



**12th
International
Corrosion
Congress**

PRECEEDINGS

AD-A273 662



7



S DTIC
ELECTE
DEC 09 1993
A

September 19-24, 1993
VOLUME 2
Houston, Texas USA

This document has been approved
for public release and sale; its
distribution is unlimited.

93-29556



**PROCESS INDUSTRIES
PLANT OPERATIONS**

NACE
International



CORROSION CONTROL FOR LOW-COST RELIABILITY



**12th
International
Corrosion
Congress**

PRECEEDINGS

VOLUME 2

**PROCESS INDUSTRIES
PLANT OPERATION**

93 12 21 00

The information is advisory only, and use of the materials and methods is solely at the risk of the user.

DTIC QUALITY INSPECTED 3

PRECEEDINGS CONTENTS

Paper #

Page #

Paper #

Page #

VOLUME 1

PLENARY LECTURES

- Corrosion: Its Effect on Society
N. Hackerman Plenary 1
- Low-Cost Corrosion Engineering and Risk Potential, Operational and Environmental Safety - nad Irreconcilable Antagonism in the Chemical Process Industry
H. Spahn Plenary 4
- Methodology of Predicting Materials Failures in Advance Nuclear Systems
T. Kondo Plenary 20
- Corrosion Control by Transferring Knowledge
R. Parkins Plenary 43

COATINGS ON STEEL

- 514 Advancements in Automotive Corrosion Resistance
M. Ostermiller, L. Lee-Piepho, and L. Singer 1
- 268 Automotive Phosphating Technology 1975 - 1995
R. Miller, M. Petschel Jr., and R. Hart 16
- 400 Hydrothermal Properties of Protective Polymer Coatings on Steel
R. Granata and K. Kovalski 24
- 293 Corrosion Behavior of Oxide Coated Cold-Rolled and Electrogalvanized Sheet Steel
W. Nowak, H. Townsend, and L. Li 42
- 039 Electrodeposition of Zn-Fe Alloy at High Current Densities
L. Yanping and W. Jixun 53A
- 569 Study of Enameling Properties on the Hot-Rolled Ti-Containing Steel Sheets
X. Xiaolian, Z. Kegang, and L. Ri 54

COATINGS

- 025 Study of Anticorrosion Properties of Metal Arc-Sprayed Coatings on a Carbon Steel for use in Petro Products
A. Groysman and V. Belashchenko 63
- 266 A Discussion on the Role of Cations in Enhancing Internally Coated Metal Container Corrosion Failure
W. Tait and K. Handrich 77
- 085 The Detrimental Effect of Water-soluble Contaminants at the Steel/Paint Interface
M. Morcillo 87

- 106 Anticorrosive Coatings Based on Phase Decomposed Polymer Blends
V. Verkholtantsev and M. Flavian 99
- 097 Application of Electrochemical Impedance Spectroscopy to Study the Efficiency of Anti-Corrosive Pigments in and Epoxy Resin
A. Amirovadin, C. Barreau, and D. Thierry 114
- 346 Determination of Protective Properties of Polymer Coatings from High-Frequency Impedance Data
F. Mansfeld and C. Tsai 128
- 156 Long-Term Electrochemical Characterizations of MIL-P-24441 Epoxy Coated Steel Using Electrochemical Impedance Spectroscopy (EIS)
J. Murray and H. Hack 151
- 073 Electrochemical Methods to Monitor Degradation of Organic and Metallic Coatings
T. Simpson 157
- 096 Determination of Coating Delamination & Underfilm Corrosion during Atmospheric Exposure by Means of Electrochemical Impedance Spectroscopy
A. Amirudin, P. Jernberg, and D. Thierry 171
- 486 Characterization of Corrosion under Marine Coating by Electrochemical Noise Methods
D. Mills, G. Bierwagen, D. Tallman, and B. Skerry 182
- 066 New Accelerated Test Simulating the Atmospheric Undercoat Corrosion
A. Martello 195
- 044 Compatability of Organic Coatings with Flame Spraying Zn, Al and Zn-Al Alloy Coatings
Z. Zhaoqing 204

METALLIC COATING AND SURFACE TREATMENTS

- 036 Surface Modification by Chemical and Electrochemical Processes
F. Mansfeld, V. Wang, S. Lin, and L. Kwiatkowski 219
- 180 Laser Melting of Plasma Sprayed Alumina Coatings
A. Escudero, V. Lopez, A. Jimenez-Morales, E. Vida, and J. Galvan 240
- 244 Corrosion and Oxidation Behavior of Ti-Al Surface Alloys Formed Using Laser Irradiation
A. Khamis, V. Desai, and G. Goswami 250
- 254 Corrosion and Heat Resistance of Alumina Coated Iron to Alkali Carbonate at 700°C
M. Okuyama, T. Noshiro, and S. Kambe 259

Paper #	Page #
319 Corrosion Resistance of Amorphous Plasma Sprayed Coatings <i>N. Bacha and C. Roy</i>	271
350 Formation of Protective Wearresistant Oxide Coatings of Aluminum Alloys by the Microplasma Methods from Aqueous Electrolyte Solutions <i>A. Timoshenko, B. Opara, and Y. Magurova</i>	280
356 Superior Corrosion Resistance by Niobium Coating <i>S. Ylassaari, M. Turkia, and O. Forsen</i>	294
394 Effects of Laser Transformation Hardening on the Corrosion Resistance of AISI ₆₁ Tool Steel <i>L. Yang, S. Jana, S. Tam, L. Lim, and M. Lau</i>	307
423 A Comparison of the Corrosion Properties of Thick Layers of Chromium and its Alloys with Nickel Deposited from Chromium (III) Electrolytes <i>M. El-Sharif, A. Watson, X. Wang, and C. Chisholm</i>	315
424 Studies of Chemical Conversion Treatments of Electrodeposited Zinc-Chromium and Zinc-Nickel-Chromium Alloys <i>M. El-Sharif, Y. Su, A. Watson, and C. Chisholm</i>	329
461 Study of Corrosion Resistance of Electroless Ni-P Platings <i>L. Yi</i>	341
472 Resistance to Aqueous Corrosion of Steels Protected by a Cr-Si Diffusion Coating <i>X. Wan, G. Wang, and R. Rapp</i>	353

NON-METALLIC COATINGS ON STEEL SUBSTRATES

150 Fluorescent Materials as Corrosion Sensors for Coatings <i>R. Johnson and V. Agarwala</i>	370
175 The Investigation of a New Autodeposition Coating System <i>Z. Pan, D. Qiu, Z. You, and Y. Zhao</i>	379
213 The Influence of Absorbed Layers of Silane Coupling Agents on Protective Properties of Polymer Coatings <i>M. Petrunin, A. Nazarov, and N. Mikhailovski</i>	386
309 Research of Weather Resistant Bridge Paint and Wear Resistant Primer and Finish for Bridge Cover Plates <i>Y. Shaoyu</i>	398
290 Determination of Water Transport Properties of Organic Coatings with EIS <i>L. Nicodemo, F. Monetta, and F. Bellucci</i>	406
324 Characterization of Organic Coatings with Impedance Spectroscopy <i>J. de Wit</i>	420
331 Substrate Effects on the Corrosion Performance of Coated Steels under Immersed Conditions <i>J. Costa, S. Faidi, and J. Scantlebury</i>	437
333 Why the Best Performance of Phosphoric Acid Pretreatments when Activated with Aluminium Hydroxide <i>E. Almeida and D. Pereira</i>	449
007 A Unique Plasma Spray Process to Create Corrosion Control Surfaces <i>G. Sweet and W. Bristowe</i>	460

Paper #	Page #
193 Evaluation of Corrosion Resistant Coating for Mild Steel <i>M. Trivedi, H. Mandalia, and C. Mital</i>	473
332 Electrocorrosion-inhibiting Behaviour of Flame Retarding PVC Pressure-sensitive Adhesive Tape <i>W. Tao, H. Ge, and Y. Qing</i>	484

VOLUME 2

ATMOSPHERIC CORROSION

335 Materials Damage Caused by Acidifying Air Pollutants - 4 Year Results from an International Exposure Program within UN ECE <i>V. Kucera, A. Coote, J. Henriksen, D. Knotkove, C. Leygraf, and B. Stockle</i>	494
145 Worldwide Data on the Atmospheric Corrosion Resistance of Weathering Steels <i>M. Komp, S. Coburn, and S. Lore</i>	509
040 The Effects of Acid Deposition on the Atmospheric Corrosion Behavior of Structural Materials in California <i>F. Mansfeld, H. Xiao, and R. Henry</i>	529
584 The Influence of Environmental Acidification on the Atmospheric Corrosion of Zinc <i>E. Johansson and M. Linder</i>	549
042 Atmospheric Corrosivity Classification Results of the International Testing Program ISOCORRAG <i>D. Knotkova</i>	561
230 Techniques Applied to the Analysis of the Atmospheric Corrosion of Low Carbon Steel, Zinc, Copper, and Aluminum <i>A. Fernandez, M. Leiro, B. Rosales, E. Ayllon, F. Varela, C. Gervasi, and J. Vilche</i>	574
530 Indoor Gaseous Sulfide and Chloride Pollutants and Their Reaction with Silver <i>L. Volpe and P. Peterson</i>	590
222 Field Exposure Studies of Corrosion Products on Metals <i>C. Leygraf, I. Odnevall, D. Persson, and J. J. Tidblad</i>	600
437B Protective Rust Layer Formed on Weathering Steel by Atmospheric Corrosion for a Quarter of a Century <i>T. Misawa, M. Yamashita, H. Miyukii, and H. Nagano</i>	612
005 Structure of Rust on Weathering Steel in Rural and Industrial Environments <i>H. Townsend, T. Simpson, and G. Johnson</i>	624
351 Effects of Seasalt on Corrosion Attacks at 8 Years Exposure of Metals in a Small Geographical Area of the Swedish West Coast <i>J. Gullman</i>	642
305 Chemical Characterization of the Corrosion Products Formed on Plain C Steel, Zinc, Copper, and Aluminum <i>S. Granese, A. Fernandez, and B. Rosales</i>	652
294 Initial Stages of SO ₂ Induced Atmospheric Corrosion of Zinc Investigated by In-Situ IR Spectroscopy and Time Resolved Trace Gas Analysis; Synergistic Effects of NO ₂ and O ₃ <i>J. Svensson and L. Johannsson</i>	662

Paper #	Page #
377 Galvanic Corrosion of Zinc/Steel Under Thin Layer Electrolytes <i>X. Zhang and E. Valeriotte</i>	676
416 Experimental Approaches to the Study of Corrosion in Thin Water Layers <i>V. Brusic, G. Frankel, T. Peterson, and S. Huang</i>	687
420 Simulation of the Degradation of Limestone and Dolomitic Sandstone under Dry Deposition Conditions <i>S. Haneef, J. Johnson, G. Thompson, and G. Wood</i>	700
308 Dissolution and Precipitation Phenomena in Atmospheric Corrosion <i>T. Graedel</i>	711
439 Atmospheric Corrosion Model for Zinc and Copper <i>S. Cramer, L. McDonald, and J. Spence</i>	722
043 Defects of Steel Structures Caused by Atmospheric Corrosion <i>D. Knotkova, J. Vlackova, and L. Rozlivka</i>	734
382 Environmental Effects in the Atmospheric Corrosion of Zinc: An Immersion - Drying Study <i>A. Valencia, R. Perez, C. Arroyave, and S. Mesa</i>	748
463 Estimate of Economic Damage of large Industrial Cities Infrastructure from Corrosion Caused by Pollutions into Environments <i>A. Lyagh</i>	761B

CHEMICAL PROCESS INDUSTRY WORKSHOP

092 The Mechanism and Control of Stress Corrosion Cracking of Zirconium in Sulfuric Acid <i>B. Fitzgerald and T. Yau</i>	762
035 What Has Happened to SA-516-70? <i>T. Phillips and D. Kloss</i>	778
028 Corrosion of Weld Zone of Stainless Steels in Industrial Urea Media <i>H. Xizhang, R. Xiaoshan, C. Xiaojun, H. Wenan, and Z. Feng</i>	784
105 The Fractality of Corroding Metallic Surfaces <i>K. Trethewey, J. Keenan, D. Sargeant, S. Haines, and P. Roberge</i>	795
379 Methods to Combat Liquid Metal Embrittlement in Cryogenic Aluminum Heat Exchangers <i>S. Wilhelm, R. Kane, and A. McArthur</i>	807
132 Prevention of Localized Corrosion Caused by Thiosulphate in Paper Mill Environments <i>V. Marichev, T. Saario, and V. Molokanov</i>	826
253 Corrosion of Stainless Steels in Kraft Process Liquors <i>A. Klarin, J. Westermarck, S. Ylasaari, J. Aromaa, and O. Forsen</i>	834
004 The Electrochemical Protection of Nickel in an NaOH + NaCl Solution <i>R. Juchniewicz, W. Sokolski, J. Walaszowski, P. Domzalcki, and B. Piorozynski</i>	849
435 Proactive Corrosion Program Improves Process Heater Reliability <i>K. Baumert, B. Heft, and S. Dean</i>	855

Paper #	Page #
102 Plant Measurement Cell for Carrying Out Electrochemical Corrosion Investigations on the Plant <i>G. Wagner and R. Munster</i>	862
061 Experience with Neutron Activation for Real-time Corrosion Monitoring in a Urea Plant <i>G. Notten, J. Thoelen, H. Verhoef, and R. Van Sluijs</i>	869
330 Corrosion Upsets are Probably More Costly Than You Know <i>A. Perkins</i>	882
378 Automated Ultrasonic Corrosion Mapping <i>C. Sinclair</i>	891
104 Autoadaptive Email Test AZ 90 for Corrosion Monitoring of Glass Lined Reactors <i>J. Hamert</i>	906

HIGH TEMPERATURE CORROSION

345 Rare Earth Element Effect on Oxidation Behavior of Chromia Forming Alloys <i>L. Ramanathan</i>	914
018 A Study of the Metal-Oxide Diffusion Barrier Coatings <i>G. Hengrong, S. Xiaofeng, and S. Biwu</i>	923
082 High-Temperature Sulfidation Properties and Demixing Process of Sulfide Scale of Fe-25Cr-9Mn Ternary Alloy <i>H. Qi, R. Zhu, and Y. He</i>	934
214 Influence of Nd on Oxidation of Ti-5621S Alloy and Adherence of Oxide Scales <i>L. Meishuan and L. Tiefan</i>	943
113 High Temperature Corrosion Behavior of Fe-Cr-Al Alloys with and without Y Addition in Pure S_{O_2} Gas Atmosphere <i>Y. Zhang</i>	951B
468 Rupture in a Steam Boiler Tube <i>B. Rezgui and M. Larbi</i>	963
069 Na_2SO_4 Deposits Induced Hot Corrosion of Iron Based Alloys at Intermediate Temperatures <i>Y. Zhang, L. Shi, and S. Shih</i>	971
391 Electrochemical Noise Measurement of Iron in Equimolar $NaNO_3$ - KNO_3 Melt at Various Temperatures <i>I. Singh, G. Venkatachari, and K. Balakrishnan</i>	979
114 Corrosion Kinetic Study at High Temperature of the In 657 Superalloy after Laser Surface Treatment in Contact with the Eutectic Melt 82% $K_2S_2O_7$ - 18% V_2O_5 <i>A. Pardo, E. Otero, F. Perez, and J. Alvarez</i>	987
316 Performance of Cr-Al Coating on Carbon Steel to Control High Temperature Corrosion due to Ash Deposit <i>G. Navas, C. Leal, E. Baron, and O. Rincon</i>	999
409 High Temperature Sulfidation of CO-CR Binary Alloys in H_2/H_2 Mixture in Co_3S_4 Stability Region <i>Z. Zurek, M. Zilik, and A. Szuryn</i>	1008

PLANT MATERIALS

- 317 Failure of Alloy 800 Steam Super Heating Coils in Refinery Hydrocracker
M. Islam and H. Shalaby 1022
- 216 The Effect of Blaze on the Mechanical and Corrosion Properties of Isfahan Refinery Distillation Unit Towers
A. Saatchi and A. Pishnamazi 1032
- 367 New Alloys for High Temperature Applications in Incineration Plants
H. Martinz and W. Kock 1039
- 260 Corrosion Evaluation of Materials in Sulfur Compound Environments
M. Teng and I. Yang 1056
- 447 Materials Selection Considerations for Vapor Collection Systems at Marine Tanker Facilities
T. Dunford, K. Lewis, and D. Rein 1064
- 169 Cracking of Weldments in Feed Water Deaerator Systems
T. Gooch, D. Noble, and R. Walker 1076
- 410 Using Fuel Oils with Different Sulphur Content and Treatment of Waste Waters Polluted with Heavy Metals in Thermoelectric Power Plants
L. Dukic 1090B
- 492 Case Study of a Service Water System Piping Corrosion Assessment
R. Tatara, K. Rhoades, and H. Olstowski 1091

VOLUME 3A

CORROSION: MATERIALS PERFORMANCE

- 210 Corrosion-Resistant Amorphous Chromium-Valve Metal Alloys
K. Hashimoto, J. Kim, E. Akiyama, H. Habazaki, A. Kawashima, and K. Asami 1102
- 089 A New Ni-Mo Alloy with Improved Thermal Stability
D. Klarstrom 1111
- 277 Corrosion Behaviour of Stainless Maraging Steel in Acidic Chloride Solutions
M. Viswanathan and K. Balakrishnan 1124
- 372 Electrochemical Characterization of Ni-Based Soft Magnetic Alloys
G. Ball and J. Payer 1132
- 413 Evaluation and Application of the EPR-double Loop Test to Assess the Degree of Sensitisation in Stainless Steels
R. Jargelius-Pettersson and P. Szakalos 1143
- 406 Corrosion Behaviour of Sintered Austenitic Stainless Steels in Sulphate and Chloride Media
E. Angelini, P. Bianco, F. Rosalbino, M. Rosso, and G. Scavino 1154
- 125 Advances in Technology Produce New Materials for Challenging Applications
N. Schmidt and T. DeBold 1170

- 512 Passive Behavior of Niobium and Niobium-Titanium Alloys in Sulfuric Acid Solutions
L. Bulhoes and D. Rehfeld 1183
- 464 The Effects of Microstructure (Cast versus Wrought) on the Wear and Corrosion Properties of a Cobalt-based Alloy
T. Meyer and P. Crook 1191
- 184 Effect of Aging Treatments on the Intergranular Corrosion of 22Cr-5Ni Duplex Stainless Steel
K. Ravindranath, S. N. Malhotra 1202
- 120 Optimized Lean-Pd Titanium Alloys for Aggressive Reducing Acid and Halide Service Environments
R. Schutz and M. Xiao 1213
- 049 Corrosion Characteristics and Applications of Newer High and Low Nickel Containing Ni-Cr-Mo Alloys
D. Agarwal, U. Heubner, and W. Herda 1226
- 178 Duplex Stainless Steels for Demanding Applications
J. Nicholls 1237

CORROSION: MODES AND BEHAVIOR

- 100 Investigation of Modified Schiff Bases for High Temperature Applications in the Area of Tribology
K. Rajan, P. Sen, A. Snelson, V. Agarwala, and A. Conte Jr. 1252
- 255 Corrosion Inhibition of Calcium Chloride Brines
K. Sotoudeh and P. Cote 1262
- 313 The Effect of Temperature and Chloride Concentration on Stainless Steels in Ammonium Chloride Solutions
O. Forsen, J. Virtanen, J. Aromaa, and M. Tavi 1278
- 109 Rest Potential Measurements for Stainless and Low-Alloy Steels in High Temperature Water
A. Charles and J. Congleton 1287
- 215 Managing Galvanic Corrosion in Waters
A. Tuthill 1300
- 119 Combination of Acoustic Emission & Electrochemical Techniques in Erosion-Corrosion Studies of Passive Stainless Steels in Acidic Media
L. Renaud, B. Chapey, and R. Oltra 1315
- 188 Accelerated Corrosion Testing of CrNi Stainless Steels in Nitric Acid by Electrochemical Methods
G. Schanz and S. Leistikow 1327
- 288 Tunneling Corrosion Mechanism of the Hot Forged Austenitic Stainless Steel in Highly Oxidizing Nitric Acid
H. Nagano and H. Kajimura 1341
- 440 Corrosion and Wear in White Cast Iron
S. Watson, S. Cramer, and B. Madsen 1353

ELECTROCHEMICAL TECHNIQUES

- 055 Scanning Microelectrochemical Methods to Study the Corrosion Behavior of Metals
T. Suter and H. Bohri 1367
- 496 PVC Film-Modified Electrodes Studied by EHD Impedance
C. Sousa da Silva, O. Barcia, O. Mattes, and C. Deslouis .. 1378
- 533 Electrochemical Noise Analysis of Iron Exposed to NaCl Solution of Different Corrositivity
F. Mansfeld and H. Xiao 1388
- 139 Characteristics of Electrochemical Noise Generation During Pitting Corrosion
S. Muralidharan, G. Venkatachari, and K. Balakrishnan 1403
- 573 Electrochemical Noise as the Basis of Corrosion Monitoring
A. Legat 1410
- 506 Electrochemical Relaxation Techniques for the Measurement of Instantaneous Corrosion Rates
V. Lakshminarayanan and S. Rajagopalan 1420
- 111 Rapid Evaluation of Corrosion Behavior by Using Random Potential Pulse Method
Y. Sugie and S. Fujii 1430
- 070 Application of Modern Electronic Technique in Corrosion
F. Qiu 1445
- 094 Improvement of Mansfelds Method for Computing Electrochemical Parameters from Polarization Data
G. Rocchini 1450
- 532 Assessment of Corrosion of Laser Surface Alloyed Aluminum & Steel by Electrochemical Technology
R. Li, M. Ferreira, A. Almeida, R. Vilar, K. Watkins, and W. Steen 1460
- 067 Marine Corrosion Resistance of Aluminum and Aluminum-Lithium Alloys
P. Roberge and D. Lenard 1466
- 209 Measuring Corrosion Resistance of Stainless Steels Using the 'Avesta Cell' - Experiences and New Applications
P. Arnvig and R. Davison 1477
- 226 Corrosion Resistance and Behavior of Construction Materials Exposed to Dilute Sulfuric Acid at Elevated Temperatures Under Static Conditions
D. Nguyen and R. Daniels 1491

ENVIRONMENTAL CRACKING

- 241 Crack Initiation and Growth of Sensitized Type 304 Stainless Steel in NaF Solution
T. Shibata, T. Oki, and T. Haruna 1509
- 211 Localized Corrosion Problems in Austenitic Stainless Steel Feed-water Heater Tubing
G. Wood 1523
- 063 Stress Corrosion Cracking of Sensitized Type 316 Austenitic Stainless Steel in Pure Sulfuric Acid Solution
R. Nishimura and A. Sulaiman 1542

- 117 The Influence of H⁺ and Cl⁻ Ions on SCC of Austenitic 304SS in Acidic Chloride Solutions at Ambient Temperature
Z. Fang, R. Zhu, and Y. Wu 1542
- 296 Differentiation Between Sulphide Stress Corrosion Cracking in 13% Cr and Duplex Stainless Steels
J. Barker, J. Yu, and R. Brook 1549
- 118 Stress Corrosion Cracking of 321 Austenitic Stainless Steel Single Crystal Under Mode II Loading
L. Qiao, D. She, W. Chu, and C. Hsiao 1560
- 010 Effect of Heat Treatment on SCC Behavior of 40 CrMnSiMo A Steel
S. Jin, S. Li, and X. Liu 1564
- 425 Corrosion Kinetics within Pits or Stress Corrosion
Y. Liu, Y. Cen, and J. Zuo 1572
- 497 Investigation of Mechanical & Environmental Effects on the Occluded Cell withing Stress Corrosion Cracks of 1Cr13 Martensitic Stainless Steel
Y. Liu, Y. Cen, and J. Zuo 1580
- 596 A Fully-Plastic Micro-Cracking Model for T-SCC in Planar-Slip Materials
W. Flanagan, M. Wang, M. Zhu, and B. Lichter 1588
- 509 Improved Stress Corrosion Performance for Alloy 718 via Melt Practice and Heat Treatment Variation
M. Miglin, J. Monter, C. Wade, J. Nelson 1600
- 485 Competition between Anodic Dissolution and Hydrogen Effects During Stress Corrosion Cracking of a 7150 Aluminum Alloy
D. Najjar, O. Moriau, R. Chieraqatti, T. Magnin, and T. Warner 1613
- 112 The Peculiarities of Electrochemical Behaviour and Stress Corrosion for Aluminium Alloys with Lithium Additives
V. Sinyavsky 1623
- 122 Cathodic Corrosion and Hydrogen Effect in TiAl & Effects of Hydrogen
W. Chu, K. Gao, J. Jin, and L. Qiao 1637
- 380 Using Real-Time Holography to Monitor Stress Corrosion Cracking Initiation
V. Desai, E. Principe, L. Quian-Falzone, and F. Moslehy ... 1649
- 564 Pre-Crack Fatigue Damage and Crack Initiation under Corrosion Fatigue Conditions
J. Seidel and D. Duquette 1658
- 327 Corrosion Fatigue of Marine Structural Steels in Saline Environments
M. Kermani and F. Abbassian 1671
- 297 Corrosion Fatigue Propagation of Higher Yield Strength Offshore Structural Steel in Artificial Seawater
J. Yu, R. Brook, I. Cole, D. Morahito, and G. Demofonti ... 1692
- 002 Corrosion Fatigue in Fossil-Fueled Boilers
G. Ogundele, E. Ho, and D. Sidey 1702
- 484 Influence of Surface Microcracks on the Corrosion Fatigue Mechanisms of Ferritic and Austenitic Stainless Steels
T. Magnin 1720

- 448 Influence of Applied Potential on Corrosion Fatigue Life and Crack Chemistry of Low Carbon Steel
H. En-Hou, H. Yuma, and K. Wei 1727

VOLUME 3B

INHIBITORS

- 020 Corrosion in Heavy Duty Diesel Engine Cooling Systems
B. Salas 1736
- 053 Synthesis and Study of Different Thioamides as Corrosion Inhibitors
K. Ahmed, S. Oun, and M. Shariff 1743
- 058 Corrosion Resistance of Copper and Copper Alloys Surface Treated with a Benzotriazole Derivative in Sodium Chloride Solutions
F. Zucchi, G. Brunoro, C. Monticelli, and G. Trabanelli 1758
- 078 Study of the Effect of Inhibitors on the Removal of Scale from Mild Steel Surface During Pickling
G. Banerjee and S. Malhotra 1766
- 088 Theoretical Calculation and Experimental Verification of Critical Passivation Concentration of Oxidizing Inhibitors in Acid Solutions
M. Zhao 1773
- 144 Chemical Composition and Structure of Surface Layer Forming in Solutions of Chromate-ions and Corrosion Behaviour of Carbon Steel
E. Enikeev, M. Panov, I. Krashennnikova, and A. Feoktistov 1784
- 149 A Quantum Chemical Study of Inhibition Effect of Isoquinoline Derivatives
L. Yao, M. Lou, P. Kong, E. Kung, and C. Yao 1794
- 200 A Spectroscopic Investigation on Inhibition Mechanism of Dibenzyl Sulfoxide for Iron Corrosion in a Hydrochloric Acid Solution
K. Aramaki, N. Ohno, and H. Nishihara 1804
- 287 The Study on Synergistic Effect of corrosion Inhibitor
E. Kalman 1814
- 411 Effect of Some Organic Inhibitors on Corrosion of Stainless Steel in Hydrochloric Acid
A. Ismail and S. Sanad 1826
- 508 Corrosion Inhibition Study of Different Azoles on Copper Using Carbon-Paste Electrodes
V. Lakshminarayanan, R. Kannan, and S. Rajagopalan 1854
- 605 Inhibition of the Corrosion of Carbon Steel in Hydrochloric Acid by Phosphonium Species
B. Barker, I. Beech, and F. Walsh 1864

LOCALIZED CORROSION/CREVICES

- 225 Prediction of Crevice Corrosion Resistance of Stainless Steels in Aqueous Environments: A Corrosion Engineering Guide
J. Oldfield, and R. Kain 1876
- 347 Seawater Testing to Assess the Crevice Corrosion Resistance of Stainless Steels and Related Alloys
R. Kain 1889
- 246 Modelling Crevice Corrosion of Fe-Cr-Ni-Mo Alloys in Chloride Solution
P. Gartland 1901
- 284 Crevice Corrosion of a Ni-Based Superalloy in Natural and Chlorinated Seawater
B. Shaw, P. Moran, and P. Gartland 1915
- 300 The IR Mechanism of Localized Corrosion
H. Pickering 1929
- 446 Corrosion Behavior of High Nitrogen Stainless Steels for Biomedical Applications
A. Cigada, G. Rondelli, B. Vicentini, and G. Dallaspezia... 1938
- 470 Nitrogen Bearing Austenitic Stainless Steels - A Promising Replacement for Currently Used 316L Stainless Steel Orthopaedic Implant Material
M. Sivakumar, U. Kamachi-Mudali, and S. Rajeswari 1942
- 471 Pit-induced Corrosion Failures in Stainless Steel Orthopaedic Implant Devices
M. Sivakumar, U. Kamachi-Mudali, and S. Rajeswari 1949
- 376 Studies on the Environmental Degradation of Metal Matrix Composite Materials
A. Rawat, V. Desai, P. Ramakrishnan, and R. Prasad 1960
- 346 Corrosion Behavior of Alumina/Al and SiC/Al Metal Matrix Composites
P. Nunes and L. Ramanathan 1974
- 252 Effect of Cold-Working on the Crevice Corrosion of Austenitic Stainless Steels
T. Handa, Y. Miyata, and H. Takazawa 1986

LOCALIZED CORROSION/PITTING

- 500 Application of In-Situ Scanning X-ray Fluorescence to Study the Concentration of Metal Ions in Simulated Pits
H. Isaacs, J. Cho, A. Davenport, M. Rivers, and S. Sutton .. 1997
- 599 Pitting Conditions Evolution of 316L Stainless Steels During Aging in Sea Water: A Statistical Approach
M. Ghiazza, D. Festy, J. Leonard, and C. Lemaître 2005
- 179 Pitting Behaviour of UNS N08904 Stainless Steel in Salt Solutions
V. Gouda and W. Abd-El Meguid 2011
- 086 Corrosion Monitoring of Aluminum Easy-Open Ends by Area Polarization Technique
O. Seri, K. Furuma, and Y. Matsumura 2022
- 565 Passivity and Passivity Breakdown in Sputtered Aluminum and Iron Alloys
Z. Szklarska-Smialowska and R. Inturi 2030

Paper #		Page #
059	Localized Corrosion Phenomena Study in 304L and 316L Stainless Steel Prepared by Power Metallurgy <i>E. Otero, A. Pardo, V. Utrilla, and E. Saenz</i>	2037
087	In-Situ Measurement of the Cl^- Concentration Distribution in Two Dimensions of Metal Surface <i>C. Lin</i>	2045

PASSIVITY AND BREAKDOWN

024	Influence of Anions on the Surface Enhanced Raman Spectre of Passive Films Formed on Iron <i>T. Devine and J. Gui</i>	2052
262	Vacancy Condensation as the Precursor to Passivity <i>D. MacDonald</i>	2065
323	Passivity of FeCr Alloys <i>J. de Wit</i>	2077
340A	Passive Oxide Films on Well-Defined Nickel Surfaces: An Examination of Film Growth on Ni(100) with Ex-Situ Scanning Tunneling Microscopy <i>C. Vitus and A. Davenport</i>	2091
371A	Passivity and Pitting Corrosion <i>M. Ives</i>	2096
398	Atomic Structure of Passive Films on Nickel <i>P. Marcus, H. Talah, and V. Maurice</i>	2105
453	The Effect of Temperature on the Passive $Ni(OH)_2$ Growth on Nickel in 1M NaOH Using Rehopping Motion Model <i>C. D'Alkain and H. Mascaro</i>	2112
071	XPS Study of Passive Films on Stainless Steels in Neutral Solutions <i>A. Rossi, and B. Elsener</i>	2120
567	Passivity of Carbon Steel in Organic Solutions <i>D. Schiffler, P. Moran, and J. Kruger</i>	2131
568	In-situ STM Characterization of Passivity and its Breakdown on Stainless Steels <i>S. Virtanen, A. Schreyer, and H. Bohni</i>	2142
015	An Investigation of the Stability of Transpassivated Film on 304 Stainless Steel <i>G. Song, C. Cao, and H. Lin</i>	2155
130	Photoelectrochemical Studies of the Passive Films on Copper and Brass <i>G. Rajagopal, S. Sathiyarayanan, and K. Balakrishnan</i> ...	2162
212	The Ion-Exchange Behaviour of the Corrodible Metal Surfaces <i>A. Nazarov and M. Petrunin</i>	2175
283	Non-Equilibrium Aluminum Alloys. Effects on Passivity in Chloride Environments <i>E. Principe</i>	2187
315	The Effect of Ion Implantation on the Passivation Behavior of Pure Copper <i>E. Wright, V. Ashworth, B. Procter, and W. Grant</i>	2207

Paper #		Page #
392	Effect of Oxygen-Containing Oxidizers on Fe, Cu, and Sn Dissolution Rates in Acidic Sulphate Electrolytes <i>N. Chebotaryova, A. Marshakov, V. Ignatenko, and Y. Mikhailovsky</i>	2223
451	Kinetic Study of the $PbSO_4$ Reduction on Lead Using Rehopping Motion Model <i>C. D'Alkain and H. Mascaro</i>	2232
452	Variation of the Dielectric Constant and Resistivity During the Anodic Growth of $Ni(OH)_2$ <i>C. D'Alkain and H. Mascaro</i>	2240
454	The Oxidation/Reduction Reaction of Zinc at the Zn/ZnO Interface <i>C. D'Alkain and H. Mascaro</i>	2248
488	Electrochemical and Corrosion Behaviour of Passive Film on Stainless Steels After Gamma-Ray Irradiation <i>G. Capobianco, A. Glisenti, T. Monetta, and F. Bellucci</i> ...	2255

VOLUME 4

CATHODIC PROTECTION

001	Stray Current Interaction in the System of Two Extensive Underground Conductors <i>W. Machczynski</i>	2268
041	An Initial Investigation of Calcareous Deposits Upon Cathodically Polarized Steel in Brazilian Deep Water <i>R. Vianna and G. Pimenta</i>	2278
161	The Isolator/Surge Protector: A Superior Alternative to Polarization Cells <i>T. Scharf</i>	2285
223	Laboratory Evaluation of the Effectiveness of Cathodic Protection in the Presence of Iron Bacteria <i>K. Okamura, Y. Koyama, F. Kajiyama, and K. Kasahara</i>	2293
580	Modification of the Corrosion Environment beneath Disbonded Coatings by Cathodic Protection <i>K. Fink and J. Payer</i>	2302
598	Pipeline Inspection and Rehabilitation - An Overview <i>G. Matocha</i>	2311
607	Prediction of Dynamic Current Density on Cathodically Protected Steel in Seawater at Different Depths <i>R. Griffin, J. Yan, R. White</i>	2324

HYDROGEN EFFECTS

524	Hydrogen Embrittlement in Steels: Mechanical Aspects <i>R. Magdowski</i>	2332
238	Hydrogen Embrittlement in Steels: Metallurgical Aspects <i>M. Speidel</i>	2339
299	Electrochemical Aspects of Hydrogen Embrittlement in Steels: (i) IPZ Model of Hydrogen Permeation (ii) IR Voltage-Induced Hydrogen Charging <i>H. Pickering</i>	2346

Paper #	Page #	Paper #	Page #
147	Predicting the Susceptibility to Hydrogen Embrittlement <i>B. Pound</i> 2356	570	Use of Composite Materials on Offshore Platforms <i>O. Sætre</i> 2529
322	Evaluation of Three Different Surface Modification Techniques for Resisting Hydrogen Embrittlement in Steel <i>S. Chan, C. Ho, and J. Lin</i> 2367	014	Corrosion Performance and Application Limits of Materials in Oil Fields <i>A. Miyasaka and H. Ogaloa</i> 2537
602	Modeling of Nonsteady State Hydrogen Permeation <i>P. Janavicius, S. Amey, J. Payer, and G. Michal</i> 2377	093	Corrosion Resistant Alloys UNS NO9925 and NO7725 for Oil Field and Other Applications <i>E. Hibner and R. Moeller</i> 2548
011	A Sensor for Measuring the Permeation Rate of Atomic Hydrogen and its Applications in HIC Inspection <i>Y. Du</i> 2383	207	Stress Corrosion Cracking Behavior of Austenitic and Duplex Stainless Steels in Simulated Sour Environments <i>K. Saarinen</i> 2566
393	The Mechanism of the Effect of Oxygen-Containing Oxidizers on the Rate of Hydrogen Cathodic Evolution and Hydrogen Permeation into Metal <i>L. Maksaeva, A. Marshakov, Y. Mikhailovsky, and V. Popova</i> 2395	427	Role of Expert Systems in Technology Transfer of Materials for Petroleum Applications <i>S. Srinivasan</i> 2574
342	On Mechanism of Hydrogen Embrittlement of Metals and Alloys <i>Y. Archakow</i> 2405	528	The Effect of Certain Compositional Aspects on the Behavior of Tank and Pipe Linings Under Laboratory and Field Conditions <i>M. Winkler</i> 2585
121	Effect of Composition on Hydrogen Induced Ductile Loss and K_{IC} in Ni-Fe FCC Alloys <i>W. Hu, Y. Wang, W. Chu, and C. Hsiao</i> 2411	549	Methods to Develop a Performance Envelope for Internal Linings in Oilfield Production Environments <i>G. Ruschau, L. Bone III, and O. Moghissi</i> 2601
OIL AND GAS PRODUCTION AND REFINING WORKSHOP		550	Polymer Coating Degradation Mechanisms Related to Hot Production <i>R. Granata, R. MacQueen, and K. Kovaleski</i> 2612
490	Corrosion Management <i>D. Williams</i> 2420	090	Oxidation of Carburised and Coked Heat-Resistant Steels <i>D. Young, D. Mitchell, and W. Kleeman</i> 2625
586	Development of Super 13Cr Stainless Steel for CO ₂ Environment Containing Small Amounts of H ₂ S <i>T. Okazawa, T. Kobayashi, and M. Veds</i> 2425	203	The Effect of Environmental Variables on Crack Propagation of Carbon Steels in Sour Media <i>M. Kermani, R. MacCuish, J. Smith, R. Case, and J. Vera</i> .. 2639
587	Corrosion Resistance of 13 and 15% Martensitic Stainless Steels in Oil and Gas Wells <i>O. Hashizume, Y. Miname, and Y. Ishizawa</i> 2439	133	Sulfide Scales for the Protection of Steels in H ₂ S-Containing Atmospheres <i>M. Schulte and M. Schutze</i> 2650
588	Development of Safe Use Limits for Martensitic and Duplex Stainless Steels <i>R. Kane and S. Srinivasan</i> 2451	194	Wall Shear Stress & Flow Accelerated Corrosion of Carbon Steel in Sweet Production <i>K. Eifird, E. Wright, J. Boros, and T. Hailey</i> 2662
585	Effect of Flow Velocity on CO ₂ Corrosion Performance of 13Cr, Super 13Cr, and A-Y Duplex Phase Stainless Steels <i>A. Ikeda, M. Ueda, J. Vera, A. Vilorio, and J. Morales</i> 2464	307	Effect of Flow Velocity on Carbon Steel CO ₂ Corrosion and Surface Films using a Dynamic Field Tester <i>J. Vera, J. Morales, A. Vilorio, A. Ikeda, and M. Ueda</i> 2695
590	The Effect of Temperature on Sulphide Stress Corrosion Cracking Resistance of Martensitic Stainless Steels used in Oil & Gas Industry <i>T. Cheldi, A. Kopliku, A. Cigada, M. Cabrini, G. Rondelli, and B. Vicentini</i> 2482	385	A Proposed Mechanism for Corrosion in Slightly Sour Oil and Gas Productions <i>S. Smith</i> 2695
278	Environment Sensitive Cracking of Titanium Alloys in Offshore Equipment <i>I. Azkarate, H. Flower, I. Aho-Mentila, and L. Lunde</i> 2492	511	Rotating Cylinder Electrode (RCE) Simulation of Flow Accelerated Corrosion in Sweet Production <i>K. Eifird, E. Wright, J. Boros, and T. Hailey</i> 2707
478	Stress Cracking & Crevice Corrosion Resistance of Pd-enhanced Ti-38644 Titanium Alloy Products in Deep Sour Gas Well Environment <i>R. Shutz, M. Xiao, and J. Skogsberg</i> 2506	606	Inhibitor Performance in Annular Mist Flow <i>H. Geretsen and A. Visser</i> 2726
099	Study of Oil Aluminium Alloy Pipes With Improved Corrosion Resistance <i>V. Kuznetsova</i> 2520	552	Evaluation of Magnetic Flux Leakage (MFL) Intelligent Pigging Results from Recurring Arctic Pipeline Inspections <i>G. Williamson</i> 2734
		325	Practical Approach to Evaluating a Corrosion and Scale Inhibitor Program in a Gathering System <i>R. Bess, D. Monical, and E. Yanto</i> 2749

Paper #	Page #	Paper #	Page #
579	The Importance of Wettability in Oil and Gas System Corrosion <i>J. Smart III</i> 2758	536	Corrosion and Behaviour of SAW Stainless Steel Filler Metals with N ₂ and Mn <i>A. Gil-Negrete</i> 2925
594	Corrosion Inhibition in Wet Gas Pipelines <i>J. Palmer, J. Dawson, K. Lawson, J. Palmer, and L. Fonczek</i> 2768	539	Beneficial Effects of Nitrogen Additions on the Micro & Structure Stability & Corrosion 52N & Super Duplex Stainless Steel <i>J. Charles</i> 2926
574	Behavior of Corrosion Resistant Alloys in Stimulation Acids, Completion Fluids, and Injected Waters <i>R. Kain</i> 2780	537	Corrosion Properties of Duplex and Super Duplex Stainless Weld Metals after Isothermal Aging <i>L. Karlsson and S. Pak</i> 2944
553	Effects of Acidizing on High Alloy Springs After H ₂ S Exposure <i>B. Bailey</i> 2795	459	Corrosion Characteristics of Plasma Weld Surfacing with the Duplex Materials, X2 CrNiMo22 53 and X2 CrNiMoN 257 4 <i>U. Draugelates, B. Bouaifi, A. Stark, I. Garz, and S. Schulze</i> 2959
038	Study of Corrosion Inhibitors in Waste Water Reuse System in the Oilfield <i>L. Zhu</i> 2803B	535	Alloy 625 Weld Overlays for Offshore and Onshore Projects <i>D. Capitanescu</i> 2973
258	The Preparation of Corrosion Inhibitor for Water Flooding in the Oil-field and Mechanism Evaluation <i>L. Zhu, H. Guangtuan, and Y. Wenjuan</i> 2804	458	Characterization of the Corrosion Behaviour of Surface Welded Protective Claddings of Nickel and Titanium Alloys <i>B. Bouaifi, U. Draugelates, H. Steinberg, J. Gollner, and A. Burkert</i> 2987
343	Low Cost Material Selection for Produced Water Tank <i>T. Havn</i> 2814	540	Some More About Electrochemical Tests to be Performed on the Field as Non-Destructive Quality Control Inspection <i>M. Verneau, F. Dupoiron, and J. Charles</i> 2996

PIPELINE CORROSION

551	Corrosion Prevention on the Iroquois Gas Transmission System by a Reliability Based Design Philosophy <i>T. Hamilton</i> 2823
566	Pitting Corrosion Behaviour of Pipeline Steel in Solutions with Coating Disbonded Area Chemistry and in Bicarbonate Solutions <i>X. Liu, X. Mao, and R. Revie</i> 2831
510	Prediction of Microstructural Effect on Corrosion of Linepipe Steels in CO ₂ - Brine Solution <i>B. Mishra, D. Olson, and M. Salama</i> 2840
250	The Effects of Latex Additions on Centrifugally Cast Concrete for Internal Pipeline Protection <i>R. Buchheit, T. Hinkelbein, P. Hlava, and D. Melton</i> 2854
256	A New Process for Internal Welding Joint Corrosion Protection of a Pipeline with Cement Liners <i>L. Fa and C. Jimin</i> 2865
563	Progress Toward a Modified B31G Criterion <i>P. Vieth and J. Kiefner</i> 2869

RELIABILITY AND CORROSION CONTROL OF WELDMENTS/CORROSION RESISTANT ALLOYS

538	Welding of UNS S32654 - Corrosion Properties and Metallurgical Aspects <i>M. Liljas and P. Stenvall</i> 2882
358	Pitting Resistance of Autogenous Welds in UNS S31254 High Alloy Austenitic Stainless Steel <i>B. Ginn and T. Gooch</i> 2895
541	Localized Corrosion of the Unmixed Zone in Nickel-Base Alloy Weldments <i>L. Flasche and H. Ahluwalia</i> 2907

VOLUME 5A

AIRCRAFT

605	The Role of Corrosion in Aging Aircraft <i>G. Koch and T. Bieri</i> 3007
151	Hidden Corrosion - Needs and Requirements <i>P. Bhagat and G. Hardy</i> 3018
196	The Corrosion Prevention & Control Program of the German Air Force for the PA200 Tornado Aircraft <i>J. Fuhr</i> 3033
403	Corrosion Control as a Necessary Treatment Following the Requirements of Aircraft and Environment Safety <i>E. Durig</i> 3043
152	A New Eddy Current Inspection System for Quantitative Corrosion Depth Measurement on AC Wing Skins <i>H. Grauvogl, F. Regler, and H. Thomas</i> 3058
608	Computer Assisted Aircraft Paint Stripping Technology <i>R. Carnes</i> 3069
185	Accelerating Factors in Galvanically Induced Polyimide Degradation <i>M. Rommel, A. Postyn, and T. Dyer</i> 3077
141	Reducing Aircraft Corrosion with Desiccant Dehumidifiers <i>D. McCarthy, D. Kosar, and S. Cameron</i> 3086
137	Corrosion Contribution to Environmental Cracking Failures of Critical Aircraft Parts <i>J. DeLuccia</i> 3099

Paper #		Page #
474	Use of VCI's (Volatile Corrosion Inhibitors) for Aircraft Protection <i>A. Eydelnant, B. Miksic, and S. Russell</i>	3109
359	Designing Metallic Surface Coatings for Improved Corrosion Resistance <i>R. Narayan</i>	3118
336	Corrosion Behavior of W Implanted Aluminum <i>J. Fernandes and M. Ferreira</i>	3130
428	Development of Chromium Based Composite Coatings for Tribological Applications <i>R. Narayan</i>	3139
168	Evaluation of Chromate Free Corrosion Inhibited Primers for Airbus Aircrafts <i>C. Matz</i>	3149
204	Development of a Non-Cyanide Cadmium Pulse Plating Process <i>J. Steppan, D. Rocca, J. Carraway, and V. Agarwala</i>	3156

AUTOMOTIVE/ACCELERATED TESTING

030	Effect of Surface Impurities on the Corrosion Behavior of Type 434 Stainless Steel <i>R. Baboian</i>	3179
153	Optimization of Corrosion and Wear Properties of Steel Component Surfaces by Controlled Gas Nitriding <i>M. Biestek, A. Czelusniak, J. Iwanow, M. Korwin, W. Liliental, and J. Tacikowski</i>	3188
581	In-Situ Analysis of Corrosion in the Crevice of Automotive Body by A.C. Impedance Measurement <i>S. Fujita and K. Matsamura</i>	3200

CORROSION IN CONCRETE

388	Designing a Reinforced Concrete Against Corrosion in Chloride Containing Environments: Choosing the Cement by Applying a Diffusion Model and Using Electrochemical Methods <i>E. Triki, L. Dhouibi-Hachani, and A. Raharinaivo</i>	3207
337	A Current-Based Criterion for Cathodic Protection of Reinforced Concrete Structures <i>J. Bennett</i>	3220
076	Carbonation of Flyash-Containing Concrete Electrochemical Studies <i>M. Montemor, A. Simoes, M. Ferreira, and M. Salta</i>	3235
301	Performance of Concrete with Microsilica in Chemical Environments <i>N. Berke, T. Durning, and M. Hicks</i>	3242
072	Inspection and Monitoring of Reinforced Concrete Structures - Electrochemical Methods to Detect Corrosion <i>B. Elsner, H. Wojtas, and H. Bohni</i>	3260
302	Evaluation of Concrete Corrosion Inhibitors <i>N. Berke, M. Hicks, and P. Tournay</i>	3271
115	Cathodic Protection of New Steel Reinforced Concrete Structure <i>A. Tvarusko</i>	3287

Paper #		Page #
507	Measurement of Corrosion Rate of Reinforcing Steel and Electrical Resistivity of Concrete using Galvanostatic Steady State Polarisation Technique <i>V. Lakshminarayanan, P. Ramesh, and S. Rajagopalan</i>	3295
057	Corrosion and Prevention of Ferrocement Roofing Slabs in Electrical Furnace Processing Workshop <i>H. Sun, M. Chou, and Y. Yong Yang</i>	3308
700	Management of Corrosion Control of Reinforced Concrete in the Channel Tunnel <i>A. Pourbaix</i>	3314

ELECTRONICS

098	Reliability and Corrosion Testing of Electronic Components and Assemblies <i>J. Sinclair, R. Frankenthal, and D. Siconolfi</i>	3332
131	In-Situ Investigation of the Initial Stages of the Electrochemical Deposition of Metals by Contact Electric Resistance Method <i>V. Marichev</i>	3344
142	Corrosion Study of Polymer-on-Metal Systems Modified by Processing Conditions <i>K. Nenov, P. Nagarkar, D. Mitton, and R. Latanision</i>	3355
157	Quantitative Corrosion Testing of EMI Materials for Aerospace Applications <i>P. Lessner</i>	3366
183	Corrosion of Electronics: Effect of Ionic Particulates <i>R. Frankenthal, R. Lobnig, D. Siconolfi, and J. Sinclair</i>	3378
234	Accelerated Gaseous Corrosion Testing <i>R. Schubert</i>	3385

EXPERT SYSTEMS

289B	How to Formulate Corrosion Knowledge for Expert Systems <i>T. Hakkarainen, and T. Hakkarainen</i>	3396
236	Transforming Computerized Information for its Integration into a Hyper Tutorial Environment <i>P. Roberge</i>	3404
206	Integrated Diagnostic System for Intelligent Processing of Field Inspection Data for Transmission Line Structures <i>P. Mayer and S. Moraes</i>	3413
123	Data Acquisition Update <i>R. Eberlein</i>	3424
048	Corrosion Prediction from Laboratory Tests Using Artificial Neural Networks <i>D. Silverman</i>	3430

LIFE PREDICTION

- 037 The Deterministic Prediction of Failure of Low Pressure Steam Turbine Disks
D. Macdonald and C. Liu 3446
- 228 Prediction of Pitting Damage Functions for Condensing Heat Exchangers
C. Liu, M. Urquidi-Macdonald, and D. Macdonald 3460
- 279 An Estimation of Maintenance Costs Related to Corrosion in Brazilian Electric Power System
A. Marinho Jr. 3477
- 312 Numeric Model for Hydrogen Embrittlement Prediction for Structures Cathodically Protected in Marine Environments
J. Regnier and D. Festy 3484
- 318 Use of Fuzzy Logic as a Decision Making Tool in the Rehabilitation of Concrete Bridge Structures
M. Islam and P. Simon 3489
- 320 The System Analysis of a National Scale Refining Equipment Corrosion Database
Y. Luo 3503
- 455 Interpretation of Electrochemical Impedance Data for Damaged Automotive Paint Films
C. Diaz, M. Urquidi-Macdonald, D. Macdonald, A. Ramamurthy, W. Van Ooij, A. Sabata, M. Strom, and G. Strom 3508
- 456 A Test of the Reliability of Mathematical Modeling of Corrosion
P. Ault Jr. and J. Meany Jr. 3519

VOLUME 5B

- 460 Degradation by Ripple-Load Effect - Impact on Life Prediction
P. Pao, R. Bayles, D. Meyn, and G. Voder 3531
- 465 Some Through-Life Risk/Reliability Considerations for Components Subject to Corrosion - A Safety Assessors View
R. Crombie 3540
- 466 Management of Corrosion in the Power Industry
H. Flitt 3551
- 469 Prediction of Corrosion Rate and Probability on Underground Pipes
Y. Katano, T. Kubo, and Y. Igawa 3561
- 477 A Dominant Flaw Probability Model for Corrosion and Corrosion Fatigue
D. Harlow and R. Wei 3573

MARINE

- 074 The Effects of Complexing Agents on the Corrosion of Copper/Nickel Alloys in Sulfide Polluted Seawater under Impingement Attack
M. Rada and J. Alhajji 3587

- 079 A Study of Flow Dependent Corrosion of Nodular Cast Iron in Arabian Gulf Seawater
A. Al-Hasham, H. Shalaby, and V. Gouda 3600
- 138 Effect of Sulfide Ions on the Corrosion Behavior of Aluminum Alloy (H2O) Synthetic Sea Water
M. Valliappan, M. Natesa, G. Venkatachari, and K. Balakrishnan 3613
- 220 Corrosion Protection of Submerged Steel Structures by the Combined Use of Protective Coatings and Impressed Current Cathodic Protection
M. Arponen 3617
- 237 On the Influence of Hydrostatic Pressure on the Corrosion Behavior of 42CD4 Steel in Natural Seawater: A Mossbauer & X-Ray Study
J. Le Breton, J. Teillet, and D. Festy 3634
- 421 Corrosion Characterization of Explosively Bonded Materials in Marine Environment
N. Lindsey 3645
- 432 Corrosion and Stress Corrosion Cracking of a Marine Steel in Artificial and Natural Sea Water
M. Golozar and A. Saatchi 3660
- 441 Environmental Degradation of Polymer Matrix Composite Exposed to Seawater
V. Stolarski, A. Letton, W. Bradley, and R. Cornwell 3671

MICROBIOLOGICALLY INDUCED CORROSION

- 136 The Impact of Alloying Elements on Microbiologically Influenced Corrosion - A Review
B. Little, P. Wagner, M. McNeil, and F. Mansfeld 3680
- 554 Early Stages of Bacterial Biofilm and Cathodic Protection Interactions in Marine Environments
H. Videla, S. Gomez de Saravia, and M. de Mele 3687
- 479 Factors Contributing to Ennoblement of Passive Metals Due to Biofilms in Seawater
P. Chandrasekaran and S. Dexter 3696
- 189 Ennoblement of Stainless Alloys by Marine Biofilms: An Alternative Mechanism
M. Eashwar, S. Maruthamuthu, S. Sathyanarayanan, and K. Balakrishnan 3708
- 249 Characterization of the Bio-Film Formed on a Steel Electrode in Seawater by Analyzing the Mass Transport of Oxygen
D. Festy, F. Mazeas, M. El-Rhazi, and B. Tribollet 3717
- 158 Microfouling Induced Corrosion of Alloys
Z. Ying and W. Qiu 3726
- 555 Microbiological Aspects of the Low Water Corrosion of Carbon Steel
I. Beech, S. Campbell, and F. Walsh 3735
- 190 Anaerobic Corrosion of Steel by Phototrophic Sulfur Bacteria
M. Eashwar, S. Maruthamuthu, S. Sebastian-Raja, and S. Venkatakrishna-Iyer 3747

Paper #	Page #	Paper #	Page #
482	Effect of Biofilms on Crevice Corrosion of Stainless Alloys in Coastal Seawater <i>H. Zhang and S. Dexter</i> 3761	401	Comparative Analysis by AES and XPS of Passive Films on Fe-25Cr-X Model Alloys Formed in Chloride and in Sulfate Solution <i>C. Hubschmid, H. Mathieu, and D. Landolt</i> 3913
304	Role of Metal Uptake by the Mycelium of the Fungus <i>Hormoconis resinae</i> in the MIC of Al Alloys <i>B. Rosales, A. Puebla, and D. Cabral</i> 3773	340B	In-Situ Studies of Passive Film Chemistry Using X-ray Absorption Spectroscopy <i>A. Davenport, J. Bardwell, H. Isaacs, and B. MacDougall</i> .. 3921
217	Electrochemical Noise Analysis as an Indicator of Microbiologically Induced Corrosion <i>A. Saatchi, T. Pyle, and A. Barton</i> 3786	027	Laser Spot Imaging of Passive Films on Stainless Steels <i>P. Schmuki and H. Bohni</i> 3929
480	Use of Nucleic Acid Probes in Assessing the Community Structure of Sulfate Reducing Bacteria in Western Canadian Oil Field Fluids <i>D. Westlake, J. Foght, P. Fedcrak, G. Voordouw, and T. Jack</i> 3794	232	Effect of Rinsing on Analytical Results for Passivity of Amorphous Iron-Chromium-Metalloid Alloys <i>K. Hashimoto, S. Kato, B. Im, E. Akiyama, H. Habakazi, A. Kawashima, and K. Asami</i> 3940
481	Control of Microbial Biofilm by Electrically-Enhanced Biocide Treatment <i>W. Costerton</i> 3803	384	Surface Analytical and Electrochemical Examination of Passive Layers on Cu/Ni Alloys <i>P. Druska and H. Strohblow</i> 3951
483	Use of a Biofilm Electrochemical Monitoring Device for an Automatic Application of Antifouling Procedures in Seawater <i>A. Mollica and G. Ventura</i> 3807	126	Laser Raman and X-Ray Scattering Studies of Corrosion Films on Metals <i>C. Melendres</i> 3973
557	Results of Electrochemical Monitoring of Microbiological Activity <i>G. Nekoksa and G. Licina</i> 3812B	544	Studies by Scanning Auger Microscopy of Electrochemical Corrosion: Serendipity and the SAM <i>J. Castle</i> 3982
271	Evaluation of Materials and Coatings for use in Wastewater Lift Stations Subjected to Biologically Induced Corrosion <i>H. Saricimen, M. Shamim, and M. Maslehuddin</i> 3813	545	Alloy Oxidation: Who is in Control as Studied by XPS <i>D. Cocke</i> 3991

SURFACE ANALYSIS TECHNIQUES

363	An ¹⁸ O/SIMS Study of Oxygen Transport in Thermal Oxide Films Formed on Silicon <i>R. Hussey, G. Sproule, D. Mitchell, and M. Graham</i> 3831
054	SNMS Studies on the Oxidation Behaviour of Titanium Aluminides <i>W. Quadackers, A. Elschner, N. Zheng, and H. Nickel</i> 3842
543	Growth Mechanism of Alumina Scales on FeCrAl Alloys <i>M. Boualam, G. Beranger, M. Lambertin, E. Sciora, R. Hussey, D. Mitchell, and M. Graham</i> 3863
548	Passive Film Studies using Neutron Reflectivity <i>L. Krebs, J. Kruger, G. Long, D. Wiesler, J. Ankner, C. Majczak, and S. Salija</i> 3863
199	Corrosion of Iron in Electrolytic Anhydrous Methanol Solutions with and without Complexing Agents <i>K. Aramaki, M. Sakakibara, and H. Nishihara</i> 3868
135	In-Situ Gravimetry of Corrosion of Iron Thin Films Combined with Surface Analytical Techniques <i>M. Seo and K. Yoshida</i> 3878
445	Passivation of High Alloyed Stainless Steel in HCl at 22°C and 65°C <i>L. Wegrelius and I. Olefjord</i> 3887
505	XPS and Electrochemical Studies of the Dissolution and Passivation of Molybdenum-implanted Austenitic Stainless Steels <i>E. De Vito</i> 3898

NUCLEAR ENERGY AND WASTE STORAGE

282	The Effect of Surface Conditions on the Localized Corrosion of a Candidate High-Level Waste Container <i>D. Dunn, N. Sridhar, and G. Cragolino</i> 4021
303	The Influence of Long-Term Low Temperature Aging on the Performance of Candidate High-Nickel Alloys for the Nuclear Waste Repository <i>F. Hodge and H. Ahluwalia</i> 4031
295	On-Line Monitoring of Corrosion in Field Pipe Gathering Systems <i>K. Lawson, A. Rothwell, L. Fronczek, C. Lange</i> 4046
518	Corrosion Potential Monitoring and Its Simulation in BWR Conditions <i>M. Sakai, N. Ohnaka, and K. Ohsumi</i> 4060

WATER

- 583 Twenty Years of Experience of Dezincification Resistant Brasses in Swedish Tap Water Systems
M. Linder 4069
- 243 Corrosion Protection due to Deaeration using a Hollow Fiber Membrane for Water Distribution Systems in Buildings
T. Fujii, Y. Ochi, Y. Ukena, and Y. Tobisaka 4080
- 609 The Impact of Environmental Consideration on Corrosion Control Economic and Technology
T. Laronge 4088

VOLUME 6**ELECTRIC POWER INDUSTRY WORKSHOP**

- 341 Cutting the Cost of Corrosion and Fouling by Real-time Performance Monitoring
P. Stokes, W. Cox, M. Winters, and P. Zuniga 4093
- 418 Service Water Electrochemical Monitoring Development at Ontario Hydro
A. Brennenstuhl 4102
- 517 Monitoring of Corrosion in a Spray Dryer Absorption FEG Plant
N. Henriksen and J. Kristgeirson 4121
- 476 On Line Monitoring of Fireside Corrosion in Power Plant
D. Farrell 4131
- 521 FSM - A New and Unique Method for Monitoring of Corrosion and Cracking Internally in Piping Systems and Vessels
R. Strommen, H. Horn, and K. Wold 4141
- 582 Experience with Neutron Activation for a Real-time Corrosion Monitoring in a Urea Plant
G. Notten, J. Thoelen, H. Verhoef, and R. van Sluijs 4154
- 311 Monitoring of Microbiological Activity in Power Plants
G. Nekoksa and G. Licina 4166
- 021 Electrochemical Monitoring of Erosion-Corrosion in Multiphase Flows
I. Ehmann, E. Heitz, K. Miers, A. Schnitzler, K. Schroeder, and X. Shimeng 4176
- 419 Monitoring and Prediction of Environmentally Assisted Crack Growth in Stainless Steel Piping
S. Ranganath, T. Diaz, F. Ford, R. Pathania, A. Pickett, S. Ranganath, G. Stevens and D. Weinstein 4185
- 429 Corrosion Monitoring Using Harmonic Impedance Spectroscopy
N. Thompson and B. Syrett 4200
- 576 Electrochemical Noise Methods as a Possible In-Situ Corrosion Sensing Technique
G. Bierwagen, D. Mills, and D. Tallman 4208
- 516 Simultaneous Rig Investigations of Electrochemical and Chemical Corrosion of Low Carbon Steel in Feedwater with Oxygen and Ammonia
A. Sirota, V. Latunin, and V. Donnikow 4219
- 251 Electrochemical Sensors for Application to Boiling Water Reactors
M. Indig 4224
- 321 Electrochemical Potential Monitoring in the Feedwater at the St. Lucie 2 PWR
W. Kassen, J. Seager, and K. Beichel 4237
- 407 On-line Chemistry Control in EDF Nuclear Power Plants
J. Doyen 4259
- 436 Potential Transients, Transmission and Electrochemical Corrosion Detection
H. Isaacs and J. Cho 4267
- 261 Development of Sensors for In-Situ Monitoring of Corrosion and Water Chemistry Parameters for the Electric Power Utility Industry
D. Macdonald, J. Pang, C. Liu, E. Medina, J. Villa, and J. Bueno 4274
- 270 An Electrochemical Sensor for Oxygen and pH in Aqueous Systems
C. Alcock, L. Wang, B. Li, and N. Bakshi 4286
- 310 On-Line Particulate Iron and Sulfur X-Ray Monitor
D. Connolly 4295
- 520 On-Line Dissolution and Analysis of Corrosion Products
M. Robles 4305
- 437A Remote Monitoring of Corrosion Chemicals via Fiber Optic Raman Spectroscopy
L. Jeffers and J. Berthold 4313
- 575 Surface Enhanced Raman Scattering as an In-Reactor Monitor of Phenomena of Interest to the Nuclear Power Industry
T. Devine 4321
- 134 A New Contact Electric Resistance Technique for In-situ Measurement of the Electric Resistance of Surface Films on Metals in Electrolytes at High Temperatures and Pressures
T. Saario and V. Marichev 4325

**Materials Damage Caused by Acidifying Air Pollutants -
4-Year Results from an International Exposure
Programme within UN ECE**

Vladimir Kucera
Swedish Corrosion Institute
Roslagsv 101, Bld 25
S-104 05 Stockholm
Sweden

Jan Henriksen
NILU
N-2001 Lillestrøm
Norway

Christofer Leygraf
Royal Inst of Technology
S-100 44 Stockholm
Sweden

A. T Coote
Building Research
Establishment
Garston, Watford
WD2 7JR, U.K.

Dagmar Knotkova
SVUOM
CS-19011 Praha 9 -
Bechovice, Czech Republic

B Stöckle
Bayerisches Landesamt
für Denkmalpflege
W-8000 München 22
Germany

Abstract

The aim of the programme which is performed as an 8-year exposure at 39 test sites in 14 countries is to quantify the effects of sulphur pollutants in combination with NO_x and rain acidity on the corrosion of selected materials from the following material groups: Structural metals, calcareous stones, paint coatings and electric contact materials. After 4-year exposure preliminary dose-response relations have been derived for some structural metals, calcareous stone materials and electric contact materials. Dry deposition of SO_2 exerts the main corrosive effect, for some materials also wet deposition is a contributing factor. The use of surface analytical techniques and chemical analyses of corrosion products can greatly enhance the understanding of the corrosion mechanisms involved.

Key terms: Atmospheric corrosion, test sites, air pollution, acidification, sulphur dioxide, nitrogen dioxide, structural metals, calcareous stones, paint coatings, electric contact materials.

I. Introduction

The increasing concern on the effects of anthropogenic acidifying air pollutants and their deposition in large areas of the northern hemisphere has resulted in adoption of the Convention on Long-range Transboundary Air Pollution within the United Nations Economic Commission for Europe in 1979. In order to obtain a scientific basis for planning effective and cost efficient emission controls the Executive Body of the Convention initiated a series of International Cooperative Programmes (ICP) for assessment of the effects of pollutants on important parts of the ecosystem. Deterioration of materials including historical buildings and monuments was considered an important effect area and consequently in 1985 an ICP on effects on materials was launched in order to fill some of the main gaps of knowledge.

Among the questions which are of relevance in this respect is the effect of dry and wet deposition as both may cause corrosion damage. Among the dry deposited pollutants SO_2 has been known for a long time as a powerful corrosion accelerating agent for several materials. The increasing levels of NO_2 rise however the question of its corrosive action. A synergistic corrosive effect of SO_2 and NO_2 has been shown by laboratory studies for some materials, the effect under outdoor conditions has so far not been clarified.

The ICP is expected to give quantitative data on the effects of acidifying air pollutants on degradation of materials. For development and implementation of control strategies for transboundary air pollutants, the recently developed critical load concept has been found valuable. The critical load is defined as a quantitative estimate of the loading of one or more pollutants below which significant harmful effects on specified sensitive elements of the environment are not likely to occur. For materials it seems more appropriate to define critical levels of pollutants as it has been shown that corrosion of materials is often closely linked to concentrations of pollutants. However, there is today for the most materials no evidence that there is any critical threshold pollutant concentration above which the mechanism of corrosion should drastically increase. It seems thus more appropriate to discuss accepted or target levels. The long-term steady state corrosion data which will be obtained in this ICP are expected to give dose-response relations which will be important for policy decisions on future emissions connected to defined target levels, for mapping of corrosivity and for calculation of economic damage.

The present paper will give a brief survey of the organization and scope of the programme and a choice of results obtained after 4 years of exposure. A more detailed description of the programme and results obtained may be found elsewhere^{1,10}.

II. Aim

The aim of the programme is to perform a quantitative evaluation of the effect of sulphur pollutants in combination with NO_x and other pollutants as well as climatic parameters on the atmospheric corrosion of important materials in a wide geographical zone of Europe and North America.

III. Organization of the Programme

A Task Force has been appointed for organizing the programme with Sweden as lead country and the Swedish Corrosion Institute serving as the Main Research Centre. Research subcentres in the Czech Republic, Germany, Great Britain and Norway are together with Sweden responsible for the choice of materials and methods of evaluation, for preparation and distribution of specimens to the participating countries and for evaluation of the corrosion attack after exposure. The Norwegian subcentre is moreover responsible for a data bank containing all environmental parameters measured at the test sites. In all participating countries a national contact person has been appointed who is responsible for the exposure and withdrawal of specimens, and reporting of environmental parameters. A list of the responsible organizations and present national contact persons are given in the acknowledgement.

IV. Experimental

A technical manual describing in detail the exposure programme and a report with a characterization of the test sites have been published within the ICP^{1,2}. Here only a short presentation will be given.

A. Test Sites and their Characterization

The network consists of 39 sites in 14 ECE countries including three sites in Northern America. The location of the sites which covers a broad geographical zone in Europe is given in FIG 1. A list of the test sites and of the parameters used for characterization of the corrosion environment are listed in TAB 1. The pollution of the atmosphere is characterized by measurement of SO₂ and NO₂ and optionally also by determination of O₃. Collection and analyses of precipitation are used for characterization of the wet deposition of pollutants.

B. Materials and Exposure Conditions

The investigated materials can be subdivided into the following four groups, with research subcentres responsible for preparation and evaluation of specimens given in the parenthesis:

Structural metals: Steel, weathering steel, zinc and aluminium (National Research Institute for Protection of Materials - SVUOM, Prague, the Czech Republic).

Copper and cast bronze (Bavarian State Conservation Office, Munich, Germany).

Stone materials: Portland limestone, White Mansfield dolomitic sandstone (Building Research Establishment, Watford, U.K.)

Paint coatings: Coil coated steel with alkyd melamine, steel with silicon alkyd paint, wood with alkyd paint system and wood with primer and acrylate (Norwegian Institute for Air Research - NILU, Lillestrøm, Norway).

Electric contact materials: Nickel, copper, silver and tin as metallic strips; Eurocard connectors of different performance classes (Swedish Corrosion Institute/Royal Institute of Technology, Stockholm, Sweden).

The specimens are mounted on identical racks permitting both free and rainsheltered exposure. All materials except electric contact materials are exposed freely in unsheltered conditions. In addition all materials except paint coatings are exposed in sheltered conditions. The electric contact materials are placed in an aluminium box with two ventilation holes and this box is placed within the shelter. This should simulate the environment for electronic devices in unheated storage. The exposure programme started at all test sites in September 1987. The withdrawal of specimens has so far been performed after 1, 2 and 4 years exposure. The last set of specimens is planned to be evaluated after 8 years. At the end of each exposure period three parallel specimens are withdrawn.

C. Evaluation Methods

The main aim of the programme is to establish quantitative effects of air pollutants on the corrosion rate. Consequently the evaluation has followed international standards or well established methods. The experimental material permits however also i.a. to study the composition of corrosion products and distribution of pollutants in porous materials, which may contribute to a better understanding of the mechanisms of their action in the corrosion process. The evaluation methods differ with material group investigated and include: visual examination, optical microscopy, SEM, X-ray diffraction, XPS, FTIR, Laser Ablation Microprobe Mass Spectroscopy (LAMMS), chemical analysis, determination of soluble salt distribution in stone specimens, gravimetric and microgravimetric methods for assessment of mass loss or mass gain, determination of electric contact resistance and of colour changes.

V. Results and Discussion

The results from the first two years of exposure have been published in separate reports for the individual material groups⁴⁻⁸. Also the environmental data for the first four years of exposure have been compiled in special reports^{3,9,10}. The evaluation of corrosion

attack after 4 years of exposure has been performed. The statistical analysis of the effects of environmental parameters on the corrosion rate has not yet been completely finished. For this reason and for reason of space here only some selected results will be given.

A. Environmental Data

The weakest point of most corrosion exposure programmes performed in the past is the inferior quality of the environmental data from the test sites. The present ICP constitutes an essential progress in this respect as not only SO_2 -, but also NO_2 - and on the majority of sites even O_3 -concentrations are measured. The data bank created at the Norwegian subcentre is based on data reported on daily, weekly or monthly basis. The quality assurance programme adopted within the ICP ensures that the obtained data will be of good quality especially for the sites reporting on daily basis.

1. Pollution Parameters. The ambition when selecting test sites for the ICP has been to obtain sites with SO_2 , NO_2 and pH normally distributed in a broad concentration range covering both clean, moderately and heavily polluted sites. The annual mean values for the 4-year exposure period show that the solution has been reasonably successful, see FIG 2. The yearly mean concentrations for SO_2 varies between 1 and 80 $\mu\text{g}/\text{m}^3$. The cumulative distribution function shows, however, that the distribution is not normal as the majority of sites has values below 30 $\mu\text{g}/\text{m}^3$. For NO_2 the distribution is better with yearly mean concentrations ranging from 4 to 80 μm with one site (Milan) showing 110 $\mu\text{g}/\text{m}^3$. The pH values varies between 3.9 and 6.2 with a normal distribution.

A problem which arises at evaluation of the effects of the pollution parameters is the intercorrelation between some of the parameters. The intercorrelation of SO_2 and NO_2 concentrations ($R=0.6$) and of O_3 concentration with NO_2 resp. SO_2 -concentrations ($R=-0.6$ resp $R=-0.8$) has to be taken into account when trying to separate the corrosive effect of these pollutants.

It should also be noticed that even if marine locations were avoided there are several sites closer to the Atlantic Ocean which are affected by marine aerosols. This is particularly the case for the sites in the United Kingdom, in Portugal and for two of the Norwegian sites. In addition high chloride values also occur at the Italian sites and in Bilbao. This will be taken into account in the regression analysis where for chloride sensitive materials separate evaluation can be done for the group of sites with low chloride levels. In this connection also the special pollution conditions on the Norwegian site Borregaard (22) should be mentioned. The site has a high concentration of chlorine from a nearly pulp factory which increases the corrosivity against certain materials and appears often as an outlier when plotting the corrosion rate against the SO_2 concentration.

The concentration resp. deposition rates of SO_2 at free exposure, under the shelter and in the electronic box has been subject to a separate study at four Scandinavian sites and a limited study at three Czech sites. The study showed that the SO_2 deposition rate inside the box is approximately 10 times lower than under the shelter. This difference could be separated into different air flow conditions (a factor of 2) and different concentrations (a factor of 5). The SO_2 concentrations under the shelter have been calculated from deposition measurements and found to be in good agreement with concentrations measured at free exposure outside the shelter. The SO_2 deposition rate inside the shelter was, however, about a factor 2 lower than at free exposure.

2. Climatic parameters. The 39 test sites cover a broad geographical region. Even if all sites are situated in the temperate climatic zone there are substantial differences in climate parameters. It could be mentioned that the time of wetness (defined as the time with $RH > 80^\circ$ and $T > 0^\circ C$) varies between round 1000 hrs/year for some years in Rome or Madrid to round 6000 hrs/year at some U.K. sites. Both the time of wetness and the temperature and relative humidity are normally distributed which is beneficial for the statistical treatment.

B. Corrosion Effects on Different Materials

In general great differences have been found in corrosion attack at different sites in the network. In most cases the corrosion attack is considerably more severe at polluted sites than at rural sites with background pollution. For some materials like nickel or carbon steel the correlation of the corrosion rate and the pollution parameters was obvious already after one year of exposure. For other materials like copper or painted surfaces the significance of the investigated parameters starts to show first after 4 years of exposure. The reason being that for several of the materials within a 2-year period the corrosion attack is still in an initiation period. During this period the corrosion mechanism and thus also the affecting factors could be different compared to prolonged exposure when the corrosion rate has reached the steady state.

C. Statistical Evaluation

The statistical evaluation including correlation analysis and single and multiple regression analysis for the 1 and 2 years' exposure has been performed and published by the individual research subcenters⁴⁻⁸. Also most of the 4-year data have been analyzed by the subcentres. A part of the analyses, however, still remains to be done as well as a central treatment of the whole material. In the following a choice of results for the individual material groups will be presented.

1. Structural metals. For steel, weathering steel and zinc a regression analysis has been performed using SO_2 , NO_2 and time of wetness as significant independent variables. For unsheltered exposure the following dose-response relations have been obtained if all test sites are included:

$$WL_{1\text{-steel}} = 59.3 + 3.8 SO_2 + 0.029 TOW \quad R^2 = 0.71 \quad (1)$$

$$WL_{4\text{-weat steel}} = 46.4 + 2.9 SO_2 + 0.06 TOW \quad R^2 = 0.37 \quad (2)$$

$$WL_{4\text{-zinc}} = 7.4 + 0.50 SO_2 + 0.003 TOW \quad R^2 = 0.31 \quad (3)$$

The correlation improves if sites with high chloride deposition are excluded:

$$WL_{4\text{-weat steel}} = 43.8 + 3.15 SO_2 + 0.06 TOW \quad R^2 = 0.46 \quad (4)$$

$$WL_{4\text{-zinc}} = 5.9 + 0.46 SO_2 + 0.004 TOW \quad R^2 = 0.62 \quad (5)$$

where WL = weight loss (1 resp. 4 yrs expos.) in g/m^2
 SO_2 = concentration in $\mu g/m^3$
 TOW = time of wetness in hrs/year

The analysis of the contribution of the individual environmental factors included shows the decisive influence of SO_2 pollution, see FIG 4. The most important of the other factors seems to be time of wetness which is demonstrated by low corrosion rates at the south European sites.

For aluminium which shows an increasing corrosion rate with time of exposures so far no dose-response relation have been obtained. Even if the mass loss does not always give the best characteristics of the corrosion attack on aluminium the effect of elevated pollution especially by chlorides is evident especially in sheltered position, see FIG . For copper and bronze samples after 1 and 2-year exposure no dose-response relations were obtained. After 4-year exposure the effect of especially the SO₂ level and the conductivity of precipitation is stronger but the regression analysis is not yet completed. Another possibility of evaluation of the effects of air pollutants constitutes of grouping of the sites into pollution classes, see FIG 8. This concept may be useful for evaluation of the so called target levels.

2. Calcareous Stone Materials. The regression analysis performed so far has shown that SO₂ significantly contributes to the degradation of unsheltered stones, see FIG 5. Beyond the dry deposition of SO₂ it has also been shown that rain acidity and natural dissolution by rain are important factors especially in areas with low SO₂ levels. The following dose-response relations have been found for the weight loss of unsheltered sandstone and limestone:

$$WL_{\text{sandstone}} = 0.293 + 0.027 \text{ SO}_2 + 0.000034 \text{ rain} + 0.0080 \text{ H}^+ \quad R^2 = 0.71 \quad (6)$$

$$WL_{\text{limestone}} = 0.051 + 0.026 \text{ SO}_2 + 0.00018 \text{ rain} + 0.00396 \text{ H}^+ \quad R^2 = 0.69 \quad (7)$$

where WL = weight loss (4 yrs exposure) in %
 SO₂ = concentration in µg/m³
 rain = total amount for 4 years in mm
 H⁺ = H⁺-concentration in µeq/l

compared to the relations obtained after 2-year exposure the present equations show considerably higher correlation coefficients.

3. Paint Coatings. Since deterioration of paint coatings is a comparatively slow process it was not possible to find any quantitative effects of the environmental parameters after one and two years exposure. After 4-year exposure the main changes have been observed in damage from cut, chalking, dirt and fungi. A correlation analysis, see TAB 2, has shown that for damage from cut on steel panels the SO₂ concentration was the most significant parameter. For damage from cut on galvanized steel panels the pH in precipitation shows a significant effect. For occurrence of fungi high precipitation and time of wetness are important parameters whereas high SO₂ levels may prevent the growth of fungi. For chalking the correlation has shown that the degradation cannot be explained by a single environmental parameter. The statistical treatment has, however, not yet been finished.

4. Electric Contact Materials. The evaluation of silver and nickel has resulted in the following equations:

$$WI_{\text{nickel}} = 5.5 + 15.8 \text{ SO}_2 \quad R^2 = 0.78 \quad (8)$$

$$WI_{\text{silver}} = 22.6 [\text{SO}_2]^{0.21} [\text{NH}_4]^{0.36} \quad R^2 = 0.60 \quad (9)$$

where WI = weight increase (4 yrs exposure) in µg/cm²
 SO₂ = concentration in µg/m³

NH_4 = concentration in precipitation in mg/l

For nickel a very strong linear effect of the SO_2 concentration is observed, FIG 6. The weight increase also slightly depends on chloride in precipitation which indicates the presence of chloride containing gases or particulates. The analyses of corrosion products by XPS, DRIFT and XRD show the presence of crystalline basic nickel sulphate but also carbonate, nitrate and chloride to lesser extent.

The equation for silver contains SO_2 and NH_4^+ in precipitation as explanatory variables. This is due to the formation of a layer of Ag_2S and also due to formation or deposition of chemical species, possibly NH_4Cl and/or $(\text{NH}_4)_2\text{SO}_4$. Since H_2S is not measured within the programme, it has not been possible to estimate its contribution to the total Ag_2S formation as compared to the contribution from SO_2 . An extension of the programme with measurements of H_2S on selected sites would provide valuable information.

The evaluation of tin is not yet completed. It is obvious that the SO_2 concentration does not have the same strong corrosive effect as for many of the other materials, see FIG 7. There are indications that the most important parameters responsible for the weight increase are not measured within the exposure programme. Also the evaluation of copper is not yet completed but seems to be more promising than the 1 and 2-year evaluations. A correlation between weight increase and conductivity in precipitation is observed and the relative behaviour of the corrosion attack inside the aluminium box approaches that of the sheltered copper samples outside the box as the exposure time increases.

VI. Conclusions

- The ICP which comprises exposure of different material groups will create a unique data bank for quantification of the effects of acidifying air pollutants on corrosion of materials.
- After 4 years of exposure preliminary dose-response relations have so far been obtained for calcareous stone materials, zinc, steel, nickel and silver.
- For most materials dry deposition of SO_2 exerts the strongest corrosive effect. The role of NO_2 has not yet been clarified, the strong synergistic effect with SO_2 observed in laboratory studies has not been observed in field studies.
- Wet deposition of pollutants expressed as rain acidity or conductivity has a corrosive effect on certain materials, which in general is weaker than the effect of dry deposition.
- The use of surface analytical techniques and chemical analyses of corrosion products can greatly enhance the understanding of the corrosion mechanisms involved.

Acknowledgement

The UN ECE exposure programme is a result of co-operation between the organizations listed below with the names of the national contact persons given in brackets. Each of the organizations has been responsible for gathering meteorological and pollution data, and for providing sites for the exposure of materials:

National Res. Inst. for Protection of Materials, Czech Republic (D.Knotkova); Technical Research Centre of Finland-VTT (T.Hakkarainen); Bayerisches Landesamt für Denkmalpflege, Germany (A.Reisener); Agency for Energy Sources (ENEA), Italy (G.Guidotti); TNO Division of Technology for Society, Dept. of Environmental Chemistry, the Netherlands (K.Hollander); Norwegian Institute for Air Research, Norway (J.Henriksen); Swedish Corrosion Institute, Sweden (C.Leygraf); Building

Research Establishment, Dept. of Environment, United Kingdom (A.T.Coote); Ministerio de Obras Publicas y Urbanismo (MOPU), Spain (J.Salazar-Mitchell); Institute of Physical Chemistry, Russian Academy of Sciences, Russian Federation (Yu.A.Michailovski); Ministry of the Environment, Estonia (J.Saar); Institute of Technology, Laboratory of Mineralogy and Petrology, Portugal (L.Aires-Barros); National Research Council of Canada and the Ministries of the Environment of Canada and of Ontario, Canada (J.J.Hechler); United States Environmental Protection Agency, USA (J.Spence).

VII. References

- 1 ICP on effects on materials including historic and cultural monuments. Report No. 1: Technical manual. Swedish Corrosion Institute, Stockholm, Sweden, 1988.
- 2 ICP on effects on materials. Report No. 2: Description of test sites. Swedish Corrosion Institute, Stockholm, Sweden, 1989.
- 3 Henriksen, J.F. & Arnesen, K. & Rode, A.: Environmental data report September 1987 to August 1989. Norwegian Inst. for Air Research, Lillestrøm, Norway.
- 4 Coote, A.T. & Yates, T.J. & Chakrabarti, S. & Bigland, D.L. & Ridal, J.P. & Butlin, R.N.: ICP on effects on materials. Report No. 4: Evaluation of decay to stone tablets: Part 1 After exposure for 1 year and 2 years. Building Research Establishment, Watford, U.K., 1991.
- 5 Stöckle, B. & Pöhlman, G. & Mach, M. & Snetlage, R.: ICP on effects on materials. Report No. 5: Corrosion attack on copper and cast bronze. Evaluation after 1 and 2 years of exposure. Bavarian State Conservation Office, Munich, Germany, 1991.
- 6 Holler, P & Knotkova, D & Bouskova, A.: ICP on effects on materials. Report No. 6: Corrosion attack on steel, zinc and aluminium. Evaluation after 1 and 2 years of exposure. Nat. Res.Inst. for Protection of Materials, Prague, Czech Republic, 1991.
- 7 Henriksen, J.F. & Anda, O. & Rode, A.: ICP on effects on materials. Report No. 7: Evaluation of the painted systems after two years of exposure. Norwegian Institute for Air Research, Lillestrøm, Norway, 1992.
- 8 Tidblad, J. & Leygraf, C & Kucera, V.: ICP on effects on materials. Report No. 8: Corrosion attack on electric contact materials. Evaluation after 1 and 2 years of exposure. Swedish Corrosion Institute, Stockholm, Sweden, 1991.
- 9 Henriksen J.F. & Bartonova, A. & Arnesen, K. & Rode, A.: ICP on effects on materials. Report No. 9: Environmental data report September 1989 to August 1990. Norwegian Institute for Air Research, Lillestrøm, Norway, 1992.
- 10 Henriksen, J.F. & Bartonova, A. & Arnesen, K. & Rode, A.: ICP on effects on materials. Report No. 10: Environmental data report September 1990 to August 1991. Norwegian Institute for Air Research, Lillestrøm, Norway, 1992.

Table 1. List of test sites and mean values of environmental parameters during the four year exposure period, September 1987 – August 1991

	Country	No Site	Climatic parameters				Gases			Precipitation					Precipitation (optional)					
			Temp °C	Rh %	Tow h/yr	Sun h/yr	SO2 µg/m3	NO2 µg/m3	O3 µg/m3	mm/yr	pH	SO4 mg/l	NO3 mg/l	Cl mg/l	Cond µS/cm	NH4 mg/l	Na mg/l	Ca mg/l	Mg mg/l	K mg/l
Czech Republic	1	Prague-Leitany	9.5	76	2877	1718	67.8	36.0		469	4.26	5.27	1.41	2.47	70.9	0.89			0.79	
	2	Kasperske Hory	6.8	77	3261		19.6	12.6		784	4.13	2.81	1.45	1.00	31.2	0.97			1.31	
	3	Kopisty	9.5	73	2265	1552	83.2	38.2		427	4.53	10.51	1.06	1.96	86.4	1.97			1.50	
	4	Esposo	5.9	79	3750	1770	14.8	20.4		675	4.35	2.11	0.84	1.39	35.3					
Finland	5	Ahtari	3.5	79	3081	1623	3.8	4.9	52	670	4.54	0.60	0.29	0.26	18.1	0.31	0.12	0.11	0.03	0.07
	6	Helsinki-Vallila	6.4	79	3776	1773	18.0	33.8		667	4.32	2.33	0.92	2.03	41.3					
Germany	7	Waldhof-Langenbrügge	9.6	81	4573		12.2	12.0	59	527	4.36	1.36	0.85	1.25	37.0	0.87	0.58	0.60	0.14	0.17
	8	Aschaffenburg	11.8	70	3508		17.5	39.2	28	652	4.71	2.31	1.04	2.13	51.7	1.75	1.82	2.01		
	9	Langenfeld-Reusrath	10.5	79	4570	1471	23.7	45.7		707	4.42	1.81	0.76	1.58	38.6	1.46	1.16	1.04	0.18	0.32
	10	Bottrop	10.9	76	4195	1645	50.1	47.7	27	731	4.44	2.55	0.77	3.76	49.9	1.35	1.78	1.55	0.34	0.87
	11	Essen-Leithe	10.3	78	4376	1645	27.2	43.8		650	4.40	1.85	0.80	1.81	37.9	1.23	1.41	1.10	0.19	0.34
	12	Garmisch-Partenkirchen	7.6	83		1722	8.9	13.3	53	1245	4.79	0.80	0.51	0.24	18.7	0.57	0.18	0.42		0.05
Italy	13	Rome	16.3	65			34.0	68.7	24	511	4.69				34.1					
	14	Casaccia	14.4	71	3460		6.9	14.1	51	668	5.00	0.92	0.11	4.02	33.9	2.18	2.00	0.81	0.26	
	15	Milan	15.0	73	3246		67.4	109.4	19	862	4.34	8.56	3.88	3.47	60.1	1.64	1.27	3.97	0.60	0.71
	16	Venice	13.8	79	4200		21.1	44.9	25	637	5.18	3.37	0.94	3.64	57.1					
Netherlands	17	Vlaardingen	10.6	83	5438	1565	32.5	55.0	30	770	4.44	1.66	0.57	5.33	51.6	1.01	2.85	0.46	0.36	0.20
	18	Eibergen	10.0	81	4911	1448	9.0	25.3	43	756	5.44	1.45	0.54	2.32	30.8	1.70	1.57	0.21	0.14	0.16
	19	Vredepeel	10.4	81	5002	1518	10.8	32.2	39	663	5.38	1.77	0.60	2.14	33.5	1.88	1.25	0.31	0.16	0.16
	20	Wijnandsrade	10.4	80	4895	1494	12.0	29.8	41	675	4.80	1.60	0.61	1.79	33.7	1.35	1.02	0.54	0.14	0.15
Norway	21	Oslo	7.8	71	2783	1710	10.9	50.6	19	640	4.55	1.61	0.65	1.63	32.7	0.47	0.75	1.86	0.18	0.16
	22	Borregard	6.6	76	3449		40.5	17.7		614	3.97	2.87	0.78	3.31	67.6	1.32	1.64	0.60	0.23	0.33
	23	Birkenes	6.9	78	4296	1860	1.1	3.5	56	1589	4.30	0.94	0.58	2.62	35.3	0.56	1.47	0.26	0.18	0.17
	24	Stockholm South	8.0	72	3272	1740	11.0	29.3	45	515	4.41	0.94	0.42	0.42	25.9	0.38	0.22	0.41	0.04	0.05
Sweden	25	Stockholm Centre	8.2	72	3272	1740	16.0	42.5		515	4.41	0.94	0.42	0.42	25.9	0.38	0.22	0.41	0.04	0.05
	26	Aspvreten	6.7	79	3681	1737	2.4	4.6	57	445	4.34	1.12	0.56	0.63	32.0	0.62	0.45	0.22	0.07	0.11
United Kingdom	27	Lincoln Cathedral	10.3	84	5908		18.2	46		292	4.24	1.94	0.67	3.98	55.2	0.82	1.68	1.80	0.27	0.25
	28	Wells Cathedral	12.0	83	5991		6.5	23.3		464	5.44	1.83	0.50	5.80	64.4	2.93	4.40	1.16	0.39	2.30
	29	Clatteringshaws Loch	9.9	96			3.9	3.8	55		4.73	0.89	0.16	6.41		0.29	3.59	0.45	0.41	0.24
	30	Stoke Orchard	9.7	77	5188		16.1	41.8	89	596	3.66	1.92	0.39	4.49		1.03	1.90	1.29	0.30	0.35
Spain	31	Madrid	14.8	58	1620	2749	15.5	24.7	26	340	5.44	1.59	0.40	0.66	27.5	0.68	0.73	2.04	0.20	0.14
	32	Bilbao	15.1	73	4193	1668	37.3	37.8		1018	4.86	10.77	3.04	7.73	65.1	2.25	2.94	5.16	0.00	0.00
	33	Toledo	14.6	60	1813	2571	8.0	14.2		575	5.46	0.51	0.15	0.56	12.1	0.18	0.60	0.72	0.10	0.13
CIS	34	Moscow	6.1	75	2562	1566	25.8	61.2		713	5.47	2.40	0.13	0.58	35.4	0.64				
Estonia	35	Lahemaa	6.1	82	4076	1732	0.6	3.8		533	4.63	0.87	0.29	0.61	17.1	0.20	0.45	0.67	0.06	0.34
Portugal	36	Lisbon	16.9	62			9.1	30.3	34	914	5.56	8.04	1.53	3.64	56.8	0.56	3.02	2.47	0.45	0.49
Canada	37	Dorset	5.3	76	3231	2041	3.3	1.7	59	1019	4.33	0.80	0.53	0.11	25.3	0.36	0.05	0.20		
USA	38	Research Triangle Park	15.3	59	2375		9.2	25.7	53	1115	4.36	0.67	0.27	0.35	22.1	0.20	0.16	0.06	0.02	0.04
	39	Steubenville	12.0	63	1737	1803	59.3	44.5	39	893	3.96	1.84	0.49	0.54	49.6	0.38	0.13	0.56	0.12	0.09

Table 2. Correlation of deterioration of paint coatings with environmental parameters after 4 year exposure

Damage	Paint system	No. of observations	Environmental factors	Correlation for 4 year's results
		4 years		
C U T	Silicon alkyd on steel (H)	37	SO ₂ mean	R = -0.64 **
		32	TOW (mean) x SO ₂	R = -0.57 **
		37	pH mean	R = +0.24
	Alkyd melamine on galv. steel (G)	37	SO ₂ mean	R = -0.30 *
		36	mm mean	R = -0.35 **
		37	pH mean	R = +0.55 **
F U N G U S	Silicon alkyd on steel (H)	32	% TOW	R = -0.27
		36	mm (mean)	R = -0.32 *
		39	SO ₂ (mean)	R = +0.21
	Alkyd melamine on galv. steel (G)	32	% TOW	R = -0.29 (*)
		36	mm (mean)	R = -0.43 **
		39	SO ₂ (mean)	R = +0.41 **
	Alkyd on wood (I)	32	% TOW	R = -0.40 **
		36	mm (mean)	R = -0.36 **
		39	SO ₂ (mean)	R = +0.37 **
	Acrylate on wood (K)	32	% TOW	R = -0.15
		36	mm (mean)	R = -0.34 (*)
		39	SO ₂ (mean)	R = +0.21
C H A L K I N G	Silicon alkyd on steel (H)	24	% sun hours	R = -0.21
		37	SO ₂ (mean)	R = +0.45 **
	Alkyd melamine on galv. steel (G)	24	% sun hours	R = -0.23
		37	SO ₂ (mean)	R = +0.47 **
	Alkyd on wood (I)	24	% sun hours	R = -0.16
		37	SO ₂ (mean)	R = -0.20
	Acrylate on wood (K)	24	% sun hours	R = -0.12
		37	SO ₂ (mean)	R = -0.26
D I R T	Silicon alkyd on steel (H)	37	SO ₂ (mean)	R = -0.35 **
		37	NO ₂ (mean)	R = -0.38 **
	Alkyd melamine on galv. steel (G)	37	SO ₂ (mean)	R = -0.65 **
		37	NO ₂ (mean)	R = -0.51 **
	Alkyd on wood (I)	37	SO ₂ (mean)	R = -0.23
		37	NO ₂ (mean)	R = -0.03
	Acrylate on wood (K)	37	SO ₂ (mean)	R = -0.31 *
		37	NO ₂ (mean)	R = -0.27 *

- ** 95% level of significance, 25 observations R > 0.40, 30 observations R > 0.36, 40 observations R > 0.31
 * 90% level of significance, 25 observations R > 0.34, 30 observations R > 0.31, 40 observations R > 0.26

Note: Since the deterioration increases with decreasing rating number, "minus" before the correlation means increasing deterioration with increasing concentration of pollutants.
 For pH "plus" before the correlation, means decreasing pH (higher acidity) gives increased deterioration.

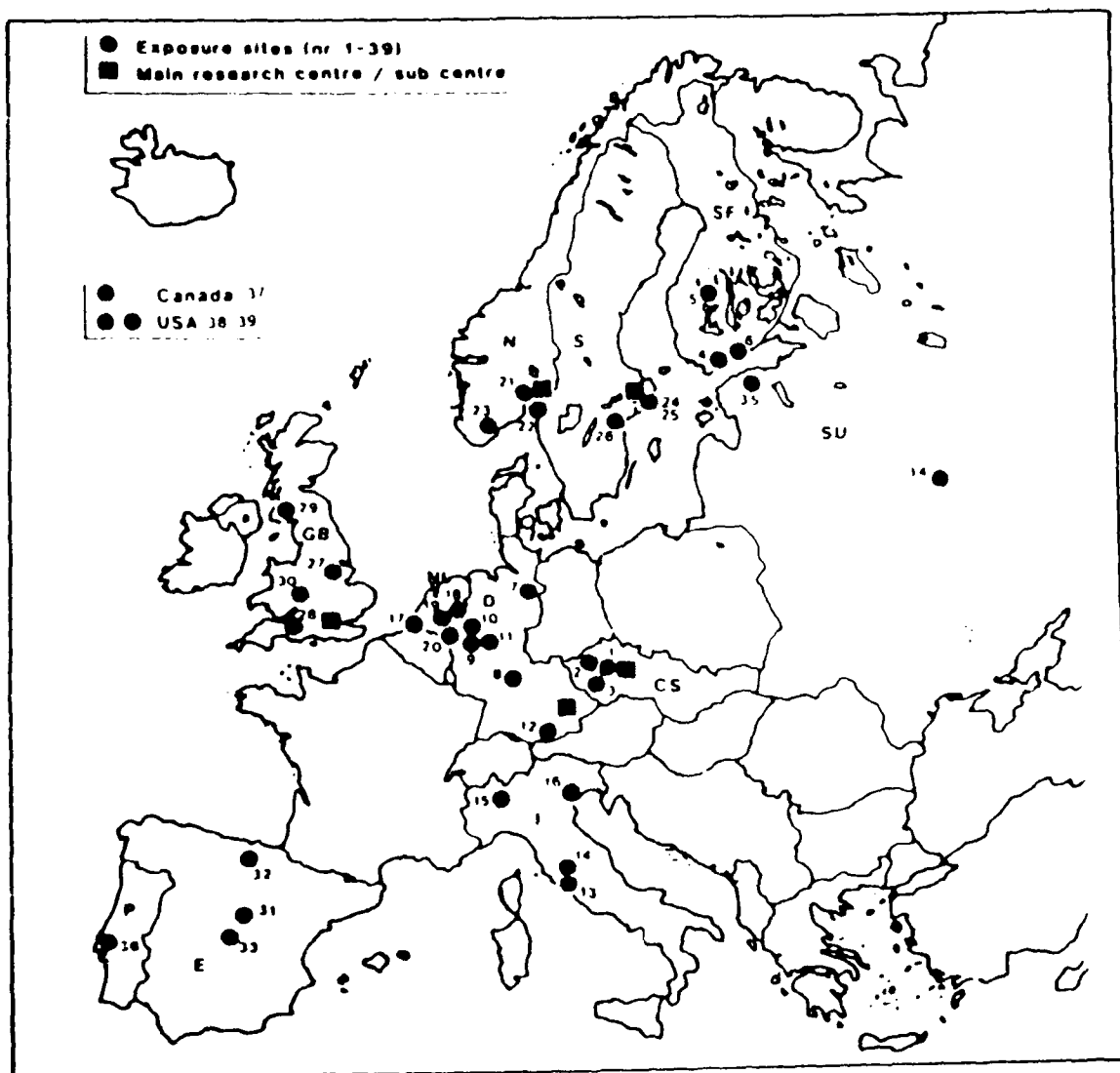


FIG 1. Network of test sites identified by the numbers found in Table 1

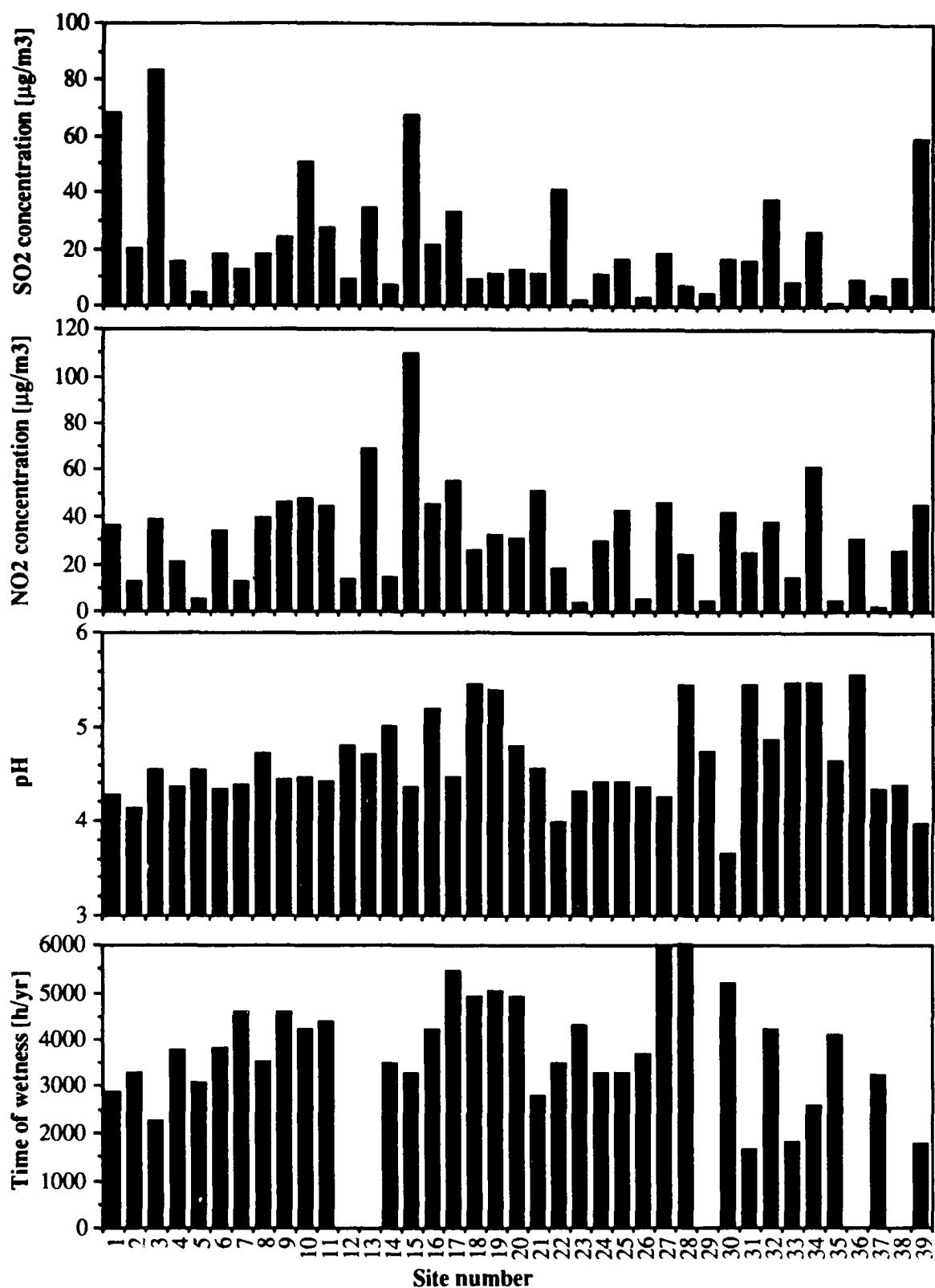


FIG 2. Mean values of sulfur dioxide concentration, nitrogen dioxide concentration, pH of precipitation, and time of wetness during the four year exposure period, September 1987 – August 1991

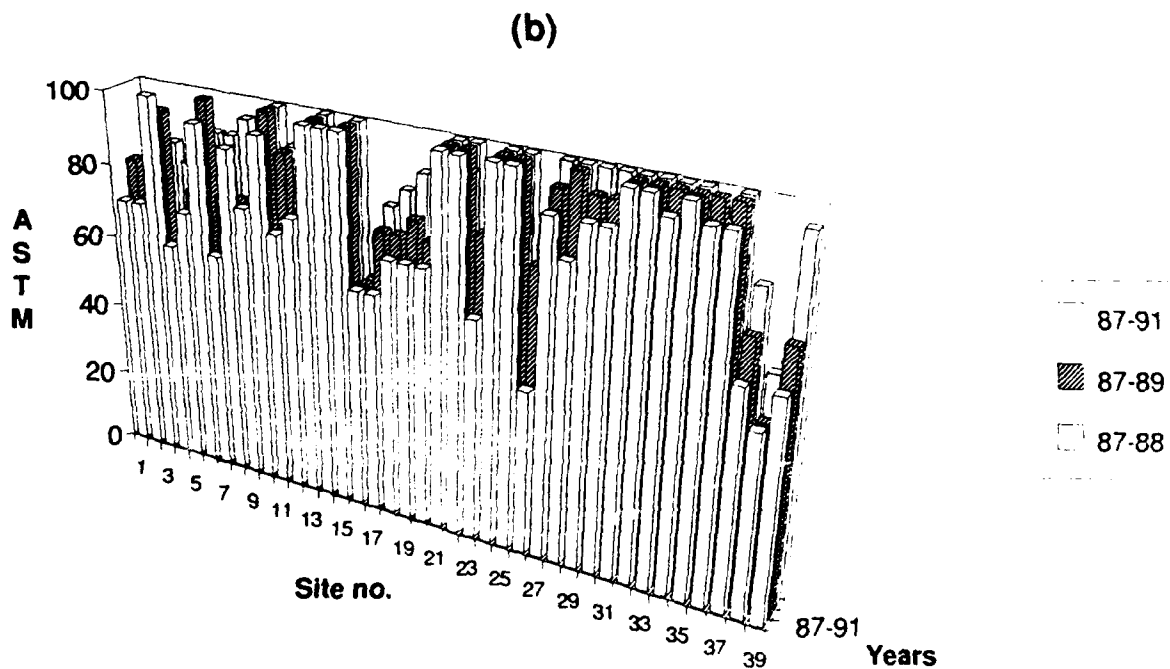
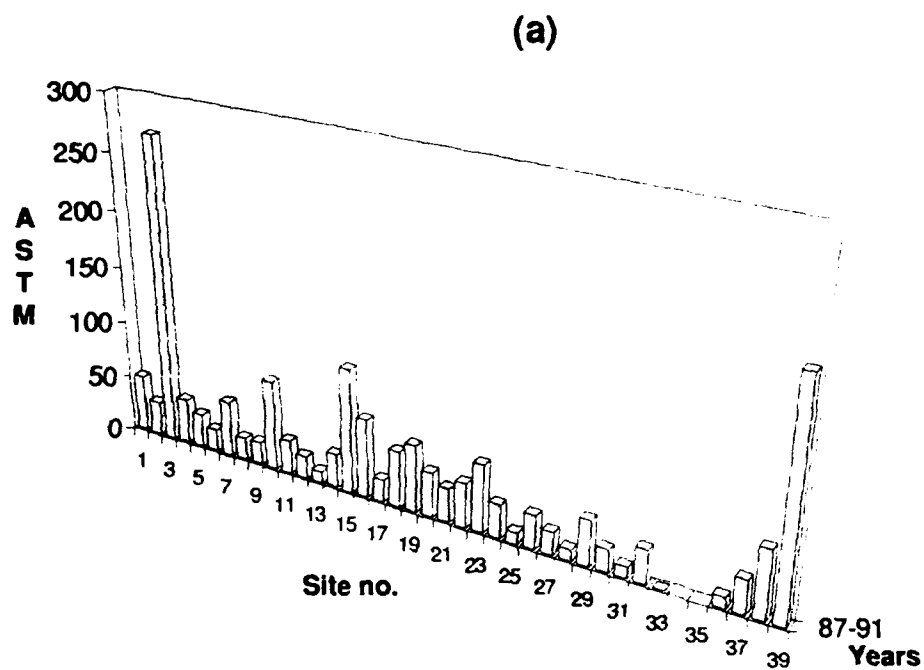


FIG 3. Steel specimens painted with a silicon alkyd paint:
 (a) spread of defect from scratch after 4 year exposure, and
 (b) occurrence of fungi after 1 to 4 year exposure

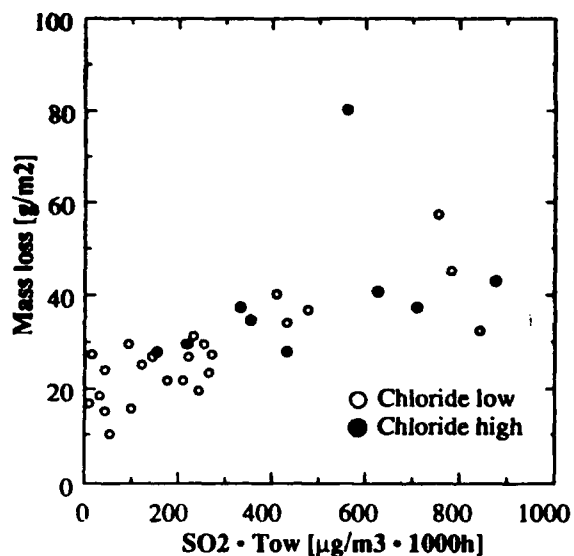


FIG 4. Mass loss of unsheltered zinc vs. SO_2 concentration \times time of wetness after 4 year exposure

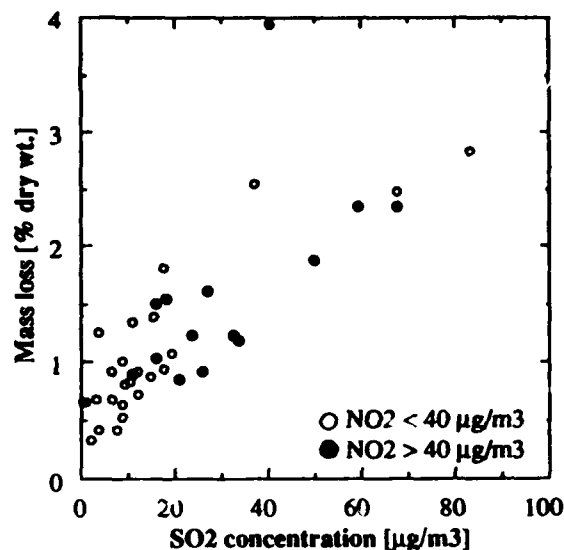


FIG 5. Mass loss of unsheltered sandstone vs. SO_2 concentration after 4 year exposure

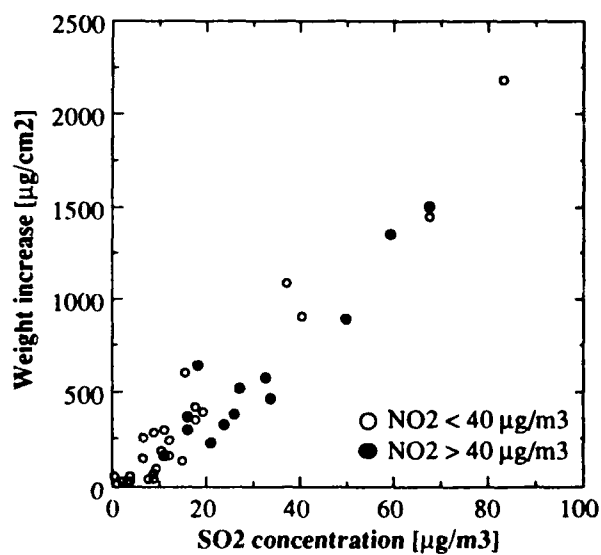


FIG 6. Weight increase of nickel vs. SO_2 concentration after 4 year exposure

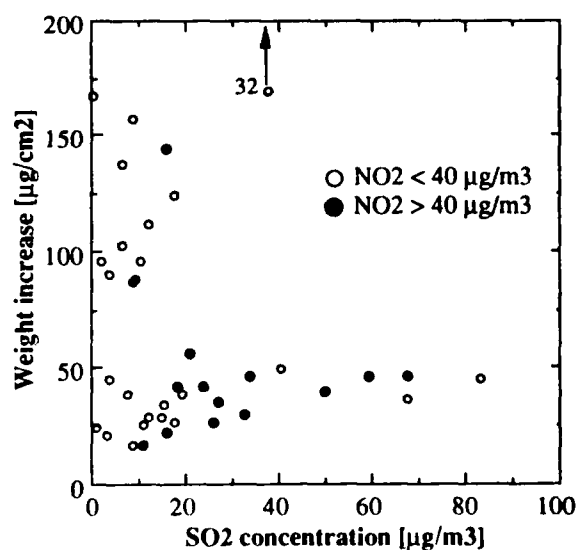


FIG 7. Weight increase of tin vs. SO_2 concentration after 4 year exposure

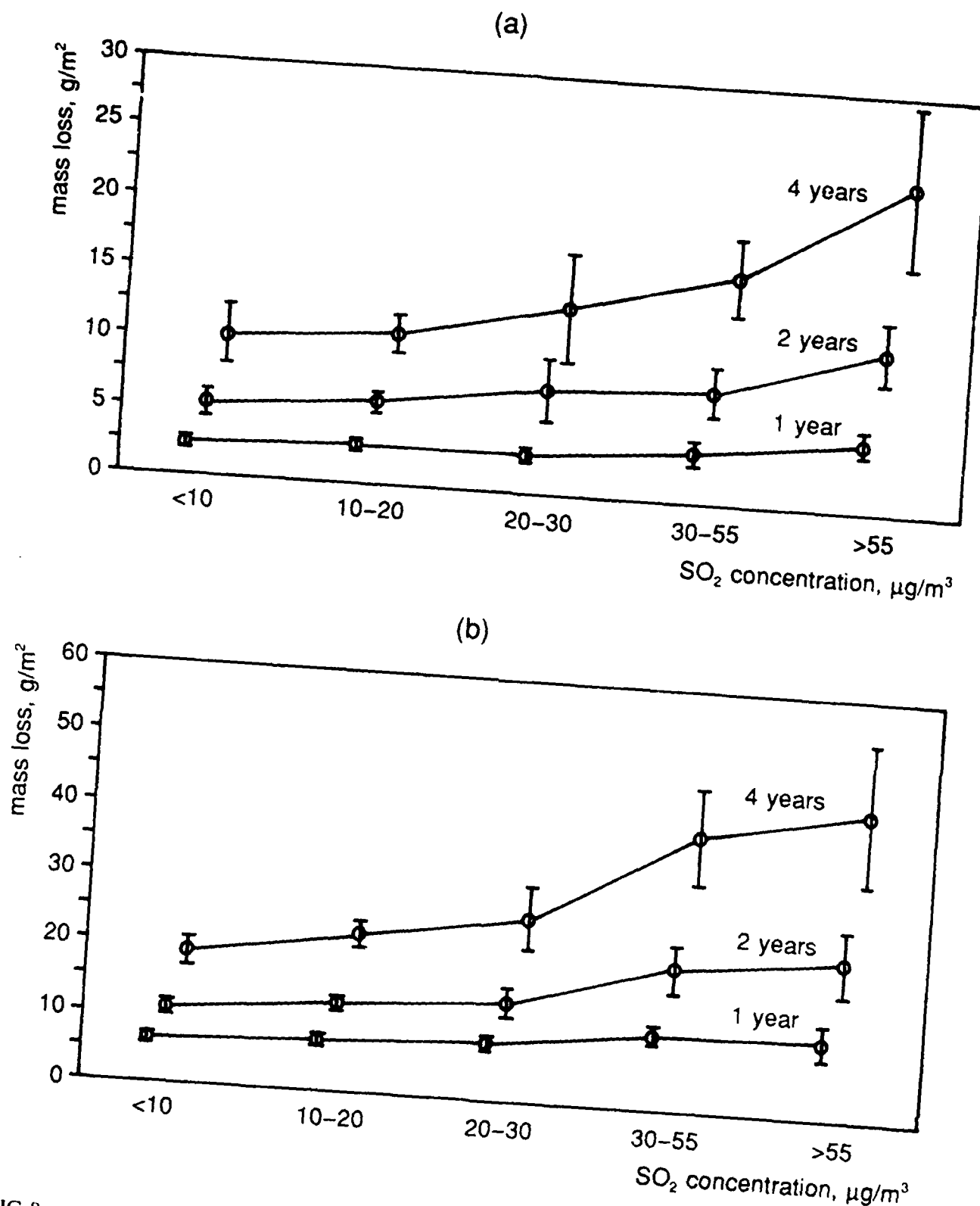


FIG 8. Mass loss of (a) sheltered and (b) unsheltered bronze specimens vs. SO₂ concentration intervals after 1, 2 and 4 year exposure

Worldwide Data on the Atmospheric Corrosion Resistance of Weathering Steels

M. E. Komp
Consultant
129 Westminster Dr.
Monroeville, PA 15146

S. K. Coburn
Corrosion Consultants, Inc.
P. O Box 81085
Pittsburgh, PA 15217

S. C. Lore
USX Engineers and Consultants, Inc.
600 Grant Street
Pittsburgh, PA 15219-4776

Abstract

To obtain corrosion data for weathering steels on a worldwide basis, USX Engineers and Consultants, Inc., and its USS COR-TEN steel licensees initiated an extensive atmospheric exposure program in the early 1970's. In this program test panels of the weathering steels ASTM A242 (USS COR-TEN A) and ASTM A588 (USS COR-TEN B), along with panels of copper-bearing steel and carbon steel, were exposed for time periods up to 16 years at test sites in the United States, Great Britain, Belgium, Japan, France, South Africa, Sweden and Germany. The sites included urban-industrial, rural, and moderate-marine atmospheres. Test panels were exposed at 30 degrees to the horizontal facing north and facing south (30°N, 30°S) and vertically facing north and facing south (90°N, 90°S).

The results of this unprecedented program document the atmospheric corrosion performance of the test steels worldwide. At virtually all the test sites the results confirmed the superior resistance of the weathering steels as compared to that of copper-bearing steel and carbon steel. However, there was a rather broad range of corrosion rates when comparing the data from the three types of environments in the different countries. For example, at the moderate-marine test sites, average corrosion rates for the 8-to-16 year period (for all test panel orientations) ranged from 2.3 to 13.9 $\mu\text{m/yr}$ (0.09 to 0.55 mils/yr) for A242 steel, 3.8 to 14.7 $\mu\text{m/yr}$ (0.15 to 0.58 mils/yr) for A588 steel, 5.7 to 24.8 $\mu\text{m/yr}$ (0.22 to 0.98 mils/yr) for copper-bearing steel, and 5.2 to 87.7 $\mu\text{m/yr}$ (0.20 to 3.45 mils/yr) for carbon steel.

With respect to the effect of test panel orientation, at about 80 percent of the urban-industrial sites the north-facing panels (south-facing in the southern hemisphere) showed greater corrosion losses than did the south-facing panels (north-facing in the southern hemisphere). The same was true at about 50 percent of the rural sites and at about 70 percent of the marine sites. At the remaining test sites there was no appreciable difference in results between the north- and south-facing panels. Vertically exposed (90°) test panels showed greater losses than did inclined (30°) panels at about 40 percent of the urban-industrial sites, 70 percent of the rural sites, and about 30 percent of the moderate marine sites. At the remaining sites there was no appreciable difference between the 90° and the 30° exposed panels.

Introduction

Because of their enhanced atmospheric corrosion resistance, weathering steels such as ASTM A242 (USS COR-TEN A) and ASTM A588 (USS COR-TEN B) can be used in the unpainted condition for outdoor structures in many geographic locations. The largest such use has been in bridges and other highway structures. Elimination of the need for initial painting (and subsequent periodic repainting) can result in substantial cost savings over the life of a structure. However, the corrosion performance of weathering steels varies depending upon local environmental conditions. There are some locations where these steels should not be used in the unpainted condition. Thus, there is a need for specific corrosion performance data in a variety of geographic sites.

To obtain comparative corrosion data for weathering steels on a worldwide basis, USX Engineers and Consultants, Inc. (Pittsburgh, Pennsylvania) and its licensees initiated an atmospheric exposure program in the early 1970's. In this program test panels of A242 steel, A588 steel, copper-bearing steel and carbon steel were exposed for time periods up to 16 years at corrosion test sites in the United States, Great Britain, Belgium, Japan, France, South Africa, Sweden and Germany. The sites included urban-industrial, rural, and moderate-marine atmospheres. Test panels were exposed in four different orientations: 30 degrees to the horizontal facing north and facing south (30°N, 30°S) and vertically facing north and facing south (90°N, 90°S). The results of this exposure program are reported in this paper.

Materials and Experimental Work

Steel Compositions

Duplicate test panels of the four steel types were tested for each time period at all the test sites. Steel compositions are shown in Table I. (Note: The A588 steel used is of the pre-1978 composition for USS COR-TEN B. The present composition of this steel has higher nickel and silicon contents, and has greater atmospheric corrosion resistance, particularly in marine environments.)

Test Panel Description

The test panels were 4 inches (10 cm) wide by 6 inches (15 cm) long by 1/8 to 3/16 (3 to 4.75 mm) thick. Before exposure each panel was marked for identification, pickled to remove mill scale, weighed, and painted on one side and the edges.

The paint system used to protect the unexposed side was as follows:

Primer: DuPont Dulux red-lead iron-oxide primer (Dupont Engineering No. 1008), brushed to a dry-film thickness of two mils (0.05 mm).

Topcoats: Two coats of DuPont Dulux metal protective paint (DuPont Engineering No. 5102), brushed to a dry-film thickness of two mils for each coat.

Exposure Locations

As indicated earlier, three different types of exposure locations were used: (1) urban-industrial (not inside the boundaries of steel or chemical plants); (2) rural (remote

from industry); and (3) moderate-marine (0.25 to 0.5 km, or 800 to 1600 ft from the surf). To minimize the influence of the microclimates produced by proximity to structures, exposure racks were installed at ground level rather than on building roofs. Also, all test panels were more than 1 m (40 inches) above the ground.

Exceptions to these conditions were that in France, at the urban-industrial site, racks were placed 17 m (56 ft) above the ground, and at the moderate-marine site they were placed 36.5 m (120 ft) above sea level and 0.05 km (164 ft) from the surf. No rural site was used in France. In Germany, an industrial site located within a steel plant in Oberhausen was used, along with an urban-industrial site in Essen. No rural or marine sites were used in Germany.

The test locations are listed in Table II, along with their approximate longitude and latitude.

Exposure Orientation

To investigate the effect of orientation on corrosion rates at each location, test panels were exposed on racks that provided orientations of vertical facing south, vertical facing north, 30° to the horizontal facing north, and 30° to the horizontal facing south. Two racks of this design were installed at each location. A photograph of one of the test racks at a rural site in the United States is shown in Figure 1.

Exposure Periods

Test panels were provided to allow for exposure periods of 1, 2, 4, 8, and 16 years. An additional set of panels was exposed at some locations at the same time and these panels were removed after approximately six months. In Japan, one set of panels was removed after six years. In Great Britain, removal times were different than in the other countries, except for the 8-year and 16-year sets. No 16-year data were obtained from the sites in France or Japan.

Cleaning of Exposed Test Panels

Cleaning of the panels after exposure times up to and including eight years was accomplished by immersing them in one to two percent sodium hydride dissolved in molten sodium hydroxide at 700° F (370° C). This treatment removed the rust on the exposed surface of the panels and the protective paint on the back side of the panels. For the 16-year panels, sodium hydride cleaning facilities were no longer available and cleaning with inhibited hydrochloric acid solution (per ASTM Specification G1) was used. Prior to the acid cleaning, the protective paint on the back side was removed with a commercial solvent-type paint stripper. Although early test had indicated that inhibited-acid cleaning results in a slightly greater mass loss as compared to sodium hydride cleaning, tests with 16-year panels exposed in the United States showed that the possible error due to acid cleaning would be less than two percent.

Evaluation

Mass loss was used as the primary experimental qualitative measure of corrosion. A weighing accuracy of 0.1 gram was used. The average loss in thickness (penetration) was calculated from the mass loss, and average corrosion rates for the 8-to-16 year period were calculated. For locations where no 16-year data were available, the 16-year losses were estimated using a log-log linear regression analysis, per ASTM G101.

Log-log plots of corrosion penetration vs. time, extrapolated to 50 years, were constructed for the weathering steels at each test site using the linear regression method described in ASTM G101. For these plots, data for the test-panel orientations exhibiting the greatest corrosion loss were used.

Results and Discussion

The mass losses, in grams, measured for each test panel exposed for up to and including 16 years are given in the Appendix.

Effect of Steel Type

The average corrosion penetrations in 16 years, and the average corrosion rates for the 8-to-16 year period, are summarized for all the test sites in Table III (urban-industrial sites), Table IV (rural sites), and Table V (moderate-marine sites). In addition, the corrosion rate data are presented graphically in Figures 2, 3 and 4. With few exceptions, A242 steel showed the lowest corrosion rate of the steels tested, and A588 steel the next lowest rate. The only exceptions were at the urban-industrial sites in Japan and France, where the A588 steel showed slightly higher rates than did copper steel, and in the moderate-marine site in France, where A242 steel showed a higher rate than did A588 steel or copper steel. The reasons for these exceptions are not clear.

The range of corrosion rates for a given steel in the different countries was quite substantial. For example, in the moderate-marine atmospheres (Table V), average rates for A242 steel varied by a factor of 6 (2.3 to 13.9 $\mu\text{m}/\text{yr}$), A588 steel by a factor of 4 (3.8 to 14.7 $\mu\text{m}/\text{yr}$), copper steel by a factor of 4 (5.7 to 24.8 $\mu\text{m}/\text{yr}$) and carbon steel by a factor of 17 (5.2 to 87.7 $\mu\text{m}/\text{yr}$).

Effect of Orientation

A review of the mass loss data indicates that the greatest effect of orientation was in the urban-industrial sites, where in approximately 80 percent of the locations the north-facing panels (south-facing in the southern hemisphere) showed greater corrosion losses than did the south-facing panels (north-facing in the southern hemisphere). In the rural and moderate-marine atmospheres, the same effect was noted but to a lesser extent (in about 50 percent of the rural sites and 70 percent of the marine sites). This north vs. south effect was not noted to any great extent at any of the test sites in Japan.

With respect to the vertical (90°) versus inclined (30°) panels, the 90° panels showed greater corrosion losses in about 40 percent of the urban-industrial sites, 70 percent of the rural sites, and 30 percent of the moderate-marine sites.

Average 8-to-16 year corrosion rates for all the test locations at the different orientations are summarized in Table 6 and presented graphically in Figure 5. It can be seen from these data that the effect of orientation was greatest for the weathering steels in the urban-industrial environments, whereas for the copper steel and carbon steel the effect was greatest in the moderate-marine sites.

These orientation effects can be attributed to the direction of incidence of solar radiation at the different latitudes. Heat from solar radiation dries exposed steel, thus decreasing the time of wetness during which the steel corrodes. Direct solar radiation

is mainly from the south in northern latitudes and from the north in southern latitudes, with the differences between north and south being greater at the higher latitudes.

The major effect that produces differences between vertical and inclined panels in non-marine atmospheres, where the major corrosion-inducing contaminants are gaseous, is the greater exposure of the inclined panels to radiation from the sky, which reduces the time of wetness of the panels. At marine sites, chloride particulate deposition (which is greater on inclined panels) is a strong factor in determining the corrosion rates.

Effect of Location and Meteorological Factors

Differences in corrosivity at the various test sites are perhaps best summarized by the log-log plots of corrosion penetration vs. time, extrapolated to 50 years, shown in Figure 6. The most striking differences were noted in the industrial environments, where much higher corrosion rates were exhibited in the north European countries as compared to those in the United States, South Africa and Japan.

With the exception of South Africa, each of the test locations is located within a band north of the equator between 35°N (Japan) and 59°N (Sweden). They have nearly the same amounts of rainfall and ranges in temperatures. The primary difference is probably in the time-of-wetness of the test panels. For the test sites in Europe (50 to 60°N) the angle of the sun's rays during the colder months of the year is such that the test panels are likely to remain wet longer and experience fewer hours of sunshine than those countries closer to the equator such as the United States (40°N) and Japan (35°N), and especially South Africa (25°S).

The next most important factor on the European continent is that Sweden is sandwiched between the southwesterly winds from England and the southeasterly winds from Poland and Russia. In each case the cross boundary movement of industrially polluted air can result in periodic episodes of acid rain fallout. In similar fashion Germany is the victim of air movement from Russia, Poland, Hungary, the Czech Republic and Slovakia.

In the early 1960's many large power plants in the United States using fossil fuels built very tall exhaust stacks so as to alleviate local pollution fallout. Unfortunately, these exhausts were merged and moved like a herd of animals in the west-to-east jet stream giving rise to the "acid-rain" phenomenon. This effect, to some degree, altered the corrosivity of specific environments and gave rise to both ecological and metallurgical damage. The rural test site in the United States was in the direct path of the jet stream and slowly turned more aggressive to the test panels. By contrast, the aggressive industrial site in Kearny, New Jersey, owing to the imposition of lower sulfur levels for fossil fuels, lost much of its corrosive nature and acted toward the test panels somewhat like a rural test site.

The foregoing mass loss data were obtained from test panels exposed at industrial, rural and marine sites selected by the respective weathering-steel licensees in their own countries. These sites could be expected to vary in their aggressiveness toward the test panels. Nevertheless, the respective environments in each of the countries were capable of distinguishing between the four steel compositions.

Appearance

In virtually all cases, the exposed A242 and A588 test panels showed a more pleasing appearance than that of the copper steel and carbon steel. At most of the urban-industrial sites, the weathering steels tended to develop a blue-gray patina, as opposed to a brownish color at the other test sites. In most cases, the inclined (30°) panels showed a smoother surface than did the vertical panels. Also, except for the moderate-marine sites, panels exposed facing south appeared somewhat smoother than those facing north.

Significance of "Heat Sink" Effect

It should be recognized that small, isolated test panels represent the most severe form of an exposure test. Because of their small mass such panels are quite sensitive to exposure conditions such as orientation and angle to the sun. While such small-scale exposures are useful in identifying various forms of atmospheric aggressiveness, experience with massive steel structures has demonstrated that some of the behavior exhibited by the small test panels, based on orientation, can be misleading due to being masked by the "heat sink" effect of a large structure.

The "heat sink" effect involves the daytime absorption (by the massive concrete and steel elements of a bridge or building structure) of a considerable amount of heat from the sun. Hence, nightly condensation of dew is minimized by the relatively short period the temperature of the structure may have dipped below the dewpoint. Thus, measurements of the time-of-wetness of small test panels at a proposed construction site have little relevance to the time-of-wetness likely to be sustained by a massive structure. While such data are indicative of local environmental conditions, engineering judgment must be exercised on the basis of current experience as exemplified by the numerous existing structures throughout the world.

Examples of Successful Use

Despite the variation in the mass loss of the test panels exposed in industrial, rural and marine environments in the various countries, structures fabricated from weathering steels continue to provide excellent service after 15 to 25 years in many locations throughout the world. In the United States monumental office buildings such as the USX Tower in Pittsburgh, the Chicago Civic Center in Chicago, the Deere Buildings in Moline, Illinois, and the Ford Foundation in New York City, among others, are prominent examples of the use of unpainted weathering steel. These applications are in addition to bridges and electrical power transmission towers, and thousands of railroad hopper cars.

In England numerous unpainted weathering steel bridges have been erected. In Sweden there are transmission towers and hundreds of chimneys as well as sculptures. In Germany, likewise, are numerous bridges as well as building façades. In Finland there are large gas holders. South Africa and Japan similarly employ weathering steel for bridges and transmission towers with great success.

Precautions and Limitations

As with any building material, certain precautions must be taken in the use of unpainted weathering steel. The recommendations of the steel producers should be followed in this regard. Unpainted weathering steel should not be used in atmospheres containing high concentrations of chemical fumes, or where it would

be exposed to recurrent wetting by salt water or salt fogs. Also, it should not be immersed in water or buried in soil. Design of structures should avoid pockets, crevices, faying surfaces or locations that can retain liquid water, damp debris, and moisture. The U. S. Federal Highway Administration and AISC Marketing, Inc., have recently published guidelines for use of unpainted weathering steel for structures.^{1,2}

Acknowledgements

The authors wish to acknowledge significant contributions to this test program by personnel at the following companies: British Steel plc, Cockerill Sambre, S. A. (Belgium), ISCOR Ltd. (South Africa), Nippon Steel Corp. (Japan), Svenskt Stal Akiebolag (Sweden), Thyssen Stahl AG (Germany) and USINOR SACLOR Groupe (France). Also, the work of former USX employees W. P. Gallagher and E. H. Phelps in setting up and implementing the program is acknowledged. Finally, the authors wish to thank USX Engineers and Consultants, Inc., for supporting the preparation of this paper and for the permission to publish it.

References

1. Federal Highway Administration Technical Advisory T 5140.22, Uncoated Weathering Steel in Structures, October 3, 1989.
2. Mathay, W. L., "Uncoated Weathering Steel Bridges", Highway Structures Design Handbook, Vol. I, Chap. 9, AISC Marketing, Inc., Pittsburgh, PA, January 1993.

Table I
COMPOSITION OF TEST PANELS

Steel Type	Weight Percent										Al (Total)
	C	Mn	P	S	Si	Cu	Ni	Cr	V		
Carbon	0.046	0.38	0.012	0.022	0.016	0.014	0.012	0.025	<0.01		0.004
Copper	0.042	0.35	0.002	0.012	0.004	0.26	0.014	0.014	<0.01		0.003
ASTM A242 (USS COR-TEN A)	0.11	0.31	0.092	0.020	0.42	0.30	0.31	0.82	<0.01		0.018
ASTM A588 Gr. A (USS COR-TEN B*)	0.13	1.03	0.006	0.019	0.25	0.33	0.015	0.56	0.038		0.043

*Pre-1978 composition

Table II

TEST SITES AND APPROXIMATE LATITUDE AND LONGITUDE

<u>COUNTRY</u>	<u>TYPE</u>	<u>LOCATION</u>	<u>LATITUDE</u>	<u>LONGITUDE</u>
UNITED STATES	Industrial	Kearny, NJ	40°30'N	74°W
	Marine	Kure Beach, NC	35°N	78°W
	Rural	Potter Co., PA	42°N	78°W
S. AFRICA	Industrial	Pretoria-8km W	25°45'S	28°E
	Marine	Kwa Zulu Coast	32°S	
	Rural	Pretoria-8km E	25°45'S	28°E
JAPAN	Industrial	Kawasaki	35°32'N	140°E
	Marine	Hikari	35°55'N	132°E
	Rural	Yamanaka	35°25'N	138°E
BELGIUM	Industrial	Liege	50°39'N	6°E
	Marine	Ostende II	51°13'N	3°E
	Rural	Eupen	50°38'N	6°E
FRANCE	Industrial	St. Denis	48°56'N	2°E
	Marine	Biarritz	43°29'N	2°W
GERMANY	Industrial	Oberhausen	51°28'N	7°E
	Industrial	Essen Frintrop	51°28'N	7°E
GR. BRITAIN	Industrial	Stratford	52°12'N	0°
	Marine	Rye	50°57'N	1°E
	Rural	Avon Dam	50°17'N	2°W
SWEDEN	Industrial	Stockholm	59°20'N	18°E
	Marine	Bohus Malmö	58°N	12°E
	Rural	Ryda Kungsgård	60°36'N	17°E

Table III

**SUMMARY OF AVERAGE PENETRATION DATA AND
CORROSION RATES FOR URBAN-INDUSTRIAL SITES**

AVERAGE OF ALL ORIENTATIONS (30°S, 30°N, 90°S, 90°N), EXCEPT AS NOTED

COUNTRY	AVERAGE PENETRATION IN 16 YEARS, μm				AVERAGE CORROSION RATE, 8 TO 16 YEARS, $\mu\text{m/yr}$			
	A242	A588	Copper	Carbon	A242	A588	Copper	Carbon
S. Africa	22	34	51	58	0.1	0.3	1.1	1.2
United States	45	70	84	91	1.5	2.4	3.5	3.2
Japan*	91	156	149	227	2.0	4.5	4.2	5.3
Sweden	138	186	192	205	2.9	5.1	6.2	6.4
Belgium	148	206	235	272	3.8	5.6	8.0	9.0
Gr. Britain	198	250	265	317	7.5	8.6	10.6	12.6
Germany**	208	306	285	360	7.2	12.5	12.6	14.9
France*	221	328	300	404	11.2	17.2	15.1	20.1

Table IV

**SUMMARY OF AVERAGE PENETRATION DATA
AND CORROSION RATES FOR RURAL SITES**

AVERAGE OF ALL ORIENTATIONS (30°S, 30°N, 90°S, 90°N)

COUNTRY	AVERAGE PENETRATION IN 16 YEARS, μm				AVERAGE CORROSION RATE, 8 TO 16 YEARS, $\mu\text{m/yr}$			
	A242	A588	Copper	Carbon	A242	A588	Copper	Carbon
S. Africa	28	42	56	62	0.3	0.8	0.9	1.4
Sweden	58	78	85	88	1.7	2.9	3.6	3.2
Japan*	60	75	91	91	2.0	2.4	3.4	3.3
United States	73	112	145	159	2.5	4.2	6.9	7.2
Belgium	126	171	-	224	5.6	7.9	-	11.5
Gr. Britain	147	190	216	231	6.6	10.7	11.1	12.9

Table V

**SUMMARY OF AVERAGE PENETRATION DATA AND
CORROSION RATES FOR MODERATE-MARINE SITES**

AVERAGE OF ALL ORIENTATIONS (30°S, 30°N, 90°S, 90°N)

COUNTRY	AVERAGE PENETRATION IN 16 YEARS, μm				AVERAGE CORROSION RATE, 8 TO 16 YEARS, $\mu\text{m/yr}$			
	A242	A588	Copper	Carbon	A242	A588	Copper	Carbon
Japan*	86	131	151	159	2.3	3.8	5.7	5.2
Sweden	116	135	188	202	5.5	6.8	10.2	11.1
S. Africa	134	201	614	2088*	5.4	7.6	13.1	87.7*
United States	158	224	380	801*	8.8	12.5	24.4	45.5*
France*	165	145	183	274	8.8	5.9	6.0	11.9
Belgium	209	225	340	429	9.4	10.7	16.1	18.9
Gr. Britain	249	257	417	541*	13.9	14.7	24.8	34.2*

NOTE: 1 μm = 0.04 mils

*16-year data estimated from log-log linear extrapolation of 8-year data.

**Only 90°S and 90°N orientation were tested in Germany.

Table VI

**EFFECT OF TEST PANEL ORIENTATION
ON AVERAGE CORROSION RATES**

AVERAGE OF ALL COUNTRIES*

STEEL TYPE	AVERAGE CORROSION RATE, 8 TO 16 YEARS, $\mu\text{m}/\text{yr}$											
	URBAN INDUSTRIAL SITES				RURAL SITES				MODERATE MARINE SITES			
	30°S	90°S	30°N	90°N	30°S	90°S	30°N	90°N	30°S	90°S	30°N	90°N
A242	1.8	2.0	6.2	7.3	2.3	2.9	3.4	3.8	5.1	6.8	9.3	9.8
A588	3.2	4.8	7.5	10.8	3.9	4.6	5.0	5.8	6.9	8.1	8.8	11.6
Copper	4.5	6.3	8.4	10.0	4.9	6.0	4.8	5.0	11.0	16.1	11.2	18.8
Carbon	6.0	7.0	9.8	11.7	6.2	6.9	6.0	7.3	17.4	32.3	42.9	30.0

NOTE: 1 $\mu\text{m}/\text{yr}$ = 0.04 mils/yr

*Data from South Africa was transposed, north \leftrightarrow south.

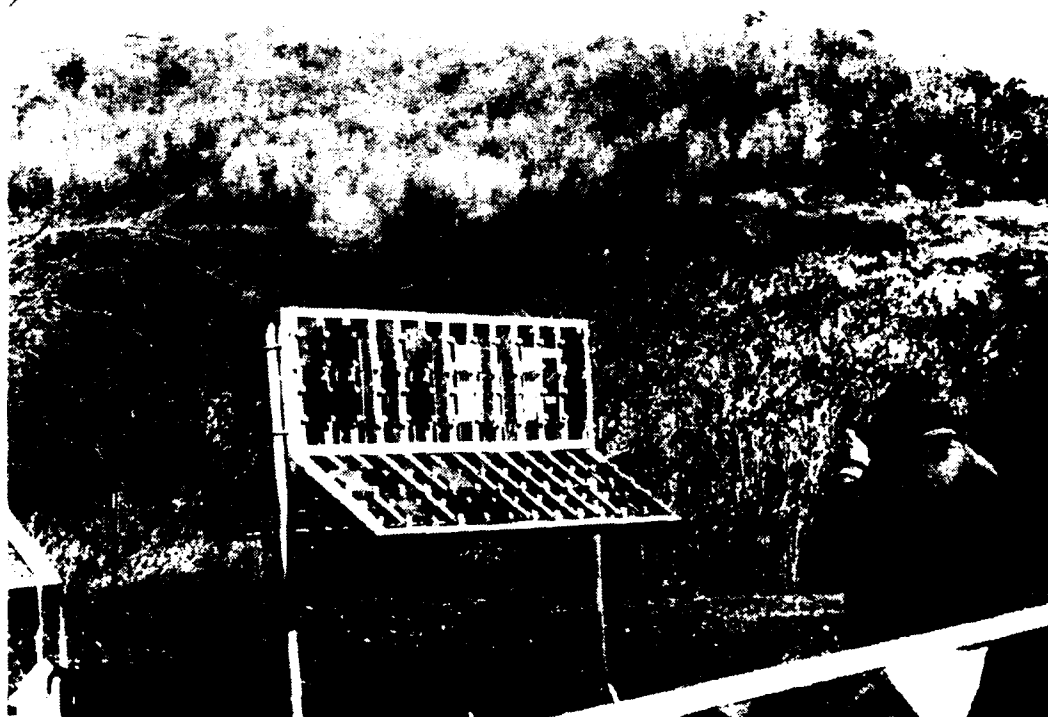


Figure 1. Atmospheric Test Rack at the Rural Site
in Potter County, Pennsylvania

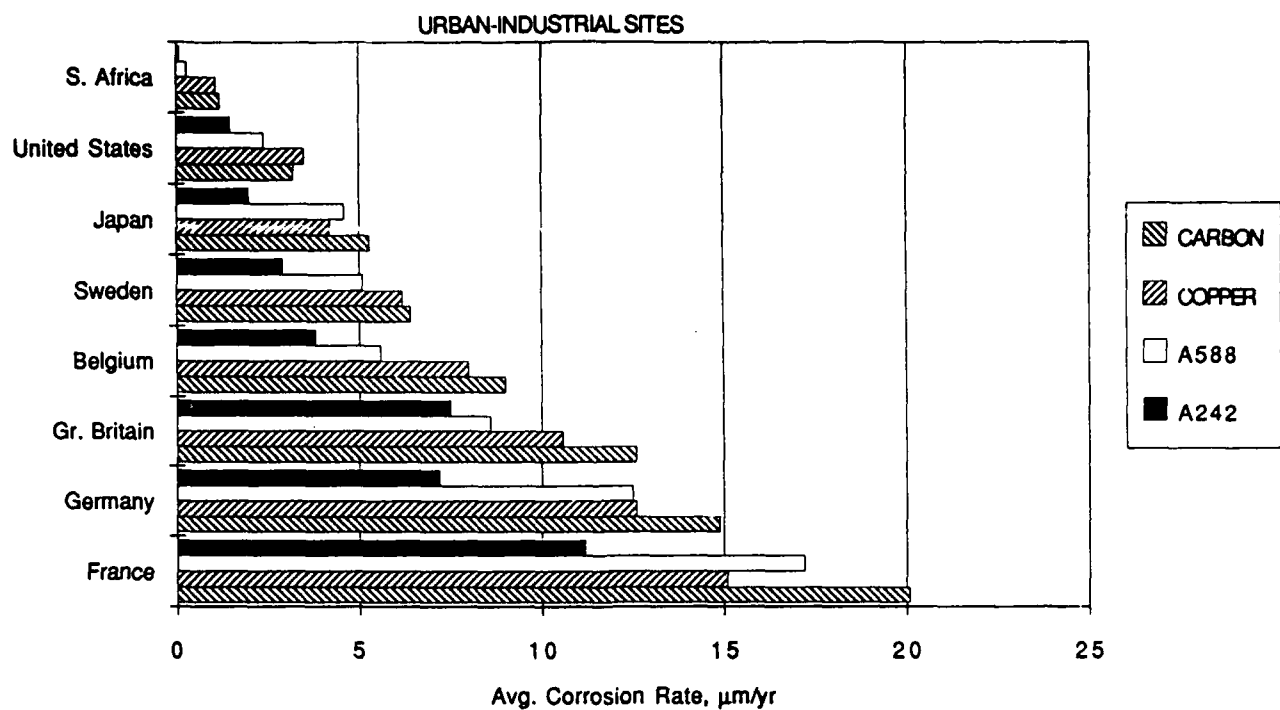


Figure 2. SUMMARY OF AVERAGE 8-TO-16 YEAR CORROSION RATES FOR URBAN-INDUSTRIAL SITES

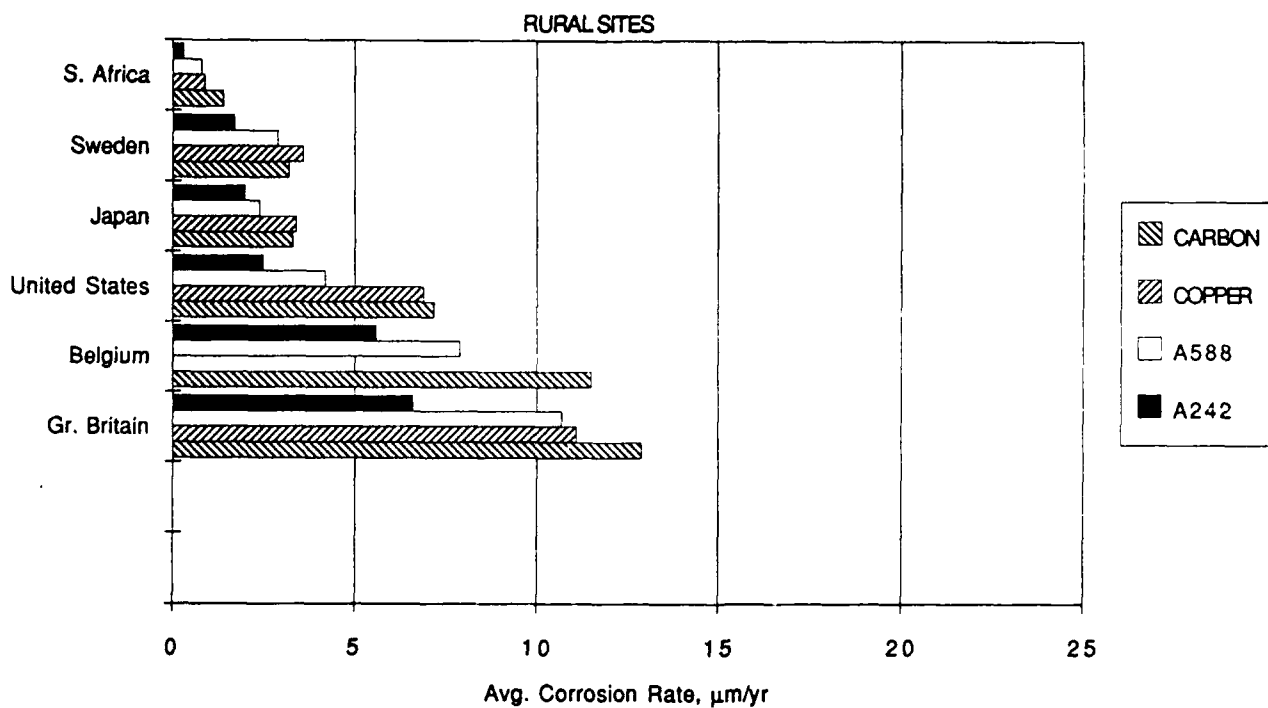


Figure 3. SUMMARY OF AVERAGE 8-TO-16 YEAR CORROSION RATES FOR RURAL SITES

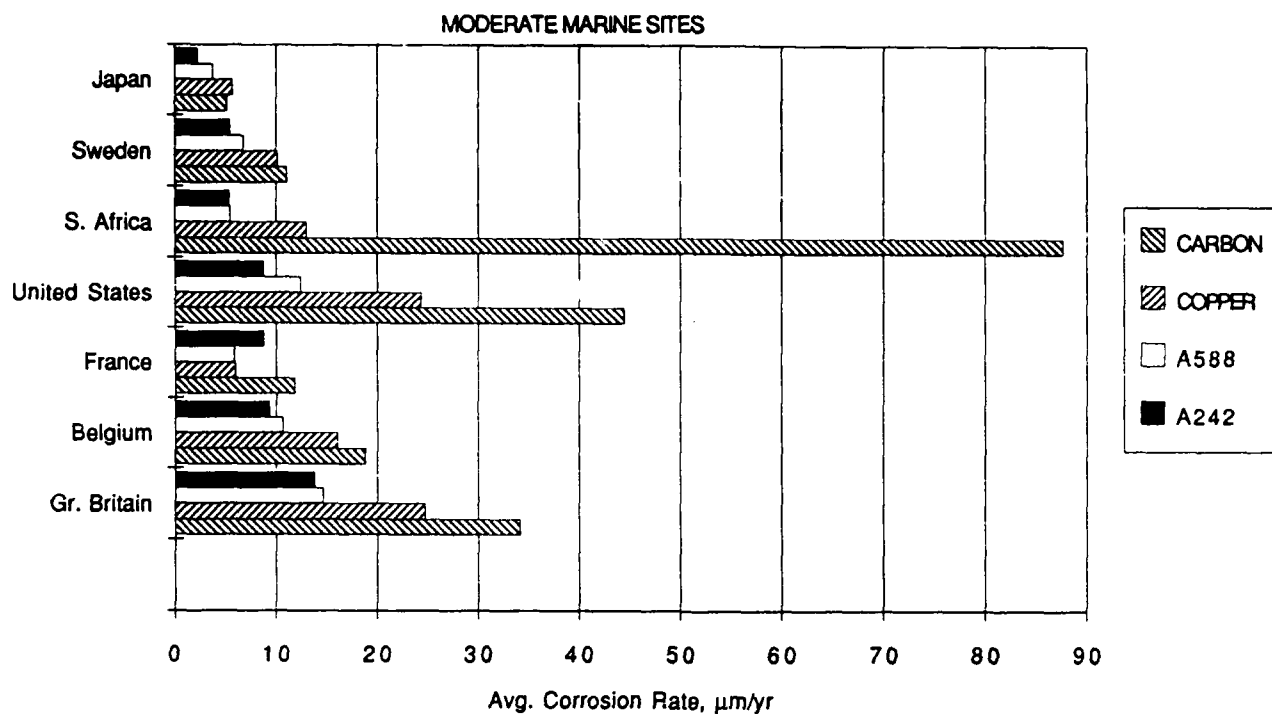


Figure 4. SUMMARY OF AVERAGE 8-TO-16 YEAR CORROSION RATES FOR MODERATE-MARINE SITES

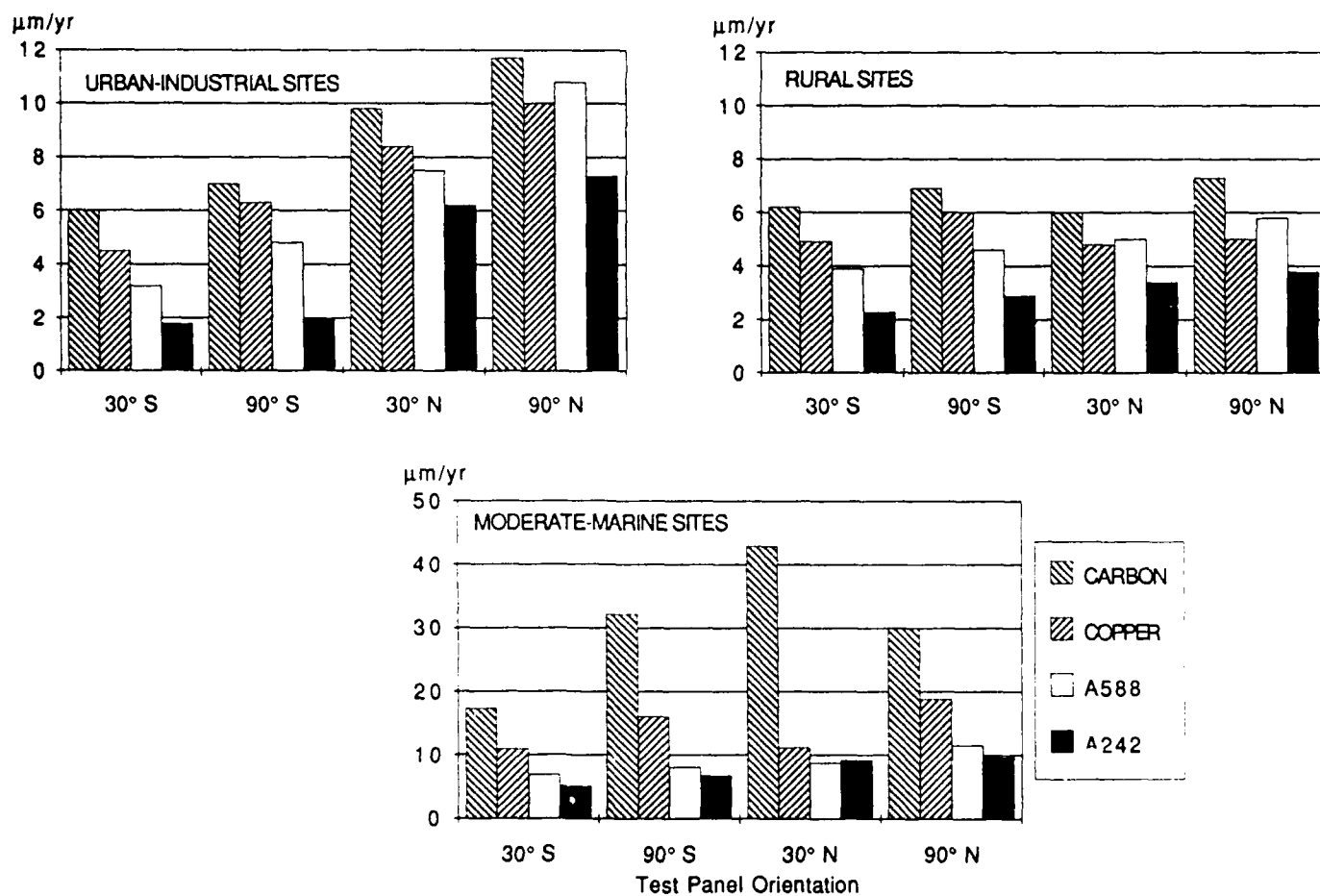


Figure 5. EFFECT OF TEST PANEL ORIENTATION ON AVERAGE 8-TO-16 YEAR CORROSION RATES

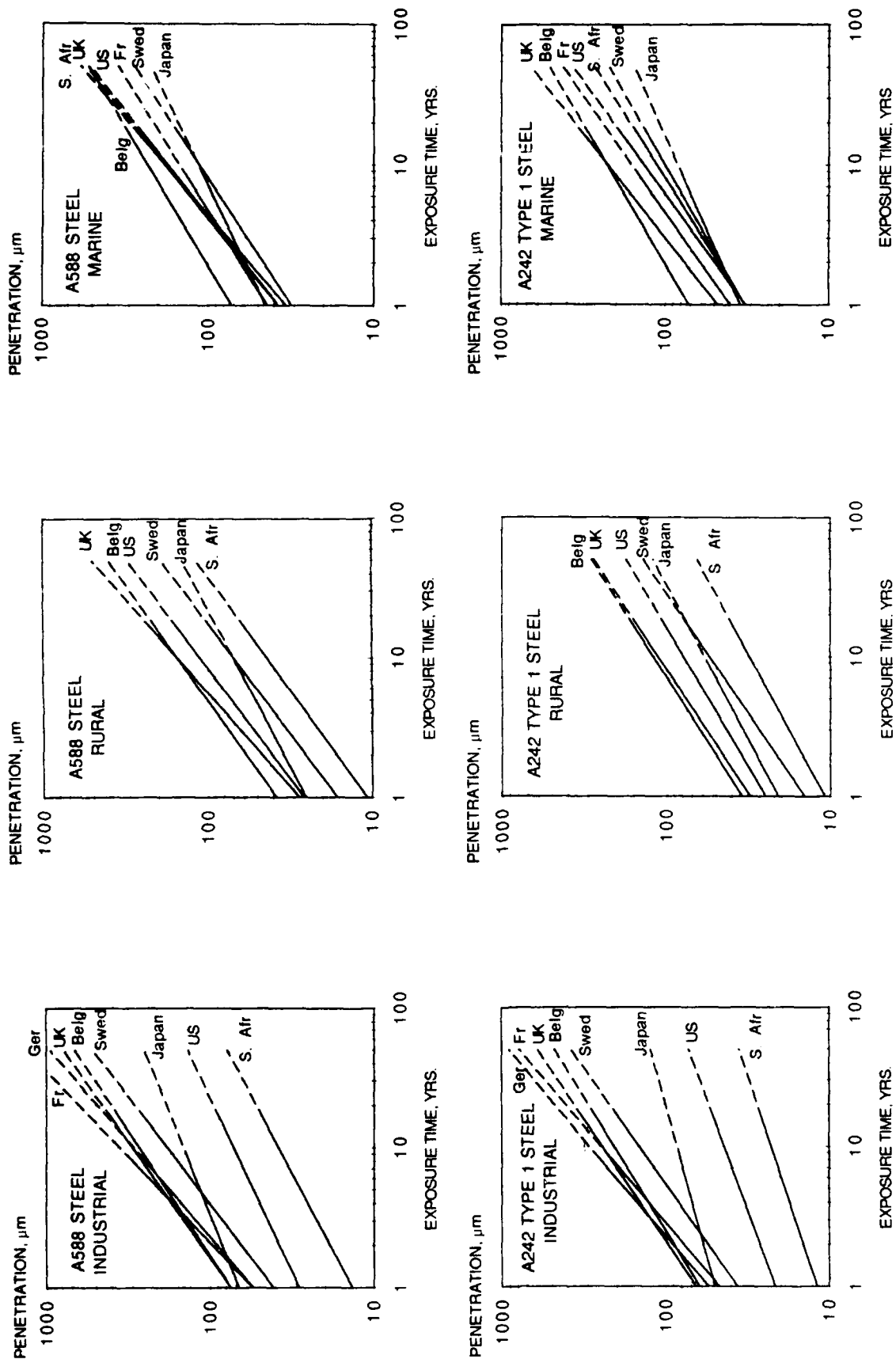


Figure 6. Projected Corrosion Penetrations for ASTM A242 and A588 Steels in Various Countries
(Based on test-panel orientations exhibiting the greatest amount of corrosion loss.)

APPENDIX
TABULATION OF MASS LOSS DATA

Table A1 - United States

Table A2 - Great Britain

Table A3 - Belgium

Table A4 - Japan

Table A5 - France

Table A6 - South Africa

Table A7 - Sweden

Table A8 - Germany

Table A1. UNITED STATES
Corrosion Losses, grams - Exposed Area: approx. 24 in² (155 cm²)

Years	A242						A588						Copper Steel						Carbon Steel											
	30.S			30.N			30.S			30.N			30.S			30.N			30.S			30.N			30.S			30.N		
	90.S	90.S	90.N	90.S	90.S	90.N	90.S	90.S	90.N	90.S	90.S	90.N	90.S	90.S	90.N	90.S	90.S	90.N	90.S	90.S	90.N	90.S	90.S	90.N	90.S	90.S	90.N			
URBAN-INDUSTRIAL SITE - KEARNY, NJ																														
0.5	2.2	2.2	2.4	2.1	2.1	2.1	2.6	2.4	3.5	2.5	2.5	2.4	2.3	2.4	2.9	3.9	2.8	2.6	2.9	3.9	2.8	2.8	2.6	2.9	3.9	2.8	2.6			
0.5	2.1	2.3	2.1	2.1	2.1	2.1	2.2	2.3	2.4	2.7	2.1	2.3	2.3	2.0	2.8	3.1	2.7	2.9	2.8	3.1	2.7	2.9	2.8	3.1	2.7	2.9				
1	2.4	2.5	2.7	2.6	2.6	2.6	3.0	2.8	4.0	3.2	3.1	3.2	3.0	2.8	3.5	4.2	3.6	3.1	3.5	4.2	3.6	3.1	3.5	4.2	3.6	3.1				
1	2.6	2.6	2.9	2.6	2.6	2.6	2.9	3.6	3.2	3.4	2.9	3.2	2.9	2.6	4.0	4.1	3.5	3.3	4.0	4.1	3.5	3.3	4.0	4.1	3.5	3.3				
2	2.8	3.3	3.2	3.4	3.4	3.4	4.1	5.1	4.4	5.2	4.4	5.0	4.5	4.6	5.3	6.1	4.7	4.9	5.3	6.1	4.7	4.9	5.3	6.1	4.7	4.9				
2	2.7	3.0	3.2	3.2	3.2	3.2	3.5	4.6	4.2	4.7	3.8	4.4	3.9	3.9	4.4	5.3	4.2	4.5	4.4	5.3	4.2	4.5	4.4	5.3	4.2	4.5				
4	3.3	3.7	3.5	4.0	4.0	4.0	4.5	5.4	5.8	6.7	5.0	6.1	5.6	5.8	6.3	7.1	6.2	6.6	6.3	7.1	6.2	6.6	6.3	7.1	6.2	6.6				
4	3.4	3.7	3.6	4.2	4.2	4.2	4.1	5.3	5.6	6.5	4.6	5.8	5.4	6.1	6.0	7.1	5.7	6.5	6.0	7.1	5.7	6.5	6.0	7.1	5.7	6.5				
8	3.3	4.3	3.9	4.7	4.7	4.7	4.9	6.3	5.8	7.8	5.8	7.1	6.9	7.9	7.3	9.2	7.3	8.5	7.3	9.2	7.3	8.5	7.3	9.2	7.3	8.5				
8	3.3	4.0	3.8	4.6	4.6	4.6	4.7	6.1	5.9	7.5	5.9	6.9	6.4	7.6	7.0	8.8	7.1	8.1	7.0	8.8	7.1	8.1	7.0	8.8	7.1	8.1				
16	4.7	5.7	5.1	6.2	6.2	6.2	6.7	8.2	10.7	10.2	8.9	10.8	10.0	11.7	9.6	12.2	9.8	11.9	9.6	12.2	9.8	11.9	9.6	12.2	9.8	11.9				
16	4.9	5.2	5.3	6.7	6.7	6.7	6.1	8.7	7.4	10.3	8.3	10.8	9.6	11.9	10.6	11.9	10.6	11.7	10.6	11.9	10.6	11.7	10.6	11.9	10.6	11.7				
RURAL SITE - POTTER COUNTY, PA																														
0.5	1.5	1.6	1.7	1.8	1.8	1.8	1.7	1.8	1.7	2.0	1.6	1.5	1.8	1.7	1.9	2.1	2.0	2.0	1.9	2.1	2.0	2.0	1.9	2.1	2.0	2.0				
0.5	1.7	1.7	1.5	2.0	2.0	2.0	1.8	1.7	1.9	1.9	1.6	1.6	1.6	1.8	2.0	1.9	2.0	2.1	2.0	1.9	2.0	2.1	2.0	1.9	2.0	2.1				
1	2.5	2.6	2.7	2.9	2.9	2.9	2.5	3.0	3.0	2.9	2.7	2.6	2.8	2.5	2.9	3.0	3.2	3.2	2.9	3.0	3.2	3.2	2.9	3.0	3.2	3.2				
1	2.2	2.5	2.5	3.1	3.1	3.1	2.6	2.9	2.9	3.2	2.6	2.5	2.7	2.7	3.2	3.8	3.2	3.0	3.2	3.8	3.2	3.0	3.2	3.8	3.2	3.0				
2	3.2	4.0	3.8	4.8	4.8	4.8	4.4	5.0	4.8	5.4	4.7	4.8	4.7	5.5	5.4	5.3	5.3	5.9	5.4	5.3	5.3	5.9	5.4	5.3	5.3	5.9				
2	3.1	4.3	3.8	4.8	4.8	4.8	4.3	5.1	4.6	5.5	4.7	4.7	4.9	5.7	5.2	5.5	5.2	6.0	5.2	5.5	5.2	6.0	5.2	5.5	5.2	6.0				
4	3.8	5.7	5.0	6.8	6.8	6.8	6.2	7.4	6.9	8.1	7.2	7.5	7.2	8.7	7.9	8.8	8.1	9.5	7.9	8.8	8.1	9.5	7.9	8.8	8.1	9.5				
4	4.1	5.7	5.3	6.9	6.9	6.9	6.2	7.3	6.7	8.2	7.0	7.4	7.5	8.7	7.9	8.5	8.3	9.5	7.9	8.5	8.3	9.5	7.9	8.5	8.3	9.5				
8	4.0	7.7	5.6	8.7	8.7	8.7	7.4	10.4	8.7	11.7	9.8	10.8	10.4	12.7	11.6	12.4	12.5	14.3	11.6	12.4	12.5	14.3	11.6	12.4	12.5	14.3				
8	4.2	7.2	5.6	8.7	8.7	8.7	7.6	10.4	8.6	11.7	10.1	10.7	10.6	12.7	11.4	11.9	10.8	13.7	11.4	11.9	10.8	13.7	11.4	11.9	10.8	13.7				
16	5.7	10.1	7.9	9.3	9.3	9.3	10.7	13.8	12.6	16.8	16.4	17.0	17.2	20.7	17.7	18.6	19.7	20.3	17.7	18.6	19.7	20.3	17.7	18.6	19.7	20.3				
16	8.9	10.9	6.0	12.4	12.4	12.4	10.9	15.9	11.9	16.8	16.0	17.1	16.4	--	17.2	--	19.9	22.9	17.2	--	19.9	22.9	17.2	--	19.9	22.9				
MODERATE MARINE SITE - KURE BEACH, NC																														
0.5	2.3	2.5	2.2	2.7	2.7	2.7	3.0	3.1	3.1	3.3	3.1	3.3	3.0	3.3	3.2	3.6	3.0	3.8	3.2	3.6	3.0	3.8	3.2	3.6	3.0	3.8				
0.5	2.4	2.4	2.4	2.6	2.6	2.6	2.9	3.4	2.7	3.1	2.8	3.1	2.8	3.2	3.4	3.6	2.9	3.6	3.4	3.6	2.9	3.6	3.4	3.6	2.9	3.6				
1	3.3	3.4	3.0	3.9	3.9	3.9	4.3	4.3	4.0	4.3	4.9	5.1	4.6	5.4	4.9	6.1	5.1	5.9	4.9	6.1	5.1	5.9	4.9	6.1	5.1	5.9				
1	3.5	3.8	3.1	4.4	4.4	4.4	4.0	4.4	4.2	4.5	4.4	4.8	4.4	5.4	5.8	5.9	4.7	5.9	5.8	5.9	4.7	5.9	5.8	5.9	4.7	5.9				
2	4.3	5.6	4.4	6.0	6.0	6.0	6.1	7.0	6.1	7.7	7.7	8.3	7.8	8.4	11.1	11.3	10.8	11.8	11.1	11.3	10.8	11.8	11.1	11.3	10.8	11.8				
2	4.7	5.4	4.5	5.5	5.5	5.5	6.3	8.0	6.1	6.8	7.7	8.2	7.8	8.8	10.5	12.0	9.6	12.7	10.5	12.0	9.6	12.7	10.5	12.0	9.6	12.7				
4	6.3	7.7	6.0	8.1	8.1	8.1	8.7	10.0	9.2	10.1	12.5	12.9	14.0	14.5	17.3	25.7	27.9	28.0	17.3	25.7	27.9	28.0	17.3	25.7	27.9	28.0				
4	6.5	8.1	6.5	8.8	8.8	8.8	8.9	9.8	9.4	10.1	12.7	13.2	13.8	14.6	18.2	22.2	24.6	33.5	18.2	22.2	24.6	33.5	18.2	22.2	24.6	33.5				
8	8.9	11.0	8.3	13.7	13.7	13.7	13.7	15.7	14.2	17.8	19.4	22.6	22.3	26.7	46.3	50.7	35.1	82.0	46.3	50.7	35.1	82.0	46.3	50.7	35.1	82.0				
8	9.3	12.0	9.2	13.0	13.0	13.0	13.1	15.8	14.0	17.0	19.7	23.1	22.0	26.5	36.2	42.8	34.7	98.3	36.2	42.8	34.7	98.3	36.2	42.8	34.7	98.3				
16	15.3	18.2	17.9	24.9	24.9	24.9	23.6	27.3	24.2	35.1	37.1	45.1	40.5	66.9	56.8	132*	146*	195*	56.8	132*	146*	195*	56.8	132*	146*	195*				
16	14.7	20.0	17.8	24.9	24.9	24.9	23.4	28.5	24.2	32.2	36.4	46.0	40.4	57.9	92.5*	--	149*	143*	92.5*	--	149*	143*	92.5*	--	149*	143*				

*Severe edge attack

Table A2. GREAT BRITAIN
Corrosion Losses, grams - Exposed Area: approx. 24 in² (155 cm²)

Years	A242				A588				Copper Steel				Carbon Steel			
	30 S	30 N	90 S	90 N	30 S	30 N	90 S	90 N	30 S	30 N	90 S	90 N	30 S	30 N	90 S	90 N
URBAN-INDUSTRIAL SITE - STRATFORD																
0.5	4.4	5.7	4.5	5.9	4.9	6.2	4.9	6.7	--	--	--	--	4.7	5.4	5.1	6.3
1	5.0	7.3	5.0	7.0	5.7	8.0	5.8	8.0	6.3	8.0	6.3	9.3	7.6	9.2	7.0	8.6
6	7.9	22.2	9.0	23.0	12.1	25.0	13.6	27.0	14.0	24.0	15.3	25.0	18.0	28.3	17.0	28.1
8	8.1	23.8	--	25.5	14.0	27.7	--	32.2	15.8	26.1	--	30.8	20.4	31.7	--	33.8
16	11.1	33.6	12.8	37.8	16.8	38.7	17.9	48.3	20.5	40.5	24.0	44.1	29.4	48.9	30.1	50.4
16	10.3	35.1	11.8	40.4	--	--	--	--	--	--	--	--	26.4	48.9	25.8	48.4
RURAL SITE - AVON DAM																
0.5	2.8	3.1	2.4	2.6	3.2	2.0	2.4	2.6	3.4	3.5	2.8	3.1	3.4	3.4	2.7	3.2
6	8.8	11.7	8.0	10.3	11.8	14.0	10.0	14.0	13.1	15.0	12.9	13.0	14.7	14.8	13.3	14.2
8	9.1	12.0	8.7	11.4	12.2	14.9	11.5	13.8	14.3	15.2	13.3	14.2	15.4	16.5	15.1	14.7
16	--	19.8	15.1	19.2	21.6	25.7	20.9	25.1	25.2	27.1	26.3	--	28.0	28.9	27.8	27.6
MODERATE MARINE SITE - RYE																
1	4.2	5.8	4.2	5.9	4.3	5.9	3.9	5.4	5.6	6.8	5.3	5.3	6.3	7.8	6.6	8.1
1	4.2	--	4.0	--	4.0	--	4.0	--	5.8	--	5.8	--	7.0	--	6.6	--
6	12.1	17.8	11.0	20.0	12.8	18.7	12.0	9.7	22.2	29.0	18.9	34.0	19.0	34.2	22.7	41.1
8	12.1	20.2	13.6	21.7	13.7	20.7	12.3	21.1	20.1	32.8	19.2	34.8	22.3	39.0	23.2	46.1
16	22.2	37.9	20.9	38.9	23.8	37.2	21.4	37.4	36.7	62.9	34.4	61.6	51.4	90.7*	58.1	119*
16	22.2	39.7	21.2	39.9	23.9	40.9	23.5	42.1	36.6	69.4	36.4	69.1	47.1	117*	52.4	124*

*Severe edge attack

Table A3. BELGIUM
Corrosion Losses, grams - Exposed Area: approx. 24 in² (155 cm²)

Years	A242				A588				Copper Steel				Carbon Steel			
	30 S	30 N	90 S	90 N	30 S	30 N	90 S	90 N	30 S	30 N	90 S	90 N	30 S	30 N	90 S	90 N
URBAN-INDUSTRIAL SITE - LIEGE																
1	5.6	--	--	7.8	8.7	10.2	10.1	8.3	6.9	7.9	8.5	8.5	8.9	9.2	9.4	9.5
1	5.8	6.4	--	7.4	8.2	8.1	8.6	9.7	7.4	8.4	7.6	8.4	9.1	9.2	9.6	9.8
2	5.8	7.3	7.2	10.0	7.2	8.9	9.5	12.6	8.4	10.0	10.5	12.4	10.2	11.5	11.9	12.6
2	5.8	7.4	7.2	10.3	7.2	8.7	9.7	12.5	8.1	9.8	10.3	12.0	9.8	11.7	11.6	12.8
4	7.2	10.7	9.0	16.4	9.6	12.7	13.9	22.5	11.1	15.1	14.4	19.9	14.1	17.4	16.4	22.4
4	7.0	11.0	8.8	16.9	10.0	12.7	13.2	21.5	11.1	14.9	14.6	20.9	14.0	17.2	15.9	22.4
8	8.2	16.0	9.0	23.4	11.3	18.9	16.2	31.3	13.2	21.5	18.9	29.5	18.6	25.6	21.5	30.5
8	7.4	16.2	9.1	25.0	11.7	18.9	16.0	32.7	13.2	21.9	18.6	29.9	18.5	25.7	21.6	32.7
16	9.0	21.7	10.8	29.0	14.4	25.4	20.0	38.6	17.2	30.5	24.8	41.0	24.4	35.7	28.0	43.6
16	9.1	22.4	11.1	30.6	14.8	25.9	21.1	40.1	17.9	31.3	24.1	42.0	24.1	36.3	26.8	46.3
RURAL SITE - EUPEN																
0.5	4.1	4.0	3.1	2.8	4.2	4.7	4.0	3.8	--	--	--	--	--	4.2	4.0	3.6
0.5	4.1	4.1	3.2	3.1	4.5	4.2	4.0	4.1	--	--	--	--	--	4.4	4.0	3.7
2	4.1	5.0	4.4	6.0	5.5	6.4	6.1	7.0	--	--	--	--	--	8.1	6.7	7.5
2	3.8	5.0	4.5	5.9	5.0	6.4	6.3	6.8	--	--	--	--	--	8.0	7.0	7.1
4	5.6	7.9	6.9	9.0	7.8	10.2	9.2	11.3	--	--	--	--	10.4	11.9	10.5	12.0
4	5.3	7.9	7.1	9.3	7.9	10.1	9.5	11.5	--	--	--	--	10.5	12.2	10.3	11.8
8	7.3	10.7	8.8	12.8	10.4	14.0	12.4	15.5	--	--	--	--	14.0	17.6	14.5	17.7
8	7.2	10.5	8.9	12.7	10.5	14.1	--	15.6	--	--	--	--	14.7	17.3	14.9	17.6
16	11.3	16.8	13.4	19.4	16.2	22.4	20.0	24.8	--	--	--	--	25.5	27.8	26.0	30.1
16	11.4	16.5	13.8	19.6	16.0	22.0	20.0	24.9	--	--	--	--	24.8	28.1	24.9	30.7
MODERATE MARINE SITE - OSTENDE																
0.5	5.8	9.5	5.9	10.4	5.6	7.7	5.7	8.0	5.2	9.3	5.9	10.5	6.4	11.9	6.6	15.1
0.5	5.5	8.5	5.4	--	5.9	6.9	4.9	9.1	5.3	9.3	5.9	10.5	6.6	11.0	7.1	13.4
2	6.1	12.1	6.2	12.2	6.9	9.5	6.8	12.5	8.1	13.4	9.3	16.8	9.2	16.5	10.2	23.9
2	5.9	10.9	6.4	12.9	6.9	9.5	6.6	13.7	8.2	13.8	9.3	19.7	9.2	16.1	9.8	29.0
4	8.5	13.3	8.5	17.7	9.7	11.8	9.6	17.5	11.0	19.3	12.8	27.5	13.0	23.1	14.8	48.6
4	8.7	12.7	8.9	17.9	9.9	11.8	9.9	17.0	11.2	20.1	12.8	26.4	13.1	23.7	14.7	45.1
8	12.2	16.7	12.9	22.7	13.6	16.4	14.9	22.8	16.6	27.7	20.0	39.8	20.0	32.0	22.2	66.4
8	11.5	18.2	12.9	22.5	13.1	16.6	14.8	23.2	16.5	27.3	19.8	37.8	19.9	31.1	21.9	58.1
16	17.4	28.7	18.6	39.5	21.1	26.7	22.8	37.8	27.4	46.1	32.1	63.0	31.4	51.3	35.6	--
16	18.0	27.4	19.5	34.2	21.2	27.5	22.6	39.0	28.2	45.1	30.7	58.2	32.2	48.4	35.4	--

Table A4. JAPAN
Corrosion Losses, grams - Exposed Area: approx. 24 in² (155 cm²)

Years	A242				A588				Copper Steel				Carbon Steel			
	30 S	30 N	90 S	90 N	30 S	30 N	90 S	90 N	30 S	30 N	90 S	90 N	30 S	30 N	90 S	90 N
<u>URBAN-INDUSTRIAL SITE - KAWASAKI</u>																
1	4.7	4.9	5.5	5.7	6.0	6.6	7.3	7.6	6.5	6.5	6.6	6.3	9.3	10.8	9.5	10.4
1	4.8	4.8	6.0	6.4	6.3	6.5	7.6	8.3	6.2	6.9	7.2	7.2	8.5	10.3	9.2	11.8
2	5.6	6.3	7.6	7.7	7.9	8.6	10.1	10.0	8.6	8.9	10.4	8.8	10.6	12.6	11.9	13.1
2	6.3	6.0	8.3	8.7	7.5	8.0	12.0	11.6	8.0	8.4	10.4	10.2	11.4	13.1	13.2	14.5
4	6.8	8.3	8.0	8.4	10.1	11.7	13.7	13.5	10.2	11.8	11.7	10.8	14.3	16.4	14.6	16.7
4	6.2	6.7	8.2	9.3	9.6	10.4	14.0	12.2	10.5	11.8	11.6	11.6	17.3	17.2	14.2	15.6
8	7.9	9.1	8.9	8.9	13.7	--	15.2	15.9	12.9	--	14.8	13.4	15.9	--	20.6	18.6
8	9.2	9.3	10.4	9.9	12.0	12.6	16.7	17.2	14.5	14.3	11.2	16.0	24.5	27.9	21.9	23.2
<u>RURAL SITE - LAKE YAMANAKA</u>																
1	2.5	2.5	2.3	2.2	3.4	3.4	3.0	3.4	3.1	3.0	2.9	2.9	4.0	3.9	2.9	3.0
1	2.4	2.6	2.3	2.4	3.2	3.2	3.3	3.1	3.0	3.1	2.8	2.8	3.2	3.9	3.4	3.2
2	3.3	3.9	3.8	3.9	4.1	4.2	3.7	4.2	3.8	4.1	3.9	3.9	4.5	4.9	4.4	4.1
2	3.6	4.1	3.9	4.0	4.0	4.1	4.3	4.5	4.2	4.4	4.1	3.9	4.8	5.0	4.6	4.5
4	3.9	4.2	5.0	4.7	5.6	5.6	6.0	6.2	6.1	5.9	6.3	6.0	6.6	6.9	6.7	6.1
8	4.5	4.4	5.9	5.5	5.9	5.4	7.4	7.7	7.3	5.8	9.2	7.5	8.6	7.0	8.5	7.2
8	4.1	6.7	5.9	6.4	6.0	7.4	7.9	8.1	7.8	8.1	8.3	7.7	8.8	9.1	8.6	7.7
<u>MODERATE MARINE SITE - HIKARI</u>																
1	3.9	3.6	3.6	4.0	4.3	5.1	4.6	5.4	4.6	4.3	4.5	4.7	6.1	5.8	5.3	5.7
1	4.0	4.0	4.2	4.2	5.6	4.8	5.2	5.7	4.6	4.4	4.7	4.7	6.3	5.3	5.9	5.6
2	4.7	5.2	5.6	5.7	5.5	6.0	6.2	6.9	5.7	6.0	5.7	5.9	6.7	7.6	7.1	7.6
2	5.0	5.2	5.1	6.1	5.6	5.7	6.4	7.1	5.8	5.9	5.8	5.7	6.5	7.2	7.0	8.0
4	5.5	6.3	6.8	6.8	9.1	9.1	11.2	11.0	9.6	9.3	10.4	9.5	11.1	11.6	12.1	11.6
4	--	--	--	--	7.1	7.3	8.7	8.7	8.5	8.2	9.7	8.8	9.5	9.3	10.2	9.4
8	7.7	8.4	7.6	9.4	11.1	12.8	11.4	13.3	13.1	12.7	12.0	13.7	13.5	13.8	14.2	13.2
8	7.4	--	7.7	9.4	11.2	--	12.1	12.5	13.2	--	14.8	12.4	15.3	--	14.5	13.1

Table A5. FRANCE
Corrosion Losses, grams - Exposed Area: approx. 24 in² (155 cm²)

Years	A242				A588				Copper Steel				Carbon Steel			
	30 S	30 N	90 S	90 N	30 S	30 N	90 S	90 N	30 S	30 N	90 S	90 N	30 S	30 N	90 S	90 N
<u>URBAN-INDUSTRIAL SITE - SAINT DENIS</u>																
0.5	2.5	3.3	2.7	3.0	2.7	3.5	2.8	3.4	3.0	3.1	3.2	3.2	3.4	3.8	3.6	3.6
1	5.1	6.8	5.0	6.5	5.5	7.1	5.5	7.5	5.2	5.8	5.2	5.9	6.3	7.2	6.5	7.0
2	6.1	9.6	5.9	10.6	7.1	10.5	7.9	13.3	7.3	8.7	8.6	9.9	9.1	11.7	10.1	11.9
4	7.2	16.3	7.2	15.2	10.7	17.7	11.4	19.0	11.2	15.4	12.7	16.9	14.5	20.0	14.5	20.1
8	7.2	25.7	7.3	24.0	13.2	28.8	15.3	35.4	14.8	27.2	19.5	25.8	20.2	33.3	21.8	35.5
<u>MODERATE MARINE SITE - BIARRITZ</u>																
0.5	2.5	2.3	1.9	2.5	3.0	2.7	2.8	3.1	3.7	4.5	3.7	4.4	4.0	5.1	3.8	4.8
1	4.6	6.9	4.9	6.9	4.6	6.4	4.8	6.5	4.8	7.1	4.5	7.0	5.4	8.3	5.2	8.0
2	5.4	8.6	6.3	8.0	5.1	7.6	6.0	8.3	6.1	9.4	6.4	8.2	6.9	12.5	7.9	9.7
4	7.7	11.6	9.5	11.7	7.4	10.0	7.9	11.1	8.6	13.4	9.0	13.2	10.9	19.9	13.1	19.7
8	8.8	14.1	9.4	13.6	9.8	12.5	9.8	15.1	13.2	20.0	13.8	18.4	20.7	21.9	21.6	23.4

Table A6. SOUTH AFRICA
Corrosion Losses, grams - Exposed Area: approx. 24 in² (155 cm²)

Years	A242					A588					Copper Steel					Carbon Steel				
	30 S	30 N	20 S	20 N	90 N	30 S	30 N	20 S	20 N	90 N	30 S	30 N	20 S	20 N	90 N	30 S	30 N	20 S	20 N	90 N
	URBAN-INDUSTRIAL SITE - PRETORIA WORKS										RURAL SITE - EAST OF PRETORIA									
0.5	1.2	1.2	1.3	1.3	1.3	1.3	1.4	1.3	1.4	1.3	1.2	1.2	1.2	1.3	1.3	1.4	1.6	1.4	1.5	1.5
0.5	1.2	1.2	1.3	1.2	1.2	1.2	1.3	1.3	1.4	1.3	1.2	1.2	1.3	1.2	1.2	1.4	1.6	1.4	1.4	1.4
1	1.3	1.2	1.3	1.1	1.1	1.4	1.2	1.5	1.4	1.4	1.3	1.4	1.4	1.4	1.4	1.6	1.6	1.5	1.6	1.6
1	1.3	1.2	1.4	1.2	1.2	1.3	1.3	1.6	1.4	1.5	1.4	1.4	1.4	1.4	1.4	1.6	1.5	1.4	1.7	1.7
2	1.7	1.5	1.5	1.6	1.6	1.9	1.8	1.9	2.0	2.2	2.1	2.1	2.1	2.2	2.2	2.5	2.3	2.4	2.5	2.5
4	2.1	1.8	2.3	2.2	2.2	2.6	2.3	3.4	3.3	3.6	3.2	4.2	4.2	3.9	4.1	4.1	3.7	4.5	4.4	4.4
8	2.5	2.0	2.8	3.0	3.0	3.1	3.0	5.0	4.0	5.0	4.0	6.2	5.0	5.0	6.0	6.0	5.0	6.4	6.0	6.0
16	2.6	2.2	3.0	2.7	2.7	3.9	3.0	5.0	4.4	5.9	4.9	7.7	6.1	6.1	7.2	5.6	8.7	6.6	6.6	6.6
0.5	1.0	1.0	1.0	0.9	0.9	0.9	1.0	0.8	0.9	0.9	0.8	0.8	0.8	0.8	0.9	0.9	0.9	0.8	0.8	0.8
0.5	1.0	0.9	0.9	0.9	0.9	1.0	0.9	0.8	0.9	0.9	0.9	0.8	0.8	0.8	0.9	0.9	0.9	0.8	0.8	0.8
1	1.3	1.2	1.2	1.2	1.2	1.3	1.3	1.3	1.2	1.5	1.5	1.4	1.3	1.3	1.6	1.5	1.5	1.3	1.3	1.3
1	1.3	1.2	1.3	1.3	1.3	1.3	1.2	1.3	1.3	1.5	1.4	1.3	1.4	1.4	1.5	1.5	1.5	1.4	1.4	1.4
2	1.8	1.5	1.8	1.9	1.9	2.0	1.8	2.0	2.1	2.5	2.3	2.1	2.2	2.2	2.6	2.4	2.2	2.2	2.5	2.5
4	2.2	2.1	2.6	2.9	2.9	2.8	2.6	3.3	3.5	3.8	4.5	3.8	4.1	4.1	3.9	3.7	3.9	4.2	4.2	4.2
8	2.8	2.9	3.6	3.6	3.6	4.0	3.4	5.0	5.0	6.0	5.1	6.0	6.0	6.0	6.4	5.4	6.0	7.0	7.0	7.0
16	3.1	3.0	4.3	3.3	3.3	4.7	4.2	6.1	5.5	6.4	6.0	7.4	7.3	7.3	7.0	6.8	8.1	8.2	8.2	8.2
MODERATE MARINE SITE - KWAZULU																				
0.5	3.3	4.1	3.9	4.9	4.9	3.0	3.6	3.2	4.4	3.7	3.2	3.4	3.0	3.0	5.0	4.1	4.5	3.7	3.7	3.7
0.5	2.4	2.4	2.2	2.4	2.4	3.1	2.5	2.8	2.7	3.7	3.2	3.3	3.2	3.2	5.1	4.0	4.5	3.8	3.8	3.8
1	3.9	3.1	3.4	3.7	3.7	4.0	3.4	3.7	3.6	5.7	4.4	5.0	4.3	4.3	9.9	5.9	6.6	5.6	5.6	5.6
1	3.7	3.1	3.6	3.7	3.7	4.2	3.4	3.9	3.4	5.6	4.4	5.0	4.6	4.6	8.2	6.3	6.6	5.6	5.6	5.6
2	4.7	4.0	4.4	4.5	4.5	4.7	4.6	5.0	4.7	8.0	6.1	6.9	6.1	6.1	11.0	9.7	8.9	9.0	9.0	9.0
4	7.3	6.0	6.9	7.3	7.3	9.3	7.4	8.3	8.5	14.5	10.7	13.5	14.1	14.1	50.4	21.4	21.0	39.7	39.7	39.7
8	11.1	8.7	11.0	13.2	13.2	34.4	12.0	14.0	16.0	28.2	18.0	32.0	76.0	76.0	351.0	87.1	218.4	137.1	137.1	137.1
16	16.7	13.1	15.4	19.8	19.8	26.2	19.9	23.2	28.5	39.1	30.7	46.8	182*	182*	--	--	--	--	--	--

*Severe edge attack

Table A7. SWEDEN
Corrosion Losses, grams - Exposed Area: approx. 24 in² (155 cm²)

Years	A242				A588				Copper Steel				Carbon Steel			
	30 S	30 N	90 S	90 N	30 S	30 N	90 S	90 N	30 S	30 N	90 S	90 N	30 S	30 N	90 S	90 N
<u>URBAN-INDUSTRIAL SITE - STOCKHOLM</u>																
1	4.0	4.8	3.8	5.0	4.6	6.0	4.2	5.5	4.5	5.7	4.2	6.2	5.6	7.0	4.9	6.4
1	4.2	4.8	4.0	5.0	4.9	5.4	4.3	5.6	5.4	7.0	4.5	6.0	4.5	5.6	4.5	5.3
2	6.6	5.5	7.2	5.7	7.1	6.9	8.2	6.6	8.9	7.3	9.4	7.1	10.4	7.7	9.9	7.1
2	6.5	5.6	7.1	5.6	7.4	6.7	6.4	6.7	8.7	7.7	9.2	7.2	10.3	8.8	9.4	7.8
4	9.1	8.9	9.6	9.2	11.4	11.4	11.7	12.3	14.9	12.2	10.9	12.8	12.1	14.0	11.8	13.8
4	8.9	9.1	9.3	9.9	11.4	10.6	11.7	11.9	10.7	12.1	11.4	12.5	12.4	13.9	12.3	14.1
8	11.4	14.5	12.3	17.7	16.0	17.6	15.8	21.6	15.0	17.6	16.3	19.8	18.0	19.5	16.3	21.0
8	11.6	13.1	13.0	18.3	16.0	16.4	16.3	21.7	15.0	17.7	16.4	20.3	18.0	19.0	18.3	20.6
16	12.7	17.9	13.8	22.4	19.3	23.0	19.5	29.2	20.8	23.0	22.9	26.4	22.5	25.5	22.9	28.6
16	12.8	17.8	14.4	22.5	18.8	22.6	19.8	29.1	20.1	23.6	23.5	26.6	23.6	25.5	24.1	27.7
<u>RURAL SITE - RYDA KUNGSGARD</u>																
1	2.0	1.8	1.9	1.7	2.3	2.2	2.2	2.0	2.2	2.2	2.2	1.8	2.3	2.1	2.4	1.8
1	2.0	1.9	1.8	1.8	2.4	2.1	2.1	1.9	2.1	2.0	1.9	1.7	2.0	1.8	2.0	1.6
2	2.6	2.8	2.7	2.5	3.2	3.2	3.2	3.2	3.4	3.2	3.0	3.0	3.2	3.2	3.2	3.2
2	2.6	2.8	2.8	2.6	3.1	3.3	3.2	3.1	3.2	3.1	3.1	3.1	3.5	3.1	3.4	3.3
4	3.9	4.1	3.9	4.0	4.7	5.0	4.7	4.7	4.5	4.4	4.8	4.4	4.8	4.8	5.2	4.6
4	3.9	3.9	4.0	4.1	4.5	4.7	4.5	4.7	4.6	4.6	4.8	4.4	4.6	4.9	5.1	4.7
8	5.0	6.0	5.0	6.0	6.0	7.0	6.4	7.2	6.1	7.0	7.2	7.1	7.0	7.0	8.0	7.2
8	5.0	5.4	5.0	6.0	6.0	7.0	6.5	7.4	6.0	7.0	7.0	7.2	7.0	7.4	8.0	8.0
16	6.1	6.9	6.8	8.6	7.9	9.2	9.4	11.7	8.5	8.1	11.7	11.0	8.8	9.1	11.4	11.1
16	6.2	7.5	6.4	8.4	8.1	9.5	9.2	11.2	9.0	10.4	11.9	11.7	9.6	10.1	12.3	12.5
<u>MODERATE MARINE SITE - BOHUS MALMON</u>																
1	3.1	3.9	3.1	3.9	3.4	4.3	3.4	4.3	4.1	4.1	3.8	3.9	4.3	4.7	4.0	4.9
1	3.3	4.0	3.4	4.5	3.4	4.2	3.3	4.3	4.2	4.9	4.2	4.7	3.9	4.4	3.9	4.6
2	3.8	5.1	4.4	5.1	4.2	4.9	4.0	4.8	4.7	6.0	4.6	5.6	5.4	6.9	5.1	5.8
2	4.0	5.4	4.6	5.5	4.1	5.2	4.5	5.2	5.0	6.2	4.9	5.6	5.3	6.8	5.1	6.1
4	5.8	8.0	5.5	7.4	6.1	7.9	5.5	7.8	6.5	10.2	7.2	9.2	8.1	11.1	7.6	10.0
4	5.8	7.6	5.5	7.8	6.4	8.0	5.7	8.2	8.2	10.1	7.3	10.4	8.4	10.7	7.8	10.6
8	7.6	9.3	7.0	10.5	8.5	11.1	7.7	11.6	12.1	15.1	10.7	14.5	11.7	15.8	11.2	16.4
8	7.5	9.7	7.1	10.7	8.6	11.4	7.7	12.2	11.5	15.1	10.8	15.2	12.1	15.9	11.0	15.6
16	11.1	15.3	13.8	16.3	13.6	18.9	14.2	19.2	19.7	26.2	18.7	25.7	21.2	28.2	19.8	27.9
16	9.1	17.6	12.7	16.6	13.8	19.3	12.9	20.0	19.8	26.7	20.0	27.8	20.4	29.0	20.9	29.1

Table A8. GERMANY
Corrosion Losses, grams - Exposed Area: approx. 24 in² (155 cm²)

Years	A242				A588				Copper Steel				Carbon Steel			
	30 S	30 N	90 S	90 N	30 S	30 N	90 S	90 N	30 S	30 N	90 S	90 N	30 S	30 N	90 S	90 N
<u>INDUSTRIAL SITE - OBERHAUSEN</u>																
0.5	--	--	--	2.6	--	--	--	2.7	--	--	--	1.7	--	--	--	2.7
0.5	--	--	--	2.2	--	--	--	2.7	--	--	--	2.3	--	--	--	2.7
1	--	--	4.7	6.1	--	--	5.1	6.8	--	--	5.1	6.6	--	--	7.6	8.5
1	--	--	4.1	5.3	--	--	4.6	6.1	--	--	4.7	5.3	--	--	7.1	6.9
2	--	--	5.6	8.6	--	--	7.4	11.1	--	--	7.8	9.8	--	--	11.2	12.8
2	--	--	6.5	8.6	--	--	7.4	10.2	--	--	8.7	9.5	--	--	11.3	13.4
4	--	--	8.1	15.4	--	--	11.0	18.1	--	--	11.3	14.7	--	--	16.6	23.8
4	--	--	8.9	15.9	--	--	10.5	17.8	--	--	12.0	15.9	--	--	16.8	24.4
8	--	--	14.3	29.4	--	--	17.0	32.3	--	--	17.7	26.7	--	--	28.5	41.5
8	--	--	11.0	18.8	--	--	17.3	32.3	--	--	19.6	27.0	--	--	26.1	35.1
16	--	--	13.9	31.8	--	--	21.7	48.1	--	--	24.7	40.7	--	--	33.8	49.4
16	--	--	14.6	37.3	--	--	23.6	50.1	--	--	25.7	42.5	--	--	35.4	50.5
<u>URBAN-INDUSTRIAL SITE - ESSEN FRINTROP</u>																
1	--	--	5.2	5.7	--	--	6.2	7.2	--	--	7.1	5.8	--	--	8.4	8.3
1	--	--	4.9	5.7	--	--	6.2	6.5	--	--	6.5	5.8	--	--	7.6	7.6
2	--	--	6.7	9.9	--	--	7.4	11.1	--	--	8.3	10.4	--	--	11.9	12.7
2	--	--	6.4	8.9	--	--	8.7	10.7	--	--	9.8	9.7	--	--	11.0	11.7
4	--	--	10.5	16.3	--	--	12.1	17.2	--	--	14.3	15.7	--	--	17.9	20.9
4	--	--	10.3	16.6	--	--	12.2	18.1	--	--	14.8	15.7	--	--	19.1	21.7
8	--	--	16.5	30.0	--	--	19.5	32.0	--	--	21.8	26.1	--	--	30.1	37.2
8	--	--	10.1	24.8	--	--	20.1	31.5	--	--	21.5	27.8	--	--	27.2	36.7

The Effects of Acid Deposition on The Atmospheric Corrosion Behavior of Structural Materials in California

F. Mansfeld

Corrosion and Environmental Effects Laboratory
Department of Materials Science and Engineering
University of Southern California
Los Angeles, CA 90089-0241, USA

H. Xiao

Corrosion and Environmental Effects Laboratory
Department of Materials Science and Engineering
University of Southern California
Los Angeles, CA 90089-0241, USA

R. C. Henry

Department of Environmental Engineering
University of Southern California
Los Angeles, CA 90089-2531, USA

Abstract

Several materials of economic significance have been exposed at three sites in Southern California (Burbank, Long Beach and Upland) and at a background site in Central California (Salinas) during the time between March 1986 and August 1990. These materials were galvanized steel, nickel, aluminum, two types of flat latex exterior house paint and nylon fabric. Corrosion damage was determined by weight loss for galvanized steel, nickel, aluminum and the two paints. For the nylon fabric the loss of breaking strength was used as a measure of corrosion damage. Corrosion rates were very low at all four locations. For galvanized steel, nickel, and aluminum corrosion rates were higher in the summer than in the winter, which is opposite to the time dependence observed at most other locations worldwide. It is very likely that the time dependence of atmospheric corrosion rates observed in Southern California is due to photochemically produced acids, particularly HNO_3 , for which concentrations peak during the summer months. However, reliable long term HNO_3 monitoring data were not available for the four test sites during the study.

Key terms: atmospheric corrosion, galvanized steel, nickel, polymer coatings, aluminum, nylon, atmospheric data, weight loss.

Introduction

The Kapiloff Acid Deposition Act of 1982 requires the California Air Resources Board (CARB) to assess the economic impact of acid deposition upon materials as part of a comprehensive research program to determine the nature, extent and potential effects

of acid deposition in California. Field exposure tests have been conducted with the ultimate goal to determine damage functions that could be used in an economic analysis of the costs of materials damage caused by acid deposition in California. Most of these exposure tests were concluded in 1988 (1), preliminary results have been presented elsewhere (2,3). The role of acid fog has also been addressed in field exposure tests (4). At the end of these studies, some samples were left at the test sites. These samples were removed during the summer of 1990, damage measurements were made and the total data set collected during the field studies (not including the acid fog study (4)) was analyzed. The experimental results and the conclusions of the data analysis will be presented here. The results of a multivariate statistical analysis used to estimate the relationships between atmospheric corrosion rates, air quality and meteorological parameters, which had been collected by CARB at all test sites, will be described elsewhere (5,6).

Experimental Approach

Sample preparation and exposure procedures and methods of damage assessment were based on the guidelines in ASTM G 50 "Standard Practice for Conducting Atmospheric Corrosion Tests on Metals," ASTM G 1 "Standard Practice for Preparing, Cleaning and Evaluating Corrosion Test Specimens," ASTM D 1682 "Breaking Load and Elongation of Textile Fabrics" and specific material procedures developed in U. S. Environmental Protection Agency (EPA) programs.

Materials

The choice of the materials exposed in this study was based primarily on the potential economic consequences of damage to materials susceptible to degradation due to acid deposition. The materials were chosen based on the extent of usage, susceptibility to damage due to acid precipitation, costs of materials, maintenance, repair, and replacement costs (7). Considerations also included limitations due to available field exposure times, sample size and methods of damage assessment. The following materials were exposed: zinc (as galvanized steel) (Zn), nickel (Ni), flat latex exterior house paint with carbonate extender (on stainless steel) (H-C), flat latex exterior house paint without carbonate extender (on stainless steel) (L-C), aluminum (commercially pure) (Al) and nylon fabric (Fabric). Zn, Ni, H-C and L-C were first exposed between February and March 1986, the other two materials were added in July 1987.

Exposure Conditions and Test Sites

Four tests sites were selected for this project, three of which are located in the South Coast Air Basin (Burbank (BR), Long Beach (LB) and Upland (UP)), while the fourth (Salinas (SL) in Northern California) serves as a relatively unpolluted background site. The annual average SO₂ concentration for Salinas has been reported as 0.2 ppb, while for the three test sites in Southern California values between 2.1 ppb (Upland)

and 9.8 ppb (Long Beach) have been reported (1,2).

Duplicate samples for each exposure period were mounted per ASTM G 50 on exposure racks inclined at 30° to the horizontal and facing south. The samples were held in place by porcelain insulators in order to avoid galvanic corrosion between the samples and the rack material (galvanized steel). For the concrete and the nylon fabric samples, somewhat different mounting procedures were used (3,4). All materials were at least 1.2 m above the ground. All test racks were situated above gray-white crushed-rock-covered roofing paper or gravel-covered ground.

Samples first exposed in December 1987 or later remained exposed for periods of nine months or longer. Eight sets of galvanized steel, nickel and two paints on stainless steel carbonate were first exposed between February 1986 and September 1989. Four sets of aluminum and nylon fabric were exposed between July 1987 and September 1989.

Damage Measurements

The degree of damage after a given exposure period was determined by weight loss measurements for the metals and the paint on stainless steel and by strength loss for the nylon fabric. Since the stainless steel substrate can be assumed to experience no weight change, the measured weight loss can be attributed to the weight loss of the paint. For Al, weight loss data are only available for samples collected after October 1987.

The weight loss, W , is determined as the difference of the weight of the unexposed sample $w(0)$ and the weight after exposure $w(t)$ for a time period t corrected for the weight loss, w_b , of an unexposed sample in the descaling solution which is used for the removal of corrosion products:

$$W = w(0) - w(t) + w_b \quad (1).$$

All samples were first photographed when they were returned from field exposure. They were then rinsed in deionized water and immersed in a descaling solution which was material specific. Finally the samples were rinsed, dried, equilibrated and weighed. A detailed account of these procedures is given elsewhere (1).

Experimental Results and Discussion

In the following, the damage data for the period between the first exposure in February 1986 and the removal of the last samples in August 1990 will be discussed.

Damage Data

The experimental weight loss data have been inspected by plotting the weight loss (or loss of breaking strength for nylon) as a function of exposure time for the four test

sites - Burbank (BR), Long Beach (LB), Upland (UP) and Salinas (SL). The nylon samples which were collected in the summer of 1990 could not be analyzed due to excessive degradation or total destruction.

In the following, the results obtained for all sets of a given material will be shown for Burbank. In addition, the results for the first set of a material will be plotted for all four sites. A survey of the experimental data for all test sites and sets of material will be presented as plots of log W (weight loss) vs log t (exposure time).

Galvanized Steel

Fig. 1 is an example of weight loss data obtained for all sets of a given material at a given test site as a function of exposure time. The data in Fig. 1 are those for the eight sets of galvanized steel samples exposed at Burbank. The most significant result is the almost zero value of corrosion rates in the winter for the time period starting in October/November and ending in February/March. This observation is contrary to the results obtained in other parts of the world, where corrosion rates are usually higher in the winter due to the increased SO₂ levels (8). The higher corrosion rates observed in Southern California in the summer might be due to the higher levels of HNO₃ which is produced by photochemical processes (1,5,6). An explanation of the close to zero corrosion rates in the winter is difficult. Rain in the South Coast Air Basin is not very acidic (pH about 5) and can have a cleaning action which would reduce corrosion rates observed in the rainy season between November and March. However, other factors must be involved in producing this quite unusual phenomenon.

For galvanized steel and nickel, average corrosion rates are lower than 1 µm/year, which characterizes the atmosphere in the South Coast Basin as rural according to the ASTM classification. Figure 2 is a graph of the weight loss data for the first set of galvanized steel which was exposed at the four test sites in February and March 1986. Very low corrosion rates were observed in the fall and winter periods of the first year. For the maximum exposure period of 4.5 years, the largest total corrosion loss was observed at Long Beach followed by Burbank and then Upland. The smallest corrosion loss was observed at Salinas which serves as background site.

In order to estimate the time dependence of corrosion rates and at the same time survey the quality of the entire data set, the weight loss data were also plotted as log W vs log t. This type of data display is common in studies of atmospheric corrosion (8), where it is assumed that the weight loss (W) depends on the exposure time (t) in the form:

$$W = a t^b \quad (2a)$$

From Eq.2a the corrosion rate r_{corr} can be calculated as:

$$r_{corr} = (1/A) (dW/dt) = (ab/A) t^{b-1} = ct^{b-1} \quad (2b).$$

where A is the sample area.

In Equation 2, a is a characteristic parameter for the corrosivity of the test site for a certain material and b is a parameter which depends on the corrosion mechanism. If diffusion of a corrosive species is the rate determining step, $b = 0.5$, for a charge transfer controlled process, $b = 1.0$ (8). A classification of different test sites based on their corrosivity for a given material can be made based on the experimental values of the parameter a , which is defined as the weight loss after one year (Eq. 2a) or the parameter c , which is defined as the corrosion rate (in $\text{g/m}^2\cdot\text{year}$) after one year. Plots of $\log W$ vs $\log t$ according to Equation 2a are shown in Figure 3a for all eight sets of galvanized steel at Burbank. Most data points fall on the straight line, which was determined by statistical analysis. The two data points with very low weight loss during the winter periods were excluded from the analysis. These very low weight loss data points correspond to the third set for exposure between October 1986 and January 1987 and the sixth set for exposure between October 1987 and January 1988. The slope of the straight line in Figure 3a is 0.744, which suggests mixed diffusion and charge transfer control. Agreement with Eq. 2 was also observed for galvanized steel at Salinas (Figure 3b), Long Beach (Figure 3c) and Upland (Figure 3d) with b ranging from 0.58 at Salinas to 0.95 at Upland (Table 1). This result suggests a gradual change from diffusion control due to the presence of protective corrosion product layers at the background site to charge transfer control at more corrosive test sites on surfaces which were either bare or were not covered with layers which reduce diffusion of corrosive species to the metal surface. A certain compensation effect can be observed in Fig. 3, which leads to similar corrosion rates after about one year for cases, where low values of the slope b are accompanied by high values of the value a and vice versa.

Nickel

The results obtained for the weight loss of nickel are shown in Fig. 4 - 6. The plots for all eight sets at Burbank (Fig. 4) are very similar to those for galvanized steel in Fig. 1 with close to zero corrosion rates in the winters of 1986 and 1987. This unusual behavior is also detected in Fig. 5 for first set of nickel at the four test sites. After exposure for 4.5 years, corrosion losses were the highest at Burbank and Long Beach followed by Upland and Salinas for which the lowest corrosion rates were observed. In the $\log W$ vs $\log t$ plots in Fig. 6 slopes exceeding 0.9 were determined for Upland, Long Beach and Salinas, while the slope for Burbank was $b = 0.744$ (Table 1).

Aluminum

Fewer data points are available for Al (Fig. 7 - 9), which makes the analysis of the $\log W$ vs $\log t$ plots (Fig. 9) more difficult. However, close to zero corrosion rates in the winter of the first year of exposure are obvious in Fig. 7 and 8. Due to the availability of fewer data points, the analysis of the weight loss data for Al and the resulting values of a and b in Table 1 are less reliable.

Paint on Stainless Steel

The two paints on stainless steel show a corrosion behavior which is quite similar to that observed for the metals insofar as most weight loss data points fall on a straight line in the $\log W$ vs $\log t$ plots. For the L-C paint some evidence can be found from an inspection of Fig. 10 and 11 that corrosion rates were close to zero in the winter months of 1986 and 1987. At the end of the test, the weight loss for the samples, which had been exposed for 4.5 years, was about the same at Burbank, Long Beach and Upland, but much less at the background site in Salinas (Fig. 11). The slopes of the $\log W$ vs $\log t$ lines for the L-C paint are between 0.5 and 0.8, indicating that diffusion of corrosive species plays a larger role for the paints than for the metals (Fig. 12 a-d). For the H-C paint on stainless steel, a decrease of corrosion rates was also observed in the winter (Fig. 13 and 14). The weight loss for the first set at the end of the final exposure period decreased in the order Long Beach > Burbank > Upland > Salinas. In general, the weight loss for the H-C paint was higher than that for the L-C paint. The dependence of weight loss of H-C paint on time is similar to that for the L-C paint, indicating a mixed diffusion/charge transfer controlled corrosion process (Fig. 15).

A survey of the $\log W$ vs $\log t$ plots for galvanized steel, nickel and the two paints on stainless steel shows that the data usually fall close to the straight line based on Eq. 2a and can therefore be considered to be quite reliable. The data for Al, for which fewer data points are available, show more scatter. Very low corrosion rates were observed for the Al samples of the third and the sixth set exposed at Burbank, Long Beach and Upland. Table 1 gives a summary of the a and b values for all materials exposed in this program. In Table 1, a is defined as the weight loss after one year, according to Equation 2a. The highest values of a for galvanized steel, Al and H-C paint were observed at Long Beach. For Ni and L-C paint a had the highest values at Burbank and Long Beach. Care must be taken in the interpretation of the data in Table 1, since apparently a compensation effect occurs with low values of the slope b coinciding with high values of a as mentioned above. This result makes extrapolation of the experimental data to longer exposure times than 4.5 years difficult.

An interesting result of this study is the fact that the loss of breaking strength of nylon fabrics follows very similar trends as the weight loss for the other samples. Fig. 16 summarizes all results obtained for the two sets at the four sites. The very low rates of degradation observed for the metals and the house paints during the fall and winter can also be seen in Fig. 16 for the nylon fabric between November 1987 and April 1988. It should be noted that this effect is clearly evident for the nylon samples of the first set exposed at Salinas, where apparently no further loss of strength occurred during this time. On the other hand, for exposure at Long Beach, the loss of strength increased from 40% to 60% during the same time period. After one year, the loss of breaking strength of the first set was the highest at Long Beach followed by Burbank and Upland which had very similar results. By far the lowest damage was observed at the background site Salinas.

Summary and Conclusions

Exposure tests have been carried out between March 1986 and August 1990 at three test sites in Southern California (Burbank, Long Beach and Upland) and at a background site in Central California (Salinas). The materials investigated in this study were chosen based on their economic importance and included galvanized steel, nickel, aluminum, two types of flat latex exterior house paint, nylon fabric, polyethylene and concrete.

Corrosion rates were very low at all four test sites. Using galvanized steel, which has been employed as a "standard material" in most atmospheric corrosion tests, a relative measure of the corrosivity of the four test sites can be estimated. The average corrosion rate at the three sites in Southern California was $7.0 \text{ mg/m}^2\cdot\text{day}$ ($2.56 \text{ g/m}^2\cdot\text{year}$) or $0.36 \text{ }\mu\text{m/year}$, which is a very low value usually observed only at "clean" sites (8). For comparison, corrosion rates for pure zinc determined in the program ISO CORRAG sponsored by the International Standards Organization (ISO) ranged from 1.6 to $2.0 \text{ }\mu\text{m/year}$ for test sites at Kure Beach, NC, Newark Kearny, NJ and Point Reyes, CA (9). At a test site in Los Angeles, CA (University of Southern California (USC)) an average annual corrosion rate over a four year period of $1.15 \text{ }\mu\text{m/year}$ was determined between March 1987 and March 1991 (9). For Al, for which fewer data points were available, an average corrosion rate of $0.42 \text{ }\mu\text{m/year}$ was determined in the study discussed here. This result agrees well with the average corrosion rates between 0.45 and $0.61 \text{ }\mu\text{m/year}$ measured at USC in the ISO CORRAG study (9). It is interesting to note that corrosion rates determined at the other three test sites in the USA were lower (0.16 - $0.29 \text{ }\mu\text{m/year}$) than those measured at the test sites in the South Coast Air Basin. Obviously, the atmospheric pollutants which cause higher corrosion rates for Al at the test sites in Southern California than at other sites in the USA do not accelerate corrosion rates of zinc or galvanized steel.

Closer analysis of the time dependence of corrosion rates for galvanized steel, nickel and aluminum reveals unusual trends insofar as corrosion rates are higher in the summer months than in the winter months. In most published exposure studies the opposite behavior has been observed with corrosion rates being higher in the winter when SO_2 concentrations are higher. In fact, a review of damage functions for zinc and galvanized steel has shown that corrosion rates have been correlated only with the SO_2 concentration or with SO_2 concentration and RH or time-of-wetness (8). Clearly such damage functions cannot be used to explain the time dependence of the corrosion rate data determined at the test sites used in this project, where SO_2 concentrations are very low. It is very likely that the higher corrosion rates observed in the summer are due to increased levels of photochemically formed acidic gases - HNO_3 vapor and perhaps also HCl vapor and organic acids. However, valid data for these pollutants were not available. In the winter, corrosion rates for galvanized steel and nickel were very low, which could be due to the low SO_2 concentration, the cleaning effect of rain and other factors which could not be determined in this study.

Acknowledgement

The work described here has been supported by the California Air Resources Board (CARB) under Contracts No. A4-110-32, A5-137-32 and A932-113. The authors acknowledge many helpful discussions with the Project Officers M. Ahuja and M. Muller. Most of the earlier weight loss data were determined by R. Hillstead of the Environmental Monitoring and Services (EMS) Group of Combustion Engineering, Inc.

References

1. R. Vijayakumar, F. Mansfeld and R. Henry, "Investigation of the Effects of Acid Deposition on Materials", Final Report, CARB Contract Nos. A4-110-32 and A5-137-32, October 1989.
2. F. Mansfeld and R. Vijayakumar, *Corros. Sci.* 28, 939 (1988)
3. F. Mansfeld and R. Vijayakumar, "Corrosion Damage due to Acid Deposition in Southern California", APCA'88, June 1988, paper No. 1514
4. F. Mansfeld, R. Henry and R. Vijayakumar, "The Effects of Acid Fog and Dew on Materials", Final Report, CARB Contract No. A4-138-32, October 1989
5. F. Mansfeld and R. C. Henry, "Effects of Acid Deposition on Materials in California", Final Report, CARB Contract No. A932-113, March 1993
6. R. Henry and F. Mansfeld, in preparation
7. Y. A. Horie, A. Shrope and R. Ellefsen, "Development of an Inventory of Materials Potentially Sensitive to Ambient Atmospheric Acidity in the South Coast Air Basin", Final Report, CARB Contract No. A6-079-32, March 1989
8. V. Kucera and E. Mattson, "Atmospheric Corrosion", in "Corrosion Mechanisms", F. Mansfeld, editor, M. Dekker, 1986
9. S. W. Dean, "ISO CORRAG Collaborative Exposure Program, Fourth Exposure Report on the USA Program", Air Products and Chemicals, Inc., December 1992

Table 1. a & b values for all materials at all sites

	Zn	Ni	Al	H-C	L-C
a	BR	81.5	77.3	29.2	123.7
	LB	107.9	76.9	43.6	135.8
	UP	60.9	48.4	17.1	106.3
	SL	82.8	25.1	38.6	86.4
b	BR	0.744	0.744	1.290	0.801
	LB	0.866	0.932	1.190	0.631
	UP	0.949	0.947	1.012	0.782
	SL	0.580	0.917	0.899	0.565
					0.640
					0.738
					0.801
					0.503

a is the weight loss (in mg) after one year;
b is a dimensionless parameter.

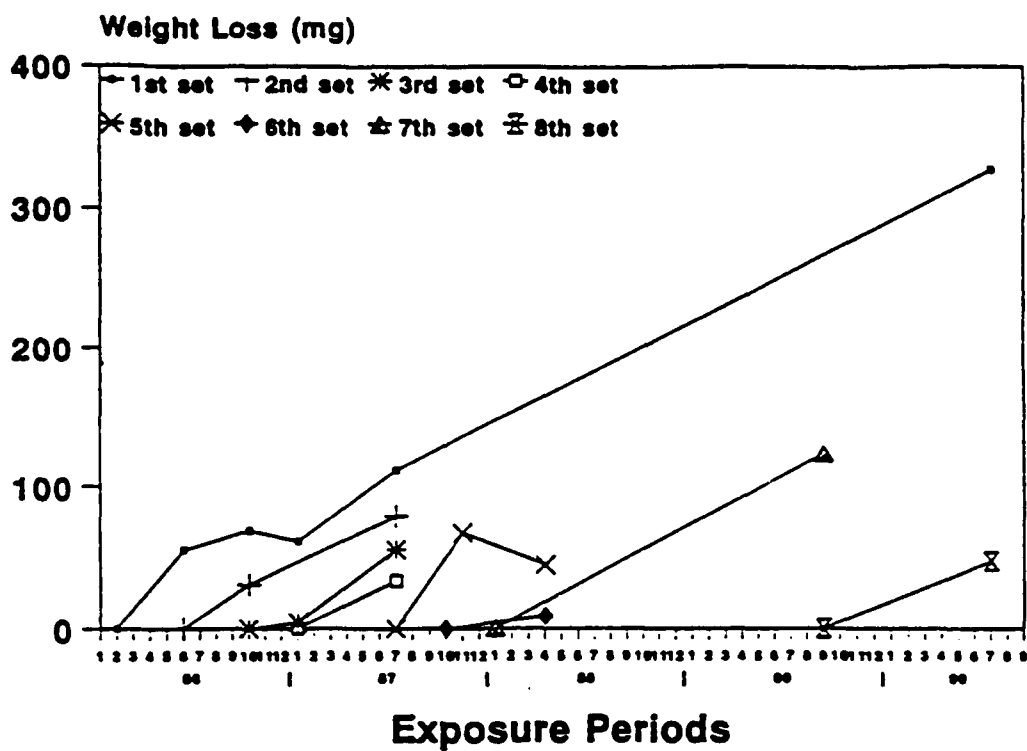


Figure 1. Weight loss for eight sets of galvanized steel as a function of exposure time at Burbank.

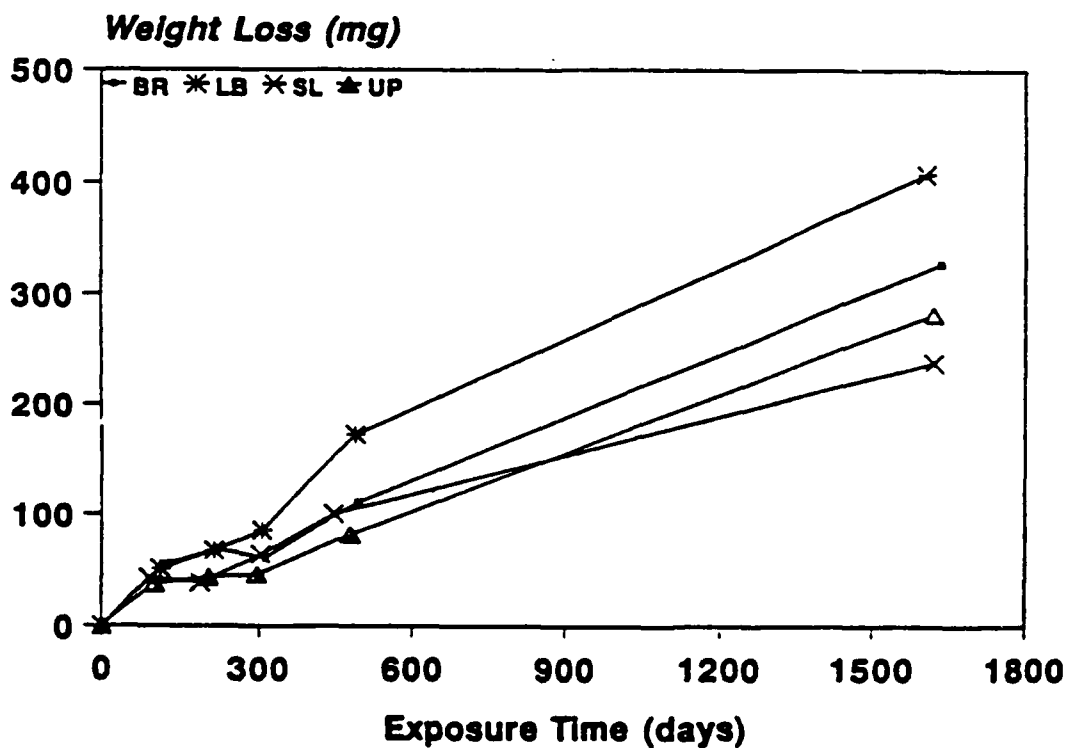


Figure 2. Weight loss for the first set of galvanized steel as a function of exposure time at the four test sites.

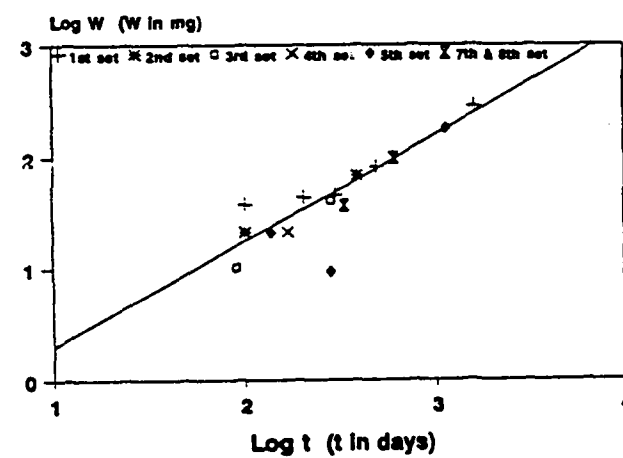
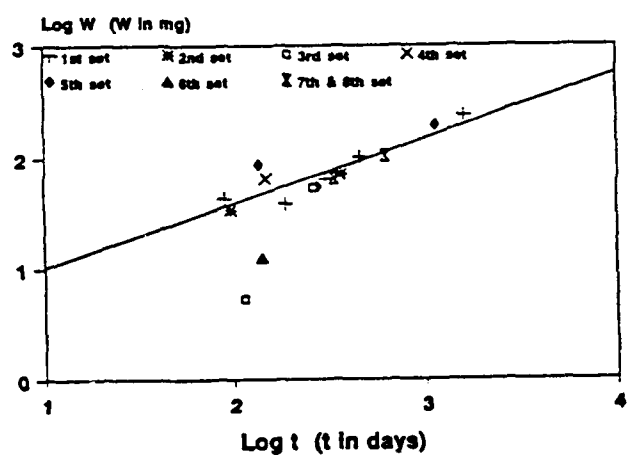
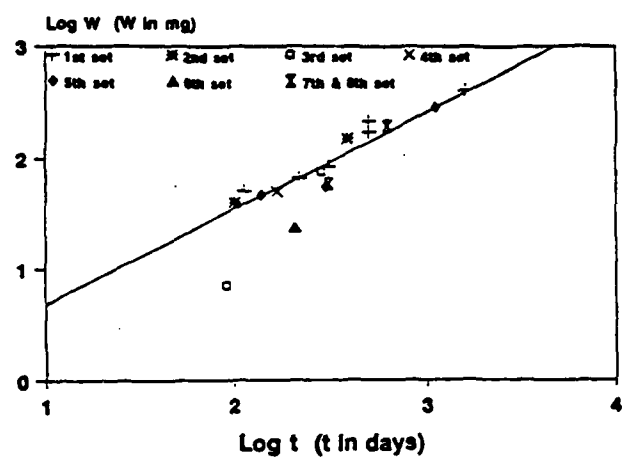
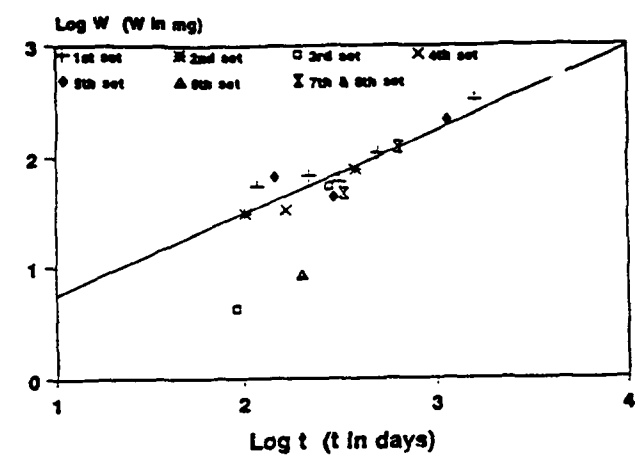


Figure 3. Plots of log W vs. log t for Galvanized steel at Burbank (Fig. 3a), Salinas (Fig. 3b), Long Beach (Fig. 3c) and Upland (Fig. 3d).

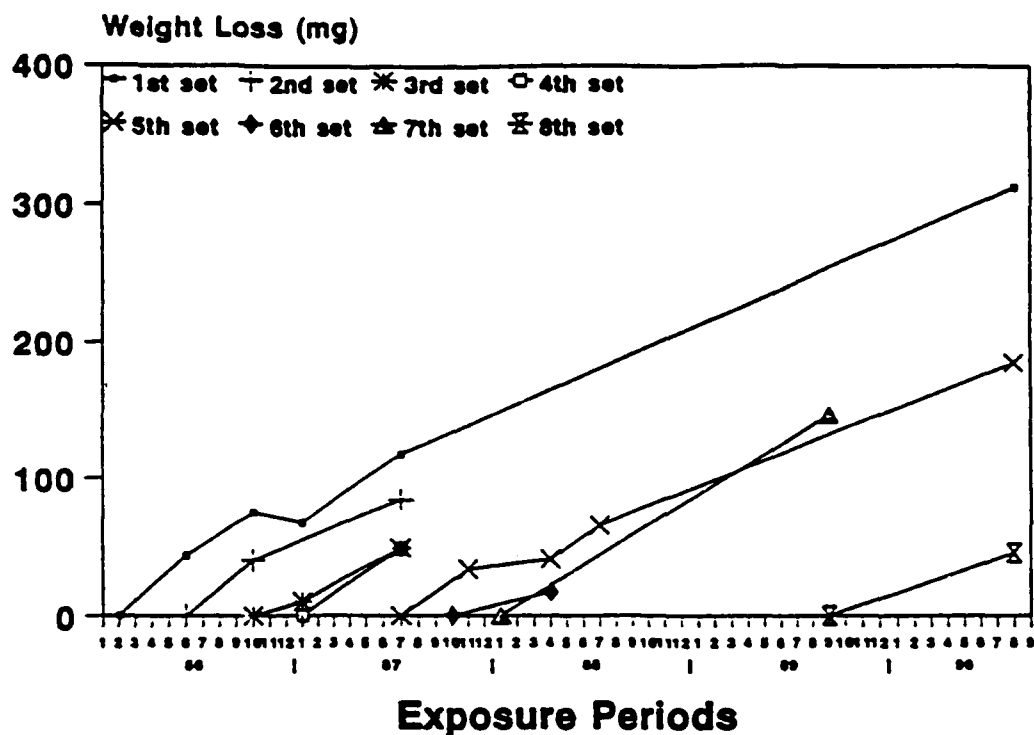


Figure 4. Weight loss for eight sets of nickel as a function of exposure time at Burbank.

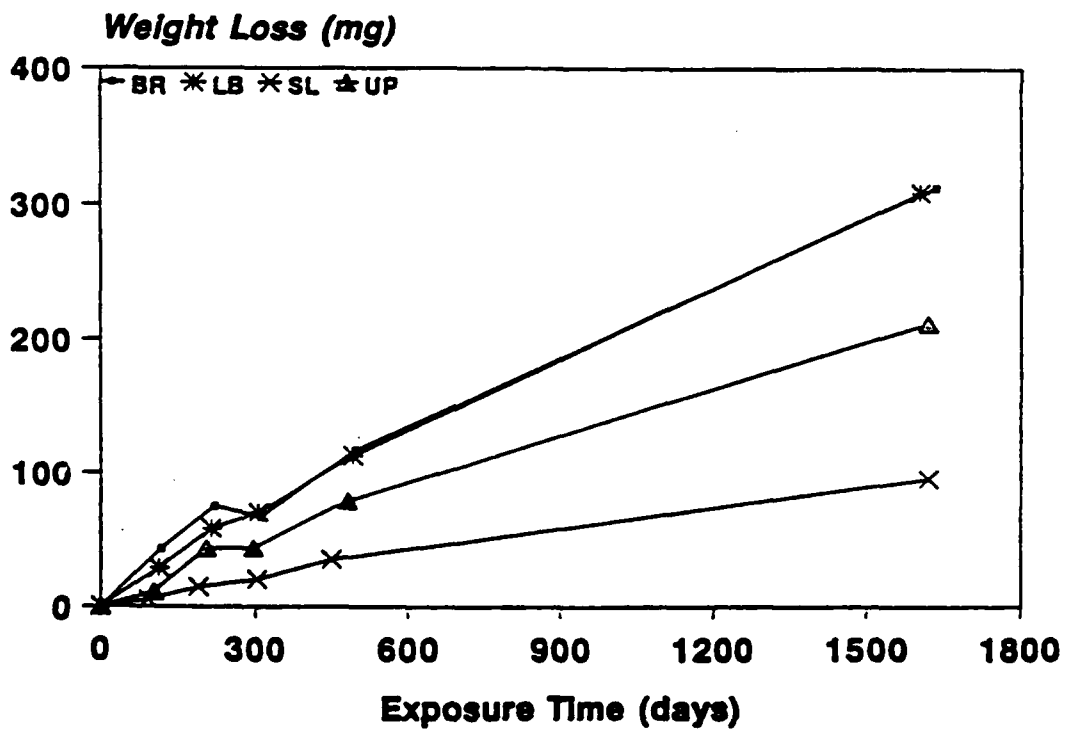


Figure 5. Weight loss for the first set of nickel as a function of exposure time at the four test sites.

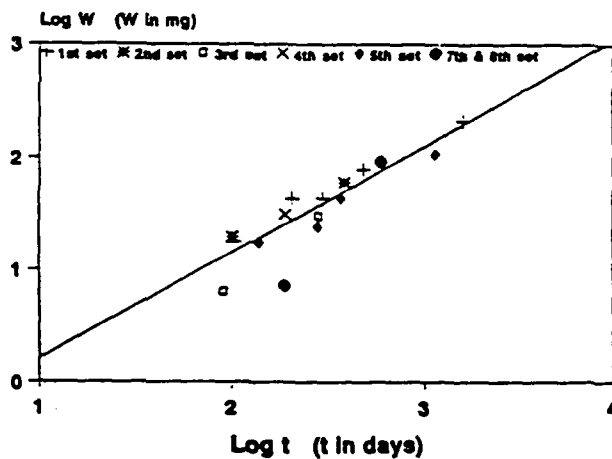
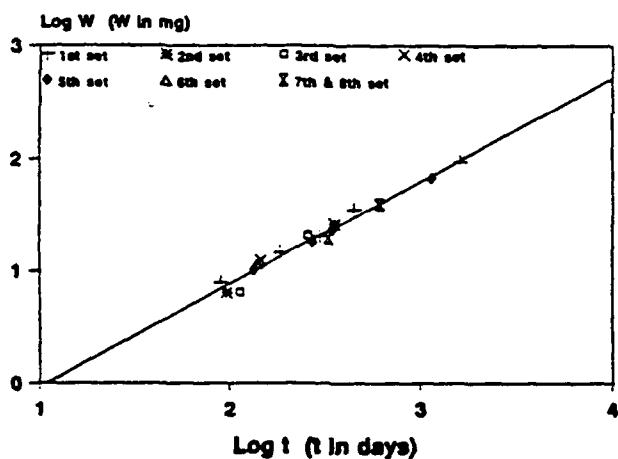
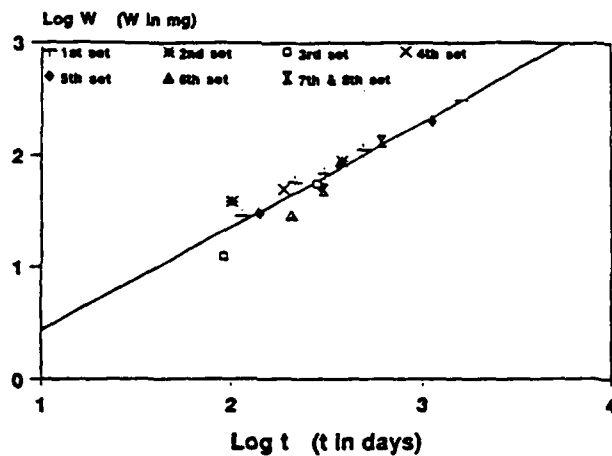
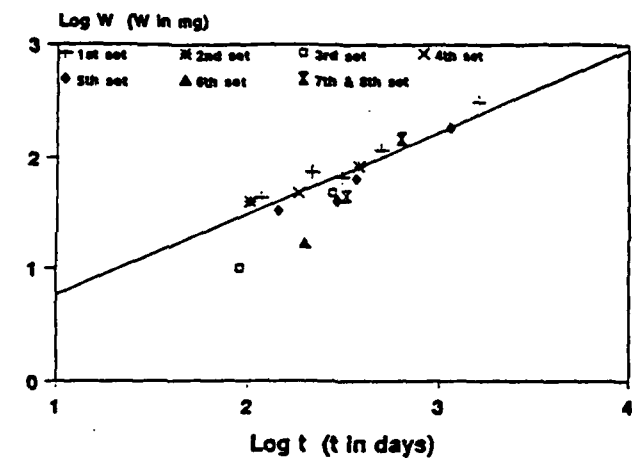


Figure 6. Plots of $\log W$ vs. $\log t$ for nickel at Burbank (Fig. 6a), Salinas (Fig. 6b), Long Beach (Fig. 6c) and Upland (Fig. 6d).

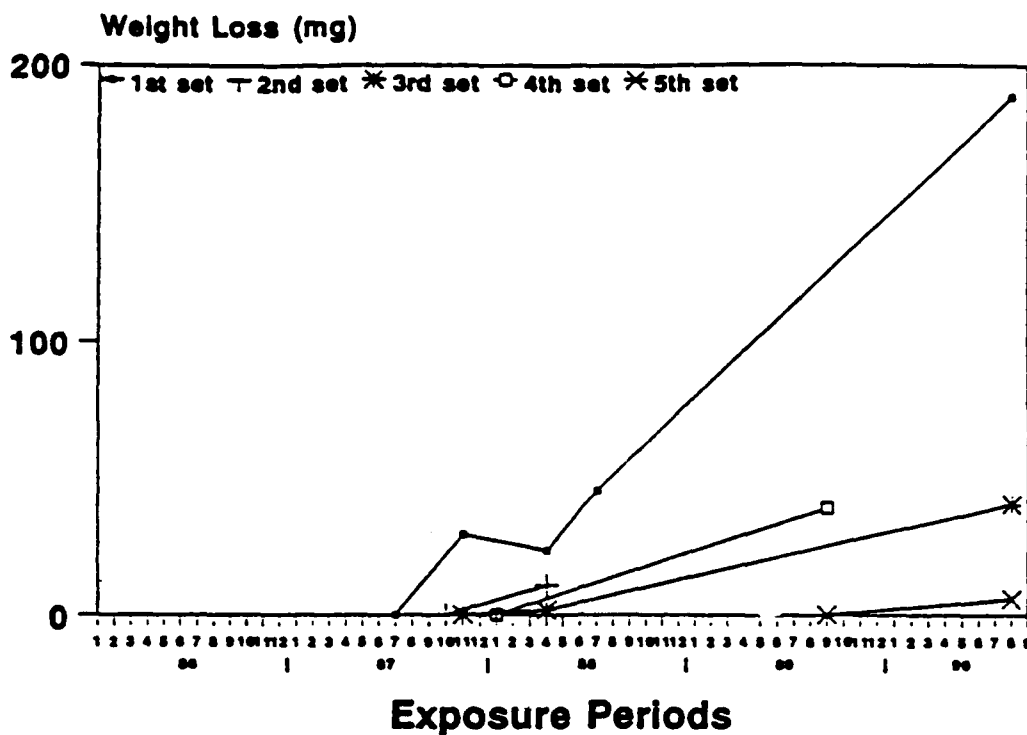


Figure 7. Weight loss for the first set of aluminum as a function of exposure time at the four test sites.

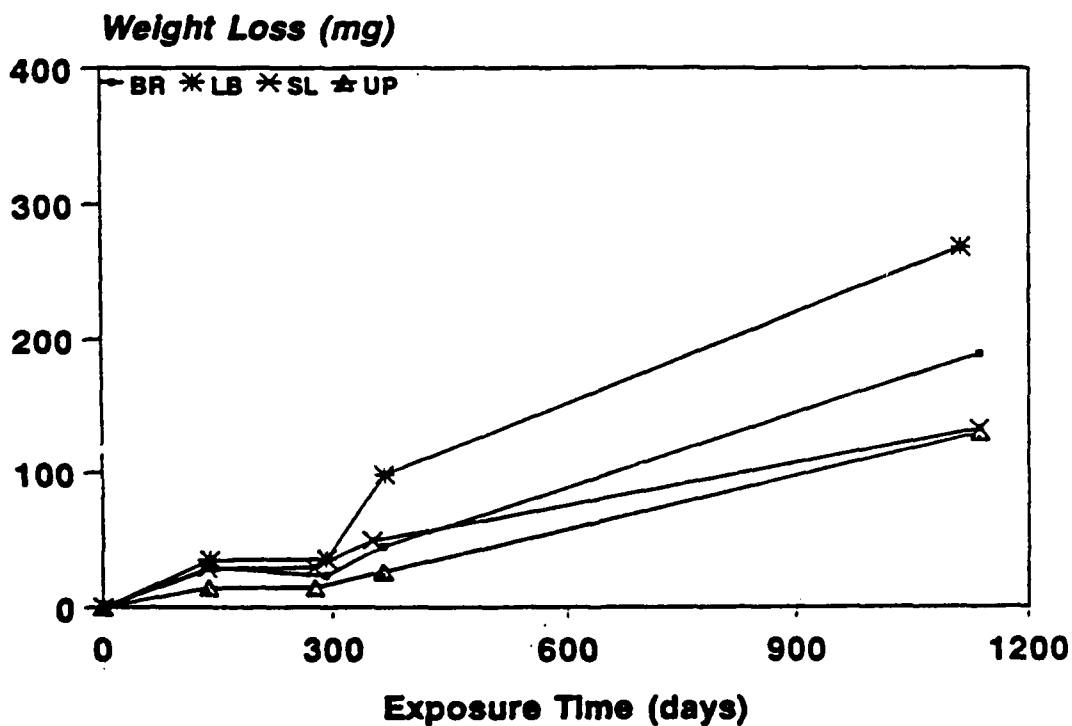


Figure 8. Weight loss for eight sets of aluminum as a function of exposure time at Burbank.

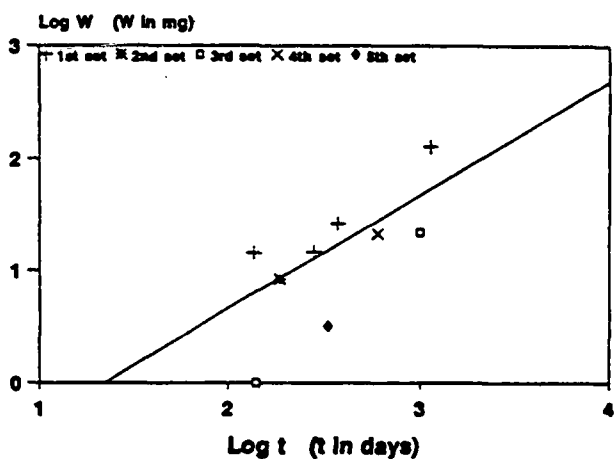
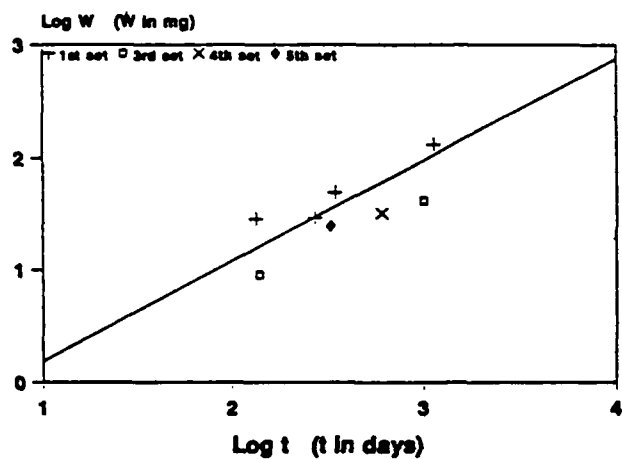
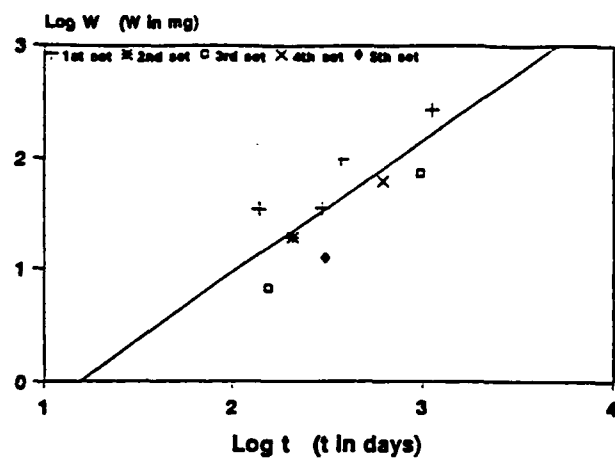
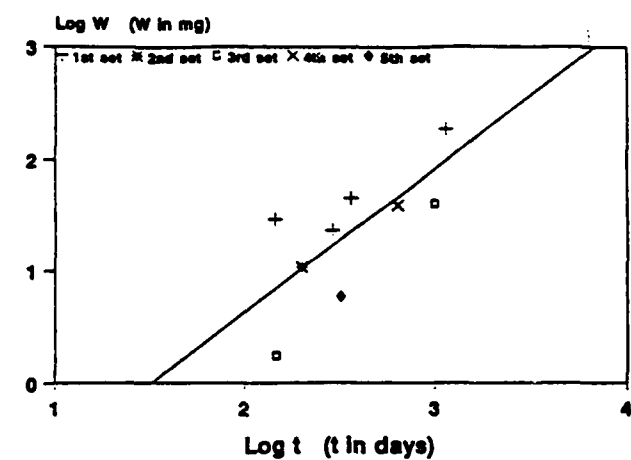


Figure 9. Plots of log W vs. log t for aluminum at Burbank (Fig. 9a), Salinas (Fig. 9b), Long Beach (Fig. 9c) and Upland (Fig. 9d).

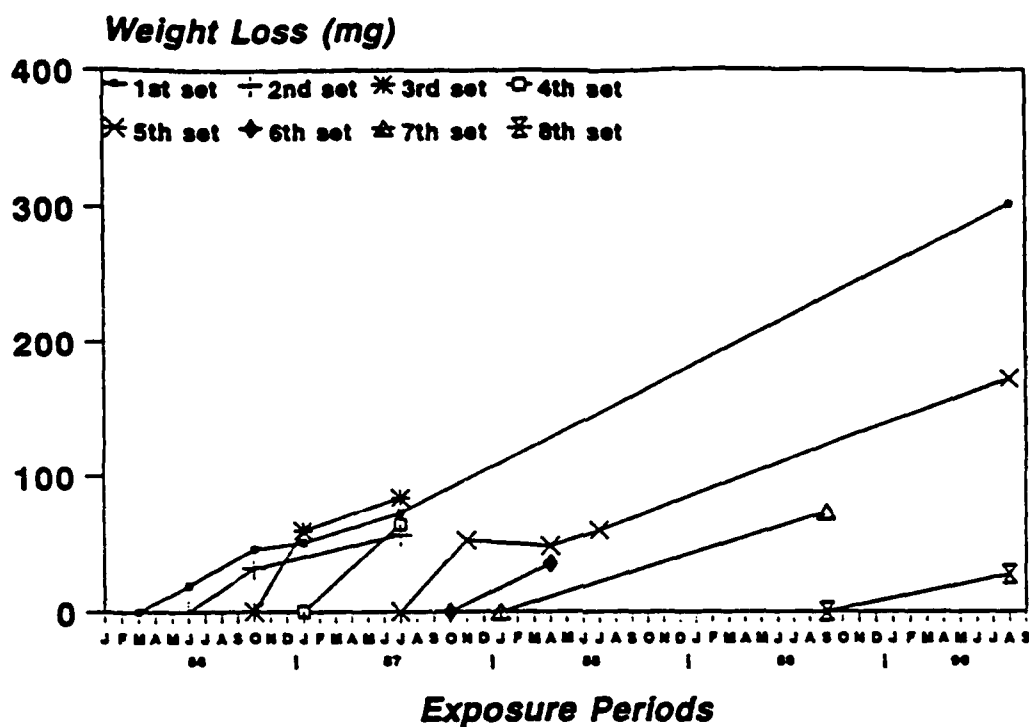


Figure 10. Weight loss for eight sets of L-C paint as a function of exposure time at Burbank.

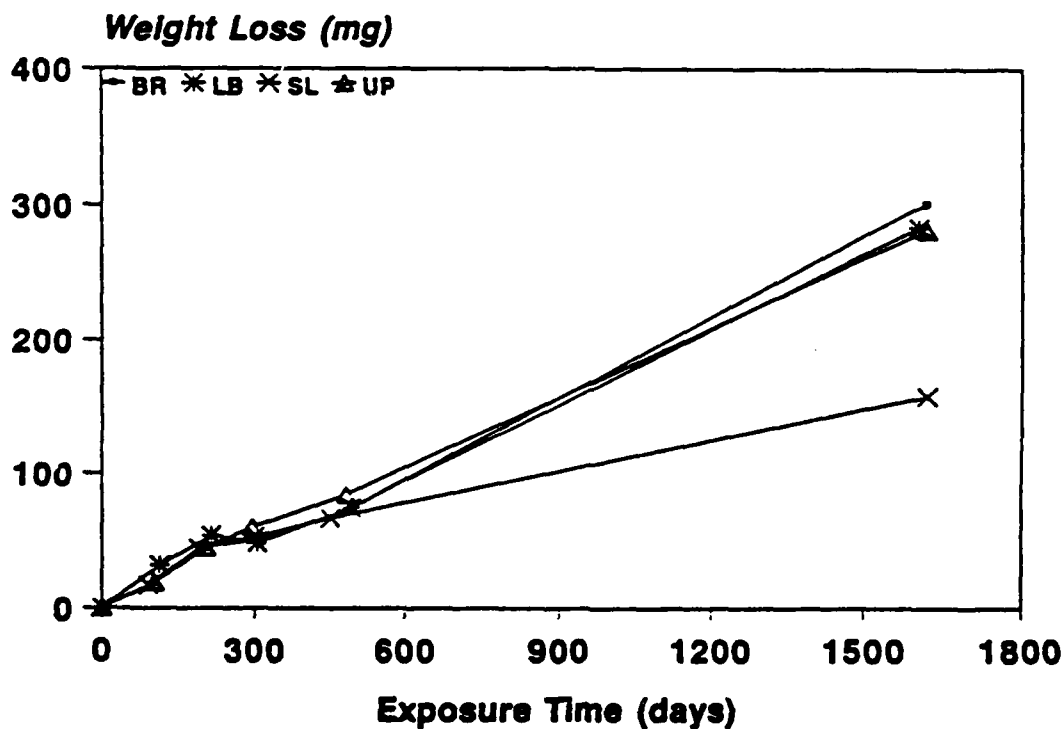


Figure 11. Weight loss for the first set of L-C paint as a function of exposure time at the four test sites.

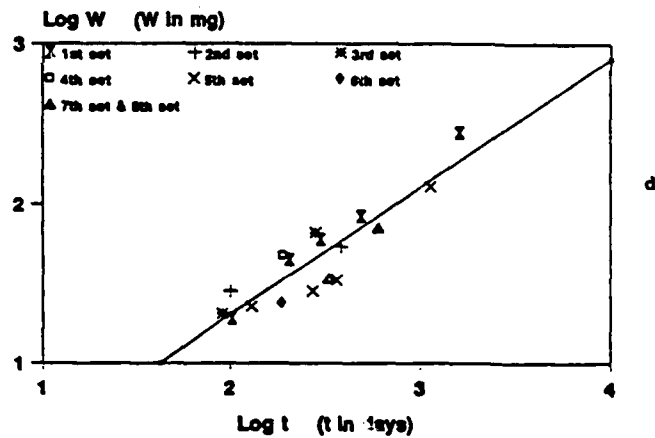
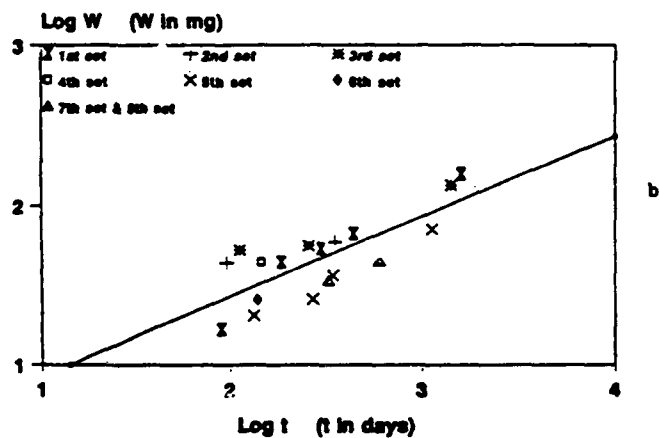
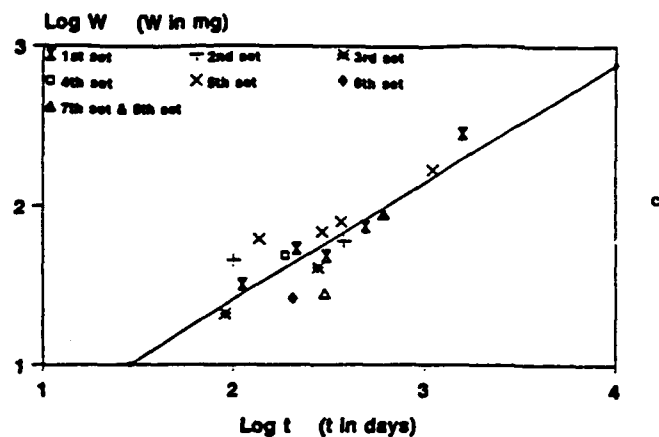
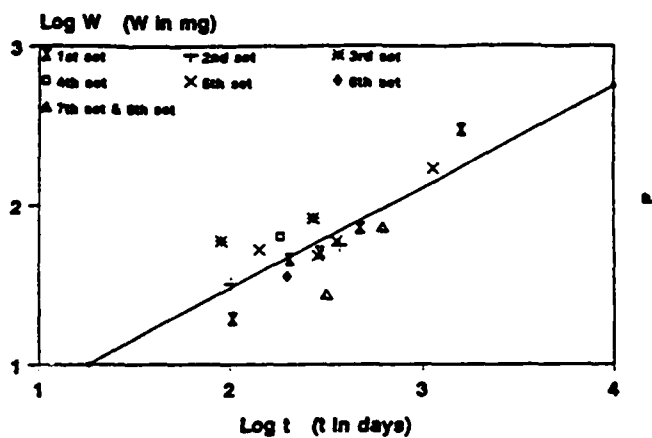


Figure 12. Plots of $\log W$ vs. $\log t$ for L-C paint at Burbank (Fig. 12a), Salinas (Fig. 12b), Long Beach (Fig. 12c) and Upland (Fig. 12d).

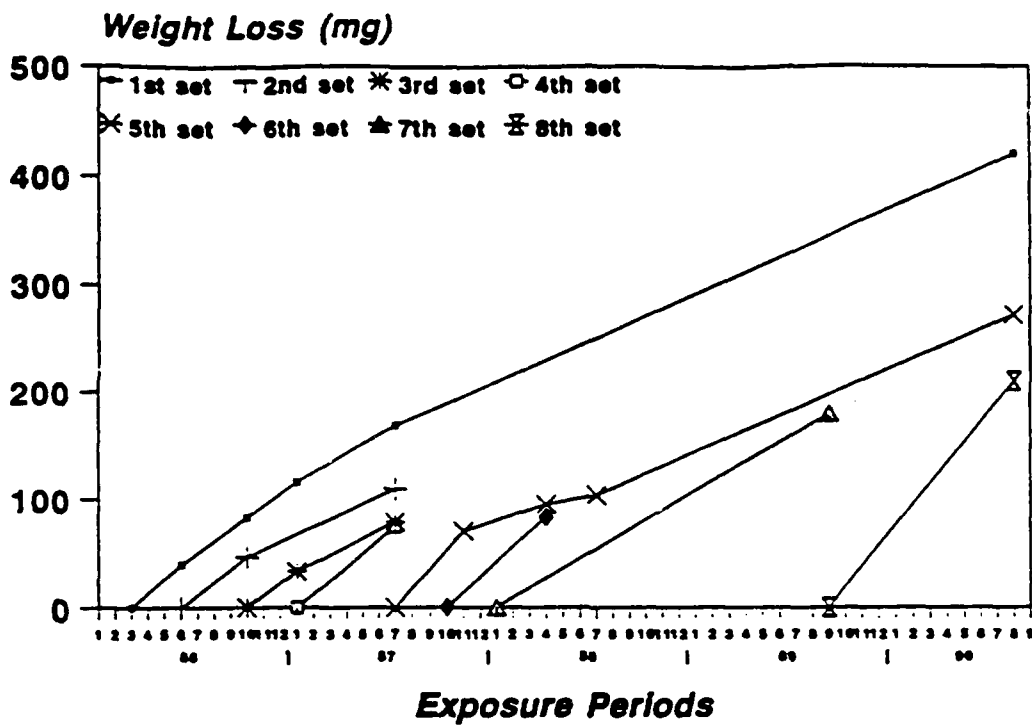


Figure 13. Weight loss for eight sets of H-C paint as a function of exposure time at Burbank.

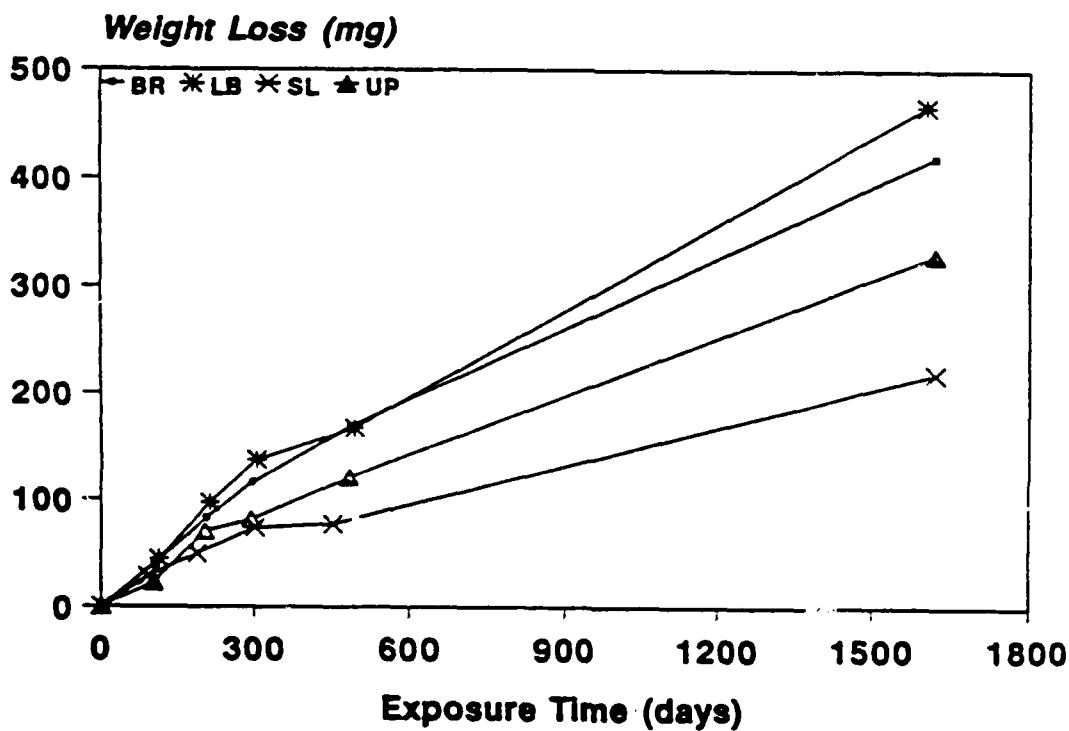


Figure 14. Weight loss for the first set of H-C paint as a function of exposure time at the four test sites.

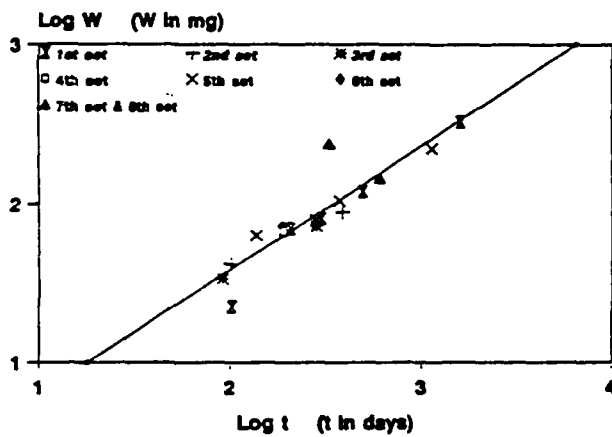
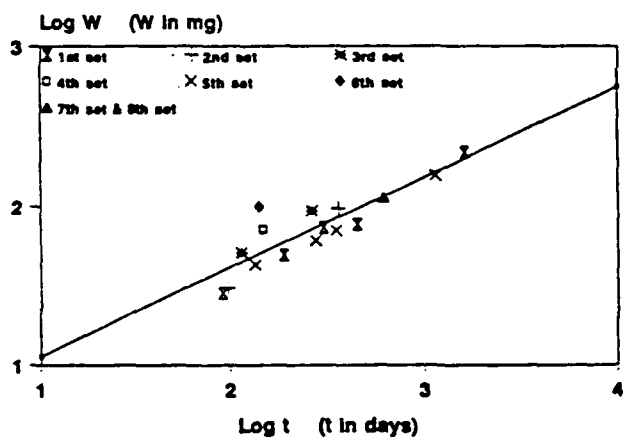
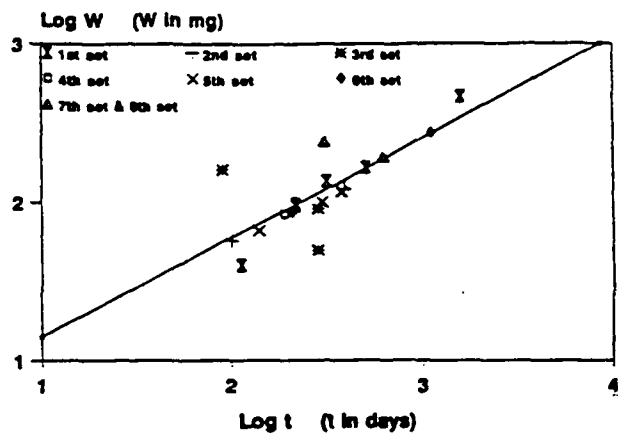
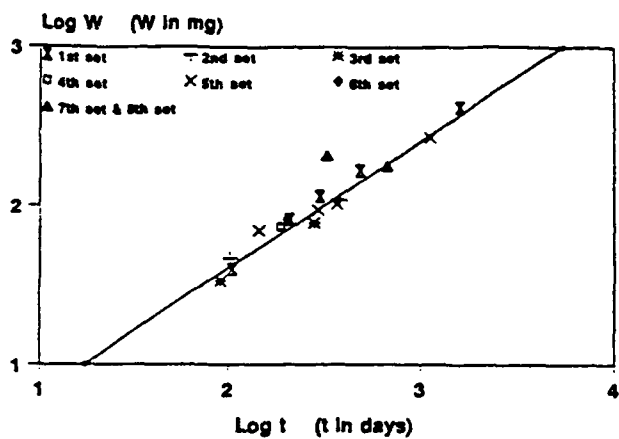


Figure 15. Plots of log W vs. log t for L-C paint at Burbank (Fig. 15a), Salinas (Fig. 15b), Long Beach (Fig. 15c) and Upland (Fig. 15d).

Percent Loss of Breaking Strength

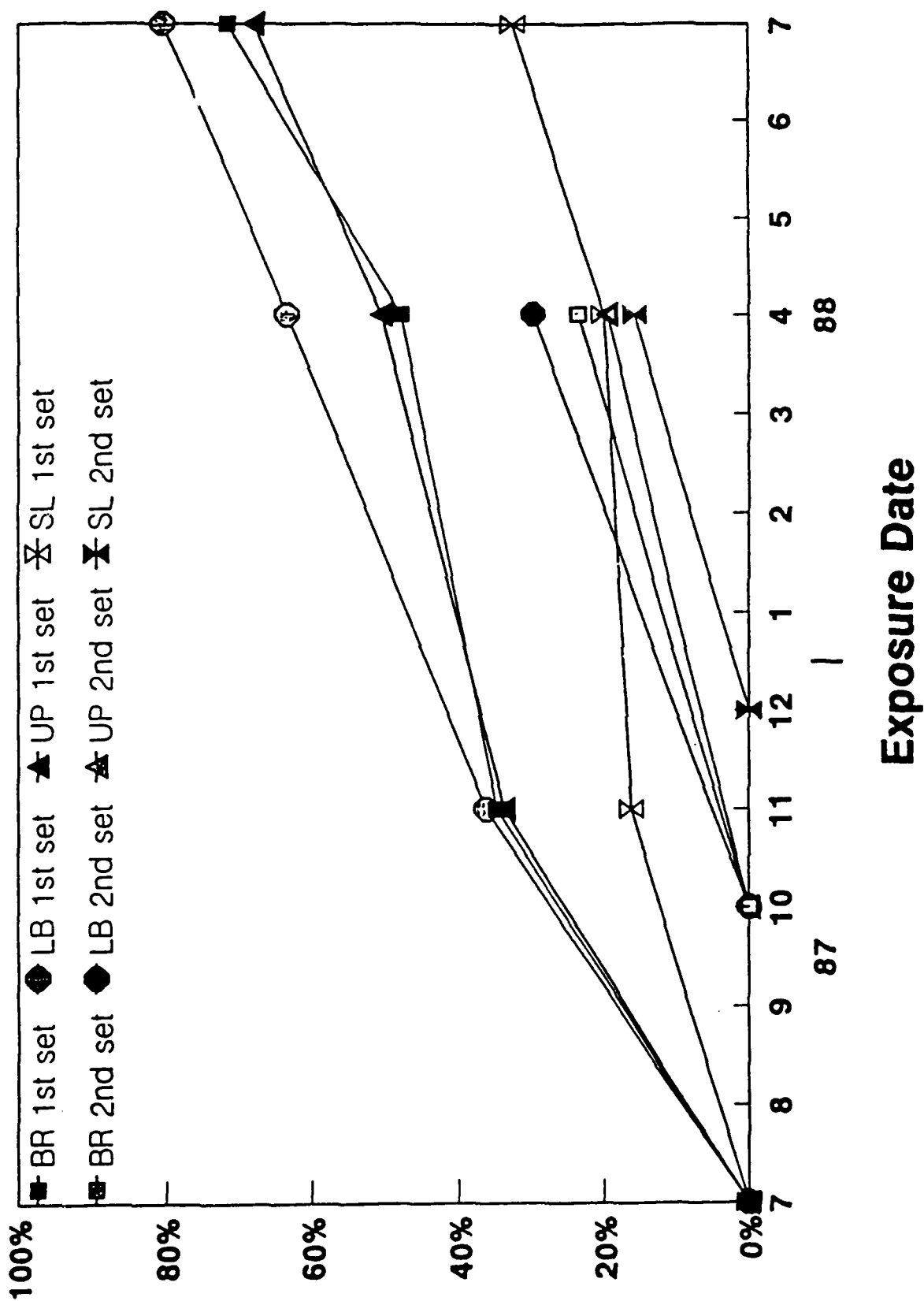


Figure 16. Loss of strength as a function of exposure time for two sets of nylon fabric at the four test sites.

The Influence of Environmental Acidification on the Atmospheric Corrosion of Zinc

Eva Johansson
Swedish Corrosion Institute
Roslagsvägen 101, Hus 25
S-104 05 Stockholm Sweden

Mats Linder
Swedish Corrosion Institute
Roslagsvägen 101, Hus 25
S-104 05 Stockholm Sweden

Abstract

The influence of acid rain on the atmospheric corrosion of zinc has been studied during a combined laboratory rain exposure and a rainprotected field exposure. The exposure has been performed during one year which permits conclusions to be drawn on the long term corrosion behaviour of zinc under realistic conditions.

Panels mounted on racks were exposed under rainshelter and once a week exposed to synthetic rain in a rain device in the laboratory. Each rain event lasted for 3 hours. After the rain exposure the panels were replaced under the rainshelter. For comparison one set of panels was exposed freely outdoors and one set rainsheltered without synthetic rain.

Rain waters with the pH values 3, 4, 5, 6 and 7 were studied for two compositions of rainwater, one containing sulphate and one containing sulphate and nitrate.

The corrosion was evaluated as mass loss by pickling after 4, 8 and 12 months. Environmental measurements were performed during the exposure.

The investigation showed that the variation of the rain acidity at pH-values 5 to 7 had no significant effect on the corrosion rate of zinc under the present exposure conditions. Rain with pH 3 gave however a strongly increased corrosion rate. It also turned out that the addition of nitrate to the sulphate containing rain had no effect on the corrosion rates.

Key terms: atmospheric corrosion, field exposure, laboratory exposure, zinc, galvanized steel.

Introduction

It has been shown in several investigations that the usually good corrosion resistance of zinc coatings can be adversely affected by acid species in the environment. An important reason for this is that the protective coating of basic salts which normally is developed on zinc in atmosphere has a higher solubility in acid solutions.

Dissolution of zinc corrosion products by acid species needs a supply of these species to the surface. This supply can be brought about by dry deposition and wet deposition of the species in question.

The dry deposition originates from deposition of gases reacting with the surface and particles that are impacted. Several field exposures have been carried out concerning the relation between the atmospheric corrosion rate of zinc and the SO_2 -pollution level. The relation found from field exposures in Scandinavia and the Czech Republic shows that the dry deposition of SO_2 has a major effect on the corrosion rate of zinc¹. Much less attention than to SO_2 has been drawn to the influence of NO_x on zinc corrosion. Even if the NO_2 -concentration in cities today is often higher than the SO_2 -concentration. Investigations of the influence of NO_2 in laboratory studies have given results which to some extent are contradictory² and ³.

The wet deposition is brought about by rain precipitation on the surface. As to the influence of rain acidity the dissolution of zinc corrosion products has mainly been attributed to H_2SO_4 originating from sulphur pollution. It seems obvious that H_2SO_4 should predominate this influence, but there have been reasons to assume that a contribution of HNO_3 plays a not negligible part at least in some areas.

In this investigation the influence of acid rain on the atmospheric corrosion of zinc has been studied during combined laboratory rain exposures and rainprotected outdoor exposure. Rain waters with the pH values 3, 4, 5, 6 and 7 were used in two variants one containing sulphate and the other containing sulphate and nitrate.

Experimental

Material

Panels of zinc with 99.67 % purity with the following additional constituents in weight% were used:

0.003 Sn, 0.003 Pb, 0.003 Fe, 0.0006 Cd, 0.22 Cu, 0.10 Ti, 0.003 Al and 0.0001 Mg.

To a minor extent panels of continuously hot-dip galvanized steel, with a coating thickness of about 10 μm were included.

The size of the panels was 100 x 100 mm^2 . The thicknesses of the zinc and hot-dip galvanized panels were 1 mm and 0.8 mm respectively.

The backside of the panels were masked with a commercial tape of type Nitto. For the panels with zinc coatings the edges were protected with tape of type Tesa, resulting in a test area of 92 x 92 mm.

The panels were degreased in trichloroethylene in a repeated procedure in gaseous and liquid phases in an ultrasonic device.

Exposure

The exposure is a combined outdoor and laboratory test. Sets of panels were exposed outdoors under rainshelter and once a week brought into the laboratory for exposure to synthetic rain. For comparison one set of panels was exposed freely outdoors and one rainsheltered without laboratory rain. The panels were exposed during in total one year with withdrawals after 4, 8 and 12 months. For each exposure variant triplicate panels were used.

Outdoor Exposure. The panels were mounted on racks with 45° inclination outside the building of the Swedish Corrosion Institute in Stockholm. The test site is located only 1000 meters from the test site Stockholm - Vanadis. The environment on this site is very well characterized by regularly measurements of temperature, relative humidity, sulphur dioxide concentration and rain precipitation. The environmental measurements can be considered equal for the two test sites. The SO₂-concentration is measured as monthly average with passive samplers. The rain precipitation is measured with an open collector. During the exposure the deposition of particles was measured under the rainshelter using Petri dishes. The dishes were weighed on an analytical balance before and after the exposure and then washed with 15 ml deionized water after the exposure. The washing solutions were analyzed with ion chromatography. Two dishes were exposed in parallell for each evaluation period i.e. 4, 8 and 12 months.

Monthly mean values of temperature and relative humidity are summarized in Table 1. The time of wetness and mean values from monthly measurements of sulphur dioxide for the different exposure periods are given in Table 2. The time of wetness is defined as the time when the relative humidity is above 80 % and the temperature is above 0 °C. The amount and the results from the analyses of the rain precipitation are given in Table 3. The dry deposition of particles and the contents of SO₄²⁻ and Cl in g/m² for the different exposure periods are summarized in Table 4.

Laboratory Exposure. The panels were exposed to synthetic rain in rain devices for three hours once a week. The devices consisted of a box with the dimension 800x600x400 mm. The rain water was pumped up to a tube of plexiglass. The tube was at its bottom side at regular distances perforated with small holes from which the water could drip down to a plexiplate. This arrangement gave a splash of fine and even water drops over the surface of the test panels. In each rain device 9 panels were simultaneously exposed, 5 and 4 at each side of the rain groove. During each of the rain events the amount of rainfall was determined by collection in a hopper. The groups of panels for the different rain compositions were alternated between the different devices according to a special scheme. Furthermore the panels were exposed "up and down" in an alternating scheme. This was made to avoid too large differences in total rain amount for the different groups due to systematic errors. The total amount and mean value of rainfall at each rain event are summarized in Table 5.

Rain water with the pH values 3, 4, 5, 6 and 7 were studied. Two compositions of rain were used one containing sulphate and one containing sulphate and nitrate. The acidity of the water was obtained by addition of H₂SO₄. The higher pH-values were adjusted with NaOH. All rain waters had a constant concentration of NH₄⁺ and Cl of 1 mg/l and 2 mg/l respectively. In the nitrate containing rain nitrate was added as NaNO₃ to a NO₃⁻-content of 4.5 mg/l. The rain composition and its conductivity are summarized in Table 6 and 7. Before each rain event the pH and conductivity were measured and corrected if necessary.

Methods of Evaluation

Corrosion Rate. After the exposure the corrosion products on zinc and hot-dipped galvanized zinc were removed by repeated pickling in 5 % acetic acid at room temperature for in total 25 minutes. The panels were weighed on an analytical balance with an accuracy of ± 0.5 mg. The mass losses were calculated with linear regression analysis and extrapolation to the pickling time zero. The latter is carried out to compensate for a possible metal loss at the pickling.

Corrosion Products. Samples exposed to sulphate and nitrate containing rain of pH

3 and 7 and rainprotected samples were examined with scanning electron microscopy (SEM) with an energy dispersive spectroscopy analyzer (EDS).

Results

Corrosion Evaluation

Mass losses in g/m² after 4, 8 and 12 months and the corresponding standard deviations of triplicates of panels in the different types of exposures are summarized in Table 8. The mass losses versus exposure time for zinc panels exposed to synthetic sulphate rain are shown in Figure 1. Corresponding diagramme for sulphate+nitrate rain is shown in Figure 2.

Mass losses in g/m² for the different pH values after 1 year's exposure are shown in Figure 3.

A comparison between mass losses for zinc and hot dipped galvanized panels is shown in Figure 4.

Corrosion Products

The EDS-analysis of panels exposed to synthetic rain of pH 3, containing sulphate and nitrate, show that there were two types of corrosion products; one containing zinc and oxygen and one with zinc, oxygen and sulphur. For panels exposed to synthetic rain of pH 7 the situation was similar. However the amount of corrosion products containing zinc, oxygen and sulphur was larger. In this case there were also parts of the surface where chlorides were incorporated. The corrosion products on rainprotected samples were similar to those on panels exposed to synthetic rain with pH 7.

Discussion

The main consideration in the planning of this investigation was to study the effect of pH in rain while keeping the other conditions as near a natural level as possible. The rain amount in the free exposure in Stockholm was about 450 mm during the 1 year period while the rain amount in the laboratory was about 800 mm. This difference does not seem to have any marked influence on the investigated pH-effect. The time of wetness calculated from values of temperature and relative humidity can be assumed to have been rather equal for the panels exposed at free and sheltered position due to a sufficient gap between the panels and the shelter. Also remaining environmental parameters have because of the arrangement of the investigation been the same for panels exposed in free position and under shelter.

The Effect of pH and Composition of Rain

Rain with pH 3 gives a strong increase of the corrosion rate both for sulphate and sulphate+nitrate containing rain. At pH 4 a marked increase of the corrosion rate could be detected. Variations of the rain acidity at pH-values 5 to 7 gave no significant effect on the corrosion rate of zinc under the present exposure conditions. This is clearly shown in Figure 3. No large difference has been found between the influence of rain with only SO₄²⁻ and SO₄²⁻ + NO₃⁻ addition. The natural rain had an average pH over the year of 4.8. The mass loss for the freely exposed panels was 3.6 g/m² after 1 year. This is almost on the curve at pH 4.8 in Figure 3 which indicates that the investigation has been performed in a relevant way.

For both types of synthetic rains at all pH-values studied and at the free exposure the corrosion rate of zinc was higher compared with the rain-protected zinc panels, which were only exposed to dry deposition of pollutants. The very low mass loss for rain protected zinc panels is mainly due to the low SO_2 -concentration, 5-10 $\mu\text{g}/\text{m}^3$, found today in the Stockholm atmosphere.

The higher corrosion rate for the freely and laboratory exposed panels is due to the effect of periodic dissolution of the protective film of corrosion products by precipitation. It is probably mainly basic zinc carbonate and sulphate that are formed on surfaces exposed both sheltered, freely and to synthetic rain. The basic zinc sulphate has been found on zinc surfaces exposed both in free and rain sheltered positions in an earlier study performed at the Stockholm-Vanadis test site⁵. The basic zinc salts possess certain protective properties. However the salts are soluble in rain water, the solubility being dependent on the pH of the solution. They are therefore washed away during exposure of zinc panels exposed to rain. For panels exposed in sheltered position, however, the salts and especially an outer layer containing sulphates may reduce the further deposition of e.g. SO_2 on the surfaces.

Galvanized panels showed in general higher mass losses than corresponding zinc panels. However the difference between the mass losses for zinc and hot dipped galvanized zinc panels is nearly constant, about 2 g/m^2 , independent of exposure time as can be seen in Figure 4. This indicates that the phenomenon does not depend on the difference in real corrosion rate on free surfaces. It is more likely that the difference in mass loss depends on edge effects such as localized galvanic attacks at the edges during the pickling procedure. This fact emphasizes one of the advantages of using solid zinc panels in systematic investigations. The results and conclusions from the pH study of the zinc panels are thus in principle valid also for hot-dipped galvanized steel.

Calculated Contributions from Wet and Dry Deposition

Dissolution of zinc corrosion products by acid species needs a supply of these species to the surface. This supply to freely exposed surfaces is conventionally subdivided into two categories: dry deposition and wet deposition. The dry deposition consists of gases reacting with the surface and of impaction of particles.

The contribution to the corrosion from the dry deposition (C_d) is in the present study, 0.9 g/m^2 , during one year, which corresponds to the corrosion rate for the rain protected panels.

The wet deposition is brought about by rain precipitation on the surface. The corrosion effect of precipitation can in principle be subdivided into the effect caused by the acidity due to dissolved antropogenic acid pollutants (C_{RA}) and to the dissolved CO_2 (C_{RC}). The contribution from C_{RC} is more important at higher pH-values.

The maximum contribution, C_{RA} to the corrosion rate due to the reaction of zinc and its corrosion products with hydrogen ions from the rain water can be stoichiometrically calculated:

$$C_{RA} = (10^{-\text{pH}} \times p) \times M_{Zn}/2$$

C_{RA} = corrosion rate in g/m^2 ,year

p = precipitation in mm/year

M_{Zn} = atomic mass for zinc (65.4) - the figure 2 reflects that 2 H^+ -ions are needed for dissolution of each Zn^{2+} -ion.

For sulphate rain of pH 3 a total precipitation of 734 mm gives a calculated $C_{RA} = 23.9$ g/m²,year compared with measured 18.8 g/m². This hypothetical influence of rain water acidity is very simplified and the deviation from reality can depend among other things on the fact that a part of the acid in the acid rain on the surface might run off the surface before it has reacted completely. Similar calculations for pH 4, 5 and 6 give: 2.7, 0.3 and 0.03 g/m² respectively. This should be compared with the measured values: 4.1, 2.5 and 2.5 g/m². With a constant contribution of 0.9 g/m² from the dry deposition measured under the shelter the corrosion expressed as $C_d + C_{RA}$ gives 3.6 g/m² for pH 4. This is somewhat lower than the measured corrosion. For sulphate+nitrate rain similar calculations of the contribution from rain acidity give, 27, 3.1, 0.3 and 0.03 g/m² for pH 3, 4, 5 and 6 respectively. Also here the sum of the calculated contributions from dry and wet acid deposition is just somewhat lower than the measured corrosion at pH 4. However it is likely that on surfaces regularly washed by rain solutions the dry deposition will be higher than on surfaces where the protective coating is permanent. For pH values higher than 4 the sum $C_d + C_{RA}$ gives constantly too low corrosion rates compared with the measured. This may be explained by the contribution of the effect of C_{RC} which is discussed below.

The difference between the corrosion rate of zinc panels exposed to synthetic rain at pH 3 for the two types of rains can be explained by the differences in rain precipitation in laboratory. The total precipitation for the rain containing sulphate was 734 mm and for the sulphate+nitrate containing rain 825 mm, see Table 5. Calculations of the contribution from the acid deposition (C_{RA}) according to this difference is 3.0 g/m² and the measured difference is 3.1 (Table 8). This shows that the addition of nitrate to the sulphate containing rain does not have any effect on the atmospheric corrosion of zinc.

Comparison with Published Data

A damage function for predicting the corrosion of galvanized steel structures by wet and dry deposition has recently been developed in a study performed for the National Acid Precipitation Assessment Program (NAPAP)⁶. This damage function consists besides the contribution from dry deposition and acid rain deposition also of a contribution from deposition of "neutral rain", containing dissolved CO₂. Using this function the prediction of corrosion of zinc caused by neutral rain, C_{RC} , is about 70 % of the total corrosion at the SO₂- level of 10 µg/m³ in the atmosphere. For the present study this corresponds to a corrosion of 2.5 g/m² (70 % of 3.6 g/m²) at the free exposure. The contribution from dry deposition C_d , as measured in the rain protected position is 0.9 g/m² and the calculated contribution C_{RA} from acid rain of pH 4.8 is 0.2 g/m². The sum of these three components is 3.6 g/m² which is equal to the measured corrosion at free exposure of panels. The same calculation for panels exposed to sulphate containing rain of pH 5 gives:

$$C = C_d + C_{RA} + C_{RC} = 0.9 + 0.3 + 1.7 = 2.9 \text{ g/m}^2,$$

to compare with the measured corrosion of 2.5 g/m².

The present investigation shows thus a good agreement with previous studies of corrosion of zinc. This makes it clear that the exposure time and the exposure conditions have been realistic for making conclusions regarding the effect of pH in rain on the corrosion of zinc.

Conclusions

From the present study of the influence of environmental acidification on the atmospheric corrosion of zinc following main conclusions can be drawn:

- The corrosion of zinc was strongly increased at exposures to acid rain with pH 3.
- At pH 4 a marked increase of the corrosion rate was obtained, whereas variations in the rain acidity at pH-values 5 to 7 had no significant effect.
- The addition of nitrate to the sulphate containing rain did not have any effect on the atmospheric corrosion of zinc.
- The used method with combined outdoor and laboratory exposure is useful and reliable for the study of environmental effects on the atmospheric corrosion.

Acknowledgment

The investigation has been funded wholly by the International Lead Zinc Research Organization.

The authors are indebted to Mr Sten Palmgren for his careful preparation of samples and extensive work with the laboratory raining.

References

- 1 V.Kucera, D.Knotkova, J.Gullman, P.Holler, "Corrosion of structural metals in atmospheres with different corrosivity at 8 years' exposure in Sweden and Czechoslovakia". Proceedings of the 10th International Corrosion Congress in Madras. November 1987, p 167-178.
- 2 J.F.Henriksen, "Corrosion rates of various metals in SO₂/NO₃ polluted atmospheres", 10th Scandinavian Corrosion Congress, Stockholm 1986, s 39-42.
- 3 P.Ericsson, L-G.Johansson, "The role of NO₂ in the atmospheric corrosion of different metals", 10th Scandinavian Corrosion Congress, Stockholm 1986, s 43-48.
- 4 E.O.Edney, "Galvanized steel controlled field and chamber experiments", Materials and Cultural Resources Effects, Task Group VII Research Summaries, January 1989, Charleston.
- 5 E.Johansson, J.Gullman, "The influence of different environmental parameters on the corrosion of carbon steel, zinc, aluminium and galvanized steel during field and climate chamber exposure", Part 1. Swedish Corrosion Institute, Stockholm Sweden, SCI-report 1990:7
- 6 J.W.Spence, F.H.Haynie, "Derivation of a Damage Function for Galvanized Steel Structures: Corrosion Kinetics and Thermodynamic Considerations", Corrosion, Testing and Evaluation: Silver Anniversary Volume, ASTM STP 1000, R. Baboian and S.W. Dean, Eds., American Society for Testing and Materials, Philadelphia, 1990, pp. 208-224.

Table 1. Monthly mean values of relative humidity and temperature during the exposure period.

Month	06	07	08	09	10	11	12	01	02	03	04	05
%RH	73	65	72	69	81	85	80	71	79	74	72	52
Temp., °C	12	19	18	12	8	5	2	2	2	3	4	14

Table 2. Time of wetness and SO₂ concentration during the different exposure periods.

Exposure period	0 - 4 months	4 - 8 months	8 - 12 months
Time of wetness, h	943	1510	878
SO ₂ -conc., µg/m ³	3.7	7.2	5.6

Table 3. Amount and analyses of precipitation during the exposure periods.

Exposure period, months	Amount mm	pH	Conductivity µS/cm	SO ₄ ²⁻ -S mg/l	Cl ⁻ mg/l	NO ₃ ⁻ -N mg/l	NH ₄ ⁺ -N mg/l
0 - 4	248	4.8	16	0.7	0.4	0.3	0.3
4 - 8	102	4.6	29	1.1	2.1	0.7	0.5
8 - 12	107	4.9	29	1.3	1.4	0.9	0.8

Table 4. Dry deposition of particles and their contents of sulphate, nitrate and chloride during the exposure periods.

	4 months	8 months	12 months
Mass increase, g/m ²	2.7	4.8	9.9
SO ₄ ²⁻ -cont., mg/m ²	28	48	69
Cl ⁻ cont., mg/m ²	31	84	87

Table 5. Total amount and mean values of rainfall at each rain event in the laboratory exposure.

	pH 3	pH 4	pH 5	pH 6	pH 7
<i>Sulphate rain</i>					
Total amount, mm	734	840(815)*	857	819	815
Mean value, mm/event	16	17(16)*	17	16	16
<i>Sulphate+nitrate rain</i>					
Total amount, mm	825	951	867	892	887
Mean value, mm/event	16	19	17	18	17

* Hot-dip galvanized panels.

Table 6. Composition of rain water in mole/litre (M).

<i>Sulphate rain</i>					
Sulphuric acid	pH 3	pH 4	pH 5	pH 6	pH 7
	5x10 ⁻⁴ M	0.5x10 ⁻⁴ M	0.05x10 ⁻⁴ M	no	no
Ammonium sulphate	3 x 10 ⁻⁵ M				

Sodium chloride	5.6 x 10 ⁻⁵ M
<i>Sulphate + nitrate rain</i>	
Composition as above + Sodium nitrate	7.1 x 10 ⁻⁵ M

Table 7. Conductivity in $\mu\text{S}/\text{cm}$ for the different synthetic rain waters.

<i>Sulphate rain</i>				
pH 3 379	pH 4 51	pH 5 17	pH 6 15	pH 7 14
<i>Sulphate and nitrate rain</i>				
pH 3 390	pH 4 55	pH 5 24	pH 6 21	pH 7 21

Table 8. Mass losses in g/m^2 for zinc and hot-dip galvanized steel after 4, 8 and 12 months exposure and the corresponding standard deviations of triplicates.

	4 months		8 months		12 months	
	Mean value	Stand. dev.	Mean value	Stand. dev.	Mean value	Stand. dev.
PURE ZINC						
<i>Sulphate rain</i>						
pH 3	6.2	0.3	13.5	0.4	18.8	0.4
pH 4	1.1	0.3	2.9	0.2	4.1	0.3
pH 5	0.5	0.1	1.9	0.2	2.5	0.1
pH 6	0.6	0.1	1.7	0.1	2.5	0.1
pH 7	0.4	0.2	1.7	0.1	2.5	0.0
<i>Sulphate + nitrate rain</i>						
pH 3	6.6	0.4	13.8	0.5	21.9	0.5
pH 4	0.9	0.1	2.8	0.1	4.3	0.1
pH 5	0.7	0.0	1.7	0.1	2.5	0.1
pH 6	0.5	0.1	1.6	0.1	2.2	0.1
pH 7	0.7	0.0	1.7	0.2	2.5	0.3
<i>Rain protected</i>	0.1	0.1	0.8	0.1	0.9	0.1
<i>Freely</i>	2.1	0.2	3.4	0.2	3.6	0.1
HOT-DIP GALVANIZED STEEL						
<i>Sulphate rain</i>						
pH 4	3.0	0.4	5.2	0.4	6.6	0.3

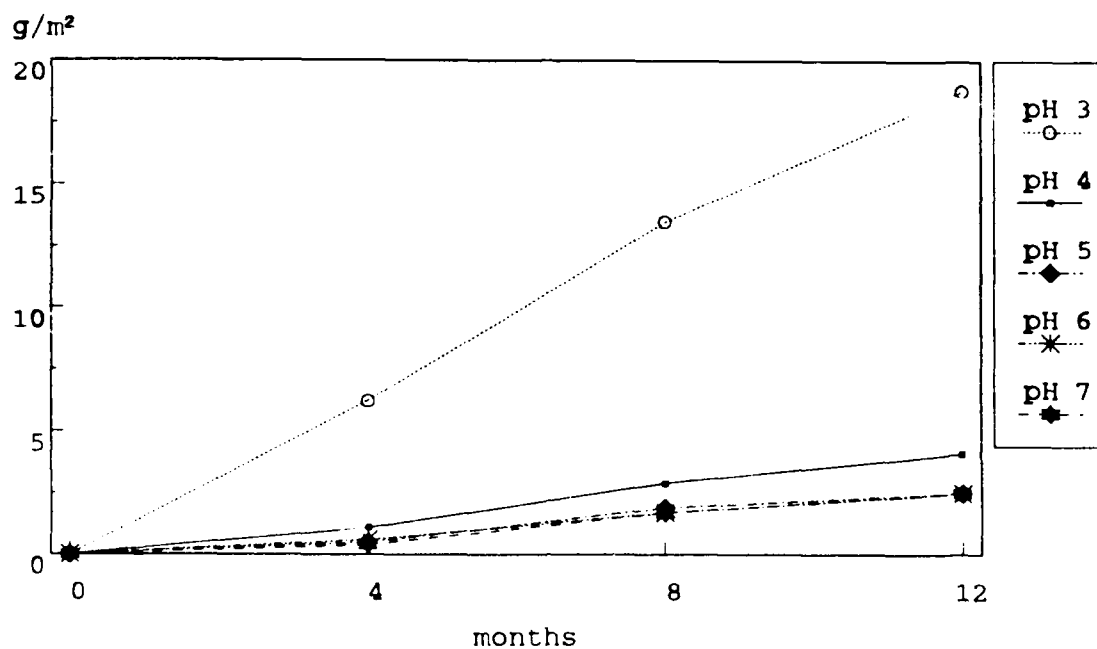


Figure 1. Mass losses for zinc panels exposed to synthetic rain containing sulphate at different pH values after 4, 8 and 12 months exposure.

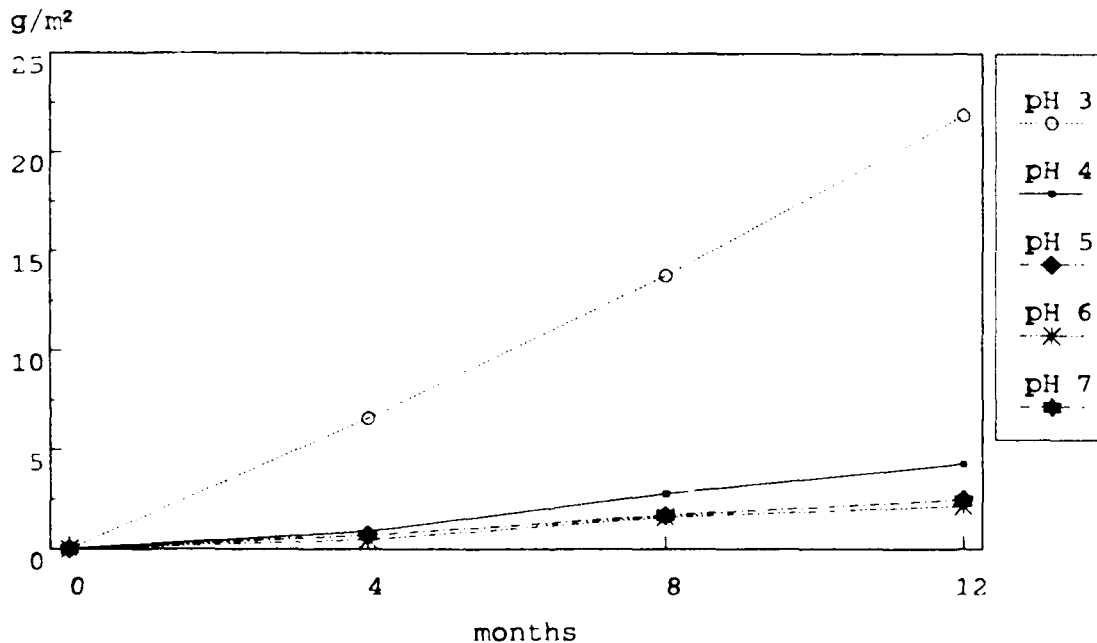


Figure 2. Mass losses for zinc panels exposed to synthetic rain containing sulphate and nitrate at different pH values after 4, 8 and 12 months exposure.

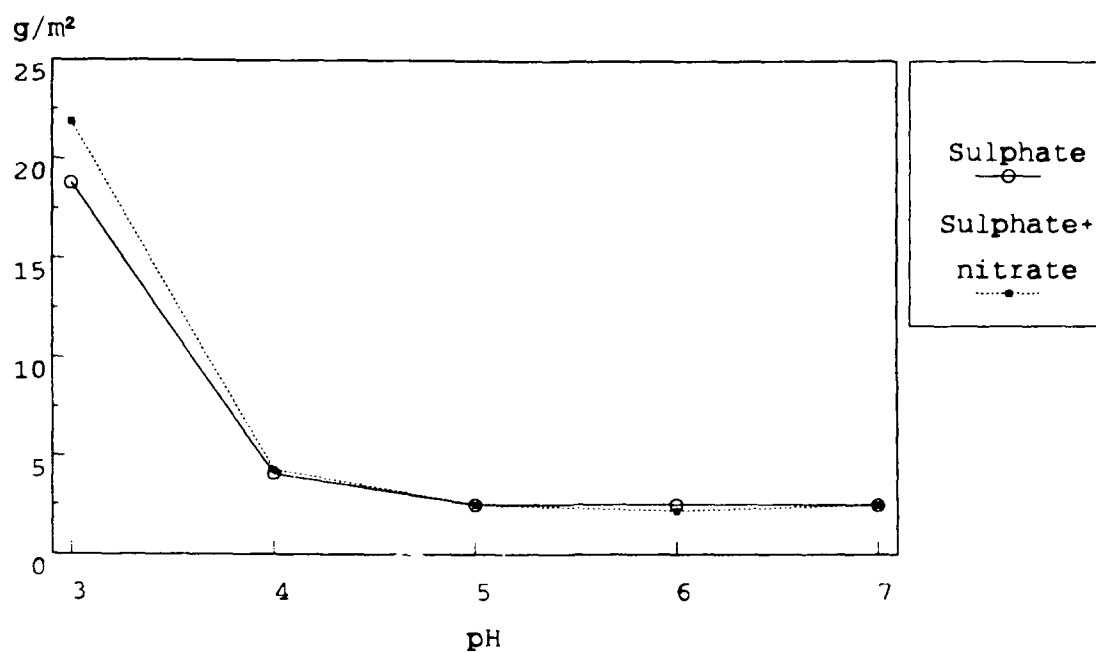


Figure 3. Mass losses for zinc panels after 1 year's exposure with synthetic rain of different composition and pH values.

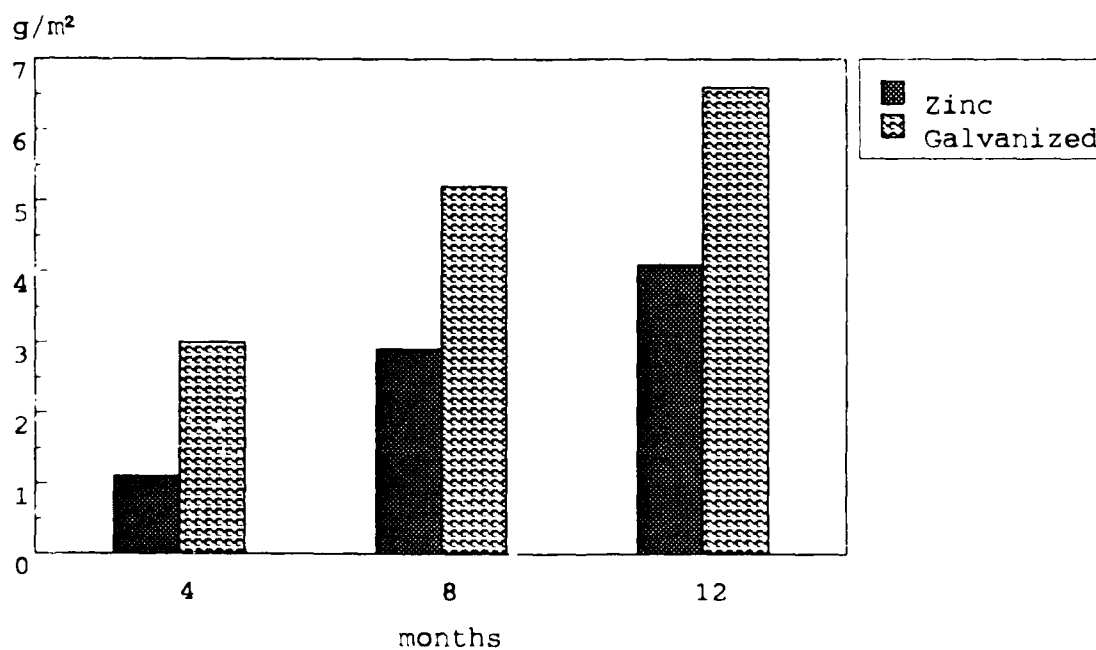


Figure 4. Comparison of mass losses for zinc and hot dipped galvanized zinc exposed to sulphate containing rain of pH 4.

Atmospheric Corrosivity Classification
Results of the International Testing Program ISOCORRAG

Dagmar Knotková
convener
Secretariat of ISO/TC 156/WG 4
SVÚOM - U Měšťanského pivovaru 4
170 00 Praha 7
Czech Republic

Members of WG 4
Classification of corrosivity of atmosphere (1)

Abstract

ISOCORRAG - worldwide atmospheric testing program was opened in 1987-1989 to provide data (corrosion losses of structural metals and environmental characteristics) using methods and procedures standardized within ISO/TC 156 with the goal to bring results for improvement of ISO corrosivity classification standards ISO 9223 - ISO 9226.

Results of 4 years of exposure are summarized and approach for changes in revision of classification standards is recommended.

Key terms: corrosivity of atmosphere, classification system, classification criteria, corrosion loss of structural metals, pollution (SO₂ and airborne salinity)

I. Introduction

Atmospheric corrosion is often a limiting factor for the service life of products. Classification of atmospheric corrosivity represents a modern approach helping to optimization of the choice of materials and protective systems. New ISO standards on atmospheric corrosivity classification form a guidance for engineers in evaluation of expected corrosion danger and in selecting anticorrosion measures. Four standards 1-4 have been published forming a complex system for atmospheric corrosivity derivation, giving methods for measurement of decisive characteristics of corrosion attack and environmental parameters (both on yearly basis) and introducing prognostic guiding values of corrosion rates of structural metals for short term (up to 10 years) and long term (more than 10 years) service life.

(1) N. de Christofaro (Argentina); J.J. Hechler (Canada); T. Hakkarainen (Finland); J. Legrand (France); M. Schröder (FRG); J. Togawa (Japan); J.F. Henriksen (Norway); P.V. Strekalov (Russia); M. Morcillo (Spain); V. Kucera (Sweden); P. McIntyre, M. McKenzie (UK); S.W. Dean, F. Mansfield (USA).

The system covered with these standards is based on the experiences of specialists - members of WG 4 and many technical and scientific results of institutions in countries participating in the activity of WG 4. Classification criteria and guiding corrosion values were derived in generalization of published exposure results from 220 testing sites in different climatic conditions and types of atmospheres. The validity of this data basis has, surely, some limitations

- non unified and with ISO standards compatible methods for exposure, measurement of parameters and evaluation of corrosion attack,
- differences in the composition of exposure materials,
- environments not covering all possible atmospheric open air conditions.

ISOCORRAG program was formulated and opened in 1987 - 1989 to provide corrosion data from a wide variety of testing sites using methods and procedures standardized within ISO/TC 156 with the goal to verify the classification philosophy and methods.

The aim of ISOCORRAG program consists in the studies of methodological, theoretical and technical aspects of the system and techniques included in ISO classification standards 1-4 and in forming a large data basis of high reliability for eventual qualified changes in the future revised version of the ISO classification standards. This worldwide exposure program (14 participating countries, 53 testing sites in 4 continents including high variety of climatic and pollution situations) is the largest atmospheric exposure program ever to be undertaken.

This paper introduces in short the results from the period 1987 - 1992. All results are summarized and analyzed in a ISO Technical Report 5, prepared to publication on the end of 1993.

II. Description of the program

A. Tested material

- unalloyed carbon steel
- zinc
- aluminium
- copper

Steel for flat and helix specimens was produced in British Steel Corp. (0.056% carbon, 0.060% silicon, 0.012% sulfur, 0.013% phosphorus, 0.02% chromium, 0.01% molybdenum, 0.04% nickel, 0.03% copper, 0.01% niobium, 0.01% titanium, 0.01% vanadium, 0.02% aluminum, 0.005% tin, 0.004% nitrogen, 0.39% manganese), all helix specimens were prepared in Germany (Staatliches Materialprüfungsamt, Dortmund). Flat specimens of zinc, copper and aluminium were of national production of single participating countries in agreement with prescribed properties.

B. Types of specimens

- flat plate specimens
- metallic wire - open helix specimens

C. Exposure sequences

- 6 one-year exposure (2)
- 1 two-year exposure
- 1 four-year exposure
- 1 long term exposure (8 years)

Details are given in ISO classification standards and in the manual to the program⁶. The survey of the test sites is in Table 1 and Fig.1 .

III. Results

The set of corrosion data available to the date of evaluation of the results (November 1992) includes corrosion losses of the flat and helix specimens for unalloyed steel, zinc, copper and aluminium for 6 one-year exposure sequences and two and four-years exposures. The theoretical number of corrosion data is 3392 values as mean values from triplicates of samples with relevant environmental characteristics. Mean values are summarized in Table 2 .

IV. Data treatment

The aim of experimental data treatment was to assess the reliability of collected data and to express the relation between corrosion loss and significant environmental parameters applied in corrosivity classification in the view point to the standardized measurement methods and corrosivity derivation.

Step in data treatment

- grouping and sorting of the data using statistical and classification criteria,
- derivation and statistical comparison of corrosivity categories basing on corrosion losses (flat and helix specimens) and/or environmental parameters,
- prognosis of average corrosion rates for 10 years exposure from the exposure period of four years, comparison with the guiding corrosion values in ISO 9224,
- regression analysis for corrosion losses and environmental characteristics important for the classification procedure.

The extent of treated results is enorm and cannot be presented in a relatively short paper. Results are more only illustrated by Tables 3.4 and 5 and Figures 2 and 3. All results together with the analysis of the results obtained are included in the ISO Technical Report listed.

(2) Three set of specimens of each metal are exposed for a year starting both in spring and autumn.

V. Conclusions

Both set of data, corrosion losses, as well as environmental characteristics are reliable enough to can form a basis for later treatment.

The transformation of the results (corrosion losses) from flat and helix specimens for reliable derivation of corrosivity categories is in principle possible, but with good validity for limited environmental conditions only (for relatively wide intervals of TOW and SO₂, relative narrow for salinity).

It is not a simple relation between corrosion attack and environmental parameters on the worldwide scale. Similar results have been published in the past ⁷ and are formulated in the reports with results to the ICP UN ECE ⁸ and in other recent publications ^{9,10}. The relative importance of environmental parameters changes from metal to metal and is different in individual climatic zones. For better fit is necessary in later treatment of data to respect binary interactions and use more complex models.

The classification system presented in the standards ISO 9223, ISO 9224, ISO 9225 and ISO 9226 is a good quantified generalization of knowledge in atmospheric corrosion of metals corresponding to the period of formulation of these standards and represents a new step in this technical activity.

The results of new worldwide programs - ISOCORRAG, ICP UN ECE, MICAT ^{8,11} form basis for better understanding of atmospheric corrosion, giving some answers but also open questions. The process of corrosion in environments with high variety cannot be fully described by rather simplified approach accepted before. The technical application of scientific results consists always in generalization, the possibilities or boundaries of this procedure is necessary to formulate in respect to the requirements of engineering practice.

Information about the severity of the atmospheric environment presented in the corrosivity classification system with quantitative criteria, based on relatively high level of generalization of results of testing and technical experience is a single realistic engineering approach for optimization of corrosion protection.

The philosophy of ISO classification standards is good. In the future revised edition of these standards some classification values and their interactive influences can be newly and better prescribed on the basis of the results of ISOCORRAG program.

ISO classification standards provide first guidance for corrosion engineers and designers in selecting materials and protective systems. The second step will always consist in creative solutions of technicians applying the standards. WG 4 is now working on a guidance as help in this respect ¹².

Acknowledgement

This work is the result of cooperation between the members of ISO/TC 156/WG 4 Classification of corrosivity of atmosphere and organizations supporting the program in participating countries: Instituto Argentino de Racionalizacion de Materiales (Buenos Aires); Instituto de Investigaciones Cientificas y Técnicas de las Fuerzas Armadas (Buenos Aires); Instituto Nacional de Tecnologia Industrial (Buenos Aires); National Research Council Industrial Materials Research Institute (Quebec); Bundesanstalt für Strassenwesen (Bergisch Gladbach); Staatliches Materialprüfungsamt N.W. (Dortmund); Technical Research Centre of Finland, Metallurgy Laboratory (Espoo); EDF - DER, Département ENA (Ecuelles); Cegedur Pechiney (Voreppe); Centre Technique du Zinc (Levallois Perret); Institut de la Recherche la Sidérurgie Francaise (St. Germain en Laye); Nippon Test Panel Co. (Tokio); Building Research Association of New Zealand, Building Science Group (Porirua); Norwegian Institute for Air Research (Lillestrom); Centro Nacional de Investigaciones Metalurgicas (Madrid); Escuela Tecnica Superior de Ingenieros Industriales, Departamento Ingeniera Quimica (Vigo); LABEIN, Dep. Materials and Contruction (Vizcaya); Swedish Corrosion Institute (Stockholm); Central Electricity Research Laboratories (Learherhead); British Steel Swinden Laboratories (Rotherham); LaQue Centre for Corrosion Technology (Wrightsville Beach); Department of Materials Science VHE, University of Southern California (Los Angeles); ASTM Committee G 1 (Philadelphia); IFCHAN (Moskow).

References

1. ISO 9223 Corrosion of metals and alloys - Classification of corrosivity of atmospheres.
2. ISO 9224 Corrosion of metals and alloys - Corrosivity of atmospheres - Guiding values for the corrosivity categories.
3. ISO 9225 Corrosion of metals and alloys - Corrosivity of atmospheres - Measurement of pollution.
4. ISO 9226 Corrosion of metals and alloys - Corrosivity of atmospheres - Determination of corrosion rate of standard specimens for the evaluation of corrosivity.
5. ISO Technical Report
ISOCORRAG - International Testing Program in the frame of ISO/TC 156/WG 4 Classification of corrosivity of atmosphere. Results and proposals for improvement of ISO corrosivity classification standards (ISO 9223 - ISO 9226) (in preparation)
6. The collaborative testing program ISOCORRAG. Technical Manual ISO/TC 156/WG 4 - N 131 (1986).
7. F.H.Haynie, J.P.Upham, Corrosion in Natural Enviroments. (ASTM/STP 553: S.W.Dean Ed.: Philadelphia 1974):p.33

8. International Cooperative Program (UN ECE) - Effects of acidifying air pollutants on materials including historic and cultural monuments; Report No. 12
D.Knotková, K.Kreislová, P.Holler, J.Vlčková, Corrosion attack on weathering steel, zinc and aluminium. Evaluation after 4 years of exposure; February 1993
9. S. Feliu, M. Morcillo, S. Feliu Jr., Corrosion Science, Vol 34, 3, (1993): p.403 - 414
10. S. Feliu, M. Morcillo, S. Feliu Jr., Corrosion Science, Vol 34, 3, (1993): p.415 - 422
11. M.Morcillo, head of the project "Ibero-American Map of Atmospheric Corrosiveness (MICAT)", (Mar del Plata, Argentina: Proc. 1st Pan-American Congress on Corrosion and Protection, Oct. 1992)
12. Protection methods on the basis of corrosivity classification, Working item of ISO/TC 156/WG 4 - WI 11303

Table 1. Atmospheric Corrosion Test Sites included into the Program

Country	Code	Name of Testing Site	Type of Atmosphere
Argentina	ARG 1	Iguazu	semiarid, wet, rural
	ARG 2	Camel	subtropical zone, marine, wet
	ARG 3	Buenos Aires	subtropical zone, marine, wet
	ARG 4	San Juan	subtropical zone, dry, rural
	ARG 5	Tubany Base	antarctic desertic zone
Canada	CND 1	Boucherville	moderate zone, rural
Czechoslovakia	CS 1	Kašperské Hory	moderate zone, rural
	CS 2	Praha-Běchovice	moderate zone, urban
	CS 3	Kopisty	moderate zone, heavy industrial
FRG	D 1	Bergisch Gladbach	moderate zone, urban
Finland	SF 1	Helsinki	moderate zone, urban
	SF 2	Otanieni	moderate zone, rural/urban
	SF 3	Ähtäri	moderate zone, rural
France	F 1	Saint Denis	moderate zone, urban - semi industrial
	F 2	Ponleau Martigues	moderate zone, marine
	F 3	Picherande	moderate zone, rural
	F 4	Saint Remy les Landes	moderate zone, marine
	F 5	Salins de Giraud	moderate zone, marine
	F 6	Ostende (Belgique)	moderate zone, marine
	F 7	Paris	moderate zone, urban
	F 8	Auby	moderate zone, heavy industrial
	F 9	Biarritz	moderate zone, marine
Japan	JAP 1	Choshi	moderate zone, rural
	JAP 2	Tokyo	moderate zone, urban
	JAP 3	Okinawa	subtropics, marine
New Zealand	NZ 1	Judgeford, Wellington	moderate zone, marine - rural
Norway	N 1	Oslo	moderate zone, urban
	N 2	Borregaard	moderate zone, industrial
	N 3	Birkenes	moderate zone, acid (acid rain)
	N 4	Tannanger	moderate zone, marine splash
	N 5	Bergen	moderate zone, marine - urban
	N 6	Svanvik	cold zone, arctic
Spain	E 1	Madrid	moderate zone, urban
	E 2	El Pardo	moderate zone, urban
	E 3	Lagoas - Vigo	moderate zone, industrial
	E 4	Baracaldo, Vizcaya	moderate zone, urban
Sweden	S 1	Stockholm-Vanadis	moderate zone, urban
	S 2	Bohus Malmön, Kattlesand	moderate zone, marine
	S 3	Bohus Malmön, Kvarnvik	moderate zone, marine - splash
UK	UK 1	Stratford, East London	moderate zone, industrial
	UK 2	Crowthorne, Berkshire	moderate zone, rural
	UK 3	Rye, East Sussex	moderate zone, marine
	UK 4	Fleet Hall	moderate zone, urban
USA	US 1	Cure Beach, N. Carolina	moderate zone, eastern marine
	US 2	Newark-Kerney, New Jersey	moderate zone, industrial
	US 3	Panama Canal - zone	tropical zone, marine - splash
	US 4	Research Triangle Park, N. Carolina	moderate zone, urban
	US 5	Point Reyes, California	moderate zone, western marine
	US 6	Los Angeles, California	moderate zone, marine - urban
USSR	SU 1	Murmansk	cold zone, marine - rural
	SU 2	Batumi	subtropical marine - urban
	SU 3	Vladivostok	far-east marine - urban
	SU 4	Oymyakon	extremely cold

Table 2. Means of mean yearly values of classification criteria

site code	corrosion loss ($\text{g.m}^{-2}\text{a}^{-1}$)								environmental characteristic		
	flat				helix				TOW (hrs)	SO ₂ ($\mu\text{g}/\text{m}^3$)	Cl ⁻ (mg/m^2)
	Fe	Zn	Cu	Al	Fe	Zn	Cu	Al			
ARG 1	5.8	1.6	0.8	0.05					5680		
ARG 2	36.8	1.3	2.2	0.19					6088		
ARG 3	16.2	1.0	0.6	0.05					4645		
ARG 4	4.6	0.2	0.2	0.03					855		
ARG 5	36.6	1.9	2.0	1.31					2693		
CND 1	23.2	1.4	1.1	0.40	27.5	2.0	1.3	0.4	1396	15.9	59.0
CS 1	26.0	1.9	2.0	0.50	47.6	2.2	2.6	0.3	3206	17.1	
CS 2	47.4	2.8	1.3	0.60	68.4	3.3	1.9	0.5	2991	67.5	
CS 3	70.7	3.5	3.3	0.70	108.0	4.8	4.2	0.7	2444	89.9	
D 1	36.2	1.6	0.6	0.30	52.1	1.8	0.8	0.6	4267	18.0	
SF 1	33.3	1.3	0.7	0.30	42.7	2.6	1.3	0.5	3578	18.9	3.7
SF 2	25.6	0.9	0.8	0.10	37.8	1.8	1.5	0.3	3256	15.3	2.5
SF 3	12.8	0.7	0.7	0.10	16.1	1.2	1.1	0.5	3105	4.1	
F 1	37.2	1.5	1.2	1.20	49.6	3.6	2.8	2.1	4268	49.6	27.8
F 2	72.4	2.6	2.7	1.00	126.0	13.4	9.7	13.5	3846	87.0	241.0
F 3	16.1	0.9	1.4	0.30	22.8	2.2	2.0	0.5	4171	9.1	6.5
F 4	44.1	1.5	1.8	0.70	94.7	4.2	5.3	1.5	6310	30.3	378.0
F 5	73.0	4.6	3.2	0.70	132.0	5.7	5.3	2.8	3311	20.0	184.0
F 6	99.3	5.1	3.1	1.50	130.0	10.6	3.5	3.3	6083	24.0	173.0
F 7	41.7	3.0	1.4	0.90	51.7	2.8	2.6	1.2	3180	53.4	
F 8	106.0	5.6	1.9	1.70	145.0	8.5	2.4	3.8	4571	188.0	16.0
F 9	87.2	4.3	3.7	1.20	67.9	8.2	4.5	2.4			193.0
JAP 1	43.3	1.4	1.4	0.33	93.7	2.8	2.3	0.7	5704	7.7	66.8
JAP 2	39.5	1.5	0.7	0.54	39.1	1.5	1.1	0.4	2173	14.6	4.4
JAP 3	75.2	3.4	2.1	0.26	109.0	8.8	4.3	1.0	3852	11.1	130.0
NZ 1	19.3	0.7	1.4	0.06	36.3	1.2	1.6	0.4			
N 1	25.2	1.3	0.6	0.20	35.0	1.8	0.9	0.2	2641	13.8	2.1
N 2	61.7	3.8	1.4	0.60	90.9	5.7	2.7	1.7	3339	44.2	8.2
N 3	19.7	2.3	1.3	0.10	27.0	2.0	1.3	0.1	4138	1.2	
N 4	59.6	3.0	1.9	0.60	74.1	3.3	3.2	0.9	4583	4.0	321.0
N 5	27.9	2.1	1.0	0.10	32.8	2.2	1.1	0.3	4439	8.6	7.1
N 6	20.2	0.8	0.8	0.10	29.0	1.4	1.0	0.2	2605	16.7	1.0
E 1	27.7	0.6	0.5	0.07	29.3	1.6	0.8	0.2	2060	44.2	
E 2	15.5	0.5	1.1	0.05	21.6	1.2	1.2	0.1	3223	4.9	
E 3	26.9	1.0	1.0	0.20	35.9	2.5	1.2	0.3	2840	48.7	21.2
E 4	43.9	1.2	1.2	0.20	56.0	2.6	1.5	0.3	4375	32.1	29.2
S 1	24.4	0.6	0.6	0.20	41.5	1.5	1.1	0.4		9.8	
S 2	35.2	1.5	1.7	0.40	60.8	2.8	2.3	0.9		5.0	85.5
S 3	61.6	1.8	2.8	0.60	67.7	3.5	4.9	1.5		5.0	667.0
UK 1	38.7	1.7	1.1	0.29	50.3	1.5	1.4	0.2	5783	19.9	15.1
UK 2	37.4	1.1	1.1	0.12	57.9	1.2	1.4	0.2			
UK 3	58.5	2.5	1.9	0.42	92.5	2.0	4.2	0.5		21.2	300.0
UK 4	39.0	1.3	0.9	0.36	56.9	2.3	1.6	0.4			
US 1	37.9	2.0	2.9	0.29	81.8	3.9	4.6	0.9	4289	9.6	184.0
US 2	26.4	2.0	1.4	0.28	27.3	2.2	1.9	0.6			
US 3	373.0	17.5	5.5	0.57	297.0	7.6	11.6	1.7	7598	51.5	619.0
US 4	23.1	0.8	2.4	0.11							
US 5	40.1	1.7	2.4	0.22	147.0	3.5	4.4	1.3			
US 6	21.4	1.1	1.2	0.56	19.2	1.8	2.0	1.5	4003	20.0	
SU 1	30.8	1.1	1.7	0.80	51.7	2.1	2.8	1.8	3227	5.0	19.9
SU 2	28.7	1.6	2.0	0.10	28.7	2.0	1.9	0.3	3216	25.8	1.0
SU 3	25.9	2.3	1.4	0.30	66.8	3.1	2.4	0.7	3920	28.6	18.4
SU 4	0.8	0.4	0.1	0.07	1.9	0.6	0.1	0.1	381	5.0	

Table 3. Linear regression of corrosion and environmental data using the equation

$$\text{Corr} = a + bx\text{SO}_2 + cx\text{TOW} + dx\text{Cl}$$

(one-year exposure)

Metal	specimen	Regression coefficient				Correl.	Number of data
		a	b	c	d		
steel	flat	30.20	0.410			0.39	211
		-10.90	0.440	0.011		0.56	183
		-3.80	0.370	$7.6 \cdot 10^{-3}$	0.13	0.59	85
		39.50			0.10	0.43	117
	helix	44.20	0.640			0.47	204
		-23.20	0.670	0.018		0.69	176
		3.35	0.520	0.011	0.16	0.72	81
		59.30			0.08	0.35	111
zinc	flat	1.45	0.024			0.34	212
		-0.97	0.024	$6.7 \cdot 10^{-4}$		0.49	184
		-0.39	0.022	$3.7 \cdot 10^{-4}$	$8.4 \cdot 10^{-3}$	0.56	86
		1.81			$7.0 \cdot 10^{-3}$	0.43	119
	helix	2.04	0.045			0.51	201
		-0.58	0.046	$7.3 \cdot 10^{-4}$		0.59	174
		1.98	0.046	$1.1 \cdot 10^{-4}$	$7.0 \cdot 10^{-3}$	0.60	79
		3.49			$3.9 \cdot 10^{-3}$	0.23	111
copper	flat	1.33	$7.0 \cdot 10^{-3}$	$2.9 \cdot 10^{-4}$		0.23	209
		0.24	$7.7 \cdot 10^{-3}$	$8.8 \cdot 10^{-5}$		0.47	181
		0.91	$1.9 \cdot 10^{-3}$		$4.4 \cdot 10^{-3}$	0.69	84
		1.38			$4.0 \cdot 10^{-3}$	0.65	118
	helix	2.09	0.017	$7.0 \cdot 10^{-4}$		0.22	203
		-0.57	0.019	$-6.9 \cdot 10^{-5}$		0.42	176
		1.86	0.012		0.012	0.55	81
		2.14			$6.5 \cdot 10^{-3}$	0.45	111
aluminium	flat	0.25	$6.5 \cdot 10^{-3}$			0.54	205
		0.53			$2.2 \cdot 10^{-4}$	0.10	115
		0.27	0.033			0.43	195

Table 4. Correlation/regression analysis of corrosion data, comparison of flat and helix specimens (equation $Y = b.X$)

Variables				Regression/Correlation	
X (independent)	Y (dependent)			b	r
steel	flat	steel	helix	1.250	0.67
zinc	flat	zinc	helix	1.270	0.36
copper	flat	copper	helix	1.630	0.66
aluminium	flat	aluminium	helix	2.580	0.53
steel	flat	zinc	flat	0.049	0.86
		copper	flat	0.030	0.45
		aluminium	flat	0.001	0.47
steel	helix	zinc	helix	0.056	0.75
		copper	helix	0.039	0.61
		aluminium	helix	0.022	0.50
zinc	flat	copper	flat	0.754	0.64
		aluminium	flat	0.174	0.28
zinc	helix	copper	helix	0.880	0.51
		aluminium	helix	0.438	0.73
copper	flat	aluminium	flat	0.282	0.46
copper	helix	aluminium	helix	0.540	0.62

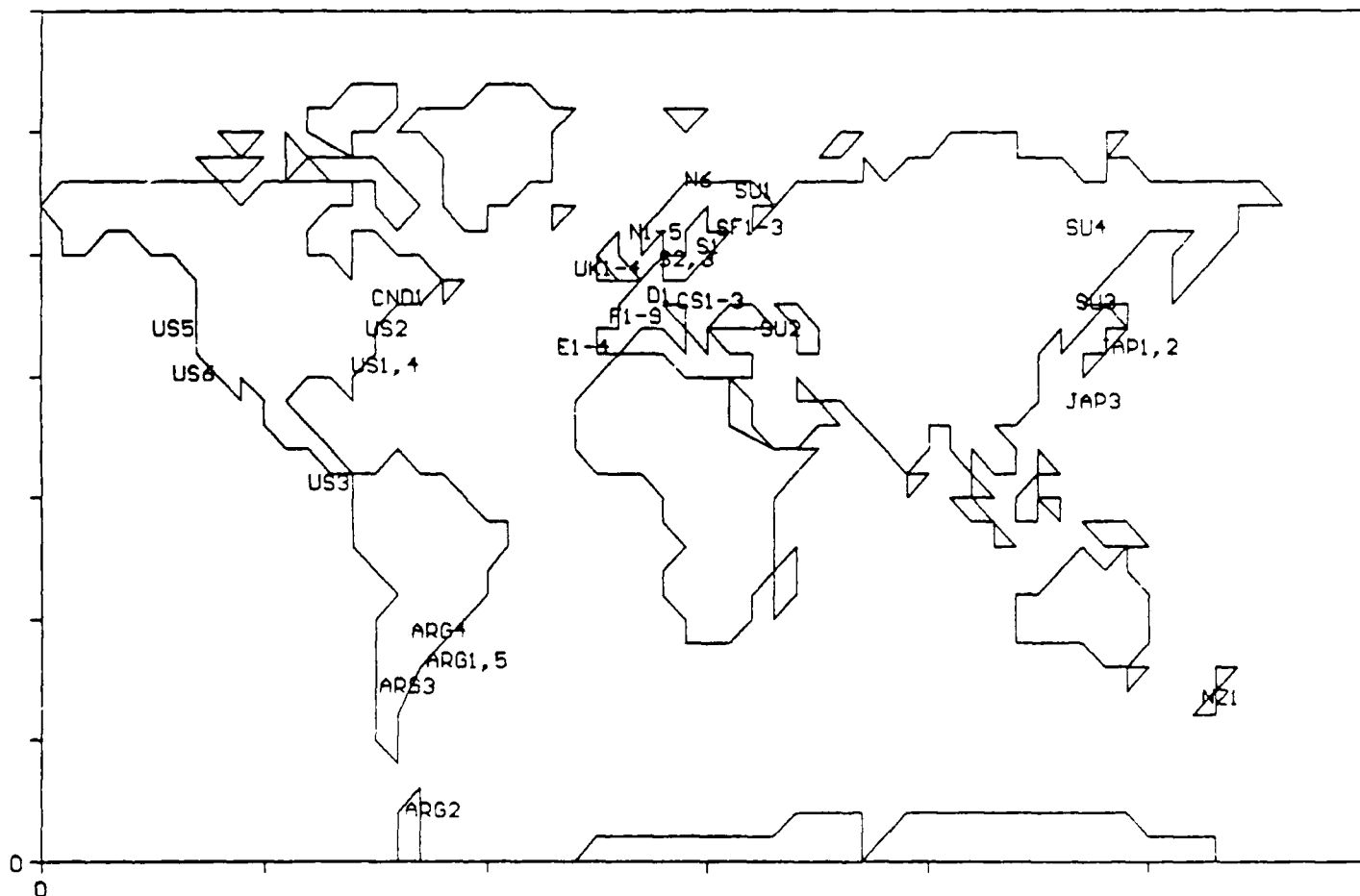


Figure 1. Map showing location of exposure sites

Figure 2. Unalloyed steel - corrosion of flat and helix specimens
Comparison of corrosion rates for one-year exposure

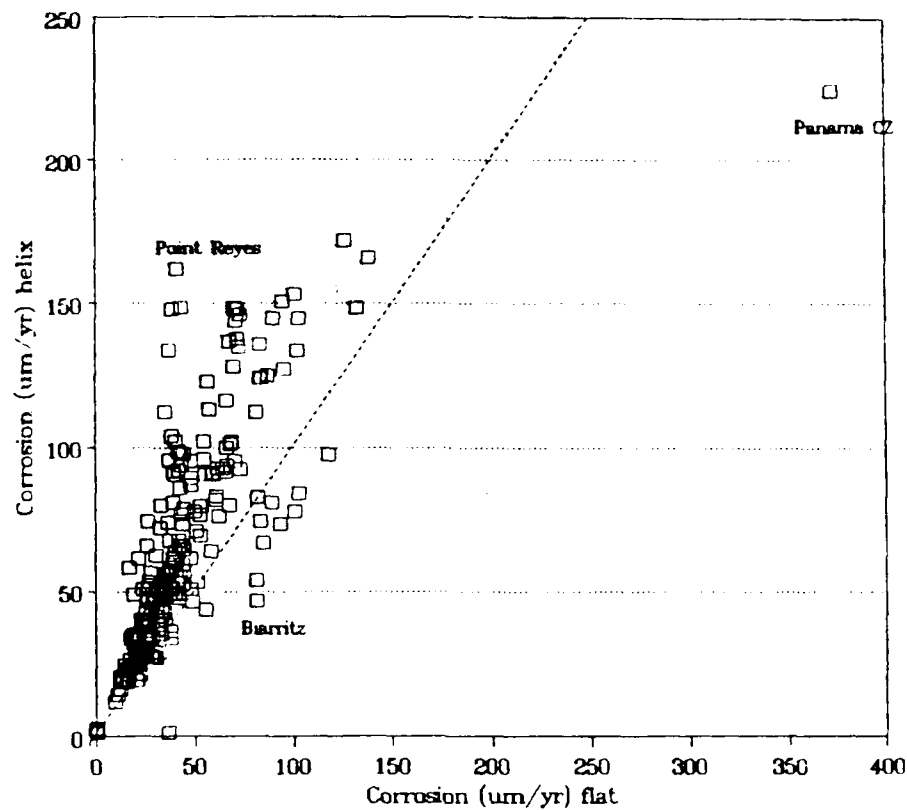


Figure 3. Copper - corrosion of flat and helix specimens
Comparison of corrosion rates for one-year exposure

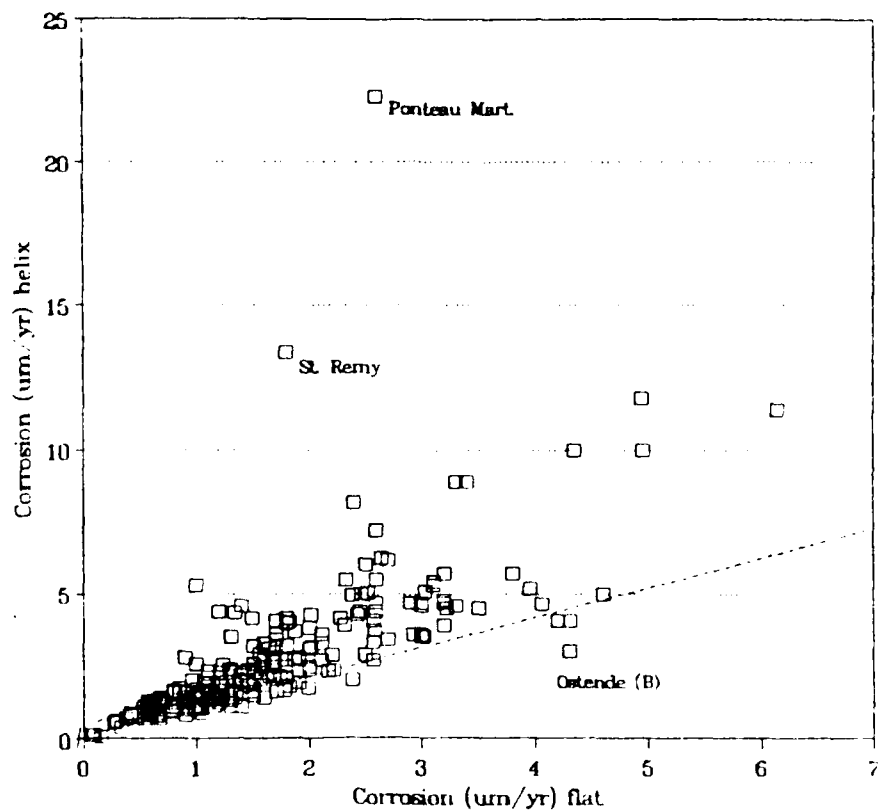


Figure 4. Corrosion rates of unalloyed steel (one year of exposure, flat specimens) as function of the SO_2 concentration with distinguished deposition rate of NaCl

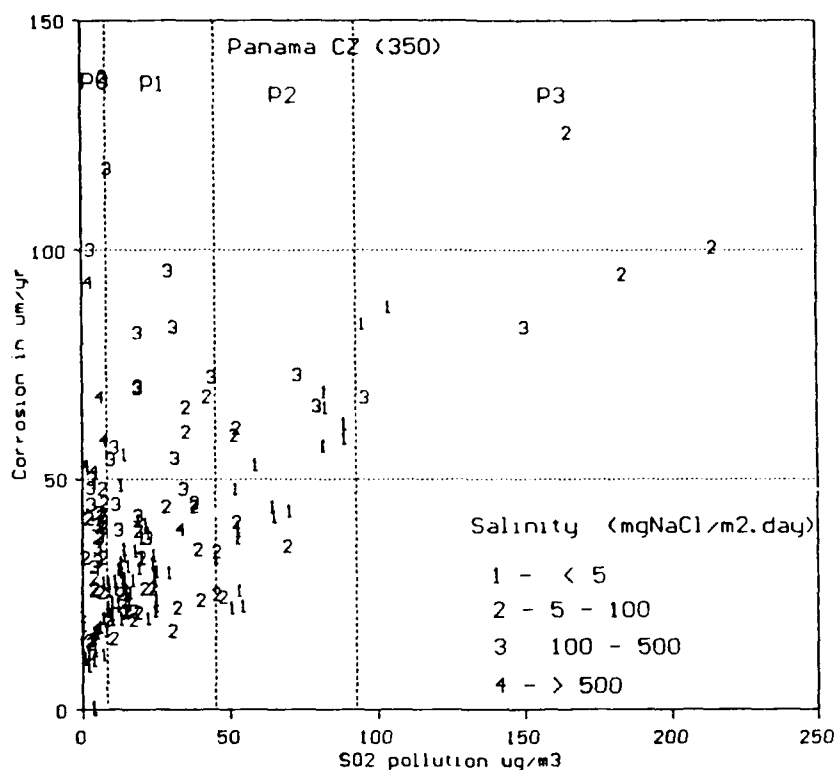


Figure 5. Corrosion rates of zinc (one year of exposure, flat specimens) as function of the SO_2 concentration with distinguished deposition rate of NaCl

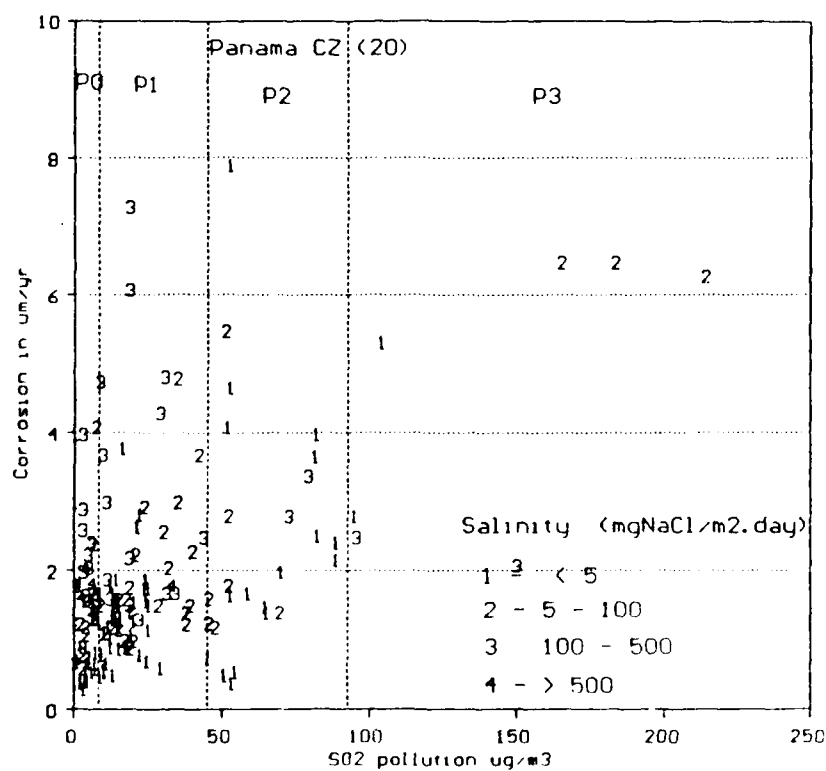
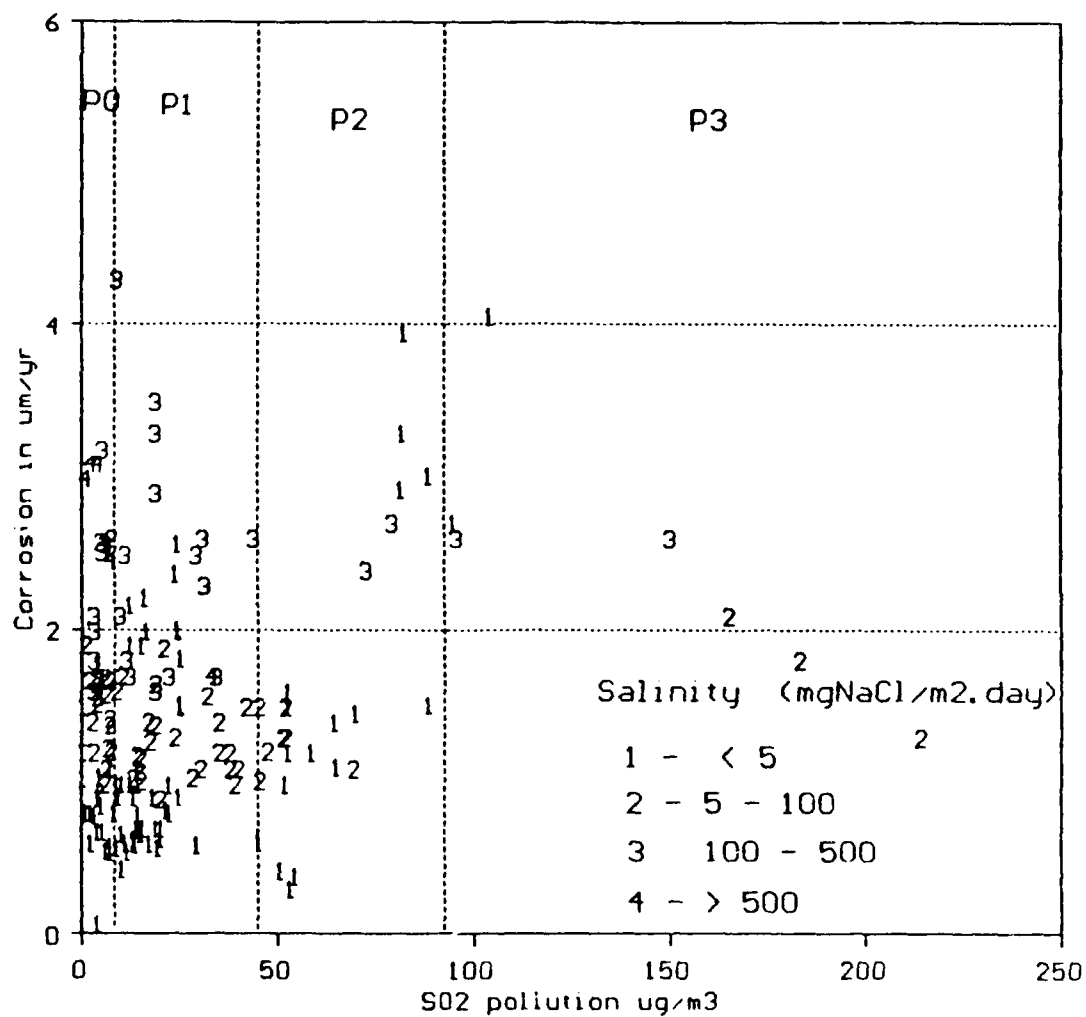


Figure 6. Corrosion rates of copper (one year of exposure, flat specimens) as function of the SO_2 concentration with distinguished deposition rate of NaCl



Techniques Applied to the Analysis of the Atmospheric Corrosion of Low
Carbon Steel, Zinc, Copper and Aluminum

Alejandro Fernandez
CITEFA
Zufriategui 4380
(1603) V. Martelli- Argentina

Maria del Carmen Leiro
CITEFA
Zufriategui 4380
(1603) V. Martelli- Argentina

Blanca M. Rosales
CITEFA
Zufriategui 4380
(1603) V. Martelli- Argentina

Eduardo S. Ayllon
CITEFA
Zufriategui 4380
(1603) V. Martelli- Argentina

Francisco E. Varela
INIFTA
Suc. 4, CC 16
(1900) La Plata- Argentina

Claudio A. Gervasi
CIDEPIINT
522 entre 121 y 122
(1900) La Plata- Argentina

Jorge R. Vilche
INIFTA
Suc. 4, CC 16
(1900) La Plata- Argentina

Abstract

The purpose of this work was to compare results of evaluation techniques applied to plain C steel, Zn, Cu and Al submitted to atmospheric corrosion after exposures in different test sites with known ambient conditions. Electrochemical dc and ac techniques were applied to determine the protectiveness of the films developed on the distinct metals and environments. Weight losses after different outdoor exposition periods were compared to the polarization resistance (R_p) measured through electrochemical pulses and impedance spectroscopy (EIS) in aerated static solutions of 0.1 M Na_2SO_4 , on the exposed face of the test samples. SEM-EDAX of the rusts provided information about the structure and the presence of pollutants in the rusts.

Key terms: Atmospheric corrosion, techniques, protectiveness of rusts.

Introduccion

This work was performed in the frame of the cooperative CYTED-D program

sponsored by Spain, to characterize the protective properties of the atmospheric corrosion products and to elucidate unknown aspects of the mechanisms involved. The metallic materials used were low carbon steel, Zn, Cu and Al weathered in different ambient conditions of the Iberoamerican network of Outdoor Test Stations.

A good correlation was not always obtained among weight losses and R_p determined by different dc or ac electrochemical techniques. From previous work¹, polarization curves were discarded as a useful tool to compare protectiveness of rusts formed in distinct environments and the corrosion rate of the respective metal, measured through weight loss during the same exposition period in well defined meteorological and pollution conditions.

However the electrochemical nature of the atmospheric corrosion² suggests the usefulness³⁻⁵ of a such technique to evaluate the controlling factors in its occurrence.

The application of an anodic or cathodic polarization step after distinct immersion times and measurements of the current decay produced, gave high dispersive results.

EIS data were not always reproducible, depending of the metal, test period and selected area of the sample considered.

Experimental

Samples of low carbon steel, aluminum, copper, and zinc (Table I) were exposed for different periods of one year at several locations in Iberoamerica covering rural, urban, marine, and industrial atmospheric conditions. The environmental factors prevailing in the outdoor test stations were well monitored in order to study their influence on the atmospheric corrosion process. The corrosion products thus formed were removed to determine corrosion rates of the metals while rusted samples were characterized by using electrochemical dc and ac measurements, SEM observations, and surface chemical analysis (EDAX).

ISO norms were followed for the outdoor expositions ambient characterization of the test sites and pickling of the rusted samples to determine weight loss.¹⁰

The electrochemical experiments were performed in 0.1 M Na_2SO_4 at 20°C. The electrolyte solution was prepared from analytical grade (p.a. Merck) reagents and triply distilled water purified in a Milli-Q reagent grade system. A three-compartment electrolysis Pyrex cell was employed. Potentials were measured and referred to in the text, against a SCE reference electrode properly shielded. A large-area Pt plate was used as counter electrode.

The dc electrochemical tests consisted on anodic and cathodic steps of 15 minutes duration and 20 mV after 1, 24 and 48 hs. of immersion and determination of the current decay attainment. The results obtained are summarized in Table II and compared with the respective corrosion rates determined from weight losses.

For impedance measurements an activated platinum probe was coupled to the reference electrode through a 10 μF capacitor to reduce phase shift errors at high frequencies. A detailed description of both hardware arrangement and data processing have been given elsewhere [6-9]. Impedance spectra were obtained at the corrosion potential in the frequency range $10^{-3} \text{ Hz} \leq f \leq 50 \text{ kHz}$ using a frequency response analyser (Solartron FRA 1250) and an

electrochemical interphase (Solartron EI 1186), which were integrated with both an Apple IIe computer and a PC compatible system. Geometrical area of the working electrodes was 1.13 cm^2 .

The SEM observations were made using a Philips 515 microscope, which was coupled to a 9100 EDAX for the surface analysis. The test samples were metallized with Al, previous to the SEM observation. Accordingly, data obtained from SEM and EDAX were used to characterize the morphology and chemical heterogeneities of the corrosion products.

Results and Discussion

SEM analysis allowed us to partly understand the uneven behavior detected through the electrochemical techniques used on the basis of the very heterogeneous morphology of the films grown on the distinct substrata and ambients. From the compact, homogeneous and thin films formed on Al in several ambients to the cracked, heterogeneous and thick rusts of steel in marine environments, the great variety of morphologies observed could justify the scattered results obtained for the different metals weathered in the distinct conditions analyzed, as can be seen in Fig. 1 for rusts formed on steel in an Antarctic and a very dry and hot test site.

The uneven affinity of the metallic surfaces and of the corrosion products formed, for the marine, industrial and solid pollutants detected by EDAX, suggested that other factors than the morphology could also influence the R_p results. In Fig. 2 SEM of corrosion products of Zn, Cu and Al and the respective EDAX after two year at Jubany Base in the Antartics. SEM-EDAX of the cross sections of the 4 metals weathered during the same period in the last Test site are given in Fig. 3. Caves are observed in all of them in connection with pollutants accumulation.

The condition to establish a useful technique for the samples of the 4 metals after exposition to the different environmental conditions of the Iberoamerican Region and outdoor test periods makes difficult to get one that provided the expected good correlation.

In fact, while in a very dry ambient with short duration wet periods the rust formed on a given metal will be enough protective to produce a low weight loss, the same metal exposed to long wetting times will suffer a high weight loss. This demonstrates that the rusts formed in environments producing long times of wettness of the metals have a lower protective character than those formed in a dry ambient.

The R_p or the decay current attained after application of a pulse is also dependent of the immersion time in the solution previous to the electrochemical measurement, for times shorter than the necessary to saturate all the existing diffusional ways for water and oxygen in the film, as can be seen in Table II. Once embebed, the measurement of the R_p would only be dependent of the protectiveness of that rust reproducing during the electrochemical measurement the condition of a long duration wet period that generally occurred during the outdoor test. This long immersion time could differently affect the protectiveness of the films formed in environments with short and long wet periods.

Impedance spectra for the different tested electrode materials are depicted in Figs. 4 to 7. Data analysis through non-linear complex fit routines were performed in order to obtain the polarization resistance (R_p) values defined by:

$$R_p = \lim_{s \rightarrow 0} Z(s)$$

were $Z(s)$ is the electrode impedance corrected for the ohmic resistance contribution and s the complex variable ($s = j\omega$) for a sinusoidal small signal perturbation.

Impedance measurements in the low-frequency region required special precautions to obtain reliable data since even at frequencies in the vicinity of 10^{-3} Hz, some experimental spectra displayed a reactive impedance. In those cases where considerable extrapolation is required to estimate the value of R_p , the corresponding data are not informed in this paper. However, computer analysis of impedance spectra with multiple time-constants can be performed to derive R_p even if less than a full semicircle in the low frequency range is determined and/or the semicircle is depressed with its center below the real axis.

It is interesting to note that this simple analysis of the corrosion behaviour, based on R_p values represents an initial approach to determine whether impedance techniques can prove useful to compare the relative corrosiveness of different atmospheric conditions. Further work is required for deriving mechanistic and kinetic information for processes occurring at the corroding interface.

The corrosion rates of metals determined from weight-loss measurements are presented in Table III, whereas data obtained from EIS are summarized in Tables IV. Comparing the corrosion rates shown in Table III, in terms of weight-loss of metals, the best correlation with electrochemical results was achieved for Cu using EIS measurements.

Further works to introduce system models based on theoretical transfer function to simulate impedance spectra as well as the use of IR, X-ray, and Mössbauer spectroscopies to determine the chemical composition of corrosion products are in progress.

Acknowledgments

The authors acknowledge to Lic. Monica PINTO from INTI, Applied Electrochemistry Sector, who performed the R_p measurements on all the Cu samples. Also they thank to Mr. Gustavo MORIENA and Juan NAVARRO for their valuable collaboration during the experimental work.

References

1. S.L. Granese, E.S. Ayllon, B.M. Rosales, F.E. Varela, C.A. Gervasi, J.R. Vilche - Characterization of the Atmospheric Corrosion Products formed on Low Carbon Steel, Aluminum, Copper, and Zinc Specimens. Proc. 1st. Panamerican Corrosion and Protection Congress, 1 (1992): p. 191.
2. U.R. Evans, Nature (1965): p. 206.
3. M. Pourbaix, Une Méthode Electrochimique Rapide de Prédétermination de la Corrosion Atmosphérique. Rapports Techniques CEBELCOR, Belgique, 109 (1969): p. 1.
4. B.M. Rosales and E.S. Ayllon, Atmospheric Corrosion (Edited by W.H. Ailor), John Wiley & Sons Inc., New York, (1982): p. 501.
5. E.S. Ayllon, S.L. Granese and B.M. Rosales, Proceedings 3rd. Iberoamerican Congress of Corrosion and Protection, Brazil, (1989): p. 427.
6. E.B. Castro, S.G. Real, S.B. Saidman, J.R. Vilche and R.H. Milocco, Materials Science Forum, 44/45 (1989): p. 417.
7. R.H. Milocco, E.B. Castro, S.G. Real and J.R. Vilche, Transient Techniques in Corrosion Science and Engineering (Edited by W.H. Smyrl,

- D.D. Macdonald and W.J. Lorenz), The Electrochemical Society Inc., Pennington, (1989): p. 88.
8. E.B. Castro, S.G. Real, R.H. Milocco and J.R. Vilche, *Electrochim. Acta*, 36 (1991): p. 117.
9. E.B. Castro and J.R. Vilche, *J. Electroanal. Chem.*, in press.
10. ISO/DP 9223 Corrosion of Metals and Alloys. Classification of Corrosivity Categories of Atmospheres. ISO/DP 9224. Guiding Values for the Corrosivity Categories of Atmospheres. ISO/DP 9225. Aggressivity of Atmospheres. Methods of Measurements of Pollution Data. ISO/DP 9226. Methods of Determination of Corrosion Rate of Standard Specimens for the Evaluation of Corrosivity.

Table 1. Chemical Composition of The Exposed Metals (% w/w)

STEEL	C	0.076	S	0.010	Cu	0.03
	Mn	0.39	Cr	0.03	Sn	0.003
	Si	0.065	Ni	0.04	Al	0.057
	P	0.015	Mo	0.001	Ti	0.003
COPPER	Pb	0.005	Ni	0.01	P	0.0067 (Sn vestiges)
ZINC	Pb	0.0063	Cu	0.0004	Sn	< 0.0005
	Cd	0.0009	Fe	0.0007	Al	< 0.0008
ALUMINUM	Si	0.06	Mn	0.002	Cr	0.002
	Fe	0.12	Mg	0.001	Zn	0.003
	Cu	0.003	Ti	0.007	B	0.001
	Pb	0.001				

TABLE III: Corrosion Rates of the 4 Metals at the 6 Argentine Outdoor Test Stations

Station		San Juan				Iguazú			
Exposition Periods		Corrosion Rate($\mu\text{m}/\text{y}$)				Corrosion Rate($\mu\text{m}/\text{y}$)			
		St.	Zn	Cu	Al	St.	Zn	Cu	Al
1 Year	1.1.	4.62	0.26	0.19	0.015	5.74	2.39	0.99	0.03
"	1.2.	4.55	0.13	0.16	0.057	5.76	1.17	0.81	0.08
"	1.3.	5.57	0.22	0.17	0.015	5.46	1.18	0.76	0.10
2 Years	2.1.	3.09	0.15	0.15	0.012	5.04	1.74	0.91	0.06
3 Years	3.1.		0.11	0.15	0.005	3.64	1.24	0.86	0.02

Station		Camet				M. Martelli			
Exposition Periods		Corrosion Rate($\mu\text{m}/\text{y}$)				Corrosion Rate($\mu\text{m}/\text{y}$)			
		St.	Zn	Cu	Al	St.	Zn	Cu	Al
1 Year	1.1.	24.90	1.30	2.41	0.14		1.12	0.81	0.05
"	1.2.	54.80	1.17	2.00	0.21	16.1	1.05	0.63	0.03
"	1.3.		2.37	2.26	0.29	12.4	1.41	0.93	0.06
2 Years	2.1.	23.1	1.28	1.65	0.13	13.3	0.87	0.53	0.02
3 Years	3.1.	28.9	1.15	1.30	0.08		0.90	0.52	0.03

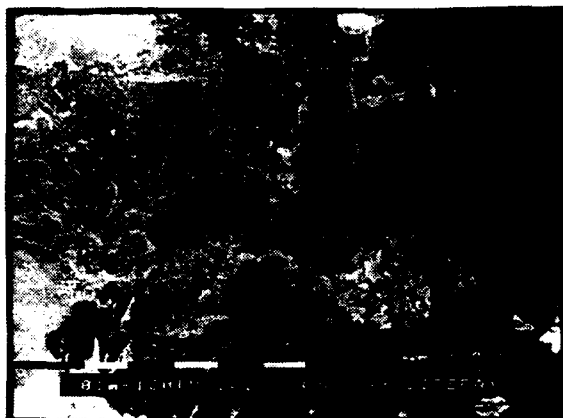
Station		Base Jubany				CIDEPIINT - La Plata			
Exposition Periods		Corrosion Rate($\mu\text{m}/\text{y}$)				Corrosion Rate($\mu\text{m}/\text{y}$)			
		St.	Zn	Cu	Al	St.	Zn	Cu	Al
1 Year	1.1.	37.29	1.98	1.98	1.54	25.30	0.77	1.32	0.049
	1.2.	35.92	2.48	2.10	1.07				
	1.3.								
2 Years	2.1.	24.99	1.07	1.17	1.19				
3 Years	3.1.								

TABLE IV: Polarization Resistance Data Calculated From
Impedance Spectra ($R_p / \text{M}\Omega$)

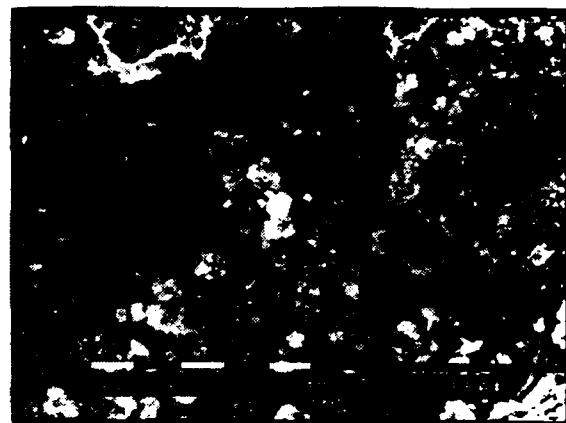
Test Station		Al	Cu	Zn
Canet	1 Year	33.78	0.060	0.062
"	2 years	8.23	---	0.100
Iguazú	1 Year	4.60	0.616	0.014
"	2 years	2.02	---	0.007
San Juan	1 Year	56.00	0.710	0.002
"	2 years	3.11	---	0.003
V. Martelli	1 Year	8.27	0.620	0.021
	2 years	5.10	---	0.020
Jubany	1 Year	2.14	0.120	0.003

Fig. 1 SEM, EDAX and Weight Loss of the Steel Weathered 2 Years in Very Different Ambient Conditions

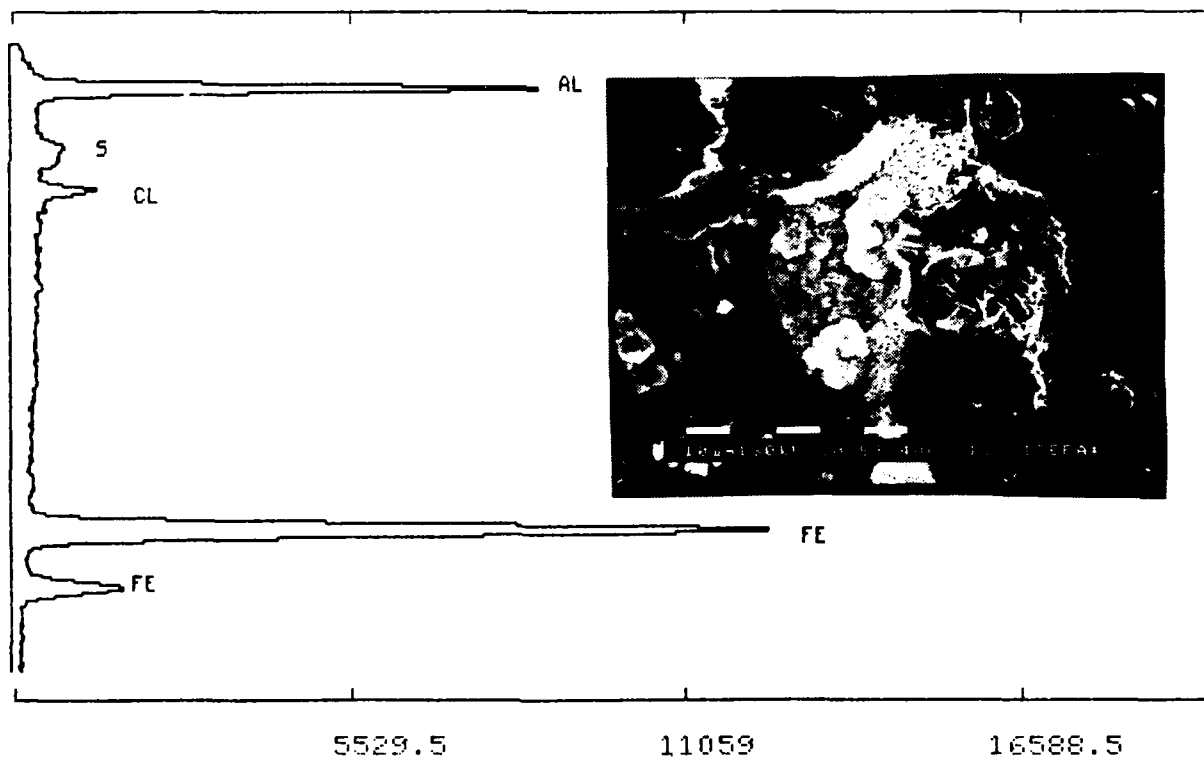
a) JUBANY BASE - Antartics



X 100



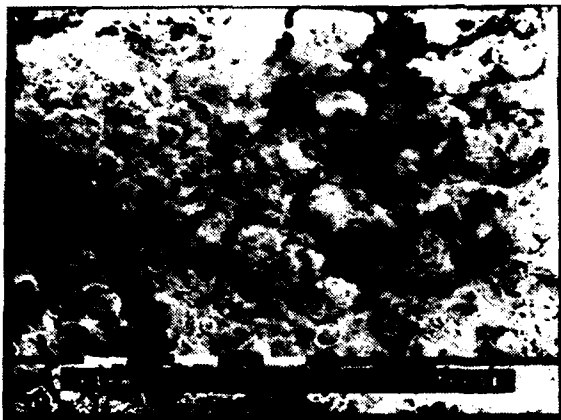
X 1000



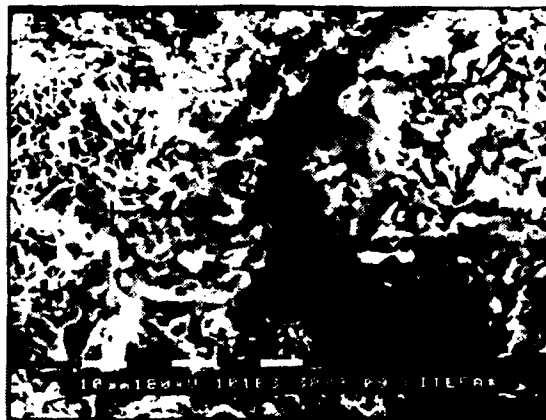
Ambient Conditions	JUBANY BASE Test Station								Corrosion Rate ($\mu\text{m} \cdot \text{year}^{-1}$)
	T ($^{\circ}\text{C}$)			Hr (%)			(hs)	($\text{mg}/\text{m}^{-2}\text{d}$)	
	Mean	Max.	Min.	Mean	Max.	Min.	TOW	[Cl ⁻]	Steel
Year 1	-2.0	0.3	-4.3	84	91	76	2693	12	37.3
Year 2	-3.1	-1.1	-5.1	84	91	77	2425	18	25.0

Fig. 1 Cont.

b) SAN JUAN Test Station



X 100



X 1000

EDAX X 100:

Element	Weight %
Si	1.39
S	1.46
Cl	4.64
Fe	<u>92.51</u>
	100.00

Ambient Conditions SAN JUAN Test Station

	T (°C)			Hr (%)			(hs)
	Mean	Max.	Min.	Mean	Max.	Min	TOW
Year 1	18	26	10	51	72	29	1002
Year 2	20	28	12	49	71	28	847

Corrosion Rate

($\mu\text{m} \cdot \text{year}^{-1}$)

Steel

5.6

3.1

Fig. 2 SEM, EDAX and Weight Loss of Zn, Cu and Al Weathered 2 Years in the
JUBANY BASE Test Station

a) Zn

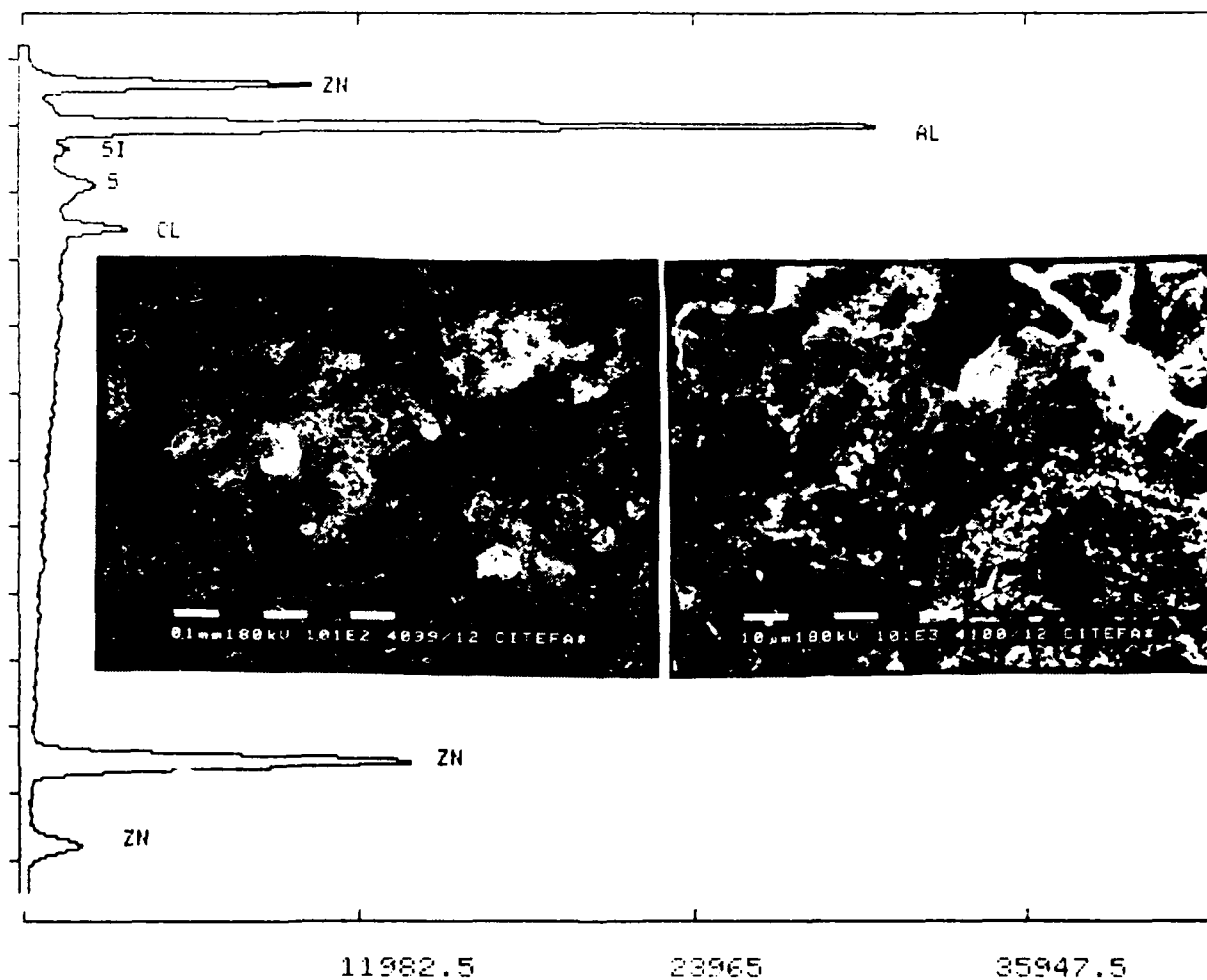


Fig. 2 Cont.

b) Cu



X 100



X 1000

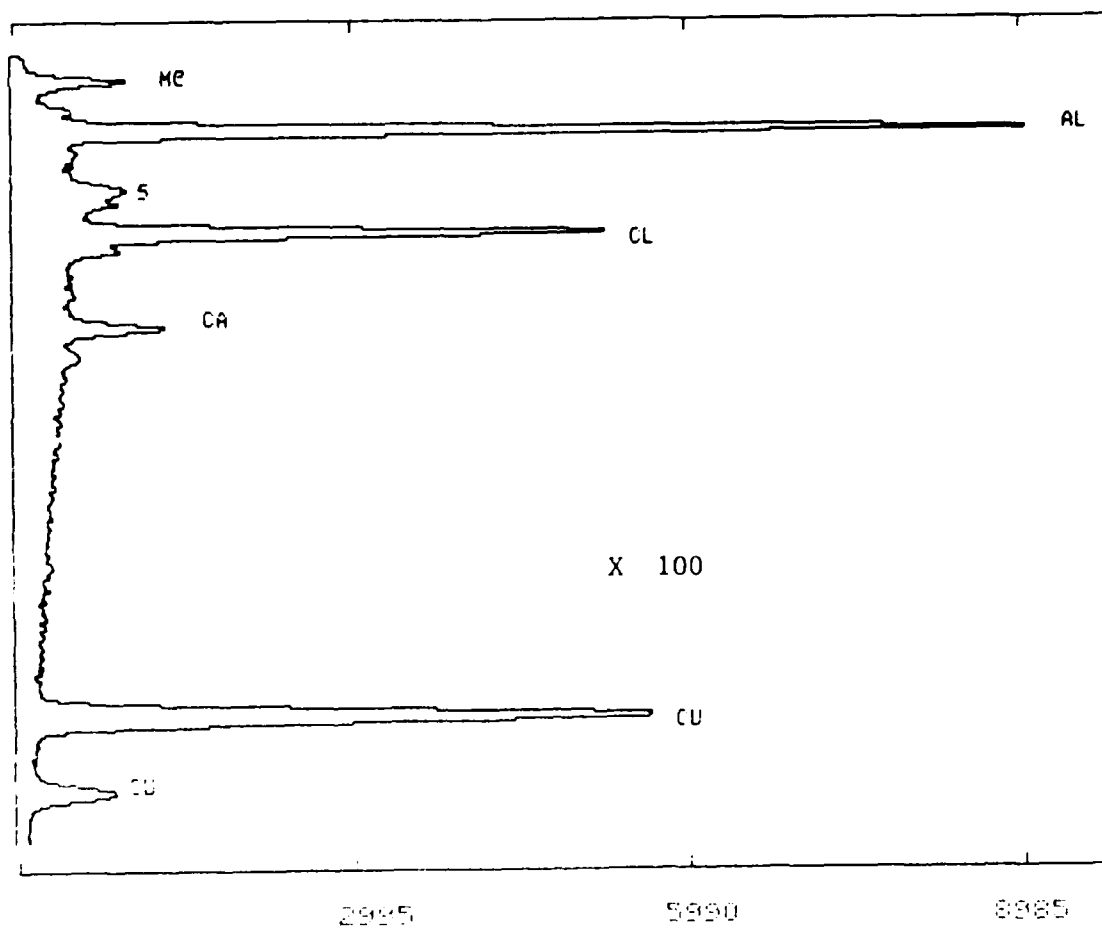
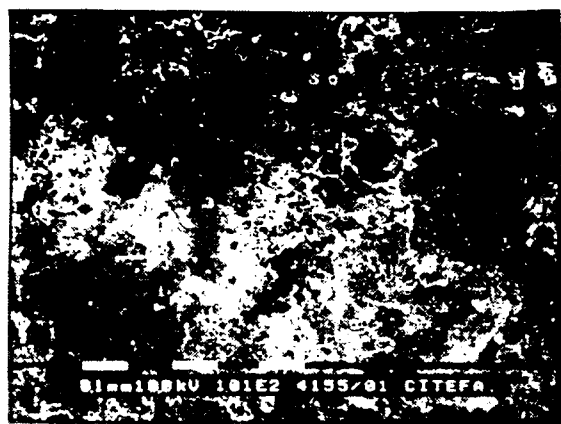
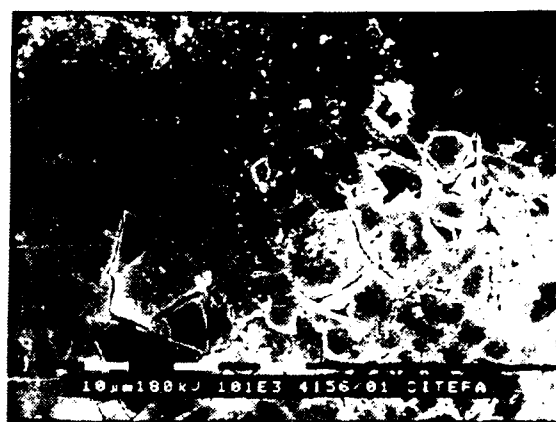


Fig. 2 Cont.

c) Al



X 100



X 1000

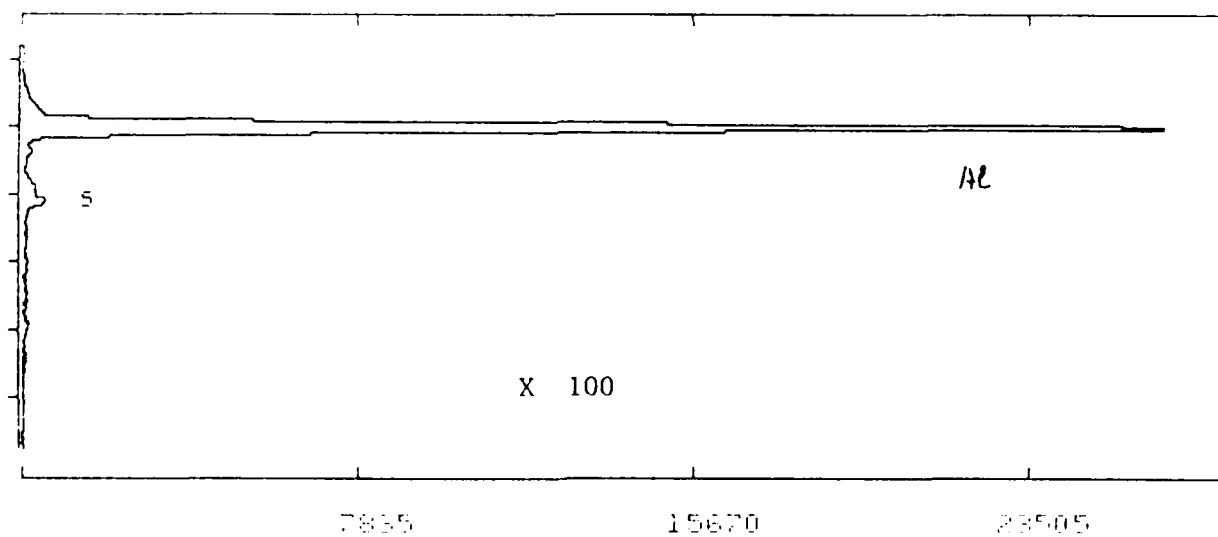


Fig. 3 SEM and EDAX in Cross Sections of the 4 Metals Weathered 2 Years
in JUBANY BASE Test Station

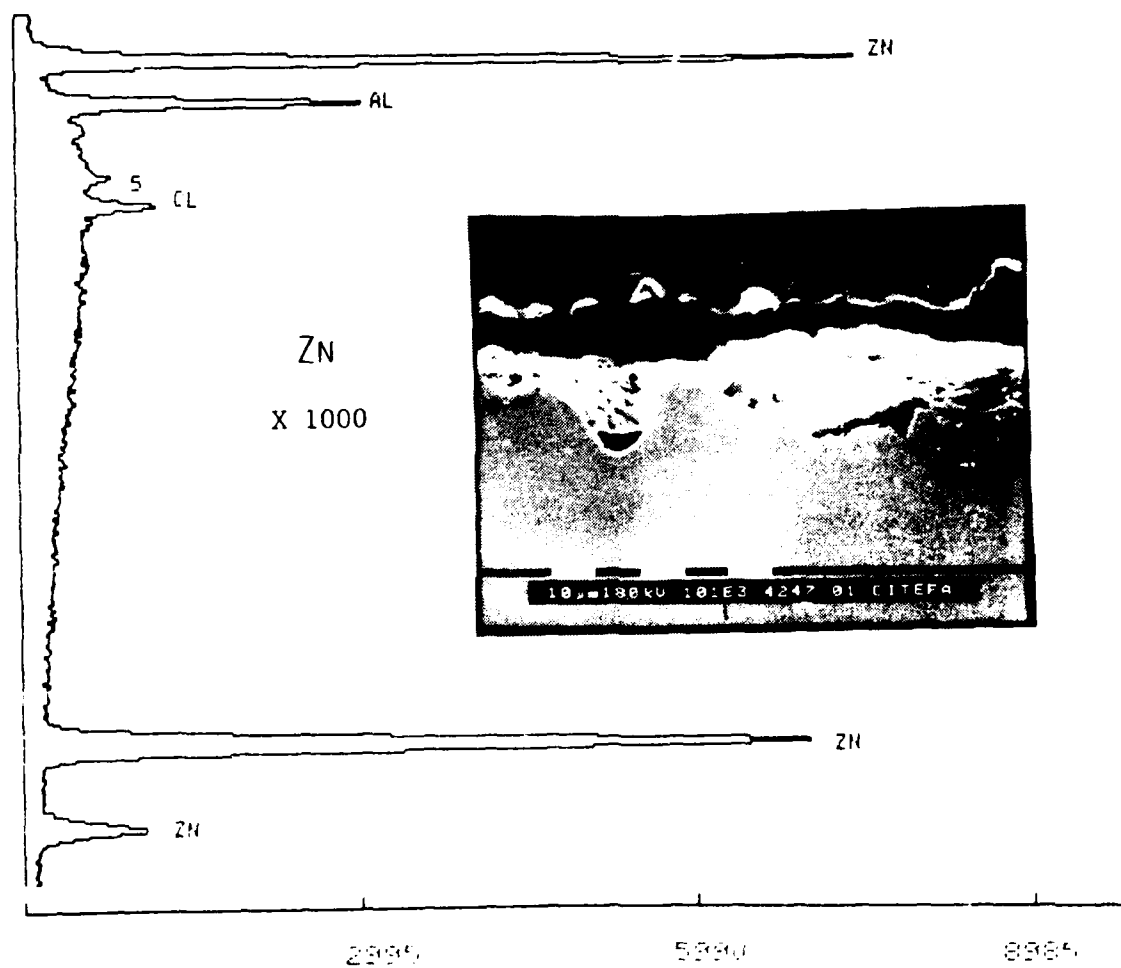
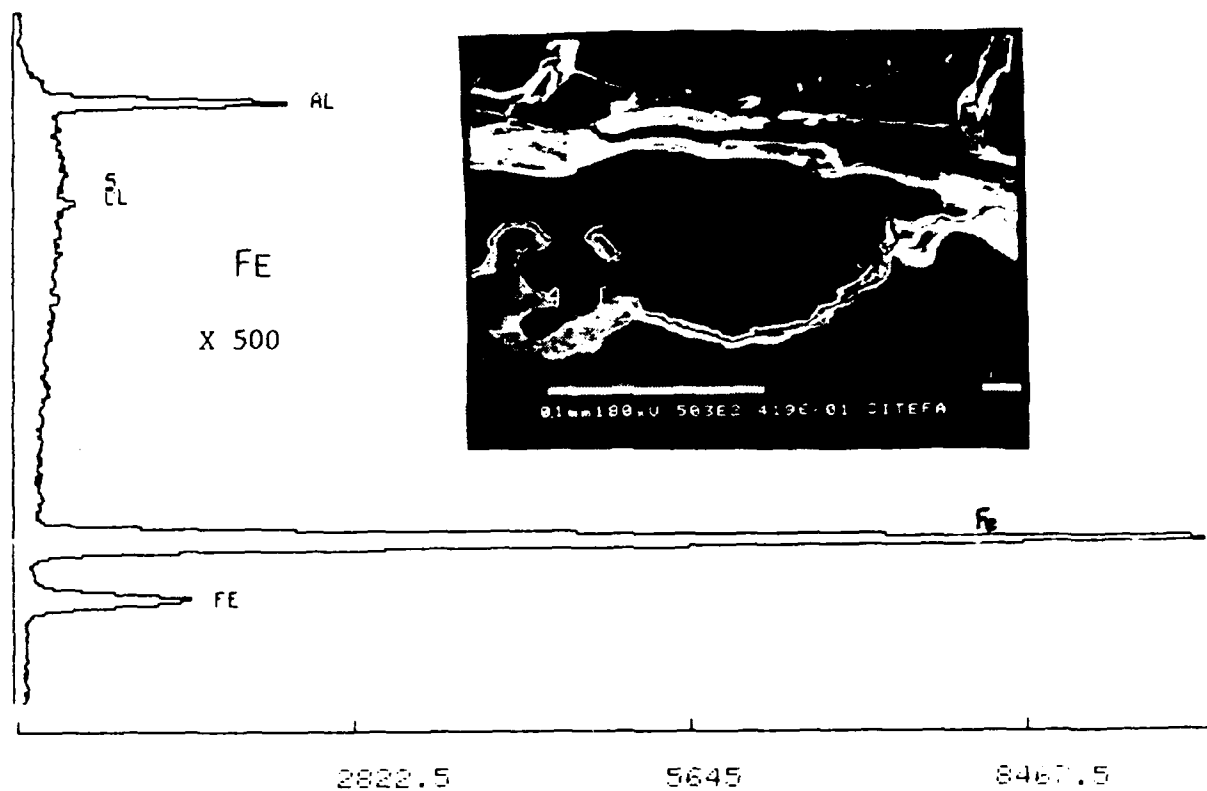


Fig. 3 Cont.

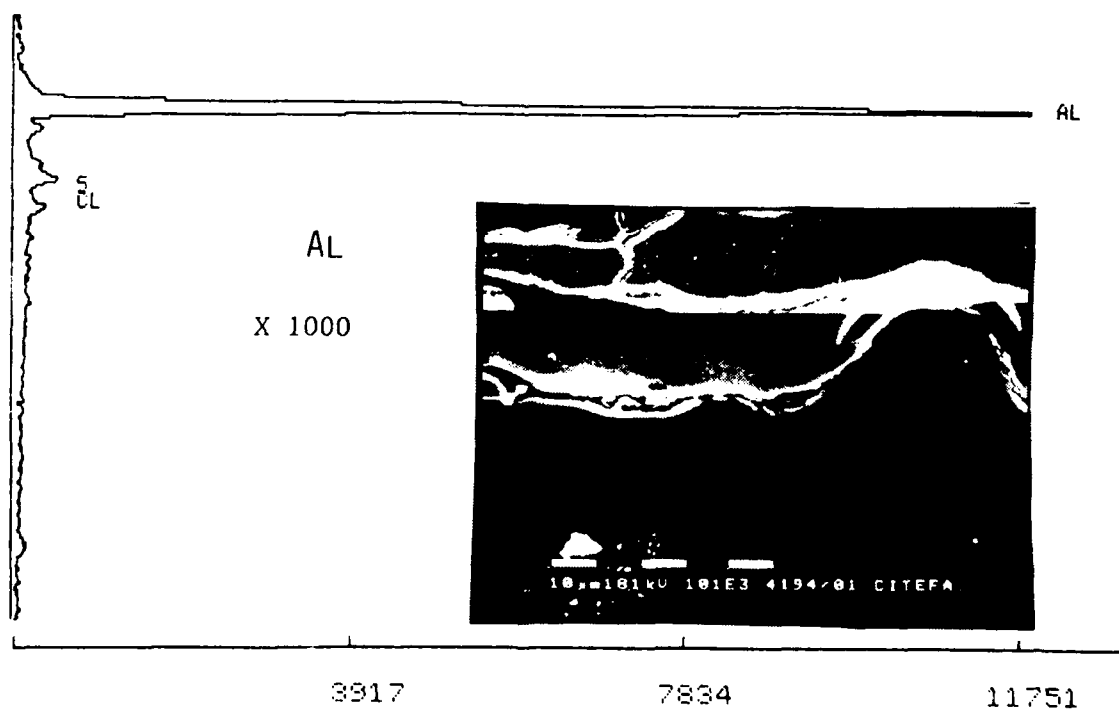
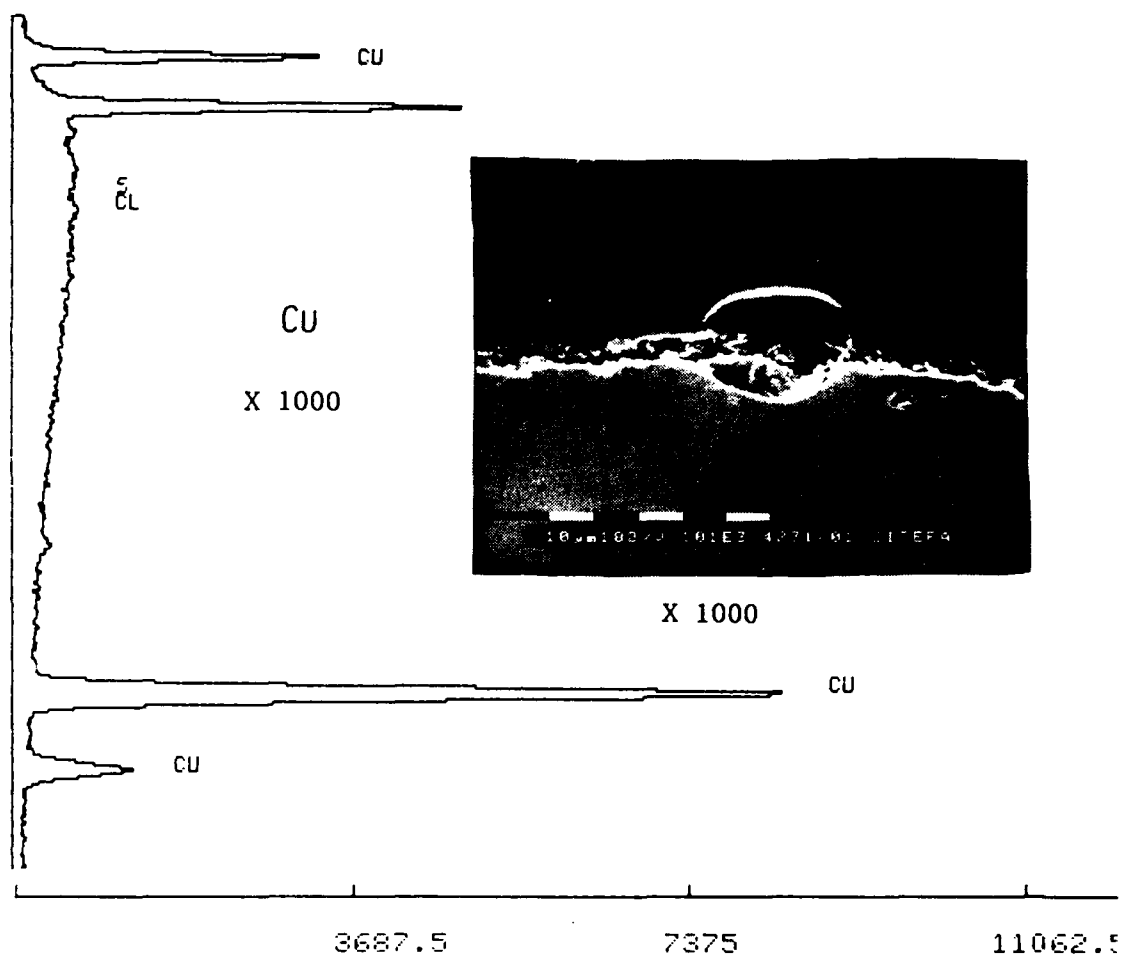


Fig. 4 Impedance Spectra of Al Weathered 1 and 2 years in SAN JUAN Test Station. Typical Capacitive Response of Passive Layers Formed on Low Corrosive Ambient Conditions.

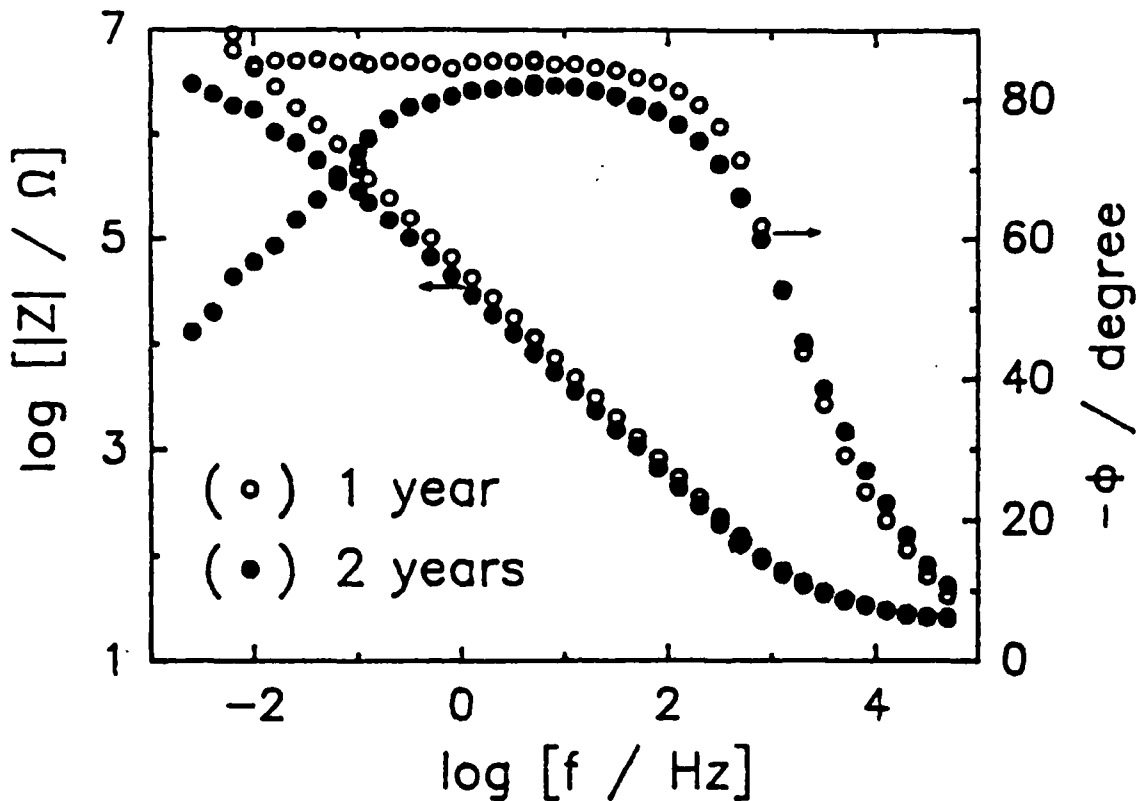


Fig. 5 Impedance Spectra of Al Weathered 1 year in JUBANY BASE Test Station (Antartics). Typical Response of Passive Layers Formed on High Corrosive Ambient Conditions (High Cl^- Concentration).

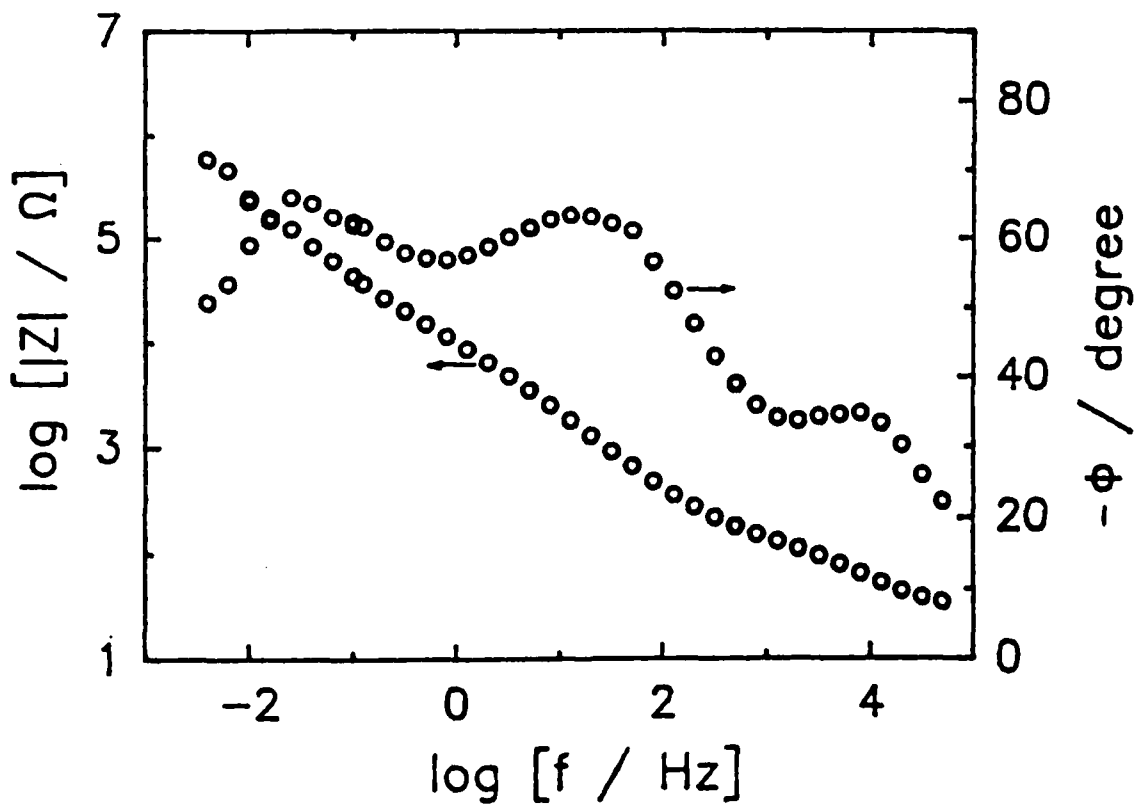


Fig. 6 Impedance Spectra of Cu Weathered 1 year in IGUAZU Test Station.

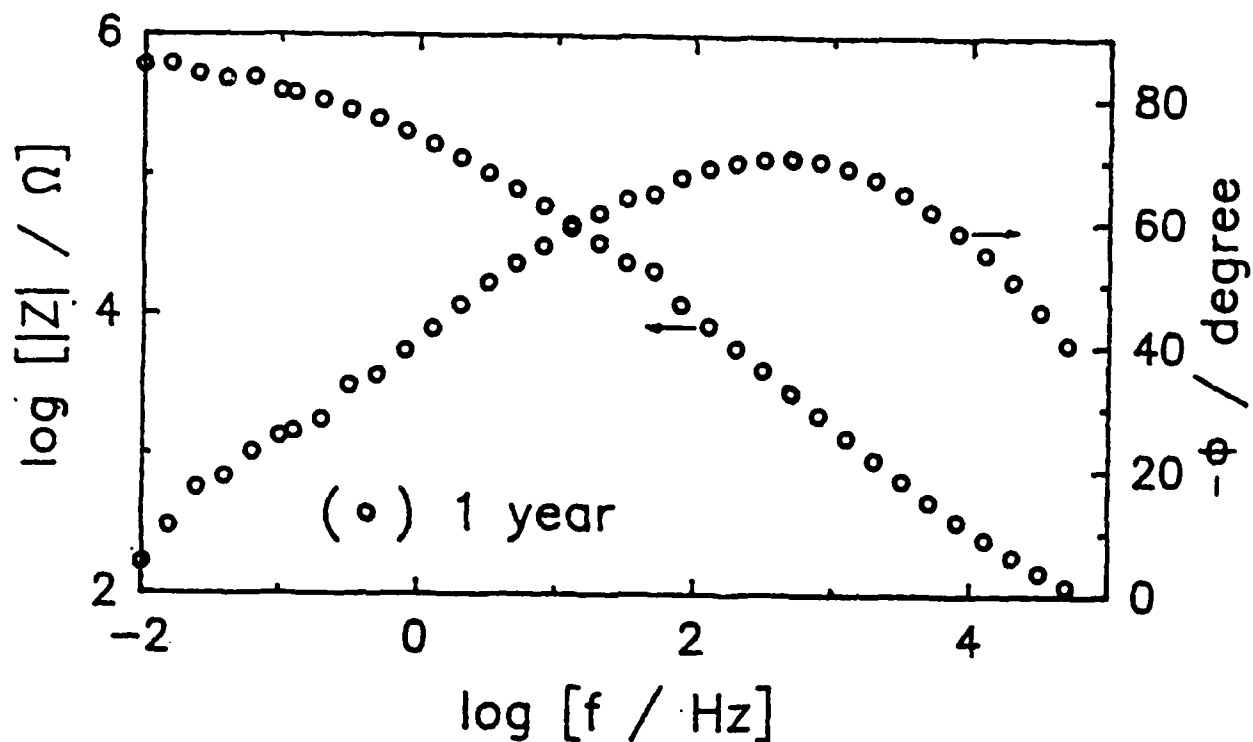
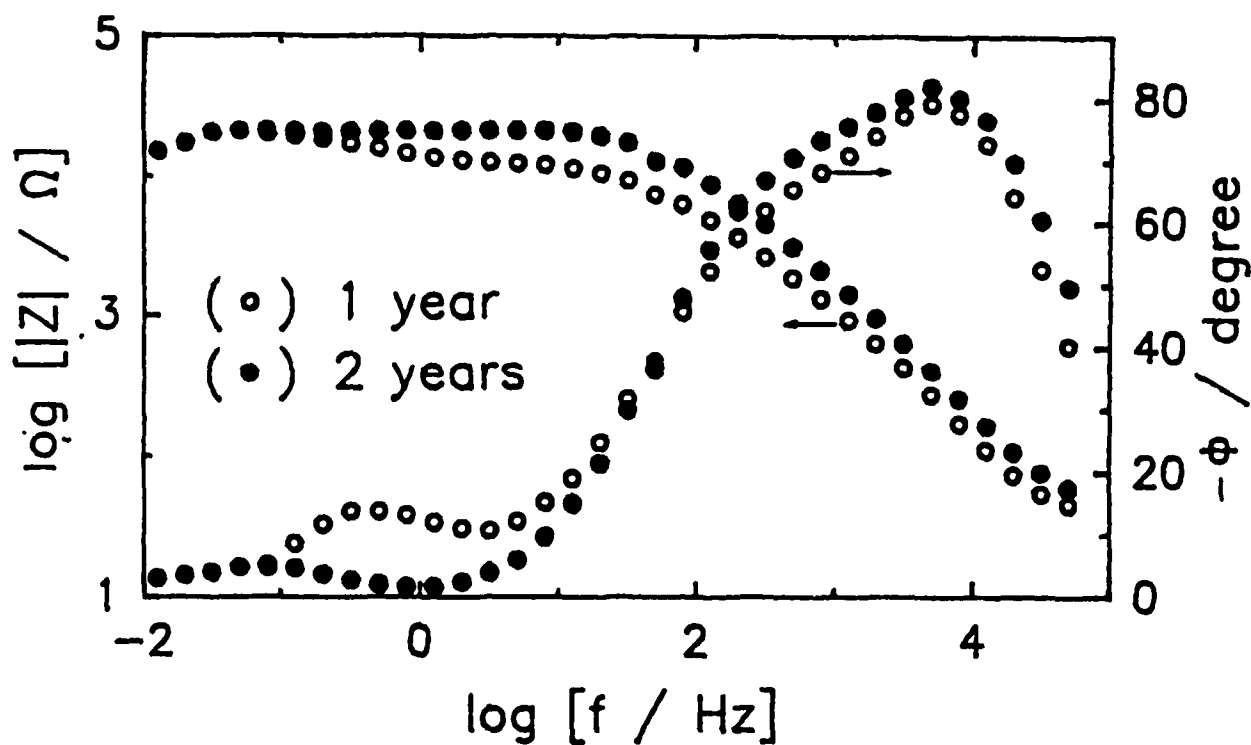


Fig. 7 Impedance Spectra of Zn Weathered 1 and 2 years in VILLA MARTELLI Test Station.



Indoor Gaseous Sulfide and Chloride Pollutants and Their Reaction with Silver

Leo Volpe
IBM ADSTAR
5600 Cottle Road
San Jose, California 95193 U.S.A.

Phillip J. Peterson
IBM ADSTAR
5600 Cottle Road
San Jose, California 95193 U.S.A.

ABSTRACT

Data on airborne reduced sulfur and acidic chlorine gases at 28 indoor locations are presented and compared with data on sulfide and chloride corrosion products formed on 1,992 silver foils. The field data were collected inside or near computer rooms in the US and other industrialized countries. These are by far the largest databases on volatile sulfide and chloride ever reported.

In one field program, reduced sulfur and acidic chlorine gases were monitored for over two years with an air sampler. Monthly average concentrations were found to range from 5×10^{-3} to $10 \mu\text{g m}^{-3}$ for sulfur gases and from 5×10^{-3} to $1 \mu\text{g m}^{-3}$ for chlorine gases. These ranges encompass most of the previously reported values, from background levels in remote locations to high levels near localized sources. The values followed lognormal distributions, except at the highest and lowest concentrations. The mean values for S and Cl gases were 0.449 and $0.181 \mu\text{g m}^{-3}$, respectively. The sulfide and chloride at the same field sites were uncorrelated, which means that their sources are mostly unrelated. Locations with simultaneously high levels of both corrodents are therefore not particularly common.

In another field program, silver foils were exposed in computer rooms for one year and then analyzed for corrosion products. The Ag_2S and AgCl amounts were found to be distributed much like the sulfur and chlorine gas concentrations measured in the air-sampling program. A relation between metal tarnishing and corrodent level was established with a mathematical model based on the fact that Ag corrosion is limited by mass transfer of H_2S and HCl from ambient air to the foil surface. With this model, airborne concentrations calculated from the foil data are in reasonable agreement with the air-sampler data.

These data are suitable for evaluating the corrosion resistance of electronic office products. The fact that the sulfide and chloride distributions are so wide means that no corrosion reliability assessment can rely on mean concentration values. The entire distribution must be taken into account.

Key Terms: atmospheric corrosion, silver, sulfide, chloride, air pollution, corrosion reliability

INTRODUCTION

It is universally recognized that air pollutants are key contributors to atmospheric corrosion. Together with airborne moisture, they take part in corrosive attack by providing ionic electrolyte, breaking down passivation, and reacting with the metal. The corrosivity of air largely depends on the type and amount of corrosive contaminants. Among the more important airborne corrodents are certain gases containing sulfur and chlorine. Due to high surface reactivity of sulfide and chloride, even minute concentrations of those gases can cause much damage. The literature contains an abundance of data on many corrosive air pollutants. Reports on sulfide- and chloride-forming gases are relatively few, however, because of their extremely low airborne concentrations and because of experimental complications.

The most important reduced sulfur gases are H_2S and OCS , while other compounds, such as CS_2 and mercaptans, are both less abundant and less corrosive.¹ For H_2S , the background concentrations are 7 to 70 ng m^{-3} in remote marine atmosphere² and < 0.1 to $0.5 \mu\text{g m}^{-3}$ in rural inland areas.³ The concentrations in urban and industrial areas range from 0.02 to $7 \mu\text{g m}^{-3}$.⁴ Near localized sources, peak values on the order of 1 mg m^{-3} and average values of as high as $32 \mu\text{g m}^{-3}$ were reported.⁵ Concentrations of carbonyl sulfide were measured to be in a narrow range from 1.0 to $1.2 \mu\text{g m}^{-3}$ in remote and urban areas alike.^{6,7}

Among chlorine-containing gases, HCl and Cl_2 are by far the most aggressive. It has long been accepted that in the atmosphere HCl accounts for most of the corrosive chlorine gas, and Cl_2 contributes relatively little.⁸ Reported values of outdoor HCl concentration range from $0.1 \mu\text{g m}^{-3}$ over the ocean⁹ to $12 \mu\text{g m}^{-3}$ in residential Tokyo.¹⁰ The mean literature value is $1 \mu\text{g m}^{-3}$.¹¹

Almost all reported data on sulfur and chlorine gases are from outdoor studies. The only exception was an earlier report from this laboratory covering six office buildings in major U.S. cities.¹² It gave concentrations of reduced sulfur gases from 0.2 to $100 \mu\text{g m}^{-3}$, and concentrations of chlorine gases from 0.03 to $0.57 \mu\text{g m}^{-3}$. Comparison of those values with outdoor concentration at the same locations yielded indoor-to-outdoor ratios of 1 and 0.13 for S and Cl gases, respectively. That study generally emphasized that the pollutant sources and concentrations indoors can be quite different from those outdoors.

The present work is concerned with indoor S and Cl gases at locations where large computers and other types of electronic equipment are used. It reports data from two worldwide field programs, one on airborne sulfur and chlorine at 28 sites and another on sulfide and chloride corrosion products formed on 1,992 silver samples exposed inside computer rooms. Both programs were aimed at obtaining data useful to determine field reliability of electronic products.

EXPERIMENTAL

The data were collected in two separate field programs. The first program monitored the indoor concentration of airborne sulfide, chloride, and other corrosive gases. This paper addresses sulfide and chloride; it does not report on the other pollutants. The second program exposed silver and other metal coupons to flowing air. Only the corrosion response of the silver coupons is reported here.

The concentration of airborne corrodents was obtained with an air sampler. The design, operation, and capabilities of this instrument were previously described.¹³ Briefly, the air sampler is a compact, inexpensive device for simultaneous monitoring of airborne dust, acidic chlorine gases, sulfiding gases, ammonia, sulfur dioxide and nitrogen dioxide. The instrument is designed for continuous unattended sampling of large air volumes for up to three months. Its flow system consists of a removable filter cartridge to collect the corrodents, a vacuum pump to draw air through the cartridge, and a critical orifice to control the flow rate. Also included are a vacuum gauge to indicate proper operation of the flow system, a clock to

monitor running time, and a fan for cooling the pump. The entire apparatus is housed in a small case with a door through which the filter cartridge can be removed.

The cartridge consists of a stack of filter holders and spacers supporting several pollutant filters. The first filter is used to remove airborne dust. It is made of fiberglass treated with silane to minimize adsorption of corrosive gases. The second and third filters are used to collect gaseous corrodents containing reduced sulfur (H_2S , OCS) and chlorine (HCl , Cl_2). They are made of surface-oxidized silver in the form of porous membrane (Hytrex Filter Division of Osmonics, Inc., 2.5-cm diameter, 1.2 μm porosity). The S- and Cl-containing gases convert nearly quantitatively forming Ag_2S and AgCl , respectively. The Ag filters will also react with other halogen-containing gases (HBr , Br_2 , HI , I_2). The reaction products can be reliably identified and quantified by coulometric reduction.¹⁴⁻¹⁶ Downstream from the silver-membrane filters, the cartridge contains other filters designed to collect NH_3 , NO_2 , and SO_2 . In the end of the sampling interval, the cartridge is removed from the case and shipped for laboratory analysis.

The analysis accuracy and collection efficiency for the silver filter were determined with gas-permeation devices. The detection limits for S^2 and Cl^- were 2 and 4 μg , respectively. Interaction with other corrodents and water vapor was checked with a well-characterized mixed flowing gas chamber representing a mildly polluted environment.¹⁷ No interactions were observed, except the presence of large amounts of reduced sulfur and nitrogen dioxide gases decreased the chloride sensitivity. The collection efficiency, with the two silver membranes, exceeded 95% at all test conditions.

The air-sampler data are due to a two-year monitoring program conducted in the mid-1980s. The samplers were used to monitor pollutant levels at 28 worldwide sites in or near IBM high-end computer rooms. The sites were selected by field engineers, with a bias toward locations suspected to have high pollutant concentrations. Although the extent of this bias cannot be assessed, these monitoring sites could be regarded as relatively polluted computer installations. The air sampling at each site lasted ca. one month, and so the concentration data represent one-month averages.

The other field program involved exposure of metal foils to indoor air. The samples were 2.54×2.54-cm coupons of silver (Western Gold and Platinum Company, 99.9%, thickness 25 μm), as well as of copper and Permalloy. The coupons were parallel and adjacent to each other, 0.32 cm apart, mounted inside a polycarbonate holder open on two sides perpendicular to the foils. The Ag coupon had the Cu coupon on one side and the NiFe coupon on the other. The holder with the coupons was placed inside the air-intake port of an IBM high-end disk drive. The drive used a constant flow of surrounding air for cooling during operation. As a result, ambient air was flowed past the foils parallel to the surface. The average flow velocity through the holder was 25 cm s^{-1} , as measured with a hot-wire anemometer.

The metal coupons were placed inside disk drives shipped in the mid-1970s to customer sites worldwide. The field consisted of 1,992 samples, 1,104 of which were located inside high-end computer rooms in the United States and 888 in other countries of the industrialized world. Thus, the program represented a population of large computer users. After the drives were installed and operated continuously for ca. 1 year, the coupons were returned for laboratory analysis. Then the Ag coupons were analyzed for Ag_2S and AgCl by coulometric reduction exactly the same way as the Ag membranes from the air-sampler program.

RESULTS AND DISCUSSION

Figure 1 shows the results of the field program using air sampling. It gives the sulfide and chloride data points on a lognormal probability plot, which is a common and convenient means of visualizing pollutant data. The abscissa is the measured concentration on the logarithmic scale, and the ordinate is the percentile, or cumulative frequency in %, scaled for the normal distribution. The ordinate value can be viewed as the likelihood that the pollutant concentration is lower than the corresponding abscissa value. The data indicate that the levels of H_2S and other reduced sulfur gases are between 5×10^{-3} and $10 \mu\text{g m}^{-3}$.

For HCl and other acidic chlorine gases, the range is between 5×10^{-3} and $1 \mu\text{g m}^{-3}$. The sulfur gases are clearly more abundant than the chlorine gases. These corroderent distributions encompass most of the sulfide and chloride levels reported in previous studies, from background concentrations in remote outdoor locations to high concentrations near localized sources.

Most of the sulfide data and about half of the chloride data in Fig. 1 follow the straight lines drawn through the points. In these coordinates, a straight line corresponds to lognormal functional dependency. The lognormal probability density function is

$$f(x) = \frac{1}{(2\pi)^{1/2} \sigma x} \exp \left[-\frac{(\ln x - \mu)^2}{2\sigma^2} \right] \quad (1)$$

where x is the argument (concentration), μ is the \ln of the mean or 50th percentile value of x , and σ is the shape parameter. Table 1 gives the values of mean concentration and σ for the straight lines in Fig. 1. Also tabulated are concentration values for the 90th percentile. The values of σ , indicating the distribution width, are similar for the two corroderents.

The lognormal shape is encountered in the environment and is supposed to be a good approximation for randomly distributed pollutant data.^{18,19} This shape is not universal, however; some literature data can be better fitted with other distribution functions, such as Weibull, gamma, and beta.⁵ An attempt was made to apply those other distributions to the data in Fig. 1, but it produced poorer fits than the lognormal distribution.

The data deviate from the lognormal straight lines. At high concentrations the sulfide data have downward curvature, and at low concentrations both corroderents have upward curvature, especially pronounced in the case of chloride. Downward curvature at the high end agrees with common sense because, in general, the highest concentration measured cannot exceed the level emitted at the most potent source.¹⁹ Another general argument can be applied to account for upward curvature at the low end, i.e., the lowest concentration cannot fall below the background level. It can also be argued that low end deviations should be particularly pronounced for these air-sampler data because the field sites are biased toward locations with high pollutant levels, and sites with the lowest concentrations are underrepresented.

Figure 2 plots the sulfide vs. chloride concentration at the same air sampling location. The comparison clearly indicates that the two corroderents are uncorrelated. Good correlation is expected when pollutants have common sources. The absence of correlation means that the sources of sulfide and chloride are unrelated.

The data from the field program involving exposure of silver foils are presented in Fig. 3. The amounts of sulfide and chloride in the tarnish films formed on the foil samples at locations in the US (Fig. 3a) and in other countries (Fig. 3b) are shown as lognormal plots. The US and non-US data are virtually indistinguishable. Comparison of Ag_2S and AgCl amounts formed on the foils shows that the former is significantly higher. The vast majority of the points fall on the straight lines providing lognormal fits to the data. For the highest and lowest tarnish amounts, the data deviate from lognormality, as did the concentration data from the air-sampling program, but the extent of those downward and upward deviations is far smaller.

Table 2 lists the values of 50th and 90th percentiles and of σ for all the distributions. The distributions of both corrosion products span ca. 3 orders of magnitude, much like those of sulfur and chlorine gases from the air-sampling program. For the foils, the calculated distribution widths for Ag_2S and AgCl are nearly the same. The values of σ in Table 2 are only slightly higher than those in Table 1.

It is interesting to relate the data on Ag tarnish to the levels of airborne sulfide and chloride. One can reasonably assume that the Ag_2S and AgCl films on the foils are produced by silver reaction with ambient reduced sulfur gases and acidic chlorine gases, respectively. With regard to surface reactivity, the silver foils are identical to the silver membranes used to collect H_2S and HCl in the air-sampling program. What is different is the relationship between the tarnish amount and the ambient concentration. With the membranes, the concentration is simply equal to the ratio of the tarnish amount and the air volume passed through the air sampler, both of which are experimentally determined. With the foils, the relation is considerably more complicated. The corrosion process is generally a function of both the kinetics of interfacial reaction between the corrosive gas and the metal and of the mass transfer of that gas from the air to the foil surface. For atmospheric sulfidation of silver foils, the surface kinetics is relatively fast, and the overall tarnish rate is totally governed by mass transfer.²⁰ This fact is due to a combination of high Ag reactivity, low ambient concentration of H_2S , and its slow diffusion in air. Silver chloride formation is probably also controlled by mass transfer, viz., the delivery of HCl from the air to the foil surface, but, since Ag chlorination is not as fast as sulfidation, the interfacial kinetics may also play a noticeable role.

It is possible to deduce the connection between the foil tarnish products and ambient pollutant levels, if the following simplifying assumption are made. First, air movement between the foils in the sample holder is treated as flow in a channel between two parallel plates. The plates can be regarded as infinite because the foil width perpendicular to the flow ($W = 2.54$ cm) is almost an order of magnitude larger than the interfoil distance ($2h = 0.32$ cm). This means that hydrodynamic deviations at the foil edges are disregarded. The flow regime between infinite plates is characterized by the Reynolds number,

$$Re = \frac{2hu}{\nu} \quad (2)$$

where $u = 25 \text{ cm s}^{-1}$ is the average flow velocity, and $\nu = 0.143 \text{ cm}^2 \text{ s}^{-1}$ is the kinematic viscosity of air. The flow is laminar if $Re \lesssim 2000$. In this case, $Re = 56$. Flow between parallel plates has a parabolic velocity profile, except at the channel entrance where it changes from flat to parabolic. The parabolic profile begins to develop immediately at the foil leading edge and is fully formed after the air passes the entrance length²¹

$$L_e = 0.08 h Re \quad (3)$$

In the present situation, $L_e = 0.72$ cm. This corresponds to more than a quarter of the total foil length ($L = 2.54$ cm), but for simplicity the inlet effects will be ignored, and the flow will be treated as parabolic starting at the entrance. Next, one can reasonably argue that the sulfidation and chlorination are totally limited by the delivery of airborne H_2S and HCl to the Ag sample. Mathematically, this means that the gas concentrations at the foil surface are zero, or at least negligibly small compared to the bulk levels in the surrounding environment. An equally high corrodent scavenging effectiveness is assumed for the Cu and NiFe coupons in the sample holder on either side of the Ag foil. This is probably valid for Cu reactions with both gases and for NiFe reaction with HCl but not with H_2S . At any rate, the pollutant mass transfer in the air flowing between the parallel plates is treated as symmetric about the plane that is parallel to, and equidistant from, the coupons. Finally, the rate of longitudinal mass transfer due to the flow is assumed to be significantly greater than that due to diffusion. Diffusive transfer depends on the gas diffusivity D in air, which is $0.16 \text{ cm}^2 \text{ s}^{-1}$ for H_2S and slightly higher for HCl .²¹ Longitudinal diffusion can be neglected if the Péclet number

$$Pe = \frac{hu}{D} \gg 1 \quad (4)$$

This condition was analyzed for similar heat-transfer problem in pipes.²² Since in this case $Pe = 25$, the approximation is justified.

These assumptions make the Ag tarnish process analogous to the classic problem of particle deposition from laminar flow onto the walls of a parallel plate channel. Its solution is given as the ratio pollutant concentrations (α) at the outlet and the inlet of the channel²³

$$\alpha = 0.9149 e^{-1.885\mu} + 0.0592 e^{-22.3\mu} + 0.0258 e^{-151.8\mu} \quad (5)$$

where

$$\mu = \frac{DL}{h^2 u} \quad (6)$$

With the present values of parameters, Eq. 5 yields $\alpha = 0.272$. A mass balance directly relates the ambient corroder concentration C to α and the tarnish film thickness

$$C = \frac{nM}{2huWt(1-\alpha)} \quad (7)$$

where n is the molar amount of corrosion product on the Ag foil, M is the molecular weight of the corrosive gas, and $t = 1$ year is the exposure time.

The last two columns of Table 2 list values of C , calculated with Eq. 7, from the amounts of Ag_2S and AgCl formed on the foils at the 50th and 90th percentiles of the distribution. These values can be compared with the corroder concentrations from the air-sampler program in Table 1. The concentrations deduced from the foil exposure are 1½-2 times lower for H_2S and 5-6 times lower for HCl . For the sulfide, the agreement is very good considering the difference in the data bases and the crudeness of the model. For chloride, the agreement is only fair. The reason for the larger difference is not entirely clear, but it may be partly due to corroder scavenging by surfaces of components surrounding the coupon holder, as most materials getter HCl more readily than H_2S .

Figure 4 compares the sulfide and chloride amounts formed on the same silver foil. The comparison for US and non-US locations is shown in Figs. 4a and 4b, respectively. There is clearly no correlation at all between the Ag_2S and AgCl levels. Therefore, the sulfide and chloride sources are unrelated. This is consistent with absence of correlation between airborne H_2S and HCl for the air-sampling program.

The fact that ambient sulfide and chloride are uncorrelated has an important implication for corrosion testing and evaluation. Laboratory corrosion tests usually combine high levels of several corrosives to achieve an acceleration factor. Since in the field simultaneous encounter with high sulfide and chloride concentrations is not a particularly common occurrence, the results of such tests can be misleading. Specifically, the silver samples exposed in this field program were found to form both Ag_2S and AgCl . In mixed-flowing-gas chambers containing relatively high concentrations of both H_2S and HCl (or Cl_2), however, almost all the tarnish product is silver sulfide, and silver chloride is barely observable.¹⁷ This is because in the chamber the corroder delivery to the metal surface is relatively fast, the H_2S reaction competes with the HCl reaction, and with Ag the sulfidation reaction prevails.²⁰ In the field, silver tarnishing is governed by mass transfer of airborne corrosives to the metal, H_2S and HCl do not have to compete at the surface, and chlorination is not suppressed.

CONCLUSION

Evaluation of corrosion reliability requires information on the distribution of corrosive gases in the field environment. Assessment that is based on a mean or "typical" concentration value overestimates the degree of corrosion resistance, especially if the field distribution is broad. For electronic products requiring high reliability levels, the high end of the distribution is far more relevant.

The two field programs described in this paper provide solid input for the assessment of corrosion associated with two of the more damaging types of atmospheric pollutants. The first program provides distributions of corrosive gases containing reduced sulfur and acidic chlorine. The second program gives the distribution of data on silver corrosion and deduces the corresponding concentrations of gaseous sulfide and chloride in ambient air. The population covers worldwide indoor locations where powerful computers and other office electronics are used. Together these programs comprise by far the largest database on volatile sulfur and chlorine ever reported. Analysis of the data allows one to reach these conclusions:

- Indoor concentrations, for both corrodent types, are distributed over three orders of magnitude, spanning most of the range of previously reported values, from background levels in remote areas to high levels near localized sources.
- Overall, sulfide is at least twice as abundant as chloride.
- Lognormal distributions provide good fits to most of the data, except at the highest and lowest concentrations.
- Sulfur and chlorine gases at the same locations are uncorrelated, implying that simultaneous encounter with high levels of both corrodents is not particularly common.
- The sulfide and chloride distributions in the US are virtually indistinguishable from those in a combination of other industrialized countries.
- In the field, silver tarnishing is limited by mass transfer of the corrosive gases to the metal surface from surrounding air, while the interfacial kinetics of Ag_2S and AgCl formation are relatively fast.
- The distributions of sulfur and chlorine gases are suitable for evaluating the corrosion resistance of computers and other kinds of electronic office equipment.

ACKNOWLEDGEMENTS: K. F. Sommers performed analytical work for the field program on air sampling, F. Y. Lieu designed the program on foil exposure, C. B. Goetz tracked the field samples, and D. Tappa analyzed foil corrosion products.

REFERENCES

1. T. E. Graedel, G. W. Kammlott, J. P. Franey, *Science*, 212 (1981): p. 663.
2. B. J. Slatt, D. F. S. Natusch, J. M. Prospero, D. L. Savoie, *Atmos. Environ.*, 12 (1978): p. 981.
3. R. J. Breeding, J. P. Lodge, J. B. Pate, D. C. Sheesley, H. B. Klonis, B. Fogle, J. A. Anderson, T. R. Englert, P. L. Haagenson, R. B. McBeth, A. L. Morris, R. Pogue, A. F. Warburg, *J. Geophys. Res.*, 78 (1973): p. 7057.
4. T. E. Graedel, in *Handbook of Environmental Chemistry*, (O. Hutzinger, Ed., Heidelberg: Springer, 1980), vol. 2, part A, p. 107.
5. T. E. Graedel, B. Kleiner, C. C. Patterson, *J. Geophys. Res.*, 79 (1974): p. 4467.
6. F. J. Sandalls, S. A. Penkett, *Atmos. Environ.*, 11 (1977): p. 197.
7. P. J. Maroulis, A. L. Torres, A. R. Bandy, *Geophys. Res. Lett.*, 4 (1977): p. 510.
8. T. E. Graedel, N. Schwartz, *Mater. Perf.*, 16 (1977): p. 17.
9. B. Vierkorn-Rudolph, K. Bachmann, B. Schwartz, F. X. Meixner, *J. Atmos. Chem.*, 2 (1984): p. 47.
10. T. Okita, K. Kaneda, T. Yanaka, R. Sugai, *Atmos. Environ.*, 8 (1974): p. 927.
11. D. Grosjean, *Environ Sci. Technol.*, 24 (1990): p. 77.
12. D. W. Rice, R. J. Cappell, W. Kinsolving, J. J. Laskowski, *J. Electrochem. Soc.*, 127 (1980): p. 891.
13. P. J. Peterson, R. J. Cappell, "An Integrating Air Sampler," *CORROSION/83*, paper no. 235 (Houston, TX: National Association of Corrosion Engineers, 1983).
14. W. E. Campbell, U. B. Thomas, *Trans. Electrochem. Soc.*, 76 (1939): p. 303.
15. L. E. Price, G. J. Thomas, *Trans. Electrochem. Soc.*, 76 (1939): p. 329.
16. R. H. Lambert, D. J. Trevoy, *J. Electrochem. Soc.*, 105 (1958): p. 18.
17. D. W. Rice, P. J. Peterson, E. B. Rigby, P. B. P. Phipps, R. J. Cappell and R. Tremoureux, *J. Electrochem. Soc.*, 128 (1981): p. 275.
18. R. I. Larsen, *J. Air Pollut. Control Assoc.*, 19 (1969): p. 24.
19. W. R. Ott, *J. Air Waste Manage. Assoc.*, 40 (1990): p. 1378.
20. L. Volpe, P. J. Peterson, *Corros. Sci.*, 29 (1989): p. 1179.
21. H. Schlichting, *Boundary-Layer Theory*, (7th Ed., New York: McGraw-Hill, 1979), p. 186.
22. S. N. Singh, *Appl. Sci. Res.*, A7 (1958): p. 325.
23. W. DeMarcus, J. Thomas, *U.S. Atom. Commis., ORNL-1413* (1952).

Table 1. Analysis of gaseous sulfur and chlorine distributions in air

	Concentration ($\mu\text{g m}^{-3}$)		Shape parameter
	50th percentile	90th percentile	
Sulfide	0.449	1.252	0.80
Chloride	0.181	0.599	0.94

Table 2. Analysis of Ag_2S and AgCl distributions on silver foils

	Yearly tarnish amount (μmol)		Shape parameter	Deduced concentration ($\mu\text{g m}^{-3}$)	
	50th percentile	90th percentile		50th percentile	90th percentile
Sulfide					
US sites	3.06	12.53	1.10	0.229	0.941
non-US sites	2.87	11.88	1.11	0.215	0.892
Chloride					
US sites	0.338	1.325	1.07	0.0273	0.107
non-US sites	0.373	1.695	1.18	0.0302	0.137

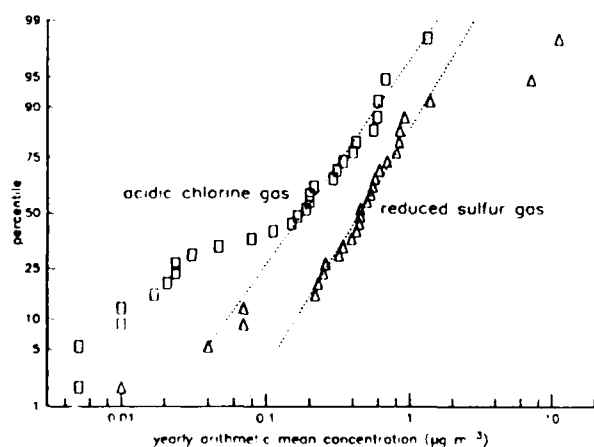


Fig 1. Distribution of corrosives in air

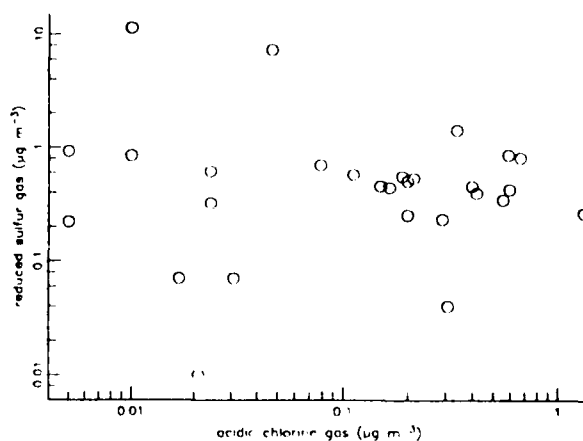


Fig 2 Sulfur vs chlorine in air samples

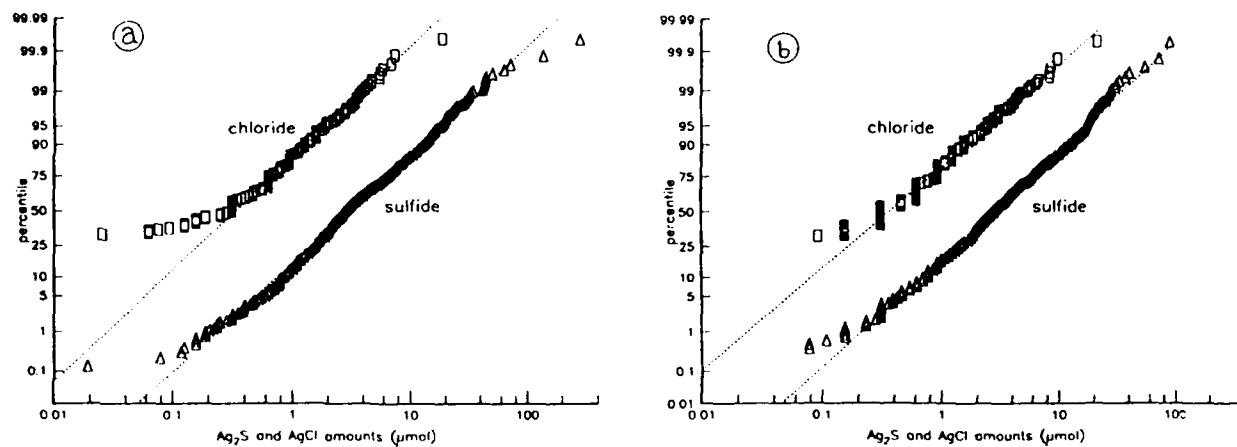


Fig. 3. Distribution of silver corrosion products: a—US sites, b—non-US sites

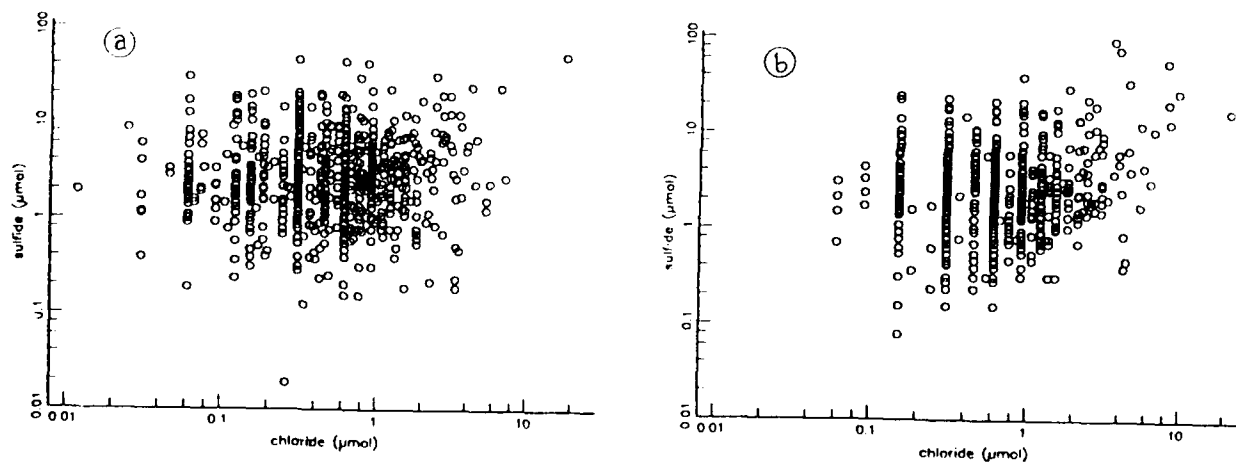


Fig. 4. Sulfide vs. chloride Ag tarnish product: a—US sites, b—non-US sites

FIELD EXPOSURE STUDIES OF CORROSION PRODUCTS ON METALS

C. Leygraf
Royal Institute of Technology
Osquidas väg 4-6
S-100 44 Stockholm, Sweden

I. Odnevall
Royal Institute of Technology
Osquidas väg 4-6
S-100 44 Stockholm, Sweden

D. Persson
Royal Institute of Technology
Osquidas väg 4-6
S-100 44 Stockholm, Sweden

J. Tidblad
Royal Institute of Technology
Osquidas väg 4-6
S-100 44 Stockholm, Sweden

Abstract

The last two decades or so have seen a rapid development of new analytical methods and today there exists a large number of different techniques, which are able to probe different properties of corrosion products. Based on experience from the authors laboratory, the aim of this work is to present selected results from various research programs involving multianalytical characterisation of corrosion products formed in natural atmospheric environments. This presentation includes some analytical techniques, which so far have found very little use in corrosion science, such as diffuse reflectance infrared fourier transform spectroscopy for phase identification and ion chromatography for quantitative analysis of water dissolved ionic species. In combination with more commonly used analytical techniques, such as x-ray powder diffraction, scanning electron microscopy with x-ray microanalysis, x-ray photoelectron spectroscopy and electrolytic cathodic reduction they have provided new insight into the complex growth of corrosion products on nickel, zinc, and silver exposed to a variety of different natural atmospheric environments.

Key terms: atmospheric corrosion, deposition, field exposure, nickel, zinc, silver, diffuse reflectance infrared fourier transform spectroscopy, ion chromatography, x-ray powder diffraction, scanning electron microscopy with x-ray microanalysis, x-ray photoelectron spectroscopy, electrolytic cathodic reduction

I. Introduction

By far the most common procedure to evaluate metallic samples exposed to a natural atmospheric environment is by means of weight loss measurements after removal of corrosion products. This procedure has resulted in a large body of weight loss data *e.g.* for performing environmental classification, determining historical trends in corrosivity variations or exploring the applicability of a material in a given environment.

Only a relatively small fraction of all weight loss determinations have been preceded by some chemical analysis of the corrosion products formed. For a deeper understanding of atmospheric corrosion phenomena it is evidently insufficient to rely solely on weight loss data and over the years it has become obvious that a detailed characterisation of corrosion products not only may improve the basic knowledge of atmospheric corrosion phenomena but also may aid in interpreting weight loss data from field exposure programs. Due to rapid developments over the last two decades or so new analytical methods are available which are able to probe different properties of corrosion products. A complete survey of analytical techniques for corrosion studies is far beyond the present context and the reader is referred to text-books given elsewhere^{1,2}.

The aim of this work is to present experience from the use of a variety of complementary techniques for characterisation of corrosion products formed during atmospheric corrosion. Some of the techniques used have so far found only limited use, such as diffuse reflectance infrared fourier transform spectroscopy for analysis of both crystalline and non-crystalline phases and ion chromatography for quantitative analysis of water soluble ionic species in corrosion products. Other analytical techniques used are x-ray powder diffraction (identification of crystalline phases), scanning electron microscopy with x-ray microanalysis (morphology, quantitative and qualitative bulk elemental analysis), x-ray photoelectron spectroscopy (elemental surface analysis) and electrolytic cathodic reduction (corrosion film thickness and composition). In combination with information on atmospheric pollutant levels and climatic parameters this multianalytical approach is shown to provide new insight into the complex growth of corrosion products on nickel, zinc, and silver exposed to a variety of different natural atmospheric environments.

II. Studies of the initial atmospheric corrosion of zinc

Field exposure programs are mostly long term experiments where fully developed corrosion films are analysed after months or years of exposure. From this follows that very little information is available on the initial stages of atmospheric corrosion. In the case of zinc there are several observations that suggest a strong influence of initial weathering conditions on the subsequent atmospheric corrosion rate³. A field exposure program was designed with the main purpose to study the initial weathering conditions over the first days, weeks and months of exposure and the simultaneous formation of initially formed corrosion products and their further growth to fully developed corrosion films. To achieve this, a

multianalytical approach was used ranging from environmental characterisation (SO_2 , NO_2 , temperature, relative humidity and precipitation chemistry) over dry deposition measurements (SO_4^{2-} , Cl^- , NO_3^-) to corrosion product characterisation including x-ray photoelectron spectroscopy (XPS), scanning electron microscopy with x-ray microanalysis (SEM/EDS), ion chromatography (IC) and x-ray powder diffraction (XRD).

A way to trace the origin of air pollutants that are transported to and incorporated into the exposed zinc surfaces is to combine dry deposition data with IC data⁴. It is then necessary to assume that all water soluble anions in the corrosion products are dissolved in the water extracts for IC analysis. In the field exposure program the filters for dry deposition measurements are placed horizontally up side down, from which follows that they mainly monitor deposition from suspended pollutants such as gases and most aerosols. The exposed zinc surfaces, on the other hand, are able to collect not only gases and aerosols but also pollutants in particulate form. Hence, if the ratio between the amount of any water soluble ion (IC data) and the amount of dry deposition of the same anion is larger than one, it is an indication that the deposited anion originates not only from suspended form but also from particulate form. On the other hand, if the ratio is less than one, the deposited anion mainly originates from gases and aerosols. An example is given in figure 1, where this ratio is plotted versus the logarithm of time for zinc exposed in a marine atmosphere under sheltered conditions. The low ratios seen in the figure indicate that the anions of the surface have been captured as gases and/or aerosols. Together with low concentrations of measured SO_2 and NO_2 the results suggest that the main source for the anions studied most likely are aerosols.

A powerful method to study the formation of different corrosion products as well as their growth and transformation into other compounds is by means of SEM/EDS. A prerequisite is that the thickness of the corrosion layer is sufficient ($\geq 1 \mu\text{m}$) and XPS can be used as an alternative technique if this is not the case. A quantitative x-ray microanalytical procedure has been developed which enables SEM/EDS to be used in order to follow the growth and transformation process from one phase in the corrosion product into other phases⁵. This approach is shown in figure 2a-c where the chlorine, sulfur and sodium content of the corrosion products are given in ternary diagrams after different exposure times. The given example is from the field exposure program performed in the marine atmosphere in which the corrosion products occur as islands with layered structures. Studies by means of XRD have identified two structurally related phases in the islands, namely $\text{Zn}_5(\text{OH})_8\text{Cl}_2 \cdot \text{H}_2\text{O}$ and $\text{NaZn}_4\text{Cl}(\text{OH})_6\text{SO}_4 \cdot 6\text{H}_2\text{O}$. The results of quantitative x-ray microanalysis are presented as average values, in atomic percent, from investigated islands and each point in the ternary diagram represents an independent measurement. Hence, a point positioned in the chlorine corner corresponds to an island with a composition corresponding to chlorine:sulfur:sodium ratios of 1:0:0. The chlorine corner is in these diagrams equivalent with the composition of $\text{Zn}_5(\text{OH})_8\text{Cl}_2 \cdot \text{H}_2\text{O}$. The filled circle in the middle of the diagram corresponds to a chlorine:sulfur:sodium ratio equivalent to $\text{NaZn}_4\text{Cl}(\text{OH})_6\text{SO}_4 \cdot 6\text{H}_2\text{O}$. Figure 2a exhibits the compositional range of islands after two days of exposure. The islands seems to consist of pure

$\text{Zn}_5(\text{OH})_8\text{Cl}_2 \cdot \text{H}_2\text{O}$ or of $\text{Zn}_5(\text{OH})_8\text{Cl}_2 \cdot \text{H}_2\text{O}$ with small amounts of sulfur. After 5 days of exposure, figure 2b, the amount of incorporated sulfur has increased and there are also a few islands with small amounts of sodium. After 30 days of exposure, figure 2c, the composition of some islands is approaching the theoretical composition of $\text{NaZn}_4\text{Cl}(\text{OH})_6\text{SO}_4 \cdot 6\text{H}_2\text{O}$. The diagrams clearly illustrate the initial formation of $\text{Zn}_5(\text{OH})_8\text{Cl}_2 \cdot \text{H}_2\text{O}$, the subsequent incorporation of first sulfur and then sodium in the gradual transformation of $\text{Zn}_5(\text{OH})_8\text{Cl}_2 \cdot \text{H}_2\text{O}$ into $\text{NaZn}_4\text{Cl}(\text{OH})_6\text{SO}_4 \cdot 6\text{H}_2\text{O}$.

These results are in close agreement with the deposition studies, figure 1, where a high deposition rate of chloride ions during the first day of exposure can be connected with a rapid formation of $\text{Zn}_5(\text{OH})_8\text{Cl}_2 \cdot \text{H}_2\text{O}$, and where an increase in the amount of deposited sulfate after 5 days of exposure can be connected with the initial formation of $\text{NaZn}_4\text{Cl}(\text{OH})_6\text{SO}_4 \cdot 6\text{H}_2\text{O}$.

By combining these results with identification of crystalline phases using XRD a complete picture of different reaction path sequences is revealed which involves the initial formation of a basic zinc carbonate. Depending on the type of environment with its specific chloride and sulfate deposition rates the sequence continues with either basic zinc chloride or basic zinc sulfate and may eventually end with some basic zinc chlorosulfate. It appears that the multitude of structurally related phases of corrosion products of zinc formed in marine, urban, rural and industrial environments and their correlation to variation in deposited amounts of chloride and sulfate are key ingredients for the understanding of the influence of initial weathering conditions on the atmospheric corrosion of zinc.

III. Analysis of crystalline and non-crystalline corrosion products

In September 1987 an international exposure program was implemented within the United Nations Economic Commission for Europe (UN ECE) with the general aim to quantify acidification effects on the atmospheric corrosion of different kind of materials. 39 different test sites were selected in 12 European countries, United States and Canada where acidifying pollutants were expected to be the major anthropogenic emissions. Materials investigated in the program have been exposed for 1, 2, and 4 years and a longer time not yet decided, and include structural metals, stone materials, paint coatings, and electric contact materials⁶.

As a part of the program corrosion effects were analysed on nickel, which belongs to the electric contact materials group⁷. Introductory studies by XRD revealed that the corrosion products formed on nickel after 1 and 2 years of rain sheltered exposure were both crystalline and non-crystalline. Efforts to identify the crystalline phase were unsuccessful. In order to obtain more information on the chemical composition of the corrosion products formed it was decided to undertake a characterisation based on diffuse reflectance infrared fourier transform spectroscopy (DRIFT) complemented by XPS and elemental analysis.

As a tool for characterisation of corrosion products infrared spectroscopy has several advantages. It can analyse a broad range of samples using different

transmission and reflection techniques, requires little material and can identify both crystalline and amorphous phases if reference spectra are available. Even if reference data are absent, comparisons and correlations with spectra of similar compounds can be used to characterise unknown corrosion products. The technique of diffuse reflectance for infrared spectroscopy became feasible with the development of fourier transform spectrometers and effective diffuse reflectance accessories⁸. It enables, among others, to overcome several of the disadvantages of traditional sampling in transmission infrared techniques, such as reduced sample preparation time and reduced ion exchange with the KBr matrix.

Altogether 58 samples, exposed for 1 or 2 years and selected from the 39 test sites, were analysed by means of DRIFT. It was found that all DRIFT spectra exhibit similar features, namely strong bands around 600 and 1100 cm^{-1} due to sulfate ions and several peaks due to water and hydroxyl groups in the region from 3000 to 3600 cm^{-1} . Bands at 1600 and 1400 cm^{-1} were also seen, the former due to water and the latter assigned to carbonate. The spectra could be classified into two groups. Spectra of type I are characterised by well resolved components of the asymmetric stretching mode of sulfate at 1100 cm^{-1} and three distinct peaks due to the stretching modes of hydroxyl groups just around 3600 cm^{-1} . Spectra of type II have poorly resolved components of the asymmetric stretching mode of sulfate with broad bands at slightly different positions compared to type I and a broad unresolved band below 3600 cm^{-1} due to hydroxyl groups. The spectra of type II exhibit in general stronger bands due to carbonate and water than spectra of type I. Spectra representative of the two types are presented in figure 3. A closer examination of the number of spectra of each type that were found after 1 and 2 years of exposure shows that the relative proportion of spectra of type II decreases with increasing exposure time and that many samples with spectra of type II after one year are of type I after two years.

Complementary information of the two types of corrosion products were obtained by XRD and elemental analysis. The results of XRD show that the spectra of type II correspond to an amorphous phase whereas spectra of type I correspond to a well defined diffraction pattern unknown in the literature. By elemental analysis it was shown that the most abundant elements in the corrosion products were oxygen, nickel, sulfur and hydrogen, small amounts of carbon were also found but nitrogen was not detected. These data are consistent with the assignments of the DRIFT data, namely that the spectra are dominated by bands due to sulfate, hydroxyl groups and water and that small bands due to carbonate groups can be seen. The non-crystallinity of type II corrosion products is reflected in the broad and unresolved sulfate and hydroxyl bands and this together with the observation that type II seems to be transformed into type I after two years of exposure suggest that type II is an intermediate state in the development of the more stable type I. The XPS measurements show only minor variations between the different sites manifesting that sulfate is the main component in the corrosion product with small amounts of chloride present on several samples. The observations suggest that both types of spectra correspond to basic nickel sulfates of different types. Type II is probably a relatively well defined but disordered basic nickel sulfate phase with intercalated carbonate ions and water

molecules and type I represents a stable and crystalline phase with less intercalated water and carbonate.

Attempts to correlate weight increase and environmental data with DRIFT spectra were made and showed that samples with DRIFT spectra of type II after one year exhibited higher weight increase during the second year than samples with DRIFT spectra of type I after one year, see figure 4. This is in agreement with the observation that type II spectra originate from corrosion products of lower stability than type I spectra. Efforts were also made to correlate the results from characterisation of corrosion products with environmental data. Figure 5 displays the occurrence of spectra of type I and II after 2 years of exposure plotted against average values of temperature of the exposure sites. It can be seen that type II is found at sites with high temperature.

From the experimental results and from information available in the literature a reaction sequence was proposed, which starts with the instant formation of monomolecular thick layers of $\text{NiO}/(\text{Ni}(\text{OH})_2)$, continues with the growth of a layered structure with intercalated water, carbonate, and sulfate ions eventually forming a basic nickel sulfate of type II, which later crystallizes into the more stable basic nickel sulfate of type I⁷. Further investigations have been made on samples exposed for 4 years, and the results of DRIFT analysis of selected samples show that all samples that exhibited spectra of type II after two years exhibit spectra of type I after 4 years⁹. This confirms the results obtained for samples exposed 1 and 2 years.

IV. Interpretation of empirically derived damage functions

The main task of the UN ECE program is to produce damage functions, linking the amount of corrosion of materials to environmental characteristics measured simultaneously at the test sites. These measurements include climatic parameters (temperature, relative humidity, time of wetness, and sunshine hours), gaseous pollutants (SO_2 , NO_2 , and O_3), and precipitation (mm, conductivity, pH, SO_4^{2-} , NO_3^- , Cl^- , NH_4^+ , Na^+ , Ca^{2+} , Mg^{2+} , and K^+). Enormous amounts of data are produced within the project and the task of developing usable damage functions can be insurmountable if not a clear strategy is applied.

The evaluation of silver after 4 years of exposure will serve as an example of the use of surface analysis of corrosion products as a complement to the statistical analysis¹⁰. Similar to nickel, silver belongs to the electric contact materials group of the UN ECE program. It is known to be more sensitive to reduced sulfur compounds such as H_2S than to acidifying pollutants^{11,12}. These compounds are not measured within the program because they are thought to be a minor part of the pollutants on most of the test sites.

When applying statistical analysis of corrosion effects of silver and of climatic parameters, the following equation was obtained,

$$r = 5.8[\text{SO}_2]^{0.20}[\text{NH}_4^+]^{0.38}$$

$$R^2 = 0.59$$

where r is the average weight increase rate of silver in $\mu\text{gcm}^{-2}\text{yr}^{-1}$ during the first 4 years of exposure, $[\text{SO}_2]$ is the average concentration in μgm^{-3} and $[\text{NH}_4^+]$ the average concentration measured as nitrogen in mg l^{-1} .

In order to interpret the equation, samples from selected sites were analysed with XPS. This technique should be able to tell whether sulfur on the silver surface was in the form of sulfide or sulfate. In fact, both sulfide and sulfate were detected at comparable levels on all silver samples investigated. Chloride and ammonium was also found, however not on all samples. Ammonium was weakly correlated to sulfate and also detected when the ammonium and chloride concentrations in precipitation both were at elevated levels.

When electrolytic cathodic reduction was applied to detect the nature and amount of the corrosion products only Ag_2S was found. In combination with previous XPS results this indicates that particulate ammonium sulfate had been deposited on the surface. Furthermore, when replacing the total weight increase in the statistical analysis with the weight increase due to Ag_2S formation, the correlation with SO_2 was improved but the correlation with NH_4^+ was changed for the worse.

It seems unlikely that SO_2 would eventually form a silver sulfide even though this reduction path has been considered¹³. However, the mechanism was proposed for copper and iron at much higher SO_2 levels than under present exposure condition. A more probable explanation for the correlation between SO_2 and sulfide formation would be the mutual correlation of SO_2 to reduced sulfur compounds.

To conclude, a damage function for the weight increase of silver was obtained using gaseous SO_2 and NH_4^+ in precipitation as explanatory variables. The physical meaning of these parameters was elucidated by examining the corrosion products by XPS and electrolytic cathodic reduction. It was shown that the origin of ammonium could be explained by deposition of particulate ammonium sulfate, probably as $(\text{NH}_4)_2\text{SO}_4$. Correlation with SO_2 and weight increase could also partly be explained by the presence of ammonium sulfate but to a larger extent by a possible correlation between SO_2 and H_2S resulting in the formation of Ag_2S .

V. Concluding remarks

The examples given have shown that significantly new information can be gained if a combination of suitable techniques are used for characterisation of corrosion products. A most useful approach is to involve different methods for surface and bulk analysis of corrosion products together with measurements of climatic parameters and deposition rates of the most important corrosion stimulating atmospheric constituents. Using such a multianalytical approach it has been possible to identify new reaction sequences in the atmospheric corrosion of zinc and relate these to actual deposition rates.

In particular zinc, but to a lesser extent also nickel, seem to be metals that exhibit a variety of different reaction sequences which involve the instant formation of thin layers of hydroxide (both metals), basic carbonates (both metals), basic sulfates (both metals), basic chloride (zinc) and basic chlorosulfates (zinc). The phases formed can be both crystalline and non-crystalline. They possess different protective abilities and, as a consequence, it is anticipated that their formation has a significant influence on atmospheric corrosion kinetics.

Analysis of corrosion products also aids in interpreting empirically derived damage functions. In the example given a statistical analysis resulted in an equation involving certain atmospheric parameters without any obvious connection to real corrosion effects of silver. Only by applying surface analysis it could be concluded that the mass gain of silver was the combined effect of silver sulfide formation and deposition of ammonium sulfate.

Acknowledgments

Financial support from the Swedish National Board for Industrial and Technical Development (NUTEK), the Swedish Steel Company (SSAB), Borlänge, and the Swedish Corrosion Institute, Stockholm, is greatly acknowledged.

References

1. "Techniques in Electrochemistry, Corrosion and Metal Finishing. A Handbook", Ed. A.T. Kuhn, (John Wiley & Sons Ltd., Chichester, 1987).
2. H.H. Willard, L.L. Merritt, Jr., J.A. Dean, F.A. Settle, "Instrumental Methods of Analysis", (Wadsworth Publishing Company, Belmont, Ca, 1981).
3. O. B. Ellis, Proc., ASTM, 47 (1947): p. 152.
4. I. Odnevall, C. Leygraf, Proc. 12:th Scand. Corros. Congr. & Eurocorr 92, Helsinki (1992).
5. I. Odnevall, C. Leygraf, Corros. Sci., in press.
6. J. Tidblad, C. Leygraf, V. Kucera, J. Electrochem. Soc., 138 (1991): p. 3592.
7. D. Persson, C. Leygraf, J. Electrochem. Soc., 139 (1992): p. 2243.
8. M. P. Fuller, P. R. Griffiths, Anal. Chem., 55 (1978): p. 1906.
9. J. Tidblad, C. Leygraf, V. Kucera, submitted for publication.
10. J. Tidblad, C. Leygraf, V. Kucera, Proc. 12:th Scand. Corros. Congr. & Eurocorr 92, Helsinki (1992).
11. J.P. Franey, G.W. Kammlott, T.E. Graedel, Corros. Sci., 25 (1985): p. 133.
12. D.W. Rice, P. Peterson, E.B. Rigby, P.B.P. Phipps, R.J. Cappell, R.J. Tremoureux, J. Electrochem. Soc., 128 (1981): p. 275.
13. I.L. Rozenfeld, in "Atmospheric corrosion of metals", (National Association of Corrosion Engineers, Houston, 1972).

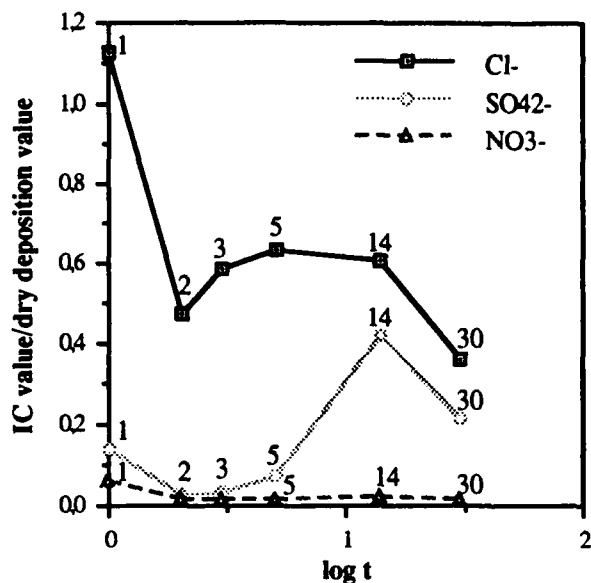


Figure 1. Ratio between IC-data and dry deposition data at the marine test site, sheltered exposure, vs. log time [days].

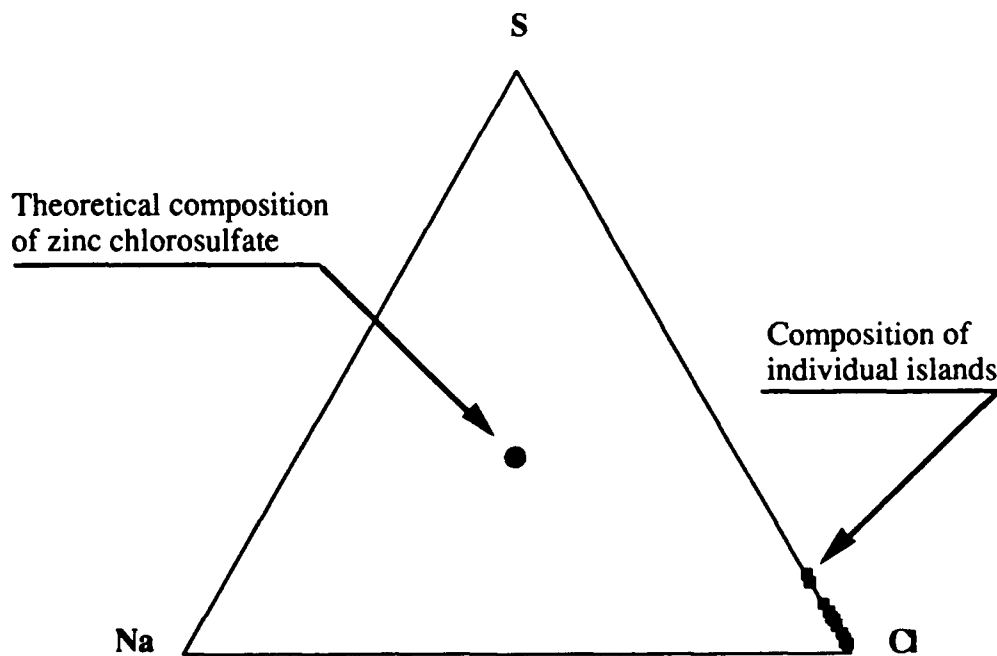


Figure 2a. Ternary diagram showing the quantitative amount of sulfur, chlorine and sodium in atomic percent by means of EDS after 2 days of exposure.

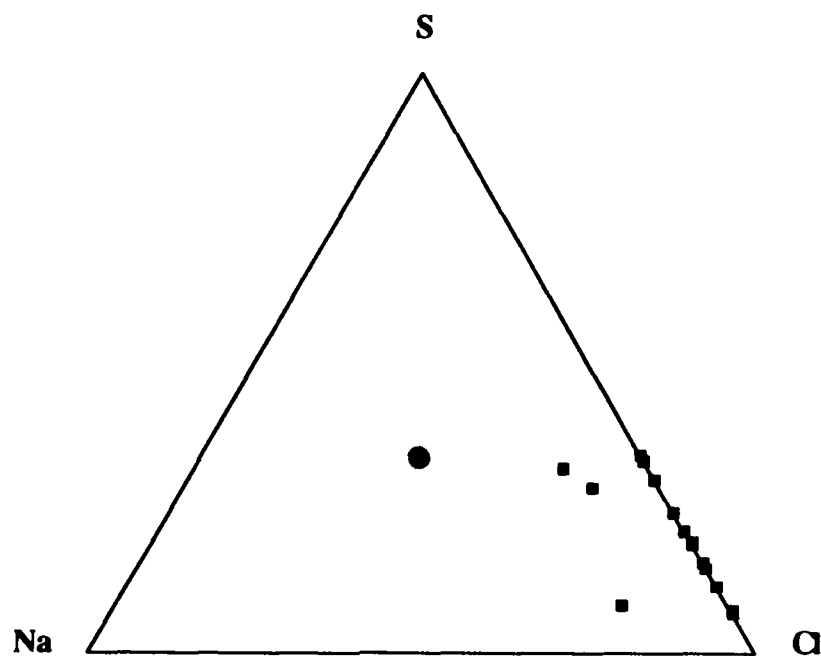


Figure 2b. Ternary diagram showing the quantitative amount of sulfur, chlorine and sodium in atomic percent by means of EDS after 5 days of exposure.

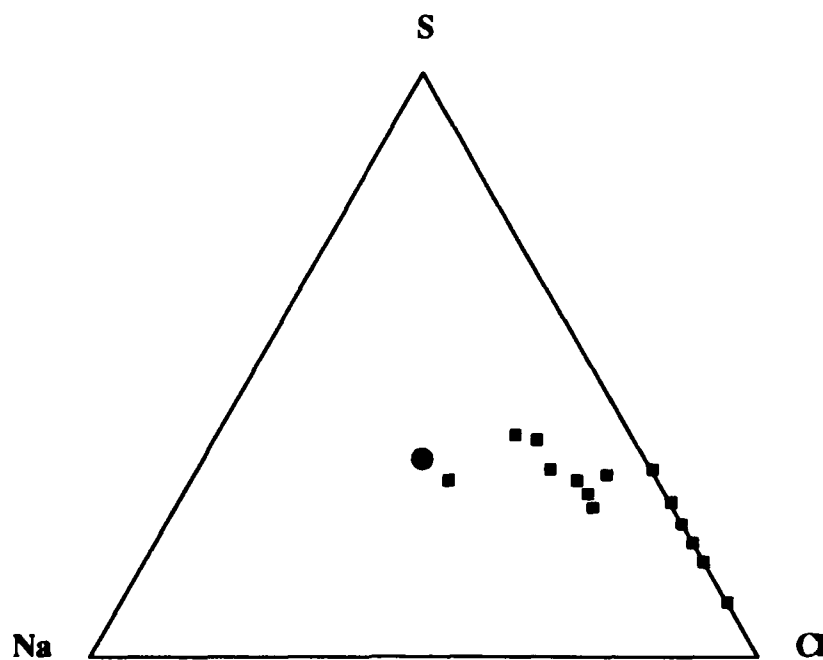


Figure 2c. Ternary diagram showing the quantitative amount of sulfur, chlorine and sodium in atomic percent by means of EDS after 30 days of exposure.

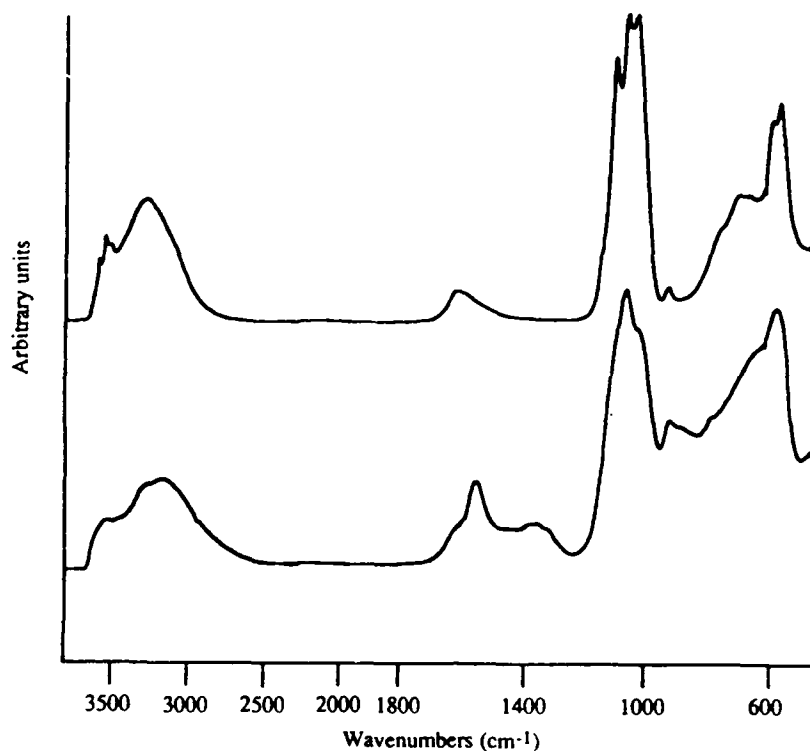


Figure 3. DRIFT spectra from basic nickel sulphate, lower spectrum type II (amorphous), upper spectrum type I (crystalline).

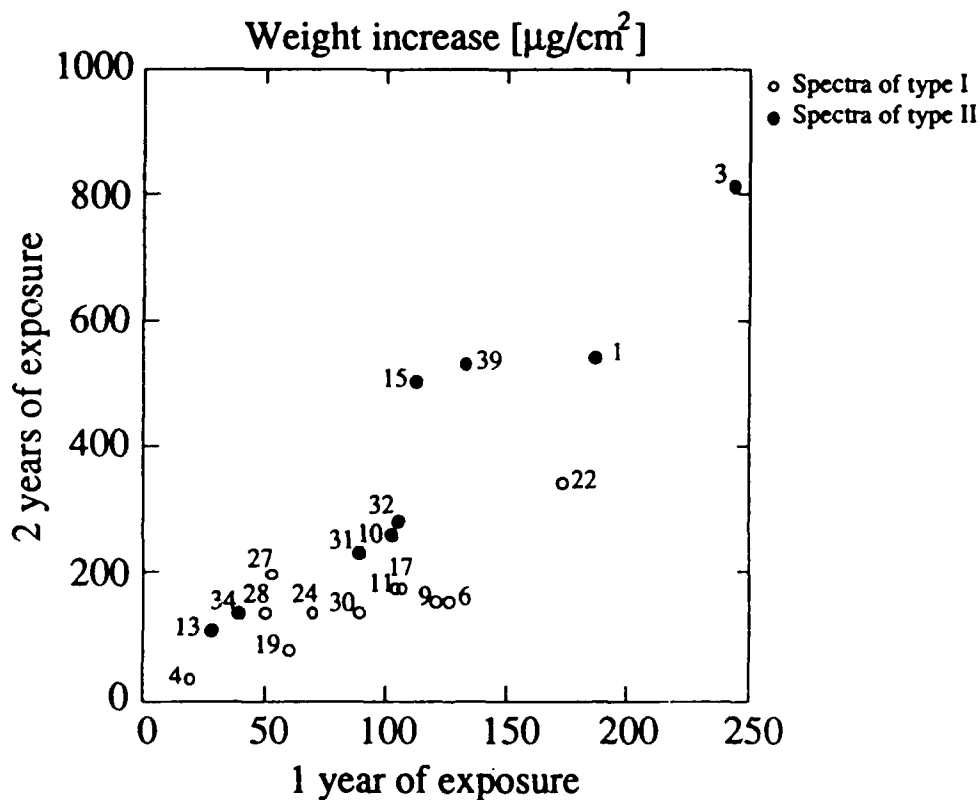


Figure 4. Weight increase after two years vs. weight increase after one year of exposure and with indications whether DRIFT spectra of type I or of type II were observed after one year of exposure. Numbers in the figure refer to test site number as described in (6).

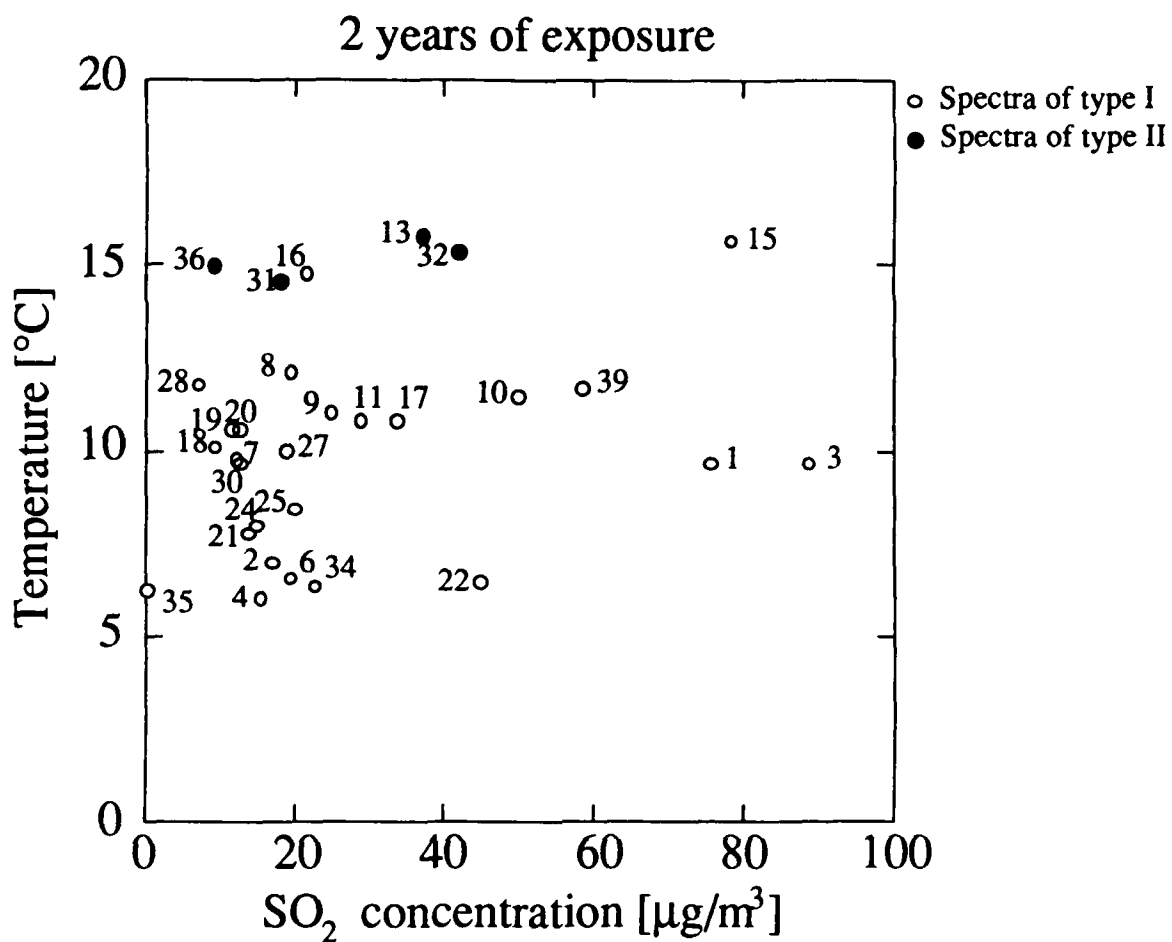


Figure 5. Type of spectra found after 2 years of exposure, plotted against average sulfur dioxide concentration and average temperature. Numbers in the figure refer to test site number as described in (6).

Protective Rust Layer Formed on Weathering Steel by Atmospheric Corrosion for a Quarter of a Century

Toshihei Misawa

Department of Materials Science and Engineering
Muroran Institute of Technology
Muroran-050, Japan

Masato Yamashita, Hideaki Miyuki, Hiroo Nagano

Research and Development Center
Sumitomo Metal Industries Ltd.
Amagasaki-660, Japan

Abstract

The structure of rust layer formed on a weathering steel by atmospheric corrosion in an industrial atmosphere for a quarter of a century has been investigated using various analytical techniques. It is elucidated that the inner stable and protective rust layer formed on the weathering steel mainly consists of fine-particle α -FeOOH containing a considerable amount of Cr.

The relative change in the amount of rust constituents for low-alloy steels supports well that a newly proposed schematic progress of long-term alteration in rust layer formed on a weathering steel in an industrial environment. That is, the γ -FeOOH, as an initial rust layer, is transformed into a final stable rust layer of α -FeOOH, via amorphous oxyhydroxide substance, during the long-term atmospheric corrosion of a weathering steel.

Key terms: atmospheric corrosion, weathering steel, oxyhydroxide, protective rust

Introduction

The main products of rusts formed on steels corroded in the atmosphere under the repeated condition of wet by very thin electrolyte layer and its drying out are α -FeOOH, γ -FeOOH, Fe_3O_4 and X-ray amorphous substance¹⁾⁻⁵⁾. The processes of rusting and phase transformation of iron oxides and oxyhydroxides have been reported by Misawa⁷⁾, as shown in Fig.1.

It has been well recognized that the rust layer formed on a weathering steel which contains a small amount of Cr, P and Cu gives certain beneficial effects for protection of the steel against atmospheric corrosion. The protective ability of the rust layer emerges after a few years exposure; the stable rust is composed of two layers of the inner and outer ones. It has been pointed out by Okada et al.²⁾ that the inner layer responsible for the protection from atmospheric corrosion consists of X-ray amorphous spinel type iron oxide containing some effective elements such as Cr, Cu and P. Misawa et al.⁴⁾ reported that amorphous ferric oxyhydroxide containing a significant amount of water acts as a protective barrier against atmospheric

rusting, by means of infra-red spectrometry. The present authors pointed out that the protective rust layer is finally transformed into stable rust matter of α -FeOOH³.

It recently becomes possible to examine the protective rust layers formed by the exposure of weathering steels to the weather for decades. In the present study, the corrosion products formed on the weathering steel exposed to an industrial environment for 26 years are characterized, especially focusing on the inner protective layer, and a process of long-term growth of the protective rust layer is newly proposed.

Experimental

I. Specimens

A. Atmospheric Rusting

Plates of weathering ($60 \times 100 \times 4\text{mm}^3$) and mild steels ($60 \times 100 \times 3\text{mm}^3$) were exposed to an industrial atmosphere at an angle of 30° facing south for 26 years. This exposure period is considered to be long enough to form sufficiently stable and protective rust layer on the weathering steel. The chemical compositions of the steels used for the long-term exposure test are listed in Table 1. The amount of corrosion of steel was evaluated in terms of the decrease in thickness obtained from a loss in weight.

B. Preparation of Specimens

The corrosion products formed on the steel surfaces were removed by a razor until the steel surfaces appeared, and then ground into powder. The powdered rust samples were desiccated for a week in advance of the subsequent analyses.

Following the reinforcement employing a vapour deposited Au and an electrodeposited Ni on the rusted surfaces of the steel plates, the specimens, employed for the examination of the cross-sections of the rust layers, were cut and fixed by an epoxy resin. The cross-sections of the fixed specimens were mechanically polished on emery papers and then with a diamond paste.

II. Analysis

A. Analysis of the Powdered Rust

The powdered samples were characterized by means of infrared transmission spectroscopy and X-ray diffraction method.

A Japan BIO-RAD Laboratories Model FTS-65A infrared spectrophotometer was used to measure spectra of the powdered samples which were pressed into a KBr matrix by scanning in the range of 400 and 4000 cm^{-1} for 10000 times within an accuracy of better than 8 cm^{-1} .

The X-ray diffraction measurements were carried out by using a Rigaku-Denki Model RU200 diffractometer employing Co target under the condition of 30kV - 100mA and a scanning speed of $2\text{ deg}\cdot\text{min}^{-1}$. The quantitative determination of α - and γ -FeOOH's and the remainder substance mainly containing an amorphous substance, was carried out by measuring the diffraction intensities. The diffraction intensities of (011) reflection of α -FeOOH and (020) reflection of γ -FeOOH were measured and referred to (200) reflection of KCl powder which had been mixed with rust samples as an internal standard⁴⁾.

B. Analysis of the Rust Layer

The cross-sections of the rust layers were characterized by means of observation of the reflection behaviour of polarized light in an optical microscope, scanning electron microscopy, Raman spectroscopy and electron probe microanalysis.

Raman spectra were measured using a Japan Spectroscopic Model NR-1100. The Ar^+ laser with the 514.5 nm wave length was used as the excitation source. The beam diameter was approximately 2 μm and the power was controlled lower than 0.1 mW at the sample surface in order to avoid the rise in temperature.

The distribution of several important elements in the rust layers was investigated using a Shimadzu Model EPM810 electron probe microanalyzer under the conditions of 15kV in accelerated voltage and 0.1 μA in the sample current.

Results and Discussion

1. Characteristics of Stable and Protective Rust Layer

A. Observation of Rust Layer

The surface of the weathering steel is covered with dark-brown rust, while that of the mild steel red brown one. The corrosion losses of the weathering and the mild steels are 355 μm and 1025 μm in the thickness, respectively. This clearly demonstrates that the protective ability of the rust layer formed on the weathering steel is decidedly superior to that on the mild steel.

It was found by the microscopic observation using reflected polarized light and crossed nicols that the rust layer formed on the weathering steel exposed for 26 years can be divided into two layers; one corresponds to the outer layer which is optically active (illuminated) and the other is the inner layer which is optically isotropic (darkened). On the other hand, the surface rust formed on the mild steel is composed of the mottled structure consisting of the optically active and isotropic corrosion products. Okada et al.^{1),2)} pointed out that the inner optically isotropic layers of the surface rusts formed on weathering steels exposed for a few years are composed of X-ray amorphous spinel type iron oxide which can protect the steel matrix.

It was observed by the scanning electron microscopy that the component particles whose mean diameter is approximately 0.5 μm in the outer layer of the weathering steel loosely aggregate, whereas the inner layer is composed of densely packed fine particles which form the larger secondary-particles. The corrosion product formed on the mild steel contains a number of voids and micro-cracks.

B. Constituent Compounds of Rust

It becomes evident by examining the X-ray diffraction patterns and the infrared absorption bands that both of the rust layers formed on the weathering and mild steels are mainly composed of α -FeOOH and γ -FeOOH as crystalline constituents. The presence of a little Fe_3O_4 can also be detected.

The outer and inner layers of the rust formed on the weathering steel are characterized by examining the Raman spectra, which are shown in Fig.2.

A Raman spectrum of the outer layer for the weathering steel is shown in Fig.2(a). The major bands observed at the vicinities of 255, 380, 530 and 655 cm^{-1} are clearly due to the presence of γ -FeOOH as the main constituent. On the one hand, it should be noted in Fig.2(b) that the observed bands at the vicinities of 245, 300, 397, 485, 550 and 685 cm^{-1} in the spectrum of the inner layer correspond to those of α -FeOOH. Raman spectra of several different areas of the inner layer were almost identical, thus it is said that the composition of the inner layer is homogeneous. Based on the present results, it can be said that the surface rust formed on the weathering steel exposed for 26 years in an industrial region consists of the outer layer which mainly comprises γ -FeOOH and the inner layer mainly composed of fine-particles of α -FeOOH.

On the other hand, the corrosion product formed on the mild steel is composed of the mottled structure consisting of γ - and α -FeOOH parts; the former is illuminated under the observation of the reflected polarized light and the latter corresponds to the darkened region, as shown in Fig.2 (c) and (d).

C. Distribution of Several Elements in the Rust Layer

Most striking feature found in the distribution of several elements in the present rust layers is the concentration of Cr observed only in the inner layer on the weathering steel. This enrichment of Cr agrees with the result reported by Okada et al.^{1),2)} who pointed out that the inner layer of the corrosion product on the weathering steel exposed for a few years contains a considerable amount of Cr, Cu and P. However, neither Cu nor P concentrates in the present 26-years corrosion product.

Another significant feature is the existence of Si only in the outer layer. It is considered that a cloud of dust in the air penetrated into and accumulated in the outer layer. Nevertheless, the inner layer might be compact enough to shut out the dust. In addition, S is detected both in the outer and the inner layers, whereas Cl is scarcely present in the corrosion products.

Although, Cr, P and Cu are naturally not present in the rust formed on the mild steel, Si exists in almost whole of the mild steel rust layer. The distribution of S and Cl in the rust on the mild steel is similar to that on the weathering steel mentioned above.

D. Characteristic Features of Rust Layer

The characteristic features of the rust layers formed on the weathering and the mild steels exposed for 26 years in an industrial atmosphere are summarized in Table 2. As has been mentioned above, the rust formed on the weathering steel consists of two layers; one is the outer layer which mainly comprises γ -FeOOH and the other corresponds to the inner layer mainly composed of densely packed fine-particles of α -FeOOH. It can be said that the densely aggregated inner layer, which contains a considerable amount of Cr and is free from Si penetration, possesses the superior ability for protection of the weathering steel against the atmospheric corrosives. On the contrary, the rust layer formed on the mild steel, which is composed of the mottled structure consisting of γ - and α -FeOOH parts, contains a number of voids and micro-cracks. The most significant result clarified in the present investigation is that the protective rust layer covering the weathering steel surface mainly consists of α -FeOOH.

Keiser et al.⁹⁾, Stockbridge et al.¹⁰⁾ and Cohen and Hashimoto¹¹⁾ have studied the electrochemical nature of various ferric oxyhydroxides. It was demonstrated that α -FeOOH is resistant to electrochemical reduction, whereas γ -, δ - and amorphous ferric oxyhydroxides can be reduced to magnetite. The reduction of corrosion product which covers a steel surface results in the cathodic reaction which balances the anodic dissolution of Fe. If it is assumed that the surface rust layer is compact enough to avoid the penetration of water and oxygen into the steel surface and that the compact rust layer is the final stable corrosion product resistant to electrochemical reduction, like the densely aggregated fine-particles of α -FeOOH rust matter, then it can be said that the surface rust layer possesses an extremely high ability in the protection of the steel against the atmospheric corrosion.

Therefore, it is concluded that the ferric oxyhydroxide of α -FeOOH is the final stable corrosion product in an atmospheric environment. Once the densely packed aggregate of fine-particle α -FeOOH, which is formed associated with enrichment of Cr, covers the weathering steel surface, formation of micro-cracks and voids due to the variation in volume as a result of phase transformation can be avoidable. This α -FeOOH rust layer exhibits a great ability in the protection against an atmospheric attack in an industrial environment after the exposure for decades.

Another important fact obtained in the present investigation is that Cu and P are not concentrated in the protective inner α -FeOOH layer, whereas Cr is present at a relatively high concentration after the 26-years exposure. However, the existence of Cu and P has been noted as beneficial elements for the formation of protective rust layer formed on a weathering steel exposed for a relatively short period^{2)-4), 6), 12)-20)}, as will be mentioned below. It is possible to consider that Cu and P play important roles on the formation of the uniform protective rust layer on the surface of the weathering steel, especially at the early stage of atmospheric corrosion, though the concentration of Cu and P in the corrosion product is not confirmed in the present 26-years weathering steel.

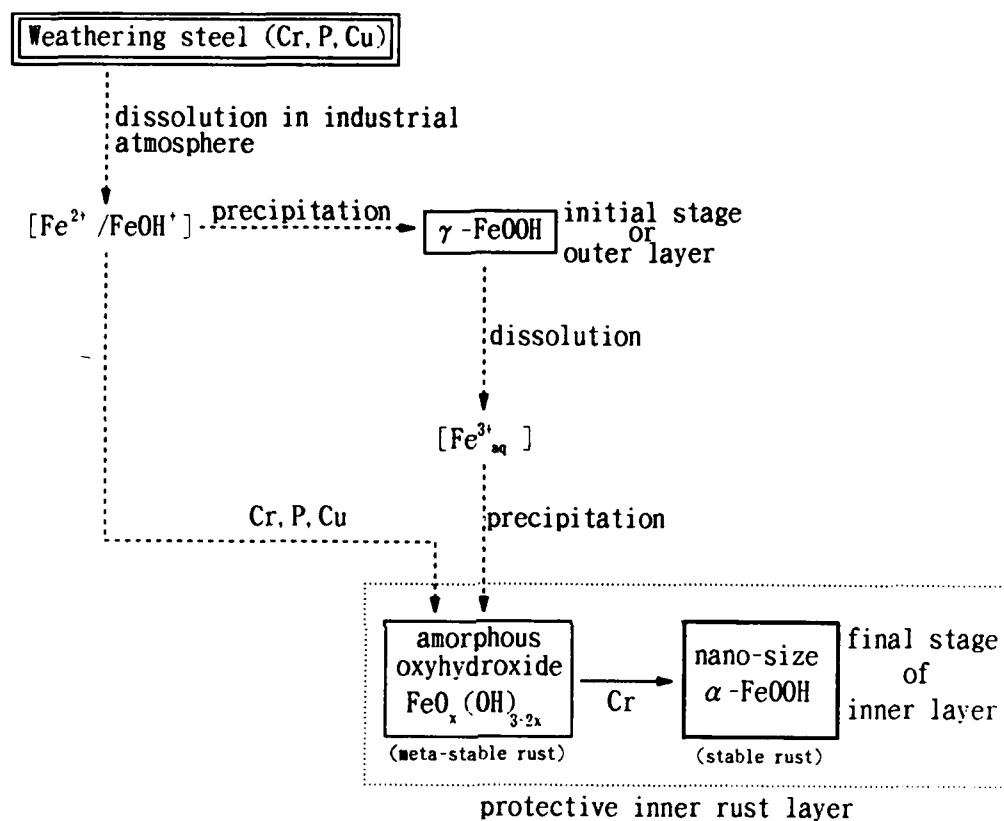
II. Change of Rust Constituents with Exposure Period

In order to know the change of rust constituents with exposure period, the quantitative fractions of α -FeOOH, γ -FeOOH and the remainder substance in the rust layers formed on the low-alloy steels which contain a small amount of Cr, Cu and P exposed for 0.5-26 years²¹⁾, including the present 26-years sample, are investigated by examining the X-ray diffraction intensities. All of the low-alloy steels were exposed in an industrial or a rural (7 and 8 years exposure) environment.

The exposure-time dependence of the fractions of three constituents in the rusts examined can be summarized in Fig.3. There exist three regions, i.e. I; γ -FeOOH-rich region less than a few years, II; amorphous-oxyhydroxide-rich region at several years and III; α -FeOOH-rich region after decades. It is concluded that the main constituent of the rust layers formed on low-alloy steels is altered from γ -FeOOH (less than a few years), via amorphous substance (several years), to α -FeOOH (decades).

III. Long-Term Growth of Stable and Protective Rust Layer

Following Misawa et al.^{4), 22), 23)} who showed the process of rusting and phase transformation of iron oxide and oxyhydroxide in an industrial region with a slightly acidic aqueous environment, a rust formation process of a weathering steel in an industrial atmosphere is newly proposed on the basis of the present results as follows;



(1).

Accordingly, a model of the progress of alteration in stable and protective rust layer formed on a weathering steel in an industrial region can be newly proposed, as schematically shown in Fig.4. As was mentioned in equation (1), γ -FeOOH is formed on the steel surface at the initial stage of atmospheric corrosion with a thin layer of slightly acidic electrolyte, as shown in Fig.4(a). Then, the inner portion of the initial corrosion product may change to amorphous ferric oxyhydroxide, via the dissolution of γ -FeOOH accelerated by acid rain and the precipitation of amorphous ferric oxyhydroxide by wet-dry cycles in industrial atmosphere, as shown in Fig.4(b). It is supposed that Cr, P and Cu dissolved out from the steel matrix exert a favorable influence on the uniform formation of the protective rust layer. Finally, during a long period exposure, the amorphous inner layer can transform to densely packed aggregate of fine-particle or nano-size α -FeOOH which is stable both electrochemically and thermodynamically, as shown in Fig.4(c). The final stable corrosion product, fine particle or nano-size α -FeOOH, which is formed associated with enriched Cr in the inner layer, is the densely packed uniform rust layer. It

is concluded that this final stable product of nano-size α -FeOOH rust possesses an extremely high protective ability against atmospheric corrosives.

Conclusion

The surface rusts formed on the weathering and mild steels by atmospheric corrosion in an industrial region for 26 years were characterized mainly by means of X-ray diffraction method, infrared spectroscopy, Raman spectroscopy and electron probe microanalysis. The quantitative change of the rust constituents of low-alloy steels with exposure period was analyzed and the long-term growth of protective rust layer on the weathering steel was discussed. The conclusions obtained are summarized as follows;

- (1) The surface rust formed on the weathering steel consists of two layers; one is the outer layer which mainly comprises γ -FeOOH and the other corresponds to the inner layer mainly composed of densely packed fine-particles of α -FeOOH.
- (2) The densely aggregated fine-particles of α -FeOOH, which are formed associated with enriched Cr in the inner layer, is the stable and protective uniform rust layer.
- (3) The main constituent of the rust layers formed on low-alloy steels is altered from γ -FeOOH (less than a few years), via amorphous substance (several years), to α -FeOOH (decades).
- (4) It is proposed that the γ -FeOOH, as an initial rust layer of weathering steel, is transformed into the final stable protective rust layer consisting of fine-particle α -FeOOH, via amorphous ferric oxyhydroxide, during the long-period atmospheric corrosion.
- (5) A rust formation process of a weathering steel in an industrial atmosphere is presented, and a model of the progress of growth of the stable and protective rust layer formed on a weathering steel is newly proposed.

Acknowledgment

One of the authors (T.M) would like to thank the financial support of The Iron and Steel Institute of Japan, as a Grant-in-Aid for Steel Research Promotion.

References

1. H.Okada, J.Soc.Mater.Sci.Japan, 17(1968):p.705.
2. H.Okada,Y.Hosoi,K.Yukawa,H.Naito, J.Iron Steel Inst. Japan, 55(1969):p.355.
3. T.Misawa,K.Hashimoto,S.Shimodaira, Corros. Engineering Japan, 23(1974): p.17.
4. T.Misawa,K.Asami,K.Hashimoto,S.Shimodaira. Corros.Sci., 14(1974):p.279.
5. T.Misawa, Corros. Engineering Japan, 32(1983):p.657.
6. H.Kihira,S.Ito,T.Murata, Corros.Sci., 31(1990):p.383.
7. T.Misawa, Corros. Engineering Japan, 37(1988):p.501.
8. T.Misawa,M.Yamashita,Y.Matsuda,H.Miyuki,H.Nagano, J.Iron Steel Inst. Japan, 79(1993):p.69.

9. J.T. Keiser, C.W. Brown, R.H. Heidersbach, J. Electrochem. Soc., 129(1982): p. 2686.
10. C.D. Stockbridge, P.B. Sewell, M. Cohen, J. Electrochem. Soc., 108(1961): p. 928.
11. M. Cohen, K. Hashimoto, J. Electrochem. Soc., 121(1974): p. 42.
12. H. Sugawara, M. Takano, H. Ebiko, K. Hashimoto, W. Suetaka, S. Shimodaira, J. Soc. Mater. Sci. Japan, 17(1968): p. 710.
13. M. Stratmann, K. Bohnenkamp, T. Ramchandran, Corros. Sci., 27(1987): p. 905.
14. K. Inoue, S. Ishii, K. Kaneko, T. Ishikawa, Z. Anorg. Allg. Chem., 381(1972): p. 86.
15. K. Inoue, S. Ishii, K. Kaneko, T. Ishikawa, Corros. Sci., 16(1976): p. 507.
16. N. Masuko, Y. Hisamatsu, Corros. Engineering Japan, 17(1968): p. 465.
17. N. Masuko, Y. Hisamatsu, Corros. Engineering Japan, 17(1968): p. 539.
18. E.P. Egan, Jr., Z.T. Wakefield, B.B. Luff, J. Phys. Chem., 65(1961): p. 1265.
19. M. Cher, N. Davidson, J. Am. Chem. Soc., 77(1955): p. 793.
20. J. King, N. Davidson, J. Am. Chem. Soc., 80(1958): p. 1542.
21. M. Yamashita, H. Miyuki, H. Nagano, T. Misawa, unpublished data.
22. T. Misawa, Corros. Sci., 13(1973): p. 659.
23. T. Misawa, K. Hashimoto, S. Shimodaira, Corros. Sci., 14(1974): p. 131.

Table 1 Chemical compositions of the weathering and mild steels tested. (mass.%)

	C	Si	Mn	P	S	Cu	Cr	Ni
Weathering steel	0.12	0.49	0.50	0.149	0.020	0.57	1.19	0.49
Mild steel	0.12	0.01	0.09	0.018	0.026	0.01	0.01	0.01

Table 2 Characteristic features of the corrosion products formed on the weathering (W) and mild (M) steels by atmospheric corrosion in an industrial environment for 26 years.

	Observation by polarized light	X-ray diffraction	Infrared spec- troscopy	Raman spectroscopy	EPMA (Remarkable characteristics)	aggregative state
W	Bright layer (outer layer)	α -FeOOH + γ -FeOOH	α -FeOOH + γ -FeOOH	γ -FeOOH	Si storage.	Loosely packed.
	Dark layer (inner compact layer)	\gg Fe ₃ O ₄	\gg Fe ₃ O ₄	α -FeOOH	Cr enrichment. Little enrichment of P and Cu. Si free.	Densely packed fine-particles.
M	Bright	α -FeOOH + γ -FeOOH	α -FeOOH + γ -FeOOH	γ -FeOOH	Absence of Cr, P and Cu. Widely penetrated Si.	Presence of voids and cracks.
	Dark	\gg Fe ₃ O ₄	\gg Fe ₃ O ₄	α -FeOOH		

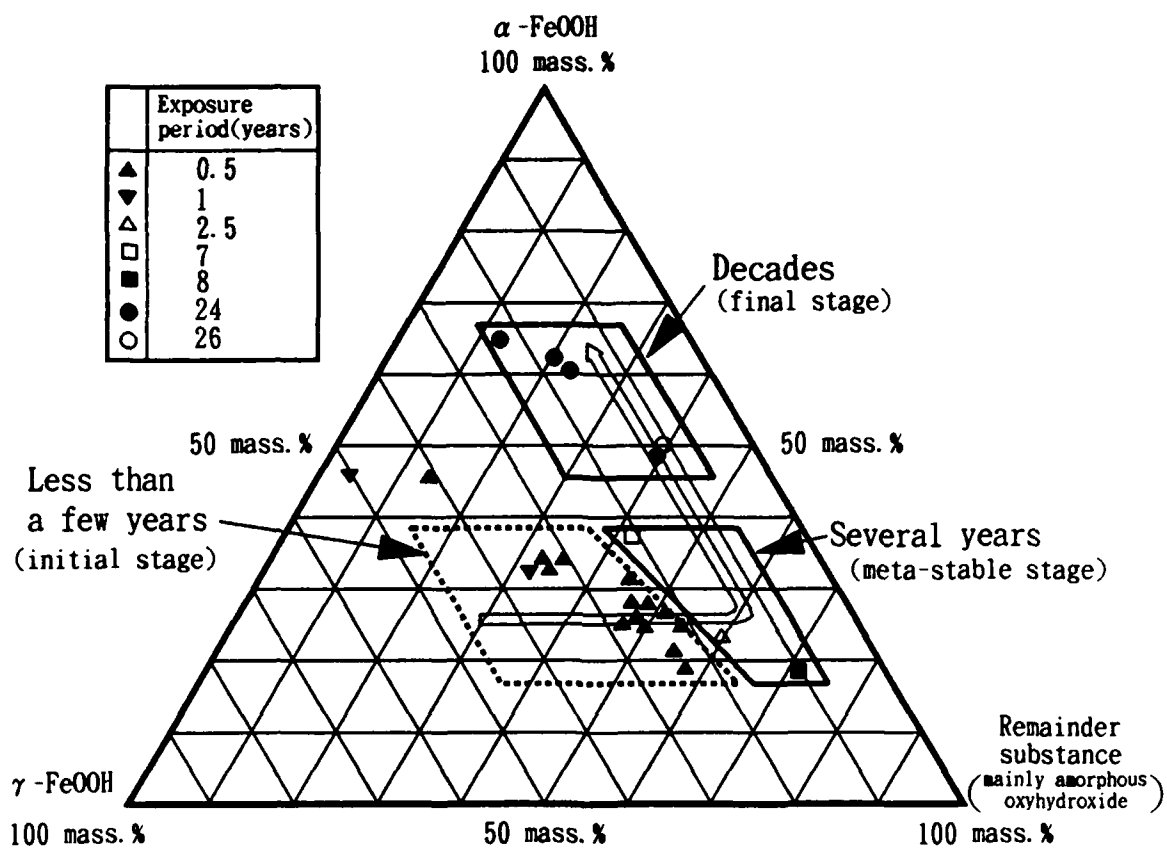


Fig. 3 The exposure-time dependence of the fractions of rust constituents formed on low-alloy steels by atmospheric corrosion in an industrial and a rural regions. The fraction changes along an open arrow.

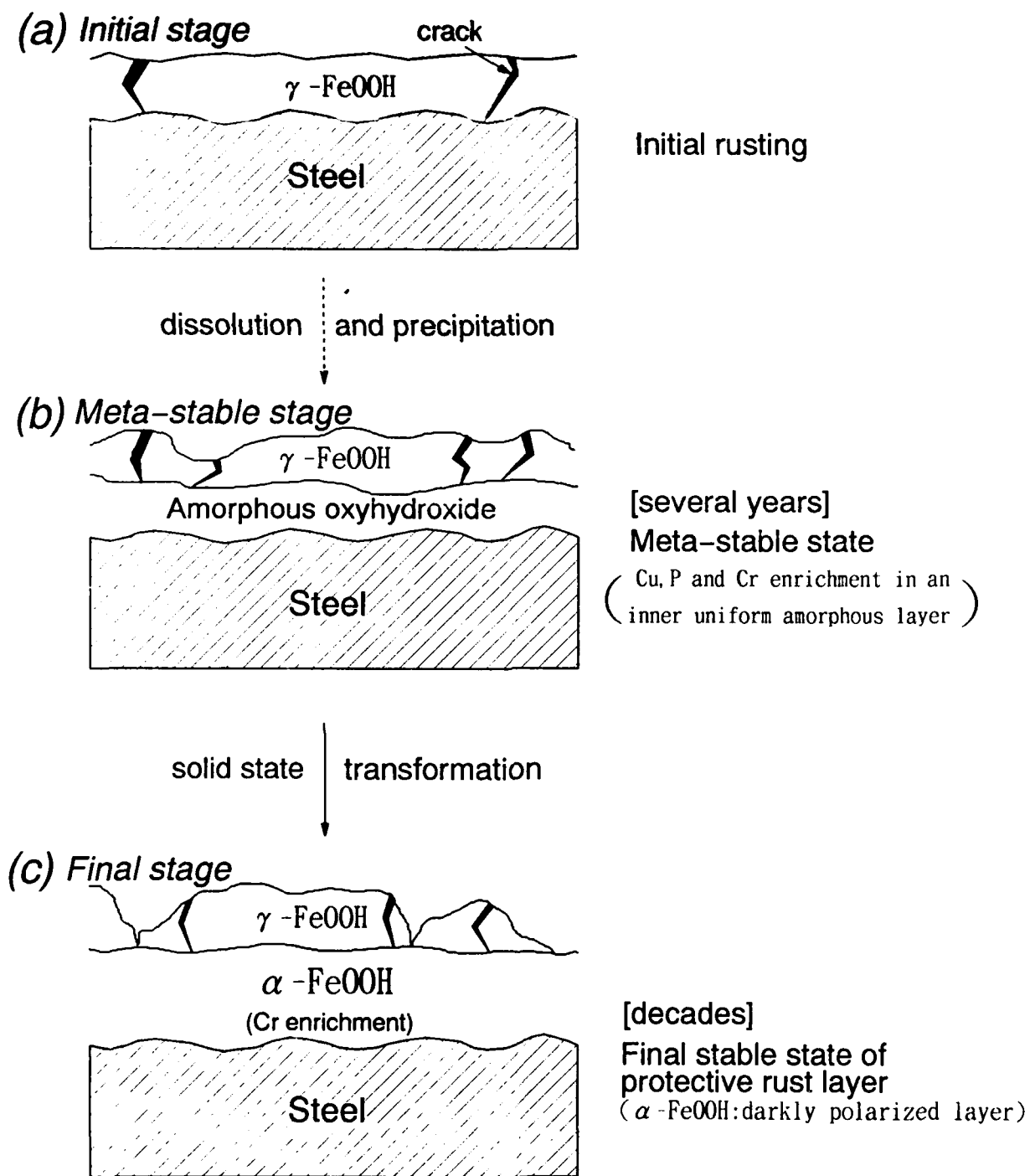


Fig. 4 Newly proposed schematic progress of alteration in stable and protective rust layer formed on a weathering steel in an industrial region.

Structure of Rust on Weathering Steel in Rural and Industrial Environments

Herbert E. Townsend
Bethlehem Steel Corporation
Homer Research Laboratories
Bethlehem, Pa. 18016 USA

Theresa C. Simpson
Bethlehem Steel Corporation
Homer Research Laboratories
Bethlehem, Pa. 18016 USA

Gary L. Johnson
Air Products and Chemicals, Inc.
7201 Hamilton Boulevard
Allentown, Pa. 18195 USA

Abstract

Rust on weathering steels exposed for up to 11 years in industrial and rural environments exhibits a spotty, non-uniform appearance owing to contrast between light and dark areas on the surface. The area of the lighter regions increases with exposure time as well as with increasing alloy content.

Microscopic examination of cross sections reveals that the dark regions have a porous appearance. The light regions are similar except for the presence of a relatively thin, smooth outer surface layer. Raman spectroscopy indicates that the dark, porous rust is comprised of goethite and lepidocrocite, while the smooth outer layer on the light areas is composed of hematite and magnetite. Electrochemical potential measurements indicate that the lighter areas are more passive.

Overall, these results suggest that formation of the thin outer layer of hematite and magnetite is an important part of the mechanism of protective rust formation on weathering steels in these environments.

Key terms: electrochemical potential, industrial environment, Raman spectroscopy, rural environment, rust, weathering steel, goethite, lepidocrocite, hematite, magnetite

Introduction

The term, "weathering steels," describes a class of low-alloy steels with enhanced resistance to atmospheric corrosion. Although the underlying mechanisms are not completely understood, it is well known that alloying elements such as copper, chromium, nickel, phosphorus, and silicon somehow promote formation of protective rust layers during outdoor exposure. Weathering steels generally contain a combination of these elements totaling less than about 3 w/o.

Owing to barrier protection imparted by the protective rust layers, weathering steels are used outdoors without paint or other protective coatings. Corrosion testing of weathering steel for up to 16 years in a variety of environments has been previously reported¹.

It should be noted that certain environmental conditions may be unfavorable for development of protective rust on weathering steel. According to US guidelines², the following conditions should be avoided: (1) high levels of salt (chloride greater than 0.5 mg /100 cm²/day), (2) high time of wetness (average time of wetness greater than 60%), and (3) direct exposure to high levels of industrial pollutants (for example, sulfur trioxide greater than 2.1 mg /100 cm²/day). When these guidelines have been adhered to, unpainted weathering steels have been successfully used in applications such as bridges, utility towers, and highway guardrails.

In the course of conducting long-term corrosion tests, we have observed that the rust layers on weathering steel exposed at rural and industrial test sites develop a spotty, non-uniform appearance. After several years of exposure at these locations, the rusted surfaces developed dark patches within a lighter background that give the spotted appearance shown in Figures 1 to 3. Previous studies of the structure of weathering-steel rusts do not provide an explanation for this phenomenon³⁻⁹.

The work described in this report was conducted in order to uncover the structural differences between the dark and light rust regions. To this end, a series of laboratory analyses, including X-ray diffraction, electron microprobe energy and scanning electron microscope dispersive X-ray fluorescence, infrared, and laser Raman spectroscopy, were performed to characterize the rust formed on samples selected from a series of weathering steels exposed for up to 11 years at our outdoor corrosion test sites.

Experimental

Materials

The steels in this study were selected from a larger, ongoing program aimed at determining the effects of composition and heat treatment on the atmospheric corrosion resistance of weathering steels that will be reported elsewhere. Of particular interest to this study are the steels with the compositions given in Table 1. These include commercially produced plain carbon steel, copper-bearing steel, A588 and A242 weathering steels, and nine laboratory-melted A588-like weathering steels with varying amounts of silicon and nickel.

All steels were hot rolled to 2.5 mm in thickness and cut into 100- x 150-mm panels. The panels were shot blasted to remove hot-rolling scale, stamped with identification markings, degreased, and weighed prior to exposure.

Atmospheric Corrosion Tests

Test panels were exposed at three test locations in an acid-rain region where precipitation has an average pH of about 4.3¹⁰:

- Rooftop site, Bethlehem, Pa. -- This site is located on the roof of an office building in downtown Bethlehem, adjacent to the blast furnaces of an integrated steel plant. This is considered to be an industrial environment of moderate severity.
- Mountaintop site, Bethlehem, Pa. -- This site is situated on the south slope of South Mountain overlooking the steel plant's coke works which are about 3 km away. This location is also considered to be a moderate industrial environment.
- Rural site, Saylorsburg, Pa. -- This site is located in the Pocono Mountains, about 50 km north of Bethlehem.

These materials were also exposed at a marine site at the Laque Center for Corrosion Technology at Kure Beach, N. C.

- 250-meter lot -- Located 250 meters from the Atlantic Ocean, this site is a moderate marine site.

Panels were exposed at 30 degrees from the horizontal and faced South. All analytical results were determined on skyward surfaces.

Metallography

Metallographic cross sections were prepared by cutting small pieces from the rusted corrosion test specimens and mounting on edge in room-temperature curing epoxy. The mounted cross sections were mechanically ground and polished with successively finer grits. The final polish was done with 0.25 μm diamond grit.

To facilitate examination in the light microscope, contrast among constituents of the rust layers was enhanced by use of Nomarski differential interference contrast¹¹. In this method, split beams of polarized light are superimposed after being reflected from the specimen surface. Because the combined image results from differences in the path lengths of the two beams, small changes in surface elevation on the specimen surface are highlighted, thus increasing differences in the surface texture among phases.

Laser Raman Spectroscopy

Raman spectra were obtained with an Instruments SA S3000 microprobe spectrometer equipped with a 1-inch (1024 pixels) intensified diode array detector from Princeton Instruments. An argon ion laser was used for excitation at 514.5 nm with 10 mW of power. Approximately 1 mW of laser power was directed onto the sample with a 10% reflective beam splitter inside the microscope. The low laser power was necessary to prevent thermal degradation of the rust structure. The laser was slightly defocused onto the sample to further minimize the possibility of thermal damage. The backscattered Raman signal was collected with an 80X long working distance objective (Olympus MSPlan) and integrated for 64 seconds. The spectra were recorded by co-adding up to 64 integrations.

A second Raman study was performed using a large area (1152 x 298 pixels) CCD chip detector from Instruments SA. A krypton laser was used for excitation at 647.1 nm with 10 mW of power. The spectra were obtained by co-adding 10 integrations of 120 seconds.

Raman peaks were identified according to spectra for the various iron oxide and hydroxide compounds from the references summarized in Table 2.

Corrosion Potentials

Small electrochemical cells were formed on the surface of weathered panels by gluing rubber O rings (6 mm inside diameter) and adding several drops of 0.1 N Na_2SO_4 solution. The O rings were placed in such a way as to isolate areas of light or dark rust. Corrosion potentials were measured against a platinum-wire reference electrode by use of an EG&G Princeton Applied Research Model (PAR) 273 potentiostat interfaced to a 386-SX compatible computer. PAR 342C or 352 electrochemical software were used for data acquisition.

Results and Discussion

Appearance of Corrosion-Test Panels

The skyward-surface appearances of corrosion-test specimens after exposure for 5 and 10-11 years are shown in Figures 1 and 2, respectively. The uniformity of surface appearance varies according to steel composition and environment.

Considerable non-uniformity in surface appearance is evident at the rural and industrial sites. For example, at the rural site, surfaces range from uniform dark brown on plain carbon steel to spotted on A242. The spotted appearance results from contrast between light and dark areas. At first glance the dark spots suggest the presence of broad, shallow pits. However, upon removal of the rust layers for determination of mass loss, it was clear that the dark regions were not related to any features on the steel surface.

In general, the amount of the light-colored rust formed at the rural and industrial sites increases with the alloy content of the steel. This suggests that the light rust is somehow associated with greater corrosion resistance, since the corrosion rate of these steels also decreases with alloy content¹. Moreover, by comparison of Figures 1 and 2, a trend towards increasing amount of light rust with time is also apparent. This effect is also consistent with a relationship between light rust and corrosion resistance because it has been shown that the corrosion rates of these steels decrease with time¹.

The effect of alloy content on the relative amounts of light and dark rust is further apparent in Figure 3. Increases in silicon and/or nickel content of A588 result in an increase in the amount of light rust.

At the marine site, all rusted surfaces are relatively uniform, although the color of the rust generally tends to be a darker brown as the alloy content of the steel increases.

Note that the plain carbon steel has perforated after 11 years at the marine location.

Metallography

Metallographic cross sections show a difference in the structures of the light and dark rust layers, Figure 4. Dark areas are comprised of layers of rough, porous rust. Light areas are similar except that they are covered by an additional layer that is relatively thin, smooth and compact. Elemental analyses of the layers by use of an electron microprobe or a scanning electron microscope did not reveal differences in chemical composition between the light and dark regions.

Laser Raman Spectroscopy

Raman analyses of the rust cross sections showed three types of region, Figure 5. In the case of both light and dark areas, the porous rust immediately adjacent to the steel was identified as lepidocrocite, see Figure 5C. Above this area, the less porous region was found to consist of a mixture of lepidocrocite ($\gamma\text{-FeOOH}$) and goethite ($\alpha\text{-FeOOH}$), see Figure 5B.

Finally, the smooth, dense layer found only on the light areas was identified as a mixture of hematite ($\alpha\text{-Fe}_2\text{O}_3$) and magnetite (Fe_3O_4), Figure 5A.

Raman analyses conducted normal to the surface of the rust layers show that the light rust consists of hematite, magnetite, and goethite, Figure 6A. This result agrees with the above findings from analyses of cross sections if we accept that some goethite is showing through from the underlying layers. Areas of dark rust, Figure 6B, showed only goethite and lepidocrocite.

Corrosion Potentials

Corrosion potentials at areas of light rust were relatively stable with time for up to one hour at -70 mv, see Figure 7. Potentials at the dark areas, although somewhat more erratic are generally about 300 mv more active.

The difference in potential suggests that the light areas are more stable and protective. Previously, Legault *et al.* have reported that the corrosion potentials measured on a series of steels exposed to an industrial environment become less active with increasing alloy content and decreasing corrosion rate¹⁴. Pourbaix has also shown that the potentials of more corrosion-resistant low-alloy steels are less active in an accelerated laboratory test¹⁵.

X-Ray Diffraction

X-ray diffraction (Cr K-alpha radiation) of rusted surfaces identified only two crystalline corrosion products, namely goethite and lepidocrocite. No obvious differences in the relative diffraction-peak intensities for these were noted according to material or exposure site. Moreover, because the 1- x 2-cm area analyzed by the X-ray spectrometer is several times larger than the light and dark regions, it was not possible to directly compare the two regions on a particular sample by use of this method.

The absence of hematite or magnetite in the x-ray diffraction results can be attributed to the relatively small amounts of these compounds in the thin surface layer, and the difficulty in identifying low-intensity peaks within the complex spectra from larger quantities of goethite and lepidocrocite.

Infrared Analyses

Infrared analyses of rusts scraped from light and dark areas, were conducted according to the method described by Misawa *et al.*¹⁸, and compared to reference spectra given by Schwertmann and Cornell¹⁹. As shown in Figures 8 and 9, goethite and lepidocrocite were the only oxides detected. Also, we were unable to detect non-crystalline iron oxides of the type reported by Misawa *et al.*¹⁸.

Conclusions

Eleven-year outdoor corrosion tests and laboratory analyses of the rusted surfaces on weathering steels lead us to the following conclusions:

1. During exposure to rural and industrial environments, weathering steels develop areas of light and dark rust which give the surface a spotty appearance.
2. The extent of the light areas increases with time and with increasing alloy content.
3. Dark areas are composed of a porous mixture of goethite (α -FeOOH) and lepidocrocite (γ -FeOOH).
4. Light areas are similar to the dark areas except that they are covered with a thin, additional layer comprised of a mixture of hematite (α -Fe₂O₃) and magnetite (Fe₃O₄).
5. Areas of light rust exhibit a more noble corrosion potential, thus indicating that the light rust is more protective.

These results suggest that the decreasing rate of corrosion with time observed for weathering steels is related to the lateral spread of the light-colored outer layer of hematite and magnetite. From this it seems that the light layer has a key role in the mechanism of corrosion resistance for weathering steels in industrial and rural environments.

References

1. C. R. Shastry, J. J. Friel, H. E. Townsend, in Degradation of Materials in the Atmosphere, ASTM STP 965, S. W. Dean and T. S. Lee, Eds., American Society for Testing and Materials, Philadelphia, PA (1988): pp. 5-15.
2. Uncoated Weathering Steel Structures, US Department of Transportation Technical Advisory T5140.22, Federal Highway Administration, Washington, DC (1989).
3. D. C. Cook, Hyperfine Interactions, 28 (1986): pp. 891-894.

4. T. Moroishi, J. Satake, N. Fujino, M. Kowaka, *Trans. ISIJ*, 116 (1971): p. 390
5. J. T. Keiser, C. W. Brown, R. H. Heidersbach, *Corrosion Science*, 23 (3) (1983): pp. 251-259.
6. T. Misawa, *Corrosion Engineering*, 37 (8) (1988): pp. 441-446.
7. I. Suzuki, Y. Hisamatsu, N. Masuko, *J. Echem. Soc.*, 127 (10) (1980): pp. 2210-2215.
8. N. L. Thomas, in *Proceedings of the Conference on Microscopy of Oxidation*, The Institute of Metals, London (1991): pp.42-48.
9. F-I Wei, *British Corrosion Journal*, 26 (3) (1991): pp. 209-214.
10. NADP/NTP Annual Data Summary, *Precipitation Chemistry in the United States, 1989*, National Atmospheric Deposition Program, Colorado State University, Fort Collins, Colorado (1990).
11. C. E. Price, in *Metals Handbook, Ninth Edition, Volume 9, Metallography and Microstructures*, American Society for Metals, Metals Park, Ohio (1985): pp.150-152.
12. R. J. Thibeau, C. W. Brown, R. H. Heidersbach, *Applied Spectroscopy*, 32 (6), (1978): pp. 532-535.
13. J. Dunnwald, A. Otto, *Corrosion Science*, 29 (9) (1989): pp. 1167-1176.
14. R. A. Legault, S. Mori, H. P. Leckie, *Corrosion*, 29 (5) (1973): pp. 169-179.
15. M. Pourbaix, *Cebelcor Report No. 2087* (1969).
16. D. Thierry, D. Persson, C. Leygraf, D. Delichere, S. Joiret, C. Pallotta, A. Hugot-Le Goff, *J. Echem. Soc.*, 135 (2) (1988): pp. 305-310.
17. T. Ohtsuka, K. Kubo, N. Sato, *Corrosion*, 42 (8) (1986): pp. 476-481.
18. T. Misawa, K. Asami, K. Hashimoto, S. Shimodaira, *Corrosion Science*, 14 (1974): pp. 279-289.
19. U. Schwertmann, R. M. Cornell, *Iron Oxides in the Laboratory: Preparation and Characterization*, VCH Publishers, Inc., New York (1991).

Table 1. Compositions of Test Materials

<u>Steel Grade</u>	<u>Composition, w/o</u>							
	C	Mn	P	S	Si	Ni	Cr	Cu
Plain Carbon	.18	.73	.007	.017	<.01	<.01	.02	.015
Cu-Bearing	.04	.36	.006	.024	<.01	.01	.01	.26
A588	.14	1.07	.011	.022	.28	.32	.55	.28
A242	.09	.65	.110	.032	.29	.66	.52	.27
A588, low Si, variable Ni	.14	.93	.008	.025	.15	.01	.53	.37
	.18	1.01	.009	.014	.15	.16	.56	.34
	.14	.97	.012	.016	.12	.31	.59	.35
A588, med Si, variable Ni	.18	1.00	.011	.020	.49	.02	.55	.32
	.13	1.01	.010	.017	.47	.17	.57	.34
	.18	1.00	.010	.017	.49	.38	.58	.33
A588, high Si, variable Ni	.12	1.06	.006	.013	.77	.01	.59	.33
	.18	.97	.008	.020	.73	.16	.51	.35
	.14	1.00	.009	.018	.75	.31	.57	.35

Table 2. Reported Raman Lines of Iron Corrosion Products

<u>Corrosion Product</u>	<u>Relative Wave Numbers, cm⁻¹</u>							<u>Reference</u>
Goethite,	<u>298</u>	<u>397</u>	414	474	550			[12]
α -FeOOH	248	<u>303</u>	<u>397</u>		485	554	680	[13]
	250	300	<u>385</u>		470	560		[16]
		308	<u>397</u>		489	557		[16]
	245	300	<u>390</u>	420	480	550	685	[17]
Hematite,	<u>227</u>	245	<u>293</u>	298	<u>414</u>	501	612	[12]
α -Fe ₂ O ₃	225	247		299	<u>412</u>	500	613	[16]
	<u>225</u>	245	<u>295</u>		<u>415</u>	500	615	[17]
Lepidocrocite,	<u>252</u>	380						[12]
γ -FeOOH	<u>255</u>	380	528	654				[13]
	<u>252</u>	380		660				[16]
Magnetite,					616	<u>663</u>		[12]
Fe ₃ O ₄	298	319	418	550		<u>676</u>		[13]
				550		<u>670</u>		[16]
				540		<u>665</u>		[17]

Largest peaks are underlined

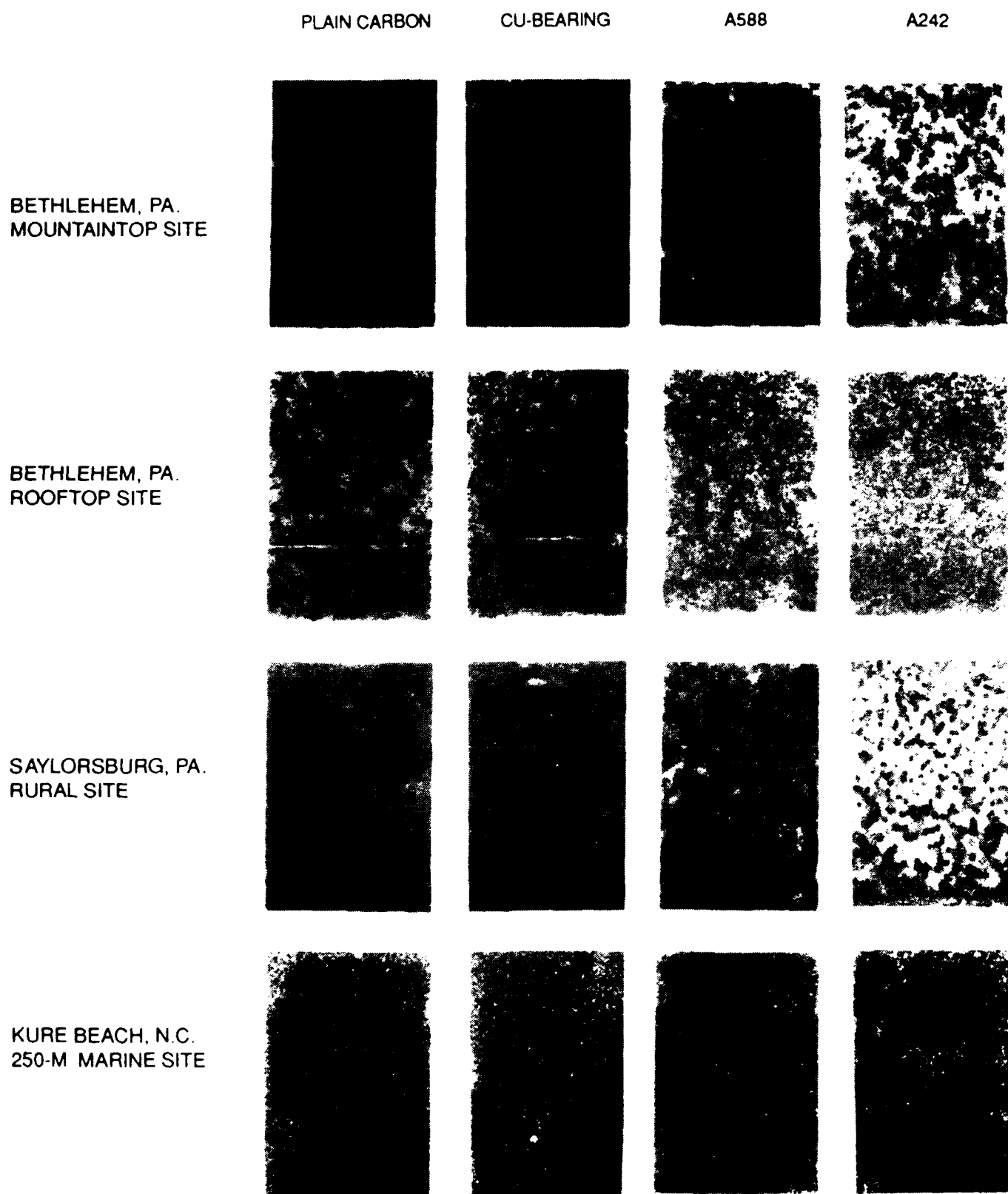


Figure 1. Appearance of Test Specimens After 5-year Exposure in Various Environments.

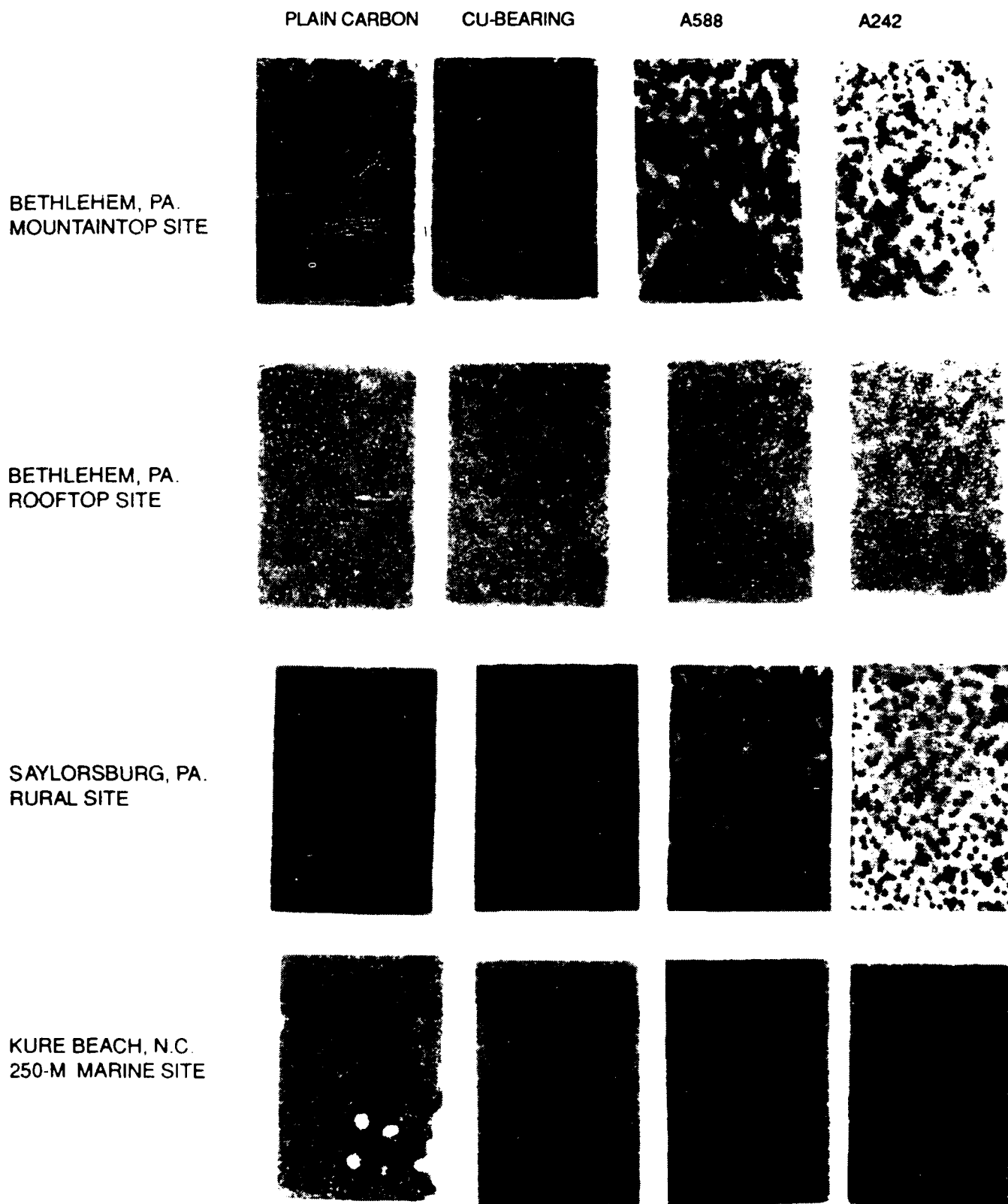
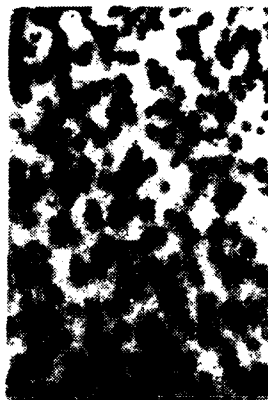


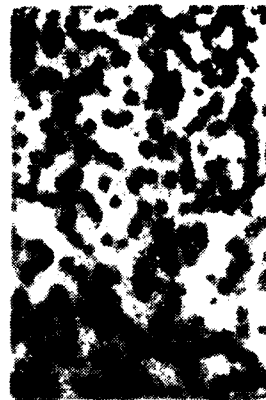
Figure 2. Appearance of Test Specimens After 10- to 11-year Exposure in Various Environments.



0.15 Si / 0.01 Ni



0.15 Si / 0.16 Ni



0.12 Si / 0.31 Ni



0.49 Si / 0.02 Ni



0.47 Si / 0.17 Ni



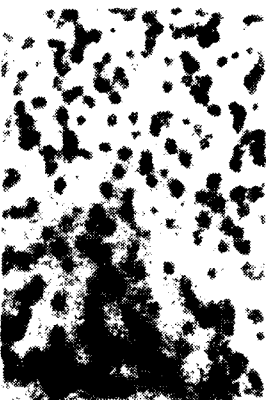
0.49 Si / 0.38 Ni



0.77 Si / 0.01 Ni



0.73 Si / 0.16 Ni



0.75 Si / 0.31 Ni

Figure 3. Effect of Nickel and Silicon on Appearance of Test Specimens After 11-year Exposure at Mountaintop Industrial Site.

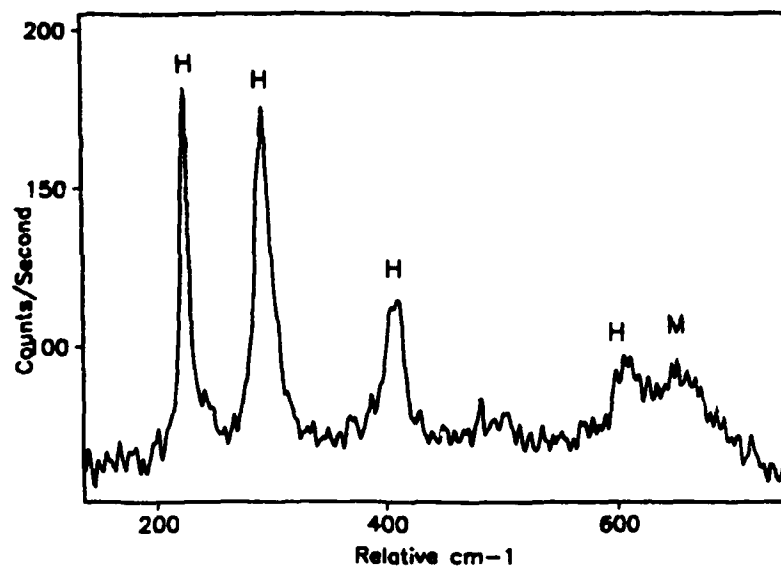


A - Light Area



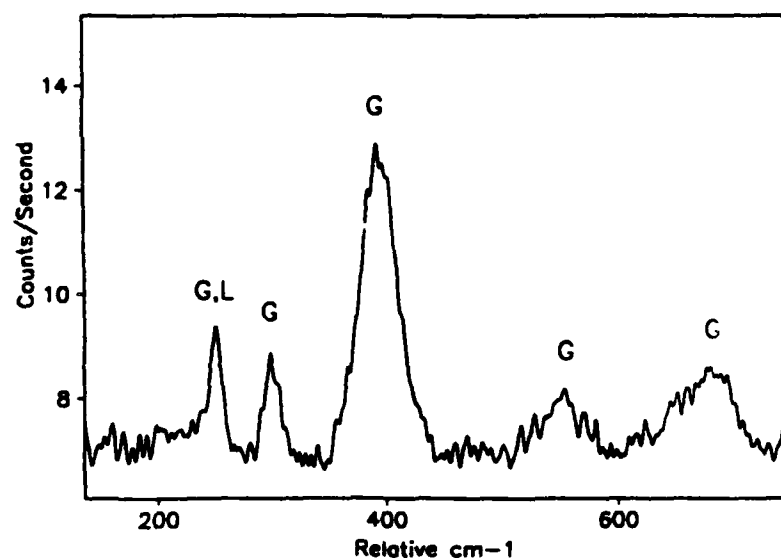
B - Dark Area

Figure 4. Metallographic Cross Sections of Dark and Light Areas in Rust Layers. A588 with 0.75%Si and 0.31%Ni. 11-year Exposure at Mountaintop Industrial Site. X400.



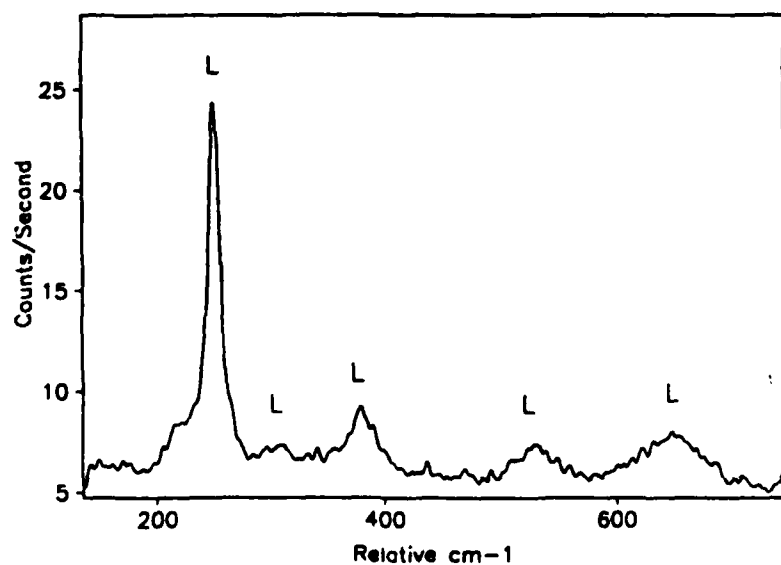
A – Light Outer Layer

(Hematite and Magnetite)



B – Intermediate Layers

(Goethite and Lepidocrocite)

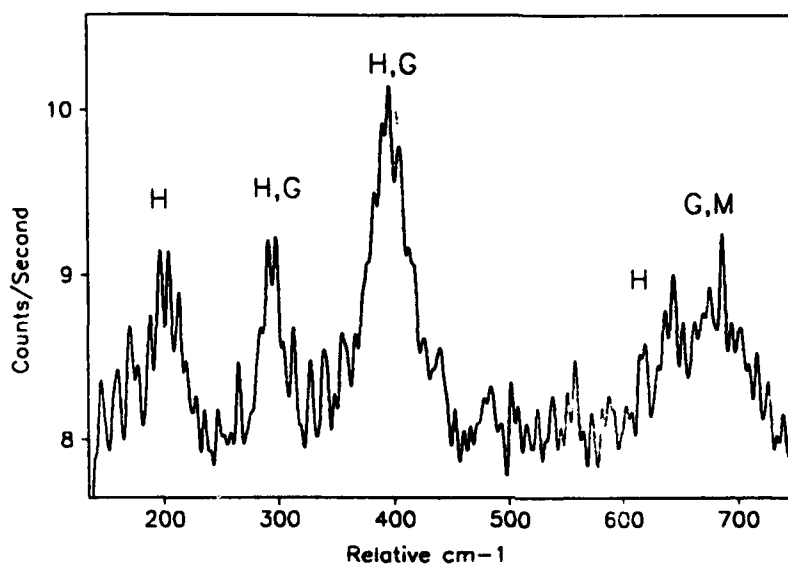


C – Adjacent to Steel

(Lepidocrocite)

Figure 5. Raman Spectra of Rust-Layer Cross section in Light Area. A588 with 0.75% Si and 0.31%Ni. 11-yr Exposure at Mountaintop Industrial Site.

A — Light Area. (Hematite, Goethite, and Magnetite)



B — Dark Area. (Goethite and Lepidocrocite)

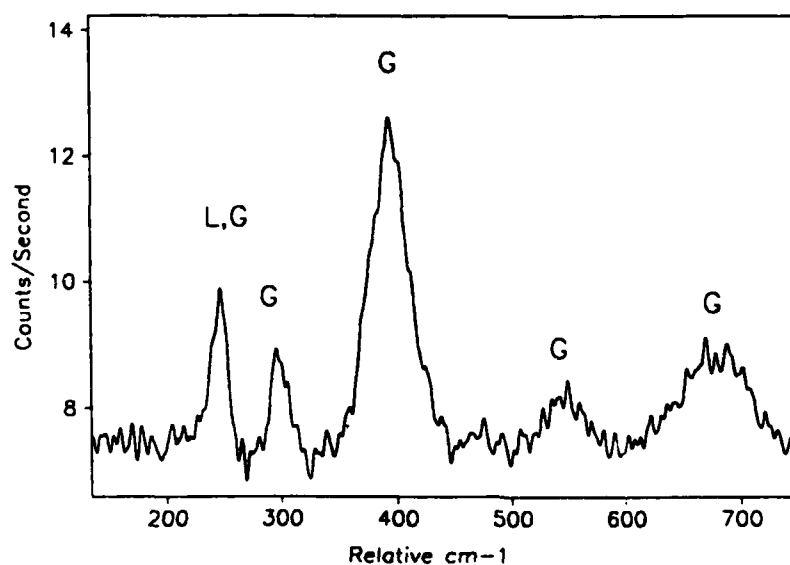


Figure 6. Raman Spectra Normal to Rusted Surface. A588 with 0.75% Si and 0.31%Ni. 11-yr Exposure at Mountaintop Industrial Site.

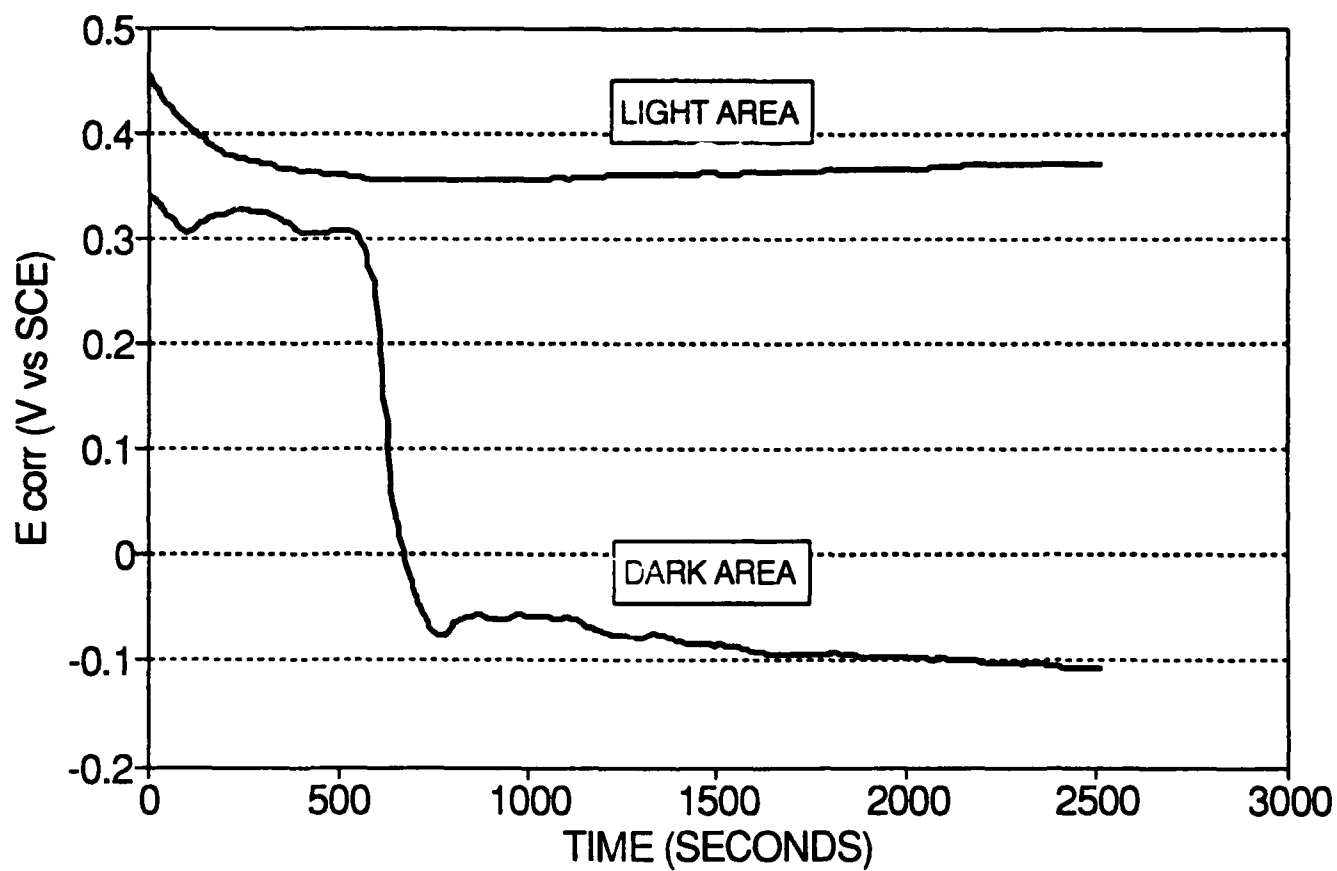


Figure 7. Corrosion Potentials in 0.1N Na_2SO_4 for Typical Light and Dark Areas 11-yr Exposed 11 Years at Mountaintop Industrial Site.

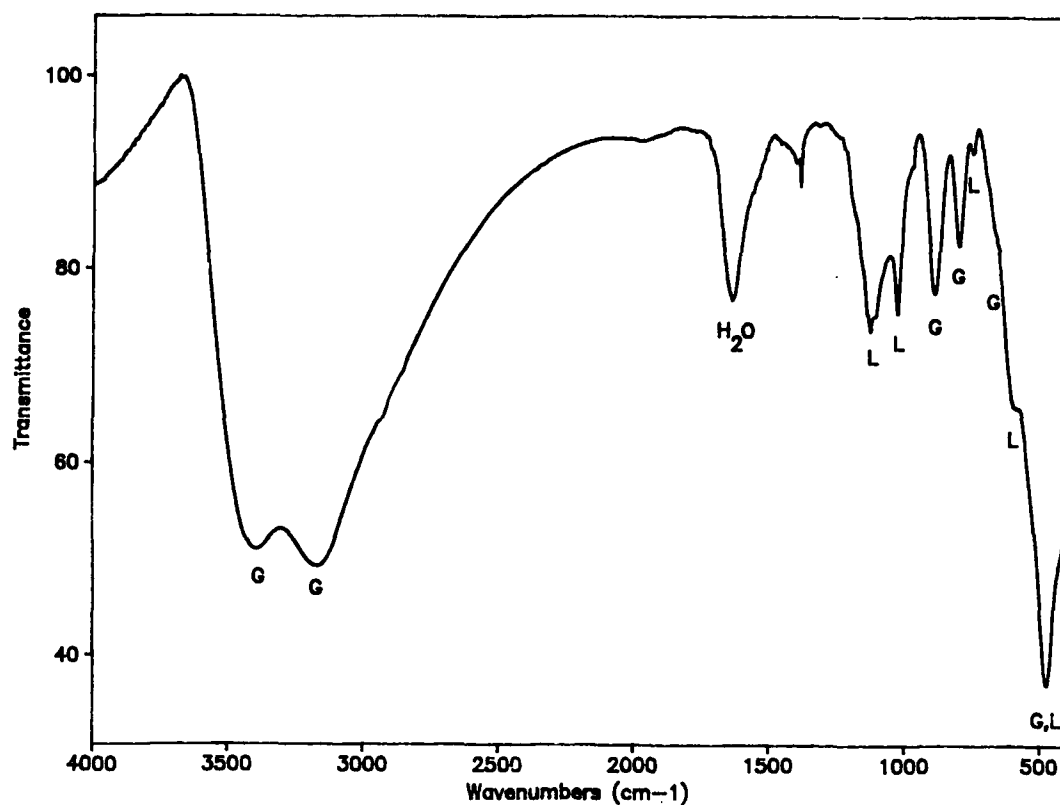


Figure 8. Infrared Spectra of Particles from Light Area.

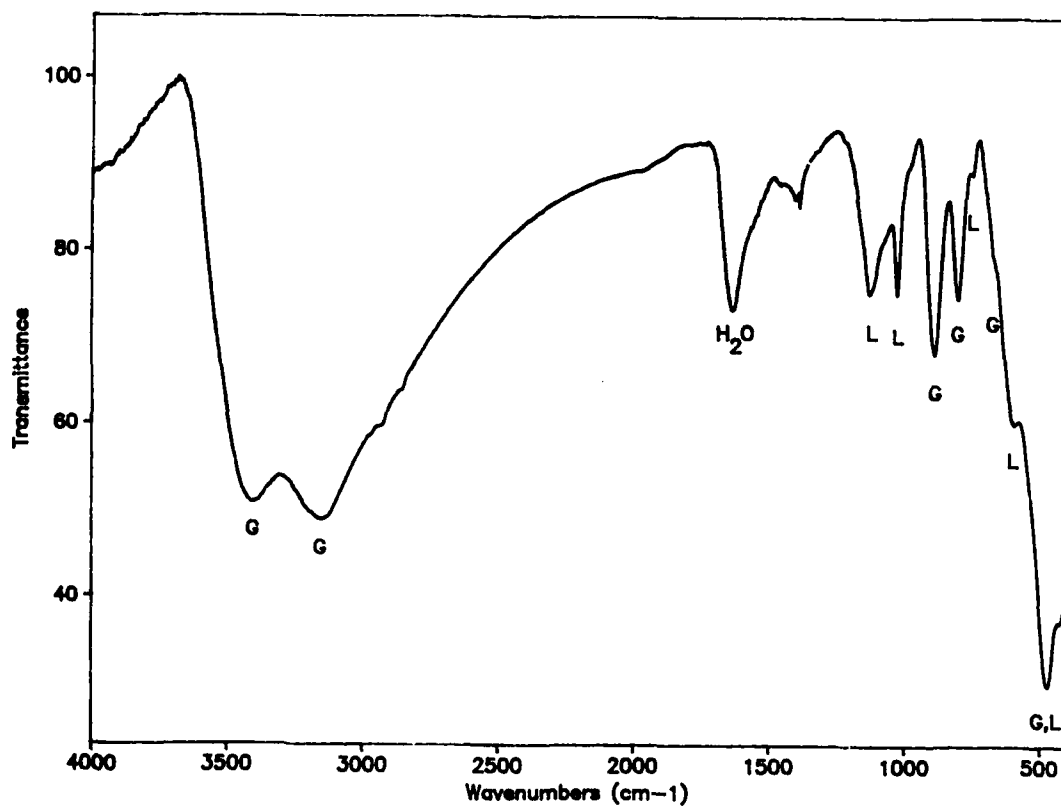


Figure 9. Infrared Spectra of Particles from Dark Area.

Effects of sea salt on corrosion attacks at 8 years' exposure of metals in a small geographical area of the Swedish west coast.

Jan Gullman
Central Board of National Antiquities, Conservation Institute
Box 5405
S-114 84 Stockholm, Sweden.

Abstract

Standard uncoated metal samples have been freely exposed at 4 test sites for 1, 2, 4 and 8 years. The test sites experience sodium chloride deposition rates of ca 50 - ca 1400 mg Cl/m².day. The chloride deposition rates were measured as several years averages with the wet candle method.

The metals investigated were carbon steel, corten A, corten B, zinc, copper and aluminium. Steel samples have also been exposed under rain-protected conditions.

It was found that the corrosion attacks on freely exposed steel panels could be well modelled by using mathematical models of the form:

$$K = (C_A + C_B \cdot Cl) \cdot (1 - \exp(-t/C_D)) + (C_E + C_F \cdot Cl) \cdot t$$

where C_A , C_B , C_D , C_E and C_F are constants, characteristic for each kind of steel and t is time of exposure in years and Cl is yearly average deposition rate of chloride in mg/m².day. For the other metals linear expressions could be used. The following expressions give good fits to the experimental data:

Zinc: $K = 0.000507 \cdot Cl + 3.55 + (0.0049 \cdot Cl + 7.08) \cdot t$

Copper: $K = 0.0081 \cdot Cl + 6.52 + 4.70 \cdot t$

Aluminium: $K = 0.00026 \cdot Cl + 0.01 + (0.00009 \cdot Cl + 0.41) \cdot t$

The results obtained are believed to serve as good approximations to the magnitude of corrosion attacks on freely exposed metal surfaces in environments which are close to the sea coast and where the SO₂ pollution levels are low. The relations are probably good approximations for the temperate climatic region.

The results of the present investigation are connected to a larger study mainly in SO₂ affected environments (1,2). In that study also measurements on two of the test sites in the present investigation were included.

Key words: Atmospheric corrosion, marine, steel, zinc, copper, aluminium, rain protection, dose-response relations, corrosivity.

* The results were obtained during the period when the author was employed in the Swedish Corrosion Institute.

Introduction

During the last decade results from several years of out-door metal exposures in different environments in Scandinavia and Czechoslovakia have been published¹⁻³. In these works influence of SO₂ pollution on the corrosion rates have been studied. In reference 1 also influence of chloride in marine test sites have been included in simple mathematical models.

As a complement to the above mentioned studies which deals mainly with SO₂ influence another field exposure was started in June 1979. It was designed within a rather limited economic framework and had two main aims:

- To fill a gap of knowledge regarding technical dose-response relationships between atmospheric corrosion rates on some technically important metals and sea salt deposition measured with different methods.

- To obtain measures of corrosion attacks on steel alloys in marine environments. This would be useful for estimating corrosion risks on objects of weathering steels, including influence of rain protection.

Some results from the first year of exposure have been published earlier⁴. The present paper gives the results after 8 years of exposure.

Experimental

The investigation was performed as a field exposure on atmospheric test sites. It was planned with removals of test specimens after 1, 2, 4 and 8 years. Since it was made in order to elucidate the magnitude of chloride influence on atmospheric corrosion rates, efforts were made to minimize effects of scatter in the data for other reasons than characterized differences in exposure conditions.

The atmospheric test sites used were the following regular test sites of the Swedish Corrosion Institute:

- Bohus Malmon Kvarnvik, marine with occasional salt spray
- Bohus Malmon Kattesand, moderately marine
- Ryda Kungsgård, rural

In the test site Kvarnvik two test racks at different distances from the sea (about 30 respectively 60 m) were used. Kattesand is situated about 1 km from the sea. A temporary test site with lower marine influence : Bohus Malmon Harbor on the mainland side of the island was also used (ca 3 kms from the open sea). As background level, virtually without chloride influence, the permanent test site Ryda Kungsgård (about 80 kms from Stockholm) was chosen.

The different chloride levels of the test sites are given in Tab 1. - It should be noted that the chloride level "0" of the test site Ryda Kungsgård was not measured. The value is however reasonable in comparison to the other test sites, since the test site is situated in inland Sweden.

Zinc, copper and aluminium samples were freely exposed at 45° inclination. The steel samples were exposed in four different ways:

- Freely exposed 45°
- Partially rain protected vertically
- Partially rain protected horizontally
- Rain protected vertically
- Rain protected horizontally

The rain protection was accomplished by simple roofs according to Fig 1. The size of all metal samples used was 100x150 mm.

It was later considered suitable to remove one set of rain-protected samples after 1.25 years. In the rural site only steel samples were exposed. The number of specimens in the rural test site was also reduced so that free exposure was studied only after 1 and 4 years since the long term behavior of steel at that test site is known from another exposure programme¹.

The mass losses due to corrosion attack on steel samples were determined by pickling in Clark's solution. The copper samples were pickled in 10 % sulfuric acid under brushing with a soft brush, the zinc specimens exposed for 1 and 2 years in chromic acid containing silver chromate, the zinc samples exposed for 4 and 8 years in 5 % acetic acid and the aluminium samples in concentrated nitric acid saturated with chromic acid. All picklings except the chromic acid picklings were carried out at room temperature. The zinc pickling in chromic acid was carried out at 80°C. All picklings of the samples were performed with ultrasonic agitation except for the copper samples. The mass losses of the samples were determined by repeated pickling and extrapolation to zero pickling time from the linear part of the mass loss versus pickling time curve. This procedure leads to a correction for the attack of the pickling agent on the base metal and only a minor systematic underestimation of the mass loss.

The mass losses of the freely exposed panels were calculated as averages and standard deviations from triplicates at every removal of specimens. The exceptions from this rule are given as remarks in Tab 1.

The mass losses of the sheltered panels were obtained from single specimens in every position for each exposure period of 1, 2 and 4 years.

At the marine test sites chloride deposition was monitored by use of wet candles of the type introduced by Ambler⁵. It was planned to collect chloride samples for every month during the entire period. It later turned out to be difficult to obtain samples from some winter months due to difficulties to reach the equipment when the rocky terrain was covered with snow and ice. Therefore most years have missing data from these months. Since these months often are very windy a great part of the total deposition is obtained during that time period. Such months therefore contributes much to a yearly average. Therefore the average chloride deposition is calculated from years with the least number of missing data and is in the present study in this way used as a characteristic of the salinity of each test site. It should be noted that the salinity in the present study is given as milligram **chloride** deposited per square meter and day and **not** as **sodium chloride**.

Results

A. Mass losses of freely exposed panels.

The mass losses of the freely exposed panels and the yearly average deposition rates of chloride on wet candles are given in Tab 1. From the calculated standard deviations it can be seen that the deviations from the average of the triplicate were higher in the markedly marine environments, but also that the scatter was relatively small throughout.

The major contribution to the scatter is believed to be caused by varying influence of neighboring panels on the test rack regarding deposition of chloride on the rear sides of the panels.

B. Comparative steel exposure.

The mass losses of freely and rain-protected steel panels are shown in Tab 2. There are reasons to assume that the influence of exposure factors other than salinity is a little larger for the rain-protected samples than for the freely exposed ones. This is more marked in the environment of highest salinity where influence of shelter from neighbor samples can clearly be seen as the samples exposed 1.25 years show lower mass losses than those exposed only for 1 year. The former were partly sheltered by the latter

during the first 12 months and the following 3 summer months were not extremely windy.

Mathematical modelling

A. Zinc, copper and aluminium

The corrosion attacks on zinc, copper and aluminium after 1, 2, 4 and 8 years of exposure can in all cases be rather well expressed as

$$K = a + b \cdot t$$

for each metal and each test site, where t is the time of exposure and a and b are constants. The zinc and copper data give very good fits to straight lines. Linear regression of the "constants" a and b in terms of average chloride deposition rate gave rise to the following expressions:

$$\text{Zinc: } K = 0.000507 \cdot Cl + 3.55 + (0.0049 \cdot Cl + 7.08) \cdot t$$

$$\text{Copper: } K = 0.0081 \cdot Cl + 6.52 + 4.70 \cdot t$$

$$\text{Aluminium: } K = 0.00026 \cdot Cl + 0.01 + (0.00009 \cdot Cl + 0.41) \cdot t$$

The generally very good agreement, between observed and calculated corrosion attacks using the mathematical models obtained, are shown in Tab 4.

B. Freely exposed steels

The data for marine exposure of the freely exposed steel panels have been fitted to a mathematical model which is an evolution of an expression which has been proposed by Michailovskij for a description of the time dependence of the atmospheric corrosion on steel samples in a given out-door environment:

$$K = \alpha(1 - \exp(-t/\beta)) + \tau t$$

where t is the time of exposure and α , β and τ are constants. In the exponential term Michailovskij has written time multiplied with a constant instead of divided by a constant. In the present work division was chosen since then β gets the dimension time instead of inverted time. It can then be interpreted as a measure of the deviation of a value of the corrosion attack from the linear expression which is valid after long time exposures:

$$K = \alpha + \tau t \quad (1)$$

Since the deviation is $\alpha \exp(-t/\beta)$ it can easily be seen that the deviations from the straight line for e.g. $t = \beta$ and $t = 2\beta$ are 0.37α respectively 0.14α . Analogous the deviation for $t = 3\beta$ is 0.05α . Hence as a rule of thumb one can say that the linear expression is an excellent approximation for practical purposes for exposure times $> 3\beta$.

The model used for fitting of the present data uses linear expressions in chloride deposition rates of the "constants" α and β i.e.:

$$\alpha = C_A + C_B \cdot Cl \quad (2)$$

$$\tau = C_E + C_F \cdot Cl \quad (3)$$

$$\beta = C_D \quad (4)$$

where C_A , C_B , C_D , C_E and C_F are constants.

The program used for least squares fitting of the data was an old general least squares one (POWOW), originally written in the 1960ies to calculate crystallographic parameters. It is written in FORTRAN and contains a special subroutine in which the mathematical model is defined. This subroutine must be specially written for each model.

The constants obtained from the fittings are shown in Tab 3. The good agreements between observed and calculated corrosion attacks for marine test sites are shown in Tab 4.

Discussion

In the present paper results from evaluations of influencing factors are presented together with extensive information of quantitative details in the measured effects. The reason for that is a strive to spread informations about magnitudes of different effects so that similar works in other environments can be planned in such a way that there will be good opportunities to evaluate significant effects. At the time when the present work was planned there were some debates on possibilities to formulate dose-response relationships. A common argument in those days were that since many different relations had been published, which seemed to be contradictory, there might not exist any "true" relationships, but only specific relationships changing from investigation to investigation. The fact that often the details of most older investigations were very superficially treated should be remembered.

The present study has rather good assets although its limited size: It covers a large range of air salinity, 50 - about 1400 mg Cl/m²·day and is based on corrosion measurements with better precisions than in most studies. It would have given better results if it had been made in a scale which was some times larger in terms of test sites. Still it is hoped to be of use as a kind of pilot study that can be complemented with further data and in such a way contribute to further work, which can also test the validity of the models obtained.

The derived models and the results from various degrees of rain shelter deserve some discussion.

A. Linear models.

As has been shown for atmospheres with main influence on corrosion from SO₂, corrosion on freely exposed zinc and copper panels can be described as linear models in terms of both corrosion stimulator and time of exposure.

Aluminium corrosion is difficult both to evaluate quantitatively and to model. A linear model for marine environments gives a fair representation. The limitation might be included in the model but lies probably chiefly in the fact that aluminium is attacked in the form of pitting and hence a stochastic factor from initiation and development of the limited number of pits on test panels might have significant influence.

B. Mathematical models for steels.

The type of mathematical model for steels can be seen as a linear model in the long time perspective, but with an initiation period of a few years during which time the rust layer is maturing to such a property that it gives a practically constant partial protection against further corrosion attack. - The time periods of maturing of the layers of corrosion products on copper and especially zinc seems to be much shorter.

The results from fitting the steel data to the model used, show some expected and some perhaps not generally expected features. As could be expected the "constant" α , which reflects the contribution to the corrosion attack from the initial period of exposure when the rust layer is maturing, has a significant dependence on the chloride deposition rate. The constant α increases with salinity with the amount C_a multiplied by the yearly average deposition rate of chloride.

The corrosion rates at long time exposure for the three steels are, as could be expected, decreasing in the order carbon steel, corten B and corten A.

It is noteworthy that no significant increase in the long time corrosion

rate of each steel with chloride deposition rate could be detected. C_p is small and of the same magnitude as its estimated standard deviation from the POWOW program (Tab 3).

The same result has, however, been obtained earlier for two of the present test sites¹. The corrosion rate between 4 and 8 years of exposure was then found to be 79 and 80 g/m²·year for Kattesand and Kvarnvik respectively, which is in perfect agreement with the presently found value of 84 with an estimated standard deviation of 9.

This long-term corrosion rate in locations with significant influence of chloride is about twice the value compared to rural conditions¹. From Tab 4 it can be seen, that when the models were applied for the data for the rural site, they strongly overestimates the corrosion, even when the chloride level is set equal to zero.

A reasonable conclusion from this fact seems to be that there is some kind of fundamental difference in quality between mature rust-layers on freely exposed steel surfaces, formed in environments with a chloride level above some specific value (or interval), compared to such formed in rural atmospheres.

It might also seem somewhat surprising that the values of CA does not too much reflect the differences between the steels. Since the present study is based only on 16 observations for each steel, and the standard deviations are relatively large, definite conclusions regarding these differences based only on the present data should be avoided.

C. The influence of rain-protection on steel corrosion.

Rain shelter in a rural environment decreases the time of wetness - at least in the early stages of an exposure of several years. In a longer time perspective the nature of the rust formed and its content of corrosion stimulating salts seems to diminish this effect (Tab 4).

In marine atmospheres the influence of accumulation of chloride on rain-protected surfaces increases the corrosion rates significantly. The reason is probably at least twofold: a salt solution on the surface should stimulate the corrosion processes and the time of wetness can be increased due to hygroscopicity of the chlorides on the surfaces. - It was observed at the removal of rain-protected samples in Kvarnvik after 2 years of exposure that the plastic bags in which the samples were packed got a layer of condensed water when they were kept for some half-hour in the sun. And this was a sunny day in the summer.

The question on how to best simulate rain-protected conditions in a field exposure cannot be answered simply. Especially not in a marine exposure when the corrosion stimulant comes from a few specific directions. The problem with shelter from neighboring samples must always be kept in mind. In the present investigations there are such influences. Their magnitudes can fairly well be estimated (Tab 4) by a critical reader.

Regarding usefulness of weathering steels in marine atmospheres the results can be summarized so that constructions which can be made without rain-protected areas can be expected to have long service lives. Weathering steel constructions with areas which are not cleaned by rain need anti-corrosive treatments on some parts, or those parts made of another material.

D. Geographical applicability of the models.

Concerning the geographical validity of the models obtained it should first be remembered that they are based on data from a small geographic area. Results, from atmospheric corrosion field tests in the southern half of Sweden and in Czechoslovakia during eight years of exposure, have shown no significant influence of difference in climate but only by air pollution on the corrosion rate on steel, zinc, copper and aluminium^{2,3}. It can

therefore, after all, be expected that the models might serve as fairly good approximations for corrosivity in a rather large part of the European Atlantic coast where the SO₂ pollution is rather low. As pointed out above, the results from the present investigation can be used as parts of complimentary investigations, which can give answers to questions regarding validities for other geographical areas.

Conclusions

The conclusions of the present investigation can be summarized as follows:

- The corrosion rates of freely exposed low alloy steels are, during the first years of exposure, markedly higher in moderately and pronounced marine atmospheres than in unpolluted non-marine environments.
- The dependence of chloride influence on the corrosion attack on freely exposed panels of the metals investigated, can be described by mathematical models based on two parameters: exposure time and yearly average chloride deposition rates on wet candles.
- Rain protection increases corrosion rates on steel in marine environments, in both short and long time perspectives, especially on horizontal surfaces.

References

1. V. Kucera, S. Haagenrud, L. Atteraa and J. Gullman, ASTM STP 965 p.264 (1988).
2. D. Knotkova, J. Gullman, P. Holler and V. Kucera, Proc. 9th ICC, Toronto 1983.
3. V. Kucera, D. Knotkova, J. Gullman and P. Holler, Proc. 10th ICC, Madras 1987.
4. J. Gullman and P. Swartling, Koroze a ochrana materialu 27 3 (1983) p.52 (in Czech).
5. H.R.Ambler and A.A.J.Baine, J. appl. Chem., 1955 5 p.437.

Table 1. Mass losses of freely exposed specimens (g/m^2) and average yearly chloride deposition rates on wet candles ($\text{mg Cl}/\text{m}^2\text{-day}$). The figures given within parenthesis are the standard deviations of the triplicates, expressed in units corresponding to the last figure given.

Time	Chloride	C-steel	Ctn A	Ctn B	Zn	Cu	Al
1	1411	360(28)	246(21)	248(14)	15(2)	23(2)	0.65(0)
2	1411	573(29)	354(26)	342(11)	31(3)	27(2)	1.13(9)
4	1411	910(26)	458(4)	477(4)	55(4)	36(4)	2.89(3)
8	1411	1387(38)	662(32)	734(9)	114(14)	53(1)	4.13(21)
1	931	354(18)	235(10)	239(6)	16(1)	18(1)	0.74(0)
2	931	508(17)	337(9)	334(8)	30(2)	23(1)	1.23(6)
4	931	850(8)	449(28)	458(1)	53(1) ¹	34(1)	3.26(9)
8	931	1300(41)	636(30)	692(9)	99(7)	54(1)	4.50(0)
1	143	236(11)	167(6)	189(7)	12(1)	13(0)	0.36(6)
2	143	339(8)	239(1)	266(10)	21(1)	18(2)	0.64(16)
4	143	582(16)	352(17)	401(3)	35(1)	27(1)	2.30(18)
8	143	962(23)	516(7)	650(13)	68(1)	43(1)	3.33(25)
1	47	202(3)	154(4)	171(0)	9(1)	11(1)	0.33(0)
2	47	306(4)	225(10)	248(15)	17(1)	15(1)	0.51(16)
4	47	507(9)	323(8)	362(13)	30 ³	26(1)	2.11(23) ¹
8	47	803(28) ¹	470(6)	613(4)	60(3)	45(1)	2.90(215) ²
1	"0"	111(0) ¹	86(2) ¹	88(0) ¹			
4 -	"0"	307 ³	214(5)	259(2)			

1) Two specimens

2) Considerably more pits on the rear of one of the three samples

3) One specimen

Table 2. Mass losses of exposed steel specimens. The corrosion losses are given in g/m^2 , the time of exposure in years and the yearly average deposition rate of chloride in $\text{mg}/\text{m}^2\text{-day}$. The freely exposed samples have been exposed at an inclination of 45 degrees. Partly and completely and rain-protected samples have been exposed horizontally and vertically, respectively.

Time	Chlo ride	Csteel free	CtnA free	CtnB free	part. vert	C-steel			Corten A				Corten B			
						rainp. horis	rain vert	prot. horis	part. vert	rainp. horis	rain vert	prot. horis	part. vert	rainp. horis	rain vert	prot. horis
1	1411	360	246	248	834	1049	1041	1042	350	423	685	766	258	292	493	516
1.25	1411				415	864	979	1000	235	307	665	721	229	255	478	546
2	1411	573	354	342	1322	1884	1552	2003	475	528	1196	1644	350	429	1030	1185
4	1411	910	458	477	1095	3679	2957	3593	701	884	1791	2257	449	588	2113	2267
8	1411	1387	662	734												
1	931	354	235	239												
2	931	508	337	334												
4	931	850	449	458												
8	931	1300	636	692												
1	143	236	167	189												
2	143	339	239	266												
4	143	582	352	401												
8	143	962	516	650												
1	47	202	154	171	235	264	401	393	164	186	308	321	166	184	292	302
1.25	47				209	235	294	300	135	153	250	278	148	168	237	258
2	47	306	225	248	361	371	545	524	227	242	472	472	229	276	386	407
4	47	507	323	362	507	547	577	910	291	323	689	721	342	365	646	642
8	47	803	470	613												
1	0	111	86	88	87	92	75	74	80	84	73	71	81	86	73	74
1.25	0															
2	0				226	221	170	176	144	159	126	132	158	177	137	141
4	0	307	214	259	293	320	278	275	210	229	212	218	239	278	233	253

Table 3. Results from least squares fittings of corrosion mass losses of freely exposed steel samples. The mathematical model used is given below. The corrosion losses are given in g/m², the time of exposure in years and the yearly average deposition rate of chloride in mg/m²·day. The figures given within parenthesis are the standard deviations (in the last figure) estimated by the POWOW program for the constants in the expression:

$$K = (C_A + C_B \times Cl) \times (1 - \exp(-t/C_D)) + (C_E + C_F \times Cl) \times \text{time}$$

Const C Steel Corten A Corten B

C _A	164(37)	159(14)	133(8)
C _B	0.12(4)	0.09(1)	0.067(9)
C _D	0.80(29)	0.80(12)	0.61(13)
C _E	84(9)	41(3)	61(3)
C _F	0.04(1)	0.005(4)	0.002(3)

TAB 4 Observed and calculated mass losses of freely exposed metal samples (g/m²·day).

Time Chloride Cstobs Cstcalc CtnAobs CtnAcalc CtnBobs CtnBcalc Znobs Znalc Cuobs Cucalc Alumobs Alumcalc

1	1411	360	378	246	252	248	247	15	18	23	23	0.65	0.91
2	1411	573	587	354	359	342	347	31	32	27	27	1.13	1.45
4	1411	910	893	458	476	477	483	55	60	36	37	2.89	2.52
8	1411	1387	1457	662	670	734	738	114	116	53	56	4.13	4.67
1	931	354	318	235	219	239	220	16	16	18	19	0.74	0.75
2	931	508	496	337	314	334	314	30	27	23	23	1.23	1.24
4	931	850	759	449	424	458	447	53	51	34	33	3.26	2.23
8	931	1300	1246	636	608	692	698	99	97	54	52	4.50	4.20
1	143	236	219	167	164	189	176	12	11	13	12	0.36	0.47
2	143	339	346	239	241	266	260	21	19	18	17	0.64	0.89
4	143	582	539	352	338	401	388	35	35	27	26	2.30	1.74
8	143	962	899	516	506	650	633	68	66	43	45	3.33	3.43
1	47	202	207	154	158	171	171	9	11	11	12	0.33	0.44
2	47	306	327	225	232	248	253	17	18	15	16	0.51	0.85
4	47	507	512	323	327	362	380	30	33	26	26	2.11	1.68
8	47	803	857	470	493	613	625	60	62	45	45	2.90	3.34
1	0	111	(201) ¹	86	(154) ¹	88	(168) ¹						
4	0	307	(499) ¹	214	(322) ¹	259	(377) ¹						

¹ Overestimated calculated values from application of a model for marine atmospheres on rural conditions.

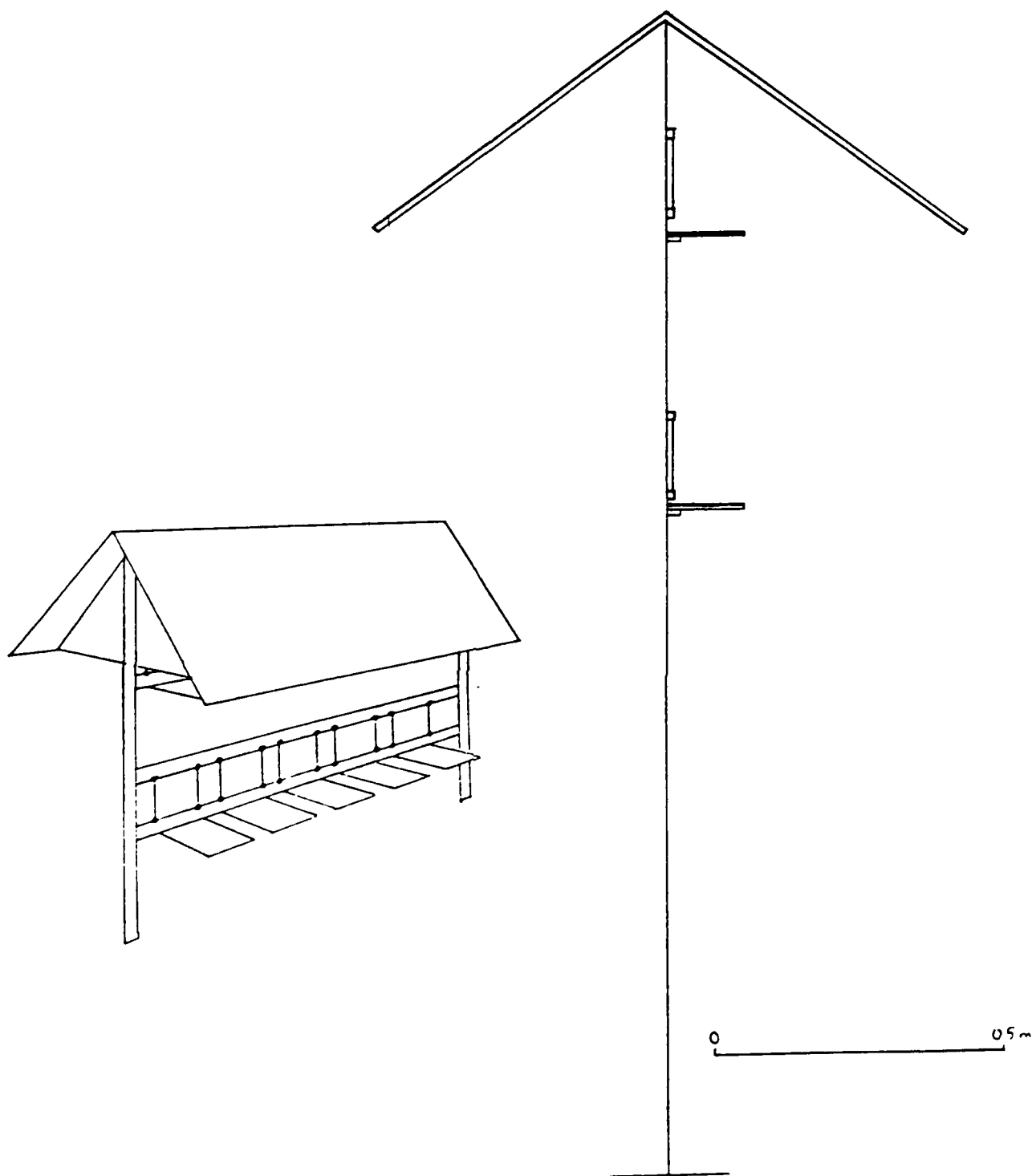


Figure 1. Exposure rack for partial and complete rain protection.

**Chemical Characterization of the Corrosion Products Formed on Plain
C Steel, Zinc, Copper and Aluminum**

Salvador L. Granese
CITEFA
Zufriategui 4380
(1603) V. Martelli-Argentina

Alejandro Fernandez
CITEFA
Zufriategui 4380
(1603) V. Martelli-Argentina

Blanca M. Rosales
CITEFA- CONICET
Zufriategui 4380
(1603) V. Martelli- Argentina

Abstract

Corrosion behaviour of plain C steel and 99.5 % w/w zinc, copper and aluminum in different outdoor atmospheric conditions was evaluated in the frame of the Iberoamerican Map of Atmospheric Corrosion (MICAT) Program. Its purpose is to characterize the aggressiveness of specific atmospheres of that region and the mechanisms involved in the corrosion of the most used technological alloys.

To separate the relative effect of each ambient variable 7 days expositions of small samples of the mentioned materials, prepared following the same procedure applied to the outdoor tests, were performed in distinct controlled conditions in a laboratory experimental loop.

In this equipment each ambient parameter was independently modified to analyze its influence in the overall process. Tests were performed at a relative humidity of the 98%, and two different temperatures, 30 and 50 °C, in the presence of 50 ppm of SO₂, with UV radiation to produce the partial photooxidation of the SO₂ to SO₃.

Among the techniques to characterize the corrosion products formed on metals exposed to different environments IR and X-ray spectroscopies are the most frequently used. In this paper we also applied differential scanning calorimetry (DSC) and obtained very interesting results not provided by the previously mentioned. On that basis the mechanistic proposals of the literature were evaluated concluding that the analysis in progress could provide useful complementary information.

Key terms: corrosion products, plain C steel, Zn, Cu and Al, chemical characterization, differential scanning calorimetry.

Introduction

The atmospheric corrosion occurs in nature in very uneven ambient conditions depending on the meteorological parameters as much as natural or industrial pollutants. On the contrary, laboratory tests in chambers provide fixed, conveniently chosen values of the main parameters affecting the reactions, allowing the separate analysis of each one on the overall process. Even when not all the ambient natural effects can be reproduced in a given laboratory test, a simplified model of a real desired situation can be designed for

study purposes.

There are previous research work performed with this purpose.¹⁻⁵

ISO Norms to evaluate atmospheric corrosion define times of wettness (TOW) of metallic substrata as the period during which a metallic surface is covered by adsorptive and or phase films of electrolyte that are capable of causing atmospheric corrosion. Its length is estimated considering the ambient situations of temperatures above 0 °C and relative humidities above 80%.

Experimental

In our experimental loop the variables considered were temperature (T), relative humidity (Hr), SO₂ concentration in the air [SO₂] and UV radiation. No wind, dust, cyclic changes in humidity and temperature, etc. effects were simulated.

Test samples of plain C steel, Zn, Cu and Al of 50 x 10 x 1 mm, were polished up to emery paper 600 grade, degreased with acetone and dried in hot air.

The experimental loop specially designed to simulate atmospheric corrosion was conditioned to provided the following conditions.

The main corrosion controlling parameter, the time of wettness of the exposed surfaces, was always coincident with the test time, according its ISO definition.

A 3 liters acrylic test chamber was thermostatzed with a Forma Scientific model 2006. The T sensor was a thermocouple made of constantan Fe and Hr was measured with a Cole Parmer 3309-50 LCD digital hygrometer.

An UV generator and a radiometer Cole Parmer, model 9815 and 9811, were used to produce and measure respectively the radiation applied.

A compresor provided the air flux, filtered to avoid dust and dried through 2 desicators with silicagel and driedrite, used as corrier of the pollutant.

The SO₂ gas was 99.9 % purity with [H₂O] < 70 ppm and [H₂SO₄] < 35 ppm. Both gases were introduced in the chamber through precision fluximeters giving a mix current with constant [SO₂] = 50 ppm.

The gas elimination to the atmosphere, after its use in the chamber, was done previous reaction of the residual pollutants in an alkaline solution.

UV radiation of 254 nm wave length was used to induce the most efficient fotooxidation of SO₂ to SO₃, simulating the natural atmospheric effect produced by the sun radiation.

The test samples were vertically suspended from the chamber cover, in triplicate for the chemical characterization of the rusts formed at the end of the test period.

The corrosion products analysis were performed in an X ray Philips 1370/10 diffractometer with Cu radiation and Ni filter at 40 kV by a proportional detector.

EDAX was performed in a model 9100 coupled to a Philips 515 SEM microscope at a vacuum level of 10⁻⁶ mm Hg.

The DSC tests were performed in a Dupont Instrument at 20 mV.cm^{-1} , heating at $20^\circ\text{C} \cdot \text{min}^{-1}$, on samples of 4 mg, in an inert atmosphere of N_2 with static purge.

Results

The corrosion products formed on the 4 metals in the experimental loop were analyzed by the ex-situ techniques X ray diffraction, IR, EDAX and DSC spectroscopies.

The ambient effect of the temperature was studied by means of tests at 30 and 50°C at constant high relative humidity, pollution level and UV radiation.

The corrosion products formed on Cu at 30°C and 50°C gave an X ray spectrum indicating as main crystalline components antlerite ($3\text{CuO} \cdot \text{SO}_3 \cdot 2 \text{H}_2\text{O}$) and cuprite (Cu_2O) with low intensity pics attributable to CuO. EDAX diagram confirmed the presence of Cu, S and O.

The respective thermograms indicated the presence of 97% of $\text{CuSO}_4 \cdot 5\text{H}_2\text{O}$, confronted with that of the pure substance (Table III).

The IR spectra obtained of the corrosion products formed at both temperatures confirmed the results of the other techniques, showing a nitrid absorption band corresponding to SO_4^{2-} , at $1100 - 1200 \text{ cm}^{-1}$. A broad band due to H_2O was observed, associated to the strong hydration of the Cu corrosion products.

For the other tested metals the IR spectra presented broad bands difficult to associate to defined chemical species, not providing significant information.

The X ray spectra of the steel rusts at both temperatures evidenced the presence of $\text{FeSO}_4 \cdot 6\text{H}_2\text{O}$, $\text{FeSO}_3 \cdot 3\text{H}_2\text{O}$, α and γ FeOOH .

EDAX results confirmed the presence of Fe, O and S. On the contrary DSC of the rusts, confronted with the diagrams of synthetical α , β and γ oxhydroxides and that of pure $\text{FeSO}_4 \cdot 7\text{H}_2\text{O}$, showed that the outer and inner layers of the rusts contained $\text{FeSO}_4 \cdot 6\text{H}_2\text{O}$, $\text{FeSO}_3 \cdot 3\text{H}_2\text{O}$ and α and γ oxhydroxides in different proportions as resumed in the Table IV.:

A thermogram corresponding to steel corrosion products is shown in Fig. 2. The absence of β oxhydroxide is due to the absence of Cl^- on the test samples during the corrosion products formation.

The presence of the α FeOOH was confirmed confronting the spectra of the rusts with that of the witness, even when it did not fit with other ones informed⁶. The γ FeOOH spectrum on the contrary was very similar to that obtained by other researchers⁶.

The thermogravimetric analysis of the steel rusts evidenced a total H_2O weight loss of 27% from the inner layer while the respective loss, of crystallization H_2O from the salts and decomposition of the oxhydroxides, was 30.5% for the outer layer. That allowed us to conclude that the outer layer contained a greater proportion of salts while the inner one which was enriched on oxhydroxides, being the more abundant one the α FeOOH .

The X ray analysis of the Zn corrosion products evidenced the presence of $2 \text{ZnSO}_3 \cdot 5\text{H}_2\text{O}$ as the main crystalline component and cinkite (ZnO) as a secondary one with some pics attributable to metallic Zn. EDAX spectra

confirmed the presence of Zn, O and S.

For the DSC analysis, which confirmed the X ray results, witness of ZnO and $\text{ZnO} \cdot x\text{H}_2\text{O}$ and reference for the $2\text{ZnSO}_4 \cdot 5\text{H}_2\text{O}$ decomposition, with H_2O and SO_2 evolution, were used (Table V).

The corrosion product formed on Al was amorphous Al_2O_3 at both temperatures. The EDAX spectra showed the presence of Al and O while the X ray ones only showed evidence of metallic Al due to the absence of crystallinity in the Al_2O_3 formed.

Discussion

During the atmospheric exposition of metals to natural as much as to laboratory controlled conditions, trigger factors appear that make possible corrosion occurrence (thermodynamic) and conditioning ones that only influence the rate or amount of propagation (kinetic).

The main, among the first ones, is the existence of a continuous film of liquid water condensed on the metal surface when a critic threshold of relative humidity is overcome. That threshold depends not only of the ambient conditions but also of the surface properties (temperature, texture, color surface tension, presence of hygroscopic, substances, etc.)

Surface characteristics determine the water absorption and retention capacity. Hygroscopic rusts, for instance, produce long TOW of the underlaying metal thus stimulating corrosion in two synergic ways: through the growth in the amount of hygroscopic rust and by the consequent increase in the TOW. They modify the critical threshold in relative humidity and in the amount of absorbed electrolyte.

In this paper the surface roughness of the test metals was normalized to 600 grade emery paper. The initial corrosion rates for all the metals at both temperatures change with time because products of different properties affect in a distinct way the kinetic process on the underlaying metals.

Non ferrous metals produced protective films which decreased their initial corrosion rates to different asymptotic values with time⁵. The increase with temperature is related to the synergic effect of T on the SO_2 action, that was clearly seen during the present work even at first sight.

Kunze⁸ verified that from the initial steps of the Zn and Cu corrosion the films formed prevented that the controlling reactions occurred at the metal film interface. The corrosion process would proceed, according to the scheme of Fig. 3, on the thin films of ZnO and Cu_2O .

The controlling step on both metals would be displaced to the outer face of the oxydes films, growing both of them by incorporation of the SO_2 as hydrated Zn sulfite and hydrated Cu sulfate.

The reactive surface for the electrochemical reaction is the metal-film interface which corrodes, through a catalytic hydrolisis process coupled to the redution of intermediaries, up to reach the dippest stratum of the metal, giving a mixture of oxhydroxides. The blocking effect to H_2O , O_2 and SO_2/SO_3 by the films formed at 30 and 50°C would control the respectrol producing corrosion rates. SO_2 would incorporate to the surface strata of the rusts as hydated sulfite through secondary reactions with the Fe oxhydroxides.

In the case of Al, during the initial steps, the bare metallic surface would adsorb SO₂ producing Al₂O₃ by hydrolisis at increasing rate with temperature (Fig. 1). The morphology of the film grown would be responsible for the distinct corrosion rates measured at 30 and 50°C.

The first corrosion product formed on Cu is cuprite (Cu₂O), from which are formed at 30 °C antlerite (3 CuO.SO₃.2H₂O) and CuSO₄.5 H₂O at 50°C.

N.6. Vannenberg et al.⁹ demonstrated that the first step in the corrosion was the SO₂ adsorption on the metal surface. They also showed the effect of the Hr and preformed corrosion products on the adsorption rate of SO₂. The critical relative humidity was always between 80 and 90% being the adsorption rate very low under that levels.

In previous research⁴ it was demonstrated that steel corroded in the presence of low SO₂ pollution levels (< 1 ppm) by steps with Fe SO₄ formation and H₂SO₄ as catalizer. Once grown the first products the adsorption capacity showed an appreciable increase even at low Hr levels, being Fe the metal which corrosion products evidenced the highest SO₂ adsorption capacity.

The differential adsorption depends of the corrosion products formed in different controlled atmospheres.¹⁰⁻¹¹ Meisel¹² found as the main corrosion product of Fe, at 25°C and 100% Hr, the γ oxhydroxide, being α the predominat form at higher temperatures¹³.

Ishikawa et al.¹⁴ found that α and γ FeOOH presented very similar SO₂ adsorption capacities and β showed a much higher capacity in a shorter time. These oxhydroxides have different but interconvertible structures. For instance β requires the presence of Cl⁻ ions to stabilize but can be transformed to α through δ by heating.

Some autors¹⁵⁻¹⁶ suggested that Fe and Zn could adsorb SO₂ on their metallic oxides in the presence of high SO₂ concentrations. These complexes could oxydize by the O₂ dissolved in the electrolyte surface giving sulphates or stabilize as sulphites, as was found in this work.

in the case of Zn uniform adsorption on all the surface was observed occurring the reactions on a thin electrolyte surface stratum. On Fe and steel, on the contrary, the model of discrete adsorption areas allowed a better interpretation of the results obtained¹⁷.

In steel corrosion FeSO₄.6H₂O is a stable product even in high Hr ambients, mainly localized at the metal oxyde interface. The first crystalline compound formed was probably the FeSO₂.7H₂O, loosing one hydrating molecule when the Hr lowered. The presence of salts decreases thus the critical relative humidity i.e. the Hr level under which no significant corrosion occurs. When Fe and steel corrosion products do not contain salts, but only FeOOH, low corrosion rates are measured at any Hr.

The steel atmospheric corrosion is a diffusion controlled process which propagation rate depends on the chemical composition, morphology and thickness of the corrosion products film formed.

Previous¹⁸ polarization studies of Zn in NaHSO₃ solution showed evidence of the higher protective character of the corrosion products formed in environments with higher SO₂ pollution than those grown in low polluted ones, being this behaviour related to the different compositions determined. XPS

and X ray analysis of Zn rusts in natural atmospheres showed for high SO₂ levels (10-15 ppm) basic Zn sulfate ($\text{ZnSO}_4 \cdot 3\text{Zn}(\text{OH})_2 \cdot 4\text{H}_2\text{O}$) and hidrozcite (ZnO) while rural atmospheres (low SO₂) produced basic Zn carbonates ($\text{Zn}(\text{CO}_3)_2(\text{OH})_2$) and hidrozcita (ZnO).

Electrochemical test of Zn in deareated NaHSO₃ solution provided mechanistic explanation of the corrosion process in SO₂ polluted environments, through an adsorption-oxidation model with pentahydrated Zn sulfite as end product, in good agreement with the results obtained in this work.¹⁹

Acknowledgments

The authors gratefully acknowledge to Mr. Gustavo Moriena for his cooperation during the experimental work and to Lic. Ricardo Viviani for the helpful discussion of the DSC results.

References

1. G. Schikorr - Werkstoffe Korr, 14 (1963): p.69.
2. J.A. Gonzalez, J.M. Bastidas, Rev. Iberoam. Corros. y Prot., 13 (1982): p.7.
3. N.G. Vannenberg, T. Sydberg - Corr. Sci., 12 (1972): p. 775.
4. B.M. Rosales, S.L. Granese, A. Fernández - 4º Congreso Iberoamericano de Corrosión y Protección, M. del Plata, Argentina, 1 (1992): p. 133.3.
5. C. Balboni, G. TrabANELLI, Doctoral Thesis "Indagine Dell'influenza Di Radiazione Luminosa Sulla Corrosione Del Ferro In Ambiente Atmosferico Inquinato Da SO₂", Università Di Ferrara, Italia, (1974).
6. ISO/DP 9226. Methods of Determination of Corrosion Rate of Standard Specimens for the Evaluation of Corrosivity.
7. N. Mackenzie - Dif. Thermal Analysis, (1958): p. 418.
8. E. Kunze, Neue Hütte, 19 (1974): p. 295.
9. S.L. Granese, B.M. Rosales-Rev. Iberoam. Corros. y Prot., 17 (1986): p. 197
10. R.L. Logani, W.W. Smeltzer - Can. Metal. Quart., 10 (1971): p. 149.
11. K. Hauffe - Oxidation of Metal, Plenum Press, N.Y (1965).
12. W. Meisel - Z. Chem., 11 (1971): p. 238.
13. T. Misawa, K. Asami, K. Hashimoto, K. Shimodaira-Corr. Sci., 14 (1974): p. 279.79.
14. T. Ishikawa, K. Ionye - J. Chem. Soc., Japan, 91 (1970): p. 935.
15. M.J.D. Low, A.J. Goodsel, N. Takezawa-Env. Sci. Technol., 6 (1972): p. 268.
16. R.A. Shoenheydt, J.H. Lundsford - J. Catalysis, 26 (1972): p. 261.
17. J.R. Duncan, D.J. Speeding, E.E. Wheeler - Corr. Sci., 13 (1973): p. 69.
18. S.L. Granese, B.M. Rosales, A. Fernandez - Bull. of Electrochem., India, 7 2 (1991): p. 67.67.
19. S.L. Granese, B.M. Rosales - J. Electrochem. Soc., 132 (1985): p. 1281.
20. R.D. Penzhornn, O.E.A. Monogr., 7, (1972): p. 34.

Table I

Materials compositions (% w/w)

Plain C steel	C 0.076	P 0.15	Cu 0.03
	Mn 0.39	Cr 0.03	Al 0.057
	Si 0.065	Mo 0.001	Ti 0.003
	S 0.01	Ni 0.04	Sn 0.003
Zn	Pb 0.0063	Cd 0.0009	Fe 0.0007
	Cu 0.0004	Al < 0.0008	Sn < 0.0005
Al	Fe 0.12	Si 0.06	Ti 0.007
	Cu 0.003	Zn 0.003	Mn 0.002
	Cr 0.002	Mg 0.001	B 0.001
	Pb 0.001		
Cu	Ni 0.01	P 0.0067	Pb 0.001
	Sn vestiges		

Table II

Test conditions in the loop

Test time (days)	7
T (°C)	30 and 50
Hr (%)	98
[SO ₂](ppm)	50
UV radiation wave length	254 nm, constant power 0.014 mW.cm ⁻²
Air flux (ml.min ⁻¹)	35

Table III

Corrosion products formed on Cu.

T (°C)	Product	% w/w
30 and 50	Antlerite (3 CuO.SO ₃ .2H ₂ O)	97
	Cuprite (Cu ₂ O)	3

Table IV Corrosion products formed on plain C steel.

T (°C)		Product	% w/w
30 and 50	Inner layer	$\text{FeSO}_4 \cdot 6\text{H}_2\text{O}$	37
		$\text{FeSO}_4 \cdot 3\text{H}_2\text{O}$	31
		Lepidocrocite ($\gamma\text{-FeOOH}$)	
		Goethite ($\alpha\text{-FeOOH}$)	32
50	Outer layer	$\text{FeSO}_4 \cdot 6\text{H}_2\text{O}$	39
		$\text{FeSO}_4 \cdot 3\text{H}_2\text{O}$	43
		$\alpha\text{-FeOOH}$ and $\gamma\text{-FeOOH}$	18

Table V Corrosion products formed on Zn

T (°C)		Products	w/w %
30 and 50		$2\text{ZnSO}_4 \cdot 5\text{H}_2\text{O}$	95
		$\text{ZnO} \cdot x\text{H}_2\text{O}$	5

Fig. 1. Thermogram of Corrosion Products Formed on Steel in the Loop at 50°C

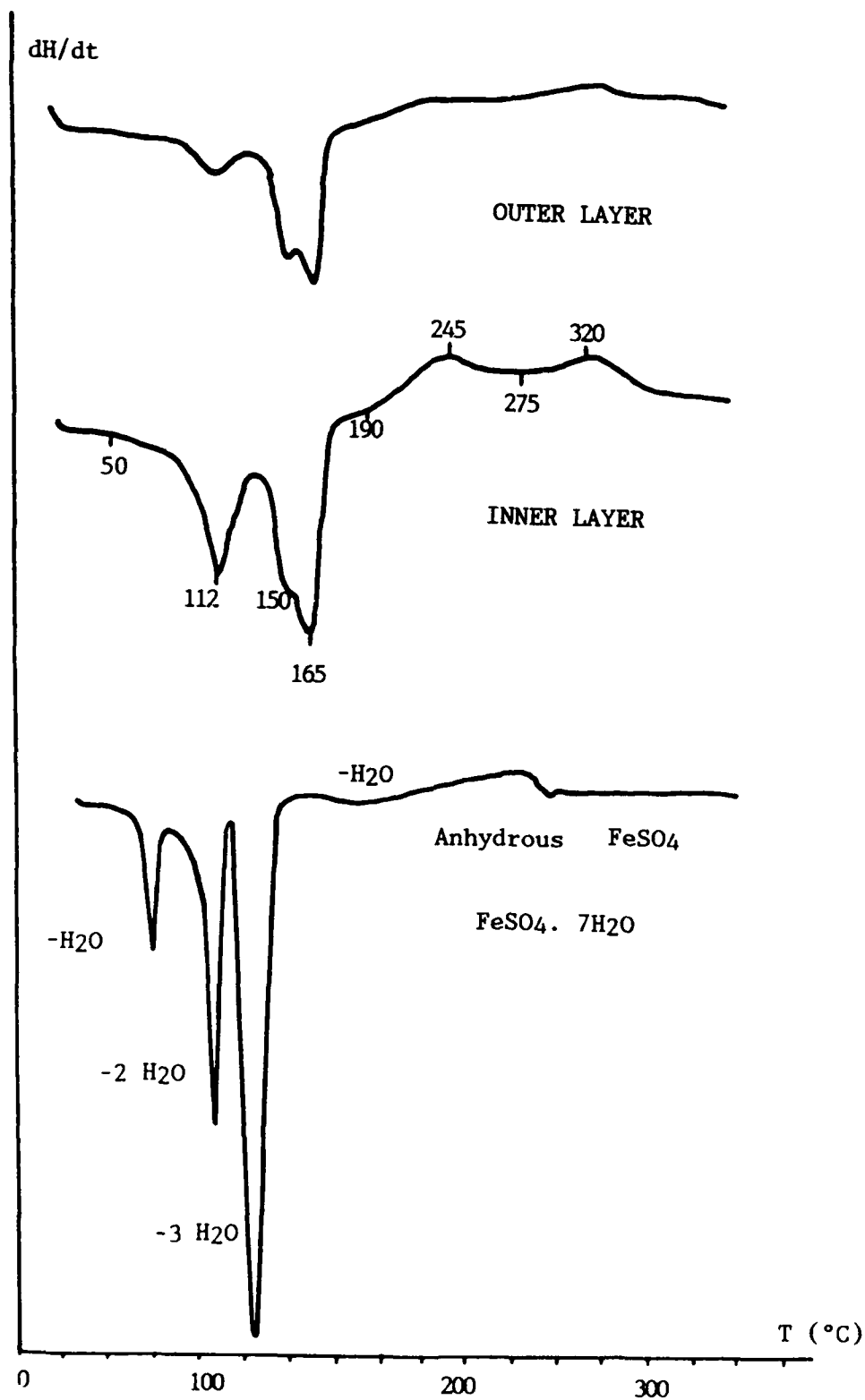
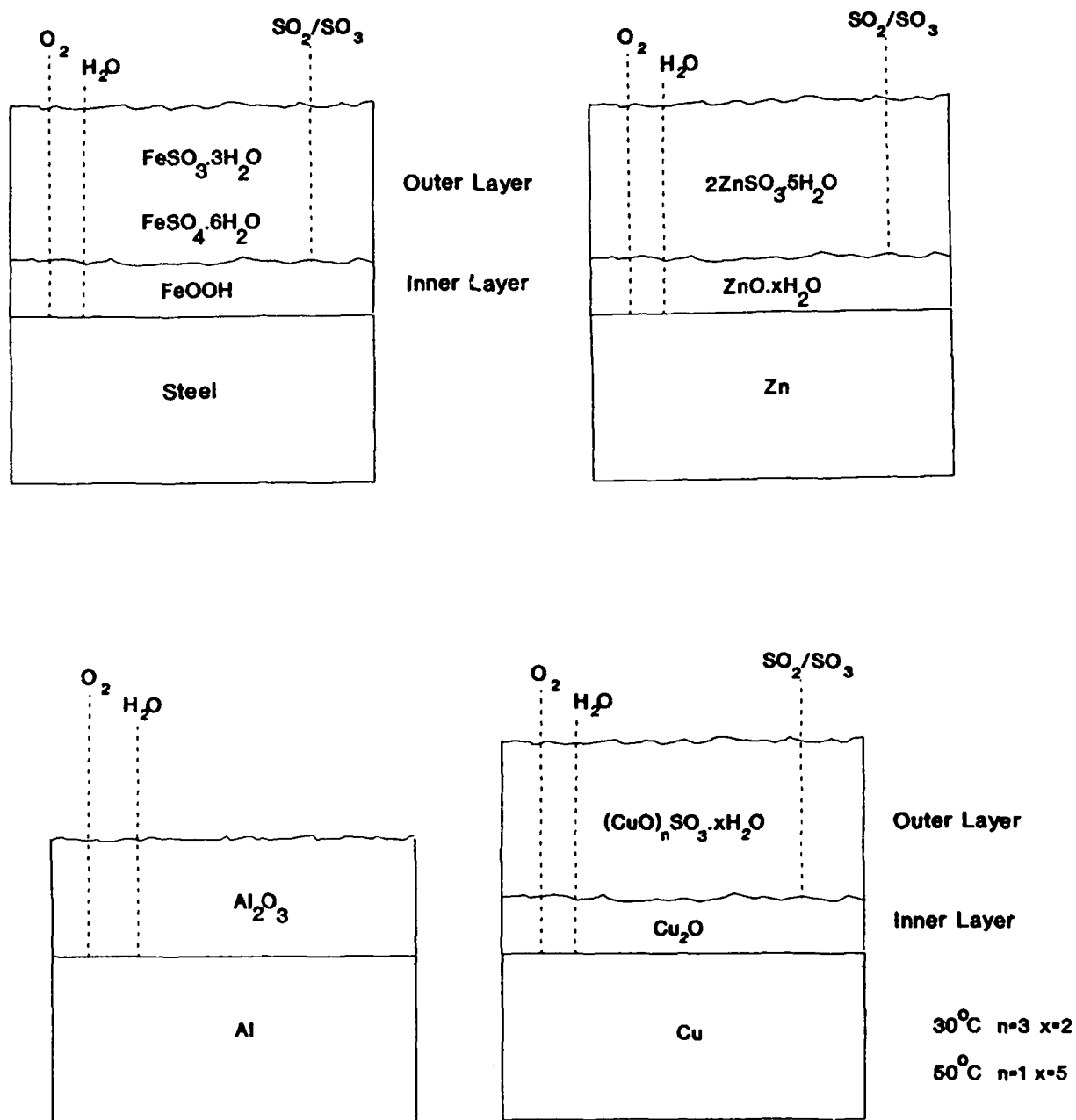


Fig. 2.- Schema of the Corrosion Process On Zn and Cu in SO₂ polluted atmospheres



Initial Stages of the SO₂-Induced Atmospheric Corrosion of Zinc Investigated by In-Situ IR Spectroscopy and Time-Resolved Trace Gas Analysis; Synergistic effects of NO₂ and O₃.

Jan-Erik Svensson
Department of Inorganic Chemistry
Chalmers University of Technology and
University of Göteborg,
S-412 96 Göteborg, SWEDEN

Lars-Gunnar Johansson
Department of Inorganic Chemistry
Chalmers University of Technology and
University of Göteborg,
S-412 96 Göteborg, SWEDEN

Abstract

The initial stages of the atmospheric corrosion of zinc in humid air (RH = 95%) containing ppm amounts of SO₂, NO₂ and O₃ were studied by in-situ Fourier transform infrared specular reflection-absorption spectroscopy on metallic zinc, in-situ Fourier transform infrared diffuse reflection spectroscopy on ZnO powder and by time-resolved analysis of SO₂, NO_x and O₃ in the output gas from a reaction chamber.

In-situ IR specular reflectance measurements show the formation of sulphite on zinc metal in humid air containing ppm amounts of SO₂, the sulphite band emerging already after 5 minutes of exposure. The growth of the sulphite band is approximately linear in the beginning of the exposure. Measurable amounts of sulphate only starts to form after 45 minutes by the oxidation of surface sulphite. The experiments show that the stability of sulphite on zinc decreases in the presence of NO₂, confirming that the synergistic effect of SO₂-NO₂ combinations on zinc corrosion reported in the literature is caused by the increased formation of sulphate in the presence of NO₂. In-situ diffuse reflectance measurements on ZnO powder indicate that the enhanced oxidation of sulphite in the presence of NO₂ also occurs in the absence of zinc metal.

In-situ IR specular reflectance measurements on zinc metal also show that O₃ rapidly oxidises sulphite on the zinc surface, the kinetic stability of sulphite being decreased much more by O₃ than by NO₂. Time resolved trace gas analysis in the ppb-ppm range showed that the deposition of SO₂ on zinc metal is enhanced in the presence of O₃ and NO₂.

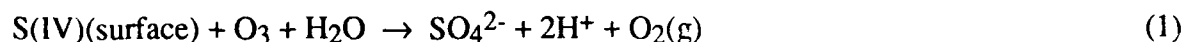
Key terms: in-situ IR spectroscopy, zinc, atmospheric corrosion, SO₂, NO₂, O₃.

Introduction

Together with the well-known corrosive effects of chlorides and acid precipitation, SO₂ is generally considered to be one of the most important factors for the corrosion of zinc in the atmosphere¹. However, there has been relatively little work on the corrosive effect on zinc of combinations of SO₂ and other reactive substances. It has been suggested that some atmospheric oxidants may accelerate the atmospheric corrosion of zinc in the presence of SO₂¹.

In previous laboratory investigations^{2, 3, 4} it was confirmed that NO₂ and O₃ are indeed able to accelerate zinc corrosion in the presence of SO₂. It was concluded that the increased deposition

of SO₂ on zinc found in the presence of NO₂ and O₃ was caused by an increased rate of oxidation of S(IV) species on the zinc surface to the S(VI) (sulphate) stage. This conclusion was based primarily on time-resolved analysis of SO₂, NO_x and O₃ in the output gas from a reaction chamber. Using this technique we showed that the interaction of SO₂ and O₃ on the zinc surface is stoichiometric corresponding to the overall reaction:



while the enhancement of sulphate formation by NO₂ does not depend on a simple redox process.

In the present study we investigate the chemistry of the corroding zinc surface during the initial stages of corrosion attack by a combination of in-situ Fourier transform infrared specular reflection-absorption spectroscopy on metallic zinc, in-situ Fourier transform infrared diffuse reflection spectroscopy on ZnO powder and time-resolved trace gas analysis.

Using in-situ Fourier transform infrared specular reflection-absorption spectroscopy on metallic zinc, we were able to corroborate our earlier conclusions³ on the enhancement of the rate of oxidation of S(IV) species on zinc by NO₂ and O₃. Thus, sulphite on the zinc surface is converted into sulphate at an increasing rate when NO₂ and, especially, O₃ are present together with SO₂.

Before exposure, the zinc metal surface will be covered by a passive film consisting of ZnO or, possibly, Zn(OH)₂. To investigate the reactions occurring in this passive film in the absence of zinc metal, the interaction of SO₂ and NO₂ with pure ZnO was studied by in-situ diffuse reflection IR spectroscopy. These experiments showed that the enhanced oxidation of S(IV) species by NO₂ found for corroding zinc metal also occurs on pure ZnO powder.

Experimental

Three different experimental approaches were used in this investigation:

- i, Time-resolved trace gas analysis of the output gas from a corrosion chamber was used to study the deposition and formation of gaseous species on the zinc metal (zinc of electrolytic grade >99.9%) quantitatively, as a function of exposure time.
- ii, In-situ IR specular reflection spectroscopy was used to provide qualitative information on the formation of adsorbates and the gradual build-up of corrosion products during the initial stages of corrosion on the zinc metal surface.
- iii, In-situ IR diffuse reflection spectroscopy was used to study the reaction on pure zincite (ZnO, Merck, analytical grade) with no metal present.

The first of these experimental techniques has been described in detail previously^{3,4}. For completeness a schematic description is given below.

The IR-spectra were obtained using a Perkin-Elmer 1800 Fourier Transform Infrared Spectrometer with a MCT detector.

In all exposures, SO₂ and NO₂ were added from temperature controlled permeation tubes using dry air as a carrier. O₃ was produced by an O₃-generator that uses UV radiation ($\lambda < 230$ nm) to

form atomic oxygen from molecular oxygen that then reacts with undissociated oxygen molecules to form O_3 .

Time-Resolved Analysis of the Deposition and Consumption of SO_2 , O_3 and NO_2

The zinc samples had a geometrical area of 26 cm^2 ($5.9 \times 2.0 \times 0.17\text{ cm}$). Prior to exposure, the samples were polished on SiC-paper in ethanol to 1000 mesh and washed in ethanol using ultrasonic agitation. The samples were then dried at 20°C in air and stored in a desiccator for 24 hours.

Figure 1 shows the experimental arrangement for the time-resolved trace gas analysis. The materials of construction are glass and Teflon. This apparatus contains one exposure chamber with continuous flow and it includes on-line analysis of SO_2 , NO_x and O_3 in the output gas from the chamber. SO_2 was analysed by a fluorescence instrument (Environnement AF21). The O_3 concentration was determined using an instrument based on UV photometry (Dasibi 1108) while NO and NO_x were analysed by a chemiluminescence instrument (Environnement AC 30). The zinc sample was suspended in a nylon string in the middle of the chamber, the direction of flow being parallel to the sample. The gas flow was $1.00\text{ dm}^3/\text{min}$ resulting in a net gas velocity of 2.7 cm/s in the cell. Flow conditions were laminar ($Re = 50$). Experiments were carried out at 95%.

Before the start of each experiment the interaction of the pollutants with the chamber walls had reached a steady state so that the output gas from the corrosion chamber had a constant composition. The experiment was started by introducing a sample into the corrosion chamber. Each specific trace gas was continuously measured during the exposures, using the decrease in the signal to calculate the consumption of the gas by the sample.

In-Situ Specular Reflection IR Spectroscopy

The specular reflectance cell was made of Teflon with BaF_2 windows placed in the open ends of the cylinder (cf. figure 2). The BaF_2 windows were covered with a $10\text{ }\mu\text{m}$ thick layer of SiO_2 . The infrared beam strikes the sample surface at 80° from the surface normal. The temperature of the sample is controlled by mounting the sample on a water-cooled brass plate. The corrosive air enters the cell through the middle gas port and leaves the cell through the two exits.

The zinc samples ($47 \times 20 \times 1\text{ mm}$) were sequentially polished with SiC paper and diamond paste down to $1\text{ }\mu\text{m}$ in ethanol. The samples were rinsed in ethanol using ultrasonic agitation and then dried in air at 20°C . The samples were stored in a desiccator for 1 hour before being transferred to the reaction cell.

At the start of each experiment a stream of dry air was allowed to pass through the cell for 30 minutes. Humid air (95% RH) was then introduced into the cell and a spectrum was recorded after 30 minutes. This spectrum was used as a reference, subtracting it from all subsequently recorded spectra during the exposure. The sample was then exposed to SO_2 (2.4 ppm) and/or NO_2 (2.2 ppm) and/or O_3 (2.2 ppm) at 95% RH. The first spectrum was recorded after 5 minutes of exposure to the corrosive gas. Spectra were then recorded intermittently during exposure. The longest exposure time was 24 hours. All spectra were obtained by adding 128 interferograms at a resolution of 4 cm^{-1} .

The experiments were carried out at 95%. The temperature during exposure was 22°C and the air flow was 200 ml/min .

In-Situ Diffuse Reflection IR Spectroscopy

The reaction cell used in the diffuse reflectance experiments was a Harrick Scientific Corporation HVC-DR3 in-situ reaction cell from equipped with $ZnSe$ windows (cf. figure 3). The materials of construction were stainless steel and Teflon. All spectra were obtained by adding 256 interferograms at a resolution of 8 cm^{-1} . The longest exposure time was 24 hours. The exposure temperature was 22°C and the air flow was 100 ml/min .

After transferring the ZnO powder to the reaction chamber, a dry air stream was allowed to pass the cell during 30 minutes. Humid air (95% RH) was then introduced into the cell and after another 30 minutes an IR spectrum was recorded which was used as a reference, subtracting it from all subsequently recorded spectra during the exposure. The sample was then exposed to SO₂ (10 ppm) and/or NO₂ (10 ppm) at 95% RH. The first spectrum was recorded after 30 minutes of exposure to the polluted air. Spectra were then recorded intermittently during exposure.

Results

Time-Resolved Analysis of the Deposition of SO₂: Influence of O₃ and NO₂

Figure 4 shows the deposition of SO₂ as a function of exposure time. The synthetic corrosive air contained SO₂ (780 ppb), SO₂ + NO₂ (1300 ppb) and SO₂ + O₃ (1300 ppb). During the first few minutes of exposure the deposition of SO₂ was very rapid in all three environments (SO₂, SO₂ + NO₂ and SO₂ + O₃). After this initial period, deposition slowed down. The decrease in the deposition rate with time was especially pronounced in the SO₂-only environment while NO₂ and especially O₃ increased the deposition of SO₂ considerably at steady state. As shown in a previous study⁴ the increase in the SO₂ deposition on zinc by NO₂ and O₃ becomes increasingly marked as the pollutant concentration decreases.

In-Situ Specular Reflection IR Spectroscopy

SO₂ Figures 5a and b show specular reflectance spectra of zinc metal exposed to 2.4 ppm sulphur dioxide in air at 95% RH at different exposure times. Already after 5 minutes of exposure a band emerged at 1000 cm⁻¹. The interpretation of IR reflection spectra is complicated by the distortion of the reflectance spectrum by anomalous dispersion. This results in changes in peak positions relative to bulk transmission spectra⁵. Taking into account these expected shifts in peak positions, the positive identification of fourvalent sulphur on zinc exposed to similar environments by other methods³ and by comparison with IR absorption data for bulk compounds containing sulphur-oxygen species this peak was attributed to sulphite stretching vibrations (cf. table 1 for IR absorption bands for some selected compounds). The assignment of the 1000 cm⁻¹ specular reflectance peak to surface sulphite on zinc is in accordance with a specular reflectance study by Persson and Leygraf⁶ on nickel where a peak at 1020 cm⁻¹ was assigned to nickel sulphite. The sulphite stretching band increased in amplitude approximately linearly with time during the first 60 minutes of exposure (cf. figure 6a). The band reached its maximum intensity after about 90 minutes, the intensity then decreasing quickly with time. The sensitivity of the measurement may be estimated to correspond to a sulphite layer with an average thickness of about 3-5 Å from the noise level of the IR measurement, the gas flow rate, the SO₂ concentration in the gas and assuming all SO₂ is absorbed by the sample surface. After 45 minutes of exposure another peak emerged at 1120 cm⁻¹. This peak was attributed to sulphate (compare table 1). The relative intensity of the sulphate peak increased with time and had become the dominating peak after 3 hours of exposure. At this stage weak peaks at 1030 and 983 cm⁻¹ were detected that were also attributed to sulphate. In addition, remnants of the sulphite stretching band were detected at 1000 cm⁻¹. Figure 6b shows the intensity of the 1120 cm⁻¹ (sulphate) band as a function of exposure time. When the sulphate peak emerges, the growth of the sulphite peak decreases and the sulphite absorption is finally lost in the sulphate peak. The growth of the sulphate peak is markedly non-linear, being very slow in the beginning and accelerating towards the end of the exposure.

SO₂ + NO₂ Figures 7a and b show specular reflectance spectra of zinc metal exposed to SO₂ (2.4 ppm) and NO₂ (2.2 ppm) at different exposure times. The spectra obtained after 15 and 30 minutes of exposure closely resemble the spectra obtained during the SO₂-only exposure (see above). The main difference is the emergence of the sulphate band at 1120 cm⁻¹ already after 30 minutes. After 60 minutes of exposure to SO₂ + NO₂ the sulphate peak at 1120 cm⁻¹ is much more pronounced than in the SO₂-only exposure. The disappearance of the sulphite peak is also

more rapid in the $\text{SO}_2 + \text{NO}_2$ environment, the peak vanishing already after 90 minutes. This should be compared to the SO_2 -only exposure where the sulphite peak is still seen after 3 hours of exposure. Figure's 8a and b show the intensity of the sulphite and sulphate bands as a function of exposure time. Comparing with figure's 6a and b, NO_2 is seen to accelerate the formation of sulphate as well as the destruction of sulphite on the zinc surface.

$\text{SO}_2 + \text{O}_3$ Figures 9a and b show specular reflectance spectra of zinc metal exposed to SO_2 (2.4 ppm) and O_3 (2.2 ppm) at different exposure times. The sulphite peak at 1000 cm^{-1} is again seen after 5 minutes of exposure, while the sulphate peak emerges already after 15 minute's exposure. The sulphate peak increased in amplitude to become the strongest peak after 30 minutes of exposure. After 60 minutes only two peaks are seen in the spectrum at 1130 and 984 cm^{-1} , while the sulphite peak at 1000 cm^{-1} has disappeared. The time-dependence of the sulphite and sulphate peaks is further illustrated in figures 10 a and b. The diminishing of the sulphite peak and the emergence of the sulphate peak is seen to be much more rapid in the presence of ozone compared to SO_2 -only and also to the $\text{SO}_2 + \text{NO}_2$ exposure.

In-Situ Diffuse Reflection IR Spectroscopy

SO_2 Figure 11a shows diffuse reflectance spectra of zincite (ZnO) exposed to 10 ppm of SO_2 in air at 95% RH at different exposure times. The first spectrum, which was recorded after 30 minutes of exposure to SO_2 , shows a peak at 950 cm^{-1} . This peak was attributed to a stretching vibration of sulphite. In the spectra recorded after 1, 2 and 3 hours of exposure this peak increased in amplitude. The spectrum after 3 hour's exposure to SO_2 showed a broad peak at 950 cm^{-1} and smaller peaks at 1000 and 860 cm^{-1} . There was also a peak at 1635 cm^{-1} corresponding to the bending vibration of water and a broad peak at $3000\text{--}3600$ attributed to OH stretching vibrations of water. There is no indication of sulphate at this stage. The spectrum recorded after 3 hours of exposure is strikingly similar to the spectrum of $\text{ZnSO}_3 \cdot 3\text{H}_2\text{O}$ reported by Lutz et al⁷.

$\text{SO}_2 + \text{NO}_2$ Figure 11b and 11c show diffuse reflectance spectra recorded in an experiment where ZnO was first exposed to SO_2 (10 ppm) for 3 hours. SO_2 was then removed from the sample gas and NO_2 (10 ppm) was introduced. The spectrum after 3 hours of SO_2 exposure was identical to the lower spectrum in figure 11a. Already after 15 minute's exposure to NO_2 a peak emerged at 1130 cm^{-1} , which were assigned to sulphate. This peak increased in amplitude and dominated the spectrum after 2 hours showing the rapid formation of sulphate when sulphite is exposed to NO_2 . Smaller peaks at 1080 , 1025 , 963 cm^{-1} were also visible that were all assigned to sulphate. Table 1 shows that the IR absorption bands found in this experiment are similar to the ones found for zinc hydroxysulphatepentahydrate ($\text{ZnSO}_4 \cdot 3\text{ZnSO}_4 \cdot 5\text{H}_2\text{O}$), synthesised according to Bear et al⁸, and normal zinc sulphate ($\text{ZnSO}_4 \cdot 7\text{H}_2\text{O}$), the spectra being obtained using the conventional KBr-disc technique. The peak at 950 cm^{-1} , assigned to sulphite, decreased in amplitude as the exposure to nitrogen dioxide continued. After 5 hours of NO_2 exposure weak absorptions emerged at 1336 1399 and 1436 cm^{-1} . These peaks were assigned to nitrate.

Discussion

The specular reflectance IR spectra in figures 5a and b show the formation of sulphite on zinc in SO_2 -polluted air. This result is in accordance with a previous study³ that reported the presence of S(IV) species on zinc in similar environments. The linear growth of the sulphite band (cf. fig. 6a) and the absence of absorption bands assignable to sulphate during the first 45 minutes of exposure illustrate the kinetic stability of S(IV) species on the zinc surface. The slowing down of the growth of the sulphite band after about 60 minutes occurs soon after the emergence of the sulphate band as illustrated by figure's 6a and 6b. This indicates that sulphite present on the zinc surface starts to oxidise at this stage, forming sulphate. The accelerating growth of the sulphate

band reflects that the surface sulphite accumulated during the early stages of exposure is being oxidised at an increasing rate. The non-linear growth of the sulphate band suggests that the oxidation of sulphite to sulphate on the zinc surface may be catalysed by the presence of liquid water on the surface, the formation of the deliquescent zinc sulphate giving rise to an aqueous solution at humidities above 89% at 22°C.

It may be noted that the growth of the sulphate band makes it difficult to measure the relatively weak sulphite band towards the end of the exposure. The previous studies^{3,4} showed the presence of S(IV) on zinc surfaces exposed to SO₂ environments even after long exposure times, although the S(IV) / sulphate ratio diminished with time.

The diffuse reflectance spectra of ZnO(s) exposed to humid SO₂-containing air shown in figure 11a, also show the formation of sulphite. In contrast to the results from the specular reflectance study on metallic zinc, sulphite on ZnO shows no tendency to oxidise to sulphate during exposure. The causes for the different behaviour of ZnO and zinc metal in this respect will be addressed in future work.

Comparing the SO₂-only results with the specular reflectance spectra obtained from zinc metal exposed to SO₂ + NO₂, shows that the presence of NO₂ decreases the kinetic stability of sulphite on zinc. Thus, oxidation of sulphite to sulphate is evident already after 30 minutes while the maximum amplitude of the sulphite band is reached after about 60 minutes (cf. 7a, b and 8a, b). As in the case of the SO₂-only runs, the sulphate formation process is highly non-linear, the s-shape of the sulphate absorption-time curve reflecting the kinetics of the oxidation of sulphite to sulphate. Once the process of sulphite oxidation is initiated, it rapidly accelerates to reach a maximum rate after about 100 minutes. This behaviour again suggests the self-catalysed nature of the process discussed above. The slowing down of the growth of the sulphate peak towards the end of the exposure reflects that most of the accumulated surface sulphite has already been oxidised at this stage, the rate of sulphate formation now being limited by the rate of deposition of SO₂ on the surface. The absence of peaks attributable to nitrate in the specular reflectance spectra is conspicuous. This is in accordance with our previous study³ where the formation of nitrate and nitrite on zinc was found to be negligible in the corresponding environment.

The diffuse reflectance experiments involving ZnO(s) also illustrate the enhancement of sulphite oxidation by NO₂ (cf. figure's 11b and c). Thus, in this experiment where SO₂ was replaced by NO₂, the sulphate peak emerged already after 15 minutes of exposure to NO₂. This result is strikingly different from the corresponding SO₂-only runs where no sulphate was detected. In the presence of NO₂, nitrate peaks were detected after 10 hours of exposure to NO₂ (not shown).

In a previous study⁴ it was shown that O₃ reacts with S(IV) species on zinc according to reaction (1), forming sulphate, hydrogen ions and molecular oxygen. The present work corroborates these findings. Thus, we find that the presence of O₃ causes a marked increase in the rate of oxidation of sulphite to sulphate. This is illustrated by figure's 9a and b, representing specular reflectance spectra of zinc metal exposed to air containing SO₂ + O₃ and by figures 10a and 10b, showing the evolution of the sulphite and sulphate bands with time, respectively. Initially, the rate of formation of sulphite on zinc in the presence of O₃ is similar to the two other environments studied. However, the slowing down of the growth of the sulphite peak and the simultaneous appearance of the sulphate peak occurs already after about 15 minutes in the presence of O₃. The sulphite peak only reaches a fraction of the intensity in the two other environments. Apparently, the rapid oxidation of sulphite on zinc by O₃ prohibits the accumulation of large amounts of sulphite on the surface, explaining the comparatively weak s-shape of the sulphate absorption-time curve compared to the case of SO₂ + NO₂. It may be noted that the previous study showed that small but significant amounts of S(IV) species are present on zinc surfaces exposed to mixtures of SO₂ and O₃, even after long exposure times^{3,4}.

As in the case of the $\text{SO}_2 + \text{NO}_2$ exposure, the difficulty to detect the sulphite band in the IR spectra after about two hours is connected to the appearance of the strong sulphate band.

The results from the experiment involving time-resolved analysis of SO_2 downstream a reaction cell containing a zinc sample are in general agreement with the results from the specular reflectance IR measurements. The greater steady-state deposition rate of SO_2 measured in the presence of NO_2 and, especially, O_3 is connected to the increased rate of oxidation of sulphite to sulphate. It is suggested that the surface sulphate creates an electrolyte that promotes the corrosion of zinc, increasing the ability of the surface to absorb SO_2 .

Conclusions

In-situ IR specular reflectance measurements show the formation of sulphite on zinc in humid air containing ppm amounts of SO_2 , the sulphite band emerging already after 5 minutes of exposure. The growth of the sulphite band is approximately linear in the beginning of the exposure. Sulphate only starts to form after about 45 minutes by the oxidation of surface sulphite.

The experiments show that the stability of sulphite on zinc decreases in the presence of NO_2 , confirming that the SO_2 - NO_2 synergism reported earlier is caused by the increased formation of sulphate in the presence of NO_2 . In-situ diffuse reflectance measurements on ZnO powder indicate that the enhanced oxidation of sulphite in the presence of NO_2 also occurs in the absence of zinc metal.

In-situ IR specular reflectance measurements on zinc metal also show that O_3 rapidly oxidises sulphite on the zinc surface, the kinetic stability of sulphite being decreased much more by O_3 than by NO_2 .

Acknowledgements

The financial support of this work from the Swedish Environmental Protection Board and OK Petroleum Environmental Protection foundation is gratefully acknowledged.

References

1. T. E. Graedel, *J. Electrochem. Soc.*, **136** 4 (1989).
2. J. -E. Svensson and L. -G. Johansson, Proc. 11th Scandinavian Corrosion Congress, Stavanger, Norway, (1989), F-47.
3. J. -E. Svensson and L. -G. Johansson, Proc. 182 Meeting of the Electrochemical Society Toronto, Canada, October 11-16, (1992).
4. J. -E. Svensson and L. -G. Johansson, to be published
5. R. G. Greenler, R. R. Hahn and J. P. Schwartz, *J. Catal.*, **23**, (1971): 42
6. D. Persson and C. Leygraf, Proc. 12th Scandinavian Corrosion Congress, Helsinki, Finland, (1992): 667.
7. H. D. Lutz, S. M. El-Suradi, C. Mertins and B. Engelen, *Z. Naturforsch.* **35b**, (1980): p. 808
8. J. Bear, I. E. Gray, E. E. Newnham and L. J. Rogers, *Aust. J. Chem.*, **40** (1987): p 539

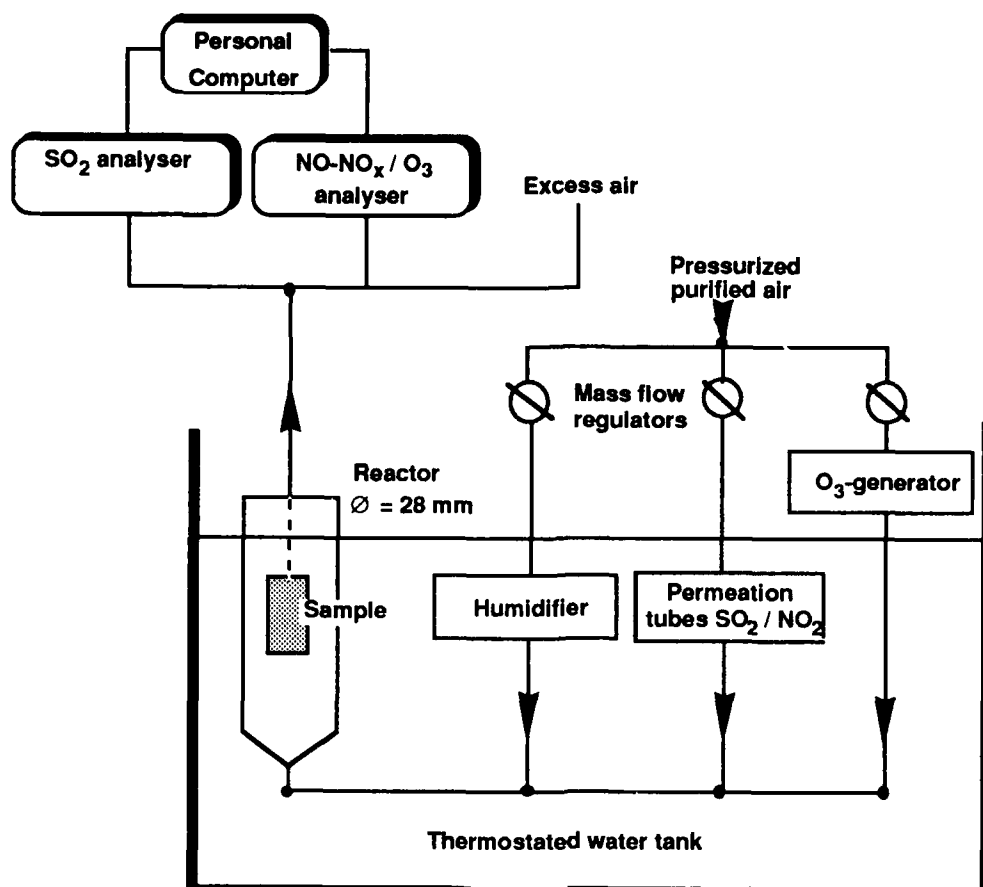


Figure 1. The experimental arrangement for time resolved trace gas analysis.

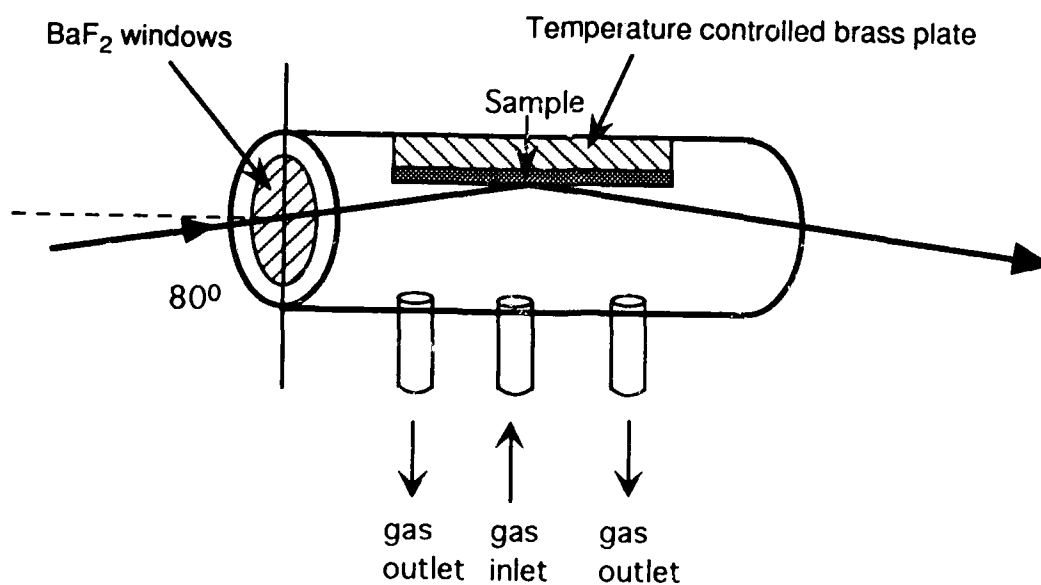


Figure 2. Schematic drawing of the reaction cell used in the specular reflectance experiments.

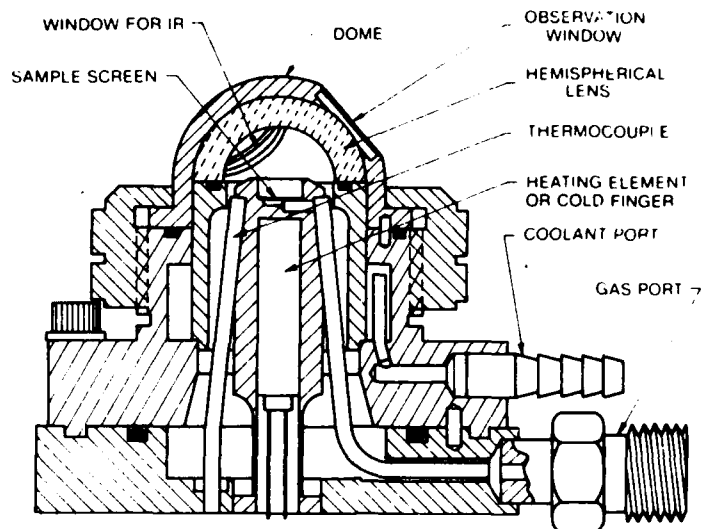


Figure 3. The reaction cell (Harrick Scientific Corporation) used in the diffuse reflectance experiments.

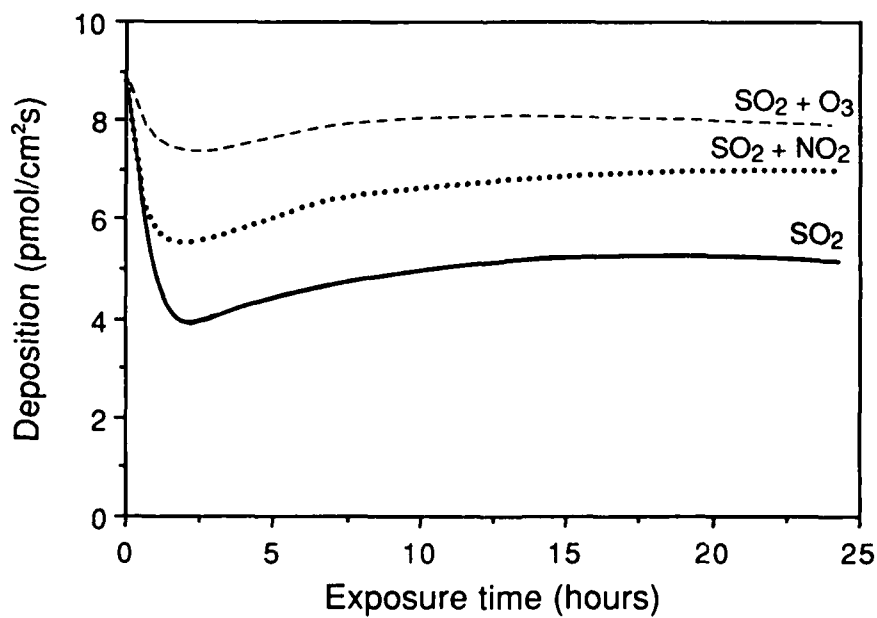


Figure 4. Deposition of SO₂ on zinc at 95% RH as a function of time. The SO₂ concentration was 780 ppb while the concentrations of NO₂ and O₃ were 1300 ppb.

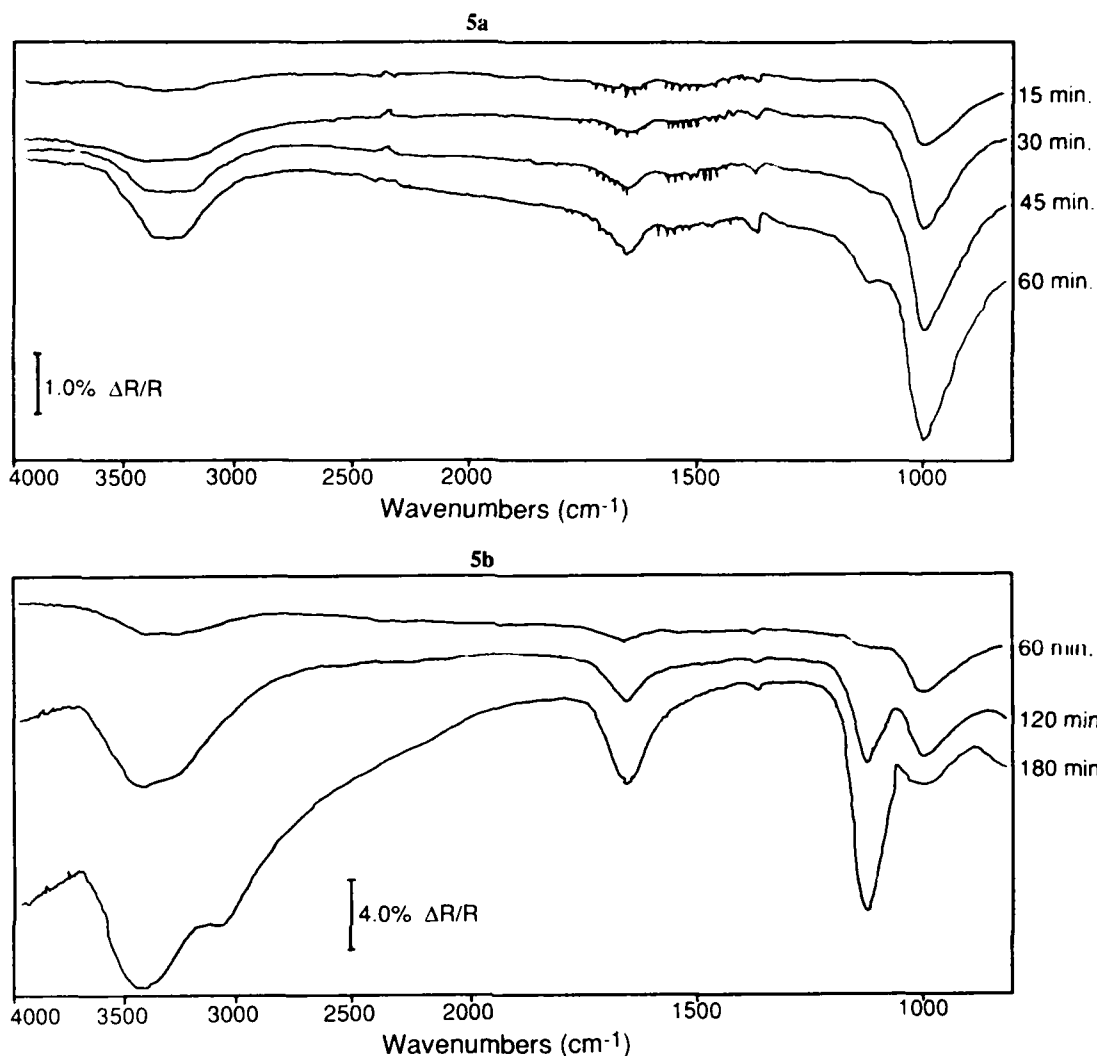


Figure 5a. Specular reflectance IR spectra of zinc metal exposed to 2.4 ppm SO₂ at 95% RH for 5, 15, 30, 45 and 60 minutes, respectively. **Figure 5b.** Same as figure 5a except for the exposure time which is 60, 120 and 180 minutes, respectively.

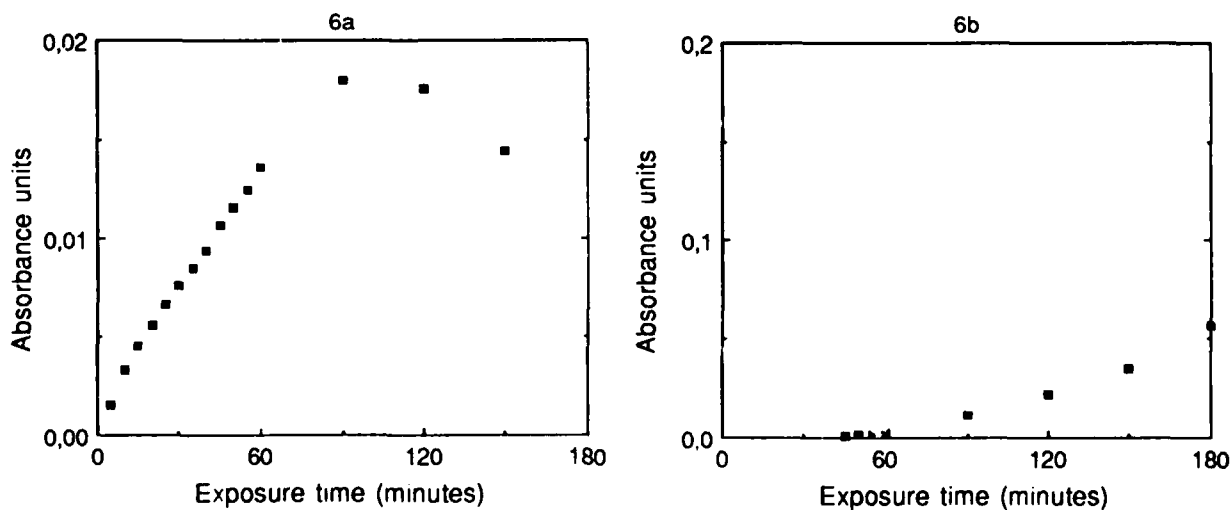


Figure 6a. Intensity of the sulphite band at 1000 cm⁻¹ as a function of exposure time for zinc exposed to 2.4 ppm SO₂ at 95% RH. **Figure 6b.** Intensity of the sulphate band as a function of exposure time for zinc exposed to 2.4 ppm SO₂ at 95% RH.

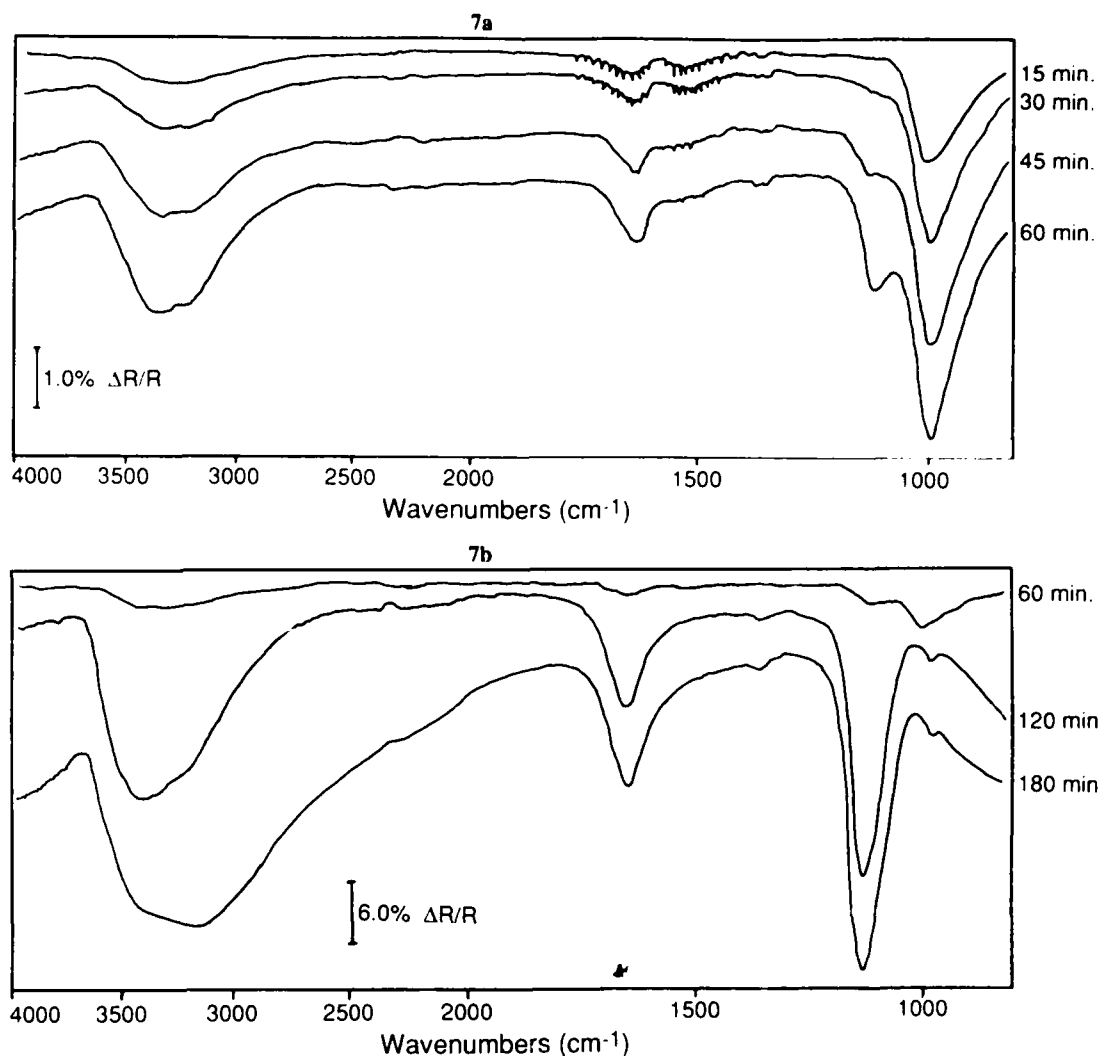


Figure 7a. Specular reflectance IR spectra of zinc metal exposed to 2.4 ppm SO_2 and 2.2 ppm NO_2 at 95% RH for 5, 15, 30, 45 and 60 minutes, respectively. **Figure 7b.** Same as figure 7a except for exposure time which is 60, 120 and 180 minutes, respectively.

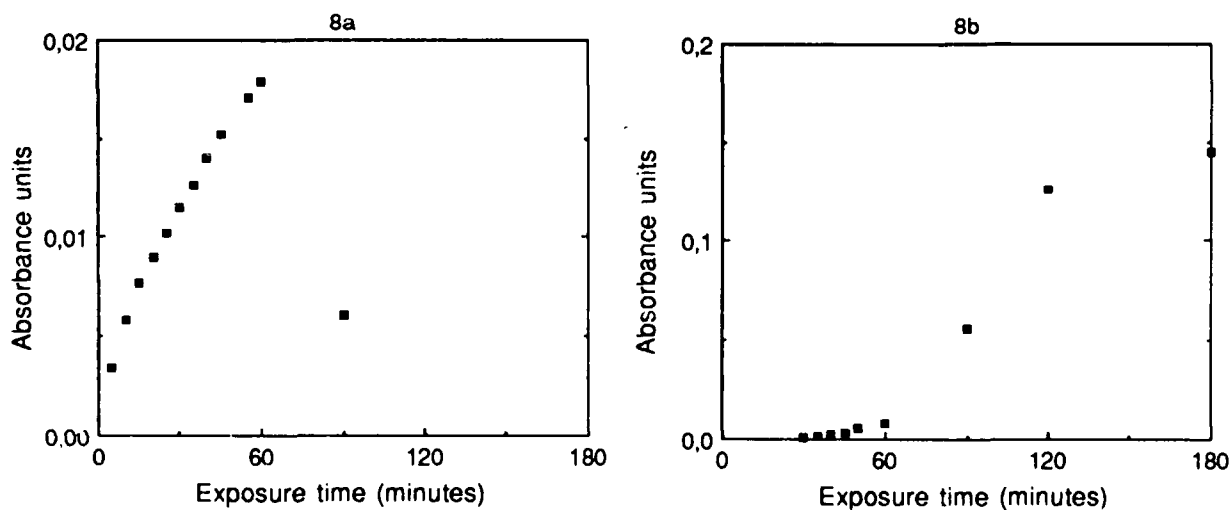


Figure 8a. Intensity of the sulphite band at 1000 cm^{-1} as a function of exposure time for zinc exposed to 2.4 ppm SO_2 and 2.2 ppm NO_2 at 95% RH. **Figure 8b.** Intensity of the sulphate band at 1120 cm^{-1} as a function of exposure time for zinc exposed to 2.4 ppm SO_2 and 2.2 ppm NO_2 at 95% RH.

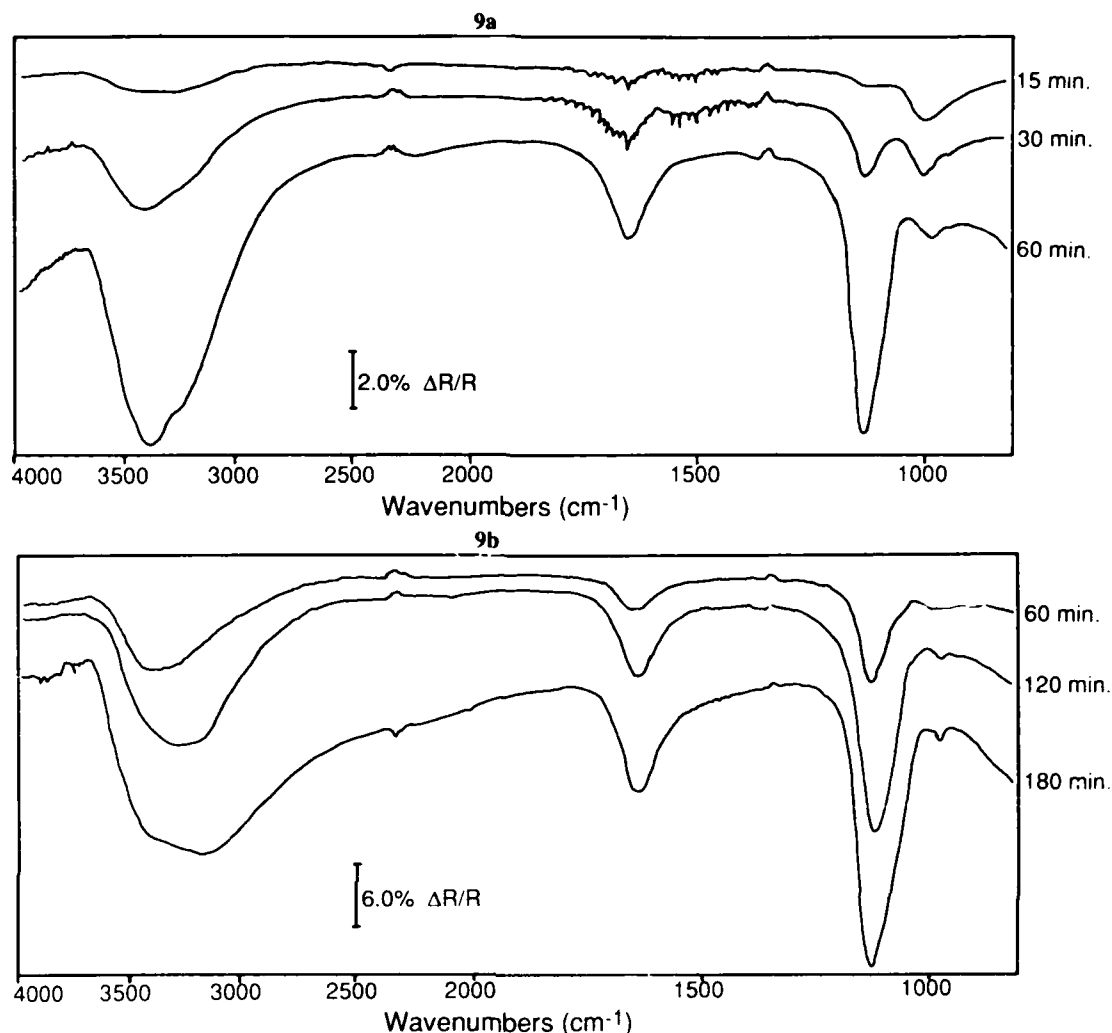


Figure 9a. Specular reflectance IR spectra of zinc metal exposed to 2.4 ppm SO_2 and 2.2 ppm O_3 at 95% RH for 5, 15, 30, 45 and 60 minutes, respectively. **Figure 9b.** Same as figure 9a except for the exposure time which is 60, 120 and 180 minutes, respectively.

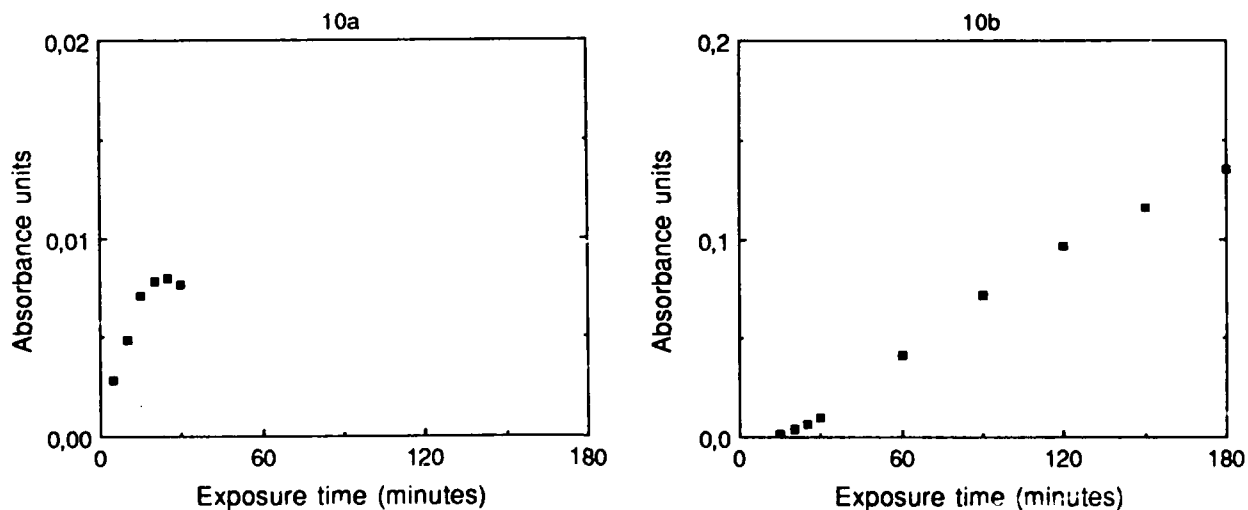


Figure 10a. Intensity of the sulphite band at 1000 cm^{-1} as a function of exposure time for zinc exposed to 2.4 ppm SO_2 and 2.2 ppm O_3 at 95% RH. **Figure 10b.** Intensity of the sulphate band at 1120 cm^{-1} as a function of exposure time for zinc exposed to 2.4 ppm SO_2 and 2.2 ppm O_3 at 95% RH.

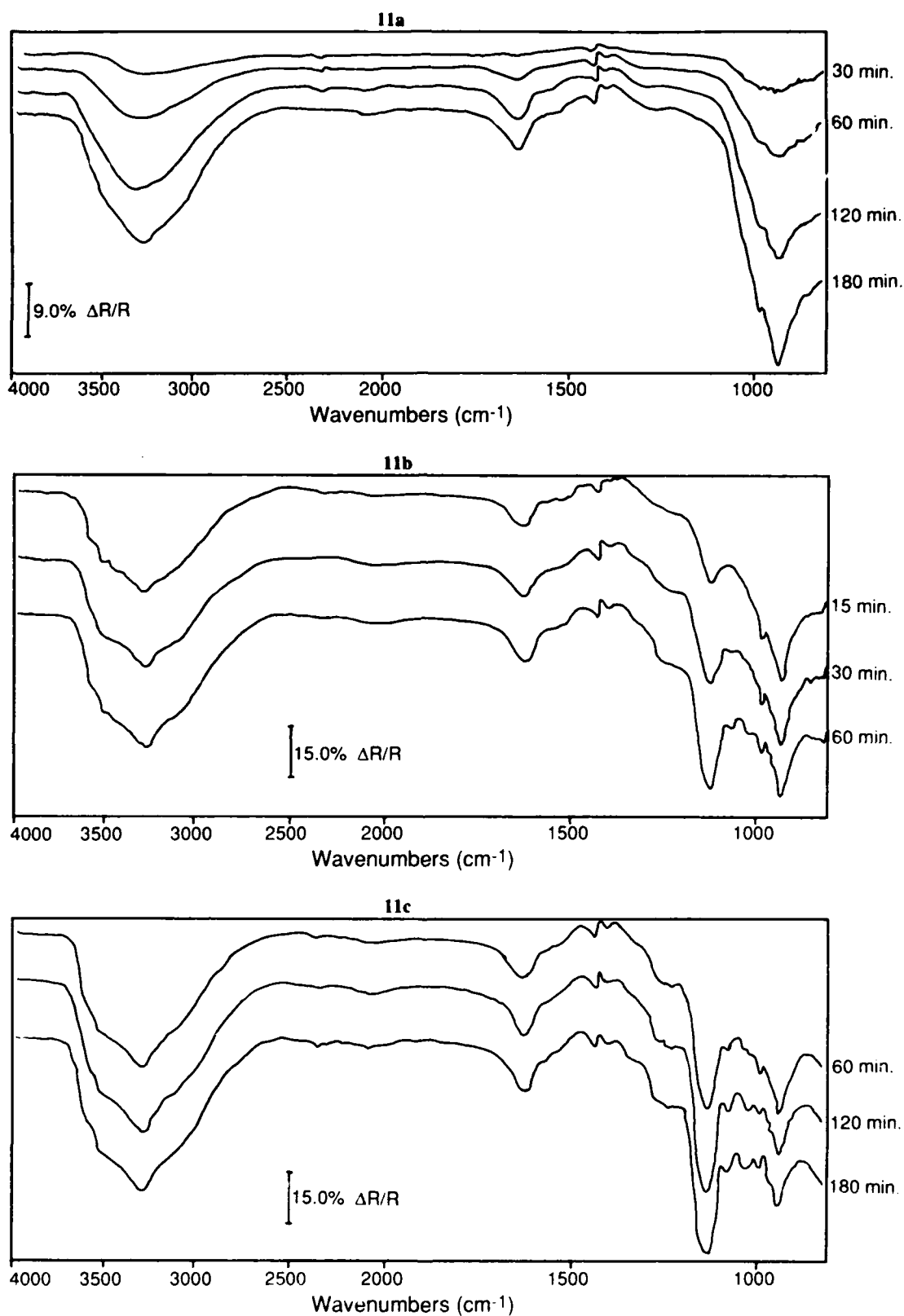


Figure 11a. Diffuse reflectance IR spectra of ZnO exposed to 10 ppm SO₂ at 95% RH for 30, 60 120 and 180 minutes, respectively. **Figure 11b.** Diffuse reflectance IR spectra of ZnO first exposed to 10 ppm SO₂ in 180 minutes and then to 10 ppm NO₂ for 15, 30 and 60 minutes respectively. **Figure 11c.** Same as figure 11b except for exposure time which is 60, 120 and 180 minutes respectively.

Table 1. Vibrational frequencies for sulphur-oxygen species in the region 1400 to 800 cm^{-1} .

Compound	Observed frequencies (cm^{-1})
$\text{ZnSO}_3 \cdot 3\text{H}_2\text{O}^{\text{a}}$	971sh, 948s, 925sh, 889sh
$\beta\text{-ZnSO}_3 \cdot 2.5\text{H}_2\text{O}^{\text{a}}$	1010sh, 975s, 900s
$\gamma\text{-ZnSO}_3 \cdot 2.5\text{H}_2\text{O}^{\text{a}}$	1037w, 1007w, 911s, 869s
$\text{ZnSO}_4 \cdot 7\text{H}_2\text{O}^{\text{b}}$	1152s, 1104s, 1007w, 983w
$\text{ZnSO}_4 \cdot 3\text{Zn}(\text{OH})_2 \cdot 5\text{H}_2\text{O}^{\text{b}}$	1153s, 1122s, 1080sh, 1027w, 966m

s=strong, m=medium, w=weak, sh=shoulder

a) Ref. (7)

b) this work

Galvanic Corrosion of Zinc/Steel Under Thin Layer Electrolytes

X.G. Zhang

COMINCO Product Technology Centre
Sheridan Park
Mississauga, ON
Canada L5K 1B4

E.M. Valeriotte

COMINCO Product Technology Centre
Sheridan Park
Mississauga, ON
Canada L5K 1B4

Abstract

The potential and galvanic current distributions of a zinc/steel couple under thin layer electrolytes of dilute Na_2SO_4 were measured using a coplanar galvanic cell, and were found to be sensitively dependent on electrolyte thickness, electrolyte concentration, steel surface area, and distance between zinc and steel. On steel, potential varied strongly but current was relatively constant across the surface. On zinc, the potential varied little but the current changed sharply across the surface. The anodic current was mostly concentrated at the edge of the zinc electrode closest to the zinc/steel boundary. The galvanic protection distance for steel and the galvanic corrosion current of zinc were quantitatively determined for the various parameters of the system.

I. Introduction

As a corrosion resistant material, galvanized steel has been used in many applications, such as in building construction and automobile bodies. Since in most natural environments zinc corrodes much more slowly than steel, by a factor of 5 to 100 times, the life of a galvanized steel structure is greatly increased compared to bare steel [1].

Numerous studies have been made on the corrosion resistance of zinc and zinc coated steel [2-6]. While most of the data are on the corrosion of zinc, relatively few studies have focused on the galvanic corrosion process for galvanized steel. The principles and theoretical understanding of the galvanic corrosion of two electrically connected metals are well documented, but the various parameters involved in the galvanic corrosion of zinc coated steel have not been quantitatively studied.

One important aspect of zinc coated steel is that it is mostly used in atmospheric environments where corrosion occurs under a thin layer of electrolyte during wetting-drying cycles. Experimental results have shown that the corrosion rate of metals under a thin layer electrolyte is very different from that in the bulk of solution [7-9]. Also, experimental results have indicated that the solvation capacity of a thin layer electrolyte for the dissolved species is very limited, which can affect the formation process of the corrosion products [10].

This paper reports experimental results on the galvanic action of a zinc/steel couple under thin electrolyte layers of various thicknesses. The potential and current distributions on electrically connected zinc and steel electrodes, lying in the same plane, with various inter-distance and surface area ratios, were measured. The objective was to obtain quantitative information on the extent of galvanic protection of steel by zinc and the galvanic corrosion rate of zinc under thin layer electrolyte conditions.

II. Experimental

The potential and current distributions of galvanically coupled zinc and steel electrodes were measured on the planar cell shown in Fig.1. The zinc electrodes and the steel electrodes were made of thin strips, moulded in epoxy. The purity of the zinc was 99.99% and the steel was cold-rolled low-carbon steel. The size and the number of electrodes, as well as the spacing between the electrodes, varied for each particular set of experiments, as will be described in the text.

The epoxy cell containing the zinc and steel electrodes was ground to #600 emery paper. The horizontal top edges of the cell were bordered by a polyimide tape (0.06 mm in thickness) to confine the electrolyte. The size of the electrodes was considerably smaller than the area defined by the borders. Na_2SO_4 solutions of different concentrations, prepared with deionized water, were used as electrolyte in the experiments. The thickness of the electrolyte was determined using a pipet to deliver a pre-determined volume, which was uniformly spread over the specimen

surface.

To obtain the potential distribution, the local electrode potential was measured relative to a saturated calomel reference electrode (SCE) using a high impedance voltmeter. The reference electrode half cell included a Luggin capillary, which was filled with the test solution and had a tip about 0.2 mm in diameter. The galvanic current from each strip was measured using an ammeter placed in the circuit as shown in Fig.1. For polarization measurements one of the zinc strips was used as the reference electrode. Since zinc demonstrated a fairly stable electrode potential, this produced reproducible polarization data. More detailed experimental procedures are described elsewhere [17].

III. Results and Discussion

A. Potential and Current Distributions

Fig.2 shows the potential over zinc and steel surfaces as a function of the distance from the centre line of the cell (as seen in Fig.1, 4 of the 6 zinc strips were electrically connected to 4 of the 6 steel strips) in 0.001 M Na_2SO_4 solutions of three different thicknesses. The zinc and steel strips each had 0.75 mm x 20 mm exposed area and were separated by gaps of 0.3 mm of epoxy. The open circuit potentials of the zinc and steel strips were about -1050 mV_{sce} and -500 mV_{sce} respectively. As seen in Fig.2 the potentials were almost the same for the four zinc strips, but were very different for each of the steel strips. The potential of the steel strips varied with the most negative closest to the zinc strip and the most positive furthest from the zinc/steel boundary.

The galvanic current flowing through each strip was measured by connecting an ammeter in series with the strip, from which the galvanic current distribution was obtained as shown in Fig.3. The current on the zinc strips was anodic and that on the steel strips was cathodic. Among the zinc strips, the one closest to the boundary had much higher current than those more distant from the boundary, showing an uneven current distribution. However, for the steel strips the current was distributed relatively equally.

The potential distribution of two coupled metal electrodes is determined by the characteristics of the anodic and cathodic polarization and the resistance of the electrolyte. For zinc, the anodic reaction is due to the dissolution of zinc which is an activation controlled process, while for steel the cathodic reaction under polarization up to around the zinc potential is predominantly controlled by the diffusion of oxygen. By knowing the open circuit potentials of the zinc and steel, the percentages of anodic polarization, cathodic polarization and ohmic potential drop between the zinc and steel electrodes can be estimated. As shown in Fig.2, the anodic polarization of all zinc strips is within 20 mV with the one closest to the steel boundary the most positive. The steel strip which is 1.4 mm from the middle line is taken as an example to discuss the ohmic contribution. Considering an electrolyte 320 μm in thickness, from Fig.2 it is seen that the ohmic potential drop between the zinc and steel strips is about 100 mV. Since the

potential difference between the open circuit potentials of zinc and steel was about 550 mV, then the cathodic polarization of this steel strip was about 430 mV. The percentages of the anodic and cathodic polarizations and ohmic potential drop were therefore about 4%, 78% and 18% respectively. As for the strips further away from the zinc, the contribution of ohmic potential drop became larger and that of cathodic polarization became smaller.

The current and potential distributions on the surface of a coplanar galvanic cell have been theoretically analyzed by Waber [12]. A polarization parameter, having a dimension of length [13], was used to characterize a galvanic corrosion cell and was defined as

$$L_i = 1/\rho \left| d\eta_i/dI_i \right| \quad (1)$$

where ρ is the specific resistivity of the electrolyte; I_i is the current density and η_i is the overpotential of the anode or the cathode. According to Waber, whether the anode and cathode behave "microscopically" or "macroscopically" is determined by the ratio of a dimension of either electrode C_i , divided by the polarization parameter L_i . The mathematical modelling indicated that, when the ratio C_i is small, the variation of current density over an electrode is small, i.e., the electrode behaves microscopically. In contrast, when the characterizing ratio is large, i.e., when the electrode dimension is much larger than L_i , the electrode process is regarded as macroscopic, and the variation of current density over the electrode surface is large.

In the present case, since the anodic reaction was activation controlled, the polarization resistance was a function of the current. At a typical current density of around $100 \mu\text{A}/\text{cm}^2$ the anodic polarization resistance of zinc $d\eta_a/dI_a$ was determined, from the anodic polarization curve, to be about $150 \Omega/\text{cm}^2$. Considering that for 0.001 M Na_2SO_4 solution ρ is about $4100 \Omega\text{-cm}$, the anodic polarization parameter L_a can be calculated from equation (1) to be 0.037 mm. For the cell shown in Fig.1, the dimension (C_a) of the anode (4 zinc strips) is 3.2 mm measuring from the centre of the cell and the ratio of C_a/L_a is 87, which is much larger than 1, meaning that the zinc anode should behave macroscopically and the current density variation over the anode should be large (as confirmed in Fig.3).

The cathodic reaction was diffusion limited and the polarization resistance was estimated from the cathodic polarization curve of the steel to be of the order of $10^5 \Omega/\text{cm}^2$ or larger. The polarization parameter is then $L_c > 24 \text{ mm}$ and $C_c/L_c < 0.13$, which is a small value indicating that the steel electrode behaved microscopically and the variation of the current over the steel surface was small as can be seen in Fig.3.

B. Effect of Electrolyte Thickness

It is seen in Fig.2 that electrolyte layer thickness does not have a noticeable effect on the potential of the zinc strips but has a large effect on that of the steel strips. One effect is to increase the resistance of electrolyte. On the zinc side the current density is very small over the whole surface except near $x=0$. Variation in electrolyte resistance will have very little effect on the potential distribution on the zinc surface. On the other hand, the current density through

the electrolyte on the steel surface is a relatively constant value. A decrease in the electrolyte thickness will lead to a significantly larger potential change over the steel strips as seen in Fig.2. Variation of electrolyte conductivity through changing the concentration has similar effect [17].

Another effect of electrolyte layer thickness is on the reaction rate of oxygen reduction which is limited by oxygen diffusion through the electrolyte. As can be seen in Fig.3, the galvanic current is larger for a thinner electrolyte layer. This is because of faster diffusion of oxygen through a thinner electrolyte layer. Fig.4 shows the galvanic current as a function of time for different electrolyte layer thicknesses for two electrically connected zinc and steel strips which were 1 mm apart. The galvanic current was relatively high at the instant when the zinc strip was connected to the steel. It decreased to a relatively low constant value in less than a minute. As is clearly seen, the current decreased with increasing layer thickness. It changed very little with further increase of thickness over 0.5 mm.

This dependence of the galvanic current on the electrolyte thickness is due to the change of oxygen transfer rate with thickness of the electrolyte. It is known that the cathodic reaction on steel in open air at potentials less negative than that for hydrogen evolution is due to oxygen reduction [14]. When the thickness of the electrolyte layer is near or smaller than the diffusion layer thickness, the reduction rate of O_2 is affected by changing the electrolyte thickness. The thinner the electrolyte layer, the higher is the diffusion rate of O_2 and thus the higher the cathodic current.

C. Galvanic Protection Distance (Throwing Power)

The cathodic protection of steel is determined by the potential of the steel. Around the corrosion potential steel will corrode. If the steel is cathodically polarized to a certain potential value by being galvanically connected to a piece of zinc, it will be protected and corrosion will not occur. The potential of the steel galvanically connected to zinc varies with electrolyte thickness, resistivity of the electrolyte, distance between the zinc and steel electrode, and area of the steel. In order to determine the effect of all these parameters under identical conditions a different type of cell was used.

The configuration and the definition of the parameters are schematically shown in Fig.5. D represents the distance between the inner edges of steel and zinc electrodes, W the width of the steel electrode, and x the distance from the inner edge of the steel electrode. By using cells with the zinc strip at different distances from the steel, the effect of distance, D , on the potential of the galvanically connected steel was characterized. By using steel electrodes of different sizes the effect of steel area on the potential of galvanically connected steel was examined. The dimension of the zinc electrode in the x direction is not controlled since, as shown previously, the current on the zinc was concentrated in a very small region, within 1 mm of the steel under a thin layer electrolyte, and the variation in the width of zinc electrode wider than 1 mm has hardly any effect on the potential or current distribution.

Fig.6 shows the potential at a position close to (at $X < 1$ mm) the edge of the steel electrode,

as a function of the distance between the zinc and the steel (D) for different thicknesses of 0.001 M Na_2SO_4 solution.

Based on the corrosion behaviour of steel in aerated solution, it can reasonably be assumed that little corrosion will occur when the potential of the steel is lower than $-700 \text{ mV}_{\text{acc}}$, which is about 200 mV more negative than the corrosion potential of steel. This potential value is then used as a criterion to estimate the galvanic protection distance of zinc for steel. As illustrated in Fig.6, taking the distance value, D , of each curve at $-700 \text{ mV}_{\text{acc}}$, the protection distances for the steel at $x < 1 \text{ mm}$ under different thickness of electrolyte are obtained. For example, as indicated in Fig.6, the protection distance in 0.001 M Na_2SO_4 was about 4 mm for a 1 mm wide steel strip under a 0.17 mm electrolyte, and it was about 47 mm under 1.36 mm thick electrolyte.

Using the same procedure, the protection distances for the steel surface at different x values for different steel widths and different solution concentrations were obtained. Fig.7 (a) shows a three dimensional plot of the protection distance for 0.01 M Na_2SO_4 solution. It is clearly seen that the protection distance increases as the electrolyte thickens or the steel strip narrows. Note that the protection distance changes less when the steel is wider than 20 mm, especially for thinner electrolyte layers. The protection distance for the steel surface at position $x = 5 \text{ mm}$ is shown in Fig.7 (b). Compared to Fig.7 (a), one can see that the protection distance for the steel surface at $x = 5 \text{ mm}$ is much smaller than at $x < 1 \text{ mm}$. When the steel strip becomes wider and the electrolyte layer thickness becomes thinner, the galvanic protection does not extend very far from the edge of the zinc steel boundary. For example, from Fig.7 (b) and Table II it can be seen there is no protection for the steel surface at $x = 5 \text{ mm}$ for a steel electrode 20 mm wide under a 0.01 M Na_2SO_4 electrolyte thickness of 0.17 mm.

Fig.7 (c) and Fig.7 (d) are the protection distances for 0.001 M Na_2SO_4 solution at $x < 1 \text{ mm}$ and $x = 5 \text{ mm}$ on the steel surface respectively. Compared to 0.01 M Na_2SO_4 solution the protection distance is much smaller. Note also that it gets even smaller at the steel surface which is 5 mm away from the edge of the electrode compared to that at the edge, i.e. at $x < 1 \text{ mm}$.

D. Galvanic Corrosion of Zinc

Galvanic corrosion of zinc occurs when it is electrically connected to steel in electrolyte. The galvanic current is thus a measure of the galvanic corrosion rate of the zinc. Fig.8 shows the galvanic current as a function of the width of the steel strip (W), the thickness of the electrolyte (t), and the distance between the zinc and steel electrodes (D) for 0.01 M Na_2SO_4 solution. The galvanic current is high when the zinc is close to the steel. It decreases as the distance between the zinc and the steel becomes larger (compare Fig.8 (a), (b), (c)), and this is more pronounced for thinner electrolyte layers than for thicker ones. It is so because when the cell scale is relatively small and the zinc is close to the steel, the cathodic current on the steel is limited by diffusion of oxygen to the steel surface [17]. As the zinc becomes more distant from the steel, the galvanic current becomes limited by the ohmic resistance of the solution, resulting in a

decrease of the total galvanic current.

The current increases sharply with steel strip width up to about 10 mm according to the result in Fig.8 (a). As the example shows, when the width of the steel strip increases to a certain value, the overall galvanic current actually decreases especially for thinner electrolyte. This is a rather interesting result. This is because increasing the width of steel will increase the reaction area, but at the same time will increase the ohmic resistance contribution which will change the potential distribution. When it is ohmic-resistance-controlled the cathodic current on steel can be much smaller than the limiting oxygen diffusion current [17]. Thus, as the width of the steel gets larger, the current density becomes smaller on the area which is more distant from the zinc/steel boundary. At a certain width, further increasing the width of steel electrode will actually result in a decrease of the total galvanic current.

According to the current distribution on the zinc surface (Fig.3), galvanic corrosion of zinc concentrates on the narrow edge which is closest to the steel. This has an important implication for the corrosion of galvanized steel in which the coating has limited thickness. It means that if a piece of galvanized steel is in touch with a piece of bare steel in a coplanar way under a thin layer of electrolyte, corrosion of the zinc coating will only occur at the edge of contact and will proceed in the direction away from the contact line.

The above is a systematic study of the effects of parameters involved in galvanic action for a zinc/steel couple. It provides a general understanding and quantitative estimate for the galvanic protection of steel and the corrosion of zinc under a thin electrolyte layer, e.g. under atmospheric conditions. In real situations, other factors may also play roles, such as the accumulation of corrosion products and formation of a passive layer, which can greatly change the overall reaction kinetics.

IV. Conclusions

The galvanic current and potential distributions of zinc and steel electrically connected in a coplanar cell under a thin aqueous layer of Na_2SO_4 electrolyte are reported. They were found to be sensitively dependent on the concentration of the electrolyte, the thickness of the layer, the area of the steel surface, and the distance between the zinc and the steel.

Except for concentrated solutions and thick electrolyte layers, the galvanic current over the zinc electrode was concentrated at a narrow edge closest to the steel, resulting in a very steep spatial current distribution. Over the steel electrode, except for a very thin electrolyte layer or for a large scale electrode, the current density was relatively constant. The potential was almost constant over the zinc surface. It remained within 40 mV of the corrosion potential of the zinc and changed little with the solution concentration, electrolyte thickness or the size of the steel electrode. On the other hand, the potential varied significantly over the steel surface, from a value close to the zinc corrosion potential to the corrosion potential of the steel, and sensitively changed with electrolyte concentration, electrolyte thickness, area of the steel surface and the

distance between steel and zinc.

The protection distance for steel galvanically connected to zinc was quantitatively determined for the various parameters involved in the system. The protection distance was found to increase with increasing conductivity of the electrolyte and with decreasing surface area of the steel. The galvanic corrosion rate of zinc increased with the area of steel up to a certain size, then decreased slightly with larger area. It decreased sharply as the distance between zinc and steel increased. The width of the zinc had little effect on the protection distance or the galvanic corrosion of the zinc.

References

1. "Zinc: Its Corrosion Resistance", International Lead-Zinc Research Organization Inc., New York, (1983)
2. H. Guttman, "Metal Corrosion in the Atmosphere", American Society for Testing and Materials, STP435, 223 (1968).
3. G.W. Walter, Corrosion Science, **16**, 573 (1976).
4. V. Kucera and E. Mattsson, in "Atmospheric Corrosion", Ed. W.H. Ailor, 561, John Wiley and Sons, New York, (1982).
5. Ichiro Suzuki, "Corrosion-Resistant Coating Technology", Marcel Dekker Inc., New York, (1989).
6. Z. Zembura and L. Burzynska, Corrosion Science, **17**, 871 (1977).
7. I.L. Rosenfel'd, First International Congress on Metallic Corrosion, 243, London, April, (1961).
8. M. Stratmann and H. Streckel, Corrosion Science, **30**, 697 (1990).
9. M. Stratmann, H. Streckel, K.T. Kim and S. Crockett, Corrosion Science, **30**, 715 (1990)
10. D.C. Stiles and E.O. Edney, Corrosion, **45**, 896 (1989).
11. E. Kennard and J.T. Waber, J. Electrochem. Soc., **117**, 880 (1970).
12. J. Waber, in "Localized Corrosion", Eds. R. Staehle, B.F. Brown, J.Kruger, A. Agrawal, 221, NACE, Houston, (1974).
13. C. Wagner, J. Electrochem. Soc., **98**, 116 (1952).
14. H.H. Uhlig and R.W.Revie, in "Corrosion and Corrosion Control", 91, John Wiley and Sons, New York, (1984)
15. J.A. Dean, in "Lange's Handbook of Chemistry", 10-5, McGraw-Hill, New York, (1985).
16. K.E. Gubbins and R.D. Walker, Jr., J. Electrochem. Soc., **112**, 469 (1965).
17. X.G. Zhang and E.M Valeriot, submitted to Corrosion Science for publication.

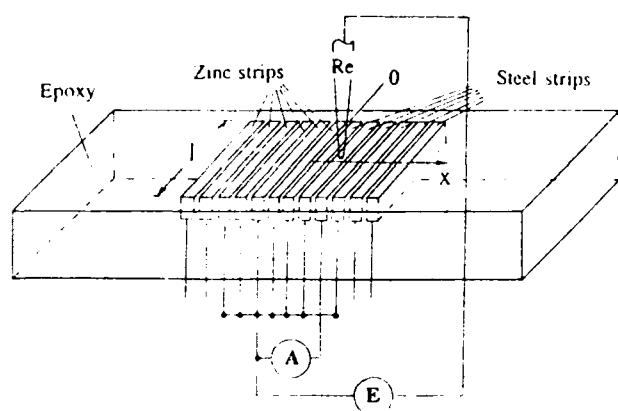


Fig.1 Schematic representation of the galvanic cell used for measuring potential and current distribution.

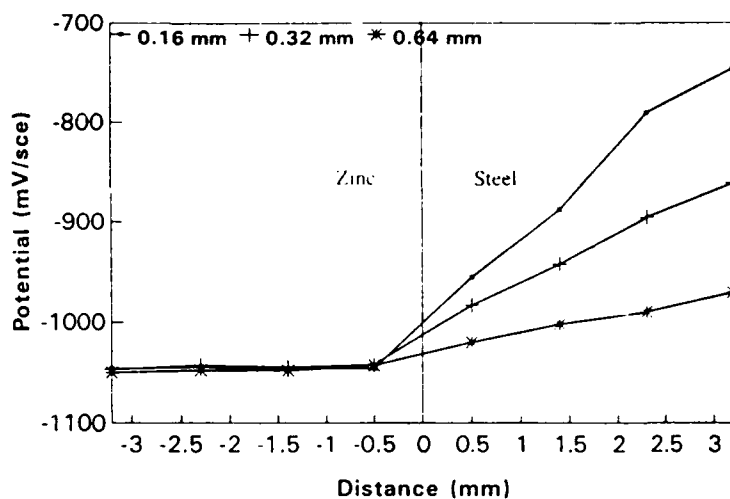


Fig.2 The potential distribution on a zinc/steel surface as a function of electrolyte thickness in 0.001 M Na_2SO_4 solution.

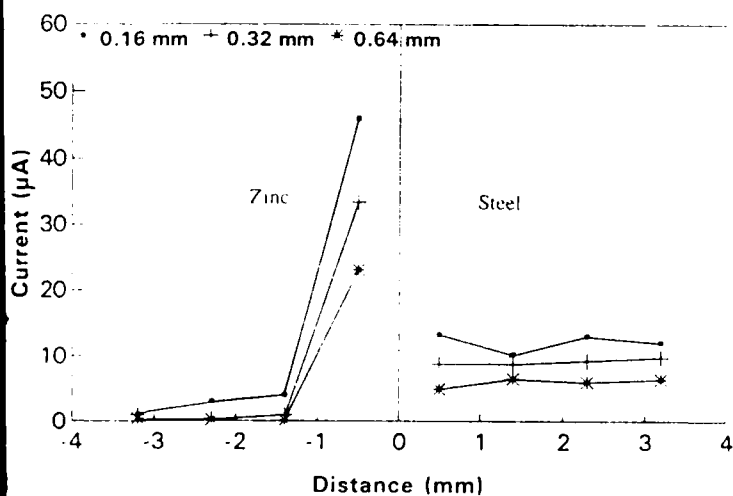


Fig.3 The current distribution on a zinc/steel surface as a function of electrolyte thickness in 0.001 M Na_2SO_4 solution.

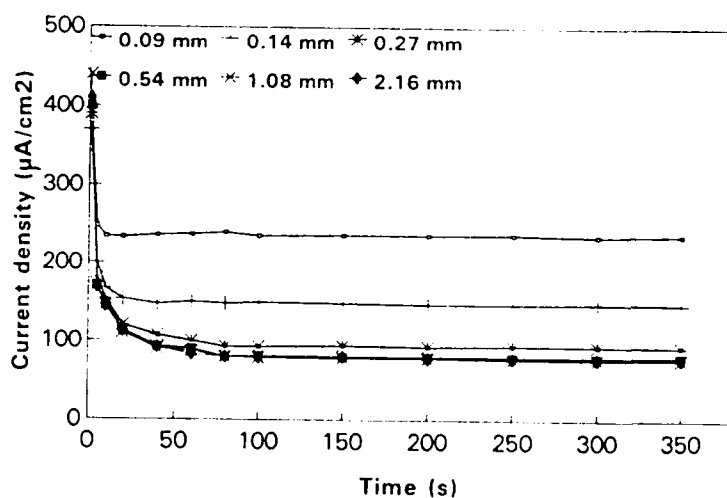


Fig.4 Galvanic current density versus time curves as a function of electrolyte thickness measured in 0.01 M Na_2SO_4 on two electrically connected zinc and steel strips which were 1 mm apart.

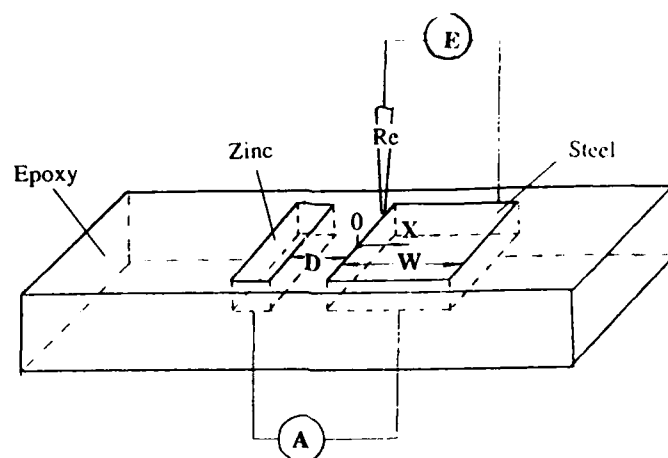


Fig.5 A schematic representation of the electrochemical cell used for obtaining data on protection distance and galvanic corrosion current; D the distance between the zinc and the steel electrode, W width of the steel electrode, and X the position on the steel electrode.

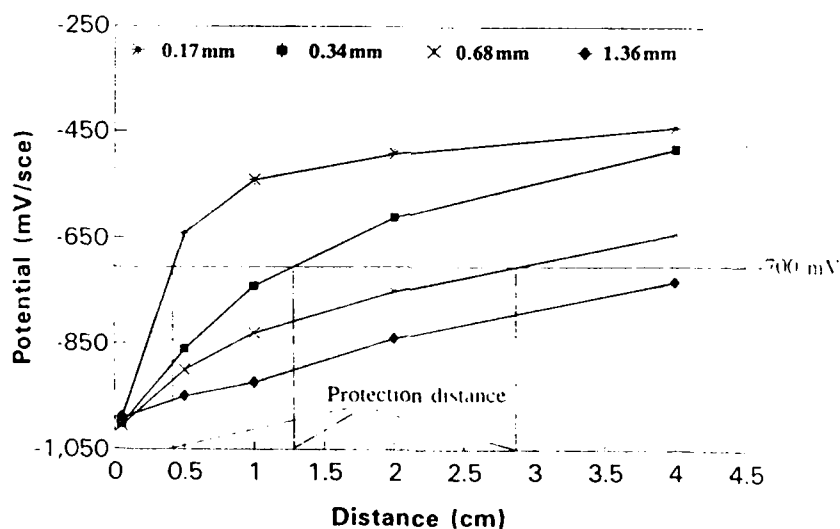


Fig.6 The potential at $x < 1$ mm as a function of the distance between the zinc and the steel in 0.001 M Na_2SO_4 solution for different electrolyte thicknesses for a steel width of 1 mm.

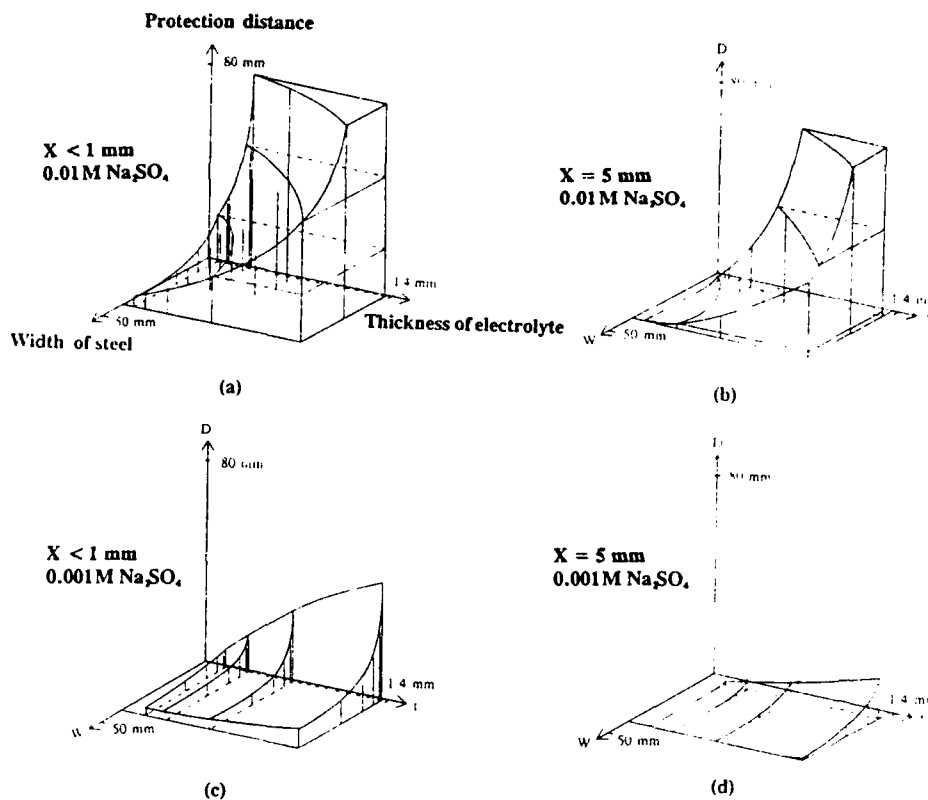


Fig.7 Three dimensional plots of the galvanic protection distance for steel at two different positions on the steel surface and two different concentrations of the solutions.

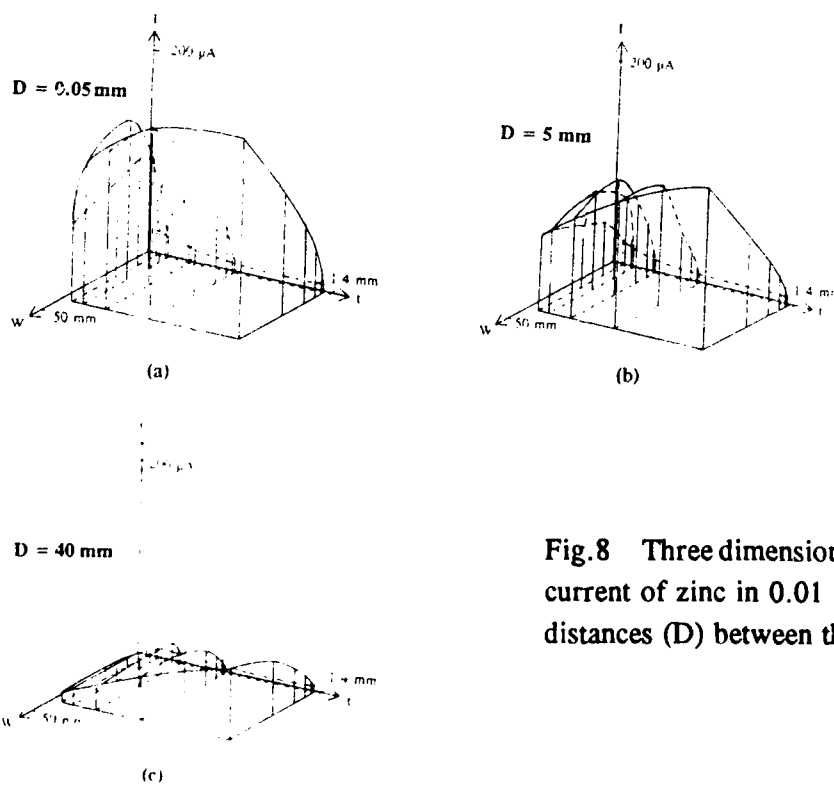


Fig.8 Three dimensional plots of the galvanic corrosion current of zinc in $0.01 \text{ M Na}_2\text{SO}_4$ solution for different distances (D) between the zinc and the steel.

Experimental Approaches to the Study of Corrosion in Thin Water Layers

V. Brusic
IBM Research Division
T.J. Watson Research Center
P.O. Box 218
Yorktown Heights, NY 10598

G. S. Frankel
IBM Research Division
T.J. Watson Research Center
P.O. Box 218
Yorktown Heights, NY 10598

T. A. Petersen
IBM Research Division
T.J. Watson Research Center
P.O. Box 218
Yorktown Heights, NY 10598

S-M. Huang
Dept. of Chemical Engineering
University of Minnesota
Minneapolis, MN 55455

Abstract

Evaluation of the corrosion rate by electrochemical techniques is direct and precise, but not readily applicable to conditions of atmospheric corrosion. This paper assesses several experimental approaches that were used in an attempt to bridge the benefits of electrochemical testing and the challenges presented by corrosion reactions under a thin layer of an electrolyte.

Key words: Corrosion, Electrochemical tests, Thin layer electrolytes

Introduction

Although the thermodynamics, electrochemical nature and kinetic principles of corrosion reactions are well understood (1, 2), corrosion continues to be poorly predictable and a sensitive function of the environment. Electrochemical techniques can provide a measure of the corrosion behavior for samples exposed to bulk electrolytes. However, the use of a standard three-electrode electrochemical cell for corrosion evaluation under thin layers of electrolytes or under the conditions of atmospheric corrosion is not straightforward. Electrolytes involved in atmospheric corrosion vary in thickness from several monolayers of water to condensation droplets. Several experimental approaches have been suggested (3-8). One of the more interesting methods has been the use of the Kelvin Probe in atmospheric corrosion (5-8), which can be applied to the thinnest of electrolytes. This paper discusses some aspects of the Kelvin Probe technique, as well as two other set-ups that were developed in our laboratory to evaluate

corrosion under a thin layer of an electrolyte by electrochemical techniques: three electrode air-tight cell for corrosion measurement under 100% relative humidity (RH) and a miniature cell for corrosion measurement in a droplet of water.

I. Metallic Corrosion in Air with 100% RH

A. Samples, Experimental Set-up and Procedure

Tests were performed in an air-tight cell, built with a KEL-F (3M, St. Paul, MN) body containing quartz windows. The cell itself was designed to be a part of an ellipsometric table, and to allow an ellipsometric characterization of the surface in conjunction with other measurements. Samples were prepared by evaporation of two different metallic film stripes, separated by 2 mm, on a single glass slide. Each film was 50 mm long, 5 mm wide and about 200 nm thick. One of the films was the metal to be studied, while the other was in all cases an Au film serving as a counter-electrode. The glass slide dimensions were 65x20 mm so that one end of each slide, with an area of 15x20 mm, was free of any metal. The sample holder provided spring-loaded, air-tight, connections to the Au and sample stripes, while holding the slide in a vertical position. The tip of the metal-free end of the slide was immersed in water at the bottom of the cell, which also contained a reference electrode, Figure 1. The following metal stripes were tested: Co, Cu, Al, Nb, W, Zr, Ti and 80Ni-20Fe. Prior to tests, samples were held in a dry nitrogen box and used without any surface pre-treatment.

The geometry of the sample and its position in the cell were dictated by the desire to make simultaneous electrochemical and ellipsometric measurements. With the sample in position, the cell was placed on the ellipsometric table, and readings were taken while dry nitrogen or oxygen was bubbled through the water. When the bubbling was stopped in a closed system, a thin layer of adsorbed water covered all surfaces and provided an electrolytic connection for the three electrodes; the working electrode (metal/alloy of choice), Au counter electrode and reference electrode. The open circuit potential became measurable about a minute after the bubbling stopped. During the next 15 minutes, the surface was monitored by ellipsometric changes and the open circuit potential was recorded. After 15 minutes, cathodic currents (from 10^{-9} to 1 A/cm^2) were applied and the change of potential was recorded. At the end of the cathodic Tafel line measurement, the bubbling of dry gas was resumed, with continued measurements of ellipsometric parameters. The cathodic Tafel lines were corrected for IR drop (with ohmic resistance measured separately by an Impedance Bridge).

B. Corrosion Rate under an Adsorbed Water Layer

1. Thickness of the adsorbed water - Under 100%RH, a surface water film could be several water layers thick, or visibly present as condensation. In our tests, water uptake on all of the tested samples was accompanied by a decrease of the ellipsometric parameter Δ by an amount ranging from 0.2° (measured on Co) to 2.14° (measured on Nb) and a corresponding increase of the parameter Ψ varying from 0.05° to 0.28° . An example of the time variation of $d\Delta$ is given in Figure 2 for aluminum. The data indicate that the initial film grows linearly

with time, before acquiring a much slower, logarithmic growth rate. The overall change is small, indicating that the newly formed surface films are very thin. In this case, the observed change in Δ is linearly related to the film thickness, with the proportionality constant depending on the refraction index of the film. If the film is solely adsorbed water, with a refraction index of 1.338, a decrease of 1° in Δ corresponds to an average film thickness of about 1 nm. Thus, the measured water thickness in all cases has to be less than 2.5 nm. In reality, a part of the observed change could be also caused by accumulation of oxidation products. This is supported by the irreversibility of the observed change upon subsequent drying. Most likely, water adsorbs and corrosion reactions lead to the formation of dissolved salts, which are left on the surface upon drying.

2. Metallic Corrosion Potential and Corrosion Rate in 100%RH. - Data for Cu and Ni-20%Fe are given in Figure 3. The corrosion potentials of the two metals are higher in O_2 than in N_2 , as would be expected. The corrosion rate for Cu is higher in O_2 than in N_2 , while for NiFe the trend is just the opposite. This can be explained by the ability of the NiFe alloy to passivate. The corrosion rates for Cu are about two orders of magnitude higher than for NiFe.

These measurements are affected by errors in ohmic resistance. The IR corrected cathodic current-potential curves exhibited diffusion limiting currents that were, in contrast to expectations, significantly lower than measured in bulk electrolytes with a well defined diffusion layer (see below). This indicates that the correction resistance was possibly too low. However, the same errors were applicable to all measurements, yet the data clearly indicate that the cathodic currents were always higher in O_2 , as expected. This (and other trends in the data) lends credibility to the approach.

II. Corrosion Tests in a Droplet of Water

A. Procedure

Following a report on the use of wet filter paper in electrochemical corrosion measurements (4), we designed a set-up to mimic the conditions of atmospheric corrosion while preserving the advantages of a three electrode cell (9). Figure 4 shows a schematic of the cell. The set-up consists of the sample (working electrode) masked with plating tape to expose a 0.32 cm^2 area, Pt mesh (counter electrode), and a mercurous sulfate electrode (reference electrode), with a filter paper disk separating each electrode. The procedure was as follows: The sample was placed on a small jack, and the working area, covered with a tightly fitted filter paper and a flat Pt mesh, was maneuvered into a center of the opening of a vertically positioned and a rigidly held Beckmann fitting. The inner diameter of the fitting was 8 mm, i. e. large enough to easily expose the entire working area that has a diameter of 6.4 mm. The sample was then raised and kept in place at a hand-tight pressure against the fitting. The second filter disk was then dropped over the working area. A droplet of electrolyte was introduced with an Eppendorf pipette, and the reference electrode was positioned over the sample using the fitting as a holder. A typical droplet size was $20\text{ }\mu\text{l}$. Due to small distances between the electrodes, the ohmic resistance in the cell was relatively small

even with electrolytes such as deionized and triple-distilled water. As the ohmic resistance of the cell was only about 800 Ω in the first seconds of measurement, insignificant errors in the evaluation of corrosion rates are introduced. The procedure was to monitor the corrosion potential for about 15 min and periodically measure the polarization resistance by scanning the potential ± 20 mV from the corrosion potential at 1 mV/s. The corrosion rate was calculated assuming anodic and cathodic Tafel slopes of 0.1 and 0.12 V/dec, respectively. The potentiodynamic polarization curve was then measured at a rate of 1 mV/s from 0.25 V cathodic of the corrosion potential. Polarization resistance measurements in a mild electrolyte such as water are particularly suitable for the study of thin films. In contrast, much or all of this film can be dissolved during potentiodynamic sweeps, but such tests are quite informative as the ability of a metal to passivate and possible galvanic exposure can be assessed.

B. Corrosion Potential and Rate in a 20 μ l of Electrolyte

An example of a linear polarization curve is given in Figure 5 for copper in water, measured one minute after water was added. The corresponding corrosion rate is 8×10^{-6} A/cm². The corrosion rates of Cu and NiFe in a droplet of water were found to be about 1000x faster than those measured in 100% RH as described above. Interestingly, the corrosion rate for Cu was still about 100x higher than that for NiFe, or Al, as measured under 100% RH. It is also interesting to note that the linearity of the measured dV/dI curves, which is expected from the basic kinetics, is not jeopardized by the technique, as visible on the Cu example. If and when a departure from the linearity is measured, it is caused by electrode reactions, such as formation of passive oxides, and not by IR drop of the cell. The results of potentiodynamic tests are illustrated in Figure 6 for Cu in water and 1.5% acetic acid. The measured cathodic rate is clearly diffusion controlled, as expected for dissolved O₂, and the overall corrosion reaction is apparently under cathodic control.

Although this electrochemical cell is small, the observed O₂-diffusion current is expected: the thickness of the two filter paper disks and a Pt mesh is about 0.55 mm, thus slightly higher than the diffusion layer thickness of a static electrolyte, 0.5 mm (10). The calculated value of the diffusion-limited current, with δ of 0.5 mm, the diffusivity of the metal ions, D, of 10^{-5} cm²/s and oxygen concentration of 1.2×10^{-6} mol/ml (11) amounts to

$$i_{\text{lim}} = zFDc/\delta = 5 \times 10^{-5} \text{ A/cm}^2.$$

This value is close to that observed in acetic acid. At this pH level, the Cu surface is oxide-free and fully available for oxygen reduction. The lower value of i_{lim} measured in water might be explained by the presence of native oxides at neutral pH, which provide a marginal hindrance to corrosion reactions. The data are in excellent agreement with published work, illustrating that the electrode kinetics in a droplet of water are similar to the kinetics measured in a bulk electrolyte.

The technique has many practical applications. It is easily used for evaluation of the corrosion behavior of a given metal in different electrolytes, in a variety of pH's, in solutions which would otherwise need special containers (such as HF and BHF), in water with or without inhibitors, etc., or for a comparative evaluation of different metals which might be candidates for the fabrication of a particular product. One criticism of the technique could be that, when the water is used, the electrolyte is quickly changed by corrosion reactions, and thus it seems to be poorly controllable. However, such a change is quite natural in atmospheric corrosion, when the adsorbed water quickly becomes a part of corrosion reactions, as well as a solvent for available pollutants. This technique has been utilized in our laboratory for an evaluation of corrosion mechanisms in thin film magnetic disks (9), characterization of AlCu exposed to reactive ion etching and a variety of cleaning steps (12), determination of solder behavior in a broad pH range (13), and evaluation of inhibitors, such as benzotriazole and its derivatives, for corrosion protection of copper (14). Some of the results, obtained for a variety of metals in water, will be discussed in section III.

III. Kelvin Potential of Metals in Humid Atmosphere

A. Apparatus and Measurement

In recent years, Strattmann and co-workers (5-8) have applied a well established technique of surface potential measurement, the Kelvin Probe, to corrosion measurements. A schematic of the apparatus is given in Figure 7. An audio-frequency current is fed into a small disk vibrator mounted parallel to the sample surface and 10-100 μm above it. When both metals are connected, their Fermi levels are identical. The two surfaces form a condenser, the capacity of which oscillates with the motion of the vibrator, resulting in an AC current in the circuit:

$$i_{AC} + dQ/dt = \Delta\Psi dC/dt$$

with $\Delta\Psi$ being the Volta potential difference between points just outside the sample/electrolyte and the vibrator. If a battery of voltage V is added to the circuit, then the Fermi levels of the two metals differ by the voltage of the battery and $\Delta\Psi$ is altered by:

$$i = (\Delta\Psi - V) dC/dt.$$

When $V = \Delta\Psi$, the AC signal vanishes. Signal amplification, analysis and nulling allow measurement of the Volta potential to an accuracy of about 1 mV.

The Kelvin potential has been correlated to the corrosion potential both by experiments with flooded electrodes as well as by fundamental electrochemical arguments (5, 8). However, it is not known if this correlation is valid for electrolyte layers only a few tenths of a nm thick.

B. Application of Kelvin Probe to Metals Exposed to Different RH

Using a Ag/AgCl probe, which has been shown to be more stable than Au or Pt (15), Kelvin potentials were measured for a variety of metals in air with RH varying from 0 to 80% at room temperature. The measured potentials decreased with increasing humidity on all samples examined thus far. An example is given in Figure 8 for Cu. The Kelvin potential obtained at 80% RH for several metals is plotted against the corrosion potential measured in water for the same samples in Figure 9. The slope of a straight line fitted to the data is close to 1. This indicates that the fundamental electrochemical arguments indeed apply to the thinnest of electrolytes. The correlation suggests that the corrosion potential of metals decreases with increasing RH. The corresponding corrosion rate was not measured. However, we can assume that the corrosion rate increases with RH. Using this assumption and the theory behind Evans diagrams (16) in data evaluation, the data indicate that, under thin electrolyte (several monolayers of water), the corrosion reaction is controlled by the anodic and not the cathodic reaction. This is illustrated in Figure 10, with a schematic of an Evans diagram for the corrosion reaction under activation control. The change in corrosion reactions, described with an increase of the corrosion rate and a decrease of the corrosion potential, can be explained by a progressive increase of the exchange current for the anodic reaction, proportional to the exodus and hydration of Cu-ions. The reaction rate is apparently limited to the amount of water available for complexing Cu-ions. For Co and metals to its right in Figure 9, the cathodic partner of the metal dissolution is oxygen reduction. The thickness of the adsorbed water should be small (between less than 1 monolayer for RH=0.1 and about 10 monolayers for RH=0.8 (17)), and thus oxygen reduction should be activation controlled and much faster than measured in bulk electrolytes. Assuming that oxygen reduction is equally fast on all metals, the relative change of the potential with humidity could indicate the extent by which the anodic reaction of each metal changed as the humidity increased. In a way then, the change of the Kelvin potential with humidity is proportional to the vulnerability of metals to corrosion. Assuming that 1) metal dissolution kinetics is activation controlled with a Tafel slope of 60 mV/decade (as for example Cu dissolution in water), 2) an increase of water on the surface changes i_0 for metal dissolution and not the dissolution mechanism, and 3) that oxygen reduction proceeds by an activation controlled kinetics with a Tafel slope of 120 mV/decade, then each 40 mV decrease in potential corresponds to an increase in metallic dissolution of 10x. The difference in the Kelvin potential measured at 0% RH and 80% RH, ΔKPV , varied from 18 mV on Zr and Hf to about 230 mV measured on Cu. We did not evaluate the corrosion rate corresponding to Kelvin potential measurement. Instead, Figure 11 shows the measured ΔKPV plotted against the corrosion rate measured on the same metals in a water droplet. There seems to be a correlation, indicating that metals with a higher corrosion rate in water also show a larger change of KPV with an increase of humidity. However, the sample size is fairly small, and much more work is needed to better understand this relationship.

Final Remarks

Three techniques were presented, two of which were developed in our laboratory, in an attempt to apply rigorous electrochemical techniques to a quantitative evaluation of corrosion processes under thin electrolyte layers. The results show some level of correlation. Of the three techniques presented here, the droplet cell is by far the simplest set-up and is amicable to an application of the basic electrochemical measurements for an evaluation of the corrosion reactions in thin electrolyte layers. The technique can be used with much of the versatility normally associated with electrochemical corrosion testing, except that it is limited to measurements in stagnant electrolytes. However, the thickness of the electrolyte, 0.55 mm, is large compared to the thickness of adsorbed water in a humid atmosphere.

The attempt to use a standard reference electrode in a combination with the thin film working and auxiliary electrode was successful, at least at 100% humidity. The technique is limited by the evaluation of the ohmic resistance and in this respect it should be improved with a use of a more sensitive, in situ measuring technique.

Kelvin Probe measurements of corrosion potential are applicable to a variety of systems, corrosive environments and electrolyte thicknesses. The results on metals exposed to a controlled levels of humidity seem to be comparable to the data obtained with the three-electrode cell in water. Wider application of this method could both broaden our understanding of corrosion reactions and evaluate their effects in thin films electrolytes.

Acknowledgments - The authors are thankful to R. D. MacInnes for his work on corrosion under 100% RH, and to R. Oriani, S. Yee, R. T. Atanasoski, and M. O'Boyle for many useful discussions.

References

1. M. Pourbaix "Atlas of Electrochemical Equilibria in Aqueous Solutions" Pergamon Press, New York (1966).
2. J. M. West "Electrodeposition and Corrosion Processes", D. Van Nostrand Co., London (1965).
3. N. D. Tomashov, G. K. Berukshtis and A. A. Lokotilov, *Zavod. Lab.*, **22**, 345 (1956).
4. M. Smallen, P. B. Mee, A. Ahmad and W. Freitag, Paper No. EA-09 presented at InterMag. Conference, St. Paul, MN (1985).
5. M. Stratmann, *Corr. Science*, **27**, 869 (1987).
6. M. Stratmann and H. Streckel, *Corr. Science*, **30**, 691, 697 and 715 (1990).
7. M. Stratmann, M. Wolpers, H. Streckel and R. Feser, *Ber. Bunsenges., Phys. Chem.* **95**, 1365, (1991).
8. S. Yee, M. Stratmann, and R. Oriani, *J. Electrochem. Soc.*, **138**, 55 (1991).
9. V. Brusic, M. Russak, R. Schad, G. Frankel, A. Selius, D. Dimilia and D. Edmonson, *J. Electrochem. Soc.*, **136** 42 (1989).
10. J. O'M. Bockris and A. K. N. Reddy, "Modern Aspects of Electrochemistry", Volume 2, Third Printing, Plenum Press, New York (1972).

11. J. M. West, "Basic Corrosion and Oxidation", Ellis Horwood, Ltd., Division of Wiley & Sons, New York (1980).
12. V. Brusic, G. S. Frankel, C-K. Hu, M. M. Plechaty and B. M. Rush, *Corrosion*, **47**, 35 (1991).
13. V. Brusic, D. D. DiMilia and R. D. MacInnes, *Corrosion*, **47**, 509 (1991).
14. V. Brusic, M. A. Frisch, B. N. Eldridge, F. P. Novak, F. B. Kaufman, B. M. Rush and G. S. Frankel, *J. Electrochem. Soc.*, **138**, 2253 (1991).
15. R. T. Atanasoski, University of Minnesota, Minneapolis/St. Paul, MN, private communication.
16. M. G. Fontana and N. D. Greene, "Corrosion Engineering", McGraw-Hill Book Co., New York (1967).
17. B. Phipps and D. Rice in "Corrosion Chemistry", G. Brubaker and B. Phipps eds., ACS Symposium Series 89, Am. Chem. Soc., Washington D. C. (1979).

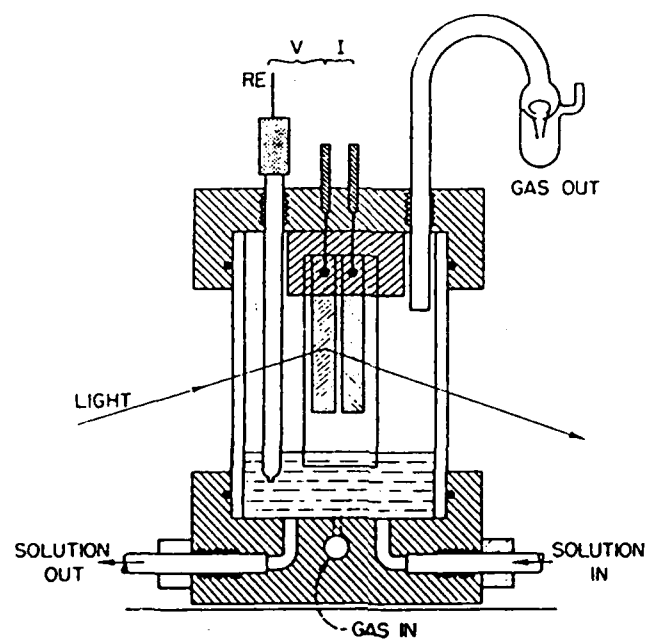


Figure 1. Cell for corrosion evaluation in wet atmosphere (100% RH).

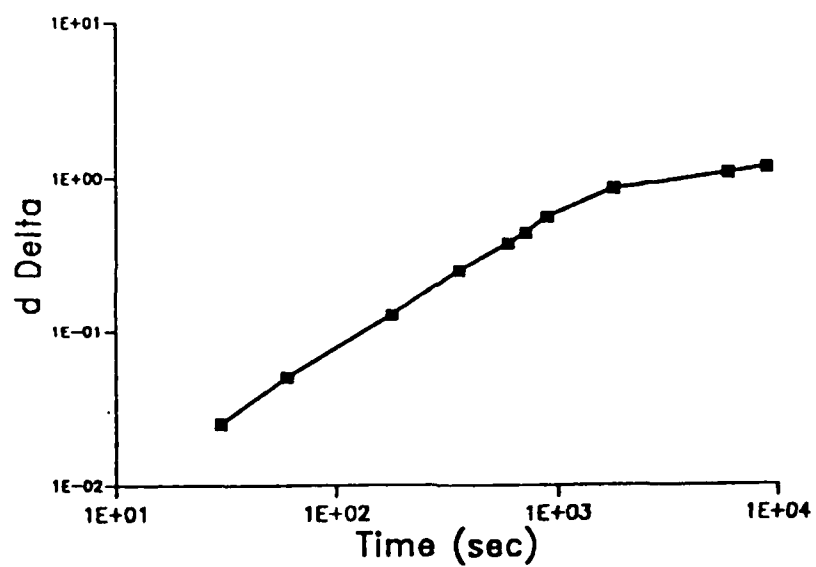


Figure 2. Change of ellipsometric parameter Δ with uptake of water on Al during the first 15 minutes in 100% RH.

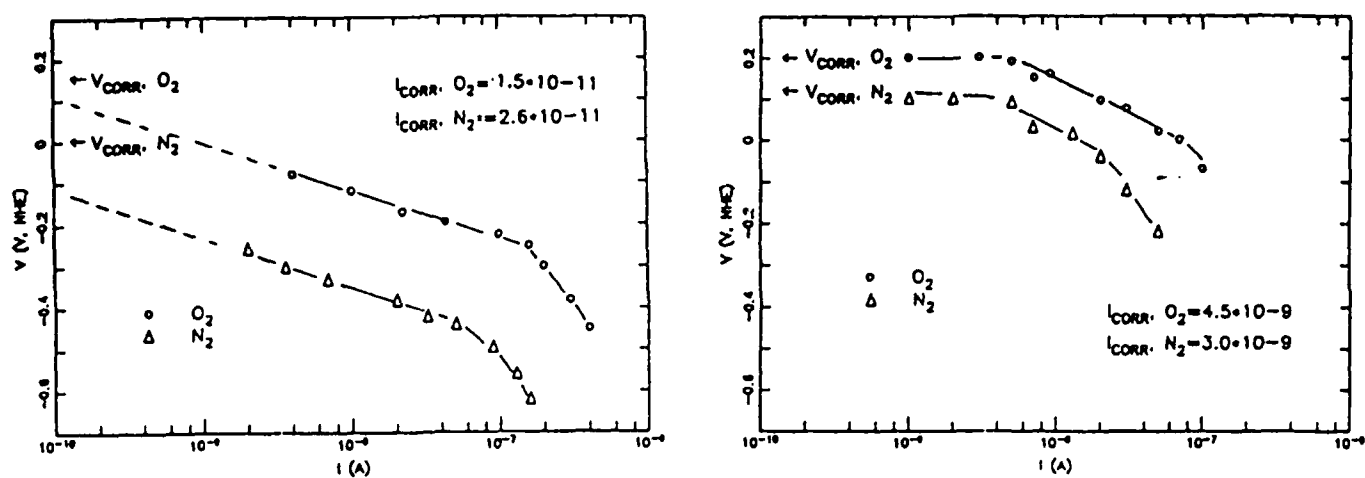


Figure 3. Corrosion potential and rate evaluated for NiFe (left) and Cu (right) in wet atmosphere (100% RH)

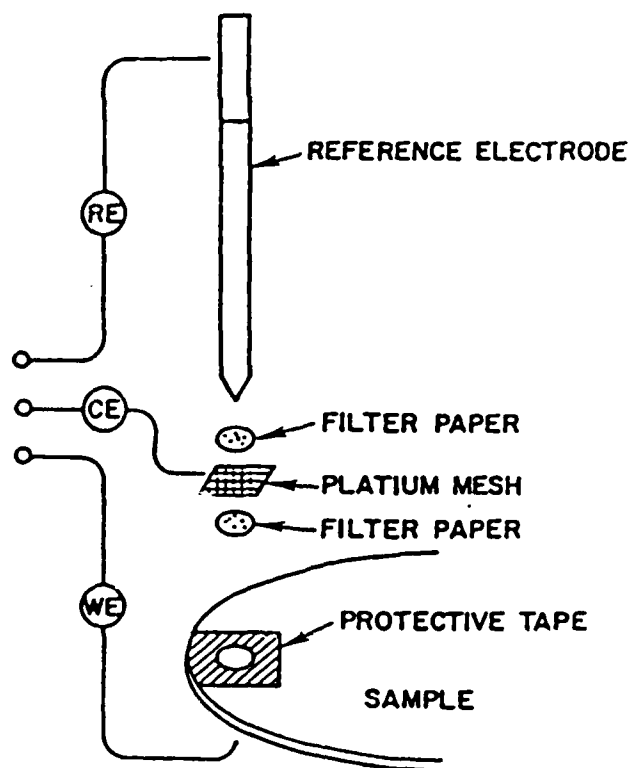


Figure 4. Schematic drawing of a three-electrode cell for corrosion evaluation in a droplet of an electrolyte.

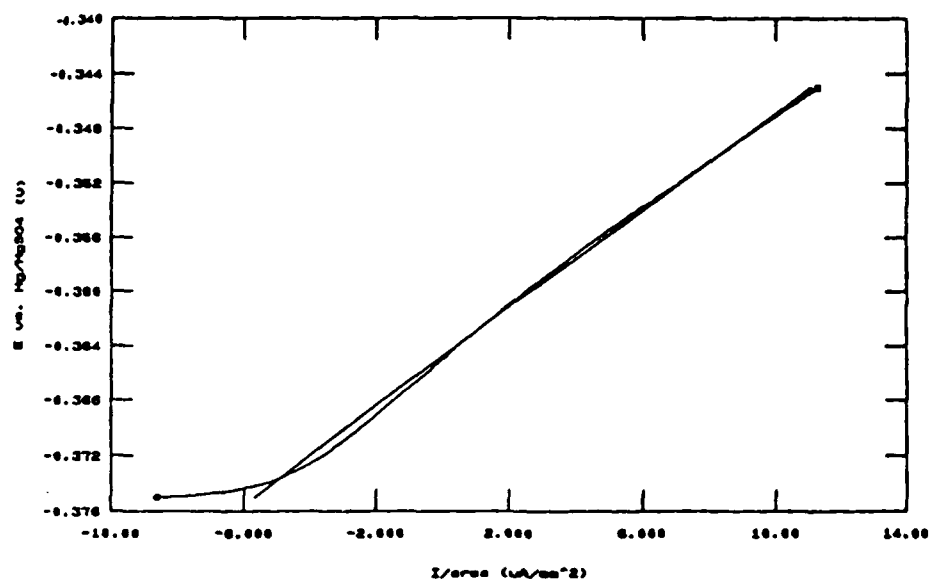


Figure 5. Linear polarization curve measured on Cu, 1 min after addition of a water droplet.

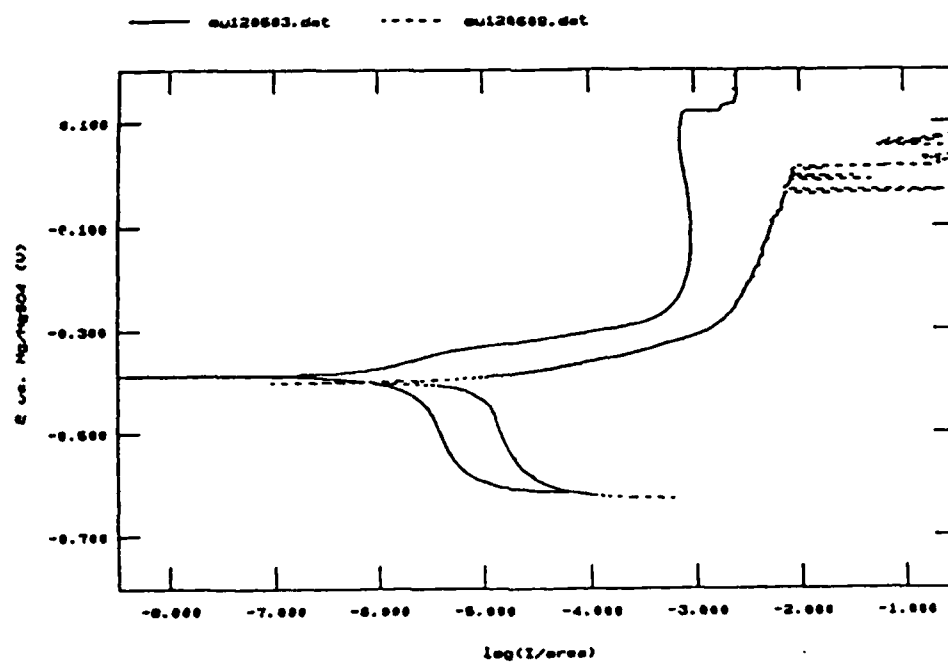


Figure 6. Potentiodynamic polarization curve for Cu in a droplet of water and acetic acid.

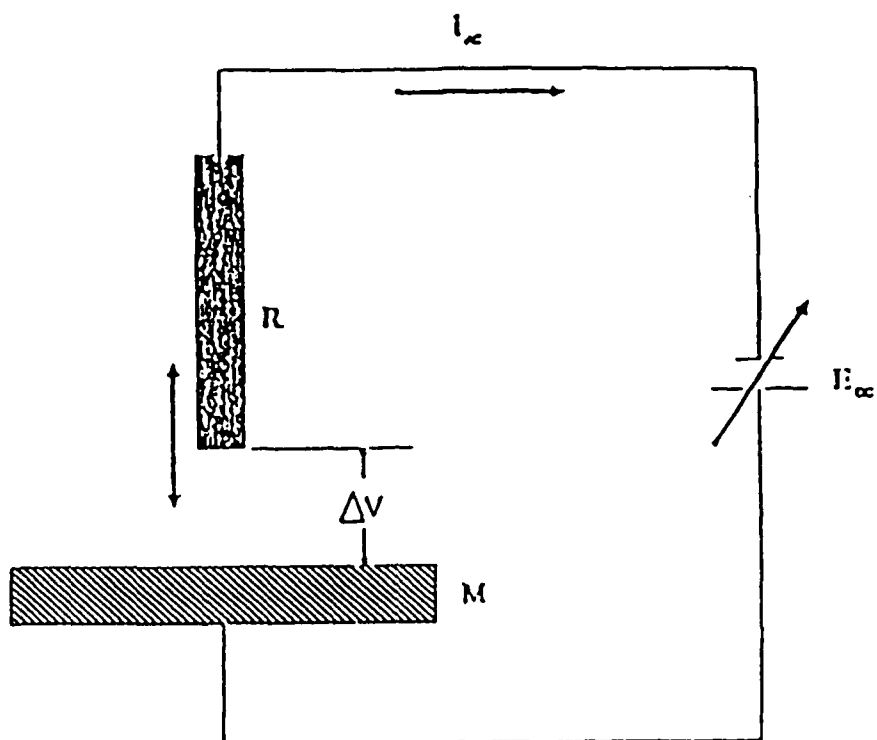


Figure 7. Schematic of Kelvin Probe

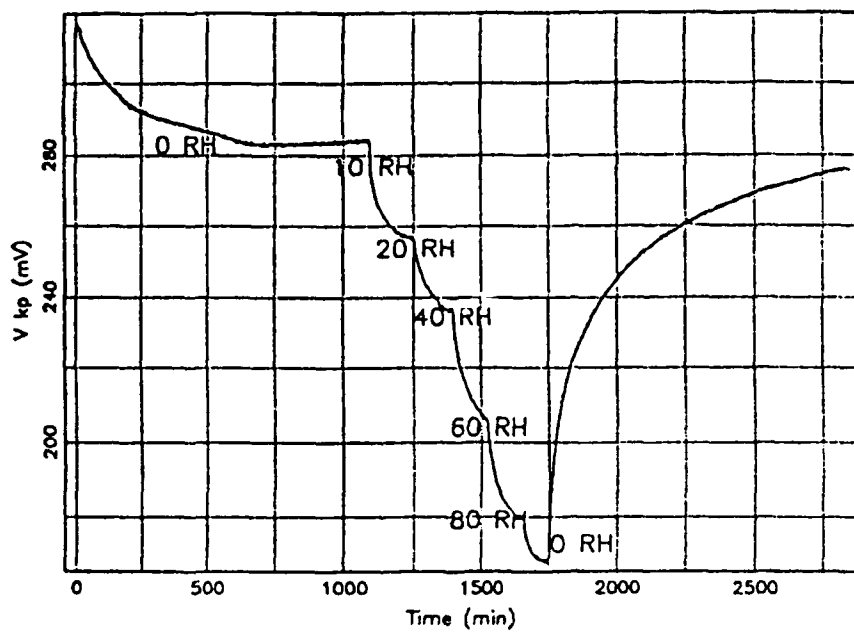


Figure 8. Variation of Kelvin potential measured on Cu in air with 0 to 80% relative humidity.

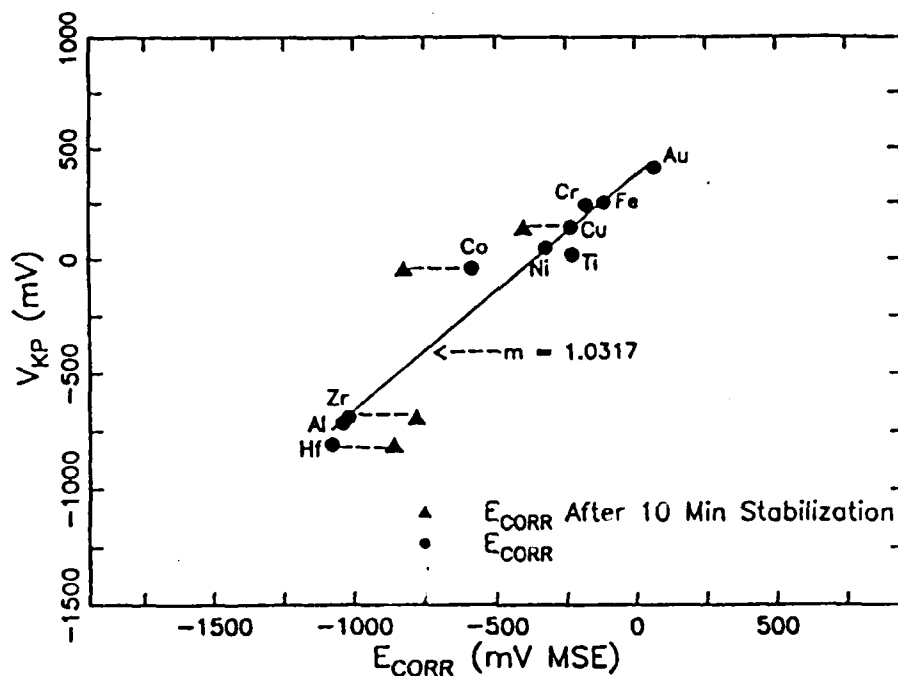


Figure 9. Variation of Kelvin potential measured in air with 80% RH in respect to the corrosion potential measured in a droplet of water on the same samples.

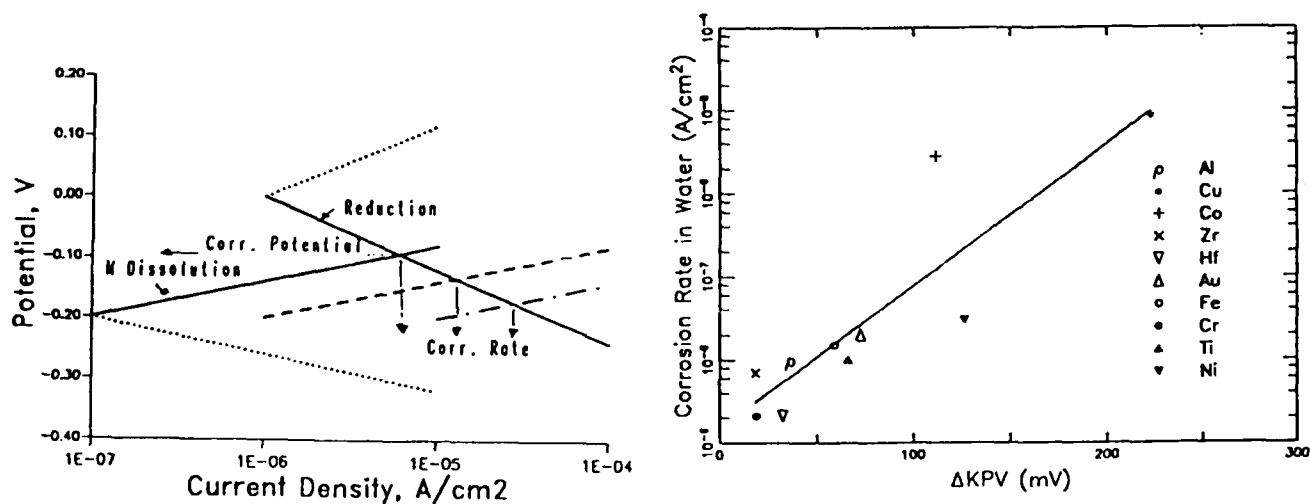


Figure 10. Evans diagram showing an increase of the corrosion rate and a decrease of the corrosion potential as the anodic exchange current density increases.

Figure 11. Variation of ΔKPV (measured at 0 and 80% RH) with the corrosion rate measured on same metals in water, 1 min after the contact.

Simulation of the Degradation of Limestones and Dolomitic Sandstone Under Dry Deposition Conditions

Shahid J. Haneef
Corrosion and Protection Centre
UMIST
P.O. Box 88
Manchester M60 1QD
United Kingdom

John B. Johnson
Corrosion and Protection Centre
UMIST
P.O. Box 88
Manchester M60 1QD
United Kingdom

George E. Thompson
Corrosion and Protection Centre
UMIST
P.O. Box 88
Manchester M60 1QD
United Kingdom

Graham C. Wood
Corrosion and Protection Centre
UMIST
P.O. Box 88
Manchester M60 1QD
United Kingdom

Abstract

A laboratory-based exposure rig has been employed to quantify the effects of the dry deposition of individual pollutants (SO_2 , NO_2 and NO), with or without ozone (O_3), on the degradation of limestones and dolomitic sandstone. In addition to employing dry stones, wetting of the stones has been used to study effects of moisture on deterioration processes. Presentation rates of pollutants have been selected to be realistic and represent atmospheric conditions encountered in the U.K. From the equivalent calcium yields calculated, quantifying the extent of reaction, the importance of pollutant gas solubility in surface water and oxidants for pollutant gas transformations to the respective acids on the limestones and dolomitic sandstone are revealed.

Electron-optical examinations reveal the importance of porosity, and physical characteristics of the stone surface, on the deterioration of stones. Compact stones lead to formation of a 'sulphate crust' on the surface, whereas porous stones allow ingress of salts to within the stones, thus aiding crystallisation related damage. Results indicate that simulation of actual outdoor degradation processes is achieved, in terms of types and degree of deterioration of samples. The exposure chambers also allow acceleration of degradation of stones (in some instances upto 3 x reality), without using unrealistic pollutant presentation rates.

Key terms: Stone degradation, exposure chambers, dry deposition, pollutant gases, oxidants.

Introduction

Monuments undergo many forms of deterioration in the external environment¹, although it is difficult to separate precisely the effects of natural weathering from those of anthropogenic pollutants². A number of studies have shown the importance of CO₂ in the degradation of stones, particularly in wet deposition conditions³. The acceleration of decay in recent decades has been attributed to the increase in man-made pollutants, above the natural levels⁴. The most important pollutants in stone decay are sulphur dioxide (from oil and coal combustion)⁵ and oxides of nitrogen (from automotive exhausts)⁴. Such pollutants are transported to stone surfaces by dry and wet deposition processes⁶. The former entails the turbulent gas transport and adsorption/absorption processes on stone surfaces (wet or dry), whereas the latter involves deposition of the pollutants, as oxidized or species dissolved in atmospheric moisture, during rain events. Pollutants delivered by turbulent processes (dry deposition) attack a greater proportion of the material surface than do large particles and precipitation, for which sheltering can limit the actual extent of deposition. Factors influencing gaseous deposition are the concentration of the pollutant in air, the turbulent transfer process, moisture presence, and the chemical and physical nature of the material; as well as the interaction of pollutants and oxidants.

Much importance, therefore, is attached to national and international exposure programmes that have been established to assess the responses of a range of materials to various external environments³. However, the number of variables involved and their lack of control; makes difficult the determination of the relative importance of individual factors. It is thus necessary to complement field work with controlled laboratory exposures to measure the effect of one variable while maintaining other parameters constant, as well as studying the interaction of pollutants to evaluate any synergistic effects. Such results may be used to formulate damage mechanisms and improve mathematical models and hence predict rates of material degradation⁷.

In this paper the effects of dry deposition of SO₂, NO₂ and NO pollutant gases are studied in controlled environments, with a view to use more complex mixtures of pollutants to ascertain individual effects and pollutant gas interactions.

Experimental

Design Philosophy. The interaction of an anthropogenic pollutant with a material entails consideration of many factors, eg pollutant concentration in the atmosphere, which may range widely in value, both temporally and spatially, and wind velocity with respect to the surface. Presentation rates of pollutants, defined as the rate at which gases are presented to the surface of materials per unit area per unit time⁸, are probably the best method of simulating pollutant concentrations in external conditions. Due to the high wind speeds possible outside, exposure chambers must employ concentration of pollutants which, at first sight, seem unrealistically high. However, comparison of the presentation rates used in the chambers and the environment shows good agreement. Other factors that are important in dry deposition processes are the relative humidity and water present on and in the stones, both of which are addressed in the current study.

Exposure Rig. The atmospheric flow rig consists of four exposure chamber units (Figure 1), each comprising a perspex box, of dimensions 470 x 150 x 150 mm, into which the polluted atmosphere at controlled humidity ($84\% \pm 2\% \text{ RH}$) and temperature ($292 \pm 2 \text{ K}$) is passed at 0.083 l s^{-1} . The volume concentrations of the individual pollutants was 10 vppm enabling realistic presentation rates (as compared to the external environment) ($16.2 \times 10^{-6} \text{ mg cm}^{-2} \text{ s}^{-1} \text{ SO}_2$, $8.02 \times 10^{-6} \text{ mg cm}^{-2} \text{ s}^{-1} \text{ NO}_2$, $7.41 \times 10^{-6} \text{ mg cm}^{-2} \text{ s}^{-1} \text{ NO}$ and $11.83 \times 10^{-6} \text{ mg cm}^{-2} \text{ s}^{-1} \text{ O}_3$). In addition to using dried stones (in reality coming to equilibrium with the air stream), the flow chamber allows wetting of the stones by means of peristaltic pumps; CO_2 -equilibrated de-ionised water was employed for wetting the stones. A wetting rate of $2.5 \times 10^{-6} \text{ ml cm}^{-2} \text{ s}^{-1}$ was employed, which is equivalent to the average rainfall rate in the U.K. Run-off was collected weekly and analyzed for calcium and magnesium, as well as for pH changes. Water was fed into the chamber, and directly onto the stone specimens, for 8 h followed by 16 h of drying at the ambient rig temperature. The wetting and drying cycles were repeated daily for the 30 d exposure period. An important feature of the exposures was that use of the peristaltic pumps ensured uniform wetting of appropriate specimens throughout the exposures. As anticipated, the same trends as previous work are achieved where wetting led to local channelling of stones.

Sample Preparation. Portland limestone, Massangis Jaune Roche limestone and White Mansfield dolomitic sandstone were chosen for exposure, due to their wide use as building materials in Europe, and cut into the required dimensions using a petrographic diamond saw, with water as lubricant. Before exposure, the stone samples ($50 \times 30 \times 5 \text{ mm}$) were washed in de-ionized water and dried at $328 - 333 \text{ K}$ until constant weight was achieved, or, in reality when two consecutive weighings, separated by 24 h drying period, were within $\pm 0.05\%$.

Analyses. The run-off solutions obtained from the wetted stones were collected weekly and analyzed for calcium and magnesium by flame emission spectrophotometry and atomic absorption spectrometry, respectively.

After exposure, the stone samples were again dried to constant weight and the weight change determined. Triplicate sample exposure allowed the following examinations to be performed:

- i) One sample was ground to powder and the anions (sulphates and nitrates) extracted in hot water, this procedure extracted 98 % of anions from within the stones. The filtrate thus obtained was analyzed by high performance liquid chromatography (HPLC).

- ii) Petrographic thin sections of the stones were prepared and examined by optical and electron-optical techniques.

Results

The stones were exposed to realistic presentation rates of SO_2 , NO_2 or NO , with or without ozone. Stones were either dry (ie coming to equilibrium with the 84 % RH) or wetted with CO_2 -equilibrated de-ionized water. In considering the various stone types, the stones are termed 'dry' or 'wetted', the former indicates the absence of flowing water and the latter the presence of flowing water over the surface of the stone. But regardless of the state of the stone surface, the pollutant gases are transported to the stones by dry deposition processes.

Weight Changes. Data are presented for the exposed surface area of 1500 mm^2 . Weight changes are a qualitative guide as to the reactivity of the gases towards the stones and should be treated as such, to quantify deterioration processes it is necessary to take into account

other parameters (anion contents of stones, calcium in run-off etc.).

Dry Stones: The weight changes of the stones after the 30 d exposure period reveal weight gains in all cases (Figure 2a); the relatively small weight increases suggest that little reaction proceeds over the selected period of exposure. In the additional presence of ozone significantly greater weight increases are observed.

Wetted Stones: For the wetted stones, exposures to SO₂ reveal weight increases whereas exposures to NO or NO₂ indicate weight losses (Figure 2b), although the weight losses are relatively small compared with large weight gains for other conditions. Since the weight change measurements in these instances are a combination of weight gains (reaction products) and weight losses (dissolution), the extent of reaction cannot be measured from the weight change alone.

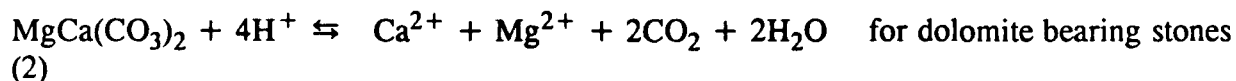
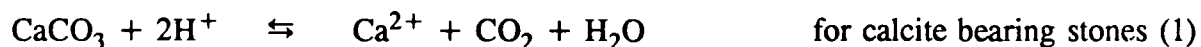
The trends of weight gains for exposures involving SO₂ and weight losses in NO₂ or NO exposures are maintained with the addition of ozone (Figure 2b). Exposures of SO₂, in the presence of ozone, lead to comparatively large weight gains for all stones. Weight losses for NO₂ and NO, in the presence of ozone, are slightly greater than for individual gases.

Retained Anions

Dry Stones: All stones show retained sulphates or nitrates (Figure 3), and a dramatic increase is seen in the presence of ozone, eg for Massangis limestone SO₂ exposures alone show sulphate retention in the order of 10 mg per stone sample; whereas, in the presence of ozone the sulphate concentration has increased to above 60 mg per stone sample.

Wet Stones: Significant quantities of sulphates and nitrates were detected for exposures involving SO₂ and NO₂ (20-50 mg per stone sample); however, exposure to NO results in reduced levels of nitrates than dry stones(0.1-2.0 mg per stone sample for wetted stones as compared to 5-20 mg per stone for dry exposures). With the addition of ozone further increase in sulphates is evident (25-130 mg). For NO exposures the presence of ozone significantly increases the concentration of nitrates extracted from the stones (20-50 mg).

Run-Off Analyses The run-off solutions were analyzed for calcium and magnesium. Concentrations of calcium in the run-off are greatest for exposures involving SO₂. In addition magnesium is evident in the run-off for Mansfield sandstone. In the presence of ozone dramatic increase in calcium (and magnesium for Mansfield sandstone) are evident (Table 1). The reaction can be represented by the following general reaction:



The above equations show only the effects of acid-base reactions (H⁺ derived from dissolution and/or oxidation of pollutant gases in the moisture films on stones), calcium in solution may also be derived from other processes eg CO₂ related dissolution, and particulate loss from stones. Analysis of run-off solutions for particulates, by neutron activation analysis, shows virtually no particulates. As for CO₂ related dissolution, this is most important in relatively pollutant free environments (during rain events) and is thus not considered here.

Electron-Optical Analyses The most readily evident change is the presence of a sulphate crust (determined by SEM/EDX analysis), on the exposed surface and lining the pores (Figure 4), in exposures involving SO₂ pollutant gas. For NO/NO₂ exposures no crust formation is evident, however roughening of the exposed surface is noted, due to dissolution of the highly soluble nitrates.

General Observations Exposures of the different stone types to the pollutants results in weight changes and the presence of the respective oxidized species ie sulphates and nitrates on or within the stones (Figure 4). The additional presence of the oxidant ozone enhances anion retention, indicating the efficacy of this species in oxidizing the pollutant gases. Absence of sulphite and nitrite suggests that if these were present at some time during reaction they have been oxidized to sulphates and nitrates. Other researchers have, however, detected sulphites on samples exposed to SO₂ alone, and nitrite leached from NO₂ exposed samples⁹. In the present work combination of exposure conditions and the period of drying employed leads to complete oxidation of nitrites and sulphates.

Water plays a principal role in damage to stones as well as being essential for chemical reactions, other important factors include physical characteristics of the stones and the environmental conditions. The NAPAP study has shown the importance of carbon dioxide in affecting damage towards stone, in relatively pollutant free regions; and during rain events⁶. Massangis limestone shows lower retention of sulphates than Portland limestone, due to the lower porosity of the former. This lack of porosity thus allows little transport of salts into the stones for retention. The effect can be readily seen by examination of petrographic thin sections (Figures 4(a) and 4(c)), the relatively compact stone shows a thin sulphate crust on the surface due to lack of porosity whereas the porous stone allowed ingress of salts and hence a thicker sulphate crust is formed.

To ascertain the overall role of pollutants' interaction with the stones, equivalent calcium yields have been evaluated (Table 2). these are derived on the assumption that the anions present on/in the stones have resulted from reaction of the acid concerned with the stone constituent, calcite for limestones and dolomite for the sandstone. From the concentrations of anions in the stones, equivalent calcium concentrations are calculated and added to the calcium present in the run-off solutions (where appropriate) to determine the total equivalent calcium yield in the degradation reaction. For the dolomitic sandstone, due consideration is given to the magnesium content; however, the conversion is expressed as equivalent calcium yield.

An overview of the processes can be achieved by comparing the equivalent calcium yields of the various exposures. The following features are readily identified:

Dry Stones It is evident that at these conditions little reaction has occurred for all exposures and stone types, due to the lack of a suitable medium (water) for reaction. Generally, sulphur dioxide shows enhanced reactivity as compared to the nitrogen oxides.

Wetted Stones In both the absence and presence of ozone the following order is clear; SO₂ > NO₂ ≥ NO.

For SO₂ gas both water and oxidant enhance the deterioration processes, whereas subtle differences are evident for NO₂/NO exposures. The reasons are discussed in the next section.

Discussion

The quantification of the extent of reaction allows comparison of the effects of individual pollutants; as well as the role of water and oxidants. It is recognised that at 84 % RH the dry stone surfaces carry a very thin moisture layer¹⁰ (about 2 nm thick), whereas, upon direct wetting this layer is increased to 0.2 mm¹⁰. Relatively gentle wetting was employed so as to avoid wash off of solid products and thus interfere in analyses.

Individual Pollutants. Dry stones show little reaction over the exposure period(30 d), with SO₂ being more reactive towards the stones than either NO₂ or NO. In the absence of catalysts or oxidants, the gas phase oxidation rates are extremely slow^{11,12}. The amount of sulphate extracted from the stones suggests that SO₂ undergoes catalytic oxidation after dissolution in the moisture film on the stone surface, since oxidation of SO₂ by O₂ alone is an extremely slow process. It has been shown that the stones contain sufficient quantities of transition metals, which are capable of catalysing the reactions¹³. Thus formation of the respective acids and subsequent reaction with the stones results in the formation of gypsum (and epsomite, in the case of Mansfield sandstone) and the various nitrate species. Due to the lower solubility (in the surface moisture film) of the nitrogen oxides, their reactivity is substantially reduced^{14,15}, thus; these gases may play an important role in long range pollutant effects as compared to the relatively short ranged sulphur dioxide.

For wetted stones the extent of reaction follows the same trend as the solubility of gases¹⁴. Thus, as a consequence of the greater solubility of SO₂ than the NO_x gases, an increased H⁺ ion concentration is available for reaction. For NO exposure, addition of water diminishes the reactivity of this pollutant; implying slow oxidation of this pollutant in the moisture and is thus lost to run-off prior to reaction with the stones.

Pollutants With Ozone In the presence of the oxidant(ozone) gas phase oxidation of NO proceeds most rapidly, with SO₂ being least affected¹⁴. However aqueous phase oxidation of SO₂ by ozone is greatly favoured. All stones shows the following order of reaction; SO₂+O₃ > NO₂+O₃ > NO+O₃. Additionally, while SO₂+O₃ shows constantly high levels of reaction for all the stones; high reactions for the NO_x gases are evident only for the more porous stones (Portland limestone and Mansfield sandstone). This is due to retention of dissolved nitrogen oxides in the moisture (within pores) and subsequent oxidation to nitrates within the stones.

For the 'wetted' stones the following order is observed in all cases; SO₂+O₃ > NO₂+O₃ > NO+O₃. Chemical reaction, with the additional presence of water, has increased for SO₂+O₃; whereas it has decreased for NO₂+O₃ and NO+O₃ (as compared with the dry stones). Oxidation of SO₂ by ozone in aqueous medium is a fast process and, therefore formation of sulphuric acid is favoured and subsequent reaction with calcite/dolomite leads to formation of gypsum/epsomite. The decrease of reaction of the nitrogen oxides, in the presence of water, suggests that oxidation in the surface water is rate controlling. Oxidation of NO/NO₂, in the presence of ozone, proceeds *via* the N₂O₅ intermediate¹⁶; and its' subsequent conversion to HNO₃, even in the presence of catalysts, is sufficiently slow so that it can be lost to the run off before complete reaction.

Effect of Stone Morphology Physical characteristics of the stone play an important role in the deterioration processes. Porosity, in particular, can influence the development of a moisture film and sites for reaction. Even for dry stones, the stones of higher porosity

showed enhanced reactivity towards the pollutant gases than the relatively compact stone (Massangis limestone). Massangis limestone shows formation of a thin crust of gypsum, with little transport of salts to the interior of the stone, whereas the porous stones show significant ingress of salts formed during exposure (Figures 4(a) and 4(b)).

The relatively thin nature of the crust formed on Massangis limestone reflects the lack of porosity in this stone and hence build up of a 'protective' layer on the surface, therefore further reaction with the stone surface is inhibited. For Portland limestone a relatively thick gypsum layer is indicative of the porous nature of the stone, thus reaction of SO_2 pollutant gas with the stone occurs throughout the duration of the test. The higher porosity of the latter also allows ingress of reaction products to within the stones.

Role of Water Water, in the form of thin moisture films or a more macroscopic surface water layer, plays a major role in stone deterioration. In addition to providing a reaction medium for calcite/dolomite dissolution, it allows dissolution of pollutants and transport to reaction sites for oxidation. For water running over the surface, the rates of chemical reactions are important; since reactants may be lost in the run-off prior to oxidation and reaction with the stones.

Surface water focuses chemical reactions in preferred regions and provides a means for removal of reaction products, which may run onto adjacent stones and provide salts for potentially damaging the stone by crystallization in the near surface regions of the stones.

Conclusions

1. Pollutant gas reactions with stones can be studied in the rigs described, and important features readily identified from measurements of weight changes, retained anion contents of stones and, where appropriate, cation losses to the run off. The total equivalent calcium yields are particularly indicative of the overall reaction between the stones and pollutant gases.
2. Comparison of results with literature indicate that SO_2 pollutant gas is not oxidized to any significant extent in the gaseous phase, with or without ozone present. The pollutant gas readily dissolves in the surface moisture films, where it undergoes oxidation by dissolved oxygen and ozone in the presence of catalysts.
3. NO and NO_2 oxidation in the gas phase, in the absence of ozone, is minimal. In addition, they dissolve only sparingly in water and thus increase in reaction is not as dramatic as for SO_2 . Ozone enhances the oxidation of these gases to NO_3 , via N_2O_5 intermediate; which hydrolyses sufficiently slowly such that flowing water may remove it prior to nitric acid formation.
4. General order of reactivity, taking into account presence of water and oxidants, can be represented as $\text{SO}_2 > \text{NO}_2 \geq \text{NO}$. Under dry conditions the low reactivity of all gases makes it difficult to assign an order of reactivity with any certainty.
5. Generally, the more porous Portland limestone and Mansfield sandstone show greater reactivity, in terms of total equivalent calcium yields, than the relatively compact Massangis limestone.

6. Total wetting of the stone surfaces leads to same general trends in the order of reactivity of the gases. Significantly, channelling of stone surfaces is avoided and a uniform reaction on the surface is attained.

Acknowledgements: The authors acknowledge support by the Commission of the European Communities, contract EV4V.0053.UK(H), Effects of Air Pollution on Historic Buildings and Monuments and the Scientific Basis for Conservation.

References

1. E. Winkler, *Engng. Geol.* 1 (1966): p. 381
2. Buildings Effect Review Group(BERG), "The Effects of Acid Deposition on Buildings and Building Materials in the United Kingdom," (London, HMSO, 1989)
3. National Acid Precipitation Assessment Program (NAPAP), Annual Report and Findings Update, Washington, DC, 1990)
4. R.A. Livingstone, N.S. Baer, "Mechanisms of Air Induced Damage to Stone," 6th World Congress on Air Quality (Paris, France , Int. Union of Air Pollution Association, 1983)
5. P. Brimblecombe, H. Rodhe, *Durab. Bldng. Mater.* 5 (1989): p. 291
6. B.B. Hicks, "Wet and Dry Surface Deposition of Air Pollutants and Their Modelling," Conservation of Historic Stone Buildings and Monuments (Washington, DC, National Academic Press; 1982)
7. T.E. Graedel, R. McGill, *Environ. Sci. Technol.* 11 (1986): p. 1093
8. J.B. Johnson, S.J. Haneef, B.J. Hepburn, A.J. Hutchinson, G.E. Thompson, G.C. Wood, *Atmos. Environ.* 24A (1990): p. 2585
9. L.G. Johansson, O. Lindquist, R.E. Mangio, *Durab. Bldng. Mater.* 5 (1988): p.439
10. K. Barton, *Protection Against Atmospheric Corrosion*, (London. Wiley, 1976)
11. A.E.J. Eggleton, R.A. Cox, *Atmos. Environ.* 12 (1978): p. 227
12. R.T. Cheng, C. Morton, J.O. Frohlinger, *Atmos. Environ.* 5 (1971): p. 987
13. C. Dickinson, S.J. Haneef, J.B. Johnson, G.E. Thompson, G.C. Wood, *Eur. Cult. Her. Newslett. Res.* 2 (1988): p. 13
14. S.J. Haneef, J.B. Johnson, C. Dickinson, G.E. Thompson, G.C. Wood, *Atmos. Environ.* 26A(1992): 2963.
15. S.J. Haneef, J.B. Johnson, C. Dickinson, G.E. Thompson, G.C. Wood, *Atmos. Environ.*(submitted).
16. R.M. Kamens, J. Guo, Z. Guo, S.R. McDow, *Atmos. Environ.* 24A (1990): p. 1161

Table 1. Calcium contents (mg) in the run-off solutions from the various wetted stones exposed to the pollutant gases in the presence and absence of ozone for 30 days.

Stone	Exposure regime					
	NO	NO ₂	SO ₂	NO+O ₃	NO ₂ +O ₃	SO ₂ +O ₃
Massangis limestone	0.9	0.1	4.8	trace	6.91	19.0
Portland limestone	0.1	0.3	12.7	1.0	7.9	12.7
Mansfield sandstone	0.1	0.1	2.8	1.1	3.0	11.7

Table 2. Equivalent calcium yields (mg) derived from retained anion contents of stones and run-off solutions, for the dry and wetted stones, exposed to the pollutant gases with or without ozone as oxidant; for 30 days.

Stone		Exposure regime					
		NO	NO ₂	SO ₂	NO+O ₃	NO ₂ +O ₃	SO ₂ +O ₃
Massangis limestone	Dry	1.7	1.1	1.7	5.7	4.1	16.8
	Wet	14.8	8.6	18.6	12.2	26.8	38.2
Portland limestone	Dry	4.7	1.3	2.2	5.8	7.7	25.8
	Wet	28.2	10.0	55.3	22.5	28.5	67.1
Mansfield sandstone	Dry	4.5	0.7	3.8	7.9	5.8	17.9
	Wet	27.4	8.2	56.4	19.8	31.8	55.7

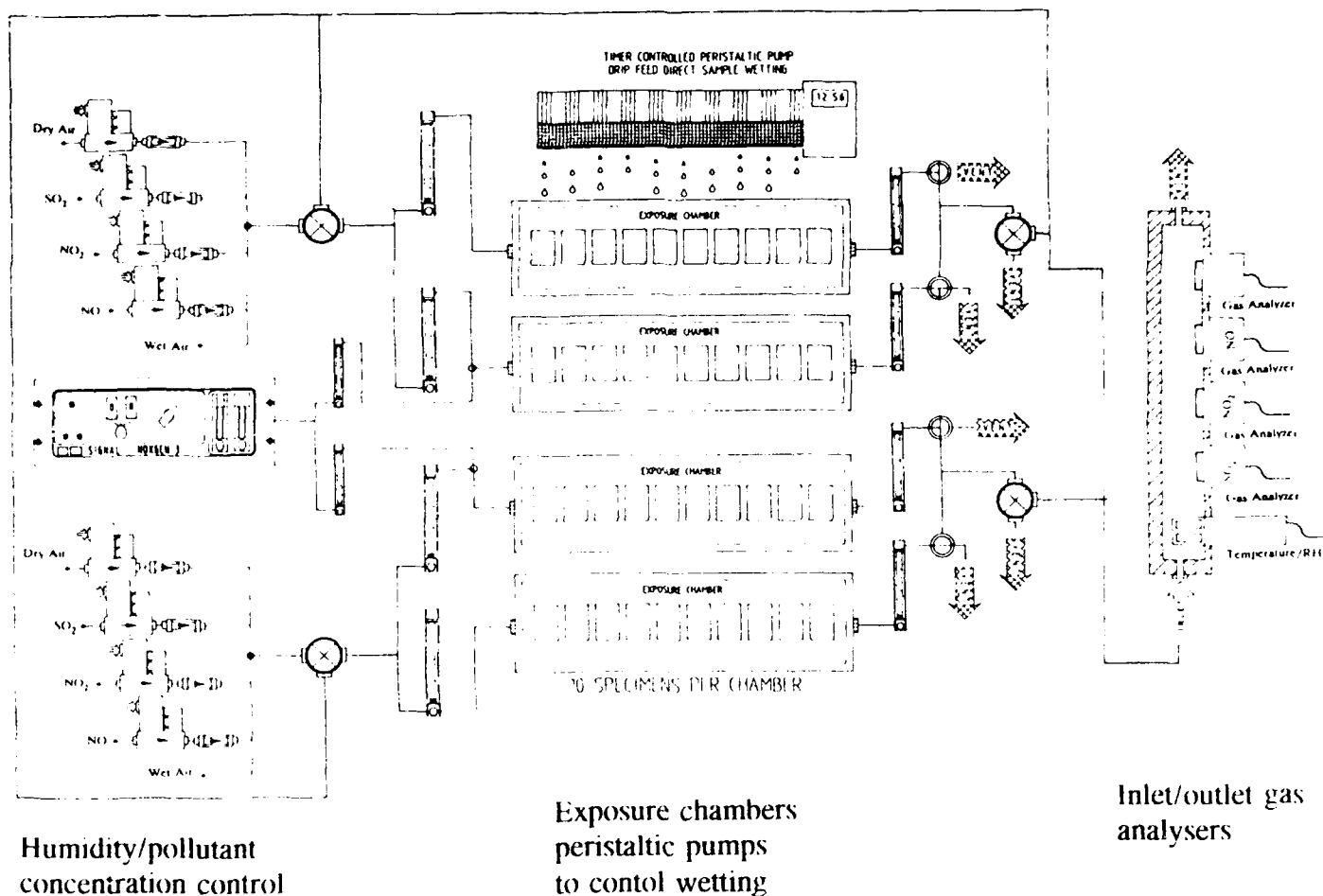


Figure 1. Diagrammatic representation of the atmospheric flow rig employed in the dry deposition studies of atmospheric pollutants.

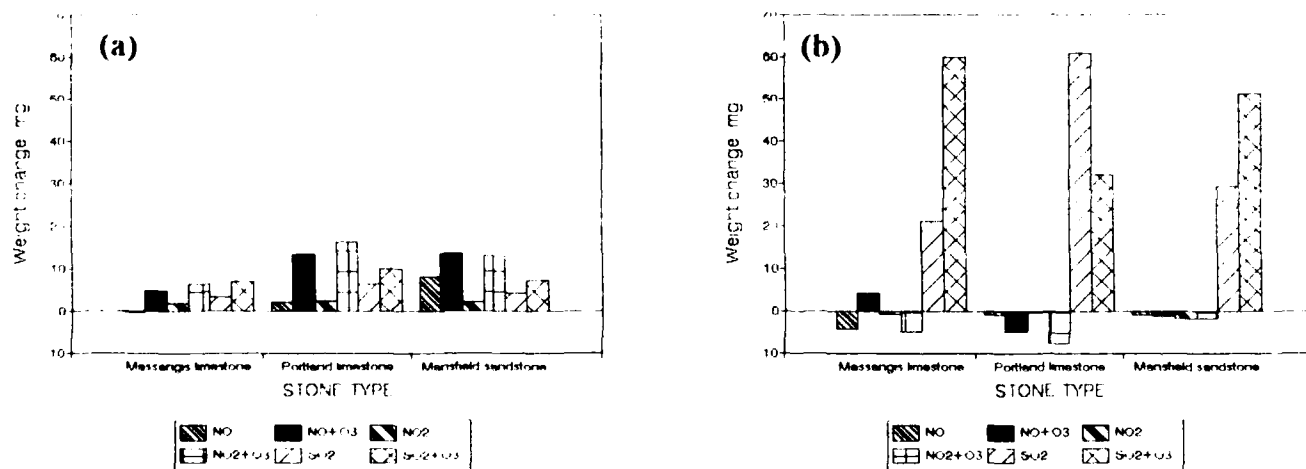


Figure 2. Weight changes for stones exposed to dry deposition of NO, NO₂, and SO₂ pollutant gases separately, with and without ozone, for 30 days: (a) dry stones, (b) wetted stones.

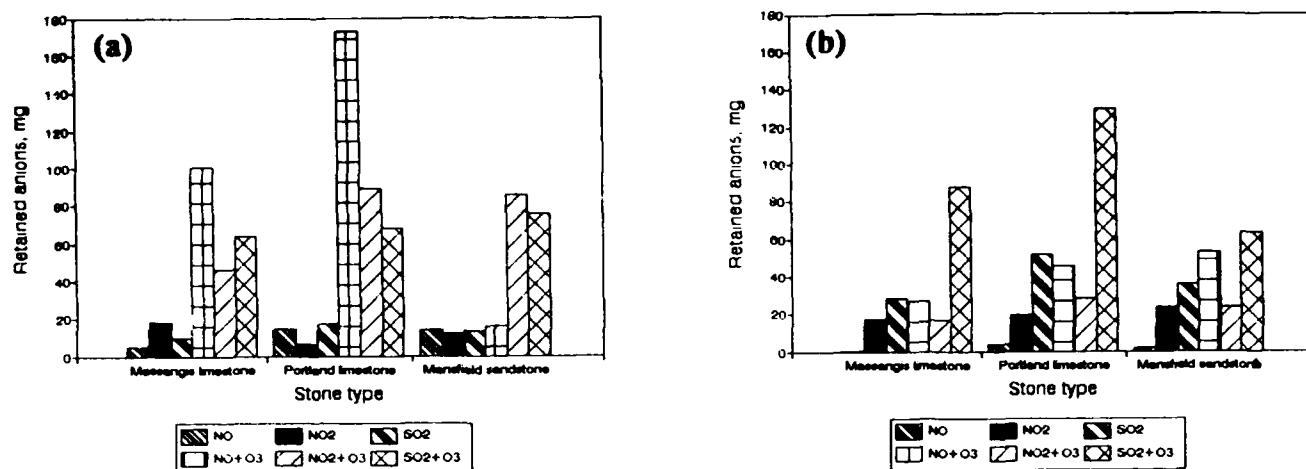


Figure 3. Retained anions in stones exposed to NO, NO₂, and SO₂ pollutant gases separately, with and without ozone, for 30 days. For NO/NO₂ exposures the anions are nitrates and for SO₂ exposures they are sulphates: (a) dry stones, (b) wetted stones.

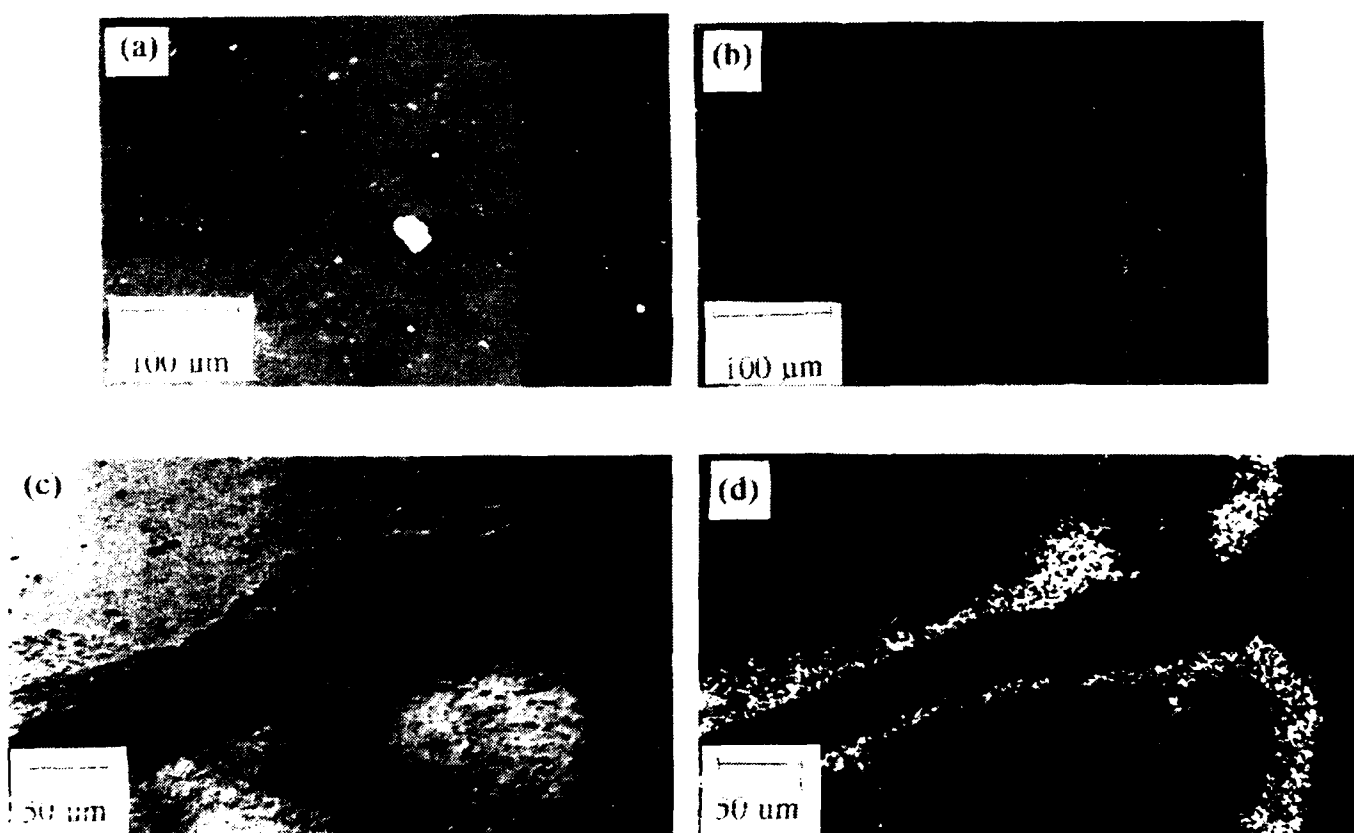


Figure 4. Scanning electron micrographs of petrographic thin sections of stones exposed to SO₂ pollutant gas in the presence of ozone, and added water, for 30 days: (a) micrograph showing formation of a very thin sulphate crust on the surface of Massangis limestone, (b) sulphur X-ray image of (a); (c) micrograph showing ingress of sulphate into the stone (Portland limestone) - depth of penetration is over 1 mm deep. (d) sulphur X-ray image of (c).

Dissolution and Precipitation Phenomena in Atmospheric Corrosion

T.E. Graedel
AT&T Bell Laboratories
Room 1D-349
Murray Hill, NJ 07974-0636
USA

Abstract

The presence on corroded metals of sulfate, nitrate, chloride, and carbonate salts implies liquid to solid transformation, since the anions are supplied to aqueous surface layers on the metals in the form of atmospheric gases or soluble aerosol particle constituents. Similarly, the presence in runoff beneath corroded metals of metal salts indicates dissolution of the metals from the solid phase into the overlying thin liquid layer. Kinetic approaches rather than thermodynamics are suitable for studying these processes in the indoor and outdoor environment, since conditions change on time scales of minutes or less during startup of air conditioning systems, rapid changes of ambient weather systems, and the like. This paper discusses the formulation of rates of mineral dissolution and precipitation, describes chemical processes for the reactions of copper and aluminum in surface aqueous solutions, and presents a few preliminary results of computations dealing with the atmospheric corrosion of wetted aluminum.

Introduction

Atmospheric corrosion is well known to be a strong function of the amount of water present, either through rain or snow fall or through wetting as a result of high humidity. This dependence implies aqueous-phase processes, particularly those relevant to the formation of minerals, because atmospheric corrosion products are invariably found to be minerals that also form naturally in geochemical environments.

Geochemical studies of mineral formation and dissolution have customarily utilized thermodynamic approaches, drawing on the reasonably well-developed data base of crystal structure stabilities, bond energies, and equilibria. Such an approach is, however, not suitable for most instances of atmospheric corrosion, in which chemical changes occur on time scales much too short for multiphase equilibria to establish themselves. As a consequence, a theoretical approach to the mechanisms of atmospheric corrosion must utilize kinetic information and kinetic techniques.

In this paper, I discuss briefly the formalism that is appropriate for describing the rates of two phase change processes crucial to corrosion: dissolution of the uncorroded surface oxide or hydroxide and precipitation of resulting corrosion products back onto the surface. These processes are functions of two important chemical variables, acidity and ionic strength, and these in turn are strongly related to the chemical properties of atmospheric corrosive gases, water droplets, and aerosol particles, and of their rates of transfer to the corroding surface.

Rates of Dissolution and Precipitation

The related concepts of the dissolution and precipitation of minerals proceed at rates that can be described by a generalized equation of the type (1)

$$R = A k (\Omega^m - 1)^n \quad (1)$$

where A is the reactive surface area of the mineral, k is the rate constant, Ω is a measure of saturation of the mineral constituents in the overlying solution, and m and n are positive adjustable parameters. In practice, the processes of dissolution and precipitation are pictured

quite differently from a mechanistic point of view, so more useful and detailed forms of Equation (1) are discussed individually below.

The solid metal surface enters into the chemical interactions of an overlying aqueous system as a consequence of the attack of the liquid-phase constituents upon it, and its subsequent dissolution. The dissolution rate is generally acid-dependent (2), and for a given supersaturation can be expressed as

$$R_{\text{diss}} = k_{\text{diss}} [a_{\text{H}^+}]^n, \quad (2)$$

n for most minerals being between 0 and 0.5, approaching unity only for hydroxide minerals and for very high proton concentrations.

A picture of proton-assisted surface dissolution has been presented by Furrer and Stumm (3). In the initial step, M-O bonds are polarized by the rapid attachment of protons to surface OH groups. The metal ion then slowly detaches itself from the surface at energy-favorable sites such as kinks or steps. Ligands in the solution may influence the dissolution rates, since metal complexes are more easily detached than are the uncomplexed metal ions. While at least minor enhancement in the dissolution rate is seen with many different ligands, the most effective are the bidentate organics such as oxalate and multiply-charged inorganics such as sulfate, which bind efficiently to the metal in the lattice. As ligand concentrations increase, the rate of dissolution increases up to the point where their effects on the metal lattice atoms are overwhelmed by supersaturation effects in the solution.

In selecting dissolution rate values for model calculations, it is obviously preferable to utilize laboratory data on the dissolution of particular minerals in solutions of specified pH and constituent concentrations. In lieu of such data, however, Wieland and coworkers (2) suggest the use of the following relationship

$$R_{\text{diss}} = k_{\text{diss}} x_a P_j S \quad (3)$$

where R_{diss} is the proton- or ligand-promoted dissolution rate ($\text{moles m}^{-2} \text{ s}^{-1}$), k_{diss} is the rate constant (s^{-1}), x_a is the mole fraction of dissolution active sites (dimensionless), P_j represents the probability of finding a specific site in the coordinative arrangement of the precursor complex (dimensionless), and S is the surface concentration of sites (moles m^{-2}). Techniques for estimating the numerical values of these parameters are given by Wieland and coworkers (2).

Precipitation rates are also related to the morphology of the solid surface, since in most cases in a non-laboratory environment, nucleation itself will not be rate-limiting and the ability of the surface to serve as a "seed crystal" for the precipitating phase will control the crystallization rate. That rate, with usual units of $\text{mole cm}^{-2} \text{ s}^{-1}$, is given by (4)

$$R_{\text{prec}} = k_{\text{prec}} \Delta c^n \quad (4)$$

where:

- k_{prec} is the effective rate constant for crystal growth, sometimes defined as $k_{\text{prec}} S$, the latter symbol referring to the effective surface area of the seed crystal. The magnitude of k_{prec} must be determined empirically.
- Δc is the degree of supersaturation of the product species (dimensionless), given for a third-order process such as the ferrous hydroxide crystallization as

$$\Delta c = ([\text{M}^{2+}] \cdot \gamma_{\text{M}^{2+}}) ([\text{X}^-] \cdot \gamma_{\text{X}^-})^2 / K_{\text{sp}} = (\text{Ion Activity Product}) / K_{\text{sp}} \quad (5)$$

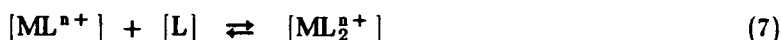
where K_{sp} is the solubility product

- n is an order parameter dependent on crystal size and morphology; its value can range between 1 and 2, but is typically about 1.6.

Given the degree of supersaturation Equation (3) is used to compute the rate of crystal growth. Where empirical values of k_{prec} are not available (a frequent occurrence), k_{prec} can be estimated by analogy with crystals of similar chemical structure and crystal habit.

Ion Pairing and Chemical Change

An interesting chemical complexity so far as precipitation is concerned is that ions in solution tend not to remain isolated from each other, assembling themselves only at the instant a mineral precipitates, but usually are present at least in part as ion pairs or more complex coordination compounds. Coordination compounds in solution are formed by stepwise reaction (5):



and so on. Stepwise stability constants can be written for each of these reactions, for example,

$$K_1 = \frac{[ML^{n+}]}{[M^{n+}][L]} \quad (9)$$

$$K_2 = \frac{[ML_2^{n+}]}{[ML^{n+}][L]} \quad (10)$$

These stability constants have been determined for a large number of the ion pairs one expects in atmospheric corrosion chemistry, and can be used to evaluate likely solution speciation of metal ions.

As an example of what needs to be considered, Table 1 presents a set of reactions potentially involved in the atmospheric corrosion of aluminum (6). From these reactions and other inferences, Figure 1 shows solution reactions leading to aluminum hydroxysulfate, the most common of aluminum's atmospheric corrosion products. The sequence begins with the dissolution of gibbsite (aluminum hydroxide) as a consequence of acidity in the surface aqueous film. Note that aluminum readily forms ion pairs with hydroxide ions and with sulfate ions, so the abundance is determined by the applicable stability constants and the abundances of the anions. Nucleation can be thought of as a four step process in this case: (1) injection of aluminum ions into solution by dissolution; (2) formation of an ion pair with either hydroxide or sulfate; (3) formation of a mixed-ligand coordination compound that serves as a precursor to the solid phase product, and (4) precipitation. The last step is described mathematically by Equation (4) above, and the other three steps occur as typical ion association reactions in the liquid layer.

In the case of cations that readily change valence in solution, the added complexities of oxidation-reduction reactions must be considered. A common example for atmospheric corrosion is copper, a reaction set for which is shown in Table 2 (6). The associated reaction sequence for the formation of several simple copper salts is shown in Figure 2 [See Mattsson (7) for additional discussion.] As with aluminum, the sequence is initiated by acid dissolution of the surface hydroxide, in this case forming the Cu^+ ion. That ion can form an ion pair with chloride, should enough be present, but it can also be oxidized to Cu^{2+} by any of several species such as hydrogen peroxide [a not uncommon atmospheric constituent]. The Cu^{2+} ion may then be reduced back to Cu^+ or it can form ion pairs as precursors to the solid salts. The most abundant of the corrosion products of copper are the mixed salts brochantite $[Cu_4(OH)_6(SO_4)]$, antlerite $[Cu_3(OH)_4(SO_4)]$, and atacamite $[Cu_2(OH)_3Cl]$, all of which are too complex to be formed entire in solution and which must be assembled on the surface from the simple salts shown in Figure 2.

Dissolution and Precipitation Data for Engineering Metals

Data for the rates of dissolution and precipitation of minerals, especially chemically complex ones, is difficult to determine, even in a laboratory setting. Nonetheless, enough data exist for the common engineering metals that one can begin to structure a perspective on the relevant kinetics. Table 3 lists some of the more common metals and their corrosion products and

indicates whether kinetic phase change data are readily available. A few comments are in order about the way in which the table was constructed. First, note that the table lists oxides or hydroxides, rather than the pure metals, since that is what an aqueous solution encounters. Second, in some cases a number of researchers have studied a particular mineral; the reference provided here is generally the most recent, containing references to the earlier literature. Third, most of the literature references to the tabular entries contain numerical data; a few give more qualitative indications of the kinetic properties of the minerals. Fourth, some of the studies provide kinetic data as a function of such useful parameters as pH or temperature, but for clarity and conciseness no indication of that additional information is shown here.

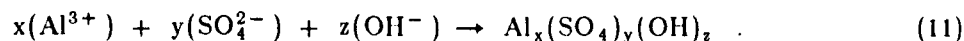
Table 3 demonstrates that some data are available for each of the metals surveyed. Dissolution data is generally more common than precipitation data. The dissolution data for the iron species is the most extensive, though none exist for iron's complicated, mixed-valence "green rust" corrosion products. It is apparent from the table that guidance is present for kinetic approaches to the chemistry, but that the phase change kinetic values remain very modestly constrained free parameters for many of the minerals of interest.

Even if data for a particular metal are available, it is not clear whether data gathered under carefully controlled laboratory conditions can be applied in a quantitative manner to more usual situations in the real world. An example of these limitations is that data for the dissolution of trace metals from atmospheric particles, a situation having much in common with atmospheric corrosion, typically shows rates much higher than anticipated on the basis of literature values (22,23). It remains unclear whether these differences are due to uncertainty regarding the particular mineral species involved, or to differences in the morphology and complexity of the mineral assemblages (24).

Model Calculations for Aluminum

As the first example of dissolution and precipitation phenomena, aluminum in an indoor environment is chosen. Aluminum is used widely in electronic and other high-technology applications despite its occasional sensitivity to corrosive species in the surrounding environment. The metal surface is initially covered by a thin layer of aluminum hydroxide (gibbsite), and it acquires a film of liquid water at humidities above about 50%. Corrosive species in gas or aerosol particles can then dissolve into this layer, creating a concentrated electrolyte.

Following the incorporation of atmospheric chemical species into moist surface films by deposition or dissolution, the aqueous phase species become modified by reactions and phase changes involving the constituents. Solution sulfur compounds are crucial reactants, since SO_2 is known to enhance aluminum corrosion in laboratory experiments (25). The rate-limiting step in the corrosion process appears to be the oxidation of sulfite to sulfate. Over periods of days to weeks under constant conditions and much shorter periods under fluctuating humidity, stable and highly insoluble basic aluminum sulfates form by stepwise reactions expressible in ensemble fashion as



The stoichiometry of the resulting product is variable, partly as a function of the amount of water conveniently available; normally the aluminum to sulfur ratio is of the order of 2 and $z \gg x \approx 2y$.

In the case of a stable aqueous layer atop the hydrolyzed aluminum, the solution chemistry changes only as a consequence of three processes: the deposition of gases and particles from the atmosphere to the surface, the dissolution of solid surface phases into the solution, and the precipitation of solid phase products from the solution to the surface.

In the scenarios dealt with here, the indoor atmosphere contains relatively high concentrations of acidic gases, and their deposition onto the aqueous film enhances solution acidity, as shown in Figure 3. The pH, initially at 5.6 (in equilibrium with atmospheric carbon dioxide), decreases

rapidly, becoming slightly less than 3 after about an hour of exposure. For the remainder of the exposure the acidity continues to increase, but the rate of increase becomes less marked (especially when plotted on a logarithmic scale).

Another parameter of interest is the concentration of aluminum in the aqueous solution, shown in Figure 4. This aluminum comes from the dissolution of the surface aluminum hydroxide (gibbsite), a process which is very slow at near-neutral pH. As the pH decreases with time, however, the dissolved aluminum concentration increases rapidly, reaching a plateau just above 10 nM after the first hour or so.

The second calculation was performed for a scenario with the same atmospheric parameters as the first, but an aqueous surface layer on the aluminum hydroxide that undergoes drying out over the three-hour exposure period. This scenario is of particular interest in view of the high ionic strengths measured in thin water films on metal surfaces by Dante and Kelly (26). Some of the results of this calculation are compared in Figures 3 and 4 with the results for the stable aqueous layer calculation.

No qualitative differences are seen between the evaporative layer calculation and the stable layer calculation, especially at early times. Later, as the layer thins and its contents become more concentrated, ionic strengths of up to 0.26 occur. Concurrently, the pH drops to 0.6. This extreme acidity promotes dissolution of the gibbsite, and the solution aluminum concentration is two orders of magnitude higher than if the layer did not evaporate. Even with these changes, none of the minerals singled out for examination approach saturation, even two minutes before drying is complete. As a consequence, the precipitation of solid phases must therefore occur very rapidly, and with little time available for the ions and atoms to assemble themselves into crystalline morphologies (27).

Finally, examining the results for aluminum speciation is of interest. Results for the two calculations are compared in Figure 5. It is seen that at early times the two cases are virtually identical, most of the aluminum being unpaired and the paired aluminum forming monohydroxy and dihydroxy complexes. With the passage of time and the deposition of sulfate from the atmosphere, the sulfate pairs become more prominent, eventually (in the evaporation case) forming nearly 40% of the aluminum in solution.

Conclusions

It is apparent from this discussion that the kinetics of phase changes are vital to a comprehensive description of the atmospheric corrosion process. A formalism for these processes is well established, though the supporting data remain sparse. Nonetheless, model calculations utilizing measurements and estimates seems likely to teach us considerable chemical information about the corrosion process. This paper has presented a few initial results from such an effort; they reveal the importance of coordination compounds as precursors to the solid phase corrosion products, and demonstrate the rapid chemical changes that occur as aqueous solutions at the metal surface undergo evaporation. Further results, now in progress, will be presented subsequently as stimuli to improved understanding of the chemistry of the degradation of metal surfaces exposed to the atmosphere.

REFERENCES

1. C.I. Steefel, P. Van Cappellen, *Geochim. Cosmochim. Acta*, 54 (1991): p. 2657.
2. E. Wieland, B. Wehrli, W. Stumm, *Geochim. Cosmochim. Acta*, 52 (1988): p. 1969.
3. G. Furrer, W. Stumm, *Chimia*, 37 (1983): p. 338.
4. J.W. Mullin, *Crystallisation*, 2nd Edition, CRC Press, Cleveland (1972).
5. C.J. Weschler, M.L. Mandich, T.E. Graedel, *J. Geophys. Res.*, 91 (1986): p. 5189.
6. T.E. Graedel, In preparation (1993).
7. E. Mattsson, *Chemtech*, 15 (1985): p. 234.
8. A.E. Nielsen, J.M. Toft, *J. Cryst. Growth*, 67 (1984): p. 278.
9. K.L. Nagy, A.C. Lasaga, *Geochim. Cosmochim. Acta*, 56 (1992): p. 3093.
10. D.K. Nordstrom, *Geochim. Cosmochim. Acta*, 46 (1982): p. 681.
11. F.R. Brown, Q. Fernando, T. Ogura, *Talanta*, 38 (1991): p. 309.
12. P. Karpinski, *Indust. Cryst.*, 78 (1979): p. 55.
13. T.L. Woods, R.M. Garrels, *Appl. Geochem.*, 1 (1986): p. 181.
14. B. Zinder, G. Furrer, W. Stumm, *Geochim. Cosmochim. Acta*, 50 (1986): p. 1861.
15. W.P. Miller, L.W. Zelazny, and D.C. Martens, *Geoderma*, 37 (1986): p. 1.
16. P.S. Sidhu, R.J. Gilkes, R.M. Cornell, A.M. Posner, J.P. Quirk, *Clays Clay Min.*, 29 (1981): p. 269.
17. C. Biegler, M.R. Houchin, *Coll. Surf.*, 21 (1986): p. 267.
18. W.A. Kornicker, P.A. Presta, C.P. Paige, D.M. Johnson, O.E. Hileman, Jr., W.J. Snodgrass, *Geochim. Cosmochim. Acta*, 55 (1991): p. 3531.
19. M.V. Ruby, A. Davis, J.H. Kempton, J.W. Drexler, P.D. Bergstrom, *Environ. Sci. Technol.*, 26 (1992): p. 1242.
20. D.C. Stiles, E.O. Edney, *Corrosion*, 45 (1989): p. 896.
21. E.B. Treivus, *Russ. J. Phys. Chem.*, 53 (1979): p. 618.
22. R. Sequeira, *Atmos. Environ.*, 22 (1988): p. 369.
23. P.T. Williams, M. Radojevic, A.G. Clarke, *Atmos. Environ.*, 22 (1988), p. 1433.
24. C. Anbeek, *Geochim. Cosmochim. Acta*, 56 (1992): p. 1461.
25. M.A. Arshadi, J.B. Johnson, G.C. Wood, *Corros. Sci.*, 23 (1983): p. 763.
26. J.F. Dante and R.G. Kelly, in *Corrosion of Electronic Materials and Devices*, R.B. Comizzoli and J.D. Sinclair, eds., The Electrochemical Society, Pennington, NJ (1993).
27. Y.-T. Cheng, W.L. Johnson, *Science*, 235 (1987): p. 997.

Table 1. Liquid Phase Chemical Reactions for Aluminum Constituents

Rx. No.	Reaction
R101	$\text{Al}^{3+} + \text{H}_2\text{O} \rightarrow \text{Al}(\text{OH})^{2+} + \text{H}^+$
R102	$\text{Al}(\text{OH})^{2+} + \text{H}^+ \rightarrow \text{Al}^{3+} + \text{H}_2\text{O}$
R103	$\text{Al}(\text{OH})^{2+} + \text{H}_2\text{O} \rightarrow \text{Al}(\text{OH})_2^+ + \text{H}^+$
R104	$\text{Al}(\text{OH})_2^+ + \text{H}^+ \rightarrow \text{Al}(\text{OH})^{2+} + \text{H}_2\text{O}$
R105	$\text{Al}(\text{OH})_2^+ + \text{H}_2\text{O} \rightarrow \text{Al}(\text{OH})_3 + \text{H}^+$
R106	$\text{Al}(\text{OH})_3 + \text{H}^+ \rightarrow \text{Al}(\text{OH})_2^+ + \text{H}_2\text{O}$
R107	$\text{Al}(\text{OH})_3 \rightarrow \text{Al}(\text{OH})_3\downarrow$
R108	$\text{Al}(\text{OH})_3\downarrow \rightarrow \text{Al}(\text{OH})_3$
R109	$\text{Al}^{3+} + \text{SO}_4^{2-} \rightarrow \text{AlSO}_4^+$
R110	$\text{AlSO}_4^+ \rightarrow \text{Al}^{3+} + \text{SO}_4^{2-}$
R111	$\text{AlSO}_4^+ + \text{SO}_4^{2-} \rightarrow \text{Al}(\text{SO}_4)_2^-$
R112	$\text{Al}(\text{SO}_4)_2^- \rightarrow \text{AlSO}_4^+ + \text{SO}_4^{2-}$
R113	$\text{Al}(\text{OH})^{2+} + \text{SO}_4^{2-} \rightarrow \text{Al}(\text{OH})(\text{SO}_4)$
R114	$\text{AlSO}_4^+ + \text{OH}^- \rightarrow \text{Al}(\text{OH})(\text{SO}_4)$
R115	$\text{Al}(\text{OH})(\text{SO}_4) \rightarrow \text{Al}(\text{OH})^{2+} + \text{SO}_4^{2-}$
R116	$\text{Al}(\text{OH})(\text{SO}_4) \rightarrow \text{Al}(\text{OH})(\text{SO}_4)\downarrow$
R117	$\text{Al}(\text{OH})(\text{SO}_4)\downarrow \rightarrow \text{Al}(\text{OH})(\text{SO}_4)$
R118	$\text{Al}(\text{OH})^{2+} + \text{Cl}^- \rightarrow \text{Al}(\text{OH})\text{Cl}^+$
R119	$\text{Al}(\text{OH})\text{Cl}^+ \rightarrow \text{Al}(\text{OH})^{2+} + \text{Cl}^-$
R120	$\text{Al}(\text{OH})_2^+ + \text{Cl}^- \rightarrow \text{Al}(\text{OH})_2\text{Cl}$
R121	$\text{Al}(\text{OH})\text{Cl}^+ + \text{OH}^- \rightarrow \text{Al}(\text{OH})_2\text{Cl}$
R122	$\text{Al}(\text{OH})_2\text{Cl} \rightarrow \text{Al}(\text{OH})^{2+} + \text{Cl}^-$
R123	$\text{Al}(\text{OH})_2\text{Cl} \rightarrow \text{Al}(\text{OH})_2\text{Cl}\downarrow$
R124	$\text{Al}(\text{OH})_2\text{Cl}\downarrow \rightarrow \text{Al}(\text{OH})_2\text{Cl}$

Table 2. Liquid Phase Chemical Reactions for Copper Constituents

Rx. No.	Reaction
R201	$\text{Cu}^+ + \text{O}_2 \rightarrow \text{Products}$
R202	$\text{Cu}^+ + \text{HO}_2 \cdot \rightarrow \text{Cu}^{2+} + \text{OH}^-$
R203	$\text{Cu}^+ + \text{HO}_2 \cdot + \text{H}_2\text{O} \rightarrow \text{Cu}^{2+} + \text{H}_2\text{O}_2 + \text{OH}^-$
R204	$\text{Cu}^+ + \text{H}_2\text{O}_2 \rightarrow \text{Cu}^{2+} + \text{HO}_2 \cdot + \text{OH}^-$
R205	$\text{Cu}^+ + \text{O}_2^- \cdot + 2\text{H}_2\text{O} \rightarrow \text{Cu}^{2+} + \text{H}_2\text{O}_2 + 2\text{OH}^-$
R206	$\text{Cu}^+ + \text{Cl}^- \rightarrow \text{CuCl}$
R207	$\text{CuCl} \rightarrow \text{Cu}^+ + \text{Cl}^-$
R208	$\text{CuCl} + \text{O}_2 \rightarrow \text{Products}$
R209	$\text{Cu}^+ + \text{SO}_3^{2-} \rightarrow \text{CuSO}_3^-$
R210	$\text{CuSO}_3^- \rightarrow \text{Cu}^+ + \text{SO}_3^{2-}$
R211	$\text{CuSO}_3^- + \text{O}_2 \rightarrow \text{Products}$
R212	$\text{Cu}^{2+} + \text{HO}_2 \cdot \rightarrow \text{Cu}^+ + \text{H}^+ + \text{O}_2$
R213	$\text{Cu}^{2+} + \text{O}_2^- \cdot \rightarrow \text{Cu}^+ + \text{O}_2$
R214	$\text{Cu}^{2+} + \text{H}_2\text{O} \rightarrow \text{Cu}(\text{OH})^+ + \text{H}^+$
R215	$\text{Cu}(\text{OH})^+ + \text{H}^+ \rightarrow \text{Cu}^{2+} + \text{H}_2\text{O}$
R216	$\text{Cu}(\text{OH})^+ + \text{H}_2\text{O} \rightarrow \text{Cu}(\text{OH})_2 + \text{H}^+$
R217	$\text{Cu}(\text{OH})_2 + \text{H}^+ \rightarrow \text{Cu}(\text{OH})^+ + \text{H}_2\text{O}$
R218	$\text{Cu}(\text{OH})_2 \rightarrow \text{Cu}(\text{OH})_2\downarrow$
R219	$\text{Cu}(\text{OH})_2\downarrow \rightarrow \text{Cu}(\text{OH})_2$
R220	$\text{Cu}^{2+} + \text{SO}_4^{2-} \rightarrow \text{CuSO}_4$
R221	$\text{CuSO}_4 \rightarrow \text{Cu}^{2+} + \text{SO}_4^{2-}$
R222	$\text{CuSO}_4 \rightarrow \text{CuSO}_4\downarrow$
R223	$\text{CuSO}_4\downarrow \rightarrow \text{CuSO}_4$

Table 3. Availability of Dissolution and Precipitation Data
for Engineering Metals and their Corrosion Products

Formula	Mineral Name	Diss. Rate Ref.	Precip. Rate Ref.
AgCl	Chlorargyrite	-	8
Ag ₂ C ₂ O ₄	-	-	8
Ag ₂ S	Acanthite	-	-
Al(OH) ₃	Gibbsite	9	-
Al(OH)(SO ₄)	Jurbanite	10	-
Cu ₂ O	Cuprite	11	-
Cu ₂ S	Chalcocite	-	-
CuSO ₄	Chalcocyanite	-	12
Cu ₃ (OH) ₄ (SO ₄)	Antlerite	-	-
Cu ₄ (OH) ₆ (SO ₄)	Brochantite	-	13
Cu ₂ (OH) ₃ Cl	Atacamite	-	-
Cu ₄ (OH) ₆ Cl ₂	Paratacamite	-	13
Fe ₂ O ₃	Hematite	14	-
α-FeOOH	Goethite	14	-
Fe oxide (amorph)	-	15	-
γ-FeOOH	Lepidocrocite	16	-
FeCO ₃	Siderite	17	-
FeSO ₄	Rozenite	-	-
PbO	Litharge	-	-
PbSO ₄	Anglesite	18	-
Pb(C ₂ H ₄ O ₂) ₂	-	19	-
ZnO	Zincite	20	-
ZnSO ₄	Zincosite	-	21
Zn ₅ (CO ₃) ₂ (OH) ₆	Hydrozincite	-	-

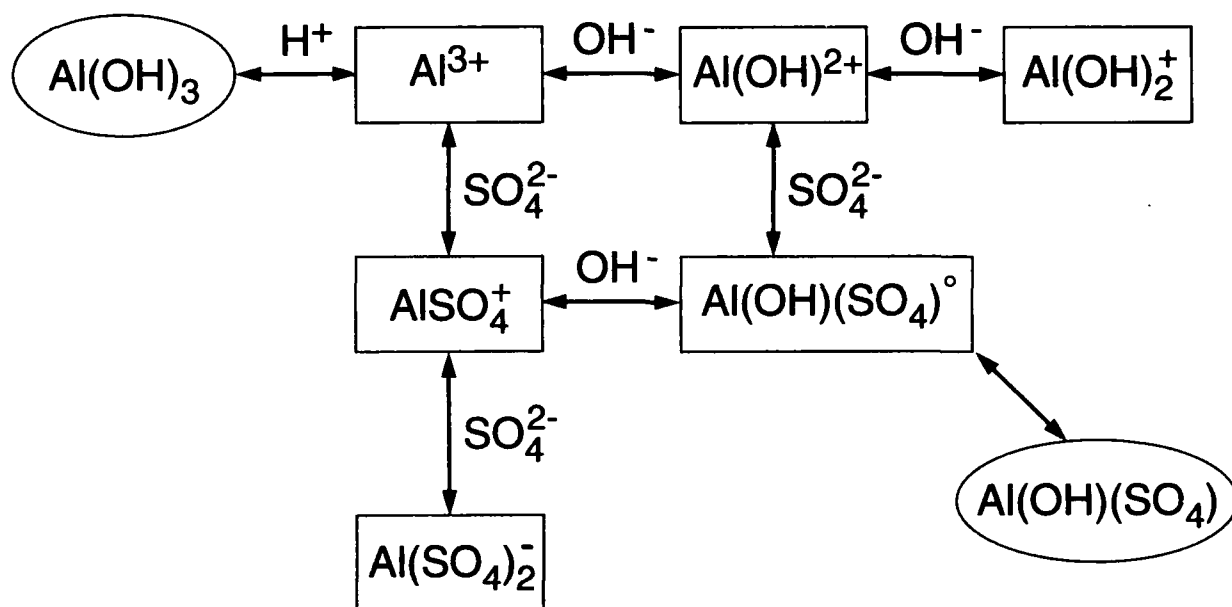


Figure 1. Reaction sequences for the formation of aluminum hydroxysulfate in atmospheric corrosion. Solid phases are shown in ellipses, liquid phase species in rectangles. The process is initiated by dissolution of the aluminum hydroxide and terminates with the precipitation of the corrosion product.

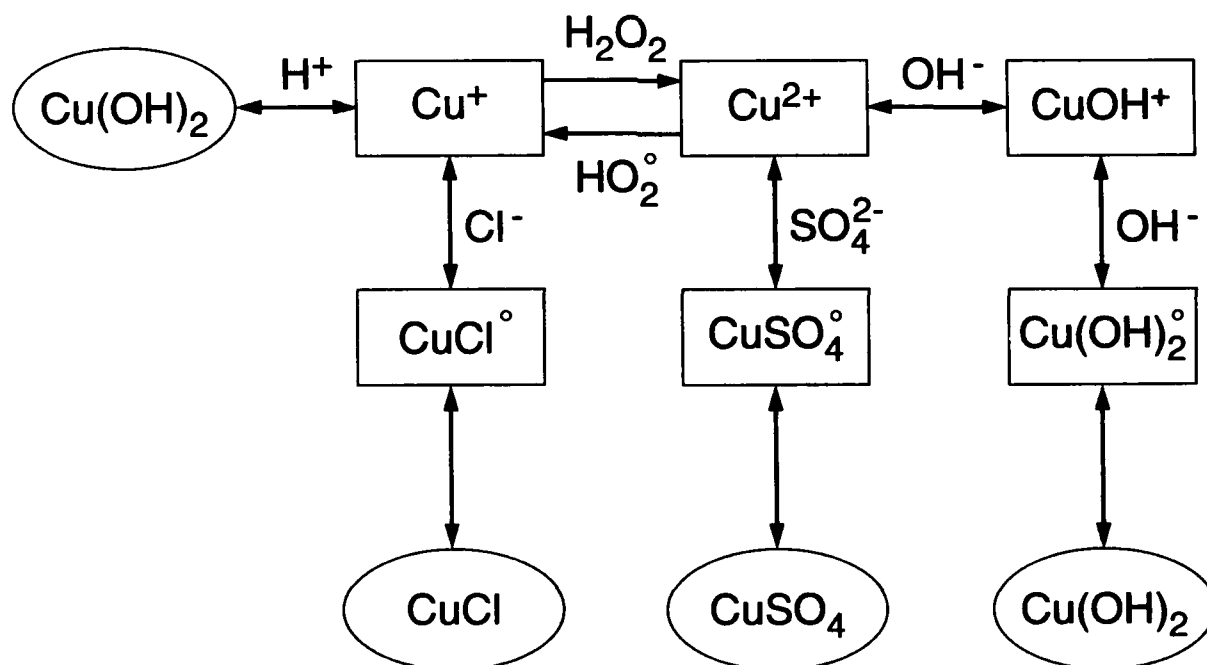


Figure 2. Reaction sequences for the formation of simple copper salts in atmospheric corrosion. Solid phases are shown in ellipses, liquid phase species in rectangles. The process is initiated by dissolution of the copper hydroxide at the solid surface and terminates with the precipitation of one of the corrosion products.

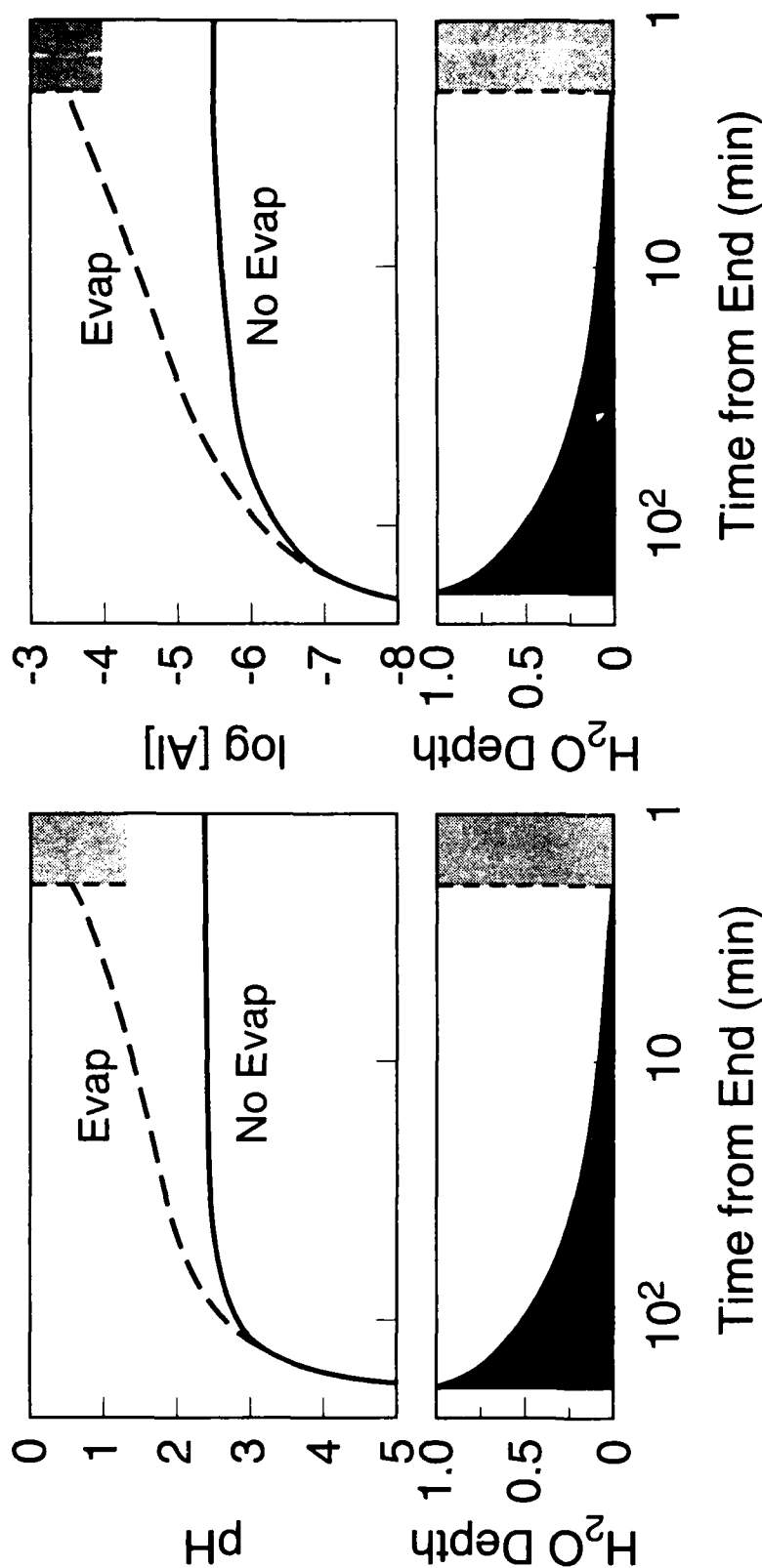


Figure 3. Comparison of the pH of the aqueous surface layer atop gibbsite (aluminum hydroxide) for two calculations: in the first, the layer is maintained at constant depth for a three-hour period while acidic gases and particles are deposited from the indoor atmosphere. In the second, the layer evaporates to dryness during the three-hour period, solution depth being shown at the bottom of the display. Two minutes from the end of the evaporation, the aqueous layer becomes so thin that the bulk chemical kinetics techniques are insufficiently accurate to permit the model to accurately represent the physical situation.

Figure 4. Comparison of the aluminum ion concentration of the aqueous surface layer atop gibbsite (aluminum hydroxide) for the two calculations described in the caption of Figure 3.

Constant Depth Layer

Evaporating Layer

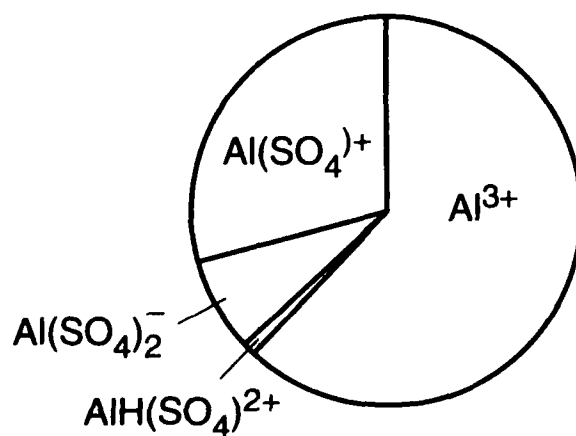
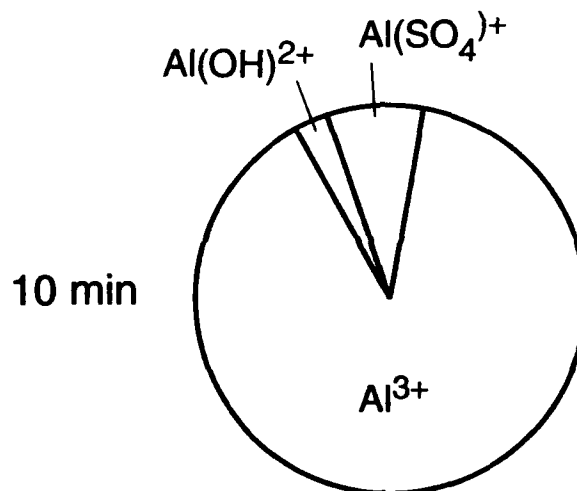
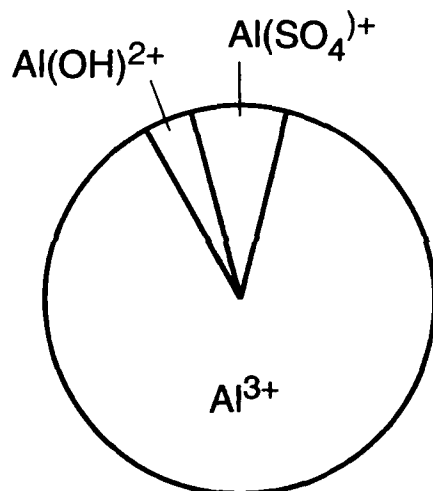
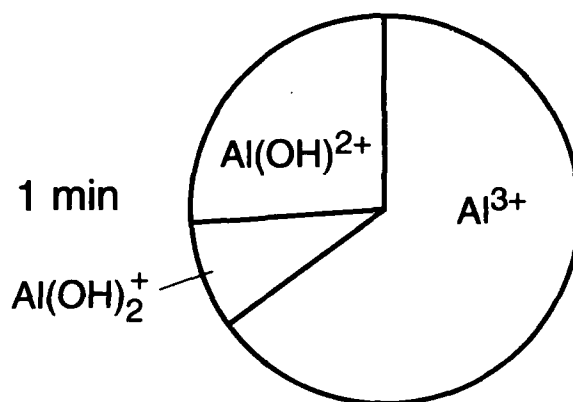
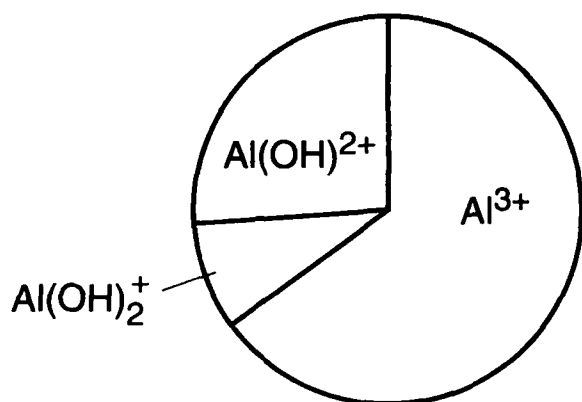


Figure 5. Aluminum speciation in the surface solution at three times during the constant depth and evaporative calculations. As the calculations proceed and sulfate is deposited on the surface from the air, the pH decreases, OH⁻ concentrations decrease, and the aluminum ions are increasingly complexed with sulfate ions.

Effects of Acidic Deposition on the Corrosion of Zinc and Copper

Stephen D. Cramer
U. S. Bureau of Mines
1450 Queen Avenue S.W.
Albany OR 97321

L. Garner McDonald
McDonald & Associates
1192 33rd Avenue S.W.
Albany OR 97321

John W. Spence
Atmospheric Research and Exposure Assessment Laboratory
Environmental Protection Agency
Research Triangle Park NC 27111

Abstract

The Bureau of Mines, in cooperation with the Environmental Protection Agency, studied the impact of acid deposition on the atmospheric corrosion of zinc and copper. A corrosion model, based on competing processes of corrosion film growth and loss, was used to analyze runoff or corrosion film losses from the metals. The model establishes quantitative, site specific measures of the dose of environmental species affecting atmospheric corrosion processes. It includes contributions to materials damage from precipitation in equilibrium with atmospheric carbon dioxide, i.e., "clean rain", from the excess hydrogen ions from the strong acids often present in precipitation in the eastern U.S., and from dry deposited sulfur dioxide and nitric acid. It also includes the effect of dry deposited basic particulates to mitigate metals damage from acidic species. These contributions help define the long term corrosion of zinc and copper. The effects of environmental species are shown to be complex, dependent on how the species are delivered to the metal surface, the chemical nature of the species, and the minerals present in the corrosion product. The solubility of zinc and copper corrosion products in precipitation in equilibrium with atmospheric carbon dioxide when acid deposition was absent was 48 $\mu\text{mol Zn/L}$ and 18 $\mu\text{mol Cu/L}$, respectively. The minerals present in the corrosion product are important to the dry deposition of the acidic gases. Acid deposition at Washington, D.C., accounts for roughly 70 pct of the long-term corrosion product losses on zinc and 80 pct of the losses on copper.

Keyterms: Atmospheric corrosion, corrosion model, acid deposition, sulfur dioxide, nitric acid, basic particulates, copper, zinc, stainless steel, deposition velocity

Introduction

The corrosion of copper and zinc in the atmosphere depends on a number of environmental parameters, including sulfur dioxide and

precipitation pH^{1-4} . Dose-response functions have been developed to quantify the effect of these parameters on corrosion⁵⁻⁷. The Bureau of Mines, in cooperation with the Environmental Protection Agency, studied corrosion damage effects of acid deposition as part of the National Acid Precipitation Assessment Program⁸. Atmospheric corrosion of zinc was modeled based on the wet and dry deposition of reactive environmental species to the metal surface and the impact of these species on the competing processes of corrosion film growth and loss^{5,7,9}. Corrosion film losses are sustained by precipitation washing the zinc surface and removing soluble compounds resulting largely from acid-base reactions with acidic gases and "acid rain"¹⁰⁻¹². The model establishes quantitative, site specific measures of the dose of environmental species affecting zinc corrosion. It includes parameters that define the well-known variation of corrosion rate with time for metals with protective corrosion films.

Only that part of the model concerned with corrosion film losses in precipitation runoff is addressed here. Runoff film losses include contributions from precipitation in equilibrium with atmospheric carbon dioxide, i.e., "clean rain", from the excess hydrogen ions from strong acids often present in precipitation in the eastern U.S., i.e., "acid rain", and from dry deposited sulfur dioxide⁸. These terms are related to the local air quality, meteorology, and precipitation and particulate chemistry. They form a stoichiometric equation relating corrosion film losses to the delivery of environmental species to the zinc and access of these species to the corrosion product.

The stoichiometric equation, which has been shown to account for a large fraction of zinc runoff losses⁵, expressed in equivalents, is

$$M = rSV + H^+ + [\text{SO}_2] \quad (1)$$

M is the corrosion product runoff loss. S is the solubility of the corrosion product in precipitation in equilibrium with atmospheric carbon dioxide; r is a residence time factor, with a value between 0 and 1, and strongly dependent on corrosion film surface roughness, water layer thickness, size and shape of the metal and temperature¹³; V is the precipitation volume. While r in theory could be computed, at present r is treated as an undetermined parameter and fit to the data. H^+ is the hydrogen ion from wet deposition consumed by acid-base reactions. This term should also include a residence time factor. However, for the thin water layers studied, excess hydrogen ions appear to react quickly and completely with the corrosion product and the residence time factor is unity^{5,11,13}. $[\text{SO}_2]$ is the dry deposited sulfur dioxide. It is determined by the ambient concentration of sulfur dioxide in the air, the time of wetness of the metal surface, and aerodynamic and

surface resistances related to movement of sulfur dioxide from the gas phase to the corrosion product.

Corrosion rates in long exposures, when the corrosion film has achieve a steady state thickness, are equivalent to the rate of the film runoff loss, Equation 1. This, of course, presumes that the terms in Equation 1 are for an aged surface or that values measured in shorter exposures are applicable to steady state conditions. Equation 1 provides insight into the environmental factors affecting corrosion in long exposures and the steady state corrosion rate. It suggests, as others have observed, that the steady state corrosion rate is determined by the level of atmospheric pollutants⁶.

Equation 1 has been expanded in this paper to include contributions from nitric acid and basic particulates. These results are based on runoff measurements in Washington, D.C., over a 33 month period. They show that the mass balance used in runoff experiments provides a sensitive method for detecting environmental effects on corrosion. The expanded Equation 1 has been used to quantify the contributions of wet and dry deposition in the atmospheric corrosion of zinc and copper. It provides a basis for assessing environmental impacts on materials damage and for examining the mass transfer processes that affect atmospheric corrosion.

Experimental Methods

Precipitation runoff measurements were begun June 1985 on the roof of the West End Library in downtown Washington, D.C., and continued to February 1988¹¹. Flat panels of rolled zinc (UNS-Z44330), electrolytic tough-pitch copper (UNS-C11000) and type 304 stainless steel (UNS-S30400) measuring 0.3x0.6 meters were mounted in separate polyethylene trays to collect the precipitation washing the skyward surface. The panels and the trays were mounted at an angle of 30 degrees to the horizon and faced south. The groundward side of each panel was masked to prevent corrosion. The site was the primary air quality monitoring site for Washington, D.C.

The panels were chemically cleaned prior to installation in the collectors using standard ASTM methods¹⁴. The stainless steel panel served as an inert reference surface to quantify acid-base reactions not related to corrosion product dissolution. Analyses for Cr in the runoff indicated the stainless steel did not corrode during the exposure period. The runoff was collected continuously by a sealed system that minimized evaporation losses and absorption of gases from the atmosphere. The collection container was changed monthly for chemical analysis.

The runoff was filtered to remove undissolved particulates and analyzed for the standard acid rain ions (H, Ca, Mg, K, Na, NH₄, NO₃, Cl, and SO₄) and selected metal ions (Cr, Fe, Zn, and Cu) by electrochemical, atomic absorption and ion chromatographic methods. Bicarbonate ion concentrations were computed from the pH assuming equilibrium with atmospheric carbon dioxide.

Precipitation (rain and snow) was continuously collected by an Aerochem Metrics wet/dry collector and analyzed on a monthly

schedule for the same ions considered in the runoff. Particulates were collected on a regular schedule in high-vol and dichotomous samplers and analyzed by EPA. Air quality (SO_2 , NO , NO_2 , O_3) was measured continuously by the D.C. government. Monitoring of atmospheric nitric acid concentrations was recently begun by the National Dry Deposition Network¹⁵. Nitric acid concentrations are not available for Washington, D.C., but were estimated, from measurements in the adjacent three state region, to be $3 \mu\text{g}/\text{m}^3$.

A number of standard 10x15 cm corrosion panels of each metal were exposed concurrently with the runoff panels for periodic removal to determine corrosion rates and corrosion film chemistry.

Results

Runoff Losses

The concentration of zinc in the runoff from the Zn panel is shown as a function of pH at 25 °C in Figure 1. The solubility curve for $\beta\text{-Zn}(\text{OH})_2$ ¹⁶ has been added to the figure. The measured values are well below the solubility curve indicating the runoff was not saturated in Zn. The term r_s is the solubility of corrosion product in runoff in equilibrium with atmospheric carbon dioxide and with no other reactive species present. The difference between this value and the measured values is attributable to acid deposition. The value of r_s shown was estimated from the expanded form of Equation 1 to be discussed later. Similar results are shown in Figure 2 for the copper runoff. The measured Cu concentrations are well above the solubility curve for cuprite (Cu_2O) and lie on the curve for tenorite (CuO)¹⁶. Basic zinc carbonate for zinc^{2,11} and brochantite for copper³ may be better bases for the solubility curves in Figures 1 and 2.

Dry Deposition

Dry deposition is the process whereby gaseous species and particulates are delivered to and retained by a surface through a combination of aerodynamic and chemical processes. The dry deposition of acidic gases is greatly enhanced by a thin layer of moisture or dew. Dry deposition cannot be measured directly in this experiment but, instead, is inferred from a mass balance involving measured quantities treating the accumulation of species in the corrosion film. Dry deposition fluxes for sulfur dioxide, sulfates, nitrates, and Ca and Mg basic particulates were computed in this way.

Basic particulates. The total Ca and Mg particulates deposited onto the stainless steel and released into solution is shown in Figure 3. A portion of these particulates consumed significant quantities of dry deposited sulfur dioxide and nitric acid and wet deposited hydrogen ions in acid-base reactions on this inert surface. The fraction of Ca and Mg particulates participating in these reactions was computed as the sum of the dry deposited sulfur dioxide and nitric acid plus the hydrogen ion loss from the precipitation. This fraction represents basic particulates. The difference between the two curves is the

fraction of Ca and Mg present in the particulates as soluble salts such as chlorides and sulfates.

Coarse mode particles ($> 2.5 \mu\text{m}$ diameter) have a deposition velocity to horizontal surfaces of 1.55 cm/s and tend to contain the Ca and Mg cations¹⁷. Coarse mode particle deposition should be the same to the stainless steel, Zn and Cu panels. In addition, the fraction of Ca and Mg present as soluble salts should be the same for each panel. Figure 4 shows the total Ca and Mg released into solution from each of the panels. The lower amounts for the Zn and Cu panels can be explained by competition between the basic particulates and basic corrosion product for the available acidic species. The largest release of Ca and Mg is from the stainless steel surface, where the basic particulates have no competition for acidic species. Lesser amounts from the Zn and Cu surfaces are related to the reactivity of the corrosion product, i.e., the minerals present in the corrosion film, the identity of the acidic species and their mode of delivery to the surface.

Sulfur deposition. The total dry deposition of sulfur species to the stainless steel is shown in Figure 5. A large fraction of this sulfur is dry deposited as sulfur dioxide. The difference between these amounts was assumed to represent sulfates present in the coarse mode particulates deposited on the stainless steel. Aerosols, which typically contain the highest concentration of sulfates, are submicron in size. They are fine mode particulates and do not deposit in a significant amounts because of their low deposition velocity¹⁷⁻¹⁸. Figure 5 shows that measurable sulfate appeared midway in the exposure period after substantial coarse particulates had accumulated and the surface had become soiled. Sulfate deposition should be roughly the same for the stainless steel, Zn and Cu panels.

Dry deposition of sulfur dioxide to the panels is shown in Figure 6. It is highest for the zinc surface. Since each of the panels was exposed to the environment in the same way, these results indicate the sulfur dioxide deposition is strongly dependent on the chemistry of the receptor surface.

Nitrogen deposition. Edney et al. has shown that the deposition velocity for NO_2 to a wet surface is 0.03 cm/s while that of nitric acid is about 2.0 cm/s ⁹. Furthermore, nitric acid was shown to deposit readily to surfaces whether they were wet or dry. In addition, equilibrium concentrations of NO_2 in surface moisture are expected to be low compared to sulfur dioxide given the Henry's law constants of 10^{12} atm and 1.24 atm , respectively. Significant concentrations of nitric acid are present in the atmosphere at background sites in the eastern U.S.¹⁵ and are expected to be higher at urban locations. For these reasons, the observed deposition of nitrates is explained here in terms of nitric acid dry deposition. Nitric acid deposition is shown in Figure 7. It is highest for copper.

Discussion

Runoff Equation

In earlier work Equation 1 resulted in computed runoff losses for zinc and copper 10 to 15 pct higher than the measured losses¹¹, suggesting the need for additional terms in the model. It is clear from the results presented here that one such term is dry deposited basic particulates, CaMg_{H^+} . Acidic species from the environment react with not just the corrosion film but with the corrosion film and dry deposited basic particulates. A second term is dry deposited nitric acid, $[\text{HNO}_3]$. Equation 1 then becomes

$$M + \text{CaMg}_{\text{H}^+} = rSV + \text{H}^+ + [\text{SO}_2] + [\text{HNO}_3] \quad (2)$$

As in Equation 1 the residence time factor, r , is only undetermined parameter in the model. A least square fit of Equation 2 to 33 months of zinc runoff data yielded a value for rS of $48 \mu\text{mol Zn/L}$ with $R^2 = 0.992$. The value of rS is consistent with the solubility of known mineral species on the zinc surface such as β -zinc hydroxide, Figure 1, or basic zinc carbonate⁷.

The results of the fit are shown in Figure 8 where the cumulative contributions of each term are stacked one on top of the other, beginning with the "clean rain" term. The sum of the terms on the right side of Equation 2 overestimates the zinc losses. However, basic particulates neutralize some of the acid species, reducing the predicted zinc losses to values consistent with the measured values. These results suggest zinc corrosion damage from wet and dry deposition of acidic species in the absence of basic particulates is more than three-fold that due to "clean rain". The actual losses are reduced 16 pct by the presence of basic particulates on the panel surface.

A least squares fit of Equation 2 to the copper runoff data yielded a value for rS of $18 \mu\text{mol Cu/L}$ with $R^2 = 0.945$. The value of rS is also consistent with the solubility of minerals known to be present in the corrosion product¹⁶. The fitted results are shown in Figure 9. The fractional contribution of dry deposited sulfur dioxide is less than for zinc corrosion while that of nitric acid is greater. These results indicate copper corrosion damage from wet and dry deposition of acidic species in the absence of basic particulates is more than four-fold that due to "clean rain". The actual losses are reduced 25 pct by the presence of basic particulates.

Deposition Velocity

The delivery of gaseous species to surfaces is commonly defined in the atmospheric chemistry literature by the deposition velocity, v_d ¹⁹⁻²⁰. For sulfur dioxide this mass transfer coefficient is given by

$$v_d = F_s/[SO_2] \propto 1/(r_a + r_s) \quad (3)$$

where $[SO_2]$ is the gas phase concentration and F_s is the dry deposition flux to the surface. The deposition velocity is inversely proportional to the sum of an aerodynamic resistance r_a and a surface resistance r_s . F_s is defined here as the amount of dry deposited sulfur dioxide per unit panel area divided by the total exposure time less the time of rainfall. (Others have divided by the time the humidity exceeds the critical relative humidity (RH_c), i.e., the humidity above which surface moisture is likely to be present. It is suggested that below RH_c the surface becomes saturated with a monolayer of adsorbed gas⁵. This approach gives a higher value for v_d and requires large amounts of meteorological data. The difference between approaches is roughly the fractional time of wetness, i.e., the time the panel is wet divided by the total exposure time.)

Deposition velocities computed from air chemistry and dry deposition data are given in Table 1 for sulfur dioxide and nitric acid. The sulfur dioxide deposition velocities for zinc and copper are not significantly different from those computed from the atmospheric corrosion model using mass loss corrosion data for five sites in the eastern U.S.¹¹. The deposition velocity for nitric acid is significantly higher than that for sulfur dioxide reflecting the ease with which nitric acid deposits on both wet and dry surfaces.

The difference in deposition velocities for the three panels can be explained by the resistance terms. The aerodynamic resistance r_a should be the same for each of the panels because size, shape, orientation, and meteorology are the same. Thus, the differences are confined to the surface resistance r_s , which is related to the rate of gas absorption by the surface and by the rate of the acid-base reactions. While these effects cannot be separated here, both depend on the minerals present on the receptor surface. Thus, as has been seen on marble²¹, the minerals present in the corrosion product strongly affect the dry deposition of acidic gases.

Acid Deposition Effects

The contribution of environmental factors to the corrosion product losses measured at the conclusion of the 33 month experiment were computed from Equation 2. The total loss was equivalent to a penetration rate of 0.92 $\mu\text{m/y}$ for zinc and 0.37 $\mu\text{m/y}$ for copper. The zinc value compares favorably to the value from mass loss measurements conducted over the same time period of $1.48 \pm 0.57 \mu\text{m/y}$ for rolled zinc and 1.10 ± 0.42 for galvanized steel. The copper value is well below the value from mass loss measurements of $0.83 \pm 0.19 \mu\text{m/y}$, reflecting the expected difference in copper corrosion rates early and late in the exposure period. The contribution of the environmental factors are given in Table 2 as a percentage of the total loss. Roughly 70 pct of the film loss on zinc is due to acid deposition. The percentage for copper is 80 pct. Clearly acid deposition can have a significant impact on the long term corrosion of Cu and Zn.

Conclusions

1. A stoichiometric equation involving the wet deposition of strong acids and the dry deposition of sulfur dioxide, nitric acid and basic particulates describes the impact of environmental factors including acid deposition on the long term corrosion of copper and zinc.

2. Basic particulates compete with corrosion product in acid-base reactions to reduce the impact of acidic environmental species on the corrosion of zinc and copper.

3. The effects of environmental species are complex, dependent on how the species are delivered to the surface, the chemical nature of the species, and the minerals present in the corrosion product.

4. Acidic deposition of environmental species at Washington, D.C., can, in the absence of basic particulates, increase more than three-fold long-term Zn corrosion damage and four-fold Cu corrosion damage.

References

1. V. Kucera and E. Mattsson, Corrosion Mechanisms, F. Mansfeld, Ed., M. Dekker, New York (1987), pp. 211-284.
2. T. E. Graedel, J. Electrochem. Soc., vol. 136, no. 4 (1989), pp. 193C-203C.
3. T. E. Graedel, Corr. Science, vol. 27, no. 7 (1987), pp. 721-740 and 741-769.
4. J. E. Svensson and L. G. Johansson, Corr. Science, vol. 34, no. 5 (1993), pp. 721-740.
5. J. W. Spence, F. H. Haynie, F. W. Lipfert, S. D. Cramer, L. G. McDonald, Corrosion, vol. 48, no. 12 (1992), pp. 1009-1019.
6. V. Kucera, Materials Degradation Caused by Acid Rain, R. Baboian, Ed., ACS Symposium Series 318, American Chemical Society, Washington, D. C. (1986), pp. 104-118.
7. J. W. Spence and F. H. Haynie, Corrosion Testing and Evaluation, ASTM STP 1000, R. Baboian and S. W. Dean, Eds., American Society for Testing and Materials, Philadelphia (1990), pp. 208-224.
8. E. O. Edney, Effects of Acidic Deposition on Materials, SOST Report 19, National Acid Precipitation Assessment Program, 722 Jackson Place, N.W., Washington, D.C. (September 1990), pp. 37-95.
9. E. O. Edney, D. C. Stiles, J. W. Spence, F. H. Haynie and W. E. Wilson, Materials Degradation Caused by Acid Rain, R. Baboian, Ed.,

ACS Symposium Series 318, American Chemical Society, Washington, D. C. (1986), pp. 172-193.

10. E. O. Edney, D. C. Stiles, J. W. Spence, F. H. Haynie, and W. E. Wilson, *Atmos. Environment*, vol. 20, no. 3 (1986), pp. 541-548.

11. S. D. Cramer and L. G. McDonald, *Corrosion Testing and Evaluation*, ASTM STP 1000, R. Baboian and S. W. Dean, Eds., American Society for Testing and Materials, Philadelphia (1990), pp. 241-259.

12. D. R. Flinn, S. D. Cramer, J. P. Carter, D. M. Hurwitz and P. H. Linstrom, *Materials Degradation Caused by Acid Rain*, R. Baboian, Ed., ACS Symposium Series 318, American Chemical Society, Washington, D. C. (1986), pp. 119-151.

13. D. C. Stiles and E. O. Edney, *Corrosion*, vol. 45, no. 11 (1989) pp. 896-901.

14. ASTM Standard G1-90, American Society for Testing and Materials, Philadelphia, PA, (1990), pp. 39-45.

15. E. S. Edgerton, T. F. Lavery, M. G. Hodges, and J. J. Bowser, *NDDN 2nd Annual Progress Report*, EPA/600/3-90/020, (August 1990), pp. 23-36.

16. M. Pourbaix, *Atlas of Electrochemical Equilibria*, National Association of Corrosion Engineers, Houston, TX, (1974), pp. 384-392 and 406-413.

17. F. H. Haynie and T. J. Lemmons, *Aerosol Science Technology*, 13 (1990), pp. 356-367.

18. F. H. Haynie, in *Aerosols*, S. D. Lee, T. Schneider, L. D. Grant, and P. J. Verkerk, Eds., Lewis Publishers, Chelsea, MI (1986), pp. 2104-2112.

19. B. B. Hicks, *Water, Air and Soil Pollution*, vol. 30 (1986), pp. 75-90.

20. J. S. Gamble and C. I. Davidson, *Materials Degradation Caused by Acid Rain*, R. Baboian, Ed., ACS Symposium Series 318, American Chemical Society, Washington, D.C. (1986), pp. 42-63.

21. D. A. Dolske, *Measurement of Toxic and Related Air Pollutants*, Air & Waste Management Assn., Pittsburgh (1992), p. 159.

Table 1. Deposition velocities, v_d , for sulfur dioxide and nitric acid to metal surfaces, cm/s.

Metal	SO ₂	HNO ₃
Stainless steel	0.047	0.068
Zinc	0.42	0.89
Copper	0.17	1.27

Table 2. Contribution of environmental factors to long-term corrosion product and basic particulate dissolution, percent.

Model term	Zinc	Copper
Precipitation, rSV	26.9	20.2
Wet deposition, [H ⁺]	19.7	33.8
Dry deposition, [SO ₂]	45.5	33.1
[HNO ₃]	5.2	12.9

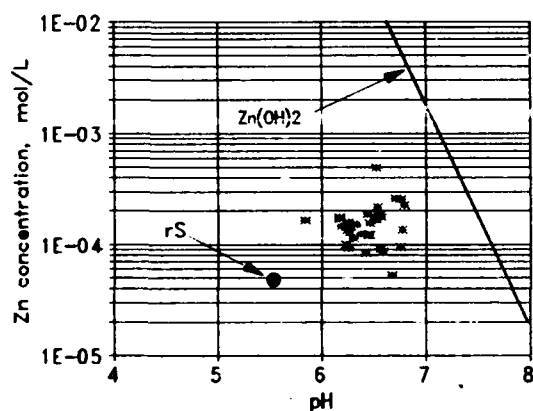


Figure 1. Concentration of zinc in 33 monthly runoff samples. Solubility curve for zinc hydroxide is shown. Zinc concentration in runoff in the absence of acid deposition is rS.

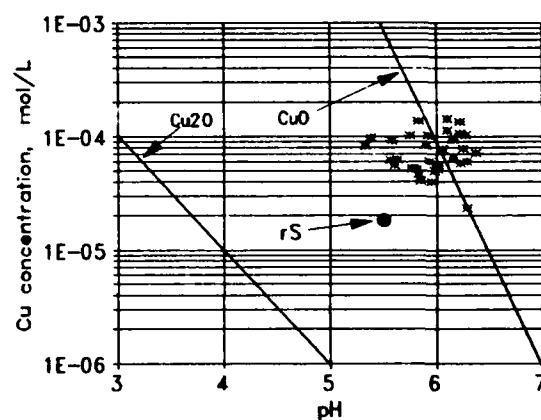


Figure 2. Cu in 33 monthly runoff samples. Solubility curves for cuprite and tenorite are shown. Copper concentration in runoff in the absence of acid deposition is rS.

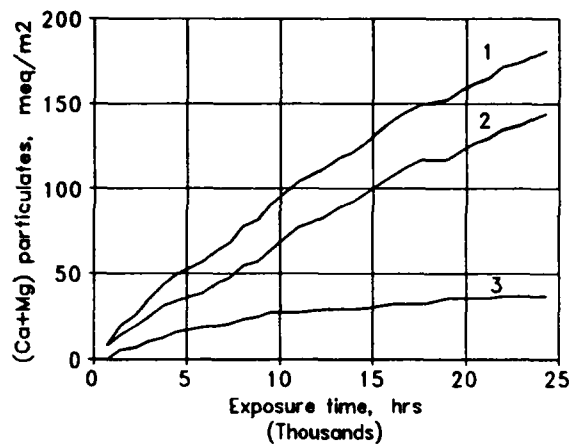


Figure 3. (Ca+Mg) particulate dry deposition on stainless steel: 1) total deposition; 2) fraction dissolved by strong acids and dry deposited acidic gases; 3) fraction soluble in precipitation.

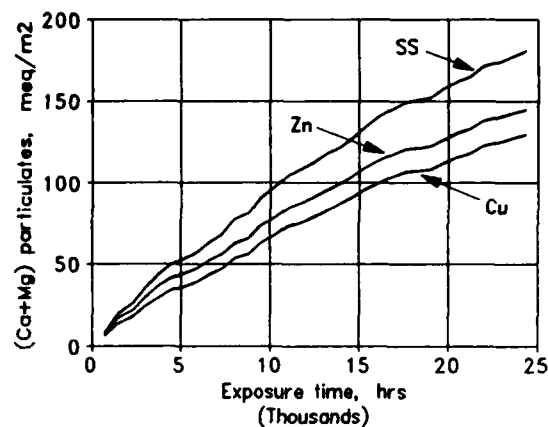


Figure 4. Total (Ca+Mg) particulates dry deposited on stainless steel, zinc, and copper.

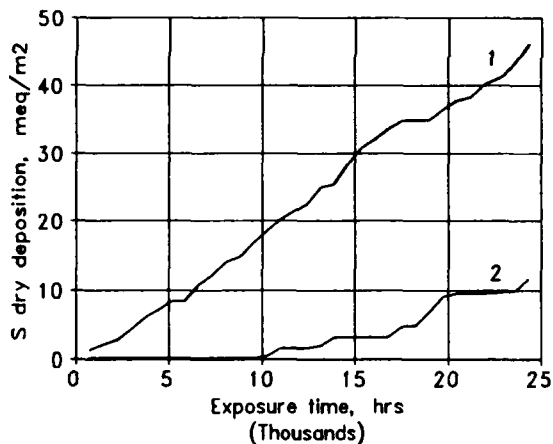


Figure 5. Dry deposition of sulfur species on stainless steel: 1) total sulfur; 2) sulfate deposited with coarse mode fraction.

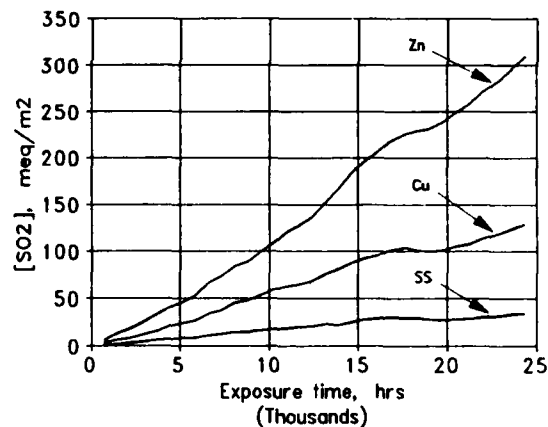


Figure 6. Sulfur dioxide dry deposited on stainless steel, zinc and copper.

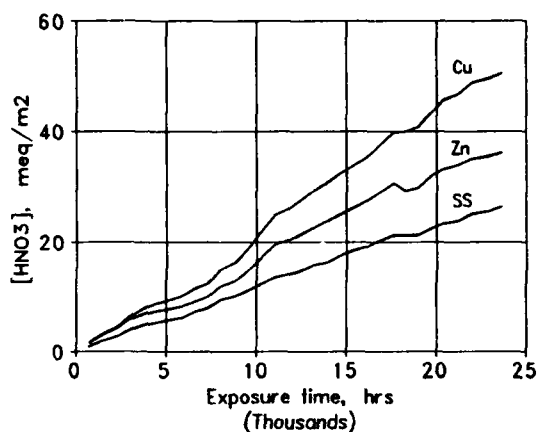


Figure 7. Nitric acid dry deposited on stainless steel, zinc, and copper.

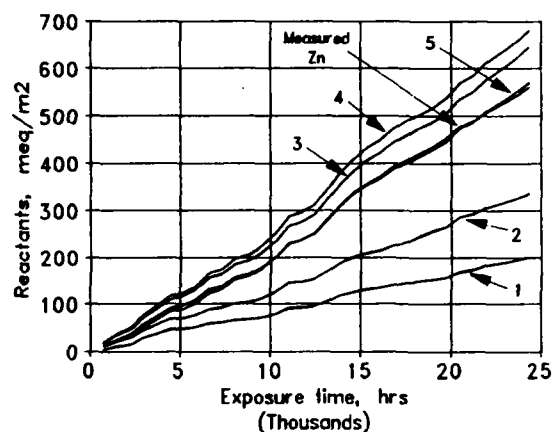


Figure 8. Cumulative model terms for zinc dissolution: 1) precipitation, rSV; 2) plus H^+ ; 3) plus $[SO_2]$; 4) plus $[HNO_3]$; 5) minus basic particulates, $[CaMg]$.

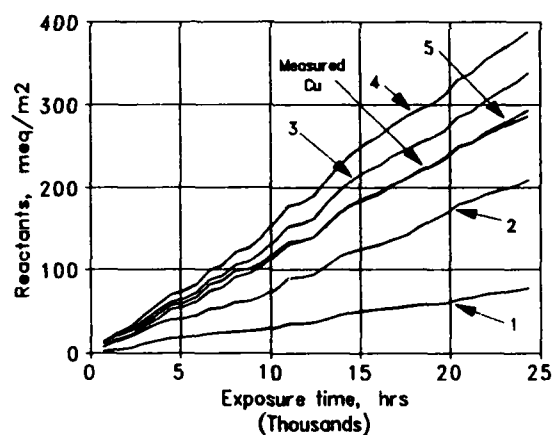


Figure 9. Cumulative model terms for Cu corrosion product dissolution: 1) precipitation, rSV; 2) plus H^+ ; 3) plus $[SO_2]$; 4) plus $[HNO_3]$; 5) minus particulates, $[CaMg]$.

DEFECTS OF STEEL STRUCTURES CAUSED BY ATMOSPHERIC CORROSION

Dagmar Knotková
National Research Institute for Protection of Materials
U měšťanského pivovaru 4
170 04 Praha 7
Czech Republic

Jaroslava Vlčková
National Research Institute for Protection of Materials
U měšťanského pivovaru 4
170 04 Praha 7
Czech Republic

Lubomír Rozlívka
ROKON - Steel Structure, Research, Engineering
Třanovského 2396
738 01 Frýdek - Místek
Czech Republic

Abstract

The best way to get information about interaction of the steel structure and environment is evaluation of the results of case-analyses of corrosion damage in longer period and investigation of the state of steel structures in service conditions.

Detailed non-destructive and destructive evaluation of corrosion effects and corrosion attack of structural elements after exposure in atmospheres with different corrosivity gives qualitative and quantitative values important for later research, but also for designers and users.

Data from more than 90 cases of corrosion damage on steel structures were collected. Corrosion effects on selected structural elements (joints, overlap, inside of section) were evaluated using different technical and scientific methods.

General view of evaluated cases shows that many of defects were caused by non optimal choice, application and maintenance of protective systems. Very important is good design and performance of joints. Very dangerous are all types of crevices.

Collected data form a part of developed Czech Information System on the Behaviour of Structures.

Key terms: corrosion effects on steel structures, corrosion attack of structural elements, information system, cause and phenomena of corrosion damage

Modern endeavour to achieve reductions of the steel induces to applying of effective structural systems (often thin-walled) at designing. In this case the corrosion phenomena can already influence useful qualities much more than in the case of structures, when the reserve of the material is usually considerable.

To follow this endeavour the aim of our work was to specify how much the atmospheric corrosion is the process leading to the limit states and which elements in the structural and technological design of the steel structure influence its durability positively or negatively lest it should be affected by atmospheric corrosion.

The principle of the solution was to study corrosion behaviour of real elements in the atmospheres with various corrosivity. A study of the interaction of the structure and environment was directed to determine the elements where the corrosion attack can be considerable. The causes can be technological, unsuitable handling with material and inner material imperfections.

The research of steel structure defects caused by atmospheric corrosion has been done in following directions:

1. The investigation of the state of steel structures in service and the conditions for their production and erection.
2. The collecting of knowledge about steel structures defects from the archives of the National Research Institute for Protection of Materials.
3. Detailed non-destructive and destructive evaluation of selected cases of corrosion behaviour of elements and models.
4. The design of questionnaires and data sheets for evaluation of the corrosion damage of the steel structure for the Czech Information System on the Behaviour of Structures.

The structural state investigations and evaluation of the results of expertise activity in longer period give the basic information about crucial effects of atmospheric corrosion on steel structures. This is the best way to get information about interaction of the steel structure and environment, especially information about determination of unsuitable design from corrosion point of view. It is necessary to have a knowledge of production and storing conditions for reliable determination of service behaviour of steel structures. These conditions can principally change the service behaviour of the structure.

The investigation in this field and expertises of service failure of steel structures use mostly non-destructive methods, especially these applicable in situ. The expert's experience and the quality of standards, used for the analysis of the damage, are very important, obtained information is mostly qualitative.

Therefore we have included detailed and often destructive evaluation of selected cases of corrosion phenomena on the elements of steel structures collected after service. For this purpose we have used different methods of evaluation at considerably corroded parts of demolished or reconstructed steel

structures. In this way it was possible to get quantitative conclusions about corrosion damage or detailed description of the corrosion effect at selected place. This process brought us much new information and ideas for the next research.

Basic process consists of inspection of the structure and in selection and taking of suitable elements. It is necessary to take photographs of the element's placing in structure and its corrosion changes. It is also necessary to estimate the environment and get information about production and service history of the structure. Then the element and its particular areas are evaluated in detail.

Following effects and magnitudes are observed:

- the residual thickness (destructively and non-destructively)
- corrosion pits incidence and their depth and dislocation
- roughness of corroded surfaces
- type and quality of protective systems, eventually the history of the maintenance (quality of protective systems, especially paints, are deduced from microscopy of the cut)
- topography of the sulphate agglomerations (nests) in the rust
- thickness and analysis (phase, elementary etc.) of the corrosion products layer
- protective ability of the rust on weathering steel
- quality of the material (structure, inclusions) and of system material-surface layer (rust, coat)
- evaluation of metallographic cross sections (weld, gap, lapped joint, corrosion pits on selected surfaces)
- surface corrosion phenomena with use of electron microscopy

Only brief account of procedures shows evaluations which are elaborate and difficult but they give very valuable information. For example the samples with different intensity of local corrosion attack can be evaluated by x-ray radiography. Intensity of blackening of sensitive photographic paper is compared with blackening of surfaces with standard slots of different depth. With a view to higher resolution the radiographs were transformed to eight colours according to the residual thickness. For digital evaluation of the radiographs system Photomation P - 1700 was used and then they were analysed and evaluated by computer.

Photographs of selected defects and examples of new methodological approach shows that systematic work helped to intensify the knowledge of corrosion defects of steel structures. (Fig. 1 - 9)

It is important for designers and users of steel structures to have knowledge of the rate of particular damages and their causes. For this purpose we evaluated the results of our research in the last period (1) and the result of archival expertise analyses of the National Research Institute for Protection of Materials (2). These conclusions are given later. More than 90 cases were processed.

Our information system forms a part of a data base of the Institute of Theoretical and Applied Mechanics (3). The data sheet is compatible with the Citation File of the data base of the AEPIIC International Center of the University of Maryland (4).

It is necessary to comment that the rate of occurrence of particular damages is rather influenced by the data collecting method. The expert analyses were asked for in the field of actual problems of practice. Relatively greater ratio of steel structures made from weathering steel Atmofix was observed because our research was connected with this problem.

In spite of these facts we decided that the account gives a good view of main types and causes of corrosion damage of steel structures. It resulted from the fact that this account is the summarization of more than ten years of expertise activity of the National Research Institute for Protection of Materials in this field and gives a good view of problems and requirements of practice.

1. Types and numbers of objects evaluated	
- steel structures of citizen constructions	17
- technological steel structures	19
- steel structures of animal production objects	10
- bridges, foot bridges	6
- crane tracks	4
- tower structures, TV towers	4
- electric distribution towers, switching stations	12
- tubular lattice steel towers	8
- accessory structures and parts	12
- jacketing	6
2. Followed phenomena of corrosion	
- damage of paints, lost of protective function	38
- damage of other surface protection systems (zinc coating)	8
- decrease of protective function of rust-patina	24
- corrosion in the joint (screw, rivet, weld)	17
- corrosion in the overlap	10
- corrosion in the inlet to the soil, footing or flooring	21
- corrosion on phase boundary (container, tank)	3
- corrosion at the place of unsuitable shape and structural design of steel structure	10
- corrosion in caverns, inside the sections, unclosed tubes	12
- material failure	2
- bimetallic corrosion and contamination of the material by rust	3
3. Cause of corrosion damage	
- unsuitable choice of material	5
- unsuitable choice of surface protection	8
- unsuitable kept surface finish	25
- application of paints on badly prepared surface	10
- bad storing of semi-products and elements	12
- design cannot make a good application and keeping of the surface protection possible	12

- execution of the steel structure aid in the course of corrosion 2
- inner defects of material 2
- specific operational causes at technological steel structures (abrasion, spray of technological agents) 15

Executed research of the steel structures state and archival expert reports processing shows, the defects of steel structures caused by atmospherical corrosion are usually of this type:

- surface protection does not function well, because it was not sufficiently dimensioned or sufficiently kept
- surface protection does not function well, because it was applied on badly prepared surface or the surface damaged by corrosion before application of the surface protection or its final layer, usually in the result of long unsuitable periods at storing and in the course of assembly
- surface protection does not function well, because constructional design does not allow quality application of protective layer
- increased corrosion arises at places of structures where constructional design aid in the intensification of corrosion effects (various joints, fixing, limitation of desiccation, creation of condensations etc.)
- occurrence of the corrosion defect is conditioned by inner defects of material
- corrosion attack was caused by specific operational causes and unsuitable combination of materials.

This summary shows that designer, producer and user of steel structure can avoid most of defects or minimize the range of corrosion damage.

At usual steel structures (masts, electric masts, usual bridges) the defects mostly occur for wrong and unsystematic maintenance of paints.

Supporting and accessory structures of objects are damaged at places where the water leaks in or condenses, in unventilated wet spaces or at places with increased influence of the environment (wet fixing, insufficient joint rigidity, joint leakage). The element design is also difficult at these objects for the surface protection to be well applicable and maintained. Some technological media can also cause.

Special defects occur in the objects made from thin sheets, where the corrosion usually arises in joints of sheets and at top and especially lower flanging sections. Use of shaped sheet for roofs brings considerable problems in joints and places of overlap. Accumulation of mechanical impurities also causes adverse effects.

Production and assembly of majority of structures takes a long time and it brings difficulties with semi-products storing. Final finish has than depressed quality in most of the cases.

Joints of any type are frequently the source of defects. A basic requirement is the joint rigidity and joint tightness. Complementary protective precautions are not usually applied.

Corrosion problems as a result of inner material defect is exceptional in atmospheric conditions. We have met the disintegration of nuts with high content of inclusions.

The operational conditions at technological structures and structures of animal production objects are often so severe that application of long-lasting surface protection is difficult and its maintenance is impossible. These objects would be protected by high quality protective systems like more layer quality paints and especially duplex coatings.

General view of evaluated cases shows that a crucial number of defects was caused by wrong application and maintenance of surface protection, even if the frequency of these defects is connected with, has relation to technical, economic and political situation in Czechoslovakia during last decades. Constructional points of view are identically important. It is necessary to give attention to the design of joints.

Negative consequences of corrosion can be prevented in the phase of technical design of steel structure by

- proper structural design of structural elements and joints and by choosing the right protective systems
- evaluated quantification of corrosion effects and their consequences to load carrying capacity and service life of supporting elements which makes it possible to strengthen adequately the structure against defined corrosion effects.

Some procedures for calculating these corrosion effects are suggested below.

Weakening of supporting cross-section is determined on the basis of corrosion characteristics rated experimentally or assessed in compliance with standards. For example ISO 9224 sets guiding values of corrosion rates for structural metals and time of exposure up to 10 and over 10 years.

Calculated values of corrosion loss over the life time of the structure for structural elements in open atmosphere and in category of location 2 is determined by the equation (7)

$$K_{tD} = K_{10} + a_{10} (T_d - 10) \alpha_d \alpha_K \alpha_U$$

where

α_d = 1.20 - the partial coefficient of reliability of corrosion loss determination

α_K = 1.00 up to 2.50 - the coefficient depending on accuracy of structural design and securing the maintenance

α_U = 1.00 up to 1.50 - the coefficient describing the effect of category of location of corroding surface

Maximum allowable value of corrosion loss (μm) for thicknesses of the elements up to 20 mm is determined from the equation

$$K_{Td}^{max} = 333 + 33 t \quad \text{for } 5 \text{ mm} \leq t \leq 20 \text{ mm}$$

It issues from presumption proved in practice that maximum allowable corrosion loss for element with thickness of 5 mm is 500 μm , for thickness about 20 mm it is 1000 μm . Analogous values are recommended also in the standards and publications (5, 6).

If these conditions are not met it is necessary to compensate the corrosion weakening by adequate corrosion allowance, it means to add the thickness of material determined from the point of view of limit state of loading capacity without considering the corrosion effects. This calculation has to be applied for weathering steels and steel structures with heavy corrosion stress wherever regular maintenance in a satisfactory way is not rational.

Calculated fatigue strength is determined for corrosion net section by decreasing the coefficient which expresses higher notch sensitivity of corroded material surface. This effect is important namely for elements with little structural or technological notches. For strongly notched details this effect is not essential.

Values of the corrosion coefficient for calculated fatigue strengths set in ČSN 73 1401 and in the Czech version of the European pre-standard for steel structures design are in following table.

Table: Coefficient of corrosion γ_k for calculated fatigue strength

Standard of designing		Coefficient of corrosion γ_K
ČSN 73 1401	EC - ENV 1993	
category of notch		
A	160 up to 140	0.80
B	125 up to 112	0.90
C	100 up to 90	0.95
D up to G	80 up to 36	1.00

We can achieve basic decrease of corrosion damages of steel structures by quality engineer work in the following directions:

- suitable selection of the place for steel structure, in the case the place is given it is necessary to deduce corrosivity of environment including service sources
- to solve structural design which avoids the rise of corrosion damages
- to optimize the use of materials, their combining and protective systems
- to ensure and control conditions for quality surface protection
- to determine and keep on regular cycles of maintenance.

It is necessary to describe better the functional effects of corrosion phenomena especially in those cases, when the material of supporting elements is considerably corroded.

The above results make it obvious, that the collection of data obtained by experimental research of corrosion problems of steel structures with better description and quantification of corrosion effects is of high technical significance and improve the knowledge of atmospheric corrosion in the viewpoint to real objects and service conditions.

References.

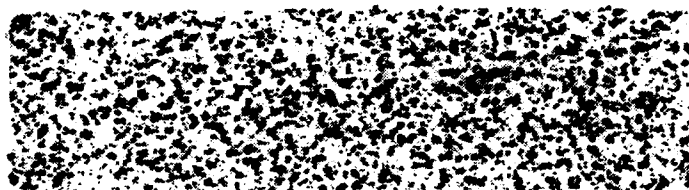
1. D.Knotková, J.Vlčková, J.Honzák, Atmospheric Corrosion of Weathering Steels in Atmospheric Corrosion of Metals, ASTM STP 767 (Dean, Rhea editors, ASTM Philadelphia, 1992), p.7
2. D.Knotková, Defects of Steel Structure Caused by Atmospheric Corrosion in Lessons from Structural Failures (M.Drdácký editor, Aristocrat Telč, 1991), p.25
3. M.Drdácký, Structural Performance Data - Their Collection, Evaluation and Utilization in Lessons from Structural Failures (M.Drdácký editor, Aristocrat Telč, 1991), p.5
4. N.Fitzsimonis, D.W.Vannoy, Architecture and Engineering Performance Information Centre (AEPIC) - What it is and what it means to you (ASCE Preprint, 1983)
5. H.E.Townsend, J.C.Zoccola, Eight-Year Atmospheric Corrosion Performance of Weathering steel in Industrial, Rural and Marine Environments in Atmospheric Corrosion of Metals, ASTM STP 767 (Dean, Rhea editors, ASTM Philadelphia, 1982), p.45
6. ČSN 03 8260 Protection of Steel Structures Against Atmospheric Corrosion. Specifications, production, quality control and maintenance, ÚNM 1983
7. Vítkovice Steel Comp. Standard VN 73 1466 - Steel Structures from Weathering Steels (Vítkovice 1990)

Figure 1 Prints of rust

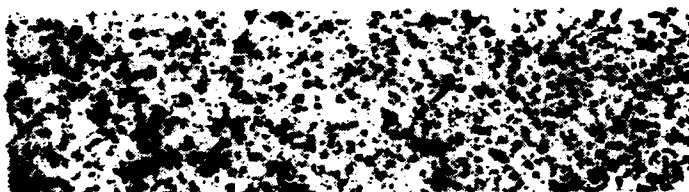
Documentation of state of rust layers with a view to free, non-adherent portion of rust.

Comparative method makes possible to evaluate:

- state of rust layer on surfaces corroding at different position on the object or structure

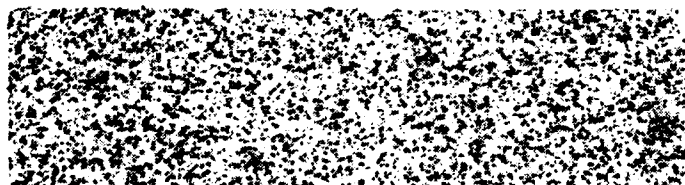


upper



lower

- state of rust layer on surfaces corroding in environments with different corrosivity



low corrosivity



high corrosivity

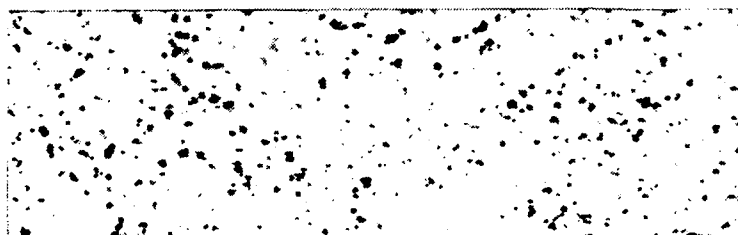
Figure 2 Topography of the active centers ("nests") in rust layers

Comparative method makes possible to evaluate:

- different steels exposed in the same conditions

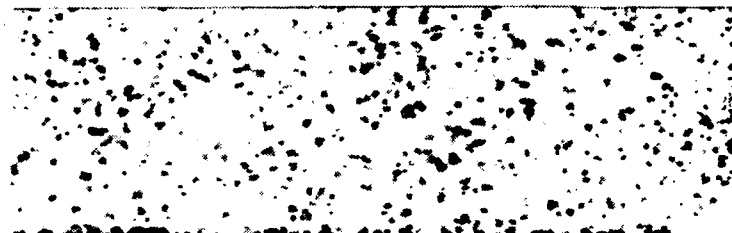


weathering steel

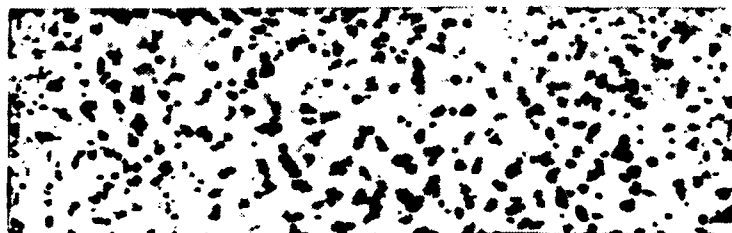


structural steel

- course of corrosion at different position and orientation of corroding surfaces on the object or structure



upper

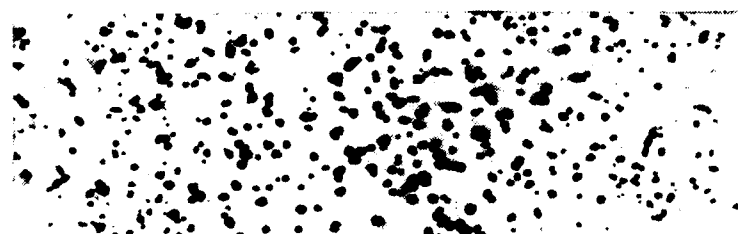


lower

- course of corrosion in environments with different corrosivity



low corrosivity



high corrosivity



Figure 3 Part of steel structure (technological crane track) applied in extreme conditions of metallurgical factory. Maintenance of protective systems was not rational, a new structure from weathering steel (with corrosion allowances of steel) was erected



Figure 4 local corrosion defects in crevices and near to crevices of screw joints on steel structure from weathering steel

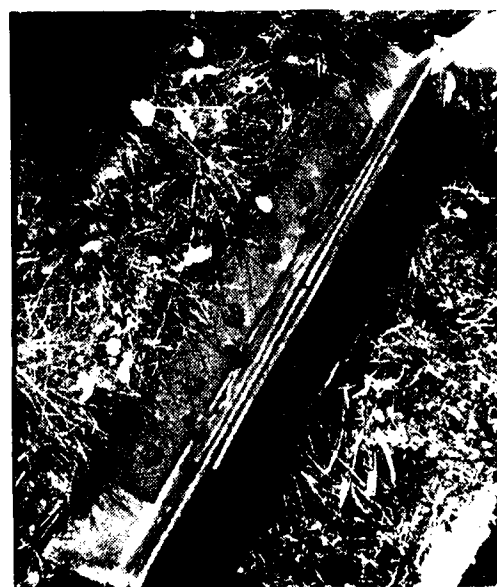


Figure 5 Layers of rust in areas of screw joints (a) deforming by pressure of rust the cover plates (b)

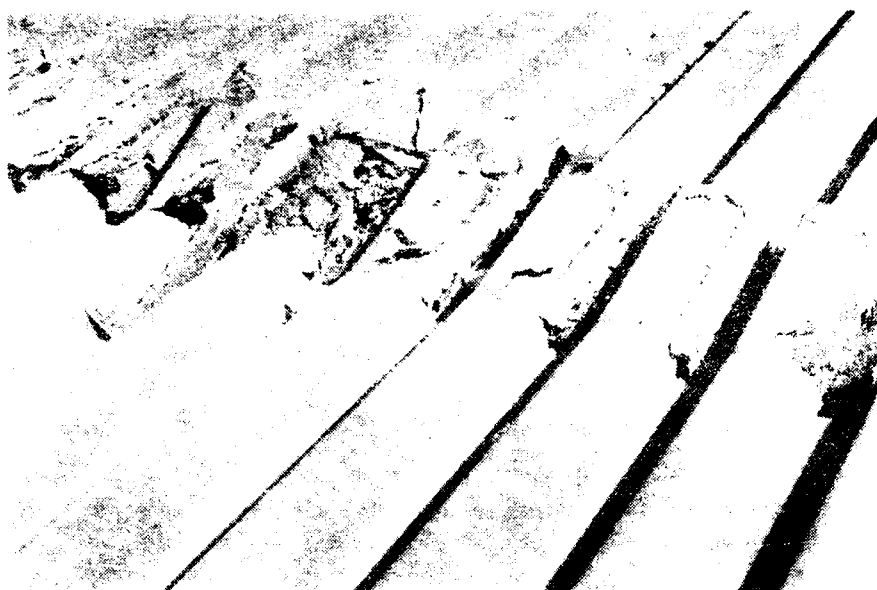


Figure 6 — reaction to crevice at overlapping of steel sheets in
; foot



Figure 7 Desintegration of screw nuts with high content of
inclusions



Figure 8 Crack of non continuous weld joint by crevice corrosion

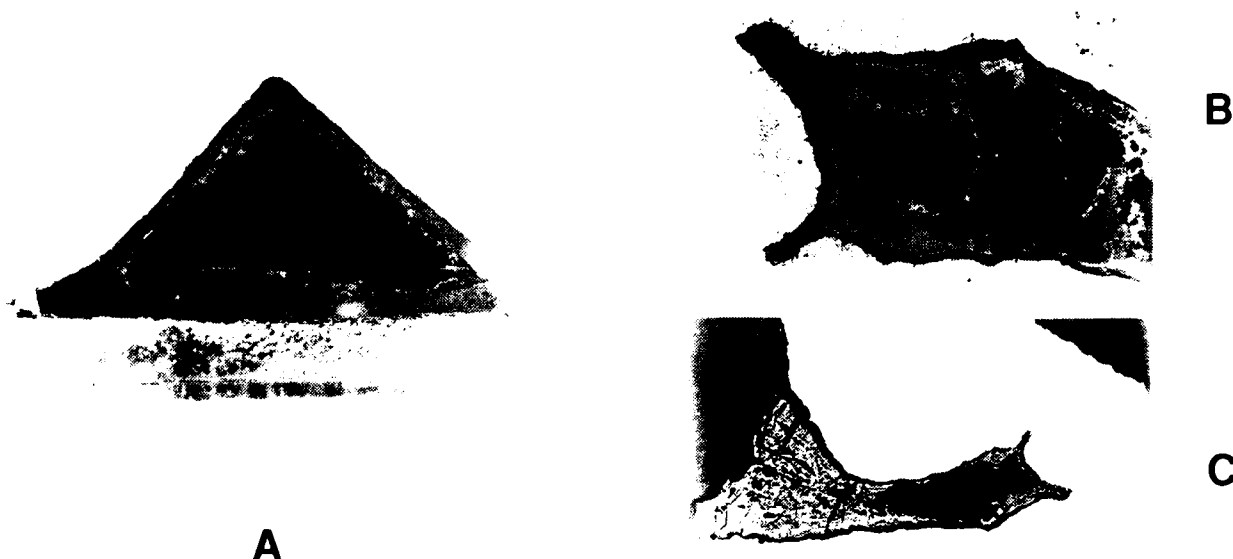


Figure 9 Cross section of a hollow structural element with layer of rust inside (a)
Cross section of weld from this element with rust and scale in crevice (b 16x), (c 50x)

Environmental Effects in the Atmospheric Corrosion of Zinc: An Immersion- Drying Study

Asdrúbal Valencia
Corrosion Group
Universidad de Antioquia - A. A. 1226
Medellín, Colombia

Ramiro Pérez
Corrosion Group
Universidad de Antioquia - A. A. 1226
Medellín, Colombia

Carlos Arroyave
Corrosion Group
Universidad de Antioquia - A. A. 1226
Medellín, Colombia

Sergio Mesa
Corrosion Group
Universidad de Antioquia - A. A. 1226
Medellín, Colombia

Abstract

During the last six years this Group have been studying atmospheric corrosion in Colombia by means of field and laboratory research. One of the complementary studies is on the corrosion behavior of zinc, which is one of the four structural metals exposed in different test sites.

The atmospheric corrosion of zinc was studied this time by using an immersion- drying system, simulating several atmospheres containing different levels of SO_2 , Cl^- and CO_2 . The potential variation with time was recorded. Corrosion damage was determined by weight loss measurements and corrosion film characterization.

The data enabled the determination of the role of pollutants in the film formation and protectiveness, as well as their synergistic action on the corrosion behavior of this metal.

Key terms: zinc, atmospheric corrosion, immersion-drying testing

Introduction

Zinc is a commonly used metal in alloys such as zamaks and brasses, but its main application is as protective coating on carbon steel. That is so because one of the most desirable characteristics of this metal is its corrosion resistance in most atmospheres. The technical and economic advantages of protecting steel by galvanizing have been known for more than 100 years.

The protection that zinc provides to steel is due to its lower corrosion rate, then acting as a barrier between iron and the atmosphere, but also there are galvanic effects, because zinc behaves as a sacrificial anode respect to the steel substrate after the coating begins to fail or is mechanically damaged.

There are other uses of zinc also based on its corrosion resistance.

The atmospheric corrosion of zinc has been widely studied in laboratory and field exposures¹⁻⁵. The general nature of the zinc corrosion process is known to some extent. Almost 30 years ago, Anderson⁶ described the atmospheric corrosion of zinc as dependant on the frequency of rain and dew, the acidity of condensates on the zinc surface, and how fast it dries. This view has been presented by Legault⁷ and corroborated by many researchers including Schikorr⁸, Guttman⁹, Rozenfeld¹⁰, Barton¹¹ and Mattson¹².

In the absence of industrial pollutants or marine influences, the atmospheric corrosion of zinc begins when the surface contacts with condensed moisture. This first involves the formation of zinc oxide or zinc hydroxide¹³. Equilibration with atmospheric carbon dioxide (CO_2) leads to the formation of basic zinc carbonate. Although basic zinc carbonate does not seem to be stable, it has been identified on zinc surfaces and may occur as a metastable species¹². In rural atmospheres this coating is apparently protective and would tend to inhibit a continuation of the corrosion process decreasing the rate of corrosion with time. However, the zinc hydroxide [$\text{Zn}(\text{OH})_2$] or zinc carbonate can dissolve by rain precipitation and wash from the surface.

On the other hand, it has been established that zinc corrodes more rapidly in highly industrialized areas than in rural ones¹⁴. Sulfur dioxide (SO_2) is the major contributing factor because it reacts with humidity providing some acidic conditions. In this case there is a reaction of the hydrogen ion with the basic zinc corrosion product available. The product is a soluble salt, such as zinc sulfate (ZnSO_4), which can be washed from the steel surface thus increasing the corrosion rate.

In marine environments, away from industrial centers and large cities, the major pollutant would be sodium chloride (NaCl). It has been shown that the corrosion rate of zinc, decreases with diminishing salinity as the distance from the ocean is increased¹⁵.

In brief, there is a reasonable good knowledge of the general nature of zinc corrosion process and the effect of the common pollutants. However, specific details of the chemical and physical processes, and complex interactions between these processes, which allow one to assess changing environmental conditions and determine their effect on corrosion, are not nearly as well known. In this paper, variations of atmosphere quality - as simulated by the immersion drying system- are studied in relation with electrode potential variation with time and weight loss. The nature and protectiveness of the films formed is analyzed as well as the synergistic action of the pollutants.

Experimental Procedure

Material

The specimens to be corroded in the various environments were pure rolled zinc that was found spectrographically to contain 0.002%Fe, 0.045%Cd, 0.079%Cu, 0.001%Pb and less than 0.001% Al, Sn and Si.

Before use in an experiment, each zinc specimen (15 cm x 2.5 cm x 0.1 cm) was thoroughly cleaned with 600 mesh polishing paper. Pickling was performed in a hot solution (80°C) of chromium trioxide (200 g CrO₃ in water up to 1000 ml). Then the specimens were scrubbed in water with a bristle brush, rinsed in water and dried with hot air. Although 36 specimens were used, 6 for environment, only 3 of them were weighted for control in each case.

Setup

The experimental setup is presented in figure 1 and described elsewhere^{18,17,18}. The system rotates exposing the samples to alternate conditions of immersion and drying, according to a prescribed cycle (a cycle of 41.38 min consisting of 11.38 min immersion and 30 min drying). The electrode potentials were measured at the begining of the immersion period by means of a EXTECH digital multimeter against a COLE PHARMER saturated calomel electrode. Initially these values were determined in the morning and the afternoon, but after two months only one daily measurement was made.

Environments

The composition of solutions used to simulate each environment is given in table 1. Solutions were well aerated by air bubbling and continuously renewed by a controlled slow overflow. In reservoirs # 1 and # 6, CO₂ was injected through the air hose, so it contained 0.07% vol. CO₂, which is equivalent to the content found in an urban polluted atmosphere. All corrosion experiments were performed simultaneously at 43°C.

Table 1 Simulated environments

Receptacle #	Solution Composition	Atmosphere
1	Distilled water	Rural
2	10 ⁻³ M NaCl	Marine
3	Distilled water + CO ₂	Urban
4	10 ⁻⁴ M NaHSO ₃	Industrial
5	10 ⁻³ M NaCl + 10 ⁻⁴ M NaHSO ₃	Industrial-marine
6	10 ⁻³ M NaCl + CO ₂	Marine-urban

Corrosion Products Analysis

After 140 days of exposure, measurements and observations, specimens were dismantled and mechanically and chemically cleaned.

Corrosion products were removed in accordance with ISO/DIS 8407 standard^{1B}. The removed power was analyzed by means of a JEOL DX-60-s X-ray diffractometer and a PERKIN ELMER 1760X Fourier Transform infrared spectroscopy working from 15000 to 50 cm^{-1} .

Weight loss was determined in accordance with ISO/DP 9226 standard^{2J} and the corroded surfaces were examined and photographed.

Experimental Results

Electrode Potential Variation

Figs. 2 to 7 show the evolution of electrode potential for the six simulated environments. Comparison of the behavior of zinc in the various atmospheres is more readily seen in Fig. 8. In figure 2, corresponding to distilled water (rural environment) the Zn potential goes down from 900 mV to 500 mV in short time and then it stabilizes around the last value. In the marine atmosphere, 10^{-3}M NaCl solution, the potential remains high (more than 900 mV) and only after 60 days it begins to decrease slowly up to 820 mV, figure 3.

The potential of Zn in the 10^{-4}M NaHSO_3 solution decreases with time from 980 mV to 850 mV in a 110 days period, figure 4.

The tendency of Zn potential in distilled water + CO_2 after 20 days varies between 900 and 1000 mV, figure 5, as it also does in the 10^{-3}M NaCl + CO_2 solution, figure 6.

In the 10^{-3}M NaCl + 10^{-4}M NaHSO_3 solution, the Zn potential behaves in a similar fashion as in NaHSO_3 , going down slowly from 950 to 850 mV in 110 days.

Weight Loss

The data on weight loss for the different atmospheres are presented in table 2. Corrosion was a little bit higher in receptacle # 5 corresponding to the industrial-marine atmosphere. Also the data from reservoirs # 2 and # 6 show that the presence of CO_2 does not seem to affect the corrosive action of salinity. On the other hand, in an urban environment containing only CO_2 as pollutant (reservoir # 3) corrosion was of comparable magnitude the one observed in # 4 receptacle (industrial atmosphere), it was even higher. Irrespective of other pollutants, corrosion in a

marine environment is very similar, according to this limited results.

Table 2. Corrosion, measured as weight loss per unit area

Receptacle	Simulated atmosphere	Corrosion value mg/cm ²
1	Rural	3.05
2	Marine	6.97
3	Urban	5.69
4	Industrial	4.18
5	Industrial-marine	7.11
6	Marine-urban	6.94

Corrosion Products

Identification of corrosion products was somewhat hindered due to the lack of enough diffraction patterns in the "Power Diffraction File" available. The same could be said of the infrared spectra that were in hand. In table 3, the compounds found in the corrosion film, by both analysis methods, are presented.

From table 3 it is apparent that the formed compounds have a well defined stoichiometry and it should be possible to describe the corresponding reactions.

Discussion

The results obtained from weight loss, electrode potential evolution, corrosion products composition and the examination of the corroded surfaces, give some ideas of the corrosion process of zinc, as simulated by the immersion-emersion method.

First of all, regarding weight loss, it is clear that the obtained data agree with the observed fact that zinc corrode more rapidly in highly industrialized areas than in rural ones. However, the data does show that corrosion is much higher in marine atmospheres. To understand this one has to bear in mind that this is an accelerated test, where long term expositions are simulated, and weight loss is not a determining parameter as the potential evolution is.

In brief, the potential versus time curves show that only in distilled water (rural environment) there is an appreciable potential decrease. This tendency is also seen, although in a much more limited way an order, in marine, industrial, industrial-marine and urban-marine; whereas the potential increases slowly in urban environment.

Table 3. Composition of Corrosion Products Found by X-Ray Diffraction and Infrared Spectroscopy.

Receptacle	Simulated atmosphere	Compounds
1	Rural	ZnO 2ZnCO ₃ .3Zn(OH) ₂ Zn(OH) ₂
2	Marine	ZnO 2ZnCO ₃ .3Zn(OH) ₂ ZnCl ₂ .4Zn(OH) ₂ Zn(ClO ₄) ₂ .6H ₂ O
3	Urban	ZnO 2ZnCO ₃ .3Zn(OH) ₂
4	Industrial	ZnO 2ZnCO ₃ .3Zn(OH) ₂ ZnSO ₄ .7H ₂ O 2ZnSO ₃ .5H ₂ O ZnS (?)
5	Industrial marine	ZnO 2ZnCO ₃ .3Zn(OH) ₂ ZnSO ₄ .7H ₂ O 2ZnSO ₃ .5H ₂ O ZnCl ₂ .4Zn(OH) ₂ ZnS (?)
6	Marine urban	ZnO 2ZnCO ₃ .3Zn(OH) ₂

The potential vs time curves obtained by linear regression, figure 8, show that zinc potential in the marine, industrial and marine industrial environments have a similar behavior, slowly decreasing with time and being almost parallel.

In urban environment, potential increases slowly and in the marine-urban atmosphere it remains almost constant, it appears to be the sum of the two individual environments.

The Zn potential in a rural environment, does not have a linear behavior as shown in figure 2, although the curve allows to see the fast potential decrease.

There is not a very good agreement in relation with the corrosion products, due to the limitations already mentioned. But this will be discussed in future work.

Conclusion

From the discussed results the following conclusions are drawn:

- The accelerated electrochemical immersion emersion test method for measuring atmospheric corrosion, is a good procedure to compare zinc behavior in various environments.
- In rural environment there is an appreciable pasivation of zinc, shown by the potential decrease.
- There is also a tendency to passivation, although in a much more limited way, in marine, industrial and marine - industrial environments.
- The corrosive action of CO₂ is remarkable in the absence of other pollutants, so the corrosion in urban environments is of a magnitude similar to that in industrial atmospheres.
- The presence of high contents of CO₂ does not modify the action of salinity on the corrosion behavior of Zinc.
- A synergistic action of SO₂ and CO₂ is apparently detected in the potential-time curve.
- It seems that there is a tendency to localized corrosion in urban atmospheres, as shown by the potential in CO₂ environments.

Acknowledgement

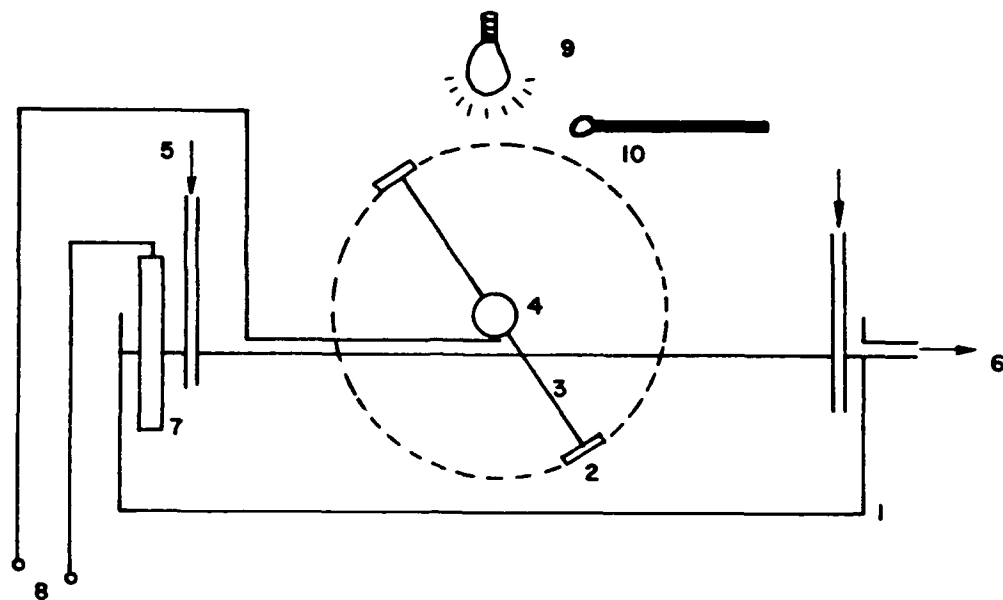
The authors wish to thank the Comité Central de Investigaciones de la Universidad de Antioquia for its financial support.

References

1. E. A. Anderson, Atmospheric Corrosion of Non Ferrous Metals. ASTM STP 175. ASTM, Philadelphia, 1955: p. 126.
2. S. R. Dunbar, W. Showak, " Atmospheric Corrosion of zinc and its alloys", Atmospheric Corrosion. John Wiley, New York, 1982: p. 529.

3. E. A. Anderson, Corrosion, 15 8(1959): p. 409t.
4. S. L. Granese, B. M. Rosales, Revista Iberoamericana de Corrosión y Protección, 17 3(1986): p. 197.
5. S. Feliu, M. Morcillo, Corrosión y Protección de los Metales en la Atmosfera, Bellaterra, Barcelona, 1982.
6. E.A. Anderson, C. E. Reinhard, "Zinc", in H.H. Uhlig (Ed.) Corrosion Handbook, John Wiley, New York, 1963, p.331.
7. R.A. Legault, O.B. Ellis, Atmospheric Factors Affecting the Corrosion of Engineering Metals, ASTM STP 646, ASTM, Philadelphia, 1978: p. 83.
8. G. Schikorr, Atmospheric Corrosion Resistance of Zinc, (New York: American Zinc Institute and London: Zinc Development Association, 1965)
9. H. Guttman, Metal Corrosion in the Atmosphere. ASTM STP 435, ASTM, Philadelphia, 1968: p. 223.
10. T. L. Rozenfeld, Atmospheric Corrosion of Metals, NACE, Houston, 1972.
11. K. Barton, Protection Against Atmospheric Corrosion, John Wiley, New York, 1973.
12. E. Mattson, Materials Performance, 21 7(1982): p. 9.
13. S.Cramer et al., Degradation of Metals in the Atmosphere. ASTM STP 965, ASTM, Philadelphia, 1988: p. 229.
14. F. H. Haynie, J. B. Upham, Materials Performance, 9 8(1970): p. 25.
15. H.R. Ambler, A.S.J. Bain, Journal of Applied Chemistry, 5 9(1955): p. 437.
16. M. Pourbaix, Rapports Techniques CEBELCOR, 109, RT 160, Brussels, 1969.
17. M. Pourbaix, " An Electrochemical Wet and Dry Method for Atmospheric Corrosion Testing", Atmospheric Corrosion, John Wiley, New York, 1982: p. 167.
18. F. Ojeda, D.C. Marin, Diseño y Montaje de un Ensayo de Corrosion Atmosférica en el Laboratorio. Ingeniería Metalúrgica, Universidad de Antioquia, Medellín. 1990.
19. ISO/DIS 8407 Metals and Alloys. Procedures for removal of corrosion products from corrosion test specimens.

20. ISO 9226 Corrosion of metals and alloys. Method of determination of corrosion rate products from corrosion test specimens.
21. S.L. Granese, B.M. Rosales, A. Ferandez, "Behaviour of Zn in atmospheres containing sulfur dioxide and chloride ions" 11th International Corrosion Congress (Florence - Italy: Associazione Italiana di Metallurgia, 1990): p. 2.71.



- 1.- Receptacle
- 2.- Specimen
- 3.- Brass rod
- 4.- Rotating Shaft
- 5.- Electrolyte inflow
- 6.- Electrolyte overflow
- 7.- Reference electrode
- 8.- Potential measurement terminals
- 9.- Lamp
- 10.- Thermometer

FIGURE 1.- EXPERIMENTAL SET-UP FOR THE IMMERSION - EMERSION TEST

Figure 2. Zinc in Distilled water

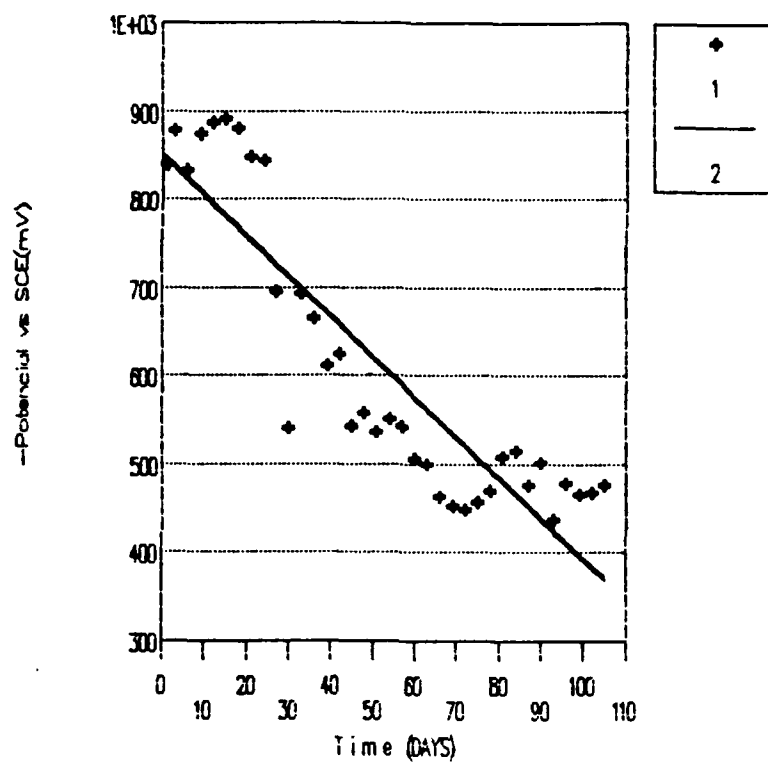


Figure 3. Zinc in $1E-3M$ NaCl Solution

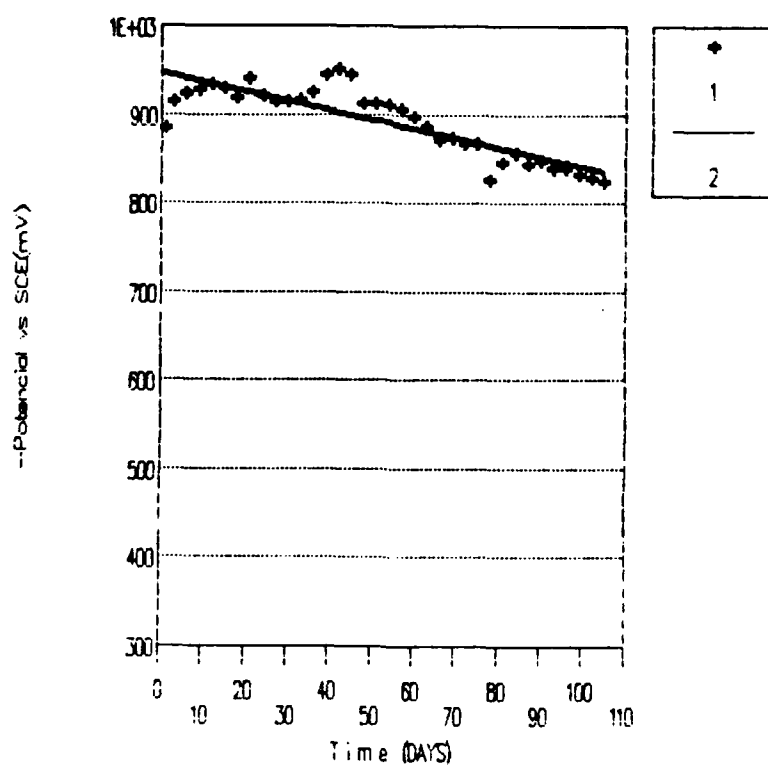


Figure 4. Zn in 1E-4M NaHSO3 solution

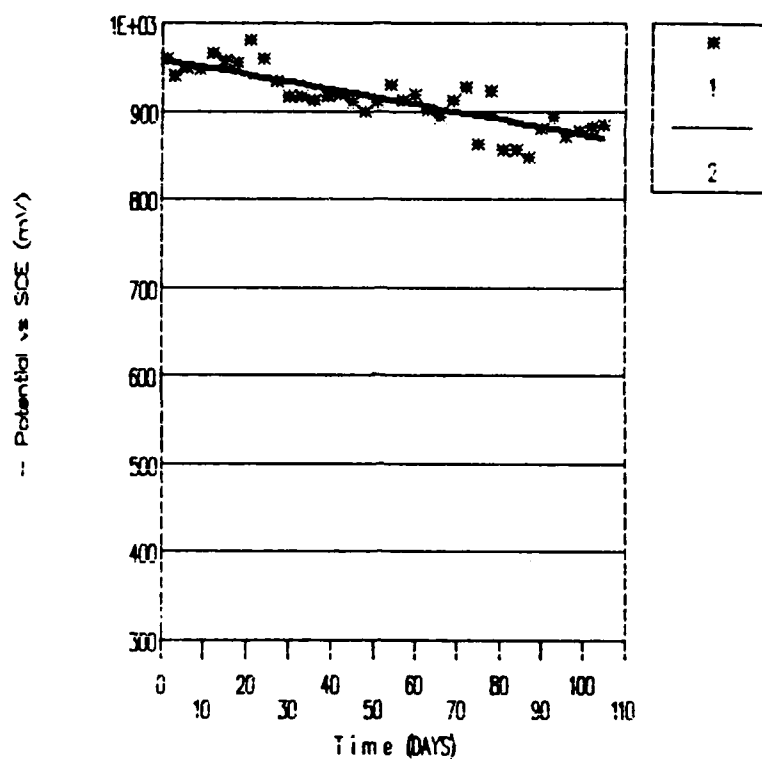


Figure 5. Zn in distilled water + CO2

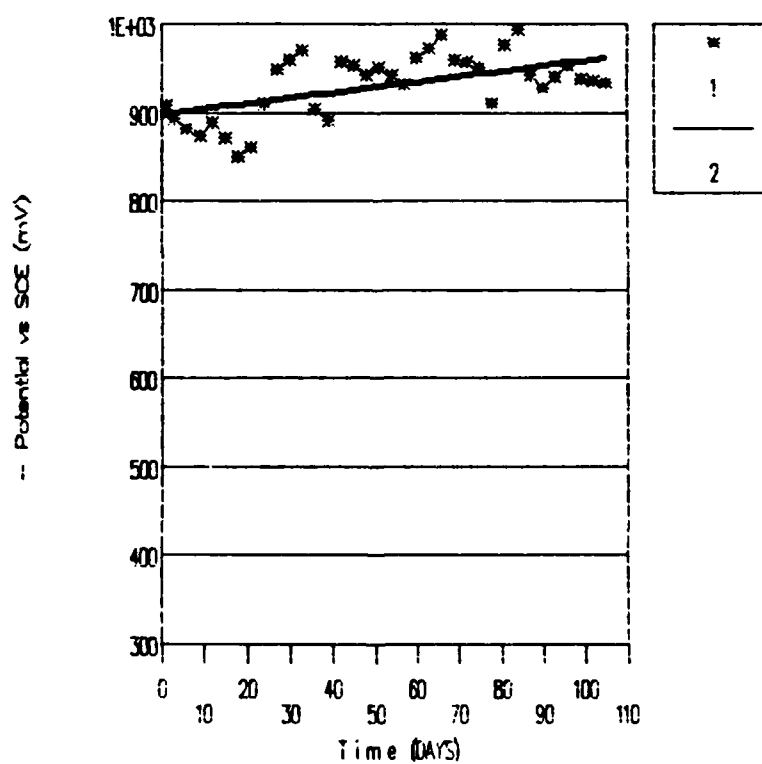


Figure 6. Zn in 1E-3M NaCl + CO₂

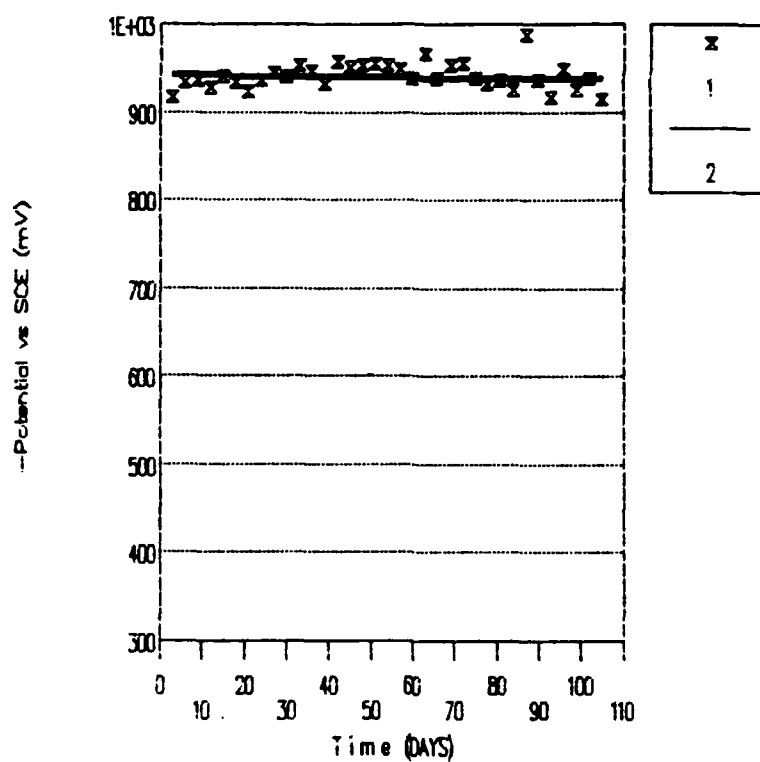


Fig. 7. Zn in 1E-3M NaCl+1E-4M NaHSO₃

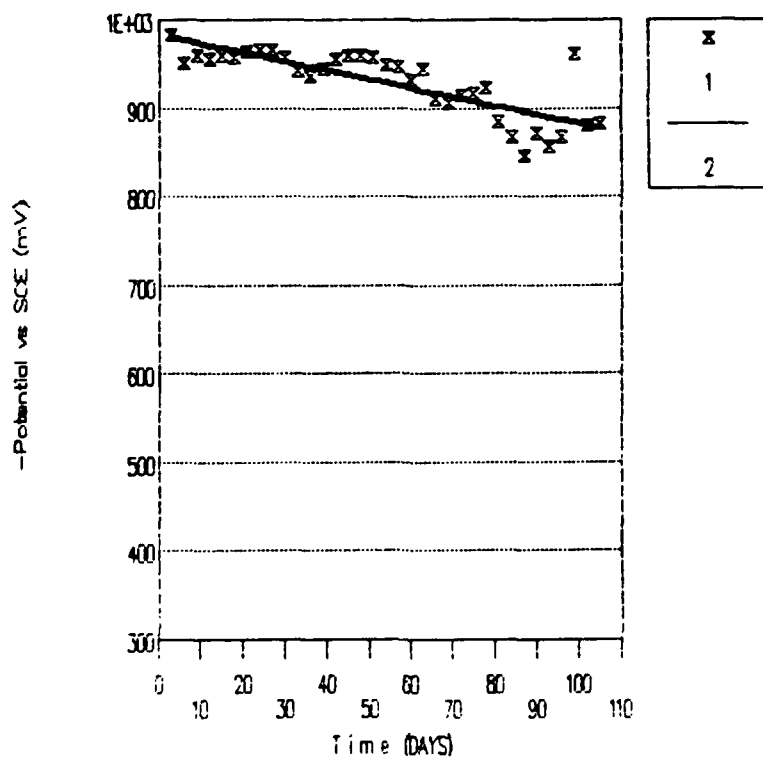
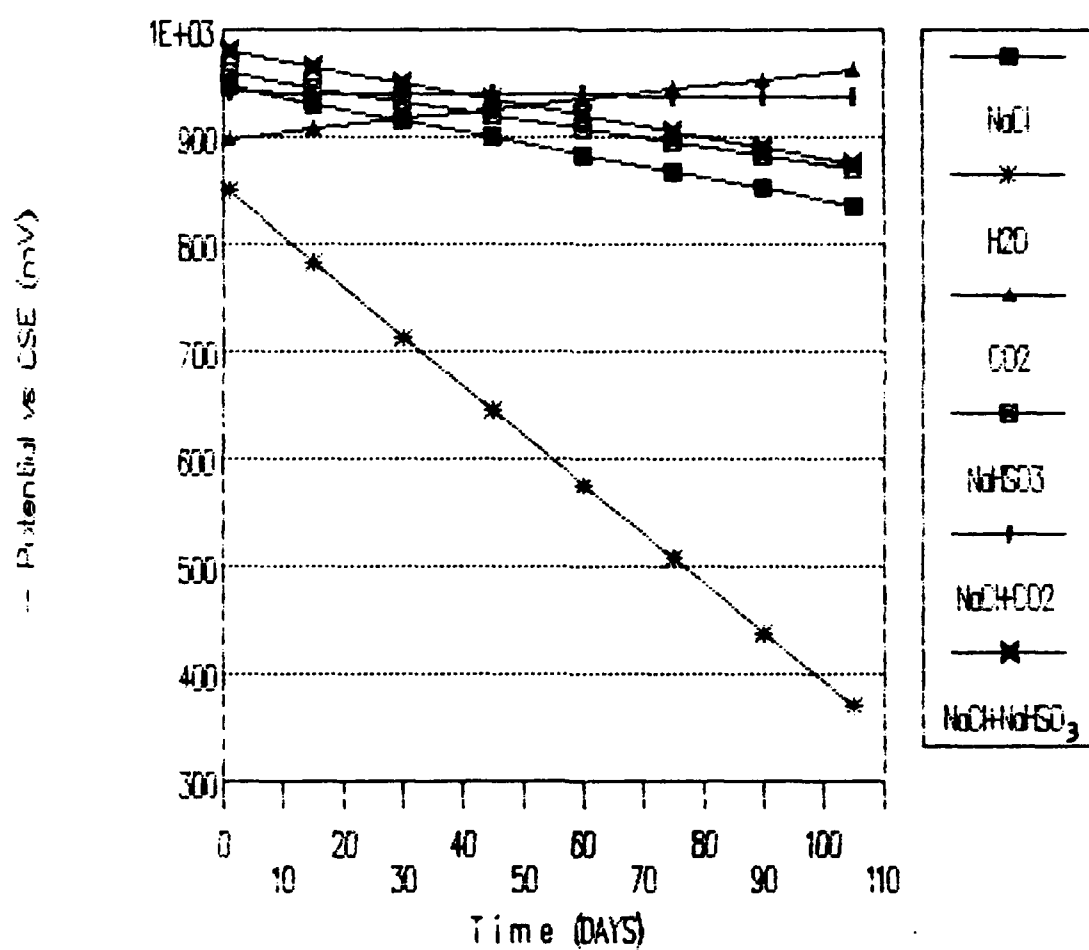


Figure 8. Potential - Time Curves for
all Six Environments



Estimations of Economic Damage of Large Industrial
Cities Infrastructure from Corrosion Caused
by Pollutions into Environment*

A. Lyajh

* Paper not available at time of printing.

The Mechanism and Control of Stress Corrosion Cracking of Zirconium in Sulfuric Acid

Brian J. Fitzgerald
Exxon Chemical Company
P.O. Box 4900
Baytown, Texas 77522

Te-Lin Yau
Teledyne Wah Chang Albany
P.O. Box 460
Albany, Oregon 97321

Abstract

Zirconium (UNS R60702) has been found to exhibit stress corrosion cracking (SCC) in 64 to 69 percent sulfuric acid. Test results indicate that SCC of zirconium develops in two steps; (1) zirconium oxide breakdown followed by (2) crack growth. Local breakdown of the zirconium oxide film exposes unfilmed zirconium to the sulfuric acid environment. Then, crack growth is determined by competition between the repassivation rate of the underlying unfilmed zirconium versus its dissolution rate.

Mechanistically, it is proposed that the breakdown of zirconium oxide film can occur by two paths (1) mechanical; for example by plastic deformation or (2) electrochemical; for example by exposure to sulfuric acid containing oxidizing ions. Cracks propagate if the repassivation rate is slightly below the dissolution rate. Test results appear to support an anodic dissolution mechanism for crack initiation and growth.

Three control measures for the SCC of zirconium in sulfuric acid have been demonstrated in laboratory and field tests. One measure is to add a hydrocarbon to the sulfuric acid. The hydrocarbon inhibits SCC although the inhibiting mechanism is not understood. The other two measures are (1) stress relieving and (2) shot peening. Both function by modifying the stress-strain field and increasing the strain required for mechanical rupture of zirconium oxide surface film.

Keywords: zirconium, sulfuric acid, stress corrosion cracking, SCC

Introduction

Sulfuric acid is a complicated corrodent, changing from the reducing nature of dilute solutions to the oxidizing nature of concentrated solutions. The corrosion of most metals and alloys in sulfuric acid depends strongly on acid concentration and temperature.

Zirconium (UNS R60702) resists attack by sulfuric acid over a wide range of concentrations (up to 70%) and temperatures (to boiling and above). Then, there is a sharp change to higher corrosion rates over only a slight increase in acid concentration. Consequently, zirconium is uniquely suitable for many sulfuric acid applications since stainless steels corrode at higher rates in less than 70% sulfuric acid.^{1,2}

One of zirconium's limits in sulfuric acid is the selective corrosion of welds. The selective weld corrosion is attack of intermetallic precipitates in the grain boundaries.³ Heat treatment at 774°C/hr/25.4mm can improve the corrosion resistance of zirconium welds.^{4,5} This treatment has been successfully employed on zirconium equipment for many years, hence, stress corrosion cracking (SCC) of zirconium in sulfuric acid did not surface as a problem.

Recently, a new zirconium clad (zirconium explosion bonded to carbon steel) vessel experienced SCC in a nominal 65 percent sulfuric acid process. It was added to the process after 10 years of successful use of post weld heat treated solid zirconium process equipment in this environment. A laboratory and field testing program exploring the cracking parameters and SCC countermeasures was undertaken. Results of this program are reported in this paper.

Experimental Approach

The materials used in all the tests conformed to commercial zirconium plate, strip or rod. They were produced in the mill annealed condition. The test solutions were made from deionized and distilled water and reagent grade chemicals. The exception was samples labeled as "plant", which were removed from the commercial operating unit.

The static SCC tests were performed with U-bend or C-ring specimens per ASTM G30 or G38 respectively. The U-bend specimens were finished through 120 grit emery paper and bend around a radius of either 0.5 inches (13mm) or 0.625 inches (16mm). The calculated strains were 5 percent and 6.25 percent, respectively, in the U-bends. The C-rings were fabricated from pipe, finished through 120 grit emery paper and strained with matching zirconium bolts to 1 percent or less.

The dynamic SCC specimens were machined from bar stock to a diameter of 0.5 inches (13mm) with a 2 inch (51mm) gage length and finished through 120 grit emery paper.

Welds in U-bend specimens were full penetration butt welds using filler metal ERZr2. The welds were in the longitudinal direction of the U-bend specimen, parallel to the direction of bending. The heat of welding was sufficient to precipitate a second phase at the grain boundaries in the heat affected zone.

Electrodes for electrochemical testing were 0.375 inches (10mm) in diameter by 0.5 inches (13mm) long. Each electrode was drilled and tapped for use with a PTFE compression fitting as described in ASTM G5. The electrode OD's were centerless ground to a surface finish equal to 600 grit emery paper.

Immediately prior to testing, the specimens were degreased in an ultrasonic cleaner with acetone, rinsed in distilled water and dried in room temperature air. U-bends and C-rings were suspended on glass hooks in 2 liter flasks fitted with water condensers. The acid strength of the solutions were measured before and after testing to ensure water evaporation did not increase the acid strength.

Results

Laboratory Studies of SCC Behavior

Effect of Oxidizing Ions on Zirconium Cracking. Zirconium is known to be susceptible to SCC in certain oxidizing environments, such as ferric chloride and nitric acid.^{6,7} Since acid analysis revealed that several of these ions could be present in the sulfuric acid, as trace contaminants, a factorial type experimental approach was taken to examine the effect of these ions. Based on the acid analysis chloride, ferric, fluoride and nitrate ions were selected for testing. The level at which each ion was tested and the results of the tests are presented in Tables 1 and 2. The results indicate that:

- Ferric and nitrate ions cause cracking of zirconium in 65% sulfuric acid at 130°C.
- Chloride ions do not cause cracking of zirconium exposed to 65% sulfuric acid at 130°C.
- Fluoride ions at the 0.3 ppm level, in combination with ferric ions, accelerate cracking of zirconium. Fluoride ions, by themselves, do not cause cracking of zirconium in 65% sulfuric acid at 130°C.
- No other combinations of the four ions affected the SCC resistance of zirconium in 65% sulfuric acid at 130°C.

The influence of the corrosion potential (E_{corr}) on the cracking of U-bends is compared in Figure 1 and Table 3. Both the plant acid sample and the reagent acid sample with trace amounts of oxidizing ions crack U-bend specimens while the reagent acid sample (without the addition of the trace oxidizing ions) does not. The E_{corr} values of the solutions producing SCC in U-bends is at least 400 mV more noble than the non cracking reagent grade acid. Schematically, this is shown in Figure 1 by comparing the E_{corr} values in the different solutions to the anodic polarization curve for zirconium in 65% sulfuric acid. Note that the E_{corr} values for SCC fall near or above the transpassive region of the polarization curve; suggesting stability of the zirconium oxide surface film is critical to the SCC process. It is interesting to note that long term U-bend exposures in sulfuric acid concentrations above and below 65 percent did not produce cracking of U-bend specimens as given in Table 4; again emphasizing the critical nature of electrode potential and film stability in the SCC process.

Effect of Acid Strength on Zirconium Cracking. Having shown that trace quantities of oxidizing ions can initiate SCC of zirconium in sulfuric acid, the effect of acid strength was investigated. These results are summarized in Table 5. Note that the oxidizing power of the solutions, as measured by E_{corr} , has been maintained by the addition of ferric ions but the acid strength has been varied. This results in the cracking of U-bend specimens only in the 65 and 67 percent sulfuric acid solutions. U-bends in acid solutions of 63 percent and 72 percent did not crack even though ferric ions were present.

The ability of the oxidizing ions to induce SCC in only a narrow range of sulfuric acid concentrations; but not across the range of acid concentrations, again suggests that SCC of zirconium in sulfuric acid is controlled by more than the redox potential of the solutions. Indeed, the lack of SCC in acid strengths outside of a relatively narrow range suggests that the acid itself is critical to the growth of the crack while the electrode potential is critical to crack initiation. Thus, while zirconium oxide film stability may be impaired by ferric ions in 63 or 72 percent sulfuric acid, cracking does not occur.

Effect of Strain on Zirconium Cracking. A factorial type approach was used to screen physical and microstructural parameter for their effect on the potential for zirconium to SCC in sulfuric acid. The factorial type approach ensures that each parameter, individually and in combinations with the other parameters, is considered for its ability to cause cracking.

Strain was chosen as a parameter because of observations that cracks were restricted to locations of unusually high strains, such as batten strip fillet welds, while lower strain locations, like circumferential butt welds, were free of cracking. In addition, laboratory screening tests, on low strain C-ring and weld specimens, did not indicate SCC. The presence of a zirconium weld was selected as a variable, not for its ability to produce a residual strain, but because welding produced an iron rich, grain boundary precipitate previously associated with intergranular corrosion in sulfuric acid. Thus, it was important to know if the cracking experienced by zirconium was really intergranular corrosion exacerbated by high strains or truly a cracking phenomena independent of grain boundary phases. Lastly, temperature was investigated because of its usual and recognized effect on corrosion and cracking processes.

The levels chosen for each of the variable and the results of the factorial tests are summarized in Table 6. Note that only the high strain condition significantly affected cracking. Temperatures between 110 to 130°C and grain boundary phases, as produced by welding, did not significantly affect the cracking process.

Slow strain rate tests were used to further investigate the mechanical factor on the cracking process. Test results are shown in Table 7. Using this test method, the 65 percent plant acid produced a failure strains of 7.3 percent while the failure strain in distilled water was 28.5 percent.

Examination of Table 7 shows the failure strain of zirconium is greatly reduced in sulfuric acid below 70 percent and above 63 percent acid strength. For example, the failure strain of zirconium in 70 percent sulfuric acid is 31.5 percent but in 67 percent sulfuric acid it is 6.3 percent. Further, secondary cracks are present on the 67 percent sulfuric acid specimen indicating a high probability of SCC. The 70 percent sulfuric acid specimen failed in a completely ductile manner and did not display secondary cracks. This type of failure morphology was repeated in sulfuric acid concentrations of 63 percent and below. These findings were consistent with or without an oxidizer in the sulfuric acid, although the oxidizer did lower the failure strain somewhat.

The data for sulfuric acid without an oxidizer is plotted in Figure 2 to emphasize the loss of ductility for zirconium in a relatively narrow range of sulfuric acid strength. This figure clearly shows that in-situ straining can induce SCC without the presence of oxidizing ions. Compare this behavior to the performance of U-bend specimens tested in identical environment as summarized in Table 7. In these tests, the U-bends, strained in the atmosphere, do not develop SCC unless an oxidizer is also present in the acid. This again emphasizes the zirconium oxide film is capable of providing protection from SCC but destabilizing the film by increasing its corrosion potential to the transpassive region, through the introduction of oxidizers, can initiate the cracking progress. However, the data also clearly shows that in-situ straining in oxidizer free environments also induces SCC. Therefore, it appears the primary role of oxidizers is to destabilize the zirconium oxide film and expose the underlying unfiled zirconium to the sulfuric acid. Crack propagation, then, depends on a critical balance between the dissolution rate of the unfiled zirconium and its repassivation rate. Hence, the low failure strains and cracked U-bends occur only in a relatively narrow sulfuric acid range of greater than 63 percent but less than 70 percent sulfuric acid.

Laboratory Studies of SCC Countermeasures.

Heat Treatment and Shot Peening. Two conventional methods to control SCC are heat treatment and shot peening. Both methods were tried on U-bend samples and the results are given in Table 8. Note, relatively low heat treatment temperatures and typical peening intensities by ZrO₂ shots were effective in preventing cracking of U-bend specimens. It should be intuitively obvious that both heat treatment and shot peening are only effective SCC mitigation methods under conditions of static strain. In situations where strain is dynamic the beneficial effects of both heat treatment or shot peening could be negated.

Hydrocarbon Addition. The addition of isopropyl alcohol to sulfuric acid was found to reduce zirconium's tendency to SCC in slow strain rate tests. The data in Table 9 shows relatively small additions of isopropyl alcohol, in the range of 0.1 to 0.2 extract saturation⁽¹⁾ (ES), greatly increases the failure strain and reduces or eliminates secondary cracking indicating a reduced tendency for SCC. It is worth noting the beneficial effects of the isopropyl alcohol were demonstrated under dynamic, slow strain rate conditions. This indicates the isopropyl alcohol alters the balance between the corrosion rate and the repassivation rate of unfiled zirconium surfaces produced by in-situ straining.

(1) Extract saturation is the ratio of moles of hydrocarbon to moles of sulfuric acid. Each 0.1 ES is approximately equal to 4% isopropyl alcohol.

Field Testing of SCC Countermeasures

Field U-bend Exposures. U-bends were installed in two locations in an operating unit:

- 65 % Plant Acid + 0 ES and
- 65 % Plant Acid + 0.1 ES.

The 0 ES condition was used to check the reliability of laboratory heat treatment and shot peening data while the 0.1 ES condition was chosen to verify the beneficial effect of hydrocarbon in preventing SCC of zirconium.

The field test results verified the laboratory data. That is, in the 0 ES location the "as fabricated" U-bends cracked while heat treated or shot peened U-bends did not. In the 0.1 ES test none of the U-bends cracked, confirming the inhibiting effect of the hydrocarbon on the SCC of zirconium in sulfuric acid. Table 10 summarizes the field U-bend tests.

Pressure Vessel Mock Up Testing. A small pressure vessel was designed so that strains in the batten strips, clad, nozzle liners, and the applied pressure stresses would equal or exceed those in the actual vessel. The operating conditions for the vessel mock up was 65 % Plant Acid (0ES), 130°C, and 425 psig.

Three vessel mock ups were fabricated. One was employed as a control to demonstrate that strains in the mock up were sufficient to induce SCC and the other two were employed to determine if heat treatment and shot peening could be effectively applied to typical fabrication geometries and actual construction techniques. A U-bend specimen was installed in each vessel mock up to ensure that the plant acid was capable of inducing SCC of zirconium. As summarized in Table 11, the "as fabricated" vessel mock up developed SCC within 3 days of start up while no SCC developed in the heat treated or shot peened vessel mock ups.

Discussion

SCC Mechanism

Corrosion potential measurements of zirconium in sulfuric acid solutions suggests a situation that is common to several recognized SCC systems; the separation of the metal - environment interface by a protective surface film. In this specific case, zirconium oxide, which is thermodynamically stable in sulfuric acid solutions of less than approximately 70 percent, is the protective surface film. In addition it is well recognized that film rupture can lead to SCC of iron based alloys.⁽⁶⁾ Following these arguments therefore, SCC of zirconium initiates when the protective surface film is mechanically or chemically damaged in a localized area. As discussed above, two means of locally rupturing the zirconium oxide exist: (1) in-situ mechanical straining or (2) electrochemical attack at film defect sites. This is sequentially shown in the schematic representation in Figure 3.

ZrO₂ film rupture, by mechanical straining or electrochemical attack, exposes unfilmed zirconium. Corrosion of the unfilmed zirconium precedes at a rate determined by the corrosion potential and current density for the specific concentration of sulfuric acid until growth of the ZrO₂ causes repassivation. Schematically, the film defect dissolves at an initial rate greater than the ZrO₂ covered surrounding surface; initiating an incipient crack. Continued growth of the film defect to form a true crack then requires the corrosion rate to be approximately equal or slightly greater than the repassivation rate. This is characteristic of the behavior between approximately 64 to 69 percent acid. If the repassivation kinetics dominate, crack growth ceases and very low, uniform corrosion would be the typical mode of metal loss. This characterizes the behavior in less than 64 percent acid. If the corrosion kinetics dominate, the incipient crack will be obliterated by high metal loss rates; as characterized by behavior in greater than 69 percent acid.

Based on the laboratory time to failure data, zirconium SCC in sulfuric acid solutions does not appear to be influenced by the presence of chloride (halide) ions and the ferric (oxidizing) ions appear to be primarily involved in film breakdown. This suggests that sulfuric acid is the environment responsible for SCC and, following the above discussion, anodic dissolution may be the prime crack propagation mechanism. That is, the sulfuric acid intensely but locally corrodes the unfilmed crack tip while the crack walls are passivated almost as fast by film growth; maintaining the critical balance for crack growth between active and passive behaviors. The relatively narrow sulfuric acid range in which zirconium appears susceptible to SCC supports this argument. In addition, this argument is also supported by the lack of hydrides on fracture surfaces, thus eliminating a hydrogen embrittlement argument. Further, the absence of striations or indications of incremental crack growth makes a film induced cleavage mechanism unlikely.

Another possible, although less likely mechanism for crack propagation, is absorption induced cracking. This mechanism must be considered because it can not be eliminated by metallographical examinations. In fact, the crack inhibiting effect of the isopropyl alcohol in sulfuric acid can support either the absorption or the anodic dissolution argument. In the case of the anodic dissolution model, the isopropyl alcohol perhaps functions by increasing the resistivity of the crack tip solution and, consequently, the corrosivity. For the adsorption induced cracking mechanism, the isopropyl alcohol may function by coating the crack surfaces and interfering with chemisorption, thus acting in a manner analogous to increasing the crack tip solution resistivity. We can only speculate that hydrogen, below the threshold level for hydride formation, may be the absorption species, although, it is certainly possible that another unidentified species is responsible.

SCC Countermeasures

Three countermeasures to zirconium SCC in sulfuric acid have been demonstrated in laboratory and field testing. Two of the countermeasures, heat treatment and shot peening, appear to function by reducing the likelihood of mechanical film rupture. As such, their effectiveness is expected to be limited to cases where the strain is somewhat less than 5%. The third countermeasure, addition of isopropyl alcohol to sulfuric acid, can be effective in cases where the strain is dynamic, however, its mechanism of inhibition is not known.

Heat treatment and shot peening mechanically modify the residual stress-strain field of the component. This is schematically illustrated by the stress-strain curves in Figure 4. Note that these curves apply equally to pressure vessels or U-bend stress corrosion cracking specimens.

The first point illustrated in Figure 4 is that fabrication, of U-bends or pressure vessels, yields areas that have been subjected to large amount of plastic strain, as represented by Point 1. The superposition of thermal stresses, pressure stresses, and other applied stresses during vessel operations pushes Point 1 along the plastic flow curve towards Point 3. The incremental strain, between Points 1 and 3, is the in-situ applied strain that can rupture the ZrO_2 film and lead to SCC.

The second point illustrated in Figure 4, is heat treating and shot peening produce identical effects, although the degree may vary. The stress reduction, with the accompanying strain relaxation, occurs in both heat treating and shot peening decreasing the likelihood the superposition of applied operation induced stresses will cause further plastic deformation (from Points 2 to 4) with the accompanying ZrO_2 cracking. Note, however, that sufficiently high strain or a dynamic load applied after heat treatment or shot peening, will render either treatment ineffective. Note, also, that shot peening modifies the stress-strain field on the near surface only; therefore exposure in environments with even low rates of uniform or localized corrosion will negate the beneficial effect with time.

Summary

Zirconium exhibits susceptibility to SCC in 64 to 69% sulfuric acid. This susceptibility significantly increases, when small amounts of oxidizing ions, such as Fe^{+3} and NO_3^- , are also present. Control measures such as heat treatment, shot peening and isopropyl alcohol addition, are found to be effective in preventing the SCC of zirconium in 64 to 69% sulfuric acid.

Acknowledgements

We would like to acknowledge the assistance of Robert Webber in conducting the field tests and Jack Cain, Tom Seabury, and Gary Cobb for assistance with the laboratory testing. The assistance of Terry Webster, retired from Teledyne Wah Chang Albany, was much appreciated and is gratefully acknowledged.

References.

1. E.W. Kleefisch, Ed., Industrial Applications of Titanium and Zirconium, (Philadelphia, Pa: ASTM STP 728, 1981), p. 181.
2. R.T. Webster, T.L. Yau, Materials Performance, 25 2 (1986): p. 15
3. B.S. Payne, D.K. Priest, Corrosion, 17 4 (1961) p. 120
4. E.W. Kleefisch, Ed., Industrial Applications of Titanium and Zirconium, (Philadelphia, Pa: ASTM STP 728, 1981), p. 85.
5. T.L. Yau, R.T. Webster, Corrosion, 39 6 (1983) p. 218
6. B. Cox, Langmuir, 3 6 (1987): p. 867.
7. R.H. Jones, Ed., Stress Corrosion Cracking, (Materials Park, Ohio: ASM International, 1992), p. 299
8. R.W. Staehle, et. al., Ed., Stress Corrosion Cracking and Hydrogen Embrittlement of from Base Alloys, (Houston, Tx: National Association of Corrosion Engineers, NACE-5, 1977), p. 180

TABLE 1		
3 X 2 Factorial - Zirconium (UNS R60702) in 65% H ₂ SO at 130°C with constant chloride ion content		
I. Matrix		
	Level	
Variable	High	Low
Fe ⁺³ (ppm)	105	0
F (ppm)	0.3	0
NO ₃ (ppm)	300	0

II. Data				
Variable			Constant	
Fe ⁺³	F	NO ₃	Cl	Test Result (Welded "U"-bend)
1. 0	0	0	200	NO CRACK 504 HRS
2. 105	0	0	200	CRACK 72 HRS
3. 0	0.3	0	200	NO CRACK 504 HRS
4. 105	0.3	0	200	CRACK 24 HRS
5. 0	0	300	200	CRACK 96 HRS
6. 105	0	300	200	CRACK 96 HRS
7. 0	0.3	300	200	CRACK 96 HRS
8. 105	0.3	300	200	CRACK 72 HRS
III. Results - Fe ⁺³ and NO ₃ ions affect time to failure - F ions with Fe ⁺³ ions decrease time to failure but F ions alone do not cause failure - Cl ions have no effect on time to failure				

TABLE 2		
3 X 2 Factorial - Zirconium (UNS R60702) in 65% H ₂ SO at 130°C with constant ferric ion content		
I. Matrix		
	Level	
Variable	High	Low
Cl (ppm)	200	0
F (ppm)	0.3	0
NO ₃ (ppm)	300	0

Data				
Variable			Constant ↓	
Cl	F	NO ₃	Fe ⁺³	Test Result (Welded "U"-bend)
1. 0	0	0	105	CRACK 72HRS
2. 200	0	0	105	CRACK 72 HRS
3. 0	0.3	0	105	CRACK 24 HRS
4. 200	0.3	0	105	CRACK 24 HRS
5. 0	0	300	105	CRACK 96 HRS
6. 200	0	300	105	CRACK 96 HRS
7. 0	0.3	300	105	CRACK 72 HRS
8. 200	0.3	300	105	CRACK 72 HRS
III. Results - F ions decrease time to failure - NO ₃ ions cause crack at slower rate than Fe ⁺³ ions - Cl ions have no effect on failure				

TABLE 3		
Corrosion Potential versus Time-to-Failure		
Environment	E _{corr} (MV, SCE)	U-bend Result ⁽¹⁾ (Time-to-Failure, HR)
65% Plant Acid	+ 220	F, (72)
65% Reagent Grade Acid + 50 ppm Fe ⁺³	+ 186	F (336)
65% Reagent Grade	-250	NF (768)
⁽¹⁾ F = Failure NF = No Failure		

TABLE 4		
Corrosion Potential Non-Oxidizing H ₂ SO ₄ versus Time-To-Failure		
Environment	E _{corr} (MV, SCE)	U-bend Result ⁽¹⁾ (Time-to-Failure, HR)
63% Plant Acid	-248	NF, (576)
65% Reagent Grade	-250	NF (768)
72% Reagent Grade	-260	NF (576)
⁽¹⁾ F = Failure NF = No Failure		

TABLE 5		
Effect of H ₂ SO ₄ Concentration on Time-to-Failure		
Environment	U-bend Result ⁽¹⁾ (Time-to-Failure, Hr)	E _{corr} (MV, SCE)
72% Reagent Grade + 50 ppm Fe ⁺³	NF (576)	+ 204
67% Reagent Grade + 50 ppm Fe ⁺³	F (24)	+ 190
65% Reagent Grade + 50 ppm Fe ⁺³	F(336)	+ 186
63% Reagent Grade + 50 ppm Fe ⁺³	NF (576)	+ 252
⁽¹⁾ F = Failure NF = No Failure		

TABLE 6		
3 X 2 Factorial - Zirconium (UNS R60702) in 65% Plant Acid		
I. Matrix		
	Level	
Variable	High	Low
Strain	$\geq 5\%$	$\leq 1\%$
Temperature	130°C	110°C
Weld	Yes	No

II. Data			
	Variable		Test Result
1. Low Stress	No Weld	Low Temp	NF ⁽¹⁾
2. Low Stress	Weld	Low Temp	NF
3. High Stress	No Weld	Low Temp	F
4. High Stress	Weld	Low Temp	F
5. Low Stress	No Weld	High Temp	NF
6. Low Stress	Weld	High Temp	NF
7. High Stress	No Weld	High Temp	F
8. High Stress	Weld	High Temp	F
III. Result			
High stress/strain affect cracking. All other primary and cross product variables are not significant.			
⁽¹⁾	NF =	No Failure	
	F =	Failure	

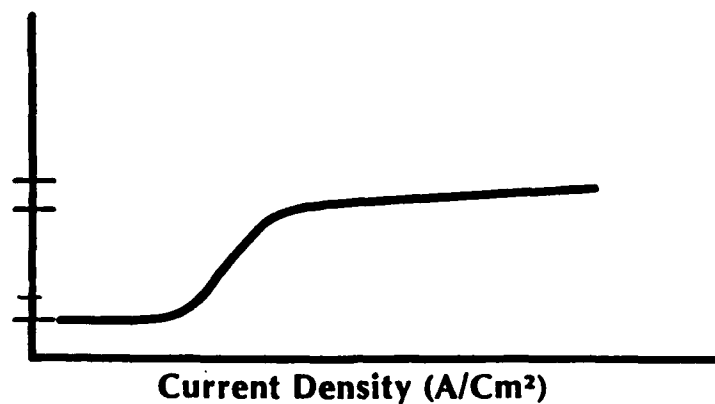
TABLE 7		
Zirconium (UNSR60702) - Comparison of Slow Strain Rate and U-bend Test Results		
Environment	Slow Strain Rate Results ⁽¹⁾ (% E _z @ 110°C)	U-bend Result ⁽²⁾ (Time to Failure, Hr 130°C)
72% H ₂ SO ₄ 72% H ₂ SO ₄ + 50ppm Fe ⁺³	38.9 20.2	NF (576) NF (576)
70% H ₂ SO ₄ 70% H ₂ SO ₄ + 50ppm Fe ⁺³	31.5 17.2	- -
67% H ₂ SO ₄ 67% H ₂ SO ₄ + 50ppm Fe ⁺³	6.3 4.9	NF (576) F (<24)
65% H ₂ SO ₄ 65% H ₂ SO ₄ + 50ppm Fe ⁺³	17.8 7.2	NF (768) F (336)
63% H ₂ SO ₄ 63% H ₂ SO ₄ + 50ppm Fe ⁺³	37.9 11.4	NF (576) NF (576)
60% H ₂ SO ₄ 60% H ₂ SO ₄ + 50ppm Fe ⁺³	31.4 16.1	NF (504) NF (504)
Plant Acid Distilled Water	7.3 28.5	F (<72) NF (672)
⁽¹⁾ Strain Rate was 2.5 x 10 ⁻⁶ Sec ⁻¹		
⁽²⁾ F = Failure NF = No Failure		

TABLE 8		
Laboratory Results of Heat Treated and Shot Peened "U"-Bend Specimens Tested at 130°C		
I. Heat Treated		
Environment	Heat Treatment °C/HRS	Cracked (HRS)
Plant Acid	425/1	N (480)
	None	Y (72)
Plant Acid	370/4	N (1080)
	None	Y (264)
Plant Acid	425/4	N (1080)
	None	Y (72)
II. Shot Peened		
Environment	Shot Peened Intensity	Crack (HRS)
Plant Acid	8A	N (864)
	10A	N (864)
	None	Y (216)
Plant Acid	6A	N (864)
	6A	N (864)
	8A	N (864)
	None	Y (216)

TABLE 9	
Effect of Hydrocarbon Addition on Dynamic Strain Tests ⁽¹⁾	
Environment	Slow Strain Rate Results (% E _r @ 110°C)
66% Plant Acid	5.2
65% Plant Acid	7.3
66% Plant Acid + 0.2 E.S. ⁽²⁾	22.9-36.2
65% Plant Acid + 0.1 E.S.	23.8-34.4
⁽¹⁾ Strain Rate was 2.5×10^{-6} /Sec ⁽²⁾ E.S. equals extract saturation. Ratio of moles of hydrocarbon to moles of sulfuric acid.	

TABLE 10		
Effect of Hydrocarbon Addition - Lab and Field Test Results		
I. 65% Plant Acid + 0 Extract Saturation		
U-bend Treatment	Lab Result ⁽²⁾	Field Result ⁽¹⁾
As-Fabricated (Control)	F	4/5 (F, <336 HR)
Heat Treated (425°C)	NF	0/2 (NF, 336 HR)
Shot Peened	NF	0/2 (NF, 336 HR)
II. 65% Plant Acid + 0.1 Extract Saturation		
U-bend Treatment	Lab Result	Field Result ⁽¹⁾
As-Fabricated (Control)	NF	0/2 (NF, 336 HR)
Heat Treated (425°C)	NF	0/2 (NF, 336 HR)
Shot Peened	NF	0/2 (NF, 336 HR)
⁽¹⁾ Number of cracked U-bends/Total number of U-bends exposed.		
⁽²⁾ F = Failure NF = No Failure		

TABLE 11		
Results of Vessel Mock-up Field Tests		
Vessel Mock-up Condition	U-bend Result	Mock-up ⁽¹⁾ Result
As-Fabricated	F	F (Nozzle Liner, 72 HR)
Heat Treated (425°C)	F	NF (504 HR)
Shot Peen	F	NF (504 HR)
⁽¹⁾ F = Failure NF = No Failure		

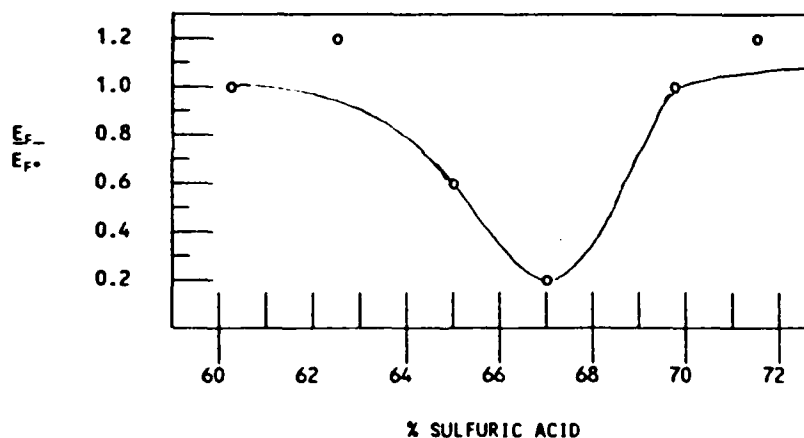


- A +220mv Plant Acid
 B +186mv Reagent Grade Acid + 50 ppm Fe³⁺
 C -250mv Reagent Grade Acid

ZIRCONIUM OPEN CIRCUIT POTENTIALS IN 65% H₂SO₄ SOLUTIONS

FIGURE 1

% H ₂ SO ₄	% Failure Strain (E _f) ⁽¹⁾	E _f /E _f [*] (2)
60	31.4	1.0
63	37.9	1.21
65	17.8	0.57
67	6.3	0.20
70	31.5	1.0
72	38.9	1.24

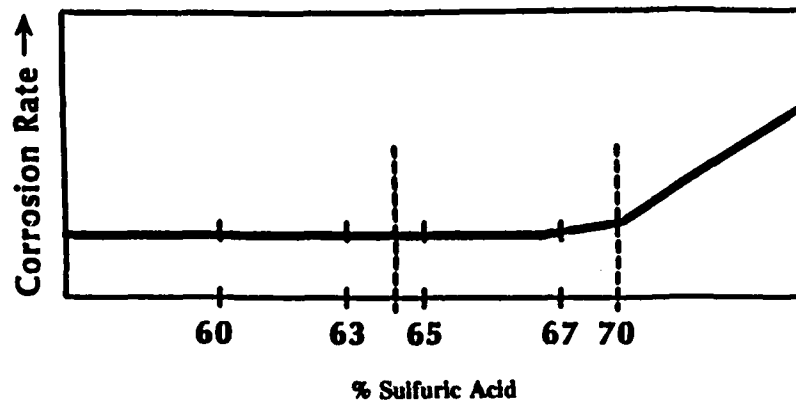


⁽¹⁾ Strain rate was 2.5×10^{-4} /Sec.

⁽²⁾ Results normalized by dividing the Failure Strain by the 60% H₂SO₄ Failure Strain.

Results of Slow Strain Rate Tests in Reagent Grade Sulfuric Acid

Figure 2



ZIRCONIUM CORROSION RESISTANCE DUE TO ZrO_2

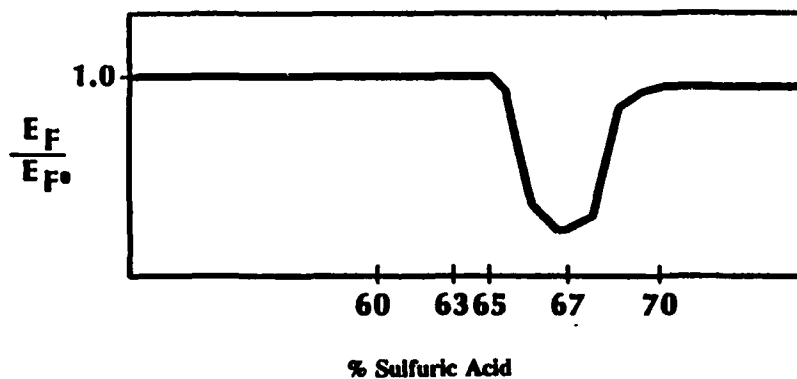
- $>70\% H_2SO_4$ - Oxide Chemically Attacked
- $<70\% H_2SO_4$ - Oxide Thermodynamically Stable

BUT

Breakdown can occur by Two Paths

- Mechanically - physical cracks by strain in oxide film
- Electrochemically - oxidizing ions degrade oxide film

FIGURE 3A
SCC OF ZIRCONIUM IN H_2SO_4



ZrO_2 BREAKDOWN EXPOSES UNFILMED METAL

- Crack initiation determined by Rate of Fresh Metal Generation (FMG) vs. Rate of Repassivation (RP)
- $<64\% H_2SO_4$
RP \gg FMG - General Corrosion, ductile failure
- $<64\%-69\% H_2SO_4$
RP \approx FMG - Local oxide breakdown, SCC
- $>69\% H_2SO_4$
RP \ll FMG - no SCC, general corrosion

FIGURE 3 B
SCC OF ZIRCONIUM H_2SO_4

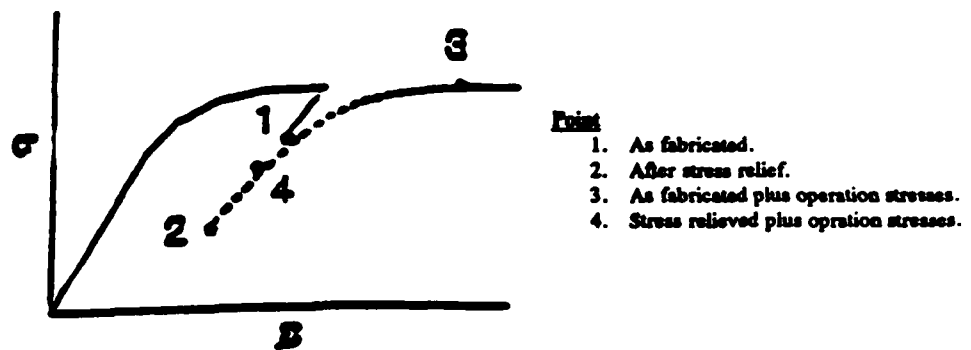


FIGURE 4A

STRESS REDUCTION BY HEAT TREATMENT

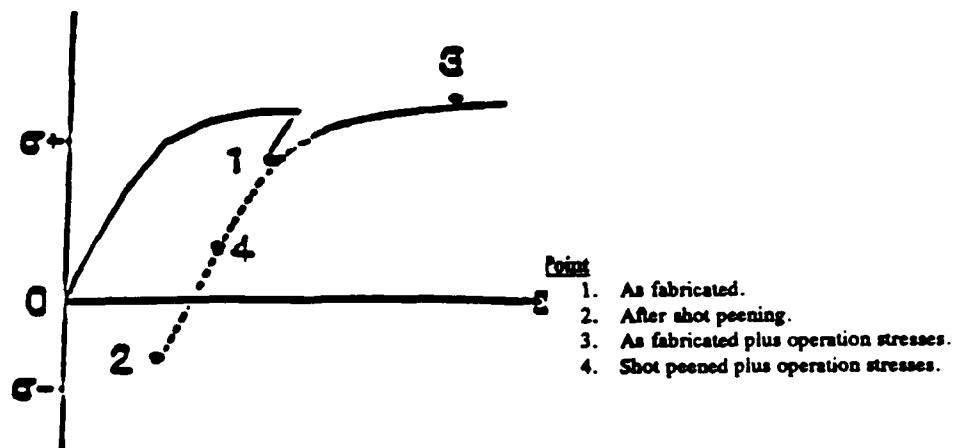


FIGURE 4B

STRESS REDUCTION BY SHOT PEENING

WHAT HAS HAPPENED TO "SA-516-70"

T.T. PHILLIPS
JACOBS ENGINEERING GROUP, INC.
P.O. BOX 53495
HOUSTON, TEXAS 77052

D.M. KLOSS
KDM & ASSOCIATES
143 KLOSS RD.
SEALY, TEXAS 77474

ABSTRACT

ASTM SA-516-70 pressure vessel steel has become the Industry standard for pressure vessel construction. Recent failures and wide spread cracking of pressure vessels in numerous environmental cracking services has prompted investigations into possible cracking mechanisms. The purpose of this paper is to demonstrate increased hardenability and resistance to postweld heat treatment softening that can be expected with microalloyed SA-516-70 pressure vessel steels containing levels of Columbium permitted by the ASME code.

INTRODUCTION

This paper will attempt to answer the question "What Has Happened To SA-516-70". Recent materials failures and difficulties with obtaining and meeting stringent HAZ hardness and base metal toughness requirements in the pressure vessel industry has prompted several research projects. This test program was undertaken to demonstrate the magnitude of the problem and to show some of the reasons why many current heats of SA-516-70 steel on the market today do not perform in the trusted and predictable manner historically established for this grade of steel.

It will be shown that the unspecified element limits contained in ASME Section II A, SA-20, the specification for pressure vessel steel plates, are too high for steels fabricated to the ASME code Section VIII Div. 1 preheat and post weld heat treatment rules when the weldments are intended for critical service applications.

It will be shown that the use of carbon equivalents to assess HAZ hardenability is invalid for steels that contain (Cb) as a microalloying element.

WHAT HAS HAPPENED TO "SA-516-70"

Page 2

It will be shown that the HAZ of steels containing (.025 - .027% Cb) when welded with the SMAW process at ambient preheat and a 335F interpass temperature will have a HAZ hardness of 340 HV 10 Kg vickers in the as welded condition.

It will be shown that steels containing (.024 - .031% Cb) resist stress relief softening at 1100F to 1200F.

BACKGROUND

ASTM SA-516-70 pressure vessel plate has become the "Bread and Butter" material of choice for modern day pressure vessel construction. Availability of the lower strength grades is poor with long deliveries and often dual certified with grade 70 on the same certified material test reports (CMTR's) when delivered.

Prior to the early '60's, SA-212B "Firebox Quality" steel was used extensively for pressure vessel construction. The need for pressure vessel steel materials with better low temperature (below -20F) toughness brought on the advent of aluminum killed fine grain steels with superior -50F impact toughness. SA-212 was discontinued and replaced with two new ASTM standards. SA-515 silicon killed course grained steels for moderated temperatures, similar to the SA-212B material, and a new SA-516 standard for fully aluminum killed steels made to fine grain practice for low temperature service were introduced. During the late 1960's and early 1970's, a number of pressure vessels constructed of SA-515 steels cracked during hydrostatic testing due to low ambient temperature toughness. SA-515 steels gradually fell out of favor with designers and SA-516 steels were specified with greater frequency.

By the mid to late 1970's, a history of predictable preheat and PWHT behavior had been developed for medium carbon, silicon, manganese steels. A comfort zone of usage with-in accepted ASME code rules for preheat and PWHT of P No.1 materials had developed for SA-516-70.

By the late 1970's and early 1980's a new breed of SA-516-70 was being sold to the pressure vessel industry under the, old and by then well established and trusted, SA-516-70 material specification.

STEEL MAKING PRACTICE

Over the period of years from 1960 to 1980, steel making practice changed in two important ways. Pipe line construction demanded higher yield strength steels with

WHAT HAS HAPPENED TO "SA-516-70"

Page 3

higher toughness and low hardenability with good weldability based on the accepted practice of low carbon equivalency. Carbon equivalents of .43% to .45% were, and still are, common.

To meet this demand, the world steel making practice developed special hot and cold finishing techniques with microalloying additions of Cb, V, Ti, N, and B to achieve specific properties for specific taylor made applications. Pipeline steels with 60, 65, and 70,000 psi minimum yield strengths were developed and a new era in steel making began.

The second change that gradually occurred over this period was an increase in the levels of tramp elements Cu, Ni, Cr, Mo in finished steel due to the increased tramp element levels in the scrap used in steel making.

These tramp elements are strengtheners and also increase yield strength. The typical carbon levels have been lowered to .16% to .18% in the new breed of steels compared to 1970's vintage SA-516-70 of .24% to .30% to compensate in part for the increased strengthening caused by the tramp element levels present in today's steels. The carbon levels are also lowered to compensate for strengthening affects caused by microalloying additions.

TEST PROGRAM

Several heats of modern SA-516-70 material containing up to .031% (Cb) representing several plate thicknesses were welded with the GTAW, SMAW, and SAW welding processes. Coupons were welded with and without preheat and tested as welded and with PWHT at various times and temperatures.

TEST RESULTS

Both Heats of material shown in Table 1 were sold as SA-516-70/65 normalized produced to fine grain practice and dual certified by the foreign steel mill. The certified material test reports (CMTR's) for each heat of steel reported the levels of Cb and V as 0.00%.

The materials were analyzed with "argon discharge optical emission vacuum spectroscopy" to obtain the results shown.

The trend in resistance to PWHT softening is obvious from the data in Table 2 and is consistent with other published data for steels containing small amounts of Cb (Ref.1-4).

WHAT HAS HAPPENED TO "SA-516-70"

Page 4

Materials with 3/8" and 1/2" thicknesses sold as SA-516-70/65 dual certified containing from 0.024% to 0.031% Cb were also welded with the GTAW, SMAW and SAW welding process with similar results. A PWHT temperature of 1200F for 8hrs was required on these welded coupons to safely reduce hardness levels to below 225 HV10kg.

CONCLUSIONS

ASME Section VIII Div. 1 permits P-1 carbon steel materials to be welded with ambient preheat up to 1-1/4" thick and requires PWHT at 1100F minimum for one hour per inch of thickness for thicknesses over 1-1/4". Test results presented in this paper demonstrate the increased hardenability and resistance to softening that can be expected with Cb containing microalloyed SA-516-70 plate that meets ASME fabrication requirements.

ASME Section II Part A, SA-20 permits up to 0.03% Cb for product analysis. As has been shown by the test results in Table 2, this limit is too high for pressure vessel steel plate fabricated to hardness limits specified for critical service applications commonly required in today's industry. These test results have demonstrated the need for a nonmicroalloyed steel industry standard for purchase of steels intended for critical service applications where hardness control is required.

The following formula is typically used to report carbon equivalents:

$$C.E. = C + Mn/6 + Cr+Mo+V/5 + Cu+Ni/15$$

This carbon equivalent formula does not account for Cb. Therefore the increased hardenability afforded by Cb is not accounted for with the conventional carbon equivalents reported.

Many fabricators in the United States purchase SA-516-70 plate from local supply houses in small quantities for pressure vessel construction. Fabricators should beware of small quantity purchases and review CMTR's for the presence of small amounts of Cb in all plate purchased. This is especially critical when hardness limits are required.

WHAT HAS HAPPENED TO "SA-516-70"
Page 5

TABLE 1

Ht#	C	Mn	P	S	Si	Ni	Cr	Mo	Cu	V	Cb
A	0.18	1.09	.013	.001	0.23	0.05	0.03	0.01	0.02	.004	.027
B	0.18	1.12	.013	.002	0.26	0.05	0.03	0.01	0.01	.002	.025

TABLE 2

Matl Ht#	CE	Matl Thk.	Weld Process	IPT	PWHT	HAZ Peak HV10Kg	Heat Input Joules/"
A/B	.38	2"	SAW	350F	None	255	96,000
					1100F @2hrs	253	
					1150F @4hrs	248	
					1200F @4hrs	223	
					1250F @4hrs	225	
A/B	.38	2"	GTAW/SMAW	335F	None	341	46,875
					1100F @2hrs	317	
					1150F @4hrs	223	

REFERENCES

1. "Clean Steel To Resist Hydrogen Embrittlement"
By J.Charles, L. Coudreuse, and R. Blondeau of Creusot-Loire Industrie, Presented at Corrosion 90, NACE paper 202 April 23-27, 1990.
2. "The Implications Of Local Brittle Zones" by Dr. Rudi M. Denys, Published in Welding Design And Fabrication, December 1989.
3. "LPG Storage Vessel Cracking Experience" by J.E. Cantwell of Caltex Petroleum Corporation, Presented at Corrosion 88, NACE paper 157 March 21-25, 1988.
4. "What's Behind The Corrosion of Microalloy Steel Weldments?" by R.D. Kane, J.P. Ribble and M.J. Schofield of Cortest Laboratories, Inc., Published in Welding Journal, May 1991.

TTP93007

Corrosion of Weld Zone of Stainless Steels in Industrial Urea Media

Hu Xizhang, Ren Xiaoshan, Chen Xiaojun
Luzhou Nature Gas Chemical Industrial Company
PO Box 646300, Luzhou, China

Han Wenan, Zou Feng
Institute of Corrosion and Protection of Metals, Academia Sinica
PO Box 110015, Shenyang, China

Abstract

The four types welded junction, 316L / 25-22-2LMn / 2RE69, 316L / 25-22-2LMn / SAF2205, 316L / 329J2L / SAF2205 and 316L / P5 / SAF2205, have been studied by means of scanning electron microscopy, electron-probe microanalysis, metalloscopy, X-ray photoelectron spectroscopy, Auger electron spectroscopy and second ion mass spectroscopy. These specimens were tested in industrial urea synthesis media for one year. It is found that the corrosion resistance of weld zone is closely related to alloy composition, structure and nature of passive film. The order of corrosion resistance of weld metal is as follow: 25-22-2LMn > 329J2L > P5. It is just the same as the order of corrosion resistance for base metal. The welding technique has obvious influence on corrosion resistance of weld zone. The technique of 2-pass filling-wire is better than that of self-melting and filling-wire. The nature of passive film formed on welded junction is similar to the base metal. The more Cr_2O_3 or $\text{Cr}_2\text{O}_3 \cdot x\text{H}_2\text{O}$ the passive film contains, the better the corrosion resistance of welded junction. Besides Cr_2O_3 , the passive films also contain Fe_2O_3 , oxides of nickel and oxides of molybdenum. It seems that the urea molecule has been incorporated in the oxides. There has a remarkable change of the ratio between α - and γ -phase and the concentration gradient of element in the metal or in the passive film in the weld junction zone. The welding flaw, alloy composition segregation and discontinuity of passive film in the weld zone will easily cause local corrosion. The measure for further improvement of corrosion resistance of weld zone is discussed.

Key terms: stainless steel, weld zone, urea medium.

Introduction

It is well known that industrial urea synthesis media may cause severe corrosion of metals. Stainless steels can be used in these media with a proper amount of oxygen. At present, the Cr-Ni-Mo stainless steels used in urea industry have two types of structure. The one is widely applied austenitic steel, such as 316L and 2RE69. The other is

austenite–ferrite duplex stainless steel, such as 329J2L and SAF2205. In urea high pressure equipments (reactor, stripper, high pressure carbamate condenser and high pressure scrubber) stainless steels go into the making of lining, tower plate, heat exchange tube, pipeline and valve etc.. Same steel or different steels are usually welded together in an equipment. Corrosion failure of equipment is of frequent occurrence in weld zone. Recently, it has been found that the heat exchange tubes in high pressure carbamate condenser was damaged, which occurred not only in weld zone in urea medium but also on outer surface of tubes in condensation water. The tubes made of 316L stainless steel suffered from stress–corrosion cracking in hot water–steam system with a certain amount of chloride and oxygen. The austenite–ferritic duplex stainless steel is far more resistant to stress–corrosion cracking in chloride solution than 316L stainless steel. However, the investigation published in literature laid emphasis on corrosion behaviour of stainless steel base metal^[1–3]. There has been only little information about the corrosion of its weld zone. The chief purpose of this work is to study the corrosion characteristic and to find the new method to improve corrosion resistance of weld zone.

Experimental

The chemical composition of stainless steels and welding wire used for this study is given in Table 1. Four types of welded junction, 316L / 25–22–2LMn / 2RE69, 316L / 25–22–2LMn / SAF2205, 316L / 329J2L / SAF2205 and 316L / P5 / SAF2205, were studied. The butt–weld of stainless steels were carried out with tungsten inert gas arc welding. The inert gas was 99.99% Ar. Two welding techniques were used, namely, two passes of filling–wire and filling wire after self–melting. Welding current was 40–60A. Welding voltage was 12–13V. The mode of butt–weld were plate–plate, plate–tube and tube–tube. The specimens for corrosion test were cut from welded junction followed by machining, washing with deionizing water and alcohol and putting into the solution at the top of a urea reactor and a HP carbamate condenser. After exposure for one year, these specimens were taken out and rinsed then dried.

The content of α –ferrite and chemical composition of main elements at welding cross–section were measured by quantitative metallography and electron–probe microanalysis(EPMA) respectively. The corrosion morphology of weld zone was observed by metalloscopy and scanning electron microscopy (SEM). The passive films on the base metal and weld zone of stainless steels were studied by X–ray photoelectron spectroscopy(XPS), Auger electron spectroscopy(AES) and second ion mass spectroscopy(SIMS).

Results and Discussion

A. Weld Zone Microstructure

Metallographic section of weld zone shows that the welding technique has an influence on macrostructure in weld zone. The macrostructure for two-pass filling-wire weld is relatively even while the macrostructure for filling-wire after self-melting is clearly divided into two parts. Because 316L, 2RE69 and 25-22-2LMn are all austenite, the microstructure of weld-metal is also austenite. For 316L and SAF2205 butt-weld, the microstructure of weld-metals are $\alpha+\gamma$ duplex phases. Their α -ferrite percentages in the middle of welding cross section or in the welding backside are given in Table 2. It can be noticed from Table 2 that the distribution of α -ferrite percentage in the weld zone exhibits a maximum and a minimum.

B. Element Distribution in Weld Zone

Distribution of main element in the middle of welding cross section is shown in Figure 2. It is evident that the distribution of element present frequently a sudden change at the weld junction zone. According to the distance for that change, the width of weld junction zone can be estimated to be about 35–210 μm . The width of weld junction zone depends on the species of element and on the concentration difference of element in the base metal and in the weld metal. The bigger the concentration difference, the wider the weld junction zone. From a corrosion-resistance viewpoint, the chromium should be firstly considered for estimating the width of weld junction zone. The data obtained by electron-probe microanalysis have indicated that the chromium content in the weld zone is generally less than that in the original welding wire.

In addition, the fluctuation amplitude of Mo, Mn, Cr and Ni content in the weld zone is stronger than that in the base metal. This means that these elements segregated in the weld zone. It is worth notice that a remarkable concentration fluctuation of Cr and Ni content occurred in 316L / 25-22-2LMn self-melting and filling wire / SAF2205, this abnormal segregation about Cr and Ni may be due to unsuitable welding operation.

C. Corrosion Morphology of Weld Zone

After corrosion test of welded junction specimens, the surface of 2RE69 base metal and 25-22-2LMn weld metal showed a bright silvery or white colour, SAF2205 and 329J2L showed a light yellow or yellow brown colour, whereas 316L and P5 exhibited brown or brown-black colour. According to the observation under stereomicroscope it is clear that the order of corrosion resistance is as follows: 316L / 25-22-2LMn / 2RE69 > 316L / 25-22-2LMn / SAF2205 > 316L / 329J2L / SAF2205 > 316L / P5 / SAF2205.

As has been discussed above, the butt-weld specimen for 316L / 25-22-2LMn self-melting and filling-wire / SAF2205 showed a bad corrosion resistance because of abnormal segregation of Cr and Ni, But its corrosion resistance was obviously improved through a suitable welding practice. From the viewpoint of corrosion resistance, in gen-

eral, the welding technique of 2-pass filling-wire was better than that of self-melting and filling-wire.

In the every welded junction, the corrosion extent of weld junction zone and heat-effect zone is larger than the other zones. For 316L and SAF2205 butt-weld, the knife-line attack(KLA) was observed in the weld junction zone at one side or both sides when use 329J2L or P5. Moreover, a corrosion ditch emerged in their heat-effect zones after the specimens exposed in urea media for two years.

Surface topography of welded specimens after corrosion test was also examined by SEM. Corrosion characteristic of welded junction in different zones was distinctive. As for welded junction of 316L / 25-22-2LMn / 2RE69, the 25-22-2LMn / 2RE69 side showed a good corrosion resistance(see Figure 2 b,c,d). However, intergranular attack occurred in the partially melted zone and heat-affect zone of 316L side(see Figure 2 a).

In the welded junction of 316L / 25-22-2LMn / SAF2205, the corrosion characteristic of 316L / 25-22-2LMn side was similar to the side in the 316L / 25-22-2LMn / 2RE69 (Figure 3a), but the other side 25-22-2LMn / SAF2205 suffered from intergranular attack in the partially melted zone and heat-affected zone(Figure 3b). However, the intergranular attack extent for SAF2205 was less than that for 316L, as shown in Figure 3c.

The corrosion resistance of welded junction 316L / 329J2L / SAF2205 was not as good as previous two welded junctions. Besides intensified general corrosion, the partially melted zone and heat-affected zone were more widened, the holes and grooves appeared locally in these zones. Moreover, the net cracks were also observed in the composite zone(see Figure 4).

The welded junction 316L / P5 / SAF2205 caused rather severe general corrosion and selective corrosion in the composite zone and knife-line attack in the weld junction zone, so that its corrosion resistance was the least.

Although there was interference of corrosion products, the surface composition in weld zone measured by SEM was substantially consistent with previous results obtained by EPMA.

D. Passive Film on the Weld Zone

Previous work^[4-5] has shown that 316L and 2RE69 stainless steels are passivated under the condition of normal supply of oxygen in the urea media. Their passive films are composed of Cr_2O_3 , Fe_2O_3 , oxides of nickel and oxides of molybdenum. Cr_2O_3 and Fe_2O_3 are much more than others. The urea molecule has been incorporated in the ox-

ides. The outmost layer of passive film contains more hydroxides and the oxides are in the inner layer. Passive film formed on the duplex stainless steel SAF2205 in the urea media has similar composition to that on the 316L or 2RE69 stainless steel. The XPS spectra of passive film formed on the SAF2205 stainless steel in the urea solution in HP carbamate condenser are shown in Figure 5. Composition profile of passive films formed on the base metal and weld zone was measured with AES and SIMS. The apparent thickness of passive film is estimated from composition profile curve and listed in Table 3.

From Table 3 it can be seen that the apparent thickness of passive film formed on the SAF2205ss lies between 2RE69 and 316Lss. This order just coincides with the order of their corrosion resistance and Cr content in the steels. Moreover, the composition and thickness of passive film on the weld zone are inhomogeneous. The passive film on the weld zone is obviously thicker than the correspondent base metal. As shown in Figure 6, a quite large composition variation, such as Cr and O occurs in the weld junction zone. This phenomenon is consistent with the result obtained from EPMA.

Owing to discrepancy, diffusion and segregation of element, existence of various welding flows and imperfection of passive film, the corrosion resistance of weld zone is certainly reduced. In order to improve the corrosion resistance of weld zone, three measures would be taken: 1. Adopt high corrosion-resisting weld wire; 2. Choose proper welding technique and good welding operation; 3. Decrease segregation in the base metal and weld wire.

Conclusion

1. The corrosion resistance of weld zone of four welded junctions in the urea media is as follow: 316L / 25-22-2LMn / 2RE69 > 316L / 25-22-2LMn / SAF2205 > 316L / 329J2L / SAF2205 > 316L / P5 / SAF2205.

2. In regard to corrosion resistance, 2-pass filling-wire are better than filling-wire after self-melting.

3. Chemical composition and microstructure of weld zone have substantial inhomogeneity. In similar manner, the composition and thickness of passive film on the weld zone are also inhomogeneous. After a long time test, the local corrosion has taken place in the weld junction zone and heat-affected zone of SAF2205 and 316Lss.

4. Increasing Cr content in the weld wire, decreasing segregation of base metal and weld wire and adopting a correct weld technique would further improve the corrosion resistance of weld zone.

Reference

- [1]. Res.Gp of IMR et al, Acta Metallurgica(China) 12, 2(1976):P.140
- [2]. K.Matsumoto, T.Shinohara, Corrosion 40, 8(1984):P.387
- [3]. Yu Fuzhou, Xu Chunchun, Yao Tianming, Proc.9th International Congress Met. Corrosion Vol.2(1984):P.558
- [4]. Sun yanfei, Han Wenan, Proc.10th International Congress Met. Corrosion Vol.3 (1987):P.2485
- [5]. Han Wenan, Sun Yanfei, Nitrogen Fertilizer(China) 1(1988): P.42

Table 1 Chemical composition of stainless steel and welding wire (wt.%)

Type	C	Cr	Ni	Mo	Mn	Si	S	P	N
316L	0.027	17.86	13.28	2.51	1.66	0.38	0.009	0.030	
2RE69	0.018	24.9	22.2	2.07	1.62	0.30	0.001	0.012	0.13
SAF2205	0.016	22.15	5.55	2.60	1.62	0.35	0.002	0.022	0.135
25-22-2LMn	0.020	24.63	22.15	2.06	4.48	0.19	0.006	0.014	0.12
TIG329J2L	0.020	22.30	7.80	2.80	1.40	0.40	0.006	<0.035	
Avesta P5	0.03	22.47	14.4	2.41	1.40	0.38	0.015	0.022	

Table 2 α -ferrite percentage of 316L / SAF205 weld zone

Welding technique	316L	UZ by 316L	Composition zone	UZ by 2205	SAF2205
329J2L, 2-pass filling-wire	0	17.1	24.0, 40, 21.5 (47)	27.3 (28.8)	50.8
25-22-2LMn, 2-pass filling-wire	0	9.4	10.9, 6.8 (9.4) (6.8)	24.0 (23.0)	50.8
25-22-2LMn self-melting and filling-wire	0	3.9	19.2 (13.9), (19.16)	19.5	52.2

Note: UZ denotes unmixed zone, parentheses denotes value in the welding backside.

Table 3 Apparent thickness of passive film on the weld zone

Type	Thickness by AES (nm)	Thickness by SIMS (min)
2RE69	3000	5
SAF2205	23400	10-20
316L	52400	
25-22-2LMn composite zone	2800, 4500	5-10
329J2L composite zone	43000	20
25-22-2LMn / SAF2205 unmixed zone	4000	8-10
329J2L / SAF2205 partially melted zone	68000	
25-22-2LMn / 316L partially melted zone	27000	
329J2L / 316L unmixed zone	84000	

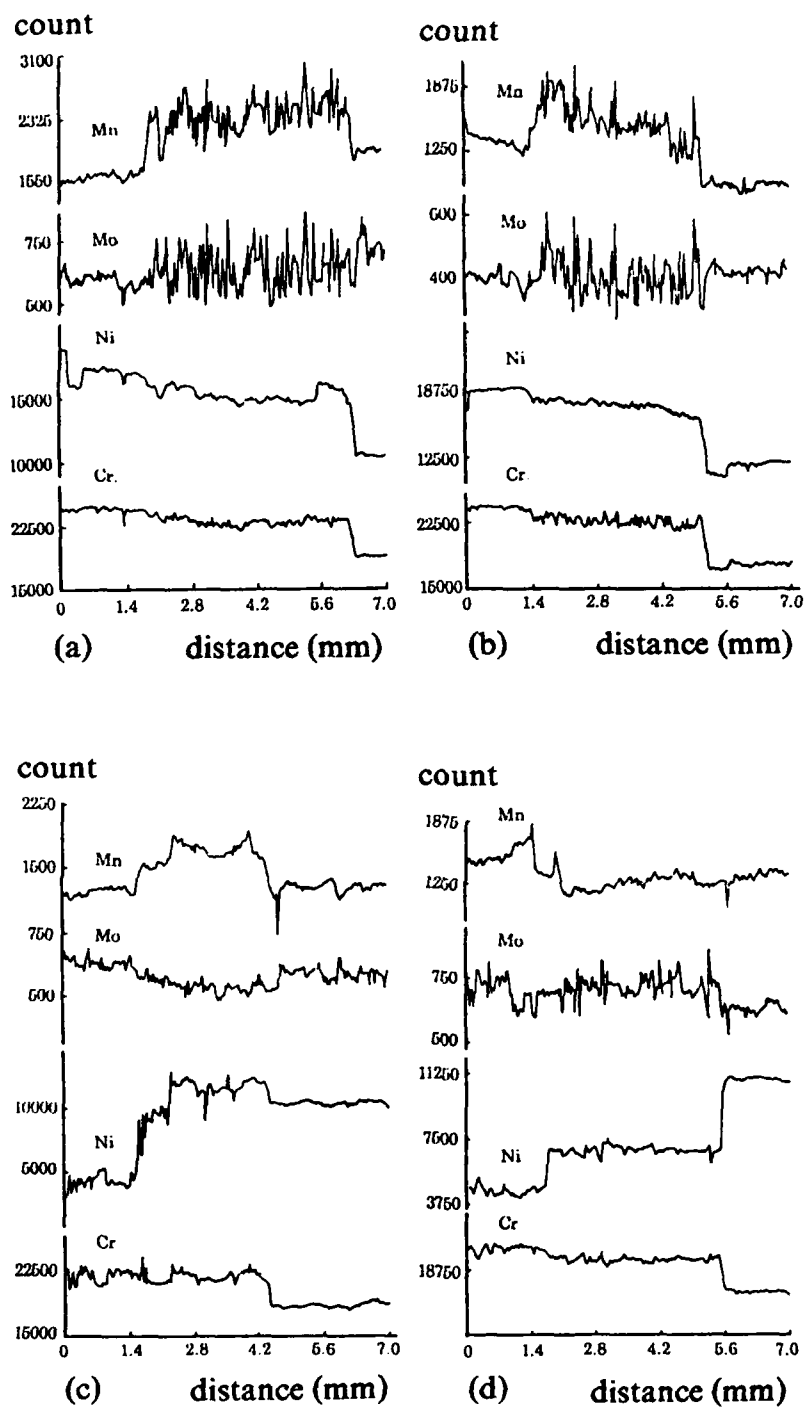
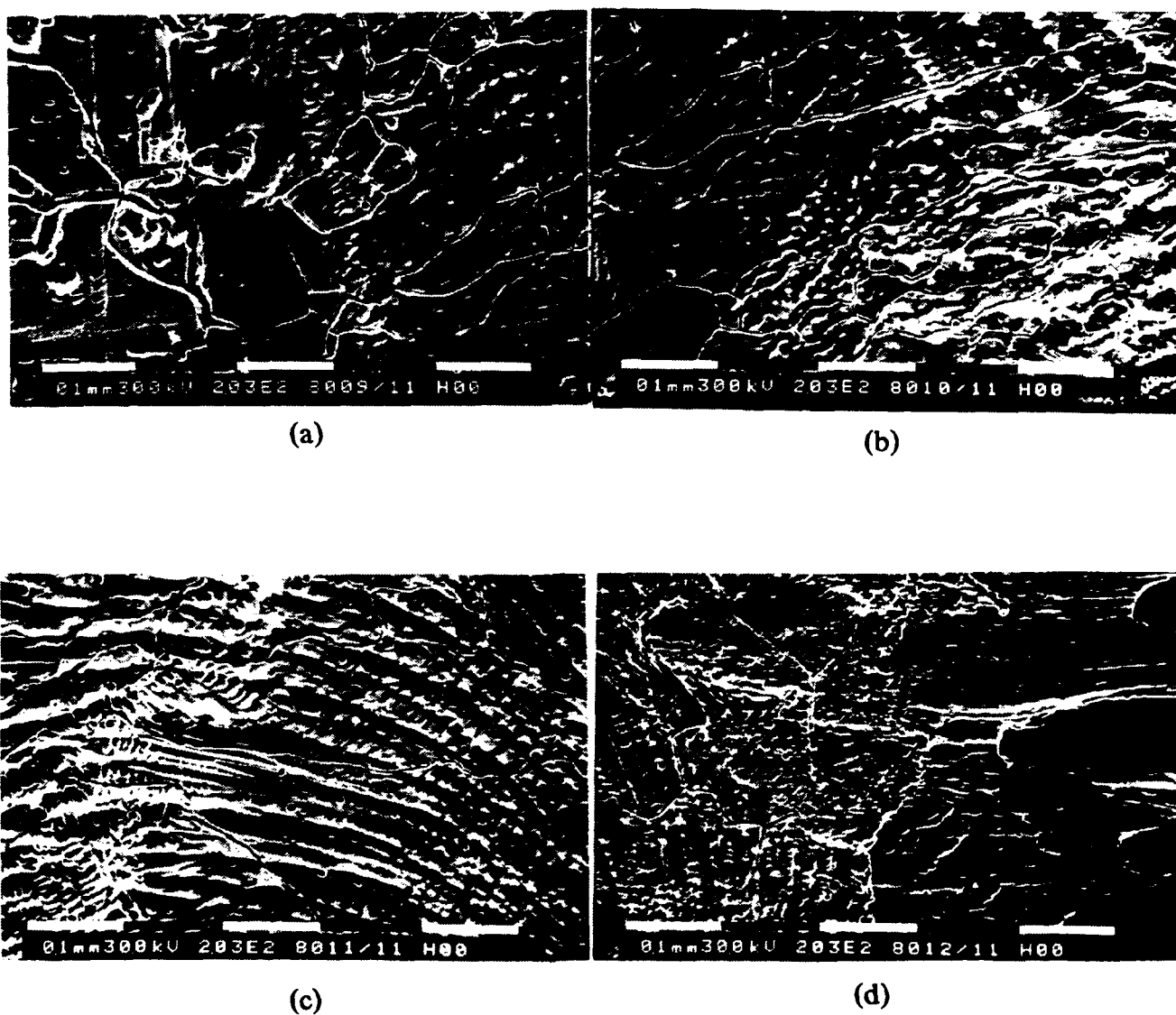


Figure 1 The main elements distribution in the middle of welding cross section

- a. 2RE69 / 25-22-2LMn 2-pass filling-wire / 316L
- b. 2RE69 / 25-22-2LMn self-melting and filling-wire / 316L
- c. SAF2205 / 25-22-2LMn 2-pass filling-wire / 316L
- d. ASF2205 / 329J2L 2-pass filling-wire / 316L



**Figure 2 Surface topography of welded junction 316L / 25-22-2LMn
2-pass filling-wire / 2RE69 after corrosion test**

- a. 316L heat-affected zone(left) to unmixed zone(right)
- b. unmixed zone of 316L side (left) to composite zone(right)
- c. composite zone of 2RE69 side (left) to unmixed zone(right)
- d. unmixed zone of 2RE69 side (left) to partially melted zone (right)

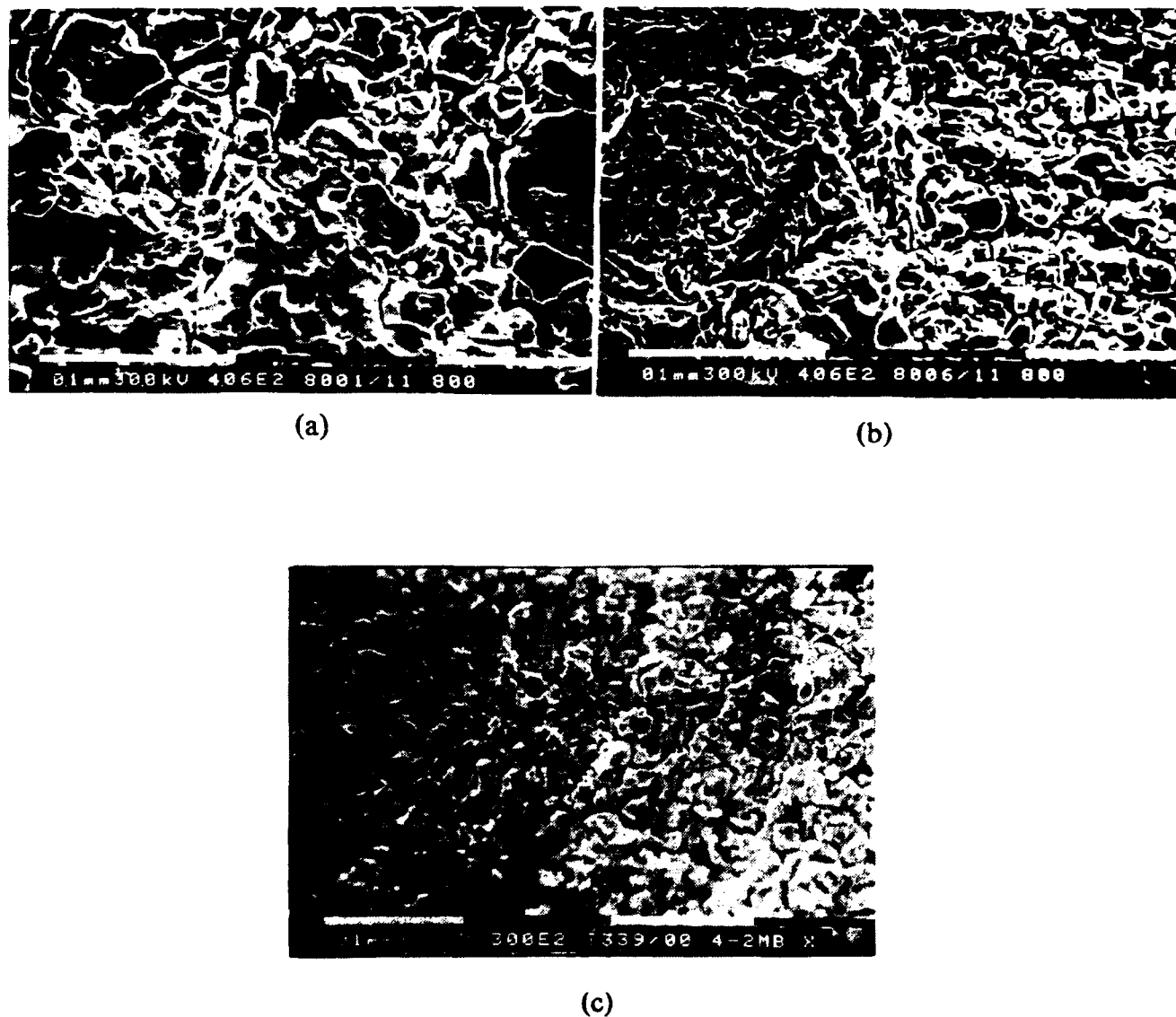


Figure 3 Surface topography of welded junction 316L / 25-22-2LMn

2-Pass filling wire / TX483 after corrosion test

a. 316L heat-affected zone(upper) to partially melted zone(lower)

b. partially melted zone of TX483(left) to heat-affected zone(right)

c. TX483 base metal



Figure 4 Surface topography of composite zone of welded junction
316L / 329J2L 2-pass filling-wire / TX483 after corrosion test

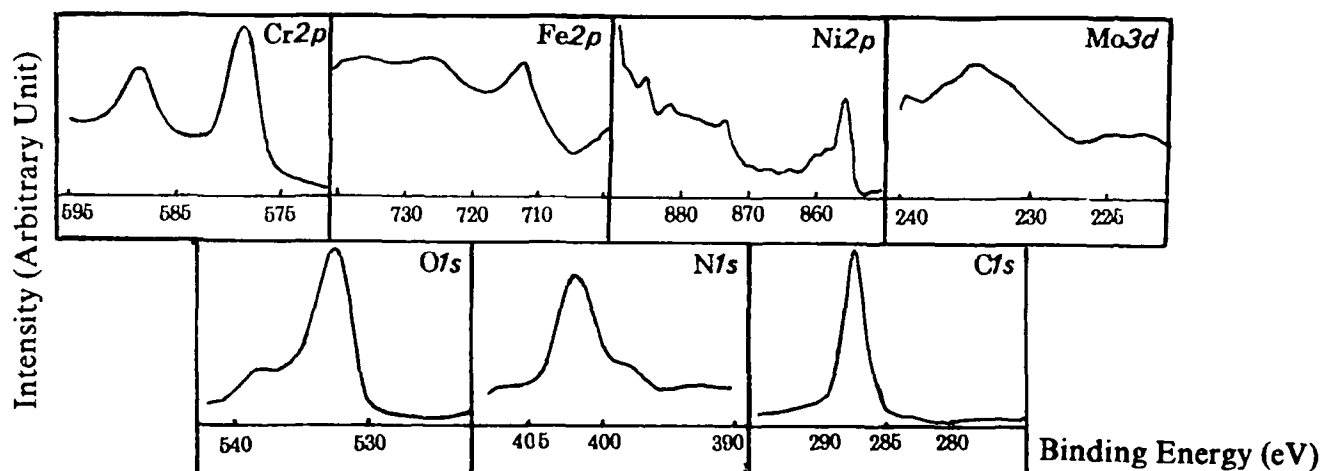


Figure 5 XPS spectra for several elements of passive film formed
on 316L in the H.P. carbamate condenser urea solution

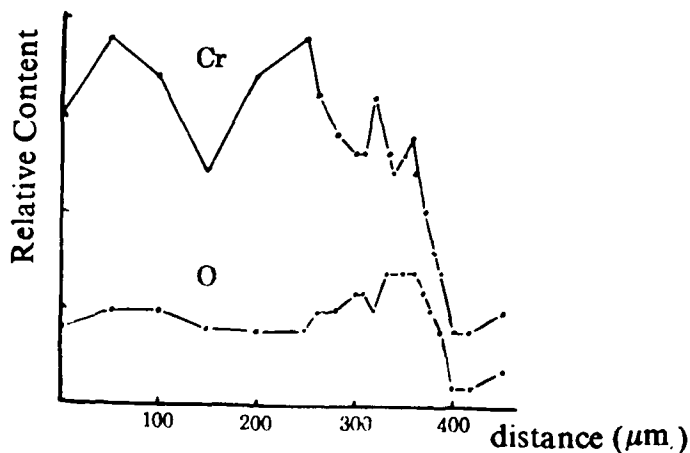


Figure 6 Cr and O contents in passive film formed on welded junction
zone 25-22-2LMn / TX483 as a function of position

The Fractality of Corroding Metallic Surfaces

K. R. Trethewey,
J. S. Keenan,
D A Sargeant,
and S Haines
Royal Naval Engineering College
Manadon
Plymouth, PL5 3AQ
UK

P. R. Roberge
Royal Military College
Kingston
Ontario K7K 5L0
Canada

Abstract

One of the greatest difficulties in current corrosion engineering is the ability to accurately quantify localized attack. Considerable efforts are made to measure corrosion rates either by electrochemical measurements or by long term exposure testing but the interpretation of results is always complicated by the presence of different forms of localized corrosion. It is thus important to characterize corrosion problems both in terms of uniform and localized metal losses. Since these problems can lead to systems-dependent surface transformations, the quantification of characteristic shapes and defects produced during corrosion attack could greatly enhance the inspection methodologies presently practised in the industry.

The description of complex self-repetitive geometries became an art and a science when the concept of a fractal was popularized in the mid-1970s by Mandelbrot. Fractal arguments involve the rules of scaling with non-integer exponents to express time or space dimensions. Such expressions have been shown to be particularly relevant for the description of natural processes and shapes including those encountered during the corrosion of metallic structures. This paper will review the experimental techniques which are used for the evaluation of surface profiles and describe the links with fractal geometry.

Key terms: corrosion, surface profile, fractals, modeling, roughness parameters.

Introduction

'Fractal' is a term coined by Benoit Mandelbrot¹ in the 1970s to describe complex patterns, shapes, curves or functions which can be expressed by

$$\text{bulk} \propto \text{size}^{\text{dimension}} \quad (1)$$

in which dimension is almost always a non-integer. Such expressions have been shown to be particularly relevant to natural processes and shapes. In particular, considerable success has been demonstrated in the application of fractals to measurements of coastlines². Since then, numerous workers have extended the theories of fractal geometry to related subjects such as flow through porous media³, theories of multilayer adsorption of gases⁴ and bimolecular chemical reactions⁵.

Chaos theory, another new tool for the understanding of complex, non-linear natural phenomena, has been recently applied to metallic dissolution^{6,7} and to electrochemical impedance in corrosion^{8,9}. Good progress has been made recently with percolation theory in so-called 'atomistic' models of corrosion¹⁰, but as yet, there are few uses of fractal geometry for similar atomic models of corroding surfaces. In the solidification of metals by dendritic growth, the Diffusion Limited Aggregation (DLA) model has been used to good effect¹¹. This type of model was constructed from the 'random walk' technique whereby individual atoms diffuse at random in the liquid and crystallise according to specified rules to form remarkably realistic dendrites. There would appear to be much scope for similar models of corrosion processes which involve the dissolution of metal atoms from solid to liquid phase with some degree of randomness, but according to rules associated with electrochemical potential and varying properties of the passive films at the interface.

The modelling of surfaces and landscapes in their broadest sense is not new and has been accomplished with spectacular success by Mandelbrot¹ and others^{12,13}. Although the application of fractal geometry has been discussed in relation to corrosion and fatigued surfaces¹⁴, this paper describes the first steps to obtain correlation of fractal models with laboratory-determined surface profile data.

A pivotal part of this approach is the correlation between the kinds of traces obtained from surface profile with time series which constitute electrical signals: both are amenable to the same kinds of analysis techniques. It will be demonstrated that corroding surfaces, in this case, of pure copper, can be modelled by fractal geometry and tools currently being used for the analysis of chaos and associated parameters in many other systems. Application of similar principles to localized corrosion of aluminium alloys has been described elsewhere⁸. Fractal representations of corroded surfaces have been studied using white noise, 1/f noise and Brownian algorithms. This

paper will describe how fractal models have been correlated with values of traditional surface roughness parameters.

Theory

In electronics, white noise is considered to represent the most random or stochastic behaviour. It consists of many separate frequencies combined over a wide spectrum. Over a period of time which is long compared to the lowest frequencies in the noise, the noise has a mean amplitude, x_0 , and the probability of the noise having any instantaneous value is given by a Gaussian distribution in which the probability, p , of a value x is of the form

$$p(x) = Ae^{-B(x-x_0)^2} \quad (2)$$

where A and B are constants and x_0 is the true mean value. In effect, a white noise time sequence is wholly uncorrelated from point to point. The effect of an algorithm for $1/f$ noise on a modelled surface profile is the same as that of an electronic filter removing high frequencies such that $1/f$ represents the spectral distribution of the profile. This results in a 'smoother' profile.

Profiles generated by Brownian fractal algorithms have a spectral distribution of $1/f^2$. Although, mathematically speaking, they are obtained by integration of the white noise ($1/f^0$) signal, the equivalent effect in electrical science is that such a time series is filtered even more than the $1/f$ models, high frequencies are less dominant and resulting profiles therefore appear even less rough than $1/f$ surfaces. Considerable use has been made of Brownian fractals for creation of computer-simulated landscapes and surfaces¹, and there are many algorithms available¹⁵. One which was selected for this study¹⁶, possessed the significant advantage of input of a value of D , the so-called fractal dimension. Previous workers have shown how, as D increases from 1.00 to 2.00, increasing amounts of surface roughness are observed^{1,15}. In corrosion it is not at all obvious what the effect on the fractal model or on the value of D will be since, depending on current density, electrochemical polishing (implying the production of a smoother surface) may occur. In the terminology of surface profiles, it could be envisaged that more material might be lost from the peaks than from the valleys. Alternatively, in localized corrosion such as pitting, the opposite might be true. Validation of a proposed model is also not straightforward, as will be demonstrated below.

Experimental

Corrosion

Samples of pure copper, 99.99% by weight, cut from bar and in the annealed condition, were polished to 0.25 μm diamond finish using a Leco automatic polishing system such that surface finish

was accurately reproducible. Specimens were then corroded in 3% NaCl solution, with added hydrochloric acid to pH 3 in order to prevent the build-up of corrosion product. Galvanostatic conditions of $100 \mu\text{A}/\text{cm}^2$ were applied so that precise amounts of charge produced measurable surface changes, as quantified by the change in the surface profile parameters. After each stage in the corrosion process, the sample was withdrawn and sets of five surface profiles taken such that parameter values for each stage could be found. Each measurement consisted of a traverse of 4 mm which covered of the order of ten grains. Thus, grain boundaries were deliberately included in each measurement. Because the act of measurement resulted in a slight scratching of the surface, care was taken to ensure that each measurement did not cross the path of any previous measurement. After each set of measurements, the specimen was returned to the corrosion cell so that the cumulative effect of galvanostatic exposure could be determined. (It was determined that the slight scratching during measurement did not affect the subsequent corrosion.)

Profile measurements

Measurements of surface profile were made by means of a Rank Taylor Hobson Form Talysurf with a $0.2 \mu\text{m}$ diamond tip probe. The instrument creates a line scan of a real surface by pulling the probe across a pre-defined part of the surface at 1 mm/s . Let us define the co-ordinate axes in the plane of the surface as x and y . Vertical deviations (in the z -axis) are measured and the data is digitised and stored in the form of an x - z map. The set of x - z co-ordinates form the familiar description of a surface. It is important to realise that since the equipment is recording a z -displacement of the probe with time, the usual x - z geometrical description is actually a time series. To facilitate the visualisation process, the display is distorted because of the use of different scales to plot the x and z information. Thus, for example, x is usually plotted in mm, whilst z is plotted in μm . The problem of human visualisation exists because a real surface plotted with two such different scales on the x - and z -axes does not 'look' real. However, when both axes are plotted on the same scale, the surface can be seen to be much 'smoother' than at first thought; indeed, it is very difficult for the human eye to distinguish the features which are under scrutiny. Scaling represents a critical part of the analysis of fractals and considerable care must be taken to ensure that errors are not made¹⁷.

Scaling

Fractal algorithms generate unscaled output and it is necessary to apply scaling to the numbers representing the co-ordinates in both the x - and z -directions. The z -direction scaling is straightforward because of the need to correlate the x -spacing with the actual times (distances) at which the Talysurf probe makes measurements. Since this distance was always $0.25 \mu\text{m}$, all modelled surfaces were plotted with this spacing. It is not

sufficient to scale z-values using single value parameters such as the maximum peak height, for example, because these may vary considerably from one profile to another. In order to sensibly scale the co-ordinates in the z-direction, use was made of the parameter, R_q which represents a root mean square value of the profile amplitudes. Co-ordinates for all modelled surfaces were scaled using the ratio $R_q(\text{real})/R_q(\text{model})$. As can be seen from the results, the effect of this is to fix R_q for both model and real surfaces. Because of its effect primarily in the z-direction, those parameter values which represent effects in that direction are also, in general, brought towards a better fit. However, this procedure also highlights the differences in parameter values which relate to the x-direction and it is here that the value of the model can be evaluated.

Modelling and software analysis

Three algorithms were used to model a copper surface: white noise, $1/f$ noise¹³ and Brown noise¹⁶. White noise was created using a random number generator such that suitably large sets of data points with a normalised distribution were obtained. In the other two cases, random number data sets were used as input for algorithms from the literature and the outputs analysed by the techniques described. Five surfaces were produced from each algorithm.

The manufacturer's software for the Talysurf instrument was used for the analysis, it being capable of generating over twenty surface profile parameters. In this study up to twelve of what were considered to be the most useful parameters were selected and monitored and of these, the six listed in Table 1 were chosen for this paper. The software carries out analysis of raw data in a sophisticated but standard way, allowing for filtering of values to remove unwanted form and waviness from the profiles. As far as possible, however, the comparison of real surface with fractal surface was made using raw data from the real surfaces because of the uncertain ways in which the software might influence the interpretation of the results. However, it is impossible to eliminate filtering effects caused by the probe tip which, depending on surface profile, is better able to measure high points on the profile than low points. Inevitably, any profile obtained by mechanical means will carry some character resulting from the measurement mechanism.

Plots were obtained using Microsoft EXCEL™ V4.0 for WINDOWS™ V3.1, which also produced a proportion of the random number files used for input to the algorithms. Other random numbers were obtained using Microsoft FORTRAN (Version 5.1). Use was also made of the Chaos Data Analyzer available from Physics Data Software.

Statistical methods

In each of the sets of data reported, whether real or model,

comparisons were made of five independent data sets. The means and standard deviations of the resulting parameter values were used. It is accepted that five sets may not be statistically significant and that many more would be desirable. Nevertheless, a pragmatic approach was necessary in balancing the need for mathematical rigour with the amount of practical effort involved.

Results

The values of surface parameters obtained from the corrosion experiments are shown in Table 2 and their variation with time is shown in Figure 1. A typical profile from each of the algorithms used to model surfaces is shown in Figure 2a-d. The white noise and 1/f profiles are shown in Figure 2a and b. Using the Brown algorithm, values of $D = 1.00$ and $D = 1.75$, Figure 2c and d, only were used for limitations of space. For comparison, a sample of a single grain from the most heavily corroded surface is included, drawn using the same scales as for the other profiles, Figure 2e. For each algorithm, analysis of five such surfaces, each containing 1,000 data points and plotted over the values stated above gave five sets of profile parameters listed in Table 3. (The parameter values for the corroded copper surface in Table 3 are for limited areas covering single grains, such as shown in Figure 2e, whilst those values in the bottom line of Table 2 are means of five sets of up to 16,000 points and include grain boundaries.)

Discussion

The data from Table 2 clearly show how roughening of the copper surface, as evidenced by increase of the traditional roughness parameter, R_a , occurred during the galvanostatic exposure. The parameters, in general, all showed increases in value to a maximum value which indicated that the copper had reached a situation in which material loss was uniformly distributed and that general corrosion was occurring by the end of the exposure. This is to be expected under the current density and electrolyte conditions used. In contrast, the parameter, λ_{mq} , continued to increase throughout the test, which must lead to the conclusion that the geometry of the copper surface was still changing. The low values of the standard deviations obtained, assisted by the high numbers of data points used, is taken as evidence that the means of five profiles were satisfactorily self-consistent.

Initial inspection of the profiles in Figure 1 leads to the conclusion that surfaces generated from white noise sources can be considered to be a 'worst-case' model upon which to build. The 1/f model also would appear not to be a satisfactory model, whilst of the two Brown models shown, the one having $D = 1.75$ would seem to represent the closest model. When the parameter values in Table 3 are examined, several conclusions can be reached. The technique of z-direction scaling by normalising R_q leads to similar values of R_a because both are averages obtained by similar methods. R_t will always be subject to fluctuation

because, being a single value parameter, it is subject to statistical variation in each data set. Of the two other parameters, it would appear that a better correlation exists between the copper surface and the Brown model with $D = 1.00$, contrary to the visual evidence of Figure 1. Obviously, this analysis is insufficient for validation of a model. Standard deviations in Table 3 are not as good as in Table 2 because the means were obtained over sets of 1,000 data points, equivalent to 250 μm in the x-direction, rather than the 4 mm traverse used in the corroded profiles.

To widen the scope of the validation process, use was made of the Chaos Data Analyzer software in order to include newer parameters from more modern analysis methods. Based upon the numbers of points (1,000) used in each data set, some problems were highlighted with respect to the algorithms being used. Frequency analysis of the profiles of Table 3, considered as time series, showed that the Brown algorithm was generating a frequency response only poorly consistent with $1/f^2$. Frequency response is thus seen to be vital in determining whether a realistic model has been achieved. Inspection of correlation dimensions, listed in Table 4, show that the corroded model does have behaviour somewhere between the Brownian $D = 1.50$ and 1.75 fractal surfaces and highlights the need for considerable care in the validation of surface models. Further work is continuing to improve upon both the algorithms and the analysis techniques.

Conclusions

Algorithms used in fractal geometry have been applied to corroding copper surfaces and correlations attempted with standard surface profile parameters. As was expected, white noise models were shown clearly not to fit a real profile, neither did models based on $1/f$ algorithms. In agreement with previous work in other fields of surface modelling, it appears that the most promising approach is to be obtained using Brownian algorithms. The correlation with traditional surface profile parameters met with mixed success. Difficulties of interpretation were found and further work is necessary to achieve better results. Full analysis of the output from algorithms is important, particularly with respect to such properties as frequency response and fractal dimensions, if models are to be successfully validated against real surfaces. Awareness of the ambiguities arising from the interpretation of the wide range of surface parameters is vital, and limitations of the applicability of the new tools of chaos and fractal geometry must be fully examined. However, considerable scope exists for the development of new models of corroding surfaces which may overcome current problems of life-prediction.

References

1. B. B. Mandelbrot, "The Fractal Geometry of Nature", W. H. Freeman and Company, New York (1983).

2. B. B. Mandelbrot, "How Long is the Coast of Britain?", in "The Fractal Geometry of Nature", W. H. Freeman and Company, New York (1983), 24-33.
3. R. Lenormand, "Flow Through Porous Media", in "Fractals in the Natural Sciences", (eds. M. Fleischmann, D. J. Tildesley and R. C. Ball), Princeton University Press, Princeton, NJ (1989), 159-168.
4. P. Pfeifer, M. Obert and M. W. Cole, "Fractal BET and FHH Theories of Adsorption: A Comparative Study", in "Fractals in the Natural Sciences", (eds. M. Fleischmann, D. J. Tildesley and R. C. Ball), Princeton University Press, Princeton, NJ (1989), 169-188.
5. A. Blumen and G. H. Kohler, "Reactions in and on Fractal Media", in "Fractals in the Natural Sciences", (eds. M. Fleischmann, D. J. Tildesley and R. C. Ball), Princeton University Press, Princeton, NJ (1989), 189-200.
6. S. G. Corcoran and K. Sieradzki, "Chaos During the Growth of an Artificial Pit", J. Electrochem. Soc., 139, p:1568-1573 (1992).
7. S. M. Sharland, Chaotic Behaviour in the Initiation of Localised Corrosion in Metals, Advances in Corrosion and Protection, Manchester, UK, Corrosion Science (1992).
8. J. S. Keenan, K. R. Trethewey, D. A. Sargeant, S. Haines and P. R. Roberge, Towards Better Quantitative Models for the Corrosion of Aluminium using Fractal Geometry, 32nd Annual Conference of Metallurgists: Light Metals, Quebec City, Canada, The Metallurgical Society of CIM (1993).
9. B. Sapoval, "Fractal Electrodes, Fractal Membranes and Fractal Catalysis", in "Fractals and Disordered Systems", (eds. A. Bunde and S. Havlin), Springer-Verlag, Berlin, Germany (1991), 207-225.
10. R. C. Newman, Q. Song, R. A. Cottis and K. Sieradzki, "Atomistic Computer Simulation of Alloy Corrosion", in "Computer Modeling in Corrosion", (eds. R. S. Munn), ASTM, Philadelphia, USA (1992), 17-27.
11. P. Meakin and S. Tolman, "Diffusion-limited Aggregation", in "Fractals in the Natural Sciences", (eds. M. Fleischmann, D. J. Tildesley and R. C. Ball), Princeton University Press, Princeton, NJ (1989), 123-148.
12. C. A. Pickover, "Computers, Pattern, Chaos and Beauty", Alan Sutton Publishing, Stroud, UK (1990).
13. R. F. Voss, "Fractals in Nature: From Characterization to Simulation", in "The Science of Fractal Images", (eds. H.-O. Peitgen and D. Saupe), Springer-Verlag, New York, USA (1988), 21-70.
14. J.-F. Gouyet, M. Rosso and B. Sapoval, "Fractal Surfaces and Interfaces", in "Fractals and Disordered Systems", (eds. A. Bunde and S. Havlin), Springer-Verlag, Berlin, Germany (1991), 229-259.
15. D. Saupe, "Algorithms for Random Fractals", in "The Science of Fractal Images", (eds. H.-O. Peitgen and D. Saupe), Springer-Verlag, New York, USA (1988), 71-113.
16. H. Takayasu, "Fractional Brownian Motion", in "Fractals in the Physical Sciences", Manchester University Press,

- Manchester, UK (1990), 95-97.
17. H.-O. Peitgen, H. Jurgens and D. Saupe, "Scaling Laws and Fractional Brownian Motion", in "Chaos and Fractals: New Frontiers of Science", Springer-Verlag, New York, USA (1992), 491-496.

Table 1 Summary of parameter values used in this analysis.

Parameter	Description
Ra	Roughness average: the average departure of the profile from a mean line. Prone to giving the same value for different waveforms.
Rq	Root mean square value of the profile: Statistically more sensitive than Ra. Used in this analysis as a means of scaling amplitude (z-coordinate) to match a real profile.
Rt	Highest peak to deepest valley from total profile
S	An average or mean spacing of the small adjacent peaks on a surface, but not those which cross the mean line. Sensitive to fine surface deviations caused by material breakdown.
Lamq	The average wavelength of the profile, adjacent and mean peaks included, based on a RMS value.
Rsk	The symmetry of the profile about the mean line. Indicates whether the spikes on the surface are predominantly above (negative) or below (positive).

Table 2: Effect of corrosion on Surface Profile Parameters

Means						
Time /s	Ra	Rq	Rt	S	lamq	Rsk
0.00E+00	0.15	0.17	0.66	1.68	18.78	-0.12
1.80E+03	0.59	0.69	2.66	2.02	69.21	0.13
1.26E+04	0.40	0.48	2.91	3.05	36.64	0.17
1.98E+04	0.94	1.08	5.08	4.97	60.00	-0.11
1.15E+05	1.50	1.89	12.21	9.23	71.49	0.80
3.67E+05	4.24	5.16	29.66	17.39	137.02	0.16
5.56E+05	4.50	5.73	32.07	16.21	134.29	0.97
9.77E+05	4.60	5.56	26.14	22.54	189.76	-0.54
Standard Deviations						
0.00E+00	0.02	0.02	0.09	0.09	3.40	0.11
1.80E+03	0.01	0.02	0.10	0.18	1.59	0.04
5.40E+03	0.02	0.03	0.15	0.26	13.38	0.03
1.26E+04	0.03	0.04	0.42	0.49	3.45	0.23
1.98E+04	0.05	0.03	0.62	0.79	9.70	0.11
1.15E+05	0.08	0.05	0.92	0.31	2.00	0.33
3.67E+05	0.33	0.42	4.33	2.19	8.95	0.24
5.56E+05	0.38	0.59	2.64	1.05	8.51	0.19
9.77E+05	0.81	0.98	5.15	2.84	34.73	0.23

Table 3: Comparison of surface profile parameters for different models and for a corroded copper surface, shown in Figure 1

Means						
Surface	Ra	Rq	Rt	S	lamq	Rsk
White noise	4.01	5.03	30.92	0.75	1.45	0.00
1/f noise	3.99	5.03	27.38	0.59	1.92	1.03
Brown noise (D=1.00)	4.41	5.03	16.76	34.35	181.59	-0.13
Brown noise (D=1.75)	4.30	5.03	20.92	5.68	21.10	0.10
Corroded copper grain	4.31	5.03	20.73	20.23	173.79	-0.33
Standard deviations						
White noise	0.08	0.09	3.06	0.02	0.03	0.07
1/f noise	0.11	0.14	1.75	0.02	0.05	0.12
Brown noise (D=1.00)	1.26	1.38	4.59	17.27	39.42	0.40
Brown noise (D=1.75)	1.04	1.10	2.95	0.47	4.08	0.12
Corroded copper grain	1.72	1.70	4.66	1.45	72.85	0.24

Table 4: Comparison of values of Correlation Dimension obtained from analysis of fractal and real surfaces.

Surface	Correlation Dimension
Brown noise (D=1.00)	1.711 +/- 0.209 (Emb. Dim. = 5)
Brown noise (D=1.50)	2.261 +/- 0.250 (Emb. Dim. = 5)
Brown noise (D=1.75)	2.506 +/- 0.260 (Emb. Dim. = 5)
Corroded copper surface	2.370 +/- 0.44 (Emb. Dim. = 5)

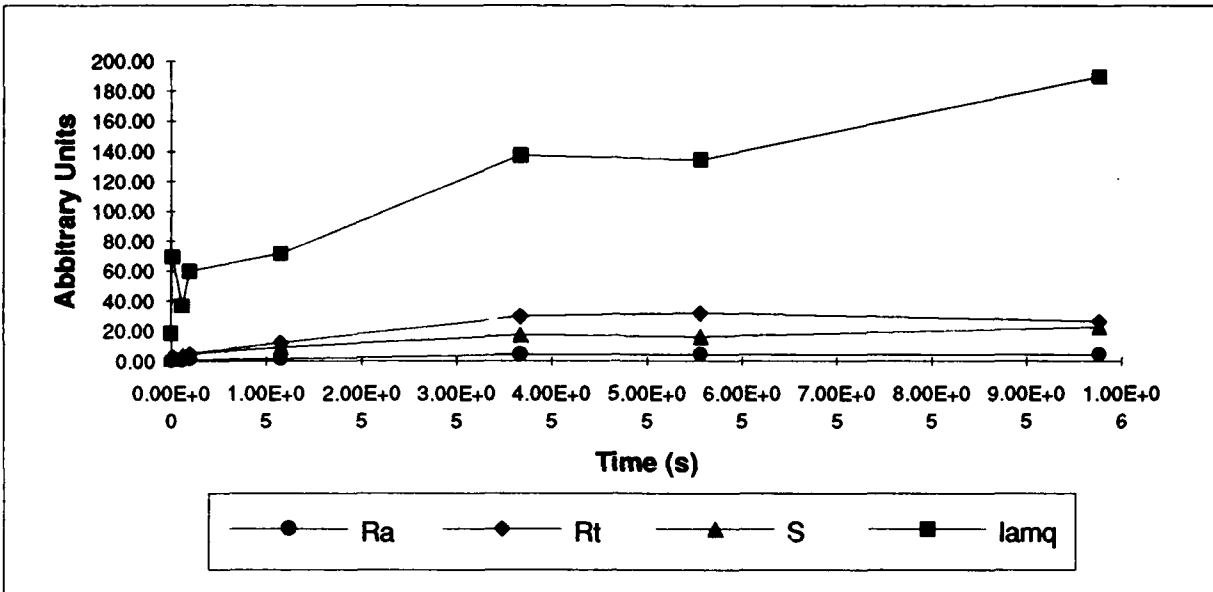


Figure 1: Effect of corrosion on surface profile parameters

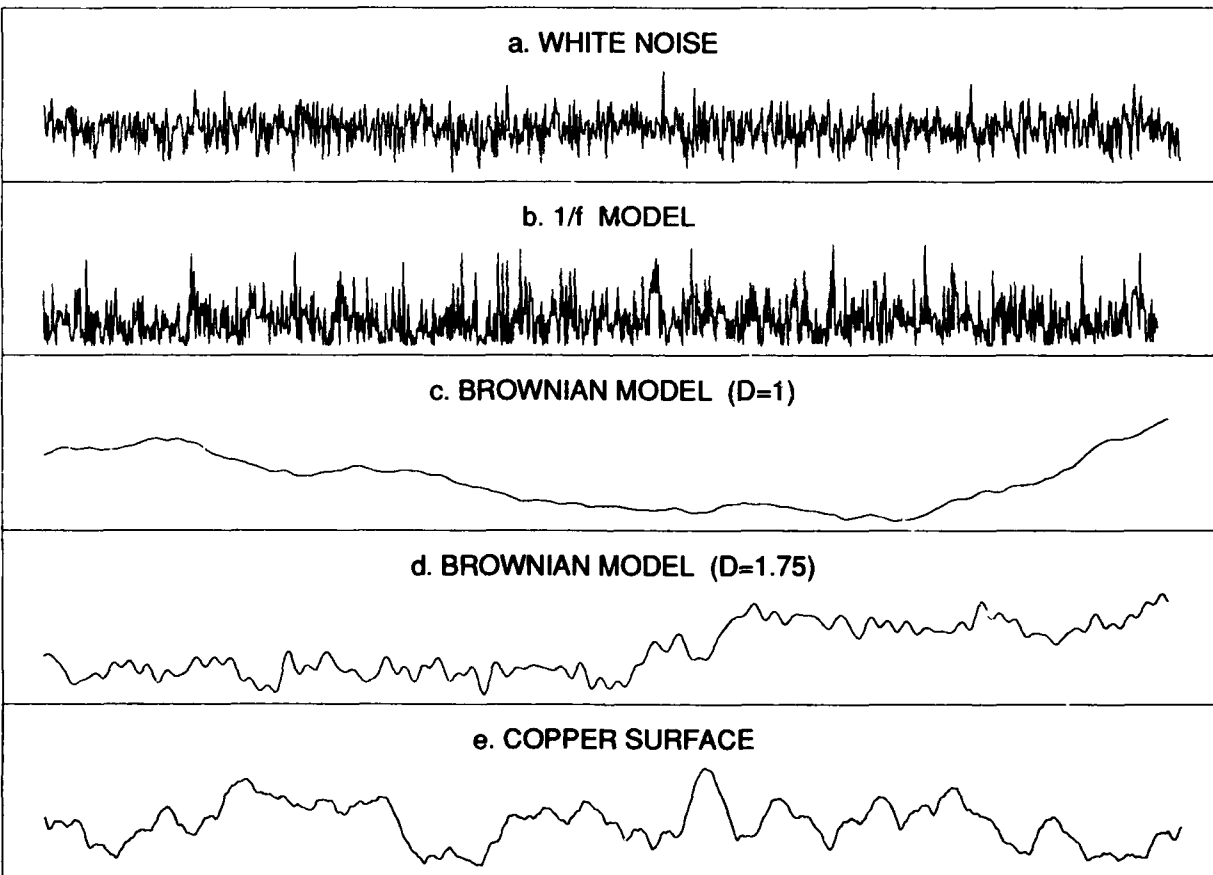


Figure 2: Sample surface profiles for white, 1/f and brown noise compared to a corroded copper surface.

METHODS TO COMBAT LIQUID METAL EMBRITTLEMENT IN CRYOGENIC ALUMINUM HEAT EXCHANGERS

S. Mark Wilhelm
R.D. Kane
Cortest Laboratories, Inc.
11115 Mills Road - Suite 102
Cypress, Texas 77429

Alan McArthur
Central Environmental, Inc.
9189 Winkler - Suite D
Houston, Texas 77017

Abstract

Liquid metal embrittlement (LME) is a rare but potentially catastrophic failure mechanism for chemical process equipment. Aluminum heat exchangers that process natural gas liquids are particularly at risk due to mercury contamination in natural gas feedstocks. Mechanisms of liquid metal attack peculiar to the Al/Hg system include amalgamation, amalgam corrosion, LME and intergranular attack that is preferential to weldments.

The paper reports the results of a program directed at prevention and remediation of liquid metal attack of cryogenic aluminum heat exchangers. The specific topics discussed are (1) detection of liquid metal embrittlement using acoustic emission techniques (2) a chemical process to remove mercury from contaminated equipment (3) surface treatment methods to prevent mercury attack of equipment exposed to mercury (4) methods to assess the condition of the oxide in aluminum equipment.

In general, corrosion and cracking of aluminum can be mitigated by several engineering approaches. Metallurgical selection of non-susceptible alloys, choice of proper welding procedures and surface treatments to strengthen the oxide can be utilized when new equipment is fabricated. For contaminated equipment, selective oxidation and complexation of mercury can be utilized to prevent mercury attack and to remove existing amalgams. LME can be detected using AE to assist decision making for critical components handling liquified natural gas. Surface condition also can be assessed using capacitance techniques to further aid decisions regarding remediation.

Introduction

Elemental mercury (Hg^0) is a contaminant to some natural gas feedstocks used in ethylene, LNG and ammonia production processes.⁽¹⁻³⁾ Mercury likely is present in a variety of other natural gas systems, however, it is only during liquefaction that significant quantities precipitate and accumulate. Cryogenic heat exchangers constructed primarily of aluminum alloys have experienced failures in welded piping due to contact with mercury during plant shutdowns or deriming operations when the temperature of the piping exceeds the melting point of Hg.

Research has been directed at understanding the chemical interactions between mercury and aluminum that give rise to catastrophic failures. The historical objectives have been:

1. To predict the most likely location for Hg attack. This includes the metallurgical questions regarding which aluminum alloys or welded metallurgical structures are most at risk.
2. To understand mechanistically the preference of Hg for grain boundaries and the role of the surface oxide on Al in mitigating Hg attack.
3. To measure the fracture properties of alloys embrittled by Hg so as to estimate serviceability.

This paper reviews a portion of the existing information on Al/Hg interactions from an engineering viewpoint in an effort to clarify methods of preventing Hg attack of aluminum.

A two year research project co-sponsored by the Gas Research Institute and four industrial sponsors (Tenneco, Dupont, Oxychem, Lyondell) was conducted in an effort to provide engineering solutions to the materials related problems in aluminum cryogenic equipment that is contaminated by mercury.

This work focused on four areas:

1. Methods to treat aluminum surfaces so that Hg attack is prevented.
2. Methods to detect and locate liquid metal embrittlement (LME) in an aluminum cold box (cold box is the industry term for a cryogenic heat exchanger).
3. Methods to assess the surface condition of contaminated surfaces.
4. Methods to remove mercury from aluminum without corrosion to the aluminum.

A condensed account of the principle objectives, results and conclusions of this research program is presented.

Technical Background

Mercury can degrade materials by four basic mechanisms:

1. amalgamation
2. amalgam corrosion
3. liquid metal embrittlement
4. galvanic corrosion

Amalgation

Amalgamation is the process by which mercury forms liquid solutions with various metals, primarily aluminum, tin, gold, silver, and zinc. Of these, only aluminum has mechanical significance. The affinity of aluminum for mercury is mediated by the oxide (Al_2O_3) that protects the aluminum surface. The oxide on aluminum is not homogenous and contains numerous defects. In general, mercury lacks the ability, because of surface tension, to diffuse through cracks or defects and hence cannot reach the underlying metal. This lack of wettability, however, can be mitigated by thermal or mechanical stresses, by chemical environments and by temperature.

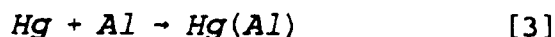
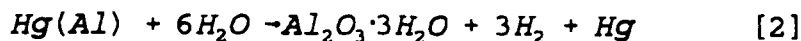
In situations in which Hg can breach the aluminum oxide and contact the underlying surface, the rate of amalgamation depends, in a major way, on metallurgical and microstructural condition. It is observed, for example, that mercury amalgamates selectively with weldments and more rapidly with particular alloys. Table 1 provides a list of aluminum alloys and the kinetic degree to which they amalgamate with Hg.

The primary manifestation of amalgamation is loss of mechanical strength in weldments. Amalgamation does not require stress nor does it require mediation by a conducting electrolyte to occur.

Amalgam Corrosion

Amalgam corrosion is the combined action of Hg and moisture on susceptible materials, primarily aluminum and tin. The difference between this mode of attack and simple amalgamation is that the corrosion process propagates with minuscule amounts of mercury.

The reaction scheme is:



etc.

Amalgam corrosion regenerates the reactant and hence is self-propagating so long as water is available. If sufficient moisture and mercury are present, aluminum structural components can be penetrated fairly rapidly. The rate of attack is mass transfer limited but does not proceed as rapidly as liquid metal embrittlement (LME) discussed below. Amalgam corrosion is selective to the same aluminum alloys as simple amalgamation, however, it can affect all aluminum alloys to some degree.

Liquid Metal Embrittlement (LME)

Liquid metal embrittlement by mercury is distinct from amalgamation in that it produces rapid brittle fracture and affects a much broader range of materials (aluminum, nickel-copper alloys, brasses, copper alloys, tin alloys, some stainless steels; see Figure 1). The mechanism of LME of aluminum involves liquid diffusion of mercury atoms in grain boundaries. Cracks usually initiate and propagate via the grain boundaries. LME is distinct from stress corrosion cracking in that no purely electrochemical processes are involved.

The unusual aspects of LME, as opposed to other fracture processes, are that the crack propagation rate can be exceedingly fast and the stress intensity required for crack propagation can be very low. Figure 2 illustrates the fracture rate with which aluminum cracks propagate in smooth tensile specimens having Hg surface contamination. The limiting crack velocity is approximately 100 cm/s which is reached due to the limit of liquid diffusion of mercury (not surface diffusion or vapor diffusion). In Figure 3, the limiting stress intensity factor for mercury LME of aluminum is shown. For weldments it can approach 5 ksi in^{1/2} which translates into a critical defect size of 10⁻¹ mm.

LME is not limited to aluminum but can affect high strength steels as well. Susceptible materials include 4140 RC 35-40 at elevated temperature, precipitation hardened stainless steels also having high strength and high hardness, and copper-nickel alloys.

Galvanic Corrosion

Galvanic corrosion caused by mercury deposits on steel in corrosive environments has been observed. Mercury serves to accelerate acid dissolution and to aggravate localized corrosion such as pitting. The situations in which mercury deposits contact steel are found in gas/water separators in gas production and when mercury from gauges contaminates process piping in chemical plants.

Engineering Solutions to Mercury Problems In Aluminum Heat Exchangers

Ethylene and LNG plant operators face tough decisions if cold box equipment becomes contaminated with Hg. Hg contamination can be avoided by employing sulfur impregnated carbon beds to adsorb Hg in gas feedstocks, however, the beds can saturate unexpectedly allowing Hg to enter the cold box. The more common occurrence is that Hg is an unknown contaminant to a feedstock that originated from an undocumented source.

If the cold box becomes contaminated, the amount of mercury and its location are often unknown and not easily estimated. As long as the cold box is operating below the freezing point of Hg (- 40 C), no acute problems exist related to materials. At some point, however, the cold box will see ambient temperatures during a scheduled outage, an unexpected shutdown or due to deriming operations (deriming is used to remove solid gas hydrates and condensed water from cryogenic equipment

by allowing it to warm above the dew point of water or above the hydrate point).

The problems that face LNG or ethylene plant operators (and engineers) involve several issues:

1. If a cold box is thought to be heavily contaminated or if actual leakage has occurred due to Hg damage, some operators elect to replace the cold box or to construct a spare if damage is detected during an outage. The question then becomes how to construct new equipment to withstand Hg attack.
2. If a cold box is placed off stream and allowed to warm to ambient, it is often necessary to assess the condition of the equipment prior to plant start-up. Assessments must be performed without causing any LME damage.
3. If mercury contamination is certain or if it is detected, then remediation of the equipment is often desirable. The questions here involve removing mercury without causing corrosion or cracking of the aluminum welds.
4. If Hg contamination is uncertain or in situations where mercury has been removed from equipment, the assessment of localized LME and/or amalgamation is of concern. Under these circumstances it is desirable to understand the condition of the oxide on aluminum.

Surface Treatments to Prevent Hg Attack

A particularly critical location of mercury attack is at a weld. For LME or amalgamation to occur, the weld metal and Hg must be in intimate contact. This can occur by pooling of mercury in low areas, by Hg accumulation behind a back-up ring used in piping welds or by surface adsorption. Two aspects of welds make them highly susceptible. The metallurgical condition, i.e. grain boundary chemistry, grain size etc., is known to be of higher susceptibility than the base metal. Once in contact with Hg, cracks form in weldments easily and they propagate readily because of residual stress resulting from welding. Secondly, the oxide (Al_2O_3) that is formed during welding is inhomogeneous and epitaxially disjointed, thus allowing Hg to penetrate and reach the underlying substrate in a facile manner.

Three approaches have been suggested for providing weldments that are resistant to Hg attack. The first involves selection of alloys and consumables that result in resistant microstructures. To date, such combinations have not been identified that satisfy all the mechanical criteria as well as the LME resistance criteria. Secondly, weld geometry has been examined from the perspective of elimination of backing rings. This approach is recommended, however, in and of itself, elimination of backing rings does not remove the possibility of Hg attack. Thirdly, surface treatments have been examined that have properties that prevent Hg ingress.

An investigation was conducted to determine the abilities of three types of surface treatments to produce surface conditions unfavorable to Hg attack. The experimental plan was developed with the knowledge the LME crack initiation is the rate determining step in equipment failure. The critical oxide properties were postulated as related to mechanical ability to resist loading (oxide strength and fracture toughness) and ability to withstand thermal stresses.

Experimental

Surface treatments examined are listed in Table 2. Aluminum plates (5083-0) were welded with 5183 filler metal then machined to produce tensile specimens. The gauge section of 50 percent of the test specimens contained a perpendicular cross section of weldment including heat affected zones (HAZ) and base metal. The remaining 50 percent of the specimens were oriented identically to the welded specimens except they were machined from base metal only.

Two test methods were used to measure the ability of the surface treatments to prevent LME. In the first method, tensile specimens were exposed to Hg under constant load using a proof ring apparatus as shown in Figure 4. The second method used a dynamic stain apparatus referred to as the slow strain rate (SSR) method⁽⁵⁾ as illustrated in Figure 5. The data generated by the constant load method are times to failure under load as a percent of yield strength. The data generated by the SSR method are times to fracture at a constant extension rate and the resultant fracture morphology.⁽⁶⁾

Results and Conclusions

Constant load data (Table 3) indicated that aluminum surfaces will withstand Hg attack for extended periods (months) under considerable loading. This is due in part to the fact that, in the absence of dynamic strain from mechanical or thermal stresses, Hg will not usually penetrate the surface oxide because of the surface tension properties of Hg. Under dynamic strain or surface wear conditions, however, the oxide can fracture due to low oxide ductility or can be physically removed. The SSR data (Table 4) indicate LME occurs at fractions of air ductility, however, significant improvement is seen for the various surface treatments.

The SSR data (Table 4) indicate that merely providing a surface treatment that makes the surface oxide thicker does not necessarily improve resistance to dynamic strain. For example, the 6 hour steam oxidation was inferior to the four hour treatment. The sulfuric anodization was generally inferior to shot peening of the air oxide in spite of the fact that anodization produces a thick (0.0005-inch) surface film. Figure 6 compares the performance of the various surface treatments.

It was concluded that surface treatments can be utilized to provide improvement to the surface condition of aluminum and thereby can reduce the likelihood of mercury attack of cold box equipment.

Detection of LME in Contaminated Equipment

Unfortunately, access to cryogenic equipment (i.e. the cold box) used in ethylene and LNG manufacture is limited. It is difficult, therefore, to use traditional methods of inspection and non-intrusive methods of detection such as radiography and ultrasonic. In fact, ultrasonic techniques will not readily identify LME nor will radiography in most situations due to the very tight cracks that are formed by LME. Visual inspections of accessible locations using borescopes will identify major accumulations of Hg, but they will not identify LME or localized amalgam corrosion.

Acoustic emission (AE) has been proposed as a viable method to detect active LME in contaminated equipment. Placement of the acoustic transducers is critical to success and, therefore, the limited access to piping and internal components hinders this approach as well, to some extent. Another concern with AE is that to record acoustic signals it is required to perturb the system, i.e. to apply an internal pressure function. This could be very detrimental to equipment in which LME has initiated given the extremely low stress intensity required to propagate LME (see Figure 3). Research was conducted in an effort to identify safe and effective techniques to detect LME in aluminum heat exchanger using AE.⁽⁷⁾

The experimental program was developed to determine the ability of AE to evaluate LME in Al-alloys. Four series of tests were performed as shown below:

- Series 1 - Evaluation of Compact Tension Specimens for AE Response in Hg.
- Series 2 - Evaluation of Pipe Specimens for AE with Internal Pressure and Hg.
- Series 3 - Evaluation of Pipe Specimens for AE Using Pressure Cycles and Hg.
- Series 4 - Evaluation of Kaiser/Felicity Effects with Compact Tension and Pipe Specimens with Hg.

Experimental

The alloy examined was alloy 5083-O which is commonly used in the construction of cryogenic equipment in ethylene plants. Pipe and plate material was evaluated in both welded and non-welded condition. Welding procedures were typical of those used in fabricating equipment.

The 1T compact tension (CT) specimens were machined per ASTM E-399. A nominal specimen thickness of 0.25 inch was used for these specimens. Side grooves were machined in the specimens in an attempt to enforce planar crack growth and test validity. Both welded and non-welded CT specimens were employed. The welded specimens were oriented so that the crack would be growing in the weld metal parallel to the direction of the weld.

Pipe specimens were fabricated from nominal 5-inch O.D. pipe. To fabricate the pipe samples, sections of pipe were butt welded together using a full penetration single V weld. Samples were tested both with and without aluminum backing rings on the inside of the pipe at the weldment. The pipe specimens were machined on the ends to provide a true O.D. on which

the pressurizing fixture could seal.

Series 1 - Evaluation of Compact Tension Specimens for AE Response in Hg. CT specimens were instrumented with a PAC R151 sensor. The sensor was a 150 KHz resonant device with a 40 dB gain, integral preamplifier and a 100 kHz to 300 kHz bandpass filter. The sensor was connected to a PAC 3000/SPARTAN AE instrument where an additional 40 dB of gain was applied. The detection threshold was adjusted to 40 dB. A total of four CT specimens were tested: Two non-welded and two welded.

Series 2 - Evaluation of Pipe Specimens for AE with Internal Pressure and Hg. Pipe specimens were monitored using the same type of AE sensors and instrumentation described in Series 1. For these tests, however, two sensors were used. The test set-up used in Series is shown in Figure 7. The AE sensors were placed on either side of the butt weld in the pipe sample. A manually operated, air driven hydraulic pump was used to hydrostatically pressurize the specimens to failure.

Series 3 - Evaluation of Pipe Specimens for AE Using Pressure Cycles and Hg. The pipe specimens in Series 3 were tested using the same AE sensor configuration used in Series 2 except that a linear array of four sensors were used. Two sensors were on one side of the butt weld and two were on the other side of the weld. The main difference in Series 2 and 3 tests were in the pressure cycles employed. The pipe specimens were initially pressurized to 450 psi for ten minutes. This pressure corresponded to approximately the normal working pressure of the Al pipe specimens. After this initial hold, the pressure was varied and then held for different periods of time. Following the pressure/hold sequence, the pipe specimens were subjected to rapid cyclic pressurization at one or more pressure levels in an attempt to initiate liquid metal attack in the pipe specimen. The initial pressure sequence was then repeated again followed by pressurization of the pipe specimens to failure.

Series 4 - Evaluation of Kaiser/Felicity Effects with Compact Tension and Pipe Specimens with Hg. Series 4 AE tests were conducted using the same AE instrument settings and similar laboratory techniques developed in the previous three series of tests. Series 4 tests involved experiments on both CT and pipe specimens using multiple load or pressure cycles. The typical cycle configuration consisted of a ramp to a designated load or pressure followed by a hold period until the AE signal subsided. Then, the load or pressure was decreased to approximately one half the previous maximum value and increasing again to a higher value of load or pressure. This sequence was continued until failure of the specimen was obtained.

Results and Conclusions

Based on the experimental program, the following conclusions were made:

1. Major differences in the performance (corrosion and cracking) were observed when Al 5083-0 was tested in inert environments as compared to the Hg environment. When Hg was present, the material was subject to amalgamation and liquid metal embrittlement (LME). This behavior was observed for both stressed 1T compact tension (CT) specimens or pressurized pipe specimens.
2. Maximum susceptibility to Hg attack was noted under conditions of (a) prolonged load cycling of the pressurized pipe specimen which produced the low failure pressures relative to similarly cycled control (Hg-free) specimens, and (b) when a surface wetting agent was used to promote surface contact of the Al-alloy and Hg which produced increased Hg attack, LME and strength loss.
3. Acoustic Emission (AE) monitoring of both CT specimens and pipe specimens was successful in observing characteristic emissions from most specimens. Low amplitude AE was most prevalent during the initiation of the tests during periods of low loads in the CT specimens or low pressure (<500 psi) in the pipe specimens particularly when surface wetting agents were used to promote active Hg-attack. The AE was somewhat random but mostly continued during hold periods following partial or total unloading of the specimen. Higher amplitude AE appear to occur during hold periods at maximum load in a particular loading cycle. By comparison, this behavior was very limited and attenuated rapidly in the control specimens.

Aluminum Oxide Assessment

The exact nature of mercury deposition on aluminum surfaces during operation of cryogenic heat exchanger equipment is not known exactly. Specifically, the physical state of the mercury (droplets, finely dispersed particles, pools) and its predominant

location of deposition cannot be predicted exactly. When the cold box or liquefaction heat exchanger is shut down and allowed to warm, the mercury coalesces to form droplets or pools which reside on an aluminum oxide covered surface.

The physical and chemical properties of the oxide determine, in large part, whether mercury will cause damage to the underlying metal. Oxide thickness, strength, and fracture toughness influence the rate of mercury ingress. The principle objective of this project was to correlate oxide dielectric properties with mercury ingress during thermal cycling and, thereby, to develop methods to assess the condition of oxides to resist mercury attack.

The capacitance of the $\text{Hg}/\text{Al}_2\text{O}_3/\text{Al}$ interface was postulated to provide the necessary information on protection. The magnitude of capacitance is related to oxide thickness and other dielectric properties (frequency dispersion is related to microstructural properties of the Al_2O_3 , such as fractures, fissures, holidays, etc). This postulate was tested by measuring oxide impedance of four surface conditions during thermal cycling. Mercury contact with the aluminum substrate was detected as an electrical short (impedance, $Z = 0$).

Experimental

The oxide assessment utilized equipment shown schematically in Figure 8. It consisted of aluminum (5083-0) block, to which was attached a plexiglass cylinder that contained mercury. The oxide on the aluminum was sandwiched between the aluminum and mercury. Electrical connection was made to the aluminum and to the mercury with leads terminating at an impedance analyzer (Solartron). The mercury and aluminum were positioned in a bath containing isopropyl alcohol which was capable of cycling between +40 C and -40 C. Dielectric properties (complex impedance) were measured as a function of temperature. Four surface conditions were examined as shown in Table 5. The test procedure entailed cooling the system to -40 C and measuring impedance as a function of time. The rate of temperature change was 5 ± 1 degrees/minute.

Results and Conclusions

The plots of impedance vs. temperature measured during thermal cycles from -40 C to +40 C for two surface conditions are provided in Figures 9 and 10. Oxide impedance data indicated that SO, SP, and SAA surface treatments did not survive a complete cycle from +40 C to -40 C. Survival in this case denotes the ability to prevent mercury from contacting (electrically) the substrate aluminum.

Presumably, oxide fractures were caused during thermal cycles by the difference in thermal expansion of metal and oxide. When covered by mercury, air oxidation is prevented; hence, the aluminum cannot heal itself and mercury can diffuse through cracks or fissures to contact the underlying metal. The chromic acid anodized surface survived in excess of nine (9) complete cycles and thus, demonstrates the feasibility of surface treatment to resist mercury degradation. It is not known conclusively what characteristic is imparted by the chromic acid treatment to improve resistance to mercury.

Mercury Remediation

Given the fact that mercury can reside on aluminum surfaces for indefinite periods without producing damage, the opportunity exists to remove it or to react it to an inert form. Such a process would restore contaminated equipment to a usable condition. Hg, however, is not easily converted to stable inorganic compounds. Hg will react with H_2S or polysulfides to form HgS . This reaction is self limiting, however, due to the accumulation of $\text{HgS}(s)$ on the surface of Hg^0 . HgS is not soluble in water or organic solvents. Secondly, Hg^0 is relatively insoluble in aqueous and hydrocarbon systems, thus precluding the opportunity to simply flush it from contaminated surfaces by contact with an appropriate solvent. Its gas phase solubility is even less, hence desorption by contact with warm gas is not feasible because of the time and quantity of gas required.

A third possibility to remove Hg is to react it with an organic based chelating agent to form a soluble organometallic compound. The transformation that must be accomplished is the oxidation of Hg to Hg^{2+} and subsequent complexation to a compound that is soluble in either an aqueous or non-aqueous system.

A chemical formulation as described has been developed and is now under patent application. The technical feasibility of mercury removal depends on (1) the cleaning solution's ability to selectively oxidize and sequester Hg and (2) being non-corrosive to other metals and alloys. Table 6 shows the corrosion rate of several engineering alloys exposed to the Hg cleaning solution. Figure 11 shows the rate of complexation of a Hg pool under mildly convective conditions at ambient temperature.

Future Trends

Hg is an extremely aggressive and detrimental corrodent to aluminum. The observed mechanisms of attack are becoming better understood as research focuses on the microstructural and metallurgical aspects of LME and amalgamation. Likewise, increasing awareness of the importance of the surface oxide on aluminum has led to new avenues of engineering research to prevent degradation of materials.

The use of stainless steels to replace aluminum in cryogenic heat exchangers is certainly an option for ethylene and LNG plant operators, however, the cost differential is a factor of 2-3. The added capital requirement may be offset by reliability in critical applications.

Another obvious way to prevent Hg corrosion of aluminum is to scavenge the Hg from all contaminated feedstocks. This technology is presently evolving along two lines. Sulfur impregnated activated carbon beds are now being used to adsorb Hg to below ppb levels in natural gas. Secondly, an ion exchange system is under development that utilizes an adsorbent that can be regenerated, thus avoiding disposal issues.

For aluminum equipment now operating in a contaminated condition or that may become contaminated in the future, the key issues discussed previously involving detection and remediation are key to prevention of damage. Lastly, by careful evaluation of operating conditions, it may be possible to prevent precipitation of Hg in aluminum equipment or to maintain the equipment below the Hg freezing point, even during scheduled outages.

Acknowledgements

The authors appreciate the permission of the Gas Research Institute (Dennis Leppin and Vern Hill, Program Managers) to publish this work and for its financial sponsorship. The participation and financial support of Oxychem (J. English), Lyondell Petrochemicals (E.R. Olivares), E.I. DuPont (G. Kobrin, J.R. Dugas), and Tenneco Oil (K. Schorre) are also gratefully acknowledged. Much of the experimental work was performed by D. Wu and K. Benoit of Cortest Laboratories, Inc.

References

1. D.R. McIntyre, J.J. English, G. Kobrin, "Mercury Attack of Ethylene Plant Alloys"; Paper No. 106, Corrosion/89; NACE, New Orleans, Louisiana, 1989.
2. W.W. Bodle and R. Serauskas for Mercury; "LNG Operations", IGT, 6th International Conference on Liquefied Natural Gas; Kyoto, Japan; April 1980.
3. S.M. Wilhelm, "The Effect of Elemental Mercury on Engineering Materials used in Ammonia Plants", Ammonia Plant Safety, AIChE, August 1990.
4. J.E. Leeper, "Mercury Corrosion in LNG Plants"; Canadian Gas Processors Association, Quarterly Meeting, Calgary; September, 1980.
5. Stress Corrosion Cracking - The Slow Strain Rate Technique. ASTM STP 665. ed. G.M. Ugiansky and J.H. Payer, Philadelphia, Pennsylvania; American Society for Testing and Materials, 1979.
6. R.D. Kane, S.M. Wilhelm, "Use of Slow Strain Rate Tests to Evaluate the Embrittlement of Aluminum and Stainless Alloys in Process Environments Containing Mercury". ASTM STP 1210, in press, Philadelphia, 1993.
7. R.D. Kane, "Evaluation of Acoustic Emission for Determination of Mercury Attack of Aluminum Alloys", Paper 243, NACE Corrosion/92, National Association of Corrosion Engineers, Nashville, Tennessee, 1992.

TABLE 1
Compositional Analysis and Corrosion Test Results for Aluminum Alloy Samples

Alloy Designation	Mg (wt %)	Mn (wt %)	Cu (wt %)	Zn (wt %)	Bi (wt %)	Fe (wt %)	Si (wt %)	Cr (wt %)	Extent of Corrosion*
99.9% Al	--	--	--	--	--	--	--	--	Yes- catastrophic pe-forating
5083	4.4	0.58	0.04	--	--	0.24	--	--	No
300-H18	Trace	1.0-1.5	0.2	--	--	0.7	0.5	--	Moderate, non-damaging
5052-H34	2.2-2.8	0.1	0.1	0.1	--	0.45	--	0.15-0.35	Yes-moderate potentially damaging
7075 W	2.1-2.9	0.3	1.2-2.0	5.1-6.1	--	0.7	--	--	No

* "yes" indicates that catastrophic corrosion was observed.

"no" indicates that it was not.

TABLE 2

Selected Surface Treatments Code

Base Metal	Welded Specimens	Treatment Code	Surface Treatment
B-0	W-0	N	No surface treatment
B-1	W-1	SAA	Sulfuric acid anodized, 0.5 mil, boiling H ₂ O seal per mil A-863
B-2	W-2	SAA	same as 1
B-3	W-3	CAA	Chromic acid anidized, 0.2 mil
B-4	W-4	CAA	same as 3
B-5	W-5	SP2	Steel shot peen, shot size MI-230, intensity .02A
B-6	W-6	SP2	same as 5
B-7	W-7	SP4	Steel shot peen, shot size MI-230, intensity .02A
B-8	W-8	SP4	same as 7
B-11	W-11	SPZ4	Ceramic shot peen, shot size MI-Z 150, intensity .004R
B-12	W-12	SPZ4	same as 11
B-13	W-13	SPZ8	Ceramic shot peen, shot size MI-Z 150, intensity .004R
B-14	W-14	SPZ8	same as 13
B-15	W-15	S0110/1	Steam oxidized, 110C/1 hr.
B-16	W-16	S0110/1	same as 15
B-17	W-17	S0110/4	Steam oxidized, 110C/4 hr.
B-18	W-18	S0110/4	same as 17
B-19	W-19	S0160/1	Steam oxidized, 160C/1 hr.
B-20	W-20	S0160/1	same as 19
B-21	W-21	S0160/4	Steam oxidized, 160C/4 hr.
B-22	W-22	S0160/4	same as 21
B-23	W-23	S0160/6	Steam oxidized, 160C/6 hr.
B-24	W-24	S0160/6	same as 23
B-25	W-25	N	No treatment
B-26	W-26	N	No Treatment

TABLE 3
Constant Load Test Data

Specimen ID	Surface Treatment	Stress (ksi)	Test Time (hours)	Failure	Surface Crack
1747-B-1 ⁽¹⁾	SAA ⁽²⁾	23.0	4069	N ⁽³⁾	N ⁽⁴⁾
1747-W-1	SAA	23.0	4141	N	N
1747-B-2	SAA	26.0	4141	N	N
1747-W-2	SAA	26.0	4141	N	N
1747-B-3	CAA	23.0	4069	N	N
1747-W-3	CAA	23.0	4141	N	N
1747-B-4	CAA	26.0	4141	N	N
1747-W-4	CAA	26.0	4141	N	N
1747-B-15	S0110/1	23.0	4069	N	N
1747-W-15	S0110/1	23.0	4069	N	N
1747-B-16	S0110/1	26.0	4069	N	N

(1) B = bare metal
W = welded

(2) see Table 2

(3) N = no fracture of tensile specimen

(4) N = no surface cracking or corrosion observed

TABLE 4

Effects of Surface Treatments on Time to Failure
Ratio and Surface Corrosion in SSR Tests

Specimen	Surface Treatment	Avg TTF (hours)	Avg TTF(s) Avg TTF(n) (1)	Surface Corrosion (2)
B	N	5.7	1.00	3
W	N	5.1	1.00	3
B	SAA	7.5	1.30	4
W	SAA	4.6	0.90	4
B	SP2	9.3	1.63	1
W	SP2	8.3	1.63	1
B	SP4	7.1	1.25	1
W	SP4	8.8	1.72	1
B	S0160/6	13.3	2.30	2
W	S0160/6	6.5	1.27	2
B	S0160/4	15.9	2.79	2
W	S0160/4	7.5	1.46	2
B	N (no Hg)	48.8	--	--
W	N (no Hg)	85.9	--	--

(1) Avg TTF(s) = average time to failure with surface treatment.

Avg TTF(n) = average time to failure without surface treatment.
Both cases exposed to Hg.

(2) Surface corrosion observations

1 = smallest amount of surface corrosion

4 = largest amount of surface attack

TABLE 5

Surface Conditions Examined for Thermal Cycling Study

Condition	Code	Description
Shot Peen	SP	Ceramic shot peen Shot size MI-2 150 Intensity 0.008/A
Chromic Acid Anodize	CAA	Boiling chromic acid for 20 minutes
Steam Oxidation	SO	Normal (see below) then 160 C steam for 1 hour
Normal	Air	Polish to 600 grit finish Water rinse Air dry at 100 C
Sulfuric Acid Anodize	SAA	Normal then boiling H ₂ SO ₄ per MIL A-863, 0.5 mil thick

TABLE 6

Corrosion Rates of Engineering Alloys
Exposed to Hg Decontamination Solution

Alloy/Metal	Corrosion Rate g/cm ² /day
Al	$< 10^{-7}$
Cu	6×10^{-7}
Steel (1010)	6×10^{-7}
Hg	0.5
304SS	$< 10^{-7}$
316SS	$< 10^{-7}$

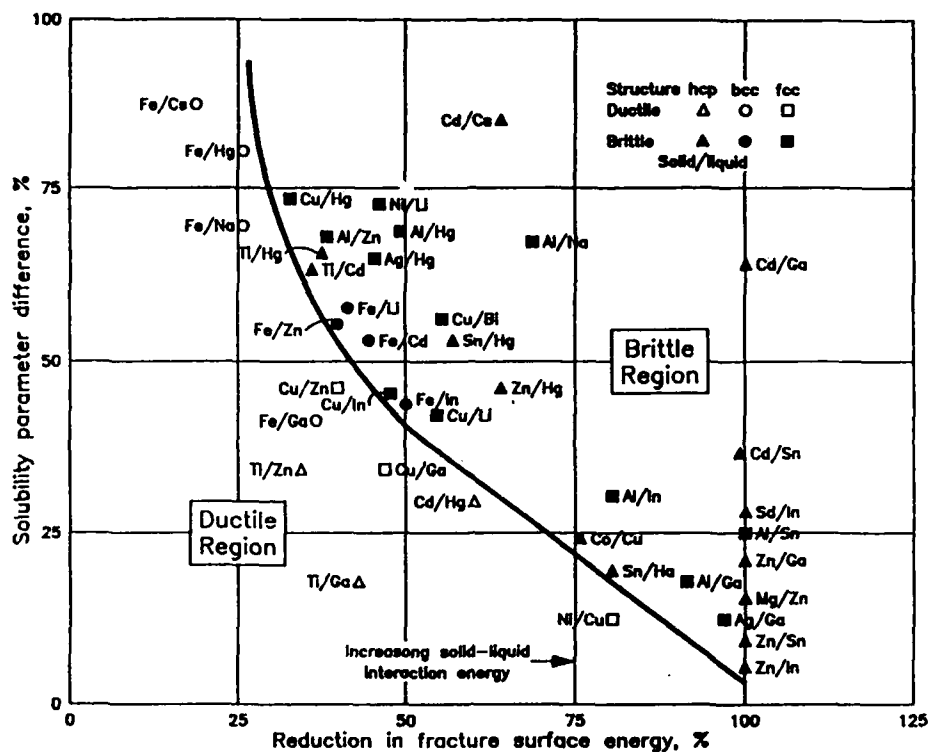


Figure 1 - LME in Solid/Liquid Metal Systems

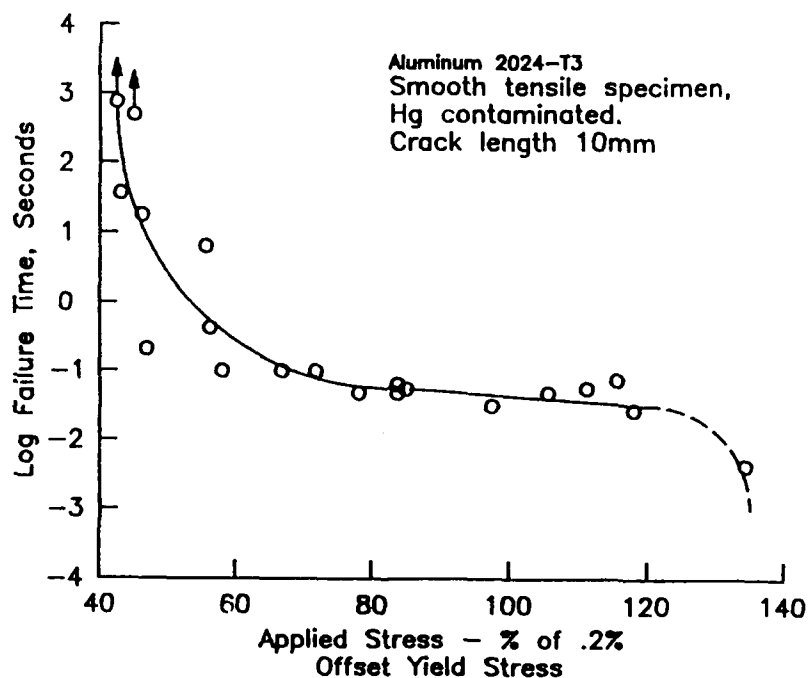


Figure 2 - Time to Fracture of Smooth Tensile Specimens Exposed to Hg

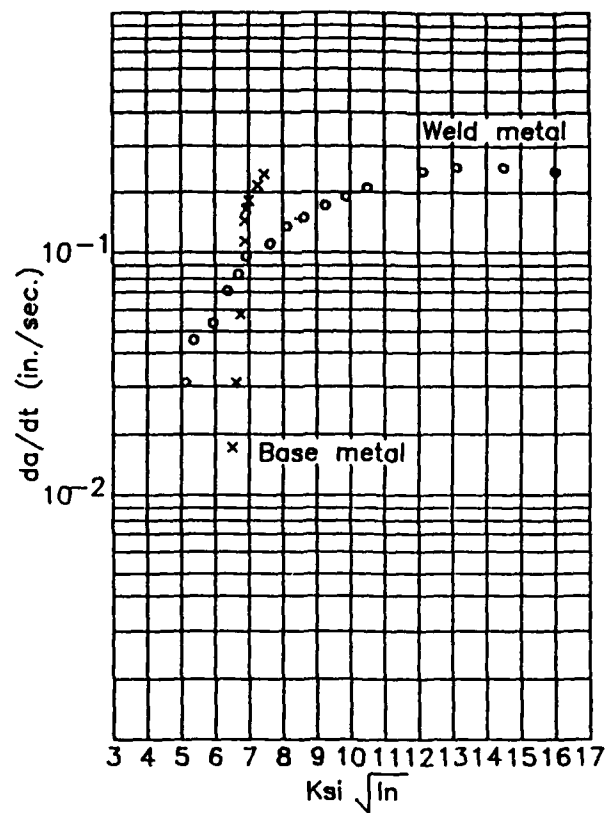


Figure 3 - Crack Growth Rates for 5083-0 Al, Room Temperature, Exposed to Hg

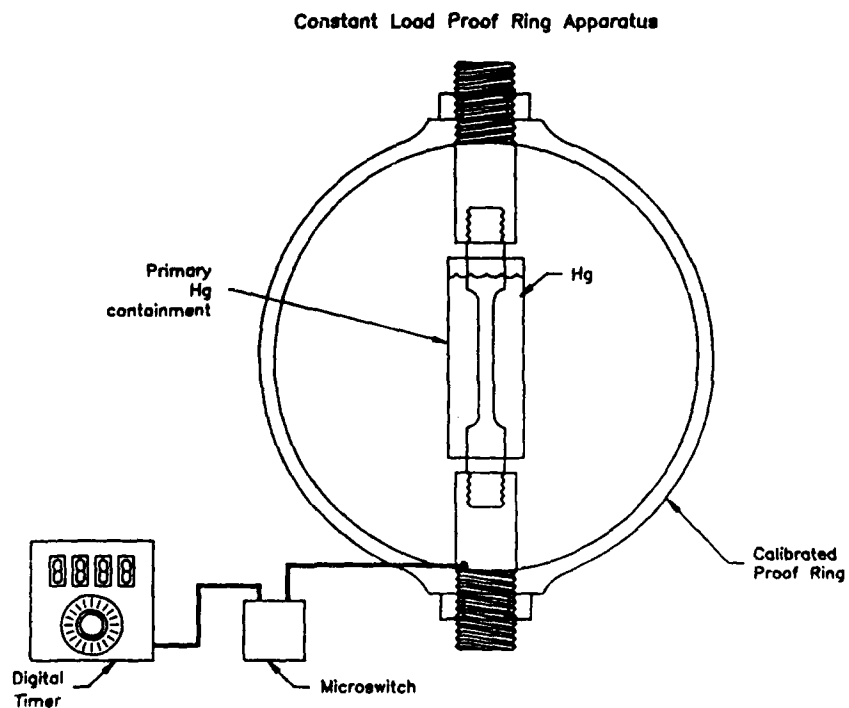
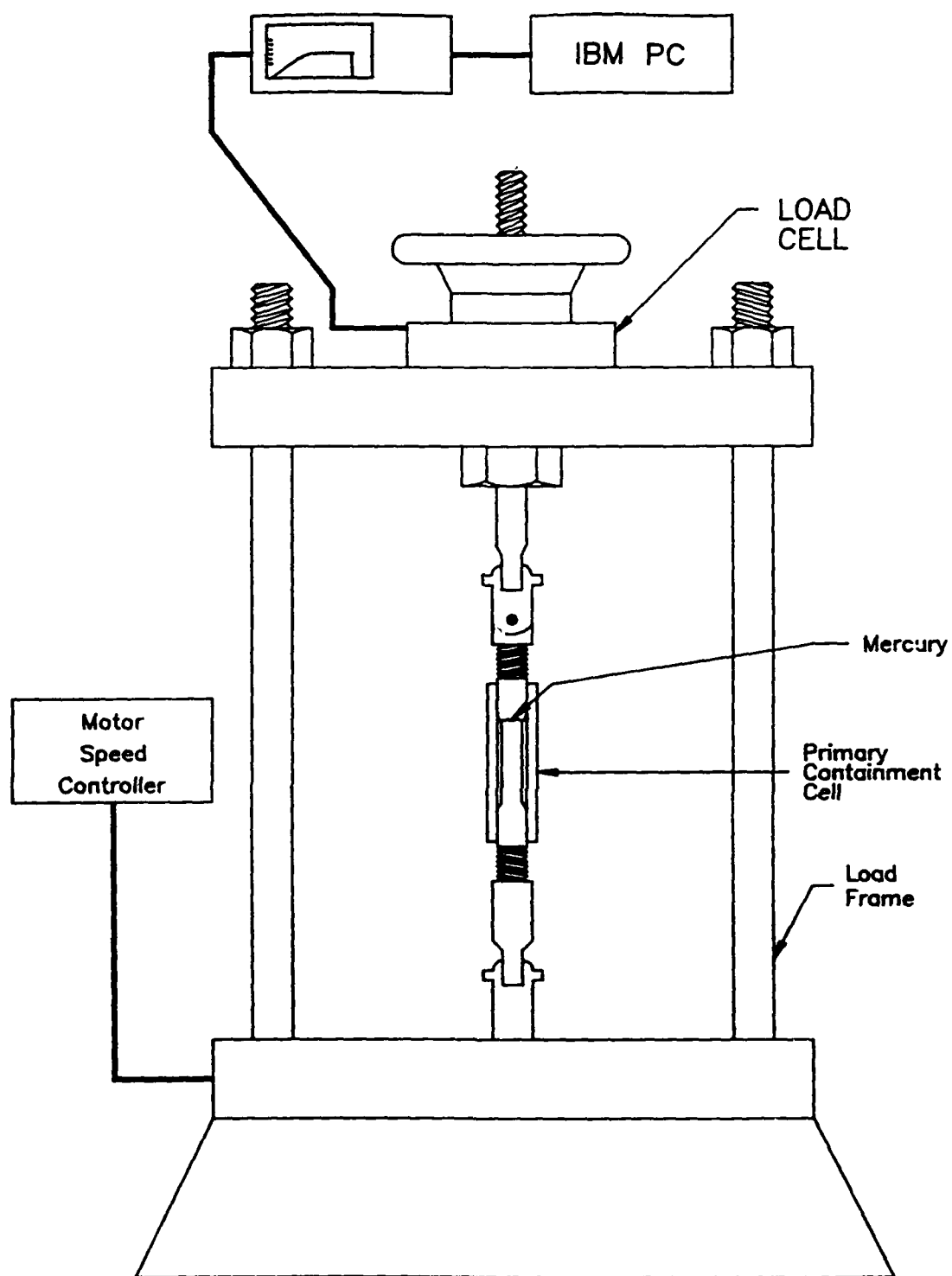


Figure 4 - Constant Load Test Apparatus for Evaluation of Surface Treatments



SSR Apparatus

Figure 5 - Slow Strain Rate Test Apparatus for Evaluation of Surface Treatments

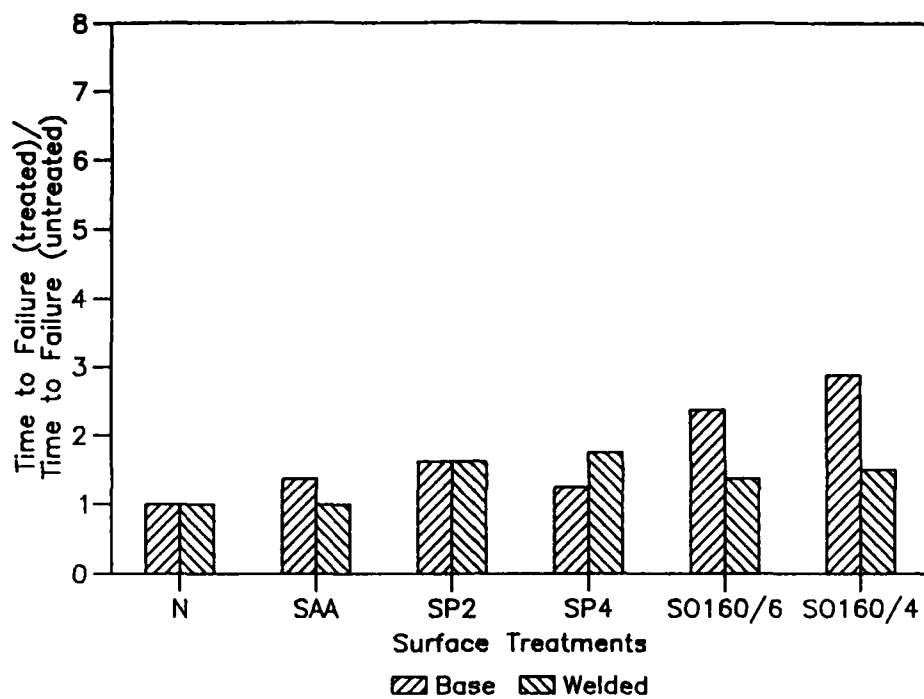


Figure 6 - Performance of Surface Treatments in SSR Tests

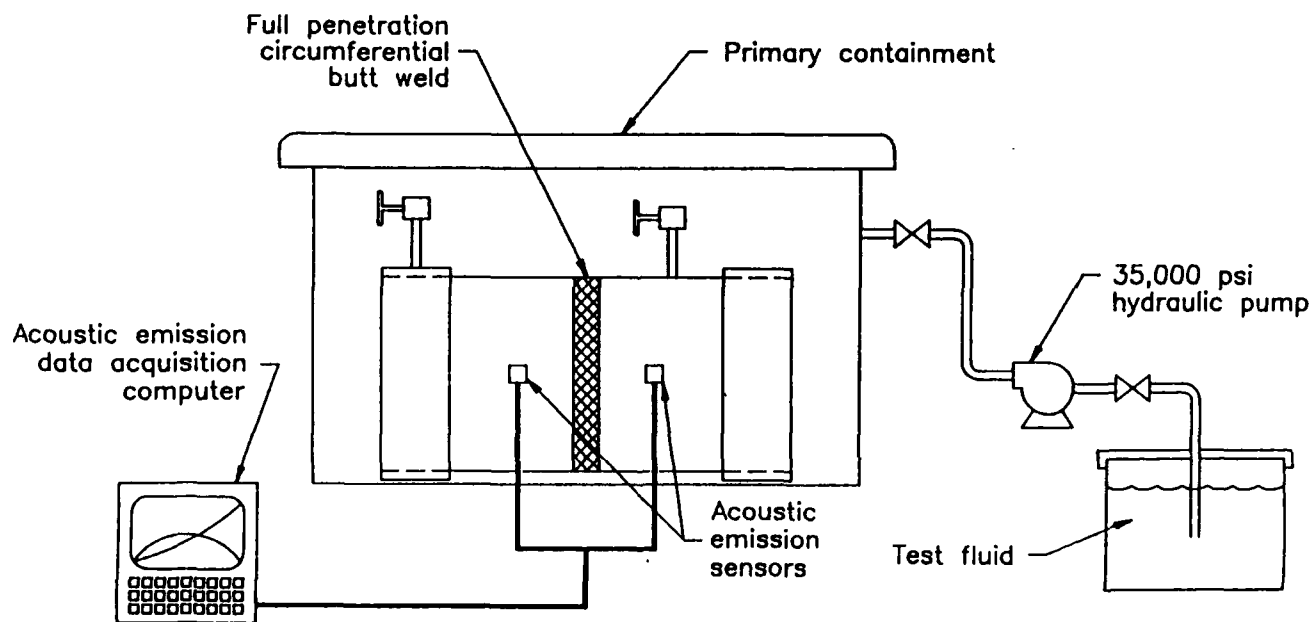


Figure 7 - Apparatus for Acoustic Emission Testing of Hg Contaminated Piping

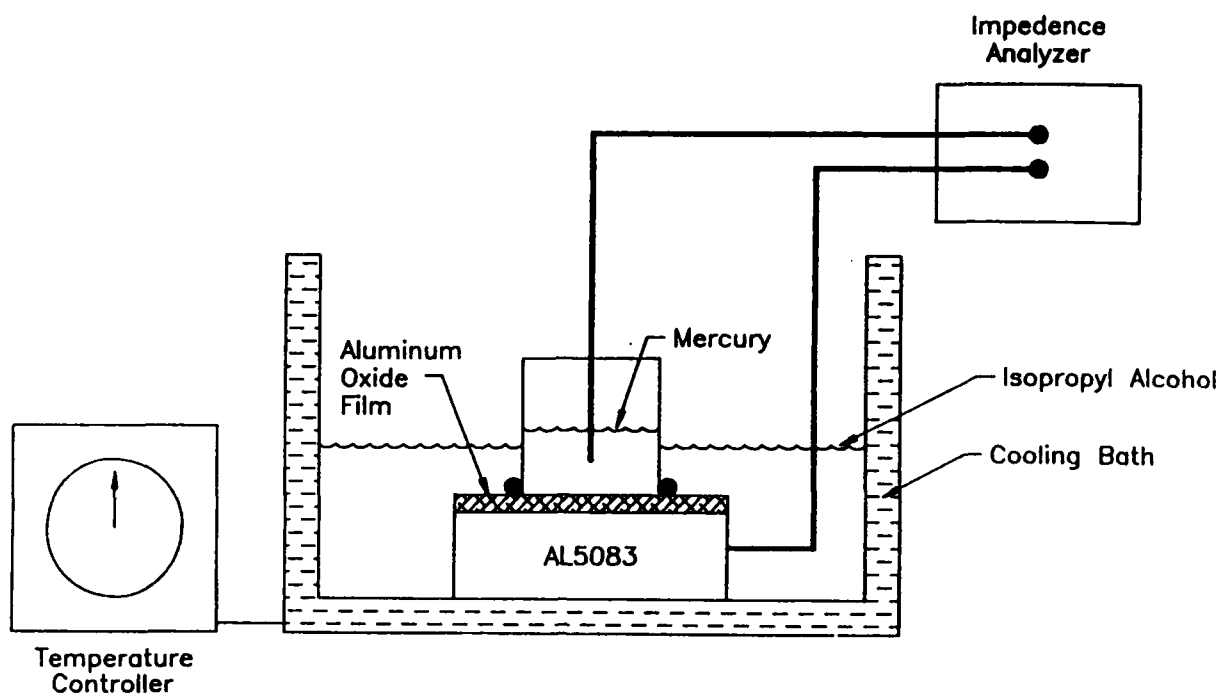


Figure 8 - Apparatus for Capacitance Testing of Surface Oxides on Aluminum

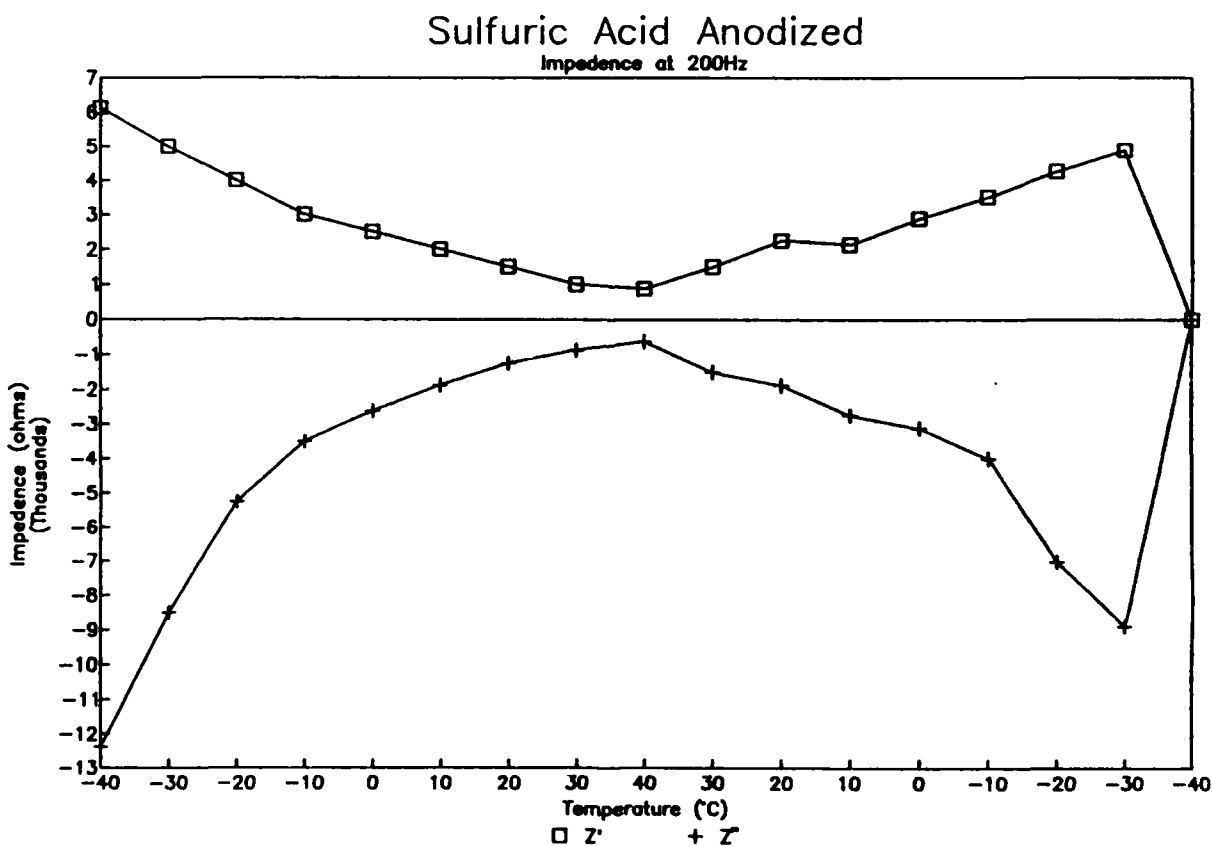


Figure 9 - Impedance versus Temperature for Thermal Cycle on Anodized Surface

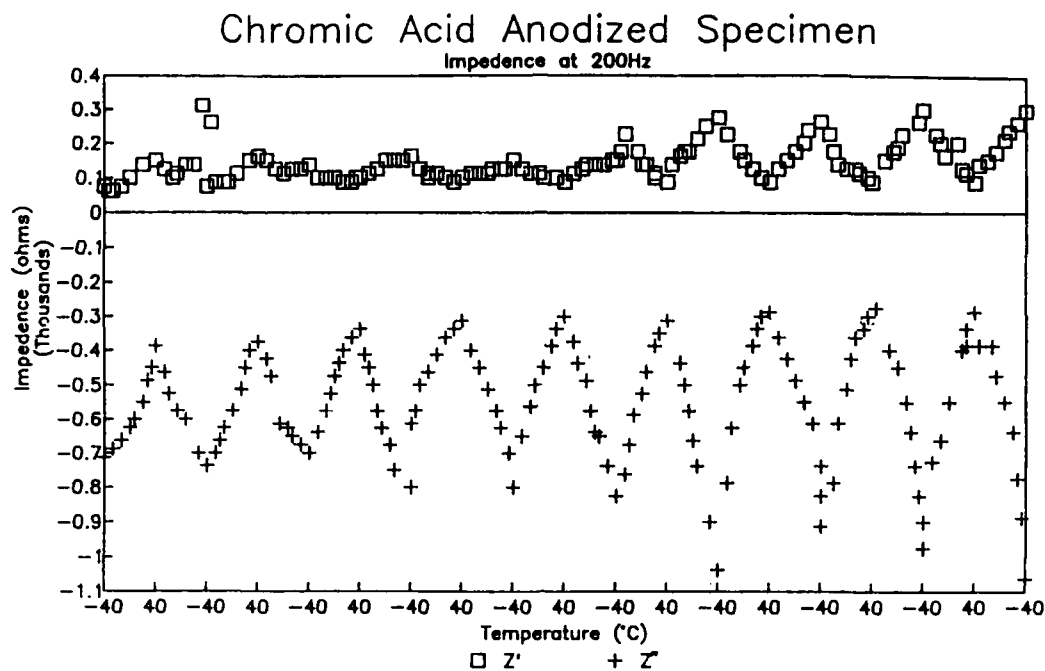


Figure 10 - Impedance versus Temperature for Thermal Cycles on Chromic Acid Anodized Specimen

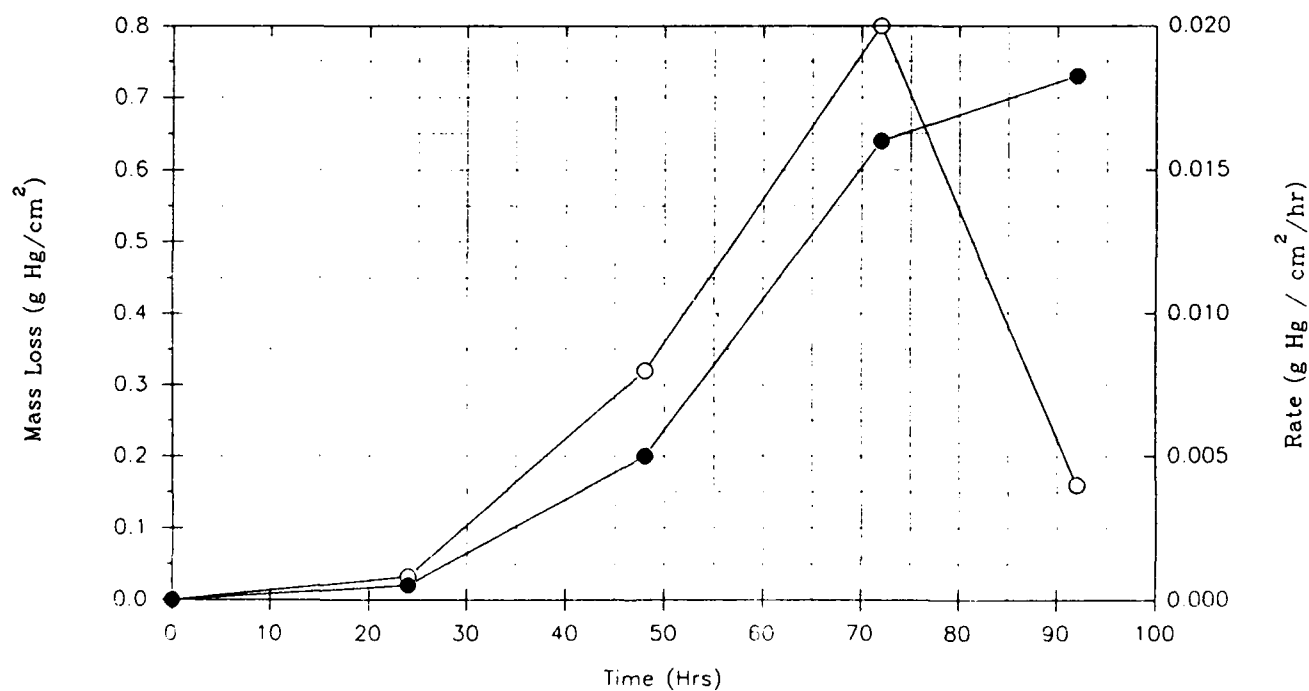


Figure 11 - Oxidation and Complexation of Hg exposed to a Hg Cleaning Solution
Solid Points - Mass Loss;
Open Points - Rate versus Time

Prevention of Localized Corrosion Caused by Thiosulphate in Paper Mill Environments

V. A. Marichev, T. Saario and V. V. Molokanov*

Technical Research Centre of Finland

Metals Laboratory, P. O. Box 26

SF-02151 Espoo, Finland

*Institute of Physical Chemistry, Russian Academy of Science

Abstract

The effect of different inhibitors on the electric resistance of the passive film on AISI 304 stainless steel in simulated paper mill environment (300 ppm SO_4^{2-} , 300 ppm Cl^- , pH = 5, $T = 55^\circ\text{C}$) was investigated by using a new Contact Electric Resistance (CER) in situ technique at room and elevated temperatures in the potential region from -1.3 to +0.2 V_{SHE} . Thiosulphate was found to decrease the surface film electric resistance by a factor of 10 to 100 at the potential range of operating paper mills. A minimum amount of about 10 mg/l of thiosulphate is needed for this detrimental effect to take place. Among the several inhibitors investigated hydrogen peroxide was found to be very effective in preventing the effect of thiosulphate. A mechanism is proposed for the effect of hydrogen peroxide. Also, a method and a technical arrangement for the prevention of the localized corrosion caused by thiosulphate in actual paper mills is presented.

Introduction

Thiosulphate, a decomposition product of the bleaching agent dithionite, is known to cause pitting of AISI 304 stainless steel in paper mill wet end environment^{1,2,3}. Pitting has been found to occur at all potentials positive to -0.15 V_{SHE} ¹ whereas in other works^{3,4} authors found an upper limit of 0.1 V_{SHE} above which pitting did not occur. The upper limit of potential is attributed to the thiosulphate ceasing to reduct to sulphide on the metal surface. It has been suggested² that formation of sulphide takes place on the nickel rich areas of steel surface. The higher the nickel content in Fe-Cr alloys is, the lower is their resistance to the pitting corrosion in thiosulphate solutions². It has been found⁵ that the addition of several anions, e.g. NO_2^- , HPO_4^{2-} , $\text{B}_4\text{O}_7^{2-}$, CO_3^{2-} , PO_4^{3-} and OH^- in solution containing thiosulphate reduced the anodic peak of the polarisation curve and inhibited stress corrosion cracking of AISI 304 SS. The effect of the above mentioned anions is accounted for changes in the repassivation process and creation of insoluble salts or hydroxides on the surface of the steel.

The present work was undertaken to investigate the effect of thiosulphate on the electric conductivity of the surface films on AISI 304 stainless steel by using the new in situ CER technique⁶ and to investigate the effectiveness of certain inhibitors in preventing the unwanted effects of thiosulphate.

Experimental

The Contact Electric Resistance (CER) method is basically similar to the direct current potential drop (DCPD) technique commonly used to measure crack length but has some important new features. The CER method consists of accurate measurement of the electric

resistance (ER) between two periodically contacted metallic specimens. In the present work these two specimens were the walls of a fatigue crack in a single edge notched plate sample cyclically loaded below the corrosion fatigue crack growth threshold. The samples of commercial grade AISI 304 stainless steel were 200 x 25 x 2 mm (Fig. 1a) with a 60° cut and with an air fatigue crack of 3 - 3.5 mm length. The sample and contacts for measuring ER of the central part of the sample with a crack (points A) were plated with a chemically stable varnish (except the 1 cm² surface area near the fatigue crack - nondashed part of the sample in Fig. 1a), placed into an electrochemical cell and fixed in electrically insulated grips of an Instron 1195 testing machine. During cyclic loading of the sample this machine provides an accuracy of 0,1 % in reproducibility of maximum and minimum loads, which results in the reproducibility of the relative displacement of the cyclically contacting crack walls at the level of 10⁻⁹ m.

A direct current of 10 A was passed through the sample generating a voltage signal depending on the ER of the sample. The ER of the sample during cyclic loading was measured using a double (Thompson) bridge, and was continuously recorded by an X -t-recorder. Since the methods of sample preparation and the details of CER measurement have been described elsewhere⁶, we note that the experimental setup provided the measurement of ER with an accuracy up to 0.02 % and the sensitivity of 10⁻⁹ Ω.

The schematic explanation of the variation of the ER of the sample at cyclic loading is given in Fig. 1b, where points A indicate the points of current supply and connections of the double bridge. If there is no crack in a sample and its ER is equal to R₁, then after growing the fatigue crack at the maximum tension load of the cycle (when the crack is fully open, i.e., its walls do not touch each other) the sample resistance grows by a factor of R₂ due to decrease of its cross-section area. At the minimum load of the cycle (zero or compression) the crack walls will touch each other which is equivalent to shunting the resistance R₂ by the contact resistance R equal to the ER sum of the successive chain: metal-film-electrolyte between the crack walls-film-metal. Thus, at the cyclic loading of a sample with a crack its ER cyclically varies from R₁ + R₂ at the maximum load and the full opening of the crack to R₁ + R₂R/(R₂ + R) at the minimum load. The variation of ER of a sample during each cycle (ΔR) is determined by the equation (1) and the contact ER at the minimum load of the cycle (R) by equation (2):

$$\Delta R = \frac{R_2^2}{(R_2 + R)} \quad (1)$$

$$R = \frac{R_2(R_2 - \Delta R)}{\Delta R} \quad (2)$$

Resistance R₂ is a constant which depends upon the specimen size, fatigue crack length and specific electric resistance of the investigated metal. For any particular specimen the ΔR value depends upon R (eq. 1), i.e. upon the electrolyte composition and the electrochemical potential. ΔR values corresponding to different potentials are continuously measured and recorded, and then used to account R from equation (2).

The experiments were carried out at the temperature 55 °C in normally aerated supporting electrolyte containing 300 mg/l of Cl⁻ and 300 mg/l SO₄²⁻. The solution pH was adjusted

at pH = 5 with sulphuric acid. The potentials were measured against Ag/AgCl-reference electrode and were recounted and reported in this work against SHE.

Experimental Results

Some experimental data and conclusions from the previous works⁶ devoted to CER-method are important for this investigation and have to be shortly listed as following. The contact electric resistance (R) is independent of the ionic electrolyte conductivity, but is defined by electronic conductivity between the crack walls. R is equal to the electric conductivity of the films on the crack walls. R is assumed to be zero at the most complete reduction of the films on the crack walls during cathodic polarization. Any increase in the R obtained by polarization to more positive potentials is due to an increase of the electric resistance of the films on the contacting crack walls. The changes of the cyclic loading frequency (0.04 - 0.4 Hz) and direct current value through the specimens (0.03 - 30 A) have no noticeable effect on the R-potential behaviour, but the changes of minimum and/or maximum loads or stress ratio of the cycling loading do have an effect on this behaviour. For this reason, all the runs in the present work were carried out by constant values of direct current (10 A), frequency (0.2 Hz) and stress ratio (0.10) of cyclic loading.

The dependence of the electric resistance of the surface film on the applied potential (R-E dependence) was obtained as follows. The surface of the sample was reduced for 10 - 30 min in the electrolyte of interest at potential -1.1 V(SHE). The surface film electric resistance at this cathodic potential was taken as a conventional zero. After stabilization at this potential, the potential was increased in steps. Each further potential step was made after a stabilisation of the surface film electric resistance at the previous potential.

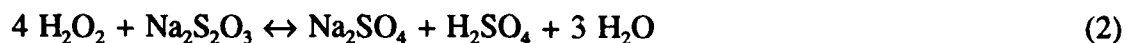
The effect of increasing amounts of thiosulphate on the electric resistance of the surface film of AISI 304 stainless steel is shown in Fig. 2 as a function of the electrochemical potential. The film resistance in supporting electrolyte increases to about $10 \times 10^{-6} \Omega$ when the potential is increased to -0.6 V. Between -0.6 V and -0.4 V the resistance decreases slightly. At -0.35 V the film resistance increases very sharply and continues to increase as the potential is further increased. Additions of thiosulphate are seen to reduce the film resistance at all potentials, this effect being most pronounced at the potentials of operating paper mills. A minimum amount of about 10 mg/l of thiosulphate is needed to have an effect on the surface film resistance at the potential of 0 V (Fig. 3).

Fig. 4 shows the effect of several added anions on the surface film resistance. The effect of 29 mg/l of sulphide is seen to be extremely deleterious in comparison of the effect of 50 mg/l of thiosulphate.

As it is clear from comparison of the data in Figs. 3 and 4, additions up to 300 - 500 mg/l NO_3^- , PO_4^{3-} , MoO_4^{2-} , CO_3^{2-} , anions into supporting electrolyte with 50 mg/l $\text{S}_2\text{O}_3^{2-}$ had no noticeable effect on the film resistivity. These anions are not possible candidates to be the inhibitors for thiosulphate containing solutions. Only NO_2^- anions have some beneficial effect which is probably connected with its competitive adsorption and/or reduction resulting in the increase of the surface pH-values.

As it is shown in Fig. 5, hydrogen peroxide additions sharply increase the electric resistance of the surface films on stainless steel in the thiosulphate containing electrolyte. This shows

that hydrogen peroxide may be used as an effective inhibitor in the paper mill industry. Its inhibition action is apparently based on two main mechanisms:



Owing to the first reaction of the cathodic reduction of hydrogen peroxide, a strong alkalization has to occur on the surface, which promotes the passivation of stainless steel independently of the thiosulphate concentration in the electrolyte. According to the second reaction hydrogen peroxide chemically oxidizes thiosulphate up to less aggressive sulphate anions. Probably this interaction proceeds very slowly at room temperature, but it sharply accelerates even by heating up to 55 °C. The data in Fig. 6 may be considered as an experimental support of this proposition.

At room temperature and at the potential $E = -0.3 \text{ V}$ the cathodic polarization current of stainless steel in the supporting electrolyte containing 0.01 M $\text{Na}_2\text{S}_2\text{O}_3$ is nearly proportional to the hydrogen peroxide concentration. It shows that reaction (2) is too slow to decrease the concentration of hydrogen peroxide participating in reaction (1). At 55 °C increasing of the hydrogen peroxide concentration up to definite limit has no effect on cathodic current. It is necessary to underline that this limit is very close to 0.03 - 0.04 M H_2O_2 , i.e. to the hydrogen peroxide concentration, which is three - four times higher than the thiosulphate concentration in the supporting electrolyte. These amounts are close to the stoichiometric ratio of hydrogen peroxide and thiosulphate (4:1) in the reaction (2). It shows that chemical interaction according to reaction (2) proceeds very fast at the temperature 55 °C and only excess of hydrogen peroxide is able to participate in the cathodic reduction.

Based on these results a simple method was proposed how to automatically control the minimum necessary hydrogen peroxide concentration to inhibit the passivity breakdown of the stainless steel in the presence of thiosulphate during paper mill operation. This method consists of the cathodic current measurements with a special three electrode system inserted e.g. in the pipe-line. If under potentiostatic control (e.g. at the potential -0.3 V) cathodic current would be lower than a definite value (e.g. $i < 0.1 \text{ mA/cm}^2$, see Fig. 6), hydrogen peroxide containing solution has to be pumped into the pipe-line until cathodic current would increase up to a desirable level and then pumping has to be stopped. After some time cathodic current will decrease again owing to possible occasional increasing of the thiosulphate concentration and/or hydrogen peroxide decomposition. At decreasing or increasing of the cathodic current out of the preadjusted limits the commands will be automatically sent to start or to stop the pumping of hydrogen peroxide. It is clear that for realization of this method there is no need to continuously measure the thiosulphate and/or hydrogen peroxide concentrations.

Conclusions

1. The electric resistance of the films on AISI 304 SS in simulated paper mill conditions was measured in situ using a new contact electric resistance method.
2. Thiosulphate was found to decrease the surface film electric resistance by a factor of 10 to 100 at the potential range of operating paper mills.

3. A minimum amount of about 10 mg/l of thiosulphate is needed for this detrimental effect to take place.
4. Hydrogen peroxide was found to be a very effective inhibitor in preventing the effect of thiosulphate.

Acknowledgements

This work has been carried out at Technical Research Centre of Finland (VTT) as part of the Surface Technology Research Program. Additional funding from the Academy of Science in Finland is acknowledged.

References

1. R. C. Newman, H. S. Isaacs and B. Alman, *Corrosion*, 38 5 (1982): p. 261.
2. A. Garner, *Corrosion*, 41 10 (1985): p. 587.
3. R. Roberge, *Corrosion*, 44 5 (1988): p. 274.
4. R. C. Newman, W. P. Wong, H. Ezuber and A. Garner, *Corrosion*, 45 4 (1989): p. 282.
5. R. C. Newman, *Corrosion*, 41 8 (1985): p. 450.
6. V. A. Marichev, *Surface Science*, 250 7 (1991): p. 220.

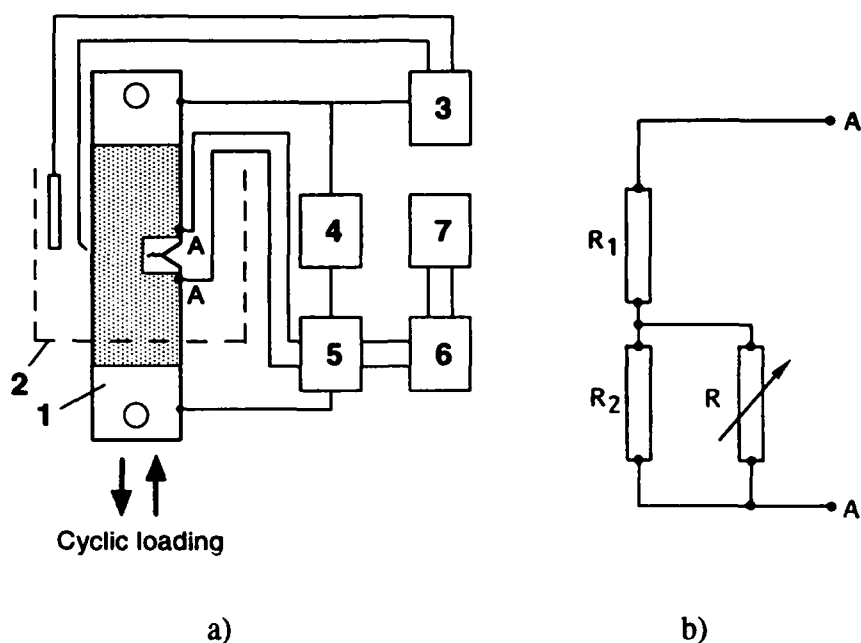


Figure 1. Scheme for measurement of the Contact Electric Resistance (CER) of the sample with a fatigue precrack (a). The electrical analog of the sample (b). (1) Sample, (2) electrochemical cell, (3) potentiostat, (4) direct current source, (5) double bridge, (6) amplifier, (7) recorder.

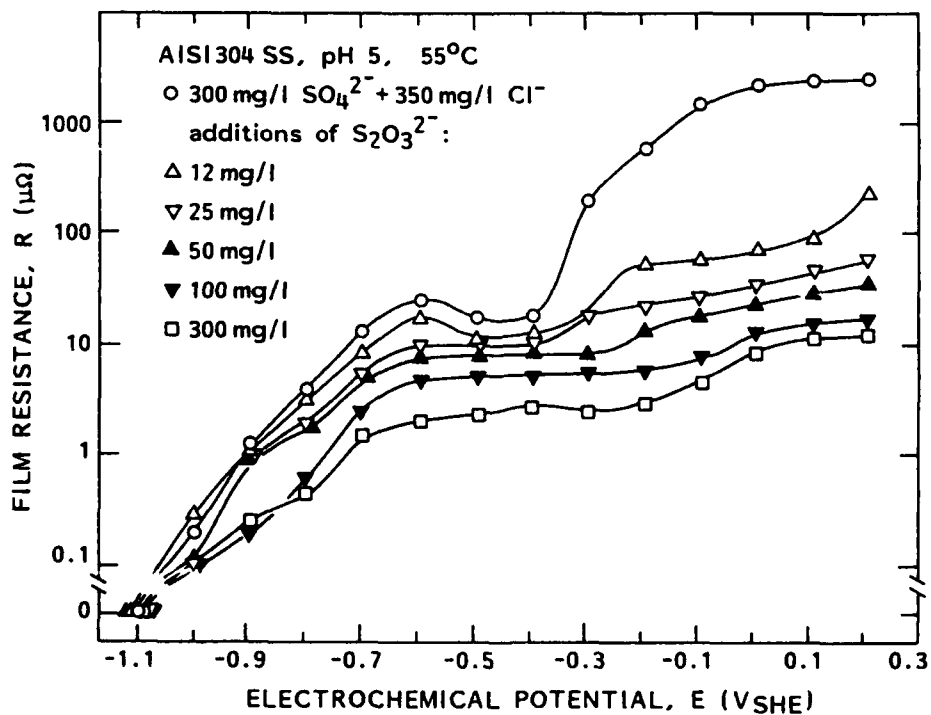


Figure 2. The electric resistance of the films on AISI 304 SS in dependence upon the electrochemical potential and thiosulphate concentration.

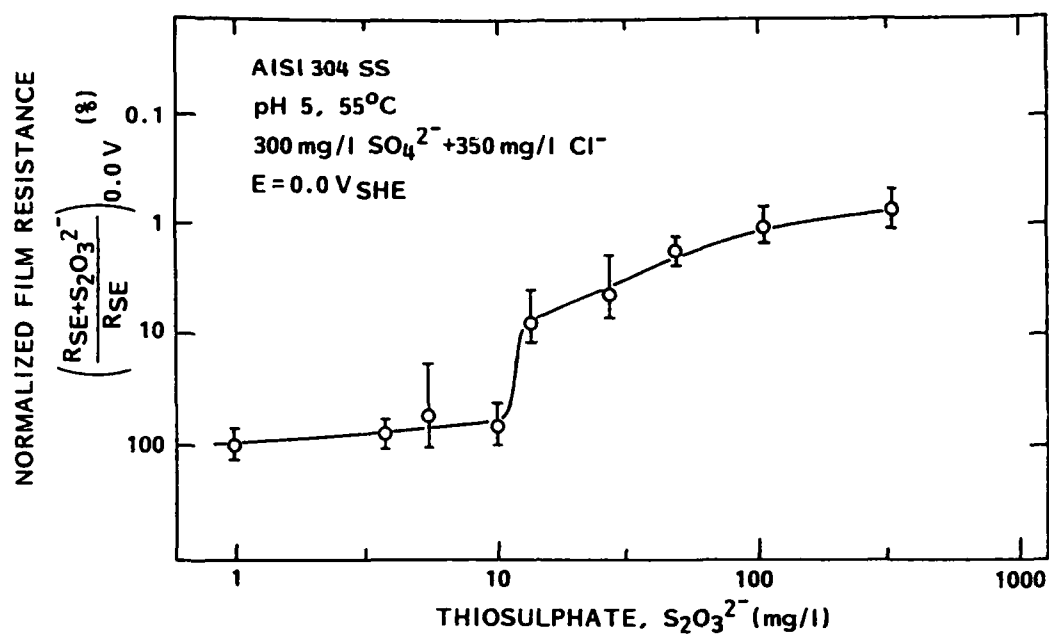


Figure 3. Dependence of the normalized film resistance at the potential $E = 0 \text{ V}_{\text{SHE}}$ upon thiosulphate concentration in the supporting electrolyte.

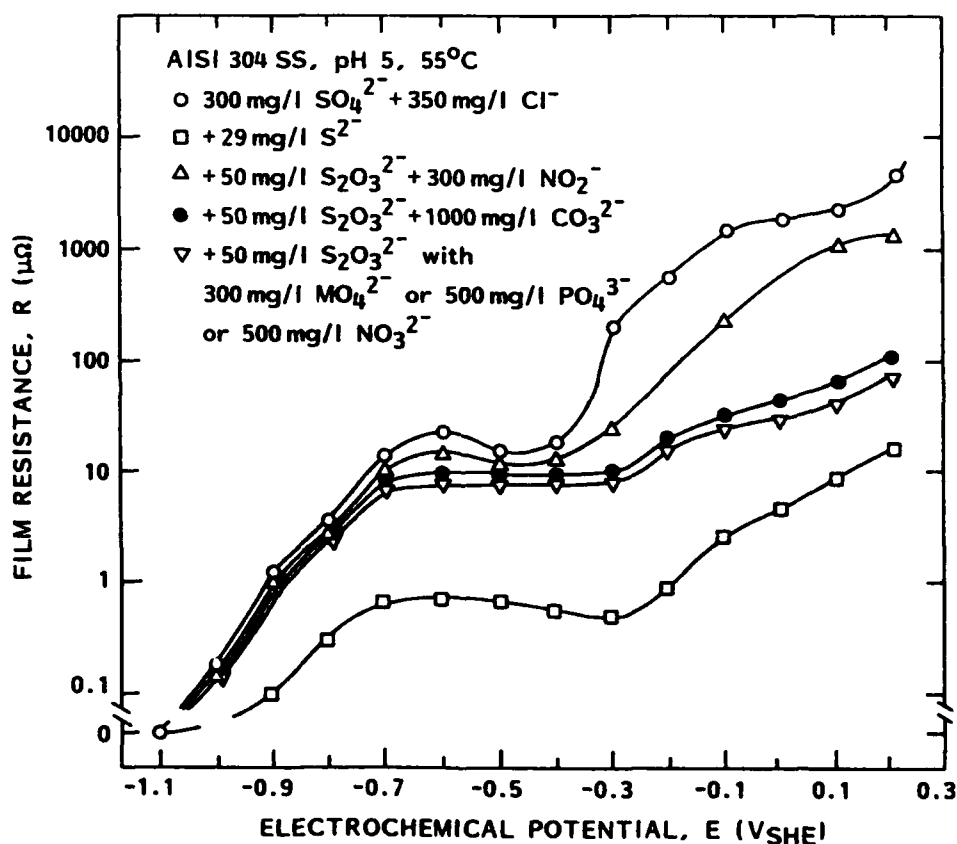


Figure 4. Dependence of the film resistance of AISI 304 SS upon the electrochemical potential and anions composition of the electrolyte.

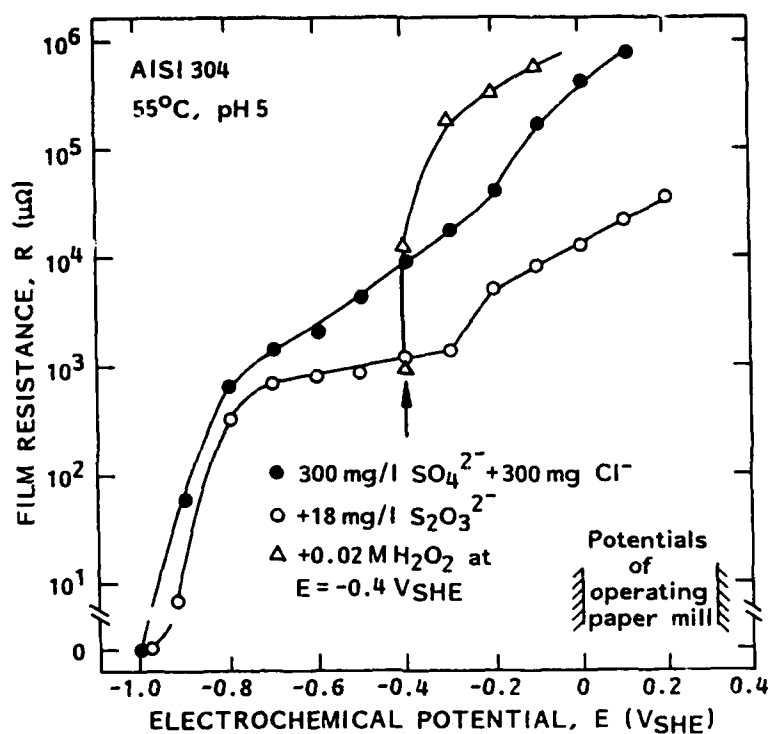


Figure 5. Dependence of the film resistance of AISI 304 SS upon the electrochemical potential, thiosulphate and hydrogen peroxide concentrations. Hydrogen peroxide was added into thiosulphate containing electrolyte at $E = -0.4 V$ (indicated by arrow).

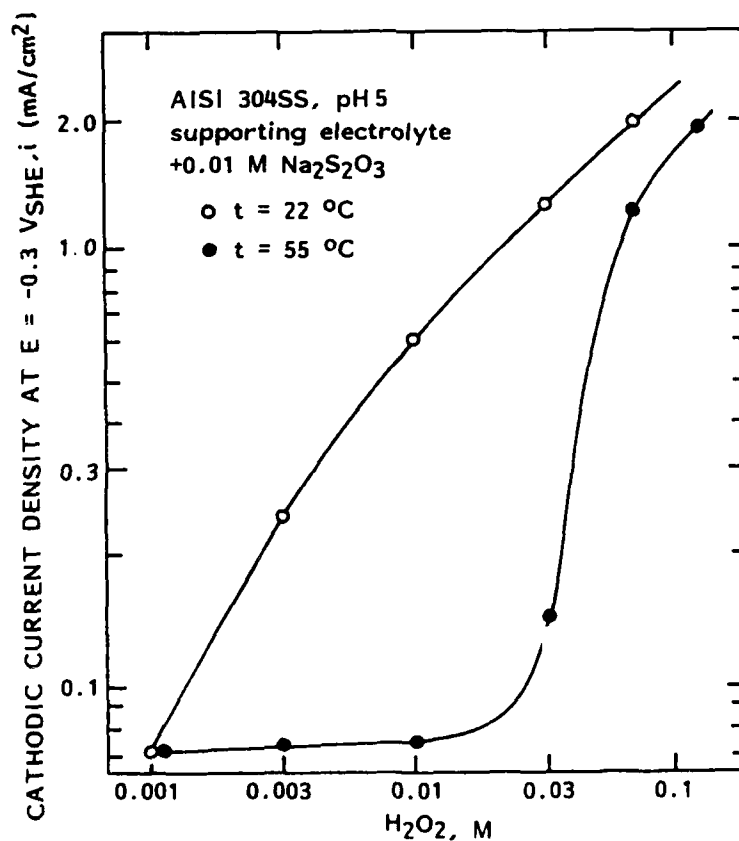


Figure 6. Dependence of the current density during cathodic polarization of AISI 304 SS at $E = -0.3 V_{SHE}$ in the thiosulphate containing electrolyte upon hydrogen peroxide concentration and temperature.

Corrosion of Stainless Steels in Kraft Process Liquors

Anja Klarin and Johan Westermarck
A. Ahlstrom Corporation
Ahlstrom Machinery
Sentnerikuja 2, P.O. Box 5
00441 Helsinki, Finland

Seppo Yläsaari, Jari Aromaa and Olof Forsén
Helsinki University of Technology
Laboratory of Corrosion and Material Chemistry
Vuorimiehentie 2
02150 Espoo, Finland

Abstract

Pulp making technology is continually undergoing process changes. In recent years, the importance of environmental aspects has increased. This has resulted in stricter environmental laws that force pulp mills to adopt processes with reduced environmental impact. Several changes in pulping processes are likely to take place in the near future, in response to environmental and market forces. One way to reduce the environmental impact is to reduce the use of fresh water and thus to recirculate process waters. It is very likely that the recirculation of process waters would result in an enrichment of chemical compounds in process waters. These changes will most probably lead to a situation where the composition of the cooking and washing liquors will change. Naturally it is considered that these changes will most probably have a negative impact on corrosion resistances of the construction materials used today. This will lead to a situation where carbon steel, which is still used in digesters and in vessels close by, does not have inherently a sufficient corrosion resistance any more. This study is mainly focused on stainless steels and their resistance towards pitting corrosion in different kraft liquors. Some experiments were also made to compare the corrosion resistances between carbon steel and stainless steels. The changes in delignification methods concern modifications in the parameters of cooking and/or adding new handling units of the pulp just after the cooking process. This study covers two extra units, i.e. a hot alkali extraction unit and an oxygen delignification unit, added into a continuous cooking line using softwood only. Electrochemical tests were performed with liquors that were taken from the process before and after installing the hot alkali extraction unit and the oxygen delignification reactor. The results indicate that these process changes made the liquors less aggressive.

I. Introduction

Studies concerning the corrosion of carbon steel in kraft pulping liquors have been published by several authors (1-6). The first theories concerning the corrosion of carbon steel in kraft liquors were formed approximately 40 years ago by Ruus and Stockman, and others (7-11). These theories are still applied today to estimate the corrosion rate of carbon steel in kraft liquors.

In recent years, the importance of environmental aspects has increased. This has resulted in stricter environmental laws that force pulp mills to adopt processes with reduced environmental impact. One way to reduce the environmental impact is to reduce the use of fresh water and thus to recirculate process waters. It is very likely that the recirculation of process waters would result in an enrichment of chemical compounds in process waters (12). This enrichment would also effect the composition of the liquors, and the liquors would most probably become more aggressive towards existing construction materials. This would lead to a situation where the corrosion resistance of carbon steels might not be sufficient. The changes in delignification methods concern modifications in the parameters of cooking and/or adding new handling units of the pulp just after the cooking process. This study covers two extra units, i.e. a hot alkali extraction (13,14) unit and an oxygen delignification unit, added into a continuous cooking line using softwood only. Delignification by hot alkali extraction is known to lower lignin contents after cooking and washing at a high pH level at high temperature, without excessive loss of yield. Hot alkali extraction (HAE) prior to oxygen delignification accelerates the lignin removal (13).

Of special interest, when using stainless steels in kraft liquors is their resistance towards localized corrosion. Localized corrosion is one of the most dangerous forms of corrosion. Pitting and crevice corrosion are two common localized corrosion types. Localized corrosion is typical for metals, e.g. stainless steels, where corrosion resistance is based on a protective passive layer. This study is mainly focused on stainless steels and their resistance towards pitting corrosion in different kraft liquors. Some experiments were also made to compare the corrosion resistances between carbon steel and stainless steels.

The electrochemical measurements showed that during the runs of the polarization curves, the reactions taking place in the test solution in order to reach the thermodynamic balance of sulfur-oxygen compounds affected by the voltage, had an effect on the polarization curve itself. Therefore one should be very careful in interpreting this kind of polarization curves. The study on the reactions taking place in the liquors will continue.

II. Experimental

In the hot alkali extraction, oxidized white liquor was used instead of sodium hydroxide. This had as a consequence that both

the potassium/sodium ratio as well as the chloride content increased more than had been the case with pure NaOH.

The corrosivity of the filtrates from the continuous cooking unit and the proceeding pressure diffuser, as well as from the pulp storage tank before and after the HAE unit and the oxygen delignification unit was measured. The filtrates were analyzed at the mill and were tested by laboratory measurements in order to see the corrosivity of these filtrates. The tests carried out in the laboratory were electrochemical in nature. The corrosive components in these filtrates were sulfides, thiosulfates, chlorides, and sulfate anions. The anodic polarization curves measured in these filtrates for three different steel grades were assumed to show the pitting corrosion resistance of these steel grades.

A. Test Materials

The experimental materials were two different types of stainless steels and a carbon steel. The nominal compositions of the test metals, S31603, S31254 and K02502, are given in Table 1. The carbon steel that was tested in this study is a commonly used structure material at Finnish pulp mills.

The stainless steels that were used in this study were austenitic. Nickel, which is needed in a stainless steel to achieve an austenitic structure, has in general a good corrosion resistance in general. Nickel is especially known for its good corrosion resistance in alkaline solutions (15). In fact, the corrosion resistance of stainless steels to sodium hydroxide is roughly in proportion to their nickel content. Both Nickel and Molybdenum are known to increase the pitting resistance of stainless steel alloys.

B. Test Liquors

Most of the experiments to evaluate the corrosion resistances of carbon and stainless steels in cooking and washing liquors have principally been made with artificial liquors. To achieve as reliable results as possible, original liquors were employed in this study. The liquors that were used were taken from both hardwood and softwood lines of a Finnish pulp mill. Altogether, 14 different liquors, from strong black liquors to weak brown stock washing liquors, were used in this study. This study also examines how some specific process changes will influence the chemical compositions and the aggressiveness of the pulping liquors. During the experiment, a hot alkaline extraction unit and an oxygen delignification unit were installed.

Laboratory analyses were performed at the pulp mill to examine the chemical compositions of the test liquors. The Redox potential, pH and temperature of each liquor were measured in connection with the sampling of the liquors. The variations of measured values are given in Table 2.

After sampling, the liquors were immediately transported to the laboratory, where electrochemical tests were performed. The electrochemical tests were made in the Laboratory of Corrosion and Material Chemistry of Helsinki University of Technology. During the transportation, the liquors were stored in heat beds. Temperature changes and long storage times can result in changes of the chemical equilibrium of the liquors. This again would effect the results in the electrochemical tests. The equilibrium between sulfur compounds is known to be sensitive to changes. It is also known that different sulfur compounds have different aggressiveness concerning the corrosion of steels.

C. Laboratory Experiments

The evaluation of the resistance towards pitting corrosion was made by laboratory tests using an electrochemical test method. The electrochemical test method that was employed in this study was the cyclic anodic polarization curve. The tests were carried out at temperatures similar to the ones in the process. All test liquors were stirred well before starting the experiments. The runs were made using an EG&G PARC 273 potentiostat and M352 SoftCorr software. The cell that was used in the test was a so-called Avesta cell, which has been developed to improve reliability of localized corrosion tests by reducing the possibilities to crevice corrosion (16). The cell provides a condition for the working electrode, where the crevice area is continuously flushed with distilled water. A platinum electrode was used as the counter electrode. At high test temperatures the heat distribution in the original cell was insufficient. By circulating the solution with a laboratory pump, a more uniform heat distribution was achieved. Local concentration variations near the specimen were also avoided by circulating the test liquor. Because of the high test temperatures the calomel reference electrode Radiometer K401 was placed in a reservoir which was maintained at room temperature. The reservoir was connected to the test cell with a salt bridge and a Luggin capillary. The test cell is shown in Figure 1.

Prior to electrochemical experiments, the test materials were ground to a surface finish of 800 mesh. After the desired surface finish was achieved, the test metals were pickled. The stainless steels were cleaned in a solution containing 15% nitric acid for 20 minutes and the carbon steel in a 10% sulfuric acid solution for 10 minutes. After cleaning, the samples were rinsed in distilled water and immediately attached to the test cell. Before starting the experiment, the test metals remained unpolarized until the change of the free corrosion potential was less than 0.2 mV/s. The cyclic anodic polarization curves were measured using a scanning rate 10 mV/min and the threshold current density for reverse scanning was set to 5 mA/cm². These values are given in the standard practice for cyclic polarization measurement, ASTM G61 (17). The size of the exposed surface was 0.95 cm². After the experiments, the samples were investigated visually in order to detect pits and other anomalies caused by the reactions that might have taken place on the exposed surface.

III. Results and Discussion

The aim of this study was to determine the corrosion resistance towards pitting. The results can be obtained in two different ways. One method is to examine the obtained polarization curve and the other method is to examine the exposed surface visually after the electrochemical test. When examining the polarization curve, the risk for localized corrosion can be seen in the hysteresis loop. In case the material is exposed to localized corrosion during an experiment, a hysteresis loop will be formed in the cyclic polarization curve. The magnitude of this loop will indicate the resistance of the test material towards pitting corrosion. The other corrosion type that also forms a hysteresis loop is crevice corrosion. When testing the pitting resistance with electrochemical test methods, one has to be sure that the possibility for crevice corrosion is eliminated. To eliminate the crevice corrosion in our experiments, a so-called Avesta cell was applied in this study. The elimination of crevice corrosion is important, as it would be very difficult to analyze the polarization curves if both corrosion forms would emerge during a test.

The other way to analyze the results in electrochemical tests is to examine visually the exposed surfaces. To achieve as reliable results as possible it is necessary to combine the polarization curve analysis with a visual analysis. For instance, the polarization curves obtained for some liquors are not reliable because of certain oxidation reactions between sulfur compounds that occur in kraft liquors when changing the potential. This will result in a polarization curve that shows the oxidation reactions of the liquor, instead of the metal's passivation behaviour. In cases like these it is important to analyze the surface visually. However, if the sweep rate is too fast, it could be possible that pits don't have enough time to emerge even if the metal is susceptible to pitting corrosion.

A. Stainless Steels

Two stainless steel types are focused in this study. Cyclic anodic polarization curves were obtained for both the steel types in each test liquor. By comparing the polarization curves of the two metals, we were able to see that there were no distinguishable differences between the polarization behaviour of the test metals in any of the tested liquors. Figures 2 and 3 present the polarization curves of the two steels in a weak brown washing liquor. By examining the figures, it can be seen that there is no noticeable difference concerning passivation between these two steels. Thus, for a more detailed examination of the polarization curves we focus only on one of the steels, i.e. S31603.

By analyzing the obtained polarization curves and exposed surfaces, we could conclude that these two stainless steels were resistant towards pitting. No results indicated that these two metals were susceptible to pitting corrosion in any of the 14 test liquors.

B. Carbon Steel

Polarization curves for the carbon steel, K02502, were also obtained in two test liquors. The two liquors that were used in the carbon steel experiments were taken from the pressure diffuser filtrate and the diffuser filtrate from the continuous digester line. This line uses softwood as raw material. The cyclic polarization curves for the carbon steel reveal that significant general corrosion took place during the experiment and that the carbon steel was susceptible to pitting corrosion in both test liquors. The cyclic anodic polarization curve for the carbon steel in diffuser filtrate liquor is shown in Figure 4. The small loop indicates that the carbon steel might be susceptible to pitting corrosion. This was confirmed when small pits were detected on the surface of the test metal, when it was examined visually after the experiment. In the second experiment, the carbon steel's passivation behaviour was examined when exposing it to pressure diffuser filtrate liquor. The cyclic polarization curve for this experiment is shown in Figure 5. This polarization curve has a large hysteresis loop, which indicates pitting. After the experiment, the exposed surface was examined and one could notice that part of the surface had been covered with pulp deposits. This part was severely corroded, which explains the large hysteresis loop in the curve. The clean part had also been attacked by corrosion but not as severely as the covered part. Pitting corrosion was detected on the clean part of the surface.

C. Process Changes

As mentioned earlier, some process changes took place during the study. A hot alkali extraction unit and an oxygen delignification unit were installed into the continuous softwood line. The polarization curves of the stainless steel for the pressure diffuser filtrate and the diffuser filtrate, before and after the installation are shown in Figures 6-9. The curves reveal that the equilibrium potentials for the steel in both liquors have moved somewhat in the oxidizing (i.e. more noble) direction. The open circuit and reversible potentials were approx. 200 and 350 mV more anodic for the test material in both liquors after the installation. The polarization curves also reveal that the test metal's corrosion resistance has improved. Tables 3 and 4 give the liquor compositions before and after the installation. The decrease of total sulfur content might be one reason for the improvement in corrosion resistance.

IV. Conclusions

The aim of this study was to analyze the aggressiveness of some common steels in different brown stock washing liquors. Several changes in pulping processes are likely to take place in the near future, in response to environmental and market forces. Significant changes will occur in the chemical recovery processes, too. These changes will most probably lead to a situation where the composition of the cooking and washing liquors will change. Naturally it is considered that these

changes will most probably have a negative impact on corrosion resistances of the construction materials used today. This will lead to a situation where carbon steel, which is still used in digesters and in vessels close by, does not have inherently a sufficient corrosion resistance any more.

In this paper, the effect of a hot alkali extraction and an oxygen delignification towards stainless steels was examined. Electrochemical tests were performed with liquors that were taken from the process before and after installing the hot alkali extraction unit and the oxygen delignification reactor. The results indicate that these process changes made the liquors less aggressive.

When comparing the cyclic anodic polarization curves of the two stainless steels in the 14 different liquors that were tested, it could be noticed that their corrosion resistances did not differ noticeably. All tests were performed in liquors that had been taken from a real kraft pulping process. Both steels showed very good pitting resistance in all test liquors. Electrochemical experiments for carbon steel were performed in two of the 14 test liquors. In both experiments, the results indicated that the carbon steel is susceptible to corrosion. The results also indicated that if the carbon steel has pulp deposits on its surface, a severe corrosion will take place beneath these deposits.

Electrochemical methods are often employed to estimate the corrosion behaviour of metals in cooking and washing liquors. To get as reliable results as possible, it is important to analyze the results, not only by examining the polarization curve, but also to examine the exposed surfaces visually. This is necessary because in some liquors the potential change will lead to some oxidation reactions between sulfur compounds, which again will result in unreliable polarization curves. This means that sulfur compounds are in a dynamic state if the temperature and/or the potential is changed.

References

1. D.A. Wensley, R.S. Charlton, Corrosion, 36 8 (1980): p. 385.
2. D.A. Wensley, "Corrosion Studies in Kraft Liquor Tankage", 1986 Corrosion Symposium, p. 15.
3. P-E. Ahlers, "Polysulphide in Kraft Cooking and Its Effect on Corrosion of Carbon Steel". 4th International Symposium on Corrosion in the Pulp and Paper Industry (1983): p. 53.
4. W.A. Mueller, "Corrosion Rates of Carbon Steel Tubes in Kraft Liquors With and Without Anodic or Cathodic Protection", 2nd International Seminar on Pulp and Paper Industry Corrosion Problems (1977): p. 140.

5. D.C. Bennett, I.J. Magar, "Carbon Steel Corrosion in Brown Stock and Post-Oxygen Washer Environments". 7th International Symposium on Corrosion in the Pulp & Paper Industry (1992): p. 111.
6. S. Ström, "Corrosion of Carbon Steels and Stainless Steels in Sulphate Black and Green Liquors". 7th International Symposium on Corrosion in the Pulp & Paper Industry (1992): p. 105.
7. L. Ruus, L. Stockman, Svenska Papperstidning, 22 (1953): p. 857.
8. L. Stockman, Svenska Papperstidning, 13 (1960): p.425.
9. B. Haegland, B. Roald, Norsk Skogsindustri, 9 10 (1955): p. 351.
10. P. Landmark, B. Roald, Norsk Skogsindustri, 15 8 (1961): p. 342.
11. W.P. Banks, M. Hutchison, R.M. Hurd, Tappi 50 2 (1967): p. 49.
12. S. Clarke, D. Singbeil, "Corrosion Phenomena Associated with Operation of Kraft Mills under Effluent Recycle or Closed-Cycle Conditions". 7th International Symposium on Corrosion in the Pulp & Paper Industry (1992): p. 11.
13. Pat. U.S. 4971 658. Method of Intensifying the Washing of Fiber Suspension, A. Ahlstrom Corp., Finland. (K. Henricson, O. Pikka, A. Vilpponen, N-E. Virkola). App. 363153, 1989-06-08. Publ. 1990-11-20. 8 p.
14. A. Vilpponen, How to reduce the lignin content of sulfate pulp with a hot alkali washing (in Finnish). PhD thesis, Helsinki University of Technology, Department of Forest Products. Espoo 1991. 103 p.
15. M.G. Fontana, Corrosion Engineering, (New York, USA: McGraw-Hill, 1986), p. 369.
16. R. Qvarfort, E. Alfonsson, "An Improved Cell for Electrochemical Pitting Corrosion Testing". 11th Skandinavian Corrosion Congress (1989), paper no. F-79.
17. ASTM G 61-86. Standard Test Method for Conducting Cyclic Potentiodynamic Polarization Measurements for Localized Corrosion Susceptibility of Iron-, Nickel- or Cobalt-based Alloys, (American Society of Testing and Materials, 1989), p. 340
18. C.W. Wegst, Stahlschlüssel, (Marbach, Germany: Verlag Stahlschlüssel Wegst, 1989), p. 175 & 374.

Table 1. Nominal compositions of the test materials in % by weight (18).

Material	C %	Si %	Mn %	Cr %	Mo %	Ni %
UNS S31603	0.03 max	1.00 max	2.00 max	16.0- 18.0	2.0 - 3.0	10.0- 14.0
UNS S31254	0.02 max	0.80 max	1.00 max	19.5- 20.5	6.0 - 6.5	17.5- 18.5
UNS K02502	0.25 max	-	0.90 max	-	-	-

Table 2. The variation of measured values.

Analysis	Variaton of Values
pH	9.2 - 11.9
Redox potential (SCE)	-704 - -130
Temperature (°C)	73 - 90
Na g/l	3.90 - 32.10
K g/l	0.09 - 2.04
S ²⁻ mg/l	0.31 - 3294
tot S g/l	0.45 - 12.00
SO ₄ ²⁻ g/l	0.37 - 5.97
S ₂ O ₃ ²⁻ mg/l	n.d. - 9498
Cl ⁻ mg/l	56 - 439
HCO ₃ ⁻ g/l	1.9 - 70.7
SO ₃ ²⁻ mg/l	0 - 40

(n.d. = not detectable)

Table 3. Chemical compositions of the pressure diffuser liquors before and after installing the hot alkaline extraction unit and oxygen delignification unit.

Pressure Diffuser		Before	After
Na	g/l	6.40	6.80
K	g/l	0.38	0.53
tot.S	g/l	8.00	4.60
S ²⁻	mg/l	736	1124
SO ₄ ²⁻	g/l	1.36	2.67
S ₂ O ₃ ²⁻	mg/l	581	153
Cl ⁻	mg/l	139	163

Table 4. Chemical compositions of the diffuser liquors before and after installing the hot alkali extraction unit and oxygen delignification unit.

Diffuser		Before	After
Na	g/l	3.90	7.20
K	g/l	0.20	0.54
tot.S	g/l	3.36	5.00
S ²⁻	mg/l	288	32
SO ₄ ²⁻	g/l	0.89	2.80
S ₂ O ₃ ²⁻	mg/l	113	170
Cl ⁻	mg/l	61	166

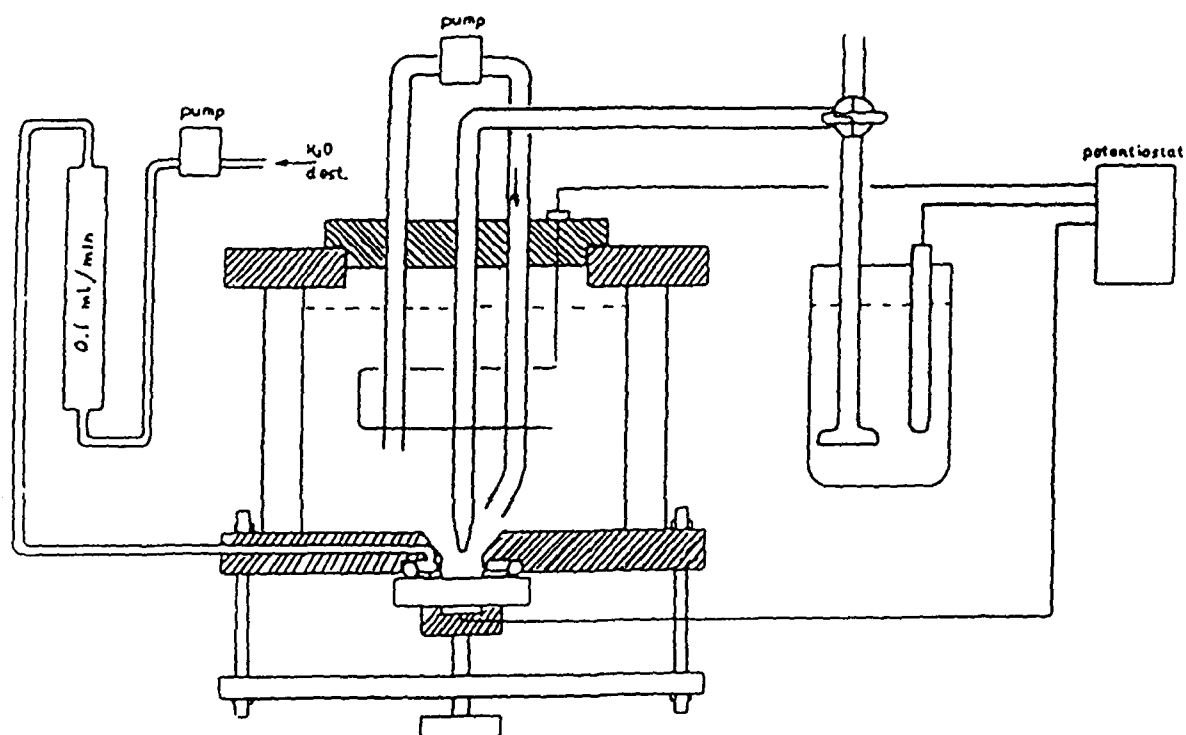


Figure 1. A draft of the test cell.

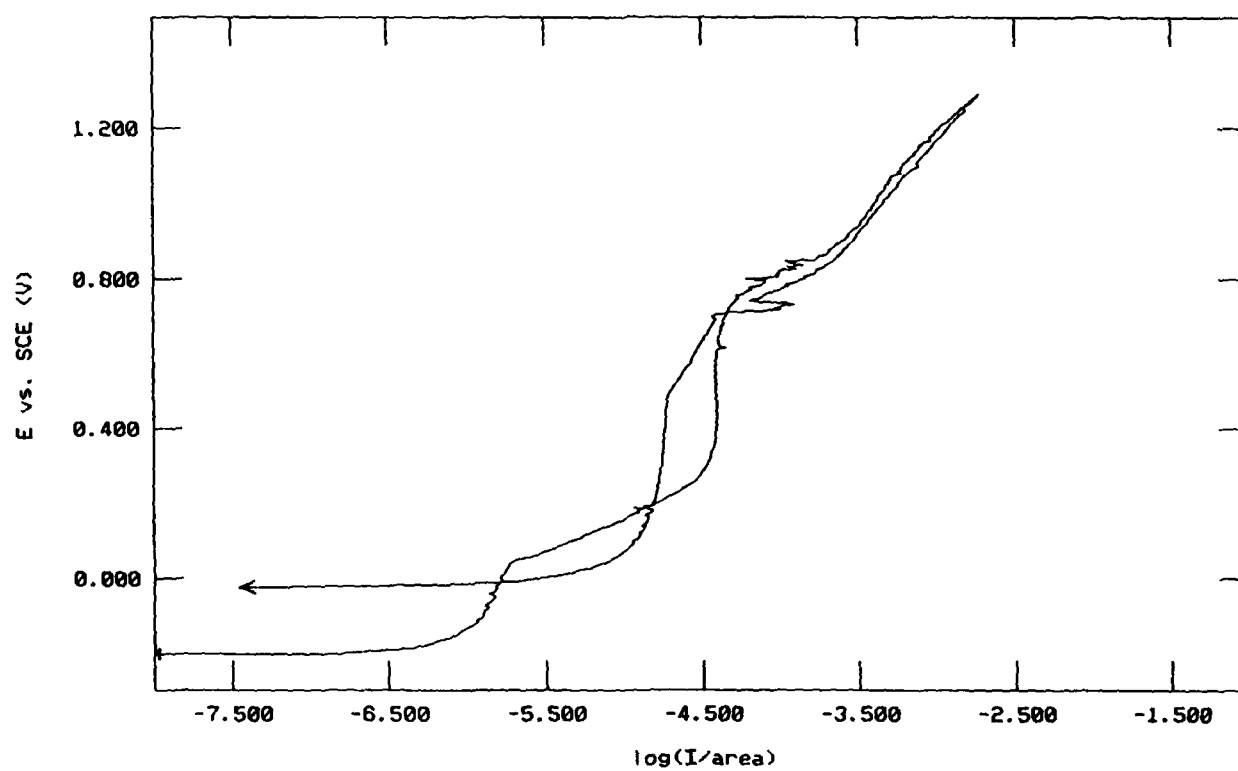


Figure 2. The cyclic anodic polarization curve of S31603 in a weak washing liquor at 90°C.

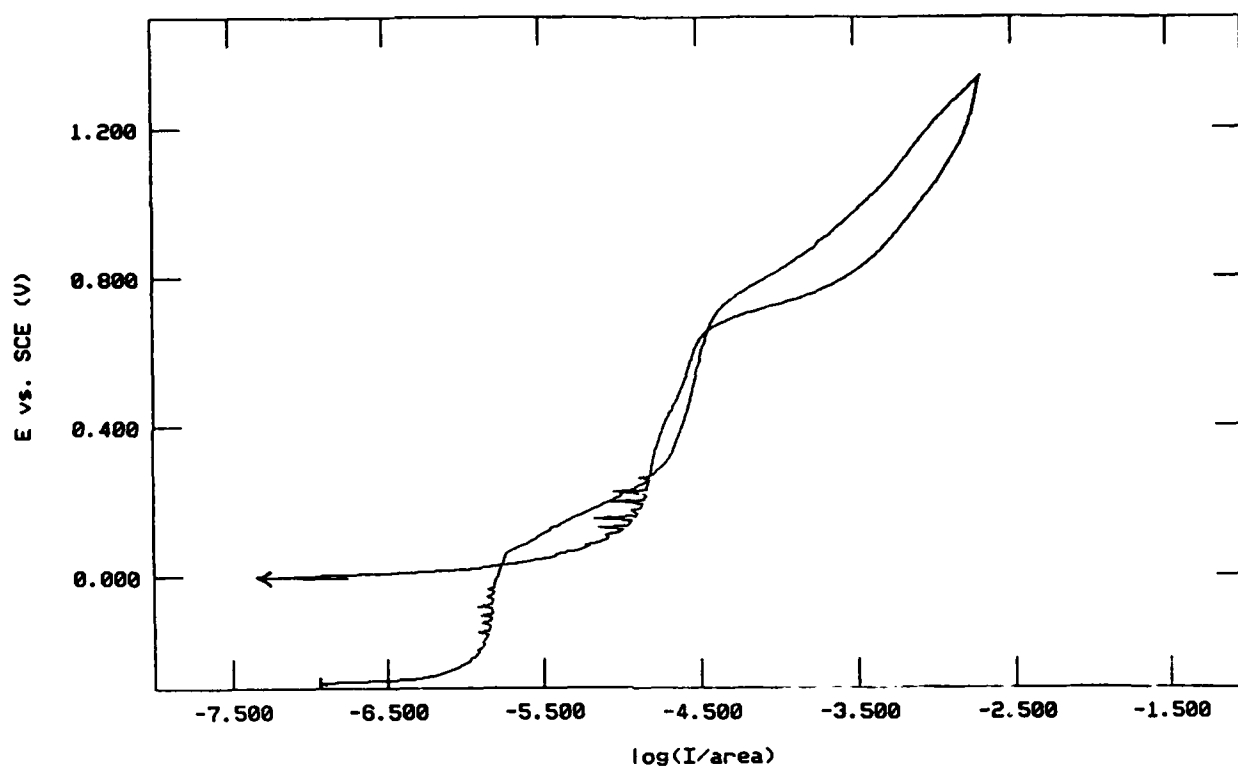


Figure 3. The cyclic anodic polarization curve of S31254 in a weak washing liquor at 90°C.

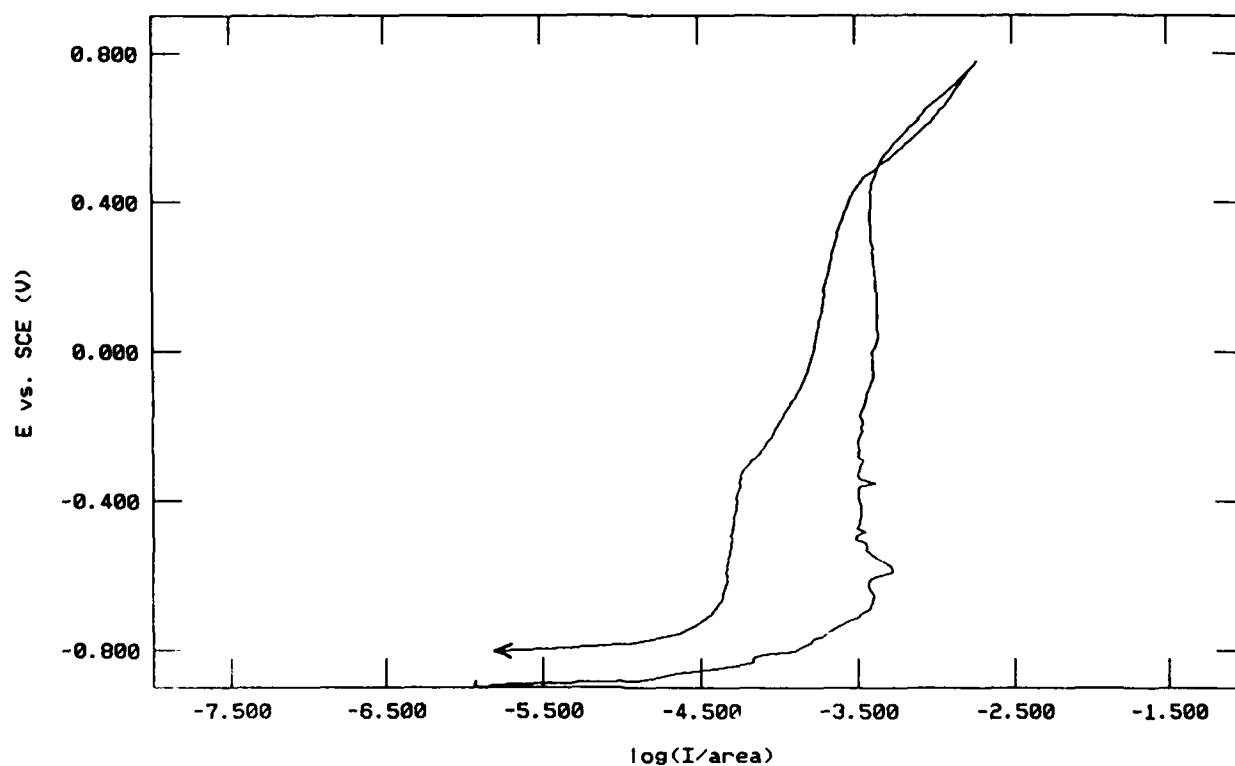


Figure 4. The cyclic anodic polarization curve of K02502 in diffuser filtrate at 85°C.

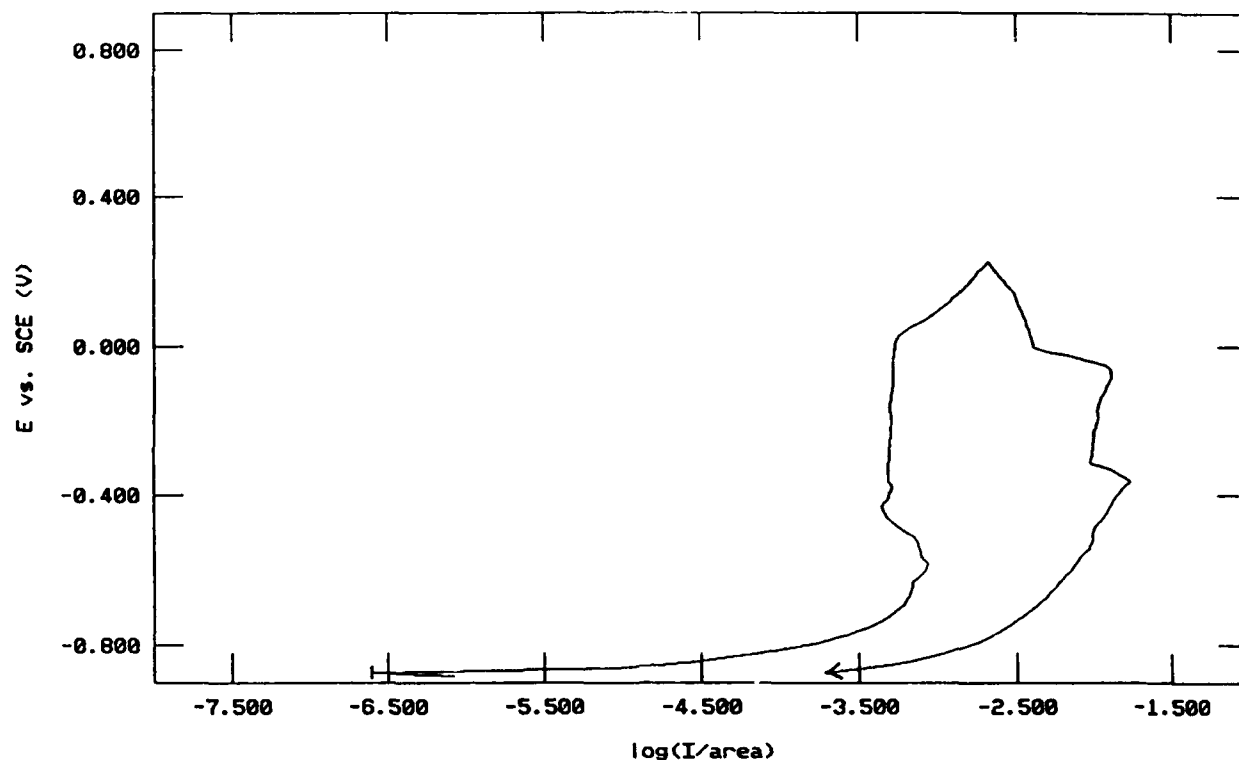


Figure 5. The cyclic anodic polarization curve of K02502 in pressure diffuser filtrate at 90°C.

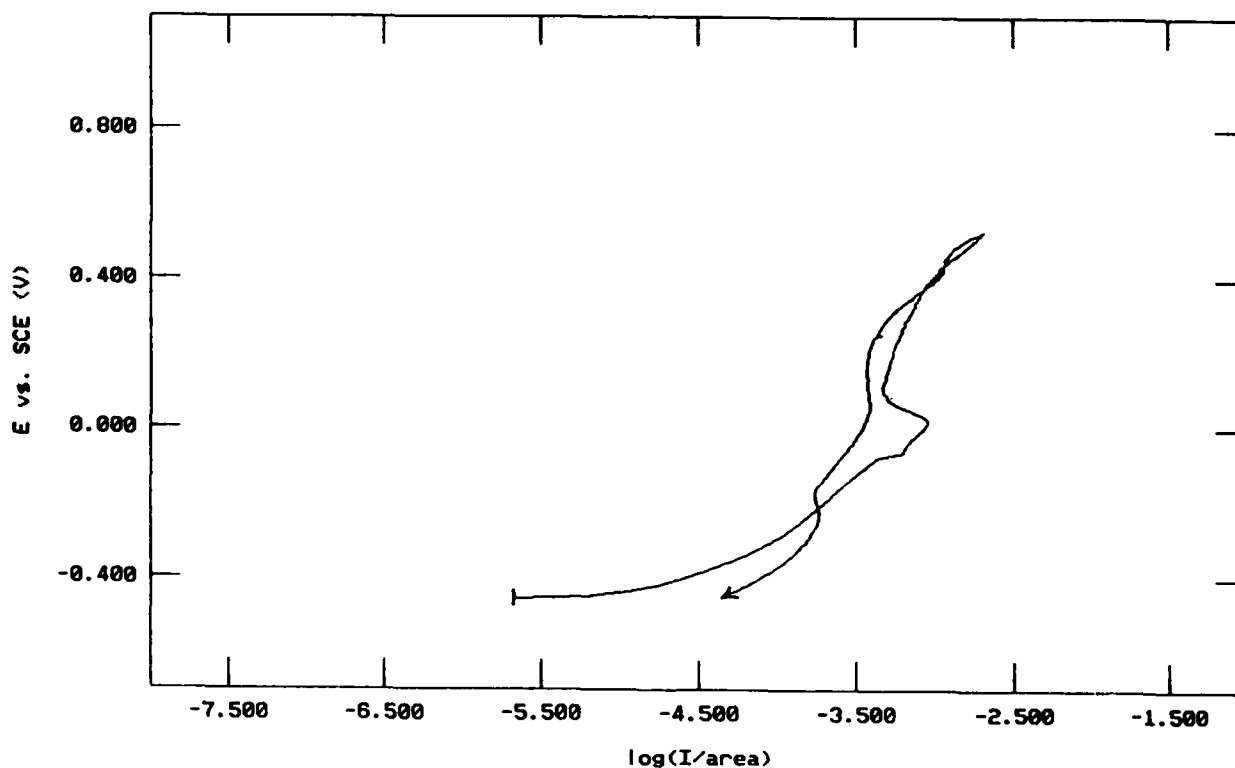


Figure 6. The cyclic anodic polarization curve of S31603 in pressure diffuser filtrate before installing the hot alkali extraction unit and the oxygen delignification unit (90°C).

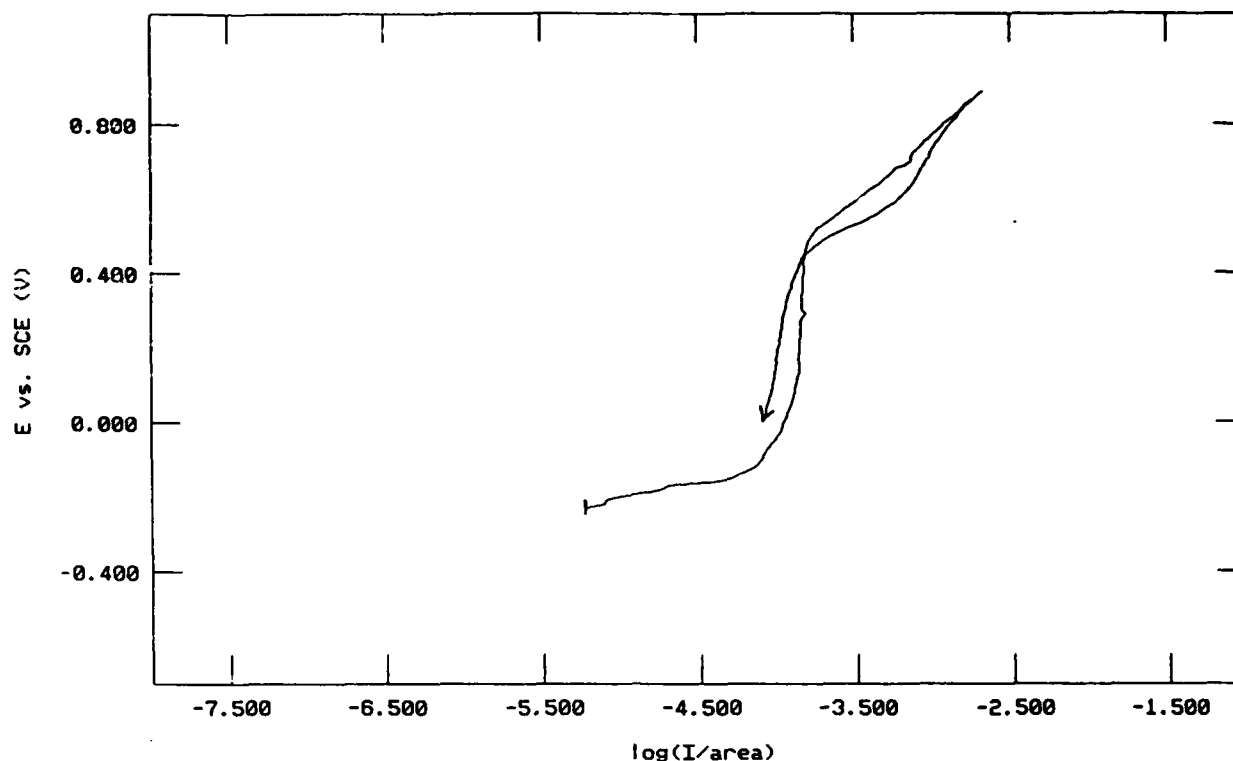


Figure 7. The cyclic anodic polarization curve of S31603 in pressure diffuser filtrate after installing the hot alkali extraction unit and the oxygen delignification unit (90°C).

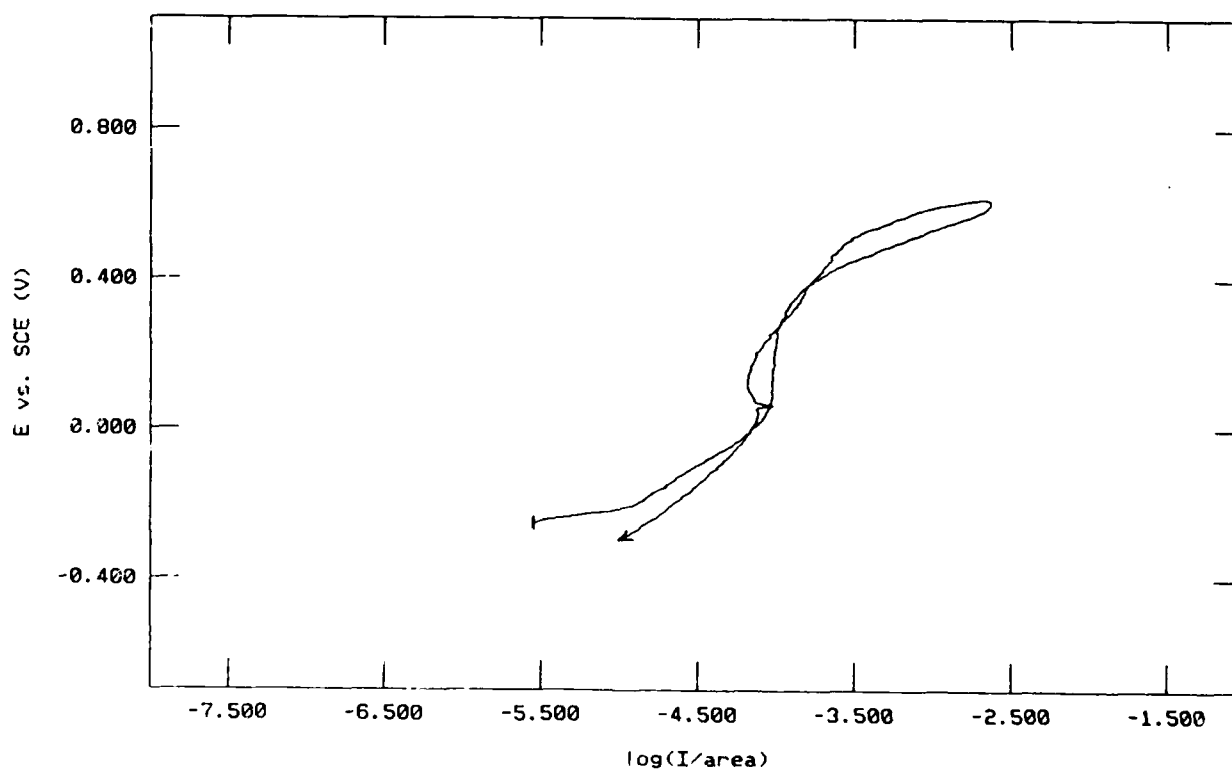


Figure 8. The cyclic anodic polarization curve of S31603 in diffuser filtrate before installing the hot alkali extraction unit and the oxygen delignification unit (85°C).

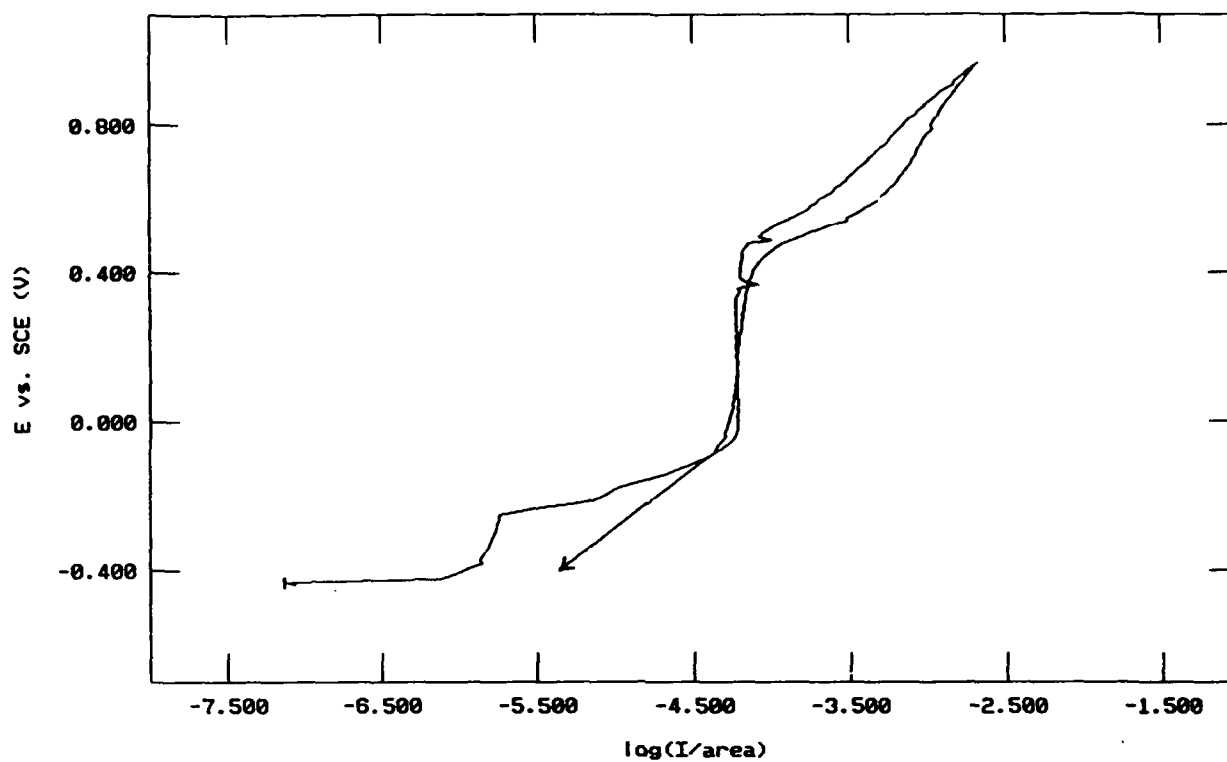


Figure 9. The cyclic anodic polarization curve of S31603 in diffuser filtrate after installing the hot alkali extraction unit and the oxygen delignification unit (85°C).

The Electrochemical Protection of Nickel in an NaOH + NaCl Solution

R. Juchniewicz
Technical University of Gdańsk
Dept. of Anticorrosion Technol.
ul. Majakowskiego 11/12
Gdańsk, Poland

W. Sokółski
Technical University of Gdańsk
Dept. of Anticorrosion Technol.
ul. Majakowskiego 11/12
Gdańsk, Poland

J. Walaszkowski
Technical University of Gdańsk
Dept. of Anticorrosion Technol.
ul. Majakowskiego 11/12
Gdańsk, Poland

P. Domżałicki
Technical University of Gdańsk
Dept. of Anticorrosion Technol.
ul. Majakowskiego 11/12
Gdańsk, Poland

B. Pierożyński
Technical University of Gdańsk
Dept. of Anticorrosion Technol.
ul. Majakowskiego 11/12
Gdańsk, Poland

Abstract

Nickel 200 is generally applied as a construction material of evaporators used during the production of sodium hydroxide. In many cases accelerated corrosion of evaporator pipes is observed. The corrosion of nickel 200 depends on many factors. The concentration of oxidizers in the concentrated solution is one of the basic factors. It was assumed that an electroless nickel Ni-P coating on nickel 200 could be one of the methods of anticorrosion protection. Solutions, similar in contents to the solution concentrated in evaporators, were used, with a variable oxidizer (sodium chlorate) concentration. The concentration of NaClO₃ has been study on the electrochemical protection of Ni 200. The corrosion current densities of electroless nickel and nickel 200 have been determined. The conditions of electrochemical protection of Ni 200 have been described.

Key terms: nickel evaporators, electroless nickel, galvanic cells, electrochemical protection.

Introduction

Nickel and its alloys are generally used in the chemical industry in view of their high corrosion resistance. One of the alloys – nickel 200 is used as a construction material during the production of sodium hydroxide, in particular for the construction of evaporators, in which extreme temperature and pressure conditions are maintained¹⁻³. In many cases significant corrosion of evaporators is observed, mainly on the internal pipe surfaces of the exchanger, in which the NaOH solution, obtained in the diaphragm electrolysis of sodium chloride, undergoes concentration. The corrosion devastation is frequently local in character. In one of the Polish factories producing sodium hydroxide by the above mentioned method, an average corrosion rate of pipes equal to 0.35 mm/year was noted. The pipe thickness, originally equal to 2.1 mm, decreased in some cases to 1.3 mm after two years of operation.

A number of factors affects the corrosion of nickel evaporators. The most important are: the temperature of the solution and the concentration of the concentrated hydroxide, the contents of oxidizing species in solution (mainly sodium hypochlorite and chlorate), oxygen contents and the turbulent flow of the solution through the evaporator pipes¹⁻⁵. Up till now, the deciding factor affecting the corrosion of nickel apparatus has not been determined. The analysis of the results of most papers has pointed to an essential role of the presence of oxidizing compounds in the concentrated solution. Sodium chlorate, formed during electrolysis, is partially degraded with the evolution of oxygen *in statu nascendi*, which is capable of oxidizing the passive layer to the nonstoichiometric oxide $\text{NiO}_{1.8}$. This oxide does not exhibit good adhesive properties and is washed out by the flowing NaCl suspension in the soda lye⁶. Counteraction to the formation of some amounts of oxidizing compounds in the catholyte of the electrolyzer is frequently very difficult.

During investigations on the possibility of decreasing the excessive corrosion rate of the exchanger pipes, we noticed that the application of an electroless nickel protective layer would be one of the possible solutions.

Electroless nickel coatings are widely used because of their quality and advantages: high resistance to corrosion, high resistance to abrasion, the possibility of producing even layers. Good protective properties are demonstrated by coatings exceeding 20 μm and with a maximum 11–13% phosphorus content⁷.

The determination of the electrochemical character of the Ni–P coating in relation to nickel 200, as well as the comparison of the corrosion rate of both materials and the investigation of the Ni–P/nickel 200 cells were the aim of this work.

Experimental

I. Electrodes

Ni 200 electrodes have been used in the form of plates (dimensions 80*12*1 mm, area 22 cm^2). Some of the plates have been covered with an Ni–P coating. Before coating, the electrodes were prepared by: treatment with abrasive paper, washing with water, pickling in 30% nitric acid (30°C), activation in a 10% HCl + 10% H_2SO_4 solution and rinsing in water. Ni–P coatings have been obtained from a bath, which contained, apart from the main components: sodium sulphate and sodium hypophosphite, also thiourea, sodium acetate, lactic acid and propionic acid^{8,9}. The temperature of the bath was equal to 85–90°C and its pH 4.3–4.8. The thickness of the obtained coatings was in the 60–70 μm range. X-Ray analysis has

shown that the Ni-P coatings contained 11–13% of phosphorus.

II. Solutions

Investigations have been carried out in solutions similar in contents to the solutions concentrated in the evaporator. A 50% NaOH and 10% NaCl solution without sodium chlorate has been used as well as solutions with the same concentrations containing 0.3, 0.6 or 1.0% of sodium chlorate. The temperature of the solution was equal to 145–150°C and was similar to conditions in the evaporator.

III. The measurement technique

DC electrochemical measurements have been carried out, including the determination of the corrosion potentials, potentiodynamic polarization curves and the registration of currents in Ni 200/Ni-P cell. The Corrosion Measurement System CMS 100 for DC measurements from Gamry Instruments was used. It functions as a potentiostat, galvanostat and zeroammeter, controlled by a computer. The enclosed software allows the determination of, amongst others, the corrosion currents and potentials, the instantaneous electrode corrosion rate and the Tafel constants for the anodic and cathodic process. Potential measurements were carried out with a calomel electrode (SCE) with an appropriate salt-bridge.

Results and Discussion

Polarization curves for Ni 200 and Ni-P, respectively, exposed to NaOH + NaCl environments with various amounts of oxidizer have been presented in Figures 1 and 2. In Table 1 the corrosion potentials (E_{corr}) and the corrosion rates (i_{corr}), determined for each electrode, have been presented. In all cases the electroless nickel coating was anodic to nickel 200, while the corrosion rate of the nickel coating exceeds the Ni 200 corrosion rate. For Ni 200 a tendency is observed of an increase of the corrosion rate with the increase of the oxidizer concentration in the solution. In the case of Ni-P coating, after a certain concentration of NaClO₃ is exceeded, a decrease of the corrosion rate to a quantity characteristic for nickel 200 is observed. This is probably caused by passivation of the coating surface. During exposition an increased passivation tendency of the Ni-P coating is observed, especially in solutions with higher sodium chlorate solutions. The electrodes were covered with black oxides. The surfaces of Ni 200 electrodes practically did not change.

Taking into account the observed differences in the electrochemical properties of both types of electrodes, the electrodes were coupled to form a cell in order to determine the galvanic currents. The changes of currents in Ni 200/Ni-P cells, investigated in each solution, have been presented in Figure 3.

In a solution with no oxidizer and a solution with a moderate oxidizer concentration the current flow ensures cathodic polarization of nickel 200. In these conditions the protecting action of the Ni-P coating is maintained during the whole investigation cycle lasting 30 hours. The presence of the oxidizer causes a significant increase of the polarization current. The positively anodic character of the coating is sustained for over 10 hours of exposition in a solution containing 0.6% of sodium chlorate. After a longer time (15 hours), a tendency is observed of pole reversal in the system. In the case of the solution with the highest concentration of the oxidizer (curve 4), this phenomenon occurs after approximately 2 hours.

The Ni-P coating, in comparison to the Ni 200 alloy, exhibits an increasing tendency to undergo passivation in the applied solutions, especially at higher oxidizer concentrations. As

the result, a decrease of the corrosion rate of this material is observed. At the same time one may conclude that the increased passivation of the coatings in solutions with high oxidizer concentrations favours the effect of pole reversal of the system. On the other hand, one should keep in mind that in industrial conditions the coating passivation could be hindered by the erosive interaction of the flowing sodium chloride suspension. As the result, constant renewal of the coating surface will proceed, favouring the maintenance of protecting properties.

During a correct electrolysis process the contents of oxidizers should be minimum and not exceed 0.3%. In these conditions the Ni-P coating will be anodic and ensure the electrochemical protection of Ni 200.

Summary

The nickel 200 alloy is resistant to corrosion in an NaOH environment due to passivation abilities. Excessive amounts of oxidizers, mainly sodium chlorate, cause a change of the corrosion potentials in the direction characteristic for the active state. As the result, the passive layers are much thinner and do not exhibit the previous protective properties.

The carried out investigations have shown that the electroless nickel coatings are anodic to nickel 200 in concentrated sodium lye solutions. The coating maintains its anodic character in low sodium chlorate concentration solutions. The obtained results of laboratory investigations are promising, they should be carried out in a larger scale and in industrial conditions as they have shown that the electroless nickel coating on a Ni 200 base may extend the lifetime of elements from this alloy, and in the case of breaks in the coating it will ensure the electrochemical protection of the exposed base.

References

1. Metals Handbook, 9th edition, vol. 13, ASM International, Ohio 1987, p. 641.
2. Inco Alloys International Catalogue, Serving the Chemical Processing and Related Industries, IAI-10/3M/1986, Resistance to Corrosion, IAI/1985.
3. T. V. Bommaraju, P. J. Orosz, Caustic evaporator corrosion: Causes and Remedy. Occidental Chemical Corporation. Private information.
4. M. Yasuda, K. Fukumoto, Y. Ogata, F. Hine, J. Electrochem. Soc., 135, 12, (1988): p. 2982.
5. P. J. Gegner, Process Industries Corrosion, (Houston: National Association of Corrosion Engineers, 1975), p. 296.
6. K. Wojtowicz, M. Tomza, Resistance of Materials in Sodium and Potassium Hydroxide and Ammonia and Aqueous Ammonia Environments, "Technorem", Kraków, 1988.
7. A. Małecki, Ochrona przed korozją, 33, 5, (1990): p. 104.
8. S. Łabuś, A. Małecki, Ochrona przed korozją, 33, 6, (1990): p. 130.
9. W. Reidel, Electroless Nickel Plating, (Finishing Pub. Ltd d. ASM Int. 1991).

Table 1. Potentials and corrosion currents for investigated electrodes.

NaClO ₃ concentration [%]	Ni-P		Ni 200	
	E _{corr.} vs. SCE [mV]	i _{corr} [mA/m ²]	E _{corr.} vs. SCE [mV]	i _{corr} [mA/m ²]
0	-1171	383	-1021	14
0.3	-1090	593	-976	70
0.6	-1047	244	-962	130
1.0	-1014	175	-948	140

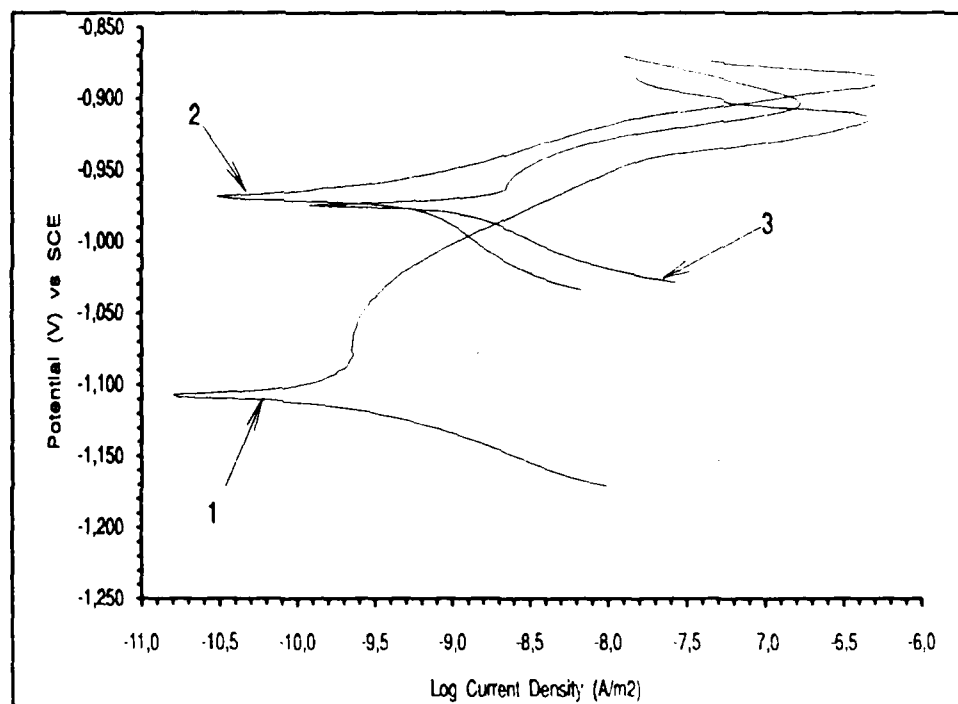


Fig. 1. Polarization curves for Ni-200, exposed in an NaOH + NaCl environment, for various chlorate concentrations.

1 - 0.0% ClO₃⁻, 2 - 0.3% ClO₃⁻, 3 - 1.0% ClO₃⁻

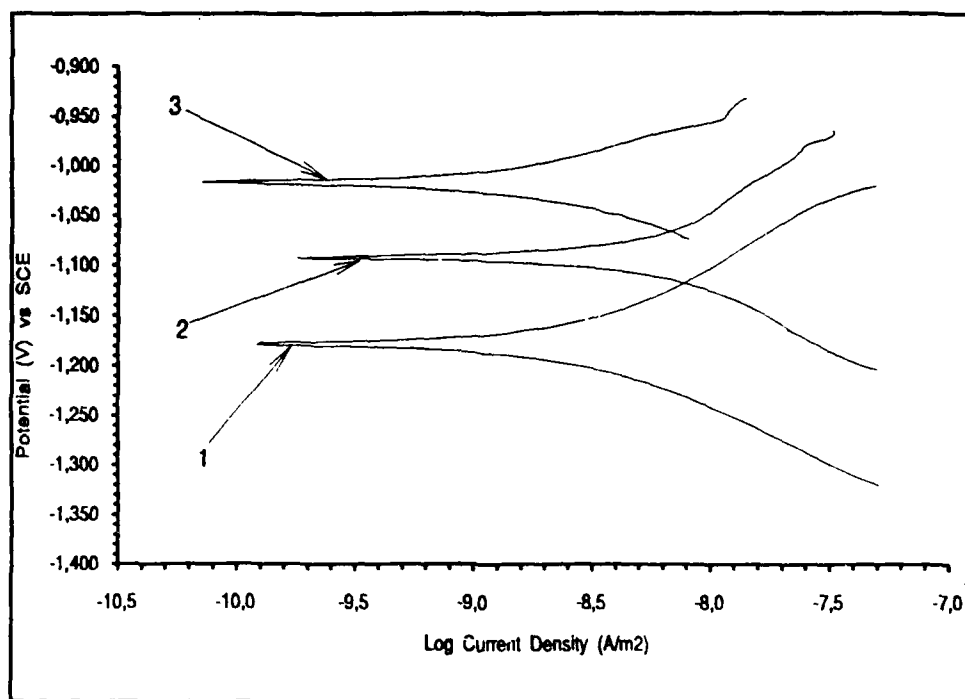


Fig. 2. Polarization curves for Ni-P, exposed in an NaOH + NaCl environment, for various chlorate concentrations.

1 - 0,0% ClO_3^- , 2 - 0,3% ClO_3^- , 3 - 1,0% ClO_3^-

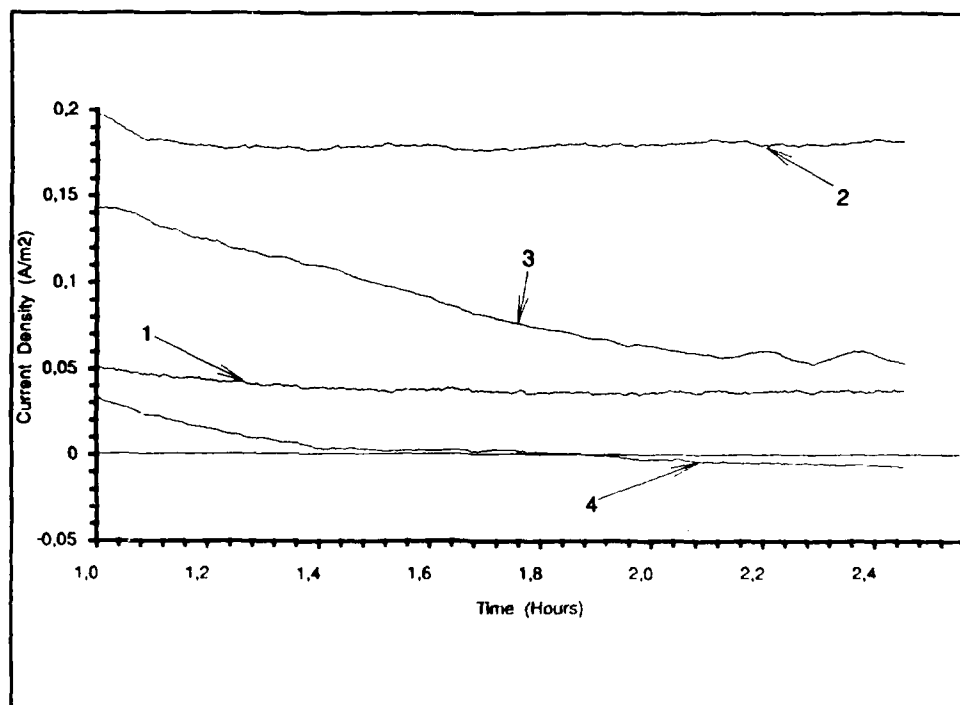


Fig. 3. Changes of currents flowing in Ni 200/Ni-P cells, tested in each solution.

1 - 0,0% ClO_3^- , 2 - 0,3% ClO_3^- , 3 - 0,6% ClO_3^- , 4 - 1,0% ClO_3^-

Proactive Corrosion Program Improves Process Heater Reliability

Kenneth L. Baumert
Senior Engineering Associate-Materials
Air Products and Chemicals, Inc.
7201 Hamilton Boulevard
Allentown, PA 18195-1501

Brian K. Heft
Senior Principal Process Engineer
Air Products and Chemicals, Inc.
7201 Hamilton Boulevard
Allentown, PA 18195-1501

Sheldon W. Dean
Air Products Fellow
Air Products and Chemicals, Inc.
7201 Hamilton Boulevard
Allentown, PA 18195-1501

Abstract

Over the course of 17 years, an amines manufacturing plant incurred three unscheduled shutdowns as a result of tube failures in a process fired heater. Corrosion failures occurred several times in the convection bank and once in the radiant section. An attempt was made to solve the problem by upgrading the materials; however, this was not successful as the replacement alloy also corroded, albeit at a lower rate. Moreover, this solution was thought to have transferred the problem downstream to the radiant section. This prompted the formation of a team consisting of plant maintenance, operations, and process engineering, plus corporate process and corrosion engineers to study conditions in the fired heater which could produce corrosion. The team also instituted a non-destructive testing, NDT, program along with criteria for equipment retirement until the corrosive species was identified.

Key terms: corrosion, proactive, nitriding, carboxylic acid.

Introduction

In an effort to control costs, manufacturing plants operate with the smallest staff deemed necessary to run the facility safely. Sometimes, this results in decisions that have to be made using a limited amount of data. A safe way to operate under these circumstances is to replace equipment before it has reached the end of its useful life. Recognizing that this conservative approach can be costly, corrosion corrective action teams have been formed to evaluate equipment life, and take a proactive approach to the issue of corrosion. This paper uses an example at a plant to describe the approach and define the benefits of the program.

Mechanical Description

The fired heater employed at one of Air Products and Chemicals, Inc. production facilities utilizes a radiant coil operating in series with multiple convection tubes to superheat the reactant streams fed to our amination reactors (Figure 1). The heater, which has the capability to burn either fuel oil or natural gas, originally utilized only the radiant coil for heat transfer purposes. The convective

section was added in the early 1980s in an effort to increase efficiency in light of the energy crisis and corresponding increase in hydrocarbon fuel costs.

The original material of construction for the radiant coil was UNS S31600, Type 316, stainless steel. The decision to use this material was based on experience from another Air Products and Chemicals, Inc. plant, which had been manufacturing amines for some time. UNS S31600 gave acceptable service life and was compatible to the process fluids.

Service History

The heater has suffered various mechanical problems since it was placed in service in the mid-1970s. The first problem occurred soon after start-up, when the flame impingement caused severe thinning of the lower wraps of the radiant coil. This problem was readily solved through realignment of the burner.

The coil was included in a maintenance inspection schedule which consisted of ultrasonic wall thickness (UT) measurements. Routine thickness measurements began to show metal loss, particularly in the lower three wraps of the coil. This was in the area near the exit where tube wall temperatures were the highest. Since the tubing was specified as schedule 40, there was ample corrosion allowance in all parts of the coil. The bottom portion of the coil was ultimately replaced during a plant outage.

Metallurgical analyses of a pipe section revealed that nitriding on the inner diameter, ID, promoted a metal dusting mechanism, Figure 2. Nitrogen was detected about 0.005 inch (0.13 mm) into the wall, with most severe attack being 1-2 grains deep. The primary constituent in the process stream was ammonia. Tube metal temperatures of ~ 1,000°F (~540°C) near the exit were sufficient to crack the ammonia and nitride the coil. The particles eroded downstream components, further compounding the metal loss problem.

A new radiant coil fabricated from UNS S34709, Type 347H SS, was placed in service in the April 1985. This alloy was chosen because of its improved high temperature properties. Because of the higher allowable stress levels the corrosion allowance was increased using the same wall thickness. Finally, nickel alloys which have good nitriding resistance were not specified because of concerns that particles originating from these metals might be incompatible with the process. The new coil performed satisfactorily until 1988 when the bottom 1/3 had to be replaced because of wall thinning. By this time, the convection section had been added to increase both the efficiency and the capacity of the heater. It was also hoped that the convection section would reduce the nitriding problem observed in the radiant coil by virtue of the reduced firing rate afforded by increased heat transfer efficiency.

The first problem with the convection section occurred in the mid-1980s when several of the finned tubes immediately above the (unfinned) shock tubes failed. The resulting fire necessitated an unscheduled outage only two years after the convection section had been placed in service. Inspection of the failed tubes and others in the immediate vicinity of the failure revealed severe thinning along the inside-bottom of the tube wall. This "trenching" effect suggested that the failure had resulted because of attack from corrosive liquid. The convection section was replaced with a new unit constructed of UNS S34709 in hopes that this alloy would provide increased corrosion resistance at elevated process temperatures.

The fact that "trenching" was found on the bottom of tube remnants indicated that liquids entered the convection section. Under normal operating conditions, only vapors should enter the fired heater inlet. Accordingly, the liquids could be formed inside or enter the heater during an upset condition. Using the temperature profile in the convection section in an analytical approach, we concluded that the most likely corrosive species were organic acids (carbamates), which became

corrosive when they concentrated as the liquid boiled to dryness.

Inspection of the radiant coil during the outage necessitated by the failure of the convection section revealed that nitriding had again caused thinning, but because of the product mix, as well as various periods of heater downtime, the actual corrosion rate was an unknown. UT measurements confirmed that only the bottom third of the coil had thinned appreciably, and this portion was replaced with the same UNS S34709 alloy utilized in the rest of the coil.

A second failure of the convection section resulted in another unscheduled outage approximately two years later. This time the ensuing fire was so extensive that no tube material could be recovered for meaningful analysis. At this time, it was decided to upgrade materials of construction to UNS N08028, Sanicro 28®. This decision was based on three reasons: (1) an austenitic alloy was needed for the temperatures in the convection section, (2) the higher Cr and Mo would offer better resistance to the assumed organic acid, and (3) the higher Ni content would offer somewhat more nitriding resistance than stainless steel, even though there was some concern from the process compatibility standpoint.

Thinning due to nitriding again necessitated replacement of the bottom third of the radiant coil roughly one year after the second failure of the convection section. Since nickel alloys were ruled out because of processing concerns, the coil was replaced with UNS S30409, Type 304H, which had been aluminized. This decision was made based on a literature review which showed that aluminum would be resistant to nitride formation. Subsequent analyses revealed that all of the aluminum corroded away within 18 months. The mechanism of corrosion is not currently understood.

Roughly 18 months later a third unscheduled outage resulted; this time from a fire that initiated when the radiant coil failed. An inspection of the radiant coil revealed that failure resulted from a trench that formed in the middle third of the coil. The trench was reminiscent of those previously observed in the convection section, suggesting that the increased resistance of the UNS N08028 had allowed the corrosive liquid and hence the corrosion problem to travel further downstream.

A final failure occurred just two months later; this time in the convection section. Inspection of the tubes revealed they had failed due to general attack associated with nitriding. No trenching in convection tubes was noted, although this phenomenon always occurred sporadically. It indicated that the nickel content of UNS N08028 was not sufficient to resist nitriding.

As a result of the repeated failures of the heater system and an apparent increase in frequency of such failures, a corrosion corrective action team was established to define procedures needed to eliminate further unscheduled shutdowns, and to launch a more detailed technical analysis into the root cause of the problems.

Corrective Action Team

The corrective action team approach was applied to this case because of the random nature of the failures. After the first failure there were opposing viewpoints as to what could have caused it. One school of thought was that it was not possible to transport liquids to the fired heater. The other viewpoint was based on analysis, which predicted the presence of liquids in the convection section. At any rate, it was felt that the problem was not a recurring one, and the plant continued to operate without adjustments. When the second failure occurred, it became evident that a more detailed approach would be needed.

The corrective action team consisted of five people each representing different disciplines in the company. They included: A materials engineer from a corporate engineering function; a process

engineer representing corporate chemicals, a plant maintenance engineer, a plant technical engineer, and a representative from plant operations. The team typically meets every month. Occasionally, these meetings are done by conference call between the plant and central engineering offices.

The agenda items consist of ongoing problems, each of which was previously assigned to one or more members. As each problem or action item is completed to the group's satisfaction, it is removed from the active list. Completion of one item often times generates additional action, which is then assigned to someone along with a due date. A list of new and incomplete action items is sent out within one week of the meeting. The minutes along with the action items are sent out at a later time to a wider distribution.

Root Cause Investigation

The corrosion corrective action team has characterized two modes of corrosive attack. The first is nitriding, which is a gradual process that causes uniform thinning of metal exposed to ammonia at metal temperatures from 700-1,100°F (370°C to above 600°C). It is the predominant mode of attack in the (higher temperature) radiant coil⁽¹⁾. Nitriding rates are generally slow enough and uniform enough to permit scheduled replacement of the radiant coil per the corrosion management plan outlined below.

The other corrosion problem, attack by a condensed liquid phase is characterized by trenching along the bottom of tubes. This phenomena is more aggressive (faster), and has resulted in the four unscheduled outages discussed above. Analysis of the convection section failures to date revealed an unusually consistent pattern:

- each failure occurred after ≈ 2 years of service despite the fact that the tube material had been upgraded.
- each failure occurred in the fin tubes located immediately above the two rows of (unfinned) shock tubes at the bottom of the convection section.

Analysis of the problems occurring in the fired heater was complicated by two major facts. First, the plant is operated in blocked-out campaigns, meaning that each of three or four separate product lines is produced in the same equipment at different times. Each of the product runs, which vary in length according to sales demand, expose the heater to different compositions, temperatures, and firing rates. Hence, one has to determine if the observed corrosion problems are related to a single product line, a consequence of the cumulative effect of multiple campaigns to produce varied products, or (since most failures occurred shortly after start-up) an artifact of start-up and/or shutdown transients.

The second item with which the corrosion corrective action team had to contend was the design of the heater itself. Originally designed for an output of 5MMBTU/hr, 1.5×10^6 J/sec, the addition of a convection section in the early 1980s (Figure 1) not only improved efficiency, but also essentially doubled the output of the heater. However, as sales increased firing rates were increased proportionately with throughput, until the design capacity of the heater was ultimately exceeded. The net result of such operation was that tube wall temperatures - though well within safe operating limits - did exceed original process criteria.

One of the first actions taken by the corrective action team involved modification of shutdown procedures so as to prevent "evidence" from being swept away. This was accomplished by replacing the (condensible) steam previously used to purge product from the heater with (gaseous) nitrogen. It was hoped that this change would prevent any corrosion residue that was deposited during a specific campaign from being washed away by condensate during the clean-up between campaigns.

A program was then put in place to collect deposits from the convection tubes after each campaign. These samples were analyzed using x-ray diffraction, x-ray fluorescence and infra-red analysis (for organic compounds). Two of the more interesting findings that resulted from these analyses were the identification of magnetite - or Fe_3O_4 - in all samples and the presence of carboxylic acid salts in some of the samples. The presence of magnetite was surprising since the process is operated under oxygen free conditions. The occasional presence of carboxylic acids was even more surprising, since carbamic acids - a common by-product of amine production - were thought to be the only acids present in the system.

Another unusual finding was the random occurrence of long-chain, aliphatic hydrocarbons in the scale samples. Since it would be very difficult to form such compounds at the operating conditions encountered in our facility, it seemed likely that their presence resulted from either trace contamination of feedstocks materials or lubricating oils that leak from rotating equipment into the process. However, checks of all feedstocks and lubricating oils used in the process failed to provide a match with the specific hydrocarbons recovered from the scale samples.

The final aspect of our root cause investigation entailed a modeling effort intended to increase our understanding of the changes in the temperature profile across the heater as a function of each campaign. The simulations indicated that tube wall temperatures in the lower portion of the convection section and radiant coil were much hotter than had previously been anticipated. This condition was verified by thermocouples which were subsequently placed in the system. The high temperature condition helped to explain the severity of the nitriding problem.

Proactive Corrosion Management

Because it was necessary to collect data for the root cause investigation over several years, a corrosion management strategy was developed to prevent additional unscheduled shutdowns until such time that appropriate corrective actions could be developed and implemented. The key elements of this strategy are the on-site availability of both a spare radiant coil and a convection section, and a monitoring program designed to track and quantify corrosion rates. In addition to providing valuable data for the root cause investigation, the monitoring program minimizes the chance of an unexpected failure by regularly quantifying the extent of metal loss. The on-site availability of the spare coils would effectively reduce downtime should an unexpected failure occur.

The monitoring program relies heavily on UT measurements taken after every campaign. Measurements are made on the ID of the convection tubes through specially designed inspection ports, at various points on the outside of the convection tubes, and at regular distances along the radiant coil. Several of the convection tubes located immediately above the unfinned "shock" tubes are also inspected visually for evidence of trench formation and/or growth when corrosion scale (discussed previously) is being collected.

Metal loss data generated from the UT measurements is used to project the useful life of the radiant coil, and replacement is scheduled accordingly. Note, however, that owing to the uncertainty inherent in corrosion rates, coil change-outs are made when metal thickness decreases to ~ 120% of that required by ASME code. A much less scientific approach is taken for scheduling change-out of the convection section: since previous failures occurred once every two years regardless of plant loading or product mix, the convection section is replaced every two years regardless of trench growth or UT measurements. It is hoped that this approach can be improved upon as our understanding of the corrosion phenomena responsible for the problem increases.

Conclusions

The root cause investigation initiated by the corrective action team has helped to shed some light on the corrosion problems afflicting the fired heater. For example, it is now known that higher than expected tube wall temperatures are responsible for the nitriding problem, and that a carboxylic acid of unknown origin is responsible for the trenching that occurs in convection section tubes. A research chemist has since been consulted to help identify possible mechanisms for the formation of this acid in our process.

The corrective action team has also reduced operating costs by eliminating unscheduled shutdowns. Representation from the various functional groups mentioned earlier has been the key to balancing the competing desires to replace equipment frequently (at great cost) so as to eliminate any chance of a failure, and the need to minimize expenditures (i.e., equipment change outs) so as to maximize profit. It is hoped that as our understanding of the relevant corrosion phenomena grows and our confidence in the UT data builds, we will be better able to maximize profits by further extending the useful life of both the coil and the convection section.

References

1. Cihal, V., Proc. 1st Int. Cong. Met. Corros., London, p. 591, 1961.

FIGURE 1

Schematic of Tube Arrangement From Fired Heater

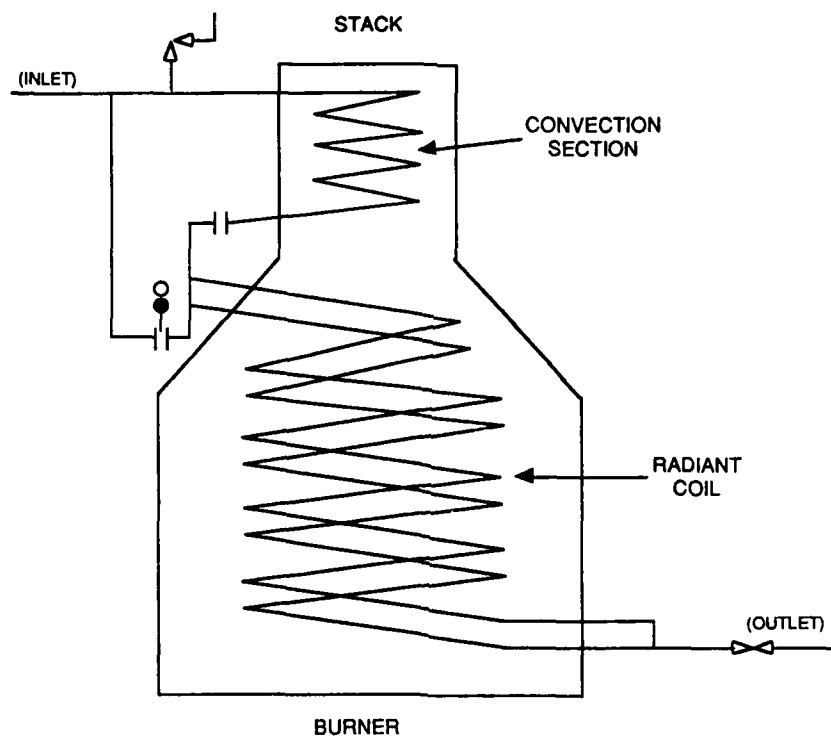
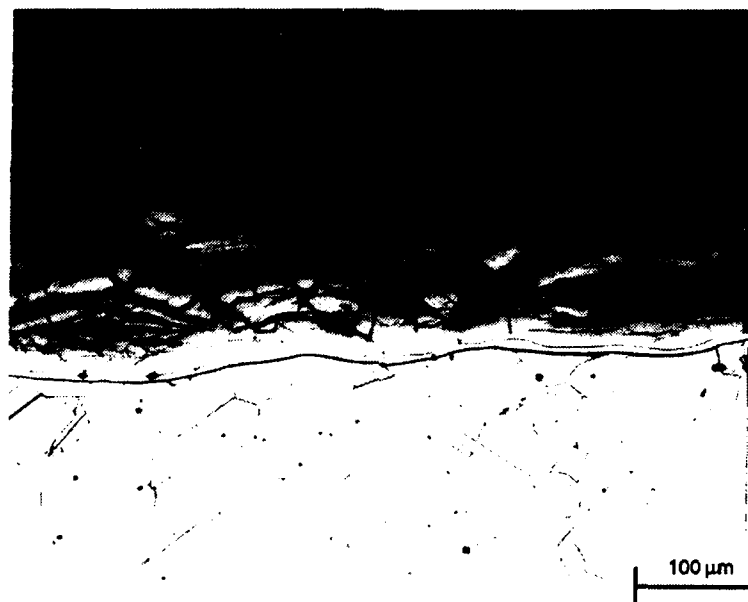


FIGURE 2

ID Surface of Heater Tube Showing a
Metal Dusting of Nitrided Grains



Plant Measurement Cell for Carrying out Electrochemical Corrosion Investigations on the Plant

Gerhard H. Wagner
BASF AG
Werkstofftechnik
6700 Ludwigshafen
Germany

Rolf L. Münster
BASF AG
Werkstofftechnik
6700 Ludwigshafen
Germany

Abstract

The solution of corrosion problems in practice may require various testing stages, which extend from simple simulation of the plant conditions in the laboratory via pilot scale tests to experiments on site, i.e. in the operating plant.

Pilot plant experiments and on-site experiments are indispensable especially if the actual critical corrosion conditions are caused by shortlived intermediate reaction stages which frequently occur in chemical reactions. Such conditions can only rarely be reproduced in the laboratory in such a way that they are stable over a sufficiently long experimental time.

The substantially more expensive on-site methods are also necessary whenever the setting of redox conditions is not reproducible in the laboratory because of the participation of the redox partners in the desired chemical reactions.

The measurement cell developed for these experiments is described and illustrated, and the potential uses of this measurement cell are demonstrated.

In addition, the use in practice and the experience gained with this measurement cell are reported.

Introduction

Materials for apparatuses (reactors, columns and heat exchangers), pipelines, pumps and fittings for the chemical industry in individual cases are chosen usually by laboratory corrosion tests, which supplement the initial selection based on experience data (standards, tables, manuals and company-own experience). In these laboratory tests, the conditions of the chemical reactions, i.e. pressure, temperature and gas atmosphere, must be simulated so that as far as possible they are comparable with the operating conditions. This means that it is necessary to

simulate not only the corrosiveness of the medium (essentially determined by the concentration) but also the redox conditions which determine the free corrosion potential of the metallic materials.

As a rule, a distinction is made between two types of tests which often also represent a necessary gradation, ie.

- a) "immersion tests" in open vessels or in autoclaves for determining the linear corrosion rate v_1 ;
- b) electrochemical tests under the same conditions for confirming the latter and especially for determining the risk due to local corrosion phenomena, eg. pitting, crevice or galvanic corrosion.

This method for selecting materials has become established in the past and is industrial practice.

In specific cases, however, it is extremely difficult to simulate the operating conditions in the laboratory. In these cases, corrosion tests are carried out, for example in pilot plants, in order to obtain reliable results and information regarding material selection. In spite of all these measures, we may find that, during subsequent operation, corrosion phenomena which are not observed under laboratory conditions occur in certain cases in parts of the plant, at materials classified as resistant. Such zones are, for example, very limited regions with columns or the vapor space of reactors. If such unforeseen corrosion damage occurs, corrosion tests must be carried out locally. Similar to the laboratory tests "a", electrically insulated coupons are then installed in the corresponding parts of the plant and are evaluated after several weeks or months. This type of corrosion test is also used when the operating conditions in the plant change, due to expansion of capacity, different provenance of starting materials or changes of the process.

Since the majority of the corrosion processes are electrochemically controlled, electrochemical corrosion tests have become an additional tool for the corrosion researcher over the past 20 years. Thus, electrochemical test methods have made it possible to gain a better understanding of fundamental processes involved in intergranular stress corrosion cracking of unalloyed steels in nitrate solutions and alkalis or the sensitivity of various austenitic CrNi steels to halide-containing media [1-4].

Such investigations make it possible in principle to monitor the corrosion, its rate and its various manifestations as a function of the potential.

The metal dissolution reactions basically are electrochemical oxidation reactions and part of the redox system of the chemical reaction medium. Since the position of the potential determines the rate of metal dissolution, it is possible, with the aid of tests at fixed potential (so-called potentiostatic tests) to investigate the dissolution behavior approximately, even outside the potential range which is established by the redox system present in each specific test. This "substitute" is however justified only if the effective redox system does not have additional - for

example inhibitory or complex-forming - effects on the corrosion system and if the intensity of metal dissolution exceeds the other redox reactions by orders of magnitude, as is frequently the case for local corrosion.

Compared with the "chemical" corrosion tests, in principle electrochemical methods also provide more information about the properties of the partial reactions, but only if the various oxidation reactions determined by the chemical reaction and by the anodic metal dissolution can be separated. This is the main difficulty, for example, in the purely electrochemical measurement of the corrosion rate in electrolytes other than model electrolytes.

In general, however, electrochemical test methods, beginning with the simple monitoring of the open-circuit potential, make the test procedure substantially more reliable and clearer but considerably more expensive in terms of apparatus and definitely more complicated. For example, in the so-called "beaker tests", the distribution of local anodes and the position of the rest potential may be completely different compared with a complicated shaped article with a large area exposed to the same corrosive medium. In this case, it may be very doubtful as to whether the conditions in such tests at rest potential resemble to conditions in practice. The electrochemical determination of the corrosion as a function of potential provides reliable information about the corrosion processes or the changes therein which must be expected if in practice the potential has a certain value or if it is shifted in one direction or other by various processes.

It was therefore an obvious step to apply the experience gained over many years with electrochemical corrosion tests in the laboratory to tests on site, ie. in the production plant. These pilot and operational tests are indispensable in particular if the actual critical corrosion conditions are caused by the intermediate reaction stages which frequently occur in chemical reactions or which are short-lived. Such conditions can rarely be simulated in the laboratory in a stable manner over a sufficiently long test period.

The substantially more expensive on-site methods are necessary also when redox conditions cannot be simulated in the laboratory, owing to the participation of the redox partners in the desired chemical reaction. In chemical reactions, the states at the beginning or end of the reaction can in principle be established over a sufficiently long period in the laboratory if it is not intended to perform such tests using expensive, fully automated "laboratory autoclaves" with continuous supply of the reactants and removal of the reaction products.

The measuring cell to be developed should thus permit, in operational corrosion systems, both the measurement of the open-circuit potential and shifting of the potential to the anodic or cathodic region (ie. polarization of the coupons). Moreover, the measuring cell should permit the measurement of the potential over relatively long periods. It should be possible to install the measuring cell with the aid of a flange, for example in a side stream of a plant or directly in a column or a reactor via a test connection. It would also be necessary to ensure that this measuring cell can be used at high temperatures and pressures.

HTHD reference electrode

An essential requirement for electrochemical corrosion tests at high temperatures and pressures is an easily handled reference electrode which is stable over long periods. The development and theoretical evaluation of such an electrode is described elsewhere [5, 6]. It uses classical reference electrode half-cells at room temperature and under pressure and taps the potential with the aid of a Haber-Luggin capillary of ceramic material at the hot measuring point. As has been shown, the so-called Soret potential (thermodiffusion potential) is stable if convection is avoided within the capillary.

The actual half-cell needs therefore to be sufficiently stable in the medium only at room temperature. Difficulties may arise here owing to the diffusion of gases such as H_2S or NH_3 through the frits into the reference electrode.

Usually, the potential values are not corrected. For conversion to a thermodynamically comparable system, for example the standard hydrogen electrode, it will be necessary to determine the exact values for the thermodiffusion potentials and chemical junction potentials, but this can be dispensed with in comparative corrosion tests.

Structure of the measuring cell

Fig. 1 schematically shows the structure of the measuring cell for "bypass" installation as an example. The reference electrode from below and a pressure-resistant, electrically insulating wire duct are mounted on a flange which meets the process conditions (pressure, temperature, material resistance). The coupons are fastened to a coupon holder and are also electrically insulated. Wires of identical or similar material are welded to the coupons. The coupon holder also permits the installation of a counter-electrode for polarization of the test pieces.

Fig. 2 shows the measuring cell, which is flanged to a T pipe section cut open longitudinally.

Example of use

In a waste gas separation column of the material 18/12/2 CrNiTi, material No. 1.4571, corresponding to AISI 316 Ti, greatly fluctuating corrosion rates were measured over a very long observation period for coupons which were installed at various points. To investigate these fluctuations and determine their causes, the measuring cell described above was mounted on a manhole cover of the column; the column solution flowed continuously through the cell. For this purpose, the solution was collected inside with a funnel and passed into the measuring cell and could flow back into the column via a wier.

Under these conditions, the open-circuit potential was monitored with various materials over relatively long periods, potentiokinetic current density-potential (i-E) curves were recorded and potentiostatic tests with weight loss determinations were carried out.

Fig. 3 summarizes, as an example, the *i*-*E* curves of three Ti-stabilized steels, a ferritic CrMo steel and two austenitic CrNi(Mo) steels. For this purpose, the coupons were first cathodically polarized for 1 h at -1200 mV against SCE_{20°C} in order to depassivate the coupon surface.

The potential was then changed with different scan rates in ascending and descending direction. The Figure shows the results for the "forward" curves with 1.3 V/h.

These potentiokinetic curves do not represent equilibrium conditions and furthermore correspond only to the sum of all electrochemical oxidation and reduction reactions taking place at the coupon surface. The partial oxidation reaction assignable to the metal dissolution can be individually determined only by potentiostatic tests. Nevertheless, certain typical potential ranges can be derived from these curves. The current curves pass through zero in the range from -800 to -900 mV SCE_{20°C} as a function of the potential change rate. In the case of the Ni-free material, it is systematically about 50 to 80 mV below that of the austenitic steels. The following increase in current corresponds initially to the active (anodic) metal dissolution. While the materials were still passive in the region of the rest potentials E_R shown, the corrosion rate increased the heavier the more potentials shifted to lower values after long test times, but as a function of the material. While the Mo-free austenitic steel was corroded at about -800 mV at 0.3 mm/a, the corrosion rate of the Mo-containing austenitic steel there still remained an order of magnitude lower and increased sharply only below this. The active range of the nickel-free material is the most negative one at about -900 mV, and the dissolution rate of this steel is higher by an order of magnitude than for the Mo-free austenitic steel.

It should be mentioned that the two peaks of the *i*-*E* curve, A and B, are not associated with correspondingly high corrosion rates but are evidently an expression of electrochemical oxidation reactions of the medium, as could be shown by potentiostatic tests in these potential ranges. While peak B is readily reproducible regardless of material and virtually regardless of the scan rate (also found in carbamate solutions of the urea process at substantially higher pressures and temperatures), peak A occurs only in the case of the Ni-containing, austenitic materials and becomes smaller with increasing scan rate. This may be the effect of the complexing reaction of Ni in the ammoniacal medium.

Summary

The selection of materials on the basis of laboratory tests can be supplemented and confirmed with the aid of on-site electrochemical measurements, which require a reliable reference electrode adapted to the conditions. An example was used to show that the different results of the abovementioned simple corrosion tests in the plant are explained by a slow potential drift with increasing operation times, which was due to a change in the redox conditions within the column.

By checking these redox conditions, which were established and monitored with the aid of potential measurements with the electrochemical measuring cell

described, it was possible to avoid further corrosion attack in the column, ie. to operate the apparatus under conditions which are safe for the material.

Over and above the mere selection of materials, such measurements can therefore also successfully be used for monitoring process engineering and operational parameters so that, once a reasonable choice of materials has been made, it is not called into question during operation as a result of temporary and particularly unfavorable conditions.

References

- [1] Radeker, W.; Gräfen, H., Stahl u. Eisen 76 (1956), S. 1616/1628
- [2] Münster, R., Gräfen, H., Arch. Eisenhüttenwes. 36 (1965)4; S. 277/284
- [3] Gräfen, H., Kuron, D., Arch. Eisenhüttenwes. 36 (1965)4; S. 285/296
- [4] Brauns, E., Schwenk, W., Arch. Eisenhüttenwes. 32 (1961)6; S. 387/396
- [5] Wagner, G.H.; Thesis Darmstadt D 17
(April 1990)
- [6] Baucke, F.G.K., G.H. Wagner;
Mat.-wiss. u. Werkstofftech. 22 (1991) 128 - 136

Electrochemical Corrosion Measurement in Plant

Example: Installation in a by-pass

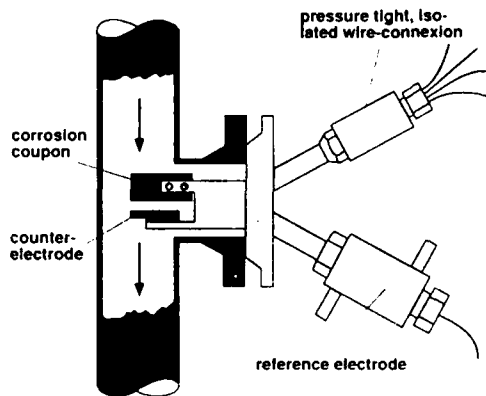


Figure 1

Figure 2

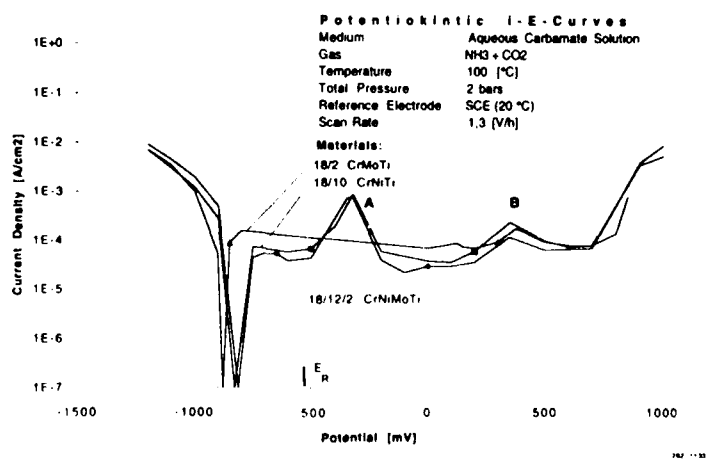


Figure 3

Experience with Neutron Activation for Real-Time Corrosion Monitoring in a Urea Plant

Giel Notten
Mechanical Plant Services, DSM
PO Box 18, 6160 MD Geleen, The Netherlands

Johan Thoelen
Mechanical Plant Services, DSM
PO Box 18, 6160 MD Geleen, The Netherlands

Hans Verhoef
Mechanical Plant Services, DSM
PO Box 18, 6160 MD Geleen, The Netherlands

Robbert van Sluijs
Radioisotope Applications and Support, DSM Research
PO Box 18, 6160 MD Geleen, The Netherlands

Abstract

Reprocessing in a urea plant of ammonium carbamate from two melamine plants was feared to cause variations in the redox potential of the urea synthesis solution. Such variations may reduce the corrosion resistance of the material of construction of the high pressure process equipment, i.e. type UNS S31603 (AISI 316L urea grade) and UNS N08310 (X2CrNiMoN 25 22 2). An on-line corrosion monitoring system was felt to be necessary for early detection of corrosion, so assuring plant safety and performance reliability.

We opted for a radioactive monitoring technique (i.e. neutron activation), because this technique does not require insertion of probes through the wall of the high-pressure equipment. Basically, the method operates by measuring the decrease in gamma radiation of an active coupon exposed to the corrosive environment.

Experience gained with this on-line corrosion monitoring technique is explained, the following aspects being highlighted:

- method of measurement
- method of activation
- system setup for industrial application
- safety regulations
- interpretation of results

Introduction

Urea plants according to the DSM stripping process use ammonia and carbon dioxide as feedstock. Equipment exposed to the process fluids in the high-pressure area of the urea synthesis section is made either in UNS S31603 (urea grade AISI 316L) or UNS N08310 (X2CrNiMoN 25 22 2). The temperature of the ammonium carbamate solution in this area of the process is approx. 180°C. Passivity, and so corrosion resistance, of the stainless steels is maintained by adding oxygen to the gaseous CO₂ feed stream. In this way, a redox system is created which ensures that the corrosion potential of the stainless steel remains in the passive region of the current vs. potential curve, where corrosion is low. Experience over many years and many plants all over the world has shown that the corrosion rate is typically 0.05 - 0.10 mm/year.

At the DSM plant in Geleen, Netherlands, the waste stream of a melamine plant is added to the feedstock. Before being supplied to the urea reactor, the ammonium carbamate is concentrated in the tie-in stage. This addition of waste carbamate causes an increased corrosion rate in the urea plant: 0.10 - 0.15 mm/year is the result of several years of experience.

A reduction of the redox potential (due to, for instance, insufficient oxygen being added) may cause the stainless steel to become active.^{1,2} A simplified representation of active and passive corrosion of stainless steel with various amounts of oxygen is given in Figure 1. In Figure 1a, the central curve shows the relation between the current and potential of a sample electrode in a urea synthesis solution without oxygen. This current actually is the algebraic sum of two partial currents: the positive current (a) that corresponds to the anodic dissolution (oxidation) of the metal and the negative current (c) that corresponds to the cathodic formation of hydrogen (reduction of the liquid). Only at the active corrosion potential E_a , do the two currents cancel each other and the resulting current is zero. Without external current being applied the metal will adopt this potential and active corrosion occurs. When some oxygen is present (Figure 1b), the cathodic current is larger (more negative), as oxygen is reduced too. There exist two potentials where the net sum current is zero: at the active potential E_a and at the more positive passive corrosion potential E_p . When active, the metal cannot pass the current peak (which is typical for passivable stainless steels) and remains active. When the metal is passive and the conditions do not change, the metal remains passive. By supplying the carbamate stream from the melamine plant process conditions change. The consumption of oxygen by this carbamate stream increases the passive corrosion rate and even may cause activation. When a high amount of oxygen is present (Figure 1c), only one zero current potential exists in the passive region: the metal is in a stable passive state and the corrosion is low.

Because the waste carbamate of a second melamine plant was to be added to the feedstock, so that the ammonium carbamate waste stream was to be substantially increased, it was feared that the redox potential might diminish so much as to allow corrosion, especially of UNS S31603, to develop. Experience is that the active corrosion rate of these steels in ammonium carbamate can be as high as 10 to 30 mm/year. Therefore, a real-time corrosion monitoring system was installed.

The main purpose of the monitoring was to alert in the case of active corrosion. Additionally, we were interested in measuring the passive corrosion rate as a function of process conditions, i.e. the waste carbamate stream. The reliability of the plant, operating at high temperature and pressure, was in no way to be endangered.

The Corrosion Monitoring Technique

Since the plant operates at pressures of about 15 MPa, insertion of probes or electrodes through the wall of the equipment was out of the question.

Being one of the most reliable non-intrusive methods, a method based on ionising radiation was chosen for the corrosion monitoring. The method had proven its applicability at DSM earlier.³

Corrosion monitoring based on a radioactive material utilizes the loss of radionuclides as a measure of surface loss brought about by corrosion or corrosion-erosion.⁴ Radionuclides are formed by activating the material under test; this may be a coupon of the material to be tested or a particular spot on the pipeline or piece of equipment under investigation.

For direct weight loss measurement of the material under test it is essential that gamma radiation emitting radionuclides be formed. Gamma radiation is only partly absorbed by material and can, within certain limits, be detected from outside of the process. The intensity of the gamma radiation is proportional to the amount of radioactivity and is measured with a NaI detector. Of course, the measuring signal needs to be corrected for radioactive decay of radioisotopes. The resulting signal is directly proportional to the thickness of the test coupon.

Another requirement for proper performance of this technique is that corrosion products be removed so they cannot interfere with the measurement.

The material can be activated by bombarding it with either high energy charged particles (in the case of thin layer activation; TLA) or with neutrons (in the case of neutron activation; NA),⁵ see Figure 2. In principle, most materials can be activated.⁶

Method of Activation

The choice of the method of activation, and thus the level of activity of the main radioisotope formed, is dictated by the required monitoring period, the desired accuracy and the anticipated corrosion rate. Essential differences between TLA and NA are given in Table 1. Table 2 shows the minimum detectable corrosion rates achievable with TLA and NA.

The key data for the monitoring system were as follows:

- overall monitoring period of about 4 years;
- penetration through 20 millimeters of stainless steel;
- anticipated passive corrosion rate approximately 0.1 to 0.15 mm/year.

The duration of the monitoring period meant that the radionuclide to be formed had to have a half life of several years and the energy of the gamma radiation had to be high enough so as not to be completely absorbed by the pipe wall. The absorption of gamma radiation is dependent on the radiation energy. High energy radiation is absorbed to a lesser extent than low energy radiation. For these reasons we opted for neutron activation of the cobalt (⁵⁹Co), present as a contaminant in the UNS S31603 stainless steel to be tested. On being activated, the ⁵⁹Co generated ⁶⁰Co, a radio-isotope with a half life of 5.27 years and emitting two gamma rays with energy levels of 1173 and 1330 keV, each with a yield of approx. 100%.

Another argument for choosing NA was the required radioactive layer thickness based on the average passive corrosion rate of 0.15 mm/year. Because of the homogeneous activation of the test coupon, any wall thickness could be chosen so long as the accuracy was not unduly impaired.

In spite of the relatively poor sensitivity, the accuracy of the method was expected to be good enough, since the monitoring system was intended to detect passive corrosion over a longer period of time and active corrosion within a few hours (see Table 2).

Irradiation of the target material must not adversely affect its corrosion resistance. Huey-testing to Stamicarbon Material Specification revealed no difference in the corrosion resistance of UNS S31603 before and after being irradiated with neutrons. The relevant literature, too, suggests that at the expected corrosion rates irradiation is unlikely to affect corrosion resistance.⁷

System Setup

The corrosiveness of the urea synthesis solution can best be measured at the top of the reactor or in the line from the reactor to the stripper. Since gamma rays are absorbed by steel, the thickness of steel intervening between the coupon and the detector should not be more than, say, 30 to 40 mm. Therefore, the monitoring system was installed in the line to the stripper (adjacent to a flange, see Figure 3).

In November 1989, two UNS S31603 coupons, whose chemical analysis, microstructure and Huey test performance were in accordance with Stamicarbon specifications, were irradiated with neutrons in the BR No. 1 reactor of SCK (StudieCentrum voor Kernenergie, Nuclear Energy Research Centre) at Mol, Belgium.

Approximately six months after irradiation, the short-lived nuclides had decayed, leaving only ⁶⁰Co, resulting in a level of activity of approx. 5 MBq. With the NA method, the whole coupon is activated. Since field welding of a radioactive material calls for special precautions, two non-radioactive strips were welded to the test coupon. This was done in the Nuclear Energy Research Center in Belgium. The welder was specially instructed and the welds were radiographed before mounting in the plant. The coupon with the best welds was chosen. Field welding was done using a special device to protect the radioactive coupon and to keep it in place during welding. The coupon was mounted in the pipe during a plant shutdown in May 1990 and was welded as shown in Figure 4, allowing the flow of fluid to remove all corrosion products from the test coupon. The second coupon was kept, but not to date used, for reference purposes.

The detector used was an industrial NaI scintillation detector giving pulses whose frequency is directly proportional to the measured gamma radiation intensity. The detector had to be very reliable over a long period of time and was cooled with water. The pulses generated by the detector are counted by a counter and then converted for readout of the surface loss or corrosion rate in the control room of the plant. This was done by means of an industrial PC and a purpose-made software program (see Figure 5). Readings, stored on hard disk, are corrected in terms of natural decay and background radiation (less than 1 % of the

measured level of activity). Figure 6 shows the setup of the monitoring system in the plant; the computer and associated hardware are shown in Figure 7.

Safety Regulations

As far as safety regulations are concerned, the NA monitoring system falls in the same category as industrial radioactive measurements for level and density. An important distinction is that the radioactive source is in direct contact with the process fluid, corrosion products may cause low-level radioactive contamination of the product or waste streams. For the government licence this meant that the system comes under the heading of tracer applications. This involved the following additional requirements:

- the NA monitoring system must be reported to the authorities;
- the level of the source activity must not exceed a given limit;
- product contamination must not exceed the maximum allowable concentration specified in the license;
- the source may be handled only under supervision of qualified personnel.

Performance

The system was started up in May 1990 after a two-yearly maintenance shutdown of the urea plant. It was inspected during the next shutdown in May 1992. We took that opportunity also to compare the then remaining wall thickness with the data generated by the on-line NA monitoring system.

The software enables the collected data to be plotted at hourly intervals. Average monthly corrosion rates are computed from the slope of the curves (the coupon surface loss being proportional to the decrease in activity). The first derivative with respect to time yields the corrosion rate. These calculations can, in principle, be done automatically in the control room to trigger an alarm when a predetermined value is exceeded. On the other hand, interference from, for instance, other radioactive sources might hamper proper interpretation of the data and cause false alarms.

Figure 8 shows the relative activity versus time from May 21, 1990 to December 31, 1991. Figure 9 shows the data from January 1, 1992 to December 31, 1992.

The figures show positive and negative spikes. In the period from October 8, 1990 to December 31, 1990, a new plant was under construction not far from the urea plant. The positive spikes observed during this period are due to radiography of field welds. The negative spikes, however, cannot be explained as yet. For the used data processing however, these spikes do not interfere.

Initially, at around July 16, 1990 the plant was down for a brief period, when the reactor-to-stripper line was flushed. This was done again in 1991 and late 1992. Increased levels of activity were measured during these three periods as there was no urea synthesis solution in the pipeline and, so, no absorption in the fluid. This is shown in the figure as relatively broad peaks.

A couple of weeks later, early 1992, the curve showed a stepwise loss of activity, which could not be explained. All system components were checked and even the detector was replaced. A temperature measurement had been added to the system in late 1991 in order to study the effect of temperature on the corrosion rate. Eventually, we found that the data processing section got upset on receiving faulty temperature values and so produced erroneous data. Omitting the temperature measurement solved the problem.

The shutdown period in May 1992 is easy to recognise by the higher level of activity. After the shutdown the level was somewhat higher than previously.

This difference is due to installation of the replacement detector: both the distance to the coupon and the detector sensitivity were different. However, this makes no difference since the measurement is a relative one.

The rough data in Figure 8 and Figure 9 can not be used directly for corrosion rate calculations. The data first were subjected to a smoothing program based on moving average. The corrosion rate is calculated from the decrease of activity during a period of time (after compensation for the natural decay). In Figure 9 the calculated slopes for three corrosion rates are shown.

A short measuring period yields a relatively large noise in the results. For the detection of active corrosion this causes no problem. The decrease in a period of, say two hours, is expected to be much larger than the scatter. However, for accurate measurements of the passive corrosion rate a much larger period is required. An accuracy of 10 μm can be obtained with a measuring period of three days.

Figure 10 shows the average monthly corrosion rates. Process conditions during the first six months may be assumed to have been constant; daily review of these conditions revealed no significant changes. Yet, the corrosion rate of the material was increasing. The explanation is that the passive oxide layer, which had been there ever since fabrication, had slowly broken down under the given process conditions. A less stable dynamic oxide layer was formed. This oxide layer is maintained by oxygen present in the process fluid. Variations in the process conditions are readily detectable in the case of passive corrosion, due to the dynamic nature of the oxide layer. Depletion of the oxygen in the urea synthesis solution would lead to active corrosion in very short time.

The next period we did see varying rates of passive corrosion. This was found to be due to changes in the carbamate flow from the melamine plant. An increased carbamate flow corresponds to an increase in corrosion rate.

During the May 1992 shutdown, the coupon was inspected in order to ascertain if the monitoring results were in agreement with the corrosion that had actually taken place. The pattern of attack found on the coupon appeared to correspond with that of the same, but non-activated, material at the top of the reactor. The measured wall thickness loss of the coupon was equal to the loss established by the NA technique. It is added here that the micrometer readings need to be corrected with respect to the surface topography of the coupon. The micrometer yields peak-to-peak readings whereas measurements of the radioactivity reveal integral material losses regardless of the surface condition.

Future Research

The software used in the NA monitoring technique is purpose-written. For commercial equipment the system can be simplified by replacing some of the software by hard software. It is further advantageous to integrate statistics in the software for easier and quicker interpretation.

In our applications the radioactive monitoring technique is applied to iron-based alloys. It might be interesting to investigate whether this technique is suitable for metals like titanium or non-metals.

Conclusions

1. Corrosion monitoring by neutron activation is well able to show the effects of changing process conditions on the corrosion performance of materials as far as overall corrosion is concerned. It is essential that the corrosion products be carried away by the process fluid. Passive corrosion increased on increase of the carbamate feed stream coming from the melamine plants.
2. Corrosion monitoring by neutron activation revealed passive corrosion of UNS S31603 material exposed to a urea synthesis process. Passive corrosion rates ranged from 50 to 200 $\mu\text{m}/\text{year}$. Active corrosion was not detected, nor did it occur, during the monitoring period.
3. A passive corrosion rate of 10 μm per year can be established in about three days. Active corrosion (at 10 to 30 mm/year) is expected to be detected within two hours.
4. The wall thickness loss of the test coupon measured by micrometer was equal to the loss established by the NA technique. Being highly reliable, this technique might allow plant operators to postpone plant turnarounds without compromising plant safety or performance reliability.

References.

1. R. de Jonge, F. Baraké and J. Logemann, "Corrosion and corrosion prevention in stainless steel urea plants," *Chemical Age of India* 26(1975)no.4: pp. 249-260.
2. J.F.M. Leerschool and J.C. Verhoef, "Corrosion Prevention in the Stamicarbon Urea Process," *Chem + Tech '80 International Congress (Symposium 3)*.
3. D.A.W. Bossus and R. van Sluijs, "Corrosion Monitoring by thin layer activation", *Proceedings of the 4th Conference on Radioisotope Application and Radiation Processing in Industry, Leipzig, DDR, 19-23 sept. 1988*.
4. D.J. Finnigan, K. Garbett and I.S. Woolsey, "The application of thin layer surface activation to the study of erosion corrosion behaviour," *Corrosion Science* 22(1982) pp. 359-372.

5. G. Notten, J. Thoelen, K. Verheesen and R. van Sluijs, "Neutron Activation for Real-Time Corrosion Monitoring in a High Pressure Process Plant", NACE, 13-18 sept. 1993, USA
6. J.A. Richardson, "Innovations in techniques for corrosion monitoring. Needs for advances in materials technology for process industries (Prof. Conf.), 29-31 Oct 1984, Atlanta, Georgia, 1985, pp. 200-218, 8609-72-0344.5.
7. D.E. Williams and J. Asher, "Measurement of low corrosion rates: comparison of a.c. impedance measurements and TLA activation methods," Corrosion Science **24**(1983): pp. 185-196.)

Table 1. Main differences between TLA and NA

	TLA	NA
Irradiated surface	beam, approx. 1 cm ²	no beam, whole surface
Irradiated layer thickness	approx. 25 - 300 μm	throughout
Useable in special locations, e.g. pipe bends	yes	no
Activity distribution	depending on particle and energy	homogeneous
Target elements in matrix	often high levels, e.g. Fe or Cr in S.S.	low levels, e.g. Co in S.S.
Suitable radionuclide formed on irradiation of S.S.	⁵⁶ Co T _{1/2} = 78 days	⁶⁰ Co T _{1/2} = 5.2 years

Table 2. Accuracy and lowest detectable corrosion rates for TLA and NA

Parameter	TLA	NA	Unit
Isotope	⁵⁶ Co	⁶⁰ Co	-
Activity	0.5	5	MBq
Wall thickness	5.0	20	mm
Transmission through walls	0.8	0.4	-
Gamma-radiation factor	0.046	0.035	(mR/h)/(MBq/m ²)
Efficiency	6000	6000	cps/(mR/h)
Distance r	0.15	0.15	m
Count rate at t=0	4900	18700	cps
Initial layer thickness	0.05	2	mm
Absolute accuracy at t=0, RA=100 %*			
Monitoring period			
T _m = 1 hour	36	730	nm
T _m = 8 hours	13	260	nm
T _m = 24 hours	7	130	nm
Minimum detectable corrosion rate at t=0, RA=100 %			
Monitoring period			
T _m = 1 hour	0.9	18.2	mm/year
T _m = 8 hours	0.04	0.8	mm/year
T _m = 24 hours	0.005	0.1	mm/year

* Minimum detectable change in layer thickness based on the activity level at the beginning of the monitoring period. At time is zero the relative activity (RA) is 100%

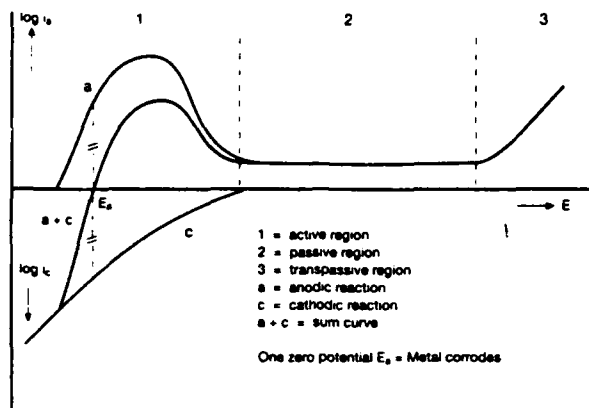


Figure 1a. Current/potential curve of stainless steel with active behaviour in ammonium carbamate

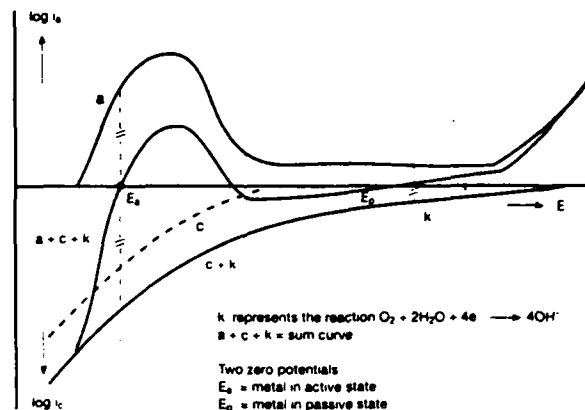


Figure 1b. Influence of oxygen on the current/potential curve

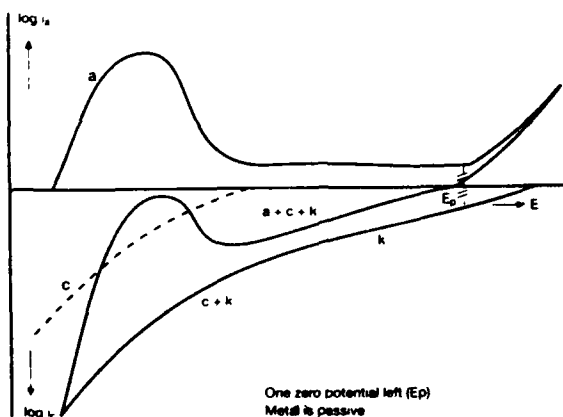


Figure 1c. Influence of an increase in oxygen on the current/potential curve

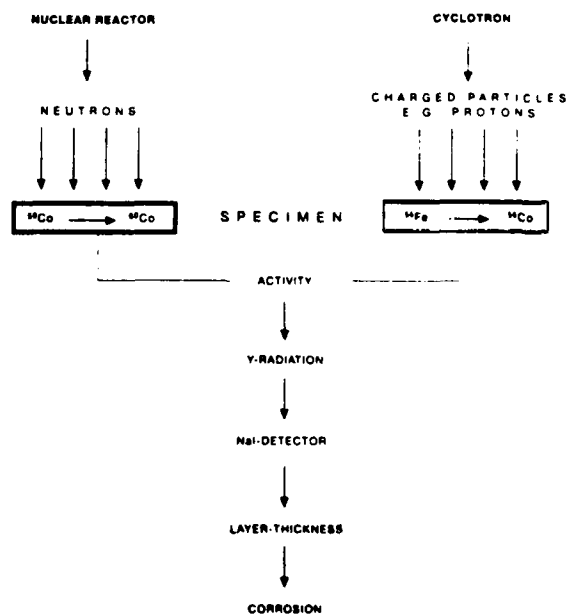


Figure 2. Schematic representation of corrosion monitoring based on TLA and NA

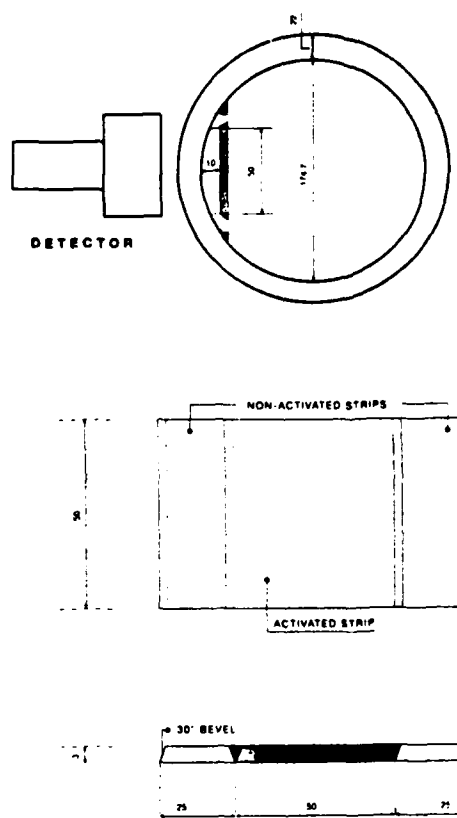
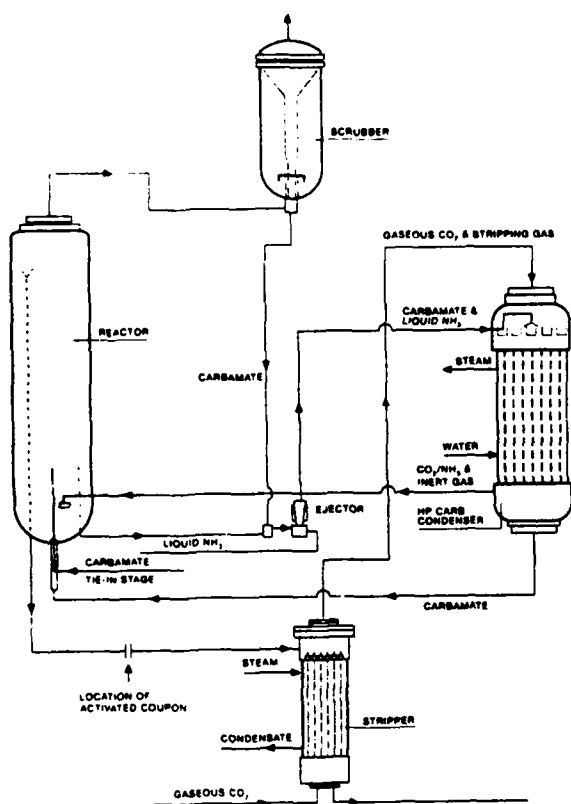


Figure 3. Urea stripping process and location of corrosion monitoring

Figure 4. Coupon mounting in pipe

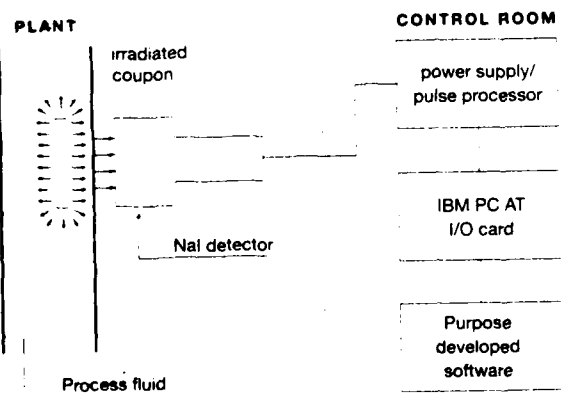


Figure 5. Schematic representation of corrosion monitoring setup

Figure 6. Corrosion monitoring assembly in plant

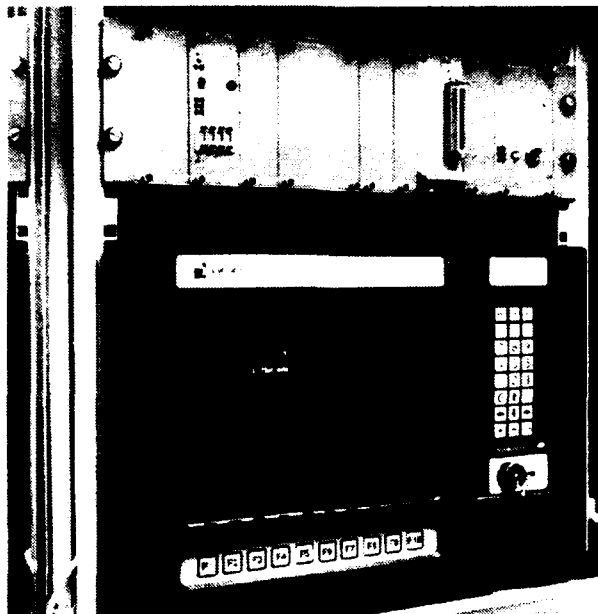


Figure 7. Corrosion monitoring assembly in control room

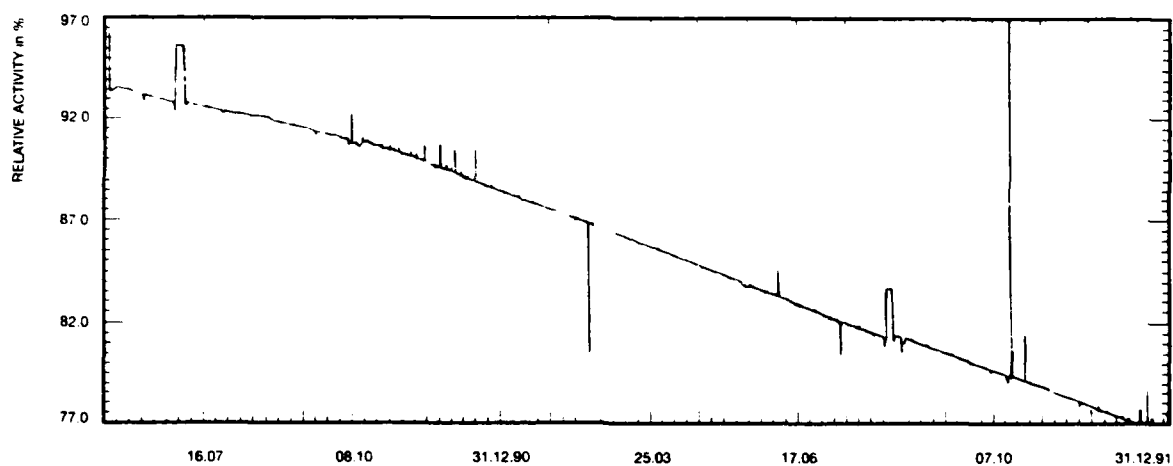


Figure 8. Relative activity versus time, 1990/1991

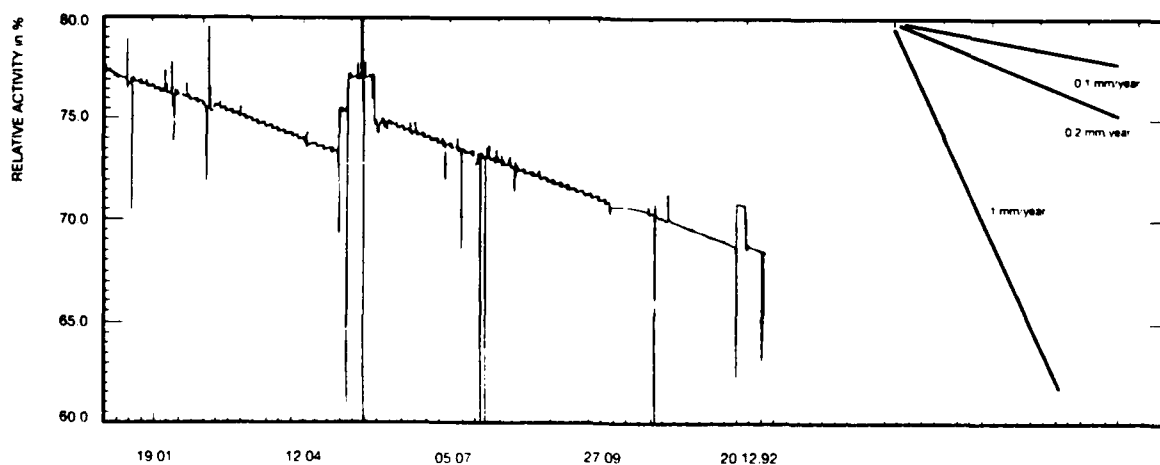


Figure 9. Relative activity versus time 1992; calculated slopes for three corrosion rates

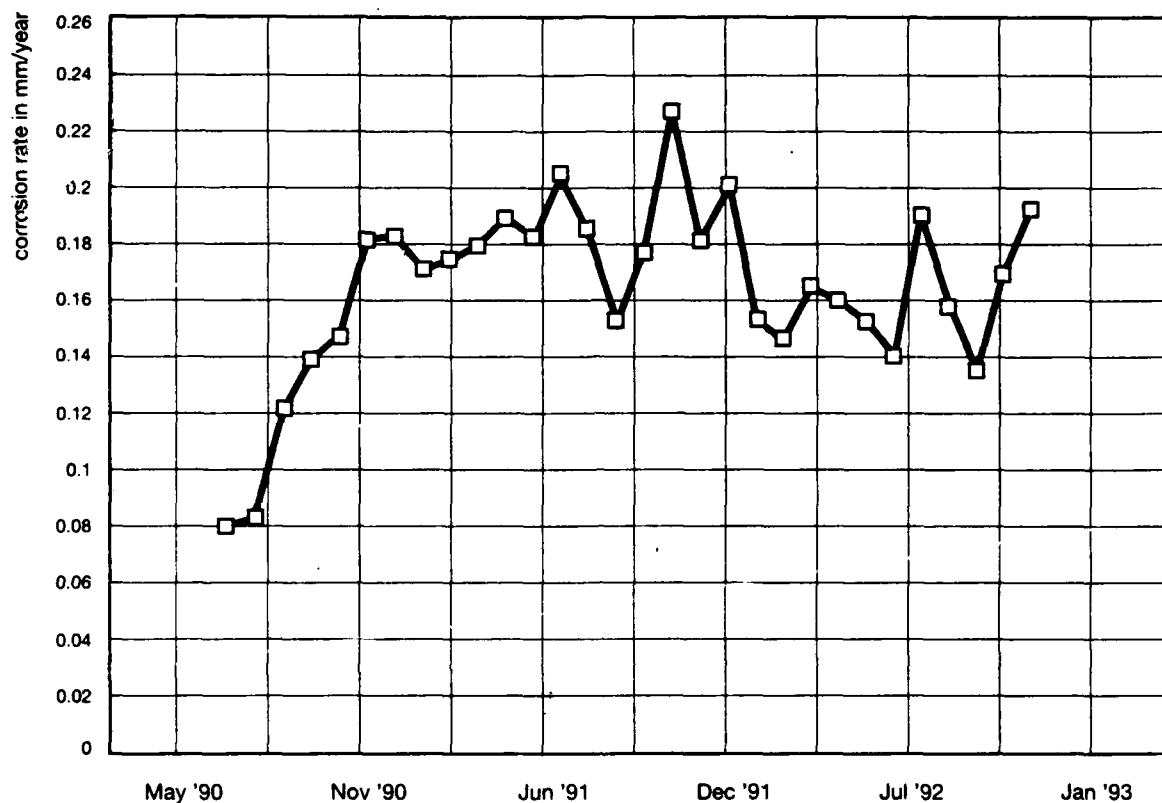


Figure 10. Average corrosion rate per month

Corrosion Upsets Are Probably More Costly Than You Know

Allan Perkins
Rohrback Cosasco Systems
11841 East Smith Avenue
Sante Fe Springs
California 90670
USA

Abstract

Traditional methods of measuring plant degradation, by ultrasonic thickness measurements or coupons, may provide adequate information on total material loss over an extended period. However, these methods frequently disguise the underlying corrosion dynamics story. Advancements in continuous on-line corrosion management systems have greatly improved the resolution and response to corrosion upsets.

In the chemical industries especially, it becomes increasingly apparent as more of these automatic monitoring systems are installed, that corrosion is anything but uniform. In many cases the "acceptable" corrosion rate may be 5 to 10 mils per year. In reality, 90% or more of the actual corrosion damage typically occurs with corrosion upsets of 50 - 100 mpy. Even values as high as 1000 mpy are not extraordinary. In this situation when corrosion upsets are relatively short, for example 60 mpy for two or three days, the average corrosion rate measured by a coupon or ultrasonics will disguise the true corrosion rate with an average corrosion rate number of 4 to 6 mpy.

When the time of upset condition can be pinpointed within hours or even minutes in some cases, it is possible to correlate this with the operating conditions, process chemistry, batch sequence or chemical treatment change that produced the upset.

Essentially we are talking about reducing corrosion rates at least an order of magnitude through identification, and reduction of the time when this rapid corrosion is occurring. This can have a major impact on process containment through corrosion control, and plant life extension.

This paper shows equipment that is available for this type of continuous corrosion management, and shows examples of upsets and actual plant applications.

Key terms: Process containment, Corrosion management, On-line corrosion monitoring, Corrosion upset detection, Corrosion detection sensitivity,

Introduction

The latest estimate from the United States National Bureau of Standards for the annual cost of corrosion in the United States alone is now \$220 Billion per year. The costs result from repair, replacement, treatment, downtime, cleanup, and fines etc. This is a substantial increase from the \$100 Billion of the previous estimate. However, much like the U.S. Federal Deficit it does not seem like real numbers, and possibly therefore does not receive the attention it deserves. Obviously, the numbers over simplify the problems of corrosion. Nevertheless, further investigation suggests that little has been done in terms of economic analyses of corrosion. More importantly, little has also been done in ways to provide management with return on investment calculations for corrosion monitoring and mitigation. For example, NACE is only now trying to prepare a document in their technical group in T-3C, and this is only in the early stages of development. Yet so far this document carries no reference to the economics, or return on investment, of monitoring methods for the detection of corrosion upsets, although such techniques are quite advanced. In reality, modern continuous monitoring methods frequently show that a corrosion problem is most frequently a series of corrosion upsets. With rapid response to the start of such upsets, an even greater contribution can be made to reducing the total corrosion occurring.

Measurement Frequency

Inspection versus On-line Monitoring

At first, the difference between inspection and on-line monitoring seems obvious. Inspection is only done occasionally, while on-line monitoring is done continuously. However, for corrosion monitoring methods, the division between the two becomes less and less obvious on further investigation. Even the fastest response on-line electrochemical technique of corrosion rate measurement is not truly instantaneous in the same sense as say measurements of temperature or pressure. The fastest corrosion rate measurement is the linear polarization technique. It typically has measurement times of two to ten minutes for a continuous on-line instrument.

In general, the electrochemical measurement methods are the nearest to being instantaneous because they are making measurements which are directly proportional to corrosion rate. Other methods of corrosion measurement generally determine remaining metal thickness. With metal thickness measurements, at least two measurements over some finite period of time are required to compute the average corrosion rate over that time.

The time between metal loss measurement may always be reduced of course, but the sensitivity and repeatability of each individual measurement limits this. As the time interval between measurements decreases, the accuracy of the corrosion rate measurement also decreases in an exponential fashion.

In essence, the key question becomes not the definition of inspection or monitoring, but the speed of response to a given corrosion rate change, versus the absolute accuracy of the measurement. On-line monitoring with a fast response technique relates to enhancing process containment by prevention. On-line monitoring with a slow response or by inspection methods relates more to predicting plant failure, but after possible considerable damage and loss of operating life.

Measurement Methods

Physical versus Electrochemical Methods

Although both physical and electrochemical methods are widely used, there is still some confusion and even myths about what the various techniques can and cannot do. This is particularly so in the real world plant environment, where many users are not corrosion engineers.

Metal loss measurement methods are universal in their application whereas electrochemical methods, though faster responding, must operate in a sufficiently conductive environment. In applications where there are multiple phases present, or only low water content, electrochemical methods become even less quantitative than normal because of variability in the effective electrode surface area. This variability can come from physical screening of the electrode area by non-conductive films, or in the case of low water content, or dewpoint areas from incomplete coverage of the electrodes and the area between the electrodes. A basic assumption of all electrochemical methods is a known surface area, since the output current signal is directly proportional to surface area.

Physical Metal Loss Measurement Methods. These are methods to determine metal loss from changes in a property of the material which relates to its physical geometry and may be summarized as follows:

1. Ultrasonics
2. Direct Electrical Measurements
3. Surface Activation and Gamma Radiometry
4. Corrosion Coupons
5. Electrical Resistance

Note that we have specifically omitted X-ray inspection here, in the sense that they do not provide a direct measurement. Any thickness measurements, when they are made at all, are derived from physical measurements on the film.

All the physical measurement methods measure the change in the physical geometry of the uncorroded metal, either on a sensing element, or directly on the plant

material. These methods may be used in virtually any environment, since they do not require a conductive media in which to operate. In addition, the conversion constants have much less variability than those for electrochemical measurements. However, corrosion rates must be determined by the change in metal loss over some finite period of time. The response time to corrosion rate changes depends on the sensitivity and frequency of measurements. The sensitivity of each method normally dictates the frequency with which measurements may sensibly be taken.

Electrochemical measurement methods. These methods all interact with electrical characteristics of the corroding surface when this can be achieved and may be summarized as follows:

1. Linear Polarization Resistance
2. Galvanic Current (Zero Resistance Ammetry)
3. Potential Measurement
4. Potentiodynamic Polarization
5. Electrochemical Impedance Spectroscopy
6. Electrochemical Noise

All the electrochemical measurement methods control either the potential or electrical current density across a metal and conductive fluid interface, and measure the other. Regardless of the exact method, all the measurements are made across the same corrosion surface and fluid interface. A vital requirement for the measurements is a sufficiently conductive fluid between the measurement electrodes and a known wetted surface area of the electrodes for determination of current density. Probably most sophisticated of these techniques for characterizing the response of a corrosion interface is Electrochemical Impedance Spectroscopy. The modeling of an equivalent circuit to match the measured response can be very helpful in understanding the corrosion mechanisms. It is also useful for calculating corrosion rates based on the equivalent circuit.

Physical Measurement on a sample versus the actual plant

The main differences in the physical measurement techniques are determined by their use either directly on the plant, or alternatively on an inserted probe or specimen. In either case, the location of any plant measurement, or location of a test specimen is critically important. It may seem obvious that you must measure where the corrosion is present and not where it is not. Yet frequently direct measurement methods miss bad corrosion areas. Probe test specimens are often located for mechanical convenience instead of corrosion severity, such as on the top of a gas pipeline instead of at the bottom where the water phase accumulates. The advantage of direct plant measurement is that it removes the question

of variations between the plant material and the material of the specimen. The disadvantage of the direct plant measurement is the reduced sensitivity and consequent loss of response to corrosion upsets as they occur.

Ultrasonic measurements give very good analysis if the measurements are made comprehensively in critical areas, a primary purposes being to pick pitting and localized corrosion. However, if only point to point measurement methods are used, pitted areas may be completely missed. The measurement sensitivity on normal ultrasonic measurements on say a one inch pipe wall is approximately 0.001" at best.

Direct electrical potential measurements on the pipe surface, with an externally applied large electrical current (sometimes called a fingerprint technique) also only have a sensitivity of 0.001" at best for general corrosion on a one inch pipe. These type of measurements do not have the resolution or discrimination of ultrasonics for detection of pitting and cracking.

With both of these direct measurement methods, a 10 mpy corrosion rate would take a period of five weeks to reach even the threshold of sensitivity of the technique. It would take considerably longer, typically ten times longer to be able to measure that rate with a tolerable accuracy.

Surface activation, corrosion coupons and electrical resistance are fundamentally more sensitive to metal loss because their measurement resolution is proportional to the specimen thickness, and their measurement specimen is much smaller than the typical one inch pipe wall. For example, an electrical resistance probe for an average 10 mpy rate would typically have a 5 mil span. With an instrument resolution of 1 in a 1000 this gives a resolution of 0.000005", i.e. approximately 200 time more sensitive than a direct measurement method. With this technique only 4.4 hours would be required to reach the threshold of sensitivity of the technique. To compute such a rate of 10 mpy would take approximately 44 hours.

Corrosion Upset Detection

In plant environments, where it is possible to use electrochemical methods, the most widely used electrochemical method is the linear polarization method. Figure 1 shows the graph produced from an LPR CORRDATA⁽¹⁾ logging system, shown in Figure 2 and 3, on a soda ash plant testing a special corrosion inhibitor change-out. Here readings are being taken at 30 minute intervals with a battery operated data logging unit. Between 11:30 am and 4:30 pm on Oct 2nd, 1992 the corrosion rate went from 5 mpy to 200 mpy.

However in most process plants it is not possible to use electrochemical techniques, and

(1) Registered Trademarks of Rohrbach Cosasco Systems

here the only effective rapid detection method is the electrical resistance metal loss technique. Figure 4 and Figure 5 show the 28 day graph of metal loss against time of a probe in a chemical plant. The system is part of an Integrated Corrosion Monitoring System (ICMS⁽²⁾) that continuously monitors a dozen points on the plant every five minutes. Figure 2 shows that the average corrosion rate for the 28 day period is 8.7 mpy. This is not an unreasonable corrosion rate and is the type of reading that would be obtained from a corrosion coupon. From Figure 4 it is apparent that the corrosion rate was almost exclusively a 57 mpy corrosion upset over a three day period from Aug 22 to Aug 25. With this system, these upsets are detectable within hours even when using the ER metal loss technique. The total metal loss in that three days was still only 0.0004 inch or about one tenth the thickness of a piece of paper.

These characteristics are much more common than they are often recognized to be. This is mostly because much of the monitoring is still done with coupons and other measurement systems which attenuate the effect of these upsets because of their slow response. We see the same effects in chemical plants, refineries, pipelines, pulp and paper, and nuclear applications.

Conclusions

In many plant applications, there is still frequently a tendency to think of THE corrosion rate, as though it is some constant value. This has been propagated to some extent by these long time scale measurements, and the idea of a target corrosion allowance for a design plant life. As continuous on-line real-time corrosion monitoring in plant environments grows, it is increasingly obvious that very few corrosive environments are at all constant. The largest proportion comprise various upsets or excursions. Developments in electronic monitoring equipment have made it much easier to observe these upsets, improve corrosion management, and assist plant life extension.

Although the enormous cost of corrosion is now estimated to be \$220 billion per annum in the USA alone, it is incredible to see that the total amount spent on in-plant corrosion monitoring equipment worldwide we estimate is less than \$30 Million. It really appears that the economics of effective monitoring has not been put effectively to management in the economic justification form that business management understands. As economics is the basis for nearly all major business decisions, the onus on the corrosion engineer is to develop and provide these economic justification methods for corrosion monitoring and mitigation techniques. Even under the most conservative assumptions, there must be more than sufficient justification to be able to invest in more and better monitoring equipment. We need to prove how much these systems can save instead of just focusing on how much they cost.

(2) Registered Trademark of Rohrback Cosasco Systems

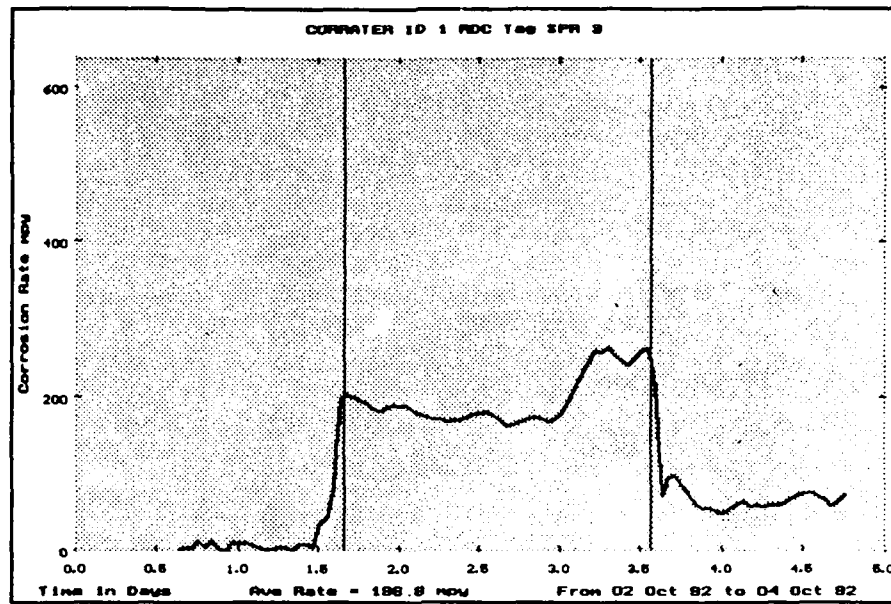


Figure 1 LPR Measurement on Data Logging System

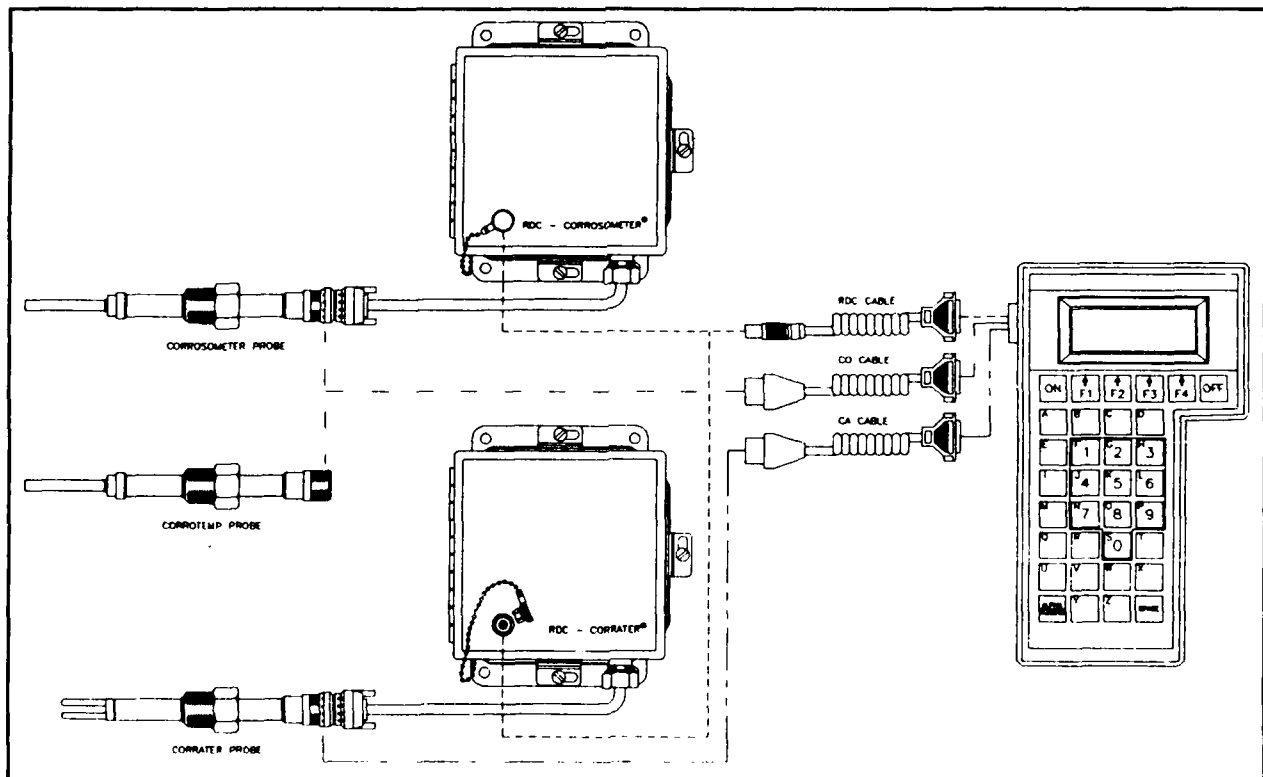


Figure 2 Data logging system at plant end

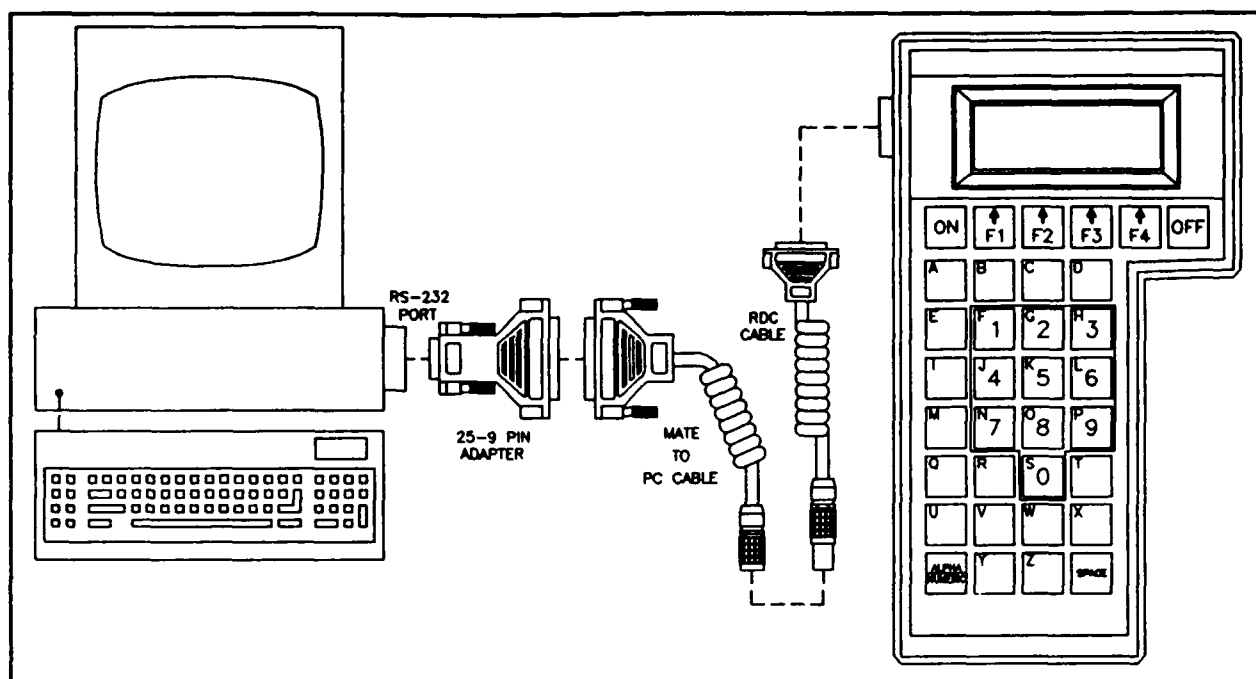


Figure 3 Data logging system at P.C. end

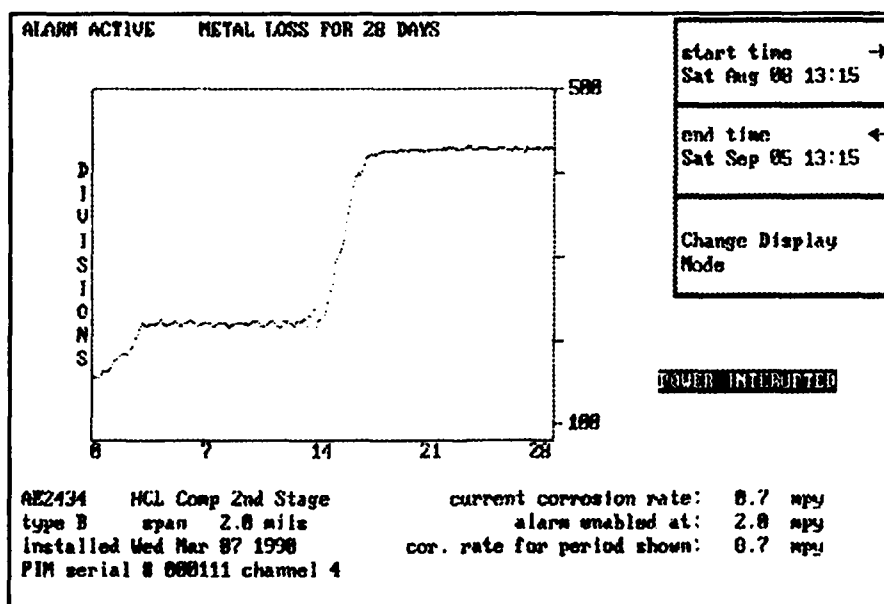


Figure 4 Display of a corrosion upset

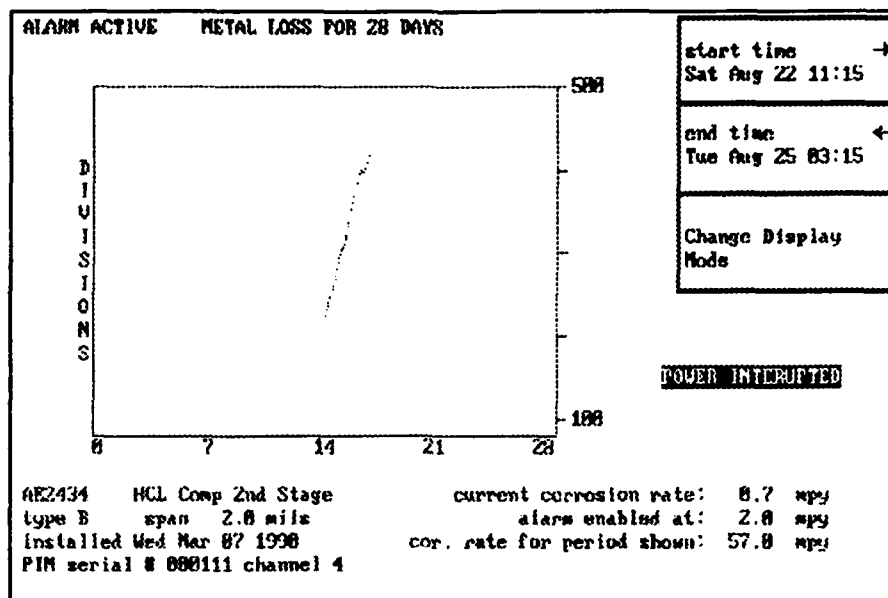


Figure 5 Upset time and rate

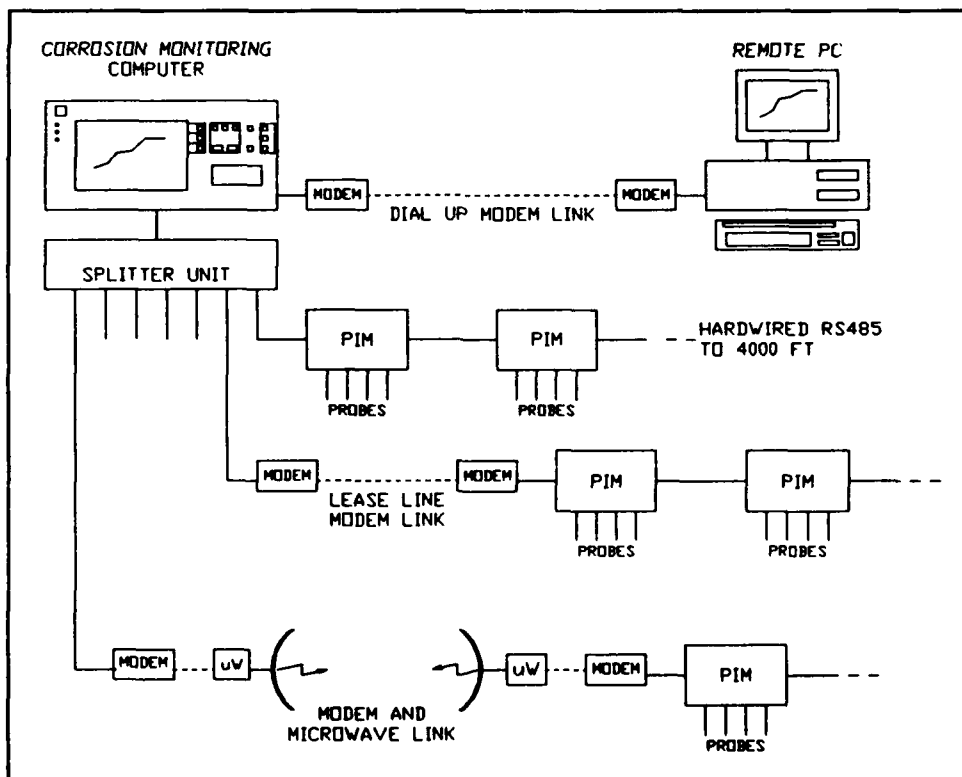


Figure 6 Continuous on-line real time corrosion monitoring

Automated Ultrasonic Corrosion Mapping

C I K Sinclair BSc
NDT Engineer
TWI
Abington Hall
Abington
Cambridge
CB1 6AL UK

Abstract

The corrosion of ferritic steel is a phenomenon which affects many industries and requires the outlay of significant capital investment. Corrosive environments may range from simple atmospheric exposure to the more aggressive conditions of marine service or process industries. All industrial areas are susceptible including power generation, transportation, food processing and oil and gas sectors. A good example is the corrosion of tank floors used in the petrochemical industry. Monitoring for the onset of corrosion and periodically determining its extent allows greater efficiency in the use of preventative measures and more accurate planning for plant maintenance and replacement.

This presentation will describe the nature of the problem from the point of view of NDT and will briefly assess the applicability of the main NDT methods to the detection and monitoring of corrosion, i.e. penetrant, magnetic particle, eddy current, radiography and ultrasonic testing methods.

Attention will then be focused on the use of automated and semi-automated ultrasonic techniques to map corrosion. The necessary attributes of the instrumentation and the relative merits of differing data acquisition techniques will be discussed and examples of ultrasonic images from corrosion mapping will be given.

Introduction

Corrosion is a detrimental process which incurs a massive cost through enforced plant replacement, preventative measures, monitoring, failures and reduced efficiency. However, the American National Bureau of Standards (NBS) estimated in 1985 (1) that 15% (or \$25 Billion) of their estimate of the total economic loss due to corrosion was avoidable had state-of-the-art practices been employed. The implication of course is that through the utilisation of advanced materials of construction, combined with accurate reliable and non-invasive monitoring techniques, significant cost savings can be realised.

A discussion of advanced materials is outside the scope of this paper, which will concentrate on comparing a selection of commonly used non-destructive testing (NDT) techniques suitable for monitoring corrosion, focusing ultimately on automated ultrasonic corrosion mapping. It is convenient at this point to make some definitions of what forms

of corrosion will be discussed and what will be meant by monitoring; both from the point of view of NDT:

- A) **Wastage.** This is a general volumetric thinning of material, e.g. "rusting". The affected surface is rough and cratered. It is monitored by detecting the wall thinning and it is quantified by specifying the affected surface area and remaining wall thickness.
- B) **Pitting.** This takes the form of isolated volumetric voids which break the affected surface. It is monitored by detecting each pit and is quantified by specifying the remaining wall thickness.
- C) **Hydrogen induced cracking¹ (HIC).** This manifests itself as a planar buried discontinuity oriented predominantly parallel to the vessel's wall. It appears "stepped" viewed from the side (Figure 1).
- D) **Stress corrosion cracking (SCC).** This is found mainly near welds where residual stresses occur. Each crack is relatively small, tight and jagged breaking the affected surface to which they are oriented predominantly normal.

NDT Techniques

It is not possible in this paper to describe all the techniques or all the different variations applicable to the monitoring of corrosion. The discussion below describes in brief the various techniques and their pertinent characteristics. Table 1 summarises this discussion.

- A) **Visual.** In conjunction with a physical dimensional survey, this is perhaps the simplest and most readily understood form of NDT for corrosion monitoring. Its main disadvantage is that access is required to the corroded surface. If that surface is inside or if it is under lagging then it may not be economically viable to gain access.
- B) **Penetrant Testing (PT).** This is a technique by which visual inspection can be enhanced by using a dye to reveal the presence of surface-breaking cracks such as SCC (2). Clearly, access is required to the corroded surface which must be dry and in good condition. Any abrasive preparation may peen-over the crack's open end and thus precluding penetrant testing. Being essentially a visual technique, PT is unaffected by material type and requires relatively little operator training/experience.
- C) **Magnetic Particle Inspection (MPI).** Like PT, MPI enhances visual inspection by using magnetic phenomena to reveal the presence of cracks such as SCC which are surface breaking or very near surface. Unlike PT however, MPI benefits from abrasive surface preparation, which usually reduces the occurrence of "false-calls", and can be applied underwater. Its main limitation is that only magnetic materials (ferritic rather than austenitic steels) can be inspected by MPI (3). Further, a medium level of operator training/experience is required.
- D) **Magnetic Flux Leakage.** This technique exploits the same principle as MPI in that a magnetic field is induced in the inspected component's surface which, in the vicinity of a near-surface flaw, will "leak" out of the surface. However, rather than use magnetic particles and visual methods, inductive coils and/or Hall-effect sensors are used to detect the "leaking flux" that is indicative of cracking. The technique is therefore more rapidly applied than MPI and can more easily be automated. Furillo and Polk (4) report the application of this technique to the inspection of above-ground storage tank floors for soil side corrosion. Applying the

technique from within the tank means that the sensitivity at the soil-side of the tank floor will be rapidly reduced with increasing floor thickness. However, the technique has been shown to be effective at floor thicknesses of 6mm. The technique is poor for determining the extent of any wastage, pitting or cracking because the degree of flux leakage is dependent upon many other factors such as flaw geometry, variations in permeability and variations in coating thickness (such as paint or liners). Although the technique can be applied rapidly using manually propelled scanning assemblies, the technique is fairly specialised and the availability of services relatively limited.

- E) **Eddy current testing (ECT).** This technique is not dissimilar to the magnetic flux leakage techniques above. However, rather than induce a magnetic field in the material, an electrical eddy current is induced by placing a coil in proximity to the component's surface which carries an alternating electric current. Changes in the material's conductivity, caused by wastage, pitting or cracking, are sensed by the same or similar coils. As this technique uses conductivity as its measurand it is only applicable to conducting materials. Further, variations in permeability tend to have a greater effect than variations in conductivity on the induced eddy currents. Therefore, the technique is more easily applied to non-magnetic materials such as austenitic steel, copper and aluminium. The technique has been used extensively in industry for the detection of wall-thinning, pitting and SCC in heat-exchanger tubing (5), though the use of multi-frequency "mixing" techniques for estimating the through-wall extent of any flaws requires a relatively high level of training and expertise.
- F) **Radiographic Testing (RT).** This technique is termed volumetric because it is sensitive to buried flaws. It is ideally suited to the detection of material loss such as wastage and pitting but will be insensitive to HIC which will be oriented perpendicular to the radiation beam. The technique will also be fairly insensitive to SCC as they are so tight and small. One advantage of RT is that the resultant radiograph provides a permanent record of the inspection from which the affected area can be determined though no estimate of the through-wall extent (or height) of any flaws can be made. The main disadvantages associated with RT are that access may be required to both sides of the corroded wall and that ionising radiation is inherently hazardous to health. Although operation of RT equipment does not require too great a level of training, interpretation of radiographs requires considerable experience and a fully trained and certified radiation protection supervisor (RPS) must be available during testing (6).
- G) **Manual Ultrasonic Testing (UT).** Whereas RT is a through-transmission technique, UT is more often a reflection or pulse-echo technique. Hence, not only is UT a volumetric technique, but the range information that is available allows an estimate of the through-wall position and height of flaws to be made. The technique relies on the transmission and reception of acoustic pulses in a direction (or beam angle) relative to the scanned surface which can be selected. Popular beam angles for manual UT are 0° (normal to the scanned surface) 45°, 60°, 70° and 90° (the so called "creep wave" which is concentrated on the scanned surface just in advance of the probe). 0° or "straight beam" probes are used for detecting wastage and pitting from the opposite surface and HIC from either surface while angled beam probes are used for detecting SCC from the opposite surface (45°, 60°) or the corroded surface (70°, "creep wave"). Obviously, UT relies on there being efficient acoustic coupling between the probe and the component. This

requires a liquid couplant and reasonably good surface condition. Manual UT flaw detectors display range and amplitude information in the form of an A-Scan (Figure 2.) from which the operator determines whether indications are of sufficient amplitude to be recordable and if so determines their range. Through a process of "plotting-out" these indications and analysing their echodynamic characteristics it is possible to determine the nature, length, height, position and orientation of flaws in the component. Straight beam scanning can be simplified in that the range to indications (indicative of remaining wall thickness) is of more importance than the amplitude. Indeed, to meet the demand for simple-to-operate ultrasonic flaw detectors for use underwater (offshore) for corrosion monitoring, compact instruments with digital thickness readout have been developed (7).

The manual application of angled beam scanning for the detection of SCC is time-consuming and laborious requiring a high degree of training and experience from the operator who must assess each significant indication at the time of scanning (regardless of the local environment which may be quite harsh) then report them in some written form some time afterwards. Thus, the results of manual UT are quite subjective and may vary significantly from one operator to another. The only assurance that the client has that coverage has been achieved and all unacceptable flaws have been reported, is that the operator is certified in accordance with a nationally approved scheme and that the procedure followed was in accordance with a national standard for manual UT. In other words, the client is totally dependent upon the integrity and competence of the UT operator. Unfortunately, there are no safeguards against operator fatigue and simple human-error.

H) **Automated UT.** The fundamental difference between automated and manual UT is that with automated UT, probe position is measured in addition to ultrasonic amplitude and range. Further, each of these properties are recorded by the system, processed and displayed in a way which allows the operator to interpret the indication some time after scanning. This relieves the operator of the burden of interpreting each indication at the time of its detection and gives automated UT these immediate advantages over manual UT:

- A much larger area can be scanned in a given time.
- A finer resolution scan (in terms of probe position) can be accommodated.
- There is a much reduced risk of inadvertently overlooking significant indications.
- The resultant image produced allows the operator to dismiss large areas of spurious "noise" and geometric echoes at once rather than taking note of each indication breaking the timebase on the A-Scan as the manual operator does. This has important implications when testing "grainy" materials such as stainless steels.
- A hard-copy print-out can be obtained of the image thus providing evidence that coverage has been achieved.
- Hard copies provide a "finger-print" of the component against which subsequent automated inspections (carried out to exactly the same procedure) can be compared allowing the spread (over time) of corrosion to be monitored.

Automation also allows the scanning of a number of probes at once thus increasing the probability of detection of flaws and reducing the occurrence of "false-calls". It also allows the use of special probe configurations for the detection and sizing of cracking

such as delta and time-of-flight diffraction (TOFD) (Figure 3). The non-linear relationship between range and depth that is characteristic of TOFD can be automatically corrected by the system.

A major disadvantage of using automated UT techniques is, that in Europe, there are no national standards governing methods and no national certification schemes to qualify those writing procedures and working to them. Consequently, clients often have to resort either to "track-record" or very costly "round-robin" validation exercises to select NDT contractors and to justify their procedures. Unfortunately, this lack of regulation can often lead to one of the main advantages of automated UT being lost: its potential for outstanding repeatability which is essential for periodic corrosion monitoring.

Automated Ultrasonic Corrosion Monitoring

The mode of operation of the equipment will depend largely on the type of corrosion which is to be detected and/or sized.

- A) **Amplitude mode.** If the system is required to detect SCC then angled beam probes will be used, as for manual UT, and amplitude and range measurement will be equally important ultrasonic measurements. In general, each indication recorded will be assigned a colour (pixel, letter or number) in proportion to its amplitude and will be positioned automatically (the software taking care of beam angle and probe skew) in a 3-dimensional "part". This "part" represents a volume of the component under test and the usual way to image it is in 3 orthogonal views described (8) as the B,C and D scans. The C-Scan is a top view, the B scan an end view and the D-Scan a side view (Figure 4). With many instruments, the B, C and D scan views represent slices through the "part". The control of cursors allows the interpreter to step through the "part" and view each slice. However, this requires that data be stored for every block comprising the "part's" volume; i.e. for a "part" 1000mm x 250mm x 40mm scanned with a 5mm probe-position resolution and with 1mm through-wall resolution there will be 400,000 blocks of data for each probe. In a special case, called P-Scan ("Projection" Scan), the volume of data is reduced by arranging for the B, C and D scans to represent projections of all the largest amplitude indications onto the outer surfaces of the "part". In this case, data is stored for every block comprising the surface area of the "part's" top, side and end; i.e. for the above "part" there will be 20,000 blocks of data for each probe. Clearly, this represents a significant reduction in data requiring processing and storage. An example of a P-Scan image (amplitude mode) of a component susceptible to SCC is shown in Figure 5; (the "echo views" represent histograms of amplitudes across the relevant views).
- B) **Time-of-flight mode.** If the system is required to detect wastage, pitting and HIC then straight beam probes may be used and range becomes more important a measurement than amplitude. This range measurement is often termed the time-of-flight of the ultrasonic pulse and the flaw detector's timebase is calibrated to measure it in units of thickness, (mm or inches). Manual UT for corrosion monitoring is often limited to a sequence of thickness measurements taken at positions marked-out on a coarse grid on the surface of the component resulting in a tabulated numerical indication of remaining wall thickness. Automating this process allows these measurements to be made on a far finer grid thus increasing significantly the probability of detection of isolated corrosion pits (7). In general,

each indication recorded will be assigned a colour (pixel, letter or number) in proportion to its time-of-flight or thickness and will be positioned automatically in a 3-dimensional "part" as above. However, unlike in amplitude mode, in time-of-flight mode, the C-Scan view conveys all the relevant information. This view is often termed the T-Scan (Thickness Scan). Figure 6 shows a T-Scan image of a corroded "part" of a ship's hull. The side view and end view represent histograms of thickness across the relevant surface, i.e. the inner surface profile along the cursors. In this case the T-Scan represents projections of all the minimum thicknesses onto the top surface.

Similarly, Figure 7 shows a T-scan image of a component which has suffered from HIC. Notice the change in "level" along the length of the image indicative of a 'stepped' profile which is characteristic of HIC.

- C) **Position measurement.** To produce a C-Scan image, regardless of whether the flaw detector is in amplitude or time-of-flight mode, it is necessary to encode the position of the probe into mutually perpendicular axes in the plane of the scanned surface.

If the component has a relatively simple geometry (such as a pipe, plate or hemispherical dome) then a mechanical scanner can be attached to the component by means of straps, vacuum cups or magnetic wheels (Figure 8). The probe or probes are then traversed, usually in a raster pattern, in accordance with the required positional resolution. The position of the probes at any instant is acquired by measuring the value of two electrical encoders coupled to the probe assembly by some linear mechanical link.

If the component has a complex geometry (reducing elbow, around fixtures etc) it may be impractical to attach a manual scanner like the one in Figure 8. To overcome this limitation there are a number of special commercial systems on the market two of which are described briefly below:

- ANDSCAN (9). This system utilises a scanning-arm assembly the base of which is fixed by vacuum cups to some convenient surface near to that requiring to be scanned. The probe is manually scanned at the end of an arm which is free to rotate and slide at the base assembly and there is some vertical freedom to aid compliance. The rotary and sliding axes are encoded and the software converts the scanner's polar co-ordinates to the image's cartesian co-ordinates.
 - SEESCAN (10). This system utilises a camera which is directed at the surface of the component under test. The probe has a source of light attached which is clearly resolvable on the camera's video image against the background of the component's surface. As the probe is scanned, a videoprocessor algorithm is applied to track the spot of light and its "X" and "Y" cartesian co-ordinates are passed to the flaw detector part of the system where they are used to position ultrasonic data on the resultant C-Scan image. In theory, any automated flaw detector system could be linked to a camera system in this way as the video processor emulates a pair of mutually perpendicular encoders provided that the videoprocessor output is scaled and coded in a way which is compatible with the relevant flaw detector.
- D) **Calibration.** Whether the flaw detector is used in amplitude or time-of-flight mode, it is important to set some reference sensitivity. In amplitude mode, this is normally done by following the same procedure as for the calibration of manual UT flaw detectors except that the time varying gain (or distance amplitude correction

- DAC) is automatic. In time-of-flight mode, it is normal to set the reference sensitivity against a single reflector (such as a flat bottom hole - FBH) at a depth equal to the wall thickness of the component under test. For the detection of pitting, the scanning sensitivity requires to be just high enough to avoid grain-noise or "grass" being recorded on the T-Scan. A typical level might be approximately 6dB above "grass". For the detection and identification of HIC and other laminations, the scanning sensitivity requires to be much lower. A typical level might be equivalent to setting the second back-wall echo (BWE) to 100% full screen-height (FSH). Automated flaw detectors normally allow the user to create more than one image from a given probe which in turn allows the concurrent acquisition of data at different sensitivities from a single probe.

Timebase calibration must be performed using the same criterion as the system's software. If the system measures time-of-flight to an echo pulse's leading edge, then the probe-delay must be established by measuring between consecutive pulse edges. If the delay were to be established to the pulse's peak but the software records time-of-flight to the pulse's leading edge then significant errors can be introduced because the wavelength of ultrasonic signals are relatively large: (e.g. a 4MHz compressional wave pulse has a wavelength in steel of approximately 1.5mm).

Position calibration is usually very simple with modern automated ultrasonic flaw detectors. The procedure usually requires the operator to "zero" the system at some datum then to move the probe(s) to some other position having entered either the coordinates of the second position (relative encoders) or the direction of travel between the datum and the second position (absolute encoders) with respect to the component under test. The flaw detector's software is thereafter "aligned" and the resultant "part" will resemble the actual component.

Concluding Remarks

If corrosion were to occur only at accessible areas of plant, and leaks and failures could be tolerated, then there would be little demand for complicated NDT systems and procedures. However, in reality, corrosion occurs where access to the corroded surface is costly or where man-access may be hazardous. At the same time, there is increasing legislative pressure to prevent leaking due to its inherent impact on the environment. Consequently, there is an increasing market for rapid, objective, non-invasive, accurate and highly repeatable NDT procedures for detecting the onset of corrosion, determining the type of corrosion and monitoring its spread over time.

Automated UT techniques are not the be-all and end-all of corrosion monitoring but do offer a viable alternative to many of the currently employed techniques. Automation can reduce the time to perform an inspection, can reduce the number of personnel required to perform the inspection, can provide a means for recording results and can increase repeatability; all of which add up to potential cost savings and increased confidence in NDT as a means of corrosion monitoring. Of course, there is a down-side. The specification of automated equipments, the methods for the application of automated UT and the certification of personnel are not currently addressed by national standards or training schemes.

Another distinct advantage of automated UT corrosion mapping is that resultant data may ultimately be automatically assessed using a fracture mechanics approach to predict very rapidly the integrity of the component. For example, the ASME 'B31G' (ii) or 'RSTRENG' (13) techniques could be applied in the case of piping.

References

1. ASTM Special Technical Publication 908, "Corrosion Monitoring in Industrial Plants using Non-destructive Testing and Electro-chemical Methods", ASTM, ISBN 0 8031 0471 5.
2. BS 6443: 1984, "Method for penetrant flaw detection", British Standards Institution.
3. PD 6513: 1985, "Magnetic particle flaw detection", British Standards Institution.
4. Furillo, F T and Polk, C J, "Tank Bottom Inspection Methods", Presented at 2nd International Symposium of Above Ground Storage Tanks, sponsored by the Materials Technology Institute of the Chemical Process Industries", 14-16 January 1992, Houston, Texas, USA.
5. BS 3889: Part 2A: 1986, "Non destructive testing of pipes and tubes - automatic eddy current testing of wrought steel tubes." British Standards Institute.
6. HMSO, "Ionising Radiations Regulations SI 1985 No. 1333", ISBN 0 11 057 3331.
7. Edwards G R, "T-Scan aids marine corrosion inspection", Welding Institute Bulletin March/April 1990, pp 34-37.
8. IIW, "Automated Ultrasonic Inspection of Welds - Guidance on its merits, performance requirements, selection and applications", BINDT, ISBN 0 903132 15 X.
9. Wells Krautkramer sales literature. "ANDSCAN", Castle Vale Ind Estate, Sutton Coldfield, West Midlands, B76 8AY, UK.
10. Sonomatic Ltd Sales Literature. "SEESCAN", 20 Rivington Court, Hardwich Grange, Woolston, Warrington, WA1 4RT, UK.
11. ANSI/ASME B31G, "Manual for determining the remaining strength of corroded pipelines", ASME 1991.
12. Andrews R M, "Pipeline corrosion-assessing the damage", Welding Institute Research Bulletin, November/December 1992, pp 124-126.

Table 1 Summary of NDT techniques and their applicability for corrosion monitoring

Technique	Detect?				Quantify?				Applicable under water?	Remove (thin) coating?	Access Required	Applicable steel
	Wastage	Pitting	HIC	SCC	Wastage	Pitting	HIC	SCC				
Visual	Y	Y	N	U	Y	N	N	U (2)	Y	Y	C	F and A
PT	N	Y	N	Y	N	N	N	Y (2)	N	Y	C	F and A
MPI	N	Y	N	Y	N	N	N	Y (2)	Y	N	C	F
Mag. Flux. Leak.	Y	Y	N	Y	N	N	N	N	U	N	C or O (3)	F
ECT	Y	Y	N	Y	U	U	N	U	Y	N	C or O (3)	F and A
RT	Y	Y	N	N	Y (1)	N	N	N	U	N	C and O (4)	F and A
Manual UT	Y	U	Y	Y	Y	Y	Y	Y	Y	N	C or O	F and A
Auto UT	Y	Y	Y	Y	Y	Y	Y	Y	Y	N	C or O	F and A

Key: Y = yes
N = not usually
U = under special circumstances

C = corroded surface
O = opposite surface

F = ferritic
A = austenitic

Notes: 1. Area only
2. Length only
3. Limited thickness
4. For SWSI technique

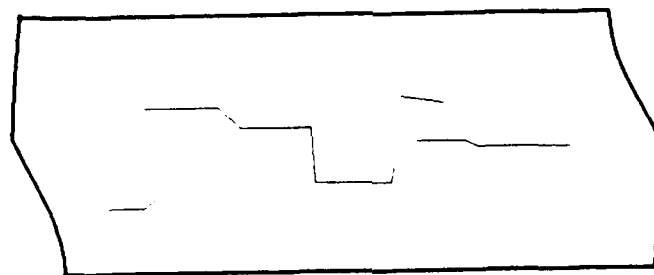


Figure 1. Hydrogen induced cracking (HIC).

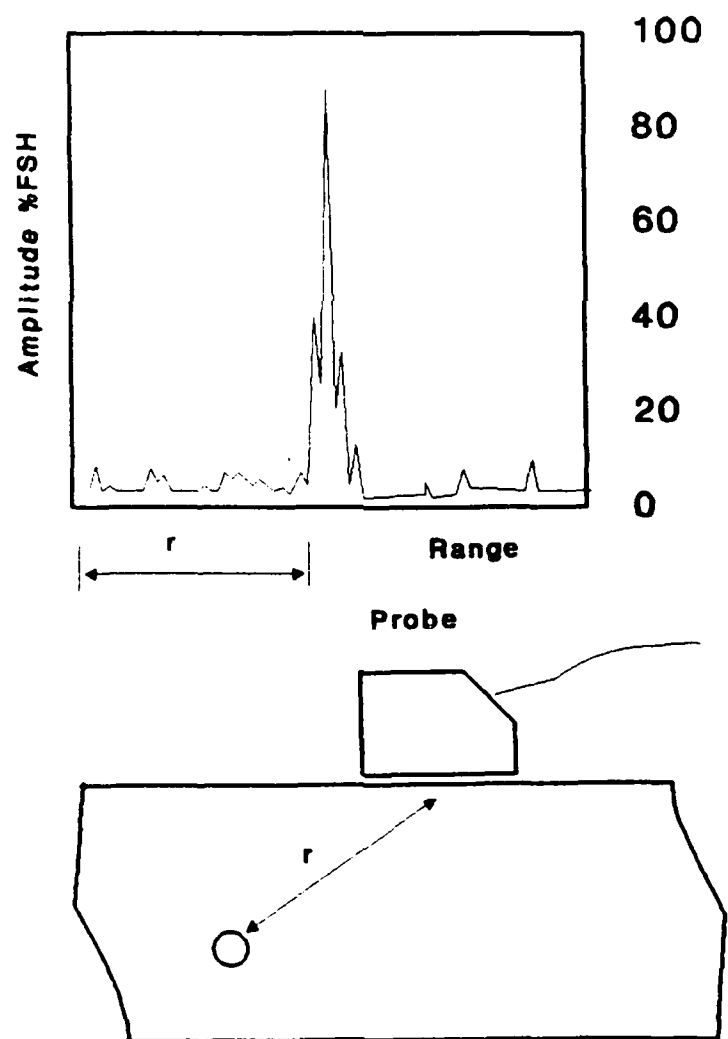
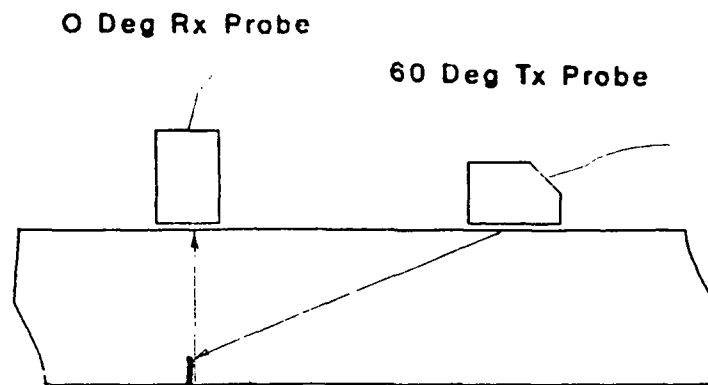


Figure 2. Manual UT A-Scan display



a) "Delta"

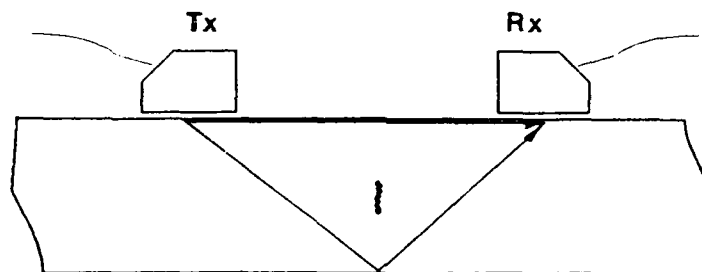


Figure 3. Special probe configurations

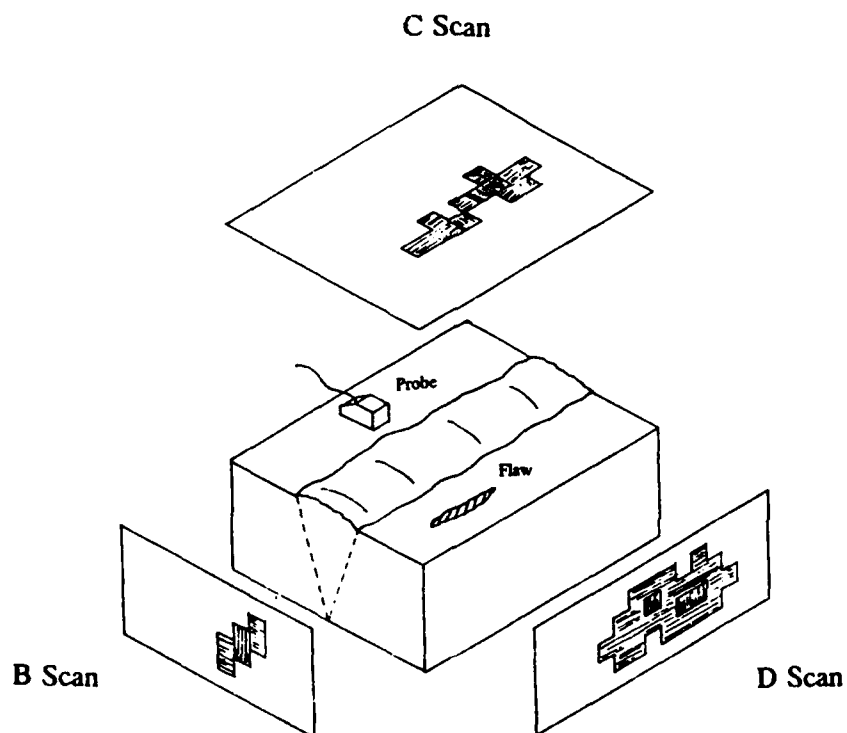


Figure 4. B.C and D-Scan definition.

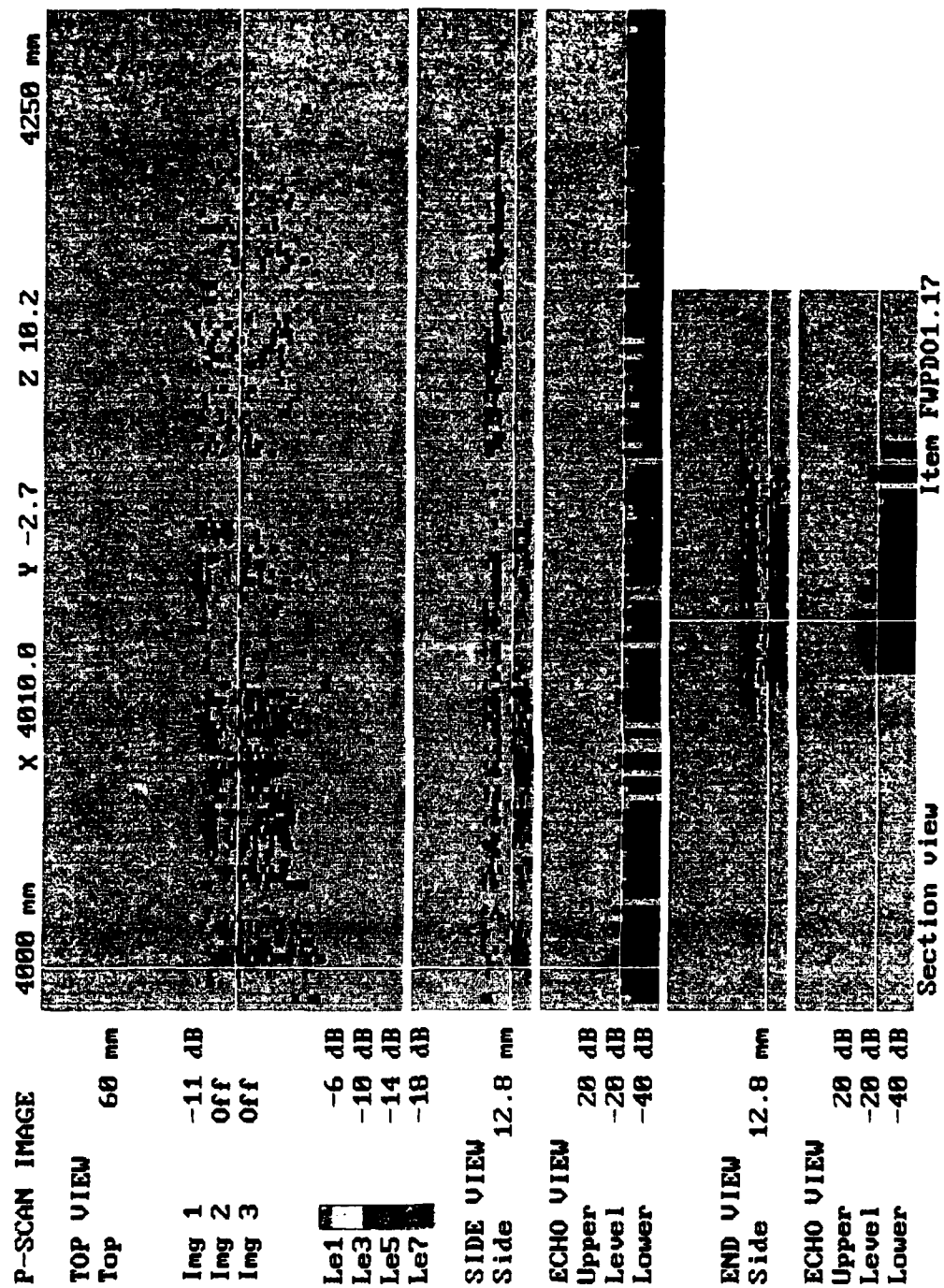


Figure 5. P-Scan image of component susceptible to SCC.

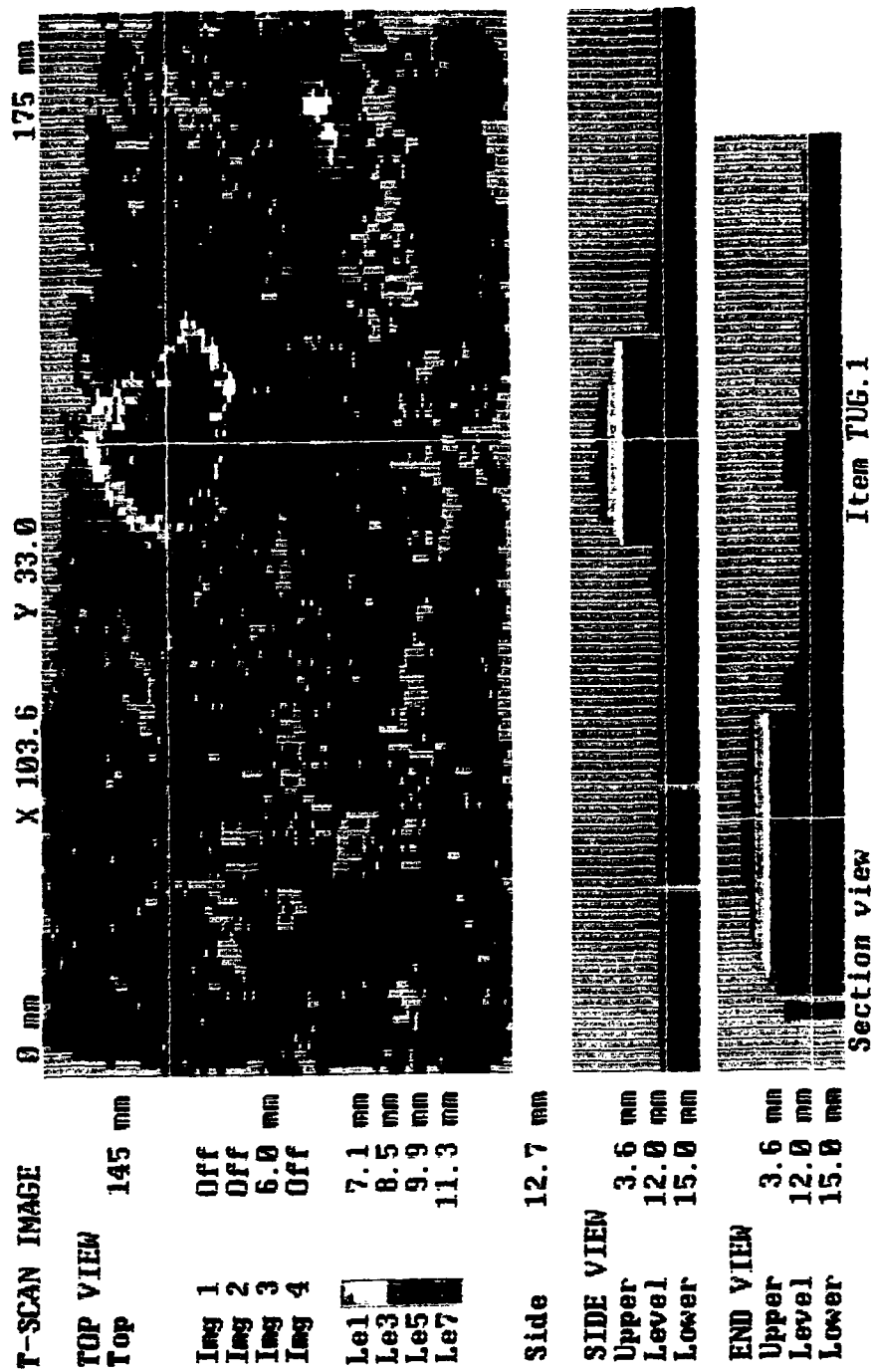


Figure 6. T-Scan image of a corroded section of ship's hull.

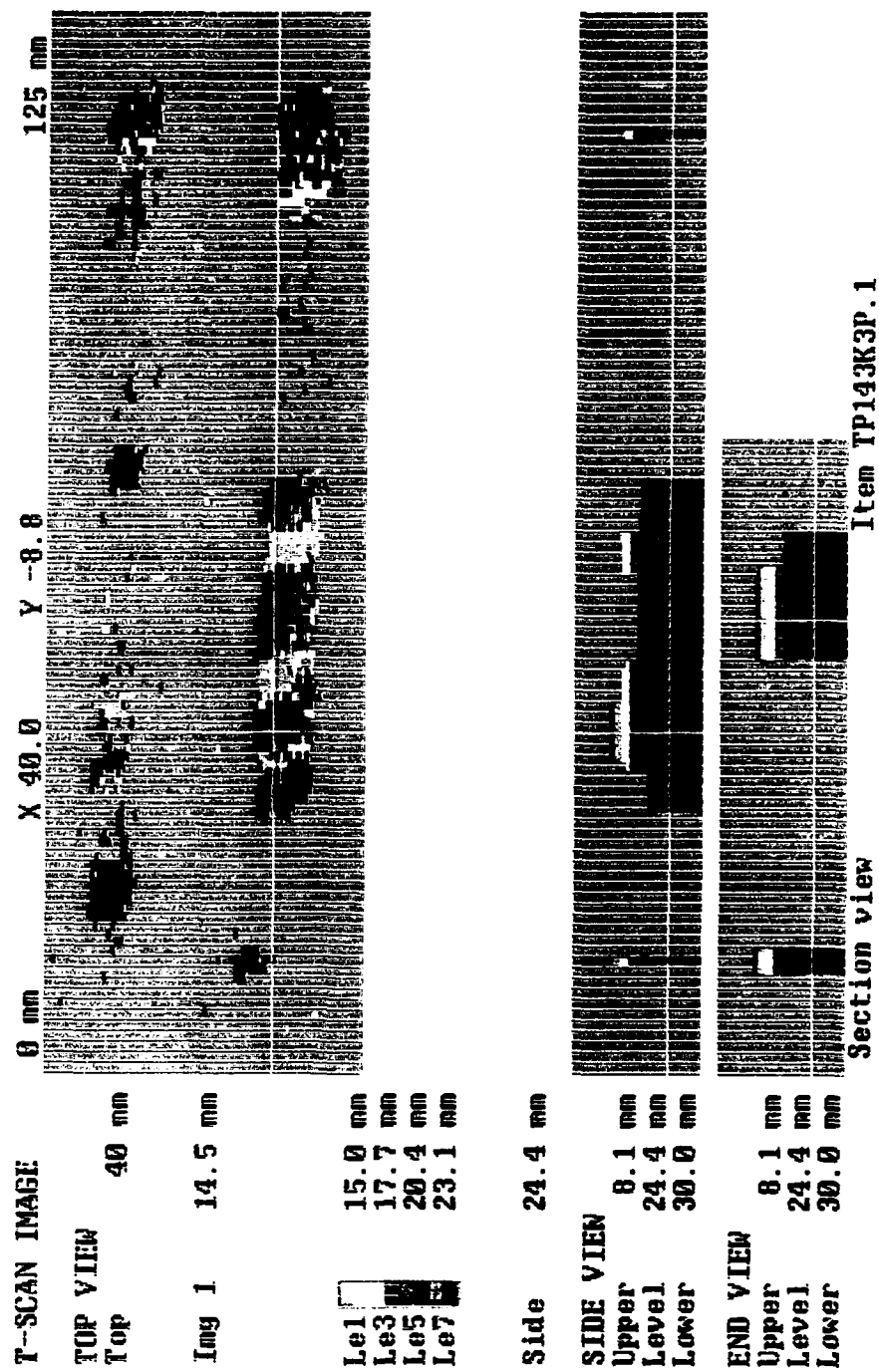
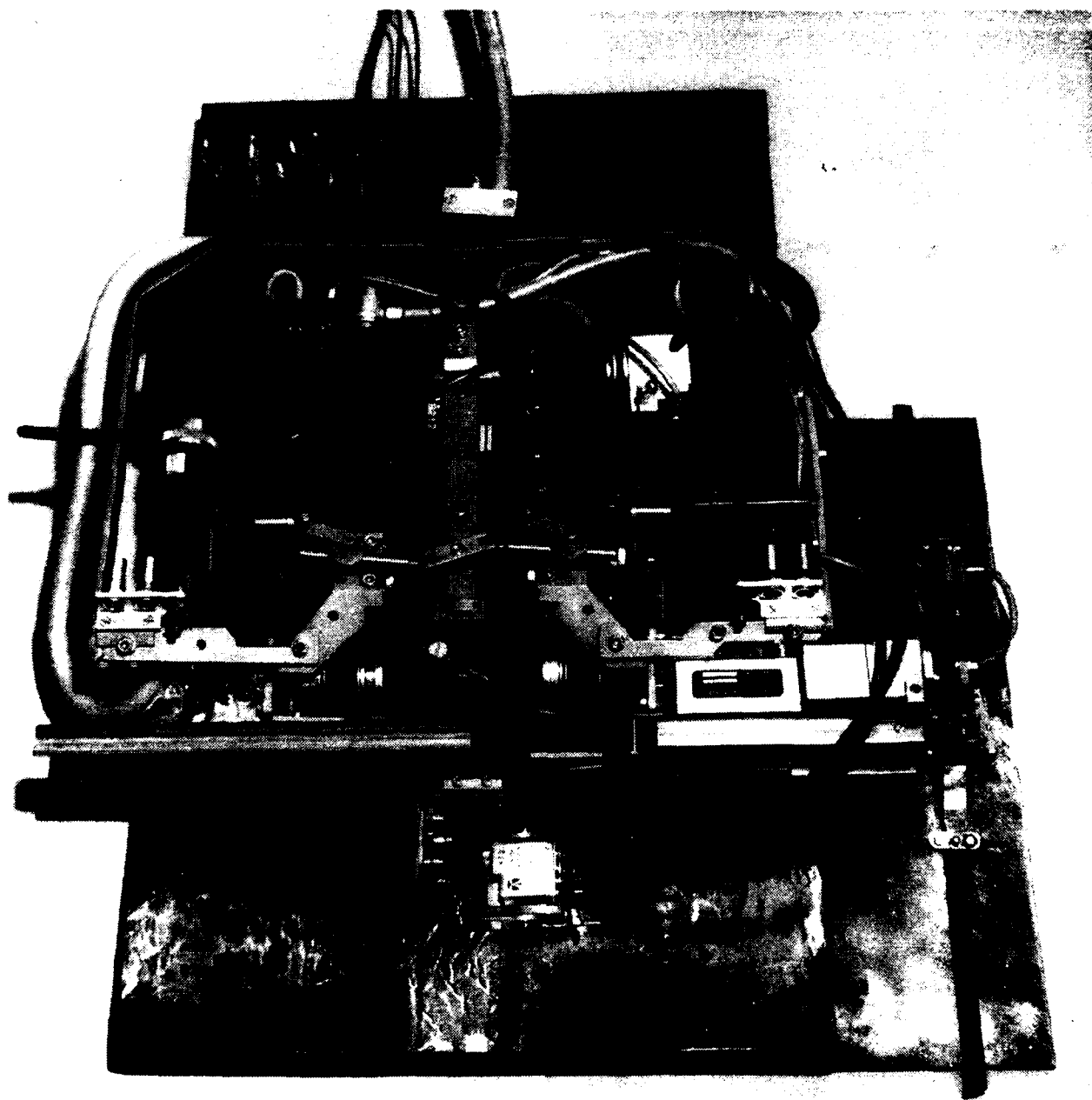


Figure 7. T-scan image of component subject to HIC.



**AUTOADAPTIVE EMAILTEST AZ90
FOR CORROSION MONITORING OF GLASS-LINED REACTORS**

**Hamert Jean-Marie
De Dietrich Equipement Chimique
67110 ZINSWILLER FRANCE**

Abstract

In the Chemical and Pharmaceutical Industry, glass-lined vessels often contain very corrosive and harmful products. To prevent major problems such as batch contamination, leakages or explosions, it is important to detect as soon as possible a failure of the glass-lining.

The well-known electrolytic method of detection has been improved by using a permanent comparison of a reference current passing between these electrodes and a defect in the glass-lining.

This is made possible with the microprocessorised glass-guard to detect a leak rate independent of the product conductivity, to be self monitoring and to give an evaluation of the conductivity.

Introduction

Glass-lined steel vessels are used in the chemical and pharmaceutical industry when the chemical conditions are too harsh for other materials or when the products can be contaminated by small amounts of metals.

As they often contain very corrosive and/or harmful products, it is easy to understand the importance of a failure detection in the glass-lining.

The most usual way to detect failures in the glass-lining is the high voltage spark test which is performed at 20,000 V during manufacturing and at 6,000 V when the vessel is installed. Field tests which are generally performed once or twice a year are very time consuming. Before entry is permitted for inspection, vessels have to be secured according to confined space entry regulations and company safety procedures (electrical lock-out, draining, cleaning). The main disadvantages of this method are :

- the high cost of the downtime of a vessel or of a whole production flow
- the possibility for a vessel to be destroyed or heavily damaged between the inspections

The continuous monitoring of the glass-lining during the process is a good solution to this problem as long as it is performed by using a reliable method allowing an early detection of a failure.

This early detection may avoid big leakages in the workshop, dangerous mixtures with heating fluids, contamination of valuable batches or explosions.

It also makes the defect potentially easier to repair and can in many cases save the cost associated with a vessel change out.

The continuous monitoring of the glass-lining is based on the electric insulating property of the glass and the electric conductivity of the fluids contained in the vessel. If a difference of potential is maintained between an electrode in contact with the fluid and the steel part of the vessel (figure 1) there is no current as long as there is no defect in the glass-lining.

I. Basic principles

For a given voltage, the intensity of the leak current flowing between the electrodes and the enamel defect depends on the conductivity of the fluid, the size of the defect and the distance between this defect and the electrodes.

A. Influence of the conductivity of the fluid (figure 2)

The intensity of the leak current measured under 12 V D.C. for a defect size of 2.5 mm² increases quickly up to a conductivity of 10 mS/cm and can be then considered as constant.

B. Influence of the size of the defect (figure 3)

The leak current increases with the size of the defect from 0.2 to 1 mm². A much slower variation is noticed for larger defects.

C. Influence of the distance between electrode and defect

1. In a reactor : in the case of a low conductivity product the distance has a small and negligible influence on the leak current.

For instance, a defect of 2.5 mm² in a 4000 l / 1,000 Gal. reactor containing a product with a conductivity of 140 μ S/cm gives a leak current of 450 μ A at distance 0 and a current of 400 μ A at 2 meters (\approx 6 feet).

As soon as the conductivity of the product is higher than 2 m S/cm the distance has no more influence.

2. In pipes : (figure 4) Distance has a strong influence which decreases when the conductivity of the product increases.

D. Influence of tantalum repairs

When placed at the positive pole of a generator, tantalum has the particularity to cover itself with a very thin insulating layer (0.1 μ) of tantalum oxide Ta₂O₅ by anodic oxidation.

We can follow this phenomenon on figure 5 and notice that it takes a long time and, that even completed, it needs a small current intensity (2 μ A/cm²) to maintain the passivation. The passivation of tantalum is not always possible, particularly in bromine compounds, hot nitric acid or in presence of abrasive products.

For these two reasons, it is necessary to insulate large tantalum repairs from the steel base by using insulating inserts in ceramic or high temperature polymers.

II. First Emailtest generation

The most simple way to detect an enamel defect is to place a limit switch amperometer in the monitoring circuit. This was the working principle of the first generation of Emailtest in which the tantalum thermowell or a tantalum ring was used as electrode (figure 6). According to the basic principles we have seen, with this method, a small defect in a product of high conductivity gives the same signal than a large defect in a product of low conductivity and it is impossible to follow the evolution of a defect.

III. Auto adaptive Emailtest AZ 90

A. Working

As previously seen the leak current in a vessel is dependent on the conductivity of the product and on the size of the defect. The Emailtest AZ 90 has been designed to give an output signal proportional to the size of the defect and corrected of the variation of conductivity in the range 0.1-20 mS/cm.

Two platinum electrodes insulated from the ground are placed on the glass of the stem/head assembly of the outlet valve or on the baffle (fig. 7). By maintaining an alternating current between these electrodes one obtains a reference current (I_{ref}) proportional to the conductivity of the medium. At the same time, the Emailtest maintains a direct voltage between the electrode and the mass of the vessel. When a defect appears in the lining, a leak current (I_f) occurs, the intensity of which varies with the conductivity of the medium and the size of the defect.

Using these two values, I_{ref} and I_f , and a linearization table, the microprocessor calculates an absolute leak rate (T_{abs}) independent of the medium's conductivity in the range 0.1-20 mS/cm. See figure 8 for some sizes of defect the variations of the leak current I_f and of the absolute leak rate T_{abs} in function of the conductivity. The absolute leak rate T_{abs} calculated by the microprocessor remains constant : this is the basis of the Emailtest AZ 90's autoadaptivity.

The main functions of the Emailtest are summarized in fig. 7.

Seven parameters can be displayed alternatively .

The reference current I_{ref} is used in conjunction with the K factor of the electrodes (calibrated in our plant) to compute the conductivity of the solution ($Cond$). An adjustable threshold "CONTROL" placed on this circuit permits to signalize through a relay output the presence or the absence of the minimum conditions of detection.

The Emailtest AZ 90 is self-monitoring.

The absolute leak rate T_{abs} can be recorded through an analogical output 4-20 mA. The initial value of the absolute leak rate can be shifted to zero in order to eliminate small leak currents due to small tantalum repairs or tiny leakages at gaskets. This shift to the absolute leak rate T_{abs} gives the relative leak rate T_{rel} . The adjustable threshold "ALARM" is set to this value (relay output and Led).

B. Advantages

The high sensitivity of the measuring circuit makes it possible to detect a tiny defect of 0.2 mm² in a product of low conductivity (0.1 mS/cm). When combined with a suitable data treatment, this allows for the detection and the follow-up of a defect. Thus avoiding the errors due to conductivity variations of the product or fouling of the electrodes.

The cleanliness of the electrodes can be followed by the measurement of the reference current in given conditions of conductivity.

The connection of the Emailtest AZ 90 into a supervisory station makes it easy to follow all these parameters and to avoid alarm errors due to earthing during filling or emptying.

The programming of the system (calibration, alarm adjustment and control threshold) is easily executed on the apparatus by using a three languages assistance.

The explosion-proof protection is assured in intrinsic safety by a Zener barrier. The AZ 90 system and the different types of probes are already certified for Europe by the French "Laboratoire Central des Industries Electriques". It has been submitted to Underwriters Laboratories in order to be UL listed.

C. Limits of use

A failure situated in the vapour phase above the liquid level cannot be detected even if condensation is flowing down since these are often thin films of high electric resistance or individual drops. To check these parts, vessels have to be filled up completely from time to time.

Big Tantalum repairs have to be insulated from the ground and in this case their tightness is also checked by the Emailtest.

The monitoring of glass-lining in continuous processes is not possible by electrolytic method because generally product can be earthed in many places.

At that time there is no method available to work in these conditions.

IV. Conclusions

The use of an updated technology to improve the reliability and sensitivity of the electrolytic control of the glass-lining led to the development of the Emailtest AZ 90 which is self-adaptive and self-monitoring.

The continuous monitoring capabilities, thus allowing for an early detection of the glass-lining failure, not only can save repair or downtime costs, but also increases the safety protection to the plant personnel and the environment.

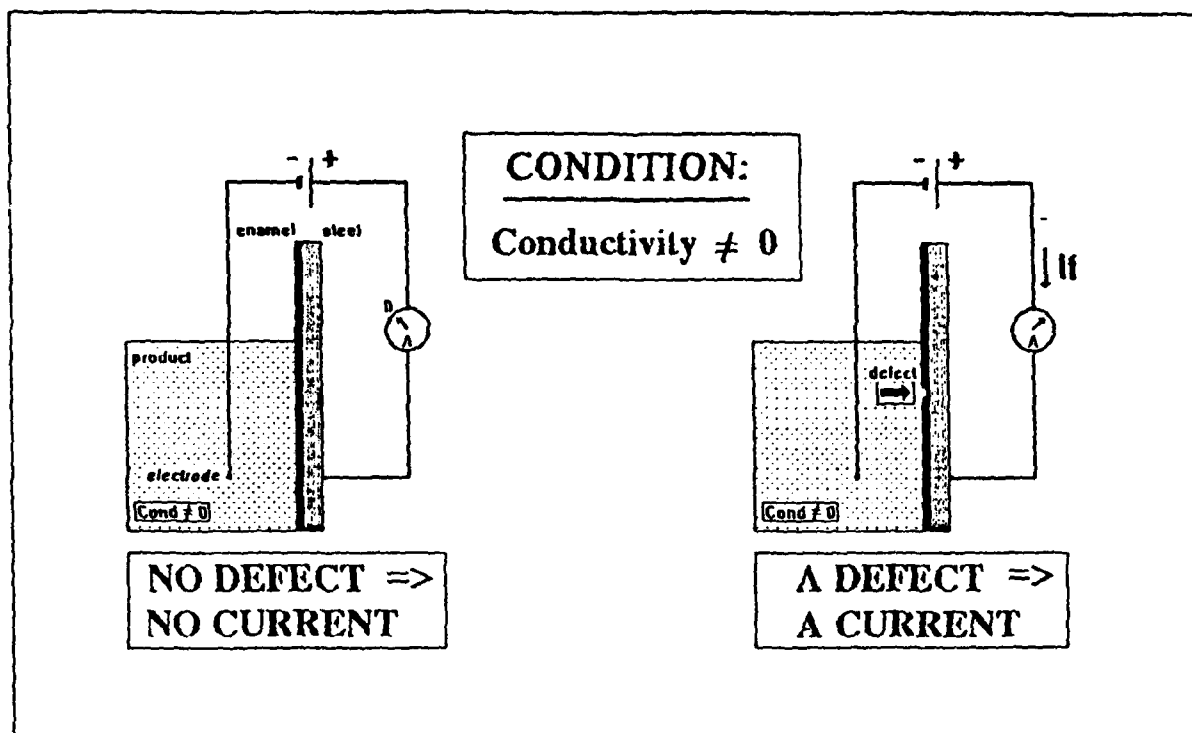


FIGURE 1: EMAILTEST WORKING PRINCIPLE

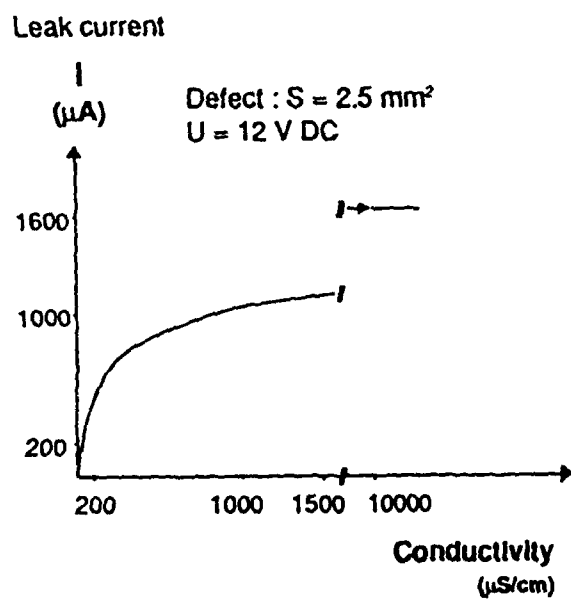


Figure 2
Variation of the leak current in function of the conductivity of the product

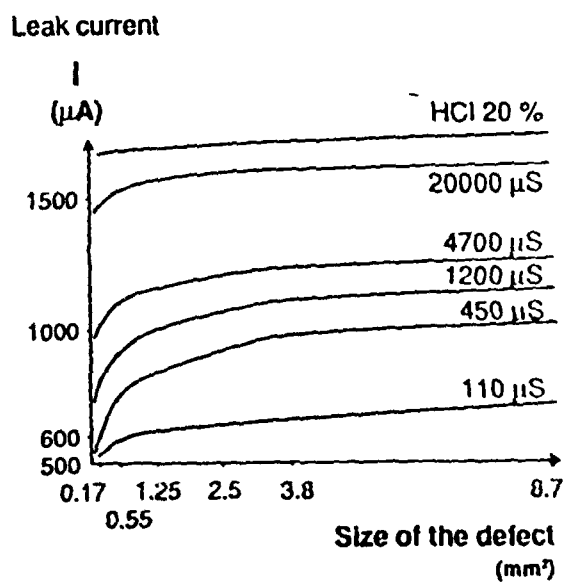


Figure 3
Influence of the size of the defect

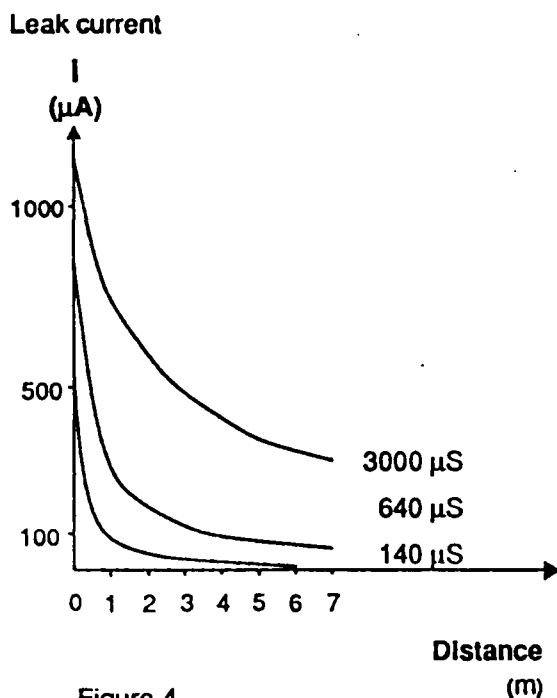


Figure 4
Influence of the distance in a pipe

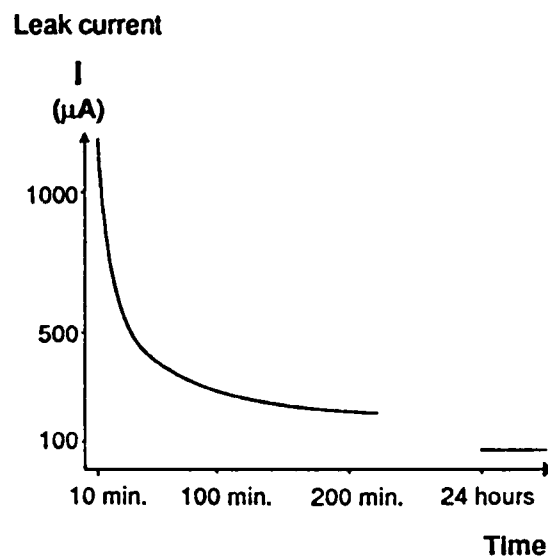


Figure 5
Anodic passivation of a tantalum plate
 $S = 37 \text{ cm}^2$
 $V = 12 \text{ V DC}$
Solution conductivity : 8.5 mS/cm

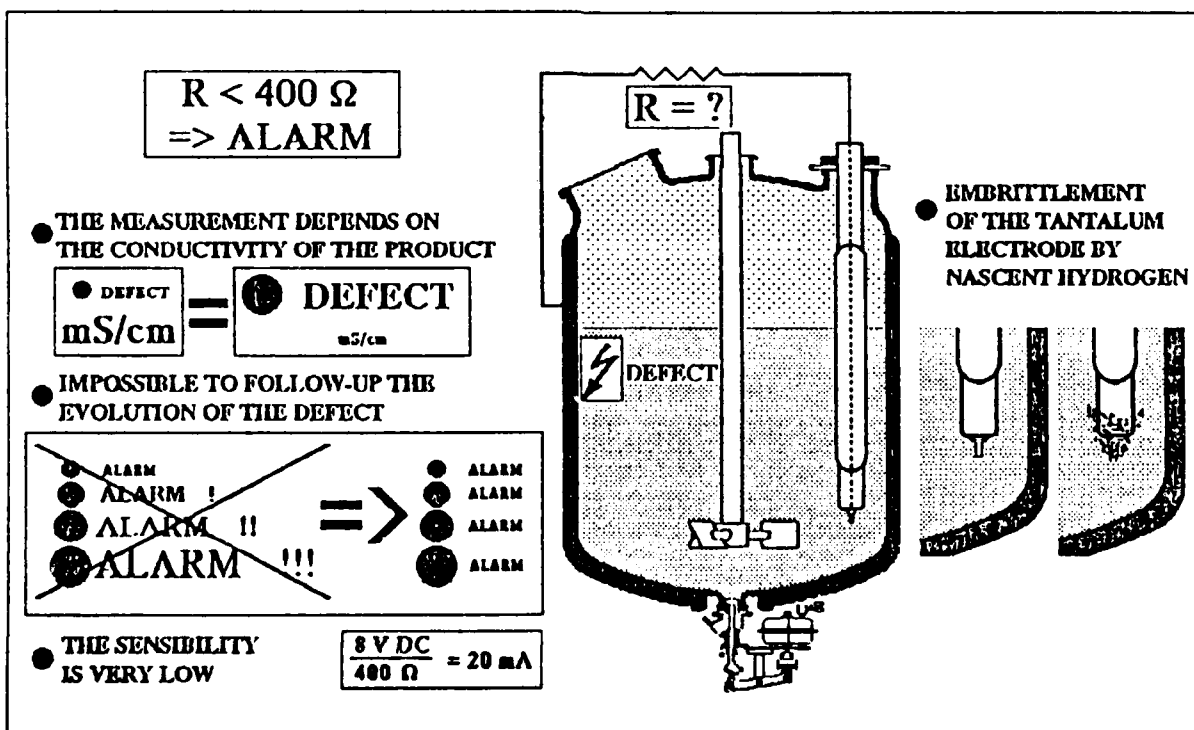


FIGURE 6: EMAIL TEST FIRST GENERATION

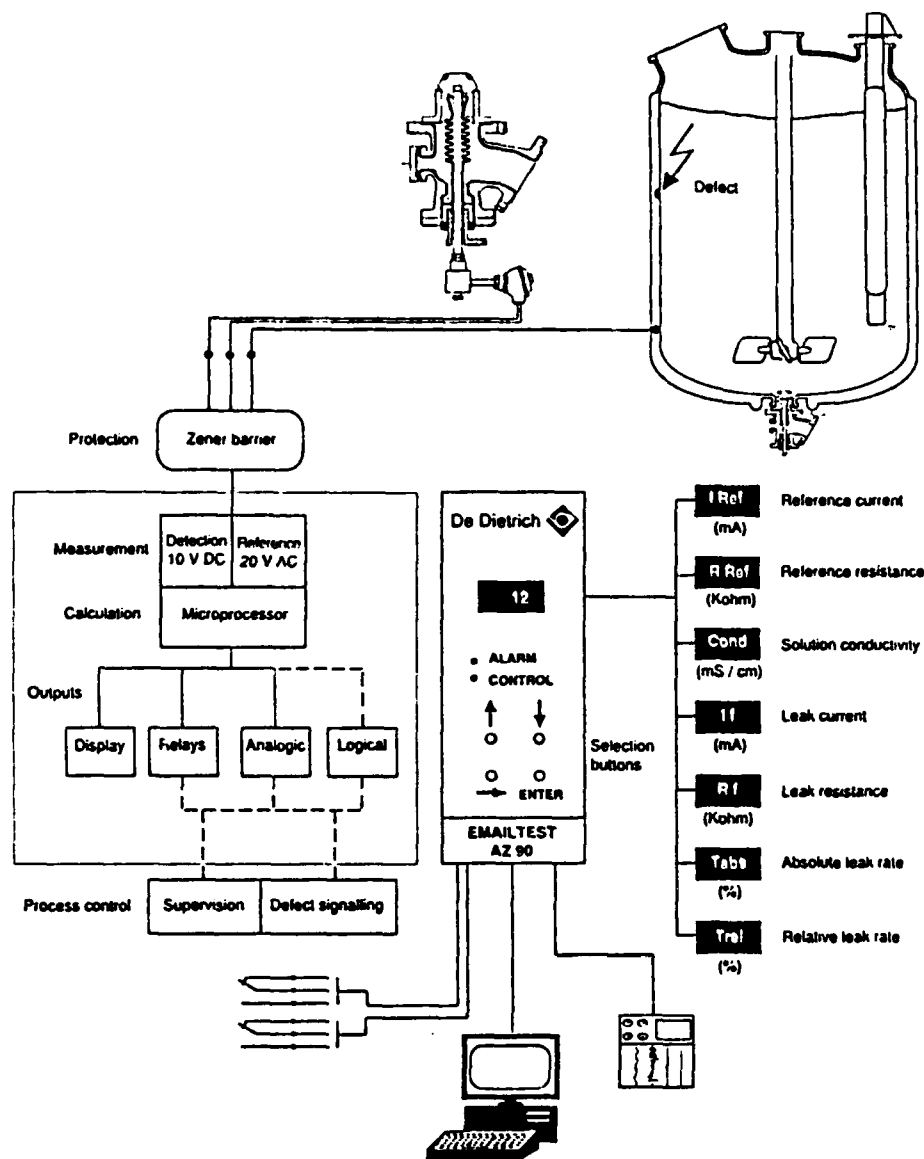


Figure 7 Auto-adaptive Emailtest AZ 90

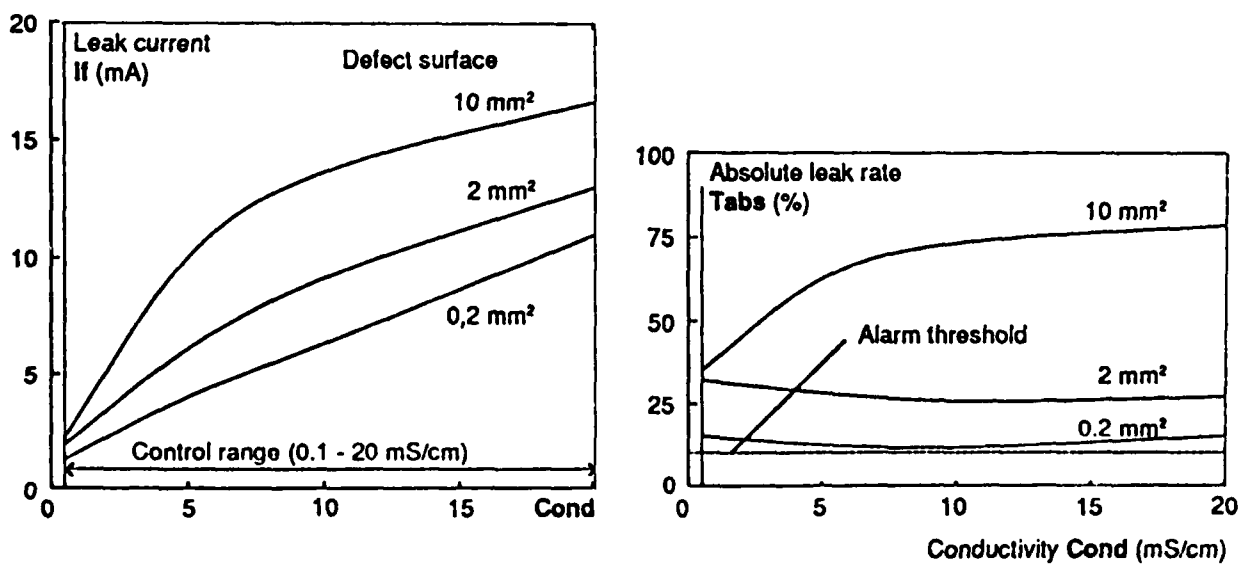


Figure 8 Linearisation of the absolute leak rate

Rare Earth Element Effect on Oxidation Behavior Of Chromia Forming Alloys.

Lalgudi V. Ramanathan,
Comissao Nacional de Energia Nuclear,
Instituto de Pesquisas Energeticas e Nucleares,
C.P. 11049, Cidade Universitaria,
Sao Paulo 05422-970,
Brazil.

ABSTRACT

The addition of rare earth (RE) elements favorably influences the oxidation behavior of high temperature alloys. Various explanations have been put forth to account for the reduction in scale growth rates and scale failures. Some have been verified for specific systems. This paper presents the influence of superficial application of RE oxides and alloying additions of RE elements and oxides on the oxidation behavior of chromia forming alloys. The role of RE elements on chromia scale growth has also been discussed. Superficial application of RE oxides and concentrates of Y and Ce improved isothermal and cyclic oxidation resistance of the relatively low Cr steel (AISI 304) but not that of the high Cr steel (AISI 310). The oxides of Y, Ce, Nd, La, Sm and Gd influenced oxidation resistance in decreasing order. Alloying additions of CeO_2 , Y_2O_3 , Ce and Y enhanced oxidation resistance of the Fe-Cr alloy in increasing order. In the presence of Y, Ce or their oxides, the scale was thin, fine grained and adherent chromia. The main stages by which oxidation resistance is enhanced are probably incorporation of the RE element in the oxide scale followed by their segregation to scale grain boundaries and consequent modification in ionic transport properties.

Key Terms : Rare earth elements, oxidation, stainless steels, chromia.

Introduction

Alloys or metallic coatings used in high temperature oxidative environments rely for their protection on a continuous and slow growing oxide scale. Ideally, these scales should be non volatile, adherent, coherent, stress free, pore free, crack free and have low defect concentrations for the transport of species. Commonly, three oxides have such capabilities, Cr_2O_3 , Al_2O_3 , and SiO_2 . All three are used in practice and the former two, Cr_2O_3 and Al_2O_3 , to a much greater extent than the latter.

The addition of small quantities (1%) of certain oxygen reactive elements to high temperature alloys is well known to reduce oxidation rates and increase scale adhesion. Several mechanisms have been proposed to account for the beneficial effects of adding the reactive elements. These include: (a) mechanical keying through formation of oxide pegs into the alloy (1), (b) promotion of preferential anionic diffusion rather than cationic diffusion in the scale, and thus oxide growth at a different interface (2-5), (c) formation of graded oxide or interlayers containing the reactive element (6), (d) reduction in accumulation of voids at the alloy/scale interface (7,8), (e) enhancement of scale plasticity by modification of the structure (9), and (f) inhibition of segregation of sulphur to the alloy/scale interface (10). Some of these explanations have been verified for specific alloys to which specific reactive elements have been added under specific conditions.

In most of the investigations, the rare earth (RE) elements were added either in metallic form or as oxide dispersions to the alloy (11,12). In some investigations, RE elements were introduced into the surface by ion implantation techniques and in others applied as oxides to the surface by various techniques (2-5,13-19). The application of RE elements to alloy substrates has the advantage of not affecting adversely the mechanical properties of the substrate alloy.

In this paper the influence of (a) superficial application of RE oxides, (b) alloying additions of RE elements, (c) additions of RE oxide dispersions to FeCrNi alloys and (d) superficial application of RE oxides to Si containing FeCrNi alloys has been studied, to extend the data available and address the effect of RE element addition on high temperature oxidation behavior of chromia forming alloys.

Methods and Materials

Commercial grade AISI 304 (Fe-18Cr-8Ni) and 310 (Fe-25Cr-20Ni) sheet specimens 1x1x0.3 cm were ground to 400 grit, degreased, rinsed and dried prior to applying the RE oxide. The RE oxide was applied by heating the specimen to 200 C followed by immersion in saturated RE nitrate solutions and drying at 200° C for 10 min (20). Oxides of Ce, La, Gd, Nd, Sm and Y as well as oxide concentrates rich in Ce and Y (as shown in table I) were applied. The specimens were isothermally oxidized in air at 900° C and 1000° C for up to 100h. AISI 304 and 310 specimens covered with RE oxides of Nd, La, Ce and Y were also tested for cyclic oxidation resistance. Each cycle consisted of 6h at 1000° C followed by cooling in air outside the furnace to room temperature.

The conjoint influence of Si as an alloying element and superficially applied RE oxide on the oxidation behavior of FeCrNi alloys was studied. In these tests CeO_2 was applied to Fe-18Cr-8Ni alloys containing 0.6 to 4.7 wt% Si and the oxidation behavior at 1000° C in air for 20h was investigated.

The effect of alloying additions of elemental RE and RE oxide dispersions to Fe-Cr alloys on oxidation behavior has also been studied. Fe-20Cr alloys containing (a) 0.1wt% Ce or Y prepared by vacuum induction melting and (b) 1wt% CeO_2 or Y_2O_3 dispersoids prepared by cold compaction from elemental powders and sintered. The alloys were subsequently homogenized in vacuum at 1000° C for 20h, 2mm thick specimens were cut, ground, rinsed, dried and oxidized in air at 1000°C for 20h.

In all experiments, the weight gain measurements were made either in a thermogravimetric balance or with a precision balance followed by examinations of the surface morphology of the oxidized specimens in a SEM coupled to a quantitative energy dispersive (EDS) system.

Results

Surface Addition of RE Oxides

The thickness of the deposited RE oxide was typically 2-4 μm and its structure depending on the composition of the oxide and condition of the substrate, consisted of either separate, closely packed grains or fractured platelets. Similar observations were made elsewhere (16). The Ce and Y oxides were found as closely packed grains.

The oxidation behavior of AISI 304 covered with RE oxides and Ce and Y concentrates at 1000°C is shown in figure 1. Straight lines have been used to join the points, since the measurements were discontinuous. Superficial application of RE oxides reduced the extent of oxidation, with Y and Ce oxides resulting in the highest overall oxidation resistance. The Y and Ce concentrates also reduced the extent of oxidation. The reduced influence of the concentrates is due to the presence and distribution of the other RE elements with reduced and/or detrimental influence on alloy oxidation. The oxides of La, Nd, Sm and Gd influenced oxidation rates to lesser extents and in decreasing order. The isothermal oxidation behavior of RE oxide covered AISI 304 at 900°C in air is shown in figure 2. Superficial addition of any of the RE oxides results in significant reduction in the extent and rate of oxidation of AISI 304. Y and Ce and their concentrates exercise greater influence than the other two oxides and La_2O_3 had greater influence than Nd_2O_3 . Figure 3 shows the isothermal oxidation curves of AISI 310 at 900°C. All the curves lie within a narrow band, indicating limited influence, if any, of the surface deposited oxides on oxidation behavior.

The cyclic oxidation behavior of AISI 304 covered with oxides of Y, Ce, Nd and La is summarized in Table 1. In the presence of Y or Ce oxides, the scale is more resistant to spalling and is due mainly to the formation of thin fine grained Cr_2O_3 on the surface.

The influence of the conjoint presence of Si and CeO_2 on the extent of oxidation is shown in figure 4. It can be seen that at 1000°C the extent of oxidation did not vary significantly with Si content. However, at higher temperatures, the oxidation rate decreased with increasing silicon. The superficial application of CeO_2 to these alloys did not result in any notable change in oxidative weight gains. The increase in oxidation resistance with increasing Si is probably due to formation of both Cr_2O_3 and SiO_2 .

Alloy Additions of Rare Earths to Fe-20Cr.

The effect of RE element addition or RE oxide dispersoids to Fe-20Cr on oxidation at 1000°C is shown in figure 5. The addition of Ce or Y in elemental form has a greater influence on reducing the oxidation rate of the alloys than the addition of ceria or yttria dispersoids. In either form, Y reduced the oxidation rate more than Ce.

Oxide Morphology

Optical and scanning electron microscopic studies on oxidized specimens were carried out. The outer oxide surface on RE free AISI 304 oxidized for 20 h at 1000°C revealed spikes of iron rich oxide (figure 6a), whereas close to the alloy/scale interface a fine grained structure was seen. SEM/EDAX measurements on sections of scale formed on AISI 304 showed a duplex scale consisting of a mixed oxide above a chromia layer. After oxidation, surface deposited RE oxides were observed at the oxide/gas interface, indicating that the deposited oxide was pushed outwards as the scale grew (figure 6b). The RE oxide particles on the scale surface were $5\text{--}25\mu\text{m}$ in size and randomly distributed. The marked improvement in the overall oxidation behavior upon addition of Y, Ce, La or Nd, is due to the formation of fine grained Cr_2O_3 as shown in figure 6c.

The addition of RE oxide to AISI 310 did not alter the oxide morphology. Fine grained Cr_2O_3 similar to that shown in figure 6c was observed on both the RE oxide covered and RE free AISI 310 oxidized for 20h at 1000°C .

The surface of oxidized AISI 304 covered with Ce or Y concentrate revealed on different regions of the surface either spike like iron oxide, rounded fine grained chromia or a mixture of both. The mixed morphology of the scale is due to the presence of RE elements with varying influence on scale growth.

General Discussion

Superficial application of RE oxides to AISI 304 improves the overall oxidation resistance. The RE elements in increasing order of influence on the oxidation behavior are Gd, Sm, Nd, La, Ce and

Y. The scale formed on (a) the Y_2O_3 covered alloy consisted of a thin layer of fine grained chromia, (b) the CeO_2 covered alloy, predominantly chromia with some iron oxide and (c) the other RE oxide covered alloys, mostly chromia with increasing amounts of iron oxide. The morphology and thickness of the scales on both RE oxide covered as well as RE oxide free AISI 310 (Fe25Cr20Ni) were similar and consisted of fine grained Cr_2O_3 . Thus superficial application of RE oxide exercised greater influence on the oxidation behavior of low Cr alloy, which normally forms discontinuous chromia scales. Hou and Stringer also observed that in the presence of surface deposited RE oxide continuous and adherent chromia scales form on alloys which normally form discontinuous scales (16).

Even though a significant part of the superficially applied RE oxide on AISI 304 was found at the scale/gas interface, the formation of fine grained chromia on specimens covered with CeO_2 or Y_2O_3 and not on specimens free from RE oxides could be attributed to the presence of the RE oxides. These RE oxides may be acting as scale nucleation sites. The presence of RE oxide in the growing scale has been reported (16,21). The surface applied RE oxide probably influenced scale growth in a manner similar to when RE elements were added to the alloy. In this study, the extent to which RE elements influence oxidation resistance, was found to be highest when present as an alloying element. It is well known that the RE elements added to the alloy become incorporated into the chromia scale as an oxide (16). It has been suggested that the RE oxide in the scale forms spinels (depending on their solubility) followed by dissociation to the RE ion, and segregation to grain boundaries where they slow the outward Cr ion movement (3). Even though direct evidence of these phenomenon are yet to be confirmed in this investigation, the observed variations in the extent of influence of the different RE elements on oxidation behavior could be attributed to their diffusion behavior in the scale.

The addition of RE oxides as dispersoids to chromia forming alloys also improves oxidation resistance. This has been observed in this investigation and elsewhere (22). The improvement in oxidation behavior is possibly brought on by the dispersoids acting as cation vacancy sinks (remote from alloy/scale interface)(23). The improvement may also be attributable to the dispersed RE oxide particles in the alloy acting as heterogenous nucleation sites (8). Thus the time required for subsequent lateral growth processes to link nuclei and form a complete protective layer is less.

In this investigation no peg formation was observed. However, based on the observed differences in scale morphologies and grain size between the RE containing and RE free alloys the improved adhesion may be attributed to increase in scale plasticity.

Conclusions

1. Superficial application of RE oxides and concentrates of Y and Ce to AISI 304 increases oxidation resistance.
2. Cerium and yttrium oxides resulted in highest isothermal and cyclic oxidation resistance. They promoted the formation of fine grained chromia on AISI 304.
3. The oxidation behavior of Si containing Fe-18Cr-8Ni alloys was not affected by superficially applied ceria.
4. The addition of 0.1wt% Ce or Y or 1wt% of their oxides as dispersions to Fe-20Cr improved their oxidation resistance.

References

1. C.S. Giggins, B.H. Kearn, F.S. Petit and J.K. Tien, Metall. Trans., 5, (1974), p.1685.
2. K. Przybylski, A.J. Garratt-Reed and G.J. Yurek, J. Electrochem Soc., 135,2,(1988),p.509.
3. K. Przybylski and G.J. Yurek, J. Electrochem Soc., 135,2. (1988), p.517.
4. C.M. Cottell, G.J. Yurek R.J. Hussey, D.F. Mitchell and M.J. Graham, Oxid. Met., 34,314, (1990), p.173.
5. C.M. Cottell, G.J. Yurek, R. J. Hussey, D.F. Mitchell and M.J. Graham, Oxid. Met., 34, 314, (1990), p.201.
6. F.A. Golightly, F.H. Stott, and G.C. Wood, Oxid Met., 10, (1976), p.163.
7. J.D. Kuenzley and D.L. Douglass, Oxid Met., 8, (1974), p.139.
8. J.Stringer, B.A. Wilcox and R.I. Jaffee, Oxid. Met., 5, (1972) p.11.
9. J.E. Antill and R. A. Paskall, J.Iron Steel Inst., London, (1967),p.1136.
10. R.W. Funkenbusch, J.G. Smeggil and N.S. Bornstein, Metall. Trans., 16A, (1985), p.1164.
11. H. Nagai, Mat.Sci. Forum, 43, (1989), p.75.
12. T.N. Rhys-Jones and H.J. Grabke, Mat. Sci. and Tech., 5,4, (1988), p.446.
13. J.E. Antill, J.J. Bennet, R.f. A. Bernsley, F.H. Fern, P.H. Goode, B.L.Myatt, J.F. Furner and J.B. Warburton, Corros. Sci., 16, (1976), p.729.
14. M. Landkof, A.V. Levy, D.H. Boone, R. Gray and E. Yanif., Corrosion, 41, (1985), p.344.
15. Y. Saito and T. Maruyama, Mat.Sci and Eng., 87, (1987) p.275.
16. P.Y. Hou and J.Stringer, Mat. Sci and Eng., 87, (1987) p.295.
17. T. Fransen, M.A. de Jough, M.M.A. Perik and P.J. Gellings, Proc.9th Int. Cong. Met. Corr., Canada, V-4, (1984), p.311.
18. R.J. Hussey, P. Papaioacovou, J. Shen, D.F. Mitchell and M.J. Graham, Mat. Sci and Eng., A120, (1989) p.147.
19. M.J. Bennet, J. Vac. Sci. Tech. B2(4), (1984), p.800.
20. L.V. Ramanathan, Proc. 9 Bras. Mat. Sci Conf., Aguas de Sao Pedro, Brazil, (1990).
21. J. Stringer, Mat. Sci and Eng., A120, (1989), p.129.
22. D. Caplan, Met. Trans A, 12A, 12, (1981), p.2135.
23. D.P. Moon, Mat. Sci and Tech., 8, 5, (1989), p.754.

Table I. Composition of oxide concentrates

Element	Y concentrate (wt%)	Ce concentrate (wt%)
Y	78	2.5
Dy	14	1.2
Gd	2	10.0
Ho	2	-
Tb	1.5	-
La	-	14.5
Ce	-	37.5
Nd	-	23.0
Sm	-	11.3
Eu	-	0.25

Table II. Cyclic oxidation resistance of RE oxide coated AISI 304. Each cycle consisted of 20h at 1000°C.
S - Spalling, NS - No Spalling

Rare Earth Oxide	Specimen after cycle					
	1	2	3	4	5	6
Y_2O_3	NS	NS	NS	NS	S	S
CeO_2	NS	NS	NS	S	S	S
La_2O_3	NS	S	S	S	S	S
Nd_2O_3	S	S	S	S	S	S

Figure 1. Isothermal oxidation behavior of AISI 304 with surface deposited RE oxides at 1000°C.

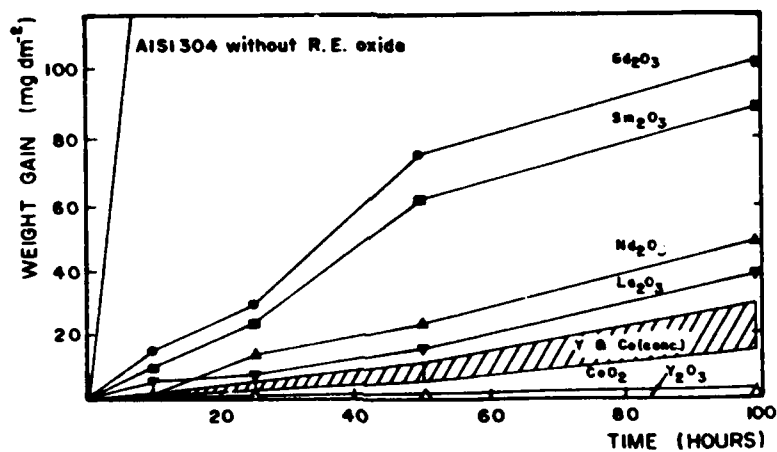


Figure 2. Isothermal oxidation behavior of AISI 304 with surface deposited RE oxides at 900°C.

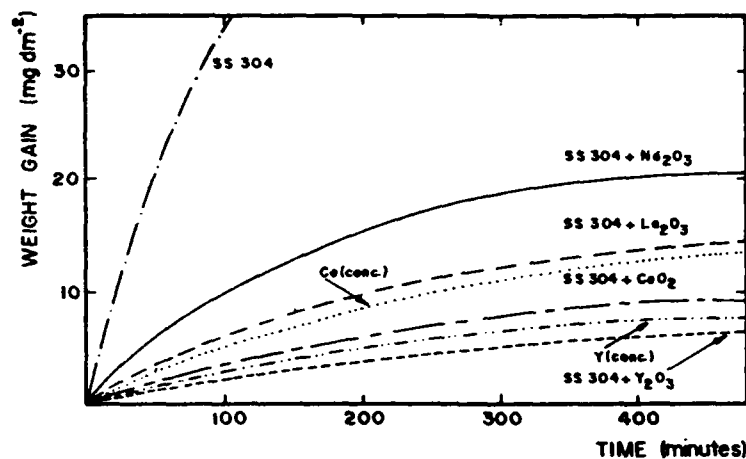


Figure 3. Isothermal oxidation behavior of AISI 310 with surface deposited RE oxides at 900°C.

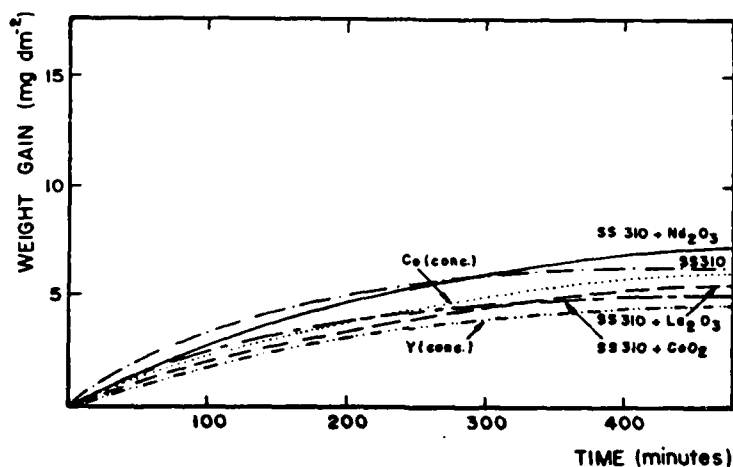


Figure 4. Isothermal oxidation behavior of Si containing Fe-18Cr-8Ni superficially coated with CeO₂.

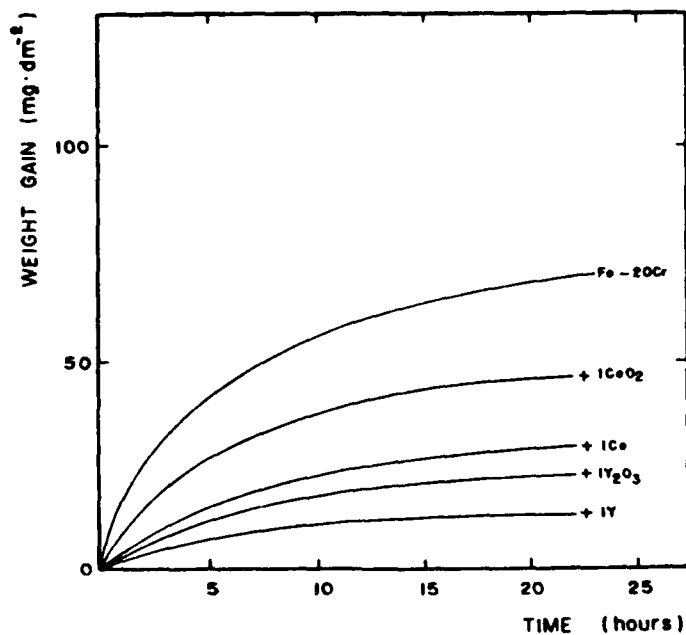


Figure 5. Isothermal oxidation behavior of Fe-20Cr at 1000°C with and without additions of 0.1wt% RE elements and 1wt% RE oxides.

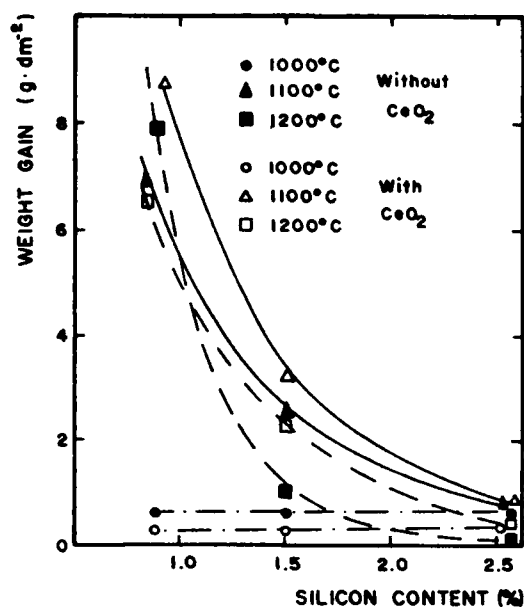
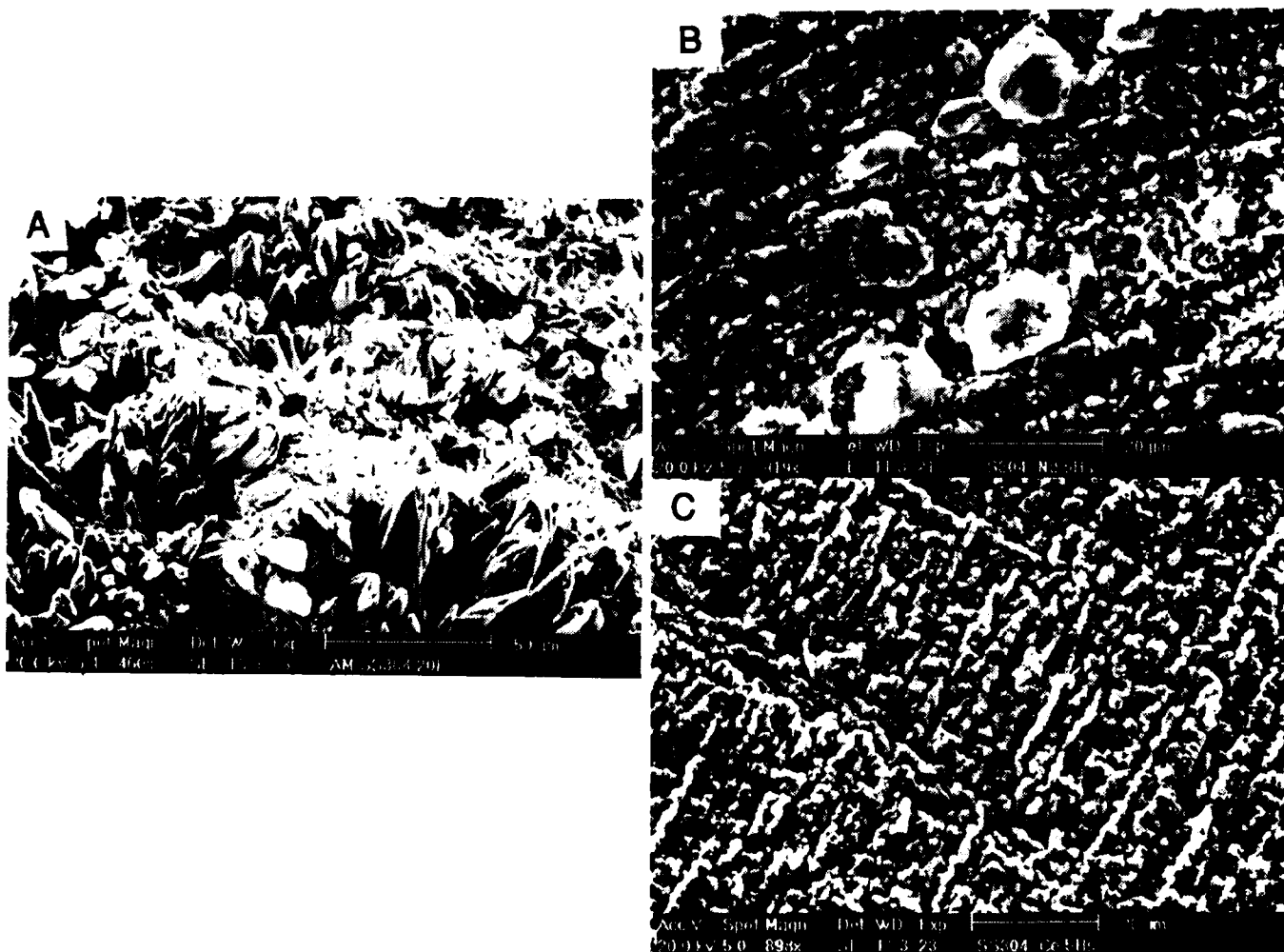


Figure 6. Scanning electron micrographs of outer oxide surface on AISI 304 specimens oxidized at 1000°C.
(a) RE oxide free (b) Nd₂O₃ deposited (c) CeO₂ deposited



A Study of the Metal—Oxide Diffusion Barrier Coatings

Guan Hengrong

Institute of Metal Research, Academia Sinica

72 Wenhua Road

Shenyang 110015, China

Sun Xiaofeng

Institute of Metal Research, Academia Sinica

72 Wenhua Road

Shenyang 110015, China

Sun Biwu

Institute of Metal Research, Academia Sinica

72 Wenhua Road

Shenyang 110015, China

Abstract

The low pressure plasma spraying (LPPS) metal—oxide diffusion barriers have been investigated in present paper. It was found that the retardation of interdiffusion is related to the amount of oxides in the diffusion barrier layer, the larger the volume fraction of oxides, the greater the effectiveness of diffusion barriers, and the post—aluminized treatment can improve the effectiveness of diffusion barriers in reducing interdiffusion between coating and substrate. Based on the above results, it is proposed that the effectiveness of diffusion barrier layer is mainly decided by (1) the volume fraction of oxides in the barrier layer, and (2) the ratio of total volume diffusion flux to total short circuit diffusion flux. The calculated results of a modified model established on the basis of the above proposal and Luthra's model are in agreement with the experimental ones.

KEY WORDS: coating, diffusion barrier, interdiffusion

Introduction

In gas turbine engines the degradation of aluminide coatings that are used to protect superalloy components from oxidation and hot corrosion usually results from the depletion of aluminium in the coating by aluminium oxide scale spallation and from the depletion of the aluminum rich coating by the interdiffusion into the substrate. The latter mechanism is often predominant above 1100°C [1]. This problem may be solved if a barrier layer could be formed between the coating and the substrate that will prevent the interdiffusion. Recently many diffusion barriers have been studied, among which there were intermediate alloys [2,3] and refractory metals etc. [4-6], but none appeared to be successful above 1100°C. Another method was to interpose a single nitride or oxide layer [7,8]. Such a layer might be brittle and might have a different thermal expansion coefficient from that of the underline substrate, which can cause spallation of the coating. Recently a diffusion barrier metal-oxide cermet has shown promise [9,10], but so far there are no systematical studies on it. In this paper, the effectiveness of the metal-oxide diffusion barrier in blocking the interdiffusion between the outer coating and the substrate has been investigated with the Ni-based superalloy M17F⁽¹⁾ as a substrate, Ni30Al-0.5Y as an outer coating, and Ni15Al-Y₂O₃ metal-oxide cermet as diffusion barriers.

Experimental Procedure

Three metal-oxide cermet powders used as diffusion barriers were prepared by means of mechanical alloying with the compositions of Ni15Al-0Y₂O₃, Ni15Al-8Y₂O₃ and Ni15Al-30Y₂O₃ (wt-%), respectively. The barrier layers and then the outer coating, Ni30Al-0.5Y, were coated with the thickness of about 40μm and 60μm respectively on the substrate M17F, which was ultrasonically washed and gritblasted before the coating was applied, by low pressure plasma spraying(LPPS). The duplex coatings are called LPPS samples for short. Some of the LPPS diffusion barrier coatings were diffused in vacuum at 1130°C for 2h, and then aluminized in pack at 900°C for 3h (simplified as post-aluminized samples), in order to increase the compactness and aluminium content of the outer coating and diffusion barrier.

For getting rid of the dilution of aluminium of the outer coating by oxidation, the

(1) The composition of the M17F alloy was 9Cr, 9Co, 4.7Al, 4.3Ti, 3.7Ta, 3.9W, 2.0Mo, 0.11C, 0.01B, balance Ni (wt-%).

specimens both before and after aluminizing were diffused at 1130°C for 10 h in vacuum at the pressure of 1×10^{-3} Pa. The composition profiles of Al, Ni, Co, Cr, Ti etc. have been quantitatively measured by EPMA across the specimen. The metallograph was used to observe the microstructure of the outer coating and diffusion barriers.

Results and Discussion

The effect of oxide fraction on the function of LPPS diffusion barrier

During the diffusing process in vacuum, the aluminium diffused from outer coating into the substrate, while Cr, Co, Ti etc. diffused from the substrate into the outer coating. Fig.1 shows the variation of Al and Cr content *versus* depth for LPPS diffusion barrier coatings which diffused at 1130°C for 10 h in vacuum. It is thought that a greater oxide fraction, a more effective diffusion barrier in blocking the interdiffusion [9]. But it can be seen in Fig.1 that the difference of the effectiveness among 0% Y_2O_3 , 8% Y_2O_3 , and 30% Y_2O_3 diffusion barriers is very small. The same results were obtained for diffusion barrier in inhibiting the diffusion of Co, Ti etc. This implies that the oxide fraction for the LPPS samples has little effect on the function of LPPS diffusion barrier. SEM and metallograph of LPPS samples showed that there were a few pores in outer coating, but diffusion barrier layer is porous and loose with small grains. This indicates that there were inner surface diffusion and interface diffusion. The percentage of short circuit diffusion (mainly including interface diffusion) has more layer than that in general states, which can explain the fact that the oxide fraction has little effect on the fraction of LPPS diffusion barrier.

The effect of aluminizing on the function of LPPS diffusion barrier

After aluminizing at 900°C for 3 h, the Al content in the outer coating and the diffusion barrier increased. For the diffusion barrier coatings with different Y_2O_3 fraction, the Al content profiles are roughly the same. Fig.2 shows the metallograph of the aluminizing LPPS diffusion barrier coating diffused at 1130°C for 10 h in vacuum. In the specimen containing 0% Y_2O_3 , the width of the diffusing band at the barrier / substrate interface is about 25 μm . In specimen containing 30% Y_2O_3 , the diffusing band is obviously narrower than the former. Fig.3 shows the variation of Al and Cr content *versus* depth for aluminized LPPS diffusion barrier coatings diffused at 1130°C for 10h in vacuum. It indicated that the more the oxide fraction in the barrier is, the less the loss of the Al content in the outer coating, and the lower the Cr content in the outer coating which diffused from the substrate. The effectiveness of the diffusion barriers in blocking the interdiffusion increases with the oxide fraction. Comparing Fig.3 with Fig.1, it can be

found that the aluminized LPPS diffusion barrier containing 30% Y_2O_3 is more effective in retarding the interdiffusion than that without aluminizing. This indicates that aluminizing increases the effectiveness of the diffusion barrier. The metallographs obtained from the post-aluminized samples showed that the state of the diffusion barrier after aluminizing is near to that of the outer coating. Compared with the LPPS samples, the aluminizing made pores decrease obviously, loose state be improved greatly and grains grow evidently, therefore lessened the pathes of short circuit diffusion distributively.

The mechanism of the diffusion barrier

A model was proposed by Luthra [9] that oxides dispersed in metal base can decrease diffusion section, lengthen diffusion path and then retard element diffusion. However, the interface diffusion was overlooked, and the effect of dispersed oxides on interface diffusion was not discussed in the model.

The results of above experiments prove that the role of diffusion barrier has a close relation to the state of barrier layer. The diffusion barriers of LPPS 8% and 30% samples show little effect on the diffusion of Al, but ones of post-aluminized 8% and 30% samples retard the diffusion of Al greatly. That the diffusion speed of Al in LPPS samples is independent of the amount of oxides in the barrier indicates that there must be a leading diffusion way and that the dispersed oxides have no effect on it in the barrier layer. It is reasonable to consider the leading diffusion way as short circuit diffusion (including interface diffusion mainly, but excluding dislocation diffusion) according to the difference in the diffusion speed of Al, in the role of diffusion barrier to retard the diffusion of elements and in the state of the barrier between LPPS and post-aluminized samples. In fact, if the size of oxides is similar to that of metal, the oxides do not disperse in the interface to influence interface diffusion, not lessen pores to decrease inner surface diffusion, not lower the number of interface, and not lengthen the pathes of interface diffusion. The dispersed oxides can only decrease the number of volume diffusion, and lengthen the pathes of it. Actually, the size of oxides is smaller than that of metal grains, therefore, the dispersed oxides raise the number of interface, which partly cancels out the role of diffusion barrier. The addition of oxides turns some metal-metal interfaces into metal-oxide interfaces and changes the properties and width of them.

Therefore, it is considered that the role of metal-oxide diffusion barrier to retard the diffusion of elements depends on the following factors: (1) the amount of oxides dispersed in diffusion barrier—the more the oxides, the more the section of volume diffusion decreases, the longer the pathes of volume diffusion, and the stronger role of the retardation; (2) the ratio of total volume diffusion flux to total short circuit diffusion

flux in barrier layer— the greater the ratio, the smaller the short circuit diffusion and the stronger the role of diffusion barrier. When the short circuit diffusion becomes predominant, the barrier does not retard the diffusion of elements. When the short circuit diffusion can be omitted, the role of the barrier reaches the maximum, which agrees with Luthra model.

The modified model of metal–oxide diffusion barrier

Generally, the diffusion of metals through oxide is in the orders of magnitude slower than through metals. Therefore, Luthra [9] expressed the diffusion flux of metal through metal–oxide diffusion barriers as follows:

$$J = -D \frac{f \partial C}{\tau \partial x}$$

where f is the volume fraction of metal in the diffusion barrier, τ is a tortuosity factor that increases the effective diffusion distance due to the addition of oxides, and it can be set from 1.5 for low amount of oxides in diffusion barriers to 10 for high amount of oxides.

According to the above analysis of the mechanism of diffusion barriers, the diffusion of elements through short circuits should not be neglected, and the oxides have the effect on short circuit diffusion and on volume diffusion in a different way. When the size of oxides is almost equal to that of metal phases, the addition of oxides does not inhibit the short circuit diffusion, only reduces the diffusion section and increases the diffusion distance. Therefore, the volume diffusive flux in diffusion barriers can be expressed in the same way as Luthra's.

$$J = -D_v \frac{f \partial C}{\tau \partial x}$$

where D_v is the volume diffusion coefficient. Since the oxides do not block the short circuit diffusion, the flux of short circuit diffusion can be represented as

$$J = -D_s \frac{f \partial C}{\tau \partial x}$$

where D_s is the short circuit diffusion coefficient and can be expressed as

$$D_s = \sum_{i=1}^n \frac{S_i}{S_g} D_i$$

here, n is the number of the manners of short circuit diffusion (not including the dislocation diffusion), S_g the total short circuit diffusion sections, and S_i and D_i are diffu-

sion section and diffusion coefficient respectively for certain short circuit diffusion.

Supposing that the concentration gradient of short circuits is the same as that in grains (actually, the former is a little less than the later, but the difference is negligible), the total diffusive flux can be expressed as

$$J = - \left(\frac{S_v}{S_t} \frac{f}{\tau} S_v + \frac{S_g}{S_t} D_g \right) \frac{\partial C}{\partial x} = - D^{\text{eff}} \frac{\partial C}{\partial x}$$

where S_v is the volume diffusion section, and S_t the total diffusion section.

The interdiffusion between the substrate and the diffusion barrier coating can be approximately considered as an one demension diffusion problem in a triple media. For the sake of simplifying calculations, the diffusion equations in a binary media have been solved with the aid of Ozisik's calculated results of thermal conduction equations [6].

At $x=0$

$$\frac{C(0,t)}{C_1} = 1 - \frac{2f}{\sqrt{D_1/D_2} + f} \sum_{n=0}^{\infty} \left(\frac{\sqrt{D_1/D_2} - f}{\sqrt{D_1/D_2} + f} \right)^n \left\{ 1 - \text{erf} \left[\frac{(2n+1)X_1}{2\sqrt{D_1 t}} \right] \right\}$$

Here:

X_1 the distance from the surface of the outer coating.

t the diffusion time

$C(0,t)$ the surface concentration of any composition in the outer coating at t .

C_1 the surface concentration at $x=0$ and $t=0$

f the metal content in the diffusion barrier

D_1 the diffusion coefficient of any composition in outer coating.

$D_2 = \frac{D^{\text{eff}}}{f}$, D^{eff} the efficient diffusion coefficient of the diffusion barrier.

Most coatings provide protection against oxidation by the formation of a continuous alumina layer [13]. A simple way to discover whether an alumina layer can form on the surface is to consider the aluminium concentration on the surface. Therefore, the effectiveness of a diffusion barrier can be ascertained by measuring the concentration on the surface as a function of time. It can be assumed that a coating loses the protective ability when the aluminium concentration on the coating surface decreases to sixty percent. Fig.4 shows the effect of oxide fraction in diffusion barriers on the coating life with different ratios $D_v / (S_g / S_t) D_g$, here $(S_g / S_t) D_g$ is short circuit diffusion

coefficient with the effect of diffusion sections. Let $\tau = 3$, and $D_v = 3.5 \times 10^{-10} \text{ cm}^2/\text{s}$ (the diffusion coefficient of aluminium through Ni5wt-%Al alloy at 1130°C [14]). In Fig.4, it is showed that the effectiveness of diffusion barriers increases with the oxide content, but the increment of the effectiveness varies with the ratio of $D_v / (S_g / S_t) D_g$. When the short circuit diffusion is the path of diffusion (ratio = 0.1), the coating life does not obviously vary with the oxide fraction. When the volume diffusivity is equal to the short circuit one, the effectiveness of diffusion barrier is small, and the barrier containing 50 wt-% oxide only increases the coating lift by a factor of 0.47. When the volume diffusion is dominant, the effectiveness of diffusion barrier increases significantly, which is in agreement with the above experimental results, and the barrier containing 50 wt-% oxides increases the coating life by a factor of 1.9. The post-aluminizing obviously reduces the short circuits, and the diffusion barrier function is similar to curves 1 and 2 in Fig.4.

Fig.5 shows the effect of $D_v / (S_g / S_t) D_g$ on the coating life for a coating with 50 wt-% oxide. The more the ratio, the more effective the diffusion barriers. When ratio is below 0.1, the effectiveness of diffusion barrier changes slightly. When it is beyond 40, volume diffusion is the dominant way, and the effectiveness hardly increases with the ratio. When it is equal to 10, the volume diffusion coefficient is an order of magnitude higher than the short circuit one, but the effectiveness varies with the ratio greatly (Fig.5). Due

to $D^{\text{eff}} = (f/\tau D_v + \frac{S_g}{S_t} D_g)$, and $f/\tau < 1$, the effect of short circuit diffusion increases

relatively. At $\tau = 3$, $f = 0.5$, $f/\tau = 0.17$, and $\frac{S_g}{S_t} D_g = 0.1 D_v$, the short circuit diffusion

still shows a relatively strong effect on the diffusion barrier function. The more the oxide content, the less the f/τ , and the greater the relative effect of the short circuit diffusion. Thus, the effect of short circuit diffusion on diffusion barriers could not be neglected, although the volume diffusion is stronger than the short circuit diffusion at high temperatures.

Conclusions

- (1) The oxide fraction in the diffusion barrier has little effect on the function of LPPS diffusion barrier, and after aluminizing the function obviously increases with the content of oxides.

- (2) There are higher porosities in LPPS diffusion barrier coatings. The short circuit diffusion should be considered in discussing the diffusion mechanism.

References

1. J.L.Smialek et al., NASA TMX-68271, (1973)
2. M.A.Gedwill et al., Met. Eng. Q., 12, 2, May (1972), p.55-61
3. M.A.Gedwill et al., Met. Prog, 106, 3, Aug (1974), p.66-68
4. F.R.Wermuth et al., NASA CR-120852, (1971)
5. M.A.Levinstein, NASA CR-121250, (1973)
6. S.G.Young et al., Thin Solid Films, 53 (1978), p.241-250
7. Y.Lindblom, U.S.Patent, PCT WO 85 / 04428, (1985)
8. J.P.Goad et al., Mat. Sci. Eng., 74(1985), p.93-103
9. K.L.Luthra, J. Vac. Sci. Technol., A3(6), Nov. / Dec. (1985) p.2574-2577
10. M.A.Gedwill et al., Thin Solid Film, 95, 65 (1982)
11. B.Lesage et al., Scripta Metall., 14, (10) (1980) p.1143-1146
12. A.Alkinson et al., Corros. Sci., 21, 1, (1981) p.49-58
13. N.Birks et al., Introduction to High Temperature Oxidation of Metals, Edward Arnold (1983)
14. A.Green et al., Mat. Sci. Technol. 1, Feb. (1985) p.101-103

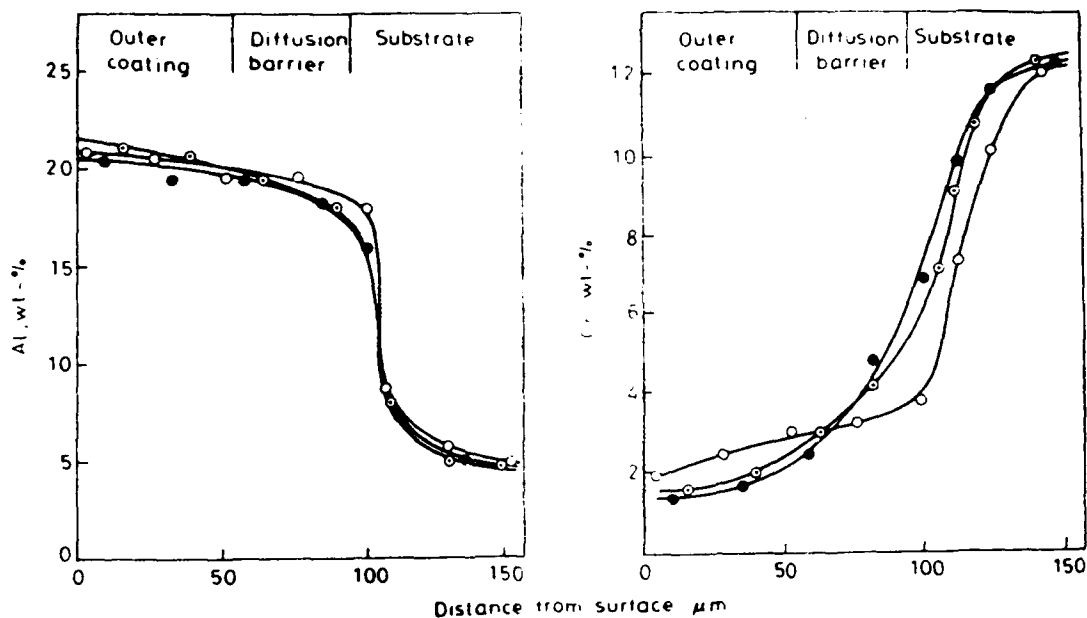


Fig.1. Variation of elemental concentration *versus* depth for LPPS diffusion barrier coatings diffused at 1130°C for 10h in vacuum.

○—0% Y_2O_3 , ⊙—8% Y_2O_3 , ●—30% Y_2O_3

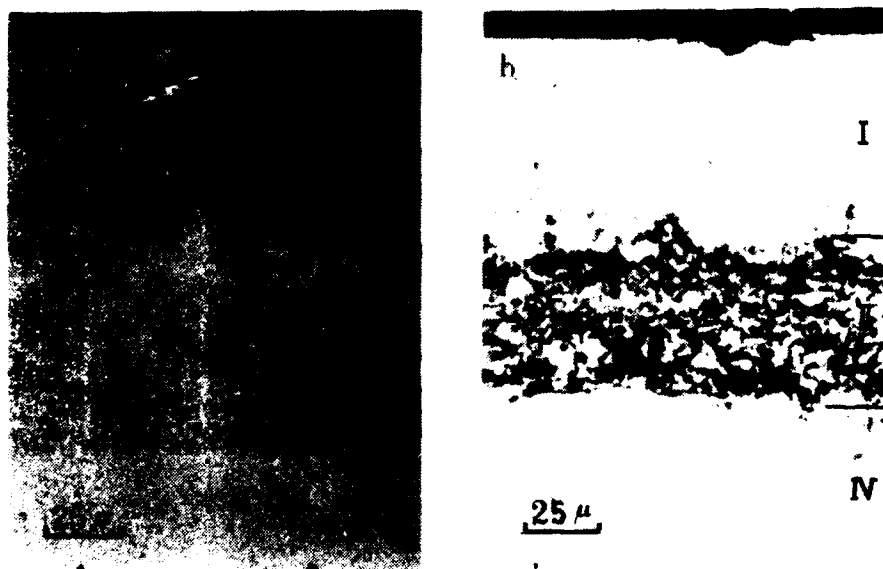


Fig.2. Metallograph of specimens with different diffusion barriers after diffusing 10 h at 1130°C in vacuum.

I —outer coating; II —diffusion barrier; III —diffusion band; IV —substrate
(a) without Y_2O_3 ; (b) containing 30wt-% Y_2O_3

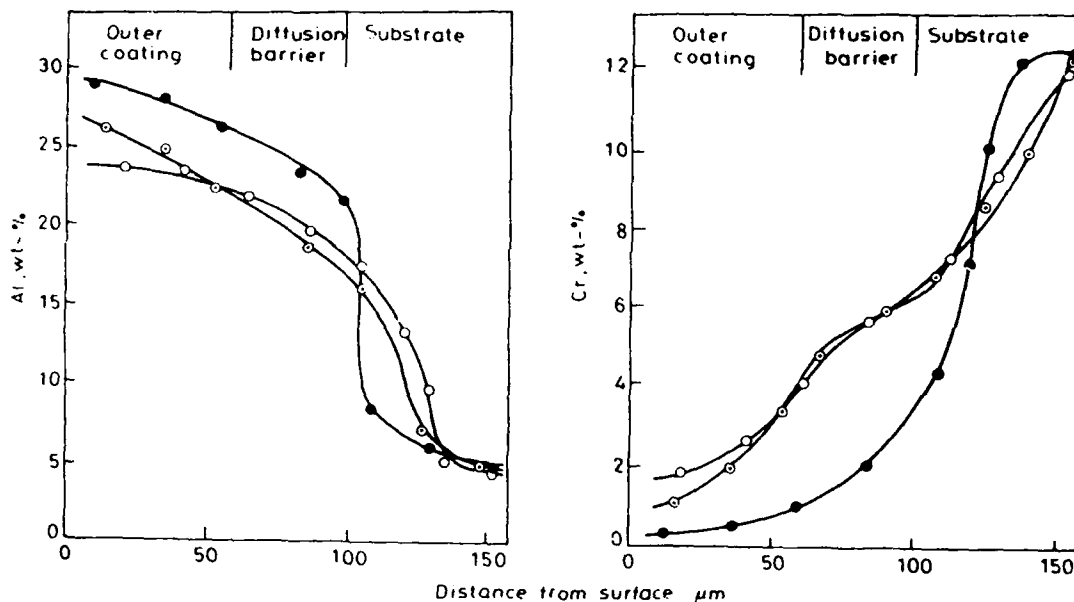


Fig.3. Variation of elemental concentration *versus* depth for aluminized LPPS diffusion barrier coatings diffused at 1130°C for 10h in vacuum

○—0%Y₂O₃ , ◐—8%Y₂O₃ , ●—30%Y₂O₃

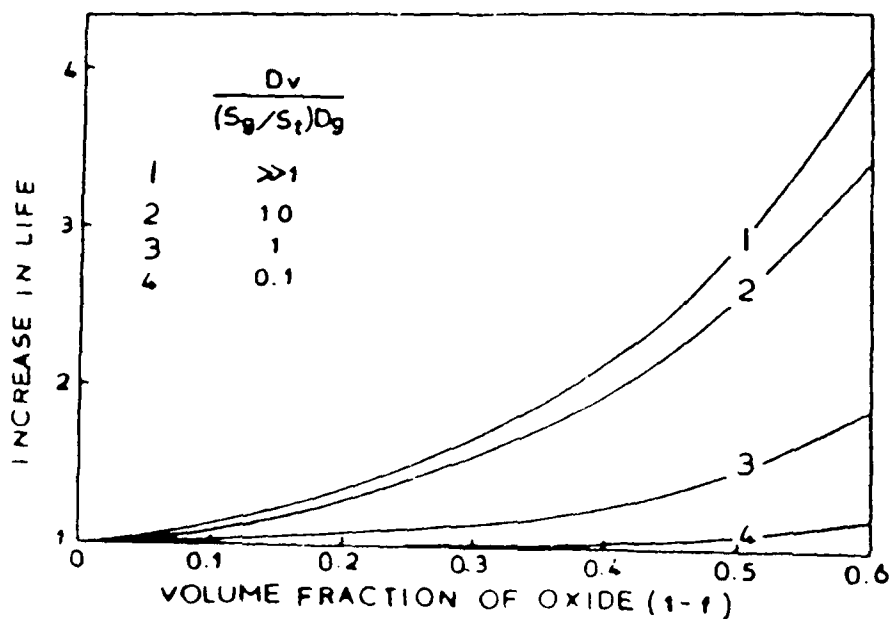


Fig.4. Effect of volume fraction of oxide in diffusion barrier on coating life with different $D_v / (S_g / S_t) D_g$

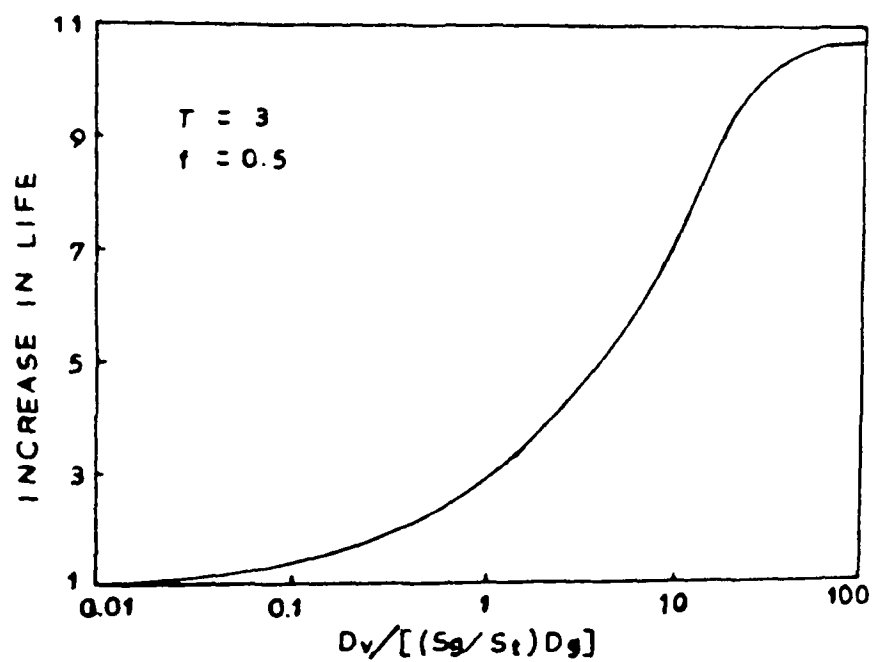


Fig.5. Effect of $D_v / (S_g / S_t) D_g$ on coating life with, oxide content of 50 V.-%

High-Temperature Sulfidation Properties and Demixing Processes of Sulfide Scale of Fe-25Cr-9Mn Ternary Alloy

Huibin Qi

Department of Surface Science and Corrosion Engineering
University of Science and Technology Beijing
Beijing 100083 China

Rizhang Zhu

UNDP Beijing Corrosion and Protection Centre
University of Science and Technology Beijing
Beijing 100083 China

Yedong He

Department of Surface Science and Corrosion Engineering
University of Science and Technology Beijing
Beijing 100083 China

Abstract

The investigation of the sulfidation of Fe-25Cr-9Mn alloy in H_2 - H_2S mixed gases, with the sulfur partial pressures in the range 10^{-3} to 1Pa at a temperature of 800°C, has been carried out. The reaction kinetics of Fe-25Cr-9Mn were measured by a quartz spring thermobalance and compared with that of Fe-25Cr. It has been found that the addition of 9Mn(w/o) enhanced the sulfidation resistance of the Fe-25Cr alloy, but the benefit was not significant. Multilayered sulfide scale formed on Fe-25Cr-9Mn. Although a rather thick α -(Mn,Fe)S layer formed on the alloy, it did not act as an effective barrier to the outward diffusion of Fe^{+2} and Cr^{+3} cations, since it was highly defective due to doping by Fe^{+2} and Cr^{+3} . The influence of the demixing of sulfide scales and the effect of the addition of manganese on the sulfidation behaviour of iron-chromium base alloys are discussed.

Key terms: sulfidation, manganese, multilayered scale, sulfide scale demixing

Introduction

Austenitic stainless steels are used extensively in process industries due to their good mechanical properties and weldability. At elevated temperatures, the corrosion resistance of austenitic stainless steels relies on the formation of chromia (or spinel) scales. However, under some sulfidizing conditions, e.g. in coal gasification and the petrochemical industry, the formation of these protective oxide scales is not possible. Usually, catastrophic sulfidation results from the formation of low-melting eutectic mixtures of Ni-Ni₃S₂ ($T > 635^\circ C$).¹ To avoid this problem, manganese is suggested as an alternative to nickel in austenitic stainless steels. Incidentally, manganese is added into steels to improve their mechanical proper-

ties (ductility, toughness).

Some authors have studied manganese for its potential benefit in sulfidation.²⁻⁶ The Mn-MnS system is much more refractory, with a eutectic temperature of 1242°C.⁶ The sulfidation of pure manganese results in the formation of a cubic α -MnS scale, which has a rather low defect concentration and diffusion coefficient.² The addition of manganese to iron leads to the formation of MnS, a more stable phase than FeS, and a greater degree of protection.⁴ The protection by MnS on Fe-Mn alloys, however, is limited because iron dissolves in the α -MnS and diffuses through it to form an outer Fe(Mn)S layer.

Up to now, only two studies have been reported on the sulfidation of Fe-Cr-Mn ternary alloys.^{6,7} At 973K and a low sulfur pressure ($P_{S_2} = 2 \times 10^{-6}$ Pa), the sulfidation rates of both Fe-20Cr-30Mn and Fe-25Cr-20Mn were higher than that of Fe-25Cr.⁷ Under these conditions, the sulfur pressure was lower than the decomposition pressure of FeS and led to the formation of multilayered sulfide scales, which were comprised of an outer (Mn,Cr)S layer, an intermediate (Mn,Fe)Cr₂S₄ layer and a (Mn,Cr)S layer next to the alloy.⁷ At 973K and 1073K and intermediate level sulfur pressures (i.e. $P_{S_2} = 10^{-3}$ Pa and 8Pa), an Fe-25Cr-10Mn alloy was found to corrode slower than Fe-25Cr.⁶ Ternary alloys provided improved performance only when a layer of Cr₃S₄ was formed. Whether it could be formed depended on the composition of alloy, temperature and sulfur activity.⁶

Fe-Cr-Mn ternary alloys have been found to form complex multilayered sulfide scales and also a single α -MnS layer at the intermediate level sulfur pressures.⁶ But α -MnS did not perform as a protective scale as in the case of sulfidation of pure manganese. The aim of the present work is to study the high-temperature sulfidation behaviour of the Fe-25Cr-9Mn alloy at 800°C and at intermediate level sulfur pressures and compare with Fe-25Cr. Through the analysis and investigation of the structure, the composition and the defects of the sulfide scales formed, further information on the mechanism of the formation and the effect of manganese is intended.

Experimental

The alloys Fe-25Cr-9Mn and Fe-25Cr used in the present study were prepared in a vacuum induction furnace by melting the pure metals under the protection of argon. The chemical compositions of the alloys are listed in Table 1. The ingots were hot rolled into bars with a diameter of about 18mm. They were annealed at 750°C for 1h. Fig.1 shows the microstructures of the alloys after their heat treatment. Samples of the dimensions of 12 × 0.9mm were cut. The sample surfaces were abraded to 1000 grit emery paper. Prior to use samples were repolished to remove the thin oxide film possibly formed on the surface at room temperature and rinsed in acetone.

The experiments were conducted at 800°C and in H₂S-H₂ gas mixtures with the sulfur partial pressures of 10⁻³ to 1Pa. The reaction kinetics were obtained by means of a quartz spring thermobalance, the sensitivity of which was about 1 × 10⁻⁵ g.⁸ Two samples were tested for each experimental condition to test the reproducibility of the experiments. The corrosion products were characterized by scanning electron microscopy(SEM), energy-dispersive X-ray analysis(EDAX), electron-probe microanalysis(EPMA) and X-ray diffraction(XRD).

Results

Reaction Kinetics

Fig.2 shows the sulfidation kinetics as mass gain against time. To show the effect of manganese, the reaction kinetics of Fe-25Cr-9Mn and Fe-25Cr under the same experimental conditions were plotted in one diagram. It can be concluded from the mass gain that both alloys were rapidly corroded under the experimental conditions used. Generally speaking, the sulfidation kinetics of both alloys obeyed the parabolic law after an initial period of time. Except for cases of Fe-25Cr at $P_{S_2} = 1\text{Pa}$ and Fe-25Cr-9Mn at $P_{S_2} = 10^{-1}\text{Pa}$, the sulfidation rate for two alloys increased with sulfur pressure. For the above mentioned two anomalous cases, the tendency of sulfidation kinetics changed during the reaction process, i.e. the mass gain vs. time curve for Fe-25Cr changed into a linear relationship after a period of time (see Fig.2a) and a turn appeared on the kinetics curve for Fe-25Cr-9Mn at about 3.0ks (see Fig.2b). This led to the mass gain of Fe-25Cr-9Mn at $P_{S_2} = 10^{-1}\text{Pa}$ lower than that at $P_{S_2} = 10^{-2}\text{Pa}$.

Except for the case at $P_{S_2} = 1\text{Pa}$, the sulfidation rate of Fe-25Cr-9Mn was slower than that of Fe-25Cr at lower sulfur pressures. Under these conditions the addition of 9Mn(w/o) improved the sulfidation resistance of Fe-25Cr. However, the improvement is not significant. It can be seen from Fig.2a that the reaction rate of Fe-25Cr was faster than that of Fe-25Cr-9Mn at the beginning of sulfidation at $P_{S_2} = 1\text{Pa}$, but slower after about 2.5ks. This change is related to the nature of sulfide scale.

Scale Morphologies and Structures

The surface product on Fe-25Cr alloy was always the large-grain phase Fe_{1-y}S , with the deviation from stoichiometry (y) of approximately 0.25 (measured by EDAX). The surface morphology and the corrosion products on Fe-25Cr-9Mn were quite similar to that of Fe-25Cr, but the product of the former contained about 2Mn(a/o). The surface grains of the product on both alloys became larger with the increase of the sulfur pressure. Also, a stripy substructure in the sulfide grains on Fe-25Cr-9Mn corroded at $P_{S_2} = 10^{-3}\text{Pa}$ appeared(Fig.3), but no remarkable composition change of the surface product was detected.

A duplex or triplex sulfide scale formed on Fe-25Cr exposed for 7.2ks depending on the sulfur partial pressures. When $P_{S_2} > 10^{-2}\text{Pa}$, the sulfide scale consisted of an outer layer of Fe_{1-y}S , an intermediate layer of FeCr_2S_4 and an inner layer of $(\text{Cr,Fe})\text{S}_x$. There was a relatively high concentration of chromium in the inner part of the outer Fe_{1-y}S layer. When $P_{S_2} < 10^{-2}\text{Pa}$, the sulfide scale of Fe-25Cr consisted of two layers, the outer layer of which was rather thick and of a nonuniform composition. The outer part of it only contained Fe and S, however, the inner part enriched in Cr in addition to Fe and S. The outer layer can be denoted as $\text{Fe}_{1-y}\text{S} + (\text{Cr,Fe})\text{S}_x$ on a quenched sample, but $\text{Fe}_{1-y}\text{S} + \text{FeCr}_2\text{S}_4$ on a furnace cooled sample. This is consistent with the result of Narita et al.⁹ This indicated that the $(\text{Cr,Fe})\text{S}_x$ phase formed at high temperature was not stable and changed into FeCr_2S_4 in the slow cooling process. The rates of this phase change were slow and dependent upon temperature and sulfur pressure.

Unlike Fe-25Cr, more complex multilayered scales formed on Fe-25Cr-9Mn. It can be seen from Fig.4-6 that the sulfide scales on Fe-25Cr-9Mn at all sulfur pressures were comprised of four layers. The higher the sulfur pressure, the thicker the innermost layer of the sulfide scale on Fe-25Cr-9Mn. Fig.4b shows that nonuniform, severe internal sulfidation of Fe-25Cr-9Mn was produced at $P_{S_2} = 1\text{Pa}$. In some

areas, sulfides protruded even to the centre of the sample. It is obvious that a porous inner sulfide layer resulted from the outward diffusions of metal ions, by the mechanism that the vacancies of metal ion diffused inwardly simultaneously. However, most of the cavities in the intermediate layer shown in Fig.5 and Fig.6 were formed by the removal of sulfide grains during polishing. It can be seen from Fig.5 that the Pt-marker was located above the innermost layer, which suggests that the outer sulfides grew by the outward diffusions of metal ions and inner sulfide by the inward sulfur diffusion, similar to the situation of Fe-25Cr.

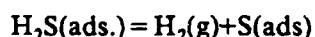
From the XRD patterns of the powder of corrosion products formed on Fe-25Cr-9Mn, it was determined that the corrosion products were mainly composed of Fe_{1-y}S , $\alpha\text{-MnS}$ and $(\text{Cr,Fe})\text{S}_x$. Combined with the analysis by EDAX, it was concluded that the outermost layer was Fe_{1-y}S . Beneath it was a $\alpha\text{-(Mn,Fe)S}$ layer, the intermediate layer was composed of $\text{Fe}_{1-y} + (\text{Cr,Fe})\text{S}_x$ and the innermost layer adjacent to the base alloy was $(\text{Cr,Fe})\text{S}_x$. Besides being enriched in $\alpha\text{-(Mn,Fe)S}$, manganese was also distributed in all other layers to about 2a/o. The mole ratio of Mn to Fe in $\alpha\text{-(Mn,Fe)S}$ is 1:1 approximately.

The sulfides formed on both two alloys were brittle and the separation of the outer sulfide layer from the inner one often occurred. This would directly influence the reaction kinetics and the sulfide morphologies. In addition, the formation of multilayered sulfide scales was a common phenomenon, and even in one layer, the composition was not uniform, e.g. the inner parts of the outer sulfide layer on Fe-25Cr and of the intermediate sulfide layer on Fe-25Cr-9Mn were highly enriched in chromium. This phenomenon may be described by the term "demixing" used in oxidation studies.¹⁰ The demixing process of sulfide scale will be discussed in detail below.

Discussion

Reaction Kinetics

The mathematical analysis of mass gain vs. time relationship shows that the basic sulfidation kinetics of the two tested alloys are an incubation period + parabolic relationship. In the initial period of time, the sulfidation process is controlled by the following reaction:¹



With the approach to equilibrium of this process, the surface sulfur activity and the sulfide scale thickness increases. As a result, the reaction becomes controlled by the outward diffusions of Fe^{2+} and Cr^{3+} , so the reaction kinetics enter the parabolic stage.

It can be determined that the change of reaction kinetics of Fe-25Cr at $P_{\text{S}_2} = 1\text{Pa}$ to the relationship similar to the linear law after the initial period of sulfidation has a relation to the detachment (no cracking) of the sulfide scale from the alloy at some local areas. It is worth point out that no cracking occurs for the sulfide scale after its separation from the alloy, so no ambient mixed gas comes into direct contact with the alloy base. The decrease of the practical reaction surface area of sample leads to the decrease in sulfidation rate.

Similar to the above case, the turn that appeared on the sulfidation kinetics curve after about 3.0ks for

Fe-25Cr-9Mn corroded at $P_{S_2} = 10^{-1}$ Pa results from the separation of the sulfide scale from the alloy and cracking of the scale, as confirmed by observation of the morphology of sulfide scales. The internal sulfidation region is thin and uniform under the separated scale without cracking, but thick and nonuniform under the separated scale with cracking (like the case shown in Fig.4).

Sulfide Scale Morphologies and Demixing

Under the experimental conditions in the present paper, multilayered sulfide scales are found on both alloys. From exterior to interior, the sulfide scales consist of $Fe_{1-y}S$, $FeCr_2S_4$, $(Cr,Fe)S_x$ on Fe-25Cr; while $Fe_{1-y}S$, $\alpha-(Mn,Fe)S$, $(Cr,Fe)S_x$ on Fe-25Cr-9Mn. Compared with Fe-25Cr, the sulfide scale structure of Fe-25Cr-9Mn does not improve protection remarkably, since the outermost $Fe_{1-y}S$ layer, consisting of large grains and being of high defect concentration, is formed. A single $\alpha-(Mn,Fe)S$ layer forms on Fe-25Cr-9Mn, but it does not give the same protection as $\alpha-MnS$ in the case of sulfidation of pure manganese.² It can be concluded from free energies of formation (Table 2) that MnS is the most stable phase among the sulfides and has the lowest equilibrium decomposition pressure. As a result, MnS should locate next to the metal. However, the $\alpha-(Mn,Fe)S$ layer formed on Fe-25Cr-9Mn is in the outer part of the sulfide scale, i.e. the order that sulfides were arranged is different from that of the sulfide stabilities shown in Table 2.

The EDAX analysis indicates that the mole fraction of FeS in the $\alpha-(Mn,Fe)S$ layer on Fe-25Cr-9Mn is about 0.5, in addition, some chromium also exists in it. $Mn_{1-y}S$ is a metal deficient p-type semiconductor, so the dissolution of Cr^{3+} of higher valence than Fe^{2+} in it will increase its defect concentration. Also, $Fe_{1-y}S$ is also a metal deficient p-type semiconductor and its deviation from stoichiometry (y) is rather high. As the result of FeS dissolved into MnS, the value of y of $Mn_{1-y}S$ would be strongly increased,⁴ thereby the decomposition sulfur pressure is elevated too. So, the appearance of an $\alpha-(Mn,Fe)S$ layer in the outer part of the scales is comprehensible. The main reason for the worse protection of $\alpha-(Mn,Fe)S$ on Fe-25Cr-9Mn than MnS on pure manganese is likely to be the doping of Fe^{2+} and Cr^{3+} . The doping of Cr^{3+} could increase the hardness and thus destroy the plasticity and the protection of $\alpha-MnS$.⁷

Schmalzried et al¹⁰ indicated that a multicomponent oxide $(A,B)O$ and even the spinel oxide AB_2O_4 would demix to AO and BO or B_2O_3 under the gradient of oxygen activity. If $D_A > D_B \gg D_O$, that D denotes the diffusivity of A, B or O, AO would segregate in the part of scale located in high oxygen activity. The rate of the demixing process and the relative thickness of each layer depends on the values of D_A and D_B . Undoubtedly, the higher the stability and the lower the defect concentration of $(A,B)O$ or AB_2O_4 , the slower the demixing process of the oxide scale.

In the present study, chromium was enriched in the inner parts of the outer sulfide layer on Fe-25Cr and the intermediate sulfide layer on Fe-25Cr-9Mn. Although no change of the scale morphology occurred, the composition in a layer was not uniform. However, the shorter the reaction time, the more uniform the chromium was distributed. This means that chromium segregated in the inner part of the layer composed of the solid solution of sulfides of chromium and iron along with the progress of sulfidation. At the same time iron segregated in the outer part of the layer. Finally, two sulfide layers of different composition appeared. The similar phenomenon was also observed by Narita et al⁹ in the sulfidation study of Fe-Cr binary alloys. Similar to the above demixing process of oxide scales, it can be inferred that under the driving force of the sulfur activity gradient between the ambient sulfur pressure and the sulfur pressure at the

sulfide / substrate interface, not only all sulfide layers were arranged from exterior to interior according to the value of decomposition pressure, but also sulfides with different composition would demix even in an individual layer. Generally speaking, the demixing of sulfide scales will destroy its protective behaviour.

Summary

In the present paper, the high-temperature sulfidation properties of Fe-25Cr-9Mn and Fe-25Cr in H_2S-H_2 gas mixtures at 800°C and $P_{S_2} = 10^{-3}-1Pa$ has been compared. The sulfidation process was mainly controlled by the outward diffusions of Fe^{2+} and Cr^{3+} cations. The sulfidation kinetics were closely related to the nature of sulfide scales (whether separating with the alloy base and / or cracking). Except for the case at $P_{S_2} = 1Pa$, the addition of 9Mn(w / o) improved the sulfidation resistance of the alloy, but the benefit was not significant. Because of the doping of Fe^{2+} and Cr^{3+} , the $\alpha-(Mn,Fe)S$ layer formed on Fe-25Cr-9Mn had a large deviation from stoichiometry, and thus did not act as a complete diffusion barrier like the $\alpha-MnS$ on pure manganese. Under the sulfur activity gradient, a demixing process of multicomponent sulfide scales occurred and led to lower corrosion protection than expected.

Acknowledgement

Financial supports for this work by Chinese National Natural Science Foundation and Chinese Corrosion Science Laboratory are acknowledged.

References

1. D.J.Young, Rev. High Temp. Mater.,4(1980): p.299.
2. S.Mrowec, K.Prszybylski, High Temp. Mater. Proc., 1(1984): p.6.
3. M.Danielewski, Oxid. Met., 25(1986): p.51.
4. K.Nishida, T.Narita, T.Tani, G.Sasaki, Oxid. Met.,14(1980): p.65.
5. W.Znamirowski, F.Gesmundo, S.Mrowec, M.Danielewski, K.Godlewski, F.Viani, Oxid. Met., 35(1991): p.175.
6. G.Southwell, D.J.Young, Oxid. Met., 36(1991): p.409.
7. P.Papaiacovou, H.J.Grabke, P.Schmidt, Werkst. Korros., 36(1985): p.320.
8. H.B.Qi, R.Z.Zhu, Y.D.He, Proc. of The 7th Asian Pacific Corrosion Control Conference, Vol.I(1990): p.118.
9. T.Narita, W.W.Smeltzer, Oxid. Met., 21(1984): p.39; 57.
10. H.Schmalzried, W.Laqua, Oxid. Met., 15(1981): p.339.

Table 1. Alloy compositions (w / o).

Nominal composition	Fe	Cr	Mn	C
Fe-25Cr-9Mn	Bal.	24.53	8.87	0.010
Fe-25Cr	Bal.	24.49	—	0.018

Table 2. Free Energies of Formation of Sulfide(kJ) per mole of S_2 (g) at 800°C.

Sulfide	FeS	FeCr ₂ S ₄	Cr ₃ S ₄	CrS	MnS
ΔG^0	-188	-214	-258	-285	-398

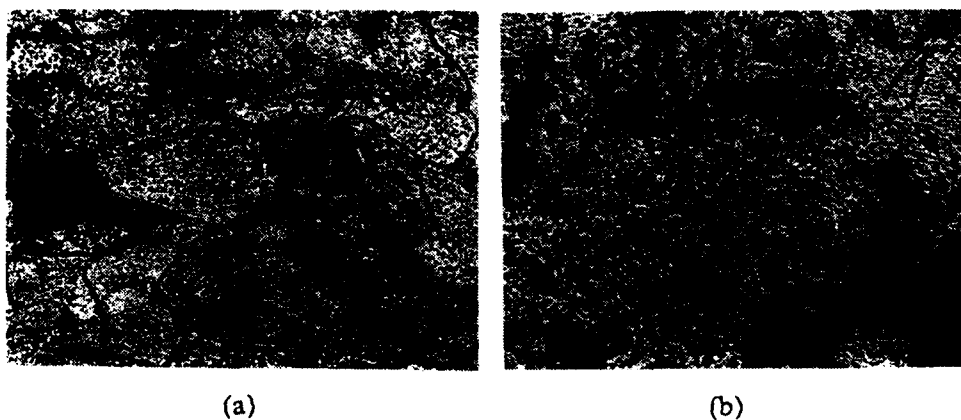
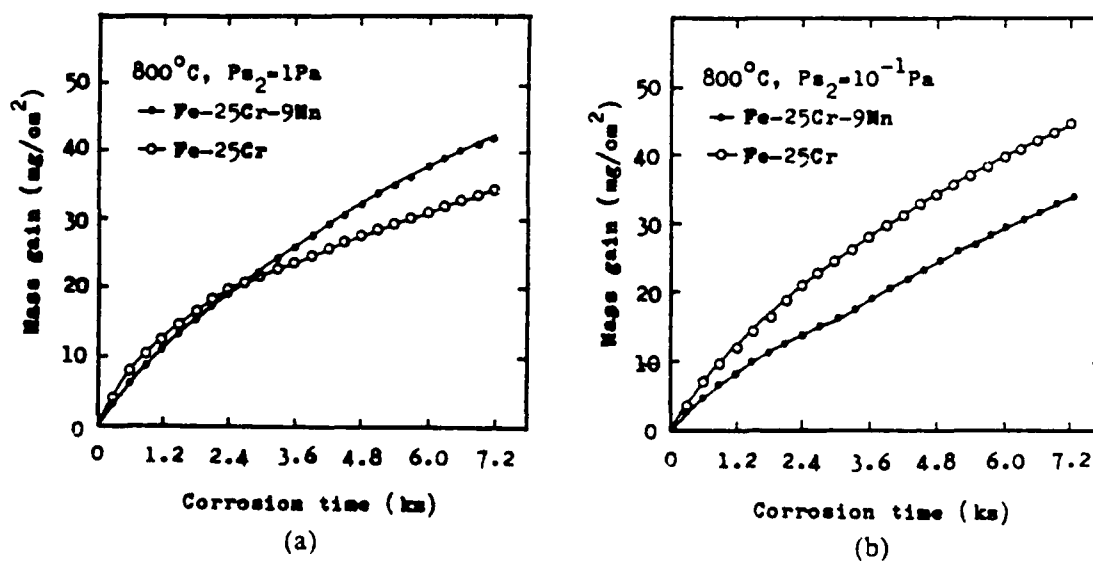
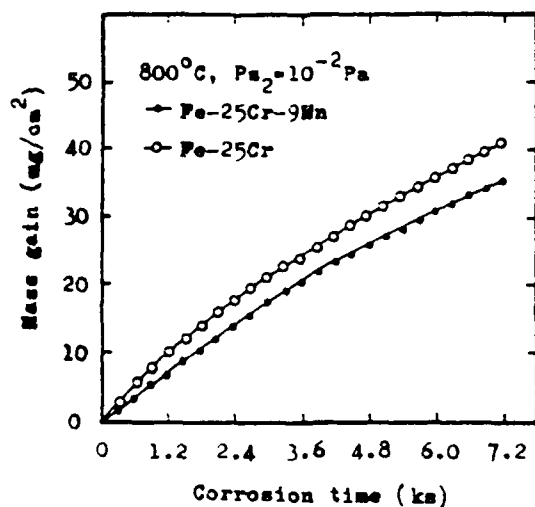
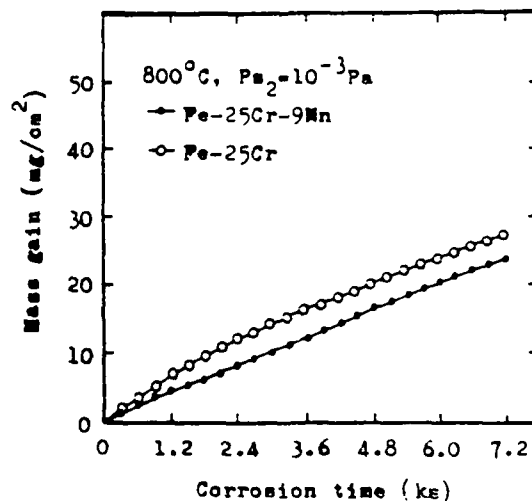


Fig.1. Metallurgical microstructures of alloys after annealing at 750°C for 1h.
(a) Fe-26Cr-9Mn, $\times 500$; (b) Fe-25Cr, $\times 200$.





(c)



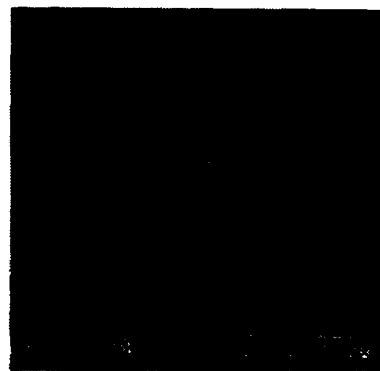
(d)

Fig.2. Sulfidation kinetics at 800°C.

(a) $P_{S_2} = 1$ Pa, (b) $P_{S_2} = 10^{-1}$ Pa, (c) $P_{S_2} = 10^{-2}$ Pa, (d) $P_{S_2} = 10^{-3}$ Pa.



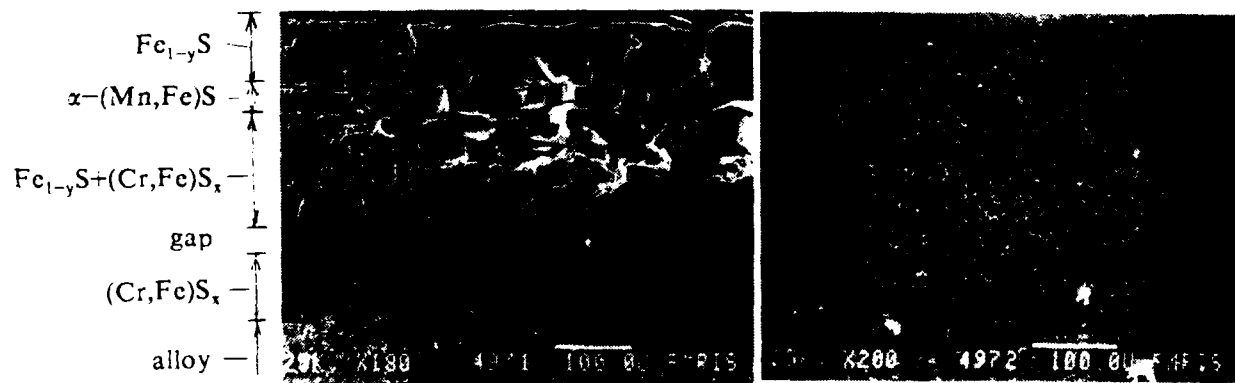
(a)



(b)

Fig.3. Surface morphologies of sulfide scales on Fe-25Cr-9Mn corroded at 800°C for 7.2 ks.

(a) $P_{S_2} = 1$ Pa, (b) $P_{S_2} = 10^{-3}$ Pa.



(a)

(b)

Fig.4. The cross-section of sulfide scale on Fe-25Cr-9Mn corroded at 800°C and $P_{S_2} = 1$ Pa for 7.2 ks. (b) is the inner sulfide layer on the same sample shown in (a).

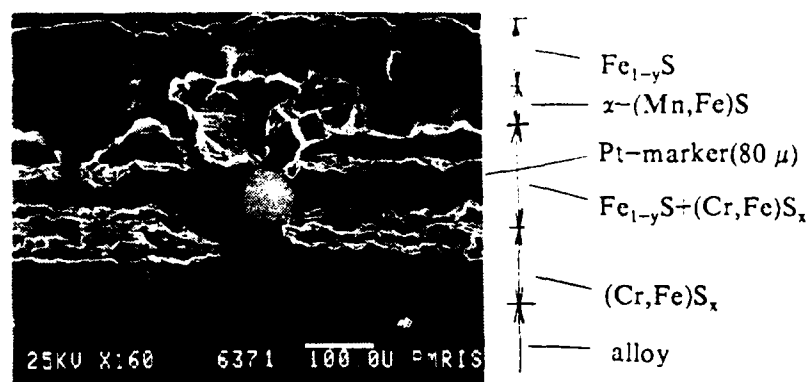


Fig.5. The position of Pt-marker in the sulfide scale on Fe-25Cr-9Mn corroded at 800°C and $\text{P}_{\text{S}_2} = 10^{-1}\text{Pa}$ for 12ks.

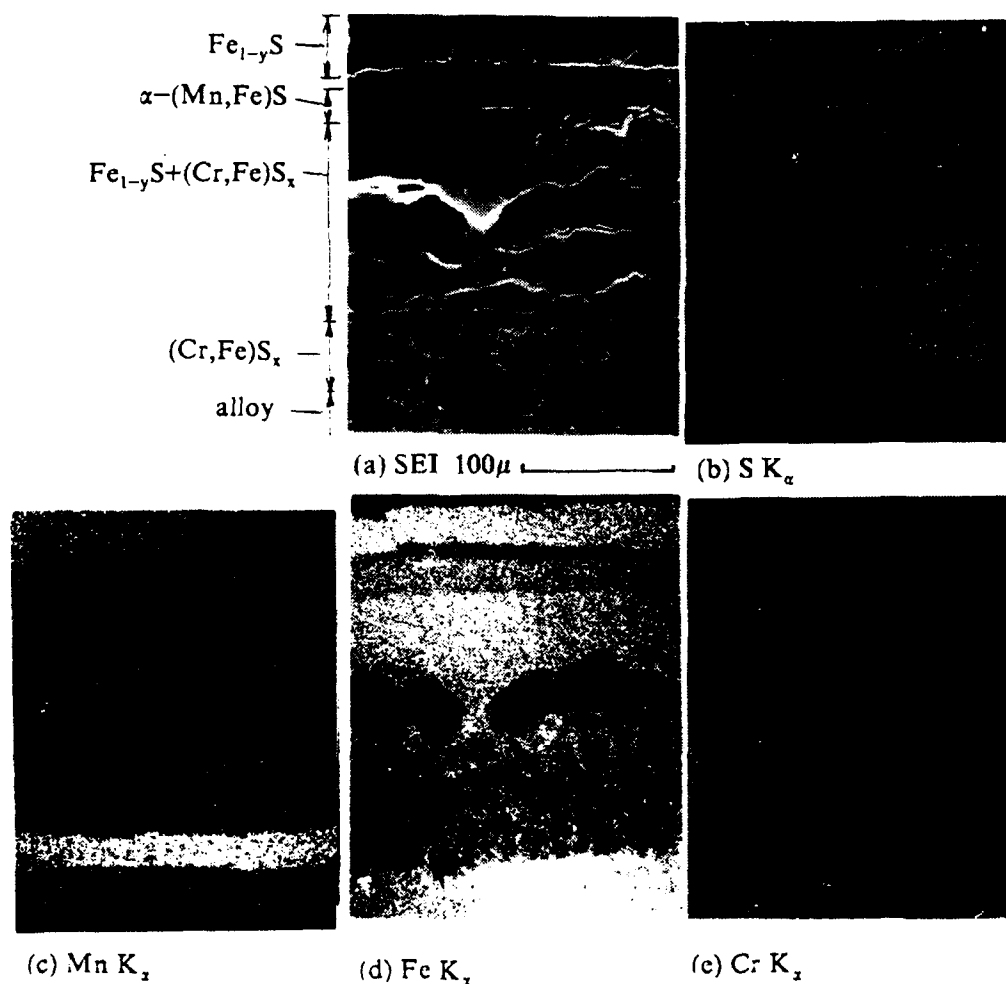


Fig.6. The elemental distribution images by EPMA of the sulfide scale on Fe-25Cr-9Mn corroded at 800°C and $\text{P}_{\text{S}_2} = 10^{-3}\text{Pa}$ for 7.2ks.

Influence of Nd on Oxidation of Ti-5621S Alloy

Li Meishuan

Corrosion Science Laboratory,
Institute of Corrosion and Protection of Metals,
Chinese Academy of Science,
No.62 Wencui Road, Shenyang 110015, China

Li Tiefan

Corrosion Science Laboratory,
Institute of Corrosion and Protection of Metals,
Chinese Academy of Science,
No.62 Wencui Road, Shenyang 110015, China

Abstract

The spalling processes of oxide scales formed on Nd-doped and Nd-free Ti-5621S (Ti-5Al-6Sn-2Zr-1Mo-0.25Si) alloys have been studied using an acoustic emission technique during cooling from 800°C. The oxidation kinetics of these two alloys also has been investigated.

The principal oxide was TiO_2 with small amounts of Ti_2O_3 , TiO , Al_2O_3 and SnO_2 . The addition of 1wt% Nd increases the oxidation rate of Ti-5621S alloy slightly, but improves the spalling resistance of the oxide scale greatly. During oxidation, a great deal of large Nd_2O_3 particles were present as spherical inclusions in the oxide layer, which were enveloped by SnO_2 and TiO_2 at the oxide/alloy interface. The inclusions generally improved the adhesion of the oxide scale. However, these inclusions suffered high thermal compressive stress during cooling, and some of them were broken off or expelled from the substrate. This type of inclusion can serve as centers for crack initiation. One simple model is proposed, and the thermal stress on the inclusion has been theoretically evaluated. The observation of surface morphologies on oxide scales verifies the analysis.

Key terms: oxidation, oxide scale, cracking and spalling, adhesion, acoustic emission, rare earth neodymium

Introduction

Titanium alloys are generally used as materials for turbine blades in aeronautical, astronautical and electric power industries due to their high strength to weight ratio. Ti-5621S (Ti-5Al-6Sn-2Zr-1Mo-0.25Si) is one of the well-known "Ti-Al-Sn-Zr" base super-alloys^[1]. It has been found that a Nd addition to Ti-5621S alloy as high as 1 wt% can play a strengthening role, and inhibits the Ti_3X phase formation^[2]. However, research on the oxidation of this complicated engineering titanium alloy is very limited. In particular, the influence of Nd on the oxidation behavior of this alloy and the adherence of the oxide scale is of interest and has

been studied at 800°C have been studied using a thermal gravimetric balance and an acoustic emission (AE) technique.

Experimental procedure and results

1. Oxidation kinetics

Ti-5621S alloy containing 1 wt% Nd was obtained by metallurgical doping, which leads to optimum strength^[2]. All specimens were cut to dimensions of 20X10X2 mm, polished with 800 grit SiC paper, planed at edges and corners, then annealed at 900°C for 1 hour and at 600°C for 2 hours in vacuum of 2.5×10^{-5} Torr (3.3×10^{-3} Pa).

Fig.1 shows the oxidation kinetics of Nd-free and Nd-doped Ti-5621S alloys at 800°C in air over 15h. The Nd addition increased the oxidation rate of the alloy slightly.

2. AE test

In the AE test, a platinum wire of diameter 1mm was used as a wave guide. It was welded onto one side of specimen using a spot welding machine. The other end of the platinum wire was welded onto a steel bar with a taper. A piezoelectric transducer with a resonant frequency of 150 kHz was fixed on the steel bar. A total system gain of 40+42 dB and threshold voltage of 1V was maintained throughout. Cumulative AE energy count was recorded. The schematic diagram of AE apparatus is shown in Fig.2. The details are described in references 3 and 4.

Cumulative AE energy counts for two specimens cooled from 800°C in and outside the furnace, respectively, are presented in Fig.3(a) and (b). No AE signal was found during isothermal oxidation in any of the experiments.

The following data can be ascertained from Fig.3 (see references 3 - 6): the time at which AE signal begins, the change of temperature corresponding to the first signal, and the final cumulative count after a certain time from beginning of cooling. During cooling in the furnace, the AE signal for Nd-free Ti-5621S occurs earlier than that for Nd-doped Ti-5621S, and the final cumulative AE energy counts are higher. For each alloy, the longer the oxidation time, the earlier the AE signal occurs during cooling and the greater the final AE cumulative counts are. In contrast, when the cooling rate is much higher (cooled outside the furnace), although Nd-free Ti-5621S develops AE signals earlier, its final cumulative AE counts are lower than those for Nd-doped Ti-5621S.

It was observed that the AE signal did not stop after the specimen had cooled to room temperature, but a few AE signals still take place. This phenomenon was also found in AE testing of Cu¹¹¹. Therefore, the processes of energy release in the oxide scale, such as plastic deformation or crack expansion, occur until the sample reaches ambient temperature.

3. Oxide phases and surface morphologies

The oxide phases were determined by XRD. Complex oxide scales were found on the two alloys oxidized at 800°C in air, which were mainly composed of TiO_2 with small amounts of Ti_2O_3 , TiO , Al_2O_3 and SnO_2 .

The oxide scales formed on all specimens appeared to partially spall. However, it is clear from the investigation of the specimen surfaces after oxidation that spalling of the oxide scale on the Nd-doped Ti-5621S is much less than that on Nd-free Ti-5621S. Many nodules were found on the surface of oxide scales formed on Nd-doped Ti-5621S alloy, as shown in Fig.4 (All specimens analyzed were cooled in the furnace). The centers of these nodules were verified to be Nd_2O_3 particles using ion micro-prob analysis. After spalling of the oxide scales, these particles may remain on the specimens wholly or only partially due to breakage, or may be separated from the alloy, as presented in Fig.5. Fig.6 shows a cross-section of Nd-doped Ti-5621S oxidized for 10h. Most of the Nd_2O_3 particles are located in the oxide/alloy interface, resulting in the formation of inclusions enveloped by Ti and Sn oxides. Further, Al is rich in the outer layer of the oxide scale. The distribution of the main alloying elements in the oxide scales did not differ for the two alloys^[8].

Results analysis

1. General analysis

Neodymium in the 1wt% Nd-doped Ti-5621S alloy exists both as a fine element dispersion and as large particles partially oxidized. These spherical particles were created during preparation of the alloy. Their size is about 100 - 200 nm^[2,8]. Therefore, this study shows that, after oxidation, the particles may coarsen and grow several times the original diameter (see Figs 4 and 5), they are composed of Nd_2O_3 .

During oxidation of Ti-5621S, the outward diffusion of Ti and Al cations predominates. However, the inward diffusion of oxygen anions also exists^[9]. It can be concluded from the fact that SnO_2 forms under Nd_2O_3 particles and that Al_2O_3 is formed with in the outer layer, that this oxidation mechanism is also applicable to Nd-doped Ti-5621S. A possible mechanism for the formation of the nodules observed is that, at the initial stage of oxidation, the large particles grow because of their oxidation. At same time, alloy elements Ti and Al are oxidized to form the scale. Finally, the rapid formation of Ti and Al oxides leads to the Nd_2O_3 particles being covered by the oxide scale.

Generally, the addition of small amount of a rare earth element can improve the oxidation resistance of Chromia-Alumina-forming alloys (the 'reactive element effect'). However, if RE concentration is a little high, its effect degrades, particularly, if large RE oxide 'pegs' are formed. It is thought that they can serve as the fast

path for diffusion of negative ions^[9,10], which causes the oxidation rate of alloys to increase. This is thought to be the main reason for the oxidation rate of Nd-doped Ti-5621S being higher than that of Nd-free Ti-5621S in this study.

The surface investigation indicates that the spalling of the oxide scale on Nd-doped Ti-5621S is much less than that on Nd-free Ti-5621S, that is, the addition of Nd to Ti-5621S alloy improves adherence of oxide scale significantly. This correlates with the results obtained in AE tests. It is proposed that inclusions have a keying effect on oxide scales. Also they can extend the expanding distance for cracks and increase the adhesive area between the oxide scale and the alloy. However, the difference between the critical temperature change ($|\Delta T|$) needed for the initial cracking of the oxide scales of these two alloys is not as great as expected. For example, the data of $|\Delta T|$ are 511°C and 585°C respectively for Nd-free Ti-5621S and Nd-doped Ti-5621S respectively oxidized at 800°C for 10h. and 400°C and 460°C for oxidation for 15h. Furthermore, for the condition of fast cooling, the final cumulative AE energy count of Nd-doped Ti-5621S is higher than that of Nd-free Ti-5621S, although the oxide scale of Nd-doped Ti-5621S cracks later. Also, the critical temperature change $|\Delta T|$ for the Nd-doped alloy is similar for cooling inside and outside the furnace. As a matter of fact, spalling of the oxide scale on Nd-doped Ti-5621S is not so serious, and only the number of the broken particles increases. Therefore, the inclusions formed during the oxidation of Nd-doped Ti-5621S have a significant influence on development of AE signals, and also therefor on the behavior of cracking of oxide scale.

The thermal expansion coefficient of the alloy is larger than that of the oxides. The contraction of the alloy is therefor larger than that of the inclusions during cooling from the oxidation temperature, so that inclusions suffer a high compressive stress in the direction perpendicular to the inclusion surface. If this stress is high enough, some of the inclusions should move outward or break. Based on this model, the thermal stress can be evaluated just as described below.

2. Thermal stress model

Fig.7 shows a simple model to ascertain the stress on the surface of inclusions. The inclusion is treated as spherical in shape. The influence of oxide layer on the deformation of alloy near the inclusion is neglected.

It is supposed that r_i is the radius of the inclusion at beginning of cooling. When the temperature change is T , the radius of the inclusion becomes r_j , the thermal stress is σ_{ox} . In order to calculate σ_{ox} , we can assume that the deformation of the inclusion and the alloy near it is independent, their radius and 'inside' radius become r_{ox}' and r_i' respectively. Therefore, we obtain

$$r_{ox}' = r_1 (1 + \alpha_{ox}^* \Delta T) \quad (1)$$

$$r_1' = r_1 (1 + \alpha_1 \Delta T) \quad (2)$$

where α is thermal expansion coefficient (* indicates average value). The stresses on the inclusion and the alloy respectively can be written as

$$\sigma_{ox} = E_{ox}^* \cdot \frac{r_2 - r_{ox}'}{r_{ox}'} \cdot \frac{1}{1 + \mu} \quad (3)$$

$$\sigma_1 = E_1 \cdot \frac{r_2 - r_1'}{r_1'} \cdot \frac{1}{1 + \mu} \quad (4)$$

Where, E is the Young's modulus, and μ is Poisson's ratio (generally equals 0.3 for both oxide and metal^[11,12]). Due to the equilibrium of two stresses indicated in the equations (3) and (4), thus $\sigma_{ox} + \sigma_1 = 0$. Finally, we can obtain σ_{ox} from all equations mentioned above, and $(1 + \alpha \Delta T)$ is replaced with 1 ($\alpha \sim 10^{-5}/^\circ\text{C}$, $|\Delta T| < 800^\circ\text{C}$), the equation of becomes very simple

$$\sigma_{ox} = \frac{(\alpha_1 - \alpha_{ox}^*) \cdot \Delta T \cdot E_{ox}^* \cdot E_1}{E_1 + E_{ox}^*} \cdot \frac{1}{1 + \mu} \quad (5)$$

This stress forces on the surface of the inclusion perpendicularly. Resulting from this stress, the perpendicular outward force in the oxide/alloy interface equals

$$F_\perp = \iint \sigma_{ox} r_2^2 \cos \theta \cdot d\theta \cdot d\psi = 2\pi r_2^2 \cdot \sin \beta \cdot \sigma_{ox}$$

So the correspondent stress equals

$$\sigma_\perp = F_\perp / (\pi (r_2 \sin \beta)_1^2) = 2\sigma_{ox} / \sin \beta \quad (\beta \neq 0, \pi) \quad (6)$$

It can be seen from equation (6) that the smaller the value of β , the less deep the inclusion intrudes the substrate, and the higher the value of σ is. However, in this case, the influence of oxide scale on the deformation of alloy near the inclusion is evident, which can't be neglected. The evaluation may cause a great error. If the inclusion is very small, the case is the same.

When $\beta > \pi/2$, most of the inclusion is located in alloy. It is very difficult for outward movement of the inclusion to occur. We can propose that this type of inclusions has a keying effect, which can

improve the adhesion of the oxide scale.

When $\beta \approx \pi/2$, the assumption is better agreement with the experimental condition, and σ_{ox} can be evaluated. The modulus and thermal expansion coefficient of the composite oxide inclusion are replaced by the corresponding data of TiO_2 ^[1,13]. Although the inclusion is mostly Nd_2O_3 , the outer layer enveloping the Nd_2O_3 particle is TiO_2 , and the inclusion separates from the alloy at the TiO_2 /alloy interface, we think that the above assumption is reasonable.

$$\begin{aligned} E_s &= 113.3 \times 10^3 \text{ MPa (20}^\circ\text{C)} \\ \alpha_s &= 9.9 \times 10^{-6}/^\circ\text{C (0 - 800}^\circ\text{C)} \\ E_{ox}^* &= E_{TiO_2} = 284.2 \times 10^3 \text{ MPa (20}^\circ\text{C)} \\ \alpha_{ox}^* &= \alpha_{TiO_2} = 8.2 \times 10^{-6}/^\circ\text{C (20 - 800}^\circ\text{C)} \end{aligned}$$

Since the temperature at which the oxide scales of two alloys first crack is nearly 200°C , $\Delta T = -600^\circ\text{C}$. Using these data and equations (5) and (6), we obtain $\sigma_{ox} = -65 \text{ MPa}$, $\sigma_1 = -130 \text{ MPa}$.

In order to verify the analysis, pull-off tests, as used early by Engell^[14], have been performed. The stress for separating the oxide scale from Nd-doped 5621S alloy (oxidized at 800°C for 10h) is 3.9 MPa. This indicates that the thermal stress on the surface of the inclusion is very high. It is possible that the inclusion was expelled or broken. We also found fissures in some nodules. Since the thermal stress forcing on the inclusion increases very quickly in the fast cooling test, the inclusion has no time to move outward, so that it is broken instead. The stress can be released rapidly by breaking the inclusion. After that, the thermal stress developed again is small, and it isn't enough to cause the crack to expand and lead to spalling. Therefore, in the condition of fast cooling, cumulative AE energy counts of Nd-doped Ti-5621S is higher than that of Nd-free Ti-5621S, but spalling of the oxide scale of Nd-doped Ti-5621S is not so serious as that of the oxide scale of Nd-free Ti-5621S.

In the analysis, we neglect the effect of the growth stress, since generally, this stress is not so important^[12,13]. As a matter of fact, in the AE test, AE signals were not received during the isothermal oxidation period. At high temperature, it is easy to accommodate the growth stress by the plastic deformation of alloy or oxide scale.

Conclusions

1. The oxide scales formed on Nd-doped and Nd-free Ti-5621S alloys during the oxidation at 800°C in air are mainly composed of TiO_2 with small amounts of Ti_2O_3 , TiO , Al_2O_3 and SnO_2 . A great deal of composite oxide inclusions in the oxide/alloy interface are developed, which cause the oxidation rate of Nd-doped Ti-5621S

alloy to increase slightly.

2. Nd addition in Ti-5621S alloy improves the adhesion of the oxide scale significantly. The inclusions are thought to 'key' the scale to the substrate, to extend expansion distance for the cracks and to increase the adhesive area between the oxide scale and the alloy. The thermal stress is the main reason for crack initiation and growth.

3. When the thermal stress is high enough, large inclusions may be expelled from the alloy or broken. These inclusions can serve as points of crack initiation.

Acknowledgment

This work was sponsored by the National Natural Science Foundation of China.

References

1. R.A.Wood, R.J.Favor, Handbook of Titanium Alloys(Vol.1), Translated by Liu Jingan, (Chongqing, Chongqing Branch of Chinese press of Science and Technology Information, 1983), p.194
2. Wan Xiaojing, Jing Kailiang, Shi Wen, Zhang Bing, Li Dong, Yang Rui, Materials Science Progress, 6(1992):p.6
3. Li Tiefan, Li Meishuan, Materials Science and Technology, A120(1989):p.235
4. Li Meishuan, Li Tiefan, Zhou Longjiang, Journal of Chinese Society of Corrosion and Protection, 11(1991):p.217
5. A.Ashary, G.H.Meier, F.S.Pettit, Proceedings of the Conference on High Temperature Protective Coatings, ed. S.C.Singhal, (Canada, Applied Science Publication, 1983), p.105
6. A.S.Khanna, B.B.Jha, Baldev Raj, Oxidation of Metals, 23(1985):p.159
7. S.Coddet, G.De Barres, G.Beranger, "Corrosion and Mechanical Stress at High Temperature", Proceeding of the European Symposium, (The Netherlands, Petten(N.H.), 1981), p.417
8. Li Meishuan, Ph.Doctor thesis, (Shenyang, Institute of Metal Research, Chinese Academy of Science, 1991)
9. H.Hindam, J.J.Hechler, D.P.Whittle, Proceedings of the 9th International Conference on Metallic Corrosion, Vol.3. p.353. (Ottawa, 1984)
10. H.Hindam and D.P.Whittle, Proceedings JIMIS-3(1983), P.261, Fuji, Japan
11. D.Delaunay, A.M.Huntz, P.Lacombe, Corrosion Science, 20(1980):p.1109
12. H.E.Evans, R.C.Lobb, Corrosion Science, 24(1984):p.209
13. The Oxide Handbook(Second Edition), ed. by G.V.Samsonov, Translated from Russian by Robert K.Johnston, (New York, Plenum Publishing Corporation, 1982), p.183
14. H.J.Engell, F.K.Peters, Arch Eisenhüttenwes, 28(1957):p.567
15. F.H.Stott, Materials Science and Technology, 4(1988):p.431

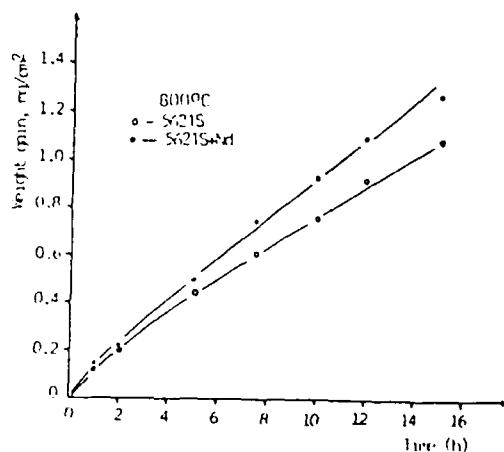


Fig.1 Oxidation of Nd-free and Nd-doped Ti-5621S alloys at 800°C in air

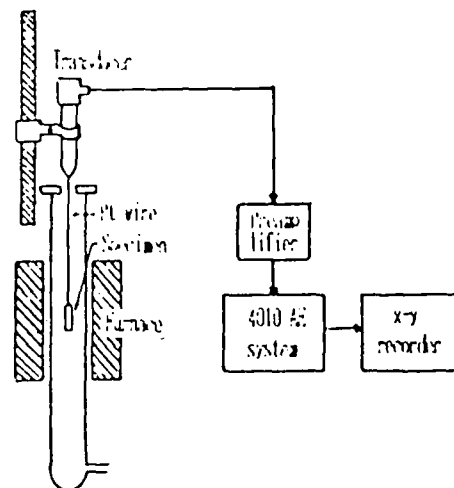
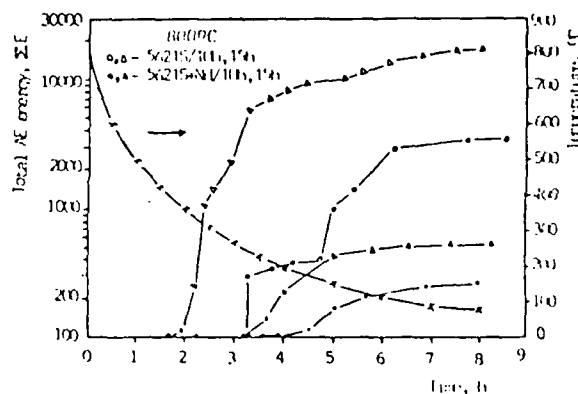
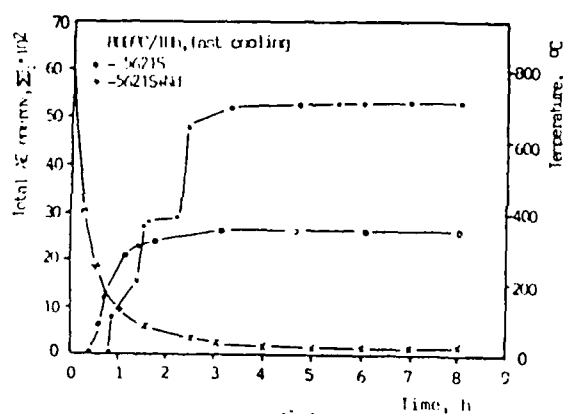


Fig.2 Schematic of acoustic emission apparatus used for detecting oxide cracking



(a)



(b)

Fig.3 Cumulative AE counts detected during cooling of Nd-free and Nd-doped Ti-5621S alloys from 800°C, (a) inside furnace, (b) outside furnace

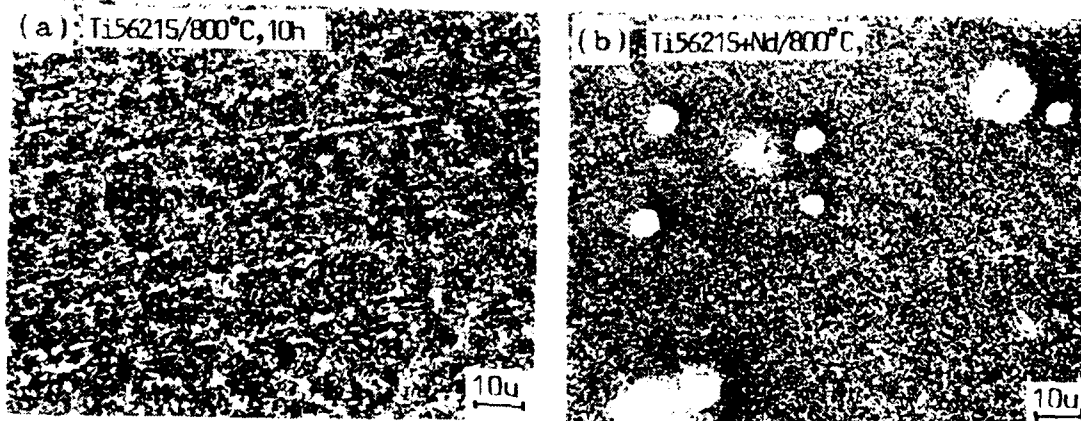


Fig.4 Surface morphologies of oxide scales formed at 800°C for 10h (furnace cooled). (a) Nd-free Ti-5621S, (b) Nd-doped Ti-5621S

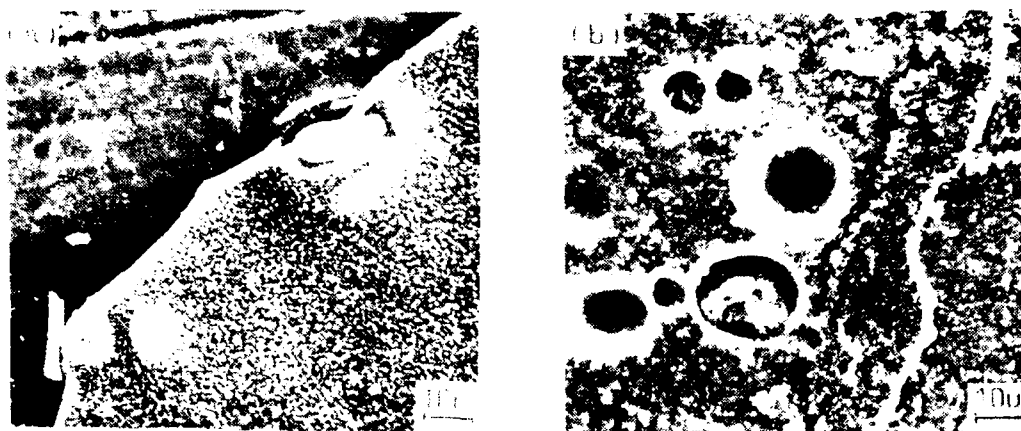


Fig.5 Micrographs showing spallation of oxide scales formed on Nd-doped Ti-5621S oxidized at 800°C for (a) 10h and (b) 15h

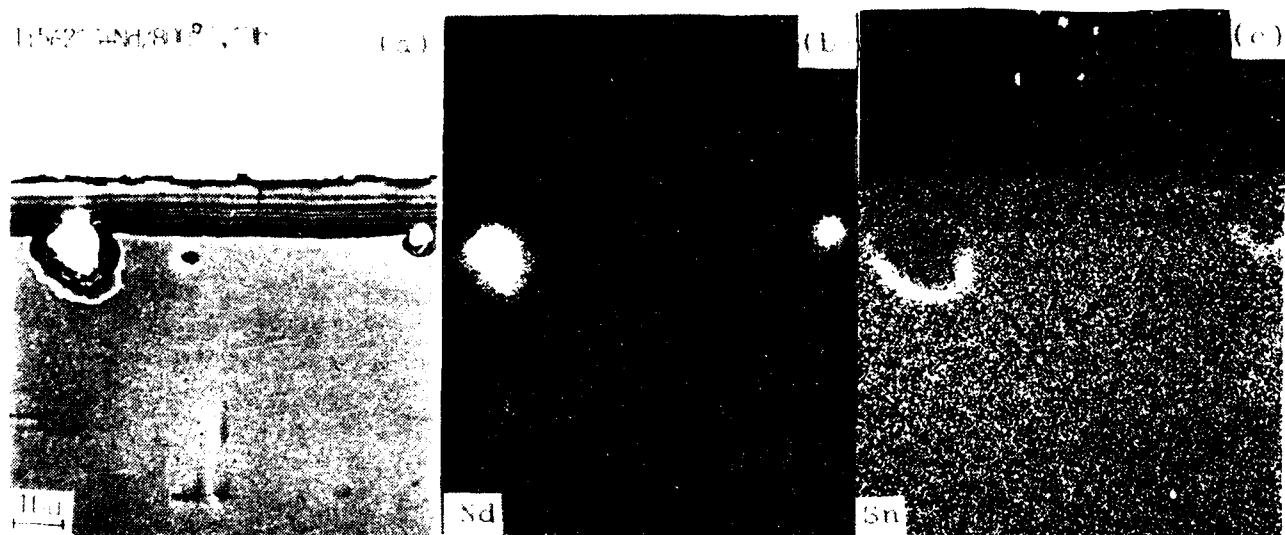


Fig.6 Cross section of the oxide scale and X-ray images of Nd-doped Ti-5621S after oxidation at 800°C for 10h

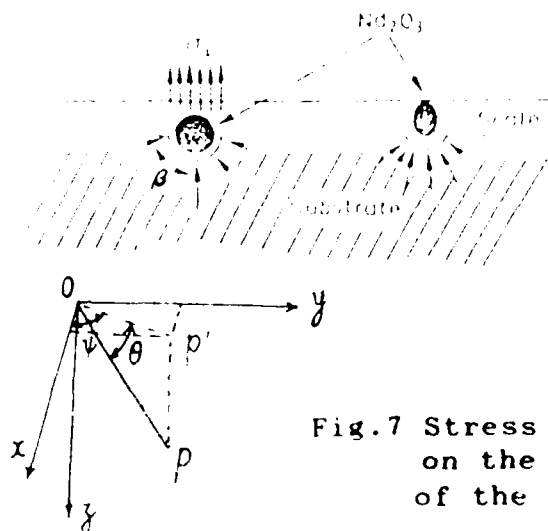
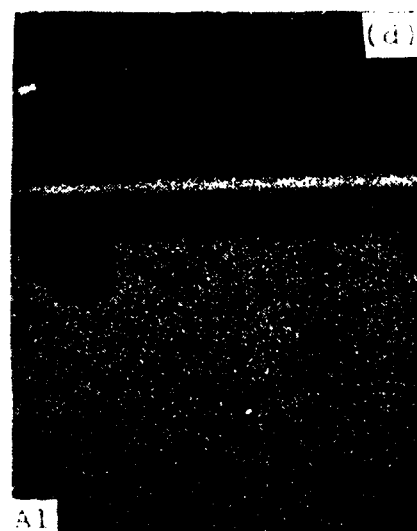


Fig.7 Stress forcing on the surface of the inclusions



High Temperature Corrosion Behavior of FE-Cr-AR Alloys with and without Y Addition in Pure SO₂ Gas Atmosphere*

Y. Zhang

* Paper not available at time of printing.

CIRCUMFERENTIAL CRACK EXTENSION CHARACTERISTICS
IN SUPERHEATER BOILER TUBES

BY

J.J. BULLOCH, J.J. HICKEY & T.B. HEALY,
ELECTRICITY SUPPLY BOARD
HEAD OFFICE
DUBLIN 2
IRELAND

ABSTRACT

The present paper describes a detailed failure study on a series of 21/4Cr1Mo superheater tubes from a peat fired boiler. Essentially the defect extension process was the result of two separate and independent initiation and propagation mechanisms.

It was observed that the defect initiation process was intimately associated with a fused outside layer of potassium sulphate. Basically tube movements caused radial cracking into or within this pure salt layer and caused it to react with sulphur trioxide to produce a liquid pyro-sulphate phase. Such a liquid phase in contact with the steel caused high temperature corrosion reactions which are electrochemical in nature.

The second phase of the defect extension, i.e. crack propagation, was attributed to a combination of an environmental component, viz., sulphidation, and a stress contribution which was thermal in nature and arose through the actions of slag and/or sootblower excursions. Essentially circumferential crack extension occurred by a sulphidation corrosion assisted thermal fatigue mechanism.

1. INTRODUCTION

When a unit of raising power plant is subjected to a forced outage, which resulted from the failure of some critical engineering component, the revenue lost can be significant. Examples of boiler failures are essentially varied in nature and include corrosion (general and localised), welding imperfections, fabrication defects, high temperature related processes, microstructural changes or degradation effects, oxidation, exfoliation and decarburisation. The manner in which different people survey boiler failures is markedly dependent upon individual specialist discipline, viz., a water chemist would develop a different perspective from that of a welding engineer, mechanical engineer or physical metallurgist. Such differing perspectives, if merged together, can yield a powerful method of understanding and solving boiler failures; indeed the modern method of dealing with boiler failures involved a multi-discipline approach.

Today, boiler failures and in particular boiler tube failures, represent the primary limiting problem which confronts steam raising utilities. Although many of the mechanisms which promote various tube failures have been successfully identified, one type of tube failure which is still not understood mechanistically is circumferential cracking. It is, however,

thought that this type of cracking results from a certain mixture of some corrosion dominated process and thermal stressing. Circumferential cracking, which is detected in an increasing extent, can initiate at outside or inside diameter locations and can be caused by fatigue or stress corrosion cracking (1). A recent survey (2) of a number of North American utilities has indicated that nearly half have been affected by circumferential cracking.

The present paper attempts to describe a failure analysis study which was conducted on a series of superheater boiler tubes, which failed as a result of circumferential cracks, from a small 45MW peat fired steam raising plant. This particular plant was around 30 years old and was sited on an inland location.

2. EXPERIMENTAL TECHNIQUES

Full and partial through thickness superheater tube defects were examined in both the as-received and oxide stripped condition. The oxide stripping procedure involved immersing the fracture surfaces in an inhibited solution of hydrochloric acid for 90 seconds in an ultrasonic bath. Fracture surfaces and crack profiles were examined in a scanning electron microscope, (SEM), and subjected to a chemical analysis using X-ray dispersive and X-ray mapping analytical techniques. The outer tube surface deposits were chemically analysed using a wetting technique.

3. EXPERIMENTAL RESULTS

3.1 METALLURGICAL AND FRACTOGRAPHIC ANALYSES

From a visual inspection it was evident that a thick adherent slag deposit, of the order of millimetres, covered the outside of the superheater tubes and a through thickness section is shown in figure 1. From this figure it can be seen that the outside slag deposit at this location was about 1.5mm thick.

The outside slag deposit was subjected to a series of X-ray dispersive analysis. A typical analysis showed significant amounts of sulphur, calcium, potassium and silicon. It can be seen from figure 2 that significant amounts of sulphur have diffused through the outer tube layer and have resided along the outer grain boundaries of the steel.

A detailed montage, illustrating a series of parallel circumferential cracks on the outer steel tube surface is shown in figure 3 and is clear that, in this particular area, the cracks are quite shallow with the crack depths being about 0.25mm maximum.

A detailed montage of a partial through thickness crack about 1.7mm deep, is illustrated in figure 4. Figure 5 shows sulphur and potassium X-ray dot maps of the same location and it can be seen that (a) a significant amount of potassium was associated with the defect on the outer surface and to a crack depth of about 0.3 mm and (b) sulphur concentrations were evident along the entire length of the defect to the crack tip location.

The topography of the fracture surfaces of a circumferential crack exhibited severe corrosion inasmuch that large corrosion tunnels of significant depth covered the fracture surface. Also isolated cases of intergranular failure facets, see figure 6, were observed on the fracture surface and the grain boundaries were decorated with carbide precipitates.

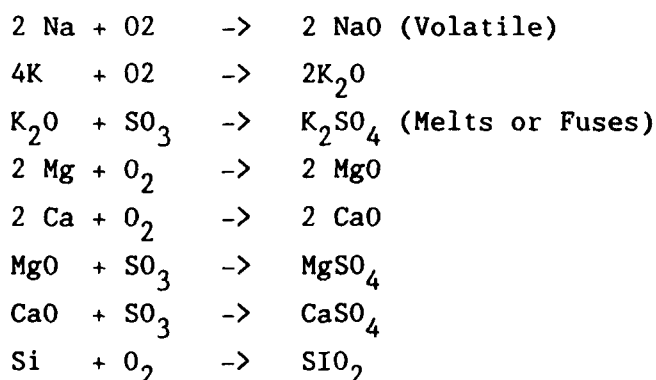
3.2 CHEMICAL ANALYSIS

Outer tube deposits of around 6 to 8mm thick were removed in four layers of approximately 2mm thick and separately analysed. These particular analyses considered water soluble and insoluble sections and loss on ignition of the insoluble section at 600°C. The analysis of each separate layer of deposit together with that of a typical peat sample are given in Table 1.

The analysis showed that the metals present, viz., sodium, potassium, magnesium and calcium, were most probably present as sulphates. The concentration of the various chemical species within the tube deposits was plotted as a function of approximate distance from the outer tube wall and this is given in Figure 7. From this figure it can be seen that the significant metallic sulphates are calcium and potassium with the latter increasing markedly in the outer tube wall location. Indeed the potassium levels at this location were about an order of magnitude higher than those found in a typical peat ash deposit. The source of potassium was the peat itself which was laid on a limestone base. The innermost layer of the deposit was almost pure potassium sulphate which appeared as a thin fused white salt layer.

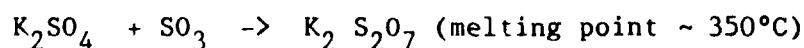
A reasonable explanation for this selective separation and concentration of potassium sulphate on the outer tube wall surface is that the furnace operation temperatures (not tube wall temperatures) were at times significantly high enough to melt the potassium sulphate i.e. greater than 1070°C, without fusing or melting the rest of the ash constituents. Sodium based salts, which fuse at even lower temperatures, volatilise in the temperature range 1000 to 1100°C and thus were not recorded in the outer wall deposits at this particular boiler location.

The chemical reactions that occur in the furnace tube wall locations may be represented by the following expressions;



The stickiness or melted state of the potassium salts allow them to adhere to and selectively concentrate on the "cool" outer walls of the superheater tubes. The remaining salts may deposit as oxides and, at a later stage, react with sulphur trioxide to form sulphates.

The potassium sulphate on the outer tube surface can further react with sulphur trioxide to form potassium pyrosulphate which fuses or melts at temperatures as low as 350°C, viz.,



Although no thermodynamic data is available to suggest that this pyrosulphate is stable at high temperature its stability will depend on the partial pressure of SO_3 in the flue gases. As a result of (i) combustion difficulties with variable (wet) fuel and (ii) air leakages into the furnace the SO_3 concentrations in the flue gases at the superheater location were estimated to be around 100ppm by volume.

According to French (3) a common feature of this particular type of corrosion attack is the circumferential penetration of the corrosion products (on the fireside location of the tubes) forming long finger-like penetrations which, in the most severe instances, leads to tube failure.

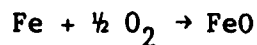
4. DISCUSSION

It was evident from the previous section that defect extension through the superheater tube was (i) initially associated with high concentrations of potassium and sulphur due to the presence of a fused layer of pure potassium sulphate on the outer tube wall, (ii) seen to be associated with high sulphur concentrations over the entire defect length, even at the crack tip location, and (iii) intergranular in nature at locations which were not significantly corroded.

It is proposed that the defect initiation process was intimately associated with the fused potassium sulphate outer tube wall deposit and that subsequent defect growth was the result of either a sulphidation corrosion assisted thermal fatigue mechanism or simply from a pure thermal fatigue process.

The outer tube wall deposits were up to 8mm thick and were very friable and, as such, prone to cracking or flaking. It is suggested that circumferential cracking of the thick outer deposit was initiated by the bending of the hanging tubes through some operational procedure(s). Such cracking would readily cause the ingress of any sulphur trioxide gases present and to come into contact with the inner potassium sulphate fused layer. When this occurs potassium pyrosulphate can readily form at such temperatures which cause it to be in the liquid state. Under such circumstances "molten salt" corrosion (4), which is highly corrosive and leads to an acceleration of tube wastage, can readily occur. This corrosion process is electrochemical in nature and involves the transfer of electrons with the liquid pyrosulphate acting in an electrolyte (5). Hence the initiation of circumferential cracks on the outer surfaces of superheater tubes caused by (i) the breakage or cracking of the outer tube deposit, (ii) the subsequent formation of liquid potassium pyrosulphate and (iii) the rapid localised electrochemical corrosion of the outer tube surface can be readily envisaged. Further evidence of the significance of the potassium salt in the defect initiation event is illustrated in figure 8 where large potassium concentrations were identified in the initial stages of the crack extension process.

From the foregoing evidence it is clear that the crack extension process is intimately connected with sulphur concentrations within the growing crack tip enclave. The propagation of circumferential cracking was caused by the significant diffusion of sulphur, present in the outer slag deposit, through the magnetite film, to the steel grain boundaries on the outer tube walls. Here corrosion can occur through a sulphidation reaction (6), i.e. when iron is heated in a gaseous environment which contains oxygen and sulphur the following reactions may occur at the metal surface,



As the sulphur can penetrate through the oxide film FeS will form preferentially when the oxygen activity is reduced. As such, the sulphide particles grow along grain boundaries causing crack initiation. Continued crack extension is thought to occur by a combination of an environmental components, the sulphidation process, and stress contribution. The stress contribution most probably is thermal in nature that results from boiler operation, e.g. slag fall and sootblower induced temperature excursions (7). Thus essentially, circumferential crack extension occurred by a sulphidation corrosion assisted thermal fatigue mechanism.

To the author's knowledge circumferential cracking has only been observed in water wall tubes (2, 8). Indeed a recent report by Cialone & Wright (2) has shown that, in a survey that covered approximately 30% of the coal fired supercritical boilers in the USA, 45% of the units were affected by circumferential cracking. also the trends were somewhat puzzling in as much that cracking was not confined to boilers of a particular manufacture, nor to those using a particular coal type, operational regime or maintenances procedures.

If it is taken that the proposed crack extension mechanism of corrosion assisted thermal fatigue is valid, it is possible to postulate a number of conditions which could embody the factors that cause circumferential cracking. In an effort to identify the nature of the fatigue component it is planned to conduct an analysis of the vibration and pressure cycles on the tubes during service and thermal stressing. Four conditions that could cause such crack extension are proposed, viz.,

(A) SLAGGING/DESLAGGING

Significant thermal cycling can result from the alternating build-up and removal, either by natural slag falls or sootblowing, of slag on the tubes. Indeed Ellery et al (9) have observed thermal shock and thermal fatigue damage when sootblowing was done with water, either intentionally or not, as a result of entrained water in the sootblower steam lines.

(B) FREQUENT LOAD CYCLING

Certain boiler units were originally designed for base-load operation can be cycled to reduce output overnight. Certain cyclic situations can develop as a result, e.g., heat flux, and such cycles could impose tube stresses that are above the design levels.

(C) RAPID START-UP PROCEDURES

The effects of rapid start-up procedures are similar to those of load cycling, except that in the former case the cyclic are greater. As such rapid start-ups will cause enhanced thermal fatigue factors.

(D) FURNACE - PRESSURE CYCLES

Furnaces pressure cycles are the result of an imbalance between the forced-draft and induced draft fans. Indeed a pressure cycle threshold amplitude, above which cracking occurred and below which slag shedding occurred without cracking has been established by one utility (2). Of the four conditions presented here only (b) does not apply to the present cracking problem.

5. CONCLUDING REMARKS

Circumferential cracking has been shown to exist in a series of boiler superheater tubes. Such cracking has been commonly observed in water wall tubes in American utilities.

It has been suggested that the circumferential cracking was initiated by a molten salt (potassium pyrosulphate) corrosion process which was electrochemical in nature. Subsequent crack propagation was thought to have occurred as a result of a sulphidation reaction superimposed on a thermal fatigue component.

The sulphur is supplied from the outer slag deposit where significant concentrations were established. The exact nature of the thermal fatigue component is less obvious.

At present circumferential cracking trends are somewhat puzzling and as such the best approach would be to establish direct measurements of certain parameters such as local temperatures, strain and environmental conditions. These could then be related to certain boiler parameters and cracking behaviour.

ACKNOWLEDGEMENT

The authors would like to thank Mr. Conleth Murphy of Lanesborough Power Station for his help in procuring tube specimens and for many stimulating discussions.

REFERENCES

- 1/ Proceedings: 1990 EPRI Workshop on Circumferential Cracking of Steam Generator Tubes.
Report No. NP-71988S-M March '90.
- 2/ H.J. Cialone & I.G. Wright, "Observations of Circumferential Cracking in the Water Walls of Supercritical Units", Conference Boiler Tube Failures in Fossil Plants, EPRI, Atlanta Georgia, November '87.
- 3/ D.N. French, "Metallurgical Failures in Fossil Fired Boilers, John Wiley & Sons, New York 1983.
- 4/ D.M. Farrell, F.H. Stott, G. Rocchini & A. Colombo, "Electrochemical Aspects of High Temperature Corrosion Reactions in Combustion Systems", Corrosion 91, European Fed. Corrosion Event 128, Inst. of Corrosion, Vol. 2 pp. 1 - 20, Manchester, U.K., October '91.
- 5/ W.T. Reid, "External Corrosion & Deposits", American Elsevier Publishing Co., 1971.
- 6/ J. Stringer, High Temperature Technology, 3, (1985) pp. 119 - 141.
- 7/ B. Smith, "Laboratory Simulation of Circumferential Cracking of Boiler Tubes", NBES, Workshop on Life Assessment and Failure Prevention of Power Plant Components", Lehigh University, Penn., USA, May 1990.
- 8/ B. Smith, Lehigh University, Penn., USA, Private Communication, April 1990.
- 9/ A.R. Ellery, T.R. Johnson & J.D. Newton, "Investigation into the Likelihood of Thermal Fatigue Damage to Furnace & Superheater Tubes caused by on-load Water Deslagging", Trans ASME, 144, (1974) pp. 138 - 144.

TABLE 1

CHEMICAL ANALYSIS (wt%) OF SUPERHEATER TUBE GAS SIDE DEPOSIT

CHEMICAL PARAMETER	OUTER LAYER (8mm from TUBE WALL	INNER WHITE FUSED LAYER (< 2mm from TUBE WALL	PEAT ASH DEPOSIT
pH	4.48	3.5	11.2
% SODIUM	0.6	1.17	2.47
% CALCIUM	25.7	17.0	55.9
% POTASSIUM	6.4	15.9	1.8
% MAGNESIUM	0.2	0.42	1.54
% IRON	0.03	0.04	-
% SULPHATE	66.0	63.1	10.4
% NITRATE	0.21	0.13	-
% PHOSPHATE	0.06	0.13	-

Outer
Slag Deposit

Magnetite
Film

Outer
Tube Wall

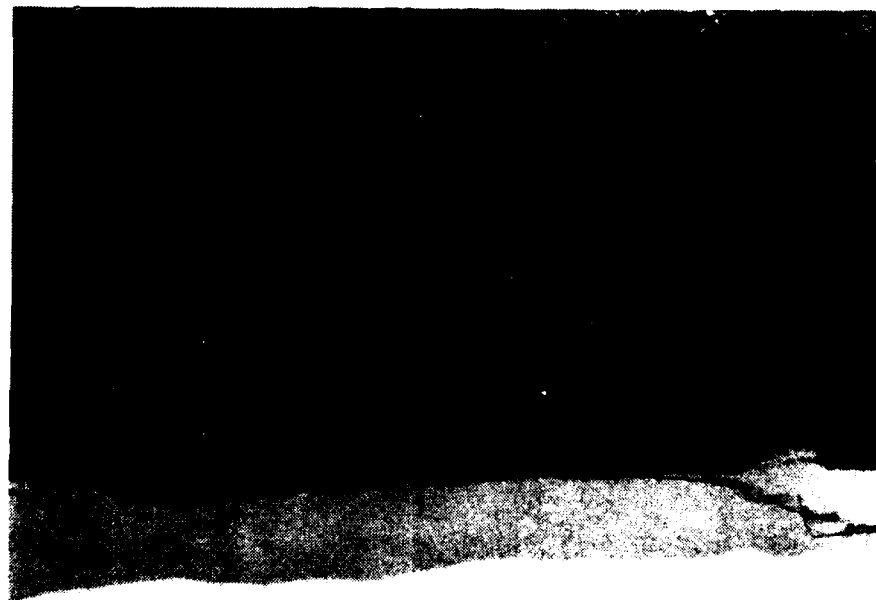


Figure 1 Through Thickness Section Illustrating
The Outer Slag Deposit (X 45)

Magnetite
Film

Outer Tube
Wall

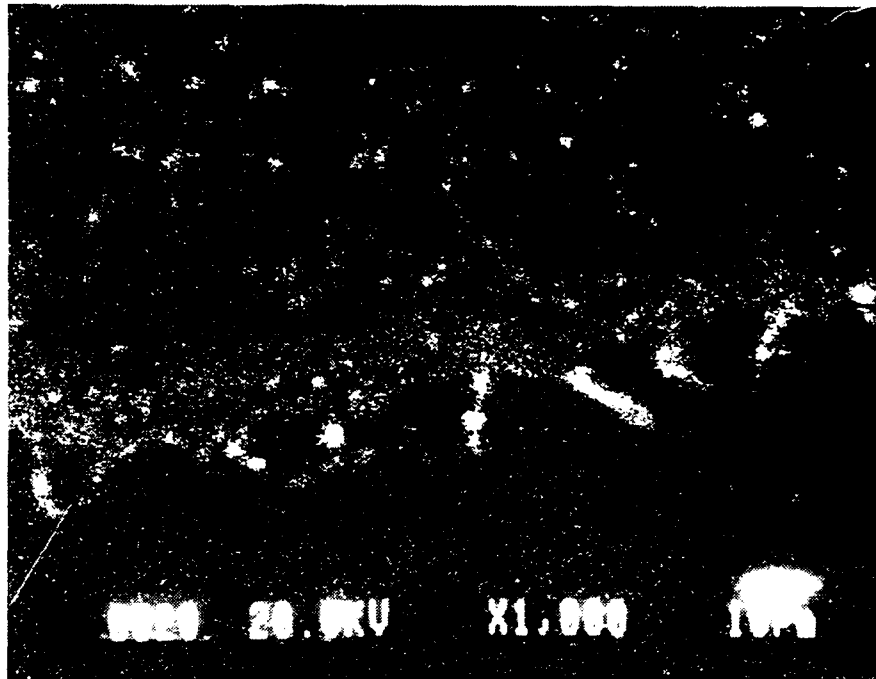


Figure 2 X-Ray Sulphur Map Of Magnetite-Steel Matrix Interface Location



Figure 3 A Detailed Montage Of The Surface Circumferential Cracking Prevalent On The Steel Tube Surface

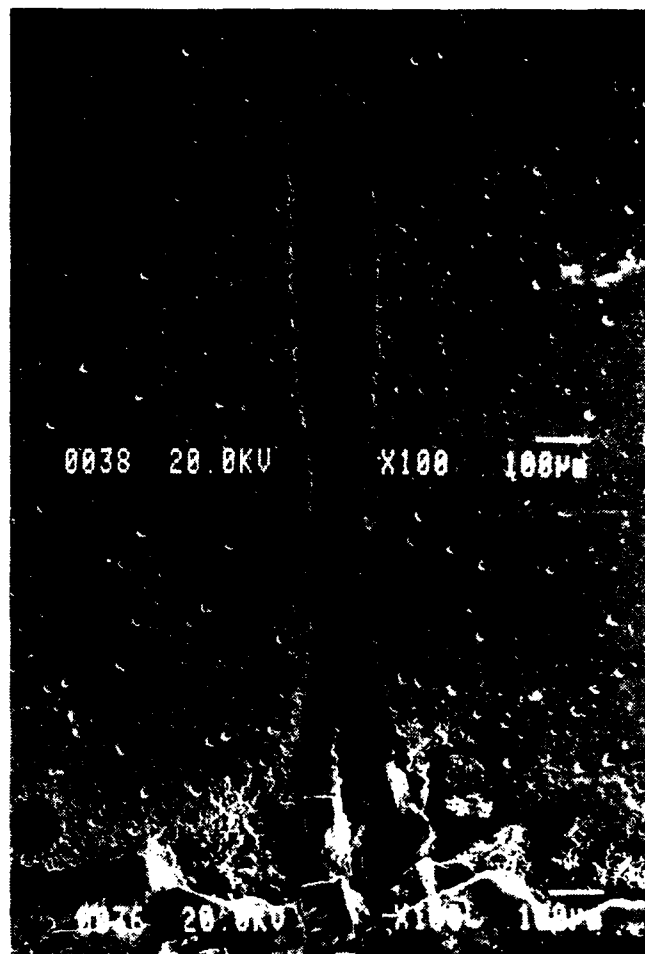


Figure 4 A Detailed Crack Profile View Of A Partial Through Thickness Circumferential Crack

A



B

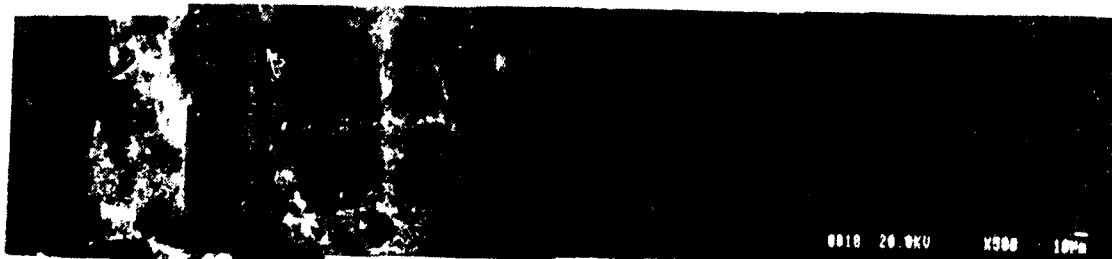


Figure 5 X-Ray Mapping Of A Partial Through Thickness Crack
(A) Sulphur X-Ray Map (B) Potassium X-Ray Map

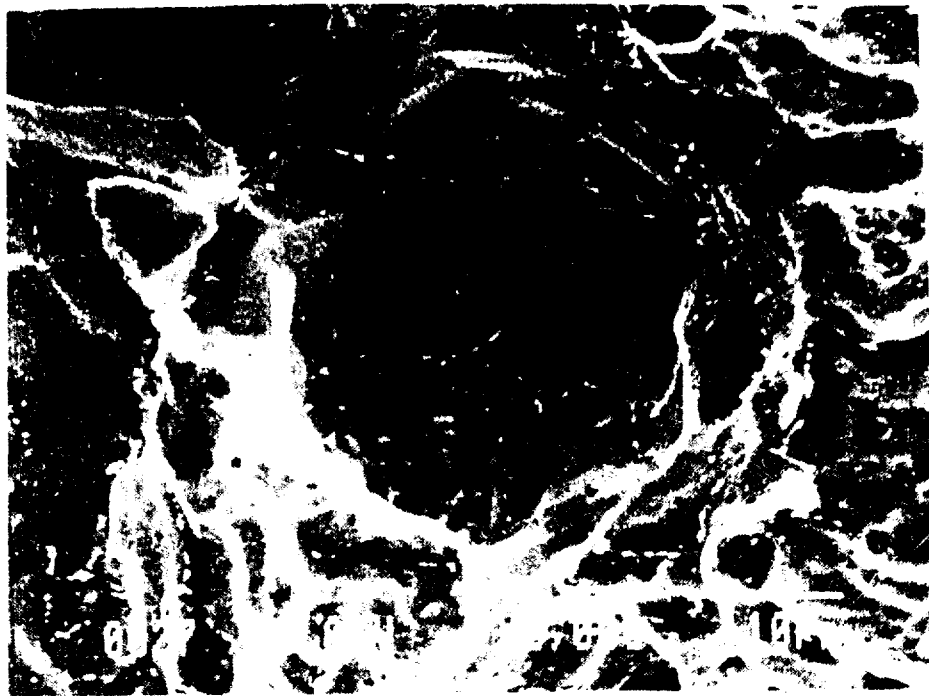


Figure 6 Fractographic Details Of Circumferential Cracking
(Isolated Intergranular Facet)

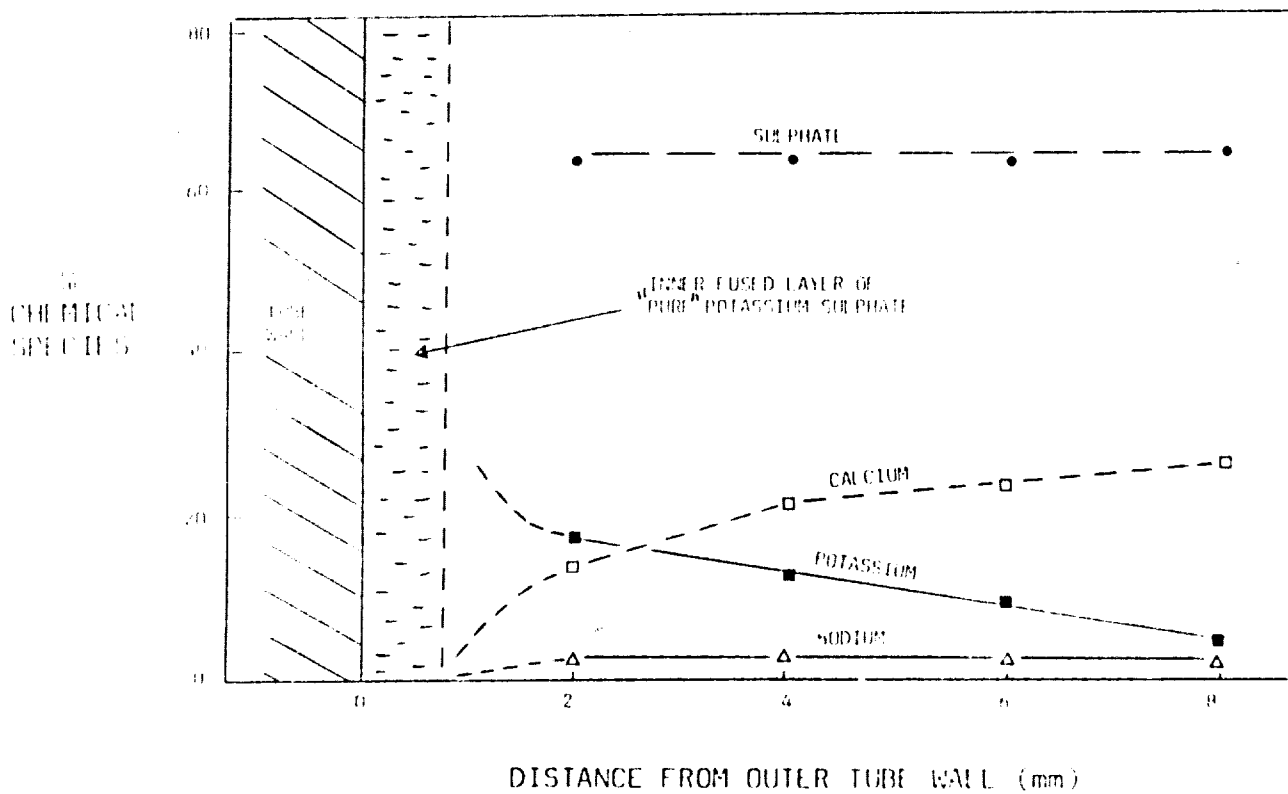


FIGURE 7 CHEMICAL COMPOSITION OF THE OUTER TUBE DEPOSIT

Rupture in a Steam Generator Tube

B. Rezgui and M. Larbi
Ecole Nationale d'Ingenieurs de Monastir
Université du Centre - 5019 Monastir - Tunisia

Abstract

This study concerns the sudden perforation and fracture caused on steel steam tubes. These tubes lined the combustion chamber walls in a steam generator, which endured 90,000 hours of service. The fracture appears as holes in some tubes reaching up to a diameter of 30 mm, and sometimes as a crack; in both cases, these lead to a burst of the tubes with a discharge of steam to the outside.

The microstructural examination of the damaged material, taken from cracked tubes, showed a high level of oxidation along the inside and the outside of the tube, as well as the cracked surfaces. However, the analysis of the surfaces of fracture shows an intergranular fracture mode, while the microstructural examination reveals an increase in grain size when compared to original material.

Results of mechanical tests, in air and at room temperature, on the damaged materials showed an increase in the hardness and tensile strength associated with a significant reduction in ductility. The fracture surface obtained from the tensile tests, although it is of transgranular type, showed the pre-existence of intergranular areas, with the appearance of carbide particles along the grain boundaries. These particles constitute favorable sites for cavitation.

Key terms: intergranular fracture, aging, creep, cavitation, oxidation

Introduction

The mechanical behaviour of a large number of engineering material components operating at high temperatures and under corrosion conditions remains an interesting research subject. To predict premature failure, many studies dealing with this problem have been carried out, on ferritic steels [1,2], and stainless steel [3,4], which have particularly shown that material aging makes any prediction approach difficult.

Our study is aimed at identifying the nature, as well as the origin, of rupture occurring in a steam heat exchanger tubes which endured 90,000 hours of service at high temperatures and under corrosive conditions. This work is concerned mainly with two aspects: a comparative study of static mechanical characteristics of original and damaged material to establish a correlation between mechanical and microstructural characteristics, and a detailed microstructural as well as fractographic analysis aimed to identify the damage process responsible for the failed tubes

Experimental procedures

Steam Exchanger Tubes

The steel tubes had lined the combustion chamber walls inside the steam generator. These tubes are 60 to 90 m long, and have an outside diameter of 57 mm and a thickness of 4.5 mm. They are heated from the outside by a gas burner at a temperature of 1200°C; heat exchange is insured mainly by radiation. Steam circulates inside the hot tubes with a working pressure of 160 bars and a temperature of 350°C

All tests were carried out on samples taken directly from tube portions in their initial and damaged states. The latter had experienced about 90,000 hours of service.

Material

The tube material is an AISI 4023 low alloy steel, with a ferrite-pearlitic structure, and a composition given in Table I.

Table I. Steel composition (wt.%)

C	Mn	Mo	Si	Cr	Ni	V	Al	S	P
0.17	0.63	0.28	0.26	0.06	0.08	0.02	0.01	0.002	0.007

Results

Mechanical Characteristics

Comparative mechanical tests in hardness and tension were performed at room temperature on specimens taken from tubes in initial and damaged conditions. Measurements made far from the fractured surfaces in damaged tubes, gave a mean value of 180 HB showing a little increase in hardness as compared with the value of 160 HB for the initial material. Results from tensile tests showed an increase in yield strength as well as ultimate tensile strength at the expense of a reduction in tensile ductility. This comparison is presented in Table 2.

Table 2 Comparative Tensile Characteristics

Material Condition	Yield Strength MPa	Tensile Strength MPa	Tensile ductility %
Initial	420	530	12
Damaged	476	580	8.5

Microstructural Analysis

Metallography

Optical microscopy observations of raw and damaged material taken from the tubes showed an important difference between the two states. Figures 1 and 2 show two micrographic pictures representing common ferrite-pearlitic structure. However, the grain size of the damaged structure is evaluated to 19 μm against only 15 μm for the virgin structure, which represents about a 25% difference in average grain size. The method used in grain size determination is based on counting the number of observed grains per unit area, then evaluating the mean grain diameter. Further microscopic examination showed the presence of large grain boundary particles which is illustrated in Figure 3.

Oxidation Aspects

From the oxidation point of view, the examination revealed the presence of thin layers of oxides overlying the inner surface of tube walls (vapor side), as well as the outside ones (gas side). The thickness of these layers varied between 0.1 and 0.28 mm as is shown in Figure 2.

A large number of corrosion pits were also found which are suspected to play a significant role in the initiation of the tube perforation. Figure 4 shows a typical picture of corrosion pits distributed over the external surface tube with the presence of a crack. Only the outside deposit was analysed by X rays diffraction and was found to be composed mainly of magnetite.

Fractography

Among the fractured tubes examined, some tubes were formed by two or more sections welded together. In such cases, when the fracture is caused by cracking, the crack originates at the welding joint and propagates in a transverse direction as shown in Figure 4. However, in most cases the failure usually occur following a perforation process. Then, the formed hole has a diameter which varies from a few millimetres to about thirty millimetres. The high degree of oxidation for rupture surfaces for both the perforation and cracking processes, made very difficult any scale analysis. However successful examination of some areas has clearly shown an intergranular mode of fracture associated with numerous triple point cracks as shown in Figure 5.

The fracture surface obtained by tensile tests performed on damaged material shows the pre-existence of intergranular areas, although the fracture is transgranular. The analysis of these areas reveals the presence of some carbide particles along the grain boundaries, which constitutes favorable sites for cavitation as it is shown in Figure 6.

Temperatures Evaluation on Inside and Outside surfaces of Tube Wall

A tube exposed to a flame is heated partially by radiation. Hot water vapor circulates inside the tube at 347°C. Assuming a shape factor equal to unity, the heat flux density received by the external tube surface is

$$\phi_p = \sigma \cdot (\epsilon_g \cdot T_g^4 - \epsilon_p \cdot T_{pe}^4) \quad (1)$$

ϵ_p is the emissivity factor of the wall tube ($\epsilon_p = 0.9$)

ϵ_g is the gas emissivity factor ($\epsilon_g = 0.25$)

σ is the Stephan-Boltzmann constant

T_g and T_{pe} are the gas temperature and the external temperature of the tube wall.

In the steady-state regime, for a uni-dimension heat exchanges the flux is conserved through the wall:

$$\sigma \cdot (\epsilon_g \cdot T_g^4 - \epsilon_p \cdot T_{pe}^4) = (T_{pe} - T_{pi}) / R \quad (2)$$

T_{pi} is the inside temperature tube wall

R is the thermal resistance equal to $0.013 \text{ m}^2 \cdot ^\circ\text{K}$

In addition, there is an equality of the flux exchanged by the outside and the inside tube wall surface

$$\sigma \cdot (\epsilon_g \cdot T_g^4 - \epsilon_p \cdot T_{pe}^4) = (T_{pi} - T_{sat}) / R' \quad (3)$$

R' is the resistance to heat transfer between vapor and the internal wall; it is a function of the flow, the physical properties of the fluid and the tube geometry. In this case $R' = 0.003 \text{ m}^2 \cdot ^\circ\text{K}$. Where T_{sat} is the vapour temperature at saturation, ($T_{sat} = 347^\circ\text{C}$).

Numerical solution of equations (2) and (3) leads to the following results :

$$T_{pi} = 480^\circ\text{C} \quad \text{and} \quad T_{pe} = 900^\circ\text{C}$$

These values are over-estimations of the temperatures.

On the other hand, the propagation of the observed cracks occurs under the action of longitudinal stress component, $\sigma_l = (P \phi) / 4e = 50 \text{ MPa}$, where P is the working pressure, ϕ is the internal diameter and e the wall thickness, as shown by the schematic representation of figure 7.

Discussion

Based on microstructural analysis, it is likely that dynamic aging is responsible for the observed increase in the strength of damaged material, as shown in table 2. On the other hand, the increase in grain size of the material is attributed to a high temperature service condition causing a probable overheating of the tubes.

Though the tube walls are submitted to of a low stress level, at 900°C , creep should play an important role in the failure of the steel. Moreover, the combined action of the high level temperature and corrosive environment lead to a combined effect of creep and stress corrosion responsible for the damage of the tubes.

The alloy exhibits a well defined 'brittle' intergranular failure associated with two modes.

1. the initiation and propagation of a creep crack,

2. a damaging process corresponding to perforation which seems to be mainly of corrosion type. Initiation of the later type of failure seems to result primarily by a corrosion pitting process at the outside surfaces of the tube walls (gas side).

Conclusions

The analysis of the failure of AISI 4023 steel steam generator tubes submitted to 90,000 hours operative conditions at elevated temperatures leads to the following results :

- A material aging leading to an increase in the material strength at the expense of reduction in ductility,
- An increase in grain size of the damaged material as compared to the original material due to the elevated temperature service,
- Abundant intergranular particles, which constitutes favorable sites for cavitation,
- Two modes of rupture one associated with the initiation and the propagation of creep crack and the second, probably a result of the initiation of corrosion pits on the outside surface of tube walls.

References

1. M. O. Speidel, " Design Against Environment Sensitive Fracture "
(Cambridge, ICM3, vol.1, 1979)
2. A. M. Abdel-Latif, J.M. Corbett, D. Sidney, D M. R. Taplin, " Effects of Microstructural Degradation on Creep Life Prediction of 2-1/4 Cr-1 Mo Steel"
(Cannes- France, ICF5, 1981, vol. 4)
3. B. Rezgui, " Creep-Fatigue-Environment Interaction on 316L Stainless Steel "
(Thesis, Paris IX University, 1982)
4. M. Yoshida, C. Levaillant, A. Pineau, " Metallographic Measurement of Creep Intergranular Damage and Creep Strain ", (Int. Conf. on Creep, Tokyo 1986).

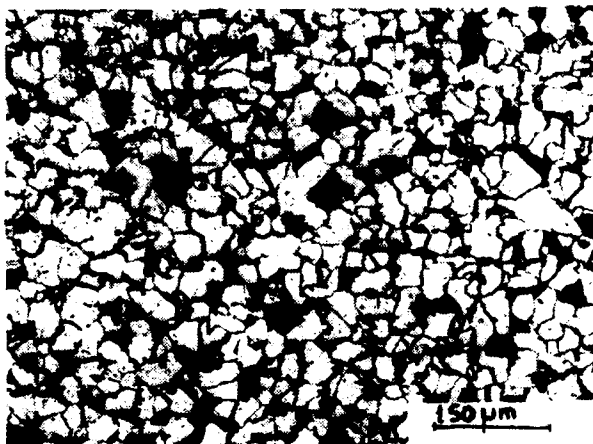


Figure 1. AISI 4023 Steel. Microstructure (Raw material)

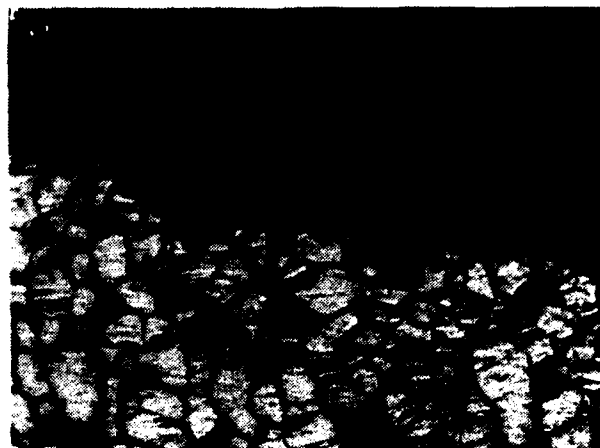


Figure 2. Damaged material



Figure 3. Massive grain boundary particles



Figure 4. Corrosion pits with Crack

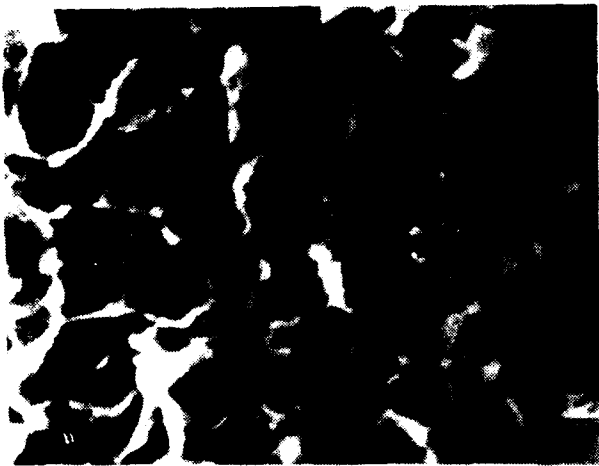


Figure 5. Intergranular Fracture. Damaged Tube

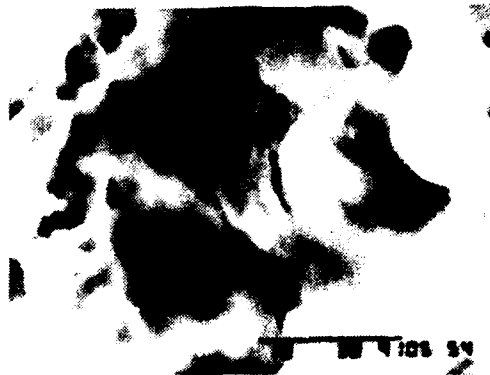


Figure 6. Tensile Fracture on damaged material

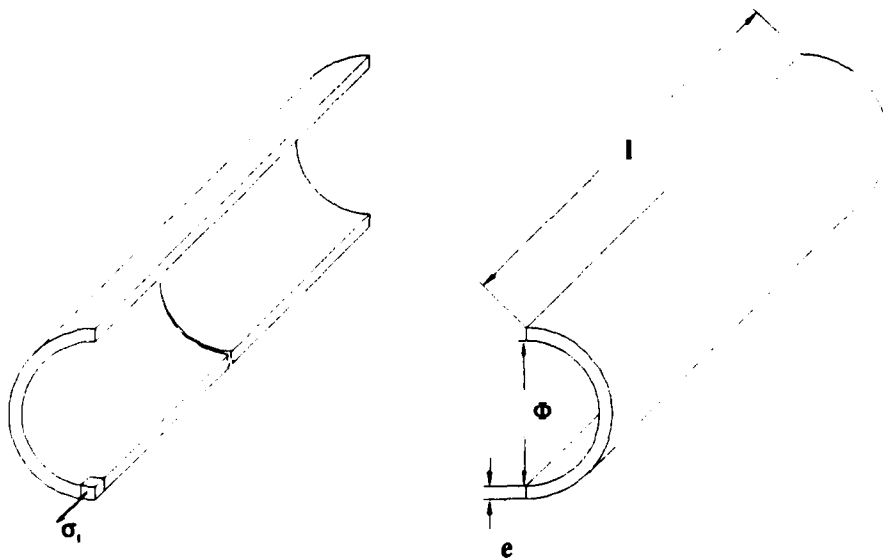


Figure 7. Crack propagation under the action of the longitudinal stress

Na₂SO₄ Deposits Induced Hot Corrosion of Iron Based Alloys at Intermediate Temperatures

Yunshu Zhang
Shanghai Institute of Metallurgy
Academia Sinica
Shanghai 200050, China

Liangquan Shi
Shanghai Institute of Metallurgy
Academia Sinica
Shanghai 200050, China

Shengtai Shih
Shanghai Institute of Metallurgy
Academia Sinica
Shanghai 200050, China

Abstract

Hot corrosion behavior of commercial iron, Fe-Cr and Fe-Al alloys in the presence of a Na₂SO₄ deposit on their surfaces in oxygen-rich atmospheres containing SO₃ at intermediate temperatures was studied. The reaction kinetics were found to be dependent upon temperature, gas composition and alloying element content. The examination of corrosion morphology indicated that the proceeding of hot corrosion was accompanied by the increase in thickness of a porous Fe₂O₃ layer and the rapid growth of a comparatively compact oxide layer on the metal surface. In addition, sulfides were observed at the metal/oxide interface as well as in the compact oxide layer. On the basis of experimental results, electrochemical mechanism is proposed to illustrate hot corrosion process of iron based alloys at intermediate temperatures. The effects of temperature, gas composition and alloying element content on corrosion behavior are also discussed.

Key terms: hot corrosion, Na₂SO₄ deposit, intermediate temperature

Introduction

Heat-resistant steels were found to undergo hot corrosion in the presence of alkali sulfate deposits on their surfaces in SO₃-containing gas environments at relatively low temperatures. Severe corrosion was reported since early this century, mainly with coal-fired boiler tubes¹⁻³. This subject was concerned in a few papers^{4,5}, and the corrosion was attributed to the formation of a low-melting complex sulfate melt on the steel surfaces. Unfortunately, this corrosion phenomenon has not been clearly understood so far. On account of its great importance in corrosion science and engineering practice, hot corrosion of iron based alloys occurring at intermediate temperatures was studied in our laboratory, and some results have been reported⁶⁻⁹. The present study was undertaken to evaluate Na₂SO₄ induced hot corrosion behavior of commercial iron, Fe-Cr and Fe-Al alloys in O₂/SO₂/SO₃ gas atmospheres at 650-750°C, and to have a good understanding of hot corrosion mechanism.

Experimental Procedures

The materials used in this study were 0.02 (wt)% carbon-containing wrought commercial iron, wrought Fe-Cr alloys with nominal compositions

of 5, 10 and 20% Cr, cast Fe-Cr alloy with 30% Cr and 5 and 10% Al-bearing Fe-Al alloys. The test specimens were measured 15×8×2 mm for the all wrought alloys and $\phi 12 \times 1.5$ mm for the cast ones.

The alloy specimens were polished through 600 grit abrasive paper, and degreased with acetone. A uniform salt deposit of $2\text{mg}/\text{cm}^2$ was obtained by brushing Na_2SO_4 solution onto a warm specimen. The salt-coated specimen was hanged in a silica crucible, and placed in a silica tube and situated in the center of the upper zone of a vertical furnace. Gas was let in and out through the silica tube. The gas inlet tube was filled with platinumized ceramic catalyst which was located right in the center of the lower zone of the furnace. The experiments were performed at 650-750°C. O_2 - SO_2 gas mixtures with 0.1(vol)%, 0.5% and 1.0% SO_2 , respectively, were used in this study. The weight changes of the specimens were monitored by a TG 328B balance with a precision of 0.1 mg.

After experiments, some corroded alloy specimens were examined and analysed by means of X-ray diffraction and EPMA to characterize the corrosion products. Chemical analyses were made to detect the existence of Fe^{2+} , Fe^{3+} , Al and Cr ions in the water soluble corrosion products.

Experimental Results

A comparison of corrosion kinetics of salt-coated and uncoated commercial iron oxidized in O_2 -0.5%(SO_2 + SO_3) gas atmosphere at 650°C is shown in Fig.1, which indicates that hot corrosion of the salt-coated iron occurred in the experimental condition. Similar behavior was also observed for all the Fe-Cr and Fe-Al alloys tested.

Fig.2 shows the dependence of corrosion kinetics of salt-coated Fe-20Cr alloy on temperature in O_2 -0.5%(SO_2 + SO_3) gas atmosphere. It is seen from Fig.2 that the maximum corrosion rate of the alloy showed up at about 700°C. The fastest corrosion of salt-coated Fe-10Al alloy occurred at about 650°C in identical series of tests. For commercial iron, however, hot corrosion rate increased with temperature monotonously.

The corrosion kinetics of salt-coated commercial iron, Fe-Cr and Fe-Al alloys were found to depend upon partial pressure of SO_3 in the system, as indicated in Fig.3 for Fe-10Al alloy at 650°C. For the mixed gases used in this study, the higher the P_{SO_3} in the system, the higher corrosion rates of the alloys were observed.

The reaction kinetics of the salt-coated alloys were also found to be dependent on Cr or Al content in the alloys, as shown in Fig.4 for Fe-Cr alloys. It is clear that a high content of Cr or Al in the alloys gave rise to an increase in corrosion resistance.

X-ray diffraction analysis results indicate that the porous corrosion product layer consisted of Fe_2O_3 and salts for all the materials tested, and that the compact layer on the metal surface consisted of Fe_2O_3 , Fe_3O_4 and FeO for commercial iron; Fe_2O_3 , Al_2O_3 and FeAl_2O_4 for Fe-Al alloys and Fe_2O_3 , Cr_2O_3 and FeCr_2O_4 for Fe-Cr ones. From EPMA analysis, iron sulfide existed in the whole compact oxide layer of commercial iron, as seen in Fig.5. For the Fe-Cr and Fe-Al alloys, the compact corrosion product layer was determined to be Fe_2O_3 -rich oxides on the top of Cr or Al-rich oxides, with a Cr or Al-rich sulfide band close to the alloy substrate. Corrosion morphology examinations also revealed that the two corrosion product layers increased in thickness with the proceeding of

corrosion, and that the compact layer grew faster than the porous one. As an example, EPMA analysis results for Fe-5Al alloy are shown in Fig.6.

The water soluble metal ions in corrosion products were identified to be Fe^{3+} , Fe^{2+} , with some Al^{3+} for Fe-Al alloys and without Cr detected for Fe-Cr alloys.

Discussion

1. Corrosion Mechanism

As indicated in the previous studies^{8,9}, hot corrosion of iron based alloys occurring at intermediate temperatures can be attributed to the formation of a low-melting $\text{Na}_2\text{SO}_4\text{-Fe}_2(\text{SO}_4)_3$ eutectic melt on the alloy surface. Hot corrosion process can be divided into two stages, namely, initial stage and steady stage. At the initial stage, the alloy is oxidized and, at the same time, the sulfation reaction of Fe_2O_3 (probably including Al_2O_3 for Fe-Al alloys) occurs, thus leading to the formation of the eutectic melt. From the experimental results described above, it is clearly seen that at the steady stage the proceeding of hot corrosion was accompanied by the increase in thickness of a porous Fe_2O_3 oxide layer and the rapid growth of a compact oxide layer on the alloy surface, and that the reaction kinetics mainly depend upon the growth of the compact Fe_2O_3 layer. This implies that although the dissolution/precipitation of Fe_2O_3 occurred, its contribution to hot corrosion was limited. Therefore, the widely accepted fluxing mechanism does not seem to be suitable for the illustration of hot corrosion process of iron based alloys occurring at intermediate temperatures. Instead, electrochemical mechanism is proposed on the basis of the present study results.

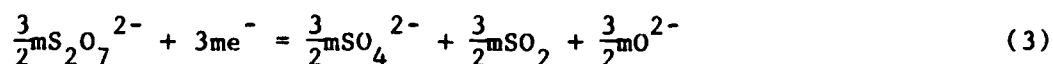
Probably because of the higher oxidation rate of the alloys compared to the sulfation kinetics, a compact oxide layer is always formed on the alloy surface. Once the eutectic melt appears, electrochemical reactions of the alloy electrode begin to occur. Iron is involved in the anodic oxidation reaction:



Some Fe^{2+} formed may be further oxidized in the compact oxide layer:



O_2 and $\text{S}_2\text{O}_7^{2-}$ can participate in the cathodic reduction reaction on the compact oxide layer, but the reduction of $\text{S}_2\text{O}_7^{2-}$ is believed to be predominant:



O^{2-} ions are incorporated into the oxide lattice and combined with Fe^{3+} ions to form Fe_2O_3 .



Reaction (4) results in the growth of the compact oxide layer. Similar reactions can be expected for element Cr or Al. As the higher affinity for oxygen and lower diffusivity in the compact oxide layer of Cr or Al compared to those of Fe, Cr or Al-rich oxides would be formed and enriched beneath the Fe_2O_3 -rich oxides. Sulfur-containing species, for example, gaseous SO_2 produced in reaction (3), may penetrate into the compact oxide layer and get reduced, thus causing Cr or Al-rich sulfides to form at the metal/oxide interface as well as in the compact oxide layer. The Fe^{2+} ions from reaction (1) can move across the compact oxide layer and dissolve in the melt since Fe^{2+} ions are more thermodynamically stable than Fe^{3+} ions in the liquid sulfate phase close to the oxide/melt interface where the oxygen activity is relatively low due to the reduction of oxygen there. Fe^{3+} ions in the eutectic melt may be involved in the cathodic reaction on the surface of the compact oxide layer:



The Fe^{2+} ions from reactions (1) and (5) diffuse outwards through the melt and get oxidized at the melt/gas interface:



Porous Fe_2O_3 particles precipitate through a secondary reaction:



When the compact oxide layer is relatively thin, the activity of Cr or Al diffusing to the oxide surface is so high that the oxygen activity in the melt close to the oxide/melt interface is significantly reduced. As a result, a great negative solubility gradient of iron ions across the melt film can be established, thus leading to the rather rapid precipitation of porous Fe_2O_3 within the melt. Afterwards, the activity of Cr or Al on the surface of the compact oxide layer is reduced with the growth of the oxide layer, and therefore, the oxygen activity at the oxide/melt interface is increased. Consequently, the development of the porous oxide layer becomes limited. Hot corrosion process is, thereby, dependent mainly on the growth of the compact product layer. The rapid growth of the compact layer is attributed to the easy diffusion of cations down through short circuit paths of sulfides contained in it.

2. The Effects of Temperature, Gas Composition and Alloying Element Content on Corrosion Behavior

The effect of temperature on corrosion kinetics of the alloys is related to the following factors. In general, the increase in temperature will cause an increase in corrosion rate. On the other hand, the temperature increase leads to the rapid development of a Cr or Al-rich oxide layer, which tends to reduce corrosion rate. As a result, a maximum corrosion

rate of the alloys would occur at certain intermediate temperatures. As corrosion kinetics of pure iron is only associated with temperature, its corrosion rate increases with temperature monotonously.

SO₃ in the system is necessary for the sulfation reaction of oxides, the formation of the sulfate eutectic melt and the formation of sulfides as corrosion product. Higher P_{SO₃} in the system will favour all these reactions, thus inducing severe corrosion, as observed in the present study.

The beneficial effect of Cr and Al content on corrosion resistance is easily understood from the fact that the content of Cr or Al-rich oxides in the compact oxide layer is associated with the content of Cr or Al in the alloys.

Conclusions

The commercial iron, Fe-Cr and Fe-Al alloys tested were found to be subject to hot corrosion attack in the presence of a Na₂SO₄ deposit on their surfaces in O₂/SO₂/SO₃ gas atmospheres at 650-750°C. The reaction kinetics were dependent upon temperature, gas composition and element content in the alloys. The proceeding of hot corrosion of the materials was accompanied by the precipitation of porous Fe₂O₃ in the melt and, mainly, the growth of compact corrosion products on the metal surface. Hot corrosion process can be illustrated in terms of electrochemical mechanism. The rapid kinetics is attributed to the fast anodic reaction caused by sulfides formed within the compact oxide layer.

References

1. W. T. Reid, R. C. Corey, B. J. Cross, Trans. ASME, 67 (1945): p. 279
2. W. Nelson, C. Cain jr, Trans. Am. Mech. Engrs. J. Eng'g Pr, 82A (1960): p. 194
3. J. Cortier, Mechanism of Corrosion by Fuel Impurities, (H. R. Janson and D. J. Litter, Eds., Butterworths, London, 1963), p. 531
4. A. Hendry and D. J. Leeds, Corr. Sci., 20 (1980): p. 383
5. V. Buscaglia, P. Nanni, C. Bottino, Corr. Sci., 30 (1990): p. 327
6. Y. S. Zhang, X. M. Li, S. T. Shih, J. Chin. Soc. Corr. Prot., 10 (1990): p. 1
7. Y. S. Zhang, X. M. Li, L. Q. Shi, S. T. Shih, J. Chin. Soc. Corr. Prot., 11 (1991): p. 17
8. Y. S. Zhang, L. Q. Shi, S. T. Shih, J. Chin. Soc. Corr. Prot., 12 (1992): p. 20
9. L. Q. Shi, Y. S. Zhang, S. T. Shih, Corrosion Control, Proc. 7th APCCC, (International Academic Publishers, Beijing, China, 1991, Vol. 1), p. 142

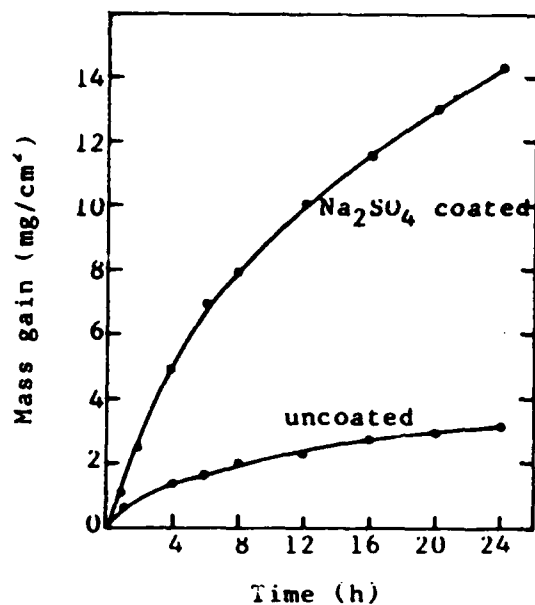


Fig.1 Corrosion kinetics of Na_2SO_4 -coated and uncoated commercial iron in O_2 -0.5%(SO_2+SO_3) gas atmosphere at 650°C

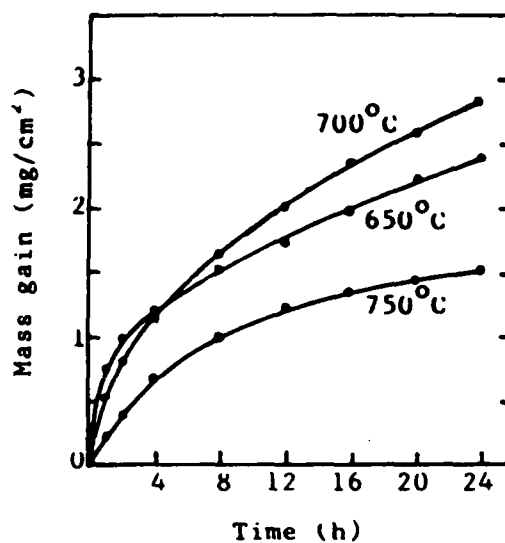


Fig.2 Temperature dependence of corrosion kinetics of Na_2SO_4 -coated Fe-20Cr alloy in O_2 -0.5%(SO_2+SO_3) gas atmosphere

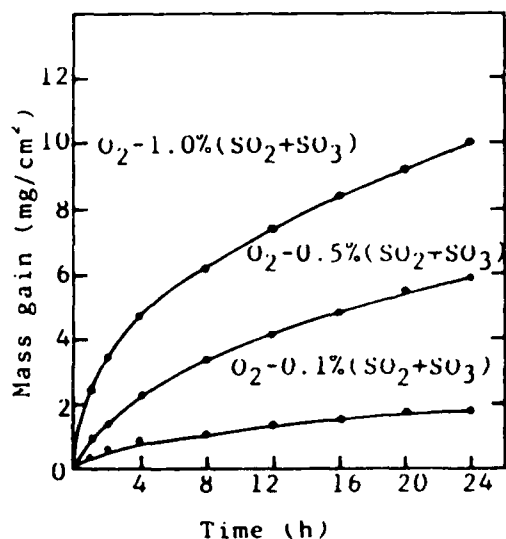


Fig.3 Dependence of corrosion kinetics of Na_2SO_4 -coated Fe-10Al alloy at 650°C upon gas composition

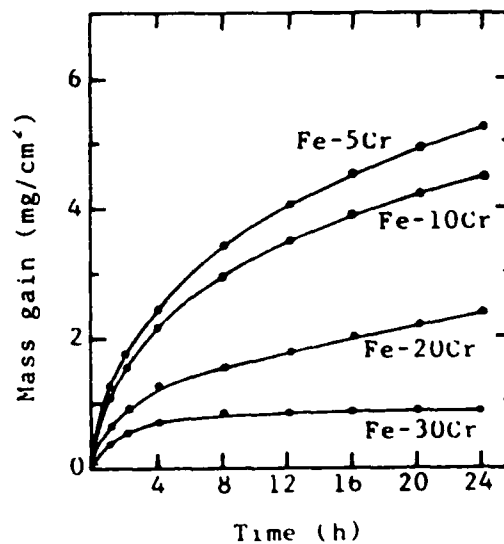


Fig.4 Influence of Cr content on corrosion kinetics of Na_2SO_4 -coated alloys in O_2 -0.5%(SO_2+SO_3) gas atmosphere at 650°C

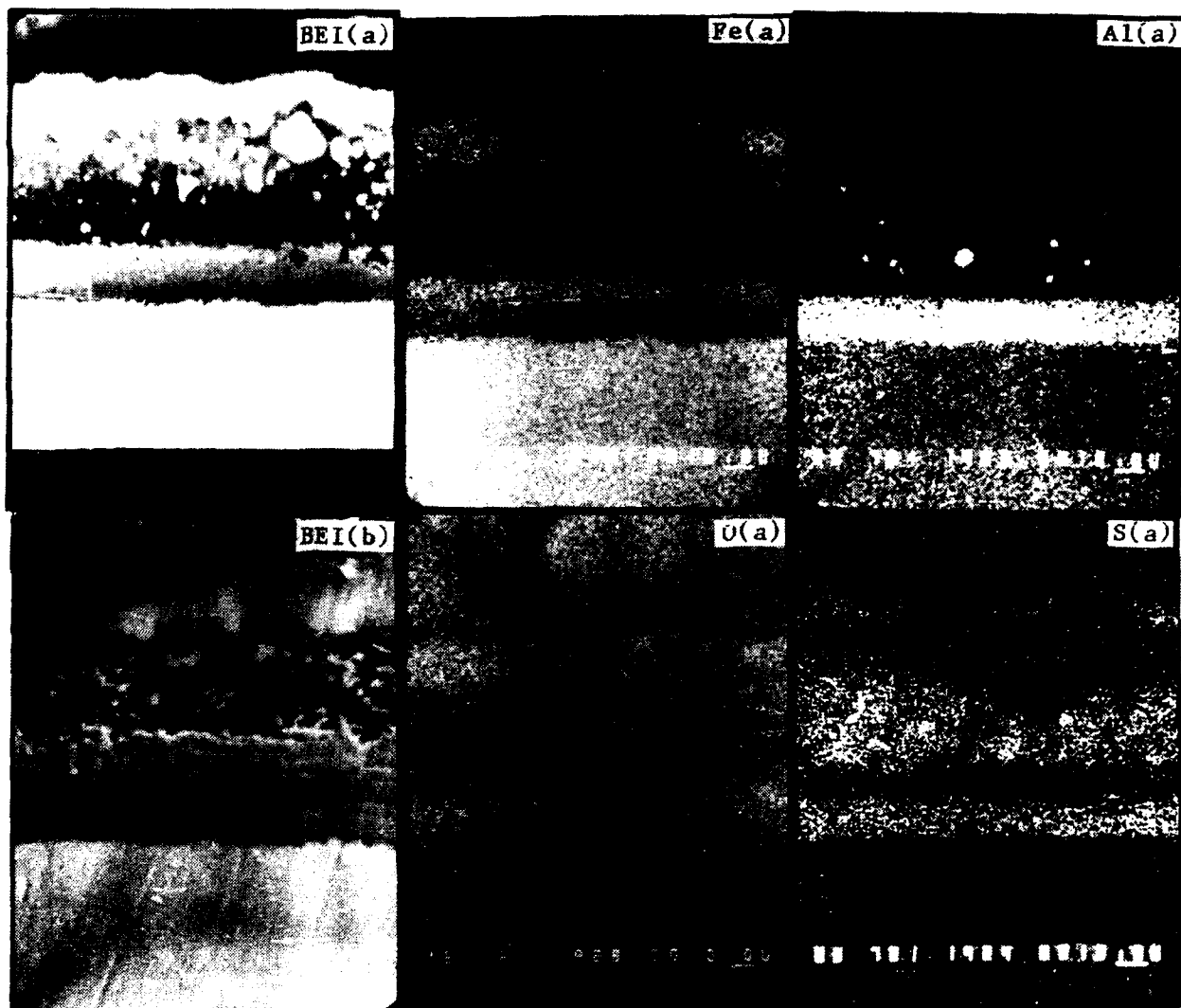


Fig.6 Corrosion morphology and elemental maps for Na_2SO_4 -coated Fe-5Al alloy corroded in O_2 -0.5%(SO_2 + SO_3) gas atmosphere at 650°C for 2 hrs (a) and corrosion morphology for the same alloy corroded for 8 hrs (b)

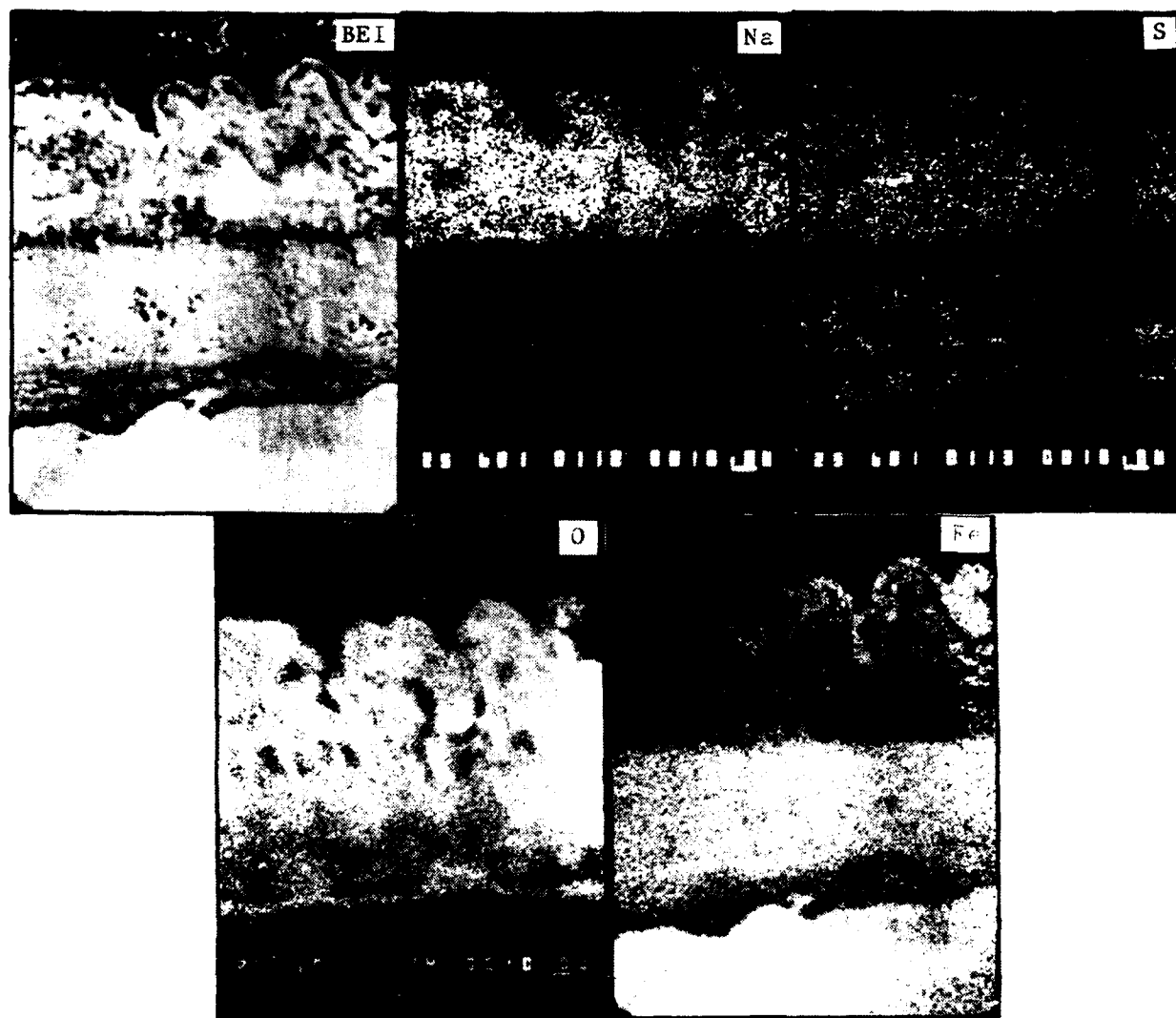


Fig.5 Corrosion morphology and elemental maps for Na_2SO_4 -coated commercial iron corroded in O_2 -0.5%(SO_2 + SO_3) gas atmosphere at 650°C for 8 hrs

Electrochemical noise measurement of iron in equimolar NaNO_3 KNO_3 melt at various temperatures.

I.B.Singh
Central Electrochemical Research Institute
Karaiikudi - 623 006
India.

G.Venkatachari
Central Electrochemical Research Institute
Karaiikudi - 623 006
India.

K.Balakrishnan
Central Electrochemical Research Institute
Karaiikudi - 623 006
India.

Abstract

The corrosion potential variation with time and electrochemical voltage noise have been recorded for pure iron in an equimolar NaNO_3 - KNO_3 melt in the temperature range of 573 K to 773 K in an inert atmosphere. The shift of corrosion potential in a noble direction with time and temperature up to 773 K, suggests the formation of a protective film. Almost four orders of magnitude of higher noise power were obtained at 773 K in comparison to 573 K, which generally indicates a decrease of compactness of the oxide film with the increase of temperature. The decrease of compactness of oxide film with increase of temperature has been further confirmed from the power spectral density plots and metallographic examination.

Key terms : Molten salt corrosion, noise power, passivation.

Introduction

An equimolar molten mixture of sodium nitrate and potassium nitrate is considered to be one of the best heat transfer and storage systems besides they enjoy common use as a heat treatment bath, because of their low corrosiveness, low eutectic temperature, high heat capacity and easy availability^{1,3}. Because of the many applications of this system, various hot corrosion studies have been carried out for iron and steels by gravimetric and electrochemical tests^{4,10}. However, most of the previous studies are related to thermodynamics and analysis of the oxide film and explaining the potential - pO_2 relationship and composition of the film. However, no attention has been paid to characterise the oxide film in terms of degree of compactness with respect to temperature.

Recently, electrochemical noise measurements are being used in aqueous systems but very little in molten salts system. Noise is a general term used to explain the fluctuating behaviour of a signal with respect to time. In the case of electrochemical corrosion, the process is stochastic, random in time and is the result of series of transients associated with the film breakdown or general corrosion. This technique provides valuable information on a corroding electrodes, such as pit initiation and propagation, unstable active - passive transitions and electrocrystallization etc. Fluctuations of potentials or current of corroding metals are generally related to sudden changes of a dissolution rate which can easily be noted in the form of electrochemical noise. In an oxidizing environment at elevated temperatures, close adherence of oxide film may also influence the metal dissolution at the electrode interface, thereby affecting the voltage or current fluctuations. Hence, some information on the compactness of the oxide film can be obtained from noise analysis. Based on the above hypothesis, the present investigation has been undertaken to examine the nature of an oxide film formed on iron surface in NaNO_3 - KNO_3 melt at various temperatures.

Experimental details

An equimolar binary mixture of NaNO_3 and KNO_3 was used as the main electrolyte. AR - grade NaNO_3 and KNO_3 were dried well separately at 473K up to 10 hours and then in their equimolar mixture at 503K for six hours in vacuum. After drying well, the equimolar eutectic mixture was kept in the inner tube of the electrochemical cell (Pyrex glass) which was placed in a vertical tubular furnace. The temperature of the melt was measured using a chromel - alumel thermocouple which was placed into the cell via a separate glass tube.

In the present investigation, the electrochemical set-up was employed as reported elsewhere⁸⁻¹⁰. The iron (Armco iron) electrodes were welded to a steel wire and were inserted into a Pyrex glass tube. The gap between the pyrexglass tube and specimen was covered by a high temperature adhesive (Ceramabond 571). The exposed area (0.16 cm^2) of the specimen was polished well by various grades of emery paper, degreased by trichloroethylene. The corrosion potential was measured with the help of Ag/Ag⁺ reference electrode. The reference electrode was made up of pure silver wire which was immersed into the equimolar NaNO_3 - KNO_3 melt containing 0.07M AgNO_3 in separate glass tube as reported elsewhere¹¹. Two identical iron electrodes were used for electrochemical noise measurements because the mean potential differences between the two identical electrodes in the same environment remain approximately zero¹². Before starting the experiment, the melt was deaerated by bubbling oxygen free dry nitrogen gas.

For measuring the noise power values (V^2), the voltage fluctuations and autocorrelation functions of the voltage Vs. time data were measured with a signal processor (1200 Solartron UK) in the band width of 20 mHz to 1 Hz. The noise power values were obtained from the autocorrelation function at time zero. The open circuit potential values with time was noted using a digital voltmeter. Metallographic examination of the cross section of the oxidized specimens was made by Scanning electron microscope (SEM).

Results

(i) Rest potential Vs time behaviour

Fig.1 shows the open circuit potential (OCP) variations with time at various temperatures for iron. The potential shifts in the noble direction with time which generally indicates the formation of an oxide layer. As the temperature of the melt is increased from 573 to 773 K, the open circuit potential becomes more noble and a steady state is attained in a shorter time. Increase of temperature increases the oxidation kinetics and the OCP attains a steady value in a shorter time. The change of OCP with time (Fig.1) shows that oxidation rate is quite high in the beginning but decreases with immersion period.

(ii) Noise power variation with temperature

Noise power is a mean value of the fluctuating current or potential with time as mentioned earlier. The variation of noise power with temperature for iron after one hour immersion at various temperatures is given in Fig.2. There is an increase of nearly four orders of magnitude of noise power when the temperature is increased from 573 to 773 K. This may be due to the increased migration rate of metal ion from the metal scale interface to the scale. The trend of increase of noise power values with temperature seems to be linear up to 723 K as shown in Fig.2.

(iii) Power spectral density analysis

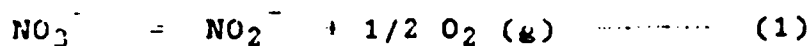
The typical power spectral density (psd) plots of iron at 573 K and 673 K after 30 minutes immersion in the melt are shown in Fig.3a and b respectively. The psd plots show that the noise is of white type at both temperatures. This indicates the presence of passive type of oxide film since such type of white noise is generally related to the presence of passive film^{14,15}. However, generation of a low frequency noise at 673 K (Fig.4a) and a discontinuous noise at 773 K (Fig.4b), and above temperature, indicates the breakdown of the oxide film^{14,15}.

(iv) Metallographic examination :

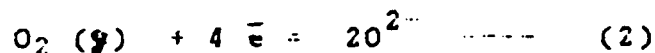
SEM photomicrographs of the cross sections of the oxidized specimens after six hours immersion in the melt at 723 and 773 K are shown in Figs. 5a and b, respectively. Presence of voids near the metal scale region at 723 K and micro cracks at 773 K are observed. Due to this, the scale seems to losses its compactness at higher temperature.

Discussion

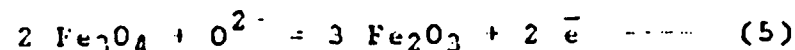
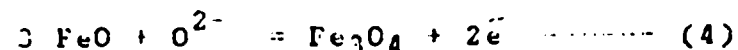
The potential time measurements at various temperatures clearly indicate not only the formation of an oxide film but also the fact that the film formation kinetics become faster when temperature increases. It has been reported¹³ that Fe_3O_4 is formed initially on bare iron surface and that Fe_2O_3 is nucleated on the Fe_3O_4 layer subsequently. Even though the melt was deaerated by oxygen free nitrogen, the presence of oxygen in the melt is possible due to generation of gaseous oxygen⁽¹⁶⁾ by the reduction of nitrate ion as.



Further reduction of oxygen into the oxide ion (O^{2-}) takes place as -



and the redox potential of O_2/O^{2-} reaction is - 0.72 V (11,17). These oxide ions react with iron to form the iron oxides and the possible reaction of FeO , Fe_3O_4 and Fe_2O_3 formation can be given as



Since FeO (Wustite) decomposes below 843 K⁽¹⁸⁾, Fe_3O_4 and Fe_2O_3 are the main oxides are formed on iron^{9,10} surface. However the incorporation of sodium in the scale^{9,10} may also start at higher temperature.

Visually, a very thin and compact oxide film was found on the surface upto 623 K. Presence of thin oxide layer is generally compact and adherent in nature which control the outward diffusion of metal ions. This may result in the generation of a low noise signal at lower temperature. The generation of noise is a result of random fluctuations of voltage-current due to the random motion of {45} electrons or ions within the system in the equilibrium state⁽⁴⁵⁾. Generation of higher noise with increase of temperature may be related to the relieving of the stresses of the growing oxide layer at the metal/scale interface since the

growth stresses in oxidizing environment is generally relieved through the detachment of the scale (20-22) near metal/scale interface or cracking of the scale. In the present investigation the relieving of stresses may likely be related to the development of voids and cracks in the scale. This has been confirmed on metallographic examination of the scale at 723 and 773 K (Fig 5a and b). Once voids are formed in the scale, migration of the metal ions from the metal/scale interface to the scale becomes fast which may subsequently influence the electrochemical equilibrium of the system resulting in generation of higher noise values.

The generation of white noise upto 623 K predict the presence of protective type compact oxide film. Above 673 K the generation of low frequency or discontinuous noise signal is observed. The generation of such noise indicates the development of voids in the scale which lead to the loss of compactness of the oxide film.

Conclusion

The noise measurements have shown that a compact oxide film is formed on iron in $\text{NaNO}_3 - \text{KNO}_3$ melt upto 623 K. At higher temperatures the compactness of oxide film tend to decrease due to development of voids in the scale.

Acknowledgement

The authors are grateful to Prof.G.V.Subba Rao, Director, CECRI, Karaikudi - 623 006 for his interest and permission to publish this work.

References

1. H.P.Voznick and V.M.Uhl, Chem. Eng. 70, (1963) p.135
2. Sundermeyer W, Angew chem, 77 (1965) p.241
3. T.N.Tallerico, Sandia Laboratories Report, SAND (1979) p.8019.
4. D.Inman and N.S.Wrench, Brit. Corros. J, 1 (1966) p.246
5. J.Notoya and R.Midorikawa, Denki Kagaku 39 (1971) 930 and 41 (1973) p.815.
6. A.J.Ariva, J.J.Podesta and R.C.Piatti, Electrochim. Acta, 16 (1971) p.1797 and 17 (1972) p.25
7. A.Baraka, A.J.Rehman and A.A.Elhosary, Brit. Corros.J., 11 (1976) p.44
8. I.B.Singh, Indian J.Technol, 30 (1992) p.347
9. I.B.Singh and U.Sen, Corros. Sci. (1993) (Inpress)
10. I.B.Singh, G.Venkatachari and K.Balakrishnan, Corrosion, to be submitted.
11. P.C.Zamboni, Electroanal.Chem.Interfacial Electro chem., 24 (1970) 365.
12. K.Hladky and J.L.Dawson, Corros.Sci,22 (1982) p.23
13. E.B.Boggs, K.H.Kachik and G.E.Pelliser, J.Electrochem.Soc.,

- 112 (1965) p.539
14. K.Nachstedt and K.E.Heusler, *Electrochim Acta*, 33 (1988) p.311.
 15. F.Flis, J.L.Dawson,J.Gill and GC Wood, *Corro. Sci.*, 32, (1991) p.710.
 16. G.Picard,J.Flament and B.Tremillon, proceeding of the International Symposium on Molten Salt Chemistry and Technology, Kyoto, Japan (1983) p.85.
 17. F.Paniccia and P.G.Zambonin, *J.Phy Chem*, 17 (1973)
 18. P.Mayer and A.V.Manulsee, Proceeding of the Higher Temperature Corrosion, Edited by R.A.Rapp, NACE 6 (1981) p. 1076.
 19. P.Bindra, M.Fleischmann, J.W.Oldfield and D.Singleton, *Discussion of Faraday Soc.*, 56 (1974) p. 180.
 20. High temperature corrosion. Per Kofstad, Elsevier Science Publishing Inc., NY (1988) p.246.
 21. D.L.Houglass, *Oxid.Met*, 1 (1969) p.127
 22. J.Stringer, *Corros. Sci*, 10 (1970) p.573.

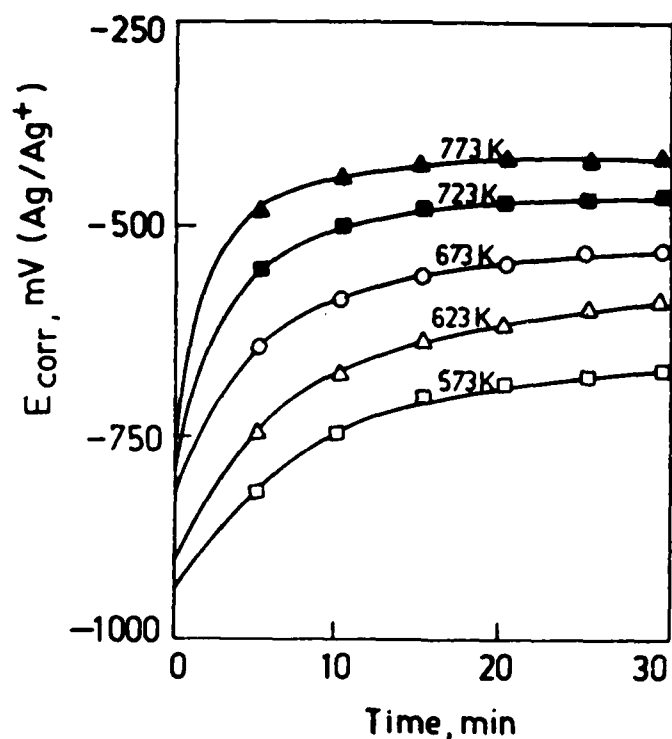


Fig.1. Variation of E_{corr} with time for iron in $\text{NaNO}_3\text{-KNO}_3$ melt.

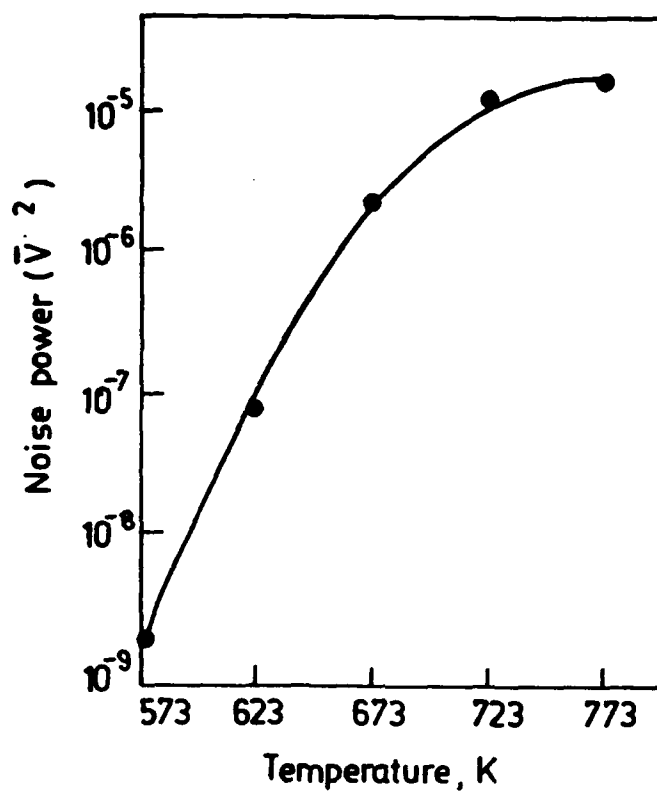


Fig.2 : Variation of noise power with temperature for iron in $\text{NaNO}_3 - \text{KNO}_3$ melt.

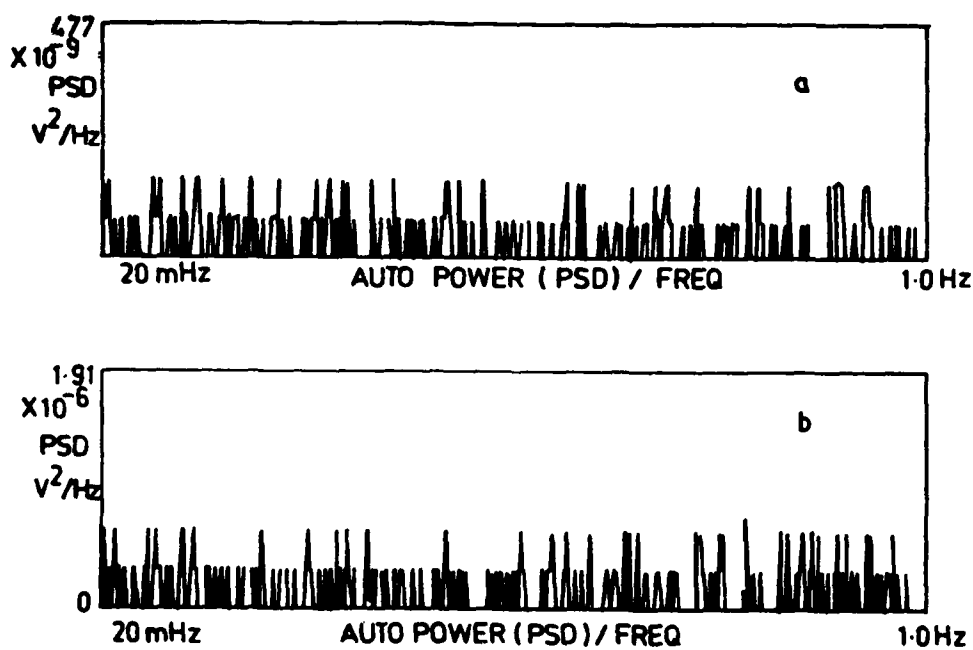


Fig.3. PSD Plot for iron in $\text{NaNO}_3 - \text{KNO}_3$ melt
(a) 573K and (b) 623K

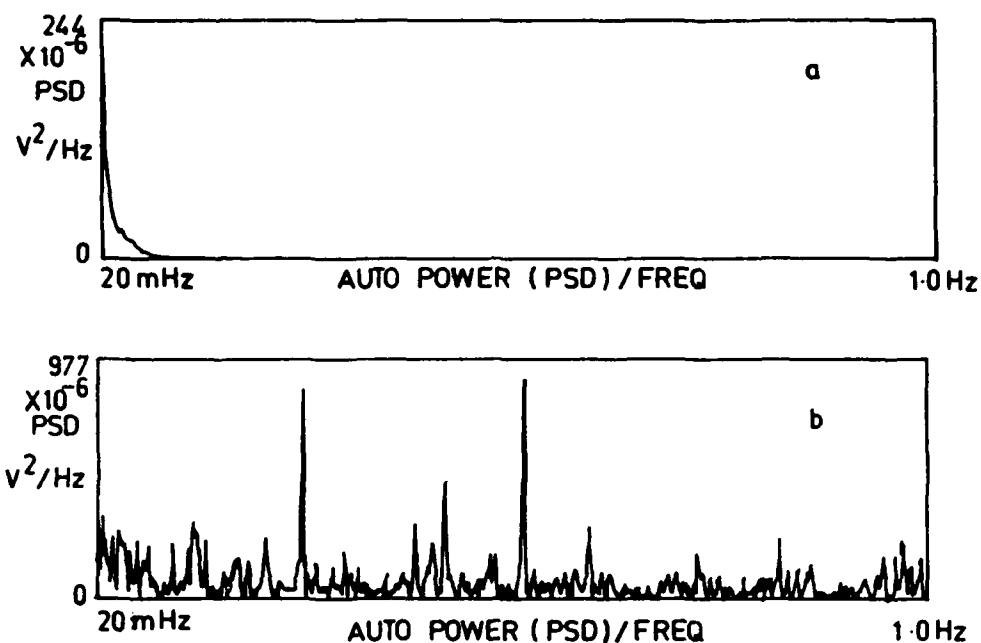


Fig. 4. PSD plot for iron in $\text{NaNO}_3 - \text{KNO}_3$ melt
(a) 673 K and (b) 723 K.



(a)



(b)

Fig. 5. SEM Photomicrographs from the cross sections of oxidized samples immersed upto six hours in the melt (a) at 723 K (b) 773 K.

CORROSION KINETICS STUDY AT HIGH TEMPERATURE OF THE IN-657
SUPERALLOY AFTER LASER SURFACE TREATMENT IN CONTACT WITH THE
EUTECTIC MELT 82% $K_2S_2O_7$ - 18% V_2O_5

A. Pardo

Dto. Ciencia de los Materiales e Ingeniería Metalúrgica.
Facultad de Ciencias Químicas. Universidad Complutense.
Ciudad Universitaria. 28040. Madrid. Spain.

E. Otero

Dto. Ciencia de los Materiales e Ingeniería Metalúrgica.
Facultad de Ciencias Químicas. Universidad Complutense.
Ciudad Universitaria. 28040. Madrid. Spain.

F. J. Pérez

Dto. Ciencia de los Materiales e Ingeniería Metalúrgica.
Facultad de Ciencias Químicas. Universidad Complutense.
Ciudad Universitaria. 28040. Madrid. Spain.

J. F. Alvarez

Instituto Tecnológico de Costa Rica, Becario Conicit.
PO Box 159-7050 Cartago, Costa Rica

Abstract

In an oxidizing atmosphere the corrosion kinetics of the IN-657 superalloy have been studied by electrochemical methods, in contact with the eutectic melt 82% $K_2S_2O_7$ -18% V_2O_5 (molar ratio) with different contents of carbon and different temperatures (773 and 823 K). The corrosion kinetic laws are determined for the material with and without laser surface treatment, comparing the results in both cases.

Key terms: IN-657, High temperature corrosion, Hot corrosion, molten salts, Laser, Laser surface treatment, Nd Laser, surface modification.

Introduction

According to current usage in the literature, the phenomenon of hot corrosion is the accelerated oxidation in a high temperature gaseous environment of a material whose surface is coated by a thin fused salt film (¹). Engineers concerned with the degradation of boiler tubes by fuel ash condensates have long been familiar with corrosive slag films (²).

The fossil fuels used in energy generation systems have chemical elements that can be transformed by the combustion reaction to form inorganic compounds with low melting point. Such deposit on metallical systems at temperatures over the melting point of these inorganic compounds cause catastrophic corrosion phenomena (^{3,4,5}).

The catastrophic corrosion results from the electrochemical nature of hot corrosion at high temperatures (^{6,7}).

The IN-657 superalloy was developed to achieve high creep

resistance. As a result, it is interesting to note its corrosion behavior at high temperature in contact with molten salts.

An important new alternative to enhance the resistance to hot corrosion is the laser surface treatment with an inherent fast heating and cooling cycle. The laser process can be controlled and applied to specific areas of the material. The surface experiences fast heating and cooling rates (On the order of 10^6 and 10^8 °C/s). This technique is used to improve the behavior of the material to wear, friction, corrosion and fatigue, due to the microstructural changes induced into the surface (^{8,9}).

The objective of this work is to determine the kinetics of the catastrophic corrosion, in the eutectic melt 82% $K_2S_2O_7$ -18% V_2O_5 (molar ratio), in contact with the IN-657 superalloy with and without laser surface treatment.

The molten salt tested was 82% $K_2S_2O_7$ - 18% V_2O_5 (molar ratio), whose melting point is approximately 600 K. It is usually present in the combustion ash, as a result of the oxidation of vanadium and sulphur from the fossil fuels (¹⁰). It is also possible to form this salt from the combustion of low quality fuels in industry and in aircraft turbines (¹¹).

Potassium pyrosulphate $K_2S_2O_7$ is formed from alkaline compounds deposited on the metallic surface, from K_2SO_4 to react with the SO_3 (¹²). The vanadium pentoxide V_2O_5 is formed from vanadium porphorine in the fossil fuels reacting in the combustion process, first to form $VO(OH)_3$ (gas), and then V_2O_5 (solid), with an excess of oxygen in the combustion gas (¹³).

The study was carried out at temperatures between 773 and 823 K, when the salt mixtures are molten. Also, at these temperatures, it is often possible to find various metallic areas showing catastrophic corrosion phenomena in equipment operating in energy transformation industries. To study the process one has used polarization resistance and intersection techniques. Such measurements have confirmed that the corrosion process, in the presence of molten salts is an electrochemical process. According to the results obtained, the authors suggest the possibility of the participation of different electron sinks in the cathodic reaction.

The Stern-Geary equation was used to obtain the corrosion intensity by determining first, the cathodic (β_c) and anodic (β_a) Tafel slopes obtained from polarization curves, and the polarization resistance values (R_p). The corrosion intensities (I_{corr}) were determined from the Tafel slopes and from the Stern-Geary equation.

In the industry, it is usual to find carbon residues in the molten salts. In this work, the effect of carbon on corrosion is analyzed for contents between 1% and 3% wt% C.

Experimental Method

The working electrode was the alloy studied: IN-657, with an exposure area to the corrosive media of 0.67 cm² (Table-1). The laser surface treatment was applied to the polished sample, by neodimium laser equipment (Nd:YAG). A pulse was used as shown in Figure 1. The energy applied was 7.7 J, with a power of 240 W. The frequency was 30 Hz. The atmosphere was controlled at 2 Bar pressure with an argon flow of 0.5 m³/h. The beam speed was 1200 mm/min with a focus of 5 mm.

TABLE 1

COMPOSITION OF THE IN-657 SUPERALLOY (wt%)

ALLOY	ELEMENTS								
	Ni	Cr	Fe	Mn	Si	Nb	V	N	P
IN-657	50.9	46.5	0.7	0.11	0.37	1.32	-	0.07	0.01

Platinum was used as a counter electrode. The electrical connection to the test electrode was shielded with a vycor glass rod sealed with ceramic paste (composed of sodium silicate with kaolin added to saturation of the mixture), to achieve the appropriate degree of protection from the melt.

The Ag/Ag₂SO₄ reference electrode consisted of a tetradic eutectic with the following molar ratio: 70.2% Li₂SO₄, 12.15% K₂SO₄, 7.65% Na₂SO₄ and 10% Ag₂SO₄ (^{14,15}).

The salt mixture was prepared with a molar ratio of 82% K₂S₂O₇ - 18% V₂O₅ corresponding to the eutectic composition which has the lowest melting point of the system K₂S₂O₇-V₂O₅ (Figure 2) (¹⁶). Carbon concentrations between 1% and 3 wt% were added to study the possible influence of this element. A quartz crucible used as a cell container was placed in an AISI 304L stainless steel sealed vessel, that permitted work in a controlled atmosphere (¹⁷⁻¹⁸). This was placed in a resistance furnace at the working temperatures of 773 and 823 K.

An AMEL potentiostat AMEL-568 and a function generator AMEL-867 were used to obtain electrochemical data. The temperature was controlled by a digital system.

Potentials of +/-10 mV were applied to the corrosion potential (scanning rate 2 mV/s) for different testing times, to determinate the polarization resistance R_p for each time.

The Tafel slopes were established from the active region of the corresponding anodic and cathodic curves. The Tafel slopes were plotted by applying a ramp of +/-100 mV to the signal generator with a polarization rate of 20 mV/s. Then R_p, obtained by the Stern-Geary equation (¹⁹), was applied

to obtain I_{corr} . Subsequently, the instantaneous corrosion rates were established for each time and different conditions using Faraday's Law.

Experimental Results and Discussion

Figure 3 shows microscopy, after laser surface treatment (Nd: YAG) of the IN-657 superalloy. The surface is homogeneous without cracks. The laser melting treatment has been used to enhance the mechanical properties of the surface and near-surface regions. The effective cooling rate can be related to two processes occurring in the melt zone:

(1) The heating process, which can control the temperature, holding time, homogeneity and stability of the liquid phase.

(2) The diffusion of elements which can control the segregation, phase transformation and precipitation phenomena within the solidified metal.

In this work a very high homogeneity of the surface composition has been obtained.

Figure 4 shows the evolution of the corrosion intensity for different times in an oxidant atmosphere ($P_{O_2} = 1 \text{ atm}$), with and without laser treatment on IN-657, in contact with the molten salt tested without carbon. The evolution of I_{corr} was similar at 823 K, but at low temperature I_{corr} was greater each time with laser surface treatment.

Figure 5 shows the integration of the Figure 4 data, which allows calculation of the weight loss for different test times. The mathematical relationship between mass loss and time (kinetic laws) are as follows:

at 773 K:

a) without laser treatment (logarithmic):

$$\begin{aligned} y &= k + 0.13 \ln(t) & t < 55 \text{ h} \\ y &= k + 0.22 \ln(t) & t > 55 \text{ h} \end{aligned}$$

b) with laser treatment (potential):

$$\begin{aligned} y &= kt^{0.55} & t < 30 \text{ h} \\ y &= kt^{0.01} & t > 30 \text{ h} \end{aligned}$$

at 823 K:

a) without laser treatment (linear-logarithmic):

$$\begin{aligned} y &= k + 0.59t & t < 25 \text{ h} \\ y &= k + 14.95 \ln(t) & t > 25 \text{ h} \end{aligned}$$

b) with laser treatment (parabolic-linear):

$$\begin{aligned} y &= kt^{0.64} & t < 100 \text{ h} \\ y &= k + 0.06t & t > 100 \text{ h} \end{aligned}$$

The worse corrosion behavior of the material with laser surface treatment can be attributed to the formation of active-passive regions in the boundary areas between those scanned by the laser pulse, changing the composition in

these limited areas, allowing the formation of localized active areas.

Figure 6 shows the evolution of the corrosion intensity for different times in an oxidant atmosphere ($P_{O_2} = 1 \text{ atm}$), with and without laser treatment on IN-657, contacting the molten salt with 1 wt% carbon. The corrosion intensities are in the same range for both temperatures tested (with and without laser treatment).

Figure 7 shows the integration of the Figure 6 data, which allows calculation of the weight loss for different test times. The mathematical relationship between mass loss and time (kinetic laws) are as follows:

at 773 K:

a) without laser treatment (linear):

$$y = k + 0.05t \quad t > 0 \text{ h}$$

b) with laser treatment (para-linear):

$$y = k + 0.12t \quad t < 140 \text{ h}$$

$$y = k + 0.05t \quad t > 140 \text{ h}$$

at 823 K:

a) without laser treatment (logarithmic):

$$y = k + 11.88 \ln(t) \quad t > 0 \text{ h}$$

b) with laser treatment (power-logarithmic):

$$y = kt^{0.7} \quad t < 80 \text{ h}$$

$$y = k + 2.95 \ln(t) \quad t > 80 \text{ h}$$

At 773 K the corrosion behavior of the IN-657 superalloy is worse than the material treated by laser, but this change in behavior in the viscosity of the molten salt (ref. 16) at 823 K allows carbon transport to the alloy surface, depositing in the active areas (boundary areas between those treated by laser areas), and so that big anodes and small cathodes decrease the corrosion rate in this case.

Figure 8 shows the evolution of the corrosion intensity for different times in an oxidant atmosphere ($P_{O_2} = 1 \text{ atm}$), with and without laser treatment of the IN-657, in contact with the molten salt tested with 3 wt% carbon. The I_{corr} at 773 K of the material without laser treatment was very low, compared with the other three corrosion intensities.

Figure 9 shows the integration of the Figure 8 data, which allows calculation of the weight loss for different test times. The mathematical relationship between mass loss and time (kinetic laws) are as follows:

at 773 K:

a) without laser treatment (linear-logarithmic):

$$y = k + 0.06t \quad t < 75 \text{ h}$$

$$y = k + 7.95 \ln(t) \quad t > 75 \text{ h}$$

b) with laser treatment (linear):

$$y = k + 0.57t$$

$$t > 0 \text{ h}$$

at 823 K:

a) without laser treatment (linear):

$$y = k + 0.75t$$

$$t > 0 \text{ h}$$

b) with laser treatment (linear):

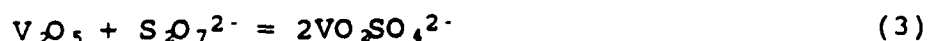
$$y = k + 0.65t$$

$$t > 0 \text{ h}$$

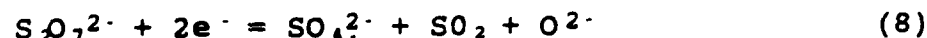
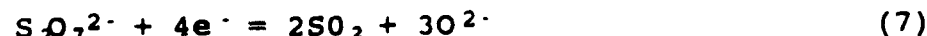
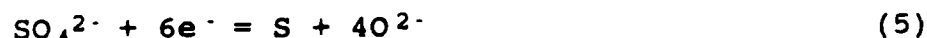
In the case with 3 wt% carbon again the viscosity of the molten salt allows the transport of the undissolved carbon, in the molten salt, and deposits it in the "boundary areas" between the pulses of laser on the material (see Figure 1).

According with the previous studies of the molten salt $K_2S_2O_7-V_2O_5$ (see ref. 16) and with the results obtained we can suggest the following chemical reactions between molten salt, carbon and IN-657.

The vanadium V^{5+} reacts in the molten media to form very stable "chemical complexes" in the test conditions as:



The amount of V^{5+} available to accept electrons in the cathodic reaction is very low. According to the last paragraph, the species rich in sulphur will play an important role in the cathodic mechanism as:



The thermal decomposition of $S_2O_7^{2-}$ plays a very important role in chemical equilibrium:

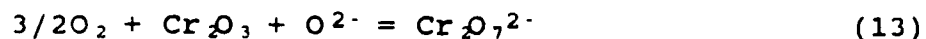


According with experimental results, the kinetic parabolic and logarithmic expressions confirm a diffusion mechanism through oxidized layers to control the kinetics. The formation of a chromium oxidized layer is:

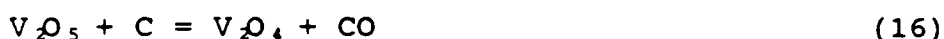
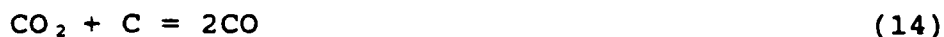




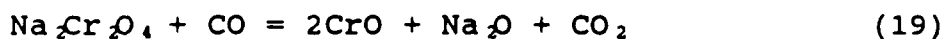
justifying the corrosion of a Cr_2O_3 layer. Allowing a reaction between the Cr_2O_3 layer and molten salts, with a "basic fluxing" as:



At the temperatures studied, the two possible reductants in the Budouard equilibrium are CO and C; but the thermodynamic reductant under 943 K is carbon. Carbon is the thermodynamic reactant, but the kinetic process is fastest with CO, because in this case the reaction is gas-liquid and in the other case the kinetic process is solid-liquid. These above discussion can be described by the following reactions:



reacting with the system components. But the action of the carbon can also occur on the protective layer.



Conclusion

1. The laser surface treatment applied to the IN-657 superalloy, obtains a superficial continuous microstructure without cracks.
2. At 773 K, independent of the carbon contents, the corrosion behavior of the IN-657 superalloy is worse than the material treated by laser surface modification.
3. At 823 K, for all the carbon contents in the molten salts tested, the corrosion resistance of IN-657 superalloy is better after laser surface modification.

Acknowledgments

The authors express their gratitude to the Consejería de Educación de la Comunidad de Madrid for the financial support of this work (Project C156-91).

References

1. R. A. Rapp, Corrosion, NACE, 42 10, (1986): p. 568.

2. W. T. Reid, R. C. Corey, B. J. Cross, Trans-ASME, 67, (1945): p. 279.
3. T. R. Griffiths, K. King and D. Mortimer, Power Industry Reserch. 2, (1982): p. 79.
4. N. S. Bornstein, M. A. DeCrescente and H. A. Roth, Corrosion. 24, (1968): p. 127.
5. N. S. Bornstein, M. A. DeCrescente and H. A. Roth, Corrosion. 28 7, (1972): p. 264.
6. P. Hancock, Corrosion Science. 22 1, (1982): p. 51.
7. L. Berchtold and L. Degussa, Werkstoffe und Korrosion. 37, (1985): p. 145.
8. P. A. Molian, Principles and Application of Laser for Wear-Resistant Coatings. Surface Modification Technologies. Ed. by Sudarshan and D. G. Bhat. The Metallurgical Society, (1988).
9. P. A. Molian, Surface Alloying Using Lasers. Surface Modification Technologies, Ed. M. Decker (1989).
10. R. J. Saunders, Material Science and Engineering, 2, (1986): p. 282.
11. K. Luthra and D. A. Spacil, Journal Electrochemical Society. 129, (1982): p. 649.
12. W.S. Reid, Mechanism of Corrosion, (New York, Ed. Elsevier, 1971).
13. K. Kim and O. Deveraux, Corrosion, 36 2, (1980): p. 262.
14. E. Erdoes und H. Altorfer, Electrochemistry Acta, 20 12, (1975): p. 937.
15. A. Rahmel, Electrochemica Acta, 15, (1970): p. 1262.
16. G. Hatem, R. Fehrmann, M. Gaune-Escard and N.J. Bjerrum, Journal Physical Chemistry, 91, (1987): p. 195.
17. E. Otero, A. Pardo, J. Hernaez and F. J. Pérez, Corrosion Science, 32 7, (1991): p. 677.
18. E. Otero, A. Pardo, J. Hernaez and F. J. Pérez, Corrosion Science, 33 11, (1992): p. 1747.
19. M. Stern y A. L. Geary, Journal Electrochemical Society, 104 1, (1957): p. 56.

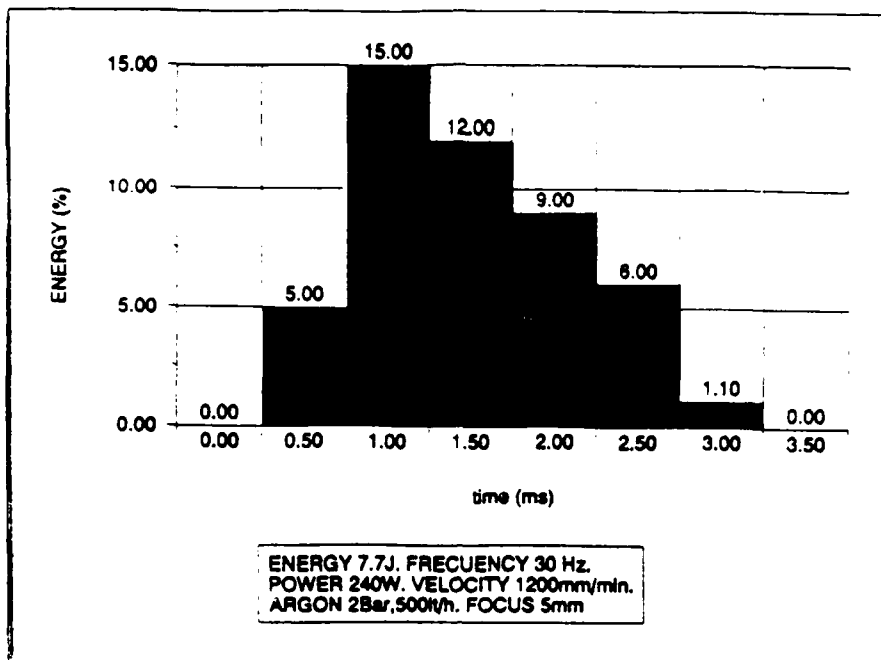


Figure 1. Laser surface treatments design, applied to the IN-657 superalloy.

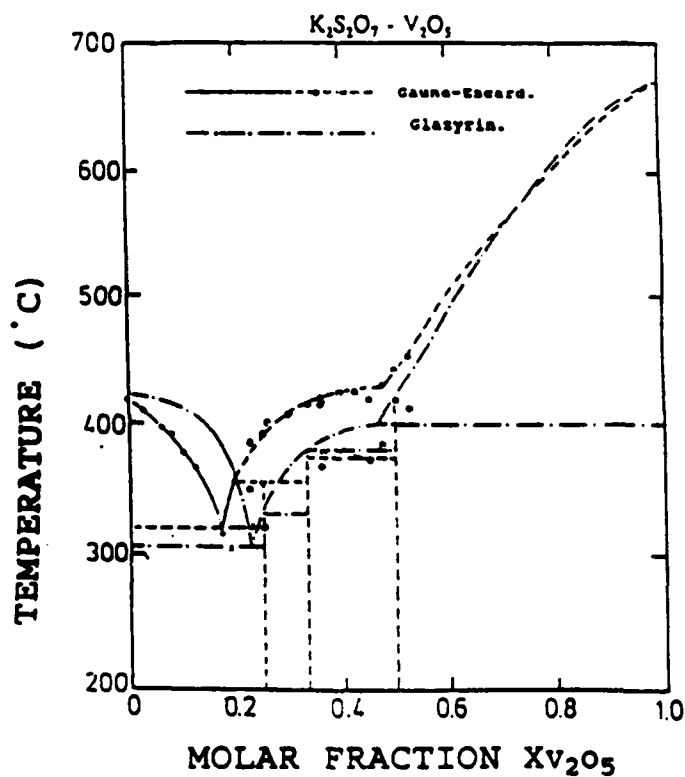


Figure 2. Equilibrium diagram of the binary system $K_2S_2O_7-V_2O_5$



Figure 3. IN-657 superalloy treated by laser, with a polarized filter (X magnification).

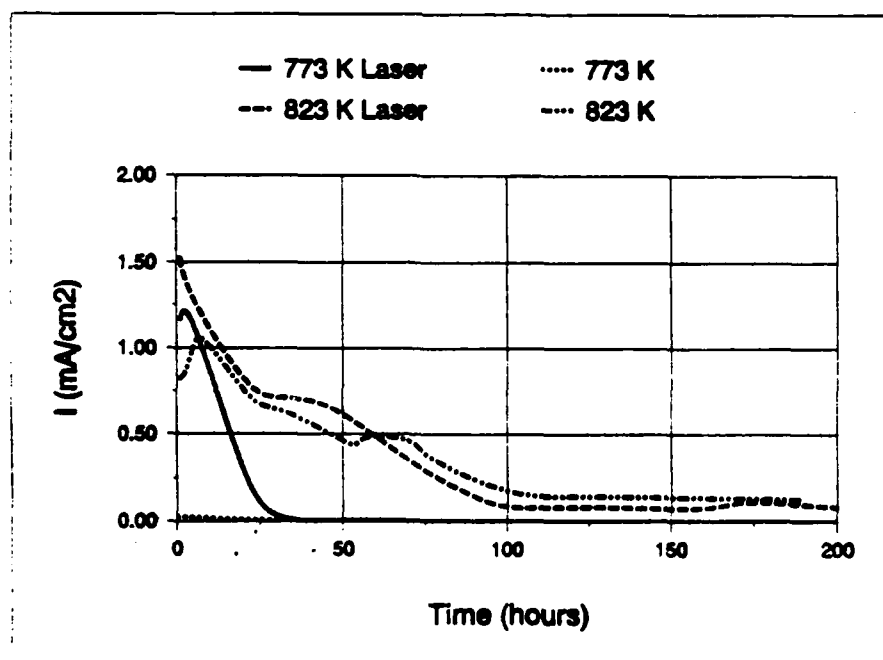


Figure 4. Evolution of I_{corr} with time in an oxidizing atmosphere for the IN-657 superalloy, with and without laser surface treatment. Molten salt with 0 wt% of carbon.

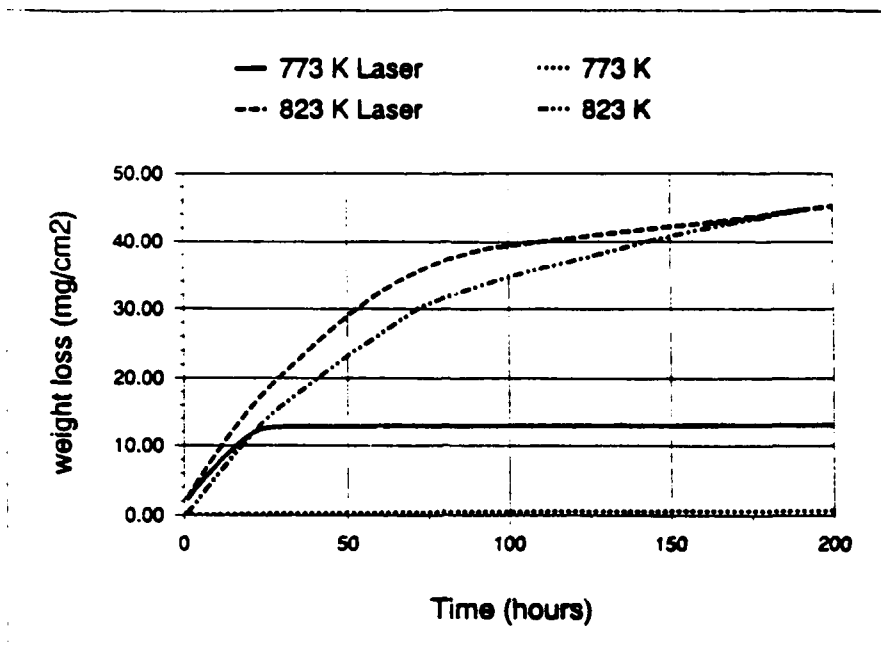


Figure 5. Loss mass with time in an oxidizing atmosphere for the IN-657 superalloy, with and without laser surface treatment. Molten salt with 0 wt% of carbon.

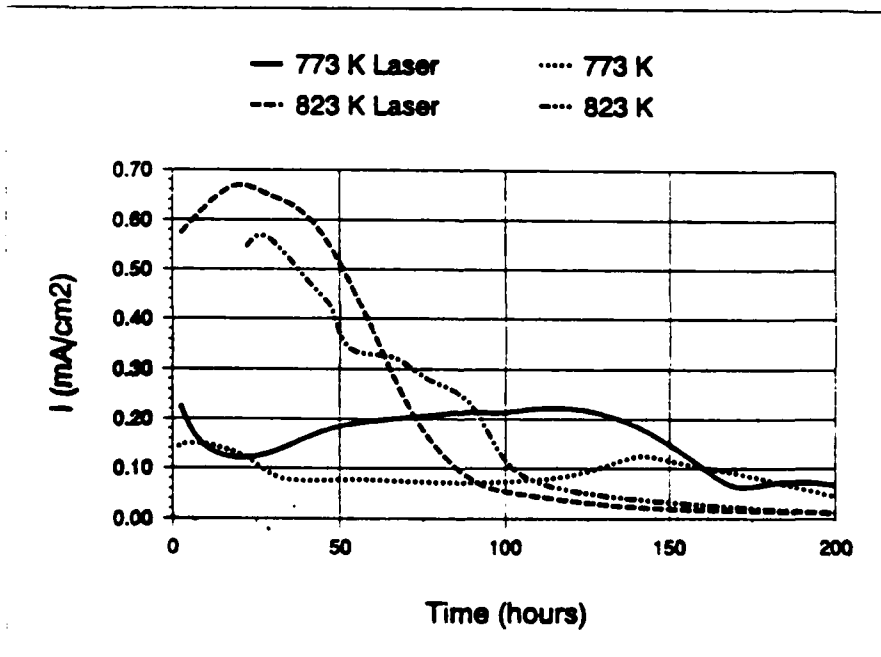


Figure 6. Evolution of I_{corr} with time in an oxidizing atmosphere for the IN-657 superalloy, with and without laser surface treatment. Molten salt with 1 wt% of carbon.

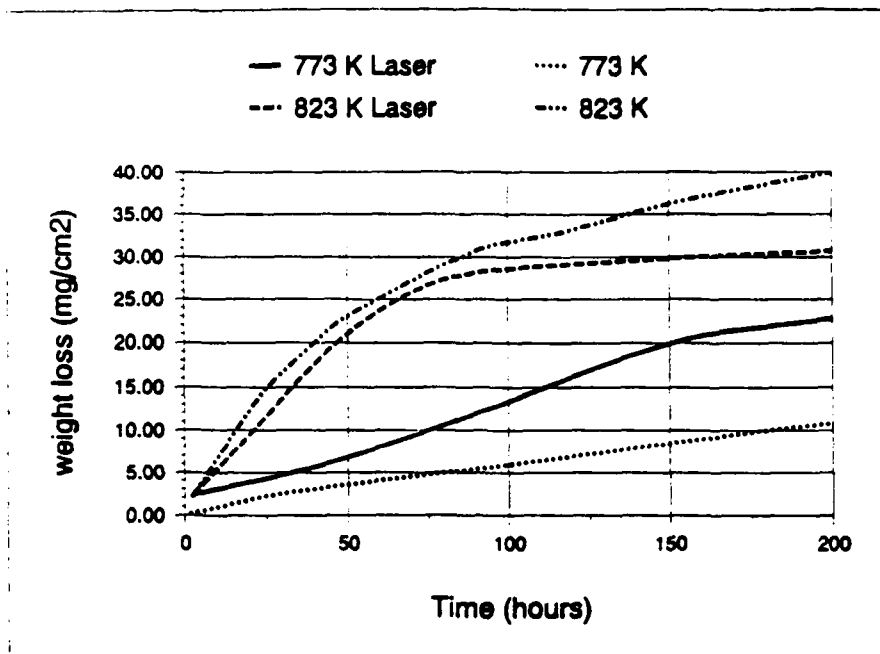


Figure 7. Loss mass with time in an oxidizing atmosphere for the IN-657 superalloy, with and without laser surface treatment. Molten salt with 1 wt% of carbon.

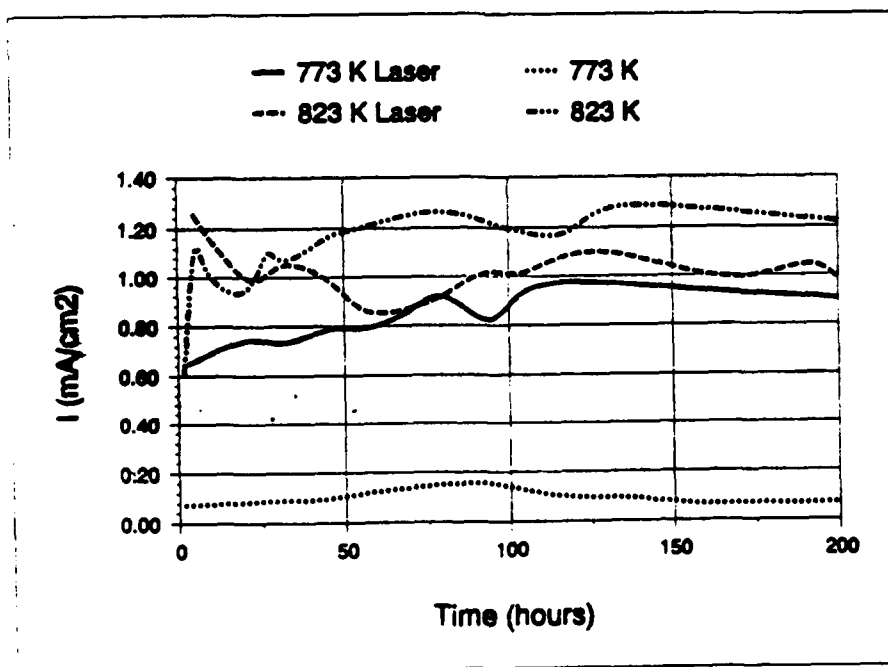


Figure 8. Evolution of I_{corr} with time in an oxidizing atmosphere for the IN-657 superalloy, with and without laser surface treatment. Molten salt with 3 wt% of carbon.

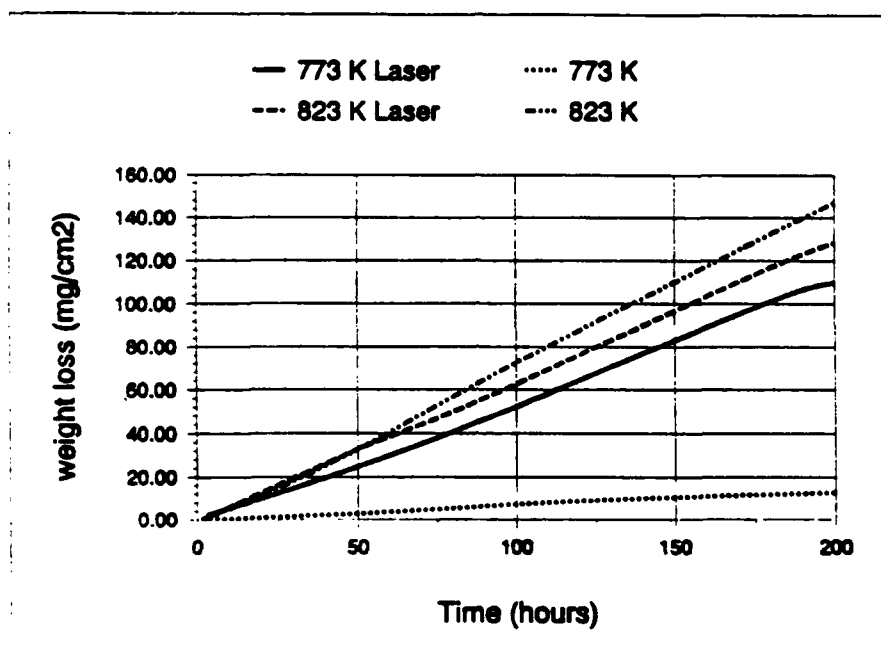


Figure 9. Loss mass with time in an oxidizing atmosphere for the IN-657 superalloy, with and without laser surface treatment. Molten salt with 3 wt% of carbon.

PERFORMANCE OF Cr-Al COATING ON CARBON STEEL TO CONTROL HIGH TEMPERATURE CORROSION DUE TO ASH DEPOSIT

Gladys Navas, Carmen. L. Leal, Evaristo Barón.
Material Technology Department, INTEVEP, S.A., Los Teques, P.O.Box 76343
Caracas, Venezuela 1070A.

Oladis de Rincón.
Corrosion Studies Center-Engineering Faculty-Universidad del Zulia
P.O.BOX 10482 Maracaibo, Venezuela.

Abstract

A common problem found during burning fuels containing vanadium, sodium and sulfur is the high temperature corrosion attack on metallic components of the combustion system. This phenomenon is of special interest due the increased use of heavy oil with high content of vanadium and sulfur.

This research describes the development of corrosion resistant metallic coating on carbon steel based on chromium -aluminium. Diffusion coating by pack cementation was the technique used to applied this coating. The optimization of the coating was performed. Then, coated and uncoated samples were exposed in laboratory test to $\text{Na}_2\text{SO}_4/\text{V}_2\text{O}_5$ fused salt in $\text{SO}_2/\text{SO}_3/\text{O}_2$ atmospheres at 700 °C.

Results of this experimental program showed that the Cr-Al coating tested adequately protected the base metal of the corrosion attack. Thickness losses on coated carbon steel were up to five times lower than on 5% Cr steel.

The work done demonstrated that the Cr-Al coatings can be used to control corrosion due to fused salts, under the tested conditions.

Key Words: Pack cementacion, high temperature corrosion, coatings, difusion, fused salts

Introduction

The use of fuels containing high concentration of contaminants such as vanadium, sulfur and sodium is limited as a result of the corrosion attack (hot corrosion) that may take place on internal components of the combustion system. It is well known that this attack is due to the formation of

low melting point vanadium-containing compounds, such as $\text{Na}_2\text{O} \cdot \text{V}_2\text{O}_4$, $5\text{V}_2\text{O}_5$ (1,2). Several mechanisms have been proposed to account for the effect of this corrosion attack. These are: vanadium compounds act as oxygen carrier (3); vanadates dissolve the protective oxides (4) vanadates penetrate the protective scales and distort the normal stable lattice, increasing the defect concentration (5) and attack by a sulfur specie. Fang (6) concluded that vanadium compounds have a chemical or electrochemical effect on the corrosion rate. All of these mechanisms involve the deterioration of the product barrier that forms on the alloys when deposits are not present. The effect that prevails depends the concentration of impurities, the alloy composition and the type of oxide that can be formed.

Several methods have been employed to reduce fused salt fireside corrosion. These include combustion control, equipment design, the use of fuel additives which are largely based on magnesium oxide, selection of high alloy materials and protective coatings.

It is well known that in Fe-base alloys, bulk addition of oxide-forming elements such as aluminium and/or chromium, facilitates the development of protective oxide scales, therefore reducing alloy degradation at high temperatures. Surface alloying by pack-diffusion processes provides a practical and cost-effective alternative to bulk alloying. In this sense, the incorporation of Cr in a protective coating is expected to promote low oxidation rates, while Al is added to improve the resistance to sulfur attack (6,7). Thus, a programme was initiated at INTEVEP, S.A (8,9) to develop this kind of surface treatment for upgrading the corrosion resistant of metallic materials. As part of the research program, chromium-aluminium diffusion coatings were applied on carbon and low alloy steels. In the present research the performance of carbon steel coated samples were evaluated in laboratory, under conditions that promote vanadate-induced corrosion.

Experimental procedure

Materials

For the laboratory tests, rectangular pieces with dimension of $2 \times 2 \times 0.1$ cm, were cut from tubes of carbon steel ASTM A-178, commonly used for boilers and other combustion systems. The composition of this steel, which were determined by Atomic Absorption Analysis, is reported in Table 1. The specimens were ground on 600 grid emery paper, degreased, air dried and weighed.

Rectangular specimens of the steel was sequentially aluminized and chromized by a proprietary pack-diffusion process, although, the process was optimized in this particular application (8,9).

Test Procedures

Laboratory corrosion tests were performed at 700 °C in a horizontal tube furnace. The specimens were placed in a crucible, immersed completely in a molten salt and exposed to a flowing SO₂/SO₃/O₂ gas mixture. This synthetic flue-gas was preheated in a platinum catalyst at 900 °C in order to convert SO₂ into SO₃. The tests were carried out during different periods of time ranging from 50 to 200 hours. The compositions of both, the salt and the synthetic flue-gas, are shown in Table 2. These conditions were selected to simulate an aggressive environment to promote high temperature corrosion due to ash deposit. The salt composition used is very corrosive due to the formation of eutectic compounds with low fusion temperatures (10).

The corrosion rate was estimated by gravimetric methods using an electrolytic descaling procedure (11) to clean the samples after the tests. Specimens were examined by optical and scanning electron microscopy (SEM) and chemical composition profiles were obtained by energy dispersive X-ray analysis (EDS).

Results and discussion

For the application of the pack cementation process on the carbon steel was necessary the optimization of the parameters such as temperature of the process, deposition time and activation gas flux (9). Figure 1 shows a photomicrograph of a cross-section aluminized/chromized carbon steel. The coating was about 60 µm thick. EDS analysis indicated up to 3% Al and a maximum of 44% Cr. Concentration profiles of Cr were characterized by a smooth gradient to a depth of 70 µm. Then a steep fall in chromium concentration followed. A compact and homogeneous coating was found.

Weight loss measurements at different times were performed to establish the corrosion kinetics data of both uncoated and coated material. Figure 2 shows the weight losses per unit area of metal specimen as a function of time, for the uncoated and coated carbon steel. For the uncoated samples, a parabolic kinetics law was observed for this steel. Initially, the corrosion rate increased rapidly and then near 100 hours the kinetics slow down and tends to be linear but with a very low slope. In the case of the Cr-Al diffusion coated samples, the corrosion kinetics was similar with uncoated steel, the corrosion rate followed a parabolic law. However, in contrast to the behavior of uncoated steels, the coated materials showed a much lower corrosion rate. In fact, a reduction of 80% in weight occurred in the coated specimens, as a result of the protection afforded by the Cr-Al coating. The carbon steel showed the smallest weight loss compared to low alloy steels (9), under the same testing conditions using the same coating. A visual microstructural examination

showed that the coating on carbon steel was more dense and defect-free than the coating on the either of the low alloy steels.

Microscopic examination of corroded samples showed that scales of uncoated specimens were 125 μm . These scales were highly porous and nonadherent as shown in Figure 3. Semiquantitative EDS revealed a mixture of iron and vanadium compounds. On the other hand, sulfur products were mainly adjacent to the metal/scale interface.

Additionally Cross-sections of exposed carbon steel coated samples (Figure 4), showed that the coating remained after the test and the thickness (50 μm) was not significantly affected by the corrosive environment. Also, the coating surface was covered with a sulfur free compact scale formed by chromium and aluminium compounds.

The formation of sulfur compounds in the base metal/corrosion products interface has been observed in different kind of steels (12,13). In some cases of severe hot corrosion where copious amounts of sulphide are formed, it appears that oxidation is following the sulphide penetration, and early investigators attributed a crucial role to the sulphur. In general, sulphur compounds form scales which have a higher defect concentration than oxides. Then, the corrosion rate tends to increase because the parabolic rate constant is proportional to the defect concentration (7). Additionally, metallic sulfides form low fusion point eutectics. Therefore, liquid phases can be formed at relatively low temperatures (14), producing the breakdown of the previously formed oxide scales.

It can be seen that different corrosion behavior was clearly defined for the tested samples. The uncoated specimen showed sulfidation while the coated ones did not show this type of degradation. This indicates that a sulfidation mechanism did not take place during the corrosion process of the aluminized-chromized materials.

Conclusions

The modification carbon steel by a surface alloying process such as pack diffusion provided materials with an improved resistance to fused salt corrosion. The results obtained with the coatings applied on this substrate, can be summarized as follows, from a standpoint of morphology and on the bases of the protection afforded:

1. From a morphology point of view, a very good aluminized chromized was obtained on carbon steel. This coating was found to be dense and defect-free.

2. With regarding to the protection afforded by the coatings, it can be concluded that it performed adequately, reducing the severity of the corrosion attack in 80%.
3. The incorporation of Al into a Cr containing film, prevented or reduced the sulfidation attack to the carbon steel.

References

1. P.Hancock.: "A critical review of alloys at high temperature in atmospheres consisting of fuel combustion products and associated impurities". Mechanics and Mechanisms Group Engineering Department Glasgow University. London 1968.
2. H. Fujikawa, H. Makiwa, N. Fujimo, H. Moroyama, M. Yagi and H. Yuzawa.: High Temperature Corrosion Conference. NACE 6: (1981) 469.
3. N. Small and L. Strawoon.: Mechanism of Corrosion by Fuel Impurities. Butterworth, London, 1963, p. 238.
4. A. Coats, J.: Inst. Fuel, 2 (1969) 75.
5. L. Faiman.: Corros. Sci., 2 (1962) 293.
6. W. Fang.: "Reaction Mechanism in Molten Sodium Sulfate Containing Vanadium oxide and Sodium Sulfate Containing Cobalt Sulfate" Ohio State University, 1982. 163-165
7. M.F.Stwosnijden and W. J. Quadakkens.: High Temperature Technology. 4 (1986) 141.
8. J. F. Nowak, E. Mirabal and A. Robles.: Patent N° 4, 929,473. May 29,1990. USA
9. G. Navas.: Revestimiento metalico a base de Al y Cr sobre aceros al carbono y de baja aleacion. Tesis de posgrado. INTEVEP, SA - L.U.Z. Venezuela. May,1991.
10. P. Elliott and T. K. Ross.: J. Inst. Fuel, 2 (1973) 77.
11. G. W. Cunningham and A. Brasunas.: Corrosion, 12 (1956) 389
12. C. L. de Leal, A. Robles.: Proceedings 3er Congreso Iberoamericano de Corrosión y Protección. ABRACO. Vol III 1646. 26 al 30 de Junio 1989. Rio de Janeiro- Brasil
13. V. N. Konev, A. K. Roslik and N. K. Farofonov.: Prot. Metals, 20 (1984) 699.
14. M. F. Stroosnijdes and W.J. Quadakkess.: 83 High Temperature Technology, 4 (1986).

ACKNOWLEDGEMENTS

The authors wishes to thank INTEVEP, S.A. for the support to carry out this work and to Petróleos de Venezuela for the permission to publish the results.

Table 1 Elemental Composition of the Steel

	Element Composition (weight %)					
ASTM Designation	C	S	Si	Mn	Cr	Mo
ASTM 178	0.158	0.015	0.01	0.50	-----	-----

Table 2 Corrosive Environment for Laboratory Test

Salt composition (weight %)	85% V ₂ O ₅ - 15% Na ₂ SO ₄
Gas composition	2400 ppm SO ₂ - 100 ppm SO ₃ - 1%O ₂ - Bal N ₂
Temperature	700 °C
Time (hrs)	50, 75, 100, 200

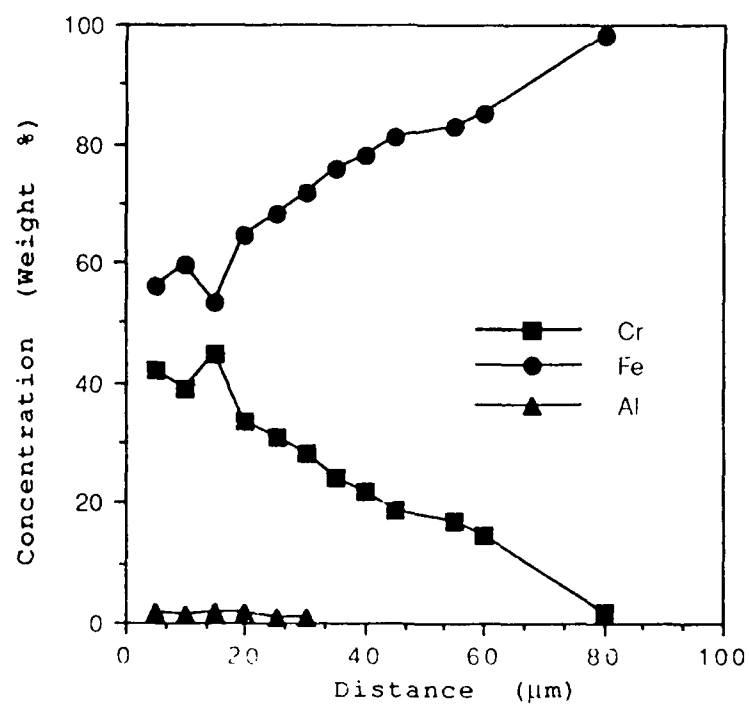


Figure 1 Coating morphology and concentration profile on carbon steel.

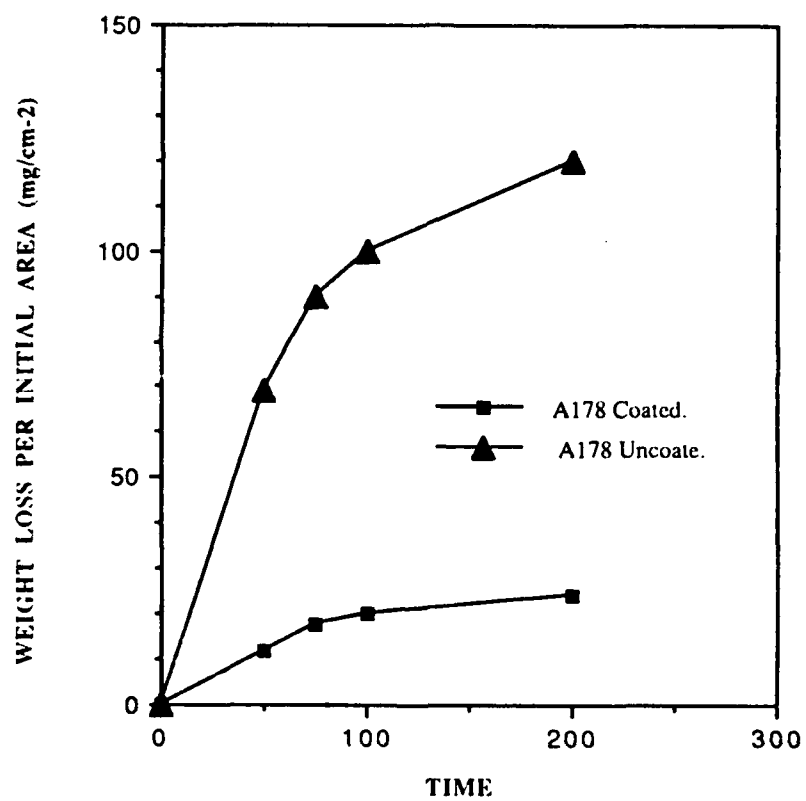
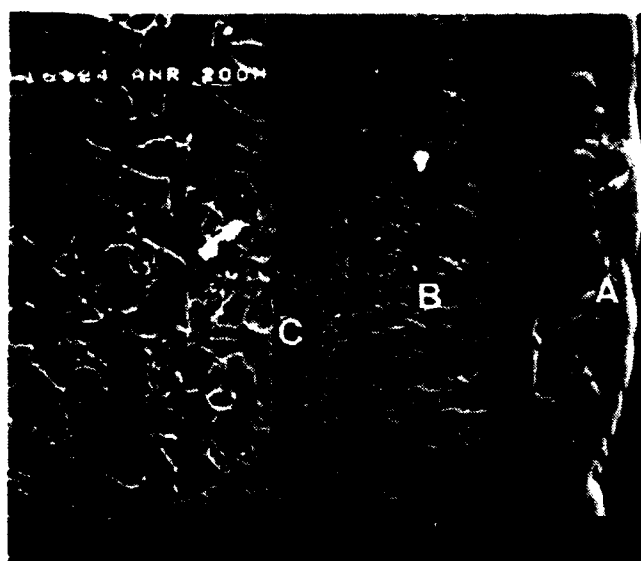
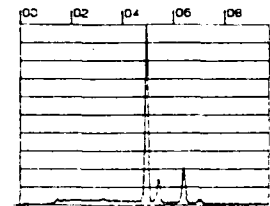


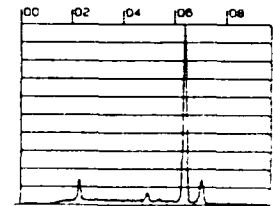
Figure 2 Kinetics behavior of uncoated and coated samples



RATE: CPS TIME SOL SEC
00-20KEV, 10EV/CH PRST, SOL SEC
A: ANR 200H A B: FS= 200
FS= 3166 MEM: A



RATE: CPS TIME SOL SEC
00-20KEV, 10EV/CH PRST, SOL SEC
A: ANR 200H B: FS= 200
FS= 3161 MEM: A



RATE: CPS TIME SOL SEC
00-20KEV, 10EV/CH PRST, SOL SEC
A: ANR 200H C B: FS= 200
FS= 3202 MEM: A

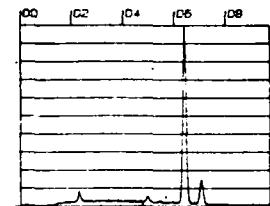


Figure 3 Corrosion products on carbon steel after 200 hours of exposure

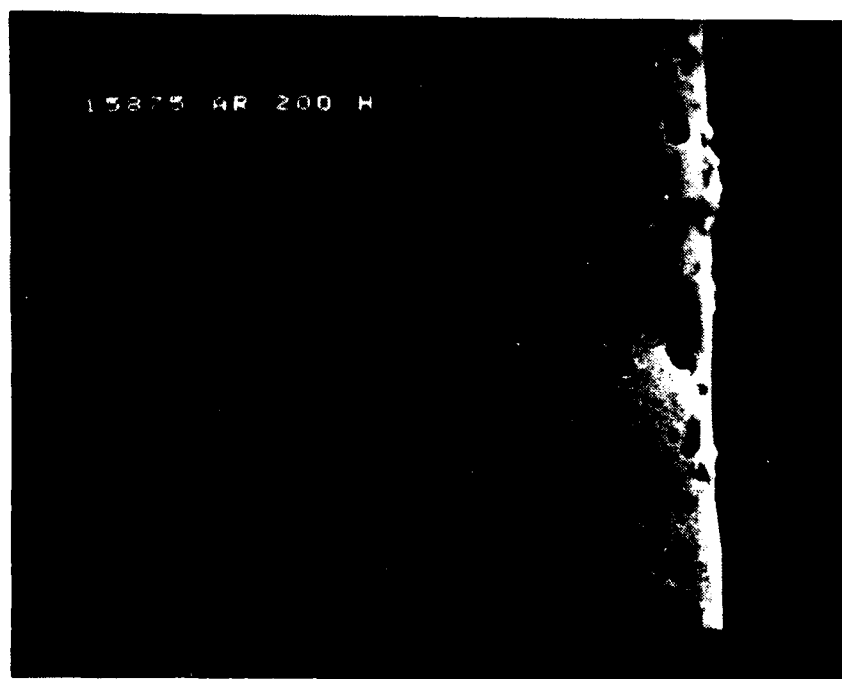


Figure 4 Corrosion products on coated carbon steel after 200 h of exposure

High Temperature Sulfidation of Co-Cr Binary Alloys in H_2/H_2S Mixture in Co_9S_8 Stability Region.

Z. Żurek

*Institute of Inorganic Chemistry and Technology,
Cracow University of Technology, 31-155 Krakow, Poland*

M. Zilik

*Institute of Inorganic Chemistry and Technology,
Cracow University of Technology, 31-155 Krakow, Poland*

A. Szuryn

*Institute of Inorganic Chemistry and Technology,
Cracow University of Technology, 31-155 Krakow, Poland*

Abstract

The kinetics and mechanism of high-temperature sulfidation of cobalt-chromium alloys were investigated. It has been found that the sulfidation rate of low-chromium alloys, in sulphur partial pressure $10^{-2,5}$ Pa and $10^{-3,5}$ Pa at 873 K to 1023 K, up to 5 wt% Cr, is higher than that of pure cobalt. The one-layer homogeneous scale on these alloys is a solid solution of chromium sulfide in cobaltous sulfide. In case of alloys containing more chromium, up to 10 wt% Cr sulfidation rate decrease gradually with chromium content, further the increase of chromium content in the alloys more than 10 wt% Cr practically does not influence on the sulfidation rate of the alloys and double scale layer is formed. At 1273 K in sulphur partial pressure $10^{-2,5}$ Pa and $10^{-3,5}$ Pa, sulfidation rate increases gradually with chromium content. The one-layer scale on these alloys are chromium sulfides. The rate-controlling mechanism appears to be diffusion of chromium ions through the chromium sulfides. Internal sulfidation of these alloys is also observed.

Key terms: high temperature sulfidation, sulfides, kinetics, hydrogen sulfide, scale

Introduction

The Co-Cr alloys are one of important system which have been extensively studied in the last decade. In spite of this, however, the mechanism of corrosion of Co-Cr alloys are still not fully explained. Cobalt based alloys exhibit good high temperature corrosion resistance in oxidizing atmosphere, but they sulfidize easily. Such a situation results mainly from the fact that the transition of metal sulfides is much more numerous than corresponding oxides [1].

Mrowec et al. [2] have studied sulfidation cobalt chromium alloys under sulphur-vapor pressure of 1 atm at 873 K - 1173 K. They have found that sulfidation rate of low-chromium alloys, up to 2% Cr, is higher than that of pure cobalt. The one-layer

homogeneous scale on these alloys is a solid solution of chromium sulfide in cobaltous sulfide. In case of alloys containing more chromium, up to 45%, sulfidation rate decreases gradually with chromium content, the scale consists of two layers.

Davin [3] has sulfidized Co-10 and Co-30 wt% Cr alloys in H_2/H_2S mixture at 1073 K and 1273 K. At sulphur partial pressure where the sulfides of both the base metal and of the alloying element are stable, the increase of chromium content in the alloy decreases the rate. This was due to the formation of increasing amounts of Cr_2S_3 which reduced the area available for diffusion through the cobalt sulfide.

Whittle, Verma and Stringer [4] have carried out sulfidation of Co-Cr binary alloys containing up to 25 wt% Cr in H_2/H_2S atmospheres of an effective sulphur partial pressure of 15 torr at 1073 K and 1273 K. They have stated that at 1073 K, the scales on the alloys consist of an inner layer of cobalt chromium sulfide solid solution and an outer layer of CoS_{1+x} containing no chromium. The scale on the 1 and 5 wt% Cr alloys also contain an intermediate layer of Co_9S_8 . The scale on the Co-17 and 25 wt% Cr alloys at 1273 K is similar to those at 1073 K.

Many industrial gases contain small amounts of sulfur compounds, so very lower sulphur partial pressure is observed. Under this condition, in agreement with theoretical prediction, on the cobalt-chromium alloys only Co_9S_8 or Co_4S_3 sulfides can form. The recent advance in an experimental procedure allows to study corrosion processes by very low sulfur partial pressures, comparable with those in the industry. This study forms part of an overall investigation into the effects of sulfur pressure, alloy content and temperature on the sulfidation behavior of Co-Cr alloys.

Experimental

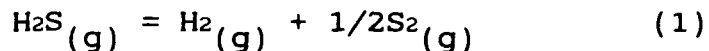
The alloys of nominal composition Co-1, 5, 10, 20 and 45 wt% Cr, were prepared by melting 99.8 per cent pure starting materials in an induction furnace under a pressure of 300 mm Hg in a round cast-iron mold coated with aluminum oxide.

All the castings were annealed in an evacuated sealed quartz for 6 hr at 1373 K to homogenize the structure and to remove the inner stresses. After annealing, all the ingots were cooled in the furnace to the room temperature and after removing the surface layer, disk-shaped samples 16 mm in diameter and 0.25 mm thick were cut out.

The surface of the sample was polished with emery paper including 5/0 and washed with water, methanol and acetone.

The investigation of sulfidation kinetics were carried out under a sulphur partial pressure of 10^{-1} Pa to 10^{-4} Pa, being achieved using H_2/H_2S gas mixture, in the range of temperature 873 - 1273 K by a continuous gravimetric method in apparatus described elsewhere [5]. The required H_2/H_2S ratio at a particular temperature is obtained from the known [6] equilibrium

constant for the reaction



under the assumptions that only diatomic sulphur molecules are present in the gas phase, and that there is no influence of hydrogen on the sulfidation reaction.

Samples were located well above the hot zone and were lowered into the furnace when the desired conditions of temperatures and atmosphere had been attained.

Results

The weight gain/time data for the sulfidation of the five alloys at a sulphur partial pressure $10^{-2.5}$ Pa at 973, 1023 and 1273 K, and $10^{-3.5}$ Pa at 873, 973 and 1273 K are presented in Fig. 1, 2. Reproducibility was generally within ± 10 per cent.

It effects from the plots that sulfidation process follows the parabolic rate law, being independent of the alloy composition, temperature of the reaction and the sulphur partial pressure, clearly indicating that in the steady state conditions the rate of scale growth is diffusion controlled. It should be noted that only in cases of low chromium content in alloys at the conditions where only chromium sulfides are stable, the sulfidation process follows the parabolic rate law after certain incubation period.

The influence of chromium concentration on the parabolic rate constants is shown in Fig. 3. It follows from these plot that a small chromium addition (below 5 wt% Cr) causes the increase in the corrosion rate and then decreases gradually with an increase of chromium concentration in the alloy up to 10 wt% Cr. Although according to Fig. 3 the weight gain experienced by the 1 per cent alloy at 973 and 1023 K is lower than that by the 5 per cent alloy, there is little difference in the parabolic rate constants. Above 10 wt% Cr the sulfidation rate becomes independent of the alloy composition. At higher temperatures ($T > 1173$ K) and sulphur pressure lower than the dissociation pressure of Co_9S_8 , the rate increases markedly with chromium concentration.

The effect of temperature on the sulfidation rate of the dilute chromium alloys is insignificant in Co_9S_8 stability region and below the dissociation pressure of Co_9S_8 (Fig. 3)

Morphology and Phase Composition of the Scale

The morphology of the scale was examined using SEM. Selected data of these investigation are shown in Fig. 4-8.

The phase composition of the scale was examined using Debye-Scherrer powder methods and also X-ray diffraction patterns obtained for the top and internal surface, polished metallographically parallel to the scale/gas interface. In case of two-layer scale each layer was examined separately. The interpretation of the X-ray patterns was carried out using data of

ASTM [7].

Fig. 4 shows SEM micrograph of the scale on the 1 wt% Cr alloy sulfidized at 1023 K in sulfur partial pressure $10^{-2.5}$ Pa. One-layer scale is formed. It follows from the X-ray diffraction data further that the scale formed on this alloy is homogeneous and contains small amounts of a dilute solid solution of chromium sulfide in Co_9S_8 .

Layered scale developed on the Co- 5 wt% Cr alloy at 1023 K in $10^{-2.5}$ Pa is shown in Fig. 5. Outer scale layer built of large columnar grains consists of a cobaltous sulfides Co_9S_8 and Co_4S_3 whereas the inner one is cobalt sulfide Co_9S_8 . On the outer most surface of the metallic core fine grains of chromium sulfide Cr_3S_4 is observed.

Figure 6 shows fracture cross sections of the one-layer scale grown on Co- 45 wt% Cr alloy at 1023 K and $10^{-2.5}$ Pa sulfur pressure. Large columnar crystals with some voids are observed. The X-ray diffraction patterns has shown that the scale is built of CoCr_2S_4 , Cr_3S_4 and Co_9S_8 .

Figure 7 shows fracture cross sections of the scale grown on Co- 45 wt% Cr alloy at 1273 K and $10^{-2.5}$ Pa sulphur pressure. The scale formed on this alloy is built with large grains; some of them are in a contact with the top of the surface of the metallic core in the toothlike shape of a saw. The X-ray investigation has identified that the scale consists in upper part chromium sulfides Cr_2S_3 and Cr_3S_4 whereas in the scale/metallic core interface Cr_3S_4 and Cr_5S_6 .

Figure 8 shows the top surface of outer very thin scale formed on Co- 1 wt% Cr alloy at 1273 K and $10^{-2.5}$ Pa. EDAX analysis has indicated that the thin film of the chromium sulfide is formed.

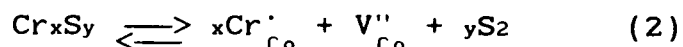
The metallographic cross section has revealed that the internal sulfidation is observed only on the alloys sulfidized under these condition where cobalt sulfides are unstable Fig. 9.

Discussion

Based on the kinetics measurement, combined with data obtained with X-ray investigation, and structure analysis, allow some conclusions to be drawn concerning the sulfidation mechanism of cobalt-chromium alloys at low-sulfur partial pressures. All alloys sulfidized at above conditions according to a parabolic rate law indicating a diffusion-controlled reaction regardless of temperature and alloy composition. However, the scale composition is strongly dependent on alloy composition.

From Fig. 3 it follows that two distinct regions can be observed for the alloys sulfidized under the conditions when both cobalt and chromium sulfides can form. In the first region, a low chromium content, the scale is single-layer and homogeneous, and the rate of sulfidation is higher than that of pure cobalt. The difference in the numerical values of the parabolic rate constants between the pure cobalt and the various alloys was only about half an order of magnitude.

The monophasic scale formed on low-chromium alloys consists of dilute solid solution Co_9S_8 or Co_4S_3 (depends on the condition) - Cr_xS_y (this chromium sulfide was virtually undetectable by X-ray only by microanalysis). The higher sulfidation rate of low-chromium alloys can be explained in terms of Wagner model. However, there is not data concerning defect structure of Co_9S_8 and Co_4S_3 but it can be assumed the both cobalt sulfides are metal-deficient p-type semiconductor. The growth of such scale should proceed due to the outward diffusion of cobalt and chromium ions and electrons via cation vacancies and electron holes. Incorporation of trivalent chromium ions into the crystal lattice of Co_9S_8 or Co_4S_3 scale results in an increase in the concentration of cation vacancies, and consequently increases the sulfidation rate. The process of cation vacancies formation can be expressed by the following equation:



where Cr_{Co}' is a trivalent chromium ion on the site of a bivalent cobalt ion; V_{Co}'' is a doubly-ionized cation vacancy.

In the second region (Fig. 3) the scale has a two-layer scale structure and the sulfidation rate decrease with increasing chromium concentration in the alloy up to 10 wt% Cr. The sulfidation rate of alloys containing more than 10 wt% Cr is practically independent of chromium concentration in an alloy. Fig. 5 shows the scale formed on these alloys. The scale consists of two layers. The outer layer of the scale is compact and built of large columnar grains and no porous was observed. X-ray diffraction has revealed that the outer scale layer contains two cobalt sulfides Co_9S_8 and Co_4S_3 . The inner scale layer contain cobalt-chromium sulfide solid solution Co_9S_8 and Cr_3S_4 . The cobalt-chromium sulfide solid solution can exist over a wide range of the composition. As might be anticipated, the chromium content in this inner sulfide increase with increasing alloy chromium content, whilst at the same time the diffusion rate of both cobalt and chromium ions through this sulfide decrease, thereby reducing the parabolic rate constant for sulfidation. The selective sulfidation of chromium has been no observed.

The sulfidation rate of alloy containing 45 wt% Cr is comparable with the sulfidation rate of alloy containing 26 wt% Cr. As follows from Fig. 6 the scale on this alloy consists of one-layer which consists mostly cobalt-chromium spinel CoCr_2S_4 and Co_9S_8 and Cr_3S_4 . In this case the scale growth occurs due to the outward cobalt and chromium ions diffusion. The sulfur activity gradient in the scale layer is now so high that internal sulfidation is observed.

The sulfidation rate of alloys at 1273 K increases with increasing of chromium concentration. In this case one-layer chromium sulfide scale is formed since cobalt sulfides are unstable. The very thin layer of chromium sulfide is formed on the surface on the alloy containing 1 wt% Cr with the clearly grain boundary visible (Fig. 8). Such situation results mainly

from the fact that grain boundary chromium diffusion and consequently internal sulfidation is observed. Fig. 7 shows a single large columnar scale composes of Cr_3S_4 and Cr_5S_6 formed on 45 wt% Cr alloy at 1273 K and $10^{-2,5}$ Pa. The mechanism growth of the scale is outward chromium ions diffusion through the scale. The sulfidation rate of this alloy is one and half order magnitude lower than the sulfidation rate of pure chromium [8], however the scale composition is practically the same. It seems, the that diffusion of chromium in the alloy plays an important role and determines the sulfidation rate.

References

1. S. Mrowec, K. Przybylski, High Temperature Materials and Processes, 6 1 & 2 (1984): 1-79
2. T. Biegun, A. Bruckman, S. Mrowec, Oxid. Met., 12 2 (1978): 157-172
3. A. Davin, D. Coutsouradis, Cobalt, 17 1 (1962):
4. D. P. Whittle, C. K. Verma, J. Stringer, Corrosion Science, 13 (1973): 247-258
5. Z. Żurek, J. Therm. Anal. 39 (1993): 15-20
6. J. Barin, O. Knacke, Thermochemical Properties of Inorganic Substances, Springer Verlag, New York 1973
7. ASTM, 1972
8. T. Narita, T. Ishikawa, K. Nishida, Oxid. Met., 27 3/4 (1987): 221-237

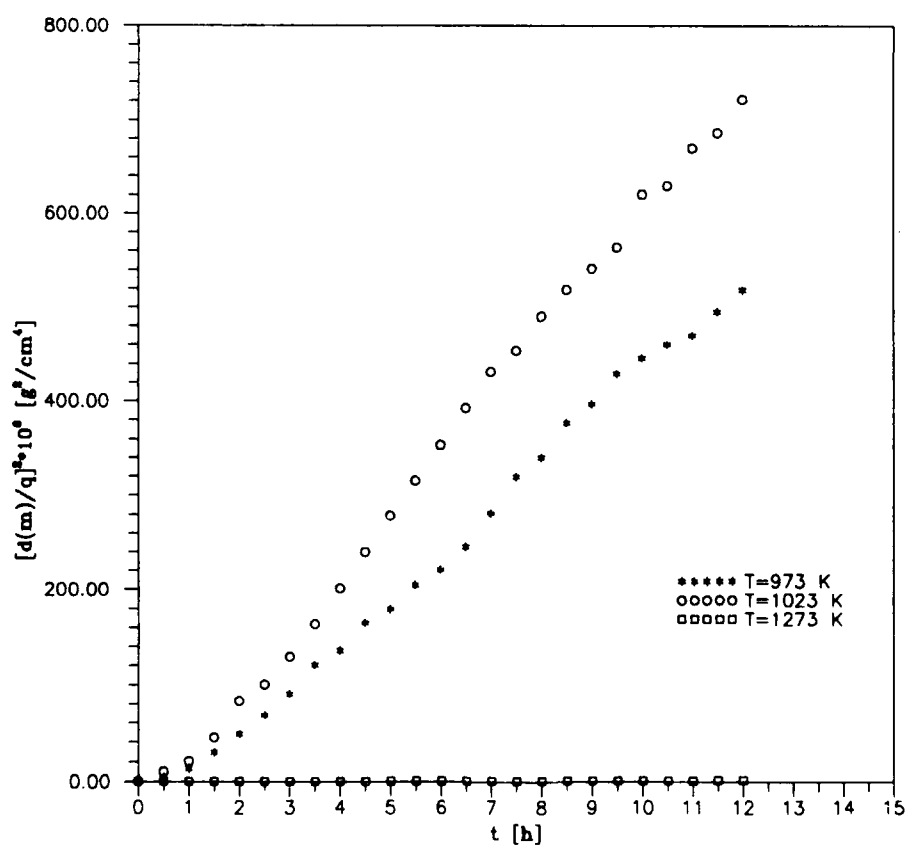
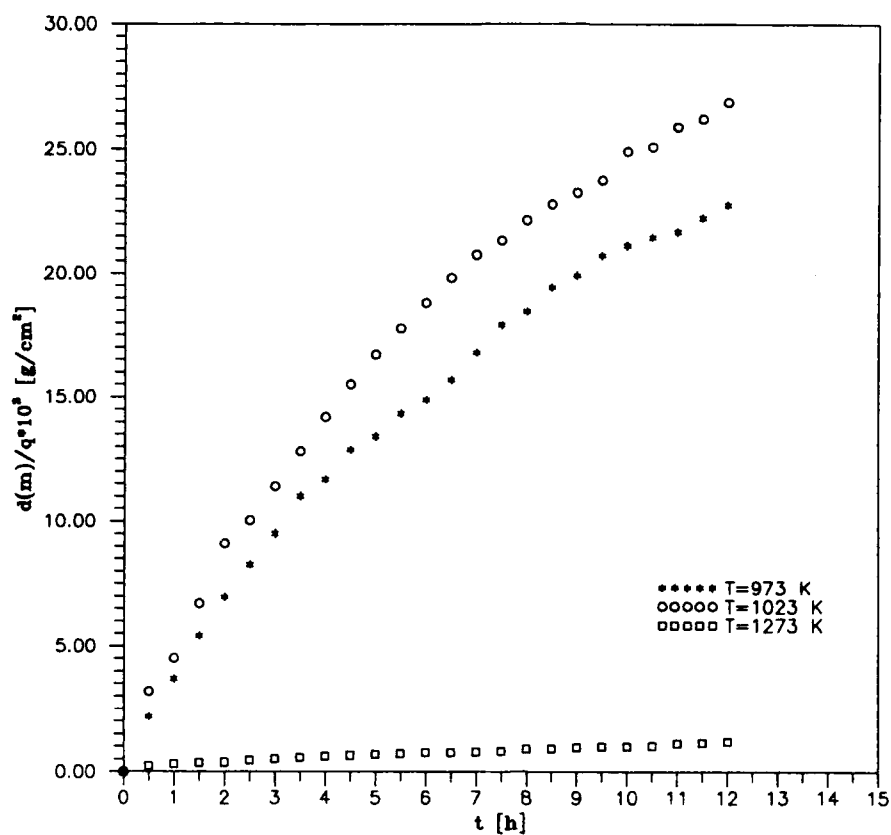


Fig.1. Linear (A) and parabolic (B) plots for sulfidation of Co-20Cr alloy at several temperatures in $\text{H}_2/\text{H}_2\text{S}$ gas mixture, $p_{\text{S}}=10^{-2.5} \text{ Pa}$.

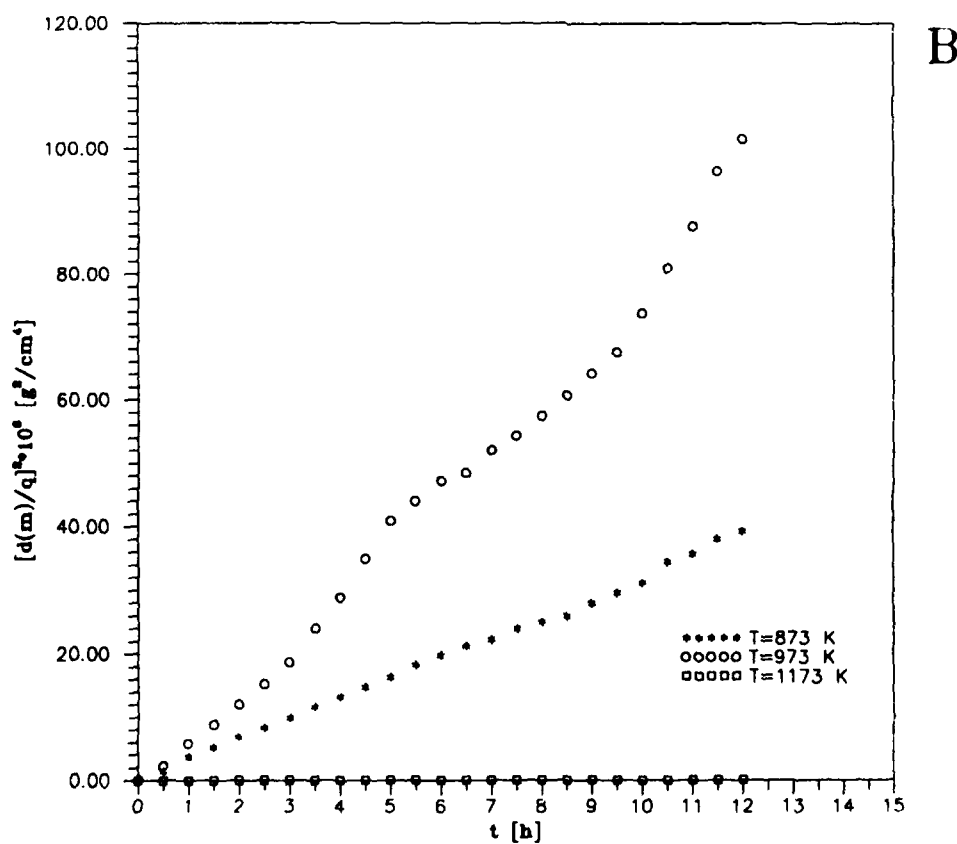
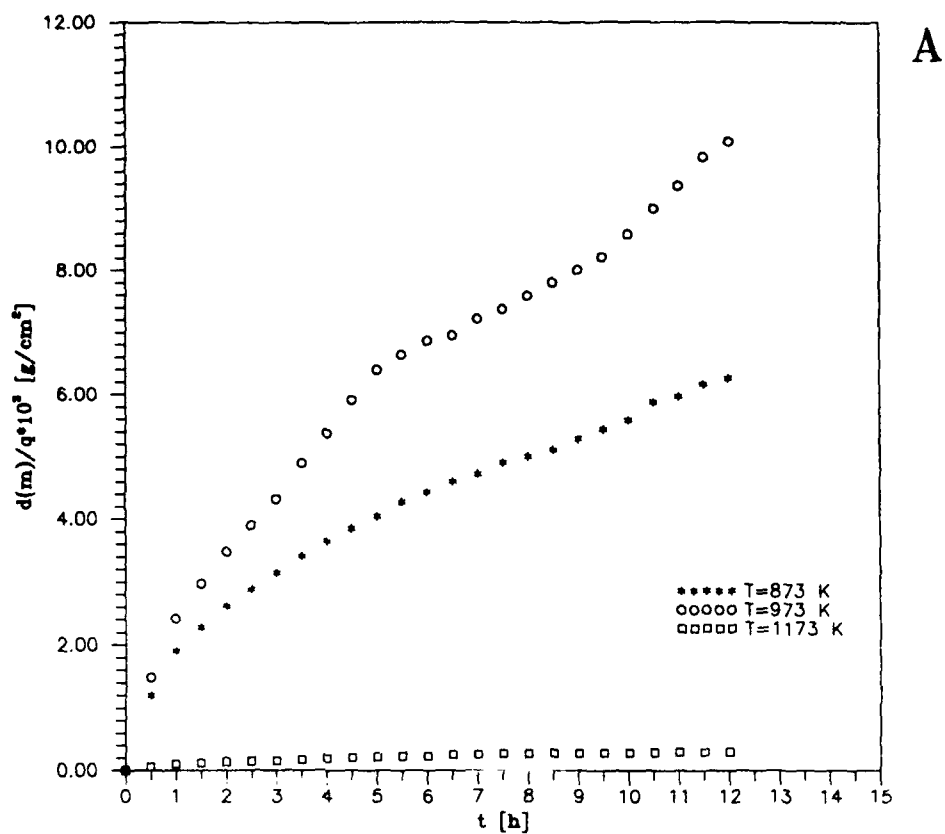


Fig.2. Linear (A) and parabolic (B) plots for sulfidation of C₉-10Cr alloy at several temperatures in H₂/H₂S gas mixture, $p_s \approx 10^{-3.5} \text{ Pa}$.

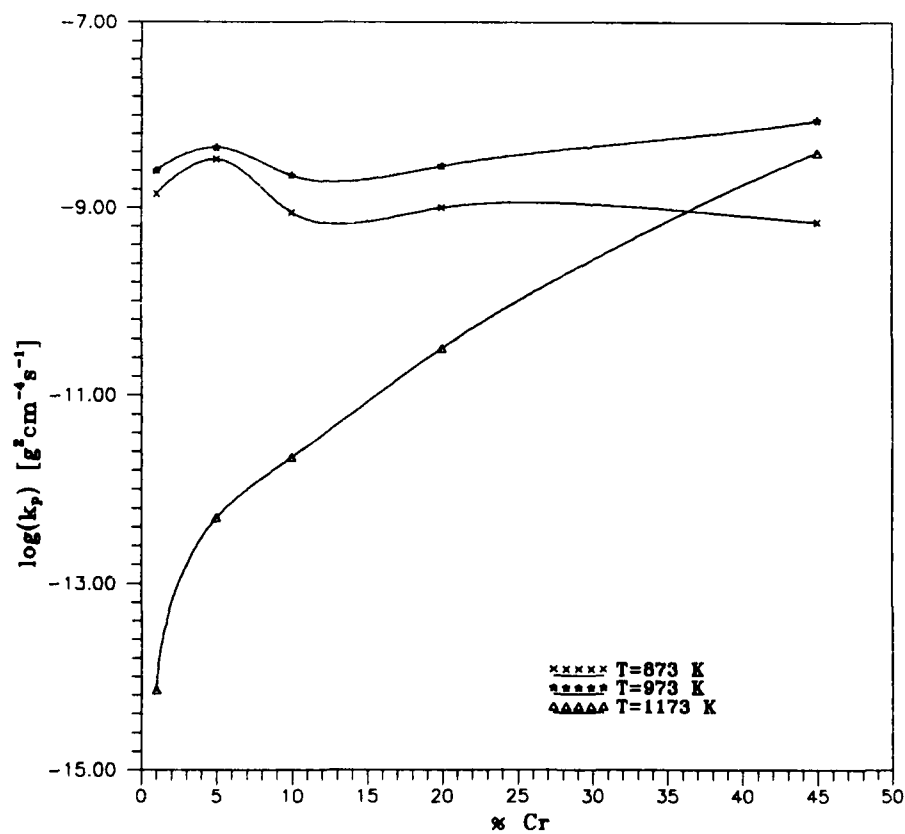
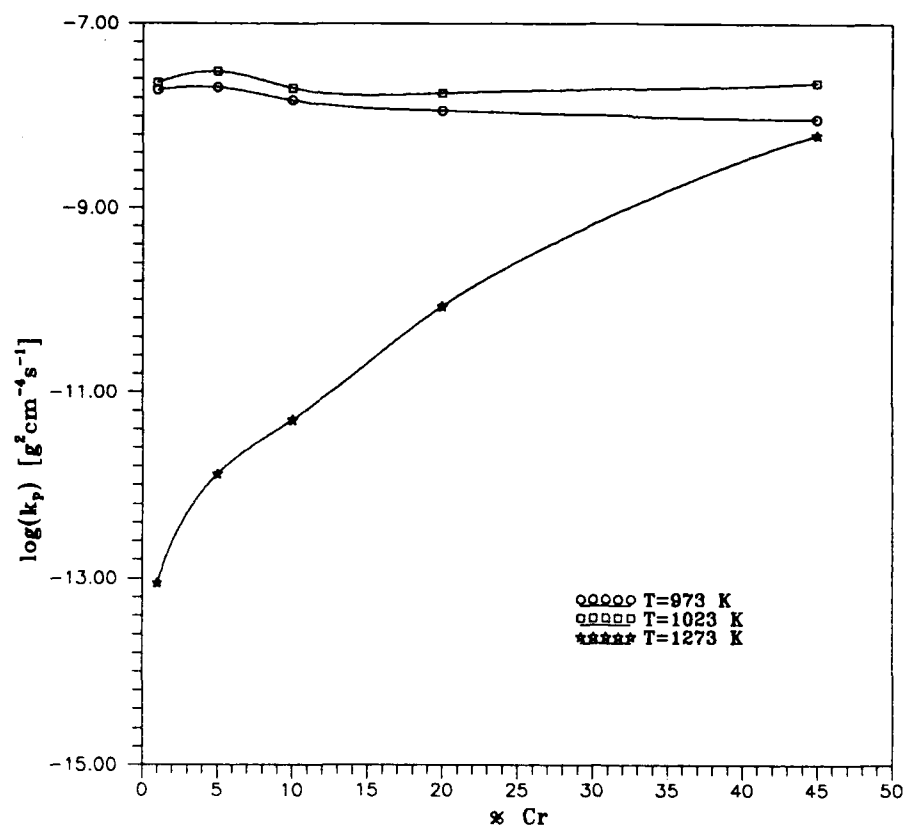


Fig.3. Dependence of parabolic rate constant of Co-Cr alloys sulfidation on chromium concentration at several temperatures in $\text{H}_2/\text{H}_2\text{S}$ gas mixture $p_s=10^{-2.5}$ Pa (A), $p_s=10^{-3.5}$ Pa (B)

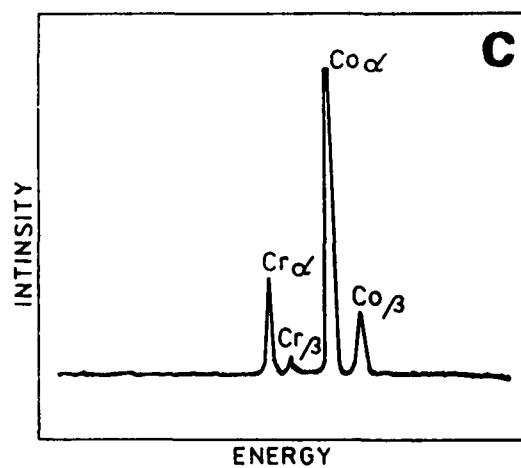
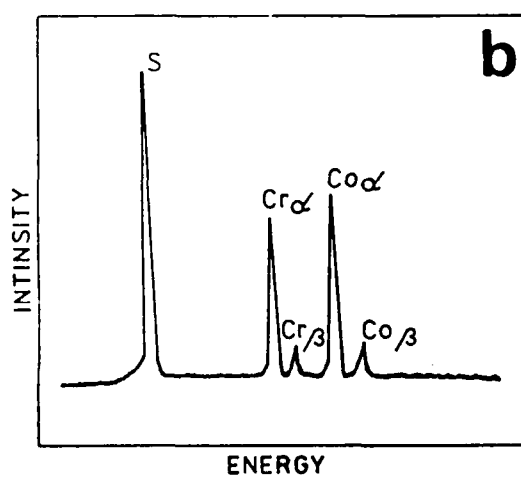
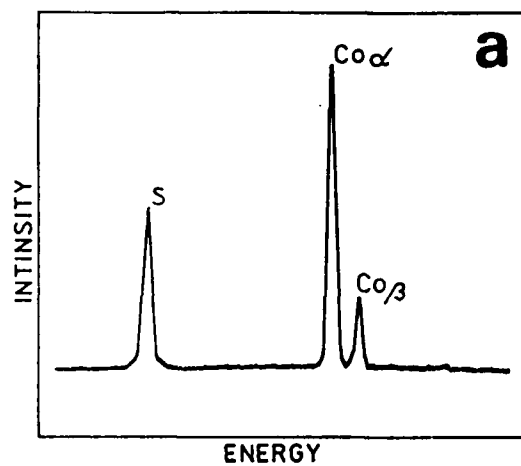
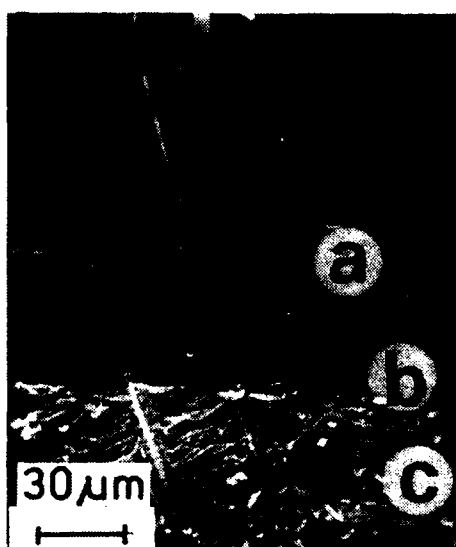


Fig.4. SEM micrograph showing the cross-section of the sulfide scale on Co-1Cr alloy ($T=1023\text{ K}$, $p_{S_2}=10^{-2.5}\text{ Pa}$)

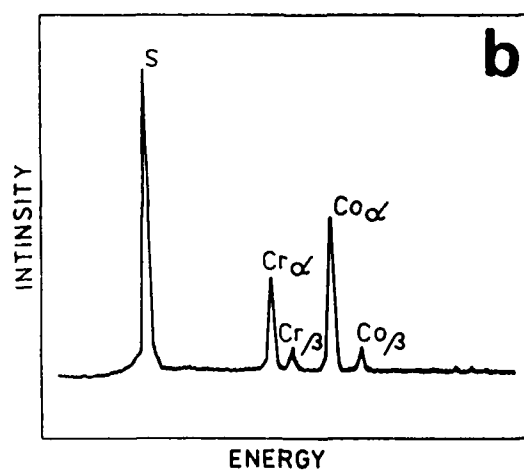
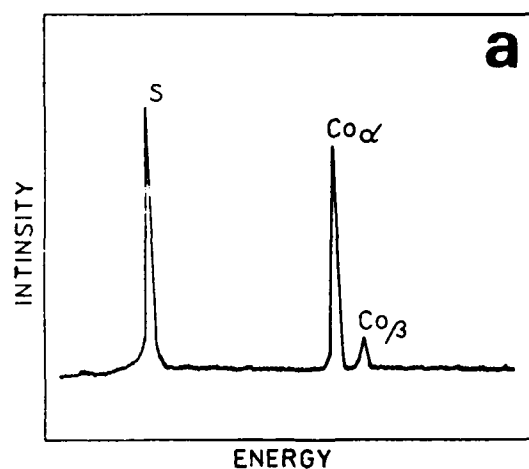
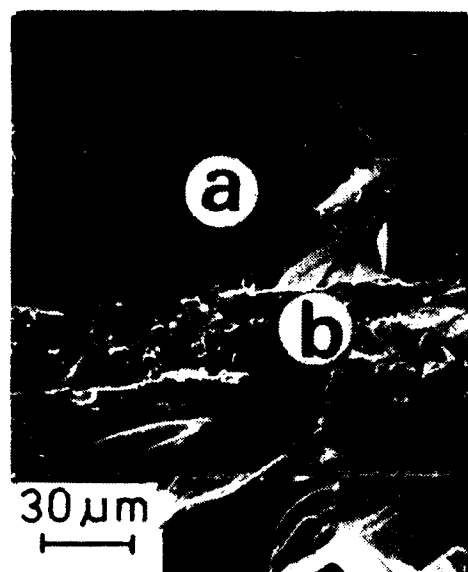


Fig.5. SEM micrograph showing the cross-section of the sulfide scale on Co-5Cr alloy ($T=1023$ K, $p_{S_2}=10^{-2.5}$ Pa)

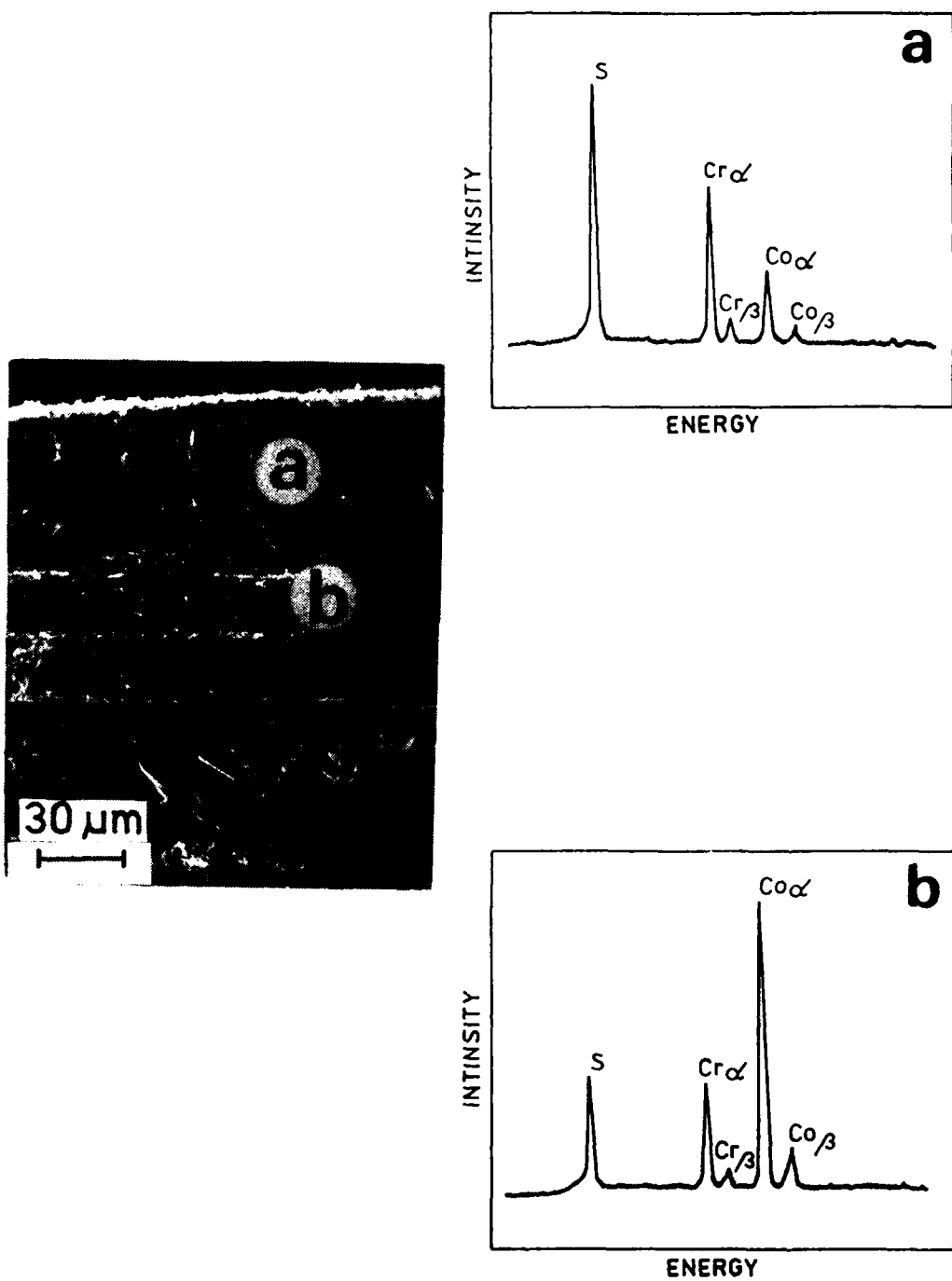


Fig.6. SEM micrograph showing the cross-section of the sulfide scale on Co-45Cr alloy ($T=1023\text{ K}$, $p_{\text{S}_2}=10^{-2.5}\text{ Pa}$)

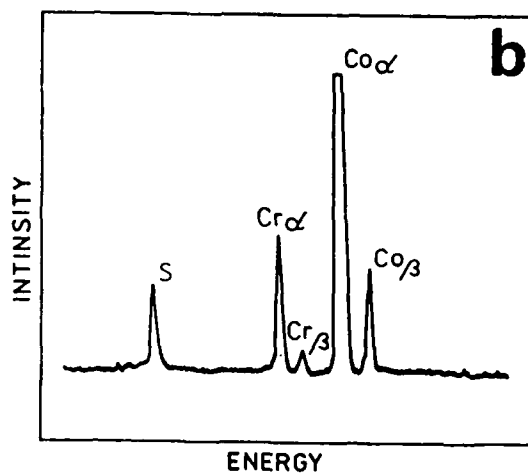
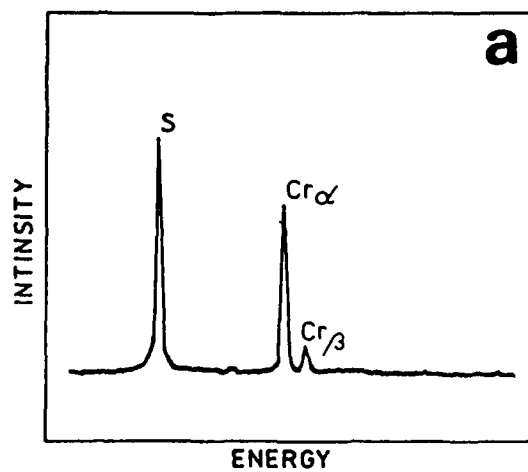
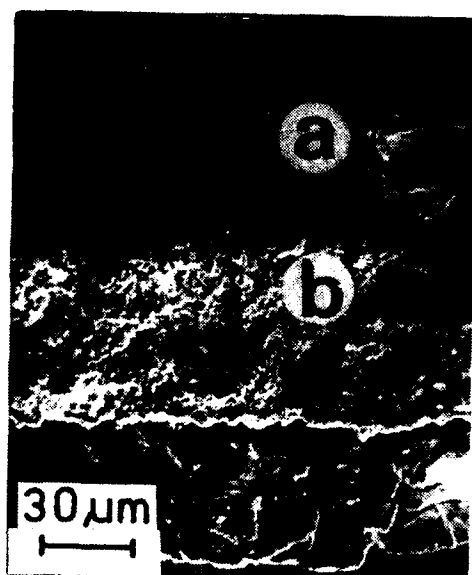


Fig.7. SEM micrograph showing the cross-section of the sulfide scale on Co-45Cr alloy ($T=1273$ K, $p_{S_2}=10^{-2.5}$ Pa)

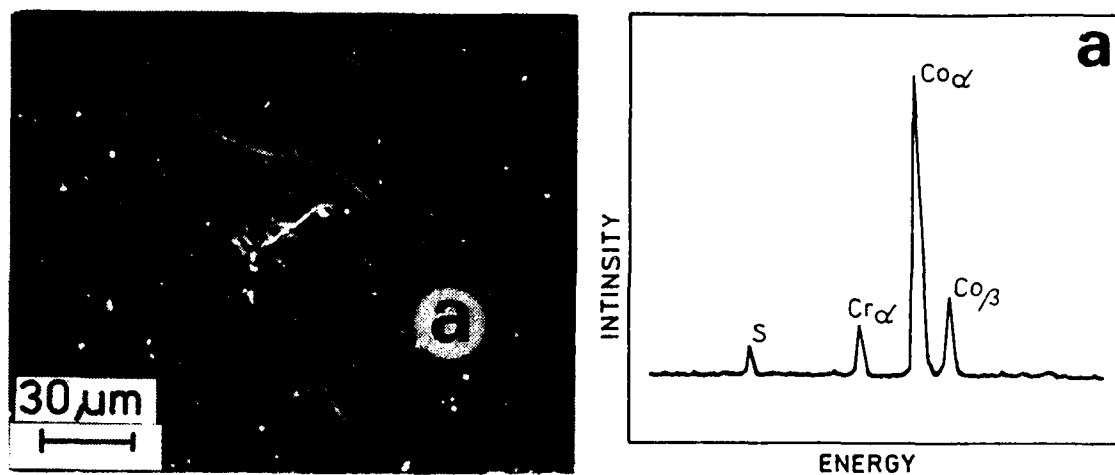


Fig.8. SEM micrograph of the surface on Co-1Cr alloy
($T=1273$ K, $p_{S_2}=10^{-2.5}$ Pa)

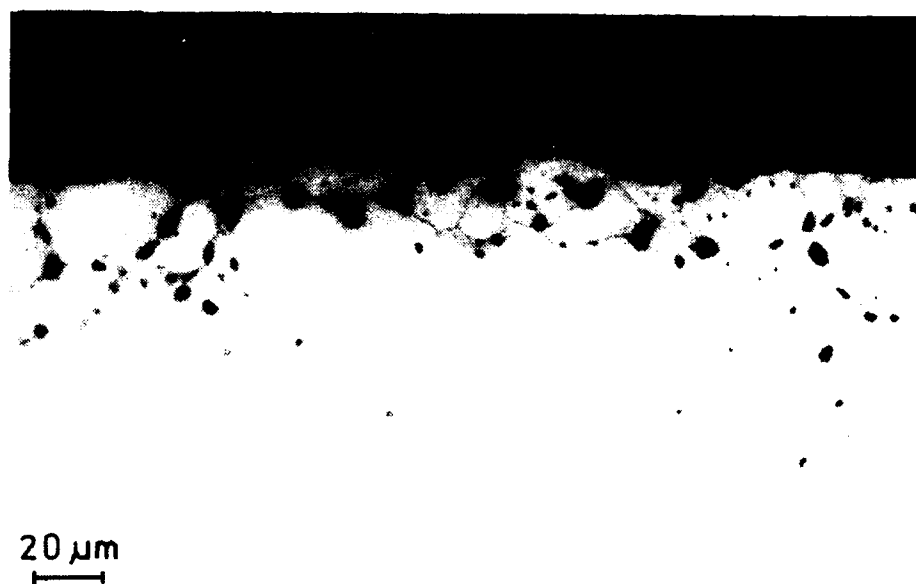


Fig.9. Optical cross-section of the metallic core
Co-20Cr ($T=1173$ K, $p_{S_2}=10^{-3.5}$ Pa)

Failure of Alloy 800 Steam Super Heating Coils in Refinery Hydrocracker Units

Moavin Islam
CC Technologies
2704 Sawbury Blvd
Columbus OH 43235

H. S. Shalaby
KISR P. O. Box 24885
Safat, Kuwait 13109

Abstract

Premature failure of Alloy 800 tubes of steam super heating coils of two hydrocracker charge heaters of a refinery were investigated. The failures of the tubes could be attributed to thermal fatigue as a result of pressure and temperature fluctuations as well as restriction to movement. Fatigue cracks initiated intergranularly from both the flue gas and steam sides. Enhanced general and grain boundary oxidation coupled with age hardening of the alloy led to the formation of incipient intergranular cracks which acted as sites for the initiation of the fatigue cracks.

Key terms: Alloy 800, thermal fatigue, steam coils, hydrocracker

Introduction

Alloy 800 is an Fe-Cr-Ni alloy containing small additions of C, Ti, Al, Cu, Mn and Si. It has a fully austenitic microstructure which is age hardened by the formation of $\text{Ni}_3(\text{Al,Ti})$ precipitates. Alloy 800 combines excellent strength and creep properties with resistance to carburization and corrosion in many aggressive environments at elevated temperatures. The alloy has become standard material for many high temperature applications such as steam generation, gas cooled reactors, steam/hydrocarbon reforming, ethylene pyrolysis etc. There are several versions of the alloy but ASTM B-407-87 specifies three types - UNS N08800 (Alloy 800), UNS N08810 (Alloy 800H), and UNS N08811. Alloy 800 is normally employed in service temperatures up to and including 1100°F, while the latter two alloys are specified for temperatures above 1100°F where resistance to creep and rupture are required.

This paper presents the results of the failure investigation carried out on prematurely failed Alloy 800 tubes of steam super heating (SSH) coils of two hydrocracker (HCR) charge heaters of a refinery.

Design of HCR Units and Locations of Failure

The tubes of the two HCR heaters (designated as units 1 and 2 respectively) have a wall thickness of 2.75 mm and a diameter of 88.9 mm. Some of the tubes are circumferentially finned on the outside with type 304 stainless steel while others are bare. The fins (thickness 1.25 mm, width 12.8 mm) are spaced approximately 7 mm apart and are joined to the tube surface by electric resistance welding. The SSH coils have super heated steam inside and hot flue gas on the outside. The design temperature is 1412°F, but the normal operating temperature is 616° F. The design pressure is 206 psig.

Unit 1 suffered five successive tube failures over a period of about three months within two years after the unit was commissioned. All failures were in the finned tubes located near the intermediate support towards the inlet side and were similar in nature, having circumferential cracks. Two of the tubes were completely fractured in two pieces. It was also noticed that the fins at the intermediate support were damaged, indicating restriction in movement. Unit 1 was recommissioned after re-tubing with Alloy 800 having double the original wall thickness (4.5 mm). Slight modifications were also made to the tube supports.

One of the finned tubes in Unit 2 failed in an identical manner three years after start up. In addition, hydro-testing of the unit during a shutdown shortly afterwards, revealed leaks in another finned tube which was located between the intermediate support and the outlet. Figure 1 shows the arrangement of the SSH coil in the HCR units and the locations of the failed tubes.

Failure Investigation

HCR Unit 1

The failure investigation was carried out on a tube section, approximately 200 mm long, which was completely fractured in two. Visually, the position of the crack appeared to coincide with the base of one of the welded fins. No secondary cracks were visible except the main one. Figure 2a shows a photograph of the failed tube with the matching fracture faces, while Figure 2b is a photograph of the fracture surface.

Metallographic cross-sectional and longitudinal sections were prepared from near the fracture area and from an area slightly away from the location of fracture. The grain size of the alloy was not uniform and varied between ASTM grain sizes 2 and 3. Inter and intragranular carbides were observed in the microstructure of the material.

Examination of the metallographic cross-sections revealed the presence of intergranular fissuring in addition to oxidation with intergranular and transgranular penetration in both sides of the tube (Figure 3a and b). The intergranular fissuring and oxidation were more pronounced on the inner surface (steam side) than on the outer surface (flue gas side). Microprobe analysis along the oxidized grain boundaries provided a mean value of 33% for

chromium, thus indicating chromium depletion from the matrix and its oxidation at the grain boundaries.

Stereo-microscopic examination of the tube outer surface after removal of the welded fins revealed the presence of a circumferential crack adjacent to the base of one of the welded areas. A metallographic cross-section revealed that the crack was transgranular without branching (Figure 3c) and it had progressed about 1/4 of the wall thickness. It may be noted that welded fins were not uniformly attached to the tube material and were disbanded in several places, which was probably because of improper welding.

The fracture surface of the tube was examined with the scanning electron microscope (SEM). Figure 4a shows a low magnification view of the area marked 'X' in Figure 2, while Figure 4b shows a higher magnification micrograph from the same area. Fatigue striations are clearly visible in Figure 4b. The relatively wide spacing of the striations suggests the occurrence of low cycle fatigue. The direction of striations indicates that the fracture path is from the steam side to the flue gas side. However, the direction of other fatigue striations found in another area of the fracture surface suggested a fracture path in an opposite direction. It is worth mentioning that the fracture surface was mostly transgranular in nature, except for some intergranular cracking near the steam side.

Rockwell B hardness tests were carried out on both the inside and the outside surfaces of the tube and tensile tests were conducted on longitudinal specimens machined from the tube material. None of these specimens had surface cracks at or near the welded areas. Table 1 shows the tensile and hardness results in addition to the values provided by the manufacturer and the ASTM specifications. The values given in table show that the tube material has high yield strength, ultimate tensile strength and grain size higher than that specified by the manufacturer or the ASTM specification. Therefore, these results suggest that the material had age hardened during service.

HCR Unit 2

The tube in HCR Unit 2 was cut in half and a section 350 mm long with 40 fins was examined. Four circumferential cracks 2 to 6 mm in length were visible on the inside surface, two of which are shown in Figure 5a. The cracks were all located in the 9 o'clock position in the direction of the steam flow. No cracks were readily visible on the finned outer side.

During removal of the fins they were found not to be uniformly welded to the tubes, in a similar manner to the tube of Unit 1. Examination of the outer surface after removal of the fins revealed that the four cracks observed on the inner surface had completely penetrated through the tube thickness. Sixteen other circumferential cracks of various dimensions were also found on the outer surface. Figure 5b shows some of these cracks. It was noticed that all the cracks were located adjacent and to the right side of the welded zones. None of the cracks originated in areas where there was lack of welding.

Examination of metallographic cross-sections showed that cracks initiated near the base of the weld and were transgranular in nature without crack branching (Figure 6a). As in the case of the tube in Unit 1, intergranular fissuring was observed on both the steam and the flue gas sides and again was more prominent on the steam side (Figure 6b and c). However, unlike the tube of Unit 1, there was no oxidation layer and the grain boundary oxidation was much less than in the tube of Unit 1. The grain size of the Unit 2 tube was found to be between ASTM No. 4 and 5.

One of the cracks shown in Figure 5a was carefully broken open to expose the fracture surface for examination with the SEM. Some intergranular and transgranular fracture features were seen in addition to fatigue striations. Again as in the tube of Unit 1, the striations were in different directions, suggesting that the fatigue cracks propagated from both the steam side and the gas side.

Because of the extensive cracking of the tube, tensile tests could not be carried out. However, hardness tests were done and the value was found to be 82 on the Rockwell B scale.

Effect of Alloy Composition

The metallurgy of Alloy 800 is rather complex and minor constituents, in particular Ti, Al and C, together with the annealing heat treatment play a critical role in determining its service performance characteristics. It has been established^{1,2} that the maximum Ti+Al level should be 0.6% and the Ti to C ratio should be a minimum of 12 to maximize the stress corrosion cracking resistance, the creep rupture strength, and rupture ductility properties. Variations of the above limits create instability in the microstructure.

The chemical composition of the two heats of Alloy 800 used in the HCR units as provided by the manufacturer in addition to ASTM B-407-88 specification are given in Table 2. It can be seen that the Ti+Al content of the failed alloy is between 0.6 to 0.72% and the Ti/C ratio is around 6. Hence some microstructural instability may be expected during service. However, it should be mentioned that the ASTM specification does not specify a Ti and Al level for Alloy 800, but does so for the higher temperature grades to be 0.85 - 1.20. The specification also does not specify a Ti/C ratio limit.

The service performance of Alloy 800 in various applications is generally good. It is not surprising, therefore, that not many instances of failures have been reported for this alloy. The one most relevant to the present failure case is that reported by Lippold³ where the author has described the creep-fatigue failure of Alloy 800 in super heated steam.

Operating Conditions and Causes of Failure

In order to identify the cause of failure of the SSH coils, it is necessary to consider the findings of the investigation in parallel with the operating conditions of the HCR charge

heaters. According to information gathered from the refinery, it was found that HCR Unit 1 was on occasions operated at the design temperature of 1412° F and the SSH coil was also run dry for sometime. The normal operating temperature should be 616° F. ASTM specifies 1100° F as the maximum service temperature for Alloy 800. The time-temperature-precipitation diagram for Alloy 800 indicates that the use of temperature >930° F would result in rapid carbide formation³. High temperatures would also induce age hardening and grain coarsening. The total effect would be to deplete the Cr content of the alloy, particularly at the grain boundaries and the surface.

With reference to HCR Unit 1, it was seen that the tube material of the unit suffered from oxidation and intergranular attack both from the steam side and the gas side (Figure 3a and b). The microstructure was quite coarse (ASTM size 2 - 3) and there was carbide precipitation at the grain boundaries. All these features are consistent with high temperature operating conditions. Moreover, the presence of striations on the fracture surface (Figure 4b) clearly indicates that fatigue was involved, and that cracking was from both sides.

The occurrence of fatigue failure in the tube of HCR Unit 1 is not readily explainable since in general the fatigue life of Alloy 800 is quite good³. However, the situation appears logical when one considers the information available in the literature on the low cycle fatigue of Alloy 800. The fatigue life of tubular samples was found⁴ to be only 20% of that of solid bar samples when tested in static steam at 1200° F with a total strain range of 0.5%. A more dramatic decrease in fatigue life was observed when a tensile and/or compressive hold period was incorporated into the fatigue test^{4,5}. Nearly a 50 fold decrease in the fatigue life was observed because of specimen geometry (solid vs tubular) and fatigue loading conditions (hold vs no hold time)³. Tensile or compressive hold time during fatigue can result in creep damage to the material during the hold period. As a result, the material damage is termed creep-fatigue behavior. rather than low cycle fatigue.

It is difficult to ascertain the exact source of fatigue in the present case. However, it is well known that steam equipment may fail by fatigue if mechanical service stresses are fluctuating or vibratory, or if thermal cycles or thermal gradients impose sufficiently high peak stresses⁶. It has also been established that a reduction in fatigue life takes place due to the occurrence of intergranular cracking and due to the effect of oxidation⁷. Grain boundary oxidation may produce a notch effect that may limit the fatigue life. In the present case, creep damage was not observed in the alloy as apparent from the absence of any significant intergranular damage within the alloy matrix.

Hence it appears that thermal fatigue was responsible for the failure of the tubes in Unit 1. Operation of the unit at high temperatures resulted in ageing, grain coarsening and carbide precipitation, all of which led to enhanced oxidation of the alloy and grain boundary attack, thus reducing the fatigue life of the alloy. Moreover, the presence of grain boundary oxidation acted as stress raisers which together with hold times during fatigue, led to the premature failure of the tubes of Unit 1.

HCR Unit 2 was found to have been operated under tighter control, i.e. the unit was not run dry and there were no excursions to high temperature. The observed microstructure (finer grain size, less carbide precipitation) and the less severe oxidation of the alloy in comparison to that of Unit 1 appears to be consistent with the operating conditions of Unit 2. The metallographic and fractographic evidences indicate that failure of the tube of Unit 2 was similar to that of Unit 1. However, because of the longer time taken to form incipient intergranular fissures, the fatigue initiation time was longer in Unit 2 and hence the service life was longer (approximately 3 years as compared to 2 years for Unit 1).

In the case of Unit 2, the fatigue cracks were mostly from the flue gas side. A few cracks were found propagating from the steam side. Crack initiation and propagation from the outer side of the tube is quite logical since the highest tensile stresses are concentrated on the outer diameter of the tube. The reason for cracking to occur near the base of the welded fins is not easily explained since no obvious microstructural changes in the parent metal were observed in the weld zone. It is possible that properly welded fins give rise to complex stress patterns in the area adjacent to the weld zone due physical restrictions.

Conclusions

1. The failure of the Alloy 800 tubes in the HCR units was due to thermal fatigue. The source of fatigue was possibly due to pressure and temperature fluctuations in addition to restriction in movement of the coils.
2. The initiation and propagation of fatigue cracks were mostly from the outside (flue gas side). However, some cracks were found to propagate from the steam side.
3. In the case of Unit 1, uncontrolled operating conditions (running dry and excursions to high temperatures), resulted in age hardening of the material and enhanced general and grain boundary oxidation with incipient intergranular cracks, leading to early initiation of fatigue cracks. In the case of Unit 2 with controlled operating conditions, the grain boundary oxidation and incipient intergranular cracking were less severe which was manifested in a longer fatigue life.

References

1. J. Orr, J. B. Marriot, Proceedings CEC Conference on Alloy 800, Brussels, Sept., 1976.
2. J. Orr, Proc. Petten International Conference on Alloy 800 (North Holland Publishing Co., Amsterdam, 1978), p. 25.
3. J. C. Lippold, Materials Performance, 24 (1983): p. 16.

4. W. B. Jones, J. A. Van Den Avyle, "Fatigue and Creep-fatigue Testing of Steam Filled Tubular Alloy 800 Specimens", Sandia National Laboratories, SAND 82-0850, May (1982) .
5. H. Teranishi, A. J. McEvily, Proc. Petten International Conference on Alloy 800 (North Holland Publishing Co., Amsterdam, 1978), p. 125.
6. Metals Handbook, "Failure Analysis and Prevention - Vol.10", Metals Park, OH: American Society for Testing and Materials, 1975), p. 639.
7. C. Levaillant, A. Pineau, Low-cycle Fatigue and Life Prediction - ASTM STP 770, (Metals Park, OH: American Society for Testing and Materials, 1982), p. 169.

Table 1. Tensile and Hardness Properties of Alloy 800

Data	YS (N/mm ²)	UTS (N/mm ²)	Elongation (%)	Hardness (Rockwell B)	Grain Size (ASTM No)
Laboratory	337	670	34	85	2 - 3
Manufacturer	238	556	55	69	4 - 5
ASTM	172 (min)	450 (min)	30 (min)	95 (max)	5

Table 2. Chemical Composition of Alloy 800

Element	%Composition Heat 1	%Composition Heat 2	%Composition ASTM
Ni	31.02	31.35	30.0 -35.0
Cr	20.20	20.39	19.0 - 23.0
Fe	46.00	45.00	39.5 min
C	0.06	0.06	0.05 - 0.10
Mn	0.72	0.89	1.50 max
Si	0.46	0.49	1.0 max
Cu	0.14	0.14	0.75 max
Ti	0.36	0.34	0.15 - 0.6
Al	0.36	0.26	0.15 - 0.6
S	0.005	0.002	0.015 max

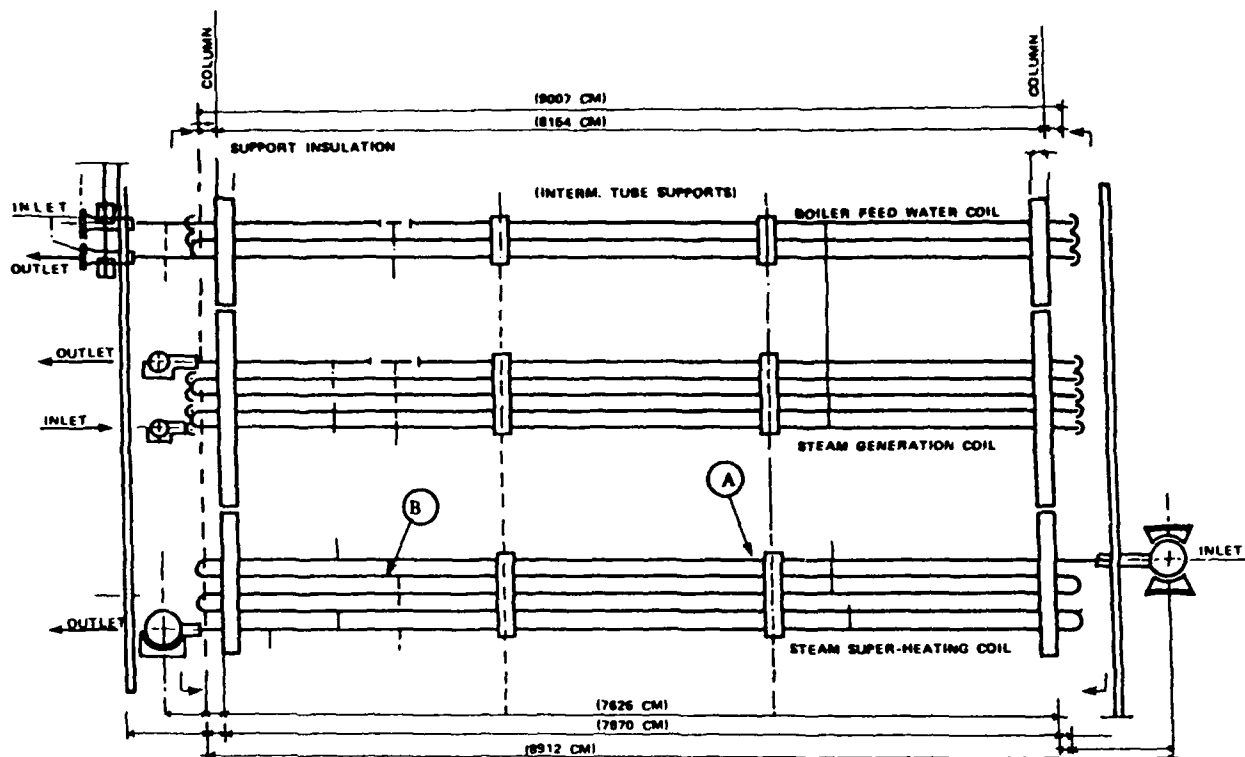


Figure 1. Schematic Arrangement of the Steam Super Heating (SSH) Coil in the Hydrocracker (HCR) Units showing Locations of Tube Failures in Units 1 and 2. (A and B respectively)

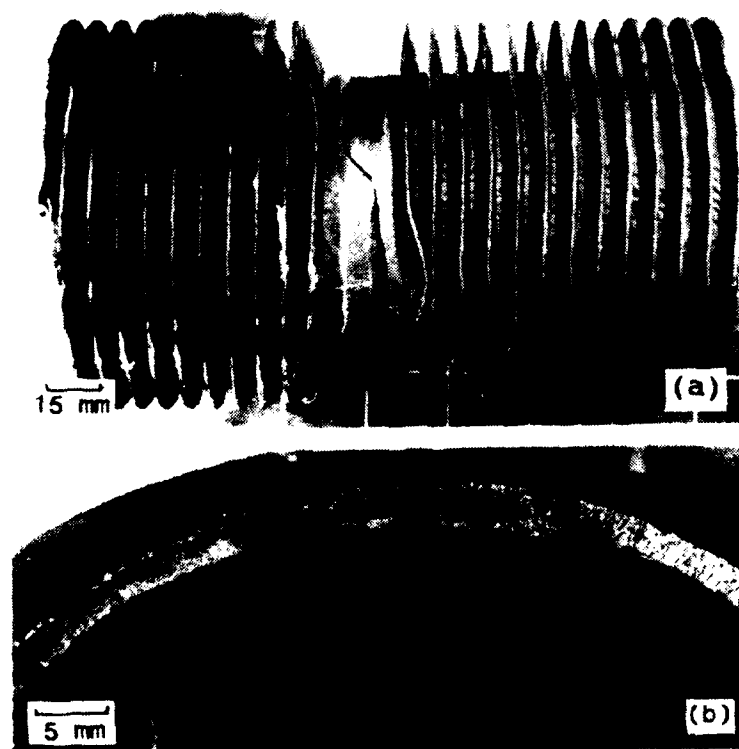


Figure 2. Photographs Showing : (a) Fractured Finned Tube from Unit 1; and (b) Fracture Surface of the Failed Tube.

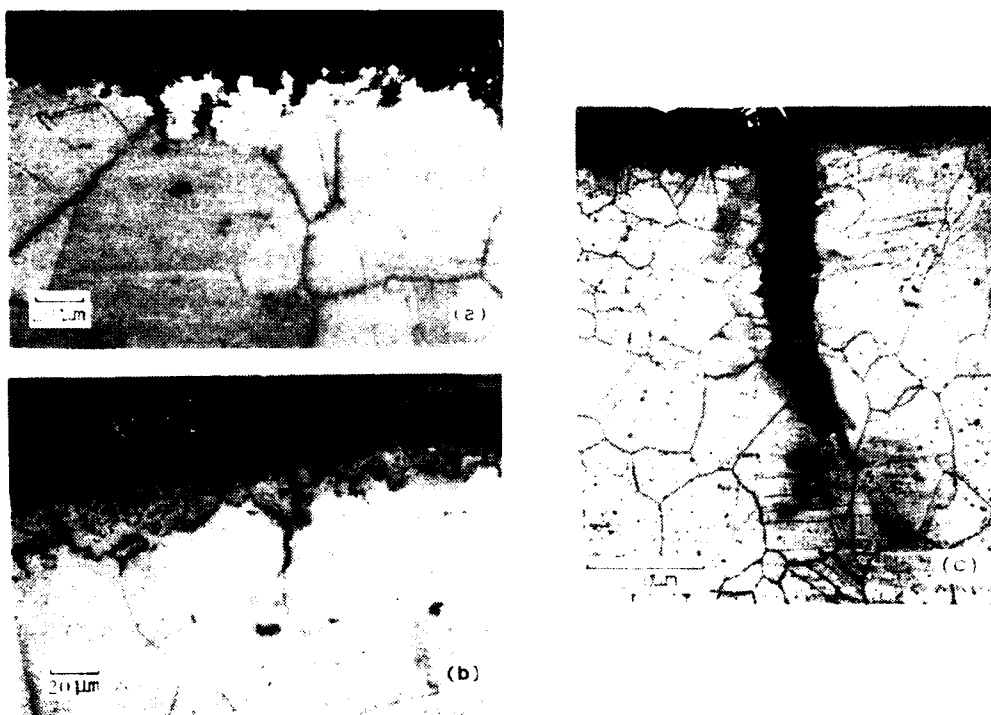


Figure 3. Micrographs of Cross-sections from the Tube of Unit 1 Showing : (a) Oxidation of the Flue Gas Side With Inter and Transgranular Penetration; (b) Intergranular Oxidation on the Steam Side; and (c) Transgranular Crack Originating From the Gas Side, Near the Base of the Welded Fin.

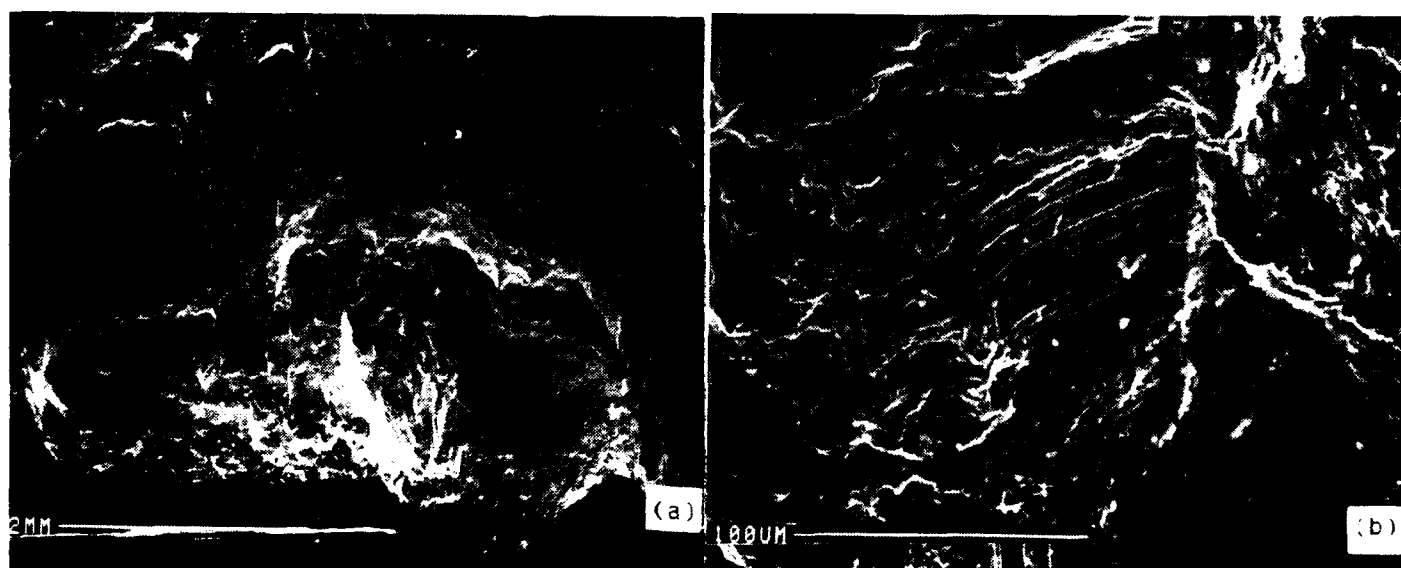


Figure 4. SEM micrographs Showing : (a) Low Magnification View of the Area Marked "X" on the Fracture Surface Shown in Figure 2; and (b) Fatigue Striations Observed in the Same Area in (a). Note - Direction of Striations is from the Steam Side to the Flue Gas Side of the Tube.



Figure 5. Photographs Showing: (a) Two of the Four Visible Cracks Observed on the Inner Surface of the Tube of Unit 2; and (b) the Outer Surface of the Tube After Removal of the Fins. Arrows Indicate Locations of Cracks Adjacent to the Welds.

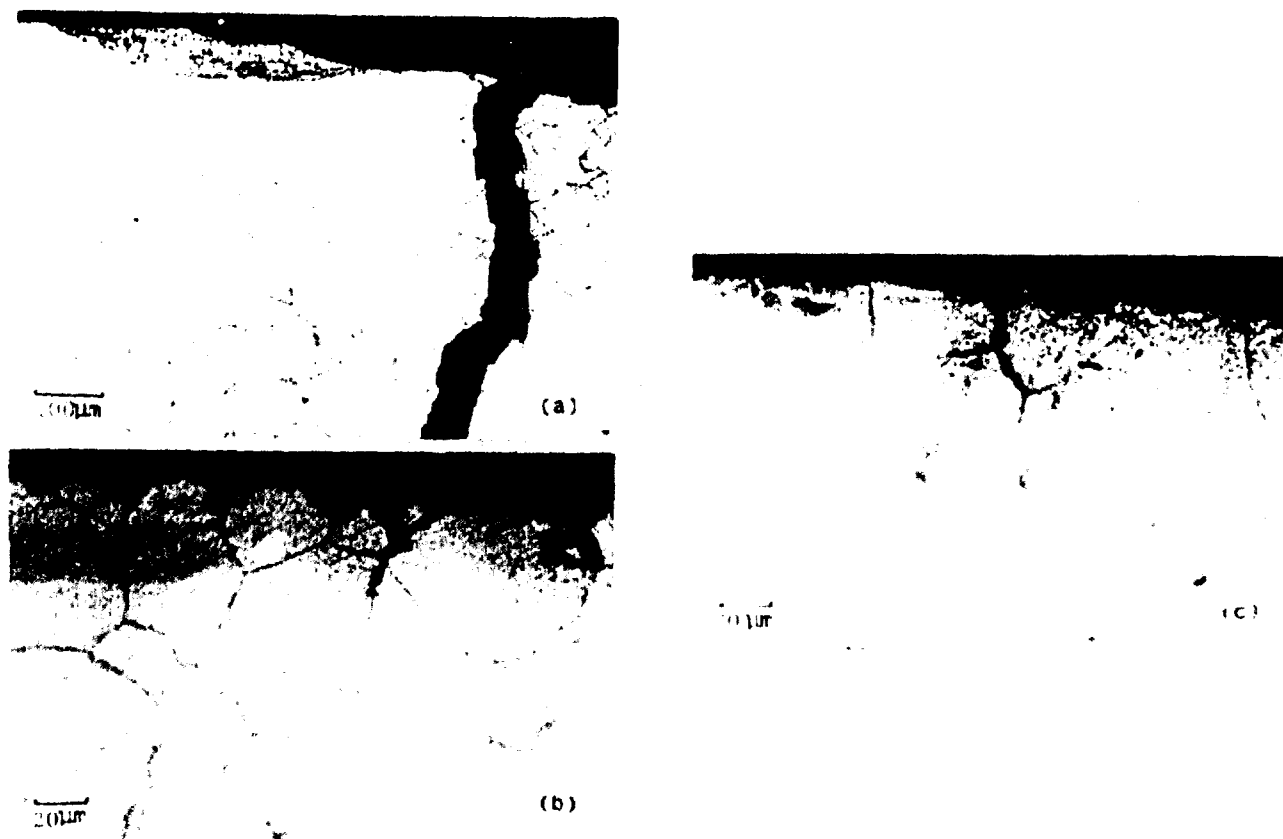


Figure 6. Micrographs Showing : (a) a Transgranular Crack Originating from Near the Base of a Weld; (b) Incipient Inter and Transgranular Fissuring on the Steam Side; and (c) Intergranular Fissuring on the Flue Gas Side of the Tube of Unit 2.

The Effect of Blaze on the Mechanical and Corrosion Properties of Isfahan Refinery Distillation Unit Towers

Ahmad Saatchi
Materials Engineering Department
Isfahan University of Technology
Isfahan Iran

Ahmad Pishnamazi
Senior Corrosion Engineer
Isfahan Refinery
Isfahan Iran

Abstract

In an air raid in October 1985, the Atmospheric and Vacuum towers of Crude Distillation Unit of Isfahan Refinery were hit by several rockets, and were set ablaze. The fire was extinguished by spraying mainly water and foam. The towers were made from low carbon Mn steel with stainless steel cladding. In order to determine the effects of the fire on the materials properties, and to check the suitability of the towers for repair and reuse various tests were performed on the materials in the damaged areas. Tests included on site and laboratory Optical Metallography, laboratory Mechanical Testing, laboratory Corrosion Testing to determine the susceptibility of the stainless steel cladding to intergranular corrosion. The results were analyzed with respect to the Constitution Diagram of the alloys. It was concluded the thermal cycle due to the fire had not affected the materials properties significantly. The materials properties were still in the specification range, and therefore they were suitable for reuse. The towers were repaired in few months and have been successfully in operation ever since.

Key terms: blaze, mechanical and corrosion properties, refinery

Introduction

In an air raid in October 1985, the Atmospheric and Vacuum towers of Crude Distillation Unit of Isfahan Refinery were hit by several rockets and were set ablaze. The rockets caused severe deformation and created holes in various locations, from which fire was coming out. The fire was extinguished after 2 hours by spraying mainly water plus foam. The towers were made from low carbon Mn steel sheet, ASME SA 516-60, with a ferritic stainless steel cladding, Type AISI 405. The thickness of the backing plate and the cladding were about 20 and 3 mm respectively. The nominal chemical composition and mechanical properties of these steels are shown in Table 1^{1,2}. The operating condition and other characteristics of the towers are as follows:

Atmospheric Tower. This towers has been designed to refine the desalted crude. The crude enters the tower at tray no. 6, with the temperature of 330 C. The height of the tower is about 52 m, internal diameter about 6 m, bottom temperature 330 C, top tem-

perature 148 C, bottom and top pressure 30 and 26 psi (210 and 180 kPa). The tower has 43 trays. The trays at the lower sections were made of AISI Type 410 stainless steel and at the upper sections were made of Monel. The volume of the injected steam at the bottom of the tower was 6 tons per hour. Film forming corrosion inhibitor and Ammonia to control pH were injected into the tower to control corrosion. The tower was designed to refine 100000 bpd of crude oil.

Vacuum Tower. This tower has been designed to refine the so called Atmospheric Bottom, i.e. the remaining of the crude in the Atmospheric Tower. Atmospheric Bottom enters this tower at tray no.6, with temperature of 427 C. The height of the tower is about 45 m, internal diameter of about 4.5 m, top and bottom temperature 57 and 354 C. This tower has 34 trays made of AISI Type 410 stainless steel. The volume of the injected steam is 2.5 tons per hours. The designed capacity is 50000 bpd of the crude.

Due to the fire, the temperature of the body of the towers had increased to red heat in several locations. The fire fighting lasted about 2 hours during which water and foam were used for lower sections. Water and foam did not reach to the very top locations on the towers and these areas were cooled in air. The time at temperature of various locations were not known exactly. This thermal cycle could cause changes in the microstructure and mechanical properties of the backing plate steel and also could cause changes in the microstructure and corrosion properties of the stainless steel cladding. The backing plate steel is a low carbon, low alloy steel, which is normally used for the construction of the pressure vessels. This steel is used in the normalized condition, i.e. the microstructure consists of ferrite plus pearlite. Fig. 1 shows the related portion of the Fe-C constitution diagram³. The vertical line on 0.3% C on this diagram shows the position of backing plate steel. This figure shows that increasing the temperature of the steel up to 720 C does not cause significant microstructural changes, unless on prolonged heating, during which the cementite will spheroidize. In this temperature range cooling rate also would not cause any change in the microstructure. On the other hand if the temperature of the steel is increased to more than 720 C, some Austenite may form, depending upon the temperature and time at this temperature. In this case cooling rate will affect the microstructure. Rapid cooling by water may cause some undesired martensite and other acicular phases which reduce the toughness of the steel dramatically. Slow cooling in air, on the other extreme, will result in the desired normalized structure.

Fig. 2 shows the vertical section of the Fe-Cr-C constitution diagram at 0.1% C⁴. The vertical line on this figure shows the approximate position of the stainless steel cladding. Based on this diagram, increasing the temperature to less than 800 C causes Chromium Carbides to precipitate. Cooling rate from this temperature range will not affect the final microstructure. Chromium Carbides, on the other hand will precipitate on the

grain boundaries and will make the steel susceptible to intergranular corrosion. This is the so called sensitized condition, and the stainless steel will not be suitable to use in this condition. Fig. 2 shows that increasing the temperature to more than 800 C, will result in austenite in the steel, the amount of which depend upon the time and the temperature. Cooling from this temperature range will result in different microstructures. Rapid cooling will result in some martensite, and thus a mixed structure, which is not good for corrosion resistance. Slow cooling, on the other hand, will result in once again, a sensitized ferritic structure.

Since the thermal cycle of various locations were not known exactly, in order to determine the effect of the fire on the backing plate and the cladding materials, and to check the suitability of the towers for repair and reuse, it was necessary to determine the actual structure and properties of these steels. This paper describes the results of such investigation.

Experimental

The microstructure of the damaged areas were studied by Optical Metallography using replica method, and also by portable microscope, on site. Some portions of the damaged areas were cut out and the following tests were performed on them in the laboratory: Metallographical examinations, Tensile Testing of the backing plate steel, testing susceptibility to intergranular corrosion of the stainless steel cladding, using ASTM A 763-83 practice⁴. For corrosion tests of the stainless steel, several specimens with the dimensions of 20 by 20 mm were abraded to no. 1000 emery paper, degreased with acetone and then electrolytically etched in 10% Oxalic acid, with a current density of 1 Ampere per square centimeter for 1.5 minutes. They were then examined under microscope and compared with the standard photomicrographs.

Results and Discussions

Backing Plate Steel. Table 2 shows the results of on site metallography of backing plate steel on various damaged locations. In this table the location, the severity of the damage, the extinguishing procedure, and the microstructure of some of the damaged areas are summarized. The microstructure of various locations did not show any evidence of accicular structure and usually contained 25 to 30% pearlite plus ferrite, irrespective of cooling rate, which is the usual microstructure of the original plate. Based on the previous discussion, it was concluded that the temperature and time had not caused any austenite and therefore the microstructure had not changed. The location no. 1 in Table 2 showed spherodised cementite in the structure. This could not be due to the thermal cycle during the fire, because this structure requires prolonged heating time at around 720 C.

Figs. 3 and 4 show the typical microstructure of the damaged

areas of the Atmospheric and Vacuum Towers. The microstructures show the usual pearlite plus ferrite of the normalized condition.

Tables 3 and 4 show the results of the Tensile Tests on backing plate steels of the towers. The comparison of these results with the standard properties of the steel, Table 1, indicates that the mechanical properties of the steel is in the standard range and thus indicates that the effect of the blaze on the properties of the backing plate materials has been insignificant.

Stainless Steel Cladding. Figs. 5 and 6 show the photomicrographs of the stainless steel claddings. The microstructures consists of normal equiaxed ferrite grains plus some chromium carbides. There were no evidence of any accicular structure in the microstructures. Based on the previous discussions, it was concluded that the temperature and the time has not caused any austenite. These results were in agreement with the previous conclusion in the preceding section. But, as it has been pointed out before, exposure to temperatures below 800 C will result in chromium carbides precipitation and sensitizes the stainless steel. Therefore, Figs. 5 and 6 which had been prepared according to the ASTM Standard for detecting the susceptibility of this material to intergranular corrosion, were compared to standard photomicrographs. Based on the ASTM A 763-83, the microstructures of the stainless steel was ranked as the dual structure, which was an acceptable structure. In this class the major areas of the grain boundaries are free from carbides, and none of the grain boundaries are completely surrounded by chromium carbides. These results indicated that the effect of the blaze on the corrosion resistance of the stainless steel had been insignificant.

Conclusion

Based on the above results, it was concluded that the thermal cycle in various locations has not resulted in any austenite in the plate materials. Therefore various cooling rates during fire fighting had not caused any major structural and properties change to occur. This thermal cycle on the other hand, had caused some chromium carbides to occur in the stainless steel, but this was not to that extent to deteriorate corrosion resistance of the material significantly. Therefore both backing plate steel and stainless steel cladding properties were acceptable and the towers could be repaired and reused.

References

1. H.E. Boyer, in Metals Handbook, Vol. 1, 9th ed. (Metals Park, Ohio: ASM, 1978), p. 138.
2. C. A. Zapffe, in Source Book on Stainless Steel (Metals Park, Ohio: ASM, 1976), p.2-7.
3. R. E. Reed-Hill, Physical Metallurgy Principles, (Van Nostrand Reinhold, New York, 1964), p.442.

4. W. D. Forgens and W. D. Forgens, Jr, in Source Book on Stainless Steel (Metals Park, Ohio: ASM, 1976),p. 398.

5. ASTM A 763-83, Annual Book of Standards, vol.01-03 (Philadelphia, PA: ASTM, 1984),p.606-621.

Table 1
Nominal Chemical Composition and Mechanical Properties of the plate Materials

Type of Steel	%C,max	%Mn	TS*	YP*	%El
SA-516-60	0.27	0.6-1.2	41-55	21-23	25.0
Type of Steel	%C,max	%Cr	TS*	YP*	%El
AISI 405	0.08	11.5-14.5	50.5	35	30

* Kg/mm²

Table 2
The Results of on site Optical Metallography of Various Locations on Vacuum Tower

Location Number	Location on Tower	Visual Appearance	Cooling Procedure	Microstructure
1	Tray 13 South	severely deformed	By Water	Ferrite+ Spheroidised carbide
2	very top	hole+fire	Air Cool	Ferrite+ 25% Pearlite
3	Tray 13 North	undeformed	By Water	Ferrite+ 25% Pearlite

Table 3
The Results of Tensile Testing on backing plate steel of Vacuum Tower

spec.no.	direction	T.S.,Kg/mm ²	Y.P.,Kg/mm ²	%El,in 2"
1	transverse	50.0	31.5	30.0
2	"	49.5	30.0	32.0
3	"	50.0	32.5	31.6
4	longitudinal	44.0	27.4	31.0
5	"	44.0	26.1	28.0
6	"	45.2	26.5	29.0

Table 4
The results of Tensile Testing of the backing plate steel of Atmospheric Tower

spes.no.	direction	T.S.,Kg/mm ²	Y.P.,Kg/mm ²	%El,in 2"
7	transverse	41.3	27.0	35.0
8	"	41.0	24.8	30.0
9	"	41.5	26.7	33.3
10	"	41.0	27.0	33.0
11	"	42.0	28.0	33.5
12	"	41.5	28.5	33.3

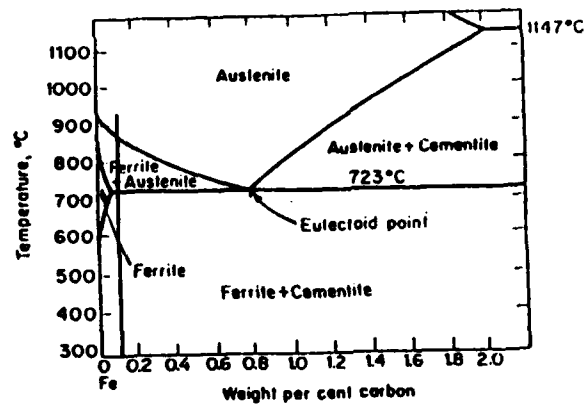


Fig. 1, The Portion of the Fe-C Constitution Diagram. The vertical line indicate the approximate location of the backing plate steel.

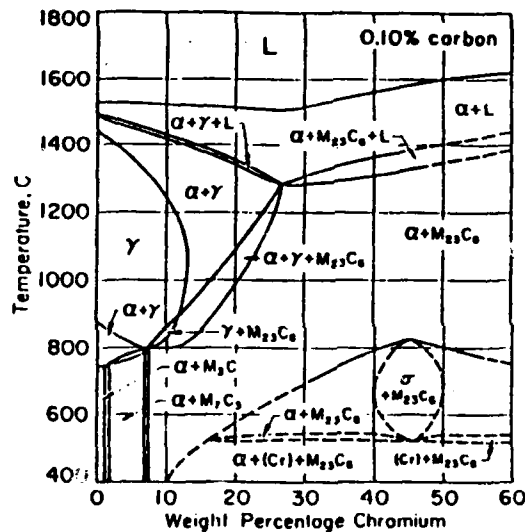


Fig. 2, The vertical section of Fe-Cr-C Constitution Diagram at 0.10% C. The vertical line indicate the approximate location of the stainless steel cladding.

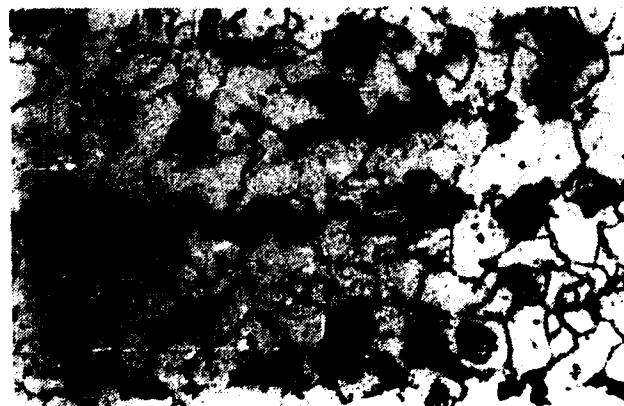


Fig. 3, Photomicrograph backing plate steel of Vacuum Tower, etched in Nital, at 400 magnification.

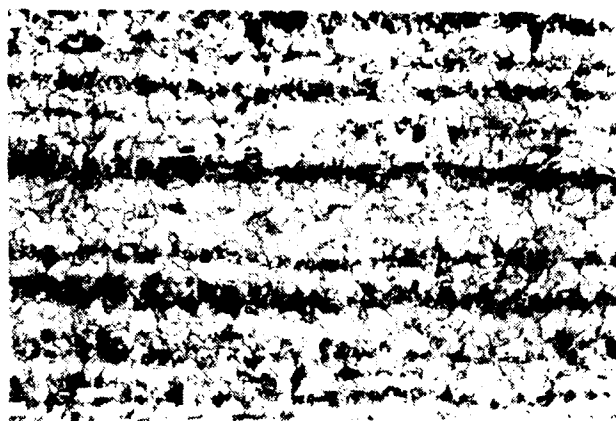


Fig. 4, Photomicrograph of backing plate steel of Atmospheric Tower, etched in Nital, at 200 magnification.

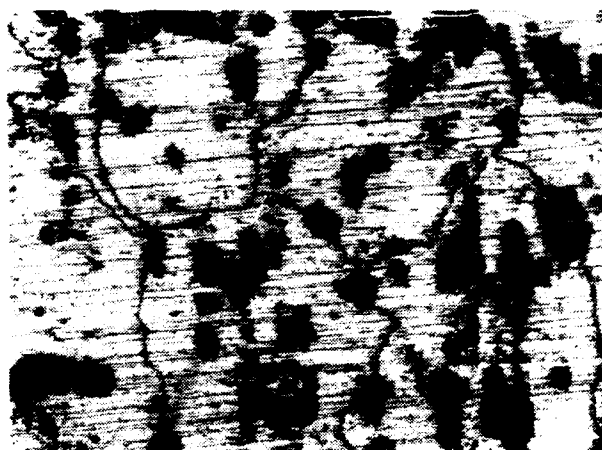


Fig. 5, Photomicrograph of stainless steel cladding of vacuum tower, electrolytically etched, at 200 magnification.



Fig. 6, Photomicrograph of stainless steel cladding of Atmospheric tower, electrolytically etched, at 200 magnification.

New Alloys for High Temperature Applications in Incineration Plants

Hans-Peter Martinz, Wolfgang Köck
Metallwerk Plansee GmbH
A-6600 Reutte Austria

Abstract

The hot components of incineration plants exposed to temperatures between 800 and 1200°C like boilers, grates, thermocouple sheaths and nozzles suffer from severe joint slag and hot gas attack. Considering corrosion resistance only, ceramic materials show excellent performance under these conditions. But because of the ceramics' brittleness metallic materials exhibit an overall advantage although being corroded faster.

Within the class of suitable metals PM-ODS(oxide dispersion strengthened)-superalloys based on iron or nickel and PM-Cr-base-alloys are among the most promising ones. This can be derived from various laboratory and field tests which were performed up to now. Laboratory oxidation tests indicate that these new alloys can be used at temperatures up to 1300°C in hot air. High temperature erosion tests with quartz particles show that PM 2000 (Fe19,5Cr5,5Al0,5Ti0,5Y₂O₃) and Ducropur (99,7 % Cr) have almost the same resistance against particle impact as alumina or zirconia at 900°C.

Agricultural waste and residues will get more interesting as non-fossile fuel for future power production. The corresponding laboratory and field tests under typical joint slag and hot gas conditions at temperatures up to 1200°C show good results for PM 2000 and already lead to the actual application of boiler components. Extensive testing has been performed in the field of municipal waste incineration. Depending on temperature, slag and hot gas composition selected grades of the PM-ODS- and Cr-base-alloy-group give satisfactory results in the field tests.

In the pulp industry black liquor, an alkaline solution with high concentrations of organic waste, is incinerated for the recovery of caustic soda. Flame sprayed coatings of Ducrolloy Cr50Ni give a sixfold increase of the lifetime of the burner nozzles compared to unprotected stainless steel.

For the applications cited above the new alloys are compared with standard materials using gravimetric, metallographic, light and electron microscopic methods for the elucidation of corrosion rates and mechanisms.

Key terms: incineration, ODS-superalloys, chromium alloys, waste, slag, oxidation

Introduction

It is well known from literature that chromium is quite resistant to hot air at temperatures up to 900-1000°C and kinetics and mechanisms have intensely been examined (1, 2, 7, 8, 9, 14, 16, 17). Above about 1000°C oxidation is accelerated by spallation of non-adherent Cr_2O_3 scale and enhanced oxidation of Cr_2O_3 to volatile CrO_3 . Furthermore the metal beneath the oxide scale is nitrided. As tight and adherent protective layers are also essential for good performance against joint slag-hot gas attack (like in waste incinerators) advanced materials have to be used in these cases. Chromia-formers can be applied up to about 1100°C if they have been improved by small additions of reactive elements or oxides of reactive elements like La, La_2O_3 , Y, Y_2O_3 , Ce, CeO_2 and others more. (9, 10, 12, 23, 14, 20, 3, 5, 6, 11). At higher temperatures up to about 1300°C alumina-formers alone remain applicable. The performance of these alloys against hot gas attack can again be improved by reactive elements or their oxides (13, 18, 20, 21, 22). ODS-superalloys furthermore exhibit enhanced mechanical properties which enables lean designs. With slags it seems to be important that the temperature is not above about 1200°C and that the oxygen potential of the atmosphere is sufficiently high; otherwise even alumina-forming ODS-superalloys fail. In the present work the above considerations from literature could essentially be confirmed with new alloys.

Experimental Procedures

In case of laboratory tests specimens of typically 10 - 20 cm² surface (ground) were exposed to hot air only or were immersed in slags for defined times in a chamber furnace. The evaluation was performed by weight- and dimensional change-measurements, surface-LiMi,-EDX and -XRD and by metallographic cross-sections (and consequent LiMi, SEM and EDX). For the field tests ("TAMARA") samples had a special shape (rings) to be easily mounted on a rod standing into the hot zone of the combustion chamber. Evaluation was done equally. For the test in the pulp industry an original burner tube was flame-spray-coated with Cr50Ni and the improvement of the endurance was registered.

Results and Discussion

Figures 1 and 2 distinctly show the beneficial effect of reactive element oxides (La_2O_3 , Y_2O_3) on the oxidation resistance of chromia-forming alloys and furtheron the excellent performance of the alumina-formers $\text{Fe}_{19,5}\text{Cr}_{5,5}\text{Al}_{10,5}\text{Ti}_{0,5}\text{Y}_2\text{O}_3$ ("PM 2000") and $\text{Cr}_{44}\text{Fe}_{5,5}\text{Al}_{10,3}\text{Ti}_{0,5}\text{Y}_2\text{O}_3$. The latter two alloys and the chromium-base-alloys $\text{Cr}_{10}\text{La}_2\text{O}_3$ and $\text{Cr}_{5}\text{Fe}_{1}\text{Y}_2\text{O}_3$ do not exhibit any internal attack beneath the protective oxide layers.

Consequently the best chromia-formers from the hot air test at 1000°C were exposed to 1080°C over 1000 hours. Additionally the content of reactive element oxides was varied. In Fig.3 the results are presented: $\text{Cr}_{0,5}\text{La}_2\text{O}_3$ and $\text{Cr}_{5}\text{Fe}_{1}\text{Y}_2\text{O}_3$ show the lowest oxidation rate under these conditions.

A further increase in temperature to 1300°C (Figs 4 and 5) clarifies the limits of the chromia-formers Cr 99,7 ("Ducropur"), $\text{Cr}_{10}\text{La}_2\text{O}_3$ ("Ducrolloy $\text{Cr}_{10}\text{La}_2\text{O}_3$ "), $\text{Ni}_{20}\text{Cr}_{0,3}\text{Al}_{10,5}\text{Ti}_{0,6}\text{Y}_2\text{O}_3$ ("PM1000") and $\text{Ni}_{30}\text{Cr}_{0,3}\text{Al}_{10,5}\text{Ti}_{0,6}\text{Y}_2\text{O}_3$ ("PM 1500").

The chromium-base-materials form very thick non-adherent scales whereas the nickel-base-alloys become porous by strong Cr-consumption on the metal gas-interface.

Even the alumina-formers (which also form Cr_2O_3 or some Fe-Cr Oxide on Al_2O_3) are not completely stable forming pores throughout the material owing to Al and Cr losses into the scale.

Besides chemical attack in practical systems erosion often plays an important role. Figs 6 and 7 show the results from tests performed by University of Dortmund for Metallwerk Plansee. Quartz-sand injected into a hot air jet was shot to preheated specimens of various alloys and ceramics.

Cr 99,7 and especially $\text{Fe}_{19,5}\text{Cr}_{5,5}\text{Al}_{10,5}\text{Ti}_{0,5}\text{Y}_2\text{O}_3$ were fairly resistant comparable to glass-bonded alumina and MgO-stabilized zirconia. This may be attributed to the tight oxide-layers formed on these materials at 800 to 900°C.

Joint hot-air- and slag-attack on various alloys has been examined in laboratory with the view to incinerators for agricultural waste and residues. Fig.8 represents the results obtained at 1100°C: The best alloys from pure oxidation tests also perform best under these conditions. At 1200°C (Fig. 9) attack is naturally more severe and lead to complete destruction in case of the steels.

"PM 2000", $\text{Cr}_{44}\text{Fe}_{5}\text{Al}_{10,3}\text{Ti}_{0,5}\text{Y}_2\text{O}_3$ and $\text{Cr}_{1}\text{La}_2\text{O}_3$ in summary were most resistant although formation of pores and mass loss by non-adherent scale respectively indicate a limited lifetime. Table 1 summarizes the results.

Field tests concerning the incineration of municipal waste were performed at KFZ-Karlsruhe, Germany in a model incinerator (Fig.10), more exactly: in the hottest zone of this plant (870 - 1050°C) within the combustion chamber. The materials (ring-shaped) were exposed to joint ash/slag (composition unknown, and hot gas attack (see Table 2). Considerable amounts of SO_2 and HCl could be found in the still oxidizing atmosphere. The results are shown in Figs 11 to 15 for various chromium-alloys and ODS-superalloys ("PM 1000", "PM 1500", "PM 2000" and $\text{Ni}_{17}\text{Cr}_{6}\text{Al}_{12}\text{Mo}_{3,5}\text{W}_{2}\text{Ta}_{0,15}\text{Zr}_{0,95}\text{Si}_{1,1}\text{Y}_2\text{O}_3$ = "PM 3030"). It is apparent that the alumina-formers "PM 2000" and $\text{Cr}_{44}\text{Fe}_{5}\text{Al}_{10,3}\text{Ti}_{0,5}\text{Y}_2\text{O}_3$ are corroded least of all and that the Cr50Ni-flame-spray-coating suffered the highest mass gain. The latter fact can be understood considering Figs 12,13 and 15: The porous spray-coating is oxidized throughout the cross-section not losing its adherence. Y_2O_3 -doped chromia-formers loose some mass by non-adherent scale but behave much better than a steel of composition $\text{Fe}_{24}\text{Cr}_{1,2}\text{Si}_{1,5}\text{Al}$ (Fig.16), which has also been tested in "TAMARA".

Finally there is some experience with Cr50Ni-flame-spray-coatings on steel in pulp industry. For recovery of caustic soda and sulfur "black liquor", an alkaline solution with high concentrations of organic waste, is incinerated. Burner tubes used in this combustion process were coated with Cr50Ni on the fire-side and could then be used about six-times longer than unprotected steel ($\text{Fe}_{17}\text{Cr}_{11}\text{Ni}_{2}\text{Mo}$).

Summary

Chromium ("Ducropur"), chromium-alloys ("Ducrolloy") and ODS-superalloys ("PM 1000, 1500, 2000, 3030") were exposed to hot air and combined systems slag/hot air at 800 to 1300°C under laboratory and field conditions. Chromia-formers show acceptable performance up to 1100°C when they are doped with lanthana or yttria. Otherwise even at 1000°C oxide growth and spallation are too severe. At temperatures up to 1300°C or joint slag/hot gas-attack Y_2O_3 -doped alumina-formers are more resistant although they suffer formation of pores throughout the material above 1200°C. Erosion tests at about 900°C with quartz-particles in hot air showed that Cr 99,7 and "PM 2000" are nearly as resistant as alumina and zirconia. Considering the above results reactive element doped chromium-base-alloys and ODS-superalloys are promising materials for tubes, grates, thermocouple sheaths and nozzles in the hot regions of incinerators.

References

- (1) E.A.Polman, F.Fransen, P.J.Gellings, *Oxid.Mat.* 32 (1989) 433-447
- (2) B.Gillot, M.Radid, *Oxid.Met.* 33 (1990) 279-299
- (3) C.H.Yang, G.Welsch, T.E. Mitchell, *J.Mater.Sci.*25 (1990) 1724-1738
- (4) J.H.Park, *Mater.Lett.*8 (1989) 405-408
- (5) P.Y.Hou, J.Stringer, Lawrence Berkeley Laboratory Report DE 88009818/XAB (1988) Pp.1
- (6) J.Przybylski, G.J. Yurek, *Mater.Sci. Forum*, 43 (1989) 1-73
- (7) R.J.Hussey, D.F.Mitchell, M.J.Graham, *Werkst.Korros.* 38 (1987) 575-583
- (8) T.A.Dzigrashvili, *Nauchn.Tr.Gruz, Politekh. Inst.* 1 (1984) 20-23
- (9) F.N.Tavadze, NP.Keshelava, O.Mikadze, T.A. Dzigrashvili, *Nauch n.Tr.Gruz. Politekh. Inst.* 1 (1984) 16-19
- (10)F.N.Tavadze, O.I. Mikadze, N.P.Keshelava, B.P.Bulia, *Oxid.Met.*25 (1986) 335-350
- (11)A.H.Rosenstein, J.K.Tien, W.D.Nix, *Metall.Trans.A*, 17A (1986) 151-162
- (12)F.N.Tavadze, O.I.Mikadze, E.R.Kuteliya, B.P.Buliya, A.N.Rakitskii, *Izv.Akad.Nauk.SSR, Neorg.Mater.* 20 (1984) 1121-1125
- (13) W.J.Quadackers, *Abstr. of 3rd Int. Symp.High Temp. Corros.1992, Los Embiez, France (F)*, p.21
- (14) H.P.Martinz, W.Köck, T. Sakaki, (F) p.26
- (15) R.Grill, W.Köck, H.P.Martinz, *VDI-Ber.Nr.917* (1992) 83-86.
- (16) R.Eck, H.P.Martinz, T.Sakaki, M.Kato, *Mat.Sci.Eng.A120* (1989) 307-312.
- (17) H.P.Martinz, R.Eck, J.Eiter, T.Sakaki, M.Kato, *Werkst. Korros.* 40 (1989) 715-719.
- (18) G.Korb, M.Rühle, H.P.Martinz, *ASME-Paper 91-GT-405*.
- (19) Y.Aito, (F) p. 27
- (20) R.J. Hussey, G.I. Sproule, M.J. Graham, (F) p.29
- (21) T.Cao, H.Pan, H.Dong, Y.Zhang, S.Shih, (F) p.36
- (22) J.Jedlinski, M.Krasovec, J.W.Quadackers, G.Borchardt, (F) p.121
- (23) R.Kilian, W.Straub, (F) p.150

Slags from incineration of:

	straw (A)
	waste from sunflowers (B)

[illegible]

Incineration of municipal waste 870 - 1050°C

oxygen (O ₂)	7 - 14 vol%
carbondioxide (CO ₂)	100 - 200 g*m ⁻³
watervapour (H ₂ O)	100 - 200 g*m ⁻³
carbonmonoxide (CO)	~ 0
sulfurdioxide (SO ₂)	0 - 1100 mg*m ⁻³
hydrogenchloride (HCl)	0 - 1100 mg*m ⁻³

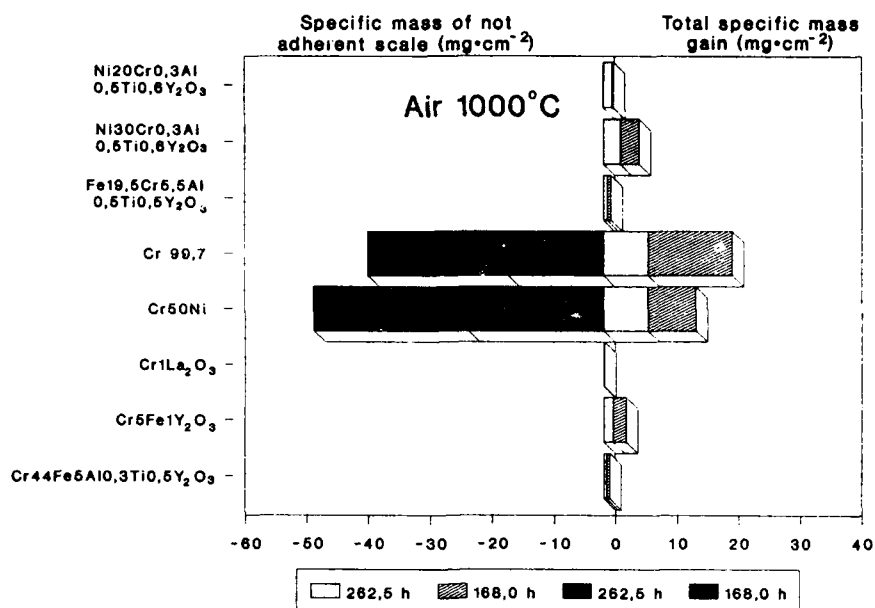


Fig. 1: Isothermal hot air oxidation of various chromium- and ODS-superalloys at 1000°C over 430,5 hours.

Air 1000°C / 430,5 hours / all x480

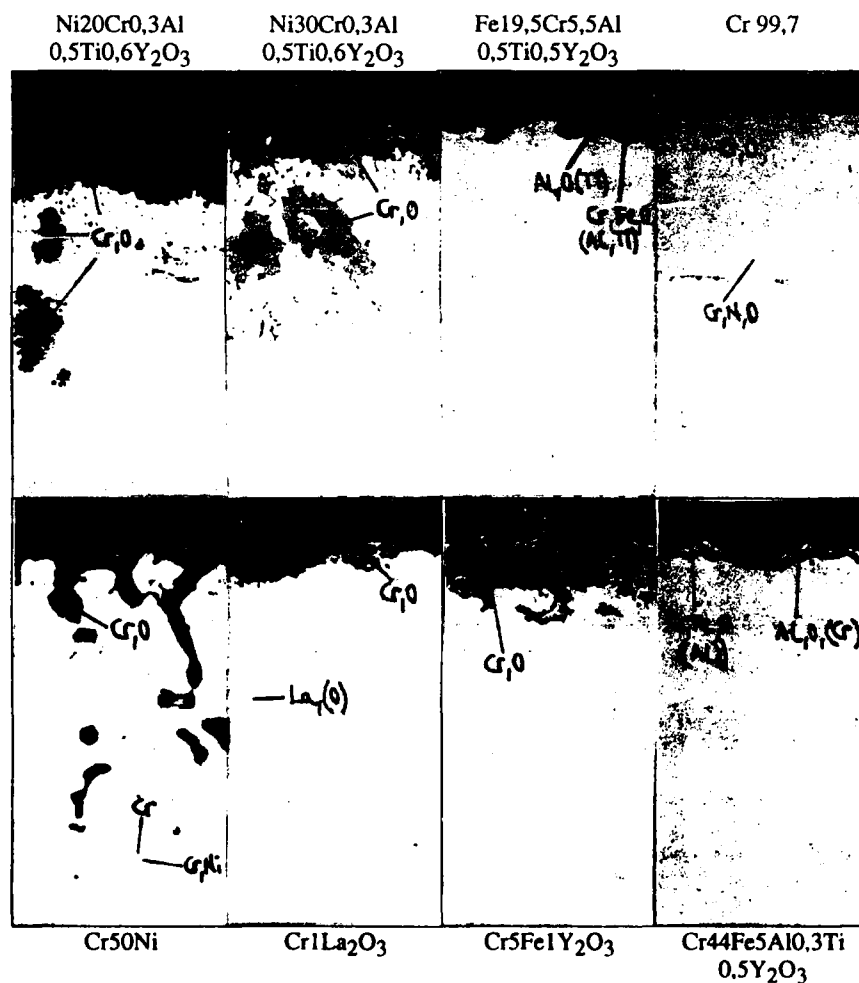


Fig. 2: Cross-sections of various chromium- and ODS-superalloys after an exposure to air at 1000°C over 430,5 hours.

Air 1080°C / 1000 hours / all x100

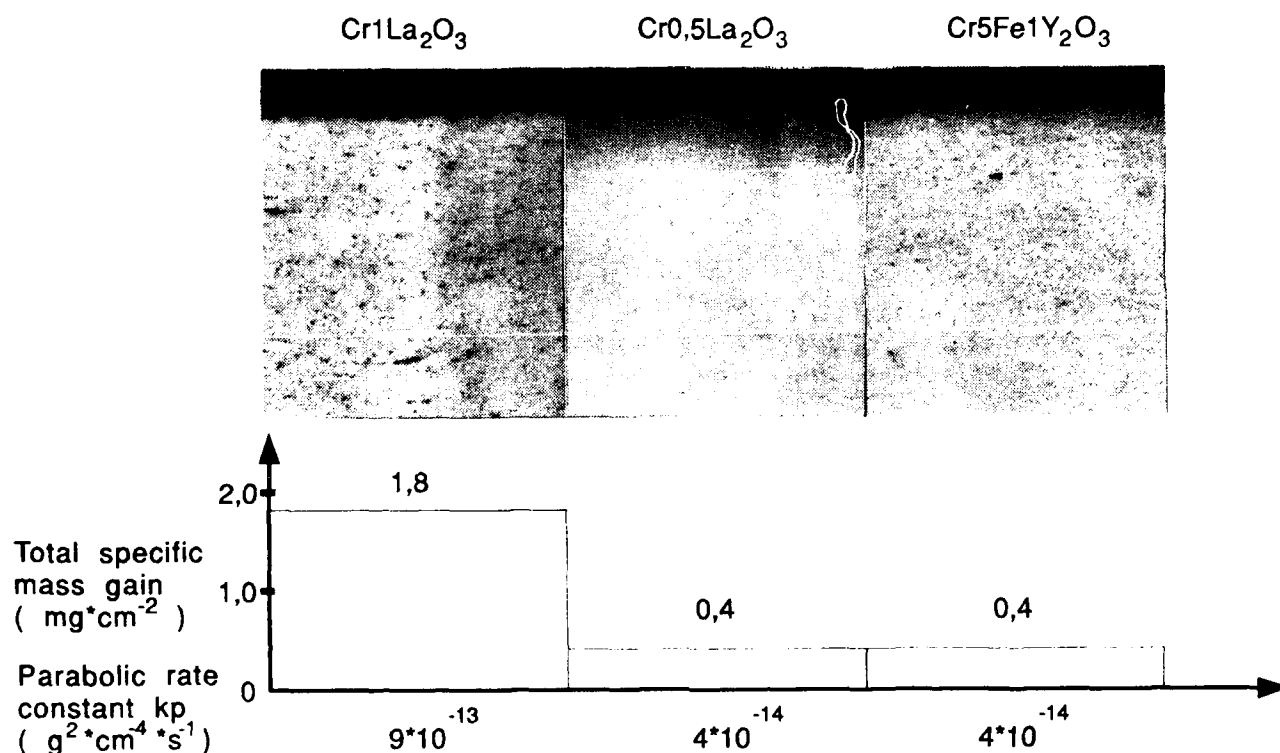


Fig. 3: Isothermal hot air oxidation of various chromium-alloys at 1080°C over 1000 hours.

Air 1300°C / 332,5 hours

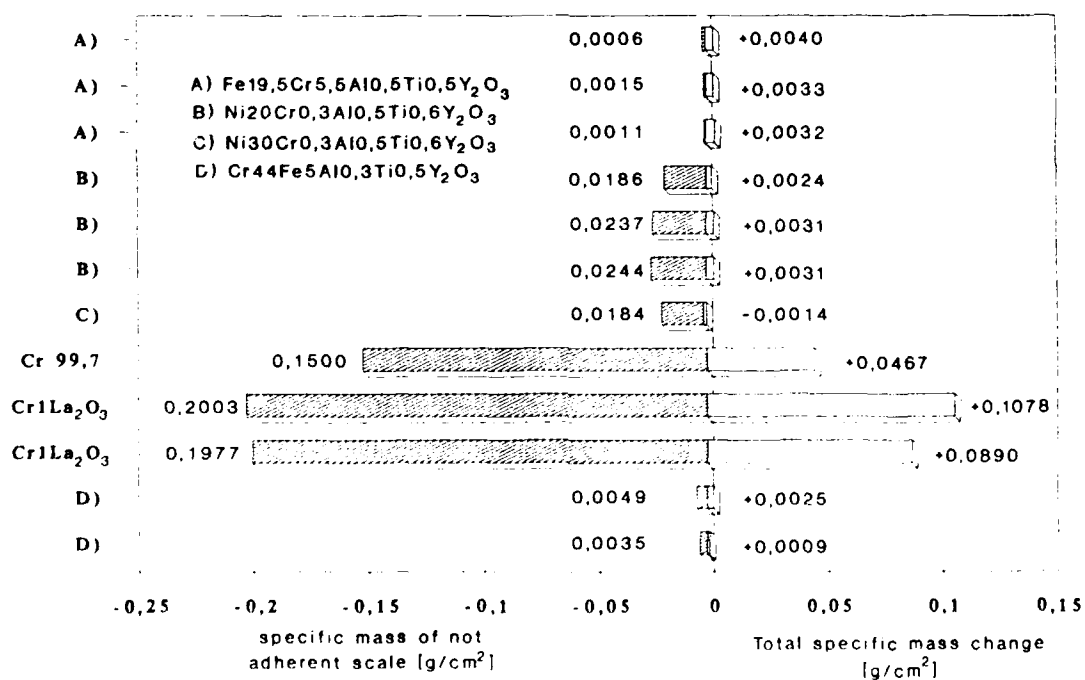


Fig. 4: Isothermal hot air oxidation of various chromium- and ODS-superalloys at 1300°C over 332,5 hours

Air 1300°C / 332.5 hours

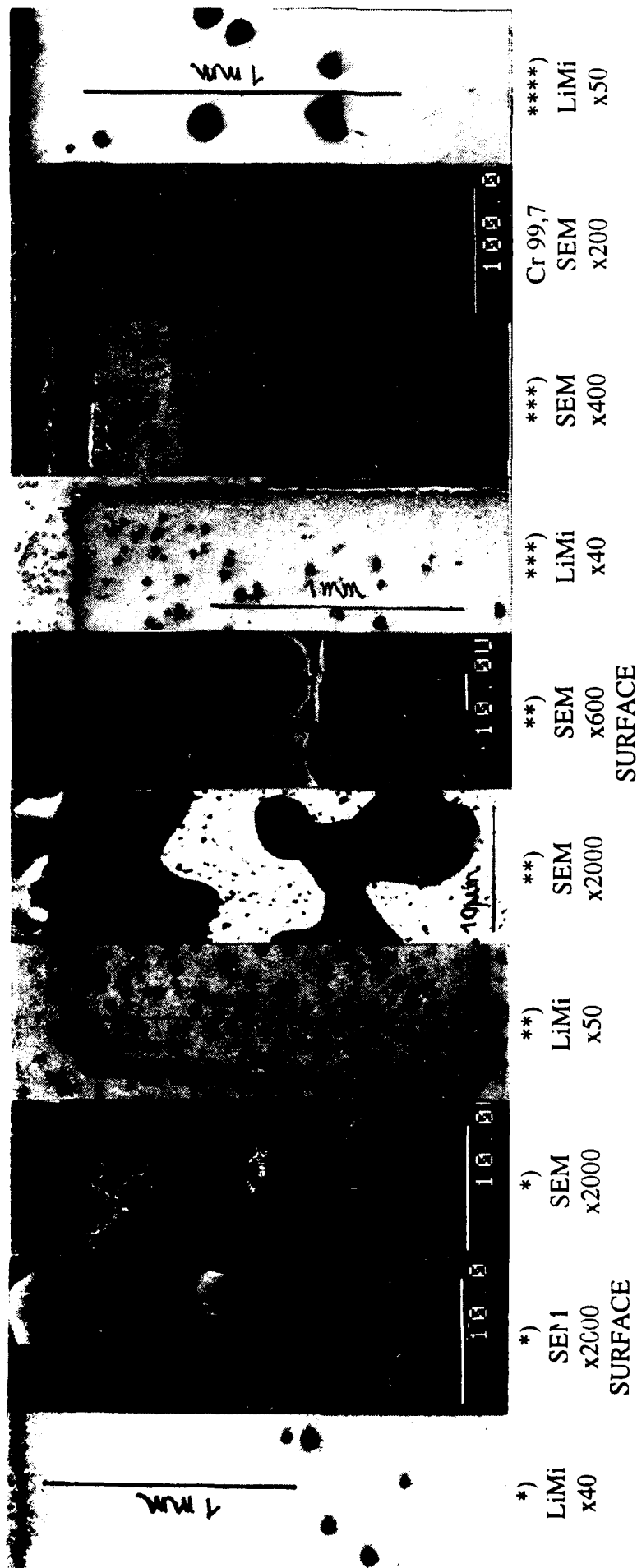


Fig. 5: Cross-sections and surfaces of various chromium- and ODS-superalloys after an exposure to air at 1300°C over 332,5 hours.

High temperature erosion test

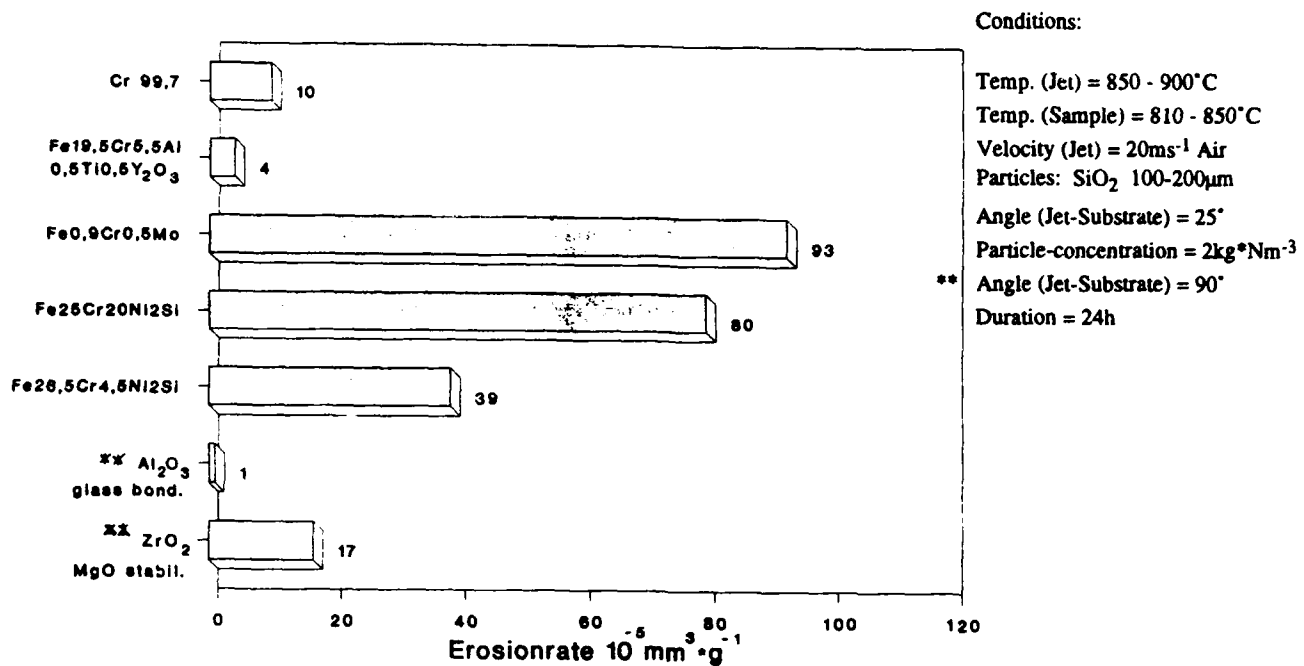
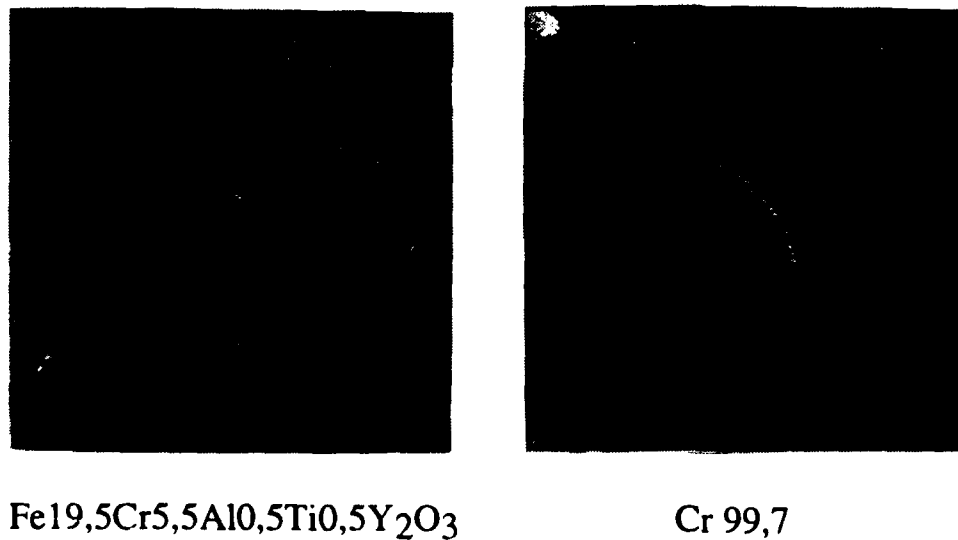


Fig. 6: High temperature erosion test of various alloys and ceramics with quartz-particles in stream of hot-air.

High Temperature Erosion Test

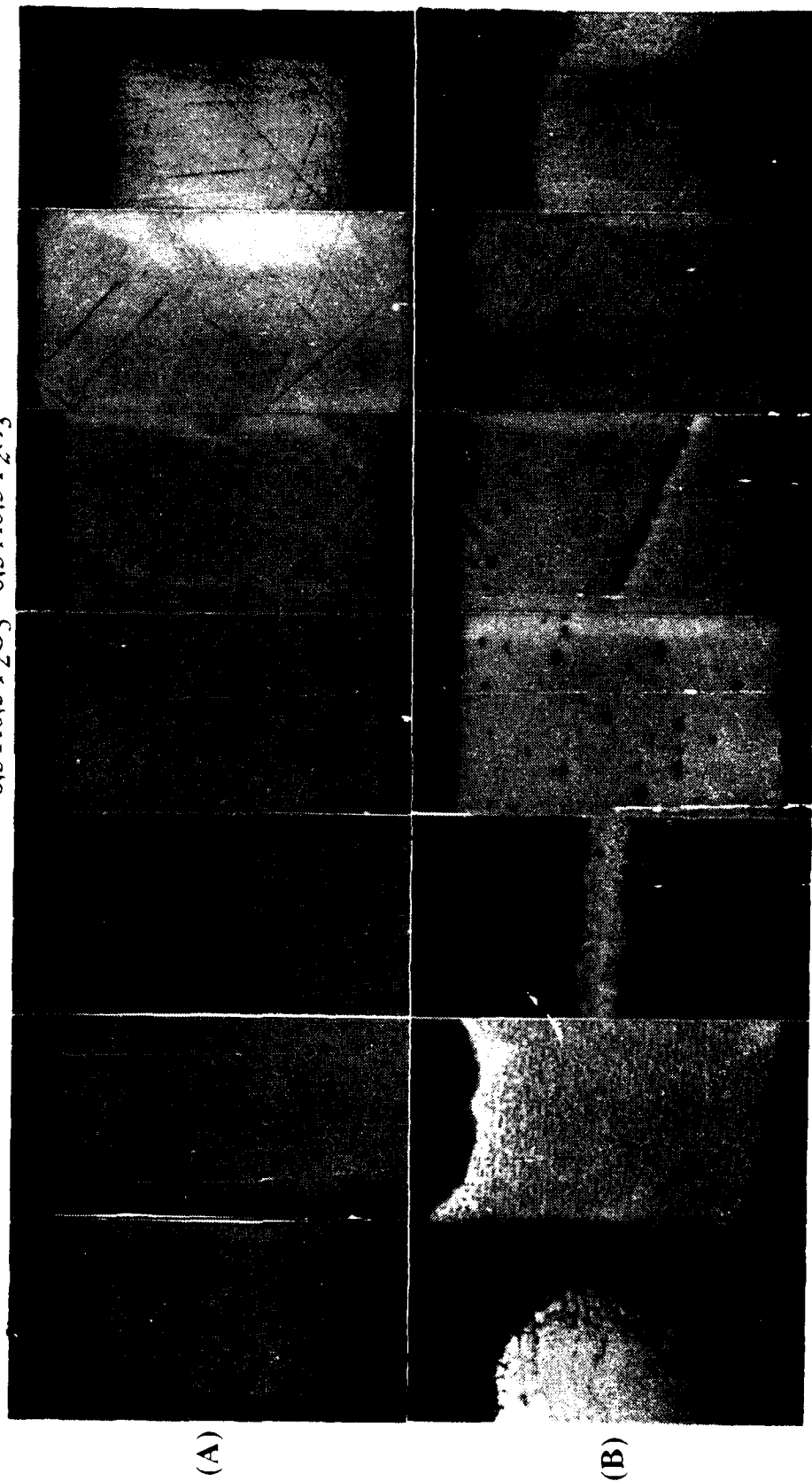


x 1,9

Fig. 7: Surfaces of a ferritic ODS-superalloy and of chromium after an high temperature erosion test.

Slags from incineration of: straw - (A)
waste from sunflowers - (B)
1100°C / 168 to 573 hours

Fe25Cr20Ni	Fe	25Cr	4Ni	F27Cr32Ni	Fe19,5Cr5,5Al	Cr44Fe5Al	Cr1La ₂ O ₃	Cr5Fe1Y ₂ O ₃
					0,5Ti0,5Y ₂ O ₃	0,3Ti0,5Y ₂ O ₃		

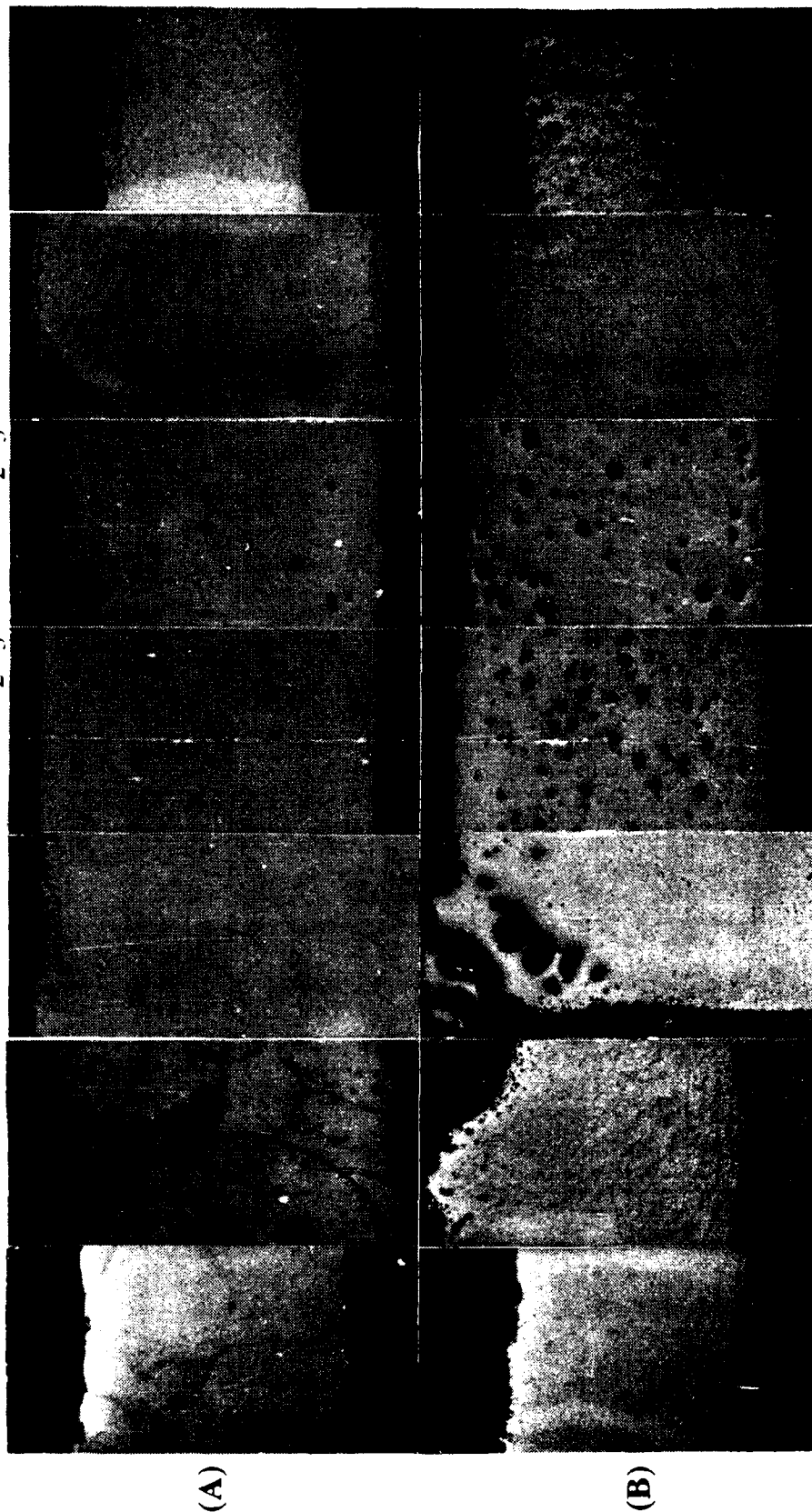


all x20

Fig. 8: Cross-sections of various alloys after an exposure to slags from the incineration of straw and waste from sunflowers at 1100°C.

Slags from incineration of: straw - (A)
waste from sunflowers - (B)
1200°C / 160 to 328 hours

Fe25Cr20Ni	Fe 25Cr 4 Ni	F27Cr32Ni	Fe19,5Cr5,5Al	Cr44Fe5Al	Cr1La2O3	Cr5Fe1Y2O3
			0,5Ti0,5Y2O3	0,3Ti0,5Y2O3		



all x20

Fig. 9: Cross-sections of various alloys after an exposure to slags from the incineration of straw and waste from sunflowers at 1200°C.

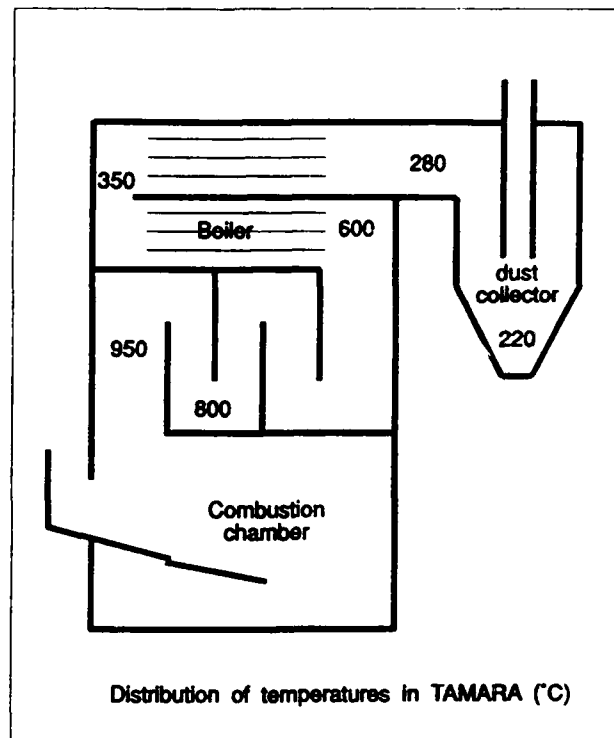
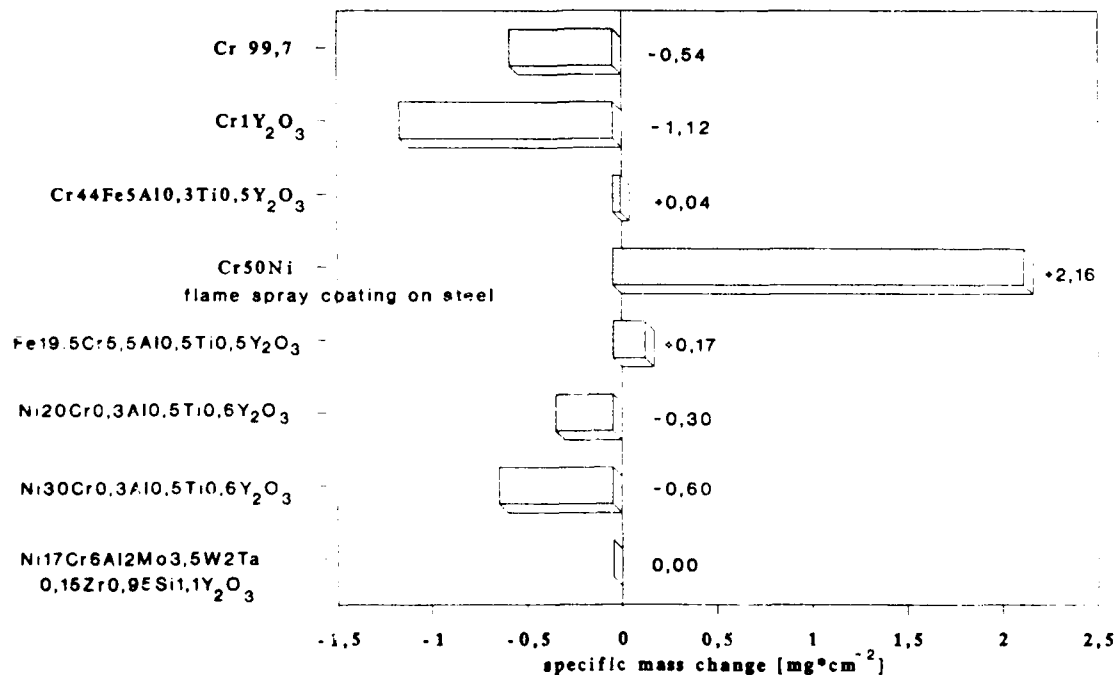


Fig.10: Schematic drawing of the model incinerator for municipal waste ("TAMARA") at KFZ-Karlsruhe with a rough distribution of temperatures.

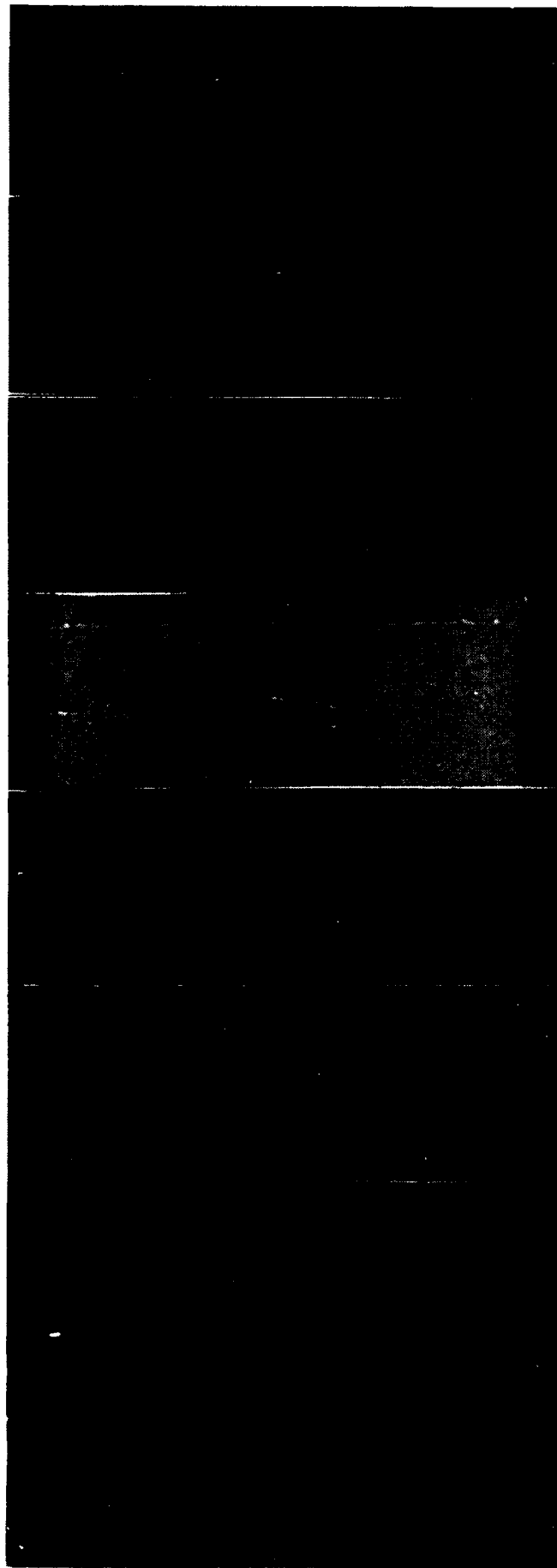
Incineration of municipal waste 960 - 1000° C (1 week)



Tests performed in TAMARA (= model incin. for munic. waste), Karlsruhe, 3/4/92

Fig.11: Field test results of various chromium- and ODS-superalloys from "TAMARA", 960 -1000°C, 1 week.

Incineration of municipal waste 960 - 1100°C (1week)



Cr99,7 x100	Cr1Y ₂ O ₃ x100	Cr44Fe5Al 0,3Ti0,5Y ₂ O ₃ x100	Cr50Ni x20	Fe19,5Cr5,5Al 0,5Ti0,5Y ₂ O ₃ x100	Ni20Cr0,3Al 0,5Ti0,6Y ₂ O ₃ x100	Ni30Cr0,3Al 0,5Ti0,6Y ₂ O ₃ x100	Ni17Cr6Al2Mo 3,5W2Ta0,15Zr 0,95Si1,1Y ₂ O ₃ x100
----------------	--	--	---------------	--	--	--	---

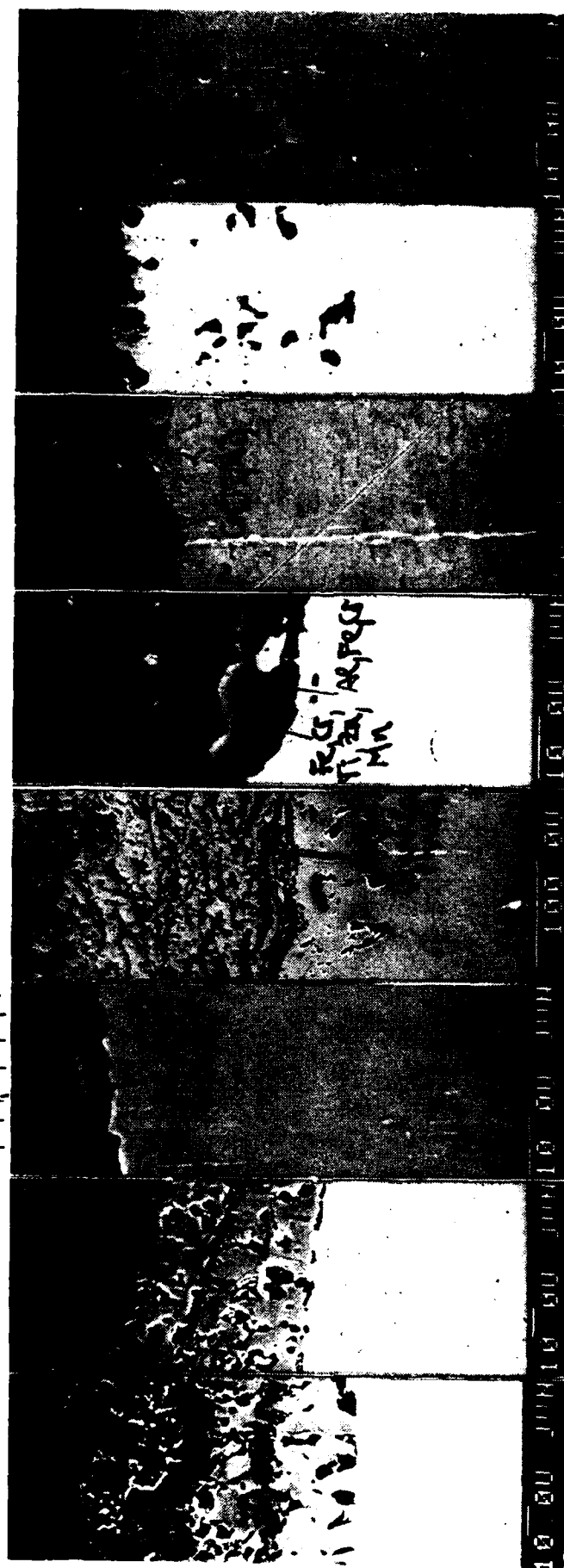
Test performed in TAMARA (= model munic. waste incin.), Karlsruhe

Fig.12: Cross-sections of various chromium- and ODS-superalloys after a field test in "TAMARA" at 960-1000°C over 1 week (LiMi)

Incineration of municipal waste

960 - 1000°C (1 week)

Al, Fe, Si, Cr, Ni, Co, Ti, S, O

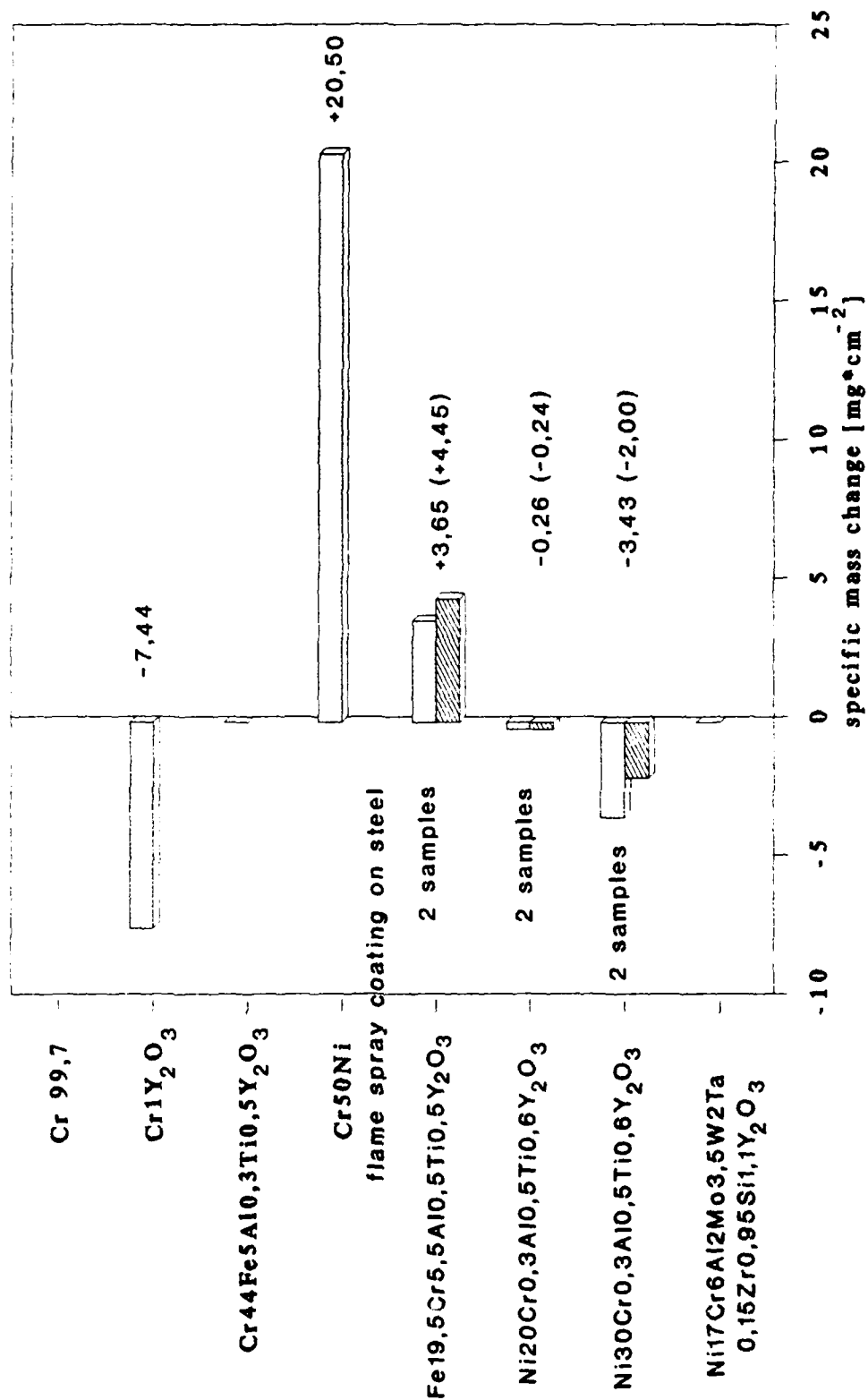


Cr 99,7	Cr1Y ₂ O ₃	Cr44Fe5Al	Cr50Ni	Fe19,5Cr5,5Al	Ni20Cr0,3Al	Ni30Cr0,3Al	Ni17Cr6Al2Mo
	0,3Ti0,5Y ₂ O ₃	0,5Ti0,5Y ₂ O ₃	on steel	0,5Ti0,5Y ₂ O ₃	0,5Ti0,6Y ₂ O ₃	0,5Ti0,6Y ₂ O ₃	3,5W2Ta0,15Zr
							0,95Si1,1Y ₂ O ₃

EDX: All Scales contain additionally: O (N) Tests performed in TAMARA (= model munic. waste incin.), Karlsruhe

Fig.13: Cross-sections fo various chromium and ODS-superalloys after a field test in "TAMARA"
960 - 1000°C over 1 week (SEM)

Incineration of municipal waste 870 - 1050°C (2 weeks)



Tests performed in TAMARA (= model incin. for munic. waste), Karlsruhe, 5/92

Fig. 14: Field test results of various chromium- and ODS-superalloys from "TAMARA", 870-1050°C, 2 weeks.

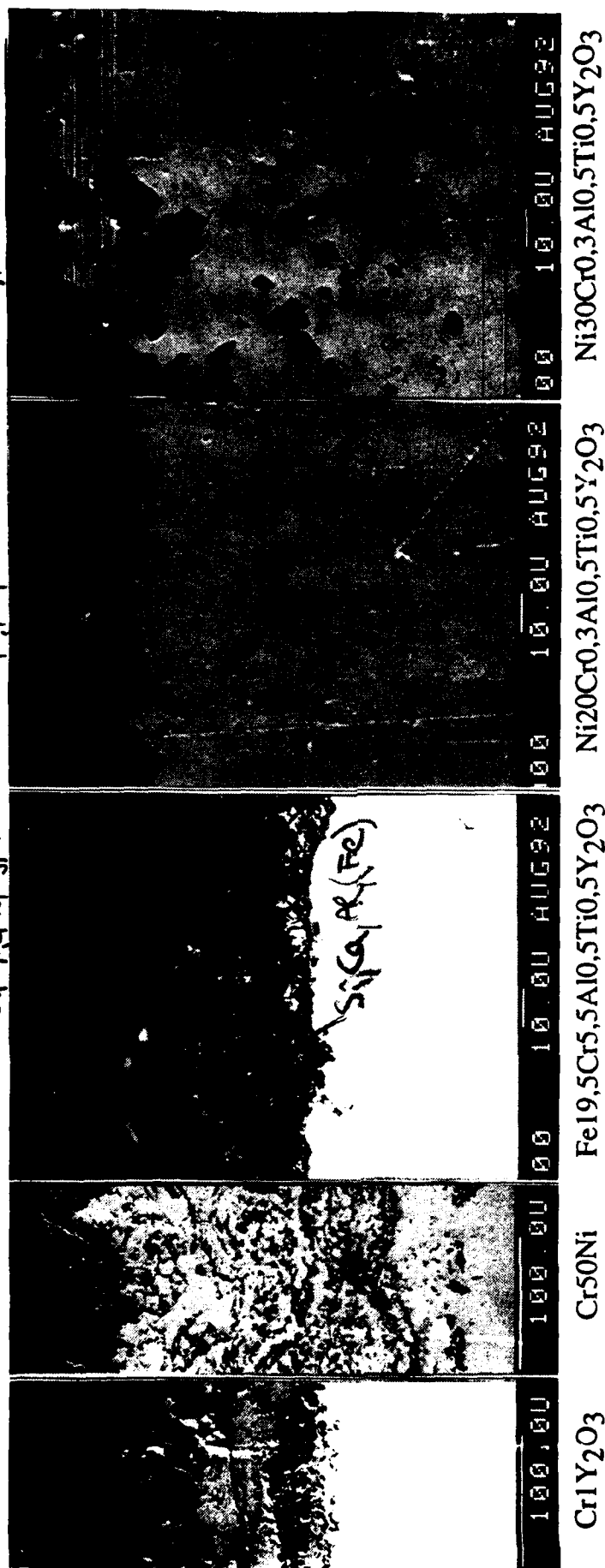
Incineration of municipal waste

870 - 1050°C (2 weeks)

Ca, Si, Fe, Al, Mg, Ti

Cr, Ti, Al, Ni

Cr, Ti, Al, Ni (Ca)



Tests performed in TAMARA (= model incin. f. munic. waste), Karlsruhe

Fig. 15: Cross-sections of various chromium- and ODS-superalloys after a field test in "TAMARA" at 870 - 1050°C over 2 weeks (SEM)

Incineration of municipal waste (TAMARA)

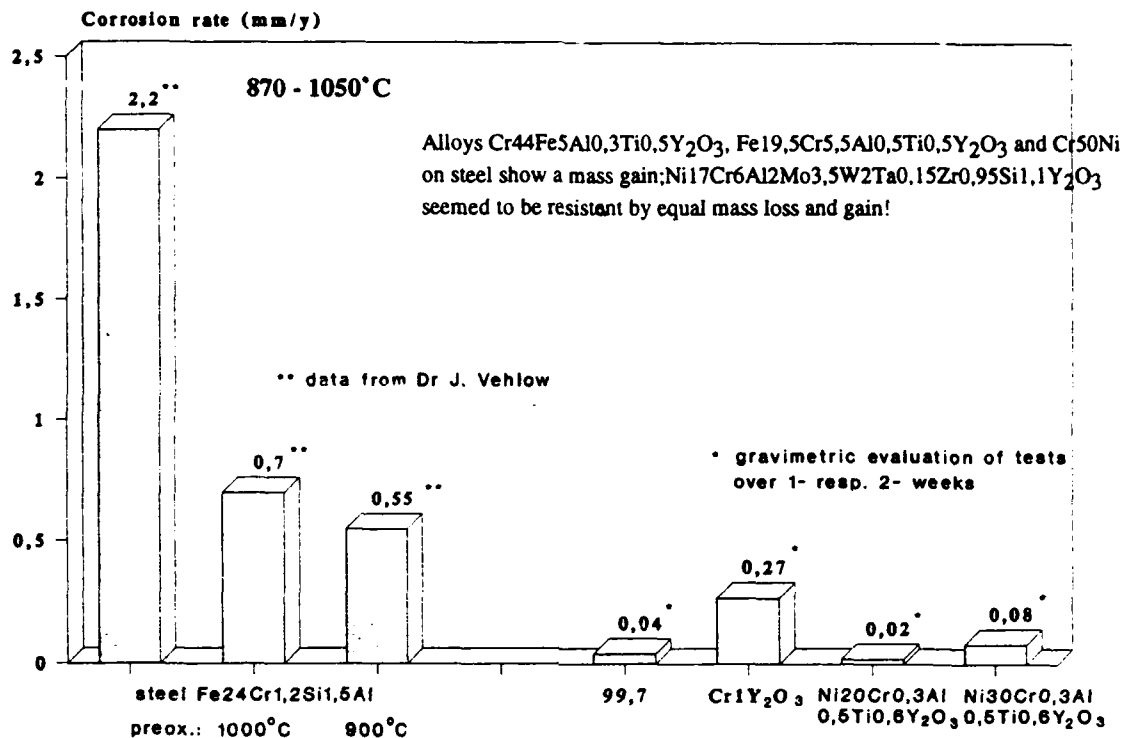


Fig.16: Field test results of various alloys from "TAMARA"

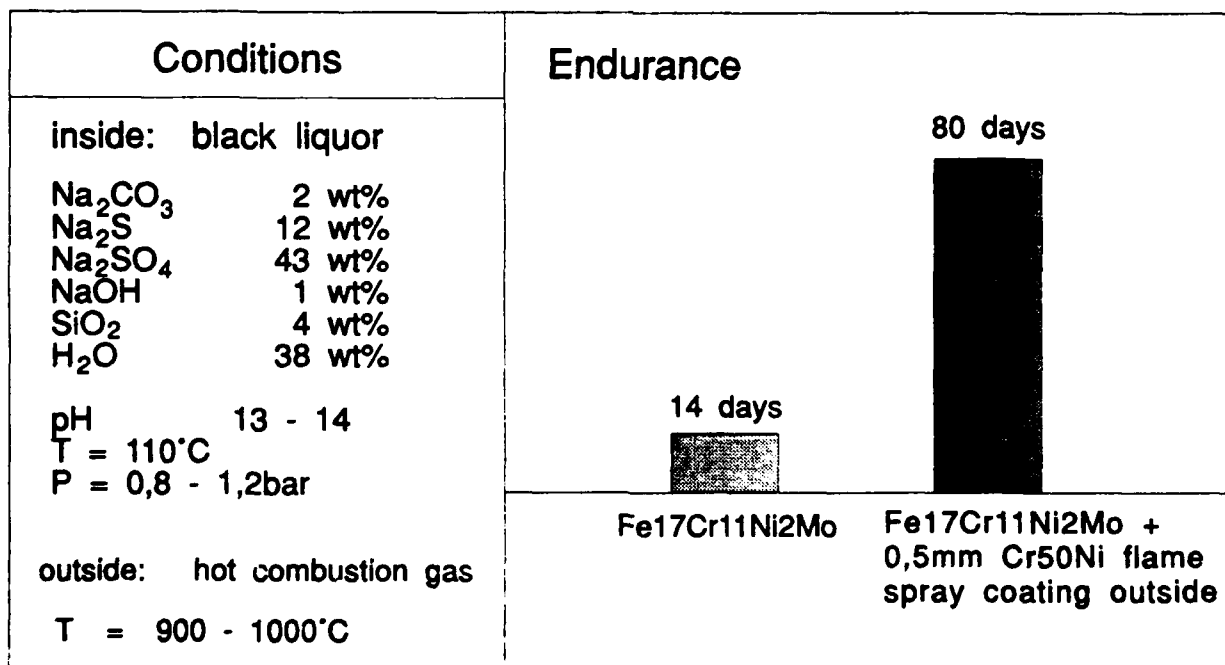


Fig.17: Field test results of uncoated and Cr50Ni-flame-spray-coated steel from the incineration of black liquor in pulp-industry.

Corrosion Evaluation of Materials in Sulfur Compound Environments

Mao-Ying Teng
Materials Research Laboratories
Chutung, Hsinchu, Taiwan, ROC

Iuan-Jou Yang
Materials Research Laboratories
Chutung, Hsinchu, Taiwan, ROC

Abstract

The para-toluene sulphonic acid (PTSA) serves as a catalyst in producing diethylene glycol dibenzoate (DEGDB) and decomposes with increasing time at elevated temperature. Due to the presence of bisulfite ion, it is important to evaluate the corrosion properties of materials in this metastable environments. Potentiodynamic method was used to screen materials' properties in PTSA solution. Surface analysis technique was also performed to investigate the oxide films. The critical current density and passive current density were substantially reduced when Fe alloyed with Cr and/or Ni. With the addition of Mo in Fe-Ni-Cr alloys, the critical current density was lowered further to show the beneficial effect of alloyed Mo.

A plot of the corrosion rate of materials in DEGDB as a function of Ni/Cr ratio shows the linearity with increasing Ni/Cr ratio, disregard the type of materials. The result suggests that nickel corrodes preferentially in DEGDB with controlling PTSA concentration. The corrosion rate of pure chromium can be estimated as ≈ 2.0 mpy by extrapolation of the linearity to Ni/Cr=0. This is also the minimum corrosion rate that even Fe-Ni-Cr alloys were alloyed with Mo. Surface analysis results showed that the dissolution of Fe and/or Ni leads to a higher surface chromium content and results in the formation of chromium oxide on metal surface. This chromium oxide then prevents metal from corrosion. It is concluded that the higher the nickel content the higher the corrosion rate of materials.

The composition potential-pH diagrams for Fe-S-H₂O and Ni-S-H₂O show that the stability fields of FeS and NiS cover a wide range of pH. The effect of sulfur or sulfide ions in promoting dissolution of Fe and/or Ni are highly possible. In view of the experimental results, the activating influence of sulfur compound on Ni is stronger than that of Fe, although the highly electronic conductivity of iron sulfides can catalyze the cathodic reaction. Undoubtedly, sulfur compound strongly depassivates high Ni contents materials.

Key terms: polarization curve, surface analysis, depassivation, sulfur compound

Introduction

According to the equilibrium relations of sulfur compound, all the substances whose oxidation numbers lie between -2(sulfides) and +6(sulfates) are thermodynamically unstable and tend to decompose. PTSA has been used as a catalyst to produce DEGDB. Since PTSA contains bisulfite ion, which may decompose to form several sulfur compounds, e.g. sulfur dioxide, thiosulfate ion, or tetrathionate ion, it is important to evaluate the corrosive interaction of sulfur compounds with technical construction materials.

Stainless steels are the most widely materials used for constructing facilities. The pitting of AISI 304 steel in thiosulfate or thiosulfate-sulfate solutions has been reported.¹⁻² Crevice corrosion testing of stainless steels in thiosulfate solutions indicated that the enhanced penetration rates were due to the formation of a reduced sulfur species in the active regions.³ Only 0.1 ppm sodium thiosulfate was found to give rise to cracking of sensitized type 304 stainless steel.⁴⁻⁵ No pitting of AISI 316L SS occurred in concentrated sulfate/thiosulfate solutions, even at 80°C. However, when chloride is the predominant anion, 316L SS undergoes thiosulfate pitting.¹

In this study an attempt was made to investigate the electrochemical properties of materials in PTSA solutions and to measure the corrosion rate of materials in DEGDB. Also, the elemental distribution of the oxide film formed in the passive region was performed by sequential Auger electron analysis and sputtering.

Experimental

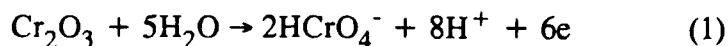
Table 1 gives the compositions of materials studied and the Ni/Cr ratios. A scan rate of 1 mV/s was chosen to construct the polarization curves. Analytical grade (MERCK) chemical reagent was used to make up PTSA solutions. The pH of the electrolyte is 0.5. An electrochemical interface (Solartron 1286) was used to sweep the potential and monitor the current. A saturated calomel reference electrode (SCE) was maintained in contact with the electrolyte. The ring-shaped platinum served as a counter electrode. The electrolyte was deaerated by purging with nitrogen before and during the test. All experiments were performed at room temperature and the potentials were reported as SCE.

A surface analysis instrument (VG Microlab Mark III) was used to investigate the composition of passive films. A 2.5 KeV primary electron beam served as a source to generate Auger electrons. The ultra high vacuum of the system was kept at 10^{-9} torr. Depth profiling was performed by filling the chamber with high purity argon generating an argon ion beam of 2.5 KeV. This beam was used to sputter the surface for controlled periods of time.

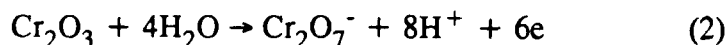
The corrosion rate of materials in DEGDB at 130°C was determined by weight difference before and after test. The specimens were polished with a silicon carbide paper (600 grid), cleaned in an ultrasonic water bath at room temperature, and finally dried in pulsed warm air. After the immersion test, the specimens were cleaned according to the ASTM G1-88 to remove corrosion products. The weight of specimens were measured by microbalance to give a reading of 0.1 mg.

Results

Fig.1 gives the polarization curves of Fe and Fe-based alloys in 2% PTSA solutions. No passive region can be observed in the case of pure Fe. When Fe was alloyed with Cr (430 SS), after passing the corrosion potential (E_{corr}), the anodic current increased continuously with the increase in potential until the passivation potential (E_p) was reached. The current density obtained at E_p was termed as the critical current density (i_{crit}). The i_{crit} was lowered for one order of magnitude with the addition of Ni in Fe-Cr alloys. When Fe-Ni-Cr alloy was alloyed with Mo, the i_{crit} was further reduced to $10 \mu\text{A}/\text{cm}^2$. It is clear that with the addition of alloying elements (Ni, Cr, and Mo) shifted E_{corr} and E_p in the positive directions, while the passive current density (i_p) kept constant. When the potential was more than +1000 mV, the anodic current decreased, suggesting the further oxidation of chromic oxide and can be formed through the following reactions in acidic media:⁶



or



The anodic polarization curves of Ni, Cr, Alloy 600, and Alloy 625 in 2% PTSA are shown in Fig.2. For pure Ni, the multi-peaks were observed in the active region, suggesting the formation of different nickel oxides with increase in potential. Cr was transpassively dissolved at high potential and shows its anti-corrosive superiority in PTSA solutions. The i_{crit} and i_p of Alloy 600 are similar to those of 304 SS, but transpassively dissolved at a more negative potential than that of 304 SS. With the presence of Mo in Ni-Cr-Fe alloy, both the i_{crit} and i_p were substantially reduced. Generally, Ni is active in PTSA solutions and the transpassive behaviour of Ni-Cr-Fe alloys follows that of pure Cr.

The major peaks chosen for this AES study were O (503 eV), Cr (529 eV), Fe (651 eV), and Ni (848 eV). A series of spectra of 304 SS oxide films passivated in 2% PTSA solutions at +200 mV for 30 minutes is given in Fig.3. The spectra of S (151 eV) and C (272 eV) were monitored on the unsputtered surface. Small quantities of the inert gas (Ar (215 eV)) were implanted in the first few surface atomic layers by the sputtering process, as seen in Fig.3(B). Fig.3(C) shows a fully sputtered surface of 304 stainless steel. The oxygen peak was so small that the positive excursion of Cr could be seen on the spectrum.

The depth profiling of 430, 304 and 316 stainless steels are given in Figs.4-6, respectively. The disappearance of the S and C peaks suggests that both components were contaminants. An enrichment of Cr in the passive films of ferritic and austenitic stainless steels can be identified. The Mo peak of 316 SS can hardly be identified and therefore did not present in AES profile diagram.

The corrosion rate of materials as a function of Ni/Cr ratio is given in Fig.7 for specimens immersed in DEGDB for 288 and 1008 h, respectively. A linear relationship can be obtained. Fig.7 also shows the corrosion rate of Mo-containing alloys (316 SS and Alloy 625) tested in DEGDB for 1008 h. An extrapolation of the linearity to Ni/Cr=0 produces a value of ≈ 2 mpy, which is thought to be the corrosion rate for pure Cr.

Discussion

When Cr was alloyed with Fe, such as 430SS, the anodic current substantially reduced and a passive region can be obtained. However, the i_{crit} ($\approx 0.1 \text{ mA/cm}^2$) was still high. The beneficial effect of Ni alloyed with Fe-Cr alloys (304 SS) is to reduce i_{crit} by one order of magnitude and shift E_{corr} and E_p toward more positive potentials, while i_p remained unchanged. The formation of the passive region was believed to be due to the formation of chromium oxide on the metal surface, since a Cr-enriched oxide film was identified by AES analysis (Figs.4-6). Although the passive oxide film may contain nickel oxide, the passive current density of the oxide layer of Fe-Cr-Ni alloys in PTSA solutions is similar to that of Fe-Cr alloys. This is also true for Mo alloyed with Fe-Cr-Ni alloys. Nevertheless, i_{crit} of 316 SS can be considerably reduced.

For Ni-based alloys, with the addition of Cr, i_{crit} of Alloy 600 was reduced by nearly one order of magnitude as compared to that of pure Ni. The further increase of Cr content and with the presence of Mo, i_{crit} of Alloy 625 was significantly reduced by 1.5 orders of magnitude.

When Mo was used as a alloying element, the active current of stainless steel was substantially reduced (Fig.1). For Ni-based alloys, both the active and the passive currents were significantly reduced (Fig.2). When Ni-based alloys were polarized at high potentials, the transpassive behaviour was controlled by Cr.

It should be emphasized that Mo in the absence of Cr may indeed be detrimental to Fe, since Mo allows more rapid dissolution of the Fe component of the oxide.⁷ Mo appears to play a role different from that of Cr; the higher the Cr content of the alloys the more the pronounced effect of Mo.⁸

With Mo alloyed with either Fe- or Ni-based alloys, the anodic active current can be considerably decreased when metals were polarized in PTSA solutions. The suppression of the active region suggests Mo helps in forming the chromium oxide in the early stage. When Fe or Ni is preferentially dissolved, more Cr is left behind (Figs.4-6) and reacts with water to form protective oxide films. The passive film which contains more Cr may thus suppress the anodic dissolution, leading to lower the active current.

It is interesting to note that the corrosion rate of Alloy 600 in DEGDB environment is higher than those of carbon steel (A508), 430 SS and 304 SS, as given in Fig.7. Undoubtedly, the higher the Ni content, the higher the corrosion rate was obtained. This result strongly supports the depassivation of Ni in sulfur compound environment. With the addition of Mo in alloys, the corrosion rate of Mo-containing materials can be reduced to that of pure Cr, shown in Fig.7 as a dotted line. It has been shown that Mo and Cr work cooperatively to form protective oxide film on metal surface.⁷⁻⁸ It seems that even with more Mo contents in alloys the minimum corrosion rate can be obtained is $\approx 2 \text{ mpy}$, since the Mo/Cr ratio of Alloy 625 is 2.7 times higher than that of 316 SS, however, the corrosion rate of the former alloy is roughly the same as that the latter.

Conclusions

Sulfur compounds strongly depassivate high Ni content materials. However, the active current can be significantly decreased by alloying metal with Mo when materials were polarized in PTSA solutions. Mo and Cr act cooperatively to suppress the dissolution. The suppression of the active regions suggests Mo helps provoke the preferential dissolution of Fe or Ni and results in an enrichment of Cr content in the passive film. The minimum corrosion rate of materials studied in DEGDB environment is $\approx 2\text{ mpy}$, disregard the Mo/Cr ratio in alloys.

References

1. R.C. Newman, W.P. Wang, H. Euber, A. Garner, *Corrosion*, 45 (1989): p.282.
2. R.C. Newman, *Corrosion*, 41 (1985): p.450.
3. D. Tromans, L. Frederick, *Corrosion*, 40 (1984): p.633.
4. H.S. Isaacs, B. Vyas, M.W. Kendig, *Corrosion*, 38 (1982): p.130.
5. R.C. Newman, K. Sieradzki, H.S. Isaacs, *Metall. Trans. A*, 13A (1982): p.2015.
6. M. Pourbaix, *Atlas of Electrochemical Equilibria in Aqueous Solutions*, (Pergamon Press, Oxford, 1974), p.546.
7. K. Sugimoto, Y. Sawada, *Corros. Sci.*, 17 (1977): p.425.
8. E.A. Lizlovs, A.P. Bond, *J. Electrochem. Soc.*, 122 (1975): p.719.

Table 1. Chemical composition of materials (Wt%)

	C	Si	Mn	P	S	Ni	Cr	Fe	Mo	Ni/Cr
A508	0.7	0.15	0.8	0.025	0.025	0.4	0.25	bal	0.1	1.6
430SS	0.12	1.0	0.9	0.045	0.03	0.7	15.5	bal	-	0.04
304SS	0.08	0.51	1.7	0.033	0.005	9.2	18.5	bal	-	0.5
316SS	0.08	0.71	1.6	0.029	0.008	12.5	17.5	bal	2.5	0.71
A600	0.08	0.25	0.5	-	-	bal	15.5	8.0	-	4.88
A625	0.05	0.2	0.5	-	-	bal	22.3	2.5	8.5	2.98

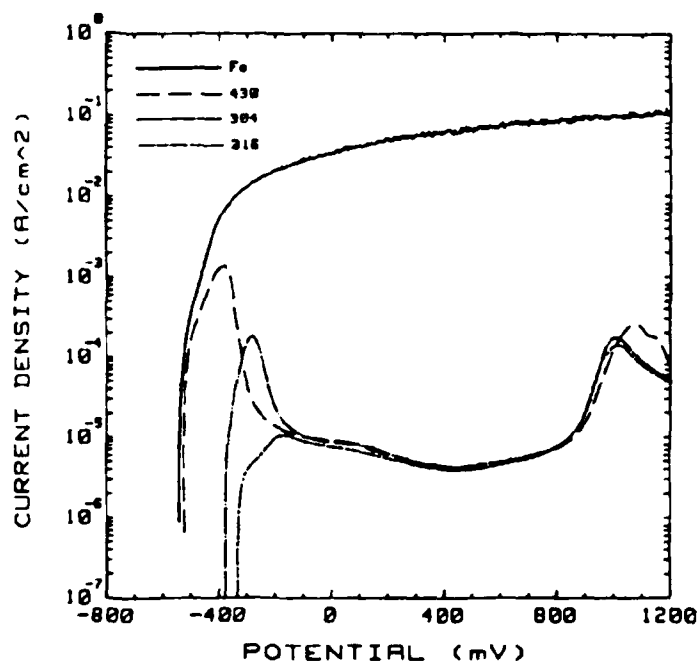


Fig.1 The polarization curves of Fe and Fe-based alloys in 2% PTSA solution at a scan rate of 1 mV/s.

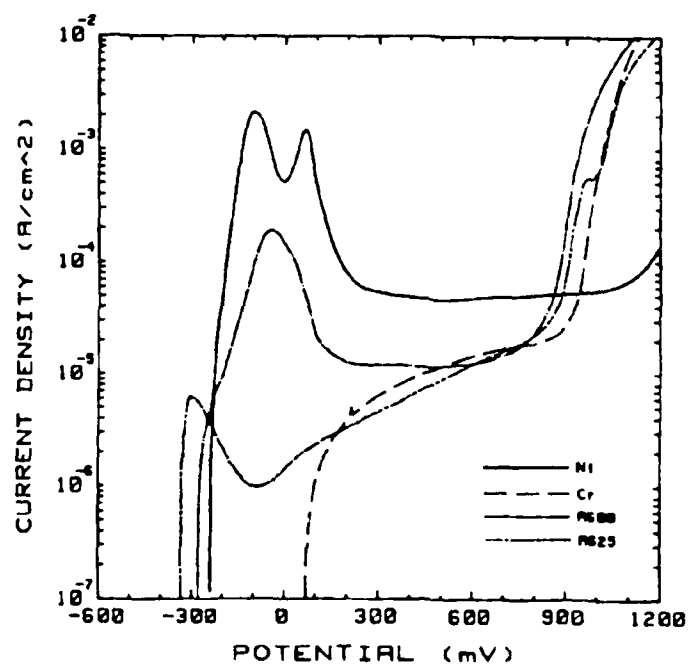


Fig.2 The polarization curves of Ni, Cr, and Ni-based alloys in 2% PTSA solution at a scan rate of 1 mV/s.

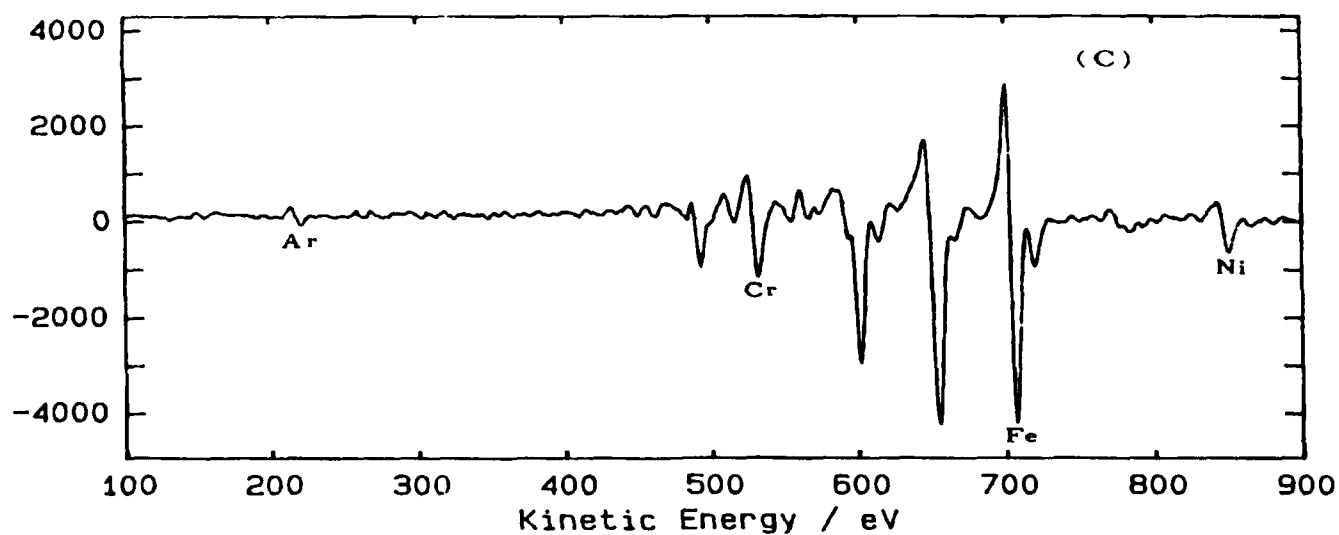
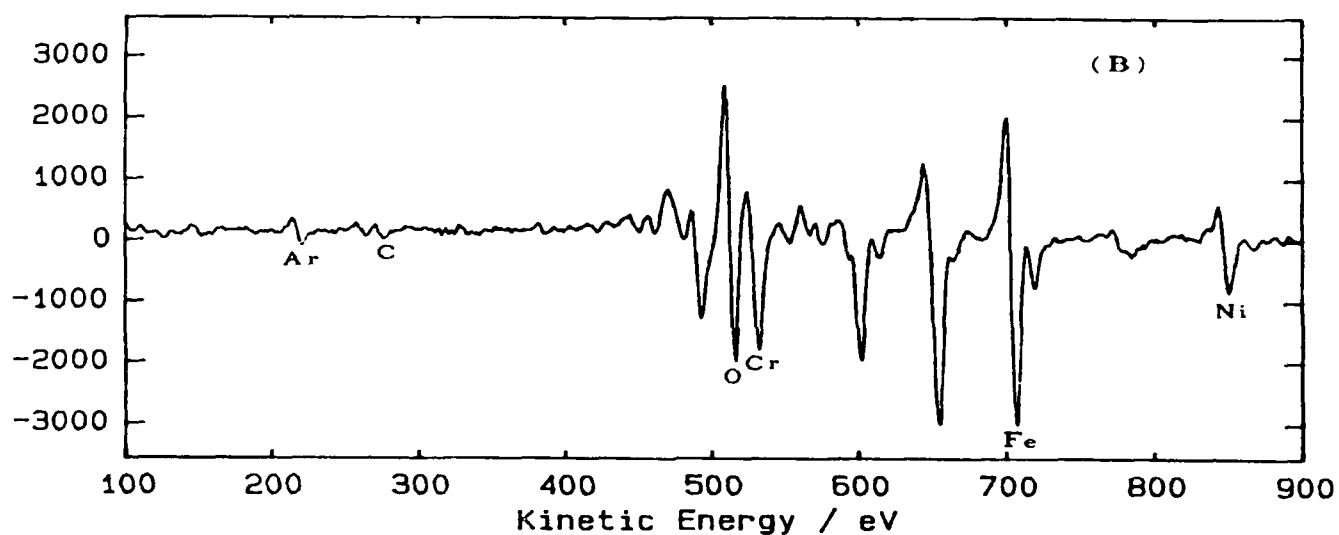
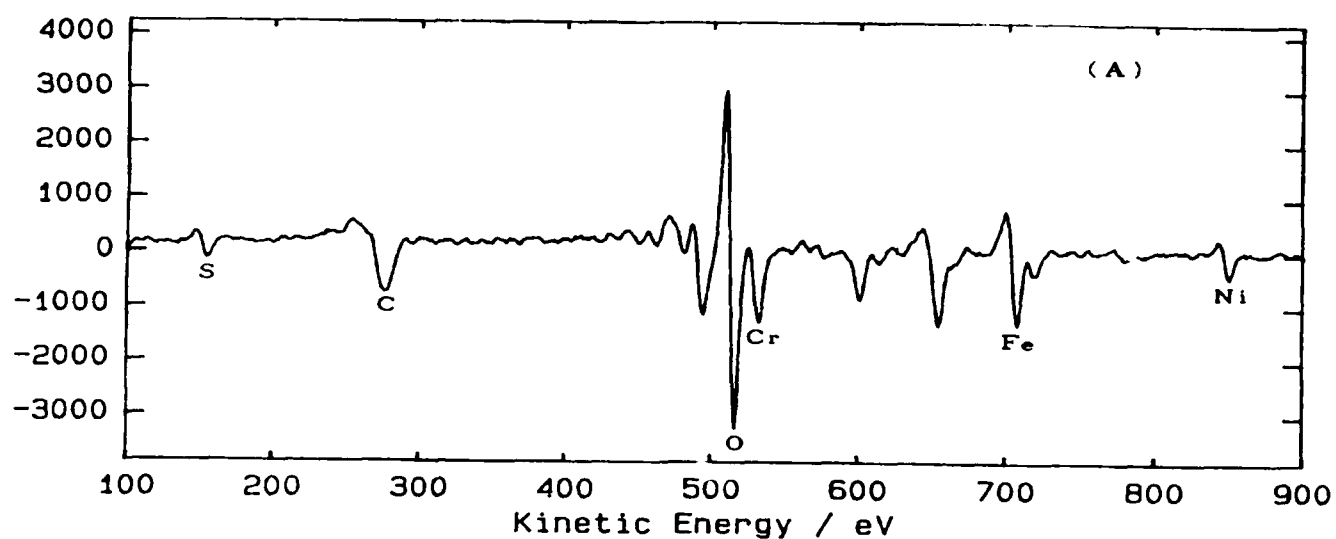


Fig.3 Typical AES spectra of 304 SS passive film passivated in 2% PTSA solution at +200 mV for 30 minutes (A) without sputtering (B) sputtered for 125 seconds (C) sputtered for 445 seconds.

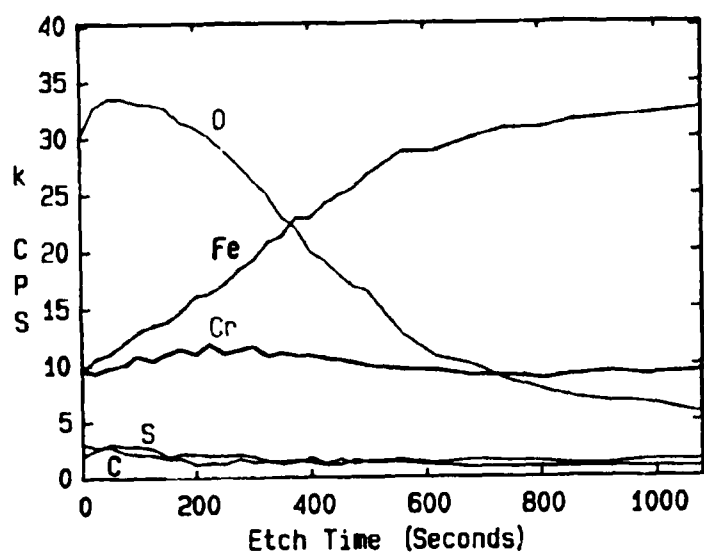


Fig.4 AES Depth profile of 430 SS passive film.

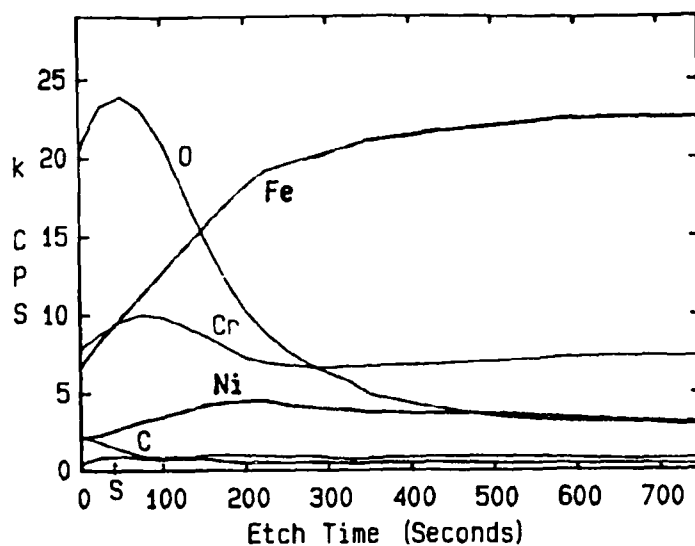


Fig.5 AES Depth profile of 304 SS passive film.

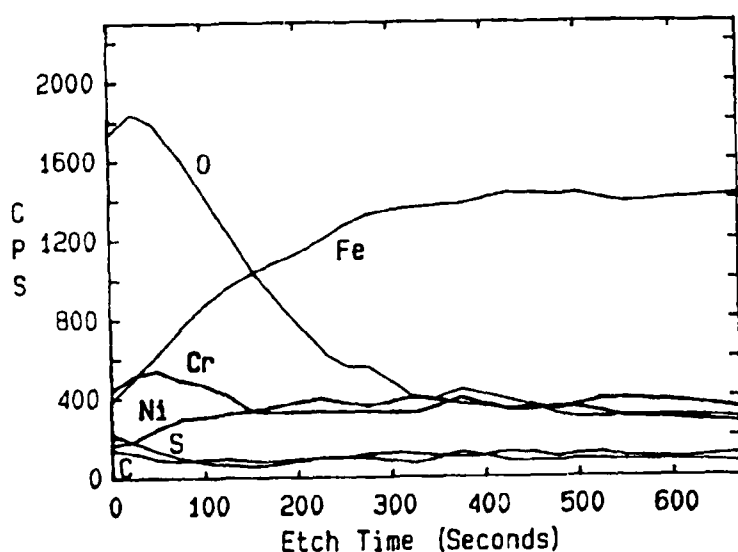


Fig.6 AES Depth profile of 316 SS passive film.

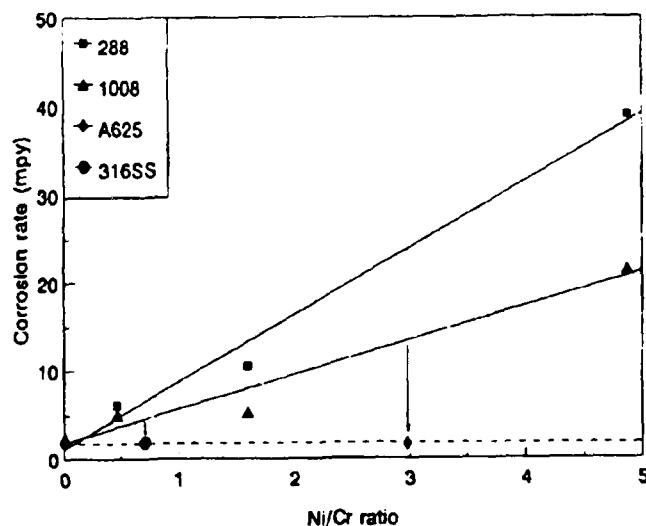


Fig.7 The corrosion rate as a function of Ni/Cr ratio of materials tested for 288 and 1008 h, respectively. The corrosion rates of Mo-containing materials (Alloy 625 and 316 SS) tested for 1008 h were also given in the figure.

Materials Selection Considerations for Vapor Collection Systems at Marine Tanker Facilities

T. G. Dunford and K. R. Lewis
Fluor Daniel, Inc.
3333 Michelson Dr.
Irvine, CA 92730

D. C. Rein
Alyeska Pipeline Service Co.
1835 S. Bragaw St.
Anchorage, AK 99512

Abstract

Selection of piping materials suitable for marine tanker vapor collection systems was determined by in-situ corrosion tests aboard marine crude oil tankers, laboratory immersion corrosion tests, and chemical analysis of fluids sampled from tanker inert gas (IG) systems. Test results have shown severe localized corrosion associated with low pH and high chloride concentration can occur with carbon steel and austenitic stainless steel. Therefore, high performance alloys are recommended for vapor collection piping at facilities loading crude with inert gas blanketing.

Key terms: vapor collection, marine tankers, inert gas, flue gas, chlorides, pH, carbon steel, austenitic stainless steel, duplex stainless steels, nickel alloys.

Introduction

Recent environmental legislation (The Clean Air Act Amendment of 1990) may require the control of volatile organic compounds (VOC's) during the loading of crude oil tankers. The inert gas (IG) vapors used to blanket the cargo spaces of tankers, and displaced hydrocarbon vapor could be collected by an on-shore vapor collection system to prevent venting VOC's to the atmosphere. Tankers use scrubbed flue gases to supply the IG needed to blanket the cargo tanks. A potentially corrosive environment exists whenever the corrosive fluids present in the flue gas scrubbing system become entrained in the IG blanket and are carried over into the vapor collection system.

The proposed vapor control system consists of vapor collection arms to capture and draw-off IG and VOC's from tankers and a large diameter vapor collection line to deliver the vapors to a compressor station where the vapor is sent to the on-shore crude oil tanks or to the incinerators. The system also includes auxiliary equipment such as pumps, valves, and collecting and discharge vessels.

The tanker flue gas scrubbers which provide vapor for IG systems use seawater to scrub the vapors prior to use. A deck seal located downstream from the scrubber serves to maintain positive IG pressure, to isolate the cargo holds from air ingress, and prevent the possibility of any ignition source reaching the cargo tanks from the flue gas system. The vapors are distributed to the various cargo holds by means of a network of piping arranged above the deck and cargo holds of tankers. During loading, these IG vapors along with crude oil vapors are currently expelled to the atmosphere through the mast riser located towards the bow of the tanker. The arrangement of a typical tanker IG system is shown schematically in Figure 1.

Tanker IG systems typically distribute vapors through carbon steel piping coated with coal tar epoxy. Some of these coated carbon steel systems have been in service more than ten years. In the IG system corrosion occurs at the bottom of couplings in the IG header where the coating is easily damaged and liquid normally collects. This problem is handled by rotating the IG piping and repair/re-coating every 3-4 years. These systems are reported to work well on

the tankers with frequent inspection and maintenance. The National Materials Advisory Board recommends coal tar epoxy lining for inert gas piping, with pure epoxy or epoxy phenolic linings as an alternative. Additional recommendations include using a flanged system to permit cleaning and maintenance, low point drains, and tests for coating imperfections¹.

Other equipment in tanker IG systems is constructed either of non-metallics or high performance alloys. Tanker experience indicates that austenitic stainless steel (SS) will fail in this service (primarily through localized corrosion). IG scrubbers have been constructed of austenitic SS, copper alloys and high nickel chromium alloys with limited success, but fiber reinforced plastics (FRP) give good service. The use of various coatings systems has been reported for carbon steel in the IG headers.

Coated carbon steel piping provides good service on crude tankers where regular shipyard maintenance can be scheduled, but is not considered viable for an on-shore vapor collection facility where the proposed system consisting of several thousand meters of large diameter piping must have a high degree of reliability. Under these conditions, a low maintenance system is required. The use of non-metallic material systems such as fiberglass reinforced polyester (FRP) and coated carbon steel were considered for the on-shore facility; however, they cannot be justified for a combination of technical reasons, installation and potential maintenance problems.

In order to validate the materials selection for the proposed vapor collection piping a corrosion test program using a wide range of candidate metallic materials was undertaken, and combined with a program to analyze samples of fluids present in IG vapors. This paper summarizes the results from these programs.

Experimental Procedure

Corrosion Testing

Two separate corrosion testing programs were undertaken. The first test was designed to support the selection of piping materials and was conducted using flat and U-bend standard corrosion coupons (25.4 x 152.4 mm) placed in-situ in the IG system of a tanker during an extended period of crude handling operations. The second test was designed to focus on the crevice corrosion performance of welds, especially duplex SS, and was an immersion test conducted on welded metal coupons in a laboratory using IG system fluid samples from operating tankers. The alloy compositions for coupons used are given in Table 1. In each of the tests the alloy materials tested fall into three classes as follows:

Class I - carbon steel A-516 grade 70 (UNS K02700) - only used for in-situ corrosion testing.

Class II - austenitic SS including: Types 316L (UNS S31603, standard grade and modified with 2.75 % molybdenum content minimum), and 317L (UNS S31703).

Class III - high performance alloys including: 22 % Cr Duplex SS (UNS S31803), 25 % Cr Duplex SS (UNS S32550 & S32750), 6 % Mo Austenitic SS (UNS S31254), Nitrogen modified SS Type 317LNM with 3-4 % Mo (UNS S31726), and Ni-Cr-Mo alloy (UNS N06625).

In-Situ Corrosion Tests

Six corrosion test coupon racks (herein referred to as holders) were exposed in the IG system of a tanker. These holders were assembled using SS hardware insulated with teflon sleeves and non-serrated teflon washers. See Figure 2 showing the in-situ corrosion coupon holder. The holders included pre-weighed corrosion coupons in U-bend (25.4 x 152.4 mm) and flat (25.4 mm x 50.8 mm, welded and unwelded) configurations of the following alloys: carbon steel (flat coupons only) and stainless steels (UNS S31603, UNS S31703), and high performance alloys (UNS S31803, UNS S32550, and UNS S31254).

The holders were located in three branches of IG header close to the cargo tanks. In one location a dam was created in order to partially immerse two coupon holders in the IG fluids present in the header. This was done since more severe corrosion is expected in the vapor condensate which may accumulate in the low points of the proposed vapor collection facility.

The holders were exposed to inert gas vapors being expelled from the tanks. This environment is considered to be very similar to the intended service of the proposed vapor collection system. The nominal composition of the inert gas is 80 % nitrogen, 12-14.5 % carbon-dioxide, less than 5 % oxygen, water, 0.03 % sulfur dioxide, with traces of carbon monoxide, and various oxides of nitrogen. Tanker IG systems operate at ambient temperatures with temperature excursions close to 38°C during loading of the warm crude oil. In addition this location exposed the holder to inert gas vapors supplied directly from the scrubber and deck seal. This is a more severe environment than is expected for vapor collection systems since the scrubber would not normally be in operation during vapor collection.

The first four holders were removed from the tanker after 163 days of service. The fifth holder was removed after 208 days of service. The sixth holder was removed after approximately 300 days of service. All but the sixth holder of coupons were metallurgically analyzed. The analysis consisted of cleaning and weighing all coupons, measuring the extent of localized corrosion (pitting and crevice corrosion), metallographically cross-sectioning through the corrosion site on several test coupons, and conducting a spectrographic chemical analysis of the corrosion by-products of a cross-sectioned coupon in a scanning electron microscope (SEM).

Laboratory Immersion Test

This test included a sampling program to provide test fluids from the IG system of tankers visiting the Alyeska Marine Terminal in Valdez, Alaska. Tankers were regularly sampled for IG fluids during a period from May through August 1992. These fluids were analyzed (using a procedure similar to that described below under "Fluid Sampling" section). Most samples were taken at the end of de-ballasting or the beginning of the crude loading which follows de-ballasting. The fluids were tested for acidity with only those samples less than pH 3 being selected for use in the test. Most had chloride levels greater than 1800 mg/L. The sampled fluids were stored at room temperature after sampling and analysis. The tray was filled with approximately 1.9 liters of fluid. These fluids were then used to immerse corrosion coupons in the as-welded condition for a period of 90 days.

One covered plastic tray partially filled with 1.9 liters of sample fluid was used to immerse the corrosion coupons. The test fluid was maintained at ambient temperature (25°C) and replaced at 2-5 day intervals with a fresh supply of corrosive fluid from storage. The test container was maintained at room temperature and was covered, but was not supplied with an inert gas blanket.

Two racks of pre-weighed coupons were arranged using mounting hardware which was assembled through holes drilled through the weld at the center of each coupon. See Figure 3 showing the laboratory corrosion coupon holder. Crevices were formed by serrated teflon washers used with the mounting hardware. The coupon holder was partially immersed with the fluid level fluctuating at the center of the coupons. In this manner each coupon had a crevice located at the air/fluid interface. The tray contained both racks side by side, each with the same nine welded alloy coupons.

The as welded corrosion coupons used in this test included:

- SS Types 316L (UNS S31603) welded with SS Type 316L filler metal.
- 317LNMO (UNS S31726) welded with SS Type 317L filler metal and welded with Ni-Cr-Mo alloy filler metal.

- 22 % Cr Duplex SS (UNS S31803) welded with 22 % Cr filler metal.
- 22 % Cr Duplex SS (UNS S31803) welded with 25 % Cr over-matching filler metal.
- 25 % Cr Duplex SS (UNS S32750) welded with 25 % Cr filler metal.
- 6 % Mo alloy (UNS S31254) welded with Ni-Cr-Mo alloy (UNS N06625) filler metal.
- Ni-Cr-Mo alloy (UNS N06625) welded with Ni-Cr-Mo alloy (UNS N06625) filler metal.

Based on work from the in-situ corrosion tests, the immersion tests focused on the performance of duplex SS. Other alloys were selected to bracket the anticipated corrosion performance of the duplex SS and offer a way to validate the immersion test relative to the in-situ tests.

Most coupons were welded from plate stock except for the UNS S31603, UNS S31803 and UNS S32750 coupons which were welded from pipe. The coupons varied in thickness between 6.4 mm and 12.5 mm, all were approximately 50.8 mm square, except the UNS S31603 coupons which were welded from pipe (12.5 mm wall thickness) and measured 12.5 x 25.4 x 50.8 mm. All of the corrosion coupons were tested in the welded condition using a 50.8 mm heterogeneous (with filler metal) butt-weld made from one side and located down the center with a 9.5 mm diameter drilled hole centered on the weld. The coupons were exposed with the weld bead intact in order to duplicate the as-fabricated condition.

The S31803 coupons with 22 % Cr Duplex SS filler metal were welded automatically using the Pulsed Gas Metal Arc Welding (PGMAW) process, all other coupons were welded manually using gas tungsten arc welding (GTAW) process.

Fluid Sampling

The IG system on crude tankers is intended to handle gases only; however, liquids originate through either condensation or entrainment of mist from the seawater scrubber. These liquids accumulate at low points; therefore, low point drains proved to be the best locations for sampling. Since each tanker has a differently configured IG system the location of the low point drains vary. To gain a basic understanding of the chemistry of the liquids present in the IG system, eight ships were sampled throughout de-ballasting and loading operations. This sampling occurred several months after the in-situ tests. Liquid collection and analysis for a greater number of ships was conducted concurrent with gathering IG system liquids for the immersion test.

Experimental Results and Discussion

In-Situ Corrosion Tests

The results of the tests are summarized in Tables 2 through 5 corresponding to the four sets of coupon holders analyzed together as a group. Tables 2, 3 and 4 show the results for holders I, II and IV respectively; all of which were located in the vapor space of IG header piping (holders I and II for a duration of 163 days and holder IV for 208 days). Table 5 shows results for holders V and VI which were both located behind the dam set up to immerse the coupon holders for 208 days. Holder III was removed after approximately 300 days but has not been analyzed and the results are not shown here.

Corrosion is grouped according to density as shown in Tables 2 through 5. Density refers to the total number of corrosion sites (pits or crevices) over the surface of the coupon. Added to this is a rating system for depth: Incipient, Mild, Moderate, and Severe based on depth of corrosion. In these tables the data for most coupons includes both numbers of corrosion sites, and the depth of

attack, separated by comma. Cracking was not found in the U-bend coupons. This was anticipated since the exposure temperature was low for stress corrosion cracking (SCC). Localized corrosion in the form of crevice corrosion and pitting distributed over the surface of the bulk coupon (at sites removed from crevice washers) was found on most of the coupons exposed in this test. The depth of corrosion was the deepest at crevices. It is not certain that the coupon holder located behind the dam was immersed in fluid since this location was dry when coupon holders were removed. However, it was noted that the coupons on this holder experienced the greatest amount of corrosion which suggests that the dam did provide intermittent immersion in fluid. This suggests that immersion in the fluids present (as with low point drains) would increase localized corrosion. Based on this it was anticipated that a laboratory immersion test should demonstrate greater localized corrosion on the materials tested.

Next to carbon steel, corrosion was greatest on the immersed UNS S31603 and UNS S31703 coupons (maximum measured depths: 0.61 mm in the crevices over a five month exposure period, corresponding to 1.45 mm per year). These are linear extrapolations of the observed corrosion rates which give conservative estimates (the corrosion rate can decelerate as corrosion by-products fill the larger pits). Figure 4 shows the crevice corrosion found on a flat, welded UNS S31603 coupon.

The results indicate severe attack of carbon steel (Class I material), extensive localized attack of austenitic stainless steels (Class II materials), and satisfactory corrosion resistance of high performance alloys (Class III materials). There was a general correlation between increased number of localized corrosion sites and greater depth of corrosion; however, specific attempt to relate number and depth of corrosion sites was not made.

Laboratory Immersion Test

The coupons removed from the fluid were rinsed, dried, photographed and visually inspected before being lightly scrubbed and reweighed.

The test results are summarized in Table 6. This table lists the coupon number, base metal, weld metal, extent of corrosion, and the weight loss for each coupon. The crevice corrosion has been separated into those locations at the weld metal, the fusion zone, and the weld heat affected zone (HAZ). For consistency the nomenclature used to describe the extent of corrosion for the in-situ corrosion test described above was modified for use for evaluating the results of the laboratory immersion test. The five groupings used above for the quantitative assessment of crevice corrosion have been combined into three groupings for qualitative use to compare the visual results obtained from this test. The three groupings used were: Incipient (< 0.04 mm), Mild to Moderate (< 0.2 mm), and Severe to Very Severe (> 0.2 mm). The examination performed was visual, so the groupings established are approximate, but are considered to be sufficient to compare the results obtained in this corrosion test.

Most coupons exhibited crevice corrosion to some extent. The Class III materials (UNS S32750 and UNS S31254) exhibited very light incipient crevice corrosion; whereas, negligible corrosion had been experienced on UNS S31254 during the in-situ test. This suggests that the laboratory immersion test was a more severe corrosion environment than for the in-situ test, although most of the materials performed similarly. The UNS N06625 coupon did not show any visible crevice corrosion. Only the UNS S31603 coupons showed any surface pitting. The extent and location (or distribution) of crevice corrosion varied from coupon to coupon, with most coupons exhibiting crevice corrosion to some degree in the weld metal. A few of the coupons were corroded in crevices located at the fusion zone (between the base metal and weld metal) or the weld HAZ.

The profile created by the weld bead was raised and uneven making a variable crevice between the weld metal and the washers thus preventing tight crevices from forming adjacent to the weld on some coupons. Large protruding weld beads tended to exhibit crevice attack to the greatest extent toward the weld

centerline where crevice washers made tight contact. Welds which protruded less tended to exhibit more crevice corrosion adjacent to the weld where crevice washers made contact (in the fusion zone or HAZ).

Pitting at locations removed from crevices was only found on UNS S31603 coupons. The UNS S31603 coupons were also the only coupons which exhibited attack on the inner bore of the machined holes used to assemble the coupons onto the holder. No significance is assigned to this corrosion on the inner bore since these locations are not intentional crevices but it does underscore the severity of localized corrosion possible with UNS S31603 in this environment.

The test showed a difference in corrosion performance between the 22 % Cr and 25 % Cr weld filler metal used on the test coupons of the S31803 base metal. Whilst the UNS S31803 base metal showed no significant attack, the 22 % Cr weld metal experienced severe attack for the liquid environment involved with this test. The 25 % Cr weld metal was needed to give comparable corrosion resistance as the UNS S31803 base metal.

Fluid Sampling

The results of the initial fluid sampling study showed that the liquid chemistry varied considerably among various ships. The sampling study confirmed the need for materials which are corrosion resistant in the presence of low pH and high chlorides. The liquid samples varied in pH from 1 to 7 with most samples below 3. The chloride levels varied from 9 to 85,500 parts per million (ppm) with most samples between 10,000 and 30,000 ppm. The high chloride level can be explained by the entrainment of the seawater in IG vapors. The low pH may be attributable to the absorption of sulfur oxide gases by entrained seawater and any condensed moisture present in IG system. IG system liquids collected during, and used for the immersion test showed similar ranges and are listed in Table 7.

Summary and Conclusions

The performance of the alloys in these corrosion tests correlates closely to the level of alloying present. Level of alloying is also related to cost. The results of these tests validate the use of high performance alloys wherever there will be accumulations of vapor condensate containing acidic aqueous chlorides in on-shore marine tanker IG vapor collection facilities. UNS S31803 with 25 % Cr filler metal, UNS S32750, UNS S31254, and UNS N06625 all performed well in the welded condition without any severe corrosion. This justifies selective use of these materials for especially severe services where low piping maintenance is required. Overall, UNS S31803 with 25 % Cr (over-matching) filler metal is recommended for bulk piping since it provides a cost effective materials selection with adequate performance in the corrosion test programs undertaken.

Acknowledgements

The authors wish to thank to the Alyeska Pipeline Service Company for allowing the publication of this information.

References

1. "Materials Aspects of Inert Gas Systems for Cargo Tank Atmosphere Control", National Materials Advisory Board Publication NMAB-372, National Academy of Sciences, Washington D. C. , 1980.

TABLE 1: Alloy Compositions

COMPOSITION (Wt %)

ALLOY		C	Cr	Cu	Mn	Mo	N	Ni	Fe
NAME	UNS #								
A516	K02700	0.27 max.			0.79 - 1.3				bal.
316L	S31603	0.03 max.	16 - 18		2.0 max.	2 - 3		10 - 14	bal.
317L	S31703	0.03 max.	18 - 20		2.0 max.	3 - 4		11 - 15	bal.
317LNMO	S31726	0.03 max.	17 - 20	0.75 max.	2.0 max.	4 - 5	0.1 - 0.2	13.5 - 17.5	bal.
2205	S31803	0.03 max.	21 - 23		2.0 max.	2.5 - 3.5	0.08 - 0.12	4.5 - 6.5	bal.
F255	S32550	0.04 max.	24 - 27	1.5 - 2.5	1.5 max.	2 - 4	0.1 - 0.25	4.5 - 6.5	bal.
2507	S32750	0.03	25		1.2 max.	4	0.3	7	bal.
254SMO	S31254	0.02 max.	19.5 - 20.5	0.5 - 1.0	1.0 max.	6 - 6.5	0.18 - 0.22	17.5 - 18.5	bal.
I625	N06625	0.10 max.	20 - 23		0.5 max.	8 - 10		bal.	5.0 max.

Table 2 Summary of Results of In-Situ Corrosion Test Holder I
Location 2C Vapor Exposure Time 163 Days

Coupon			Crevice Corrosion				Pitting			Max. Depth (mm)	
	Alloy (UNS #)		Side 1	Side 2			Top Surface	Bottom Surface	Sides	Surfaces	Sides
Flat Coupons	K02700	as-rec'd	Heavy General Corrosion				-	-	-	-	-
	S31603	as-rec'd	Sample Cut Up				-	-	-	-	-
		welded	>20, Sev.	>20, Mod.			<10, Sev.	<5, Sev.	<5, Sev.	0.16	N
	S31703	as-rec'd	N	>5, Mild			N	N	N	0.03	N
		welded	<10, I	<10, Mild			N	N	N	0.02	N
	S31803	as-rec'd	N	N			N	N	N	N	N
		welded	N	N			N	N	N	N	N
	S31254	as-rec'd	N	N			N	N	N	N	N
		welded	N	N			N	N	N	N	N
	S32550	as-rec'd	N	N			N	N	N	N	N
		welded	N	N			N	N	N	N	N
U-Bend Coupons			Side 1	Side 2	Side 3	Side 4					
	S31603	as-rec'd	>10, Mild	>10, Mild	>10, Mild	N	<20, Mod.	<20, Mod.	>20, Sev.	0.11	0.25
	S31703	as-rec'd	N	>10, Mild	N	N	>10, I	N	N	N	N
	S31803	as-rec'd	N	N	N	N	N	N	N	N	N
	S31254	as-rec'd	N	N	N	N	N	N	N	N	N
	S32550	as-rec'd	5I	N	N	N	N	N	N	N	N

**Table 3 Summary of Results of In-Situ Corrosion Test Holder II
Location 2C Vapor Exposure Time 163 Days**

Coupon			Crevice Corrosion				Pitting			Max. Depth (mm)	
	Alloy (UNS #)		Side 1	Side 2			Top Surface	Bottom Surface	Sides	Surfaces	Sides
Flat Coupons	K02700	as-rec'd	General Corrosion								
	S31603	as-rec'd	<10, Mod.	<5, Mod.			<5, Mod.	-	>20, Sev.	0.08	0.20
		welded	>20, Mod.	>20, Mod.			<10, Mod.	>5, Mild	<5, V.S.	0.11	0.35
	S31703	as-rec'd	N	<5, I			N	<5, I	N	0.08	I
		welded	N	N			N	N	N	N	N
	S31803	as-rec'd	N	N			N	N	N	N	N
		welded	N	N			N	N	N	N	N
	S31254	as-rec'd	N	N			N	N	N	N	N
		welded	Sample Cut-Up				-	-	-	-	-
U-Bend Coupons	S32550	as-rec'd	N	N			N	N	N	N	N
		welded	N	N			N	N	N	N	N
			Side 1	Side 2	Side 3	Side 4					
	S31603	as-rec'd	>20, Sev.	>10, Mild	<10, Mild	>10, Mild	>20, Mild	>20, Mild	>20, V.S.	0.15	0.39
	S31703	as-rec'd	>10, Mild	>10, Mild	>20, Mild	N	<5, Mild	N	N	0.12	I
	S31803	as-rec'd	<10, Mild	5, Mild	N	N	N	N	N	N	N
	S31254	as-rec'd	N	N	N	N	N	N	N	N	N
	S32550	as-rec'd	N	N	N	N	N	N	N	N	N

xx, yyyy
xx = number of corrosion sites
yyyy = depth of attack per legend

Legend:
N (Negligible)
I (Incipient) < 1 mil (0.025 mm)
Mild 1 < mils < 2 (0.05 mm)
Mod. (Moderate) 2 < mils < 5 (0.075 mm)
Sev. (Severe) 5 < mils < 10 (0.25 mm)
V.S. (Very Severe) > 10 mils (0.25 mm)

**Table 4 Summary of Results of In Situ Corrosion Test Holder IV
Location 5C Vapor Exposure Time 208 Days**

Coupon			Crevice Corrosion				Pitting			Max. Depth (mm)	
	Alloy (UNS #)		Side 1	Side 2			Top Surface	Bottom Surface	Sides	Surfaces	Sides
Flat Coupons	K02700	as-rec'd	Heavy General Corrosion Except Under Washes								
	S31603	as-rec'd	<20, Mod.	>20, Mod.			>20, Mod.	>20, Mod.	>20, Sev.	0.24	0.32
		welded	>20, Mod.	>20, Mod.			<10, Mild	<10, Mild	>20, Sev.	0.11	0.16
	S31703	as-rec'd	<5, Mild	>10, Mild			<5, Mild	<5, Mild	Mild	0.07	I
		welded	>10, Mild/Mod	>20, Mild			<5, Mild	<5, Mild	>5, Mild	0.09	I
	S31803	as-rec'd	N	N			>5, I	>5, I	N	I	N
		welded	N	N			N	N	N	N	N
	S31254	as-rec'd	N	N			N	N	N	I	N
		welded	N	N			<5, I	<5, I	N	N	N
U-Bend Coupons	S32550	as-rec'd	N	N			N	N	N	N	N
		welded	N	N			N	N	N	N	N
			Side 1	Side 2	Side 3	Side 4					
	S31603	as-rec'd	10 %, Sev.	10 %, Sev	50 %, Sev	N	>20, Sev.	>20, Sev.	>20, Sev.	0.09	0.21
	S31703	as-rec'd	>10, Sev./Mod	>20, Mild	>20, Mild	N	<5, Mild	<5, Mild	N	0.11	N
	S31803	as-rec'd	N	N	N	N	N	N	N	N	I
	S31254	as-rec'd	N	N	N	N	N	N	N	N	N
	S32550	as-rec'd	5 I	N	N	N	N	N	N	N	N

Table 5 Summary of Results of In Situ Corrosion Test Holder V & VI
Location 6S Liquid Condensate Exposure Time 163 Days

Coupon			Crevice Corrosion				Pitting			Max. Depth (mm)	
	Alloy (UNS #)		Side 1	Side 2			Top Stamp	Bottom	Sides	Surface	Sides
Flat Coupons Holder V	K02700	as-rec'd	Severe General Corrosion								
	S31603	as-rec'd	Sample Cut Up								
		welded	>20, Sev.	>10, Sev.			>20, Sev.	>20, Sev.	>20, Sev.	0.19	0.40
	S31703	as-rec'd	>20, Sev.	>20, Sev.			N	<10, Mild	<20, Mild	0.14	-
		welded	N	N			<20, Mild	<10, Mild	>20, Mod.	0.12	-
	S31803	as-rec'd	N	N			N	N	N	N	N
		welded	N	N			N	N	N	N	N
	S31254	as-rec'd	N	N			N	N	N	N	N
		welded	N	N			N	N	N	N	N
	S32550	as-rec'd	N	N			N	N	N	N	N
		welded	N	N			N	N	N	N	N
U-Bend Coupons Holder VI			Side 1	Side 2	Side 3	Side 4					
	S31603	as-rec'd	80 %, V.S.	20 %, V.S.	N	15 %, V.S.	>20, V.S.	>20, V.S.	>20, V.S.	0.46	
	S31703	as-rec'd	20 %, V.S.	90 %, V.S.	N	40 %, V.S.	<10, Mild	>10, Mild	<5, Mod.	0.36	I
	S31803	as-rec'd	10 %, I	I	N	N	N	N	N	N	N
	S31254	as-rec'd	N	N	N	N	N	N	N	N	N
	S32550	as-rec'd	N	N	N	N	N	N	N	N	N

xx, yyyy

xx = number of corrosion sites (or % of coupon surface)
yyyy = depth of attack per legend

Legend:

N (Negligible)

I (Incipient) < 1 mil (0.025 mm)

Mild 1 < mils < 2 (0.05 mm)

Mod. (Moderate) 2 < mils < 5 (0.075 mm)

Sev. (Severe) 5 < mils < 10 (0.25 mm)

V.S. (Very Severe) > 10 mils (0.25 mm)

TABLE 6: Assessment of Laboratory Immersion Corrosion Coupons

COUPON #	BASE METAL (UNS #)	WELD METAL	CREVICE CORROSION				WEIGHT LOSS (grams)
			WELD	FUSION	HAZ	OVERALL	
RACK I							
1	S31603	316L	S	S	-	S	0.62
2	S31603	316L	S	-	-	S	0.62
3	S31726	317L	S	M	I	S	0.11
4	S31726	I625	M	M	-	M	0.03
5	S31803	22 Cr	S	S	-	S	0.07
6	S31803	25 Cr	I	-	-	I	0.00
7	S32750	25 Cr	I	-	-	I	0.01
8	S31254	I625	I	I	I	I	0.01
9	N06625	I625	-	-	-	-	0.03
RACK II							
10	S31603	316L	S	S	-	S	0.56
11	S31603	316L	M/S	-	-	M/S	0.60
12	S31726	317L	S	S	I	S	0.11
13	S31726	I625	I	S	-	S	0.03
14	S31803	22 Cr	S	M	-	S	0.04
15	S31803	25 Cr	I/M	-	-	I	0.00
16	S32750	25 Cr	I	-	-	I	0.01
17	S31254	I625	-	I	I	I	0.01
18	N06625	I625	-	-	-	-	0.03

I = Incipient Corrosion

M = Mild to Moderate Corrosion

S = Severe to Very Severe Corrosion

Table 7
Summary of Immersion Test Liquid Chemistry

Exposure Period (Days)	pH	Chloride (mg/L)
1 - 2	2.6	5900
3 - 6	2.7	9500
7 - 8	2.2	650
9 - 13	2.5	21000
14 - 15	2.7	9500
16 - 17	2.1	450
18 - 20	2.1	24000
21 - 22	2.6	320
23 - 24	2.5	1800
25 - 29	2.1	33000
30 - 31	2.2	3000
32 - 34	2.1	24000
35 - 36	2.6	16000
37 - 38	1.8	16000
39 - 41	2.4	16000
42 - 43	2.5	1800
44 - 45	2.1	33000
46 - 48	2	25000
49 - 50	2.4	19000
51 - 52	2.7	5900
53 - 55	2.2	28500
56 - 57	2.5	16000
58 - 59	2	16000
60 - 62	2.5	16000
63 - 64	2.6	19000
65 - 66	2	15000
67 - 69	2.4	13000
70 - 71	2.5	16000
72 - 73	2.7	26000
74 - 76	2.3	16000
77 - 78	2	15000
79 - 80	2.8	26000
81 - 83	2.3	180
84 - 85	2.3	16000
86 - 87	2	15000
88 - 90	2.3	16000
91 - 92	2.8	26000

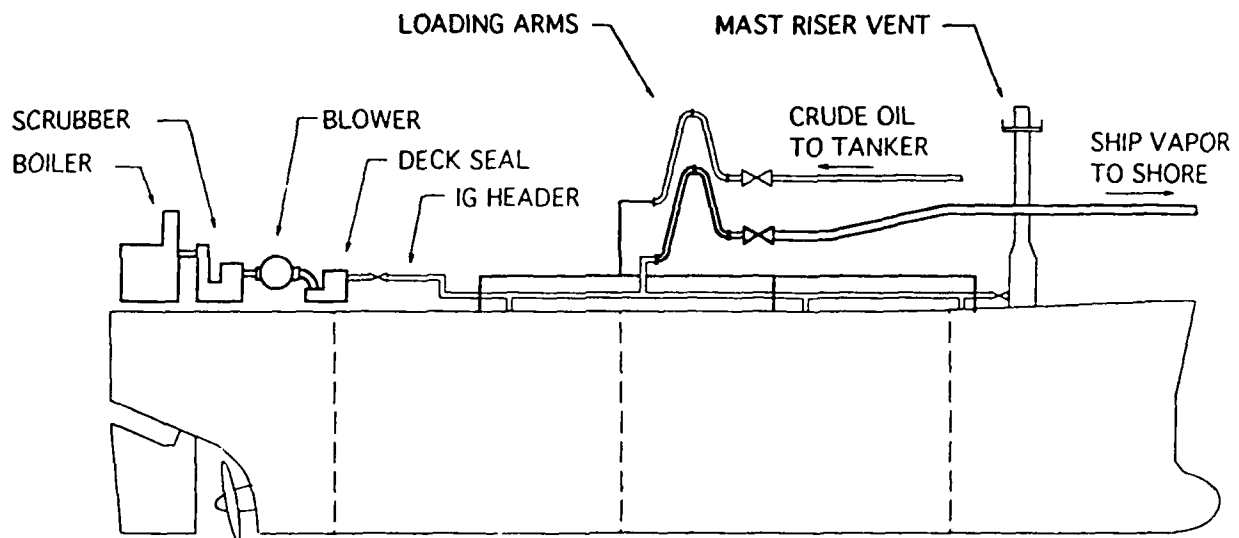


FIGURE 1. Schematic of Typical Marine Tanker IG System

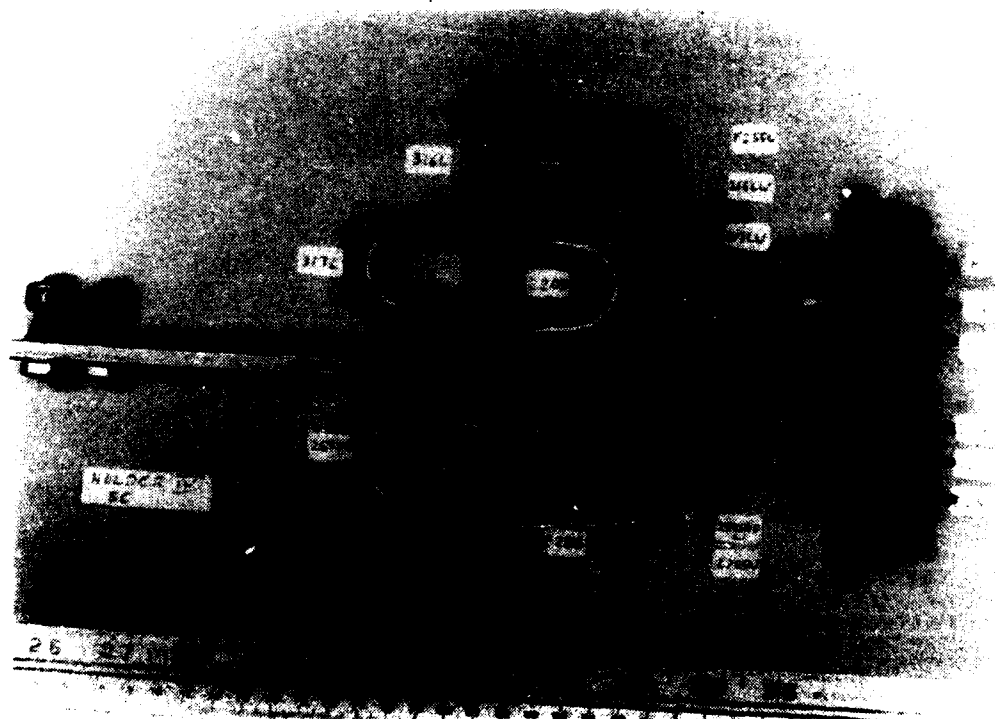


FIGURE 2. In-Situ Corrosion Test Coupon Holder

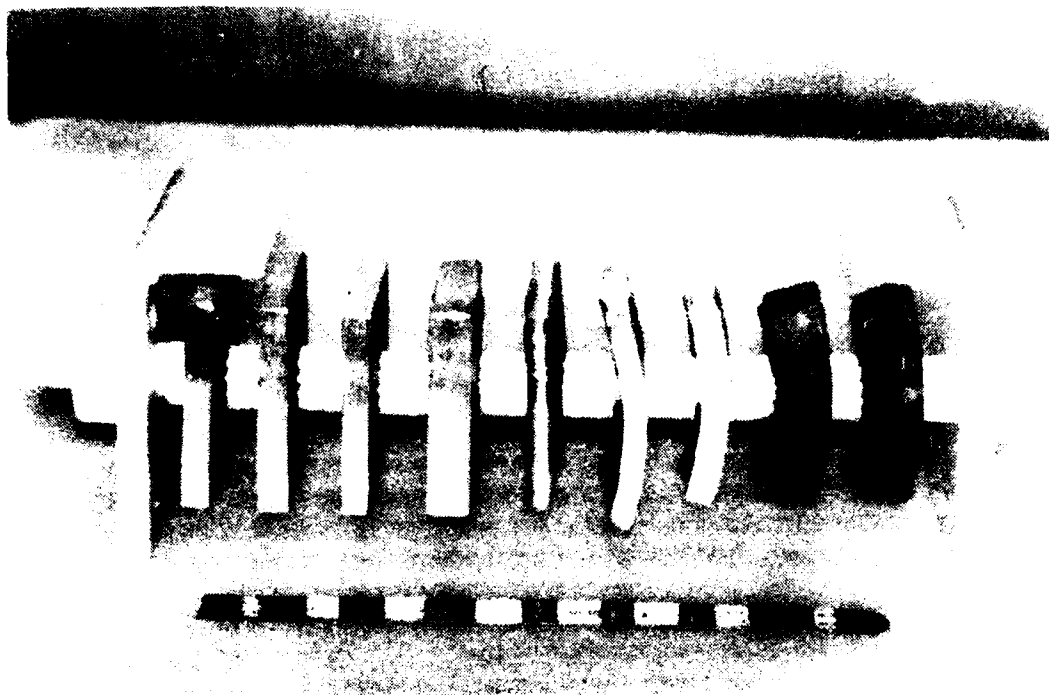


FIGURE 3 Laboratory Immersion Corrosion Test Coupon Holder



FIGURE 4 Crevice Corrosion on Type 316L SS from In-Situ Corrosion Test

Cracking of Weldments in Feed Water Deaerator Systems

T G Gooch, D N Noble and R A Walker
TWI
Abington Hall
Abington
Cambridge CB1 6AL, UK

Abstract

Factors influencing cracking of deaerator water storage vessels have been examined. Carbon and microalloyed steels and shielded metal arc weldments were employed with static, slow strain rate and fluctuating load test procedures. The effects were examined of varying water oxygen level, pH and temperature, and crack growth rate was evaluated under severe environmental conditions.

No cracking was found in statically loaded samples in water at 95°C, at pH7 or 9 and with nominally 5ppb or 2000ppb oxygen. Cracking in slow strain rate tests was induced at high oxygen levels, susceptibility being lower with pH7 rather than pH9 and at 100°C rather than 150°C. No significant cracking was found even at 150°C with 5ppb oxygen. Measured crack growth rates were about 10^{-6} mm/s.

It was concluded that cracking occurred by rupture of an otherwise protective magnetite film, with ensuing localised corrosion of the bare metal. Effects of material composition and microstructure were secondary to those of environmental conditions and service loading regime. Hence, deaerator cracks form primarily under conditions in which plastic strain is experienced at fairly high oxygen levels and at above 100°C. This indicates that cracking takes place mainly under transient conditions, whether plant warm up/shut down or when dynamic strain is experienced from temperature/pressure fluctuations, water hammer etc.

Key terms: deaerators, steel, welds, stress corrosion cracking, corrosion fatigue

Introduction

Weld area cracking in feed water deaerator systems fabricated from carbon and C-Mn steels has become recognised as a major problem in recent years. Some 30–40% of deaerator vessels may exhibit such cracking, (1–7), mainly at welds, either longitudinal or circumferential seams, or associated with attachments, eg nozzles or baffles.

Specific factors controlling the incidence of cracking have not been identified, nor the cracking mechanism, which has been described as thermal fatigue, corrosion fatigue, stress induced corrosion, stress corrosion cracking and hydrogen embrittlement (8). The cracks have, however, mainly formed below the water level in the different types of deaerator that have suffered the problem, and clearly result from environmental action. Present palliative measures are based on minimising service loads, whether static or cyclic from temperature/pressure fluctuations, water hammer etc, and on providing good water quality (9). Postweld heat treatment for stress relief has been advocated (7), with regular inspections being deemed advisable during service life (9). The present programme had two main aims. First, it was necessary to identify conditions under which deaerator cracking is most likely in order that guidelines may be provided on avoiding future failures. Second, data on crack growth rate were required to assist formulation of inspection schedules with non-destructive examination (NDE).

Experimental Programme

Approach

In most cases, deaerator cracking has developed only after a fairly long service lifetime, up to an average of 15 years (10). Accelerated laboratory test procedures were thus required. The approach adopted allowed both an increased corrosivity of operating environment and the application of severe stress conditions. In Phase 1, behaviour was examined under fairly low temperature conditions relative to normal deaerator practice, such that the surface oxide film was "defective" and afforded only inferior protection. Static load was employed, and the samples were subjected to repeated simulation of shutdown conditions. Specimens in Phase 2 were assessed by slow strain rate testing (SSRT) to obtain failure in high temperature, high pressure water; environmental and loading conditions were varied, and the effects examined of material type and microstructural changes associated with welding. Crack growth rates were measured in Phase 3, employing environmental conditions identified as

severe from Phase 2. Pre-cracked linear elastic fracture mechanics samples were tested under static, incrementally rising or fluctuating load.

Materials and Welding Procedure

Two steels were used, namely a 10mm carbon steel to BS1501: 161 grade 430 (plate 1) and a 20mm microalloyed steel to BS1501: 224 grade 490 (plate 2) (Tables 1 and 2). Multipass shielded metal arc (SMA) butt welds were produced (Table 3) with a single bevel weld preparation to give a straight fusion boundary perpendicular to the plate surface and facilitate testing of the heat affected zone (HAZ). For steel 1, rutile coated electrodes to BS639: E4333 R21 were employed, with basic coated electrodes to BS639: E5154 B120 26 (H) for the microalloyed material 2. Analyses were performed at the weld centres (Table 1). Metallographic examination and Vickers hardness measurements were carried out.

Phase 1: Static Load Tests

Cross-weld specimens 100x12x5mm were machined from steel 1 for testing in four point bend. Since there might have been some stress relaxation with time in the test rigs, U-bend samples 110x12x5mm from both steels were also produced. Prior to testing, samples were heated in water of pH9 with about 5ppb oxygen (determined by an Orbisphere instrument) in an autoclave at 200°C for 40 hrs. When removed, the specimens were coated in an adherent black scale of about 5µm thickness, confirmed as magnetite by X-ray diffraction.

Tests were carried out at high and low oxygen and pH conditions, at 95°C (Table 4). The feed water was deionised with a conductivity below 0.2µS/cm, and pH was adjusted as required with ammonium hydroxide. To produce a high oxygen content, the water was purged with air at room temperature for 2 hours. This gave about 8000ppb oxygen, and, on heating to the test temperature, an oxygen level of 2000ppb (measured at room temperature) could be maintained. To obtain a low oxygen content, the water was sprayed down a column against a counterflow of nitrogen gas: oxygen figures as low as 1ppb were reached.

The cross weld specimens were tested using rigs shown in Fig.1, calibrated via a parent material sample with a strain gauge attached to the top surface. All tests were carried out with an outer fibre stress nominally equal to the parent steel yield stress. Unstressed samples were exposed for comparison. The U-bend samples were bent conventionally to give a diameter of 5 x thickness. The load was maintained using steel bolting.

Samples and test assemblies were immersed in the required solution at 95°C with reflux condensers to avoid evaporation. A simulated shutdown period was undertaken three times per week. The vessels were cooled to room temperature, and the oxygen content of the water increased to about 8ppm. After 2 hours, the "correct" test solution was produced and the vessels were reheated to 95°C. Samples were removed after varying test durations. These were visually examined, and a metallographic section taken transverse to the weld. The scale on the samples was analysed using X-ray diffraction.

Phase 2: Slow Strain Rate Tests

Round section tensile samples were produced with 16 x 3.5mm gauge length, from parent steels and weld metals. Specimens were also prepared transverse to the weld in plate 1, and parallel to the weld in plate 2 to include as much as HAZ as possible along the gauge length. All samples were magnetite coated prior to test.

Solutions were prepared as in Phase 1 with initial room temperature oxygen contents of nominally 5 and 5000ppb and pH levels of 7 and 9. Because of partitioning between the gas and liquid phases in the autoclave, the oxygen level in solution during test could not be defined exactly. A loop was incorporated into the system so that, directly a sample failed, water could be pumped from the autoclave, cooled to room temperature for Orbisphere measurement, and returned to the autoclave which was still at about 150°C. Thus, the sample analysed should not have been subject to significant oxygen pick up from the gas phase at temperatures below that of the autoclave. In repeat trials at high oxygen level, the initial oxygen content of the water was 9000-9700ppb: this was reduced at test temperature, and sampling using the loop gave oxygen contents of 150-500ppb. Under low oxygen test conditions, an initial content of 2ppb was measured, and this increased to 4ppb during tests at temperature. Tests were carried out at 150°C, with limited studies at 100°C. For comparison, tests were undertaken in pure nitrogen gas as an inert environment. Individual samples were loaded, the autoclave was

sealed and nitrogen purged, and the test solution was then admitted. Heating to the required temperature was by external resistance mats, the temperature being controlled by an internal thermocouple.

Tests were undertaken at strain rates in the range 10^{-5} to 10^{-6} /sec. Conventional monotonically increasing load was normally employed, but in some cases the load was cycled, either via small temperature fluctuations or mechanically. Following failure, the maximum load was recorded, together with the sample elongation and reduction in area. One of the broken portions of each specimen was sectioned longitudinally and prepared for metallographic examination.

Phase 3: Crack Growth Rate Studies

Single edge notch tension (SENT) specimens 60x25x9mm were machined from steel 1 (12mm total crack depth), and magnetite coated. From Phase 2, cracking was most pronounced under high oxygen conditions. Testing was therefore based on deionised water of pH9, overpressurised with air at 150°C.

From tests in room temperature air, stress intensity levels were determined corresponding to general plastic deformation (K_Q) and maximum load (K_{max}). The tests (Table 5) proceeded to maximum load, without failure, and specimens were broken open in liquid nitrogen for fatigue crack measurement. The values for K_Q and K_{max} calculated (11) were taken to define loading conditions for the autoclave tests, but should not be regarded as exact: elastic behaviour is assumed, whereas, with the fairly low strength steel involved, the high loads applied for some tests will have led to significant plastic strain. A direct current potential drop (DCPD) technique was employed to monitor crack growth during testing. Calibration was conducted by making saw cuts to different depths in duplicate samples and monitoring the change in potential. Voltage readings were normalised by reference to plain metal adjacent to the crack. The DCPD leads were attached to an individual sample, which was loaded into the autoclave. The test solution was admitted, the assembly heated to 150°C, and the load applied.

Four loading regimes were examined. First, static load was applied over a period of time. Second, if no static crack growth was evident, the load was increased by 5% increments until stable cracking or sample rupture occurred: the aim was to obtain a measure of the critical stress intensity for crack growth, K_{SCC} . A test with increasing load was performed also in nitrogen at 150°C to determine whether or not low temperature creep was responsible for any crack growth. Third, an attempt was made to identify the K_{SCC} under load shedding conditions, the load being reduced once crack extension had occurred. Finally, some samples were cycled over a range of stress intensity, both within nominally elastic conditions, and with higher peak stress intensity corresponding to some plastic strain. As an extreme case, one sample was subjected to a concurrent temperature variation, being cooled to room temperature and off loaded at the start of each cycle.

Some specimens fractured while on test. Unbroken samples were normally broken open for measurement of crack face, although some samples were sectioned in a longitudinal plane at about one third thickness for metallographic examination, the unmounted portion again being broken open for crack measurement.

Results

Metallurgical Examination of Test Welds

Figure 2 shows a typical weld section. Both steels had a banded ferrite-pearlite structure (Fig.3a). The HAZ microstructure in both steels comprised ferrite with aligned second phase and martensite, although the martensite content and resultant hardness (Table 6) were higher in steel 2 (Fig.3b), reflecting the relative steel hardenability. Weld metal 1 microstructure consisted of grain boundary ferrite, ferrite with aligned second phase, and a small amount of acicular ferrite. In contrast, weld 2 deposit microstructure was largely acicular ferrite, although containing grain boundary ferrite and some ferrite with aligned second phase (Figs.3c and d).

Phase 1: Static Load Tests

Low oxygen, pH9 conditions produced an adherent, black magnetite scale; high oxygen, pH7 solution resulted in a similar black scale, largely covered in a thicker, soft, rust coloured iron oxide; and in the high oxygen, pH9 environment a very thick (3-4mm), hard, rust coloured scale was present. These differences persisted throughout the exposure periods and were similar for both unstressed and stressed samples, whether 4-point or U-bend. There was no difference between deposits on tension or compression sides. Similar observations were made for

both steels and welds tested. From X-ray diffraction on steel 1, the scales in all three environments were largely magnetite with some ferric oxide (Fe_2O_3), and, in the high oxygen, pH7 solution, some cementite.

The corroded metal surface had an irregular profile. General metal loss had occurred, but with a tendency to penetration in the form of open pits, more especially for the pH9, low and high oxygen conditions, in which slightly enhanced weld metal attack was also noted (Fig.4). No significant cracking was found in either steel. Crack-like intrusions were observed on the tensile faces of the U-bend samples from the microalloyed steel 2 at pH7 (Fig.4c), but total extension beyond the corroded surface was less than 0.1mm.

Phase 2: Slow Strain Rate Tests

Condition 1 - 150°C Nitrogen, Strain Rate $10^{-6}/\text{s}$. No evidence of cracking (apart from the final rupture) or corrosion was observed. (Table 7 and Fig.5). Tensile strengths were apparently higher in the SSRTs than in Table 2, possibly a consequence of the use of slower strain rates, as evidenced by the test at $10^{-5}/\text{s}$. Cyclic loading produced ductility values below those from constant strain rate tests. Plate 2 showed greater reduction of area than steel 1, as in room temperature tensile tests (Table 2).

Condition 2 - 150°C Water, 5ppm O_2 , pH9, Strain Rate $10^{-6}/\text{s}$. All tests with monotonic loading gave a decrease in reduction of area at failure compared to that in nitrogen. The test sample from steel 1 that underwent cyclic loading produced the lowest RE/RN value and had extensive cracking, along the gauge length and extending up the shoulder (Fig.6). Shallow pitting was evident. The microalloyed steel 2 showed an average RE/RN of 0.8 as opposed to 0.4 for plate 1. However, samples from plate 2 displayed cracking and corrosion as in the plate 1 tests, albeit mainly in the necked region (Fig.7). The crack morphology was similar for both plates, with transgranular growth and oxide on the crack faces (Fig.7c).

Considering the all weld metal samples, there was less effect of the environment on weld W2 than on W1. Only W1 suffered extensive surface corrosion and contained a number of small oxide-filled cracks. The cross weld sample from plate 1 also failed in the weld metal giving a low apparent RE/RN value, again with widespread pitting and cracking. The HAZ of plate 2 appeared more susceptible than the parent microalloyed steel with an average RE/RN of 0.6. Away from the final rupture, the crack depth was greater in the HAZ than in adjacent parent steel (Fig.8).

Condition 3 - 150°C Water, 5ppm O_2 , pH9, Strain Rate $10^{-5}/\text{s}$. Steel 1 showed little cracking, but shallow, oxide-filled pits. From the RE/RN value of 0.8, environmental cracking had occurred, but the strain rate of $10^{-5}/\text{s}$ was less damaging than $10^{-6}/\text{s}$.

One sample underwent cyclic loading by means of a fluctuating temperature. A reference test in nitrogen was not conducted, but the reduction of area at failure of 15% was low, implying that temperature/load fluctuation again led to marked sensitivity to cracking. Two tests used cyclic loading between two predetermined stress levels. No cracking was observed, but the hardness in the gauge length had increased by about 40 to 50 HV2.5 over the shoulder region. It is likely that, following such work hardening, the cyclic load corresponded only to elastic deformation, whereas the increasing load during the temperature fluctuation test would have induced continual plastic strain.

Condition 4 - 100°C Water, 5ppm O_2 , pH9, Strain Rate $10^{-6}/\text{s}$. Relative to tests in condition 2, reduction of area values at failure at 100°C were higher, while there was less corrosion of the sample surface, suggesting that a temperature of 150°C is more aggressive than 100°C.

Condition 5 - 150°C Water, 5ppm O_2 , pH7, Strain Rate $10^{-6}/\text{s}$. All samples showed some cracking, although in some cases only isolated pits and single cracks. The RE/RN values tended to be above those at pH9, and there was less discernable difference in the performance of plates 1 and 2.

Condition 6 - 150°C Water, 5ppb O_2 , pH9, Strain Rate $10^{-6}/\text{s}$. The RE/RN values for all parent steels and welds were above those in higher oxygen conditions, especially with cyclic loading, indicating less cracking susceptibility in condition 6. Samples from plate 1 contained wide-spread sharp intrusions up to about 0.1mm deep (Fig.9a). Plate 2 samples showed little or no cracking and minimal corrosion (Fig.9b), again suggesting lower environmental sensitivity than plate 1. Considering weld samples from both plates, no cracking or

corrosion was generally evident. A sample from weld 1 did exhibit oxide-filled cracks in the necked region, but the RE/RN ratio was high.

Phase 3: Crack Growth Rate Studies

Test in nitrogen at 150°C. A load of 10.3kN was initially applied, and then increased in 10% increments up to a maximum of 16.5kN (Table 8). The applied K values ranged from $1140\text{mm}^{-3/2}$ to $1825\text{Nmm}^{-3/2}$. Despite a total test duration of 1½ months, no crack extension was observed by DCPD or by metallographic examination.

Tests with Static or Monotonically Changing Load. No cracking was found in the samples tested at below about $1200\text{Nmm}^{-3/2}$ by either DCPD or subsequent examination, and this was the case whether the specimen was tested under purely static or incrementally increased load. Environmental cracking was induced at higher stress intensities, the maximum crack depth observed being about 2mm. The cracks were predominantly transgranular, with small regions of intergranular appearance, and were oxide-filled (Fig.10).

In the test under load shedding conditions, cracking (Fig.11) was induced at above the K_{IQ} , the DCPD trace indicating this to have developed especially in the final 10 days of the 80 day test period. The load was reduced with no evidence of further cracking after 30 days.

Tests with Fluctuating Load. Tests were carried out initially using an applied stress intensity range of about 60–80% of the K_{IQ} value. This range was progressively increased, first by reducing the lower limit to 35% K_{IQ} , and then by raising the upper limit to 100% K_{IQ} . No evidence of any environmental cracking was found, either on a section or on the fracture face. For the test at a high applied stress intensity, some 140% K_{IQ} , with regular unloading and cooling, the DCPD record indicated an overall increase in crack length, although this could not be related to either heating or peak load portions of the cycling applied. Crack extension of about 3.5mm was indicated by the DCPD trace, but a maximum crack growth of only 1.5mm was apparent on the fracture face.

Crack Growth Measurement. In most tests, total crack growth indicated by the DCPD was in reasonable agreement with the results of direct measurement on the sample following test. Certainly any crack extension in a specimen was identified by DCPD measurement. Figure 12 shows the average crack growth rates calculated from the DCPD records, plotted against the stress intensity, either that applied during a static load period or the maximum under cycling conditions. The result from the load/temperature cycled sample was obtained from the actual measurement. From Fig.12, there is a trend for growth rate to increase at higher stress intensity levels, while no cracking was found below $1200\text{Nmm}^{-3/2}$.

Discussion

General Comments

The work carried out has successfully induced environmentally assisted cracking in carbon and carbon-manganese steel exposed to high temperature water, such cracking being observed in slow strain rate and precracked sample tests. In both cases, the morphology of cracking was similar to that encountered in service (3–6,8), the cracks forming roughly perpendicular to the material surface and applied stress direction, with predominantly transgranular cracking. Single and branched cracks were noted, the width at the surface increasing as the crack depth became greater, and with formation of an oxide scale within the cracks.

There is no doubt that the cracking observed is a direct result of environmental action in that no cracking was found in tests in an inert nitrogen atmosphere, whether under slow strain conditions or with constant load precracked samples. Thus, despite the fairly short timescale of the individual tests, it can be concluded that the problem of deaerator cracking has been reproduced in the laboratory, and the test data should therefore be applicable to the practical situation.

Factors Influencing Cracking

All Phase 1 samples produced a thick rust scale for the oxygen levels and pH levels examined. The scale was layered and defective in the sense of providing little protection for the steel, but there was virtually no evidence of cracking, even in samples stressed well above the yield point. Presumably during sample exposure, all regions of the surface corroded at one time or another, so that either conditions for cracking were not fulfilled or the crack growth rate was less than general corrosion rate. Cracking may have been suppressed kinetically by the

fairly low peak temperature of less than 100°C, as suggested by the relative data obtained in the Phase 2 slow strain rate tests at 100 and 150°C (conditions 4 and 6). Whatever the reason for the lack of cracking, the extended test duration of up to 28 months must be recognised, and it does not appear that exposure to oxygen levels high enough to cause severe general attack is a sufficient condition to induce deaerator cracking.

The Phase 2 tests on environmental factors are summarised in Fig.13. The data suggest that the major factor influencing the occurrence of cracking is the oxygen level at high temperature. All samples were covered with a magnetite film, with little indication of formation of higher oxides, whether haematite etc, but low RE/RN values, say below 0.5, were found only under high oxygen conditions. Moreover, for all steels and weld metal studied, the minimum and/or average RE/RN ratios were lower with the higher oxygen level than at 5ppm oxygen. This adverse effect of high oxygen content supports recent work by Wedgbury (8). The initial 5ppm oxygen level in Fig.13a will be reduced during test, but, from the loop trials, can be expected to still be well above 100ppb. The results suggest pH9 to be more deleterious than pH7, but the role of pH over this range is secondary to that of oxygen. Although not definitive, the results in Table 7 indicate cracking sensitivity to be reduced at 100°C, and at a strain rate of 10^{-5} /s. Again, these trends follow other work (8), and indeed Copeland et al failed to obtain cracking in SSRT studies at about 105°C (12).

Surveys on cracking in operating deaerators have not unambiguously established any particular material factors as of overriding importance, but cracking has been considered more likely in higher strength steels (8). This view is not supported by the present results, in which lower RE/RN ratios were found for plate 1 than for the microalloyed plate 2 (Fig.13b). Cracking in elevated temperature water has been associated with high sulphur levels and sulphide inclusions (13). This trend is consistent with the present findings: lowest RE/RN values were found for plate 1 and weld metal 1 and both materials contained higher sulphur contents than plate 2 and its corresponding weld metal. A possible adverse effect of higher material strength levels is indicated by the relative behaviour of the steel 2 parent and HAZ samples, the latter being of higher hardness and cracking sensitivity, but the RE/RN value was not as low as found with steel 1, suggesting compositional factors to be more important. Available data are insufficient to associate increased cracking risk solely with higher sulphur materials, since the low silicon and manganese contents in plate 1 and weld 1 may also have produced higher susceptibility (14). At the same time, cracking was induced in a range of steel composition and microstructure, and thus material variables appear of secondary importance relative to the operating environment.

The present results suggest that plastic strain in the steel is necessary for deaerator cracking to take place. In the slow strain rate tests, total specimen elongations were well into the plastic range, while cracking arose in precracked samples only with applied stress intensity levels above the K_{I0} value. Further, from the Phase 2 studies, imposition of a fluctuating load component is deleterious, but only when the material is under rising load and constantly undergoing fresh plastic strain. In the Phase 3 tests, even repeated cycling under essentially elastic conditions at below K_{I0} did not cause cracking within the test period employed. Cracking may be enhanced by temperature fluctuation, as in the Phase 2 tests, and from the higher crack growth rate for the test with temperature cycling than for an incremental load test with a similar peak stress intensity of about $1640\text{Nmm}^{-3/2}$ (Fig.12).

Crack Growth Rate

The precracked sample tests suggest an approximate threshold stress intensity for cracking in aerated water at 150°C of some $1200\text{Nmm}^{-3/2}$, at least over the test durations employed. Above this value, most tests in which cracking was observed indicated a growth rate of the order of 10^{-6}mm/s , and a similar rate of penetration could be inferred from the depths of cracks away from the necked region in SSRT samples tested at high oxygen level. This rate is fairly high and, if maintained, would lead to cracking some 30mm deep after one year operation. Indeed, the data in Fig.12 represent an average of crack extension over the test period, and, from the DCPD traces, more rapid cracking may have taken place at some periods. Even at say 10^{-7}mm/s , penetration to the depth of a corrosion allowance on a vessel wall would occur well within the expected operating life.

Most surveys have indicated a lower average long term growth rate and this implies that cracking in practice has not been continuous, but has occurred mainly during transient conditions, whether warm up or shut down or from unforeseen load excursions etc. An essential caveat is that slower cracking could arise from corrosion fatigue and a possible contribution of this mechanism to service problems must be borne in mind (8).

The precracked samples did not display entirely consistent fracture behaviour. This may reflect variability in material properties, or the inexact use of an elastic parameter to describe the behaviour of a sample experiencing significant plastic strain. However, there is no doubt that under adverse environmental conditions cracks can propagate at a rate sufficiently high to be of practical concern. While only one steel was tested, it is unlikely from the Phase 2 results that the situation will be greatly different for other materials: low sulphur grades may give better behaviour, but this might be negated by the development of harder microstructures at welded joints.

Mechanism of Cracking

It is generally considered that deaerator crack growth takes place by dissolution at the crack tip (4,6,8,9). Certainly, hydrogen embrittlement would not be expected, bearing in mind the low strength level and hardness of the steels concerned, and the elevated temperature at which cracking occurs. Various workers have suggested that the problem represents a form of "stress induced corrosion" in which attack is localised, essentially as a result of rupture of an otherwise protective coating (1,15,16). The present results are consistent with this view.

First, for such a mechanism to be operative, a cathodic reactant is necessary with attainment of an appropriate metal/environment potential (14). The Phase 2 results show that no significant cracking takes place under low oxygen conditions, and presumably high oxygen levels induce cracking both by promoting the oxygen reduction reaction, and, at the expected solution levels of over 100ppb, increasing the rest potential of the system by some 200mV_{NHE}, probably to about 0mV_{NHE} (8,17). Second, the observed crack growth rate of roughly 10⁻⁶mm/sec would require an anodic current density at the crack tip of about 10mA/cm² (18). Polarisation studies by Congleton and Parkins (14) indicate a current density at 0mV_{NHE} below this value, but with a dependence on the potential scan rate. This latter implies surface filming or increased anodic polarisation with time, and 10mA/cm² could well be achieved if bare metal is exposed to the environment following coating rupture (18). Third, the present results strongly indicate that some plastic strain is required for crack extension to occur. The tensile ductility of a magnetite coating (8) is low, below 1% under tensile loading (15,19). Hence, by causing magnetite rupture, whether or not local plastic strain is experienced is likely to be critical in determining the incidence of cracking in operating deaerators. Fracture of the magnetite coating may be induced also by differential expansion/contraction strain, the coefficient of expansion for magnetite being appreciably less than for steel (19), and an adverse effect of temperature cycling is indicated by the data in Table 7 and Fig.12.

On this basis, cracking will occur most specifically under conditions in which an otherwise protective magnetite film is present on the material, but with fairly high oxygen levels, and at points where high local strain is experienced (8,16). This is entirely consistent with the reported occurrences of deaerator cracking and its preferential development at welded joints where both tensile residual stresses and local stress concentrations will be present. Cracking would seem most likely to occur when transient stress is experienced, causing rupture of the magnetite layer, probably during warm up and shut down in particular, but also if severe pressure/temperature fluctuations or water hammer are encountered. The high crack rate recorded indicates that cracking will occur only while such dynamic strain takes place: once steady state conditions have been regained, repair of the magnetite may take place, with an interruption to crack growth. This mechanism does not preclude a contribution to crack extension from corrosion fatigue, and it must be assumed that corrosion fatigue has been mainly responsible for some service failures. Indeed, to some degree, distinction between the failure mechanisms is unrealistic, and the present hypothesis of cracking can be regarded as constituting corrosion fatigue under high strain, low frequency conditions.

Practical Implications

Recommendations to avoid deaerator cracking (9) are based most especially on control of the environment to minimise oxygen levels and on reducing applied static and fluctuating loads. These measures are endorsed by the present results and careful attention to plant operation can be expected to reduce the incidence of deaerator cracking. It is suggested that low sulphur material and welding consumables are to be preferred. Moreover, since cracking is associated especially with plastic strain, it can be inferred that all measures to reduce strain levels experienced should be pursued, and, on this basis, postweld heat treatment to obtain maximum relief of residual welding stresses would seem advisable.

If the view that cracks form primarily during upset conditions is correct, it is difficult to make specific comment on the frequency of NDE during the life of an operating deaerator, since the development of cracking will depend critically on the service conditions experienced. The approach has been formulated that the frequency

of NDE should reflect the amount of cracking observed during any shutdown (9). If similar conditions are experienced from one operating period to the next, this is reasonable, but, should more irregular operation be experienced, more frequent inspection may be needed, especially in view of the present high crack growth rates. At the same time, cracking will occur during shut down and warm up and thus unnecessary interruptions to service to carry out NDE may actually be deleterious.

Conclusions

1. Cracking in deaerator vessels occurs as a result of rupture of an otherwise protective magnetite film, with ensuing localised corrosion of the bare metal. Cracking was observed only when the substrate steel experienced plastic strain during exposure to the environment.
2. No cracking was found in samples statically stressed to the yield point and above in water at 95°C. Tests were carried out at pH7 or 9 and with 5ppb or 2000ppb oxygen, and with simulated shutdowns involving exposure to high oxygen levels and formation of copious rust scale.
3. Cracking in slow strain rate tests was most pronounced at high oxygen levels (above 100ppb), and susceptibility was somewhat lower with pH7 than pH9 and at 100°C than 150°C. No significant cracking was found at 150°C with oxygen levels of 5ppb.
4. Cracking in slow strain rate tests was induced in parent steel, heat affected zone and weld metal covering a range of composition and microstructure. The role of material variables is secondary to that of environmental conditions and service loading regime.
5. Under high oxygen conditions at 150°C, cracking in precracked samples was induced only at applied stress intensity levels expected to give large scale yielding.
6. Above the threshold level, crack growth rate in high oxygen water at 150°C increases with increasing applied stress intensity, but was typically 10^{-6} mm/s.
7. Cracking in deaerators occurs primarily under conditions in which plastic strain is experienced by the material when exposed to fairly high oxygen levels and most especially at temperatures above 100°C. Thus cracking takes place mainly under transient conditions, whether plant warm up/ shut down or when dynamic strain is experienced from temperature/pressure fluctuations, water hammer etc.

Acknowledgements

Acknowledgement is made to staff who carried out the work, especially Mr D Sparkes, Mr P Rodwell, Mr M Allen and Mr M J Bennett. Thanks are given also to Members of the Sponsor Group for their support and assistance: Dienst voor het Stoomwezen, Electricité de France, United Kingdom Health and Safety Executive, National Power TEC, PowerGen Company, Norsk Hydro as, Swedish Plant Inspectorate, and Stork Boilers.

References

1. Adamsky F J and Teichmann H D: VGB Kraftwerkstechnik, **57** (11), November 1977, pp759-773.
2. Anon: TAPPI Journal, **66** (11), November 1983, p15.
3. Clevenger T G: Proc Conf Corrosion '86, NACE, Houston, March 1986, Paper 302.
4. Franco R J and Buchheim G M: Proc Conf Corrosion '86, NACE, Houston, March 1986, Paper 306.
5. Chakrapani D G and Hudson R A: *ibid*, Paper 138.
6. Kelly J A et al: Proc Conf Corrosion '88, NACE, St Louis, March 1988, Paper 350.
7. Bolten J G: Proc 9th European Congress on Corrosion, EFC, Utrecht, October 1989, Paper EG-096.
8. Wedgbury M K: "Environmentally-assisted crack growth in deaerator storage vessel steels". PhD Thesis, CNA, London, September 1990.
9. NACE Standard: "Recommended practice for prevention, detection and correction of deaerator cracking", RP0590-90.
10. Anon: National Board Bulletin, July 1984.
11. Rooke D P, Cartwright D J: "Compendium of stress intensity factors". Published by HMSO, 1976.
12. Copeland J F: Proc Conf Corrosion '87, NACE, San Francisco, March 1987, Paper 216.
13. Pednekar S et al: Proc Conf Corrosion '82, NACE, Houston, March 1982, Paper 244.
14. Congleton J and Parkins R N: Corrosion, **44** (5), May 1988, pp290-298.
15. Schoch W and Spahn H: Proc Conf Corrosion Fatigue chemistry, mechanics and microstructure. NACE, Connecticut, June 1971, pp52-64.
16. Winter M A: Proc Conf Corrosion '87, NACE, San Francisco, March 1987, Paper 211.
17. van Osch G A A and Huijbregt W M M: Corrosion, **42** (2), February 1986, pp120-123.
18. Parkins R N: Corrosion, **43** (3), March 1987, pp130-139.
19. Kussmaul K and Navab-Motlagh M: VGB Kraftwerkstec, **63** (2), February 1983, p138.

Table 6 Hardness results, HV10kg

Location		Hardness range	Hardness mean
Weld 1	(Plate	162-174	165
	(Weld metal	155-202	179
	(HAZ	217-314	244
Weld 2	(Plate	153-159	159
	(Weld metal	187-220	198
	(HAZ	258-405	300

Table 7 Results of slow strain rate testing (Phase 2)

Test condition	Sample type	Time h	Tensile strength N/mm ²	Elongation %	Reduction of area %	RE/RN	Comments
1	P1	67,69	600,670	20,22	35,33	1.0	Temperature cycled $\pm 5^{\circ}\text{C}$ (140 cycles) Strain rate $10^{-3}/\text{s}$
1	P1	58	635	18	25	1.0	
1	P1	6.0	540	19	35	1.0	
1	P2	81	595	27	60	1.0	
1	W1	62	620	19	25	1.0	Fracture in weld metal
1	W2	70	680	21	50	1.0	
1	XW1	55	620	17	40	1.0	
1	HAZ2	82	665	26	55	1.0	
2	P1	63,50,57	650,660,570	19,16,18	25,10,12	0.7,0.3,0.3	Temperature cycled $\pm 5^{\circ}\text{C}$ (120 cycles)
2	P1	49	665	15	5	0.2	
2	P2	83,73,79	590,485,555	26,23,26	50,35,55	0.8,0.6,0.9	
2	W1	47,61	675,665	10,19	10,15	0.4,0.6	
2	W2	72,75	710,690	23,23	40,40	0.8,0.8	Temperature cycled $\pm 5^{\circ}\text{C}$ (10 cycles) Load cycled 370-460N/mm ² (80 cycles). No failure. Load cycled 460-550N/mm ² (715 cycles). No failure.
2	XW1	40	615	10	12	0.3	
2	HAZ2	64,59	710,665	20,18	30,35	0.5,0.6	
3	P1	6.2	585	21	28	0.8	
3	P1	6.2	620	19	19	ND	Temperature cycled $\pm 5^{\circ}\text{C}$ (10 cycles) Load cycled 370-460N/mm ² (80 cycles). No failure. Load cycled 460-550N/mm ² (715 cycles). No failure.
3	P1	28	ND	ND	ND	ND	
3	P1	240	ND	ND	ND	ND	
4	P1	64,43	585,605	19,13	35,20	ND	
5	P1	55,76,75	610,580,650	18,20,23	10,30,28	0.3,0.9,0.8	Temperature cycled $\pm 5^{\circ}\text{C}$ (175 cycles)
6	P1	66,76,78	530,595,645	20,24,24	25,25,30	0.7,0.7,0.9	
6	P1	71	610	22	34	1.4	

Notes: P = parent plate, W = all weld metal, XW = cross weld, HAZ = heat affected zone,
RE/RN = reduction of area in test environment/reduction of area in nitrogen

Table 8 Precracked sample results (Phase 3)

Test type	Applied load, kN	Applied stress intensity, $\text{Nmm}^{-3/2}$	No of cycles	Test duration, hrs	Average crack growth rate, mm/s
N ₂ reference: incremental load increase	10.3	1140	1	24	0
	11.7	1295	1	360	0
	13.0	1440	1	310	0
	13.8	1525	1	170	0
	15.3	1690	1	70	0
	16.5	1825	1	100	0
Static load	15.0	1365 (1640)*	1	115	3.1×10^{-6}
	11.2	1395	1	1344	0
Incremental load increase	10.3	1440	1	335	1.1×10^{-6}
	11.7	1640	1	145	0.7×10^{-6}
	13.0	1330	1	265	0.5×10^{-6}
	14.3	1465 (1505)	1	6	ND
	13.0	1200	1	475	0.2×10^{-6}
	13.7	1265	1	340	0
	14.3	1321	1	945	0.4×10^{-6}
			1	190	0
	6.4	925			
	6.8	985	1	190	0
	7.5	1085	1	335	0
	8.3	1200	1	430	0
	8.7	1260 (1260)	1	70	0
Load shedding	13.7	1263	1	1390	0.4×10^{-6}
	12.7	1171	1	720	0
Fluctuating load	7.8-9.8	770-965	123	145	0
	5.9-9.8	580-965	90	240	0
	3.9-9.8	385-1165	111	551	0
	3.9-11.8	385-1165	51	335	0
	3.9-11.8	330-1005	50	350	0
Temperature and load cycled	0-10.3	0-1645	14	222	2×10^{-6} to 3×10^{-5} **

* Values in brackets indicate calculated stress intensity at failure, following any environmental crack growth.

** Growth rate from measurement of crack length on fracture face.

ND = Not determined.

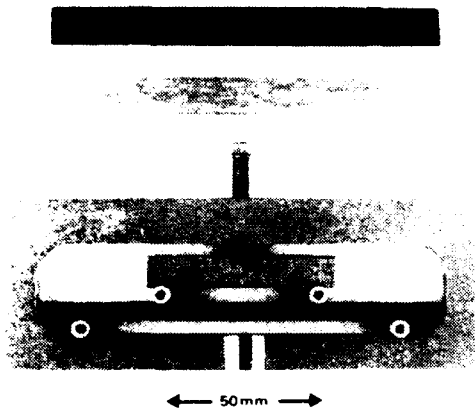


Fig.1 Machined and magnetite coated 4-point bend specimens and Phase 1 test rig.



Fig.2 Section through weld 1, X3

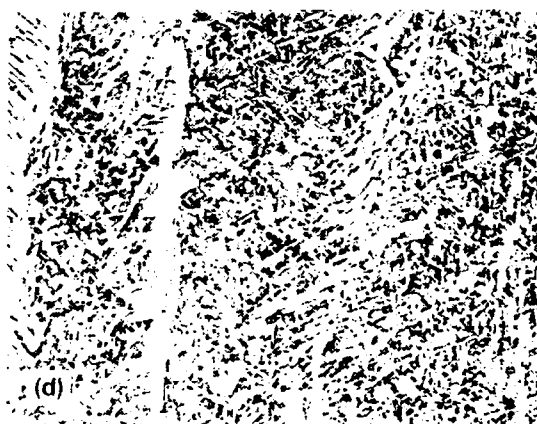
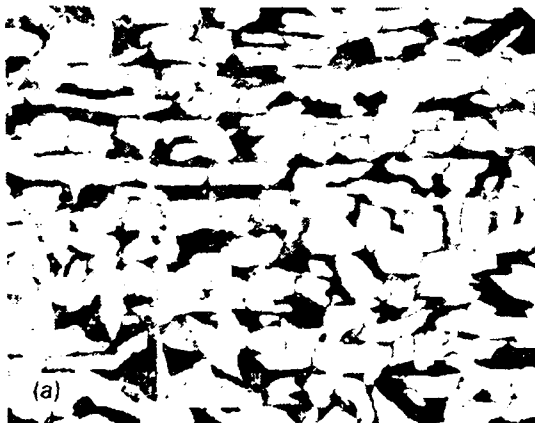
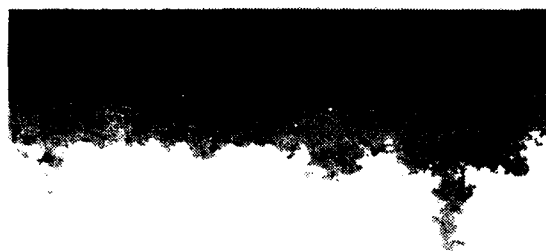


Fig.3 Representative microstructures, X400:

a) Plate 1; b) HAZ of weld 2; c) Weld metal 1; d) Weld metal 2.



(c)

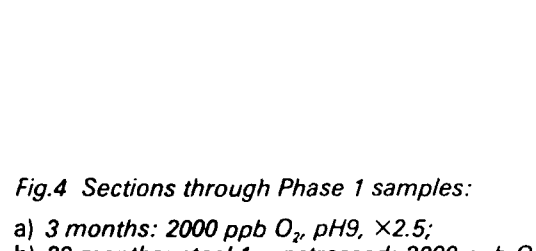
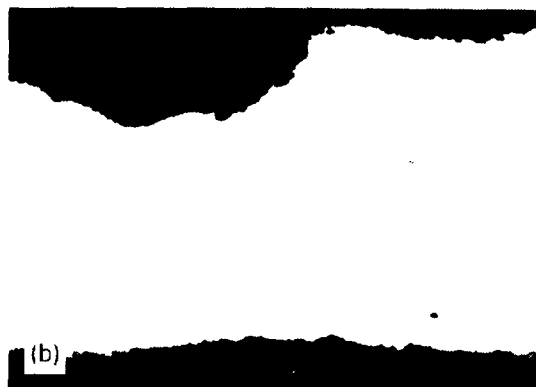
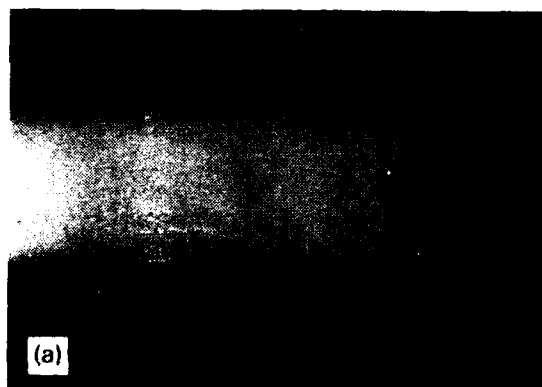


Fig.4 Sections through Phase 1 samples:

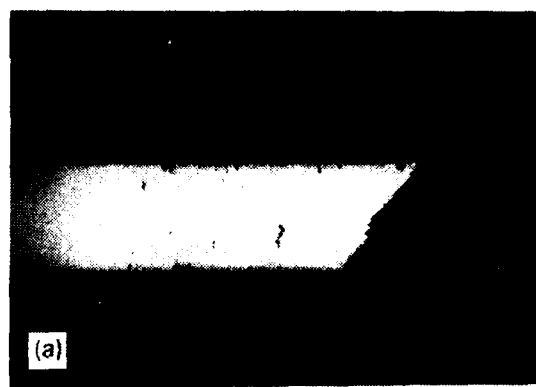
- a) 3 months: 2000 ppb O_2 , pH9, $\times 2.5$;
- b) 28 months: steel 1: unstressed: 2000 ppb O_2 , pH7, $\times 10$;
- c) 10 months: steel 2: U-bend: 2000 ppb O_2 , pH7, $\times 200$.



(b)

Fig.5 Steel 1: SSRT: 150°C, N_2 , 10^{-6} /sec:

- a) $\times 6$; b) $\times 200$.



(b)

Fig.6 Steel 1: SSRT: 150°C, 5 ppm O_2 , pH9, 10^{-6} /sec, fluctuating temperature:

- a) $\times 5$; b) $\times 50$.

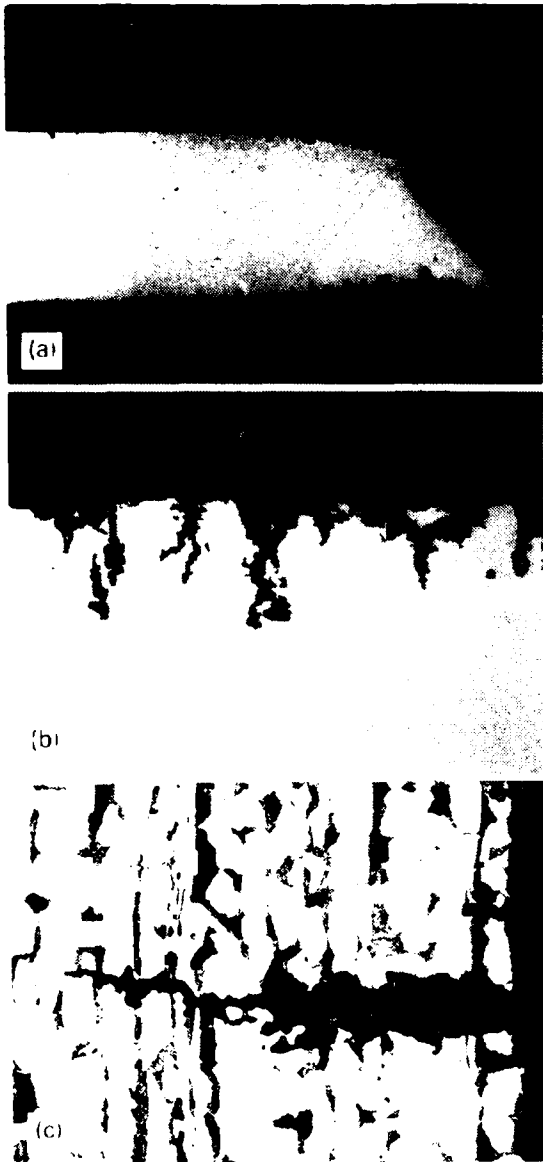


Fig.7 Steel 2: SSRT: 150° C, 5ppm O₂, pH9, 10⁻⁶/sec:
a) ×7; b) ×200; c) ×400.



Fig.8 Steel 2: HAZ SSRT: 150° C, 5ppm O₂, pH9, 10⁻⁶/sec, ×100.

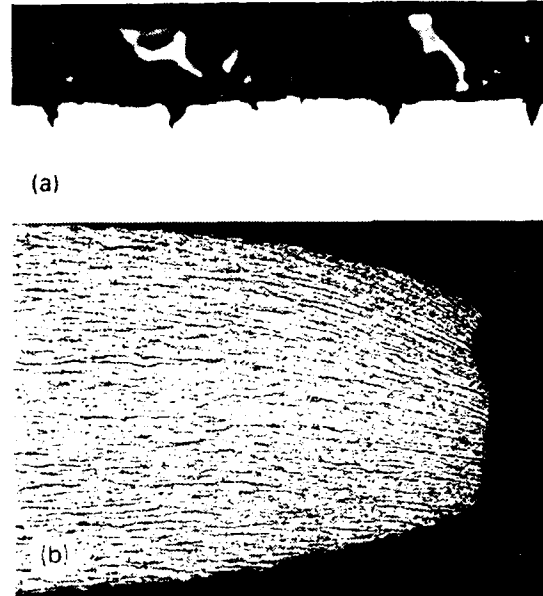


Fig.9 SSRT: 150° C, 5ppb O₂, pH9, 10⁻⁶/sec:
a) Steel 1, ×400; b) Steel 2, ×15.

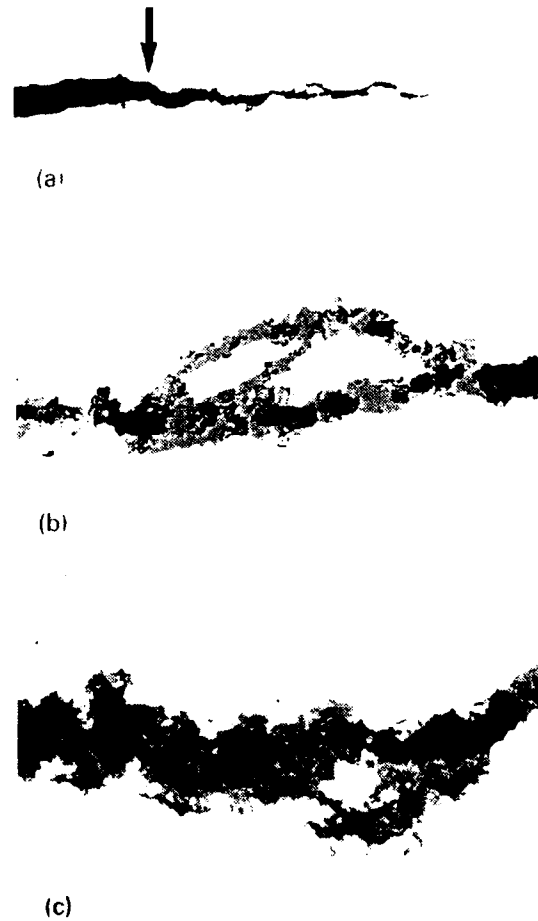


Fig.10 Cracking in SENT sample: applied K from 1440 to 1640 N/mm^{3/2}:
a) Growth from fatigue crack tip (arrowed), ×50;
b) Environmental cracking, ×400;
c) Environmental cracking, ×400.



Fig.11 Fracture face of SENT sample tested with load shedding, showing transition from fatigue crack (top) to environmental crack (bottom), $\times 10$.

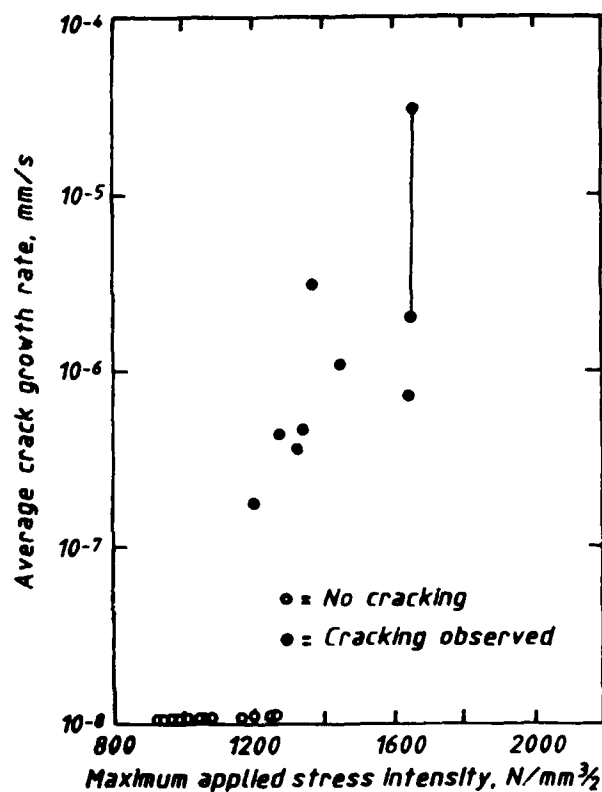


Fig.12 Relationship between average crack growth rate and maximum applied stress intensity.

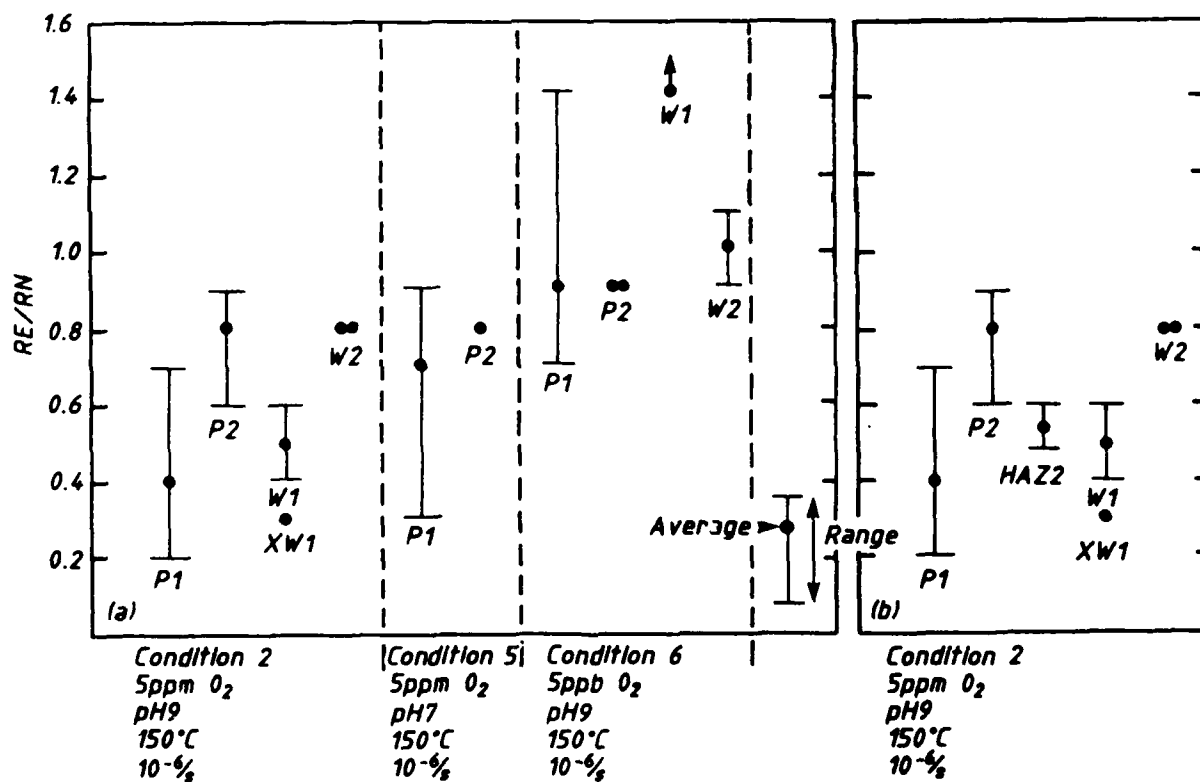


Fig.13 Summary of SSRT results:

- a) Effect of environment (conditions 2, 5 and 6);
- b) Effect of material variables (condition 2).

Using Fuel Oils with Different Sulphur Content and Treatment of Waste Waters Polluted with Heavy Metals in Thermoelectric Power Plants*

L. Dukic, Ph.D.

* Paper not available at time of printing.

Case Study of a Service Water System Piping Corrosion Assessment

R.A. Tatara, Ph.D.
ABB Impell Corporation
1333 Butterfield Rd.-Ste. 550
Downers Grove, Illinois 60515, USA

K.E. Rhoades, P.E.
ABB Impell Corporation
300 Tri-State International
Lincolnshire, Illinois 60069, USA

H.A. Olstowski, P.E.
Imperial Irrigation District
P.O. Box 937
Imperial, California 92251, USA

Abstract

An assessment of service water and auxiliary circulating water piping has been conducted at a coal-fired power generating station. The piping systems have been degraded by corrosion. The purpose of the assessment was to determine the short-term, long-term, and monitoring actions required to ensure reliable plant operation.

This integrity evaluation included the ultrasonic inspection of selected piping areas throughout the systems. To calculate the rate of wall loss, the original wall thickness, minimum measured thickness, and plant operating life were utilized for each inspected component. The rate of wall loss was projected to find the estimated remaining life of the corresponding sections of these systems. The remaining life was based on the results of code minimum wall thickness calculations with added conservatism.

It was observed that much of the piping has signs of corrosion damage. Based on remaining life calculations a significant portion is due for immediate replacement while substantial areas are to be replaced within twelve years. However, data indicate that much of the remaining pipe may be retained by continuing the station's chemistry practices and removing as much of the corrosion layer build-ups as possible. Operational recommendations have been made and include monthly flushing for all stagnant or intermittent-use lines.

Key terms: service water, piping corrosion

Introduction

A piping study is presented for a coal-fired power generating station. The study was initiated due to concerns over the integrity of the Service Water (SW) and Auxiliary Circulating Water (AW) Systems in the plant. Corrosion in these systems had plagued this 250 megawatt coal-fired power plant since it began commercial operation. Even though the plant is less than ten years old, significant lengths of SW and AW Systems piping had already been replaced due to corrosion. Until root causes were recently addressed, corrosion rates varied from in excess of 100 mils/year to less than 10 mils/year as measured with corrosion coupons. It became obvious that major expenditures could be expected in the future if nothing was done. A total replacement of these systems was estimated at over a million dollars and would require an extended outage. Another issue, besides the cost of piping repairs, was the effect on plant availability and potential

damage to equipment. A significant failure in either the SW or AW Systems would mean inability to supply cooling water to critical pieces of equipment resulting in a unit trip, equipment damage, or both. Resolving these corrosion and reliability problems became a critical issue facing the station.

Several steps were performed as part of the scope of work. To determine the status of the plant systems, information was collected from walkdowns, plant personnel interviews, drawings, and operational data. Both normal and off-normal operating modes were considered. Flowrates were measured at key locations in the system to allow a gross determination of the output of the service water pumps and the flows to various segments of the system.

To survey the condition of the piping, locations for ultrasonic examination (UT) were identified. Of course, it would have been impractical and prohibitively expensive to inspect all the piping. Thus, the approach taken in this evaluation consisted of identifying locations that are especially susceptible to fouling; inspecting such locations to determine the extent (if any) of damage; evaluating the results; and recommending corrective actions and maintenance/operations procedures. Although the data are specific for this power plant and its systems and equipment, the methodology and techniques can be applied to any plants using cooling water. Heat exchangers and pipe configurations here can be found at other power plants, and these results can serve as a guide to corrosion assessment elsewhere.

Station Operational Background

Except for lines plugged by corrosion products, there is adequate pressure and flow throughout the systems and components. New major flow demands have not been added since original construction, and the pumps can satisfy system flows if the lines are clear. The ultimate source of water is deep wells, and the plant has zero net water discharge. Prior to treatment, the well water is temporarily located in the raw water pond. The source of the cooling tower water is the same as SW and the chemistry must be balanced for both systems. Fifteen to sixteen water cycles are currently practiced at the cooling tower. The station has experienced considerable problems due to corrosion of the carbon steel piping and has taken continuous action to minimize the effects. The problems include flow blockage due to corrosion products, wall thinning, and leakage.

System Descriptions

Two cooling water sources in the plant are Service Water (SW) and Auxiliary Circulating Water (AW). The SW and AW Systems spread throughout several buildings and structures.

Service Water System. The SW System takes water from the clearwells at the Water Treatment Building and delivers it to various areas at the power plant. These areas include the Chlorination Building, Circulating Water Services Building, Gas Cleaning Building, Intake Pump Structure, Power Block, Recycle Water Pump Structure, and Water Treatment Building. The Circulating Water Service Building houses chemicals and equipment for maintaining circulating water. Equipment necessary to remove sulfur dioxide from the flue gas is contained in the Gas Cleaning Building. The Intake Pump Structure directs water from the raw water pond into the Chlorination Building. Most of the equipment necessary for the generation of electricity is housed in the Power Block, including the boiler, turbine, deaerator, and heaters. In the Recycle Water Pump Structure, bottom ash water is recycled back to the bottom ash handling system at the boiler. The SW System is designed to fulfill the following requirements: supply the demineralized water system, heat exchanger cooling, washdown water, and pump sealing. The SW System is non-recirculating, and it is constructed of lined ductile iron pipe below ground and unlined carbon steel piping above.

Auxiliary Circulating Water System. The AW System supplies various heat exchangers within the Power Block. AW is pumped by the auxiliary circulating pumps through the main and boiler feed pump turbine lube oil coolers, main and auxiliary condenser vacuum pump coolers, and hydrogen coolers. The entire AW System is constructed of unlined carbon steel pipe.

The SW is chlorinated and there is no evidence of macrobiofouling (the presence or growth of clams, mussels, etc.) in the water or systems. Microbiological counts in the water are virtually zero. No traces of slime have been found. Pyrophosphate is injected into the SW System in the Water Treatment Building and has the potential to lower corrosion rates. However, the station had not seen significant reductions below what was achieved through pH adjustments. It is postulated that corrosion rates may be reduced once the entire system becomes passivated; there may be too many corrosion products in circulation currently for the treatment to be effective.

Heat Exchangers

The station operates most equipment continuously although there are some heat exchangers that are on a standby basis for long periods. In the AW System, the hydrogen, main condenser vacuum pump, and auxiliary condenser vacuum pump coolers are in service at all times with continuous flow. The main turbine and boiler feed pump turbine lube oil cooling systems include two 100% capacity coolers which are rotated as needed. This can result in long periods of stagnation for the coolers on standby duty. The plant examines these coolers regularly especially during an outage. Cooler tubes appear free of corrosion. Nevertheless, coolers have been collection points for corrosion product pieces circulating in the AW System.

In the case of the SW System, sample coolers, humidifier lines, and many hose stations are often stagnant for long periods of time. HVAC heat exchangers may be isolated with stagnant water up to nine months. It is known that low SW flow exists in the line discharging to the Blowdown Tank. Scaling also occurs in the air compressor intercoolers due to the reverse solubility phenomenon of calcium carbonate. This makes the resulting outlet water more aggressive to the carbon steel piping. These coolers are backflushed weekly with a combination of air and water. The backflushing appears to be an effective method for clearing the exchangers.

System Corrosion

Corrosion product growth has resulted in pluggage of small bore lines up to and including 4 inch nominal diameter. These corrosion products are hard and reddish brown in color but can break off in chunks. Broken-off pieces of corrosion products have been found lodged in heat exchanger tubes. Recent inspection of a main turbine lube oil cooler located two tubes (5/8 inch diameter) almost completely occluded with corrosion pieces. Corrosion damage has been observed in cooler pass partition plates and heads; and in some cases, an entire 3/8 inch thick pass partition has been destroyed. Coatings in these areas have afforded some corrosion protection.

The station has already replaced an estimated 20% of the total piping length of the SW and AW Systems combined. Pipe replacement was usually done on a like-for-like basis and some replaced pipe has already developed leaks. Other regions with identical piping configurations and flows (sister trains) were simultaneously replaced where feasible as preventive maintenance. In some cases, PVC piping and rubber hose have been used as replacement materials for carbon steel in the case of smaller diameter piping. In general, drains, vents, and instrument tap lines have been replaced. In addition, it had been believed that some areas contain corroded pipe which had not produced leakage due to relatively low pressure.

Horizontal and vertical piping runs seem equally susceptible to corrosion; the corrosion had attacked at various circumferential positions. Weld areas and 2 inch nominal diameter and smaller threaded pipe seemed especially prone to deterioration. The corrosion can be very localized. For coolers, in general,

discharge lines have corroded faster than the inlet lines. It is interesting that no indication existed that high velocity degradation, such as erosion/corrosion and conventional erosion, was present. All of the degraded pipe showed significant corrosion products on the wall as a result of typical corrosion mechanisms. Figure 1 displays a photograph of typical corroded pipe that had been taken out of service. Tuberculation is clearly present. Some of the smaller diameter pipes were found virtually completely blocked.

Study Initiation

The task of resolving the SW and AW Systems corrosion and reliability issues was given to the Generation Engineering group at the station. Due to the many other systems connected to the SW and AW Systems, with each one having specific requirements, resolution of the root cause problems and addressing all concerns would be a complex undertaking. Corrosion rates would have to be reduced, and there were only two options available: either change the piping material or water properties. It was decided that an attempt to significantly change the SW and AW properties (still satisfying the requirements of all the other systems involved) would be initiated.

Addressing Water Properties. Work began on modifying SW and AW properties so that they would not corrode the carbon steel pipe at an unacceptable rate or foul critical heat exchangers. Listed are the deficiencies found and corrective actions performed.

- A tie between the SW and AW Systems had been made after commercial operation so that SW could be input into the AW System for additional cooling capability. A study determined that this was not necessary from an equipment cooling standpoint, and the SW and AW Systems were once again isolated from each other.
- The original SW pH control system could not maintain the pH within 1.0 of the setpoint. The pH control system was redesigned to maintain a pH within 0.1 of the setting.
- Also, the SW pH setpoint was originally 8.5. After lengthy testing, it was determined that a pH of 9.4 was optimal in order to balance the corrosion and calcium carbonate deposit concerns.
- Corrosion inhibitors were not being added to the SW System. It was determined that an injection of phosphate treatment at 5 ppm would further reduce corrosion rates.

The combination of these actions resulted in the SW and AW Systems having corrosion rates averaging below 5 mils/year as implied by coupons. As an example, one SW coupon exhibited an original, average corrosion rate of 22 mils/year; this had been reduced to an average rate of 3.5 mils/year or a reduction in corrosion rate of approximately 85%. However, corrosion rates do differ throughout the systems.

Addressing System Reliability. Engineering then began the systematic approach to obtain reliable SW and AW Systems. The plan included various steps:

- Immediately replace piping which is obviously corroded as evident by patches and small leaks including piping that ran in the proximity of equipment that would be damaged if a significant water leak occurred; piping was replaced in a sectional rather than piecemeal fashion so that clear boundaries were created between existing and new piping.
- Determine the current condition of the remaining SW and AW Systems' piping so that further replacements would be performed as needed; this would require the condition analysis and life assessment of many different sections of piping.
- Develop piping replacement criteria so that the field data could be converted into replacement

directives; these directives should neither result in leaving questionable piping in place nor replacing piping that could reliably function.

- Develop a long term inspection plan in order to ensure reliable SW and AW Systems; the plan would include both replaced and original pipe.

The implementation of these steps is the primary focus of this study. The efforts evaluating system integrity are described in detail.

Piping Assessment Methodology

Part of the approach taken in this evaluation consisted of identifying locations that are especially susceptible to corrosion and fouling and inspecting such locations to determine the extent (if any) of damage. This required several sequential steps.

Data Gathering

The purpose of this task was to prepare for the selection of the proper inspection locations. Since it is not feasible to inspect all the piping, the proper representative sampling of locations must be chosen. This task consisted of the collection of system descriptions, flow diagrams, and physical drawings as well as information on the operation of the piping systems from both normal and off-normal modes. Specific component data, such as pipe schedules and water flowrates, were also developed.

Evaluation of Piping Components

This task involved evaluating the various piping components in terms of their susceptibility to degradation. Here, the bulk water velocity in the component along with local geometry effects were considered to identify locations that are highly susceptible to erosion concerns (high velocity, highly local turbulent effects) and those prone to corrosion, silting, and biofouling (low velocity, minimal turbulence).

Selection of Inspection Locations

Twenty-eight inspection locations were chosen. The locations were based upon modeling, plant operating history and experience, and engineering judgement. The locations included areas that are particularly susceptible to high and low flow degradation as well as areas that typify the remainder of the piping. The goal was to survey the general status of the systems so that the piping could be classified as to its short term or long term need for repair. Walkdowns of the local geometries and plant personnel interviews were performed. Isometric sketches of the chosen inspection locations were prepared.

Ultrasonic Data Evaluations

Prior to UT inspections, preparations included identifying scaffolding requirements; pipe surface cleaning; and pipe surface gridding. Grids were spaced in 1 inch x 1 inch increments for piping with a nominal outside diameter of 4 inch or less and 2 inch x 2 inch increments for piping with a nominal outside diameter of 6 inch or greater. The grids contain sufficient detail to locate localized corrosion spots. To properly construct the grids, guidelines were formulated for grid extent, orientation, and reference points/lines. Figure 2 presents a sample component and its grid details. Over 9,100 total UT readings were taken for the twenty-eight inspection locations.

The ultrasonic inspections determined the amount of wall thinning based upon nominal initial thicknesses or maximum measured thicknesses, whichever were greater. A code minimum wall thickness for pressure and temperature analysis was completed for each component to assist in determining the useful remaining life of the component.

As an example, Table 1 displays UT measurements for a short, horizontal run of 2½ inch diameter pipe downstream of air compressor intercoolers. The nominal pipe wall is 0.203 inch thick. The data show significant corrosion at the bottom portions of pipe. The degradation area extends to a tee and may be progressing from an existing weld joint.

Remaining Life Calculations

From the ultrasonic measurements, pipe schedules, and plant operating time, an estimate was made for the remaining life of each of the inspected components. These results were extrapolated to the entire SW and AW Systems to project recommendations as to which piping should be replaced in the short term and in the long term.

To determine the extent of degradation, it was necessary to estimate the rate of wall loss for each component. Generally, the piping was installed per Schedule 80 for 2 inch and smaller piping, Schedule 40 for nominal sizes 2½ inch to 10 inch, and standard wall for 12 inch and larger piping. Since nominal rather than the actual original wall thicknesses are known, the original wall thicknesses for the basis of the calculations were taken as the greater of the maximum UT readings or 110% of the nominal thickness.

The measured minimum wall thickness was subtracted from the original wall thickness to calculate the apparent wear (wall loss). In the case of elbows, the maximum value of the difference between the maximum and minimum readings in each longitudinal band was used as the wear value. In the use of expanders, reducers, and tee runs, the maximum value of the difference between the maximum and minimum readings in each circumferential band was the wear value. This reduced the effect of manufactured differences in wall thickness along the surface of the components. The time period over which the wear was assumed to have occurred was taken from start of commercial operation to the present. In this way, a conservative wear rate (greater than actual) was computed. A wear rate was not generated for piping that has been previously replaced since the short operating time would lead to extremely unreliable calculated wear rates.

A code minimum wall thickness for pressure and temperature analysis was completed. This value was compared against 30% of the nominal wall thickness and 0.100 inch, and the greater of these three was used as the minimum required wall thickness for the individual component. For these water systems, a 30% wall thickness was judged to be sufficient to protect against external collapse and assure structural stability. Of course, the actual integrity of the pipe depends on other factors such as the extent and location of supports. Nevertheless, the minimum wall thicknesses used here seem reasonable for cooling water systems which have relatively low operating pressures and temperatures.

Using the minimum acceptable and measured minimum values for the wall thickness the remaining life of each component was determined by projecting the calculated wear rate. Note there is no assurance that any wear, especially in the case of under-deposit corrosion, is linear. Furthermore, the improvement in water chemistry practices by the plant was not factored into the projections of remaining life since the improved treatment may not be able to penetrate the layers of corrosion deposits that are insulating the degradation at the base metal.

Assessment Results

The inspection results ranged from severe thinning to no noticeable wear or corrosion depending on the location. Mostly random, localized pitting was observed. Some lines show significant corrosion at the bottom portions. This is characteristic of corrosion initiated under deposits which have settled on the bottom of pipe. In other cases, the degradation area occurred at a weld joint due to the use of backing rings. Regions near screwed joints in small diameter piping also appeared susceptible to corrosion attack. Inspections in an area that experienced cracked pipe indicated general loss of pipe wall. This is consistent since general thinning would cause cracking of the pipe while localized pits, more common in the systems, would produce leaks.

A few small areas showed erosion damage. There was noticeable wear in a SW elbow and its downstream pipe. The wear is characteristic of conventional erosion since the damage is localized at the extrados of the elbow and its corresponding downstream piping. Several corrosion pits were also present in these data.

Based upon the findings, the piping was grouped into three replacement categories. Segments of pipe were recommended for replacement within the next three years, replacement within 4-12 years, and long term remaining life. Where feasible, replacements were listed in order of priority. Replacement priority was based on the estimated remaining life and whether or not the piping is critical for uninterrupted service of the plant. In other words, a certain segment may be expected to have a slightly longer remaining life but is higher on the priority list since it is critical to operation of the plant.

Short-Term (3 Year) Remaining Life

A large amount of 4 inch and smaller SW and seal water piping in the Gas Cleaning Building requires replacement including all branches to pump seals. Some original portions of the lines in the Water Treatment Building were projected for replacement. This included mainly 8 inch piping and the 6 inch branch to the Reverse Osmosis System. Other near-term replacements included air compressor aftercooler discharge lines (1½ inch diameter), inlet and/or outlet chiller and humidifier piping (1 inch through 3 inch diameter), and lube oil cooler inlet pipe (3 inch diameter). Four inch and six inch sections of SW line, starting just downstream of the aftercoolers up to the Blowdown Tank, were judged inadequate. (This line is critical to plant operation and the 6 inch section is near motor control centers.) The 2 inch and 1 inch diameter Service Water lines in the Chlorination Building showed significant deterioration.

Intermediate-Term (4-12 Year) Remaining Life

Replacement recommendations in this category included the 8 inch line from the discharge of the auxiliary circulating pumps up to the main turbine lube oil coolers, the 12 inch line from the auxiliary circulating pumps up to the 4 inch tee to the main condenser vacuum pump coolers, and the 2½ inch supply lines to the auxiliary condenser vacuum pump coolers. The 2 inch and ¾ inch lines to the centrifuges in the Gas Cleaning Building also warranted replacement. Further recommendations involved the 10 inch supply header to the hydrogen coolers starting at the 4 inch tee to the main condenser vacuum pump coolers (six inch vertical supply lines to the hydrogen coolers had been replaced previously) and the 8 inch Power Block SW supply line entering at ground level up to the point where recent replacements were performed.

Additional areas identified for replacement were the 2 inch and smaller SW lines supplying seal water to the sludge pumps. Much of the piping in this area is cast iron; only the carbon steel parts were recommended for exchange. Based on similar configuration, the 2 inch and smaller lines supplying seal water to the continuous water supply pumps and sluice water recycle pumps in the Recycle Water Pump Structure also were selected.

Other plant areas affected were the 6 inch and 2 inch diameter sections in the Circulating Water Service Building and the 2 inch and 1 inch piping inside the Intake Pump Structure (the pipe contains screwed fittings). The 2 inch discharge line, from the Electric Room HVAC chiller up to the tee into the 6 inch line to the Blowdown Tank, as well as the 1 inch lines to the humidifiers had significant remaining life; but it would not be cost effective to monitor these pipes so they were included for replacement.

Long-Term Monitoring

To minimize costly replacements and ensure future piping integrity, some piping locations were targeted for reinspection in 5-10 years to determine acceptability for the remainder of plant life. Inspections should be performed using the same components and grids already completed. More inspections may be desired, and UT scanning would be appropriate. Points selected for long-term observation include 1½ inch, 2 inch, and 2½ inch discharge air compressor intercoolers pipe; certain segments inside the Recycle Water Pump Structure and the Water Treatment Building, including 12 inch pipe headers from the SW pump discharges; main turbine lube oil coolers discharge piping; and the SW to AW Systems cross-tie.

Finally, based on results from these inspections, it appears that the 8 inch and 16 inch piping downstream of the SW pumps and the 10 inch and 12 inch piping downstream of the cooling tower makeup pumps are acceptable for at least another 20 years. This is most likely due to the higher flows and constant line usage that limit conditions for corrosion.

Evaluation of Future Operations

The majority of corrosion products were found to be iron-corrosion oxides such as Fe_2O_3 and Fe_3O_4 . This is consistent with conventional electrochemical corrosion of carbon steel in an oxygen environment. The corrosion initiates at surface metal flaws such as weld areas. The discharge piping of coolers is especially susceptible since the elevated temperatures increase the rate of corrosion. (In general, every 15°F increase in water temperature will double the rate of reaction.) This phenomenon is further aggravated as buffering agents, such as carbonates, drop out and the exit water becomes more aggressive.

The build-up of corrosion products (tuberculation) insulates the degradation occurring at the pipe wall. Further, these corrosion layers may not be porous enough to permit the inhibitors to pacify the base metal. Certainly it is impractical to totally eliminate corrosion but all cost-effective attempts to remove the corrosion layer build-ups should be considered. The increased water pH level, as currently practiced, benefits the piping by enhancing the hydroxyl layer at the water/substrate interface. The hydroxyl ions impede the absorption of oxygen into the corrosion layers, and thus reduce the degradation rates. The pyrophosphate addition serves to control both mineral scaling and steel corrosion by a similar barrier mechanism. The current water treatment practices will be most effective when the corrosion layer build-ups are removed and the base metal exposed for treatment. Additionally, removal of the layers will increase the flowrates through the piping systems, aiding any concurrent flushing procedures. With proper corrective actions, large amounts of piping can be monitored while cleaning efforts and chemical treatment progress. This will be cost effective when compared to the efforts needed to replace this pipe.

Even if all possible steps are taken, due to the unpredictable nature of under-deposit corrosion, it is impossible to forecast all pipe failures. Thus the focus has been on the probable rates of wall thinning as applied to the entire systems. Some pipe areas may experience single, small leaks; since this corrosion is localized, complete pipe replacement is not called for as adequate wall exists throughout the rest of the line. In such cases, the recommendation was to monitor the lines to ensure reliable operation. This is especially true for large diameter piping with a high replacement cost; any localized damage can be weld-repaired with filler material compatible with the base material.

In parallel with the replacements, recommendations for system alternatives for maintenance/operational improvements include:

- The scheduled frequent examinations of heat exchangers should continue.
- To reduce the corrosion rates, initiate monthly flushing schedules for all intermittent-use coolers, piping, and water supply outlets throughout the plant. Begin with lines furthest from SW and AW pumps and at highest elevation and work back towards pumps in the flushing schedules.
- It is beneficial to flush all lines with water at 125% of design flow to clear as much of the corrosion layer build-up as possible. High pressure water cleaning, using a nozzle traveling the length of the pipe, is an option to remove the well-adhered layers. For large diameter piping, if water flushing does not remove corrosion layers, consider mechanical, in-line cleaning. However, it may be more cost-effective to perform reinspections and/or new inspections prior to determining the need for flushing or mechanical in-line cleaning.
- In the case of galvanic corrosion (Admiralty tube bundles and steel heads), attach sacrificial anodes to the carbon steel of the cooler heads. It may take several attempts to determine the best placement of the anodes.
- Coat all heat exchanger heads tied into the SW and AW Systems. Use a coating system that will hold up under heat exchanger head conditions.

Concluding Remarks

A piping assessment has been completed. Root causes for the corrosion degradation have been identified and resolved and recommendations made to improve system integrity. Piping replacement needs are identified. Although these are specific to this case study, the results can be used as guidelines for other plants. Also, the approach and methodology described here are general in nature and are applicable to other piping systems suffering unacceptable rates of wall thinning.

The testing identified large amounts of deterioration in the system, but it is anticipated that the corrective actions and operations have significantly reduced the degradation mechanisms. Thus, along with these optimal pipe replacement recommendations, the station is expected to have reliable operations and maintain its cooling systems in a cost-effective manner.

Table 1. Example of UT measurements showing localized wall thinning.

AXIAL GRID POINT	RADIAL GRID POINT									
	A	B	C	D	E	F	G	H	I	J
1	0.201	0.203	0.194	0.208	0.288	0.205	0.186	0.209	0.205	0.194
2	0.200	0.170	0.184	0.202	0.213	0.200	0.190	0.195	0.209	0.198
3	0.194	0.181	0.185	0.211	0.215	0.212	0.195	0.165	0.184	0.176
4	0.186	0.198	0.184	0.217	0.210	0.194	0.198	0.194	0.183	0.197
5	0.185	0.196	0.190	0.205	0.197	0.193	0.200	0.198	0.204	0.180
6	0.188	0.195	0.188	0.212	0.213	0.171	0.200	0.202	0.199	0.199
7	0.190	0.190	0.186	0.215	0.210	0.194	0.190	0.201	0.179	0.190
8	0.197	0.201	0.186	0.217	0.215	0.192	0.181	0.193	0.150	0.188
9	0.201	0.202	0.171	0.216	0.204	0.195	0.188	0.178	0.199	0.205
10	0.197	0.207	0.193	0.205	0.217	0.193	0.187	0.211	0.211	0.197
11	0.201	0.202	0.179	0.203	0.225	0.202	0.190	0.198	0.205	0.207
12	0.207	0.197	0.187	0.217	0.220	0.203	0.174	0.197	0.204	0.209
13	0.197	0.162	0.187	0.212	0.222	0.193	0.195	0.199	0.190	0.202
14	0.207	0.162	0.188	0.224	0.221	0.204	0.200	0.216	0.198	0.190

NOMINAL WALL: 0.203 inch.

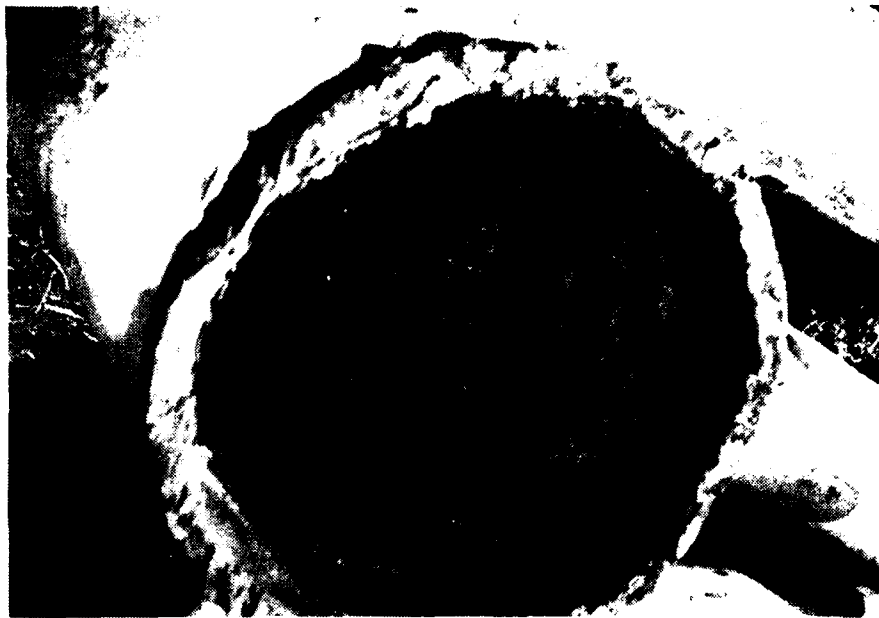
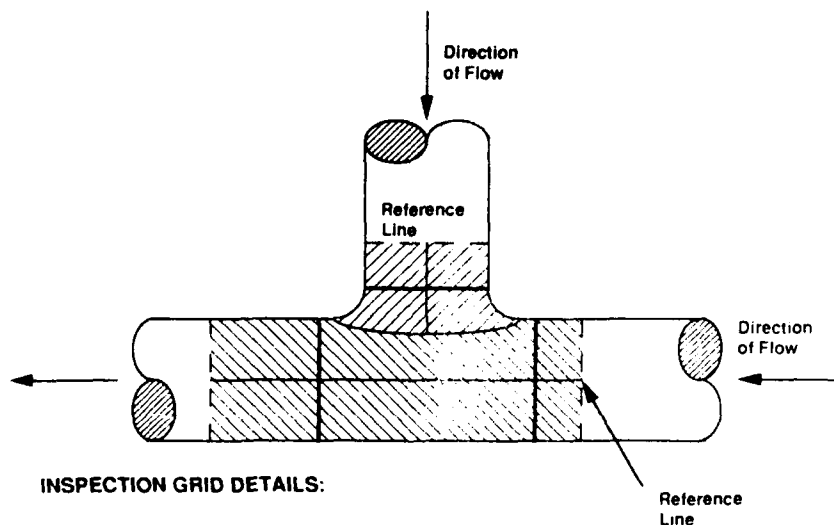


Figure 1. Typical pipe having build-up of corrosion products on wall.



INSPECTION GRID DETAILS:

1. Branch and run grids to be separate.
2. Reference line for run 90° from branch centerline.
3. Reference line for the branch radial to be on the same side as the run.
4. Branch grid to extend complete to main run connection.
5. Radial grids on fitting may be further apart than pipe due to larger outside diameter.

Figure 2. Sample ultrasonic gridding guidelines for formed tees.